



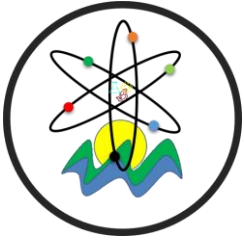
Black Sea Journal of Engineering and Science

Volume 6 | Issue 4



ISSN: 2619 - 8991


BS Journals



BLACK SEA JOURNAL OF ENGINEERING AND SCIENCE
(BSJ ENGIN SCI)


BS Journals

Black Sea Journal of Engineering and Science (BSJ Eng Sci) is a double-blind peer-reviewed, open-access international journal published electronically 4 times (January, April, July and October) in a year by since January 2018. It publishes, in English and Turkish, full-length original research articles, innovative papers, conference papers, reviews, mini-reviews, rapid communications or technical note on advances in a wide range of scientific disciplines from all fields of engineering and science and from any source.

ISSN 2619 - 8991

Phone: +90 362 408 25 15

Fax: +90 362 408 25 15

Email: bsjsci@blackseapublishers.com

Web site: <http://dergipark.gov.tr/bsengineering>

Sort of publication: Periodically 4 times (January, April, July and October) in a year

Publication date and place: October 15, 2023 - Samsun, TÜRKİYE

Publishing kind: Electronically

OWNER

Assoc. Prof. Uğur ŞEN

DIRECTOR IN CHARGE

Prof. Dr. Hasan ÖNDER

EDITOR BOARDS

EDITOR IN CHIEF

Prof. Dr. Hasan ÖNDER, Ondokuz Mayıs University, TÜRKİYE

Assoc. Prof. Uğur ŞEN, Ondokuz, Mayıs University, TÜRKİYE

SECTION EDITORS*

Prof. Dr. Ahmet UYANIK, Section Editor of Chemistry, Ondokuz Mayıs University, TÜRKİYE

Prof. Dr. Berna KILIÇ, Section Editor of Fisheries Engineering, Ege University, TÜRKİYE

Prof. Dr. Çiğdem TAKMA, Section Editor of Statistics, Ege University, TÜRKİYE

Prof. Dr. Ertan BUYRUK, Section Editor of Mechanical Engineering, Sivas Cumhuriyet University, TÜRKİYE

Prof. Dr. Gökhan CİVELEKOĞLU, Section Editor of Environmental Engineering, Akdeniz University, TÜRKİYE

Prof. Dr. Hasan TANAK, Section Editor of Physics, Amasya University, TÜRKİYE

Prof. Dr. Hasan TEMİZ, Section Editor of Food Engineering, Ondokuz Mayıs University, TÜRKİYE

Prof. Dr. İbrahim Özgür DENEME, Section Editor of Civil Engineering, Aksaray University, TÜRKİYE

Prof. Dr. İbrahim UĞUR, Section Editor of Mining Engineering, Süleyman Demirel University, TÜRKİYE

Prof. Dr. Ümit Cafer YILDIZ, Section Editor of Forest Engineering, Karadeniz Technical University, TÜRKİYE

Assoc. Prof. Dr. Belgin KARABACAKOĞLU, Section Editor of Chemical Engineering, Eskişehir Osmangazi University, TÜRKİYE

Assoc. Prof. Dr. Bülent BOSTANCI, Section Editor of Geomatics Engineering, Erciyes University, TÜRKİYE

Assoc. Prof. Dr. Ergün EKİCİ, Section Editor of Industrial Engineering, Çanakkale Onsekiz Mart University, TÜRKİYE

Assoc. Prof. Dr. Kadyrbay CHEKİROV, Section Editor of Biology, Kyrgyz Turkish Manas University, KYRGYZSTAN

Assoc. Prof. Dr. Mehmet EBEOĞLUGİL, Section Editor of Metallurgical and Materials Engineering, Dokuz Eylül University, TÜRKİYE

Assoc. Prof. Dr. Nilüfer YURTAY, Section Editor of Computer Engineering, Sakarya University, TÜRKİYE

Assoc. Prof. Dr. Özgür Hakan AYDOĞMUŞ, Section Editor of Mathematics, Social Sciences University of Ankara, TÜRKİYE

Assoc. Prof. Dr. Sinan AKISKA, Section Editor of Geological Engineering, Ankara University, TÜRKİYE

Asst. Prof. Dr. Mehmet GÜÇYETMEZ, Section Editor of Electrical and Electronics Engineering, Kırşehir Ahi Evran University, TÜRKİYE

Asst. Prof. Dr. Melahat CİHAN, Section Editor of Aerospace Engineering, Samsun University, TÜRKİYE

Asst. Prof. Dr. Sedat KARADAVUT, Section Editor of Agricultural Engineering, Trakya University, TÜRKİYE

* The ranking is arranged alphabetically within the academic title

EDITORIAL - ADVISORY BOARD*

Prof. Dr. Aglaia (Litsa) LIOPA-TSAKALIDI, Institute of Western Greece, GREECE

Prof. Dr. Ercan EFE, Kahramanmaraş Sutcu Imam University, TÜRKİYE

Prof. Dr. Mohammad Masood TARIQ, University of Balochistan, PAKISTAN

Prof. Dr. Mustafa Çağatay TUFAN, Ondokuz Mayıs University, TÜRKİYE

Prof. Dr. Özkan GÖRGÜLÜ, Ahi Evran University, TÜRKİYE

Assoc. Prof. Dr. Taner TUNÇ, Ondokuz Mayıs University, TÜRKİYE

Asst. Prof. Dr. Emil OMURZAK, Kyrgyz-Turkish Manas University, KYRGYZSTAN

Asst. Prof. Dr. Yılmaz KAYA, Ondokuz Mayıs University, TÜRKİYE

* The ranking is arranged alphabetically within the academic title

STATISTIC EDITOR

Prof. Dr. Mehmet TOPAL, Kastamonu University, TÜRKİYE

ENGLISH EDITOR

Asst. Prof. Dr. Betül ÖZCAN DOST, Ondokuz Mayıs University, TÜRKİYE

TURKISH EDITOR

Prof. Dr. Serkan ŞEN, Ondokuz Mayıs University, TÜRKİYE

REVIEWERS OF THE ISSUE*

Prof. Dr. Adem ÖNAL, Tokat Gaziosmanpaşa University, Department of Analytical Biochemistry, TÜRKİYE

Prof. Dr. Bayram TOPAL, Sakarya University, Department of Time-Series Analysis, TÜRKİYE

Prof. Dr. Birsen AYDIN, Amasya University, Department of Nutrigenomics, TÜRKİYE

Prof. Dr. Gerhard-Wilhelm WEBER, Poznan University of Technology, Department of Computing in Mathematics, POLAND

Prof. Dr. Ergin KARİPTAŞ, Samsun University, Department of Industrial Biotechnology, TÜRKİYE

Prof. Dr. Hakkı Gökhan İLK, Ankara University, Department of Electrical-Electrical Engineering, TÜRKİYE

Prof. Dr. Haluk Çağlar KAYMAK, Atatürk University, Department of Vegetable Growing and Breeding, TÜRKİYE

Prof. Dr. İskender IŞIK, Kütahya Dumlupınar University, Department of Mineralogy-Petrography, TÜRKİYE

Prof. Dr. Kadir AY, Manisa Celal Bayar University, Department of Organic Chemistry, TÜRKİYE

Prof. Dr. Mehmet BEKTAŞ, Fırat University, Department of Mathematical Sciences, TÜRKİYE

Prof. Dr. Metehan TOLON, Ankara Hacı Bayram Veli University, Department of Customer Relationship Management, TÜRKİYE

Prof. Dr. Metin DAĞTEKİN, Çukurova University, Department of Agricultural Machines, TÜRKİYE

Prof. Dr. Onur KOYUNCU, Eskişehir Osmangazi University, Department of Biological Sciences, TÜRKİYE

Prof. Dr. Ömer EYERCİOĞLU, Gaziantep University, Department of Finite Element Analysis, TÜRKİYE

Prof. Dr. Ömer Faruk ERTUĞRUL, Batman University, Department of Signal Processing, TÜRKİYE

Prof. Dr. Taner Abdullah OĞUZER, Dokuz Eylül University, Department of Engineering Electromagnetics, TÜRKİYE

Prof. Dr. Zeynel CEBECİ, Çukurova University, Department of Information and Computing Sciences, TÜRKİYE

Assoc. Prof. Dr. Ali İhsan ATALAY, Iğdır University, Department of Animal Production, TÜRKİYE

Assoc. Prof. Dr. Aysel VEYİSOĞLU, Sinop University, Department of Bacteriology, TÜRKİYE

Assoc. Prof. Dr. Ayşe ÖZGÜVEN, Van Yüzüncü Yıl University, Department of Environmental Pollution and Prevention, TÜRKİYE

Assoc. Prof. Dr. Bilal Barış ALKAN, Akdeniz University, Department of Applied Statistics, TÜRKİYE

Assoc. Prof. Dr. Burak ALTINIŞIK, Pamukkale University, Department of Architectural History, Theory and Criticism, TÜRKİYE

Assoc. Prof. Dr. Cem TIRINK, Iğdır University, Department of Animal Science, Genetics and Biostatistics, TÜRKİYE

Assoc. Prof. Dr. Emre ŞİRİN, Ahi Evran University, Department of Animal Reproduction and Breeding, TÜRKİYE

Assoc. Prof. Dr. Ercan AYDOĞMUŞ, Fırat University, Department of Polymer Science and Technologies, TÜRKİYE

Assoc. Prof. Dr. Erhan KEYVAN, Burdur Mehmet Akif Ersoy University, Department of Food Microbiology, TÜRKİYE

Assoc. Prof. Dr. Esra UÇAR, Sivas Cumhuriyet University, Department of Biologically Active Molecules, TÜRKİYE

Assoc. Prof. Dr. Fadime ÖZDEMİR KOÇAK, Bilecik Şeyh Edebali University, Department of Industrial Biotechnology, TÜRKİYE

Assoc. Prof. Dr. Fatih ÖNER, Ordu University, Department of Field Crops and Pasture Production, TÜRKİYE

Assoc. Prof. Dr. Fuat LÜLE, Adıyaman University, Department of Solar Energy Systems, TÜRKİYE

Assoc. Prof. Dr. Funda TAŞDEMİR, Yozgat Bozok University, Department of Algebra and Number Theory, TÜRKİYE

Assoc. Prof. Dr. Güzin İPLİKÇİOĞLU ARAL, Ankara University, Department of Veterinary Food Hygiene and Technology, TÜRKİYE

Assoc. Prof. Dr. Hacer YALIM KELEŞ, Hacettepe University, Department of Computer Science, TÜRKİYE

Assoc. Prof. Dr. Hikmet ELDEK GÜNER, İzmir Demokrasi University, Department of Architectural Heritage and Conservation, TÜRKİYE

Assoc. Prof. Dr. Hüseyin ERDEM, Ondokuz Mayıs University, Department of Stock Farming and Treatment, TÜRKİYE

Assoc. Prof. Dr. İlker ÖZKAN, Dokuz Eylül University, Department of Ceramics in Materials Engineering, TÜRKİYE

Assoc. Prof. Dr. İlknur ŞENTÜRK, Sivas Cumhuriyet University, Department of Surface Water Quality Processes and Contaminated Sediment Assessment, TÜRKİYE

Assoc. Prof. Dr. İpek ŞAHİN, Ege University, Department of General Physics, TÜRKİYE

Assoc. Prof. Dr. K Ganpati Shrinivas SHARMA, Research Scholar at Bhilai Institute of Technology Raipur, Department of Deep Learning, INDİA

Assoc. Prof. Dr. Koray KARABULUT, Sivas Cumhuriyet University, Department of Thermodynamics and Statistical Physics, TÜRKİYE

Assoc. Prof. Dr. Levent UĞUR, Amasya University, Department of Finite Element Analysis, TÜRKİYE

Assoc. Prof. Dr. Mehmet HASKUL, Şırnak University, Department of Mechanical Engineering, TÜRKİYE

Assoc. Prof. Dr. Muhammet Hüseyin ÇETİN, Konya Technical University, Department of Machine Design and Machine Equipment, TÜRKİYE

Assoc. Prof. Dr. Mustafa ALTIN, Bingöl University, Department of Algebraic and Differential Geometry, TÜRKİYE

Assoc. Prof. Dr. Onur KARAAĞAÇ, Samsun Seed Certification Test Directory, Department of Vegetable Growing and Breeding, TÜRKİYE

Assoc. Prof. Dr. Orhan ER, İzmir Bakırçay University, Department of Algorithms and Calculation Theory, TÜRKİYE

Assoc. Prof. Dr. Özgül PERSİL ÇETİNKOL, Middle East Technical University, Department of Biologically Active Molecules, TÜRKİYE

Assoc. Prof. Dr. Refiye Refika AKÇALI GIACHİNO, Ege University, Department of Field Crops and Pasture Production, TÜRKİYE

Assoc. Prof. Dr. Sedat BOYACI, Ahi Evran University, Department of Agricultural Structures, TÜRKİYE

Assoc. Prof. Dr. Serhat Berat EFE, Bandırma Onyeddi Eylül University, Department of Electrical Energy Transmission, Networks and Systems, TÜRKİYE

Assoc. Prof. Dr. Sevcan MAMUR, Gazi University, Department of Biological Sciences, TÜRKİYE

Assoc. Prof. Dr. Sevgi ÜNAL KARAKUŞ, Bartın University, Department of Genetics, TÜRKİYE

Assoc. Prof. Dr. Şengül GÜVEN, Pamukkale University, Department of Renewable Energy Resources, TÜRKİYE

Assoc. Prof. Dr. Yıldırım YILDIRIM, Düzce University, Department of Industry, TÜRKİYE

Assist. Prof. Dr. Abdullah TUNÇ, Bingöl University, Department of Animal Cell and Molecular Biology, TÜRKİYE

Assist. Prof. Dr. Adnan AYDIN, Iğdır University, Department of Epigenetics, TÜRKİYE

Assist. Prof. Dr. Ahmet UÇAR, Ankara University, Department of Poultry Farming and Treatment, TÜRKİYE

Assist. Prof. Dr. Bahar ONARAN ACAR, Ankara University, Department of Food Chemistry and Food Sensory Science, TÜRKİYE

Assist. Prof. Dr. Coşkun KONYALI, Çanakkale Onsekiz Mart University, Department of Animal Biotechnology, TÜRKİYE

Assist. Prof. Dr. Ece AVULOĞLU YILMAZ, Amasya University, Department of Cytogenetic, TÜRKİYE

Assist. Prof. Dr. Edip ÇETKİN, Batman University, Department of Resource Technologies, TÜRKİYE

Assist. Prof. Dr. Elif Zeynep ÖZTÜRK, Artvin Çoruh University, Department of Medical Biochemistry and Metabolomics, TÜRKİYE

Assist. Prof. Dr. Esra DAMAR, Hitit University, Department of Mathematics, TÜRKİYE

Assist. Prof. Dr. Fadıl KUYUCUOĞLU, Manisa Celâl Bayar University, Department of Photonics, Optoelectronics and Optical Communications, TÜRKİYE

Assist. Prof. Dr. Göksel GÖKKUŞ, Nevşehir Hacı Bektaş Veli University, Department of Electrical Energy Generation (Incl. Renewables, Excl. Photovoltaics), TÜRKİYE

Assist. Prof. Dr. Harun YAKA, Amasya University, Department of Production Technologies, TÜRKİYE

Assist. Prof. Dr. Hasan ARSLAN, Erciyes University, Department of Associative Rings and Algebras, TÜRKİYE

Assist. Prof. Dr. Hasan CANGİ, Hasan Kalyoncu University, Department of Electrical-Electrical Engineering, TÜRKİYE

Assist. Prof. Dr. İklim GEDİK BALAY, Ankara Yıldırım Beyazıt University, Department of Statistics, TÜRKİYE

Assist. Prof. Dr. Mehmet ETLİOĞLU, Konya Food and Agriculture University, Department of Innovation Management, TÜRKİYE

Assist. Prof. Dr. Mehmet Serhat CAN, Tokat Gaziosmanpaşa University, Department of Control Engineering, Mechatronics and Robotics, TÜRKİYE

Assist. Prof. Dr. Merve BALLI YÜKSEL, İstanbul Topkapı University, Department of Cell and Nuclear Division, TÜRKİYE

Assist. Prof. Dr. Murat Erhan ÇİMEN, Sakarya Applied Science University, Department of Deep Learning, TÜRKİYE

Assist. Prof. Dr. Mustafa Yusuf YAZICI, Samsun University, Department of Thermodynamics and Statistical Physics, TÜRKİYE

Assist. Prof. Dr. Ömer ERTUĞRUL, Ahi Evran University, Department of Agricultural Machine Systems, TÜRKİYE

Assist. Prof. Dr. Özkan ARSLAN, Tekirdağ Namık Kemal University, Department of Artificial Intelligence, TÜRKİYE

Assist. Prof. Dr. Salih SARICAOĞLU, Ondokuz Mayıs University, Department of Bacteriology, TÜRKİYE

Assist. Prof. Dr. Selami BAĞRIYANIK, İstanbul Topkapı University, Department of Computer Software, TÜRKİYE

Assist. Prof. Dr. Serdal ARSLAN, Harran University, Electrical Engineering, TÜRKİYE

Assist. Prof. Dr. Serdar GENÇ, Ahi Evran University, Department of Genetically Modified Animals, TÜRKİYE

Assist. Prof. Dr. Sıdıka GENÇ, Bilecik Şeyh Edebali University, Department of Animal Cell and Molecular Biology, TÜRKİYE

Assist. Prof. Dr. Şerif ÖZLÜ, Gaziantep University, Department of Mathematical Sciences, TÜRKİYE

Assist. Prof. Dr. Taner ÇARKIT, Kırklareli University, Department of Machine Learning, TÜRKİYE

Dr. Abdulhamit SEVGİ, OSTİM Technical University, Artificial Intelligence, TÜRKİYE

Dr. Aslı ARPAK, Yaşar University, Information Technologies in Architecture and Design, TÜRKİYE

Dr. Ayodeji OMOTEHINSE, Benson Idahosa University, Department of Industrial Engineering, NIGERIA

Dr. Cenk YANEN, Fırat University, Department of Composite and Hybrid Materials, TÜRKİYE

Dr. Ebru ERGÜNEŞ BERKİN, Hassa District Directorate of Agriculture and Forestry, Department of Biostatistics, TÜRKİYE

Dr. Esen Bilge BİÇER, Sivas Cumhuriyet University, Department of Phytopathology, TÜRKİYE

Dr. Esra ÇİĞNİTAŞ, Antalya Batı Akdeniz Agricultural Research Institute Directorate, Department of Herbology, TÜRKİYE

Dr. Francis INEGBEDION, University of Benin, Department of Engineering Materials, NIGERIA

Dr. Hicret HOPOĞLU, Sivas Cumhuriyet University, Department of Nanofotonic, TÜRKİYE

Dr. İsmail YARİÇİ, Aydın Adnan Menderes University, Department of Electromagnetic, TÜRKİYE

Dr. Muhammad GULİSTAN, Hazara University, Department of Mathematics, PAKISTAN

Dr. Murat LUZUM, Van Yüzüncü Yıl University, Department of Algebra and Number Theory, TÜRKİYE

Dr. Mustafa ALTINTAŞ, Yozgat Bozok University, Department of Information Security Management, TÜRKİYE

Dr. Norfarah NORDIN, University Sains Malaysia, Department of Machine Learning, MALAYSIA

Dr. Nurettin ŞENYER, Samsun University, Department of Image Processing, TÜRKİYE

Dr. Selin TÜNK, Çukurova University, Department of Herbology, TÜRKİYE

Dr. Yasin BEKTAŞ, Aksaray University, Department of Electrical Machines and Drives, TÜRKİYE

* The ranking is arranged alphabetically within the academic title

Table of Contents

Research Article

1. **ASSESSMENT OF ELECTRICITY CONSUMPTION CHARACTERISTIC: TEXTILE FACTORY CASE STUDY**
Cihat Çağdaş UYDUR.....308-316
2. **GERZE TAVUKLARINDA YUMURTA AĞIRLIĞI VE ŞEKİL İNDEKSİNİN YAŞA BAĞLI DEĞİŞİMİ**
Cansu ARSLAN, Elif CİLAVDAROĞLU, Umut Sami YAMAK.....317-320
3. **PROTEİN İÇERMİYEN MEDYA İLE OLGUNLAŞTIRILAN İMMATÜR SIĞIR OOSİTLERİNİN İN VİTRO FERTİLİZASYONU VE BLASTOSİSTE KADAR GELİŞİMLERİ**
Yusuf Ziya GÜZEY.....321-324
4. **DETERMINATION OF HARNESS PRODUCTION TIME AND DEFECTIVE PRODUCT FORMATION RISK FACTORS WITH ARTIFICIAL NEURAL NETWORK**
Gülşah KURNAZ, Naci MURAT.....325-329
5. **A NEW SOFT SET OPERATION: COMPLEMENTARY SOFT BINARY PIECEWISE INTERSECTION (\cap) OPERATION**
Aslıhan SEZGİN, Fitnat Nur AYBEK, Akın Osman ATAGÜN.....330-346
6. **OPTIMIZATION USING TAGUCHI METHOD TO INVESTIGATE THE EFFECTS OF PROCESS PARAMETERS ON THE HARDNESS OF DEVELOPED ALUMINIUM ROOFING SHEETS**
Dickson David OLODU, Andrew ERAMEH.....347-355
7. **SEFTRİAKSON ETKEN MADDELİ İLACIN İNSAN PANKREAS HÜCREŞİ ÜZERİNDE SİTOTOKSİK ETKİLERİNİN MTT TESTİ İLE DEĞERLENDİRİLMESİ**
Asena KURT, Zinet ÇÖL, Ömer ERTÜRK.....356-362
8. **İKLİM DEĞİŞİKLİĞİ İLE MÜCADELEDE KURUMSAL KARBON EMİSYON FARKINDALIĞINI ARTTIRMA: ZONGULDAK BÜLENT ECEVİT ÜNİVERSİTESİ DEVREK MESLEK YÜKSEKOKULU ÖRNEĞİ**
Serkan ÖREN, Sefa KOCABAŞ.....363-368
9. **LED BASED LOW-COST PHOTO-ACOUSTIC SETUP BY USING STETHOSCOPE**
Emine Ela DURMUŞ, Ensar KARABULUT, İbrahim AKKAYA, Yavuz ÖZTÜRK.....369-374
10. **EFFECTS OF HIGH LEVEL OF LEAD (II) OXIDE (PBO) USAGE ON ACCUMULATOR AND RESPONSE SURFACE METHOD**
Emrah PIÇAKÇI, Zehra Gülten YALÇIN.....375-386
11. **CORN DISEASE DETECTION USING TRANSFER LEARNING**
Cevher OZDEN.....387-393
12. **AKUT AKCİĞER HASARI MODELİNDE HİSPİDULİNİN HEPATOPROTEKTİF ROLÜNÜN KARACİĞER BİYOMOLEKÜLER KOMPOZİSYONU DEĞİŞİMLERİ AÇISINDAN DEĞERLENDİRİLMESİ**
Nihal ŞİMSEK ÖZEK.....394-400

| | |
|--|---------|
| 13. ON DARBOUX FRAMES OF INDICATRICES OF SPACELIKE SALKOWSKI CURVE WITH SPACELIKE BINORMAL IN E13 | |
| <i>Birkan AKSAN, Sümeyye GÜR MAZLUM</i> | 401-413 |
| 14. BIBLIOMETRIC ANALYSIS OF THE STUDIES DETERMINED BY THE MONTE CARLO SIMULATION TECHNIQUE OF THE POWER OF THE TEST | |
| <i>Malik ERGIN, Rabia ALBAYRAK DELIALIOĞLU, Yasin ALTAY, Özgür KOŞKAN</i> | 414-420 |
| 15. FORECASTING COVID-19 CASES IN TÜRKİYE WITH THE HELP OF LSTM | |
| <i>Nurgül GÖKGÖZ KÜÇÜKSAKALLI</i> | 421-425 |
| 16. ETLİK PİLİÇ YETİŞTİRİCİLİĞİNDE ÇEVRE KOŞULLARININ İZLENMESİNE YÖNELİK WEB TABANLI BİR UZAK İZLEME SİSTEMİNİN GELİŞTİRİLMESİ | |
| <i>Hayrettin KARADÖL, Ali ÇAYLI1, Adil AKYÜZ, Serdar ÜÇÖK</i> | 426-433 |
| 17. A NEW SOLUBLE COPPER PHTHALOCYANINE DERIVATIVE AS A SMART MATERIAL | |
| <i>Fuat ERDEN, Ebru YABAŞ</i> | 434-441 |
| 18. NEUROANATOMY OF ENTREPRENEURSHIP AND BIBLIOMETRIC ANALYSIS OF STUDIES WITH VOSVIEWER | |
| <i>Abdullah BALLI</i> | 442-457 |
| 19. MECHANICAL PERFORMANCE OF SALVADORA PERSICAL (MISWAK) REINFORCED POLYLACTIC ACID MATRIX COMPOSITES FOR THREE DIMENSIONAL PRINTING | |
| <i>Fuat KARTAL, Arslan KAPTAN</i> | 458-468 |
| 20. THE ANGULAR USE OF LIGHT IN ARCHITECTURE AND THE CONCEPT OF SPACE | |
| <i>Mehmet Sait CENGİZ</i> | 469-476 |
| 21. A PARALLEL ALGORITHM FOR DESIGNING PRIMER AND PROBE FOR ACCURATE DETECTION OF SEVERE ACUTE RESPIRATORY SYNDROME CORONAVIRUS | |
| <i>Hilal ARSLAN, Rıza DURMAZ</i> | 477-485 |
| 22. INVESTIGATION OF USE OF HYDROCHARS OBTAINED FROM LEGUME WASTES AS FUEL AND THEIR CONVERSION INTO ACTIVATED CARBON FOR AMOXICILLIN REMOVAL | |
| <i>İsmail Cem KANTARLI</i> | 486-501 |
| 23. BIODIVERSITY OF ACTINOBACTERIA ISOLATED FROM MARMARA AND AVŞA ISLANDS IN TÜRKİYE | |
| <i>Ahmet Ridvan TOPKARA, Kamil ISIK</i> | 502-521 |
| 24. DETERMINATION OF HMF VALUE AND DIASTASE ACTIVITIES IN STRAINED HONEYS SOLD IN MARKETS | |
| <i>Seda Dicle KORKMAZ</i> | 522-526 |
| 25. INVESTIGATION OF DEFECTS OCCURRING IN THE CASTING SHOP PROCESS OF CERAMIC SANITARYWARE ON THE FINAL PRODUCT | |
| <i>Nihal Derin COSKUN, Eray CASIN, Cumhur Eren ISIK</i> | 527-534 |
| 26. DAYLIGHT ANALYSIS IN TERMS OF BUILDING DIRECTION AND ONE-WAY ROOF | |
| <i>Mehmet Sait CENGİZ</i> | 535-539 |
| 27. INVESTIGATION OF THE GENOTOXIC EFFECTS OF THE ANALGESIC DRUGS PIROXICAM AND TENOXICAM IN HUMAN LYMPHOCYTES | |
| <i>Humeyra GUL, Ece AVULOGLU YILMAZ</i> | 540-549 |

28. SCATTERING FROM PARABOLIC CYLINDRICAL REFLECTOR ANTENNA USING PHYSICAL OPTICS

Fadil KUYUCUOĞLU.....550-556

29. COMPREHENSIVE ANALYSIS AND EVALUATION OF DC-DC CONVERTERS: ADVANCEMENTS, APPLICATIONS, AND CHALLENGES

Fuad ALHAJ OMAR.....557-571

30. ELEVATING THYME SPECIES IDENTIFICATION: EXPLOITING KEY CHLOROPLAST GENES (matK, rbcL, AND psbA-trnH) THROUGH DNA BARCODING AND PHYLOGENETIC ANALYSIS

Mehmet Alp FURAN.....572-582

31. 3 BOYUTLU GÖRÜNTÜLEME KULLANILARAK BİR AĞAÇ GÖVDE ÇAP ÖLÇÜM UYGULAMASININ GELİŞTİRİLMESİ

Hayrettin KARADÖL, Mehmet GÖK, Mehmet TEKEREK.....583-588

32. OPTI-WAFFLE: A TECHNOLOGICAL FURNITURE DESIGN AND MANUFACTURING MODEL

Erdem YILDIRIM.....589-599

33. CHROMOSOME BANDING PROPERTIES OF *Neogobius fluviatilis* (PALLAS, 1814) (PERCIFORMES, GOBIIDAE)

Sevgi UNAL-KARAKUS, Muradiye KARASU-AYATA, Muhammet GAFFAROĞLU.....600-603

34. ESTIMATION OF AIR LIGHT WITH DEEP LEARNING FOR A NEAR REAL-TIME IMAGE DEHAZING SYSTEM

Yücel ÇİMTAY.....604-612

35. ÇOK NOKTALI DERİN ÇEKME PROSESİNDE FARKLI PİM RADYUSLARININ ETKİSİNİN İNCELENMESİ

Kaan Emre ENGIN.....613-623

36. LAHANAGİLLER FAMILİYASINA AİT BAZI SEBZE TÜRLERİNİN VEJETATİF BÜYÜME ÖZELLİKLERİNİN İNCELENMESİ

Dilek KANDEMİR, Kübra PALA, G. Tuğba ŞAHİN, Ahmet BALKAYA.....624-632

37. COMPARING OF CFD CONTOURS USING IMAGE ANALYSING METHOD: A STUDY ON VELOCITY DISTRIBUTIONS

Ahmet ERDOĞAN, Mahmut DAŞKIN.....633-638

38. MAXIMUM LIKELIHOOD ESTIMATION FOR THE LOG-LOGISTIC DISTRIBUTION USING WHALE OPTIMIZATION ALGORITHM WITH APPLICATIONS

Adi Omaia FAOURI, Pelin KASAP.....639-647

Review Articles

39. FARKLI ÖZELLİKLERİ VE ÖZEL YÖNLERİ İLE BİR BİTKİ HORMONLARI GRUBU: STRİGOLAKTONLAR

Özge DURMAZ, Alper DURMAZ, Erdi Can AYTAZ, Yasemin ÖZDENER KÖMPE.....648-657

40. BULUT SERVİSLERİ VE BULUT GÜVENLİĞİ İÇİN ONTOLOJİ TABANLI HİZMET DÜZEYİ SÖZLEŞMELERİ

Sena YAKUT, Özgü CAN.....658-667



ASSESSMENT OF ELECTRICITY CONSUMPTION CHARACTERISTIC: TEXTILE FACTORY CASE STUDY

Cihat Çağdaş UYDUR^{1*}

¹Trakya University, Technical Sciences Vocational School, Department of Electrical and Energy, 22030, Edirne, Türkiye

Abstract: Currently, electrical energy tariffs are a crucial factor in the electricity market, as they significantly impact the decisions made by end users. They play a vital role in the effectiveness of energy management systems (EMS). Tariffs are not solely considered a fixed component of expenditure calculations. Instead, they are indirectly linked to the costs of power generation, electricity transmission, and electricity distribution, as well as other determinants such as government taxation. In certain regions, improper tariff calculation methodologies have resulted in substantial power losses, superfluous investments, increased operating costs, and environmental pollution because of the underutilization of available renewable energy sources. This study examined the electrical energy consumption values and characteristics of an integrated textile factory. Additionally, analyses were conducted on the electricity tariffs published by the Energy Market Regulatory Authority (EMRA) Electricity Energy Market management, in order to decrease the electrical energy consumption costs of the textile factory. Based on the findings of the analyses, suggestions were put forward for regulating the electrical energy consumption characteristics and reducing the electrical energy consumption costs.

Keywords: Electricity consumption, Electricity tariffs, Energy management, Energy markets

*Corresponding author: Trakya University, Technical Sciences Vocational School, Department of Electrical and Energy, 22030, Edirne, Türkiye

E mail: ccagdasydur@trakya.edu.tr (C. C. UYDUR)

Cihat Çağdaş UYDUR



<https://orcid.org/0000-0002-0908-2722>

Received: May 04, 2023

Accepted: July 06, 2023

Published: October 15, 2023

Cite as: Uydur CC. 2023. Assessment of electricity consumption characteristic: textile factory case study. BJS Eng Sci, 6(4): 308-316.

1. Introduction

Energy management is a process application consisting of procedures for monitoring and optimizing energy consumption used in buildings. It needs to be sustainable and constantly reviewed. The main aim of energy management is to take initiatives to cost-effectively reduce the energy consumption required and to reduce the energy consumption without reducing the productivity (Zaki and Hamdy, 2022).

Electricity tariffs are guides with energy unit fees that determine the amount of bills that consumers will pay for electricity use. Electricity tariffs play an important role in the electrical energy market, they directly affect consumers' decisions and energy usage habits (Grimm et al., 2021). They are also very important to increase competition in the electricity market. Today, local consumers can respond to bill amounts and seek different ways to reduce their energy consumption (Ren et al., 2016). In this case, revenues from electricity bills may tend to decrease. This trend will not reduce costs and will pave the way for the rest of the consumers to obtain energy at higher prices in order to meet the operating expenses. As a result, the expediency of electrical installations will disappear. It will cause problems throughout the system and increase energy costs (Felder and Athawale, 2014; Brown and Sappington, 2018). In this context, a preferable tariff design should appeal to different user profiles but be

applicable at the same time. It should be able to cover energy costs without causing inequalities. This situation was frequently discussed in studies in the literature (Borenstein, 2016; Neuteleers et al., 2017). In order to accurately determine the energy costs in the electricity tariffs, factors such as the cost of electricity production, the costs of operation and maintenance that make the operation of transmission and distribution networks possible and sustainable should be taken into account (Ansarin et al., 2020; Batlle et al., 2020). Electricity pricing has a significant impact and a delicate balance on the demand-based generation and distribution of energy. As a natural consequence of this situation, considering the environmental conditions and geographical effects, it has been determined that energy costs vary between different countries or different regions within (Hinz et al., 2018; Sulaima et al., 2019). The widespread use of renewable energy sources such as wind, solar and hydroelectricity in the electricity grid has affected the electricity unit prices for residential, commercial and industrial sectors.

In recent years, many methodologies have been developed to detect current loads and develop Energy Management System (EMS) strategies (Li et al., 2019). Evaluation of generation plans to understand current energy requirements and power generation techniques were discussed. Forecasts based on load models were made using artificial neural networks (Poongavanam et



al., 2023). A supporting energy management system regulating electrical energy use had been proposed (Zorita et al., 2016). This system was designed to improve the EMS of buildings. The energy performances of the facilities were analyzed comparatively. The relationship between EMS and electricity tariffs following the load profile was discussed in detail with different variations. In another study, a set of EMS methodologies were discussed in (Ouédraogo et al., 2021), and the fee advantages provided for PV and electric vehicle systems that provide electrical energy to a residential building are examined and compared from different perspectives. Calculation of the energy cost obtained and consumed provides a total profitability and thus the most suitable method was determined. In a study (Wu et al., 2022), a new method, which includes a multifunctional strategy, was proposed by adjusting the charge and discharge states of the PV system with a life cycle planning. A new EMS methodology was introduced to control pricing manipulation. The effect of the four-time energy pricing tariff on the planning of energy consumption discussed in (Zhao et al., 2023). In addition, the approach of load sharing configurations of different levels of stakeholders within the microgrid is examined in order to reduce financial costs. A predictively optimized energy procurement model was discussed, which minimizes energy costs and reveals the best energy sharing strategy for stakeholders (Qayyum et al., 2022). In another study, EMS as energy planning was carried out with reference to ISO 50001 standard, and the first step is the optimal tariff management analysis. It has been emphasized that the implemented EMS provides absolute benefits (Iscan and Arikan, 2022).

In this study, the electrical energy consumption characteristics of an integrated textile factory were examined. Analyzes were carried out to reveal the electricity energy consumption costs of the textile factory within the scope of the electricity tariffs published by the Energy Market Regulatory Authority (EMRA) Electricity Energy Market management. A remote monitoring system were installed in order to monitor the electrical energy consumption instantly and to keep the electricity consumption characteristics under control. In this context, instant monitoring and determination of hourly consumption data are provided. With the findings obtained, energy costs were reduced by changing the factory working hours.

2. Materials and Methods

In this section, detailed information about “Tariff Tables Based on Electricity Bills” published by EMRA is shared (EMRA, 2023). Activity-based tariffs approved and published by EMRA are published four times a year, in January-April-July-October. In 2022, an exceptional application was made within this process, with tax reductions in March and price changes in June and September. Then, the practice of publishing the updated tariffs in quarterly periods continued.

When the activity-based tariff tables are examined, it is seen that two different types of users are defined as transmission and distribution system users. While there is only one pricing option for transmission system users, different options are specified for distribution system users: industry, public sector, residential, agricultural activities and lighting. In addition, medium voltage and low voltage options are presented, where the voltage type of the connection point is determined.

For consumers who purchase electrical energy with a medium voltage connection; apart from the single-term tariff where only the electricity consumption value is priced, there is also the double-term tariff option that charges the demand consumption value as the power price. For the consumer tariffs where all these definitions are met, two different energy cost options are offered for the electrical energy consumption cost within the 24-hour period, as full-time and three-time. Finally, all tariff options include a fixed distribution fee. In the light of all this information; Considering the tariff published by EMRA in April 2023, the details of the unit electrical energy consumption cost for a single term, full-time tariff residential subscriber connected to the electricity grid from low voltage are presented in Table 1.

Table 1. Details of electrical energy consumption cost (EMRA, 2023)

| Parameter | Amount | Amount |
|-------------------|-------------|------------|
| Consumption Cost | 0.558378 TL | 0.02893 \$ |
| Distribution Cost | 0.778883 TL | 0.04035 \$ |
| Consumption Tax | 0.027919 TL | 0.00144 \$ |
| Subtotal | 1.365180 TL | 0.07073 \$ |
| Value-added Tax | 0.109214 TL | 0.00565 \$ |
| Bill Amount | 1.474394 TL | 0.07639 \$ |

The electricity consumption cost and distribution cost in Table 1 were taken from the relevant EMRA tariff and the electricity consumption tax was calculated by calculating 5% of the electricity consumption price. The subtotal value is calculated by summing the electricity consumption cost, distribution cost and electricity consumption tax. Value added tax is determined by calculating 8% of the subtotal value. In this context, the electricity bill amount consists of the sum of the subtotal value and the value added tax. In addition, the average value of USD/TL parity between 1-31 April was calculated as 19.3. With the help of this value, electricity consumption cost values were also shared in USD (\$).

Residential subscribers with an average daily electricity consumption of more than 8 kWh are faced with electricity bills calculated with a gradual electricity tariff. For example, a residential subscriber who consumes 300 kWh of electrical energy within the billing period has to pay for the first 240 kWh of electrical energy at a unit price of 0.558378 TL/kWh, while for 60 kWh, he has to pay at a unit price of 1.208462 TL/kWh.

In the three-time electricity tariffs, the electrical energy

consumption during the day is divided into three different time periods as daytime, peak and night. The electrical energy consumed between 06-17 hours is calculated as Daytime, the electrical energy consumed between 17-22 hours as Peak and the electrical energy consumed between 22-06 hours as Night. There is no gradual electricity tariff in the three-time electricity energy tariff. The distribution fee is the same for one-time and three-time tariffs.

In the Turkish electricity energy market; the change in unit electrical energy consumption price, including taxes, over the years for a single term, single-time tariff residential subscriber connected to the electricity grid from low voltage is given in Table 2.

Table 2. Change of electricity cost for residential subscriber (EMRA, 2023)

| Period | Bill Amount |
|----------------|-------------|
| 2021 January | 0.796131 TL |
| 2021 April | 0.796131 TL |
| 2021 July | 0.915551 TL |
| 2021 October | 0.915551 TL |
| 2022 January | 1.373327 TL |
| 2022 March | 1.256943 TL |
| 2022 June | 1.445485 TL |
| 2022 September | 1.734582 TL |
| 2022 October | 1.734582 TL |
| 2023 January | 1.734582 TL |
| 2023 April | 1.474394 TL |

In Table 3, for the month of April 2023, the unit price of electricity energy consumption, including all taxes, are shared for the residential, commercial, industrial, martyr families and agricultural irrigation options for distribution system users.

Table 3. Electricity costs by subscriber type (EMRA, 2023)

| Subscriber Type | Bill Amount |
|------------------------------|-------------|
| Residential | 1.474394 TL |
| Commercial | 2.837906 TL |
| Industrial | 3.670157 TL |
| Martyr Families and Veterans | 0.698965 TL |
| Agricultural Irrigation | 2.211597 TL |

3. Electricity Consumption Characteristic of Textile Factory

In this section, electrical energy consumption data was analyzed in order to determine the electrical energy consumption characteristic of the factory. In the textile factory in Marmara region, 10 oil-type transformers with a power of 1600 kVA are connected to each other at 31.5 kV voltage level to form a ring grid. The analyses started with a factory-wide evaluation and were detailed on the basis of department and time.

3.1. Analysis of Electricity Consumption

In Figure 1, the electrical energy consumption values of the textile factory for the last five years are shared.

When Figure 1 is examined, it is seen that the total electrical energy consumed in 2018 is 33,707.46 MWh. In 2019, this value increased by 6.5% and reached 35,890.76 MWh hours. Due to the global corona epidemic that occurred in 2020, electrical energy consumption has tended to decrease. The total consumed electrical energy value in 2020 was recorded as 29,603.72 MWh. In 2021, with the increase in electrical energy consumption especially in the second half of the year, 31,383.52 MWh of electricity was consumed. In 2022, with the living conditions returning to normal, the factory working order was re-established and the consumption record of the last five years was broken with 37,615.24 MWh electrical energy consumption at the end of the year.

When the electrical energy consumption data of the last five years are analyzed monthly, it is seen that seasonal transitions are felt. In this context, considering that the workload is also a determining factor, it turns out that evaluating the data in general will not be consistent and determining the main factor causing electricity consumption will lead to an erroneous diagnosis. As a result, more data that are detailed should be obtained in order to determine the electrical energy consumption characteristics. Electricity consumption values monitored hourly in 2022 are arranged to meet the time periods determined in EMRA tariffs and are shared monthly in Table 4. Considering the consumption trends of the data in Table 4, daytime consumption rates are 47% in January, 46.78% in February, 47.13% in March, 47.35% in April, 47.3% in May, 47.72% in June, 46% in July, It was calculated as 46.64% in August, 46% in September, 45.77% in October, 45.7% in November and 46.1% in December. Considering that the instantaneously consumed power value does not change during the whole day, this value is known to be 45.83%. It has been determined that this critical threshold has been exceeded for nine months as of the year. In this context, it turns out that the production planning is not evaluated based on the electrical energy consumption value and cannot be controlled by receiving feedback. The consumption behavior of 2022 is shared in Figure 2 based on time periods.

When Figure 2 is evaluated, the time-dependent change of the electricity consumption trend in 2022, the daytime consumption rate is 46.425%, the peak consumption rate is 21%, and the nighttime consumption rate is 32.572%. As a result of a more detailed examination of these values, the electricity consumption character will be revealed and the basis for the efforts to reduce the electricity bill amount can be laid. In this context, it has been determined that the overall consumption of the factory becomes more intense during the daytime and peak time hours. This point will be used as a support and will play an active role in the analysis of electrical energy consumption components.

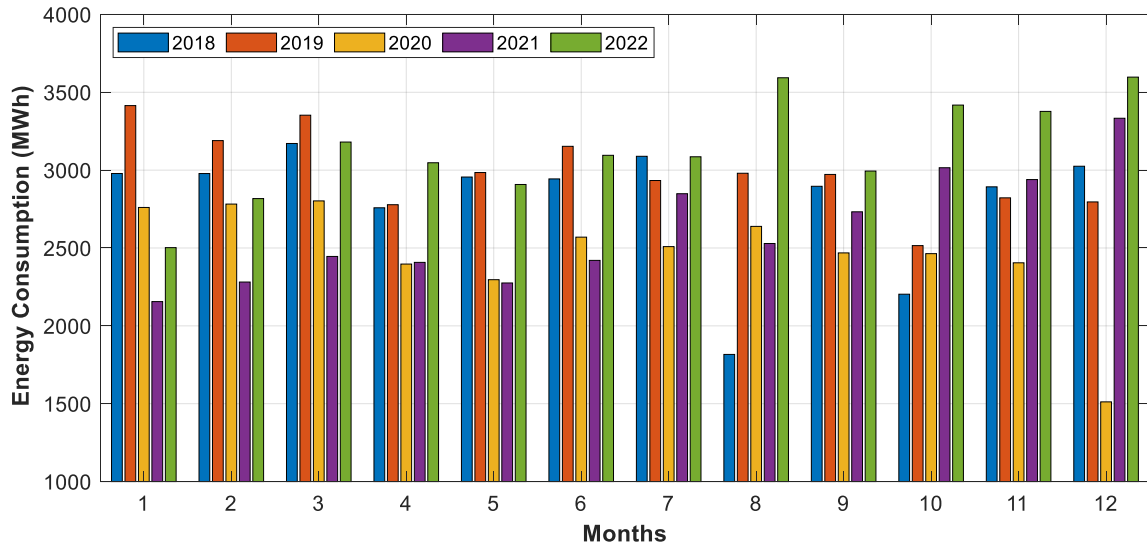


Figure 1. Electricity consumption of textile factory.

Table 4. Electricity consumption of textile factory in 2022

| Month | Daytime (kWh) 06-17 [11 h] | Peak (kWh) 17-22 [5 h] | Night (kWh) 22-06 [8 h] | Total (kWh) |
|-----------|-------------------------------|---------------------------|----------------------------|--------------|
| January | 1,177,762.95 | 526,950.90 | 797,570.55 | 2,502,284.40 |
| February | 1,318,000.95 | 597,863.70 | 901,397.70 | 2,817,262.35 |
| March | 1,498,779.45 | 676,308.15 | 1,005,300.45 | 3,180,388.05 |
| April | 1,442,996.10 | 653,514.75 | 950,821.20 | 3,047,332.05 |
| May | 1,375,211.25 | 591,192.00 | 941,418.45 | 2,907,821.70 |
| June | 1,446,180.75 | 657,512.10 | 991,465.65 | 3,095,158.50 |
| July | 1,420,476.75 | 644,149.80 | 1,021,119.75 | 3,085,746.30 |
| August | 1,639,764.00 | 753,930.45 | 1,199,412.90 | 3,593,107.35 |
| September | 1,378,717.20 | 625,523.85 | 989,840.25 | 2,994,081.30 |
| October | 1,564,315.20 | 706,293.00 | 1,147,078.80 | 3,417,687.00 |
| November | 1,543,619.70 | 713,323.80 | 1,120,155.75 | 3,377,099.25 |
| December | 1,657,180.61 | 753,623.82 | 1,186,470.37 | 3,597,274.80 |

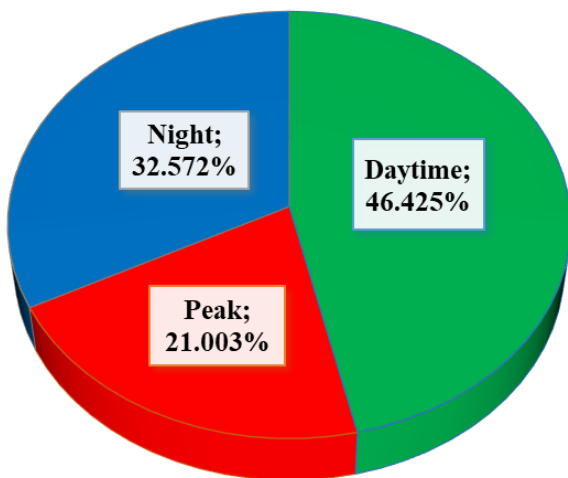


Figure 2. The consumption characteristic of factory in 2022.

3.2. Department-Based Analysis of Electricity Consumption

The factory structure consists of six different departments: spinning mill, weaving preparation,

weaving-1, weaving-2, dyeing and finishing and auxiliary enterprises. While denim fabrics has been produced in the weaving-1 section, shirt and tent fabrics has been woven in the weaving-2 section. Auxiliary businesses include electrical, electronic and mechanical workshops, as well as boiler rooms and water treatment plants. Until 2022, the electricity consumption values of the factory were obtained from only electricity bills. In 2021, NEXUS 1500+ power analyzer mounting at the factory main supply point and ELNET LT energy analyzers were installed in order to monitor the electrical energy consumption of the departments within the factory. The NEXUS 1500+ power analyzer and ELNET LT series energy analyzer is shown in Figure 3.

In this study, a total of 90 energy analyzers were installed, taking into account the main production sections of the factory. The installation of the energy analyzers took approximately 6 months. Of these energy analyzers; 24 of them were established in the spinning mill department, 10 in the weaving preparation department, 12 in the weaving-1, 12 in the weaving-2, 24 in the dye finishing department and 8 in the auxiliary

businesses. In this context, electrical energy consumption by the departments began to be monitored and recorded on a machine-based basis. The distribution of electricity consumption values for 2022 by departments is presented in Table 5.

When the electricity consumption data shared in Table 5 is analyzed, it can be said that factory electrical energy consumption sources in 2022 consist of four basic parts. These departments were determined as spinning mill,

weaving (consisting of weaving preparation, weaving-1 and weaving-2 sections), dyeing and finishing and auxiliary businesses. In this context, 32.49% of the total electrical energy is consumed by spinning mill, 47.35% by weaving, 15.12% by dye finishing and finally 5.04% by auxiliary enterprises.

In Figure 4, the electrical energy consumption rates of all departments are shared on a monthly basis.



Figure 3. Energy analyzers used to monitor factory electricity consumption; (a) NEXUS 1500+, (b) ELNET LT series.

Table 5. Electricity consumption values for 2022 by departments

| Month | Spinning Mill (kWh) | Weaving Preparation (kWh) | Weaving-1 (kWh) | Weaving-2 (kWh) | Dye-finishing (kWh) | Auxiliary Enterprises (kWh) |
|-----------|---------------------|---------------------------|-----------------|-----------------|---------------------|-----------------------------|
| January | 809,989.46 | 53,048.43 | 402,367.33 | 745,680.75 | 350,319.82 | 140,878.61 |
| February | 781,790.30 | 58,317.33 | 486,822.93 | 876,732.04 | 462,031.03 | 151,568.71 |
| March | 891,462.77 | 55,020.71 | 532,715.00 | 999,914.00 | 539,075.77 | 162,199.79 |
| April | 909,323.88 | 45,709.98 | 489,401.53 | 980,936.19 | 479,650.06 | 142,310.41 |
| May | 920,616.35 | 45,943.58 | 474,847.28 | 879,034.50 | 451,003.15 | 136,376.84 |
| June | 950,523.18 | 50,141.57 | 568,580.62 | 881,191.62 | 497,391.97 | 147,329.54 |
| July | 1,019,839.15 | 38,571.83 | 511,308.16 | 935,289.70 | 441,261.72 | 139,475.73 |
| August | 1,294,237.27 | 45,991.77 | 543,277.83 | 1,026,550.77 | 514,173.66 | 168,876.05 |
| September | 1,022,778.17 | 38,324.24 | 460,789.11 | 882,954.58 | 436,537.05 | 152,698.15 |
| October | 1,243,012.76 | 48,189.39 | 487,362.17 | 965,154.81 | 498,982.30 | 174,985.57 |
| November | 1,174,892.83 | 55,722.14 | 507,240.31 | 971,253.74 | 486,977.71 | 181,012.52 |
| December | 1,202,209.24 | 67,628.77 | 550,023.32 | 1,047,886.15 | 531,317.49 | 198,209.84 |

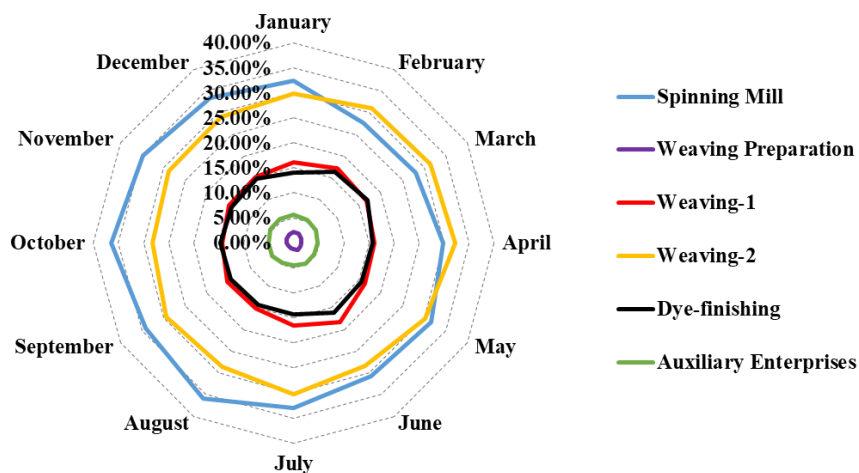


Figure 4. Electrical energy consumption rates of textile factory by departments.

Looking closely at Figure 4, it is seen that among the six different sections defined within the factory, the section where electrical energy is consumed for nine months of the year is the spinning mill. The spinning mill section is followed closely by the weaving-2 section. In fact, the weaving-2 department in February-March-April passed it. This is due to the intensive use of air conditioning devices such as compressors and air conditioners, which are used to provide the ambient conditions required by the weaving looms in the weaving-2 section. The electrical energy consumption values of the paint finishing department vary between 14% and 17% during the year according to the production planning. Although auxiliary enterprises are in the passive user class since they are not the main factor in the factory production

processes, they generally constitute 5% of the factory electrical energy consumption value. Seasonal conditions have little effect on this situation.

3.3 Time-Based Analysis of Electricity Consumption

In this section, in the light of the electrical energy consumption values of December 2022, the consumption values of the textile factory sections are classified according to time and evaluated in detail within the time periods specified in the electricity tariffs determined by EMRA. In this context, the assessment of the electricity consumption values of factory departments over time is the main factor in determining the electricity consumption characteristic of the textile factory. The electrical energy consumption values for December 2022 are given in Table 6.

Table 6. Electricity consumption of textile factory in December 2022 by departments

| Department | Daytime (kWh) | Peak (kWh) | Night (kWh) | Total (kWh) |
|-----------------------|---------------|------------|-------------|--------------|
| | 06-17 | 17-22 | 22-06 | |
| Spinning Mill | 549,770.28 | 249,939.30 | 402,499.65 | 1,202,209.24 |
| Weaving Preparation | 32,123.66 | 13,775.98 | 21,729.12 | 67,628.77 |
| Weaving-1 | 256,640.88 | 116,219.93 | 177,162.51 | 550,023.32 |
| Weaving-2 | 484,437.77 | 219,636.94 | 343,811.45 | 1,047,886.15 |
| Dye-finishing | 241,802.59 | 112,586.18 | 176,928.72 | 531,317.49 |
| Auxiliary Enterprises | 92,405.43 | 41,465.50 | 64,338.91 | 198,209.84 |

When the data in Table 6 were analyzed, it is revealed that the electrical energy consumed by the spinning mill section was 45.73% during the daytime, 20.79% at the peak time and 33.48% during the night time. These rates were respectively 46.8%, 20.82% and 32.38% for weaving sections. In the dye finishing section, the rates of 45.51%, 21.19% and 33.30% were obtained.

In Figure 5, the time-dependent consumption rates of electricity consumption for December 2022 are shared.

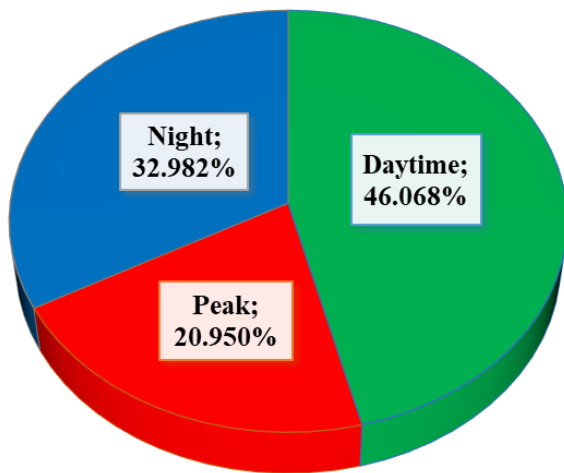


Figure 5. The consumption behavior of factory in December 2022.

When the electrical energy consumption values of the textile factory are analyzed based on time, it has been determined that all departments are the main factor in determining the electricity consumption characteristic. In

this context, it is necessary to review the working order throughout the factory in order to control electricity consumption. Assessment of these factors is discussed in detail in the next section.

4. Discussion

According to EMRA tariffs, the electrical energy consumed during the day is measured between 06-17 hours, the electrical energy consumed during the peak time is between 17-22 hours and the electricity consumed at night is measured between 22-06 hours. In this context, the day time zone is 11 hours, the peak time zone is 5 hours and the night time zone is 8 hours. If the instant electricity consumption of the textile factory remained constant throughout the day, the daytime electricity consumption rate would be 45.833%, the rate of peak electricity consumption would be 20.833% and the nighttime electricity consumption rate would be 33.333%. However, when the electrical energy consumption values in December 2022 are analyzed, it is seen that the daytime, peak and nighttime electricity consumption rates are 46.068%, 20.95% and 32.982%, respectively.

This is the main factor affecting electricity energy costs. In order to analyze the factor directly, it would be a more accurate form of analysis to discuss the electricity consumption cost rather than the electricity bill amount. The effect of 2022 electrical energy consumption on electricity consumption characteristics and energy costs is given in Table 7.

Table 7. Energy costs based on monthly electricity consumption characteristics in 2022

| Month | Consumption Cost (TL/kWh) | Daytime | Peak | Night | Energy Cost (TL/kWh) |
|-----------|---------------------------|---------|---------|---------|----------------------|
| January | 2.456997 | 47.068% | 21.059% | 31.874% | 2.417368 |
| February | 2.456997 | 46.783% | 21.221% | 31.996% | 2.418358 |
| March | 2.456997 | 47.126% | 21.265% | 31.609% | 2.423825 |
| April | 2.456997 | 47.353% | 21.445% | 31.202% | 2.431667 |
| May | 2.456997 | 47.294% | 20.331% | 32.375% | 2.399936 |
| June | 2.456997 | 46.724% | 21.243% | 32.033% | 2.418231 |
| July | 2.456997 | 46.033% | 20.875% | 33.092% | 2.399412 |
| August | 2.456997 | 45.636% | 20.983% | 33.381% | 2.397473 |
| September | 2.456997 | 46.048% | 20.892% | 33.060% | 2.400066 |
| October | 2.456997 | 45.771% | 20.666% | 33.563% | 2.390335 |
| November | 2.456997 | 45.708% | 21.122% | 33.169% | 2.402254 |
| December | 2.456997 | 46.068% | 20.950% | 32.982% | 2.401918 |

Table 8. Energy costs based on department of textile factory in December 2022

| Department | Consumption Cost (TL/kWh) | Daytime | Peak | Night | Energy Cost (TL/kWh) |
|-----------------------|---------------------------|---------|---------|---------|----------------------|
| Spinning Mill | 2.456997 | 45.730% | 20.790% | 33.480% | 2.393277 |
| Weaving Preparation | 2.456997 | 47.500% | 20.370% | 32.130% | 2.403583 |
| Weaving-1 | 2.456997 | 46.660% | 21.130% | 32.210% | 2.414287 |
| Weaving-2 | 2.456997 | 46.230% | 20.960% | 32.810% | 2.404217 |
| Dye-finishing | 2.456997 | 45.510% | 21.190% | 33.300% | 2.401670 |
| Auxiliary Enterprises | 2.456997 | 46.620% | 20.920% | 32.460% | 2.407949 |

The electricity consumption cost in Table 7 is taken from the activity-based electricity tariffs table published by EMRA in April 2023. Calculations were made using the electricity consumption costs of the double-term tariff, which includes the power cost for the industrial type user connected from the medium voltage connection point, which is already in the electricity bills of the textile factory. Here, the electricity price stated as 2.456997 TL/kWh is valid for the all-day. In this context, electricity consumption costs are 2.489192 TL/kWh for daytime, 4.028333 TL/kWh for peak and 1.246951 TL/kWh for nighttime. The electrical energy cost of the factory was determined by using the electricity consumption characteristics of the factory and the electricity consumption costs.

Considering the data in Table 7, it is seen that the energy costs are cheaper than the one-time electricity consumption cost. A direct assessment of this information is misleading. The main reason for this is that the energy cost of an industrial enterprise that consumes constant power throughout the day has been calculated as 2.395766 TL/kWh. This should be the critical threshold value to be taken as a basis when making the comparison. From this point of view, it is striking that the electrical energy costs of the textile factory are quite variable. The energy costs obtained in July and August in 2022 are very close to each other. However, energy costs below the critical threshold value were achieved in October 2022. In Table 8, the electricity consumption values and energy cost analyzes of the factory departments for December 2022 are shared.

As can be seen in Table 8, the section with the lowest electricity consumption cost is the spinning mill section.

For this reason, production planning has been reviewed in departments with high costs. When this situation is evaluated, the production planning in the weaving-1 and dye finishing departments, which work intensively at the peak time, has been reviewed and the working hours have been rearranged. The first priority of this arrangement is to be able to apply constant power consumption throughout the day. When the determined target is achieved, business plans for reducing the electrical energy consumed in peak time will be discussed. Assuming that an average of 3,100,000 kWh/month electrical energy is consumed in 2022, the effect of the 2 kr decrease in the electrical energy cost will emerge as a savings of approximately one million liras in the annual total electricity consumption cost. This value will increase even more with the taxes in the electricity bill calculation.

5. Conclusion

In this study, the electrical energy consumption characteristics of an integrated textile factory were examined by examining the electrical energy consumption characteristics. Analyzes were carried out to reveal the electricity energy consumption costs of the textile factory within the scope of the electricity tariffs published by the Energy Market Regulatory Authority (EMRA) Electricity Energy Market management.

In this context, the results can be listed as follows;

- It has been determined that the use of single-term tariff is misleading when evaluating the electricity consumption characteristics of a factory.
- In the evaluation of the electricity consumption characteristic, it should be assumed that the

instantaneous power consumption is constant and the unit electricity consumption price determined under these conditions should be accepted as the main criterion.

- According to the 2023 April tariffs, the critical threshold value has been determined as 2.395766 TL/kWh.
- 83.333% of the departments in the factory produce with energy costs above the critical threshold.
- The department that consumed the most electrical energy in the factory in 2022 was the spinning mill with a rate of 32.489%.
- The energy cost of the electricity consumption characteristic of spinning mill was determined as 2.393277 TL/kWh.
- Weaving-1 department has the most costly electricity consumption characteristic throughout the factory.
- It has been observed that the electrical energy cost of the Weaving-1 department is 2.414287 TL/kWh.
- The only departments within the factory where electricity consumption characteristics cannot be interfered with are auxiliary enterprises.

In future studies, it is planned to evaluate the electrical energy quality of the textile factory by using the data obtained from the energy measurement and monitoring system.

Author Contributions

The percentage of the author contributions is presented below. The author reviewed and approved the final version of the manuscript.

| | C.Ç.U. |
|-----|--------|
| C | 100 |
| D | 100 |
| S | 100 |
| DCP | 100 |
| DAI | 100 |
| L | 100 |
| W | 100 |
| CR | 100 |
| SR | 100 |
| PM | 100 |
| FA | 100 |

C=Concept, D= design, S= supervision, DCP= data collection and/or processing, DAI= data analysis and/or interpretation, L= literature search, W= writing, CR= critical review, SR= submission and revision, PM= project management, FA= funding acquisition.

Conflict of Interest

The author declared that there is no conflict of interest.

Ethical Consideration

Ethics committee approval was not required for this study because of there was no study on animals or humans.

References

- Ansarin M, Ghiassi-Farrokhfal Y, Ketter W, Collins J. 2020. The economic consequences of electricity tariff design in a renewable energy era. *Appl Energy*, 275: 115317. DOI: 10.1016/j.apenergy.2020.115317.
- Batlle C, Mastropietro P, Rodilla P. 2020. Redesigning residual cost allocation in electricity tariffs: A proposal to balance efficiency, equity and cost recovery. *Renew Energy*, 155: 257-266. DOI: 10.1016/j.renene.2020.03.152.
- Borenstein S. 2016. The economics of fixed cost recovery by utilities. *Elect J*, 29(7): 5-12. DOI: 10.1016/j.tej.2016.07.013.
- Brown DP, Sappington DEM. 2018. On the role of maximum demand charges in the presence of distributed generation resources. *Energy Econ*, 69: 237-249. DOI: 10.1016/j.eneco.2017.11.023.
- EMRA. 2023. Electricity tariff tables valid as of 1/4/2023. URL: <https://www.epdk.gov.tr/Detay/Icerik/3-1327/elektrik-faturalarina-esas-tarife-tablolari> (accessed date: February 10, 2023).
- Felder FA, Athawale R. 2014. The life and death of the utility death spiral. *Electricity J*, 27(6): 9-16. DOI: 10.1016/j.tej.2014.06.008.
- Grimm V, Orlinskaya G, Schewe L, Schmidt M, Zöttl G. 2021. Optimal design of retailer-prosumer electricity tariffs using bilevel optimization. *Omega*, 102. DOI: 10.1016/j.omega.2020.102327.
- Hinz F, Schmidt M, Möst D. 2018. Regional distribution effects of different electricity network tariff designs with a distributed generation structure: The case of Germany. *Energy Pol*, 113: 97-111. DOI: 10.1016/j.enpol.2017.10.055.
- Iscan S, Arıkan O. 2022. Energy management planning according to the electricity tariff models in Turkey: A case study. *Turkish J Elect Power Energy Syst*, 2(1): 46-57. DOI: 10.5152/tepes.2022.22010.
- Li S, Luo F, Yang J, Ranzi G, Wen J. 2019. A personalized electricity tariff recommender system based on advanced metering infrastructure and collaborative filtering. *Int J Electr Power Energy Syst*, 113: 403-410. DOI: 10.1016/j.ijepes.2019.05.042.
- Neuteleers S, Mulder M, Hindriks F. 2017. Assessing fairness of dynamic grid tariffs. *Energy Pol*, 108: 111-120. DOI: 10.1016/j.enpol.2017.05.028.
- Ouédraogo S, Faggianelli GA, Pigelet G, Notton G, Duchaud JL. 2021. Performances of energy management strategies for a Photovoltaic/Battery microgrid considering battery degradation. *Solar Energy*, 230: 654-665. DOI: 10.1016/j.solener.2021.10.067.
- Poongavanam E, Kasinathan P, Kanagasabai K. 2023. Optimal energy forecasting using hybrid recurrent neural networks. *Intell Automat Soft Comput*, 36(1): 249-265. DOI: 10.32604/iasc.2023.030101.
- Qayyum F, Jamil H, Jamil F, Kim D. 2022. Predictive optimization based energy cost minimization and energy sharing mechanism for peer-to-peer nanogrid network. *IEEE Access*, 10: 23593-23604. DOI: 10.1109/ACCESS.2022.3153837.
- Ren Z, Grozev G, Higgins A. 2016. Modelling impact of PV battery systems on energy consumption and bill savings of Australian houses under alternative tariff structures. *Renew Energy*, 89: 317-330. DOI: 10.1016/j.renene.2015.12.021.
- Sulaima MF, Dahlan NY, Yasin ZM, Rosli MM, Omar Z, Hassan MY. 2019. A review of electricity pricing in peninsular Malaysia: Empirical investigation about the appropriateness of Enhanced Time of Use (ETOU) electricity tariff. *Renew Sustain Energy Rev*, 110: 348-367.

- Wu Y, Liu Z, Li B, Liu J, Zhang L. 2022. Energy management strategy and optimal battery capacity for flexible PV-battery system under time-of-use tariff. *Renew Energy*, 200: 558-570. DOI: 10.1016/j.renene.2022.09.118.
- Zaki DA, Hamdy M. 2022. A review of electricity tariffs and enabling solutions for optimal energy management. *Energies*, 15(22): 8527. DOI: 10.3390/en15228527.
- Zhao J, Wang W, Guo C. 2023. Hierarchical optimal configuration of multi-energy microgrids system considering energy management in electricity market environment. *Int J Elect Power Energy Syst*, 144: 108572. DOI: 10.1016/j.ijepes.2022.108572.
- Zorita AL, Fernández-Temprano MA, García-Escudero LA, Duque-Perez O. 2016. A statistical modeling approach to detect anomalies in energetic efficiency of buildings. *Energy Build*, 110: 377-386. DOI: 10.1016/j.enbuild.2015.11.005.



GERZE TAVUKLARINDA YUMURTA AĞIRLIĞI VE ŞEKİL İNDEKSİNİN YAŞA BAĞLI DEĞİŞİMİ

Cansu ARSLAN¹, Elif ÇİLAVDAROĞLU¹, Umut Sami YAMAK^{1*}

¹Ondokuz Mayıs University, Agricultural Faculty, Department of Animal Science, 55139, Samsun, Türkiye

Özet: Bu çalışma ülkemize ait yerli Gerze tavuklarının yumurta ağırlığı ve yumurta şekil indeksinde yaşa bağlı meydana gelen değişimleri ortaya koymaktadır. Bu amaçla on sekiz haftalık yaşta 120 yerli Gerze tavuğu kümese yerleştirilerek aydınlatma başlatılmıştır. İlk yumurtlamanın gerçekleştiği 22 hafta ile üretim dönemi sonu olarak değerlendirilen 52 haftalık yaş döneminde üretilen tüm yumurtalarda ağırlık ve şekil indeksleri bireysel olarak belirlenmiştir. Bu dönemde toplam 6913 yumurta üretilmiştir. İlk hafta elde edilen yumurtaların ortalama ağırlığı 34,48 gram olarak tespit edilirken 52 haftalık yaşta elde edilen yumurtaların ağırlığı 52,58 grama yükselmiştir. Üretim dönemi boyunca ortalama yumurta ağırlığı 48,32 gram olarak gerçekleşmiştir. Ortalama yumurta eni 39,74 mm olarak hesaplanırken, yumurta boyu 53,76 mm olarak hesaplanmıştır. Gerze tavuklarında ortalama şekil indeksi 74,05 olarak belirlenmiştir.

Anahtar kelimeler: Gerze tavuğu, Yerli tavuk, Yumurta ağırlığı, Yumurta şekil indeksi

Age-Related Changes in Egg Weight and Shape Index in Gerze Chickens Eggs

Abstract: This study reveals the age-related changes in egg weight and egg shape index of native Gerze chickens of our country. With this aim, 120 native Gerze chickens at the age of eighteen weeks were placed in the house and lighting was started. Weight and shape index were determined individually for all eggs produced during the 22 weeks of the first laying and the 52 weeks of age, which is considered as the end of the production period. During this period, a total of 6913 eggs were produced. While the average weight of the eggs obtained in the first week was determined as 34.48 grams, the weight of the eggs obtained at the age of 52 weeks increased to 52.58 grams. The average egg weight during the production period was 48.32 grams. While the average egg width was calculated as 39.74 mm, the egg length was calculated as 53.76 mm. The average shape index of Gerze chickens was determined as 74.05.

Keywords: Gerze chicken, Indigenous chicken, Egg weight, Egg shape index

*Sorumlu yazar (Corresponding author): Ondokuz Mayıs University, Agricultural Faculty, Department of Animal Science, 55139, Samsun, Türkiye

E mail: usyamak@omu.edu.tr (U. S. YAMAK)

Cansu ARSLAN



<https://orcid.org/0009-0007-8480-3503>

Elif ÇİLAVDAROĞLU



<https://orcid.org/0000-0002-8258-2416>

Umut Sami YAMAK



<https://orcid.org/0000-0002-6435-4866>

Gönderi: 30 Mayıs 2023

Kabul: 16 Temmuz 2023

Yayınlanma: 15 Ekim 2023

Received: May 30, 2023

Accepted: July 16, 2023

Published: October 15, 2023

Cite as: Korkmaz A, Akınoğlu G, Boz E. 2023. Age-related changes in egg weight and shape index in Gerze chickens eggs. BJS Eng Sci, 6(4): 317-320.

1. Giriş

Türkiye'nin saf tavuk ırkı olarak Gerze ve Denizli tavukları bulunmaktadır. Gerze tavuk ırkı, Sinop'un Gerze bölgesinin lokal bir ırkıdır. Çatal ibikli, yüz yapısı orta uzunlukta ve hafif tüylüdür. Gözler orta büyüklükte yuvarlak ve kahverengidir. Burun delikleri büyük ve gaga üzerinde çıkıntılı, gaga gri renk tonlarında ve orta uzunluktadır. Kulaklar kısa tüylerle kaplı, kulak lopları erkeklerde çok belirgin her iki tarafta beyazdır. Sakal geniş ya da orta genişlikte ve erkeklerde uzundur. Boyun yapısı erkeklerde uzun ve tüylü, dişilerde orta uzunlukta ve tüylüdür. Kuyruk sağlam yapılı, erkeklerde gösterişlidir. Kanat büyük ve geniştir. Göğüs orta derinliktedir. Vücut siyah tüylerle kaplıdır. Erkeklerde kuyruk tüyleri ışık altında yeşil-siyah bir görünüm verir. Deri rengi beyazdır. İncik, ayak derisi ve pulları gri renk tonlarında, tüsüz, dört parmaklı ve mahmuzludur. Bacaklar erkeklerde sağlam yapılı, yüksek ve sağlam duruşlu, dişilerde daha kısadır. Yumurta kabuk rengi beyazdır (Şekeroğlu ve Özen, 1997).

Gerze tavukları %5 verime ortalama 160-166 günde ulaşmaktadırlar. Dişilerde bu yaştaki canlı ağırlıkları ise 1400 gram civarındadır (Şekeroğlu ve Özen, 1997). % 50 verim yaşı ise ortalama 186 gündür. Dişilerde ergin canlı ağırlığı 1700 gram erkeklerde ise 2300 gram seviyesindedir. Yumurta veriminin hayvan başına yılda 80-98 adet arasında değiştiğini belirleyen çalışmalar mevcuttur (Şekeroğlu, 1994; Özdoğan ve Gürcan, 2006). Yumurta verimleri düşük olarak kabul edilse de yumurta ağırlıkları yüksek sayılabilecek seviyede, 47-51 gram arasında değişmektedir. Türkiye evcil gen kaynakları raporunda civcivlerin kuluçkadan çıkış ağırlığı ortalama 37 gram olarak belirtilmiştir. Bu tavuklardaki verim düşüklüğü, ticari hibritler ile mücadele etmelerinin önüne geçmektedir. Ayrıca, yerel ırklar ile yapılan ticari üretim de oldukça kısıtlıdır. Ancak, dünyanın farklı bölgelerinde düşük verimli yerel tavuk ırklarının ıslah çalışmaları neticesinde ticari üretimde kullanıldığı bilinmektedir (Sarıca ve Yamak, 2010).



Tavuk yumurtası şeklinin tanımı, çok sayıda uygulama ve çalışma için önemlidir. Genel olarak, kuş yumurtaları hakkında konuşurken (hem evcil hem de yabani türler), geometrik parametrelerinin bilgisi, popülasyon ve ekolojik morfoloji (Mänd, 1998), civciv ağırlığının tahmin edilmesi (Narushin ve ark., 2002), yumurta kuluçka kabiliyeti (Narushin ve Romanov, 2002), kabuk kalitesi (Şekeroğlu ve Altuntaş, 2009), yumurta iç parametreleri, kuş biyolojisi, taksonomi, sınıflandırma, üreme, kanatlı seçimi, genetik ve işleme gibi bir dizi çalışma ile ilgilidir. Şekil indeksi de kuluçkalık yumurtalar için önemli bir faktör olarak tanımlanmaktadır (Başpınar ve ark., 1997; Esen ve Ozelik, 2002). Seker ve ark. (2005) yaptıkları çalışmada yumurta şekil indeksi değerlerinin kuluçka üzerinde önemli bir etkiye sahip olduğunu belirlemişlerdir. Bu konuda yapılan çalışmaların benzer sonuçlar vermesi kuluçka çalışmalarında yumurta şekil indeksinin de dikkate alınması gerektiğini göstermektedir (Shanawany, 1987). Sarı ve ark. (2010) ise yumurta şekil indeksinin verimliliğin önemli bir göstergesi olabileceğini öne sürmüştür. Bu çalışmada Gerze tavuklarında, yaklaşık 30 haftalık bir üretim dönemi boyunca elde edilen yumurtalarda yumurta ağırlığının ve şekil indeksinin yaşa bağlı değişimi ortaya koyulmaya çalışılmıştır.

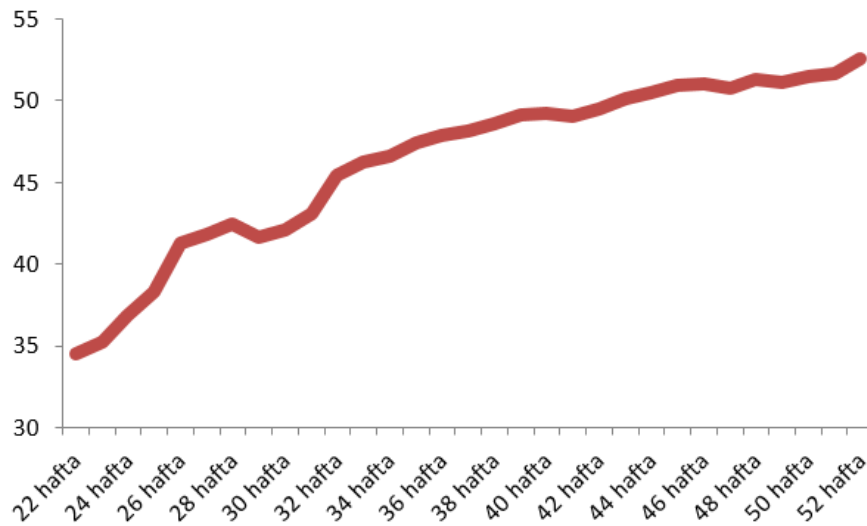
2. Materyal ve Yöntem

Bu çalışma Ondokuz Mayıs Üniversitesi Ziraat Fakültesi Araştırma ve Uygulama Çiftliğinde yürütülmüştür. Çalışma Ondokuz Mayıs Üniversitesi Hayvan Deneyleri Yerel Etik Kurulunun 2020/63 nolu onayı ile kabul edilen "Gerze Tavuklarında seleksiyon ile canlı ağırlık ve besi performansının artırılması" başlıklı projeden elde edilen yumurtalarda yapılmıştır. On sekiz haftalık yaştaki, toplam 120 dişi 16 erkek Gerze tavuğu, 1,5x1,5 metre ölçülerindeki 8 bölmeye, her birinde 15 dişi ve 2 erkek olacak şekilde rastgele yerleştirilmiştir. Günlük 8 saat olacak şekilde başlatılan aydınlatma, üçer gün ara ile birer saat artırılarak 19 haftalık yaşta 10 saat; 20

haftalık yaşta ise 12 saatlik aydınlatma uygulanmıştır. Yine bu dönemde folluklar açılarak hayvanların alışmaları sağlanmıştır. Üç gün sonra aydınlatma 13 saate çıkarılmıştır. Beş hafta sonra tavuklar 25 haftalık yaşta iken aydınlatma yarım saat artırılarak 13,5 saat olmuştur. 34 haftalık yaşa geldiklerinde 14 saat aydınlatmaya ulaşılmış ve deneme sonuna kadar sabit bırakılmıştır. Tavuklar 52 haftalık yaşlarını tamamlayana kadar deneme devam ettirilmiştir. Üretim dönemi boyunca hayvanlara serbest yem ve su verilmiştir. Yumurta verimleri günlük olarak kaydedilmiştir. Tüm yumurtaların ağırlıkları alınıp eni ve boyu dijital kumpas yardımı ile belirlenmiştir. Bu veriler ile yumurta şekil indeksi $\text{Yumurta eni/Yumurta boyu} * 100$ formülü ile hesaplanmıştır. Elde edilen SPSS paket programında, tek yönlü varyans analizi ile karşılaştırılmış ve gruplar arasındaki farklılığın belirlenmesinde Duncan çoklu karşılaştırma testinden yararlanılmıştır.

3. Bulgular

Tavuklar 22 haftalık yaşa geldiklerinde yumurtlama başlamıştır. 52. Haftanın sonuna kadar devam eden yumurtlamanın haftalara göre değişimi Tablo 1'de verilmiştir. Bu 30 haftalık üretim sürecinde toplam 6913 yumurta üretilmiştir. İlk hafta elde edilen yumurtaların ortalama ağırlığı 34,48 gram olarak tespit edilirken 52 haftalık yaşta elde edilen yumurtaların ağırlığı 52,58 grama yükselmiştir. Üretim dönemi boyunca ortalama yumurta ağırlığı 48,32 gram olarak gerçekleşmiştir. Bu dönemde gerçekleşen değişim Şekil 1'de gösterilmektedir. Bu dönemde yumurtalarda ölçülen yumurta en ve boyları da Tablo 1'de verilmiştir. Ortalama yumurta eni 39,74 cm olarak ölçülürken, yumurta boyu 53,76 cm olarak ölçülmüştür. Yumurta en ve boyları kullanılarak hesaplanan şekil indeksi üretim döneminde ortalama olarak 74,05 olarak hesaplanmıştır. Bu dönemde şekil indeksinin haftalara göre değişimi Şekil 2'de gösterilmektedir.

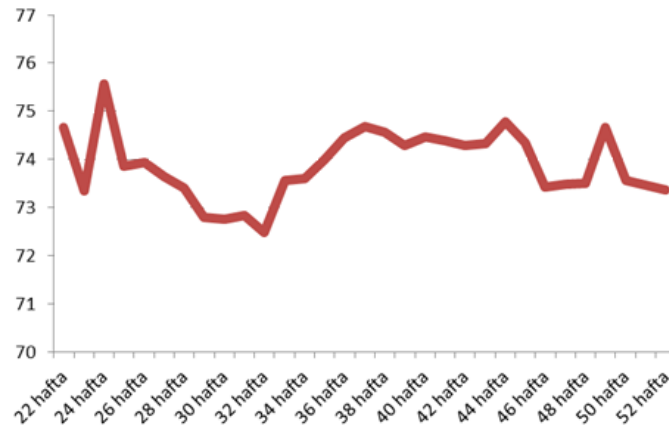


Şekil 1. Yumurta ağırlığının haftalara göre değişimi.

Tablo 1. Gerze tavuklarında üretim döneminde yumurta özellikleri

| Yaş (Hafta) | n | Ağırlık (gram) | Yumurta en (mm) | Yumurta boy (mm) | Şekil İndeksi |
|-------------|------|----------------------|----------------------|----------------------|----------------------|
| 22 hafta | 8 | 34,48 ^r | 35,51 ⁿ | 47,58 ^m | 74,66 ^{abc} |
| 23 hafta | 32 | 35,27 ^r | 35,48 ⁿ | 48,45 ^l | 73,35 ^{cde} |
| 24 hafta | 128 | 36,85 ^p | 36,21 ^m | 48,30 ^l | 75,57 ^a |
| 25 hafta | 183 | 38,33 ^o | 36,67 ^l | 49,81 ^k | 73,86 ^{bcd} |
| 26 hafta | 127 | 41,23 ⁿ | 37,63 ^k | 51,03 ^j | 73,93 ^{bcd} |
| 27 hafta | 107 | 41,85 ^{mn} | 37,77 ^k | 51,38 ^{ij} | 73,65 ^{b-e} |
| 28 hafta | 79 | 42,45 ^{mn} | 37,90 ^k | 51,70 ^{hij} | 73,40 ^{b-e} |
| 29 hafta | 38 | 41,59 ⁿ | 37,95 ^k | 52,23 ^h | 72,80 ^{de} |
| 30 hafta | 46 | 42,05 ^{mn} | 37,74 ^k | 51,95 ^{hi} | 72,75 ^{de} |
| 31 hafta | 87 | 43,10 ^m | 38,05 ^k | 52,32 ^h | 72,83 ^{de} |
| 32 hafta | 158 | 45,37 ^l | 38,63 ^j | 53,39 ^{fg} | 72,49 ^e |
| 33 hafta | 216 | 46,26 ^{kl} | 39,10 ⁱ | 53,22 ^g | 73,56 ^{b-e} |
| 34 hafta | 226 | 46,56 ^{ikl} | 39,16 ⁱ | 53,27 ^{fg} | 73,60 ^{b-e} |
| 35 hafta | 238 | 47,37 ^{ijk} | 39,45 ^{hi} | 53,40 ^{fg} | 73,99 ^{bcd} |
| 36 hafta | 381 | 47,81 ^{hij} | 39,78 ^{gh} | 53,50 ^{efg} | 74,45 ^{abc} |
| 37 hafta | 379 | 48,10 ^{ghi} | 39,84 ^{gh} | 53,41 ^{fg} | 74,68 ^{abc} |
| 38 hafta | 378 | 48,57 ^{ghi} | 39,88 ^{fgh} | 53,60 ^{efg} | 74,56 ^{abc} |
| 39 hafta | 378 | 49,11 ^{e-h} | 40,02 ^{efg} | 53,95 ^{d-g} | 74,28 ^{abc} |
| 40 hafta | 367 | 49,21 ^{e-h} | 40,15 ^{c-g} | 53,99 ^{d-g} | 74,46 ^{abc} |
| 41 hafta | 354 | 49,02 ^{fgh} | 40,07 ^{d-g} | 53,94 ^{d-g} | 74,38 ^{abc} |
| 42 hafta | 310 | 49,46 ^{d-g} | 40,16 ^{c-g} | 54,12 ^{def} | 74,28 ^{abc} |
| 43 hafta | 321 | 50,07 ^{c-f} | 40,31 ^{b-f} | 54,30 ^{cde} | 74,33 ^{abc} |
| 44 hafta | 319 | 50,47 ^{b-e} | 40,54 ^{abc} | 54,44 ^{bcd} | 74,79 ^{ab} |
| 45 hafta | 307 | 50,90 ^{bc} | 40,41 ^{a-e} | 54,48 ^{bcd} | 74,35 ^{abc} |
| 46 hafta | 293 | 51,00 ^{bc} | 40,38 ^{a-e} | 55,06 ^{abc} | 73,43 ^{b-e} |
| 47 hafta | 302 | 50,75 ^{bcd} | 40,36 ^{a-e} | 54,99 ^{abc} | 73,49 ^{b-e} |
| 48 hafta | 274 | 51,29 ^{abc} | 40,47 ^{a-e} | 55,15 ^{ab} | 73,50 ^{b-e} |
| 49 hafta | 225 | 51,14 ^{bc} | 40,51 ^{a-d} | 54,49 ^{bcd} | 74,66 ^{abc} |
| 50 hafta | 185 | 51,50 ^{abc} | 40,59 ^{abc} | 55,26 ^{ab} | 73,57 ^{b-e} |
| 51 hafta | 236 | 51,63 ^{ab} | 40,62 ^{ab} | 55,37 ^a | 73,47 ^{b-e} |
| 52 hafta | 231 | 52,58 ^a | 40,79 ^a | 55,67 ^a | 73,37 ^{cde} |
| Ortalama | 6913 | 48,32 | 39,74 | 53,76 | 74,05 |

^{a,b}: aynı sütunda farklı harflerle gösterilen değerler arasındaki farklar istatistik olarak önemlidir (P<0,05).



Şekil 2. Gerze tavuklarında şekil indeksinin haftalara göre değişimi

4. Tartışma ve Sonuç

Çalışmada 22 haftada yumurtlamaya başlayan Gerze tavuklarında ilk hafta yumurta ağırlığı 34,48 gram olarak tespit edilmiştir. İlerleyen tüm haftalarda artış göstererek 52 hafta sonunda 52,58 grama ulaşmıştır.

Yumurta ağırlığındaki bu artış, yumurta ağırlığı üzerine yaş ve genotipin (Doyon ve ark., 1985; Sarıca ve ark., 2010) önemli olduğunu oraya koyan çalışmaların sonuçlarına benzerlik göstermektedir. Tavuklar 52 haftalık yaşa gelene kadar ürettikleri yumurtaların

ortalama ağırlığı 48,32 gram olarak tespit edilmiştir. Elde edilen yumurta ağırlıkları, Şekeroğlu ve Özen (1997)'in tespit ettiği 47,6 gram ağırlığı ile uyumludur. Benzer şekilde Özdoğan ve Gürcan (2006), yumurta ağırlık ortalamalarını 47,85 ile 51,13 gram aralığında tespit etmişlerdir.

Yumurta şekil indeksi, yumurta eninin yumurta uzunluğuna oranıdır (Narushin ve Romanov, 2002). Yumurtanın şekli, tavuğun anatomik yapısına, özellikle yumurta kanalının yapısına bağlıdır (King'ori, 2012). Tavuk yumurtaları için ideal şekil indeksi 74'tür. 72-76 arasındaki şekil indeksine sahip olan yumurtalar normal şekillidir. İndeksin 76'dan büyük olduğu yumurtalar yuvarlak, 72'den küçük olduğu yumurtalar ise sivri şekillidir (Sarıca ve Erensayın, 2009). Çalışmamızda elde edilen yumurtaların şekil indeksi, ilk haftadan çalışmanın sonuna kadar ideal şekilli olarak tanımlanan 72-76 aralığındadır (Şekil 2). Kanatlı türlerini karakterize etmek için önemli bir faktör (Song ve ark., 2000) ve yumurta kalitesinin bir göstergesi olarak kabul edilen şekil indeksi, civcivlerin hayatta kalması için de çok önemlidir. Üretim döneminde elde edilen yumurtaların ortalama şekil indeksi 74,05 olarak belirlenmiştir. Bu değer Kaya ve Yıldız (2014)'ün tespit ettiği 75,07 ve Şekeroğlu ve Özen (1997)'in belirlediği 75,05 değerlerine benzerdir. Bu durum Gerze tavuklarına ait yumurtanın ideal yumurta şekline sahip olduğunu ortaya koymaktadır. Şekil indeksinde yaşa bağlı olarak düzenli bir artma ya da azalma meydana gelmemiştir. Bu durum, Sarıca ve ark. (2010)'nın değişik yumurtacı hibritlerde şekil indeksinin yaşa bağlı olarak azaldığı görüşünün aksine gerçekleşmiştir. Yumurta eni ve boyu ilerleyen yaşla birlikte artış göstermiştir. Bu durumda şekil indeksinde de çok ciddi artışlar meydana gelmemiştir.

Katkı Oranı Beyanı

Yazar(lar)ın katkı yüzdesi aşağıda verilmiştir. Tüm yazarlar makaleyi incelemiş ve onaylamıştır.

| | C.A. | E.C. | U.S.Y. |
|-----|------|------|--------|
| K | 30 | 30 | 40 |
| T | 30 | 30 | 40 |
| Y | 30 | 30 | 40 |
| VTI | 30 | 30 | 40 |
| VAY | 30 | 30 | 40 |
| KT | 30 | 30 | 40 |
| YZ | 30 | 30 | 40 |
| KI | 30 | 30 | 40 |
| GR | 30 | 30 | 40 |
| PY | 10 | 10 | 80 |
| FA | | | 100 |

K= kavram, T= tasarım, Y= yönetim, VTI= veri toplama ve/veya işleme, VAY= veri analizi ve/veya yorumlama, KT= kaynak tarama, YZ= Yazım, KI= kritik inceleme, GR= gönderim ve revizyon, PY= proje yönetimi, FA= fon alımı.

Çalışma Beyanı

Yazarlar bu çalışmada hiçbir çıkar ilişkisi olmadığını beyan etmektedirler.

Etik Onay Beyanı

Bu araştırma Ondokuz Mayıs Üniversitesi Hayvan Deneyleri Yerel Etik Kurulu tarafından onaylanmıştır (onay tarihi: 27 Kasım 2020, onay numarası: 2020/63).

Destek ve Teşekkür Beyanı

Bu çalışma Ondokuz Mayıs Üniversitesi Bilimsel Araştırma Projeleri PYO.ZRT.1904.22.009 nolu proje ile TAGEM ARGE 20/10 nolu projelerin verilerinden üretilmiştir.

Kaynaklar

- Başpınar E, Yıldız MA, Özkan MM, Kavuncu O. 1997. The effect of egg weight and shape index on hatchability in Japanese Quail eggs, *Turkish J Vet Anim Sci*, 21(1): 53-56.
- Doyon G, Bernier-Cardou M, Hamilton RMG, Castaigne F, MacLean H. 1985. Egg quality: 1. shell strength of eggs from five commercial strains of white leghorn hens during their first laying cycle. *Poultry Sci*, 64: 1685-1695.
- Esen A, Özcelik M. 2002. The effect of age of parents, egg weight and shape index on hatchability in quails. *Firat Univ J Health Sci*, 16(1): 19-25.
- Kaya M, Yıldız MA. 2014. Tavuğun evcilleştirilmesi ve Türkiye yerli tavuk ırkları. *Tavukçuluk Araşt Derg*, 11(2): 21-28.
- King'ori AM. 2012. Poultry egg external characteristics: egg weight, shape and shell colour. *Res J Poultry Sci*, 5(2): 14-17.
- Mänd R. 1998. Intrapopulation variation of avian eggs. *T Sutt*, ed. Valgus, Tallinn, Estonia.
- Narushin V, Romanov MN, Bogatyr V. 2002. AP-animal production technology: relationship between pre-incubation egg parameters and chick weight after hatching in layer breeds, *Biosyst Eng*, 83(3): 373-381.
- Narushin VG, Romanov MN. 2002. Egg physical characteristics and hatchability. *World's Poultry Sci J*, 58: 297-303.
- Özdoğan N, Gürcan İS. 2006. Denizli ve Gerze yerli tavuk ırklarında yumurta verimine ait bazı özellikler. *Lalahan Hayv Araşt Enst Derg*, 46(2): 13-21.
- Sarı M, Tilki M, Saatci M, Işık S, Önk K. 2010. Japon bıldırcınlarında (*Coturnix coturnix japonica*) ebeveyn yaşı, yumurta ağırlığı ve şekil indeksinin kuluçka özellikleri ve yaşama gücü üzerine etkisi, *Firat USBV Derg*, 24(2): 93-97.
- Sarıca M, Erensayın C. 2009. Poultry products. *Bey-Ofset*, Ankara, Türkiye, pp: 89-138.
- Sarıca M, Yamak US, Boz MA. 2010. Dış kaynaklı ve yerli hibritlerde yumurta kalitesinin yaşa bağlı değişimi. *Tavukçuluk Araşt Derg*, 9: 11-17.
- Sarıca M, Yamak US. 2010. Yavaş gelişen etlik piliçlerin özellikleri ve geliştirilmesi. *Anadolu Tar Bil Der*, 25(1): 61-67.
- Seker I, Kul S, Bayraktar M, Yildirim O. 2005. Effect of layer age on some egg quality characteristics and egg production in Japanese quail (*Coturnix coturnix japonica*), *J Fac Vet Medic Istanbul Univ*, 31(1): 129-138.
- Shanawany M. 1987. Hatching weight in relation to egg weight in domestic birds, *World's Poultry Sci J*, 43(2): 107-115.
- Song KT, Choi SH, Oh HR. 2000. A comparison of egg quality of pheasant, chukar, quail and guinea fowl. *AJAS*, 13(7): 986-990.
- Şekeroğlu A, Altuntaş E. 2009. Effects of egg weight on egg quality characteristics, *J Sci Food Agri*, 89(3): 379-383.
- Şekeroğlu A, Özen N. 1997. Gerze (Hacıkadı) ve Denizli tavuk ırklarının bazı verim özellikleri bakımından karşılaştırılması. *Akdeniz Üniv Ziraat Fak Derg*, 10: 41-57.



PROTEİN İÇERMİYEN MEDYA İLE OLGUNLAŞTIRILAN İMMATÜR SIĞIR OOSİTLERİNİN *İN VİTRO* FERTİLİZASYONU VE BLASTOSİSTE KADAR GELİŞİMLERİ

Yusuf Ziya GÜZEY^{1*}

¹Mustafa Kemal University, Agricultural Faculty, Department of Animal Sciece, 31060, Hatay, Türkiye

Özet: Henüz doğmamış buzağılardan elde edilen fetal buzağı serumu, buzağının acı çekmesine neden olmaktadır. Hayvanlara daha az acı çektilmesi ve hayvan refahı gibi konularda süregelen tartışmalar neticesinde özellikle son yıllarda, *in vitro* embriyo ve hücre kültüründe fetal serum ikamelerinin kullanıma olanaklarına dair çok sayıda araştırma yapılmaktadır. Bununla birlikte serum içerisinde mevcut olan ve konsatrasyonu tam olarak belirlenemeyen moleküllerin hücrel işlevler üzerine etkilerinden dolayı özellikle tekli moleküler yolların araştırıldığı çalışmalarda serum kullanımı bazı çakışmalara neden olabilmektedir. Bu amaçla, serum ikamelerinin kullanım olanaklarının araştırıldığı bu çalışmada, *in vitro* matürasyon için knockout serumTM kullanımının ilk bölünme ve blastosiste kadar gelişen embriyo sayısının önemli oranda artırdığı tespit edilmiştir. Bununla birlikte sentetik serum ikamesi ve serum ikamesi 2 kullanımının ise elde edilen embriyo sayılarını bir miktar düşürdüğü belirlenmiştir.

Anahtar kelimeler: IVF, Serum ikamesi, Sığır, Olgunlaştırma, Blastosist, Oosit

In Vitro Fertilization of Immature Bovine Oocytes Matured In a Protein-Free Media and Their Subsequent Development to the Blastocysts

Abstract: Fetal calf serum obtained from unborn calves causes pain to the calf. As a result of the ongoing discussions on issues such as less suffering to animals and animal welfare, especially in recent years, there has been a lot of research on the possibilities of using fetal serum substitutes in *in vitro* embryo and cell culture. However, the use of serum may cause some conflicts, especially in studies investigating single molecular pathways, due to the effects of molecules present in serum and whose concentration cannot be determined precisely on cellular functions. For this purpose, in this study, in which the possibilities of using serum substitutes were investigated, it was determined that the use of knockout serumTM for *in vitro* maturation significantly increased the number of embryos developing until the first division and blastocyst. On the other hand, it was determined that the use of synthetic serum substitution and serum substitution 2 slightly reduced the number of embryos obtained.

Keywords: IVF, Serum replacement, Bovine, Maturation, Blastocyst, Oocyte

*Sorumlu yazar (Corresponding author): Mustafa Kemal University, Agricultural Faculty, Department of Animal Sciece, 31060, Hatay, Türkiye

E mail: yzguzey@gmail.com (Y. Z. GÜZEY)

Yusuf Ziya GÜZEY <https://orcid.org/0000-0002-4900-6038>

Gönderi: 11 Haziran 2023

Kabul: 16 Temmuz 2023

Yayınlanma: 15 Ekim 2023

Received: June 11, 2023

Accepted: July 16, 2023

Published: October 15, 2023

Cite as: Güzey YZ. 2023. *In vitro* fertilization of immature bovine oocytes matured in a protein-free media and their subsequent development to the blastocysts. BSJ Eng Sci, 6(4): 321-324.

1. Giriş

Özellikle verim yönünde yapılan iyileştirmeler sonucunda buzağılama oranı düvelerde %55-60, sağmal ineklerde ise %35-40 seviyelerine kadar düşmüştür. Bu noktada, sürü seviyesinde, üretim ve üreme özellikleri arasındaki negatif genetik korelasyonlar etkilidir (Lonergan ve ark. 2016).

Hayvansal kaynaklı protein içermeyen medyaların *in vitro* fertilizasyonda (IVF) kullanımı hipoalerjenik bileşenleri bulundurmaması, içeriği tam tanımlanabilir olduğundan embriyo gelişimi üzerinde daha iyi kontrol sağlanması, alıcı ile verici arasındaki immünolojik uyumluluk ve serum kaynaklı enfeksiyon risklerinin azaltılması gibi pek çok noktada avantaj sağlamaktadır. Sığır embriyolarının *in vitro* üretim koşullarının iyileştirilmesi ve daha detaylı tanımlanması üzerine,

özellikle son 20 yıllık süreç içerisinde birçok çalışma yapılmıştır. Serum içerisinde mevcut olan ve konsatrasyonu tam olarak belirlenemeyen moleküllerin hücrel işlevler üzerine etkilerinden dolayı özellikle tekli moleküler yolların araştırıldığı çalışmalarda serum kullanımı bazı çakışmalara neden olabilmektedir. Her ne kadar serumun oosit matürasyonu ve *in vitro* embriyo üzerine olumlu etkileri birçok araştırma sonucu ile ortaya konmuş olsa da bazı çekincelerin bulunması araştırmacıları ticari embriyo üretiminde hayvansal kaynaklı olmayan alternatif çözümlere yöneltmektedir (Grad ve ark., 2010; Korhonen ve ark., 2010; Çevik ve ark., 2014).

Protein içermeyen medya ile yapılan kültürde kümülüs-oosit kompleksi (KOK) ve oositler, plastik/cam malzemeye yapışabilmekte ve müdahale güçleşmektedir. Bununla birlikte serum, hormonlar, büyüme faktörleri,



vitaminler, peptitler gibi bir seri molekül içerebilmekte ve bu nedenle de serum kaynakları arasında biyolojik aktivite bakımından önemli farklılıklar olabilmektedir (Çevik ve ark., 2011). Ayrıca, hayvan kaynaklı serumlar özellikle viral ve prion kaynaklı enfeksiyonlar için potansiyel kaynaklardır (Chanson ve ark., 2001).

Mevcut serum kaynaklarının gerek hayvanlara eziyet alanındaki endişeleri ve gerekse de muhtemel kontaminasyon risklerinin elimine edilmesi bakımından serum ikameleri son yıllarda tercih edilen bir alternatif oluşturmaktadır. Yapılan bu çalışma ile IVF laboratuvarlarının çalışma protokollerinin günümüz teknolojileri doğrultusunda güncellenmesi ve böylece *in vitro* embriyo üretimindeki başarı oranının artırılması amaçlanmıştır.

2. Materyal ve Yöntem

Çalışma Hatay Mustafa Kemal Üniversitesi, Ziraat Fakültesi Embriyo Kültürü laboratuvarında yürütülmüştür. Kullanılan stok solüsyonlar Caisson Labs (Sugar City, ID, USA) isimli firmadan satın alınmıştır. Araştırma materyalini, Antakya'da özel bir kesimhanede kesilen sığırlardan alınan ovaryumlardan elde edilen KOK ve oositler oluşturmuştur. Bu amaçla uygun taşıma koşullarında laboratuvara getirilen ovaryumlar üzerindeki 2-6 mm çaplı yüzeysel foliküllerden, iğne takılı enjektör yardımı ile KOK içeren folikül sıvısı alınarak 15 mL tüp içerisinde toplanmıştır. Folikül sıvısının içerdiği KOK'lar stereo mikroskop yardımı ile 10× büyütmede bulunarak morfolojik değerlendirme sonucunda düzgün bir sitoplazma ve zona pellucida yapısına sahip, atretik olmayan ve çevresinde yeterince kümülüs hücresi bulunan oositler matürasyon için seçilmişlerdir. Seçilen oositler deneme gruplarına ayrılarak 38 °C' de, havada %5 CO₂ ve maksimum nem koşulları altında matürasyon için kültüre alınmıştır. Deneme gruplarına göre tasarlanan matürasyon medyalarının kompozisyonu aşağıdaki şekildedir.

MatC= TCM 199 + pirüvat (22µg/ml) + FSH (5 µg/ml) + LH (1 µg/ml) + E₂ (4 ng/mL) + 50 IU Penisilin + 50 mg Streptomisin + %10 fetal buzağı serumu (FBS)

MatSR2= TCM 199 + pirüvat (22µg/ml) + FSH (5 µg/ml) + LH (1 µg/ml) + E₂ (4 ng/mL) + 50 IU Penisilin + 50 mg Streptomisin + %10 Serum Replacement 2 (SR2)

MatKSr= TCM 199 + pirüvat (22µg/ml) + FSH (5 µg/ml) + LH (1 µg/ml) + E₂ (4 ng/mL) + 50 IU Penisilin + 50 mg Streptomisin + %10 Knock-out Serum (KSr)

MatSSS= TCM 199 + pirüvat (22µg/ml) + FSH (5 µg/ml)

+ LH (1 µg/ml) + E₂ (4 ng/mL) + 50 IU Penisilin + 50 mg Streptomisin + %10 Serum Substitute Supplement (SSS) Matürasyon medyalarında deneme grupları için kullanılan SR2, Sigma-Aldrich (S9388); KSr, ThermoFisher Sci (10828010); SSS ise Irvine Sci (99193) isimli firmalardan satın alınmıştır.

Matürasyon işlemi inkübatör içerisinde yaklaşık olarak 22 saat süresince devam etmiş, bu süre sonunda fertilizasyon medyalarına alınan oositlerde *in vitro* fertilizasyonun sağlanması amacıyla 1×10⁶ sperm/mL konsantrasyonunda spermatozoa ile 8-10 saat süre ile kültüre alınmıştır. Gametlerin *in vitro* fertilizasyonu amacıyla kullanılacak IVF-TALP (IVF-TL, 22 µg/mL pirüvat, 100 U/mL Penisilin, 100 µg/mL Streptomisin, 1 µg/mL, 20 µmol/L penicillamine, 10 µmol/L hypotaurine, 1 µmol/L epinephrine, 6 mg/mL BSA-FAF) ve SP-TALP (SP-TL, 22 µg/mL pirüvat, 100 U/mL Penisilin, 100 µg/mL Streptomisin, 6 mg/mL BSA-FracV) medya kullanılmıştır. Tüm medya geçişlerinde ise HEPES-TALP (Hepes-TL, 22 µg/mL pirüvat + 100 U/mL Penisilin + 100 µg/mL Streptomisin +3 mg/mL BSA-FracV) tampon solüsyon kullanılmıştır.

Fertilizasyonun sağlanması amacıyla gametler 38°C' de, havada %5 CO₂ ve maksimum nem koşulları altında inkübatör içerisinde bekletilmiştir. Ardından mefruz zigotları çevreleyen kümülüs hücreleri vorteks yardımı ile uzaklaştırılmış ve 8'inci güne kadar potasyum simpleks medya içerisinde ve 38°C, %5 CO₂, %5 O₂, %90 N₂ gaz kompozisyonu ve maksimum nem koşullarında inkübatör içerisinde kültüre alınmıştır. Embriyoların içerisinde bulunduğu medya 48 saat aralıkla tazelenmiş ve embriyo gelişimleri izlenerek kaydedilmiştir. Embriyoların kültürü için KSOM-BE (KSOM+AA, 3 mg/mL BSA-FAF, 100 U/mL penisilin, 100 µg/mL Streptomisin) medya kullanılmıştır.

Embriyonik gelişimin değerlendirilmesi amacıyla klevaj ve blastosist aşamasına kadar gelişen embriyo oranları kayıt altına alınmıştır. Bu amaçla kullanılan formüller şu şekildedir;

Klevaj oranı: ikiye bölünen zigot / toplam oosit sayısı

Blastosist oranı: blastosiste kadar gelişen embriyo / ikiye bölünen zigot sayısı.

3. Bulgular ve Tartışma

Araştırma 16 tekerrürlü olarak 4 grup üzerinde yürütülmüştür. Çalışma süresince toplam 1279 adet KOK kullanılmıştır.

Tablo 1. Gelişim aşamalarına göre farklı muamele gruplarının gelişim oranları

| | Kontrol (n=321) | SR2 (n=319) | KSR (n=319) | SSS (n=320) | P |
|------------|----------------------------------|----------------------------------|---------------------------------|---------------------------------|-------|
| 2 hücre | 84,7±0,31 ^{ab} (272) | 81,5±0,39 ^{bc} (260) | 86,5±1,52 ^a (276) | 80,0±0,38 ^c (256) | 0.000 |
| Blastosist | 32,7±0,39 ^b (89) | 29,6±0,46 ^c (77) | 37,0±0,42 ^a (102) | 28,5±0,41 ^c (73) | 0.000 |

Değerler %±ortalamanın standard hatası (n) şeklinde verilmiştir.

Araştırma sonucunda matürasyon medyasına eklenen serum ikamelerinin klevaj oranları üzerine etkisinin önemli olduğu tespit edilmiştir ($P<0,000$). Yapılan Tukey HSD çoklu karşılaştırma testi sonucuna göre in vitro kültüre alınan embriyolarda en yüksek ilk bölünme oranı Knockout Serum™ (KSR) verilen grupta elde edilmiş, kontrol grubu arasındaki farklılık ise istatistiki olarak önemli bulunmamıştır ($P>0,05$). Bununla birlikte Serum İkamesi 2 (SR2) ve Sentetik Serum İkamesi (SSS) verilen gruplarda gözlenen ilk bölünme oranları, Knockout Serum grubuna oranla anlamlı miktarda azalmıştır ($P<0,01$). En düşük ilk bölünme oranları ise %80 ortalama ile sentetik serum ikamesi verilen grupta gözlenmiştir.

Yapılan bu çalışmada medya içerisine serum yerine serum ikamelerinin ilavesi ilk bölünme oranlarının önemli ölçüde artmasına neden olmuştur. İmmatür KOK'ların olgunlaştırılması, blastosiste kadar in vitro embriyo gelişimini etkileyen en kritik aşamaların başında gelmektedir. Oositlerin olgunlaştırılması için kullanılan medyum, sığır embriyolarının gelişimini önemli ölçüde etkilemektedir. İn vitro olgunlaştırma medyalarında sıklıkla kullanılan protein kaynakları serum ve sığır serum albümini (BSA) olarak karşımıza çıkmaktadır (Jin ve ark., 2017; Mingoti ve ark., 2011; Şen ve Kuran, 2018). Serum ilavesi bifazik bir etkiye sahiptir ve embriyo gelişimini erken aşamada inhibe eder, ancak daha sonraki aşamalarda ise destekler (Ali ve Sirard, 2002; George ve ark., 2008; Sağırkaya ve Üstüner, 2010; Sakurai ve ark., 2015). Elde etmiş olduğumuz bulgular, mevcut araştırma sonuçlarının bulguları ile de desteklenmektedir.

Blastosiste kadar gelişen embriyo oranları üzerinden yapılan karşılaştırmada, ilk bölünme oranlarına benzer biçimde, en iyi sonuçlar yine Knockout Serum grubunda elde edilmiştir. Bu gruptaki blastosiste kadar gelişen hücrelerin oranı diğer gruplara oranla önemli oranda artış göstermiştir ($P<0,01$). Bu grubu takiben kontrol grubundaki blastosist oranları diğer iki grup olan sentetik serum ikamesi ve serum ikamesi 2 gruplarına oranla anlamlı biçimde yüksektir ($P<0,001$).

KSR esas olarak özelleşmemiş embriyonik kök hücrelerinin kültürü amacıyla bir serum ikamesi olarak geliştirilmiş olup, pluripoten kök hücrelerinin kültüründe yaygın biçimde kullanılmaktadır. Bununla birlikte SSS, insan albumini ve globulini içeren bir serum ikamesidir ve genel olarak insanlarda yardımcı üreme tekniklerinde kullanılmaktadır. Oositlerin in vitro olgunlaştırılması sonucu elde edilen döllerde canlılık, fötal buzağı serumu içerisindeki serum ve fetuin ile ilişkilidir. Diğer yandan, serum içermeyen ortamda BSA ile yapılan in vitro olgunlaştırma ve fertilizasyonda zona sertleşmesine bağlı olarak başarı azalmaktadır (Motohashi ve ark., 2017).

Her ne kadar serum embriyo kültür ortamına katkı yapsa da, medyadan çıkarılması durumunda belirli moleküllerin embriyo kültüründeki rolü daha iyi analiz edilebilir (Duquew ve ark., 2003). Kültür medyası içerisinde protein bulunmaması durumunda KOK ve oositlerin manipülasyonu zorlaşmakta, plastik ve cam

malzemeye yapışmalarına neden olmaktadır. Bununla birlikte serum hormon, vitamin, peptit ve protein gibi kısmen tanımlanmamış moleküller içerebilmektedir. Hayvan kaynaklı serumlar aynı zamanda viral ve prion kaynaklı enfeksiyonlara da neden olabilmektedir (Bavister ve ark., 1992; Brackett ve Zuelke, 1993; Chanson ve ark., 2001; Smetanina ve ark., 2006; Park ve ark., 2013).

Yapılan bu çalışma FBS kaynaklı protein ve fetuin olmadan da in vitro embriyo üretimi sonucunda sığırlarda canlı döllere elde edilebileceğini göstermiş fakat implantasyon öncesi gelişim potansiyelini destekleyen etkili bileşenlerin bir tanımlaması yapılamamıştır. Bununla birlikte implantasyon sonrası etkileri gösteren bir bulgu da elde edilmediğinden, daha detaylı çalışmaların yapılması gerekmektedir.

4. Sonuç

Mevcut araştırma sonuçları, in vitro fertilizasyon ve embriyo üretiminde fötal serum yerine serum ikamelerinin güvenle kullanılabilirliğini göstermiştir. Yapılan bu çalışmaya göre özellikle Knockout Serum™ sığır embriyolarının in vitro üretiminde güvenle kullanılabilir tanımlanmış kültür medyası olabileceği belirlenmiştir. Sığır oositlerinin in vitro matürasyonu aşamasında, medya içerisine serum yerine eklenen Knockout serum, oosit gelişiminin tamamlanması açısından %10 fötal seruma benzer ve hatta daha iyi sonuçlar elde edilmesine katkı yapabilmektedir. Bu sonuçların elbette ki daha detaylı araştırmalarla desteklenmesi de gerekmektedir. Lipid metabolizması, enerji tüketimi gibi detaylı çalışmalar yapılarak bu mekanizmanın ortaya çıkmasına neden olan faktörlerin belirlenmesi yerinde olacaktır. Bununla birlikte mevcut sonuçlar göz önüne alınarak serum ikamesinin sığır oositlerinin in vitro olgunlaştırmasında güvenle kullanılabilirliği söylenebilir.

Katkı Oranı Beyanı

Yazarın katkı yüzdesi aşağıda verilmiştir. Yazar makaleyi incelemiş ve onaylamıştır.

| | Y.Z.G. |
|-----|--------|
| K | 100 |
| T | 100 |
| Y | 100 |
| VTI | 100 |
| VAY | 100 |
| KT | 100 |
| YZ | 100 |
| KI | 100 |
| GR | 100 |
| PY | 100 |

K= kavram, T= tasarım, Y= yönetim, VTI= veri toplama ve/veya işleme, VAY= veri analizi ve/veya yorumlama, KT= kaynak tarama, YZ= Yazım, KI= kritik inceleme, GR= gönderim ve revizyon, PY= proje yönetimi, FA= fon alımı.

Çatışma Beyanı

Yazar bu çalışmada hiçbir çıkar ilişkisi olmadığını beyan etmektedirler.

Etik Onay Beyanı

Bu araştırmada hayvanlar ve insanlar üzerinde herhangi bir çalışma yapılmadığı için etik kurul onayı alınmamıştır.

Destek ve Teşekkür Beyanı

Hatay Mustafa Kemal Üniversitesi Bilimsel Araştırma Projeleri Koordinatörlüğü tarafından (No. 18.M.042) desteklenmiştir.

Kaynaklar

- Ali A, Sirard MA. 2002. Effect of the absence or presence of various protein supplements on further development of bovine oocytes during in vitro maturation. *Biol Reprod*, 66(4): 901-905. DOI: 10.1095/biolreprod66.4.901.
- Bavister BD, Rose-Hellekant TA, Pinyopummintr T. 1992. Development of in vitro matured/in vitro fertilized bovine embryos into morulae and blastocysts in defined culture media. *Theriogenology*, 37(1): 127-146. DOI: 10.1016/0093-691X(92)90251-L.
- Brackett BG, Zuelke KA. 1993. Analysis of factors involved in the in vitro production of bovine embryos. *Theriogenology*, 39(1): 43-64.
- Chanson A, Nocera D, Senn A, De Grandi P, Germond M. 2001. Development of a well-defined medium for the in vitro maturation of immature bovine cumulus-oocyte complexes. *J Assist Reprod Genet*, 18(2): 97-105. DOI: 10.1023/a:1026534725483.
- Çevik M, Şen U, Kocyigit A, Soydan E, Kuran M. 2011. Effects of serum, gonadotropins, epidermal growth factor and estradiol 17-Beta on cumulus expansion and nuclear maturation of bovine oocytes. *J Fac Vet Med, University of Kafkas*, 17(6): 1009-1014.
- Cevik M, Kocyigit A, Sen U, Kuran M. 2014. Can commercial human embryo culture media be used in bovine embryo culture? *J Fac Vet Med, University of Kafkas*, 20(1): 149-153.
- Duque P, Gomez E, Diaz E, Facal N, Hidalgo C, Diez C. 2003. Use of two replacements of serum during bovine embryo culture in vitro. *Theriogenology*, 59(3-4): 889-899. DOI: 10.1016/s0093-691x(02)01134-2.
- George F, Daniaux C, Genicot G, Verhaeghe B, Lambert P, Donnay I. 2008. Set up of a serum-free culture system for bovine embryos: Embryo development and quality before and after transient transfer. *Theriogenology*, 69(5): 612-623. DOI: 10.1016/j.theriogenology.2007.11.008
- Grad I, Gajda B, Smorag Z. 2010. Effect of plant protein supplementation on in vitro development of porcine embryos. *Animal Sci Papers Rep*, 28(3): 271-279.
- Korhonen K, Kananen K, Ketoja E, Matomaki J, Halmekyö M, Peippo J. 2010. Effects of serum-free in vitro maturation of bovine oocytes on subsequent embryo development and cell allocation in two developmental stages of day 7 blastocysts. *Reprod Domest Anim*, 45(1): 42-49. DOI: 10.1111/j.1439-0531.2008.01203.x.
- Lonergan P, Fair T, Forde N, Rizos D. 2016. Embryo development in dairy cattle. *Theriogenology*, 86(1): 270-277. DOI: 10.1016/j.theriogenology.2016.04.040.
- Mingoti GZ, Castro VSDC, Meo SC, Barretto LSS, Garcia JM. 2011. The effects of macromolecular and serum supplements and oxygen tension during bovine in vitro procedures on kinetics of oocyte maturation and embryo development. *In Vitro Cell Dev Biol Anim*, 47(5-6): 361-367. DOI: 10.1007/s11626-011-9400-0.
- Motohashi HH, Taniguchi R, Sakamoto J, Sankai T, Kada H. 2017. Live, full-term mouse pups from oocytes grown and matured in vitro with serum substitutes. *Reprod Biol*, 17: 180-184.
- Parl YH, Gong SP, Kim HY, Kim GA, Choi JH, Ahn JY, Lim HM. 2013. Development of a Serum-free defined system employing growth factors for preantral follicle culture. *Mol Reprod Dev*, 80(9): 725-733. DOI: 10.1002/mrd.22204.
- Sağırkaya H, Üstüner B. 2010. Replacement of fetal calf serum with two different synthetic sera in in vitro maturation medium: effects on maturation, fertilization and subsequent development of cattle oocytes in vitro. *Uludag Univ J Fac Vet Med*, 29(2): 51-56.
- Sakurai M, Suzuki C, Yoshioka K. 2015. Effect of knockout serum replacement supplementation to culture medium on porcine blastocyst development and piglet production. *Theriogenology*, 83(4): 679-686. DOI: 10.1016/j.theriogenology.2014.11.003.
- Smetenina IG, Tatarinova LV, Krivokharchenko AS. 2006. In vitro fertilization of bovine oocytes in protein-free culture system. *Ontogenez*, 37(6): 438-443.
- Sen U, Kuran M. 2018. Low incubation temperature successfully supports the in vitro bovine oocyte maturation and subsequent development of embryos. *Asian-Australas J Anim Sci*, 31(6): 827-834.



DETERMINATION OF HARNESS PRODUCTION TIME AND DEFECTIVE PRODUCT FORMATION RISK FACTORS WITH ARTIFICIAL NEURAL NETWORK

Gülşah KURNAZ¹, Naci MURAT^{1*}


¹Ondokuz Mayıs University, Department of Industrial Engineering, Faculty of Engineering, 55139, Samsun, Türkiye

Abstract: The aim of this research is to estimate the projected production times of the cable harnesses produced for the tender in a company operating in the aviation and defense industry in our country by artificial neural network. For this, artificial neural network model has been formed for the number of work order, the number of cable harness module, the number of cable harness pin, the number of cable harness label, the number of cable harness back shell, the number of cable harness heat shrink tube, and the number of cable harness terminal variables which may have an effect on the projected production times of cable harnesses for the tender. Multiple linear regression analysis method is used to compare the predictive power of this model and the most appropriate method for estimating the projected production time of cable harnesses for the tender is provided. The aim of the research is to determine the effect of cable harness connector type, cable harness label type and personnel competence level risk factors on the formation of faulty cable harnesses determined during the quality control and electrical testing steps in the production process using logistic regression analysis.

Keywords: Machine learning, Artificial neural networks, Logistic regression analysis, Determination of risk factors

*Corresponding author: Ondokuz Mayıs University, Department of Industrial Engineering, Faculty of Engineering, 55139, Samsun, Türkiye

E mail: nacimurat@omu.edu.tr (N. MURAT)

Gülşah KURNAZ  <https://orcid.org/0000-0002-1341-1517>

Naci MURAT  <https://orcid.org/0000-0003-2655-2367>

Received: May 12, 2023

Accepted: July 25, 2023

Published: October 15, 2023

Cite as: Kurnaz G, Murat N. 2023. Determination of harness production time and defective product formation risk factors with artificial neural network. BSJ Eng Sci, 6(4): 325-329.

1. Introduction

Computers and computer systems having critical role among the indispensable elements of our life have had limited capabilities such as to be able to make calculation or transfer data in the past. Nowadays, it has the ability to be able to operate and interpret its decision mechanism on existing or future situations by using large amounts of data (Alpaydın, 2010). On the other hand, the rapid digitization of the world and the increase in internet usage, which offers instant access to information and news, have increased total data (Pacci et al., 2023). In parallel with these developments in technology, the amount of numerical information produced in enterprises is increasing. It is seen that databases have reached the level of being able to store larger amounts of data and it is easier to access the data (Leech et al., 2004). This has revealed the presence of large data concept with high capacity and capacity increasingly a wide range of data (Bayır, 2006). Each day, the storage of increasing data and reaching the data have started to be difficult for businesses. For this reason, the enterprises are required to provide sustainable competitive advantage that makes it possible to provide products or services with a higher value added value. It is not always possible to work with experts who are accurate, realistic, and have sufficient knowledge and foresight in making strategic decisions

that determine the future of enterprises in order to ensure the highest efficiency (Kotsiantis, 2007). Strategic decision-making and predictions are able to save the workforce and cost when performing the computer. In addition, it provides many gains such as being able to be objective and the information needed is easily copied and replicate (Kurt et al., 2017). Machine learning is defined as a method that uses AI, statistics and mathematics to make strategic decisions, predict, and use knowledge from experience. Artificial intelligence benefiting from statistics and mathematics; The machine learning described as a method that uses the information obtained from strategic decision-making, prediction, and experiences (Jackson, 2002; Karabulut and Alpar, 2011). Inspired by the human brain, which incorporates the ability to discover or produce new information, artificial neural networks (ANNs) are a simulation of the biological nervous system that can perform complex calculations by creating relationships and performing them automatically (Beale et al., 2010). Artificial neural networks are a branch of computer science developed for systems that are difficult or impossible to program (Öztemel, 2003). Artificial neural networks are called structures consisting of many interconnected nodes, which are expressed as simple nerves and mostly function in parallel (Elmas, 2003). Artificial neural



networks are usually a structure consisting of the input layer, hidden layers and output layer (Öğücü, 2006; Buduk, 2013). In artificial neural networks, each of the neurons is connected by synaptic weight to other neurons in the previous layer (Kalogirou, 2000). The artificial nerve cell, expressed as the smallest unit of an artificial neural network, consists of five main parts: inputs, weights, joining function, activation function and output (Gürsoy, 2012). Methods used in machine learning such as classification, clustering and estimation are among the basic functions of artificial neural networks (Chiang et al., 2004; Küçükşille, 2009). In this study, it is aimed to estimate the production times of cable sets produced in a company operating in the aviation and defense industry of our country through artificial neural networks.

2. Materials and Methods

2.1. Materials

In a company that has been operating in the aerospace and defense industry for many years, approximately 650 different types of harness are produced in “IPC/EIA J-STD-001C Requirements for Soldered Electrical and Electronic Assemblies” and “IPC/WHHA-A-620 Requirements and Acceptance for Cable and Wire” Harness Assemblies standards. In order to produce these cable sets, a tender for the purchase of labor services has been opened.

This study was completed between August 2016 and November 2018 and the projected production times of the cable tools (harness) delivered for the tender were determined with the help of machine learning algorithms. For this purpose, it was determined that the cable module, cable pin, cable label, cable back-ring, cable macaroon and cable terminal were both used jointly and went through similar integration processes during the production of 187 of the 650 types of cable set produced in the company (Figure 1).

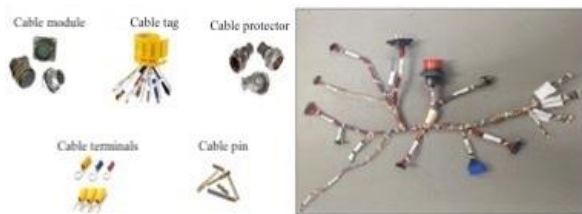


Figure 1. Materials commonly used in cable set production.

In this study, the competence level of the personnel who produce cable set connector type, cable set label type, and cable set label type was determined as independent risk factors that affected the formation of defective cable sets detected during quality-control and test processes after the production of cable sets. Therefore, the type of cable set connector, the cable set label type, the level of competence of the personnel who produce the cable set are as independent variable; whether there is a defect in the products during the quality control and testing processes of the cable sets is determined as dependent variable. The risk factors that affect the formation of defective products are shown in Figure 2.



Figure 2. Risk factors that affect defective product formation.

2.2. Method

Modeling has been established for the analysis to be carried out to determine the cable tool production time, risk factors affecting defective products and defective/defective cable sets. Artificial neural networks, which are formed by the combination of nerve cells expressed as basic units by forming parallel bonds within various layers, obtain information from the learning process just like in the human brain (Haykin, 1994; Tiryaki et al., 2015).

Although artificial neural networks usually consist of an input layer, hidden layers and an output layer, basically each neuron binds to other neurons in the previous layers with the help of their synaptic weight (Kalogirou, 2000). The structure of the artificial neural network is shown in Figure 3.

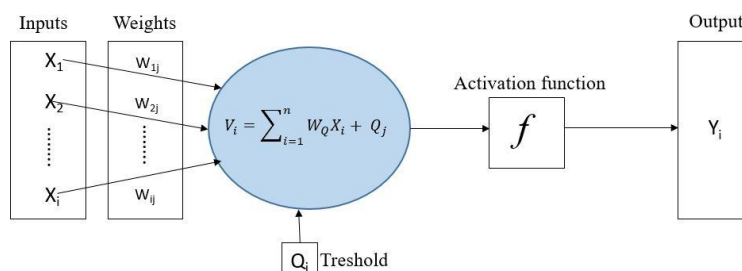


Figure 3. Structure of artificial neural network (Elmas, 2003).

In the structure of the artificial neural network shown in Figure 3, the inputs expressed with X_i transmit the information obtained from the environment to the nerve. The weights expressed by W_i determine the effect of inputs taken by the artificial nerve on the nerve. The large weight value refers to the strong binding of the corresponding input to the artificial nerve, while the small weight value refers to the weak attachment of the corresponding input to the artificial nerve (Elmas, 2003). The aggregation process indicated by V_i in the nerve is added to the activity function by adding the total of the weights to the threshold value obtained from the sum of their product (Q_i) with the inputs to which they belong. The result of the aggregation function is then passed through the activity function expressed by $f(\text{activity})$ and forwarded to the output. The activity function allows the output of the collection function to change when time is involved.

2.2.1. Modeling with artificial neural network

Since back propagation algorithm is the most frequently used algorithm for solving prediction problems with artificial neural network model in the literature, multilayer feedforward back propagation machine learning algorithm was also used in this study. In this study, 7 independent variables were determined that the projected production periods can affect the production time in order to be estimated. These variables represent the input number of the artificial neural network model (Figure 4). The output layer was determined as production times in the tender.

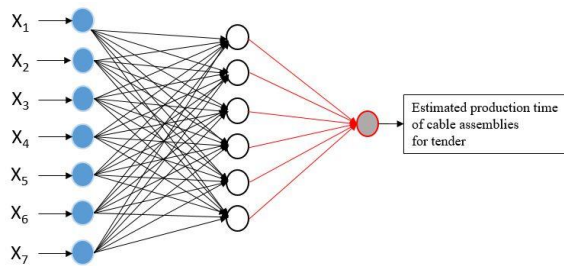


Figure 4. The artificial neural network architecture of the model.

In the study, Knime 3.6.2 program was used in the analysis of the artificial neural network model. Normalization was applied to these values in order to keep the impact of input variables in very low or very large value in the formation of the artificial neural network. The most critical stage of the neural network is the training of the network. For this, the partitioning operator in the Knime 3.6.2 program was used in order to divide 70% of the 415 datasets for training (290 units) and 30% (125 units) for testing.

3. Results and Discussion

Evaluation results of the models created for the detection of defective or flawless cable sets detected in quality control and test steps using machine learning algorithms are included.

3.1. Evaluation of the Artificial Neural Network Model

Mean absolute error (MAE), mean square error (MSE), root mean square error (RMSE) and R² values were examined as performance criteria after the application of the artificial neural network model created to determine cable tool production times (Table 1).

Table 1. Artificial neural network model predictive performance criteria and values

| Criterion | Value |
|---------------------------------|-------|
| R ² | 0.852 |
| MAE (Mean Absolute Error) | 0.013 |
| MSE (Mean Squared Error) | 0.001 |
| RMSE (Root Mean Squared Error) | 0.036 |

The relationship between the estimated values reached after the application of the artificial neural network model and the actual values is shown in Figure 5. When evaluated, this graph shows that the actual values are estimated with high accuracy.

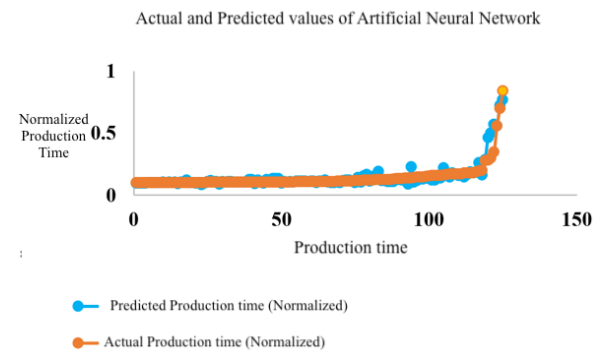


Figure 5. Relationship between predicted values and actual values according to ANN.

Multiple linear regression (MLR) models have been created to test the strength of the artificial neural network model created to estimate cable tool production times. After the implementation of this model, the performance criteria for the model are R², MAE, MSE, and RMSE values are included in Table 2.

Table 2. Multiple linear regression model forecast performance criteria and values

| Criterion | Value |
|---------------------------------|-------|
| R ² | 0.745 |
| MAE (Mean Absolute Error) | 0.013 |
| MSE (Mean Squared Error) | 0.002 |
| RMSE (Root Mean Squared Error) | 0.048 |

The estimated values obtained by the application of the multiple linear regression model and the actual values are shown in Figure 6.

A comparison of the results of the artificial neural network and multiple linear regression model for estimating cable tool production times according to performance criteria is shown in Table 3.

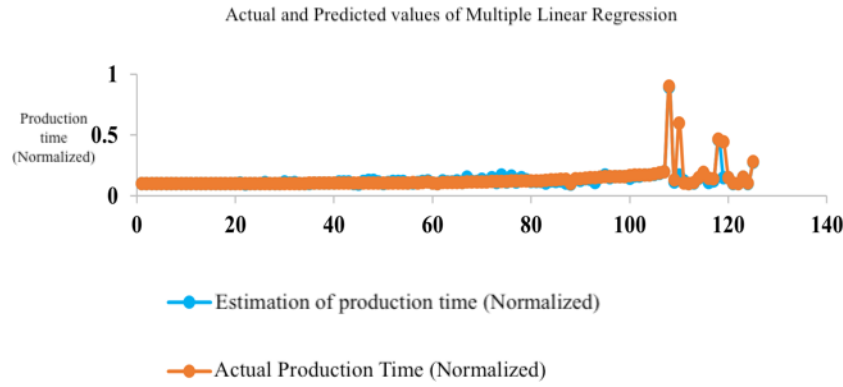


Figure 6. The relationship between predicted values and actual values in a multiple linear regression model.

Table 3. Comparative model performance criteria values

| Methods | R ² | MAE | MSE | RMSE |
|---------|----------------|-------|-------|-------|
| ANN | 0.852 | 0.013 | 0.001 | 0.036 |
| MLR | 0.745 | 0.013 | 0.002 | 0.048 |

In Table 3, the mean square error (MSE) value is evaluated as a performance measure in the forecast methods. With the artificial neural network model with the smallest MSE value, it is estimated with higher accuracy to the actual values.

Considering the results of the artificial neural network model, it is understood that 85.2% of the changes in the projected production times of the cable sets produced and delivered between August 2016 and November 2018, which are considered dependent variables, were explained by amount of work order, number of cable set modules, number of cable set pins, number of cable set labels, number of cable tool backs, number of cable set macarons and number of cable set terminals which are independent variables. According to the results of the multiple linear regression model, 74.5% of the changes in the dependent variable can be explained by the independent variables.

Considering all these criteria, it was concluded that the estimation values with the artificial neural network offer closer to the actual values.

4. Conclusion

Thanks to the technological developments today, large data sets are recorded on databases and these data can be inferred about future possible situations. Machinery learning techniques, which have the ability to learn the existing data and to control systems by basic, and the machine learning techniques that have the ability to predict future events with acquired experiences. For this reason, all organizations have to carry out studies to prevent and improve their results by predicting the uncertain situations that they may be affected in the future. In this study, the artificial neural network model was created in order to predict the production periods that are produced in a company operating in the Aeronautics and Defense Industry. Then, artificial neural

network results and multiple linear regression model results were compared in order to measure the predictive power of the model.

According to the estimation result of ANN, 85.2% success was determined by 0.001 MSE value. As a result of the estimation made with the multi-linear regression model, 74.5% success was determined with 0.002 MSE value. As a result of the applications performed, it was concluded that the artificial neural network model generated by machine learning algorithms is more successful.

Author Contributions

The percentage of the author(s) contributions is presented below. All authors reviewed and approved the final version of the manuscript.

| | G.K. | N.M. |
|-----|------|------|
| C | 50 | 50 |
| D | 50 | 50 |
| S | 50 | 50 |
| DCP | 50 | 50 |
| DAI | 50 | 50 |
| L | 50 | 50 |
| W | 50 | 50 |
| CR | 50 | 50 |
| SR | 50 | 50 |
| PM | 50 | 50 |
| FA | 50 | 50 |

C=Concept, D= design, S= supervision, DCP= data collection and/or processing, DAI= data analysis and/or interpretation, L= literature search, W= writing, CR= critical review, SR= submission and revision, PM= project management, FA= funding acquisition.

Conflict of Interest

The authors declared that there is no conflict of interest.

Ethical Consideration

Ethics committee approval was not required for this study because of there was no study on animals or humans.

Acknowledgements

It was produced from the thesis titled "Determination of harness production time and defective product formation risk factors with machine learning algorithms" at Ondokuz Mayıs University Thesis no: 571508. <https://tez.yok.gov.tr/UlusalTezMerkezi/tezSorguSonucYeni.jsp>.

References

- Alpaydin E. 2010. Introduction to machine learning (Second edition). MIT Press, London, UK, pp: 537.
- Bayır F. 2006. An application on artificial neural networks and predictive modeling. Master Thesis, Istanbul University Institute of Social Sciences, Department of Business Administration, İstanbul, Türkiye, pp: 122.
- Beale MH, HaganMT, Demuth HB. 2010. Neural network toolbox 7 user's guide. The MathWorks Inc., Natick, Massachusetts, US, pp: 424.
- Burduk A. 2013. Artificial neural networks as tools for controlling production systems and ensuring their stability. 12th International Conference on Information Systems and Industrial Management (CISIM), Computer Information Systems and Industrial Management, 25-27 October, 2013, Krakow, Poland, pp: 487-498.
- Chiang YM, Chang LC, Chang FJ. 2004. Comparison of static-feedforward and dynamic-feedback neural networks for rainfall-runoff modeling. *J Hydrol*, 209: 297-311.
- Elmas Ç. 2003. Artificial neural networks theory, architecture, education, practice (first edition). Seçkin Publishing, Ankara, Türkiye, pp: 192.
- Gürsoy A. 2012. Estimation of tire mold cost with artificial neural networks approach. Master Thesis, Kocaeli University Institute of Science and Technology, Department of Industrial Engineering, Kocaeli, Türkiye, pp: 102.
- Haykin S. 1994. Neural networks: A comprehensive foundation (First edition). Macmillan College Publishing, New York, Us, pp: 696.
- Jackson J. 2002. Data mining: A conceptual overview. *Communication of the Association for Information System Magazine*, 8(1): 267-296.
- Kalogirou SA. 2000. Applications of artificial neural-networks for energy systems. *Appl Energy*, 67(1): 17-35.
- Karabulut E, Alpar R. 2011. Logistic regression, applied multivariate statistical methods. Detay Publishing, Ankara, Türkiye, pp: 876.
- Kotsiantis SB. 2007. Supervised machine learning: A review of classification techniques. *Informatica*, 31(3): 249-268.
- Küçüksille E. 2009. Evaluation of portfolio performance using data mining process and an application in the ISE stock market. PhD Thesis, Süleyman Demirel University, Institute of Social Sciences, Department of Business Administration, Isparta, Türkiye, pp: 128.
- Kurt R, Karayılmazlar S, İmren E, Çabuk Y. 2017. Predictive modeling with artificial neural networks: The case of Turkish paper-cardboard industry. *J Bartın Fac Forestry*, 19(2): 99-106.
- Leech HL, Barrett KC, Morgan GA. 2004. Spss for intermediate statistics: use and interpretation (Second edition). Lawrence Erlbaum Associates Publishers, 240, Manwah New Jersey.
- Öğücü MO. 2006. System recognition with artificial neural networks. Master Thesis, Istanbul Technical University, Institute of Science and Technology, Department of Control and Automation Engineering, İstanbul, Türkiye, pp: 85.
- Öztemel E. 2003. Artificial neural network (first edition). Papatya Publishing, İstanbul, Türkiye, pp: 232.
- Pacci S, Safli ME, Odabas MS, Dengiz O. 2023. Variation of USLE-K soil erodibility factor and its estimation with artificial neural network approach in semi-humid environmental condition. *Brazilian Arch Biol Technol*, 66: e23220481.
- Tiryaki S, Bardak S, Bardak T. 2015. Experimental investigation and prediction of bonding strength of oriental beech (*Fagus orientalis* Lipsky) bonded with polyvinyl acetate adhesive. *J Adhesion Sci Technol*, 29(23): 2521-2536.



A NEW SOFT SET OPERATION: COMPLEMENTARY SOFT BINARY PIECEWISE INTERSECTION (\cap) OPERATION

Aslıhan SEZGİN^{1*}, Fitnat Nur AYBEK², Akin Osman ATAGÜN³

¹Amasya University, Faculty of Education, Department of Mathematics and Science Education, 05100, Amasya, Türkiye

²Amasya University, Graduate School of Natural and Applied Sciences, Department of Mathematics, 05100, Amasya, Türkiye

³Kırşehir Ahi Evran University, Faculty of Arts and Science, Department of Mathematics, 40000, Kırşehir, Türkiye

Abstract: The soft set theory developed by Molodtsov has been applied both theoretically and practically in many fields. It is a useful piece of mathematics for handling uncertainty. Numerous variations of soft set operations have been described and used since its introduction. In this paper, we define a new soft set operation, called complementary soft binary piecewise intersection operation, a unique soft set operation, and examine its basic algebraic properties. Additionally, we aim to contribute to the literature on soft sets by illuminating the relationships between this new soft set operation and other kinds of soft set operations by researching the distribution of this new soft set operation over other soft set operations. Moreover, we prove that the set of all the soft sets with a fixed parameter set together with the complementary soft binary piecewise intersection operation and the soft binary piecewise union operation is a zero-symmetric near-semiring and also a hemiring.

Keywords: Soft sets, Soft set operations, Conditional complements, Near-semiring

*Corresponding author: Amasya University, Faculty of Education, Department of Mathematics and Science Education, 05100, Amasya, Türkiye

E mail: aslihan.sezgin@amasya.edu.tr (A. SEZGİN)

Aslıhan SEZGİN



<https://orcid.org/0000-0002-1519-7294>

Fitnat Nur AYBEK



<https://orcid.org/0009-0003-7580-0264>

Akin Osman ATAGÜN



<https://orcid.org/0000-0002-2131-9980>

Received: June 25, 2023

Accepted: July 28, 2023

Published: October 15, 2023

Cite as: Sezgin A, Aybek FN, Atagün AO. 2023. A new soft set operation: Complementary soft binary piecewise intersection (\cap) operation. BSJ Eng Sci, 6(4): 330-346.

1. Introduction

Due to the existence of some types of uncertainty, we are unable to effectively employ traditional ways to address issues in many domains, including engineering, environmental and health sciences, and economics. Three well-known foundational theories that we could use as mathematical tools to deal with uncertainties are interval mathematics, fuzzy set theory, and probability theory. Molodtsov (1999) proposed Soft Set Theory as a mathematical method to deal with these uncertainties; however this method has limits as well because each of these theories has flaws of its own. Since then, this theory has been applied to a variety of fields, including information systems, decision-making as in Özlü (2022a, 2022b), optimization theory, game theory, operations research, measurement theory, and some algebraic structures such as Özlü and Sezgin (2021). The initial contributions to soft set operations were released in Maji et al. (2003) and Pei and Miao (2005). Following this, Ali et al. (2009) introduced and discussed several soft set operations, including restricted and extended soft set operations. The basic traits of soft set operations were discussed by Sezgin and Atagün (2011), and the connections between them were shown. They also investigated and defined the idea of restricted symmetric difference of soft sets. Stojanovic (2021) defined the term "extended symmetric difference of soft sets" and its

characteristics were investigated. A brand-new soft set operation called extended difference of soft sets was presented by Sezgin et al (2019). The two main categories into which the operations of soft set theory fall, according to the research, are restricted soft set operations and extended soft set operations.

The inclusive complement and exclusive complement of sets, a novel concept in set theory, were proposed and their relationships were investigated by Çağman (2021). As a result of the inspiration from this study, certain novel complements of sets were developed in (Sezgin et al., 2023c). Additionally, Aybek (2023) constructed a number of additional restricted and extended soft set operations using these complements to soft set theory. Demirci (2023); Sarılıoğlu, 2023; Akbulut (2023) defined a new type of extended operation and in-depth examined their fundamental characteristics by changing the form of extended soft set operations using the complement at the first and second row of the piecewise function of extended soft set operations. Additionally, Eren and Çalııcı (2019) created a brand-new class of soft difference operations. Soft binary piecewise operations were defined by Yavuz (2023), who also carefully analyzed their core characteristics. In addition, Sezgin and Demirci (2023), Sezgin and Aybek (2023), Sezgin et al. (2023a), Sezgin and Yavuz (2023) continued their work on soft set operations. They altered the soft binary operation's form by using the complement in the first



row of piecewise operations.

This paper contributes to the literature on soft set theory by describing a novel soft set operation, which we call "complementary soft binary piecewise intersection operation". The organization of the paper is as follows: Section 3, definition and an example of the new operation are given. Also the full analysis of the algebraic properties of the new operation, including closure, associativity, unit, inverse element, and abelian property, is then made. In Section 4, to add to the body of knowledge on soft sets, the distributions of complementary soft binary piecewise intersection operation over extended soft set operations, complementary extended soft set operations, soft binary piecewise operations, complementary soft binary piecewise operations and restricted soft set operations are specifically targeted. In the conclusion section, we put into focus the meaning of the study's findings and its potential influence on the field.

2. Preliminaries

Definition 2.1. Let U be the universal set, E be the parameter set, $P(U)$ be the power set of U and $A \subseteq E$. A pair (F, A) is called a soft set over U where F is a set-valued function such that $F: A \rightarrow P(U)$ (Molodtsov, 1999). Throughout this paper, the set of all the soft sets over U is designated by $S_E(U)$. Let A be a fixed subset of E and $S_A(U)$ be the collection of all soft sets over U with the fixed parameter set A . Clearly $S_A(U)$ is a subset of $S_E(U)$.

Definition 2.2. (K, D) is called a relative null soft set (with respect to the parameter set D), denoted by \emptyset_D , if $K(t) = \emptyset$ for all $t \in D$ and (K, D) is called a relative whole soft set (with respect to the parameter set D), denoted by U_D if $P(t) = U$ for all $t \in D$. The relative whole soft set U_E with respect to the universe set of parameters E is called the absolute soft set over U (Ali et al., 2009).

Definition 2.3. For two soft sets (K, D) and (R, J) , we say that (K, D) is a soft subset of (R, J) and it is denoted by $(K, D) \subseteq (R, J)$, if $D \subseteq J$ and $K(t) \subseteq R(t), \forall t \in D$. Two soft sets (K, D) and (R, J) are said to be soft equal if (K, D) is a soft subset of (R, J) and (R, J) is a soft subset of (K, D) (Pei and Miao, 2005).

Definition 2.4. The relative complement of a soft set (K, D) , denoted by $(K, D)^r$, is defined by $(K, D)^r = (K^r, A)$, where $K^r: D \rightarrow P(U)$ is a mapping given by $(K, D)^r = U \setminus K(t)$ for all $t \in D$ (Ali et al., 2009). From now on, $U \setminus K(t) = [K(t)]'$ will be designated by $K'(t)$ for the sake of designation.

Two conditional complements of sets, the inclusive complement and exclusive complement, were defined in (Çağman, 2021). For the ease of presentation, we represent their complements as $+$ and θ , respectively. These complements, which are binary operations, are defined as follows: Assume that D and J are the two subsets of U . The formulas for the J -inclusive complement of D and J -exclusive complement are $D+J = D' \cup J$ and J -exclusive complement of D $D \ominus J = D' \cap J'$, respectively. Here, U refers to a universe, D' is the complement of D over U .

For more information, we refer to (Çağman, 2021). New complements were created as binary operations on sets: Let U have the two subsets D and $J, D^* \ominus J = D' \cup J', D \ominus J = D \cap J, D \oplus J = D \cup J'$ are the results (Sezgin et al., 2023b). Aybek (2023) defined new restricted and extended soft set operations and looked at their characteristics by applying these set operations to soft sets.

Soft set operations can be grouped into the following categories in order to provide a summary: If " ∇ " is used to denote the set operations (i.e., here can be $\cap, \cup, \setminus, \Delta, +, \theta, *, \lambda, \gamma$), then restricted operations, extended operations, complementary extended operations, soft binary piecewise operations, and complementary soft binary piecewise operations are as follows:

Definition 2.5. Let (K, D) and (R, J) be soft sets over U . The restricted ∇ operation of (K, D) and (R, J) is the soft set (S, F) , denoted by $(K, D) \nabla_R (R, J) = (S, F)$, where $F = D \cap J \neq \emptyset$ and $\forall t \in F, S(t) = K(t) \nabla R(t)$ (Ali et al., 2009; Sezgin and Atagün, 2011; Aybek, 2023).

Definition 2.6. Let (K, D) and (R, J) be soft sets over U . The extended ∇ operation of (K, D) and (R, J) is the soft set (S, F) , denoted by $(K, D) \nabla_\varepsilon (R, J) = (S, F)$, where $F = D \cup J$ and $\forall t \in F,$

$$S(t) = \begin{cases} K(t), & t \in D \setminus J, \\ R(t), & t \in J \setminus D, \\ K(t) \nabla R(t), & t \in D \cap J. \end{cases}$$

(Maji et al., 2003; Ali et al., 2009; Sezgin et al., 2019; Stojanovic, 2021; Aybek, 2023).

Definition 2.7. Let (K, D) and (R, J) be soft sets over U . The complementary extended ∇ operation of (K, D) and (R, J) is the soft set (S, F) , denoted by $(K, D) \overset{*}{\nabla}_\varepsilon (R, J) = (S, F)$, where $F = D \cup J$ and $\forall t \in F,$

$$S(t) = \begin{cases} K'(t), & t \in D \setminus J, \\ R'(t), & t \in J \setminus D, \\ K(t) \nabla R(t), & t \in D \cap J. \end{cases}$$

(Saralioğlu, 2023; Demirci, 2023; Akbulut, 2023).

Definition 2.8. Let (K, D) and (R, J) be soft sets over U . The soft binary piecewise ∇ operation of (K, D) and (R, J) is the soft set (S, D) , denoted by $(K, D) \overset{\sim}{\nabla} (R, J) = (S, D)$, where $\forall t \in D,$

$$S(t) = \begin{cases} K(t), & t \in D \setminus J \\ K(t) \nabla R(t), & t \in D \cap J \end{cases}$$

(Eren and Çalışıcı, 2019; Yavuz, 2023).

Definition 2.9. Let (K, D) and (R, J) be soft sets over U . The complementary soft binary piecewise ∇ operation of (K, D) and (R, J) is the soft set (S, D) , denoted by $(K, D) \overset{*}{\sim} (R, J) = (S, D)$, where $\forall t \in D;$

$$S(t) = \begin{cases} K'(t), & t \in D \setminus J \\ K(t) \nabla R(t), & t \in D \cap J \end{cases}$$

(Sezgin and Demirci, 2023; Sezgin and Aybek, 2023; Sezgin et al., 2023a; Sezgin and Yavuz, 2023)

Hoorn and Rootselaar (1967) discussed general theory of near-semirings. In mathematics, a near-semiring, also called a seminearring, is an algebraic structure more general than a near-ring or a semiring. Near-semirings arise naturally from functions on monoids. Near-semirings are a common abstraction of semirings and near-rings. An algebraic system $(R, +, \cdot)$ is said to be a right (resp., left) near-semiring if R is a an additive monoid with identity 0 (not necessarily commutative) under addition, semigroup with respect to multiplication, satisfying right (resp., left) distributive law $(a+b) \cdot c = a \cdot c + b \cdot c$ (resp., $c \cdot (a + b) = c \cdot a + c \cdot b$), $\forall a, b, c \in R$ and $0 \cdot a = 0$, $\forall a \in R$ (Accordingly 0 is a one-sided (right or left, respectively) absorbing element for the multiplication operation). In addition, if $0 \cdot a = a \cdot 0 = 0$ for all $a \in R$, then we call it a zero-symmetric near-semiring (or seminearrings). For more about near-rings and ideals of near-ring and N-ideals, we refer to (Pilz, 1977; Taşdemir et al., 2013; Taşdemir and Taştekin, 2019)

The standard examples of near-semirings are typically of the form $M(\Gamma)$, the set of all mappings on a monoid $(\Gamma, +, 0)$, equipped with composition of mappings, pointwise addition of mappings, and the zero function. Subsets of $M(\Gamma)$ closed under the operations provide further examples of near-semirings.

3. Complementary Soft Binary Piecewise Intersection Operation and Its Properties

Definition 3.1. Let (F, A) and (G, B) be soft sets over U . The complementary soft binary piecewise intersection (\cap) operation of (F, A) and (G, B) is the soft set (H, A) , denoted by, $(F, A) \sim (G, B) = (H, A)$, where

$\forall \omega \in A$,

$$H(\omega) = \begin{cases} F'(\omega), & \omega \in A \setminus B \\ F(\omega) \cap G(\omega), & \omega \in A \cap B \end{cases}$$

Example 3.2. Let $E = \{e_1, e_2, e_3, e_4\}$ be the parameter set $A = \{e_1, e_3\}$ and $B = \{e_2, e_3, e_4\}$ be the subsets of E and $U = \{h_1, h_2, h_3, h_4, h_5\}$ be the initial universe set. Assume that (F, A) and (G, B) are the soft sets over U defined as following:

$$(F, A) = \{ (e_1, \{h_2, h_5\}), (e_3, \{h_1, h_2, h_5\}) \},$$

$$(G, B) = \{ (e_2, \{h_1, h_4, h_5\}), (e_3, \{h_2, h_3, h_4\}), (e_4, \{h_3, h_5\}) \}.$$

Let $(F, A) \sim (G, B) = (H, A)$. Then,

$$H(\omega) = \begin{cases} F'(\omega), & \omega \in A \setminus B \\ F(\omega) \cap G(\omega), & \omega \in A \cap B \end{cases}$$

Since $A \setminus B = \{e_1\}$ and $A \cap B = \{e_3\}$, $H(e_1) = F'(e_1) = \{h_1, h_3, h_4\}$, $H(e_3) = F(e_3) \cap G(e_3) = \{h_1, h_2, h_5\} \cap \{h_2, h_3, h_4\} = \{h_2\}$. Thus, $(F, A) \sim (G, B) = \{ (e_1, \{h_1, h_3, h_4\}), (e_3, \{h_2\}) \}$.

Theorem 3.3. (Algebraic properties of the operation)

1) The set $S_E(U)$ is closed under the operation \sim . That is, when (F, A) and (G, X) are two soft sets over U , then so is $(F, A) \sim (G, X)$.

Proof: It is clear that \sim is a binary operation in $S_E(U)$.

That is,

$$\sim : S_E(U) \times S_E(U) \rightarrow S_E(U)$$

$$((F, A), (G, X)) \rightarrow (F, A) \sim (G, X) = (H, A)$$

Hence, the set $S_E(U)$ is closed under the operation \sim .

2) $[(F, A) \sim (G, A)] \sim (H, A) = (F, A) \sim [(G, A) \sim (H, A)]$.

Proof: Let $(F, A) \sim (G, A) = (T, A)$, where $\forall \omega \in A$;

$$T(\omega) = \begin{cases} F'(\omega), & \omega \in A \setminus A = \emptyset \\ F(\omega) \cap G(\omega), & \omega \in A \cap A = A \end{cases}$$

Let $(T, A) \sim (H, A) = (M, A)$, where $\forall \omega \in A$;

$$M(\omega) = \begin{cases} T'(\omega), & \omega \in A \setminus A = \emptyset \\ T(\omega) \cap H(\omega), & \omega \in A \cap A = A \end{cases}$$

Thus,

$$M(\omega) = \begin{cases} T'(\omega), & \omega \in A \setminus A = \emptyset \\ [F(\omega) \cap G(\omega)] \cap H(\omega), & \omega \in A \cap A = A \end{cases}$$

Let $(G, A) \sim (H, A) = (L, A)$, where $\forall \omega \in A$;

$$L(\omega) = \begin{cases} G'(\omega), & \omega \in A \setminus A = \emptyset \\ G(\omega) \cap H(\omega), & \omega \in A \cap A = A \end{cases}$$

Let $(F,A) \underset{\cap}{\sim} (L,A) = (N,A)$, where $\forall \omega \in A$;

$$N(\omega) = \begin{cases} F'(\omega), & \omega \in A \setminus A = \emptyset \\ F(\omega) \cap L(\omega), & \omega \in A \cap A = A \end{cases}$$

Thus,

$$N(\omega) = \begin{cases} F'(\omega), & \omega \in A \setminus A = \emptyset \\ F(\omega) \cap [G(\omega) \cap H(\omega)], & \omega \in A \cap A = A \end{cases}$$

It is seen that $M=N$.

That is, for the soft sets whose parameter sets are the same, the operation $\underset{\cap}{\sim}$ has associativity property.

However we have the following:

$$3) [(F,A) \underset{\cap}{\sim} (G,X)] \underset{\cap}{\sim} (H,L) \neq (F,A) \underset{\cap}{\sim} [(G,X) \underset{\cap}{\sim} (H,L)]$$

Proof: Let $(F,A) \underset{\cap}{\sim} (G,X) = (T,A)$, where $\forall \omega \in A$;

$$T(\omega) = \begin{cases} F'(\omega), & \omega \in A \setminus X \\ F(\omega) \cap G(\omega), & \omega \in A \cap X \end{cases}$$

Let $(T,A) \underset{\cap}{\sim} (H,L) = (M,A)$, where $\forall \omega \in A$;

$$M(\omega) = \begin{cases} T'(\omega), & \omega \in A \setminus L \\ T(\omega) \cap H(\omega), & \omega \in A \cap L \end{cases}$$

Thus,

$$M(\omega) = \begin{cases} F(\omega), & \omega \in (A \setminus X) \setminus L = A \cap X' \cap L' \\ F'(\omega) \cup G'(\omega), & \omega \in (A \cap X) \setminus L = A \cap X \cap L' \\ F'(\omega) \cap H(\omega), & \omega \in (A \setminus X) \cap L = A \cap X' \cap L \\ [F(\omega) \cap G(\omega)] \cap H(\omega), & \omega \in (A \cap X) \cap L = A \cap X \cap L \end{cases}$$

Let $(G,X) \underset{\cap}{\sim} (H,L) = (K,X)$, where $\forall \omega \in X$;

$$K(\omega) = \begin{cases} G'(\omega), & \omega \in X \setminus L \\ G(\omega) \cap H(\omega), & \omega \in X \cap L \end{cases}$$

Let $(F,A) \underset{\cap}{\sim} (K,X) = (S,A)$, where $\forall \omega \in A$;

$$S(\omega) = \begin{cases} F'(\omega), & \omega \in A \setminus X \\ F(\omega) \cap K(\omega), & \omega \in A \cap X \end{cases}$$

Thus,

$$S(\omega) = \begin{cases} F'(\omega), & \omega \in A \setminus X \\ F(\omega) \cap G'(\omega), & \omega \in A \cap (X \setminus L) = A \cap X \cap L' \\ F(\omega) \cap [G(\omega) \cap H(\omega)], & \omega \in A \cap (X \cap L) = A \cap X \cap L \end{cases}$$

Here let handle $\omega \in A \setminus X$ in the second equation of the first line. Since $A \setminus X = A \cap X'$, if $k \in X'$, then $\omega \in L \setminus X$ or $\omega \in (X \cup L)'$. Hence, if $\omega \in A \setminus X$, then $\omega \in A \cap X' \cap L'$ or $\omega \in A \cap X' \cap L$. Thus, it is seen that $M \neq S$. That is, the operation $\underset{\cap}{\sim}$ has not associativity property on the set $S_E(U)$.

$$4) (F,A) \underset{\cap}{\sim} (G,X) \neq (G,X) \underset{\cap}{\sim} (F,A)$$

Proof: Let $(F,A) \underset{\cap}{\sim} (G,X) = (H,A)$. Then, $\forall \omega \in A$;

$$H(\omega) = \begin{cases} F'(\omega), & \omega \in A \setminus X \\ F(\omega) \cap G(\omega), & \omega \in A \cap X \end{cases}$$

Let $(G,X) \underset{\cap}{\sim} (F,A) = (T,X)$. Then $\forall \omega \in X$;

$$T(\omega) = \begin{cases} G'(\omega), & \omega \in X \setminus A \\ G(\omega) \cap F(\omega), & \omega \in X \cap A \end{cases}$$

Here, while the parameter set of the soft set of the left hand side is A ; the parameter set of the soft set of the right hand side is X . Thus, $(F,A) \underset{\cap}{\sim} (G,X) \neq (G,X) \underset{\cap}{\sim} (F,A)$.

Hence, the operation $\underset{\cap}{\sim}$ has not commutative property in the set $S_E(U)$. However it is easy to see that $(F,A) \underset{\cap}{\sim} (G,A) = (G,A) \underset{\cap}{\sim} (F,A)$. That is to say, the operation $\underset{\cap}{\sim}$ has commutative property, where the parameter sets of the soft sets are the same.

$$5) (F,A) \underset{\cap}{\sim} (F,A) = (F,A)$$

Proof: Let $(F,A) \underset{\cap}{\sim} (F,A) = (H,A)$, where $\forall \omega \in A$;

$$H(\omega) = \begin{cases} F'(\omega), & \omega \in A \setminus A = \emptyset \\ F(\omega) \cap F(\omega), & \omega \in A \cap A = A \end{cases}$$

Here $\forall \omega \in A$; $H(\omega) = F(\omega) \cap F(\omega) = F(\omega)$, thus $(H,A) = (F,A)$.

That is, the operation $\underset{\cap}{\sim}$ is idempotent in $S_E(U)$.

$$6) (F,A) \underset{\cap}{\sim} \underset{\cap}{\emptyset_A} = \underset{\cap}{\emptyset_A} \underset{\cap}{\sim} (F,A) = \underset{\cap}{\emptyset_A}$$

Proof: Let $\emptyset_A = (S,A)$. Then, $\forall \omega \in A$; $S(\omega) = \emptyset$. Let

$$(F,A) \underset{\cap}{\sim} (S,A) = (H,A), \text{ where } \forall \omega \in A,$$

$$H(\omega) = \begin{cases} F'(\omega), & \omega \in A \setminus A = \emptyset \\ F(\omega) \cap S(\omega), & \omega \in A \cap A = A \end{cases}$$

Hence, $\forall \omega \in A$; $H(\omega) = F(\omega) \cap S(\omega) = F(\omega) \cap \emptyset = \emptyset$. Thus, $(H,A) = \emptyset_A$. Note that, for the soft sets whose parameter set is A , \emptyset_A is the absorbing element for the operation $\underset{\cap}{\sim}$ in $S_E(U)$.

$$7) (F,A) \underset{\cap}{\sim} \underset{\cap}{\emptyset_E} = \underset{\cap}{\emptyset_A}$$

Proof: Let $\emptyset_E = (S,E)$. Hence $\forall \omega \in E$; $S(\omega) = \emptyset$. Let $(F,A) \underset{\cap}{\sim} (S,E) = (H,A)$. Thus, $\forall \omega \in A$,

$$H(\omega) = \begin{cases} F'(\omega), & \omega \in A \setminus E = \emptyset \\ F(\omega) \cap S(\omega), & \omega \in A \cap E = A \end{cases}$$

Hence, $H(\omega) = F(\omega) \cap S(\omega) = F(\omega) \cap \emptyset = \emptyset$, so $(H,A) = (F,A)$.

$$8) (F,A) \underset{\cap}{\sim} \underset{\cap}{U_A} = \underset{\cap}{U_A} \underset{\cap}{\sim} (F,A) = (F,A)$$

Proof: Let $U_A = (T,A)$. Then, $\forall \omega \in A$; $T(\omega) = U$. Let (F,A)

$$\underset{\cap}{\sim} (T,A) = (H,A), \text{ where } \forall \omega \in A,$$

$$H(\omega) = \begin{cases} F'(\omega), & \omega \in A \setminus A = \emptyset \\ F(\omega) \cap T(\omega), & \omega \in A \cap A = A \end{cases}$$

Thus, $\forall \omega \in A$; $H(\omega) = F(\omega) \cap T(\omega) = F(\omega) \cap U = F(\omega)$, hence $(H,A) = (F,A)$. Note that, U_A is the identity element for the operation $\underset{\cap}{\sim}$ in $S_A(U)$.

REMARK 1: By Theorem 3.3. (1), (2), (4) and (8), $(S_A(U), \underset{\cap}{\sim})$ is a commutative monoid with identity U_A .

$$9) (F,A) \underset{\cap}{\sim} \underset{\cap}{U_E} = (F,A)$$

Proof: Let $U_E = (T,E)$. Hence, $\forall \omega \in E$, $T(\omega) = U$. Let

$$(F,A) \underset{\cap}{\sim} (T,E) = (H,A), \text{ then } \forall \omega \in A,$$

$$H(\omega) = \begin{cases} F'(\omega), & \omega \in A \setminus E = \emptyset \\ F(\omega) \cap T(\omega), & \omega \in A \cap E = A \end{cases}$$

Hence, $\forall \omega \in A$, $H(\omega) = F(\omega) \cap T(\omega) = F(\omega) \cap U = F(\omega)$, so $(H,A) = (F,A)$. Note that, for all the soft sets (no matter what the parameter set is), U_E is the right identity element for the operation $\underset{\cap}{\sim}$ in $S_E(U)$.

$$10) \underset{\cap}{U_E} \underset{\cap}{\sim} (F,A) = \underset{\cap}{U_A}$$

Proof: Let $U_E = (T,E)$. Then, $\forall \omega \in E$; $T(\omega) = U$. Let $(T,E) \underset{\cap}{\sim} (F,A) = (H,L)$, where $\forall \omega \in A$;

$$H(\omega) = \begin{cases} T'(\omega), & \omega \in E \setminus A \\ T(\omega) \cap F(\omega), & \omega \in E \cap A = A \end{cases}$$

Hence $\forall \omega \in A$; $H(\omega) = T(\omega) \cap F(\omega) = U \cap F(\omega) = F(\omega)$, thus $(H,A) = (F,A)$.

$$11) (F,A) \underset{\cap}{\sim} (F,A)^r = (F,A)^r \underset{\cap}{\sim} (F,A) = \emptyset_A$$

Proof: Let $(F,A)^r = (H,A)$. Hence, $\forall \omega \in A$; $H(\omega) = F'(\omega)$. Let $(F,A) \underset{\cap}{\sim} (H,A) = (T,A)$, where $\forall \omega \in A$,

$$T(\omega) = \begin{cases} F'(\omega), & \omega \in A \setminus A = \emptyset \\ F(\omega) \cap H(\omega), & \omega \in A \cap A = A \end{cases}$$

Hence, $\forall \omega \in A$; $T(\omega) = F(\omega) \cap H(\omega) = F(\omega) \cap F'(\omega) = \emptyset$, thus $(T,A) = \emptyset_A$.

$$12) (F,A) \underset{\cap}{\sim} (G,X)]^r = (F,A) \underset{\cap}{\sim} (G,X)$$

Proof: Let $(F,A) \underset{\cap}{\sim} (G,X) = (H,A)$. Then, $\forall \omega \in A$,

$$H(\omega) = \begin{cases} F'(\omega), & \omega \in A \setminus X \\ F(\omega) \cap G(\omega), & \omega \in A \cap X \end{cases}$$

Let $(H,A)^r = (T,A)$, so $\forall \omega \in A$,

$$T(\omega) = \begin{cases} F(\omega), & \omega \in A \setminus X \\ F(\omega) \cup G'(\omega), & \omega \in A \cap X \end{cases}$$

Thus, $(T,A) = (F,A) \underset{\cap}{\sim} (G,X)$.

$$16) (F,A) \underset{\cap}{\sim} (G,A) = U_A \Leftrightarrow (F,A) = U_A \text{ and } (G,A) = U_A$$

Proof: Let $(F,A) \underset{\cap}{\sim} (G,A) = (T,A)$. Hence, $\forall \omega \in A$,

$$T(\omega) = \begin{cases} F'(\omega), & \omega \in A \setminus A = \emptyset \\ F(\omega) \cap G(\omega), & \omega \in A \cap A = A \end{cases}$$

Since, $(T,A)=U_A, \forall \omega \in A, T(\omega)=U$. Thus, $\forall \omega \in A, T(\omega)=F(\omega) \cap G(\omega)=U \Leftrightarrow \forall \omega \in A, F(\omega)=U$ and $G(\omega)=U \Leftrightarrow (F,A)=U_A$ and $(G,A)=U_A$.

$$17) \phi_A \overset{*}{\underset{\cap}{\cong}} (F,A) \sim (G,X) \text{ and } \phi_B \overset{*}{\underset{\cap}{\cong}} (G,X) \sim ((F,A).$$

$$18) (F,A) \overset{*}{\underset{\cap}{\sim}} (G,X) \overset{*}{\underset{\cap}{\cong}} U_A \text{ and } (G,X) \overset{*}{\underset{\cap}{\sim}} (F,A) \overset{*}{\underset{\cap}{\cong}} U_B$$

$$19) (F,A) \overset{*}{\underset{\cap}{\sim}} (G,A) \overset{*}{\underset{\cap}{\cong}} (F,A) \overset{*}{\underset{\cap}{\sim}} (G,A) \text{ (Yavuz, 2023)}$$

$$20) (F,A) \overset{*}{\underset{\cap}{\sim}} (G,A) = (F,A) \overset{*}{\underset{\cap}{\sim}} (G,A) \Leftrightarrow (F,A) = (G,A) \text{ (Yavuz, 2023)}$$

$$21) (F,A) \overset{*}{\underset{\cap}{\sim}} (G,A) \overset{*}{\underset{\cap}{\cong}} (F,A) \text{ and } (F,A) \overset{*}{\underset{\cap}{\sim}} (G,A) \overset{*}{\underset{\cap}{\cong}} (G,A).$$

Proof: Let $(F,A) \overset{*}{\underset{\cap}{\sim}} (G,A)=(H,A)$. First of all, $A \subseteq A$. Moreover, $\forall \omega \in A$,

$$H(\omega) = \begin{cases} F'(\omega), & \omega \in A \setminus A = \emptyset \\ F(\omega) \cap G(\omega), & \omega \in A \cap A = A \end{cases}$$

Since $H(\omega)=F(\omega) \cap G(\omega) \subseteq F(\omega)$ and $H(\omega)=F(\omega) \cap G(\omega) \subseteq G(\omega), \forall \omega \in A$, the proof is completed.

$$22) (F,A) \overset{*}{\underset{\cap}{\cong}} (G,A) \Leftrightarrow (F,A) \overset{*}{\underset{\cap}{\sim}} (G,A) = (F,A).$$

Proof: Let $(F,A) \overset{*}{\underset{\cap}{\cong}} (G,A)$, then, $\forall \omega \in A, F(\omega) \subseteq G(\omega)$ and let $(F,A) \overset{*}{\underset{\cap}{\sim}} (G,A)=(H,A)$. Then, $\forall \omega \in A$,

$$H(\omega) = \begin{cases} F'(\omega), & \omega \in A \setminus A = \emptyset \\ F(\omega) \cap G(\omega), & \omega \in A \cap A = A \end{cases}$$

Since $\forall \omega \in A, H(\omega)=F(\omega) \cap G(\omega) = F(\omega)$, hence $(H,A)=(F,A)$.

For the converse, let $(F,A) \overset{*}{\underset{\cap}{\sim}} (G,A) = (F,A)$. Since,

$$(F,A) \overset{*}{\underset{\cap}{\sim}} (G,A) \overset{*}{\underset{\cap}{\cong}} (G,A) \text{ by (21), } (F,A) \overset{*}{\underset{\cap}{\sim}} (G,A) = (F,A) \overset{*}{\underset{\cap}{\cong}} (G,A).$$

$$23) \text{ If } (F,A) \overset{*}{\underset{\cap}{\cong}} (G,A) \text{ and } (H,A) \overset{*}{\underset{\cap}{\cong}} (T,A), \text{ then } (F,A) \overset{*}{\underset{\cap}{\sim}} (H,A) \overset{*}{\underset{\cap}{\cong}} (G,A) \overset{*}{\underset{\cap}{\sim}} (T,A).$$

Proof: Let $(F,A) \overset{*}{\underset{\cap}{\cong}} (G,A)$ and $(H,A) \overset{*}{\underset{\cap}{\cong}} (T,A)$. Then, $\forall \omega \in A, F(\omega) \subseteq G(\omega)$ and $H(\omega) \subseteq T(\omega)$. Assume that $(F,A) \overset{*}{\underset{\cap}{\sim}} (H,A) = (K,A)$ where $\forall \omega \in A$,

$$K(\omega) = \begin{cases} F'(\omega), & \omega \in A \setminus A = \emptyset \\ F(\omega) \cap H(\omega), & \omega \in A \cap A = A \end{cases}$$

Let $(G,A) \overset{*}{\underset{\cap}{\sim}} (T,A) = (S,A)$ where $\forall \omega \in A$,

$$S(\omega) = \begin{cases} G'(\omega), & \omega \in A \setminus A = \emptyset \\ G(\omega) \cap T(\omega), & \omega \in A \cap A = A \end{cases}$$

Since, $\forall \omega \in A, F(\omega) \subseteq G(\omega)$ and $H(\omega) \subseteq T(\omega)$, then $K(\omega) = F(\omega) \cap H(\omega) \subseteq G(\omega) \cap T(\omega)$. Hence, $(K,A) \overset{*}{\underset{\cap}{\cong}} (S,A)$.

4. Distribution Rules

In this section, the distributions of complementary soft binary piecewise intersection (\cap) operations over other soft set operations, including complementary extended soft set operations, complementary soft binary piecewise operations, soft binary piecewise operations, and restricted soft set operations, are thoroughly examined. As a result, several intriguing discoveries are made.

4.1. Distribution of Complementary Soft Binary Piecewise Intersection Operation over Extended Soft Set Operations

4.1.1. Left-distribution of complementary soft binary piecewise intersection operation over extended soft set operations

The followings are held where $A \cap X' \cap L = \emptyset$.

$$1) (F,A) \overset{*}{\underset{\cap}{\sim}} [(G,X) \cap_\varepsilon (H,L)] = [(F,A) \overset{*}{\underset{\cap}{\sim}} (G,X)] \overset{*}{\underset{\cap}{\sim}} [(H,L) \overset{*}{\underset{\cap}{\sim}} (F,A)].$$

Proof: Let's first take care of the left hand facet of the equality and let $(G,X) \cap_\varepsilon (H,L) = (M,X \cup L)$ where $\forall \omega \in X \cup L$;

$$M(\omega) = \begin{cases} G(\omega), & \omega \in X \setminus L \\ H(\omega), & \omega \in L \setminus X \\ G(\omega) \cap H(\omega), & \omega \in X \cap L \end{cases}$$

Assume that $(F,A) \overset{*}{\underset{\cap}{\sim}} (M,X \cup L) = (N,A)$, where $\forall \omega \in A$;

$$N(\omega) = \begin{cases} F'(\omega), & \omega \in A \setminus (X \cup L) \\ F(\omega) \cap M(\omega), & \omega \in A \cap (X \cup L) \end{cases}$$

Hence,

$$N(\omega) = \begin{cases} F'(\omega), & \omega \in A \setminus (X \cup L) = A \cap X' \cap L' \\ F(\omega) \cap G(\omega), & \omega \in A \cap (X \setminus L) = A \cap X \cap L' \\ F(\omega) \cap H(\omega), & \omega \in A \cap (L \setminus X) = A \cap X' \cap L \\ F(\omega) \cap [(G(\omega) \cap H(\omega))], & \omega \in A \cap X \cap L = A \cap X \cap L \end{cases}$$

Now let take care of the right hand facet of the equality:

$$[(F,A) \overset{*}{\underset{\cap}{\sim}} (G,X)] \overset{*}{\underset{\cap}{\sim}} [(H,L) \overset{*}{\underset{\cap}{\sim}} (F,A)]. \text{ Assume that } (F,A) \overset{*}{\underset{\cap}{\sim}} (G,X) = (V,A), \text{ where } \forall \omega \in A;$$

$$V(\omega) = \begin{cases} F'(\omega), & \omega \in A \setminus X \\ F(\omega) \cap G(\omega), & \omega \in A \cap X \end{cases}$$

Let $(H,L) \overset{*}{\sim} (F,A)=(W,L)$, where $\forall \omega \in L$;

$$W(\omega) = \begin{cases} H'(\omega), & \omega \in L \setminus A \\ H(\omega) \cap F(\omega), & \omega \in L \cap A \end{cases}$$

Let $(V,A) \overset{\sim}{\cap} (W,L)=(T,A)$, where $\forall \omega \in A$;

$$T(\omega) = \begin{cases} V(\omega), & \omega \in A \setminus L \\ V(\omega) \cap W(\omega), & \omega \in A \cap L \end{cases}$$

Hence,

$$T(\omega) = \begin{cases} F'(\omega), & \omega \in (A \setminus X) \setminus L = A \cap X' \cap L' \\ F(\omega) \cap G(\omega), & \omega \in (A \cap X) \setminus L = A \cap X \cap L' \\ F'(\omega) \cap H'(\omega), & \omega \in (A \setminus X) \cap (L \setminus A) = \emptyset \\ F'(\omega) \cap [H(\omega) \cap F(\omega)], & \omega \in (A \setminus X) \cap (L \cap A) = A \cap X' \cap L \\ [F(\omega) \cap G(\omega)] \cap H'(\omega), & \omega \in (A \cap X) \cap (L \setminus A) = \emptyset \\ [F(\omega) \cap G(\omega)] \cap [H(\omega) \cap F(\omega)], & \omega \in (A \cap X) \cap (L \cap A) = A \cap X \cap L \end{cases}$$

It is seen that $N=T$.

$$2) (F,A) \overset{*}{\sim} [(G,X) \cup_{\varepsilon} (H,L)] = [(F,A) \overset{*}{\sim} (G,X)] \overset{\sim}{\cap} [(H,L) \overset{*}{\sim} (F,A)].$$

$$3) (F,A) \overset{*}{\sim} [(G,X) \lambda_{\varepsilon} (H,L)] = [(F,A) \overset{*}{\sim} (G,X)] \overset{\sim}{\cap} [(H,L) \overset{*}{\sim} (F,A)].$$

Proof: Let's first take care of the left hand facet of the equality and let $(G,X) \lambda_{\varepsilon} (H,L) = (M, X \cup L)$ where $\forall \omega \in X \cup L$;

$$M(\omega) = \begin{cases} G(\omega), & \omega \in X \setminus L \\ H(\omega), & \omega \in L \setminus X \\ G(\omega) \cup H'(\omega), & \omega \in X \cap L \end{cases}$$

Assume that $(F,A) \overset{*}{\sim} (M, X \cup L) = (N,A)$, where $\forall \omega \in A$;

$$N(\omega) = \begin{cases} F'(\omega), & \omega \in A \setminus (X \cup L) \\ F(\omega) \cap M(\omega), & \omega \in A \cap (X \cup L) \end{cases}$$

Thus,

$$N(\omega) = \begin{cases} F'(\omega), & \omega \in A \setminus (X \cup L) = A \cap X' \cap L' \\ F(\omega) \cap G(\omega), & \omega \in A \cap (X \setminus L) = A \cap X \cap L' \\ F(\omega) \cap H(\omega), & \omega \in A \cap (L \setminus X) = A \cap X' \cap L \\ F(\omega) \cap [G(\omega) \cup H'(\omega)], & \omega \in A \cap X \cap L = A \cap X \cap L \end{cases}$$

Now let take care of the right hand facet of the equality:

$$(F,A) \overset{*}{\sim} (G,X) \overset{\sim}{\cap} [(H,L) \overset{*}{\sim} (F,A)].$$

Assume that $(F,A) \overset{*}{\sim} (G,X) = (V,A)$, where $\forall \omega \in A$;

$$V(\omega) = \begin{cases} F'(\omega), & \omega \in A \setminus X \\ F(\omega) \cap G(\omega), & \omega \in A \cap X \end{cases}$$

Let $(H,L) \overset{*}{\sim} (F,A)=(W,L)$, where $\forall \omega \in L$;

$$W(\omega) = \begin{cases} H'(\omega), & \omega \in L \setminus A \\ H'(\omega) \cap F(\omega), & \omega \in L \cap A \end{cases}$$

Let $(V,A) \overset{\sim}{\cap} (W,L)=(T,A)$, where $\forall \omega \in A$;

$$T(\omega) = \begin{cases} V(\omega), & \omega \in A \setminus L \\ V(\omega) \cup W(\omega), & \omega \in A \cap L \end{cases}$$

$$T(\omega) = \begin{cases} F'(\omega), & \omega \in (A \setminus X) \setminus L = A \cap X' \cap L' \\ F(\omega) \cap G(\omega), & \omega \in (A \cap X) \setminus L = A \cap X \cap L' \\ F'(\omega) \cup H'(\omega), & \omega \in (A \setminus X) \cap (L \setminus A) = \emptyset \\ F'(\omega) \cup [H'(\omega) \cap F(\omega)], & \omega \in (A \setminus X) \cap (L \cap A) = A \cap X' \cap L \\ [F(\omega) \cap G(\omega)] \cup H'(\omega), & \omega \in (A \cap X) \cap (L \setminus A) = \emptyset \\ [F(\omega) \cap G(\omega)] \cup [H'(\omega) \cap F(\omega)], & \omega \in (A \cap X) \cap (L \cap A) = A \cap X \cap L \end{cases}$$

It is seen that $N=T$.

$$4) (F,A) \overset{*}{\sim} [(G,X) \setminus_{\varepsilon} (H,L)] = [(F,A) \overset{*}{\sim} (G,X)] \overset{\sim}{\cap} [(H,L) \overset{*}{\sim} (F,A)]$$

4.1.2. Right-distribution of complementary soft binary piecewise intersection operation over extended soft set operations

$$1) [(F,A) \cup_{\varepsilon} (G,X)] \overset{*}{\sim} (H,L) = [(F,A) \overset{*}{\sim} (H,L)] \cup_{\varepsilon} [(G,X) \overset{*}{\sim} (H,L)],$$

where $A \cap X \cap L' = \emptyset$

Proof: Let's first take care of the left hand facet of the equality and let $(F,A) \cup_{\varepsilon} (G,X) = (M, A \cup X)$ where $\forall \omega \in A \cup X$;

$$M(\omega) = \begin{cases} F(\omega), & \omega \in A \setminus X \\ G(\omega), & \omega \in X \setminus A \\ F(\omega) \cup G(\omega), & \omega \in A \cap X \end{cases}$$

Let $(M, A \cup X) \overset{*}{\sim} (H,L) = (N, A \cup X)$, where $\forall \omega \in A \cup X$

$$N(\omega) = \begin{cases} M'(\omega), & \omega \in (A \cup X) \setminus L \\ M(\omega) \cap H(\omega), & \omega \in (A \cup X) \cap L \end{cases}$$

$$N(\omega) = \begin{cases} F'(\omega), & \omega \in (A \setminus X) \setminus L = A \cap X' \cap L' \\ G'(\omega), & \omega \in (X \setminus A) \setminus L = A' \cap X \cap L' \\ F'(\omega) \cap G'(\omega), & \omega \in (A \cap X) \setminus L = A \cap X \cap L' \\ F(\omega) \cap H(\omega), & \omega \in (A \setminus X) \cap L = A \cap X' \cap L \\ G(\omega) \cap H(\omega), & \omega \in (X \setminus A) \cap L = A' \cap X \cap L \\ [F(\omega) \cup G(\omega)] \cap H(\omega), & \omega \in (A \cap X) \cap L = A \cap X \cap L \end{cases}$$

Now let's take care of the right hand facet of the equality:

$$(F,A) \overset{*}{\sim} (H,L) \cup_{\varepsilon} [(G,X) \overset{*}{\sim} (H,L)]. \text{ Let } (F,A) \overset{*}{\sim} (H,L) = (V,A),$$

where $\forall \omega \in A$;

$$V(\omega) = \begin{cases} F'(\omega) & \omega \in A \setminus L \\ F(\omega) \cap H(\omega) & \omega \in A \cap L \end{cases}$$

Suppose that $(G, X) \underset{\cap}{\sim}^* (H, L) = (W, X)$, where $\forall \omega \in X$;

$$W(\omega) = \begin{cases} G'(\omega), & \omega \in X \setminus L \\ G(\omega) \cap H(\omega), & \omega \in X \cap L \end{cases}$$

Let $(V, A) \cup_{\varepsilon} (W, X) = (T, A \cup X)$, where $\forall \omega \in A \cup X$;

$$T(\omega) = \begin{cases} V(\omega), & \omega \in A \setminus X \\ W(\omega), & \omega \in X \setminus A \\ V(\omega) \cup W(\omega), & \omega \in A \cap X \end{cases}$$

Hence,

$$T(\omega) = \begin{cases} F'(\omega), & \omega \in (A \setminus L) \setminus X = A \cap X' \cap L' \\ F(\omega) \cap H(\omega), & \omega \in (A \cap L) \setminus X = A \cap X' \cap L \\ G'(\omega), & \omega \in (X \setminus L) \setminus A = A' \cap X \cap L' \\ G(\omega) \cap H(\omega), & \omega \in (X \cap L) \setminus A = A' \cap X \cap L \\ F'(\omega) \cup G'(\omega), & \omega \in (A \setminus L) \cap (X \setminus L) = A \cap X \cap L' \\ F'(\omega) \cup [G(\omega) \cap H(\omega)], & \omega \in (A \setminus L) \cap (X \cap L) = \emptyset \\ [F(\omega) \cap H(\omega)] \cup G'(\omega), & \omega \in (A \cap L) \cap (X \setminus L) = \emptyset \\ [F(\omega) \cap H(\omega)] \cup [G(\omega) \cap H(\omega)], & \omega \in (A \cap L) \cap (X \cap L) = A \cap X \cap L \end{cases}$$

It is seen that $N = T$.

$$2) [(F, A) \cap_{\varepsilon} (G, X)] \underset{\cap}{\sim}^* (H, L) = [(F, A) \underset{\cap}{\sim}^* (H, L)] \cap_{\varepsilon} [(G, X) \underset{\cap}{\sim}^* (H, L)], \text{ where } A \cap X \cap L' = \emptyset.$$

$$3) [(F, A) \setminus_{\varepsilon} (G, X)] \underset{\cap}{\sim}^* (H, L) = [(F, A) \underset{\cap}{\sim}^* (H, L)] \cap_{\varepsilon} [(G, X) \underset{\cap}{\sim}^* (H, L)], \text{ where } A \cap X \cap L' = A' \cap X \cap L = \emptyset.$$

Proof: Let first take care of the left hand facet of the equality and let $(F, A) \setminus_{\varepsilon} (G, X) = (M, A \cup X)$, where $\forall \omega \in A \cup X$,

$$M(\omega) = \begin{cases} F(\omega), & \omega \in A \setminus X \\ G(\omega), & \omega \in X \setminus A \\ F(\omega) \cap G'(\omega), & \omega \in A \cap X \end{cases}$$

Suppose that $(M, A \cup X) \underset{\cap}{\sim}^* (H, L) = (N, A \cup X)$, where $\forall \omega \in A \cup X$;

$$N(\omega) = \begin{cases} M'(\omega), & \omega \in (A \cup X) \setminus L \\ M(\omega) \cap H(\omega), & \omega \in (A \cup X) \cap L \end{cases}$$

Hence,

$$N(\omega) = \begin{cases} F'(\omega), & \omega \in (A \setminus X) \setminus L = A \cap X' \cap L' \\ G'(\omega), & \omega \in (X \setminus A) \setminus L = A' \cap X \cap L' \\ F'(\omega) \cup G'(\omega), & \omega \in (A \cap X) \setminus L = A \cap X \cap L' \\ F(\omega) \cap H(\omega), & \omega \in (A \setminus X) \cap L = A \cap X' \cap L \\ G(\omega) \cap H(\omega), & \omega \in (X \setminus A) \cap L = A' \cap X \cap L \\ [F(\omega) \cap G'(\omega)] \cap H(\omega), & \omega \in (A \cap X) \cap L = A \cap X \cap L \end{cases}$$

Now let's take care of the right hand facet of the equality:

$$[(F, A) \underset{\cap}{\sim}^* (H, L)] \cap_{\varepsilon} [(G, X) \underset{\cap}{\sim}^* (H, L)]. \text{ Let } (F, A) \underset{\cap}{\sim}^* (H, L) = (V, A),$$

where $\forall \omega \in A$;

$$V(\omega) = \begin{cases} F'(\omega), & \omega \in A \setminus L \\ F(\omega) \cap H(\omega), & \omega \in A \cap L \end{cases}$$

Let $(G, X) \underset{\gamma}{\sim}^* (H, L) = (W, X)$, where $\forall \omega \in X$;

$$W(\omega) = \begin{cases} G'(\omega), & \omega \in X \setminus L \\ G'(\omega) \cap H(\omega), & \omega \in X \cap L \end{cases}$$

Assume that $(V, A) \cap_{\varepsilon} (W, X) = (T, A \cup X)$, where $\forall \omega \in A \cup X$;

$$T(\omega) = \begin{cases} V(\omega), & \omega \in A \setminus X \\ W(\omega), & \omega \in X \setminus A \\ V(\omega) \cap W(\omega), & \omega \in A \cap X \end{cases}$$

Hence,

$$T(\omega) = \begin{cases} F'(\omega), & \omega \in (A \setminus L) \setminus X = A \cap X' \cap L' \\ F(\omega) \cap H(\omega), & \omega \in (A \cap L) \setminus X = A \cap X' \cap L \\ G'(\omega), & \omega \in (X \setminus L) \setminus A = A' \cap X \cap L' \\ G'(\omega) \cap H(\omega), & \omega \in (X \cap L) \setminus A = A' \cap X \cap L \\ F'(\omega) \cap G'(\omega), & \omega \in (A \setminus L) \cap (X \setminus L) = A \cap X \cap L' \\ F'(\omega) \cap [G'(\omega) \cap H(\omega)], & \omega \in (A \setminus L) \cap (X \cap L) = \emptyset \\ [F(\omega) \cap H(\omega)] \cap G'(\omega), & \omega \in (A \cap L) \cap (X \setminus L) = \emptyset \\ [F(\omega) \cap H(\omega)] \cap [G'(\omega) \cap H(\omega)], & \omega \in (A \cap L) \cap (X \cap L) = A \cap X \cap L \end{cases}$$

It is seen that $N = T$.

$$4) [(F, A) \lambda_{\varepsilon} (G, X)] \underset{\cap}{\sim}^* (H, L) = [(F, A) \underset{\cap}{\sim}^* (H, L)] \cup_{\varepsilon} [(G, X) \underset{\cap}{\sim}^* (H, L)],$$

where $A \cap X \cap L' = A' \cap X \cap L = \emptyset$.

4.2. Distribution of Complementary Soft Binary Piecewise Intersection Operation over Complementary Extended Soft Set Operations

4.2.1. Left-distribution of complementary soft binary piecewise intersection operation over complementary extended soft set operations

$$1) (F, A) \underset{\cap}{\sim}^* [(G, X) \underset{\cap}{\sim}^* (H, L)] = [(F, A) \underset{\cap}{\sim}^* (G, X)] \underset{\cap}{\sim}^* [(H, L) \underset{\cap}{\sim}^* (F, A)]$$

Proof: Let's first take care of the left hand facet of the equality. Let $(G, X) \underset{\cap}{\sim}^* (H, L) = (M, X \cup L)$ where $\forall \omega \in X \cup L$;

$$M(\omega) = \begin{cases} G'(\omega), & \omega \in X \setminus L \\ H'(\omega), & \omega \in L \setminus X \\ G'(\omega) \cup H'(\omega), & \omega \in X \cap L \end{cases}$$

Let $(F, A) \underset{\cap}{\sim}^* (M, X \cup L) = (N, A)$, where $\forall \omega \in A$;

$$N(\omega) = \begin{cases} F'(\omega), & \omega \in A \setminus (X \cup L) \\ F(\omega) \cap M(\omega), & \omega \in A \cap (X \cup L) \end{cases}$$

Thus,

$$N(\omega) = \begin{cases} F'(\omega), & \omega \in A \setminus (X \cup L) = A \cap X \cap L' \\ F(\omega) \cap G'(\omega), & \omega \in A \cap (X \setminus L) = A \cap X \cap L' \\ F(\omega) \cap H'(\omega), & \omega \in A \cap (L \setminus X) = A \cap X' \cap L \\ F(\omega) \cap [(G'(\omega) \cup H'(\omega))], & \omega \in A \cap X \cap L = A \cap X \cap L \end{cases}$$

Now let's take care of the right hand facet of the equality

$$[(F,A) \sim (G,X)] \tilde{\cup} [(H,L) \sim (F,A)]. \text{ Let } (F,A) \sim (G,X) = (V,A),$$

where $\forall \omega \in A$;

$$V(\omega) = \begin{cases} F'(\omega), & \omega \in A \setminus X \\ F(\omega) \cap G'(\omega), & \omega \in A \cap X \end{cases}$$

Let $(H,L) \sim (F,A) = (W,L)$, where $\forall \omega \in L$;

$$W(\omega) = \begin{cases} H'(\omega), & \omega \in L \setminus A \\ H(\omega) \cap F(\omega), & \omega \in L \cap A \end{cases}$$

Suppose that $(V,A) \tilde{\cup} (W,L) = (T,A)$, where $\forall \omega \in A$;

$$T(\omega) = \begin{cases} V(\omega), & \omega \in A \setminus L \\ V(\omega) \cup W(\omega), & \omega \in A \cap L \end{cases}$$

Thus,

$$T(\omega) = \begin{cases} F'(\omega), & \omega \in (A \setminus X) \setminus L = A \cap X' \cap L' \\ F(\omega) \cap G'(\omega), & \omega \in (A \cap X) \setminus L = A \cap X \cap L' \\ F'(\omega) \cup H'(\omega), & \omega \in (A \setminus X) \cap (L \setminus A) = \emptyset \\ F'(\omega) \cup [H(\omega) \cap F(\omega)], & \omega \in (A \setminus X) \cap (L \cap A) = A \cap X' \cap L \\ [F(\omega) \cap G'(\omega)] \cup H'(\omega), & \omega \in (A \cap X) \cap (L \setminus A) = \emptyset \\ [F(\omega) \cap G'(\omega)] \cup [H(\omega) \cap F(\omega)], & \omega \in (A \cap X) \cap (L \cap A) = A \cap X \cap L \end{cases}$$

It is seen that $N=T$.

$$2) (F,A) \sim \underset{\cup}{\theta_\varepsilon} [(G,X) \underset{\setminus}{\theta_\varepsilon} (H,L)] = [(F,A) \sim (G,X)] \tilde{\cap} [(H,L) \sim (F,A)]$$

$$3) (F,A) \sim \underset{\cap}{\theta_\varepsilon} [(G,X) \underset{+}{\theta_\varepsilon} (H,L)] = [(F,A) \sim (G,X)] \tilde{\cup} [(H,L) \sim (F,A)]$$

Proof: Let first take care of the lefthand facet of the equality. Assume $(G,X) \underset{+}{\theta_\varepsilon} (H,L) = (M,X \cup L)$ where $\forall \omega \in X \cup L$;

$$M(\omega) = \begin{cases} G'(\omega), & \omega \in X \setminus L \\ H'(\omega), & \omega \in L \setminus X \\ G'(\omega) \cup H(\omega), & \omega \in X \cap L \end{cases}$$

Let $(F,A) \sim (M,X \cup L) = (N,A)$, where $\forall \omega \in A$;

$$N(\omega) = \begin{cases} F'(\omega), & \omega \in A \setminus (X \cup L) \\ F(\omega) \cap M(\omega), & \omega \in A \cap (X \cup L) \end{cases}$$

Thus,

$$N(\omega) = \begin{cases} F'(\omega), & \omega \in A \setminus (X \cup L) = A \cap X' \cap L' \\ F(\omega) \cap G'(\omega), & \omega \in A \cap (X \setminus L) = A \cap X \cap L' \\ F(\omega) \cap H'(\omega), & \omega \in A \cap (L \setminus X) = A \cap X' \cap L \\ F(\omega) \cap [(G'(\omega) \cup H(\omega))], & \omega \in A \cap X \cap L = A \cap X \cap L \end{cases}$$

Now let's take care of the right hand facet of the equality

$$[(F,A) \sim (G,X)] \tilde{\cup} [(H,L) \sim (F,A)]. \text{ Assume that } (F,A) \sim (G,X) = (V,A), \text{ where } \forall \omega \in A;$$

$$V(\omega) = \begin{cases} F'(\omega), & \omega \in A \setminus X \\ F(\omega) \cap G'(\omega), & \omega \in A \cap X \end{cases}$$

Let $(H,L) \sim (F,A) = (W,L)$, where $\forall \omega \in A$;

$$W(\omega) = \begin{cases} H'(\omega), & \omega \in L \setminus A \\ H(\omega) \cap F(\omega), & \omega \in L \cap A \end{cases}$$

Suppose that $(V,A) \tilde{\cup} (W,L) = (T,A)$, where $\forall \omega \in A$;

$$T(\omega) = \begin{cases} V(\omega), & \omega \in A \setminus L \\ V(\omega) \cup W(\omega), & \omega \in A \cap L \end{cases}$$

Thus,

$$T(\omega) = \begin{cases} F'(\omega), & \omega \in (A \setminus X) \setminus L = A \cap X' \cap L' \\ F(\omega) \cap G'(\omega), & \omega \in (A \cap X) \setminus L = A \cap X \cap L' \\ F'(\omega) \cup H'(\omega), & \omega \in (A \setminus X) \cap (L \setminus A) = \emptyset \\ F'(\omega) \cup [H(\omega) \cap F(\omega)], & \omega \in (A \setminus X) \cap (L \cap A) = A \cap X' \cap L \\ [F(\omega) \cap G'(\omega)] \cup H'(\omega), & \omega \in (A \cap X) \cap (L \setminus A) = \emptyset \\ [F(\omega) \cap G'(\omega)] \cup [H(\omega) \cap F(\omega)], & \omega \in (A \cap X) \cap (L \cap A) = A \cap X \cap L \end{cases}$$

It is seen that $N=T$.

$$4) (F,A) \sim \underset{\cap}{\theta_\varepsilon} [(G,X) \underset{\setminus}{\theta_\varepsilon} (H,L)] = [(F,A) \sim (G,X)] \tilde{\cap} [(H,L) \sim (F,A)].$$

4.2.2. Right-distribution of complementary soft binary piecewise intersection operation over complementary extended soft set operations

$$1) [(F,A) \underset{\theta_\varepsilon}{\sim} (G,X)] \underset{\cap}{\sim} (H,L) = (F,A) \underset{\gamma}{\sim} [(H,L) \underset{\cap}{\sim} [(G,X) \underset{\gamma}{\sim} (H,L)]],$$

where $A \cap X \cap L' = \emptyset$

Proof: Let's first take care of the left hand facet of the equality. Let $(F,A) \underset{\theta_\varepsilon}{\sim} (G,X) = (M,A \cup X)$, where $\forall \omega \in A \cup X$;

$$M(\omega) = \begin{cases} F'(\omega), & \omega \in A \setminus X \\ G'(\omega), & \omega \in X \setminus A \\ F'(\omega) \cap G'(\omega), & \omega \in A \cap X \end{cases}$$

Let $(M,A \cup X) \underset{\cap}{\sim} (H,L) = (N,A \cup X)$, where $\forall \omega \in A \cup X$;

$$N(\omega) = \begin{cases} M'(\omega), & \omega \in (A \cup X) \setminus L \\ M(\omega) \cap H(\omega), & \omega \in (A \cup X) \cap L \end{cases}$$

Thus,

$$N(\omega) = \begin{cases} F(\omega), & \omega \in (A \setminus X) \setminus L = A \cap X' \cap L' \\ G(\omega), & \omega \in (X \setminus A) \setminus L = A' \cap X \cap L' \\ F(\omega) \cup G(\omega), & \omega \in (A \cap X) \setminus L = A \cap X \cap L' \\ F'(\omega) \cap H(\omega), & \omega \in (A \setminus X) \cap L = A \cap X' \cap L \\ G'(\omega) \cap H(\omega), & \omega \in (X \setminus A) \cap L = A' \cap X \cap L \\ [F'(\omega) \cap G'(\omega)] \cap H(\omega), & \omega \in (A \cap X) \cap L = A \cap X \cap L \end{cases}$$

Now let take care of the right hand facet of the equality: $[(F,A)_{\gamma} \sim (H,L)] \cap_{\varepsilon} [(G,X)_{\gamma} \sim (H,L)]$. Assume that $(F,A)_{\gamma} \sim (H,L) = (V,A)$, where $\forall \omega \in A$;

$$V(\omega) = \begin{cases} F(\omega), & \omega \in A \setminus L \\ F'(\omega) \cap H(\omega), & \omega \in A \cap L \end{cases}$$

Let $(G,X)_{\gamma} \sim (H,L) = (W,X)$, where $\forall \omega \in X$;

$$W(\omega) = \begin{cases} G(\omega), & \omega \in X \setminus L \\ G'(\omega) \cap H(\omega), & \omega \in X \cap L \end{cases}$$

Assume that $(V,A) \cap_{\varepsilon} (W,X) = (T,A \cup X)$, where $\forall \omega \in A \cup X$;

$$T(\omega) = \begin{cases} V(\omega), & \omega \in A \setminus X \\ W(\omega), & \omega \in X \setminus A \\ V(\omega) \cap W(\omega), & \omega \in A \cap X \end{cases}$$

Hence,

$$T(\omega) = \begin{cases} F(\omega), & \omega \in (A \setminus L) \setminus X = A \cap X' \cap L' \\ F'(\omega) \cap H(\omega), & \omega \in (A \cap L) \setminus X = A \cap X' \cap L \\ G(\omega), & \omega \in (X \setminus L) \setminus A = A' \cap X \cap L' \\ G'(\omega) \cap H(\omega), & \omega \in (X \cap L) \setminus A = A' \cap X \cap L \\ F(\omega) \cap G(\omega), & \omega \in (A \setminus L) \cap (X \setminus L) = A \cap X \cap L' \\ F(\omega) \cap [G'(\omega) \cap H(\omega)], & \omega \in (A \setminus L) \cap (X \cap L) = \emptyset \\ [F'(\omega) \cap H(\omega)] \cap G(\omega), & \omega \in (A \cap L) \cap (X \setminus L) = \emptyset \\ [F'(\omega) \cap H(\omega)] \cap [G'(\omega) \cap H(\omega)], & \omega \in (A \cap L) \cap (X \cap L) = A \cap X \cap L \end{cases}$$

It is seen that $N=T$.

$$2) [(F,A)_{\varepsilon}^* (G,X)] \sim (H,L) = [(F,A)_{\gamma} \sim (H,L)] \cup_{\varepsilon} [(G,X)_{\gamma} \sim (H,L)]$$

where $A \cap X \cap L' = \emptyset$

$$3) [(F,A)_{\gamma_{\varepsilon}}^* (G,X)] \sim (H,L) = [(F,A)_{\gamma} \sim (H,L)] \cap_{\varepsilon} [(G,X)_{\gamma} \sim (H,L)]$$

where $A \cap X \cap L' = A' \cap X \cap L = \emptyset$.

Proof: Let's first take care of the left hand facet of the equality, let $(F,A)_{\gamma_{\varepsilon}}^* (G,X) = (M,A \cup X)$, where $\forall \omega \in A \cup X$;

$$M(\omega) = \begin{cases} F'(\omega), & \omega \in A \setminus X \\ G'(\omega), & \omega \in X \setminus A \\ F'(\omega) \cap G(\omega), & \omega \in A \cap X \end{cases}$$

Let $(M,A \cup X) \sim (H,L) = (N,A \cup X)$, where $\forall \omega \in A \cup X$;

$$N(\omega) = \begin{cases} M'(\omega), & \omega \in (A \cup X) \setminus L \\ M(\omega) \cap H(\omega), & \omega \in (A \cup X) \cap L \end{cases}$$

Therefore,

$$N(\omega) = \begin{cases} F(\omega), & \omega \in (A \setminus X) \setminus L = A \cap X' \cap L' \\ G(\omega), & \omega \in (X \setminus A) \setminus L = A' \cap X \cap L' \\ F(\omega) \cup G'(\omega), & \omega \in (A \cap X) \setminus L = A \cap X \cap L' \\ F'(\omega) \cap H(\omega), & \omega \in (A \setminus X) \cap L = A \cap X' \cap L \\ G'(\omega) \cap H(\omega), & \omega \in (X \setminus A) \cap L = A' \cap X \cap L \\ [F'(\omega) \cap G(\omega)] \cap H(\omega), & \omega \in (A \cap X) \cap L = A \cap X \cap L \end{cases}$$

Now let's take care of the right hand facet of the equality: $[(F,A)_{\gamma} \sim (H,L)] \cap_{\varepsilon} [(G,X)_{\gamma} \sim (H,L)]$. Assume that $(F,A)_{\gamma} \sim (H,L) = (V,A)$, where $\forall \omega \in A$;

$$V(\omega) = \begin{cases} F(\omega), & \omega \in A \setminus L \\ F'(\omega) \cap H(\omega), & \omega \in A \cap L \end{cases}$$

Let $(G,X)_{\gamma} \sim (H,L) = (W,X)$, where $\forall \omega \in X$;

$$W(\omega) = \begin{cases} G(\omega), & \omega \in X \setminus L \\ G(\omega) \cap H(\omega), & \omega \in X \cap L \end{cases}$$

Assume that $(V,A) \cap_{\varepsilon} (W,X) = (T,A \cup X)$, where $\forall \omega \in A \cup X$;

$$T(\omega) = \begin{cases} V(\omega), & \omega \in A \setminus X \\ W(\omega), & \omega \in X \setminus A \\ V(\omega) \cap W(\omega), & \omega \in A \cap X \end{cases}$$

Hence,

$$T(\omega) = \begin{cases} F(\omega), & \omega \in (A \setminus L) \setminus X = A \cap X' \cap L' \\ F'(\omega) \cap H(\omega), & \omega \in (A \cap L) \setminus X = A \cap X' \cap L \\ G(\omega), & \omega \in (X \setminus L) \setminus A = A' \cap X \cap L' \\ G(\omega) \cap H(\omega), & \omega \in (X \cap L) \setminus A = A' \cap X \cap L \\ F(\omega) \cap G(\omega), & \omega \in (A \setminus L) \cap (X \setminus L) = A \cap X \cap L' \\ F(\omega) \cap [G(\omega) \cap H(\omega)], & \omega \in (A \setminus L) \cap (X \cap L) = \emptyset \\ [F'(\omega) \cap H(\omega)] \cap G(\omega), & \omega \in (A \cap L) \cap (X \setminus L) = \emptyset \\ [F'(\omega) \cap H(\omega)] \cap [G(\omega) \cap H(\omega)], & \omega \in (A \cap L) \cap (X \cap L) = A \cap X \cap L \end{cases}$$

It is seen that $N=T$.

$$4) [(F,A)_{\varepsilon}^* (G,X)] \sim (H,L) = [(F,A)_{\gamma} \sim (H,L)] \cup_{\varepsilon} [(G,X)_{\gamma} \sim (H,L)]$$

where $A \cap X \cap L' = A' \cap X \cap L = \emptyset$.

4.3. Distribution of Complementary Soft Binary Piecewise Intersection Operation over Soft Binary Piecewise Operations

4.3.1. Left-distribution of complementary soft binary piecewise intersection operation over soft binary piecewise operations

The followings are held where $A \cap X \cap L = \emptyset$:

$$1) (F,A)_{\gamma} \sim [(G,X)_{\gamma} \cup (H,L)] = [(F,A)_{\gamma} \sim (G,X)] \cup [(F,A)_{\gamma} \sim (H,L)]$$

Proof: Let's first take care of the left hand facet of the equality, let $(G,X)_{\gamma} \cup (H,L) = (M,X)$, where $\forall \omega \in X$;

$$M(\omega) = \begin{cases} G(\omega), & \omega \in X \setminus L \\ G(\omega) \cup H(\omega), & \omega \in X \cap L \end{cases}$$

Let $(F,A) \underset{\cap}{\sim} (M,X)=(N,A)$, where $\forall \omega \in A$;

$$N(\omega) = \begin{cases} F'(\omega), & \omega \in A \setminus X \\ F(\omega) \cap M(\omega), & \omega \in A \cap X \end{cases}$$

Thus,

$$N(\omega) = \begin{cases} F'(\omega), & \omega \in A \setminus X \\ F(\omega) \cap G(\omega), & \omega \in A \cap (X \setminus L) = A \cap X \cap L' \\ F(\omega) \cap [G(\omega) \cup H(\omega)], & \omega \in A \cap X \cap L = A \cap X \cap L \end{cases}$$

Now let take care of the right hand facet of the equality:

$$[(F,A) \underset{\cap}{\sim} (G,X)] \underset{\cap}{\tilde{\cup}} (H,L) \underset{\cap}{\sim} (F,A). \text{ Let } (F,A) \underset{\cap}{\sim} (G,X)=(V,A), \text{ where } \forall \omega \in A;$$

$$V(\omega) = \begin{cases} F'(\omega), & \omega \in A \setminus X \\ F(\omega) \cap G(\omega), & \omega \in A \cap X \end{cases}$$

Let $(H,L) \underset{\cap}{\sim} (F,A)=(W,L)$, where $\forall \omega \in L$;

$$W(\omega) = \begin{cases} H'(\omega), & \omega \in L \setminus A \\ H(\omega) \cap F(\omega), & \omega \in L \cap A \end{cases}$$

Suppose $(V,A) \underset{\cap}{\tilde{\cup}} (W,L)=(T,A)$, where $\forall \omega \in A$;

$$T(\omega) = \begin{cases} V(\omega), & \omega \in A \setminus L \\ V(\omega) \cup W(\omega), & \omega \in A \cap L \end{cases}$$

$$T(\omega) = \begin{cases} F'(\omega), & \omega \in (A \setminus X) \setminus L = A \cap X' \cap L' \\ F(\omega) \cap G(\omega), & \omega \in (A \cap X) \setminus L = A \cap X \cap L' \\ F'(\omega) \cup H'(\omega), & \omega \in (A \setminus X) \cap (L \setminus A) = \emptyset \\ F'(\omega) \cup [H(\omega) \cap F(\omega)], & \omega \in (A \setminus X) \cap (L \cap A) = A \cap X' \cap L \\ [F(\omega) \cap G(\omega)] \cup H'(\omega), & \omega \in (A \cap X) \cap (L \setminus A) = \emptyset \\ [F(\omega) \cap G(\omega)] \cup [H(\omega) \cap F(\omega)], & \omega \in (A \cap X) \cap (L \cap A) = A \cap X \cap L \end{cases}$$

Here let handle $\omega \in A \setminus X$ in the first equation of the first line. Since $A \setminus X = A \cap X'$, if $\omega \in X'$, then $\omega \in L \setminus X$ or $\omega \in (X \cup L)'$. Hence, if $\omega \in A \setminus X$, then $\omega \in A \cap X' \cap L'$ or $\omega \in A \cap X' \cap L$. Thus, it is seen that $N=T$.

$$\mathbf{2)} (F,A) \underset{\cap}{\sim} [(G,X) \underset{\cap}{\tilde{\cap}} (H,L)] = [(F,A) \underset{\cap}{\sim} (G,X)] \underset{\cap}{\tilde{\cap}} [(H,L) \underset{\cap}{\sim} (F,A)]$$

$$\mathbf{3)} (F,A) \underset{\cap}{\sim} [(G,X) \underset{\cap}{\tilde{\cup}} (H,L)] = [(F,A) \underset{\cap}{\sim} (G,X)] \underset{\cap}{\tilde{\cup}} [(H,L) \underset{\cap}{\sim} (F,A)].$$

Proof: Let's first take care of the left hand facet of the equality, let $(G,X) \underset{\cap}{\tilde{\cup}} (H,L)=(M,X)$, where $\forall \omega \in X$;

$$M(\omega) = \begin{cases} G(\omega), & \omega \in X \setminus L \\ G(\omega) \cap H'(\omega), & \omega \in X \cap L \end{cases}$$

$(F,A) \underset{\cap}{\sim} (M,X)=(N,A)$, where $\forall \omega \in A$;

$$N(\omega) = \begin{cases} F'(\omega), & \omega \in A \setminus X \\ F(\omega) \cap M(\omega), & \omega \in A \cap X \end{cases}$$

$$N(\omega) = \begin{cases} F'(\omega), & \omega \in A \setminus X \\ F(\omega) \cap G(\omega), & \omega \in A \cap (X \setminus L) = A \cap X \cap L' \\ F(\omega) \cap [G(\omega) \cap H'(\omega)], & \omega \in A \cap X \cap L = A \cap X \cap L \end{cases}$$

Now let's take care of the right hand facet of the equality

$$[(F,A) \underset{\cap}{\sim} (G,X)] \underset{\cap}{\tilde{\cap}} [(H,L) \underset{\cap}{\sim} (F,A)]. \text{ Let } (F,A) \underset{\cap}{\sim} (G,X)=(V,A), \text{ where } \forall \omega \in A;$$

$$V(\omega) = \begin{cases} F'(\omega), & \omega \in A \setminus X \\ F(\omega) \cap G(\omega), & \omega \in A \cap X \end{cases}$$

Let $(H,L) \underset{\cap}{\sim} (F,A)=(W,L)$, where $\forall \omega \in L$;

$$W(\omega) = \begin{cases} H'(\omega), & \omega \in L \setminus A \\ H'(\omega) \cap F(\omega), & \omega \in L \cap A \end{cases}$$

Assume that $(V,A) \underset{\cap}{\tilde{\cap}} (W,L)=(T,A)$, where $\forall \omega \in A$;

$$T(\omega) = \begin{cases} V(\omega), & \omega \in A \setminus L \\ V(\omega) \cap W(\omega), & \omega \in A \cap L \end{cases}$$

Therefore,

$$T(\omega) = \begin{cases} F'(\omega), & \omega \in (A \setminus X) \setminus L = A \cap X' \cap L' \\ F(\omega) \cap G(\omega), & \omega \in (A \cap X) \setminus L = A \cap X \cap L' \\ F'(\omega) \cap H'(\omega), & \omega \in (A \setminus X) \cap (L \setminus A) = \emptyset \\ F'(\omega) \cap [H'(\omega) \cap F(\omega)], & \omega \in (A \setminus X) \cap (L \cap A) = A \cap X' \cap L \\ [F(\omega) \cap G(\omega)] \cap H'(\omega), & \omega \in (A \cap X) \cap (L \setminus A) = \emptyset \\ [F(\omega) \cap G(\omega)] \cap H'(\omega), & \omega \in (A \cap X) \cap (L \cap A) = A \cap X \cap L \end{cases}$$

$$\mathbf{4)} (F,A) \underset{\cap}{\sim} [(G,X) \underset{\cap}{\tilde{\cap}} (H,L)] = [(F,A) \underset{\cap}{\sim} (G,X)] \underset{\cap}{\tilde{\cap}} [(H,L) \underset{\cap}{\sim} (F,A)]$$

4.3.2. Right-distribution of complementary soft binary piecewise intersection operation over soft binary piecewise operations

The followings are held where $A \cap X \cap L' = \emptyset$.

$$\mathbf{1)} [(F,A) \underset{\cap}{\tilde{\cup}} (G,X)] \underset{\cap}{\sim} (H,L) = [(F,A) \underset{\cap}{\sim} (H,L)] \underset{\cap}{\tilde{\cup}} [(G,X) \underset{\cap}{\sim} (H,L)].$$

Proof: Let first take care of the left hand facet of the equality. Suppose $(F,A) \underset{\cap}{\tilde{\cup}} (G,X)=(M,A)$, where $\forall \omega \in A$,

$$M(\omega) = \begin{cases} F(\omega), & \omega \in A \setminus X \\ F(\omega) \cup G(\omega), & \omega \in A \cap X \end{cases}$$

Let $(M,A) \underset{\cap}{\sim} (H,L)=(N,A)$, where $\forall \omega \in A$,

$$N(\omega) = \begin{cases} M'(\omega), & \omega \in A \setminus L \\ M(\omega) \cap H(\omega), & \omega \in A \cap L \end{cases}$$

$$N(\omega) = \begin{cases} F'(\omega), & \omega \in (A \setminus X) \setminus L = A \cap X' \cap L' \\ F'(\omega) \cap G'(\omega), & \omega \in (A \cap X) \setminus L = A \cap X \cap L' \\ F(\omega) \cap H(\omega), & \omega \in (A \setminus X) \cap L = A \cap X' \cap L \\ [F(\omega) \cup G(\omega)] \cap H(\omega), & \omega \in (A \cap X) \cap L = A \cap X \cap L \end{cases}$$

Now let's take care of the right hand facet of the equality

$$[(F,A) \sim (H,L)] \tilde{\cup} [(G,X) \sim (H,L)]. \text{ Let } (F,A) \sim (H,L) = (V,A),$$

where $\forall \omega \in A$;

$$V(\omega) = \begin{cases} F'(\omega), & \omega \in A \setminus L \\ F(\omega) \cap H(\omega), & \omega \in A \cap L \end{cases}$$

Let $(G,X) \sim (H,L) = (W,X)$, where $\forall \omega \in X$;

$$W(\omega) = \begin{cases} G'(\omega), & \omega \in X \setminus L \\ G(\omega) \cap H(\omega), & \omega \in X \cap L \end{cases}$$

Suppose that $(V,A) \tilde{\cup} (W,X) = (T,A)$, where $\forall \omega \in A$;

$$T(\omega) = \begin{cases} V(\omega), & \omega \in A \setminus X \\ V(\omega) \cup W(\omega), & \omega \in A \cap X \end{cases}$$

Thus,

$$T(\omega) = \begin{cases} F'(\omega), & \omega \in (A \setminus L) \setminus X = A \cap X' \cap L' \\ F(\omega) \cap H(\omega), & \omega \in (A \cap L) \setminus X = A \cap X' \cap L \\ F'(\omega) \cup G'(\omega), & \omega \in (A \setminus L) \cap (X \setminus L) = A \cap X \cap L' \\ F'(\omega) \cup [G(\omega) \cap H(\omega)], & \omega \in (A \setminus L) \cap (X \cap L) = \emptyset \\ [F(\omega) \cap H(\omega)] \cup G'(\omega), & \omega \in (A \cap L) \cap (X \setminus L) = \emptyset \\ [F(\omega) \cup G(\omega)] \cap H(\omega), & \omega \in (A \cap L) \cap (X \cap L) = A \cap X \cap L \end{cases}$$

It is seen that (1)=(2).

REMARK 2: In Yavuz (2023), it is proved that $(S_A(U), \tilde{\cup})$ is a commutative monoid with identity \emptyset_A . And in

Remark1, we show that $(S_A(U), \sim)$ is a commutative

monoid. Moreover, $\emptyset_A \sim (F,A) = \emptyset_A$. That is to say, \emptyset_A is

the left-absorbing element for the operation \sim . Besides,

by the subtitle 4.3.2. (1), \sim satisfies the right distributive

law over $\tilde{\cup}$. As a result we can conclude that $(S_A(U),$

$\tilde{\cup}, \sim$) is a (right) near-semiring. Moreover, since

$(F,A) \sim \emptyset_A = \emptyset_A \sim (F,A) = \emptyset_A$, $(S_A(U), \tilde{\cup}, \sim)$ is a zero-

symmetric near-semiring. One can similarly show that $(S_A(U), \tilde{\cup}, \sim)$ is also a hemiring.

$$2) [(F,A) \tilde{\cap} (G,X)] \sim (H,L) = [(F,A) \sim (H,L)] \tilde{\cap} [(G,X) \sim (H,L)]$$

$$3) [(F,A) \tilde{\cup} (G,X)] \sim (H,L) = [(F,A) \sim (H,L)] \tilde{\cup} [(G,X) \sim (H,L)].$$

Proof: Let's first take care of the left hand facet of the equality. Suppose $(F,A) \tilde{\cap} (G,X) = (M,A)$, where $\forall \omega \in A$,

$$M(\omega) = \begin{cases} F(\omega), & \omega \in A \setminus X \\ F(\omega) \cup G'(\omega), & \omega \in A \cap X \end{cases}$$

Let $(M,A) \sim (H,L) = (N,A)$, where $\forall \omega \in A$,

$$N(\omega) = \begin{cases} M'(\omega), & \omega \in A \setminus L \\ M(\omega) \cap H(\omega), & \omega \in A \cap L \end{cases}$$

Thus,

$$N(\omega) = \begin{cases} F'(\omega), & \omega \in (A \setminus X) \setminus L = A \cap X' \cap L' \\ F'(\omega) \cap G(\omega), & \omega \in (A \cap X) \setminus L = A \cap X \cap L' \\ F(\omega) \cap H(\omega), & \omega \in (A \setminus X) \cap L = A \cap X' \cap L \\ [F(\omega) \cup G'(\omega)] \cap H(\omega), & \omega \in (A \cap X) \cap L = A \cap X \cap L \end{cases}$$

Now let's take care of the right hand facet of the equality:

$$[(F,A) \sim (H,L)] \tilde{\cup} [(G,X) \sim (H,L)]. \text{ Let } (F,A) \sim (H,L) = (V,A),$$

where $\forall \omega \in A$;

$$V(\omega) = \begin{cases} F'(\omega), & \omega \in A \setminus L \\ F(\omega) \cap H(\omega), & \omega \in A \cap L \end{cases}$$

Let $(G,X) \sim (H,L) = (W,X)$, where $\forall \omega \in X$;

$$W(\omega) = \begin{cases} G'(\omega), & \omega \in X \setminus L \\ G'(\omega) \cap H(\omega), & \omega \in X \cap L \end{cases}$$

Suppose that $(V,A) \tilde{\cup} (W,X) = (T,A)$, where $\forall \omega \in A$;

$$T(\omega) = \begin{cases} V(\omega), & \omega \in A \setminus X \\ V(\omega) \cup W(\omega), & \omega \in A \cap X \end{cases}$$

Hence,

$$T(\omega) = \begin{cases} F'(\omega), & \omega \in (A \setminus L) \setminus X = A \cap X' \cap L' \\ F(\omega) \cap H(\omega), & \omega \in (A \cap L) \setminus X = A \cap X' \cap L \\ F'(\omega) \cup G'(\omega), & \omega \in (A \setminus L) \cap (X \setminus L) = A \cap X \cap L' \\ F'(\omega) \cup [G'(\omega) \cap H(\omega)], & \omega \in (A \setminus L) \cap (X \cap L) = \emptyset \\ [F(\omega) \cap H(\omega)] \cup G'(\omega), & \omega \in (A \cap L) \cap (X \setminus L) = \emptyset \\ [F(\omega) \cup G'(\omega)] \cap H(\omega), & \omega \in (A \cap L) \cap (X \cap L) = A \cap X \cap L \end{cases}$$

It is seen that $N=T$.

$$4) [(F,A) \tilde{\setminus} (G,X)] \sim (H,L) = [(F,A) \sim (H,L)] \tilde{\setminus} [(G,X) \sim (H,L)]$$

4.4. Distribution of Complementary Soft Binary Piecewise Intersection Operation over Complementary Soft Binary Piecewise Operations

4.4.1. Left-distribution of complementary soft binary piecewise intersection operation over complementary soft binary piecewise operations

$$1) (F,A) \sim \underset{\cap}{\underset{*}{[(G,X) \sim (H,L)]}} = \underset{\cap}{\underset{*}{[(F,A) \sim (G,X)]}} \tilde{\cup} \underset{\cap}{\underset{*}{[(H,L) \sim (F,A)]}}$$

where $A \cap X \cap L = \emptyset$

Proof: Let's first take care of the left hand facet of the equality, let $(G,X) \sim (H,L) = (M,X)$, where $\forall \omega \in X$;

$$M(\omega) = \begin{cases} G'(\omega), & \omega \in X \setminus L \\ G'(\omega) \cup H'(\omega), & \omega \in X \cap L \end{cases}$$

Let $(F,A) \sim (M,X) = (N,A)$, where $\forall \omega \in A$;

$$N(\omega) = \begin{cases} F'(\omega), & \omega \in A \setminus X \\ F(\omega) \cap M(\omega), & \omega \in A \cap X \end{cases}$$

$$N(\omega) = \begin{cases} F'(\omega), & \omega \in A \setminus X \\ F(\omega) \cap G'(\omega), & \omega \in A \cap (X \setminus L) = A \cap X \cap L' \\ F(\omega) \cap [(G'(\omega) \cup H'(\omega))], & \omega \in A \cap X \cap L = A \cap X \cap L \end{cases}$$

Now let's take care of the right hand facet of the equality:

$$[(F,A) \sim (G,X)] \tilde{\cup} [(H,L) \sim (F,A)]. \text{ Let } (F,A) \sim (G,X) = (V,A), \text{ where } \forall \omega \in A;$$

$$V(\omega) = \begin{cases} F'(\omega), & \omega \in A \setminus X \\ F(\omega) \cap G'(\omega), & \omega \in A \cap X \end{cases}$$

Suppose that $(H,L) \sim (F,A) = (W,L)$, where $\forall \omega \in L$;

$$W(\omega) = \begin{cases} H'(\omega), & \omega \in L \setminus A \\ H(\omega) \cap F'(\omega), & \omega \in L \cap A \end{cases}$$

Let $(V,A) \tilde{\cup} (W,L) = (T,A)$, where $\forall \omega \in A$;

$$T(\omega) = \begin{cases} V(\omega), & \omega \in A \setminus L \\ V(\omega) \cup W(\omega), & \omega \in A \cap L \end{cases}$$

Hence,

$$T(\omega) = \begin{cases} F'(\omega), & \omega \in (A \setminus X) \setminus L = A \cap X' \cap L' \\ F(\omega) \cap G'(\omega), & \omega \in (A \cap X) \setminus L = A \cap X \cap L' \\ F'(\omega) \cup H'(\omega), & \omega \in (A \setminus X) \cap (L \setminus A) = \emptyset \\ F'(\omega) \cup [H(\omega) \cap F'(\omega)], & \omega \in (A \setminus X) \cap (L \cap A) = A \cap X' \cap L \\ [F(\omega) \cap G'(\omega)] \cup H'(\omega), & \omega \in (A \cap X) \cap (L \setminus A) = \emptyset \\ [F(\omega) \cap [G'(\omega) \cup H'(\omega)]], & \omega \in (A \cap X) \cap (L \cap A) = A \cap X \cap L \end{cases}$$

$A \cap X'$, if $\omega \in X'$, then $\omega \in L \setminus X$ or $\omega \in (X \cup L)'$. Hence, if $\omega \in A \setminus X$, $\omega \in A \cap X' \cap L'$ or $\omega \in A \cap X' \cap L$. Thus, it is seen that $N=T$.

$$2) (F,A) \sim \underset{\cap}{\underset{\theta}{[(G,X) \sim (H,L)]}} = \underset{\cap}{\underset{\theta}{[(F,A) \sim (G,X)]}} \tilde{\cup} \underset{\cap}{\underset{\theta}{[(H,L) \sim (F,A)]}}$$

where $A \cap X \cap L = \emptyset$

$$3) (F,A) \sim \underset{\cap}{\underset{\gamma}{[(G,X) \sim (H,L)]}} = \underset{\cap}{\underset{\gamma}{[(F,A) \sim (G,X)]}} \tilde{\cap} \underset{\cap}{\underset{\gamma}{[(H,L) \sim (F,A)]}}$$

where $A \cap X' \cap L = \emptyset$

Proof: Let's first take care of the left hand facet of the equality, let $(G,X) \sim (H,L) = (M,X)$, where $\forall \omega \in X$;

$$M(\omega) = \begin{cases} G'(\omega), & \omega \in X \setminus L \\ G'(\omega) \cap H(\omega), & \omega \in X \cap L \end{cases}$$

Let $(F,A) \sim (M,X) = (N,A)$, where $\forall \omega \in A$;

$$N(\omega) = \begin{cases} F'(\omega), & \omega \in A \setminus X \\ F(\omega) \cap M(\omega), & \omega \in A \cap X \end{cases}$$

Therefore,

$$N(\omega) = \begin{cases} F'(\omega), & \omega \in A \setminus X \\ F(\omega) \cap G'(\omega), & \omega \in A \cap (X \setminus L) = A \cap X \cap L' \\ F(\omega) \cap [(G'(\omega) \cap H(\omega))], & \omega \in A \cap X \cap L = A \cap X \cap L \end{cases}$$

Now let's take care of the right hand facet of the equality:

$$[(F,A) \sim (G,X)] \tilde{\cap} [(H,L) \sim (F,A)]. \text{ Let } (F,A) \sim (G,X) = (V,A), \text{ where } \forall \omega \in A;$$

$$V(\omega) = \begin{cases} F'(\omega), & \omega \in A \setminus X \\ F(\omega) \cap G'(\omega), & \omega \in A \cap X \end{cases}$$

Suppose that $(H,L) \sim (F,A) = (W,L)$, where $\forall \omega \in L$;

$$W(\omega) = \begin{cases} H'(\omega), & \omega \in L \setminus A \\ H(\omega) \cap F(\omega), & \omega \in L \cap A \end{cases}$$

Let $(V,A) \tilde{\cap} (W,L) = (T,A)$, where $\forall \omega \in A$;

$$T(\omega) = \begin{cases} V(\omega), & \omega \in A \setminus L \\ V(\omega) \cap W(\omega), & \omega \in A \cap L \end{cases}$$

$$T(\omega) = \begin{cases} F'(\omega), & \omega \in (A \setminus X) \setminus L = A \cap X' \cap L' \\ F(\omega) \cap G'(\omega), & \omega \in (A \cap X) \setminus L = A \cap X \cap L' \\ F'(\omega) \cap H'(\omega), & \omega \in (A \setminus X) \cap (L \setminus A) = \emptyset \\ F'(\omega) \cap [H(\omega) \cap F(\omega)], & \omega \in (A \setminus X) \cap (L \cap A) = A \cap X' \cap L \\ [F(\omega) \cap G'(\omega)] \cap H'(\omega), & \omega \in (A \cap X) \cap (L \setminus A) = \emptyset \\ [F(\omega) \cap G'(\omega)] \cap H(\omega), & \omega \in (A \cap X) \cap (L \cap A) = A \cap X \cap L \end{cases}$$

Here let's handle $\omega \in A \setminus X$ in the first equation. Since $A \setminus X =$

$$4) (F,A) \underset{\cap}{\sim} [(G,X) \underset{+}{\sim} (H,L)] = [(F,A) \underset{\setminus}{\sim} (G,X)] \underset{\cap}{\tilde{\cup}} [(H,L) \underset{\cap}{\sim} (F,A)]$$

where $A \cap X' \cap L = \emptyset$

4.4.2. Right-distribution of complementary soft binary piecewise intersection operation over complementary soft binary piecewise operations

The followings are held where $A \cap X \cap L' = \emptyset$:

$$1) [(F,A) \underset{\theta}{\sim} (G,X)] \underset{\cap}{\sim} (H,L) = [(F,A) \underset{\setminus}{\sim} (H,L)] \underset{\cap}{\tilde{\cap}} [(G,X) \underset{\setminus}{\sim} (H,L)]$$

Proof: Let's first take care of the left hand facet of the equality, let $(F,A) \underset{\theta}{\sim} (G,X) = (M,A)$, where $\forall \omega \in A$,

$$M(\omega) = \begin{cases} F'(\omega), & \omega \in A \setminus X \\ F'(\omega) \cap G'(\omega), & \omega \in A \cap X \end{cases}$$

Let $(M,A) \underset{\cap}{\sim} (H,L) = (N,A)$, where $\forall \omega \in A$,

$$N(\omega) = \begin{cases} M'(\omega), & \omega \in A \setminus L \\ M(\omega) \cap H(\omega), & \omega \in A \cap L \end{cases}$$

Thus,

$$N(\omega) = \begin{cases} F(\omega), & \omega \in (A \setminus X) \setminus L = A \cap X' \cap L' \\ F(\omega) \cup G(\omega), & \omega \in (A \cap X) \setminus L = A \cap X \cap L' \\ F'(\omega) \cap H(\omega), & \omega \in (A \setminus X) \cap L = A \cap X' \cap L \\ [F'(\omega) \cap G'(\omega)] \cap H(\omega), & \omega \in (A \cap X) \cap L = A \cap X \cap L \end{cases}$$

Now let's take care of the right hand facet of the equality:

$[(F,A) \underset{\setminus}{\sim} (H,L)] \underset{\cap}{\tilde{\cap}} [(G,X) \underset{\setminus}{\sim} (H,L)]$. Let $(F,A) \underset{\setminus}{\sim} (H,L) = (V,A)$, where $\forall \omega \in A$;

$$V(\omega) = \begin{cases} F(\omega), & \omega \in A \setminus L \\ F'(\omega) \cap H(\omega), & \omega \in A \cap L \end{cases}$$

Assume that $(G,X) \underset{\setminus}{\sim} (H,L) = (W,X)$, where $\forall \omega \in X$;

$$W(\omega) = \begin{cases} G(\omega), & \omega \in X \setminus L \\ G'(\omega) \cap H(\omega), & \omega \in X \cap L \end{cases}$$

Let $(V,A) \underset{\cap}{\tilde{\cap}} (W,X) = (T,A)$, where $\forall \omega \in A$;

$$T(\omega) = \begin{cases} V(\omega), & \omega \in A \setminus X \\ V(\omega) \cap W(\omega), & \omega \in A \cap X \end{cases}$$

Therefore,

$$T(\omega) = \begin{cases} F(\omega), & \omega \in (A \setminus L) \setminus X = A \cap X' \cap L' \\ F'(\omega) \cap H(\omega), & \omega \in (A \cap L) \setminus X = A \cap X' \cap L \\ F(\omega) \cap G(\omega), & \omega \in (A \setminus L) \cap (X \setminus L) = A \cap X \cap L' \\ F(\omega) \cap [G'(\omega) \cap H(\omega)], & \omega \in (A \setminus L) \cap (X \cap L) = \emptyset \\ [F'(\omega) \cap H(\omega)] \cap G(\omega), & \omega \in (A \cap L) \cap (X \setminus L) = \emptyset \\ [F'(\omega) \cap G'(\omega)] \cap H(\omega), & \omega \in (A \cap L) \cap (X \cap L) = A \cap X \cap L \end{cases}$$

It is seen that $N=T$.

$$2) [(F,A) \underset{\cap}{\sim} (G,X)] \underset{\cap}{\sim} (H,L) = [(F,A) \underset{\setminus}{\sim} (H,L)] \underset{\cap}{\tilde{\cup}} [(G,X) \underset{\setminus}{\sim} (H,L)]$$

$$3) [(F,A) \underset{+}{\sim} (G,X)] \underset{\cap}{\sim} (H,L) = [(F,A) \underset{\setminus}{\sim} (H,L)] \underset{\cap}{\tilde{\cup}} [(G,X) \underset{\setminus}{\sim} (H,L)]$$

Proof: Let's first take care of the left hand facet of the equality, let $(F,A) \underset{+}{\sim} (G,X) = (M,A)$, where $\forall \omega \in A$,

$$M(\omega) = \begin{cases} F'(\omega), & \omega \in A \setminus X \\ F'(\omega) \cup G(\omega), & \omega \in A \cap X \end{cases}$$

Let $(M,A) \underset{\cap}{\sim} (H,L) = (N,A)$, where $\forall \omega \in A$,

$$N(\omega) = \begin{cases} M'(\omega), & \omega \in A \setminus L \\ M(\omega) \cap H(\omega), & \omega \in A \cap L \end{cases}$$

Hence,

$$N(\omega) = \begin{cases} F(\omega), & \omega \in (A \setminus X) \setminus L = A \cap X' \cap L' \\ F(\omega) \cap G'(\omega), & \omega \in (A \cap X) \setminus L = A \cap X \cap L' \\ F'(\omega) \cap H(\omega), & \omega \in (A \setminus X) \cap L = A \cap X' \cap L \\ [F'(\omega) \cup G(\omega)] \cap H(\omega), & \omega \in (A \cap X) \cap L = A \cap X \cap L \end{cases}$$

Now let's take care of the right hand facet of the equality:

$[(F,A) \underset{\setminus}{\sim} (H,L)] \underset{\cap}{\tilde{\cup}} [(G,X) \underset{\setminus}{\sim} (H,L)]$. Let $(F,A) \underset{\setminus}{\sim} (H,L) = (V,A)$, where $\forall \omega \in A$;

$$V(\omega) = \begin{cases} F(\omega), & \omega \in A \setminus L \\ F'(\omega) \cap H(\omega), & \omega \in A \cap L \end{cases}$$

Assume that $(G,X) \underset{\setminus}{\sim} (H,L) = (W,X)$, where $\forall \omega \in X$;

$$W(\omega) = \begin{cases} G(\omega), & \omega \in X \setminus L \\ G(\omega) \cap H(\omega), & \omega \in X \cap L \end{cases}$$

Let $(V,A) \underset{\cap}{\tilde{\cup}} (W,X) = (T,A)$, where $\forall \omega \in A$;

$$T(\omega) = \begin{cases} V(\omega), & \omega \in A \setminus X \\ V(\omega) \cup W(\omega), & \omega \in A \cap X \end{cases}$$

Therefore,

$$T(\omega) = \begin{cases} F(\omega), & \omega \in (A \setminus L) \setminus X = A \cap X' \cap L' \\ F'(\omega) \cap H(\omega), & \omega \in (A \cap L) \setminus X = A \cap X' \cap L \\ F(\omega) \cup G(\omega), & \omega \in (A \setminus L) \cap (X \setminus L) = A \cap X \cap L' \\ F(\omega) \cup [G(\omega) \cap H(\omega)], & \omega \in (A \setminus L) \cap (X \cap L) = \emptyset \\ [F'(\omega) \cap H(\omega)] \cup G(\omega), & \omega \in (A \cap L) \cap (X \setminus L) = \emptyset \\ [F'(\omega) \cup G(\omega)] \cap H(\omega), & \omega \in (A \cap L) \cap (X \cap L) = A \cap X \cap L \end{cases}$$

It is seen that $N=T$.

$$4) [(F,A) \underset{\cap}{\sim} (G,X)] \underset{\cap}{\sim} (H,L) = [(F,A) \underset{\setminus}{\sim} (H,L)] \underset{\cap}{\tilde{\cap}} [(G,X) \underset{\setminus}{\sim} (H,L)]$$

4.5. Distribution of Complementary Soft Binary Piecewise Intersection Operation over Restricted Soft Set Operations

The followings are held where $A \cap X \cap L = \emptyset$.

$$1) (F,A) \underset{\cap}{\sim} [(G,X) \cap_R (H,L)] = [(F,A) \underset{\cup}{\sim} (G,X)] \cup_R [(F,A) \underset{\sim}{\sim} (H,L)]$$

Proof: Let's first take care of the left hand facet of the equality, suppose $(G,X) \cap_R (H,L) = (M, X \cap L)$ and so $\forall \omega \in X \cap L$,

$$M(\omega) = G(\omega) \cap H(\omega). \text{ Let } (F,A) \underset{\sim}{\sim} (M, X \cap L) = (N,A), \text{ so } \forall \omega \in A,$$

$$N(\omega) = \begin{cases} F'(\omega), & \omega \in A \setminus (X \cap L) \\ F(\omega) \cap M(\omega), & \omega \in A \cap (X \cap L) \end{cases}$$

$$N(\omega) = \begin{cases} F'(\omega), & \omega \in A \setminus (X \cap L) \\ F(\omega) \cap [G(\omega) \cap H(\omega)], & \omega \in A \cap (X \cap L) \end{cases}$$

Now let's take care of the right hand facet of the equality:

$$[(F,A) \underset{\cup}{\sim} (G,X)] \cup_R [(F,A) \underset{\sim}{\sim} (H,L)]. \text{ Let } (F,A) \underset{\sim}{\sim} (G,X) = (V,A),$$

so $\forall \omega \in A$,

$$V(\omega) = \begin{cases} F'(\omega), & \omega \in A \setminus X \\ F'(\omega) \cap G(\omega), & \omega \in A \cap X \end{cases}$$

Let $(F,A) \underset{\sim}{\sim} (H,L) = (W,A)$, so $\forall \omega \in A$,

$$W(\omega) = \begin{cases} F'(\omega), & \omega \in A \setminus L \\ F'(\omega) \cap H(\omega), & \omega \in A \cap L \end{cases}$$

Assume that $(V,A) \cup_R (W,A) = (T,A)$, and so $\forall \omega \in A$, $T(\omega) = V(\omega) \cup W(\omega)$. Thus,

$$T(\omega) = \begin{cases} F'(\omega) \cup F'(\omega), & \omega \in (A \setminus X) \cap (A \setminus L) \\ F'(\omega) \cup [F'(\omega) \cap H(\omega)], & \omega \in (A \setminus X) \cap (A \cap L) \\ [F'(\omega) \cap G(\omega)] \cup F'(\omega), & \omega \in (A \cap X) \cap (A \setminus L) \\ [F'(\omega) \cap G(\omega)] \cup [F'(\omega) \cap H(\omega)], & \omega \in (A \cap X) \cap (A \cap L) \end{cases}$$

Hence,

$$T(\omega) = \begin{cases} F'(\omega), & \omega \in A \cap X' \cap L' \\ F'(\omega), & \omega \in A \cap X' \cap L \\ F'(\omega), & \omega \in A \cap X \cap L' \\ [F'(\omega) \cap G(\omega)] \cup [F'(\omega) \cap H(\omega)], & \omega \in A \cap X \cap L \end{cases}$$

Considering the parameter set of the first equation of the first row, that is, $A \setminus (X \cap L)$; since $A \setminus (X \cap L) = A \cap (X \cap L)'$, an element in $(X \cap L)'$ may be in $X \setminus L$, in $L \setminus X$ or $(X \cup L)$. Then, $A \setminus (X \cap L)$ is equivalent to the following 3 states: $A \cap (X \cap L)'$, $A \cap (X' \cap L)$ and $A \cap (X' \cap L')$. Hence, (1)=(2).

$$2) (F,A) \underset{\sim}{\sim} [(G,X) \cup_R (H,L)] = [(F,A) \underset{\sim}{\sim} (G,X)] \cap_R [(F,A) \underset{\sim}{\sim} (H,L)]$$

$$3) (F,A) \underset{\sim}{\sim} [(G,X) \theta_R (H,L)] = [(F,A) \underset{\sim}{\sim} (G,X)] \cup_R [(F,A) \underset{\sim}{\sim} (H,L)]$$

Proof: Let's first take care of the left hand facet of the equality, suppose $(G,X) \theta_R (H,L) = (M, X \cap L)$ and so $\forall \omega \in X \cap L$,

$$M(\omega) = G'(\omega) \cap H'(\omega). \text{ Let } (F,A) \underset{\sim}{\sim} (M, X \cap L) = (N,A), \text{ so } \forall \omega \in A,$$

$$N(\omega) = \begin{cases} F'(\omega), & \omega \in A \setminus (X \cap L) \\ F(\omega) \cap M(\omega), & \omega \in A \cap (X \cap L) \end{cases}$$

Thus,

$$N(\omega) = \begin{cases} F'(\omega), & \omega \in A \setminus (X \cap L) \\ F(\omega) \cap [G'(\omega) \cap H'(\omega)], & \omega \in A \cap (X \cap L) \end{cases}$$

Now let's take care of the right hand facet of the equality,

$$[(F,A) \underset{\theta}{\sim} (G,X)] \cup_R [(F,A) \underset{\theta}{\sim} (H,L)]. \text{ Let } (F,A) \underset{\theta}{\sim} (G,X) = (V,A),$$

and $\forall \omega \in A$,

$$V(\omega) = \begin{cases} F'(\omega), & \omega \in A \setminus X \\ F'(\omega) \cap G'(\omega), & \omega \in A \cap X \end{cases}$$

Let $(F,A) \underset{\theta}{\sim} (H,L) = (W,A)$ and $\in A$,

$$W(\omega) = \begin{cases} F'(\omega), & \omega \in A \setminus L \\ F'(\omega) \cap H'(\omega), & \omega \in A \cap L \end{cases}$$

Assume that $(V,A) \cup_R (W,A) = (T,A)$, so $\forall \omega \in T(\omega) = V(\omega) \cup W(\omega)$,

$$T(\omega) = \begin{cases} F'(\omega) \cup F'(\omega), & \omega \in (A \setminus X) \cap (A \setminus L) \\ F'(\omega) \cup [F'(\omega) \cap H'(\omega)], & \omega \in (A \setminus X) \cap (A \cap L) \\ [F'(\omega) \cap G'(\omega)] \cup F'(\omega), & \omega \in (A \cap X) \cap (A \setminus L) \\ [F'(\omega) \cap G'(\omega)] \cup [F'(\omega) \cap H'(\omega)], & \omega \in (A \cap X) \cap (A \cap L) \end{cases}$$

Thus,

$$T(\omega) = \begin{cases} F'(\omega), & \omega \in A \cap X' \cap L' \\ F'(\omega), & \omega \in A \cap X' \cap L \\ F'(\omega), & \omega \in A \cap X \cap L' \\ [F'(\omega) \cap G'(\omega)] \cup [F'(\omega) \cap H'(\omega)], & \omega \in A \cap X \cap L \end{cases}$$

$$4) (F,A) \underset{\cap}{\sim} [(G,X) *_{\cap} (H,L)] = [(F,A) \underset{\sim}{\sim} (G,X)] \cap_R [(F,A) \underset{\sim}{\sim} (H,L)]$$

$$5) (F,A) \underset{\cap}{\sim} (G,X) \gamma_R (H,L) = [(F,A) \underset{\sim}{\sim} (G,X)] \cup_R [(F,A) \underset{\sim}{\sim} (H,L)]$$

Proof: Let's first take care of the left hand facet of the equality, suppose $(G,X) \gamma_R (H,L) = (M, X \cap L)$ and so $\forall \omega \in X \cap L$,

$$M(\omega) = G'(\omega) \cap H(\omega). \text{ Let } (F,A) \underset{\sim}{\sim} (M, X \cap L) = (N,A), \text{ so } \forall \omega \in A,$$

$$N(\omega) = \begin{cases} F'(\omega), & \omega \in A \setminus (X \cap L) \\ F(\omega) \cap M(\omega), & \omega \in A \cap (X \cap L) \end{cases}$$

Thus,

Author Contributions

The percentage of the author(s) contributions is presented below. All authors reviewed and approved the final version of the manuscript.

| | A.S. | F.N.A. | A.O.A. |
|-----|------|--------|--------|
| C | 34 | 33 | 33 |
| D | 34 | 33 | 33 |
| S | 34 | 33 | 33 |
| DCP | 34 | 33 | 33 |
| DAI | 34 | 33 | 33 |
| L | 34 | 33 | 33 |
| W | 34 | 33 | 33 |
| CR | 34 | 33 | 33 |
| SR | 34 | 33 | 33 |
| PM | 34 | 33 | 33 |
| FA | 34 | 33 | 33 |

C=Concept, D= design, S= supervision, DCP= data collection and/or processing, DAI= data analysis and/or interpretation, L= literature search, W= writing, CR= critical review, SR= submission and revision, PM= project management, FA= funding acquisition.

Conflict of Interest

The authors declared that there is no conflict of interest.

Ethical Consideration

Ethics committee approval was not required for this study because of there was no study on animals or humans.

References

Akbulut E. 2023. New type of extended operations of soft set: Complementary extended lambda and difference operations. Master Thesis, Amasya University, The Graduate School of Natural and Applied Sciences, Mathematics Department, Amasya, Türkiye, pp: 105.

Ali MI, Feng F, Liu X, Min WK, Shabir M. 2009. On some new operations in soft set theory. *Comput Math Appl*, 57(9): 1547-1553.

Aybek F. 2023. New restricted and extended soft set operations. Master Thesis, Amasya University, The Graduate School of Natural and Applied Sciences Mathematics Department, Amasya, Türkiye, pp: 186.

Çağman N. 2021. Conditional complements of sets and their application to group theory. *J New Results Sci*, 10(3): 67-74.

Demirci AM. 2023. New type of extended operations of soft set: Complementary extended plus, union and theta operations. Master Thesis, Amasya University, The Graduate School of Natural and Applied Sciences, Mathematics Department, Amasya, Türkiye, pp: 105.

Eren ÖF, Çalışıcı H. 2019. On some operations of soft sets. The Fourth International Conference on Computational Mathematics and Engineering Sciences (CMES-2019), April 20-22, 2019, Antalya, Türkiye.

Hoorn WGV, Rootselaar VB. 1967. Fundamental notions in the theory of seminearrings. *Composit Math*, 18(1-2): 65.

Maji PK, Bismas R, Roy AR. 2003. Soft set theory. *Comput Math Appl*, 45(1): 555-562.

Molodtsov D. 1999. Soft set theory-first results. *Comput Math Appl*, 37(1): 19-31.

Özlu Ş, Sezgin A. 2020. Soft covered ideals in semigroups. *Acta Univ Sapientiae Math*, 12(2): 317-346.

Özlu Ş. 2022a. Interval Valued q- rung orthopair hesitant fuzzy choquet aggregating operators in multi-criteria decision making problems. *Gazi Univ J Sci Part C: Design Tech*, 10(4): 1006-1025.

Özlu Ş. 2022b. Interval valued bipolar fuzzy prioritized weighted dombi averaging operator based on multi-criteria decision making problems. *Gazi Univ J Sci Part C: Design Tech*, 10(4): 841-857.

Pei D, Miao D. 2005. From soft sets to information systems. In: *Proceedings of Granular Computing IEEE*, 2: 617-621.

Pilz G. 1977. *Near Rings*. Amsterdam, Nederland.

Sarialioğlu M. 2023a. New type of extended operations of soft set: Complementary extended gamma, intersection and star operations. Master Thesis, Amasya University, The Graduate School of Natural and Applied Sciences, Mathematics Department, Amasya, Türkiye, pp: 78.

Sezgin A, Atagün AO. 2011. On operations of soft sets. *Comput Math Appl*, 61(5):1457-1467.

Sezgin A, Aybek F, Güngör Bilgili N. 2023a. New soft set operation: Complementary soft binary piecewise union operation. *Acta Inform Malaysia*, 7(1): 38-53

Sezgin A, Aybek F. 2023. New soft set operation: Complementary soft binary piecewise gamma operation. *Matrix Sci Math*, 7(1): 27-45.

Sezgin A, Çağman N, Atagün AO, Aybek F. 2023b. Complemental binary operations of sets and their application to group theory. *Matrix Sci Math*, 7(2): 91-98.

Sezgin A, Demirci AM. 2023. New soft set operation: Complementary soft binary piecewise star operation. *Ikonion J Math*, 5(2): 24-52.

Sezgin A, Shahzad A, Mehmood A. 2019. New operation on soft sets: extended difference of soft sets. *J New Theory*, (27): 33-42.

Sezgin A, Yavuz E. 2023. New soft set operation: Complementary soft binary piecewise lambda operation. *Sinop JNS*, (in press). DOI:10.33484/sinopfdb.1320420

Stojanovic NS. 2021. A new operation on soft sets: extended symmetric difference of soft sets. *Military Tech Courier*, 69(4): 779-791.

Taşdemir F, Atagün AO, Altındış H. 2013. Different prime N-ideals and IFP N-Ideals. *Indian J Pure Appl Math*, 44(4): 527-542.

Taşdemir F, Taştekin İ. 2019. On P-3-prime and P-c-prime ideals in near-rings. *J Algebra Number Theory Appl*, 42(1): 49-57.

Yavuz E. 2023. Soft binary piecewise operations and their properties. Master Thesis, Amasya University, The Graduate School of Natural and Applied Sciences, Mathematics Department, Amasya, Türkiye, pp: 169.



OPTIMIZATION USING TAGUCHI METHOD TO INVESTIGATE THE EFFECTS OF PROCESS PARAMETERS ON THE HARDNESS OF DEVELOPED ALUMINIUM ROOFING SHEETS

Dickson David OLODU^{1*}, Andrew ERAMEH²

¹Benson Idahosa University, Faculty of Engineering, Department of Mechanical Engineering, Benin City, Edo State, Nigeria


²Igbinedion University, Faculty of Engineering, Department of Mechanical Engineering, Okada, Edo State, Nigeria


Abstract: This study focused on the optimization using taguchi method to investigate the effects of process parameters on the hardness of developed aluminium roofing sheets. Maximizing process variables like manufacturing temperature, manufacturing pressure, cooling time, and percentage of magnesium in aluminium, the Taguchi Method, a statistical method, was used to enhance the manufacturing quality of aluminium roofing sheets. Using an orthogonal array, a signal-to-noise ratio, and an analysis of variance, the effects of process variables on the hardness of the produced aluminium roofing sheets were examined. In this analysis, four factors; manufacturing temperature, manufacturing pressure, cooling time, and the percentage of magnesium in the aluminium roofing sheet were investigated. Thus, a suitable orthogonal array was selected, and experiments were conducted. Following the trial, the process parameters were evaluated, and the signal-to-noise ratio was calculated. The best parameter values were determined with the use of graphs, and confirmation trials were performed. The results showed that an aluminium roofing sheet's maximum hardness of 65.0kgf was obtained at a manufacturing temperature of 1250 °C, a manufacturing pressure of 65 GPa, a cooling period of 95 seconds, and a magnesium content of 0.5%. The most important influences on the hardness of aluminium roofing sheets was found to be the percentage of magnesium in aluminium roofing sheets followed by manufacturing pressure and manufacturing temperature. The cooling time was found to be the least efficient one. The obtained results in this study were used to improve the material property (hardness) of aluminum roofing sheet and investigate the effects of production factors in aluminum production industries.

Keywords: Aluminium sheets, Design of experiments, Hardness, Manufacturing, Signal-to-noise ratio

*Corresponding author: Benson Idahosa University, Faculty of Engineering, Department of Mechanical Engineering, Benin City, Edo State, Nigeria

E mail: dolodu@biu.edu.ng (D. D. OLODU)

Dickson David OLODU  <https://orcid.org/0000-0003-3383-2543>

Andrew ERAMEH  <https://orcid.org/0000-0002-6463-143X>

Received: March 30, 2023

Accepted: June 23, 2023

Published: October 15, 2023

Cite as: Olodu DD, Emareh A. 2023. Optimization using Taguchi method to investigate the effects of process parameters on the hardness of developed aluminium roofing sheets. *BSJ Eng Sci*, 6(4): 347-355.

1. Introduction

Most technical applications that demand outstanding mechanical properties require the development of metal matrix composites. Moreover, applications requiring low weight, such as in the aerospace and automotive sectors, use aluminium alloys (Altan, 2010). This is because aluminium alloy has great qualities such as increased stiffness (a higher strength-to-weight ratio), increased heat conductivity, and corrosion resistance. However, compared to steels, it has a lower melting point, less temperature stability, and a lower tensile and fatigue strength (Fratilia and Caizar, 2011; Zitoun, 2019). Aluminium alloy composite materials were created with increased strength and without changing the fundamental characteristics of aluminium alloys (Zitoun, 2019; Foster, 2000). The matrix phase makes up the majority of a composite substance while the reinforcement makes up the minority (Friend, 1987). Here, the matrix phase and reinforcement phase combine to create a composite substance. Various reinforcements, including Silicon carbide (SiC) (Joardar et al., 2012), Titanium diboride (TiB₂), Titanium carbide (TiC), Boron

Carbide (B₄C), Aluminium oxide (Al₂O₃), Magnesium oxide (MgO), and fly ash (Kok, 2004; Manigandan et al., 2011), can be mixed with an aluminium matrix. Several techniques, including powder metallurgy, spray coating, electroplating, and stir casting, are used in the production of aluminium metal matrix composites (Singla et al., 2009). The production technique known as stir casting is more cost-effective and ideal for mass production. The metal matrix composite is primarily reinforced with whiskers and other particulate types using the stir casting method (Meena and Manna, 2013). Due to the lower density difference and greater wettability of Silicon carbide (SiC) compared to aluminium, it is frequently used as reinforcement in aluminium metal matrix composites (Olodu, 2018; Olodu, 2021). Prior to casting, the reinforcement and matrix were preheated individually (Osarenmwinda and Olodu, 2018; Rao et al., 2019). Aluminium- Silicon carbide (Al/SiC) composite is created by pouring reinforcement into a molten metal matrix that has reached its melting point and is being stirred with a motorized stirrer (Sozhamannan et al., 2012; Srinivas and Venkatesh,



2012; Saravanan et al., 2015).

Taguchi and Konishi created a statistical technique in 1987 known as the Taguchi method (Taguchi and Konishi, 1987). It was used to achieve the best results from the process, the Taguchi Method entails the identification of suitable control parameters. In Taguchi Method, a series of tests are carried out using orthogonal arrays (OA). These experiments' findings are used to assess the data and forecast the quality of the components that will be made (Taguchi and Konishi, 1987). The development of production processes was initially established to increase the quality of manufactured goods, but later its application was expanded to many other engineering fields, such as biotechnology (Fratilia and Caizar, 2011). The creation of analysis of variance schemes was one of Taguchi's contributions that was particularly valued by statisticians in the field. To effectively achieve the desired results, precise process parameter selection and their separation into control and noise components are essential (Taguchi and Konishi, 1987; Vaatainen and Pentti, 2016). It is important to choose the control in such a manner that the sound source has no effect. The Taguchi method entails selecting the proper control parameters in order to obtain the best process outcomes. There have been several orthogonal network (OA) experiments (Olodu, 2018). The findings of these investigations are used in data analysis and component quality prediction techniques (Friend, 1987). Foster (2000) looked into how five input parameters affected the refined goods' surface quality. Mold temperature, melting temperature, packing pressure, packing duration, and injection time were the input factors. The Taguchi method was used to lessen shrinkage in polypropylene (PP) and polystyrene (PS). In addition, Foster (2000) decreased PP and PS by 0.937% and 1.224%, respectively, using neural networks to simulate the process. The Taguchi technique was used by Vaatanen et al. (2016) to examine how injection molding parameters affected the aesthetic appeal of cast parts. The decrease of three other quality attributes; weight, welding, and kiln marks was a priority. They can optimize a variety of high-quality features that can result in cost savings with very little expertise. Economic growth is fueled by the discovery of new materials through research and design (Singla et al., 2009). That is, contemporary technology is heavily reliant on material research, which advances the economies of all nations. The mechanical characteristics of vortex-produced alloys of 2024 aluminium alloy enhanced with Al_2O_3 particles were examined by Kok (2004). The optimum melting temperature, mold preheating temperature, mixing speed, particle addition speed, mixing time, and contact pressure for the production process are 700 °C for casting, 550 °C for mold preheating, 900 rpm, 5 g/min., or 6 MPa. According to Friend (1987), the hardness and toughness of MMC A359/ Al_2O_3 increase with increasing temperature. In addition, the research showed that the use of electromagnetic agitation during production leads

to smaller particles and better adhesion from the interface of the particles to the matrix. Aluminium-Silicon carbide (Al/SiC) composites produced by powder metallurgy were studied by Venkatesh and Pentti (2016) to obtain the required properties and improve the mechanical properties of aluminium. Meena and Manna (2013) and Friend (1987) reported that aluminum strength, fatigue strength, modulus, wear resistance, and creep are improved by reinforcement. In comparison to the standard aluminium alloy, composites reinforced with Titanium diboride (TiB_2) particles showed a 30% increase in stiffness and a nearly doubling of tensile strength (Olodu, 2021). Meena and Manna (2013) looked at the effect of mixing time and speed on particle distribution in Silicon carbon-aluminum metal matrix composite (SiCAMC). The aluminium material's strength, durability, and stability, according to Meena and Manna declined (Meena and Manna, 2013). Early processing observations revealed a persistent uneven distribution of reinforcement in the form of groups or clumps of reinforcement with associated porosity. In addition, for a particular matrix alloy, raising the volume fraction reduces the break length (Singla et al., 2009). According to Fratilia and Caizar (2011) investigation on the effects of reinforcing particle shape and interface strength on the deformation and fracture behavior of an Al/ Al_2O_3 composite observed two processes for particle failure which are cracking and separation at the interface. This study therefore, focused on the optimization using Taguchi method to investigate the effects of process parameters on the hardness of developed aluminium roofing sheets

2. Materials and Methods

5052 aluminium sheet was used in this study. it is the strongest non-heat treatable sheet and plate in common use. Versatility and strong value make it one of the most serviceable alloys. When alloyed with magnesium, 5052 aluminium can be anodized. It shows good welding characteristics, and demonstrates moderate-to-good strength. It has good drawing properties and a high rate of work hardening. 5052 aluminium is resistant to saltwater corrosion, making it appropriate for roofing sheet applications. There are various types of long-span aluminium roofing products used in Nigerian construction industry. These products was analysed based on their hardness. Samples of aluminium material used for the tests were obtained from two Longspan aluminium manufacturing companies namely; AGEN Aluminium and Differential Aluminium Company all located in Benin City, Edo State, Nigeria. This material was exposed to a range of temperatures and pressures, from 30 GPa to 65 GPa and 905°C to 1250°C, respectively. In order to regulate the grain structure, limit grain growth, and avoid recrystallization following heat treatment in aluminium roofing sheets, magnesium (Mg) was added at different percentage to the aluminium. The magnesium (Mg) added was used to improve toughness

and reduces susceptibility to stress corrosion. After cooling, the mechanical properties of these materials, which were created at different pressures and temperatures, were evaluated.

2.1 Types of Hardness Testing Methods

The Brinell Hardness Test was used in this study due to its economic advantage over other methods. The following are other types of hardness testing methods used to determine the hardness of materials: Rockwell Hardness Test, Vickers Hardness Test, Shore Scleroscope Hardness Test, Knoop Hardness Test, Mohs Hardness Test, and Barcol Hardness.

2.2. Evaluation of Developed Aluminium Roofing Sheets for Hardness

The Brinell hardness test was used in this study, it involves the application of a constant load, usually in the range 500–3000 N, for a specified period of time (10–30 s) using a 5 or 10 mm diameter hardened steel or tungsten carbide ball on the flat surface of longspan aluminium roofing sheet. The Brinell hardness number (BHN) was then obtained using Equation 1 (Rao et al., 2019) (Figure 1 and 2).

$$BHN = \frac{2F}{\pi D [D - \sqrt{D^2 - d^2}]} \quad (1)$$

where F is the load in kilogram, D is the steel ball diameter in millimeter, and d is the depression diameter or indentation diameter.

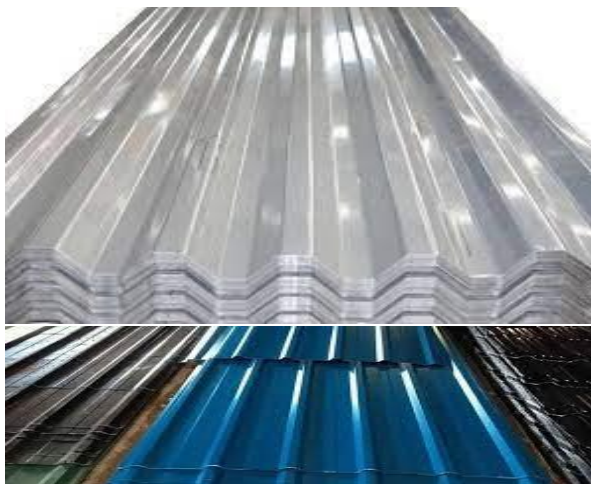


Figure 1. Samples of longspan aluminium roofing sheets.

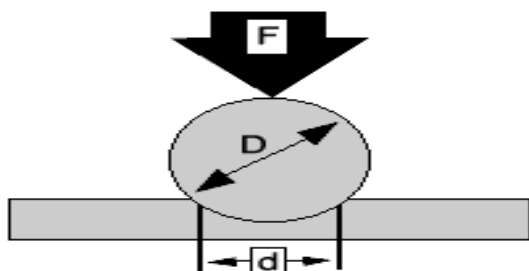


Figure 2. Impact force using brinell hardness method.

2.3. Optimization of Aluminium Roofing Sheets Process Parameters Using Taguchi Method

2.3.1. Experimental plan

In this study, experimental design was considered as one of the most comprehensive approaches to product/process development. This statistical approach attempts to provide predictive knowledge about a complex, multifactorial process through multiple trials.

2.3.2. Application of Taguchi method

A complete factorial design necessitates a great deal of testing. The more variables there are, the more complicated and time-consuming this becomes. Taguchi proposed an innovative method using an orthogonal array to explore the complete parameter space with fewer experiments to address this issue. To measure performance that deviates from the intended target value, Taguchi advises using a loss function. A signal-to-noise (S/N) ratio is then created from the value of this loss function. The signal-to-noise (S/N) ratio used by the Taguchi method shows both the mean and variability of quality characteristics. It is a metric of effectiveness for creating systems and procedures that are resistant to noisy influences.

2.4. Types of Signal-Noise (S/N) Ratio

The following are types of signal to noise ratio:

(i) Smaller-the-better: In Smaller-the-better (Equation 2),

$$Signal\ to\ noise\ ratio, \eta \left(\frac{S}{N} \right) = -10 \log_{10} \left\{ \frac{1}{n} \sum_{i=1}^n y_i^2 \right\} \quad (2)$$

when a characteristic's minimization is desired, it is utilized.

(ii) Larger-the-better: In Larger-the-better (Equation 3),

$$Signal\ to\ noise\ ratio, \eta \left(\frac{S}{N} \right) = -10 \log_{10} \left\{ \frac{1}{n} \sum_{i=1}^n \frac{1}{y_i^2} \right\} \quad (3)$$

where i ranges from 1 to n , and n is the number of iterations used to complete tasks that call for optimizing the quality traits of interest.

with S/N (signal-to-noise ratio), n (number of observations), and y_i (i -th number of observations).

(iii) Nominal-the-best: Equation 4 is used to determine the signal ratio for Nominal-the-best (Equation 4):

$$Nominal - the - best \left(\frac{S}{N} \right) = -10 \log_{10} \left\{ \frac{\mu^2}{\sigma^2} \right\} \quad (4)$$

when the mean, μ and standard deviation, σ are given. It is applied while attempting to reduce the RMS error near a particular target value. Matching the mean to the objective transforms the issue into a constrained optimization problem, regardless of the approach.

2.4.1. Selected Signal Ratio

In this study, the smaller-the-better was used. This is because production temperature ($^{\circ}C$), production

pressure (GPa), cooling time (second) and percentage of magnesium in aluminium roofing sheet (%) are intended to be lower in order to produce aluminium roofing sheets with good hardness.

2.5. Identifying the Control Factors and their levels

Three levels of processing parameters and L9 orthogonal array were selected. The process parameters and levels are shown in Table 1 and L9 orthogonal array is shown in Table 2.

3. Results and Discussion

The factors and levels listed in Table 1 were used in the trials, per the orthogonal table (OA) above. Table 3 presents the trial configuration with the chosen factor values. Each of the aforementioned 9 trials was carried

out. 36 experiments were conducted a total of 4 times to account for potential variations brought on by noise variables. The measured values of the process parameters acquired from different tests are displayed in Tables 4 through 7.

3.1. Determining the Experimental Matrix

The orthogonal table (OA) above indicates that the factors and levels used in the trials were those listed in Table 1. Table 3 displays the experimental configuration with the chosen numbers for the factors. Each of the aforementioned 9 trials was carried out. 4 times (total of 36 trials) to account for potential variations brought on by noise elements. The measured values of the process parameters derived from various tests are displayed in Tables 4 through 8.

Table 1. The process parameters and their levels

| Serial Number | Factors | Level 1 | Level 2 | Level 3 |
|---------------|--|---------|---------|---------|
| 1 | Manufacturing Temperature (°C) | 905 | 1100 | 1250 |
| 2 | Manufacturing Pressure (GPa) | 30 | 50 | 65 |
| 3 | Cooling Time (second) | 50 | 70 | 95 |
| 4 | Percentage of magnesium in Aluminium Sheet (%) | 0.2 | 0.3 | 0.5 |

Table 2. The orthogonal array for L9

| Experiment Number | Control Factors | | | |
|-------------------|--------------------------------|------------------------------|-----------------------|--|
| | Manufacturing Temperature (°C) | Manufacturing Pressure (GPa) | Cooling Time (second) | Percentage of magnesium in Aluminium Sheet (%) |
| 1 | 1 | 1 | 1 | 1 |
| 2 | 1 | 2 | 2 | 2 |
| 3 | 1 | 3 | 3 | 3 |
| 4 | 2 | 1 | 2 | 3 |
| 5 | 2 | 2 | 3 | 1 |
| 6 | 2 | 3 | 1 | 2 |
| 7 | 3 | 1 | 3 | 2 |
| 8 | 3 | 2 | 1 | 3 |
| 9 | 3 | 3 | 2 | 1 |

Table 3. Orthogonal array (OA) with control factors and hardness for aluminium roofing sheets

| Experiment No. | Control Factors | | | | Brinell Hardness (N/mm ²) |
|----------------|--------------------------------|------------------------------|-----------------------|--|---------------------------------------|
| | Manufacturing Temperature (°C) | Manufacturing Pressure (GPa) | Cooling Time (second) | Percentage of magnesium in Aluminium Sheet (%) | |
| 1 | 780 | 42 | 54 | 0.20 | 45.4 |
| 2 | 1022 | 55 | 70 | 0.22 | 48.0 |
| 3 | 1100 | 60 | 75 | 0.30 | 54.7 |
| 4 | 1110 | 65 | 70 | 0.50 | 65.0 |
| 5 | 1250 | 45 | 95 | 0.40 | 60.0 |
| 6 | 890 | 40 | 54 | 0.20 | 40.0 |
| 7 | 905 | 30 | 85 | 0.33 | 38.5 |
| 8 | 1005 | 58 | 60 | 0.42 | 50.4 |
| 9 | 850 | 35 | 65 | 0.38 | 44.0 |

Table 4. Measured values of manufacturing temperature for aluminium roofing sheets

| Experiment No. | Manufacturing Temperature (°C) | | | | | Mean |
|----------------|--------------------------------|------|------|------|------|------|
| | 1 | 2 | 3 | 4 | 5 | |
| 1 | 786 | 785 | 775 | 770 | 784 | 780 |
| 2 | 1022 | 1020 | 1024 | 1015 | 1025 | 1022 |
| 3 | 1080 | 1120 | 1100 | 1130 | 1070 | 1100 |
| 4 | 1105 | 1115 | 1100 | 1130 | 1100 | 1110 |
| 5 | 1250 | 1270 | 1230 | 1260 | 1240 | 1250 |
| 6 | 870 | 900 | 900 | 900 | 880 | 890 |
| 7 | 900 | 900 | 915 | 900 | 910 | 905 |
| 8 | 790 | 790 | 760 | 790 | 770 | 780 |
| 9 | 1022 | 1024 | 1020 | 1021 | 1023 | 1022 |

Table 5. Measured values of manufacturing pressure for aluminium roofing sheets

| Experiment No. | Manufacturing Pressure (GPa) | | | | | Mean |
|----------------|------------------------------|----|----|----|----|------|
| | 1 | 2 | 3 | 4 | 5 | |
| 1 | 42 | 43 | 40 | 42 | 43 | 42 |
| 2 | 54 | 53 | 56 | 56 | 57 | 55 |
| 3 | 57 | 62 | 62 | 61 | 58 | 60 |
| 4 | 65 | 68 | 65 | 63 | 64 | 65 |
| 5 | 42 | 48 | 43 | 45 | 47 | 45 |
| 6 | 41 | 38 | 42 | 37 | 42 | 40 |
| 7 | 28 | 32 | 30 | 28 | 32 | 30 |
| 8 | 41 | 40 | 45 | 44 | 40 | 42 |
| 9 | 50 | 60 | 55 | 50 | 60 | 55 |

Table 7. Measured values of percentage of magnesium in aluminium roofing sheets (%)

| Experiment No. | Percentage of magnesium in Aluminium Roofing Sheet (%) | | | | | Mean |
|----------------|--|------|------|------|------|------|
| | 1 | 2 | 3 | 4 | 5 | |
| 1 | 0.20 | 0.15 | 0.20 | 0.20 | 0.25 | 0.20 |
| 2 | 0.22 | 0.21 | 0.22 | 0.22 | 0.23 | 0.22 |
| 3 | 0.30 | 0.29 | 0.30 | 0.30 | 0.31 | 0.30 |
| 4 | 0.50 | 0.40 | 0.50 | 0.50 | 0.60 | 0.50 |
| 5 | 0.40 | 0.39 | 0.40 | 0.40 | 0.41 | 0.40 |
| 6 | 0.20 | 0.25 | 0.20 | 0.20 | 0.15 | 0.20 |
| 7 | 0.33 | 0.31 | 0.33 | 0.33 | 0.35 | 0.33 |
| 8 | 0.42 | 0.44 | 0.42 | 0.42 | 0.40 | 0.42 |
| 9 | 0.38 | 0.36 | 0.38 | 0.38 | 0.40 | 0.38 |

Table 8. Tabulated signal-to-noise (s/n) ratios for of aluminium roofing sheets

| Experiment No. | S/N Ratio (dB) for Manufacturing Temperature (°C) | S/N Ratio (dB) for Manufacturing Pressure (GPa) | S/N Ratio (dB) for Cooling Time | S/N Ratio (dB) for Percentage of magnesium in Aluminium Roofing Sheets |
|----------------|---|---|---------------------------------|--|
| 1 | -57.8489 | -32.4679 | -34.5579 | 13.8722 |
| 2 | -62.7618 | -34.8419 | -36.9108 | 13.1480 |
| 3 | -61.6731 | -35.5683 | -37.5028 | 10.4556 |
| 4 | -60.9069 | -36.2611 | -36.9048 | 5.9517 |
| 5 | -61.9388 | -33.0753 | -39.4100 | 7.9577 |
| 6 | -58.9887 | -32.0531 | -34.6509 | 13.8722 |
| 7 | -59.1332 | -29.5578 | -38.5889 | 9.6233 |
| 8 | -57.8430 | -32.4758 | -35.5669 | 7.5311 |
| 9 | -60.1890 | -34.8389 | -36.2603 | 8.3995 |

The S/N ratio (η) for the individual control factors are calculated as given below (Equations 5-16):

Sum of Squares for manufacturing temperature for 1 to 3

$$S_{T1}=(\varphi_1+ \varphi_2+ \varphi_3) \quad (5)$$

Sum of Squares for manufacturing temperature for 4 to 6

$$S_{T2}=(\varphi_4+ \varphi_5+ \varphi_6) \quad (6)$$

Sum of Squares for manufacturing temperature from 7 to 9

$$S_{T3}=(\varphi_7+ \varphi_8+ \varphi_9) \quad (7)$$

Sum of Squares for manufacturing pressure from 1 to 3

$$S_{P1}=(\varphi_1+ \varphi_4+ \varphi_7) \quad (8)$$

Sum of Squares for manufacturing pressure from 4 to 6

$$S_{P2}=(\varphi_2+ \varphi_5+ \varphi_8) \quad (9)$$

Sum of Squares for manufacturing pressure from 7 to 9

$$S_{P3}=(\varphi_3+ \varphi_6+ \varphi_9) \quad (10)$$

Sum of Squares for cooling time from 1 to 3

$$S_{T1}=(\varphi_1+ \varphi_5+ \varphi_9) \quad (11)$$

Sum of Squares for cooling time from 4 to 6

$$S_{T2}=(\varphi_2+ \varphi_6+ \varphi_7) \quad (12)$$

Sum of Squares for cooling time from 7 to 9

$$S_{T3}=(\varphi_3+ \varphi_4+ \varphi_8) \quad (13)$$

Sum of Squares for percentage of magnesium from 1 to 3

$$S_{C1}=(\varphi_1+ \varphi_4+ \varphi_7) \quad (14)$$

Sum of Squares for percentage of magnesium from 4 to 6

$$S_{C1}=(\varphi_2+ \varphi_5+ \varphi_8) \quad (15)$$

Sum of Squares for percentage of magnesium from 7 to 9

$$S_{C1}=(\varphi_3+ \varphi_6+ \varphi_9) \quad (16)$$

See Table 9 to choose values for $\varphi_1, \varphi_2, \varphi_3$, etc., and to calculate S_1, S_2 , and S_3 . The average S/N ratio for level 1 manufacturing temperature is $\frac{S_{T1}}{3}$. The average S/N ratio for level 2 manufacturing temperatures is $\frac{S_{T2}}{3}$. $\frac{S_{T3}}{3}$ is the average S/N ratio for level 3 manufacturing temperature. Similar formulas are used to determine the manufacturing pressure, cooling time, and magnesium content of aluminium roofing sheets, respectively. Table 9 displays the average of the signal-to-noise ratios (S/N).

Table 9. The response table for S/N ratio for aluminium process parameters

| Serial Number | Manufacturing Temperature (°C) | Manufacturing Pressure (GPa) | Cooling Time | Percentage of Magnesium in Aluminium Sheet (%) |
|---------------|--------------------------------|------------------------------|--------------|--|
| Level 1 | -60.7613 | -34.2927 | -36.3238 | +12.4919 |
| Level 2 | -60.6115 | -33.7965 | -36.9886 | +9.2605 |
| Level 3 | -59.0551 | -32.2908 | -36.8054 | +8.5180 |
| DELTA | 1.7062 | 2.0019 | 0.6648 | 3.9739 |
| RANK | 3 | 2 | 4 | 1 |

*DELTA= absolute highest signal noise ratio - absolute lowest signal noise ratio

3.2. Confirmation Experiment

The confirmation experiment, which was performed using manufacturing temperature of 1250°C, manufacturing pressure of 65 MPa, 95 s of cooling time, and 0.5% magnesium in aluminum roofing sheets, as shown in Table 11. A total of five sets of experiments were run in the confirmation experiment, and their hardness was assessed. It is evident that the outcomes were reliable.

Table 9 displays the response Table for the S/N ratio. The level with the highest value for each factor was chosen as the ideal set of combination parameters. For aluminium roofing sheets, LEVEL 1 for percentage of Magnesium, LEVEL 2 for manufacturing pressure, LEVEL 3 for manufacturing temperature, and LEVEL 4 for cooling time respectively, are the best process parameter combinations. The factor that has the greatest impact on

the hardness of aluminium roofing sheets is depicted by the Delta value in Table 9. It was discovered that the factor having the greatest impact on the hardness of aluminium roofing sheets had a Delta value of 3.9739 for percentage of magnesium. This was followed by manufacturing pressure with a Delta value of 2.0019, manufacturing temperature with a Delta value of 1.7062, and cooling time with a Delta value of 0.6648 (Table 9). Figures 1 to 4 depict a response diagram for the S/N ratio that was created. The ideal process condition relates to a manufacturing temperature of 1250°C, a manufacturing pressure of 65 GPa, a cooling time of 95 seconds, and a percentage of magnesium of 0.5%, and was determined by the maximum S/N ratio for each factor (Table 10). To improve the situation, the factor levels with the highest S/N ratio were picked.

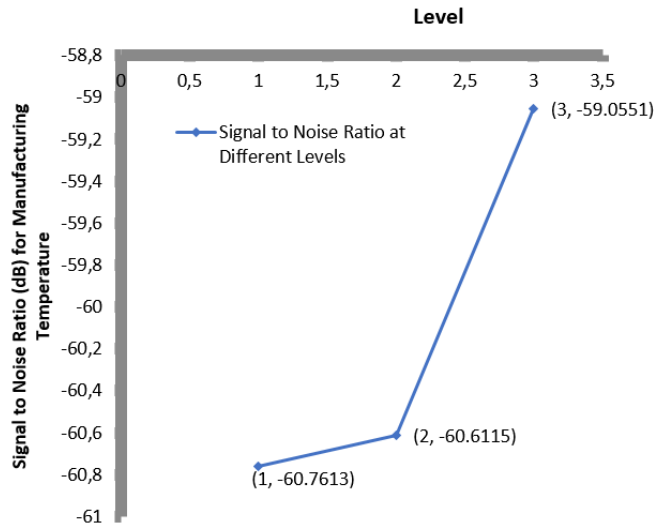


Figure 3. Signal to noise ratio (dB) for manufacturing temperature.

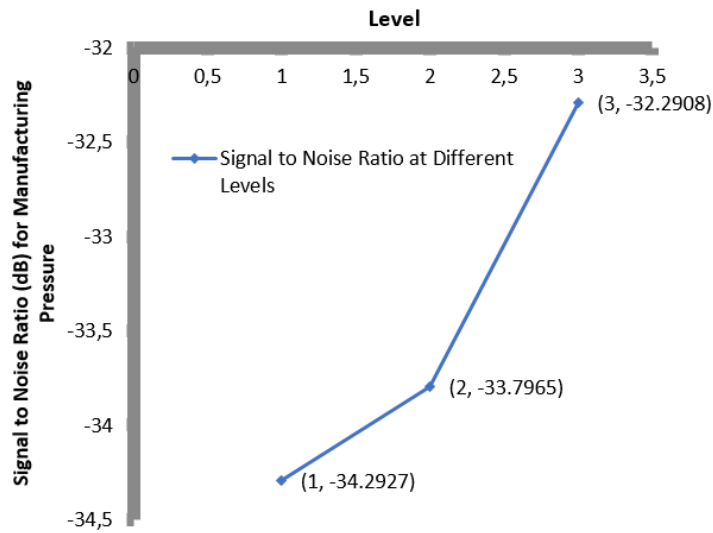


Figure 4. Signal to noise ratio (dB) for manufacturing pressure.

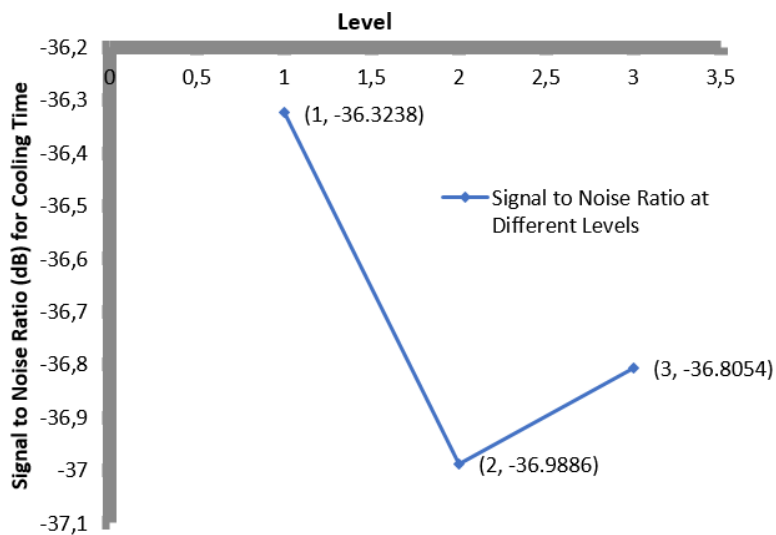


Figure 5. Signal to noise ratio (dB) for cooling time.

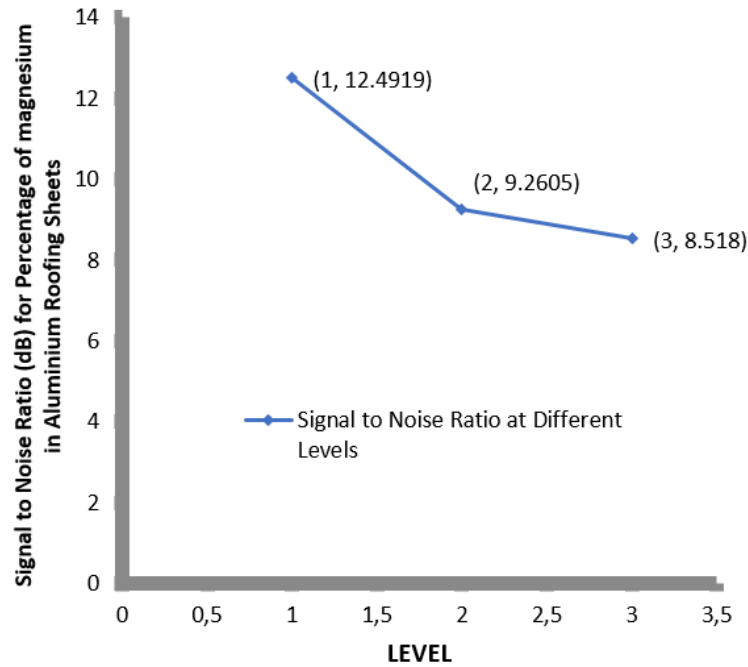


Figure 6. Signal to noise ratio (dB) for percentage of magnesium in aluminium roofing sheets

Table 10. Optimum values of factors of developed aluminium roofing sheets

| Parameter | Optimum Value |
|---|---------------|
| Manufacturing Temperature | 1250°C |
| Manufacturing Pressure | 65 GPa |
| Cooling Time | 95 seconds |
| Percentage of magnesium in Aluminium Roofing Sheets | 0.5% |

Kok (2004) looked at the mechanical properties of vortex-produced composites of 2024 aluminum alloy reinforced with Al₂O₃ particles. The appropriate melting temperatures, mold preheating temperatures, mixing speeds, particle addition rates, mixing times, and contact pressure for the production process are 700 °C for casting, 550 °C for mold preheating, 900 rpm for mixing speed, and 5 g/min for particle addition speed. The contact pressure is 6 MPa, and the mixing time is 105

seconds. The manufacturing temperature measured is consistent with the findings of this inquiry. To optimize the process parameters of medium-carbon steel joints joined by MIG welding, Altan (2010) applied the Taguchi technique. The results showed that the highest and the lowest Brinell hardness were 72 kgf and 64.2 kgf, respectively, and they were created by grooves with a 90° angle, 120 A current, and 30 V voltage. The maximal hardness of 65 kgf and the ideal hardness value of 72 kgf discovered in this study are consistent. Altan (2010) undertake a numerical analysis of the fatigue behavior of unpatched and patched aluminum and composite plates. They looked at the fatigue behavior of composite patched and unpatched Al 5083 aluminum plates using mathematics. The toughness results obtained in their study serves as a basis for the hardness obtained in this study.

Table 11. Confirmation experiment

| Serial Number | Process Parameters | | | | Hardness (Kgf) |
|---------------------|--------------------------------|------------------------------|-----------------------|---|----------------|
| | Manufacturing Temperature (°C) | Manufacturing Pressure (MPa) | Cooling Time (second) | Percentage of Magnesium in Aluminium Roofing Sheets (%) | |
| 1 | 1250 | 65 | 95 | 0.5 | 64.9 |
| 2 | 1250 | 65 | 95 | 0.5 | 65.1 |
| 3 | 1250 | 65 | 95 | 0.5 | 65.2 |
| 4 | 1250 | 65 | 95 | 0.5 | 64.8 |
| 5 | 1250 | 65 | 95 | 0.5 | 65.0 |
| Mean Hardness (Kgf) | | | | | 65.0 |

4. Conclusion

The best combinations of manufacturing conditions for

the hardness of aluminium roofing sheets were found using the Taguchi method. According to the results, the

maximum hardness was produced at manufacturing temperature of 1250 °C, manufacturing pressure of 65 GPa, 95 seconds of cooling time, and 0.5% of Magnesium. The most important aspect was discovered to be percentage of magnesium, which was followed by manufacturing pressure and manufacturing temperature. The least effective component was determined to be cooling time. This study is intended to help researchers and manufacturers of aluminium develop high-quality, defect-free aluminium roofing sheets, which would ultimately boost productivity in the aluminium industries.

Author Contributions

The percentage of the author(s) contributions is presented below. All authors reviewed and approved the final version of the manuscript.

| | D.D.O. | A.E. |
|-----|--------|------|
| C | 60 | 40 |
| D | 60 | 40 |
| S | 50 | 50 |
| DCP | 50 | 50 |
| DAI | 60 | 40 |
| L | 50 | 50 |
| W | 50 | 50 |
| CR | 60 | 40 |
| SR | 60 | 40 |
| PM | 50 | 50 |
| FA | 50 | 50 |

C=Concept, D= design, S= supervision, DCP= data collection and/or processing, DAI= data analysis and/or interpretation, L= literature search, W= writing, CR= critical review, SR= submission and revision, PM= project management, FA= funding acquisition.

Conflict of Interest

The authors declared that there is no conflict of interest.

Ethical Consideration

Ethics committee approval was not required for this study because of there was no study on animals or humans. The authors confirm that the ethical policies of the journal, as noted on the journal's author guidelines page, have been adhered to. The experimental procedures were approved by the Mechanical Engineering Department of Benson Idahosa University and Igbinedion University, Edo State, Nigeria.

Acknowledgements

The authors acknowledged the Department of Mechanical Engineering, Faculty of Engineering, Benson Idahosa University and Igbinedion University respectively for the using some of their facilities during the fabrication process.

References

Altan M. 2010. Reducing shrinkage in injection moldings through the taguchi, ANOVA and neural network methods. *J Mat Design*, 31: 599-604.

Foster WT. 2000. Basic Taguchi design of experiments. National Association of Industrial Technology Conference, May 9-11, 20000, Pittsburgh, US, pp: 1-50.

Fratilia D, Caizar C. 2011. Application of taguchi method to selection of optimal lubrication and cutting conditions in face milling of AlMg3. *J Clean Prod*, 19: 640-645.

Friend CM. 1987. The effect of matrix properties on reinforcement is short Al2O3 fiber-Al MMCs. *J Mater Sci*, 22(8): 3005-3010.

Joardar H, Sutradhar G, Das NS. 2012. FEM simulation and experimental validation of cold forging behavior of LM6 base metal matrix composites. *JMMCE*, 11(10): 989-994.

Kok M. 2004. Production and mechanical properties of Al2O3 particle-reinforced 2024 aluminium alloy composites. *J Mater Proces Technol*, 161: 381-387.

Manigandan K, Srivatsan TS, Quick T. 2011. Influence of silicon carbide particulate on tensile fracture behavior of an aluminium alloy. *Mater Sci Eng*, 534: 711-715.

Meena KL, Manna SS. 2013. Banwait, Jaswanthi, an analysis of mechanical properties of the developed Al/SiC-MCC's. *American J Mech Eng*, 1(1): 14-19.

Olodu DD. 2018. Optimization and analysis of cutting tool geometrical parameters using taguchi method. *J Appl Sci Environ Manag*, 22(3): 346-349. DOI: 10.4314/jasem.v22i3.9.

Olodu DD. 2021. Modelling and validation of the production parameters of unalloyed aluminium sheets. *Gazi Univ J Sci Part A: Eng Innov*, 8(1): 94-108.

Osarenmwinda JO, Olodu DD. 2018. Optimization of injection moulding process parameters in the moulding of high density polyethylene (HDPE). *J Appl Sci Environ Manag*, 22(2): 203-206. DOI: 10.4314/jasem.v22i2.8.

Rao RS, Kumar G, Prakasham CS, Hobbs PJ. 2019. The taguchi methodology as a statistical tool for biotechnological applications: a critical appraisal, *Biotechnol J*, 3(4): 510-523.

Saravanan C, Subramanian K, Ananda Krishnan V, Sankara Narayanan R. 2015. Effect of particulate reinforced aluminium metal matrix composite. *Mechanics Mechanical Eng*, 19(1): 23-30.

Singla M, Deepak Dwivedi D, Singh L, Chawla V. 2009. Development of aluminium based silicon particulate metal matrix composite, *J Miner Mater Charact Eng*, 8(6): 455-567.

Sozhamannan GG, Balasivanandha Prabu S, Venkatagalapathy VSK. 2012. Effect of processing parameters on metal matrix composites: stir casting process, *J Surface Eng Mater Adv Technol*, 2: 11-15. DOI:10.4236/jsemat.2012.21002.

Srinivas A, Venkatesh YD. 2012. Application of taguchi method for optimization of process parameters in improving the surface roughness of lathe facing operation. *Int Refer J Eng Sci*, 1(3): 13-19

Taguchi G, Konishi S. 1987. Taguchi methods, orthogonal arrays and linear graphs, tools for quality american supplier institute. *American Supplier Instit*, 2: 8-35.

Vaatainen O, Pentti J. 2016. Effect of processing parameters on the quality of injection moulded parts by using the taguchi parameter design method. *J Plastic Rubber Compos*, 1: 21-27.

Zitoun E. 2019. Matrix Al-alloys for silicon carbide particle reinforced metal matrix composites. *Chennakesava Reddy*, 3(12): 1184-1187.



SEFTRİAKSON ETKEN MADDELİ İLACIN İNSAN PANKREAS HÜCRESİ ÜZERİNDE SİTOTOKSİK ETKİLERİNİN MTT TESTİ İLE DEĞERLENDİRİLMESİ

Asena KURT^{1*}, Zinet ÇÖL¹, Ömer ERTÜRK¹

¹Ordu University, Department of Molecular Biology and Genetics, 52200, Ordu, Türkiye

Özet: Tıp dünyasında önemli yere sahip olan antibiyotikler bakterilerin sebep olduğu enfeksiyon hastalıklarının tedavisinde sıklıkla kullanılan bir grup ilaçtır. Yararlı etkilerin yanı sıra yan etkisiz değildir. Her zaman klinikte saptanamayan yan etkilere hücresel düzeyde saptanabilir. Hücresel düzeydeki hasarlar yeni bozukluklara yol açabilir. Seftriakson, üçüncü kuşak sefalosporinler grubuna ait antibiyotiktir. Gram negatif bakterilerin neden olduğu enfeksiyonların tedavisinde tercih edilir. Bu çalışmada, seftriakson antibiyotisinin insan pankreas hücresinde (hTERT-HPNE) sitotoksitesi araştırıldı. hTERT-HPNE hücreleri, seftriakson etken maddesi içeren ilaca maruz bırakıldı. Deney grubu konsantrasyonu, 0,097 mM, 0,195 mM, 0,390 mM, 0,781 mM, 1,562 mM, 3,125 mM, 6,25 mM, 12,5 mM aralığında hazırlanarak 24,48 ve 72 saatlik maruziyet süresine bırakılmıştır. MTT testi sonuçlarında doza bağlı hücre canlılığında düşüşler görülmüştür. Hücre canlılığında ilk azalma, 24 saatlik maruziyetten sonra 0,781 mM'lik bir konsantrasyonda ve 48 saatlik maruziyette 0,195 mM'lik konsantrasyonda gözlemlendi. 72 saatlik maruziyet süresinde ise uygulanan tüm konsantrasyonlarda hücre canlılığı azaldı. Seftriakson etken maddeli antibiyotinin maruziyeti sonrasında hücrelerin morfolojilerinde değişim ve canlılığını kaybetmiş hücreler gözlemlenmiştir. Sonuç olarak seftriaksonun dozuna bağlı olarak hücre canlılığındaki azalmalar negatif kontrole kıyaslandığında istatistiksel olarak anlamlı bulunmuştur ($P < 0,05$). Deney sonucunda seftriaksonun hTERT-HPNE üzerinde sitotoksitesine neden olduğu belirlenmiştir. Çalışmamız seftriakson etken maddeli antibiyotinin insan pankreas hücreleri üzerinde sitotoksik etkileri olabileceği hipotezini desteklemekte ve antibiyotiklerin hücresel düzeyde yan etkilerine dikkat çekmektedir.

Anahtar kelimeler: Seftriakson, Sitotoksitesite, hTERT-HPNE, Pankreas hücresi


Evaluation of Cytotoxic Effects of Ceftriaxone Active Ingredient Drug on Human Pancreatic Cell by MTT Test


Abstract: Antibiotics, which have an important place in the medical world, are a group of drugs that are frequently used in the treatment of infectious diseases caused by bacteria. Besides the beneficial effects, they are not without side effects. Side effects that are not always clinically detectable can be detected at the cellular level. Damages at the cellular level can lead to new disorders. Ceftriaxone is an antibiotic belonging to the third generation cephalosporins group. It is preferred in the treatment of infections caused by gram negative bacteria. In this study, the cytotoxicity of the antibiotic ceftriaxone in human pancreatic cell (hTERT-HPNE) was investigated. hTERT-HPNE cells were exposed to drug containing the active ingredient ceftriaxone. The concentration of the experimental group was prepared in the range of 0.097 mM, 0.195 mM, 0.390 mM, 0.781 mM, 1.562 mM, 3.125 mM, 6.25 mM, 12.5 mM and left for exposure time of 24.48 and 72 hours. Dose-related decreases in cell viability were seen in the MTT test results. The initial reduction in cell viability was observed at a concentration of 0.781 mM after 24 hours of exposure and at a concentration of 0.195 mM at 48 hours of exposure. Cell viability decreased at all applied concentrations during 72 hours of exposure. Changes in the morphology of the cells and cells that lost their vitality were observed after exposure to the antibiotic with ceftriaxone active ingredient. As a result, decreases in cell viability depending on the dose of ceftriaxone were statistically significant when compared to the negative control ($P < 0.05$). As a result of the experiment, it was determined that ceftriaxone caused cytotoxicity on hTERT-HPNE. Our study supports the hypothesis that antibiotics with ceftriaxone active ingredient may have cytotoxic effects on human pancreatic cells and draws attention to the side effects of antibiotics at the cellular level.


Keywords: Ceftriaxone, Cytotoxicity, hTERT-HPNE, Pancreatic cell

*Sorumlu yazar (Corresponding author): Ordu University, Department of Molecular Biology and Genetics, 52200, Ordu, Türkiye

E mail: asena_05_61@icloud.com (A. KURT)

Asena KURT  <https://orcid.org/0000-0003-3722-828X>

Zinet ÇÖL  <https://orcid.org/0000-0003-3762-7870>

Ömer ERTÜRK  <https://orcid.org/0000-0001-5837-6893>

Gönderi: 14 Mart 2023

Kabul: 04 Ağustos 2023

Yayınlanma: 15 Ekim 2023

Received: March 14, 2023

Accepted: August 04, 2023

Published: October 15, 2023

Cite as: Kurt A, Çöl Z, Ertürk Ö. 2023. Evaluation of cytotoxic effects of ceftriaxone active ingredient drug on human pancreatic cell by MTT test. BSJ Eng Sci, 6(4): 356-362.

1. Giriş

Antibiyotik ismi Yunanca anti(karşı) ve bios(yaşam) sözcüklerinden türetilmiştir(Yıldız ve ark., 2010). Waksman 1947 yılında antibiyotik terimini bakterilerin ve diğer mikroorganizmaların büyümesini veya metabolik aktivitelerini inhibe etmek olarak tanımlanmıştır

(Küçükbuğru,2020). XX. Yüzyılın en önemli buluşlarından biri olarak kabul edilen antibiyotikler, mantar veya bakteri gibi mikroorganizmaların sebep olduğu enfeksiyon hastalıklarının tedavisinde kullanılan ilaç grubudur. Antibiyotikler bu mikroorganizmaların gelişimini durdurma ve hatta bunları öldürebilme



yeteneğine sahip biyolojik kaynaklı ya da sentetik biyoaktif maddelerdir (Topal ve ark., 2015).

Alexander Flemming 1928 yılında *Staphylococcus* varyantları üzerinde çalışmalarını yaptığı kültür ortamına bulaşmış bir küf mantarının çevresinde stafilkokların üreyemediklerini ve öldüklerini şans eseri fark etmiştir. Flemming bu mantarların Penicillium türünden olmalarından dolayı etken maddeye penicillium adını vermiştir. Böylelikle ilk antibiyotik Sir Alexander Flemming tarafından, 1928 yılında keşfedilmiştir (Topal ve ark., 2015). Bilim insanları bu devrim niteliğindeki buluş sonrasında antibiyotikler ile ilgili çalışmalara yoğunlaşmışlardır (Yıldız ve ark., 2010). Günümüzde antibiyotik adı verilen birçok ilaç bulunmaktadır. Bunların önemli bir kısmını sefalosporin grubu antibiyotikler oluşturur. Sefalosporinler β -laktam halkası ve dihidrothiazin halkasından oluşan 7-aminosefalosporanik asid çekirdeğine sahip *Cephalosporium acremonium*'un fermentasyon ürünüdür. Sefalosporinler etki edeceği organizmaların penisilin bağlayıcı proteinlerine (PBP) bağlanarak bakteri hücre duvarındaki peptidoglikan yapının sentezini bozarlar ve bakterisid özellik gösterirler. Bu antibiyotikler antibakteriyel aktivitelerinin genel özelliklerine bağlı olarak beş kuşak şeklinde sınıflandırılırlar (Köksal,2013). Bu sınıflandırma birinci kuşak sefalosporinler, ikinci kuşak sefalosporinler, üçüncü kuşak sefalosporinler, dördüncü kuşak sefalosporinler ve beşinci kuşak sefalosporinler şeklindedir (Yıldız ve ark., 2014).

Güçlü, yarı sentetik ve üçüncü kuşak bir sefalosporin grubuna ait seftriakson antibiyotiği, güçlü bir antimikrobiyal aktivite yelpazesine sahiptir. Seftriaksonun intravenöz uygulaması, özellikle organ enfeksiyonu ve sepsis olmak üzere mikrobiyal enfeksiyonların tedavisinde sıklıkla kullanılmaktadır (Yıfan ve ark., 2020). Güvenilirlik profili net olarak bilinmemekle beraber olası yan etkileri arasında en sık görüleni makülopapüler döküntülerdir (Yıldız ve ark., 2014). Seftriakson yenidoğan çocuklarda hepatotoksisite, safra koyulaşması ve safra çamuru vakaları yaşanmaması için ilk 2-3 ay içinde tercih edilmemelidir. Anafilaksi riski vardır. Çocuklarda az sayıda da olsa anafilaksi vakaları bildirilmiştir. Çin'de yapılan bir çalışmada seftriaksona bağlı 22 anafilaksi vakasının 4'ünün çocuk olduğu bildirilmiştir (Yao ve ark., 2012). Literatürde üçüncü kuşak sefalosporinlerin çoğunun şaşırtıcı derecede az ciddi yan etkisi bildirilmiştir. Bu durum onları çok çeşitli ciddi enfeksiyonların tedavisinde kullanım için ön planda tutmaktadır.

Antibiyotikler bulunduktan sonra enfeksiyon hastalıklarına bağlı yüksek mortalite ve morbidite hızla azalmıştır (Erdemir ve ark., 2011). Fakat antibiyotiklerin yaygın ve uygunsuz kullanımının artması, mikroorganizmalara karşı dirence, maliyetin artmasına ve ikincil yan etkilerin görülme sıklığında bir artışa yol açar (Güngör ve ark., 2018). Dünya Sağlık Örgütü'ne göre bir ilacın amacına uygun biçimde profilaksi, tanı ya da tedavi amacıyla kullanıldığı dozlarda ortaya çıkan

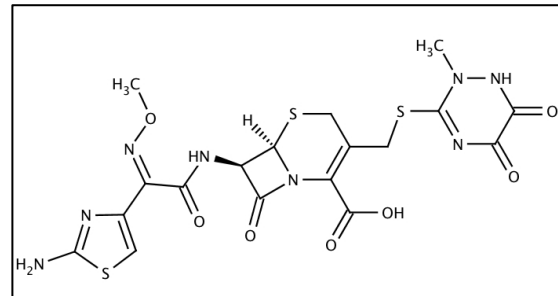
hedeflenmemiş zararlı etkiler yan etkiler olarak tanımlanmaktadır(Gökçe,2017). Klinikte rastladığımız yan etkiler alerjik reaksiyonlar, ishal, cilt reaksiyonları, hepatotoksisite, nefrotoksisite ve hematolojik yan etkiler olarak sınıflandırabiliriz (Öncü, 2013). Bununla birlikte, herhangi bir ilaç için "hücresel düzeyde ne tür bir hasara neden olduğunu" tam olarak söylemek mümkün değildir. Hücresel düzeyde hasarları in vitro kültür ortamında sitotoksisite testleri ile saptanabilir. Sitotoksisite, bir ilacın ya da maddenin hücre ölümüne yol açtığı durumdur (Şahin,2020). İlaçlar hücre zarlarının yapısını tahrip etmesi, protein sentezini baskılaması ve reseptörlere yanlış bağlanma gibi mekanizmalar sonucu hücreler üzerinde sitotoksik etkiye sebep olabilirler (Şahin 2020).

Sitotoksik etkiler hücre canlılığında azalmalar, hücre morfolojisinde değişiklikler olarak karşımıza çıkmaktadır. Hücre ölümlerinin morfolojileri apoptotik hücre ölümlerinde; hücrenin yuvarlaklaşması, hücresel ve çekirdek hacmin azalması, genetik materyal olan çekirdeğin parçalanması, sitoplazmik organellerde değişiklikler, hücre zarı yüzeyinde çıkıntı oluşurken, nekrotik hücre ölümlerinde ise sitoplazmik şişme, sitoplazmik organellerin şişmesi, orta düzeyde kromatin yoğunlaşması ve hücre zarının yırtılmasıdır (Şahin,2020). Literatür araştırmaları sonucunda daha önceki çalışmalarda seftriaksonun hücre üzerindeki toksisitesi hakkında veri eksikliği bulunmamaktadır. Bu çalışmada seftriakson içeren ilacın insan pankreas hücreleri üzerinde sitotoksik etkisi olup olmadığı araştırılmıştır.

2. Materyal ve Yöntem

2.1. Seftriakson Etken Maddeli İlaç ve Kimyasallar

Ordu'da bulunan yerel bir eczaneden seftriakson etken maddeli ilaç temin edildi. Seftriaksonun kimyasal yapısı Şekil 1'de gösterilmiştir.



Şekil 1. Seftriakson grubu antibiyotiklerin kimyasal yapısı

2.2. Hücre Kültürü

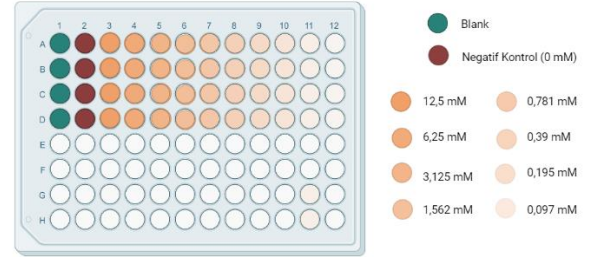
İn vitro model olarak Human Pancreatic Nestin-Expressing cells (hTERT-HPNE) (ATCC® CRL-4023™) insan pankreas epitel hücre hattı American Type Cell Culture'dan (ATCC) (Rockville, MD, ABD) temin edilmiştir. Temin edilen hTERT-HPNE hücrelerinin kültür ortamı için 500 ml Dulbecco's modified Eagle's (DMEM) besiyeri içerisine 55 ml FBS (%10) ve 0,1 ml penisilin / streptomisin (%1) ilave edilmiş ve homojen

hale getirilmiştir (Cao ve ark., 2022). Uygun kültür kaplarına 5 ml DMEM besiyeri ve 1 ml hTERT-HPNE hücreleri karışımı ekildikten sonra 37°C'de, %95 nem içeren ve %5 CO₂'li inkübatöre bırakılmıştır. Her gün invert mikroskopta hücre canlılığı gözlemlenerek besiyerleri üç günde bir değiştirilmiştir. Bu işlem hücre %70-80 yoğunluk olana kadar devam edilmiştir.

2.3. MTT Testi

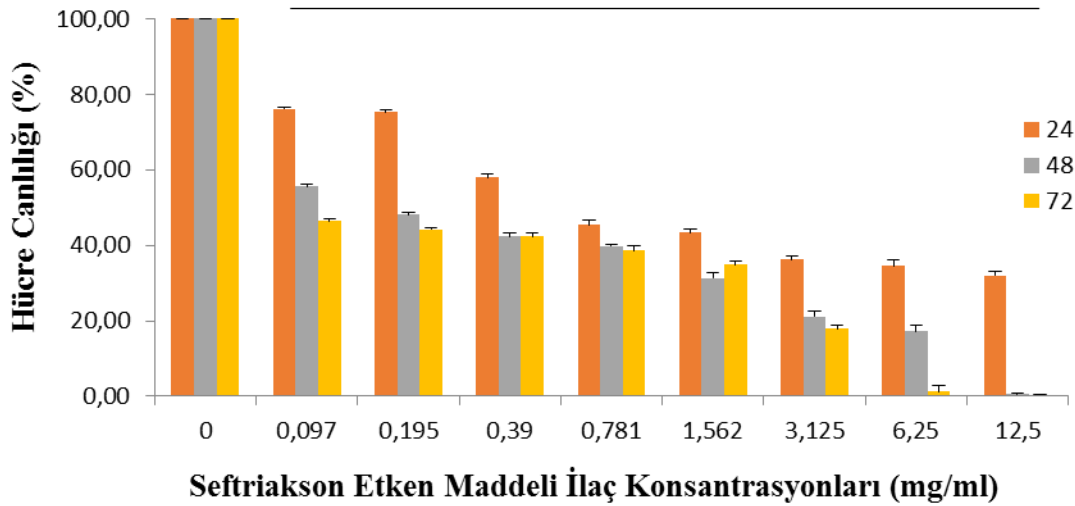
Hücre canlılığı ve sitotoksitesinin kantitasyonunda Tetrazolium tuzu kullanılarak yapılan MTT (3-[4,5-dimetil-tiyazolil-2,5-difeniltetrazolyum bromür]) testi uygulanmıştır. 96 kuyucuklu kültür kaplarının her bir kuyucuğuna 200 µl besiyeri içerisinde 1×10⁴ hücrenin ekimi gerçekleştirilmiştir. Hücrelerin normal hücre döngülerini kazanmaları için 1 gün 37°C'de CO₂ inkübatöre kaldırılmıştır. Süre sonunda hücrelerin besiyerleri aspire edilerek taze besiyeri ile yenilenmiştir. Kültür kaplarındaki hTERT-HPNE hücrelerine Şekil 2 ve

Şekil 3'te gösterildiği gibi 100 ml saf su (negatif kontrol) ve seftriakson etken maddeli ilaç 0,097 mM, 0,195 mM, 0,390 mM, 0,781 mM, 1,562 mM, 3,125 mM, 6,25 mM, 12,5 mM dozlarında maruz edilerek, 24 saat, 48 saat ve 72 saatlik maruziyet sürelerinde 37°C'de CO₂ inkübasyonuna bırakılmıştır.



Şekil 2. 96 Kuyucuklu kültür kaplarında seftriakson etken maddeli ilaç için MTT testi uygulama planı.

*



Şekil 3. 24, 48 ve 72 saatlik uygulama sonrası elde edilen ortalama hücre canlılığı verileri ve standart hata değerlerinin grafiksel olarak gösterimi [*] çözücü kontrol ile karşılaştırıldığında farklılığı gösterir (P<0,05).

24, 48 ve 72 saatlik muamele süreleri sonunda, kuyucuklara PBS içerisinde hazırlanmış %5'lik MTT solüsyonundan 20 µl eklenmiştir. Kültür kabındaki hücreler 3 saat 37°C'de inkübatörde bekletilmiştir. Süre sonunda içerisinde MTT bulunan besiyeri aspire edilerek formazan kristallerinin çözülmesi için 100 µl DMSO eklenmiş ve 15 dk bekletilmiştir. Kuyucuklardaki mor renkli solüsyonun absorbansı 570 nm'de spektrofotometrik olarak ölçülmüştür (Kahraman ve ark., 2013).

hTERT-HPNE hücrelerinin, negatif kontrol ve seftriakson etken maddesi ile maruziyet süreleri sonucundaki hücre canlılığı değerleri aşağıdaki formül ile hesaplanmıştır.

Hücre canlılığı= (Ortalama doğrulanmış muamele kuyucuğunun absorbans değeri/Ortalama doğrulanmış kontrol kuyucuğunun absorbans değeri) x 100.

2.4. İstatistik Analiz

Deney üç kez tekrarlanmış olup veriler bu üç tekrarın ortalamasını ve ± standart hatasını ifade etmektedir.

İnceleme sonucunda elde edilen tüm verilerin homojenliği ve grup ortalamaları arasındaki farkın önemli olup olmadığı SPSS programı kullanılarak tek yönlü varyans analiz metodu (ANOVA) ile belirlenmiştir. Farkın önemli olduğu gruplarda ise, elde edilen sonuçlar Student's t-testi ile karşılaştırılmıştır. Sonuçların değerlendirilmesinde P<0,05 anlamlılık seviyesi temel alınmıştır.

3. Bulgular

3.1. Hücre Canlılığı

MTT testi ile seftriaksonun tüm tedavi süreleri boyunca konsantrasyona bağlı olarak hücre canlılığını azalttığı belirlenmiştir. Seftriaksonun 24 saatlik maruziyet sonucu hTERT-HPNE hücrelerinin hücre canlılığı değerlerinin konsantrasyon artışına bağlı olarak azaldığı belirlenmiştir. Hücre canlılığı değerindeki bu azalmanın ilk olarak 0,781 mM konsantrasyonda %50'nin altına düştüğü görülmüştür. 48 saatlik maruziyet süresi

sonucunda ise, 24 saatlik uygulamaya benzer bir şekilde konsantrasyon artışına bağlı olarak hücre canlılığında düşüşler tespit edilmiştir. Hücre canlılığı değerindeki ilk düşüş 0,195 mM'lık konsantrasyon ve sonrasında %50'nin altına düşmüştür. 72 saatlik muamele sonrasında seftriaksonun hTERT-HPNE hücrelerinin hücre canlılığı üzerindeki etkisine bakıldığında, doza bağımlı olarak uygulanan tüm doz konsantrasyonlarında

%50'nin altına düşmüştür.

Bu değerler istatistiksel olarak karşılaştırıldı ve grafiklendirildi. Tüm konsantrasyonlarda seftriaksonun neden olduğu hücre canlılığındaki azalmalar negatif kontrole kıyasla anlamlı bulunmuştur ($P<0,05$). Seftriaksonun aktif bileşeninin hTERT-HPNE hücre canlılığı üzerindeki etkileri Tablo 1'de gösterilmiştir (Tablo 1).

Tablo 1. 24,48 ve 72 saatlik seftriakson etken maddesi maruziyet süresi sonrasında konsantrasyona bağlı olarak hücre canlılıkları ve hesaplanan standart hata değerleri

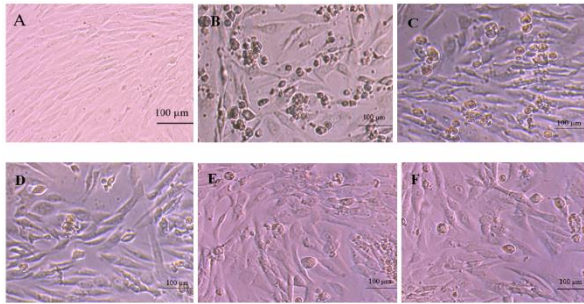
| Konsantrasyonlar | 24 Saat | 48 Saat | 72 Saat |
|------------------|---------------|--------------|--------------|
| Negatif Kontrol | 100 ± 0 | 100 ± 0 | 100 ± 0 |
| 0,097 | 76,18 ± 0,532 | 55,56 ± 0,50 | 46,40 ± 0,67 |
| 0,195 | 75,31 ± 0,499 | 48,15 ± 0,60 | 44,27 ± 0,25 |
| 0,39 | 57,97 ± 0,817 | 42,42 ± 0,84 | 42,40 ± 0,75 |
| 0,781 | 45,36 ± 1,377 | 39,73 ± 0,64 | 38,67 ± 1,07 |
| 1,562 | 43,43 ± 0,793 | 31,31 ± 1,43 | 34,93 ± 0,85 |
| 3,125 | 36,25 ± 0,876 | 21,21 ± 1,20 | 17,87 ± 0,93 |
| 6,25 | 34,50 ± 1,500 | 17,17 ± 1,55 | 1,33 ± 1,39 |
| 12,5 | 32,05 ± 1,024 | 0,67 ± 0,17 | 0,51 ± 0,58 |

3.2. Morfolojik Değişiklikler

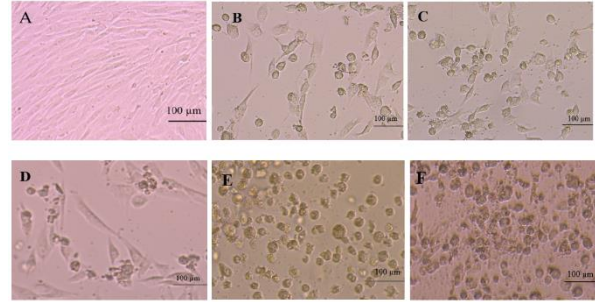
hTERT-HPNE hücre hattı seftriakson etken maddesine, 0,097 mM, 0,195 mM, 0,390 mM, 0,781 mM, 1,562 mM, 3,125 mM, 6,25 mM, 12,5 mM dozlarında 24,48 ve 72 saat boyunca maruz bırakılmıştır. Maruziyet sonucunda hTERT-HPNE hücrelerinde meydana gelen morfolojik değişiklikler Şekil 4,5 ve 6'da gösterilmiştir.

Şekil 4, 5, 6 'da yer alan A görseli negatif kontrol grubunun morfolojisini göstermektedir. Şekil 4, 5, 6'da yer alan B-F görselleri ise hTERT-HPNE hücre hattının seftriakson etken maddesi ile maruziyeti sonucundaki morfolojisini göstermektedir.

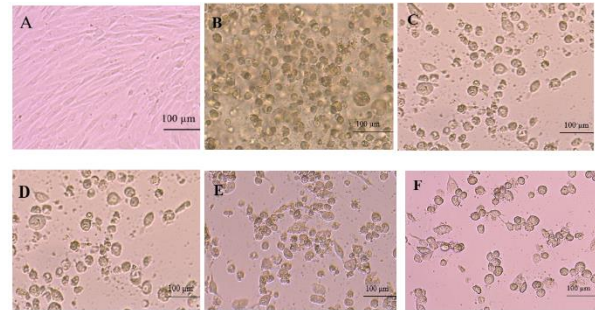
hTERT-HPNE hücre hattının seftriakson etken madde ile maruziyeti doza ve süreye bağlı olarak negatif kontrol ile kıyaslandığında canlı hücrenin morfolojisinin değiştiği, hücre ölümlerinin meydana geldiği görülmektedir.



Şekil 4. A Kontrol / B-F seftriakson etken maddeli ilacın hTERT-HPNE hücresi üzerindeki 24 saatlik morfolojik değişimleri.



Şekil 5. A Kontrol / B-F seftriakson etken maddeli ilacın hTERT-HPNE hücresi üzerindeki 48 saatlik morfolojik değişimleri.



Şekil 6. A Kontrol / B-F seftriakson etken maddeli ilacın hTERT-HPNE hücresi üzerindeki 72 saatlik morfolojik değişimleri.

4. Tartışma

Antibiyotiklerin dünyada ve ülkemizde bilinçli ve bilinçsiz şekilde kullanımı çok yüksektir. Antibiyotik ilaçlar bakterilerin büyümesini öldürme (bakterisid) ya da büyümesini engellemek (bakteriyostatik) üzere iki

hedef için kullanılırlar. İlaç ve hedef etkileşimlerinden bağımsız olarak, bakterisidal antibiyotikler bakterilerde yaygın bir oksidatif hasara neden olarak reaktif oksijen türlerinin (ROS) üretimine ve hücre ölümüyle sonuçlanan DNA, protein ve lipid hasarına sebep olabilir (Kohanski ve ark., 2007). Bununla birlikte, bakterilerin öldürülmesinde rol oynayan ortak bir mekanizma olarak oksidatif stres oluşumu tartışılmıştır. Tüm bakterisidal ilaç sınıfları, hidroksil radikali oluşumunu teşvik etmek için demir-kükürt kümelerinden salınan dahili demiri kullanabilir. Hidroksil radikalleri DNA'ya, proteinlere ve lipitlere doğrudan zarar verebilir (Karabulut ve ark., 2016). Bakterisidal antibiyotik etkileri, antioksidan N-asetilsisteinin uygulanmasıyla hafifletilebilir veya bakteriyostatik etkili antibiyotik kullanımı ile önenebilir (Çoşkun, 2017). Bakterisid grubu antibiyotikler memeli dokularına ve hücrelerine de zarar verebilir. Bununla birlikte, etkileri bakterilerde olduğu kadar iyi karakterize edilmez (Savcı, 2016). Moleküler hedefleri ne olursa olsun, başlıca mitokondriyal disfonksiyonu yani mitokondrinin fonksiyonu herhangi bir nedenle bozulursa, hücre ve vücut fonksiyonları uygun şekilde işlev görememesi ile sonuçlanmaktadır. Daha önce yapılan literatür araştırmalarında memeli hücrelerinde, özellikle hepatositlerde bakterisid antibiyotikler tarafından oksidatif ve endoplazmik retikulum (ER) stresinin indüklenmesine odaklanılmıştır ve başta karaciğer olmak üzere çeşitli insan dokularında ve hücrelerinde olumsuz yan etkilere neden olabilir. Mitokondriyal disfonksiyon ve ROS'un aşırı ekspresyonu ile ilişkili, oksidatif strese ve hücre ölümüne yol açtığı bildirilmiştir (Kocasarı ve ark., 2021). Başka bir çalışmada antibiyotiklerin osteojenik hücre canlılığı üzerine etkisi araştırılmıştır. Osteoblastları, 8 farklı konsantrasyonda 21 çeşit antibiyotik ile tedavi ettiklerinden sonra hücre sayısını ve osteojenik aktiviteyi belirlemek için osteoblast deoksiribonükleik asit içeriği ve alkalın fosfataz aktivitesi (ALP) ölçülmüştür. Çoğu antibiyotiğin hücre sayıları ve ALP ölçümleri önemli ölçüde azaldığı sonucuna ulaşmışlardır. Fakat amikasin, tobramisin ve vankomisin çok yüksek konsantrasyonlar kullanılıncaya kadar en az sitotoksikite göstermiştir. Hücre sayısını ve ALP'yi belirgin şekilde etkilemediği sonucuna varmışlardır (Rathbone ve ark., 2011).

Sitotoksikite; canlı hücreler üzerindeki toksik etki oranını ifade eder. Sitotoksikite testleri, toksik olduğu düşünülen maddenin, uygun hücre kültüründe, hücre çoğalma oranı ve hücre üzerindeki toksik etkisi dikkate alınarak değerlendirme yapılan testlerdir. Sitotoksikite çalışmaları sayesinde kimyasal maddelere maruz bırakılan hücrelerin canlılığının deneysel olarak belirlenmesi sağlanır ve çalışma sonunda canlı ve ölü hücre miktarı belirlenebilir (Niles ve ark., 2007). Ayrıca hücreler, sitotoksik etkiye sahip bir maddeye maruz bırakıldıklarında apoptoz, nekroz ve otofaji gibi olaylar sebebiyle ölebilir. Buna ek olarak, hücre gelişiminin durdurulması veya engellenmesi nedeniyle de proliferasyon özelliklerini kaybedebilirler (Galluzzi ve

ark., 2009).

İn-vitro memeli kültürlerinde uygulanan ilaçların hücrelerde oluşturduğu hasarın incelenmesinde sıklıkla MTT testi kullanılır. MTT testinde kullanılacak ilacın farklı molaritelerde hazırlanan derişimleri, kültür flaksındaki hücre hattı ve besiyeri karışımına ekilir. Bu sayede ilaç ve hücre mitokondrisi etkileşime geçer. İlaç toksik bir etkiye sahipse hücre solunumu baskılanır ve MTT test solüsyonu içeriğinde bulunan tetrazolium tuzları ile reaksiyonun azalması görülür. Mitokondriyel iki katmanlı lipoprotein zar yapısına ve yüksek metabolik aktiviteye sahip oldukları için hücrede meydana gelebilecek hasarlardan ilk etkilenir (Okatan,2017).Bir çalışmada protokatekuik asitin (PCA) insan prostat kanseri (DU145) hücreleri üzerindeki sitotoksik, morfolojik ve apoptotik etkileri 0,5 ile 3,5 mM dozlarında 24 ve 48 saatteki sitotoksik etkileri MTT yöntemi ile araştırılmıştır. Çalışma sonucunda hücrelerdeki morfolojik değişiklikler ters ışık mikroskobu ile incelenmiş ve hücrelerdeki apoptotik hücre ölümü, PCA dozlarındaki artışa bağlı olarak hücrelerin yuvarlaklaştığı ve sayıca azaldığı ve bununla beraber hücre çekirdeklerinde yoğunlaşma ve parçalanmaların olduğunu belirtmişlerdir (Öztopcu ve ark., 2018). Başka bir çalışmada insan vasküler endotelial EA.hy926 hücrelerinde valinomisin ve antimisin A'nın sitotoksikitesini değerlendirildi. Çalışmada yapılan MTT analizi sonuçlarına göre iki antibiyotiğin de hücreler üzerinde sitotoksik etkiler gösterdiği hatta valinomisin, antimisin A'ya göre daha güçlü sitotoksik ajan olduğu görülmüştür (Luzak ve ark., 2022). Duwelhenke ve ark. (2007) yaptığı bir çalışmada primer insan osteoblast, MG63 osteosarkom ve Hela epitel hücre dizisi üzerine 20 farklı antibiyotiğin sitotoksik etkisini araştırmışlardır. Primer osteoblast hücreleri üzerinde belirledikleri konsantrasyonlar da siprofloksasin ve moksifloksasin, klindamisin ve eritromisinin farklı oranlarda sitotoksik etki meydana getirdiğini göstermişlerdir. Azitromisin ve roksitromisinin primer insan osteoblast hücreleri üzerinde konsantrasyona bağlı olarak sitotoksik etkinin arttığı bildirilmiştir. Aynı çalışmada siprofloksasin ve moksifloksasin, primer insan osteoblast hücresi proliferasyonunu durduğunu bildirmişlerdir. Aynı etken maddelerinin MG63 osteosarkom ve Hela epitel hücre dizilerinde de daha yüksek konsantrasyonlarda proliferasyonu engellediğini ifade etmişlerdir (Şahin,2020). Bu çalışmalar son yıllarda yapılmıştır. Literatür araştırmaları her antibiyotiğin farklı sitotoksik etkilerinin olabileceğini ve antibiyotiğin uygulandığı hücreye bağlı olarak da farklı sonuçlara ulaşabileceğini göstermektedir. Bu sebepten, farklı hücrelerde farklı antibiyotikler üzerinde çoklu çalışmalar yapılarak daha net bir fikir birliğine ulaşılabilir.

Bu çalışmamızda ilacın etken maddesi seftriakson içeren bir antibiyotiğin in vitro kültürde sağlıklı insan pankreas hücreleri üzerinde sitotoksikitesini araştırılmıştır. Çalışmamızda kullandığımız seftriakson disodyum, geniş bir antimikrobiyal aktivite yelpazesine sahip üçüncü nesil

yarı sentetik bir sefalosporin grubu antibiyotiktir. Gram pozitif ve Gram negatif aerobik ve bazı anaerobik bakterilere karşı geniş bir aktivite spektrumuna sahiptir (Richards ve ark., 1984). Seftriakson bakteri hücre duvarı sentezini bozarak transpeptidasyon evresinde penisilin bağlayan proteinleri (PBP) durdurur. Bakteri duvarı tam sentezlenemez ve iç basınçtan dolayı lizise uğrar. Eksitator bir nörotransmitter olan glutamatin fazla salınması, N-metil-d-aspartat (NMDA) reseptörlerini sürekli uyarabilir, bu da nöronlarda kalsiyumun fazla yüklenmesine ve hücreyi apoptotik ölüme uğratar. 2016 yılında yapılan bir çalışmada Seftriaksonun Ekzitatör Aminoasit Taşıyıcı 1 (EAAT1), Ekzitatör Aminoasit Taşıyıcı 2 (EAAT2), Ekzitatör Aminoasit Taşıyıcı 3 (EAAT3) blokeleriyle birlikte kullanımının sıçan GBM hücre hattı üzerindeki etkilerinin incelenmesi üzerine bir araştırma gerçekleştirilmiştir. Bu araştırmanın sonuçları seftriakson etken maddeli antibiyotiğin çalışmada kullanılan diğer ilaç gruplarıyla kıyaslandığında hücre canlılığı bakımından en çok hücre ölümüne sebep olduğu gözlemlenmiştir (Nalcı, 2016). Bir çalışmada kıkırdak matriksini üreten kondrosit hücreleri üzerinde seftriakson sitotoksitesini araştırılmıştır. Analiz sonuçlarında seftriaksonun apoptotik hücre ölümü indüklendiği hem de transkripsiyon seviyesindeki kondrojenik işaretleyici genler üzerindeki olumsuz etkileri olduğu görülmüştür (Siengdee ve ark., 2017). Bununla birlikte, literatürde MTT ile seftriakson sitotoksitesine çalışmaları çok azdır. Bu çalışmada, hücre canlılığını gözlemlemek için ucuz, hızlı, etkili, kullanımı kolay, güvenilir ve dünya çapında yaygın olarak kullanılan MTT analiz yöntemini kullandık. hTERT-HPNE hücre hattı seftriakson etken maddesine maruz bırakıldıktan sonra mitokondriyal aktivite ölçülerek değerlendirildi. Seftriakson, 24, 48, 72 saatlik maruziyet sonrası hTERT-HPNE hücrelerinde artan konsantrasyonlara bağlı olarak sitotoksitesine neden olduğu görülmüştür. Aynı zamanda hTERT-HPNE hücreleri ve ilaca maruz bırakılan hTERT-HPNE hücrelerinin invert mikroskop ile morfolojileri kıyaslandığında sağlıklı hücre görüntüsünün bozulması ve hücre sayısındaki azalmanın varlığı görülmüştür.

5. Sonuç

Antibiyotikler tüm dünyada en çok kullanılan ilaçlar arasında ilk sıralarda yer almaktadır. Bu çalışmada kullanılan sefalosporin grubuna ait seftriakson antibiyotiği dahil olmak üzere enfeksiyon hastalıklarının tedavisinde kullanılan antibiyotiklerin belirlenmesinde hastanın yaşı, cinsiyeti, genetik özellikleri ve immün sistemdeki farklılıklar ilaç etkinliğini değiştirmektedir. Kullanılan diğer ilaçlarla, çeşitli kimyasal maddeler veya alkol ile etkileşime girerek ilaç etkinliğini değiştirebilir ve hedeflenmeyen hücrelerde istenmeyen sonuçlar ile karşılaşmamıza sebep olabilmektedir. Bu sebeplere ek olarak kullanılan ilacın sitotoksik etki gösterme potansiyeli vardır. Bu yüzden tedavide kullanılacak ilaçların doz ve maruziyet ilişkisinin belirlenebilmesi için

bu faktörlerin bilinmesi gereklidir. Yanlış ilaç kullanımı genetik materyalde bozukluklara, tamir edilemeyen DNA hasarına, doku ve hücre hasarlarına ek kanser gibi çeşitli hastalıkların temelini oluşturur. Doğru ilaç kullanımı için ilaçların toksisitesi, yapılacak laboratuvar çalışmaları sayesinde aydınlatılabilir.

Bu çalışmada tüm dünyada enfeksiyon hastalıklarının tedavisinde sıklıkla tercih edilen sefalosporin grubuna ait üçüncü nesil seftriakson antibiyotiğinin, in vitro insan pankreas hücre kültüründe sitotoksik etkileri çalışılmıştır. Literatür araştırmaları ve incelenmeleri sonucunda seftriaksonun sitotoksitesine çalışmaları çok az ve yetersiz olduğu görülmüştür. Çalışmamızda sitotoksitesini belirlemek için MTT testi kullanılmıştır. Seftriaksonun çalışılan dozlarında doza ve maruziyet sürelerine bağlı olarak negatif kontrole göre kıyaslandığında sağlıklı pankreas hücresi üzerinde sitotoksik özellik gösterdiği görülmüştür. Çalışmamızın bir diğer kısmında seftriakson etken maddeye maruz grup ile negatif kontrol grubu karşılaştırıldığında hücrelerin morfolojisinde de farklılıklar olduğu, seftriakson etken maddeye maruz deney grubunda canlılığını yitirmiş hücrelerin varlığı görülmüştür. Sefalosporin grubuna ait seftriakson ile ilgili yapılan önceki çalışmalarda da bu ilacın farklı hücreler üzerinde de sitotoksik olduğu desteklenmektedir. Yapılan in vitro çalışmaları sayesinde ilaçların en az yan etkiye sahip konsantrasyonları belirlenerek daha ileri aşama olan in vivo deney hayvanı çalışmaları için referans veri kabul edilebilir.

Katkı Oranı Beyanı

Yazar(lar)ın katkı yüzdesi aşağıda verilmiştir. Tüm yazarlar makaleyi incelemiş ve onaylamıştır.

| | A.K. | Z.Ç. | Ö.E. |
|-----|------|------|------|
| K | 30 | 30 | 40 |
| T | 100 | | |
| Y | 60 | 10 | 30 |
| VTI | 40 | 30 | 30 |
| VAY | 40 | 30 | 30 |
| KT | 70 | 20 | 10 |
| YZ | 60 | 20 | 20 |
| KI | 40 | 30 | 30 |
| GR | 100 | | |
| PY | 40 | 20 | 40 |
| FA | | | 100 |

K= kavram, T= tasarım, Y= yönetim, VTI= veri toplama ve/veya işleme, VAY= veri analizi ve/veya yorumlama, KT= kaynak tarama, YZ= Yazım, KI= kritik inceleme, GR= gönderim ve revizyon, PY= proje yönetimi, FA= fon alımı.

Çalışma Beyanı

Yazarlar bu çalışmada hiçbir çıkar ilişkisi olmadığını beyan etmektedirler.

Etik Onay Beyanı

Hayvanlar ve insanlar üzerinde herhangi bir çalışma yapılmadığından dolayı bu araştırma için etik kurul onayı alınmamıştır.

Kaynaklar

- Cao H, Högger P, Prieto M, Simal-Gandara J, Xiao J. 2022. Stability of quercetin in DMEM and cell culture with A549 cells. *EFood* 3:e13. <https://doi.org/10.1002/efd2.13>.
- Çoşkun D. 2017. N-asetil-L-Sisteinin ekstrapamukolitik etkileri. *Dicle Üniv Vet Fak Derg*, 10(2): 154–162.
- Erdemir F, Akman A, Uysal G, Polater E, Çırlak A. 2011. Yeni-Yeniden tanımlanan enfeksiyonlar ve enfeksiyon kontrolü. *Ege Üniv Hemşirelik Yüksek Okulu Derg*, 27(1): 47–60.
- Galluzzi L, Aaronson S, Abrams J, Alnemri E. 2009. Guidelines for the use and interpretation of assays for monitoring cell death in higher eukaryotes. *Cell Death Different*, 16: 1093–1107.
- Gökçe T. 2017. Birinci basamağı sağlık hapsedmesi hastalarının antibiyotik kullanımındaki davranış ve bilgi düzeylerinin araştırılması. *Uzmanlık Tezi, Pamukkale Üniversitesi, Denizli, Türkiye*, ss: 106.
- Güngör A, Çuhaci Çakır B, Yalçın H, Çakır H. T, Karauzun A. 2018. Evaluation of parents' attitudes and behaviors related to the use of antibiotics in children. *Turkish J Pediatric Disease*, 12(3): 215 – 217.
- Kahraman E, Gurhan I, Korkmaz M. 2013. Investigation of possible genotoxic and cytotoxic effects of differential boron compounds in CCL 62 (hela contaminant): human amniotic epithelial cell line. *Medicine Sci, Inter Med J*, 2(1): 454. <https://doi.org/10.5455/medscience.2012.01.8046>
- Karabulut H, Gülay MŞ. 2016. Serbest radikaller. *MAKÜ Sağ Bil Enst Derg*, 4(1): 50-59.
- Kocasarı Ş, Erdemli Köse SB, Garlı S. 2021. Hayvanlarda ilaç ve toksik maddelere bağlı olarak oluşan oksidatif stresin sindirim ve solunum sistemi toksisitesindeki rolü. *Şahindokuyucu Kocasarı F editör. İlaç ve Toksik Maddelere Bağlı Olarak Oluşan Oksidatif Stres ve Antioksidanlar. Türkiye Klinikleri, 1. Baskı, Ankara, Türkiye*, pp: 85-99.
- Kohanski M, Dwyer D, Hayete B, Lawrence C, Collins J. 2007. A common mechanism of cellular death induced by bactericidal antibiotics. *Cell*, 130(5): 797–810.
- Köksal İ. 2013. Enfeksiyon hastalıkları. *Nobel kitapevi, İstanbul, Türkiye*, ss: 75-78.
- Küçükbuğru N. 2020. Gıdalarda antibiyotik kalıntıları ve halk sağlığına etkileri. *Vet Farmak Toksikol Derneği Bülten*, 11 (3): 161-167.
- Luzak B, Siarkiewicz P, Boncler M. 2022. An evaluation of a new high-sensitivity PrestoBlue assay for measuring cell viability and drug cytotoxicity using EA.hy926 endothelial cells. *Toxicology in Vitro*, 83: 105407.
- Nalci A. 2016. Seftriaksonun eksitator aminoasit taşıyıcı 1 (eaat1): eaat2 eaat3 blokerleriyle birlikte kullanımının sıçan glioblastoma multiforme hücre hattı üzerindeki etkilerinin incelenmesi. *Trakya Üniversitesi, Sağlık Bilimleri Enstitüsü, Tıbbi Farmakoloji Ana Bilim Dalı, Edirne, Türkiye*, ss: 69.
- Niles A, Moravec R, Hesselberth E, Scurria M, Daily W, Riss T. 2007. A homogeneous assay to measure live and dead cells in the same sample by detecting different protease markers. *Analytical Biochem*, 366(2): 197–206.
- Okutan D. 2017. Antibiyotik g 418'in Toxoplasma Gondii üzerine etkisinin in vitro olarak araştırılması. *Yüksek lisans Tezi, Kırıkkale Üniversitesi, Sağlık Bilimleri Enstitüsü, Tıbbi Farmakoloji Ana Bilim Dalı, Kırıkkale, Türkiye*, ss: 58.
- Öztopcu-Vatan P, İnan E. 2018. Determination of growth inhibitory and apoptotic effects of protocatechuic acid on prostate carcinoma cells. *Biological Diver Conservat*, 11(1): 80-86.
- Rathbone C, Cross J, Brown K, Murray C, Wenke J. 2011. Effect of various concentrations of antibiotics on osteogenic cell viability and activity. *J Orthopaedic Res*, 29(7): 1070–1074.
- Richards D, Heel R, Brogden R, Speight T, Avery G. 1984. Ceftriaxone a review of its antibacterial activity pharmacological properties and therapeutic use. *Drug Evaluation*, 27: 469–527.
- Savcı A. 2016. Gentamisin sülfat amoksisilin ve sefazolin sodyum antibiyotiklerinin fare kalp dokusunda antioksidan enzim aktiviteleri protein ve gen ekspresyon düzeyleri üzerine etkilerinin incelenmesi. *Doktora Tezi, Kimya Anabilim Dalı, Biyokimya Bilim Dalı, Bingöl Üniversitesi, Bingöl, Türkiye*, ss: 100.
- Siengdee P, Pradit W, Euppayo T, Chomdej S, Nganvongpanit K. 2017. Comparison of the effects of cefazolin and ceftriaxone on canine chondrocyte culture. *Vet Pharnacol Therapeut*, 40(6): 604–617.
- strategies. *Washington DC: The National Academies Press* 2010.
- Şahin Y. 2020. Sığırlarda tulatromisin ve gamitromisinin trakea düz kasının kasılması ile trakea epitel hücreleri üzerine apoptotik nekrotik ve sitotoksik etkilerinin araştırılması. *Doktora tezi, Sağlık Bilimleri Enstitüsü, Kırıkkale Üniversitesi, Kırıkkale, Türkiye*, ss: 83.
- Topal M, Uslu Şenel G, Arslan Topal E, Öbek E. 2015. Antibiyotikler ve kullanım alanları. *Erciyes Üniv Fen Bilimleri Enstit Derg*, 31(3): 121–127.
- Yao Y, Zhou R, Wang Y. 2012. Fatal adverse effects of injected ceftriaxone sodium in China. *Pharmacoepidemiology Drug Safety*, 21(11): 1197–1201.
- Yıldız İ, Varkal M, Ünüvar E. 2014. Günümüzde sefalosporinler ve antibiyotik direnci. *Çocuk Derg*, 14(1): 22–27.
- Yifan Z, Benxiang N, Zheng X, Luwei X, Lihua Z, Yuzheng G, Ruipeng J. 2020. Ceftriaxone calcium crystals induce acute kidney injury by nlrp3-mediated inflammation and oxidative stress injury. *Oxidative Med Cellular Longev*, 2020: 6428498.



İKLİM DEĞİŞİKLİĞİ İLE MÜCADELEDE KURUMSAL KARBON EMİSYON FARKINDALIĞINI ARTTIRMA: ZONGULDAK BÜLENT ECEVİT ÜNİVERSİTESİ DEVREK MESLEK YÜKSEKOKULU ÖRNEĞİ

Serkan ÖREN^{1*}, Sefa KOCABAŞ¹

¹Zonguldak Bülent Ecevit University, Devrek Vocational School, Department of Environmental Protection, 67800, Zonguldak, Türkiye

Özet: Dünyadaki hızlı nüfus artışı ve sanayileşmenin hızla ilerlemesi doğal kaynakların tüketilmesine, fosil yakıtların kullanılmasına ve çevre kirliliğine neden olmaktadır. Bu durum, atmosfere salınan sera gazı miktarının artmasını ve küresel ısınmayı beraberinde getirmektedir. Bu etkilerin azaltılması için salınan karbon miktarının düşürülmesi gerekmektedir. Bu kapsamda ülkesel, bölgesel, kurumsal ve bireysel farkındalıklar oluşturulmalı ve salınım miktarının düşürülmesi hedeflenmelidir. Bu çalışmada, Zonguldak Bülent Ecevit Üniversitesi Devrek Meslek Yüksekokulunun karbon ayak izi İngiltere Çevre Gıda ve Köy İşleri Departmanı (DEFRA) kriterlerine göre hesaplanmıştır. Devrek Kampüsü'nün yakıt tüketimi (kömür ve doğalgaz), elektrik tüketimi, atıklar, personel araçları, öğrenci ve personel servislerinin cinsi, araçlarda kullanılan yakıt tipi ve yakıt miktarları hesaplamalara dahil edilmiştir. Sonuç olarak, CO₂ salınım miktarı 2022 yılı için 427,92 bin tCO₂e olarak hesaplanmış ve en yüksek emisyon salınımının ısınma amaçlı kullanılan yakıtlardan (yaklaşık 284 bin tCO₂e) ve personelin kullandıkları araçlardan (yaklaşık 77 bin tCO₂e) kaynaklandığı, en düşük emisyon salınımının ise atıklardan kaynaklandığı tespit edilmiştir.

Anahtar kelimeler: Sera gazı, Küresel ısınma, Karbon ayak izi, İklim değişikliği, DEFRA


Increasing Corporate Carbon Emission Awareness in Combating Climate Change: The Case of Zonguldak Bülent Ecevit University Devrek Vocational School


Abstract: Rapid population growth and rapid progress of industrialization in the world cause the consumption of natural resources, the use of fossil fuels and an increase in environmental pollution. In this context, national, regional, institutional and individual awareness should be created and efforts should be made to reduce the amount of emissions. This situation brings about an increase in the amount of greenhouse gases released into the atmosphere and global warming. In order to reduce these effects, the amount of carbon released must be reduced. In this study, the carbon footprint of Zonguldak Bülent Ecevit University Devrek Vocational School was calculated according to Department for Environment Food & Rural Affairs (DEFRA) criteria. The fuel consumption (coal and natural gas), electricity consumption, wastes, personnel vehicles, the type of student and personnel shuttles, the type of leaning used and the amount of fuel of Devrek Campus are included in the calculations. As a result, the amount of CO₂ emission was calculated as 427.9200 tCO₂e for 2022, and it was determined that the highest emission was caused by the fuels used for heating (approximately 284 thousand tCO₂e) and the vehicles used by the personnel for commuting (approximately 77 thousand tCO₂e), while the lowest emission was caused by the wastes.

Keywords: Global warming, Greenhouse gas, Carbon footprint, Climate change, DEFRA

*Sorumlu yazar (Corresponding author): Zonguldak Bülent Ecevit University, Devrek Vocational School, Department of Environmental Protection, 67800, Zonguldak, Türkiye

E mail: serkan.oren@hotmail.com (S. ÖREN)

Serkan ÖREN  <https://orcid.org/0000-0001-7699-517X>

Sefa KOCABAŞ  <https://orcid.org/0000-0002-8003-8310>

Gönderi: 05 Mayıs 2023

Kabul: 14 Ağustos 2023

Yayınlanma: 15 Ekim 2023

Received: May 05, 2023

Accepted: August 14, 2023

Published: October 15, 2023

Cite as: Ören S, Kocabaş S. 2023. Increasing Corporate Carbon Emission Awareness in Combating Climate Change: The Case of Zonguldak Bülent Ecevit University Devrek Vocational School. BSJ Eng Sci, 6(4): 363-368.

1. Giriş

Hızla artan insan nüfusu ve sanayileşmedeki ilerleme doğal kaynakların tüketilmesine, fosil yakıtların kullanımına bağlı çevre kirliliğinin artmasına neden olmaktadır. Artan insan faaliyetleri ile karbondioksit, metan ve diazot oksit gibi sera gazları yerkürenin sıcaklığının yükselmesine ve küresel ısınmaya yol açmaktadır (Kılıç ve ark., 2021). Yayılan bu sera gazlarının toplamı karbon ayak izi olarak bilinmektedir ve karbon ayak izinin hesaplanması için günlük üretilen

kirlilik veya sera gazı emisyon seviyelerinin tam olarak bilinmesi gerekmektedir (Kurnuç ve Çerçi, 2022). Bu gazların bir miktarı doğal yollarla oluşmakla beraber çok büyük bir miktarı ise insan faaliyetleri sonucu oluşmaktadır. Sera gazlarının oluşmasına fosil yakıtların kullanımı öncelikli olmasına karşın, tarımsal faaliyetler, orman alanlarının yok edilmesi de sera gazı oluşumuna neden olmaktadır. Sanayileşmenin ve insan aktivitelerinin artması ile başta karbondioksit olmak üzere metan, azot dioksit, karbonmonoksit ve diğer gazlar atmosferde birikerek güneş ve yerküre arasında



bir tabaka oluşturmaktadırlar. Atmosferde biriken sera gazları yeryüzüne gelen güneş ışığını tekrar yer küreden atmosfere yansımaları engellemekte ve yer kürenin beklenenden daha fazla ısınmasına neden olmaktadır. Sera etkisi olarak adlandırılan bu doğal süreç küresel ısınma ve iklim değişimine neden olur (Erdoğan, 2020). Elektrik tüketimi, ulaşım, malzeme, atık yönetimi, ambalaj kullanımı vb. etkenler aracılığıyla toplanan veriler yardımıyla karbon ayak izi ton CO₂ eşdeğeri (tCO₂e) olarak ölçülür ve verilerinin emisyon faktörleriyle çarpılmasıyla belirlenir (Kurnuç ve Çerçi, 2022). Elde edilen sonuçlar ile çevre korumada gerekli önlemlerin alınması, tasarrufların belirlenmesi ve sera gazı emisyonlarının azaltılması hedeflenir.

Kırbaş ve Kocakulak (2022) yapmış oldukları çalışmada Burdur ilinin karbon ayak izi değerlerini araştırmışlardır. Hesaplamalarını, konut, serbest tüketici, ticarethane ve katı atık depolama tesislerinde meydana gelen salınımlarla gerçekleştirmişlerdir. Elde ettikleri sonuç doğrultusunda Burdur ilinde yıllık 538,44 bin tCO₂e emisyon salınımı olduğunu bildirmişlerdir. Gökçek ve Arkadaşları (2019) tarafından yapılan bir çalışmada Niğde Ömer Halis Demir Üniversitesinin karbon ayak izini hesaplamışlardır. Çalışma toplam 9 fakültede öğrenim gören öğrencilerin tüketim alışkanlıklarını ölçen anket uygulaması gerçekleştirilerek yapılmıştır. Sonuç olarak CO₂ emisyonunun mekânsal dağılımı incelenerek çözüm önerileri sunulmuştur. Kumaş ve ark., (2018) Mehmet Akif Ersoy Üniversitesi Bucak Sağlık Yüksekokulunun karbon ayak izini hesaplamışlardır. Hesaplamalar DEFRA kriterlerine göre yapılmış olup karbon salınımı miktarının en fazla doğal gazdan en az ise benzinli araçlardan kaynaklandığını bildirmişlerdir. Kurnuç ve Çerçi (2022) DEFRA kriterlerini kullanarak Erzincan Binali Yıldırım Üniversitesinin karbon ayak izi hesaplamasını gerçekleştirmiştir. 2019 yılı için 2753,2 tCO₂e, 2020 yılı için ise 2383,74 tCO₂e olarak hesaplamışlardır. Böylece %13,42'lik bir azalma olduğunu bildirmişlerdir. Bu azalmayı ise Covid-19 pandemi sürecinde eğitim öğretimin uzaktan olmasına bağlamışlardır.

Yañez ve arkadaşları 2019 yılında yaptıkları çalışmalarında Talca Üniversitesinde 2012 yılından itibaren her yıl karbon ayak izi hesaplamalarını takip etmişler ve özellikle 2016 yılında kapsam 3 içerisinde personel ve öğrenci taşımacılığının en yüksek sera gazı katkısı olduğunu belirtmişlerdir.

Mendoza-Flores ve arkadaşları 2019 yılında yaptıkları araştırma makalelerinde Kolombiya Pereira Teknoloji Üniversitesinin 2017' yılındaki kurumsal karbon ayak izini hesaplamışlar ve doğrudan emisyonlar (Kapsam 1), elektrikle ilişkili dolaylı emisyonlar (Kapsam 2) ve diğer dolaylı sera gazı emisyonlarını (Kapsam 3) değerlendirmişlerdir. Buldukları sonuçları diğer üniversitelerle kıyaslamışlar ve kampüste hareketliliğin az olması ve elektrik ve ısınma gibi durumların az kullanılmasından ötürü diğer üniversitelere nazaran karbon ayak izi değerlerinin düşük olduğunu öne

sürmüşlerdir.

Bu çalışmada, Zonguldak Bülent Ecevit Üniversitesi (ZBEÜ) Devrek Meslek Yüksekokulunun DEFRA (2022) hesaplama kriterleri kullanılarak karbon ayak izi miktarı hesaplanmıştır. Hesaplamalarda, yakıt tüketimi (kömür ve doğalgaz), elektrik tüketimi, atıklar, personel araçları, öğrenci ve personel servislerinin cinsi, kullandığı yakıt tipi ve yakıt miktarları dahil edilmiştir.

2. Materyal ve Yöntem

Zonguldak Bülent Ecevit Üniversitesi, Devrek Kampüsünde 2 meslek yüksekokulu ve 1 Yüksekokul bulunmaktadır. Kampüsün kapalı alanı 11.916 m², toplam arsa alanı ise, 230.554 m²'dir. Karbon ayak izi hesabının belirlenirken yüksekokulun toplam elektrik enerjisi tüketimi ve ısınma amaçlı kullanılan kömür ve doğalgaz miktarları kullanılmıştır. Hesaplamaya dahil "edilen toplam akademik personel sayısı 48, idari personel sayısı, 27 ve öğrenci sayısı 1870' dir. Yapılan hesaplamalardan bir diğeri ise yüksekokul personeli ve öğrencilerin kullandığı araçlardan kaynaklı atık gazların oluşturduğu karbondioksit salınımdır. Salınım değerlerinin hesaplanması için birimlerde bulunan tüm personelin kullandığı araçların motor hacimleri ve günlük aldıkları mesafeler tespit edilmiştir. Öğrencilerin kullandığı toplu taşıma araçları için ilçe merkezi ile yüksekokul arasındaki mesafe 5 km kabul edilmiştir.

2.1. Hesaplama Yöntemi

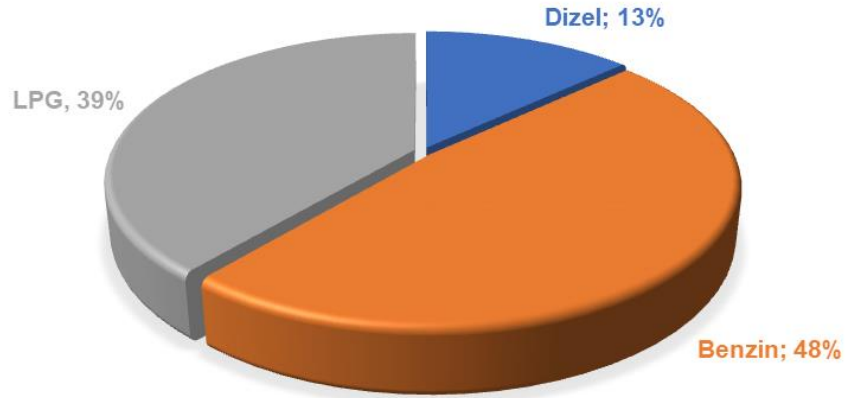
Tüm araçların aynı motor hacminde ve aynı yakıt kullanması durumundaki karbon ayak izindeki değişim İngiltere Çevre Gıda ve Köy İşleri Departmanının yayımladığı DEFRA (2022) kriterlerine göre hesaplanmıştır. Bu çalışma için 2022 yılı dönüşüm kriterleri kullanılmıştır. (Conversion factors 2022: condensed set -for most users). DEFRA'nın yayınlamış olduğu kriterler her yıl güncellenerek kullanıcıların hizmetine sunulmaktadır. DEFRA'nın yayınlamış olduğu bu hesaplama tablosunda istenilen veriler (Atık Miktarları, Personel Sayıları, Personel Araç Türleri, Katedilen Mesafeler vb.) tabloda yerlerine girilerek tüm hesaplama sonuçları eşdeğer CO₂ (eCO₂) değerinde alınmaktadır. Devrek Meslek Yüksekokulu kampüsünde 2016 yılında Karbon ayak izi hesaplamaları DEFRA metoduna göre yapılmış olup, kullanılan 2016 ve 2022 yılları verileri Tablo 1'de verilmiştir. Personelin kullandığı araçların yakıt türüne göre kat ettikleri mesafeler Tablo 2 ve Şekil 1'de verilmiştir. Ayrıca, personelin kullandığı araçların yakıt türü ve motor güçlerine göre kat ettiği mesafeler Tablo 3'de sunulmuştur. DEFRA'nın 2022 yılında yayımladığı karbon ayak izi hesaplama kriterlerine göre hesaplanan araç tipi ve yakıtına göre yapılan yıllık mesafeler ise Tablo 4'te verilmiştir.

Tablo 1. 2016 ve 2022 yılları Devrek kampüsü verileri

| | 2016 Yılı | 2022 Yılı |
|-------------------------------------|-----------------------|----------------------|
| Öğrenci Sayıları | 1547 | 1870 |
| Personel Sayıları | 60 | 75 |
| Personel Araç Sayısı | 36 | 47 |
| Görevlendirilen Personel km bilgisi | 11790 km/yıl | 15150 km / yıl |
| Organik Atık Miktarı | 2,5 ton/yıl | 0,48 ton/ yıl |
| Elektrik Tüketimi | 152.105,350 Kwh / yıl | 143.154,105 Kwh/ yıl |
| Su Tüketimi | 7514 ton / yıl | 2630 ton / yıl |
| Kömür Tüketimi | 50 ton / yıl | 40,68 ton / yıl |
| Doğal Gaz Tüketimi | - | 122.304,51 Kwh / yıl |

Tablo 2. Personelin kullandığı araçların yakıt türüne göre kat ettikleri mesafeler

| Yakıt Tipi | Toplam Yapılan Mesafe (km/yıl) |
|------------|--------------------------------|
| 1 Dizel | 31.025 km / yıl |
| 2 Benzin | 113.625 km / yıl |
| 3 LPG | 91.800 km / yıl |



Şekil 1. Personelin kullandığı araçların yakıt türü

Tablo 3. Toplam yıllık katedilen mesafe (motor gücüne göre)

| Yakıt Türü | Toplam Yıllık Katedilen Mesafe |
|------------|--------------------------------|
| 1.2 Benzin | 17.600 km / yıl |
| 1.3 Benzin | 12.600 km / yıl |
| 1.4 Benzin | 39.900 km / yıl |
| 1.6 Benzin | 43.525 km / yıl |
| 1.3 Dizel | 18.900 km / yıl |
| 1.4 Dizel | 3.800 km / yıl |
| 1.6 Dizel | 6.225 km / yıl |
| 2.0 Dizel | 2.100 km / yıl |
| 1.2 LPG | 16.800 km / yıl |
| 1.6 LPG | 75.000 km / yıl |

Tablo 4. Araç tipine ve yakıtına göre yapılan yıllık mesafeler

| Araç Tipi | Yakıt | Toplam Yapılan Mesafe (km/yıl) |
|---------------------------------|--------|--------------------------------|
| 1 Alt Orta Sınıf (Lower Medium) | Benzin | 98.925 km / yıl |
| | Dizel | 6.425 km / yıl |
| | LPG | 75.600 km / yıl |
| 2 Küçük Araç (Small Car) | Benzin | - |
| | Dizel | 22.500 km / yıl |
| | LPG | - |
| 3 Orta Sınıf Araç (Medium Car) | Benzin | - |
| | Dizel | 2.100 km / yıl |
| | LPG | - |
| 4 Üst Orta Sınıf (Upper Medium) | Benzin | 14.700 km / yıl |
| | Dizel | - |
| | LPG | - |
| 5 Supermini | Benzin | - |
| | Dizel | - |
| | LPG | 12.600 km / yıl |
| 6 Çok Amaçlı Araç (MPV) | Benzin | - |
| | Dizel | - |
| | LPG | 3.600 km / yıl |

3. Bulgular ve Tartışma

Zonguldak Bülent Ecevit Üniversitesi Devrek Meslek Yüksekokulu'nda 2016 ve 2022 yıllarında karbon ayak izi emisyonunun belirlenmesi adına 2 çalışma gerçekleştirilmiştir. Bu iki tarih arasında emisyon değerlerinin karşılaştırılması ve ne gibi önlemler alınabileceği araştırılmıştır. DEFRA Sera Gazı Emisyonları Dönüşüm Faktörü 2022 hesabına göre yapılan hesaplamalar Tablo 5' de verilmiştir. Yapılan hesaplamalara göre Zonguldak Bülent Ecevit Üniversitesi Devrek Kampüsünün doğaya saldıgı karbon miktarı 427.919,59 kg CO₂e/yıl olarak bulunmuştur. 2016 ve 2022 yılları arasındaki Karbon Ayak izi hesaplamaları karşılaştırmaları Tablo 6' da gösterilmiştir.

Tablo-5 ve Tablo-6 incelendiğinde; Kömür tüketiminin 2016 yılına oranla azaldığı ve neticesinde sera gazı salınımının yaklaşık % 25 oranında azaldığı görülmektedir, ancak bu azalmanın yaklaşık son 2 ayda doğal gaz kullanımı olup kömür kullanımı olmamasından kaynaklandığı görülmektedir. 2022 yılının ilk 9 ayı kömür kullanıldığı ve son 1,5 ayında doğal gaz kullanımı gerçekleştirildiği görülmektedir. İlk 9 aylık kömür kullanımında yaklaşık 235 ton CO₂e Sera gazı emisyonu salındığı buna karşın son 1,5 ayda doğal gaz kullanımı kaynaklı yaklaşık 50 ton CO₂e salınımı olduğu görülmektedir. 2023 ve sonraki senelerde doğal gaz kullanımını olacağından 2023 yılı ve diğer senelerde ısınma amaçlı doğal gaz kullanımı kaynaklı emisyon salınımların hesaplanması önem arz etmektedir. Elektrik tüketimine bağlı sera gazı salınımı değerleri incelendiğinde 2022 yılındaki tüketime bağlı sera gazı salınımının 2016 yılına oranla yaklaşık % 55,8 azaldığı görülmektedir. Bu azalmadaki başarı eski tip flüoresan

tarzı lambaların değiştirilerek yeni tip enerji tasarruflu lambalara geçilmesi ve neredeyse tüm bölümlerde okutulmakta olan çevre koruma dersi eğitimleri ayrıca belirli periyotlarda akademik ve idari kadrolara verilen bilinçlendirici eğitimlerin etkili olduğu görülmektedir. Ayrıca DEFRA hesaplama tablosu incelendiğinde 2016 yılında yayınladıkları hesaplama tablosu ile 2022 yılında yayınladıkları hesaplama tablosundaki kat sayıların farklılığı da dikkat çekmektedir. Son olarak bu azalmada 2016 yılındaki 5 olan ikinci öğretim program sayısının 2022 yılında 3 programa düşmesi ve eğitim gören öğrenci sayısındaki azalma da gösterilebilir. Akademik ve İdari personelin işe geliş gidiş için kullandığı özel araçlarının sera gazı emisyon değerleri incelendiğinde 2016 yılına nazaran 2022 yılındaki sera gazı salınımının %160 oranında arttığı görülmektedir. Atıklardan kaynaklanan sera gazı salınımları incelendiğinde ise 2022 yılındaki verilerin 2016 yılına göre yaklaşık 6 kat düştüğü gözlenmektedir. Bu azalmanda özellikle son birkaç yıldır üniversitemizde de etkin bir şekilde yürütülmekte olan sıfır atık sürecinin etkisinin olduğu görülmektedir. Öğrenci transferi ve personel görevlendirmeleri nedeniyle sera gazı salınım miktarları incelendiğinde öğrenci sayısında artış olmasına rağmen salınımın 2022 yılında azaldığı görülmektedir. Bu azalmadaki en büyük etkinin Devrek kampüsü yakınlarına yapılan öğrenci yurdunun öğrencilerin araç kullanmadan okula ulaşmasından dolayı olduğu düşünülmektedir.

Tablo 5. Sera gazı emisyonları dönüşüm faktörü hesaplamaları (2022 Yılı)

| Veri | Toplam Sera Gazı |
|--------------------------------|-------------------|
| Yakıt Kömür | 234.582,03 |
| Yakıt Doğalgaz | 49.477,066 |
| Elektrik | 55.366,28 |
| Personel Araçları | 77.687,1 |
| Atıklar | 326,56 |
| Öğrenci ve Personel Servisleri | 10.489,55 |
| TOPLAM | 427.919,59 |

Tablo 6. 2016 ve 2022 yılları Devrek kampüsü karşılaştırmalı karbon miktarları

| Tür | 2016 yılı | 2022 yılı |
|---|-------------------|-------------------|
| Yakıt kömür | 285.670,26 | 234.582,03 |
| Yakıt Doğal Gaz | - | 49.477,066 |
| Elektrik | 125.350,02 | 55.366,28 |
| Personel Araçları | 30.843,46 | 77.687,1 |
| Atıklar | 1.820,0 | 326,56 |
| Öğrenci Transferi ve Personel Görevlendirmeleri | 11.210,77 | 10.489,55 |
| Resmi Araç | - | - |
| Toplam Sera Gazı | 454.894,51 | 427.919,59 |

4. Sonuç

Bu çalışma, Zonguldak Bülent Ecevit Üniversitesi Devrek Kampüsündeki karbon ayak izi hesaplamaları yapılmıştır. Sera gazı emisyonunun azaltılmasına yönelik yapılan araştırmada 2016 ve 2022 yılları verileri kullanılmıştır. Çıkan sonuçlar incelendiğinde 2016 yılı için yaklaşık 454 bin tCO₂e ve 2022 yılı için 427 bin tCO₂e karbon ayak izi değerinin hesaplandığı görülmektedir. Tablo ve şekillerdeki sayısal değerler incelendiğinde ısınma amaçlı kullanılan yakıt ve personelin işe geliş gidiş için kullandığı araçlardan kaynaklı emisyon miktarlarının fazla olduğu görülmektedir. Isınma kaynaklı yaklaşık 284 bin tCO₂e ve personelin kullandıkları araçlardan ise yaklaşık 77 bin tCO₂e olduğu görülmektedir. Bu kapsamda hem ısıtma hem aydınlatma hem de personelin ulaşımı ile ilgili çalışmalar yapılması planlanmalıdır. Zonguldak Bülent Ecevit Üniversitesi Devrek Kampüsü olarak doğaya salınan karbon miktarını azaltmak için alınması gereken önlemler aşağıdaki gibi sıralanabilir:

- Devrek Kampüsü yerleşkesinde yeşillendirme çalışmaları tüm hızıyla devam etmelidir.
- Kampüs içerisinde idari ve akademik personel odalarında eski tip floresanlar enerji tasarruflu ampullerle değiştirilmiş ve tasarruf sağlanmıştır. Aynı çalışma derslikler içinde uygulanabilir.
- Kampüs içerisinde sıfır atık kapsamında atıkların ayrı toplanması için hem personel hem de öğrencilere yönelik eğitimler artırılarak devam edilebilir.
- Kampüs yakınlarında öğrencilerin ikamet edebileceği yeni yurtlar inşa edilebilir. Böylece araç kullanımı minimum düzeye indirilebilir.
- Güneş enerjisi ve rüzgar enerjisi kullanılarak kampüs

binasının ısı ve elektrik ihtiyacını karşılamaya yönelik araştırmalar ve çalışmalar yapılabilir.

- Personel servislerinin ve kurumda kullanılan araçların elektrikli araçlardan seçilmesi sağlanabilir. Tüm bölümlerde iklim değişikliği, çevre kirliliği vb. konuları içeren dersler müfredatlara eklenerek öğrencilere küresel iklim değişikliği ve çevre sorunları ile ilgili bilinçlendirilmesi sağlanabilir.

Katkı Oranı Beyanı

Yazar(lar)ın katkı yüzdesi aşağıda verilmiştir. Tüm yazarlar makaleyi incelemiş ve onaylamıştır.

| | S.Ö. | S.K |
|-----|------|-----|
| K | 90 | 10 |
| T | 100 | |
| Y | 50 | 50 |
| VTI | 50 | 50 |
| VAY | 80 | 20 |
| KT | 80 | 20 |
| YZ | 80 | 20 |
| KI | 50 | 50 |
| GR | 100 | |
| PY | 50 | 50 |

K= kavram, T= tasarım, Y= yönetim, VTI= veri toplama ve/veya işleme, VAY= veri analizi ve/veya yorumlama, KT= kaynak tarama, YZ= Yazım, KI= kritik inceleme, GR= gönderim ve revizyon, PY= proje yönetimi, FA= fon alımı.

Çatışma Beyanı

Yazarlar bu çalışmada hiçbir çıkar ilişkisi olmadığını beyan etmektedirler.

Etik Onay Beyanı

Hayvanlar ve insanlar üzerinde herhangi bir çalışma yapılmadığından dolayı bu araştırma için etik kurul onayı alınmamıştır.

Kaynaklar

DEFRA. 2022. URL: <https://www.gov.uk/government/publications/greenhouse-gas-reporting-conversion-factors-2022> (erişim Tarihi: 16 Şubat 2023).
Erdoğan S. 2020. Enerji çevre ve sera gazları. Çankırı Karatekin Üniv İktisadi İdari Bilim Fak Derg 10(1): 277-303.
Gökçek B, Bozdağ A, Demirbağ H, 2019. Niğde Ömer Halisdemir Üniversitesi örneğinde karbon ayak izinin belirlenmesi. Niğde Ömer Halisdemir Üniv Müh Bilim Derg 8(2): 721-730.
Kılıç MY, Dönmez T, Adalı S. 2021. Karayolu ulaşımında yakıt tüketimine bağlı karbon ayak izi değişimi: Çanakkale örneği.

Gümüşhane Üniv Fen Bilim Derg, 11(3): 943-955.
Kırbaş İ, Kocakulak T. 2022) Burdur İli Karbon Ayak İzinin Belirlenmesi. Dokuz Eylül Üniversitesi Müh Fakültesi Fen Müh Derg, 24(70): 317-327.
Kumaş K, Akyüz A. Ö, Zaman M, Güngör A. 2019. Sürdürülebilir bir çevre için karbon ayak izi tespiti: MAKÜ Bucak sağlık yüksekokulu örneği. El-Cezeri, 6(1): 108-117.
Kurnuç Seyhan A, Çerçi M. 2022. IPCC Tier 1 ve DEFRA metotları ile karbon ayak izinin belirlenmesi: Erzincan Binalı Yıldırım Üniversitesi'nin yakıt ve elektrik tüketimi örneği. J Natural Applied Sci, 26(3).
Yañez P, Sinha A, Vásquez M. 2019. Carbon footprint estimation in a university campus: evaluation and insights. Sustainability, 12(1): 181.
Mendoza-Flores R, Quintero-Ramírez R, Ortiz I. 2019. The carbon footprint of a public university campus in Mexico City. Carbon Manage, 10(5): 501-511.



LED BASED LOW-COST PHOTO-ACOUSTIC SETUP BY USING STETHOSCOPE

Emine Ela DURMUŞ¹, Ensar KARABULUT¹, İbrahim AKKAYA^{2*}, Yavuz ÖZTÜRK²

¹Buca İnci-Özer Tırnaklı Science High School, 35678, Izmir, Türkiye


²Ege University, Department of Electrical and Electronics Engineering, 35100, Izmir, Türkiye


Abstract: In this study, design and characterization of a low-cost photo-acoustic setup is presented. Photo-acoustic effect is a very intriguing photo-thermo-acoustic effect having applications in a wide range from biomedical science to material characterization. The basic components of a photo-acoustic setup are a sound detector with or without an acoustic cell, a modulated light source preferably with enough power, and an absorbing object. One of the challenging problems is to couple the produced photo-acoustic waves into the detector and this problem was solved by using a commercial sound sensor module connected to a stethoscope. As a modulated light source simply a high power flashlight driven with an amplifier and MOSFET circuit was used. Both detection and light modulation were designed and operated to be via sound card input/output (I/O) of a computer and/or cell phone. Light power and frequency response of the system were presented and 523 Hz was determined as a resonance frequency of the system.


Keywords: Photo-acoustic, Low-cost, Stethoscope, Sound detection


*Corresponding author: Ege University, Department of Electrical and Electronics Engineering, 35100, Izmir, Türkiye

E mail: ibrahim-akkaya@hotmail.com (İ. AKKAYA)

Emine Ela DURMUŞ  <https://orcid.org/0000-0001-9910-0578>

Ensar KARABULUT  <https://orcid.org/0000-0001-7374-907X>

İbrahim AKKAYA  <https://orcid.org/0000-0003-0605-7115>

Yavuz ÖZTÜRK  <https://orcid.org/0000-0002-9650-6350>

Received: June 21, 2023

Accepted: August 22, 2023

Published: October 15, 2023

Cite as: Durmuş EE, Karabulut E, Akkaya İ, Öztürk Y. 2023. LED based low-cost photo-acoustic setup by using stethoscope. BSJ Eng Sci, 6(4): 369-374.

1. Introduction

Photoacoustic (PA) effect was discovered by Alexander Graham Bell in 1880, while he was experimenting with sound transport with light (Bell, 1880). At the same time period, similar PA experiments were done with liquids and gasses by the famous scientists John Tyndall and Wilhelm Röntgen as well. (Tyndall, 1880; Röntgen, 1881). Following that, from 1880 up to date, PA has been studied intensely in gas, liquid, and solid materials research. Furthermore, PA found applications in many different fields such as chemical energy estimation in chemistry (Malkin and Canaani, 1994), light intensity measurement in optics (Perelta et al., 1988; Aldama-Reyna et al., 2018), PA imaging in biomedical and medicine (Lucero and Chan, 2021), plant investigations in agriculture (Hernández-Aguilar C et al., 2008; Velasco et al., 2011; Singhal et al., 2022), bread characterization in food science (Hernández-Aguilar et al., 2021), painting investigations in art (Tserevelakis et al., 2017) and so on. The origin of the PA effect is the thermal effects due to the absorption of modulated continuous or pulsed light. These thermal effects can be in the form of thermal expansion or contraction and thermal diffusion (Rosencwaig and Gersho, 1976; Rousset et al., 1983). Both these outcomes produce pressure changes on the material and so acoustic waves. Many different systems have been developed to measure these acoustic waves. These systems in general have a light source to create

thermal effects, a sound detection device, and a PA measurement cell where the light energy transforms to heat and/or pressure waves. A PA cell has been generally designed and used for gas or liquid measurements, where the sample and sound detection device are separated by channels or placed in different configurations. However, in specific types of configurations for material research, the sample of interest is in contact with the sound detection unit which can be a piezoelectric sensor, or a microphone (Somer et al., 2013). In contact systems, acoustic waves need to be transferred into the sensor. Therefore, transferring the acoustic waves efficiently into the electrical or optical microphone is crucial. The majority of the studies about PA were conducted to optimize this transfer process (Sim et al., 2017). In many cases, determining the resonance frequency is very crucial to increase the signal to noise ratio (SNR) level (Sim et al., 2017).

The sound sensor structures used in previous studies are microphones based on capacitive, piezoelectric or optical. Many of these studies use custom acoustic cells and expensive sensor arrays. Several studies focused on low-cost light sources to reduce cost in PA experiments (Zhong et al., 2018). The paper, which inspired our study as well, using an easy access stethoscope showed the possibility of sound transfer via PA for educational purposes (Nikitichev et al., 2016).

In this study, an audible photoacoustic experimental



setup built with relatively low-cost and easy to find commercially available parts is presented. The system has an amplifier and modulation circuit to modulate an LED light source and a computer audio interface used to collect data from a sound sensor coupled to a stethoscope. All-important circuit characteristics are presented, a basic black vinyl tape is used as a sample and the resonance frequency of the system determined.

2. Materials and Methods

Optically generated acoustic waves due to the conversion of absorbed electromagnetic radiation energy to heat and pressure change is called photo-acoustic (PA) (Ma et al., 2020). There are two mechanisms formulated for PA as thermal diffusion and thermos-elastic bending (Rosencwaig and Gersho, 1976; Rousset et al., 1983; Mansanares et al., 1991; Somer et al., 2013). In thermo-elastic bending, thermal shape deformation is mainly caused by thermal expansion and/or contraction due to the temperature variation in the matter as shown in Figure 1. In thermal diffusion, the light absorbed in each cycle of the modulated light transforms to heat and propagates into the surrounding gas and produces temperature gradient along the direction of the surface normal.

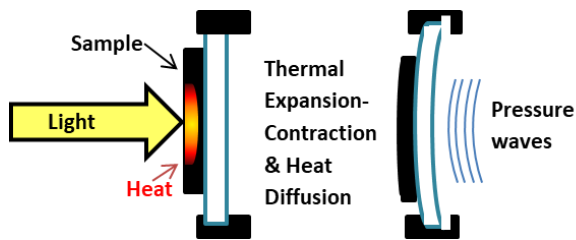


Figure 1. Mechanism of photoacoustic wave formation.

As mentioned earlier, the absorbed light energy is the source of the PA effect. This energy depends on the duration and absorbed power of the light (Rosencwaig and Gersho, 1976; Rousset et al., 1983). Therefore, PA signal amplitude is simply expected to be inversely proportional to the modulation frequency and proportional to the light power if a modulated continuous wave light is used as a source and it can be expressed as given in Equation 1 (Somer et al., 2013).

$$V_{pa}(f) = k_1(f) \frac{P}{f} + k_2(f) \frac{P}{f^{3/2}} + C \quad (1)$$

In here, P is the absorbed optical power, f is the modulation frequency of light, and $k_1(f)$ and $k_2(f)$ functions which depend on all the thermal, optical, and elastic properties of the absorbing material, ambient conditions, and the modulation frequency dependence of the electronic and mechanical system elements (Rosencwaig and Gersho, 1976; Rousset et al., 1983; Somer et al., 2013; Sim et al., 2017). In the PA detection, by measuring the $k_1(f)$ and $k_2(f)$ it is possible to

determine which mechanism is dominant between the thermal diffusion and thermos-elastic bending, respectively. C is a frequency invariant, constant value of a photoacoustic signal when there is no light excitation. For detailed information the theoretical studies can be read in the ref. Somer et al., (2013). In Equation (1), the term P/f is proportional to the energy of the incident light beam on the sample during each period of square wave modulated light. Therefore, if k is taken as a constant, it is expected to observe PA signal intensity decrease with ascending frequency.

2.1 Experimental Setup

The schematic of the designed system is given in Figure 2. The system consists of an amplifier circuit, white LED flashlight, spherical lens, stethoscope coupled by a sound sensor, computer, and a cell phone. First, to be able to obtain modulated light, an amplifier circuit was built by making some modifications based on the study of Nikitichev et al. (2013). An earphone jack was used to provide constant amplitude and variable sinusoidal frequency signals from a cell phone audio output to the amplifier circuit. Then, the amplifier circuit was directly connected to the voltage input of the light source. The projected light beams from the LED focused on to the stethoscope via the lens of the flashlight and an external lens with focal length +50 mm. A simple photodiode circuit was used to monitor the output of the light source. The photodiode was placed just in front of the light source not to prevent light from the flashlight to the stethoscope and stray light measured. The stethoscope was connected with its tube (length of 105 mm) to the sound sensor (KY-038, Joy-it, Germany). The microphone of the sound sensor was placed in the open end of the tube. The sound sensor was then connected to a computer via the microphone input port. An oscilloscope software (Soundcard Oscilloscope, Zeitnitz, Germany) was used to filter and measure the signals from the microphone unit.

The schematic of the amplifier and photodiode circuit is shown in Figure 3. The cell phone was connected to the amplifier circuit via an audio jack (3.5 mm stereo audio plug terminal block). The following high pass RC circuit ($R=75 \text{ k}\Omega$ and $C=100 \text{ nF}$), whose cutoff frequency was $\sim 150 \text{ Hz}$, used to suppress a possible DC bias of the input signal and also to filter out the network noise 50 Hz and its 2nd and 3rd harmonics due to the possible laboratory environment. If the 50 Hz network noise would be smaller, the high pass filter cutoff frequency may decrease $\sim 15 \text{ Hz}$. V_{ipp} and V_{opp} are peak-to-peak voltages of V_i and V_o , input and output amplifier voltages, respectively. The amplifier circuit designed to have gain ($G=V_{opp}/V_{ipp}$) of ~ 5 at higher frequencies than the cutoff. Also this circuit was designed to add a DC bias voltage around 3.9 V to the output of the amplifier. This DC Bias voltage can be adjusted to drive MOSFET on when there is no input voltage.

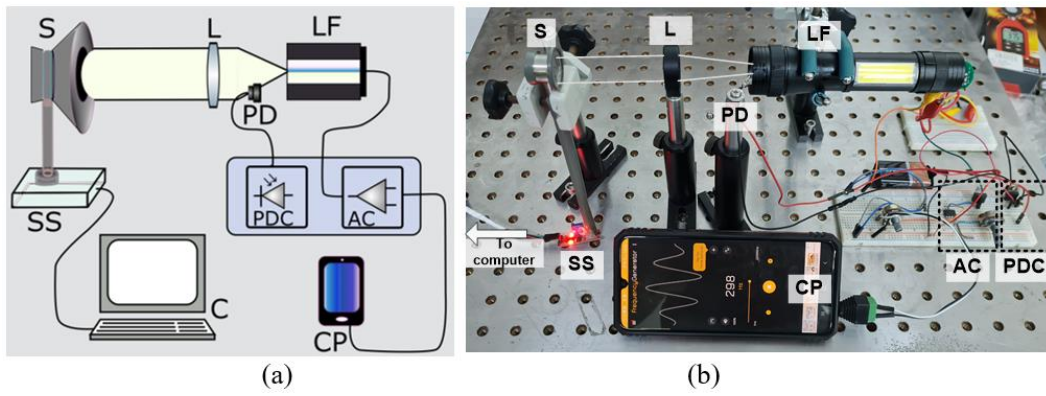


Figure 2. The experimental system design. (a) Schematic and, (b) actual view of the proposed system. AC: Amplifier circuit; C: Computer; CP: Cell phone. L: Lens; LF: LED flashlight; PD: Photodiode; PDC: Photodiode circuit; S: Stethoscope; SS: sound sensor.

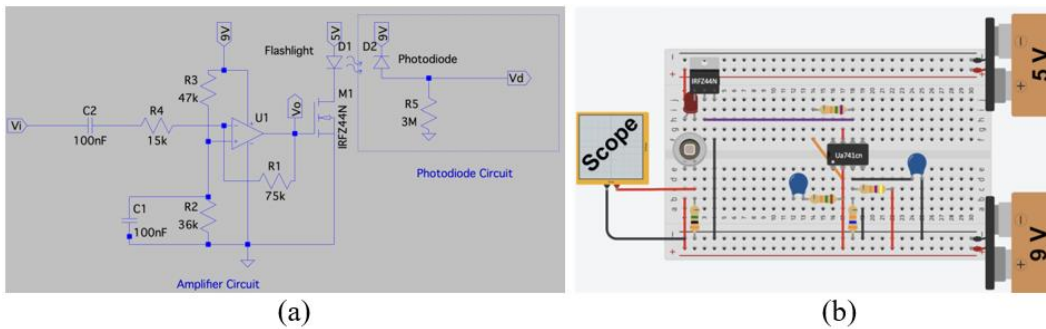


Figure 3. The proposed electrical circuit design of the amplifier and the photodiode. (a) analog circuit design and (b) the experimental design view on the breadboard.

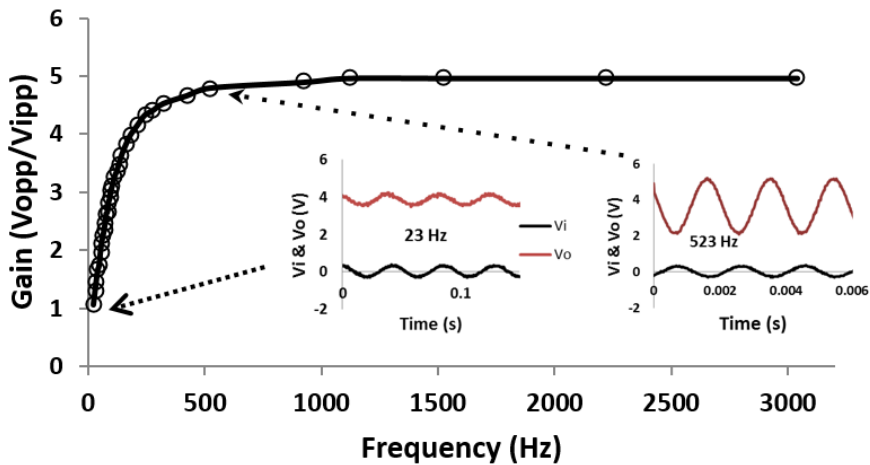


Figure 4. Gain changes against the frequency. V_{ipp} : amplifier input peak to peak voltage, V_{opp} : amplifier output peak to peak voltage.

The output of the amplifier circuit was connected to the gate pin of the MOSFET (Irfz44n, Transys Electronics, UK) to modulate the LED voltage connected to another 5 V source. V_i , V_o , and V_d voltages, monitored with the oscilloscope (GDS-2062, GW Instek, Taiwan), are all shown in Figure 3.

Although, the voltage output of the computer to the standard earphone (headphone) is expected to be $\sim 0.77 V_{RMS}$ ($2.2 V_{pp}$), the voltage range of the cell phone we used measured as $\sim 0.6 V_{pp}$. We first measured the input and output of the amplifier circuit. The average DC was 3.83

$\pm 0.1 V$ and a frequency dependent AC voltage (V_o) was observed. The ratio of input and output peak to peak voltages (V_{opp}/V_{ipp}) plotted with respect to frequency in Figure 4. The record of the oscilloscope voltages of V_i and V_o at the frequency of 23 Hz and 523 Hz is given in insets. A 3.83 V DC bias voltage was sufficient to activate the MOSFET. It is possible to adjust the on and off states duration of the MOSFET according to the transistor type and 36 and 46 k Ω resistors in the given circuit.

As an important parameter, the light output of the LED flashlight which indirectly determines the energy

absorbed by the material during excitation was measured by a photodiode shown in Figure 2. Since the flashlight was a white LED, it was arduous to measure and determine its intensity. We instead measured the light output with a lux-meter to give an idea about the light intensity. The focused non-modulated (continuous) light after the lens was first measured as 5660 Lux with an inexpensive lux-meter (UT-383, Uni-T, China). The photodiode circuit peak-to-peak voltage (V_{dpp}) was ~ 1.8 V during the constant, non-modulated light measurement. This value can give an idea about light intensity illuminating on the sample which was assumed to be proportional to the V_d voltage during the measurement of PA signal. The photodiode voltage was monitored with the oscilloscope and results of V_{dpp} presented in Figure 5, also voltage variations V_o and V_d at 523 Hz were presented in insets. The duty cycle of measured V_d was between $\sim 42\%$ and 44% in all measured frequency ranges. As can be seen from Figure 5, the gain G and DC bias values affect output of MOSFET and light modulation as well. Beyond around 150 Hz, the output of the light source was a square wave.

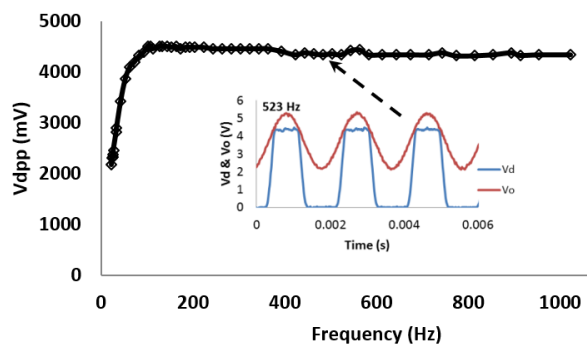


Figure 5. Photodiode circuit voltage V_{dpp} against frequency graph.

The system was built by easy to find commercial materials and components. The total cost of the system was around \$50 which is a relatively lower cost compared to other systems (Somer et al., 2013; Nikitichev et al., 2016, Zhong et al., 2018).

3. Results and Discussion

After building the experimental setup, a polyvinyl chloride (PVC) black tape was placed onto the stethoscope. During the measurements, photodiode voltage was monitored with the oscilloscope. The input voltage was set around $0.6 V_{pp}$. The created PA waves due to modulated light intensity variation on the stethoscope - sample surface was transferred to the used tube and then microphone. The electrical signal transferred into the computer microphone input was monitored and measured by soundcard oscilloscope software. A digital bandpass filter whose bandwidth was 2 Hz was applied by using the Soundcard Oscilloscope software. The filter type and order was Butterworth and 10, respectively. The mean PA signal voltage (V_{pa}) deviation was ± 0.1 mV

at a frequency range of 23 Hz to 1023 Hz. The measured V_{pa} values are shown in Figure 6. As it is seen from Eq. 1, V_{pa} is proportional to absorbed energy and light power, also inversely proportional to frequency. Additionally, V_{dpp} is proportional to light power. Therefore, V_{pa}/V_{dpp} ratio is related to V_{pa}/P . When we take the $k_1(f)$ and $k_2(f)$ values constant in Eq. 3, the ratio is inverse. However, when we acquire the resonance conditions, V_{pa}/V_{dpp} value will be higher (Rosencwaig and Gersho, 1976; Rousset et al., 1983). In Figure 6, the discrete line shows the theoretical curve which is proportional to $1/f$ and this curve overlaps with our experimental results besides the resonance interval. The PA signal can be modeled in two cases. One of them is thermal diffusion which is proportional to $1/f$, and the other one is thermoelastic bending is related to $1/f^{1.5}$ (Rosencwaig and Gersho, 1976; Rousset et al., 1983; Somer et al., 2013; Sim et al., 2017). When the PA signal is proportional to $1/f$, it means thermal diffusion mechanism is dominant (Mansanares et al.; 1998; Somer et al., 2013). The experimentally recorded signals acquired through thermally thick PVC tape. The similar results were acquired with the study in Ref Mansanares et al. (1998). In addition, the V_{pa} values from ~ 740 Hz and beyond are similar with no input light voltage value which is 0.03 ± 0.02 mV and we can call it dark voltage. Therefore, the dark voltage value was seen in the graph. One of the important findings was that the system was in resonance at 523 Hz. During measurements harmonics of the resonance frequency, with smaller amplitudes, were observed, but they did not be presented for the sake of simplicity. To make any measurements at resonance frequency 523 Hz, a higher signal to noise ratio (SNR) will be acquired than the other frequencies (Sim et al., 2017).

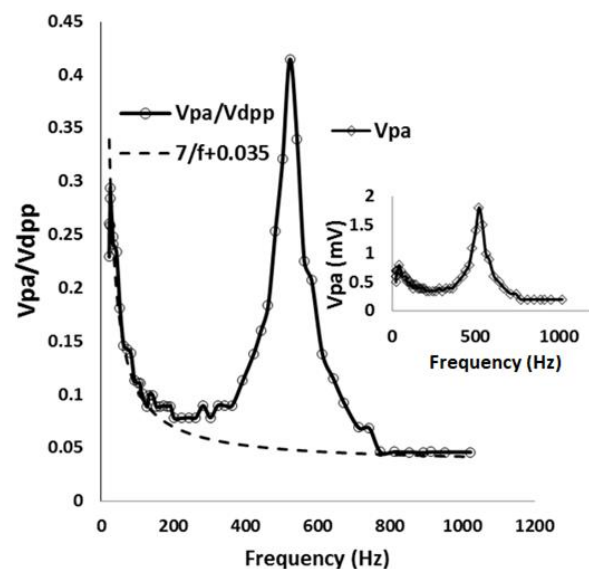


Figure 6. PA over detected light signal against frequency graph representation. Dotted line: theoretical, solid line: experimental.

After determination of the resonance frequency, $V_{dc}=5$ V voltage, given in Figure 3, changed to V_{dpp} values between 0.25 to 7.5 V via a DC power supply. V_{dpp} minimum voltage value was close to zero during all the measurements. Due to the fact that the V_{dpp} value is proportional to light power P, it shows the light power implicitly. Therefore, light power and V_{pa} are correlated with each other. Figure 7 shows this linear correlation between the light power (V_{dpp}) and V_{pa} . The outcomes are in-line with other studies in the literature where PA effect used as optical powermeter (Perelta et al., 1988; Inan et al., 2019; Ayoub et al., 2021).

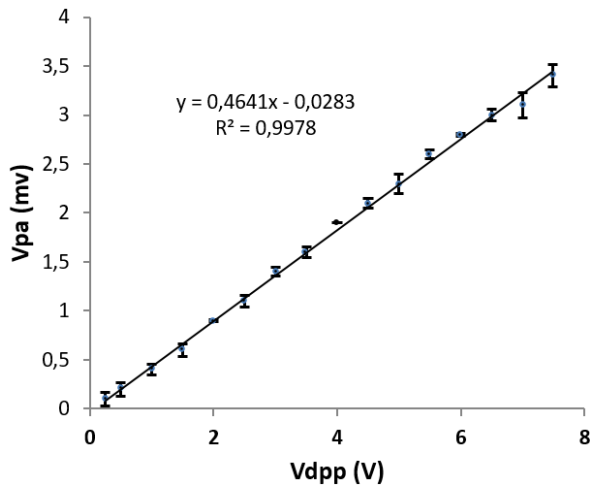


Figure 7. The correlation between the light source power and photoacoustic signal voltage.

In this research, the resonance frequency of the system was determined; the inverse relation between PA signal and modulation frequency and linear relation with the light power was shown as given in Equation 1.

4. Conclusion

In this study, a simple and low cost experimental setup was built from off the shelf components. Then, the photoacoustic (PA) effect and important parameters of this effect were given. Starting from the designed circuit, all the steps from electrical signals to optical signals within modulated in time, to acoustic waves, and then to the electrical signals again, and finally monitoring in the computer are shown. It is demonstrated that the measured PA signal by using a computer sound card as an oscilloscope is inversely proportional to light frequency and linearly proportional to light power. Furthermore, one of the important parameters for the measurements, the resonance frequency of the system was found at 523 Hz. The proposed study is considered to contribute to the photoacoustic field in research laboratory experiments and for preparing demonstrations. In addition, the proposed work is a multidisciplinary study which gathers optics, acoustics, mechanics, and electrical subjects, therefore; we believe that many undergraduate and graduate students and also researchers will favor their studies.

Author Contributions

The percentage of the author(s) contributions is presented below. All authors reviewed and approved the final version of the manuscript.

| | E.E.D. | E.K. | İ.A. | Y.Ö. |
|-----|--------|------|------|------|
| C | 20 | 20 | 30 | 30 |
| D | 30 | 30 | 20 | 20 |
| S | 15 | 15 | 25 | 45 |
| DCP | 30 | 30 | 20 | 20 |
| DAI | 30 | 30 | 20 | 20 |
| L | 30 | 30 | 20 | 20 |
| W | 25 | 25 | 30 | 20 |
| CR | 25 | 25 | 30 | 20 |
| SR | 10 | 10 | 70 | 10 |
| PM | 25 | 25 | 30 | 20 |

C=Concept, D= design, S= supervision, DCP= data collection and/or processing, DAI= data analysis and/or interpretation, L= literature search, W= writing, CR= critical review, SR= submission and revision, PM= project management, FA= funding acquisition.

Conflict of Interest

The authors declared that there is no conflict of interest.

Ethical Consideration

Ethics committee approval was not required for this study because of there was no study on animals or humans.

References

- Aldama-Reyna CW, Aldama-Guardia JD, Agreda-Delgado JF. 2018. Infrared laser pulse energy detector based on photoacoustic effect. *Momento-Revista De Fisica*, 56: 87-103.
- Ayoub HS, El-Sherif AF, Maize SM, Elbasha YH. 2021. Design and implementation of photoacoustic based beam dump-average optical power meter for fast and ultrafast lasers. *Opt Lasers Eng*, 140: 106548.
- Bell AG. 1880. On the production and reproduction of sound by light. *American J Sci*, 118: 305-324.
- Hernández-Aguilar C, Mezzalama M, Lozano N, Cruz-Orea A, Martínez E, Ivanov R, Domínguez-Pacheco A. 2008. Optical absorption coefficient of laser irradiated wheat seeds determined by photoacoustic spectroscopy. *The European Physical J Special Top*, 153(1): 519-522.
- Hernandez-Aguilar C, Dominguez-Pacheco A, Valderrama-Bravo C, Cruz-Orea A, Ortiz E M, Ivanov, R, Ordóñez-Miranda J. 2021. Photoacoustic characterization of wheat bread mixed with *Moringa oleifera*. *Curr Res Food Sci*, 4: 521-531.
- Inan I, Öztürk Y, Özdemir İE. 2019. Optical power measurement by using piezo microphone. In: *Innovations in Intelligent Systems and Applications Conference (ASYU)*, Oct. 31 – Nov. 02, 2019, Izmir, Türkiye, pp: 1-4.
- Lucero MY, Chan J. 2021. Photoacoustic imaging of elevated glutathione in models of lung cancer for companion diagnostic applications. *Nature Chem*, 13(12): 1248-1256.
- Ma Y, Qiao S, Patimisco P, Sampaolo A, Wang Y, Tittel FK, Spagnolo V. 2020. In-plane quartz-enhanced photoacoustic spectroscopy. *Appl Physics Lett*, 116(6): 061101.
- Malkin S, Canaani O. 1994. The use and characteristics of the photoacoustic method in the study of photosynthesis. *Ann Rev Plant Physiol Plant Molec Biol*, 45(1): 493-526.

- Mansanares AM, Vargas H. 1991. Photoacoustic characterization of a two-layer system. *J Appl Physics*, 70: 7046.
- Nikitichev DI, Xia W, Hill E, Mosse CA, Perkins T, Konyn K, Ourselin S, Desjardins AE, Vercauteren T. 2016. Music-of-light stethoscope: a demonstration of the photoacoustic effect. *Phys Educ*, 51: 045015.
- Perelta SB, Al-Khafaji HH, Williams AW. 1988. Photoacoustic optical power meter using piezoelectric detection. *J Physics E: Sci Instrum*, 21(2): 195.
- Röntgen WC. 1881. On tones produced by the intermittent irradiation of a gas. *Philos Mag Lett* 5, 11(68): 308-311.
- Rosencwaig A, Gersho A. 1976. Theory of the photoacoustic effect with solids. *J Appl Physics*, 47(1): 64-69.
- Rousset G, Lepoutre F, Bertrand L. 1983. Influence of thermoelastic bending on photoacoustic experiments related to measurements of thermal diffusivity of metals. *J Appl Physics*, 54(5): 2383-2391.
- Sim JY, Ahn CG, Huh C, Chung KH, Jeong EJ, Kim BK. 2017. Synergetic resonance matching of a microphone and a photoacoustic cell. *Sensors*, 17(4): 804.
- Singhal SK, Singh KP, Joshi SK, Rai AK. 2002. Diagnosis and study of fungal diseases of wheat by photoacoustic spectroscopy. *Curr Sci*, 82(5): 172-176.
- Somer A, Camilotti F, Costa G F, Bonardi C, Novatski A, Andrade AVC, Kozlowski Jr VA, Cruz GK. 2013. The thermoelastic bending and thermal diffusion processes influence on photoacoustic signal generation using open photoacoustic cell technique. *J Appl Physics*, 114: 063503.
- Tserevelakis GJ, Vrouvaki I, Siozos P, Melessanaki K, Hatzigiannakis K, Fotakis C, Zacharakis G. 2017. Photoacoustic imaging reveals hidden underdrawings in paintings. *Sci Rep*, 7(1): 1-11.
- Tyndall J. 1880. Action of an Intermittent Beam of Radiant Heat upon Gaseous Matter. *Proc Royal Soc London*, 31: 307-317.
- Velasco DS, Baesso ML, Medina AN, Bicanic DD, Koehorst R, van der Hooft JJJ, Bento AC. 2011. Thermal diffusivity of periderm from tomatoes of different maturity stages as determined by the concept of the frequency-domain open photoacoustic cell. *J Appl Physics*, 109(3): 034703.
- Zhong H, Duan T, Lan H, Zhou M, Gao F. 2018. Review of low-cost photoacoustic sensing and imaging based on laser diode and light-emitting diode. *Sensors*, 18(7): 2264.



EFFECTS OF HIGH LEVEL OF LEAD (II) OXIDE (PbO) USAGE ON ACCUMULATOR AND RESPONSE SURFACE METHOD

Emrah PIÇAKÇI¹, Zehra Gülten YALÇIN^{1*}


¹Karatekin University, Faculty of Engineering, Department of Chemical Engineering, 18200, Çankırı, Türkiye


Abstract: This study involved the preparation of lead oxide paste for use in the production of lead-acid batteries. The paste was applied to the positive plates, and its performance effects were tested on the battery. Morphological and surface area analyses were conducted using SEM and BET, respectively, after the performance tests. Two mixtures of lead oxide ratios, 25%Pb-75%PbO (sample A) and 30% Pb-70% PbO (sample B), were used. The dough was applied to positive grids and passed through the curing process. SEM images revealed that tribasic sulfate (3BS) structures had a higher charge acceptance rate than tetrabasic sulfate (4BS) structures. BET analyses showed that the surface area of the samples with A ratio was higher than that of B. Electrical tests were conducted in the laboratory, and the A sample was found to be 12% more effective in the first charging efficiency than the B sample. Sample A was also found to be 67% more efficient in charge acceptance tests and 6.5% more efficient in cycle tests. The study also showed that increasing the %Pb ratio in the product decreases the initial charge efficiency, charge acceptance, and cycle life. Finally, the response surface method was used to examine the 2D picture of the relationship between lead percentage and yield, and it was found that the highest yield was obtained at 26% lead yield, with the yield being inversely proportional to the increase in lead percentage, likely due to the effect of particle size and surface area.

Keywords: Lead (II) oxide, Lead acid battery, Positive plate, Performance tests, Surface response system

*Corresponding author: Karatekin University, Faculty of Engineering, Department of Chemical Engineering, 18200, Çankırı, Türkiye

E mail: zaltin@karatekin.edu.tr (Z. G. YALÇIN)

Emrah PIÇAKÇI  <https://orcid.org/0000-0002-7552-439X>

Zehra Gülten YALÇIN  <https://orcid.org/0000-0001-5460-289X>

Received: June 21, 2023

Accepted: August 23, 2023

Published: October 15, 2023

Cite as: Piçakçı E, Yalçın ZG. 2023. Effects of high level of lead (II) oxide (PbO) usage on accumulator and response surface method. BSJ Eng Sci, 6(4): 375-386.

1. Introduction

A battery is a device that transforms chemical energy directly into electrical energy through an electrochemical oxidation-reduction reaction, which can be reversed in rechargeable systems. This reaction involves the transfer of electrons between materials through an electrical circuit. Unlike non-electrochemical redox reactions, where only heat is affected, batteries offer high energy conversion. There are several types of batteries classified according to the metal types used, such as lead-acid, nickel-cadmium, nickel-iron, nickel-metal hydride, lithium-ion, and silver-zinc batteries. Lead-acid batteries are the most commonly used due to their durability, low cost, well-understood electrochemistry, and high recyclability. These batteries can be classified as dry or wet. The advantages and disadvantages of the lead acid battery are as follows; Gutiérrez et al. (2018); Bode (1979); Bode (1977); Eydemir (2019); (Piçakçı et al. 2021).

1.1. Advantages

- It is low cost.
- It is easy to recycle.
- It can be produced easily in high quantities.
- Recharge efficiency is high (>70%)
- Various sizes and capacity production are easy to

design.

- It is easily available in the market.

1.2. Disadvantages

- Low cycle compared to other accumulators (Approximately 500 deep discharge-charge cycles).
- Low energy density (30-40 Wh/kg)
- Sulfation problem occurs when there is no long-term use.
- Flooded batteries

Starter batteries, also known as SLI (defined by the words starting, lighting, and ignition) batteries, are the most commonly used battery types. Automobiles, trucks, tractors etc. used in the fields Garche (1990); Pavlov (2011).

1.3. Dry batteries (VRLA)

The technological infrastructure of dry batteries differs from that of wet batteries, as dry batteries are classified into two categories: AGM (Absorbent Glass Mat) and gel batteries. Unlike wet batteries, dry batteries do not contain liquid electrolytes. As a result, they eliminate the risk of electrolyte leakage and overflow, which is often a concern with flooded batteries. Additionally, dry batteries produce significantly less gas than their wet counterparts, which leads to a longer shelf life and enhanced safety (Mitchell et al., 2009; Lu et al., 2022).

The scientific literature contains numerous studies



investigating the effects of various additives on the properties of positive and negative electrodes in lead acid batteries, with the goal of enhancing battery performance. In these studies, morphological analyses using SEM and BET were conducted to examine the impact of these additives on the positive plate dough, revealing notable structural changes (Wang et al., 1995; Lach et al., 2019; Jia et al., 2020).

The initial investigation of lead acid batteries by Mayer and Rand highlighted the crucial role of increasing the electrochemical reactivity of the active mass, which is one of many factors that can significantly impact battery performance. As researchers have noted, the production of lead oxide through mixing, hardening, and forming processes is a critical part of battery design and performance. The battery industry currently employs two primary methods for lead oxide production: the ball mill and Barton-pot processes. While both methods have their own unique advantages, it remains difficult to determine which yields the best lead oxide. Nevertheless, studies have emphasized that both the ball mill and Barton-pot products are effective in the production of automotive batteries. This study explores the current procedures for lead oxide production, the desirable properties of lead oxide, and the effect of this substance on battery performance (Mayer and Rand, 1996).

In a lead acid battery discharge lead sulfate is produced and it is also known that large $PbSO_4$ crystals dissolve more slowly, thus causing the battery to fail. Little is known about the use of chemically prepared $PbSO_4$ as the active ingredient in lead acid batteries.

Zhang et al. In their study, it is seen that they are working on the preparation of $PbSO_4$ by chemically precipitating aqueous lead acetate with sodium sulfate and its use as a positive active material. In this study, it has been shown that $PbSO_4$ alone is not sufficient for this, at different mixing ratios with Pb_3O_4 at 5, 10, 20 and 30%, at a current density of 100 mA g⁻¹, 78.2, 92.9, 88.0 and 91.5 It seems that the performance of mAh g⁻¹ has been reached. In addition, there is information that it remains at a capacity of 150 with 10% Pb_3O_4 , and 93% at 100% battery charge (Zhang et al., 2016).

Zhang et al. In their study, the effects of expanded graphite, carbon fiber, needle odor and polyacene as positive electrode additives on the PbO_2 electrode behavior of lead/acid batteries were investigated. It has been found that all additives can significantly increase the utilization coefficient of the positive active material during the first phase of the charge and discharge cycle (Zhang et al., 2017).

According to Liu et al. In their study, they investigated the effect and mechanism of iron-doped lead oxide on lead acid battery. Iron doped lead oxide has been found to significantly reduce battery capacity and cycle life, as well as promote the release of hydrogen and oxygen, resulting in poor performance of the iron "redox-diffusion" process. They seem to have concluded that $PbSO_4$ formation causes poor performances (Liu et al.,

2011).

Bao et al. In their study, the mechanism of SiO_2+PbO_2 powder as a positive electrode additive for lead-carbon batteries was investigated in detail. Silica and its compounds were tested for their electrochemical stability and strong electrolyte storage capacity in sulfuric acid solution. Since SiO_2+PbO_2 has a high specific surface area and porous structure, it is seen that it gives good electrochemical performance at the anode. After these powders were added to the lead-carbon battery, this additive was found to increase ionic diffusion, creating extraordinary ion transfer channels within the positive active material (Bao et al., 2021).

According to Arun et al. In their study, it is seen that using standard production processes, lead acid batteries are formed on negative and positive plates containing two different carbon additives. They investigated the effects of morphological, porosity, BET surface area and battery performance in the dough plastered on the plates prepared with this additive. In the study conducted with carbon additives, it is seen that the effect on the discharge performance is positive. In addition, it was emphasized that the high surface area carbon additive increased the water loss and brought some disadvantages when adding it to the negative electrode (Arun et al., 2020).

Yin et al. conducted a study on lead-carbon anodes and proposed a novel approach using a carbon/lead (C/Pb) composite with electroless coating. The composite was found to reduce the hydrogen formation rate of the anode, protect its porous structure, and enhance the connection between the carbon and lead components. Additionally, the C/Pb composite was found to suppress hydrogen formation and incorporate carbon additives. The researchers highlighted the importance of reinforcing the connection between the components and the sponge lead material in their investigation (Yin et al. 2019).

Wang et al. In their study, they prepared new lead oxides with different particle sizes by the pyrolysis of lead citrate in a rotary kiln and investigated the mechanism of how the particle size affects the phase transition path of the new lead oxides during the wetting process. PbO with larger particle size (D50 diameter = 22.4 μm) converts to $3PbO \cdot PbSO_4$, $3PbO \cdot PbSO_4$ is then partially converted to $PbO \cdot PbSO_4$ while $PbO \cdot PbSO_4$ is gradually converted to $PbSO_4$. Smaller particle size PbO (D50 diameter = 8.3 μm) is directly converted to $PbSO_4$, and $3PbO \cdot PbSO_4$ has been reported to be partially converted to $PbO \cdot PbSO_4$. Since PbO_2 is the oxidation product of $PbSO_4$ in the subsequent formation process, the phase compositions after soaking determined the PbO_2 content in the positive plates. The particle size of leaded oxides determines the initial capacity of the test cells by affecting the wetting process, and it is stated that a linear correlation is obtained between the initial capacity in the positive plates and the PbO_2 content (Wang et al., 2020).

Chen et al. (2013) emphasized that the microstructure

and surface morphology of lead dioxide (PbO_2), as the positive active substance of the lead-acid battery, have a strong effect on the overall performance of the lead-acid battery. In this study, it is seen that a series of PbO_2 thin films are produced on the pure Pb surface via Pb electrochemical oxidation. Its morphological effect and electrochemical properties were investigated. At the end of the study, it was found that the PbO_2 layer formed had a high surface area, relatively small size, and especially higher discharge capacity and better cycling performance than other PbO_2 layers. It is seen that micro/nano structured PbO_2 materials improve their electrochemical performance (Chen et al., 2013; Yang et al., 2013).

Karimi et al. (2006) conducted a study aimed at enhancing the performance of lead-acid cells by improving their cycle life. In their research, they examined the use of sodium sulfate as an effective, low-cost additive for the negative paste in lead-acid batteries. The inclusion of sodium sulfate led to improvements in battery capacity, cold-start performance, and cycle life. The team carried out several practical production experiments using paste series with 0-4% of the new additive added to the negative active substances. Results showed that pastes containing sodium sulfate had significantly higher capacity, better cold-start performance, and longer cycle life than those without the additive.

According to Karimi et al. (2006) investigated the effect of sodium sulfate on the performance of sealed lead acid cells by using sodium sulfate at the positive electrode. It has found that the 4BS crystal size can be reduced in cured positive plates, thus providing a larger surface area that helps the user have better performance at high temperatures.

Kwiecien et al. (2018) in their study, they emphasized that sulphation affects the active surface area in the aging mechanisms of lead acid batteries. For this reason, it describes the accumulation of sulfate crystals on the surface of the electrodes in the reaction where corrosion resistance is also increased and spills occur. The low conductivity of the crystals results in local immobility with portions of inaccessible capacity as a result. The sulfate crystals are the product of the discharge reaction at both electrodes and are dissolved during the recharging process. It has been emphasized that the negative electrode is more exposed to sulfation due to its smaller surface area compared to the positive electrode. The response surface method is the experimental design method proposed by Kwiecien et al. (2018) in 1951. It is used to perform experiments and regressions on representative points available. It also determines the relationship between factors and outcomes in general terms (Dayton and Edwards, 2000). In the response surface method, it generates a regression that matches the equation of the process to be analyzed and estimates the value corresponding to each factor level by plotting the contour map. Response values of experimental conditions are determined separately for each factor.

Finally, a variable surface model is established through experiments to evaluate the factors affecting the results and their interactions.

Compared with traditional optimization methods, more accurate experimental results are obtained (Tong et al., 2015). In addition, it is necessary to apply various test methods in order to verify the created models. ANOVA analysis and the quality of fit of the results with the model equations were expressed using the coefficient of convergence (R^2) (Zhang et al., 2017; Zhang et al., 2022). Researchers use the (R^2) value to measure the accuracy of a model. The R^2 adj value of the model is the modified version of the R^2 coefficient. Adding factors that are known to have no effect on the model reduces the R^2 adj value (Draper and Pukelsheim, 1996; Jensen, 2017). The response surface method can generally be divided into two stages. The first stage can be called the response surface design stage and the second stage can be called the response surface optimization stage. If there are many factors to be examined in the response surface design stage, screening experiments are performed to determine the importance of each factor and finally the factor with the greatest impact is selected for further investigation. Screening experiments include partial factorial design experiments. The main goal of the first phase is to examine the relationship between the current experimental conditions and the response surface. When test conditions are far from optimal, a first-order approximation model should be applied to the optimal location of the response surface (Sagbas, 2022; Elkelay et al., 2022; Kocakulak et al., 2023). The response surface method develops an appropriate experimental design that integrates all the independent variables and uses the data input from the experiment to find a set of equations that can eventually give the theoretical value of an output. Outputs are obtained by well-designed regression experiments and results from the mathematical model (Shang et al., 2021; Xie et al., 2022; Zhang et al., 2022).

In this study, considering the values specified in the Turkish Ball mill production standard (TS EN 13086 2008) as PbO content (mass fraction) 65-82%, Free Pb content (mass fraction) 18-35%, in this study, PbO (Lead monoxide) was produced in two different metallic lead ratios and its effects on the battery were investigated. In the literature, these ratios are not clearly stated, and it has been observed that the optimum values have changed by considering the raw material and energy losses in production. In the experiments, 25-30% free lead, which is within the standards specified in TS EN 13086 2008, was used.

25% to 30% lead oxide paste was prepared and plastered on the positive plate. Performance experimental studies of the dough on the positive plate were carried out. After the plastering process on the plate, the curing process was performed and SEM and BET analyzes were examined. Capacity, starting, cycle and charge acceptance tests were carried out in the electrical test laboratory, taking into account the TS EN 50342-1 standard. In

addition, by using the response surface method, it was determined that the high efficiency was obtained with 26% lead in the relationship between the lead percentage and the yield, and the yield was inversely proportional with the increase in the lead percentage. It is thought that this situation is due to the effect of particle size and therefore the effect of changing surface area on yield.

2. Materials and Methods

In this study, lead monoxide was melted and formed into balls using pure lead with a purity of 99.996%. The balls were then processed in a ball mill to produce two different ratios of lead oxide: 25% Pb-75% PbO (A) and 30% Pb-70% PbO (B). The analysis was performed using the test method specified in the TS EN 13086 standard for lead and lead alloys-lead oxide. The batteries manufactured from the lead monoxide were charged under identical conditions and were subjected to various tests, including capacity, starting, cycle, and charge acceptance tests, as specified in the (TS EN 50342-1 Standard Technical Board, 2016).

2.1. Materials Used in Material Synthesis

In this study, the effects of lead oxide produced in lead acid batteries on the battery were investigated. The performance effects of A oxide production and B mixed

oxide production on battery quality were investigated.

Plate dough was prepared from 2 different lead monoxide with ratio A and B. Plastering was done on the positive plate from the prepared dough. These plates were subjected to the curing process under the same conditions and their moisture was removed. 10 batteries (5 A, 5 B batteries) of L2 Type 60 Ah 540 A EN type were made from the plates on the assembly line. The batteries produced on the assembly line were filled with 1.10 gr/cm³ concentrated sulfuric acid (H₂SO₄). The batteries made were charged in the same charging program in the laboratory. After charging, the acid in the batteries was discharged and a new acid with a density of 1.36 gr/cm³ was added. The batteries were kept for 1 day and capacity tests, starting tests and cycle tests were performed according to the Lead acid accumulators general rules and test methods standard (Chemistry Specialization Group, 2008).

2.2. Tests Applied in Material Synthesis

2.2.1. Free lead test in the product after lead oxide production

This test was prepared with reference to the TS EN 13086 standard. 5 g of the oxide sample was weighed and ground in a mortar. After the grinded sample was weighed, it was taken into a flask (Figure 1).



Figure 1. Oxide sample preparation.

Then, 50mL of 20% acetic acid solution was added on it (Figure 2).



Figure 2. Adding solution to the prepared sample.

It was agitated on the heater every 20 seconds until the free lead in the sample precipitated out. 2-3 drops of ascorbic acid were added (Figure 3).

The sample on the blotter was washed first with distilled water and then again with acetone (Figure 4-5).

The sample was placed in an oven with blotting paper and left for 15 minutes. At the end of 15 minutes, the sample was removed from the oven and weighed on a precision balance.



Figure 3. Dissolution of the oxide sample.



Figure 4. Filtration after dissolution.



Figure 5. Washing process after filtration.

2.2.2. Weighing process after drying

The % Pb amount was calculated (Equation 1).

$$Pb\% = \frac{(A-B)}{C \times 100} \quad (1)$$

A= Weight of sediment with blotting paper

B= Blotting paper tare

C= Oxide sample weight.

2.3. Capacity Test (Ce)

During the whole experiment, the accumulator was kept in a water bath at $25 \text{ }^\circ\text{C} \pm 2 \text{ }^\circ\text{C}$. The amount of water in the water bath must be above the battery by a minimum of 15 mm and a maximum of 25 mm. Even if there are multiple batteries, the distance between them should be at least 25 mm and the batteries should be soaked in a water bath for at least 4 hours.

The accumulator must be discharged until the voltage drops to $10.50 \text{ V} \pm 0.05 \text{ V}$, keeping the current I_n at $\pm 1\%$ of its nominal value. The $t(h)$ recorded during the discharge time constitutes the capacity time of the battery. The beginning of the discharge should be rested for a period of 1 hour to 5 hours until the end of the charge.

Nominal capacity (C_n) = C20 (20 hours capacity, electrical load that can be supplied with current; Ah) shown in the form Equation 1-2.

$$I_n = \frac{C_n}{20} \quad (2)$$

From this formula, the test continues until the final voltage value of the battery is 10.5 V.

C_e = It is the maximum Ah (capacity) value that the battery gives when discharging until it drops to 10.5 V.

The calculated value should be equal to or greater than the declared capacity.

The condition must be Equation 3

$$C_e \geq C_n \quad (3)$$

2.4. Starting Test

The charged accumulator should be placed in a circulating cooling chamber at $-18 \text{ }^\circ\text{C} \pm 1 \text{ }^\circ\text{C}$ until the medium cell temperature reaches $-18 \text{ }^\circ\text{C} \pm 1 \text{ }^\circ\text{C}$. It is considered to have reached this temperature after approximately 24 hours.

The accumulator must be discharged with a starting

current (I_{cc}) current within 2 minutes after cooling. During discharge, this current should be kept constant within $\pm 0.5\%$.

I_{cc} = Starting current (CCA)

After 10 s of discharge, the voltage U_f between the terminals should be recorded and the current should be cut off. U_f value should not be less than 7.50 V.

The test should be continued after resting for $10 \text{ sec} \pm 1 \text{ sec}$.

The battery should then be re-discharged with a current of $0.6 I_{cc}$. During discharge, the current should be kept constant within $\pm 0.5\%$. Discharge should be terminated when the battery voltage reaches 6 volts. The discharge time between $0.6 I_{cc}$ and 6 V is accepted as ($t'6V$) and this time is recorded in seconds. $t6V$ is defined as the sum of the duration of the second stage ($t'6V$) and the equivalent duration of the first discharge stage (Equation 4.)

$$t6V = t'6V + \frac{10}{0.6} = t'6V + 17 \text{ sec} \quad (4)$$

Condition shown in the form Equation 4-5.

$$t6V > 90 \text{ sec} \quad (5)$$

2.5. Cycle Test

The accumulators were connected to a series test circuit and cycled. Each cycle consists of the following two steps: The 1st step battery was discharged for 2 hours with a constant current at $I = 5 \times I_n$. The criterion for breaking this test during testing is the voltage at discharge. If it drops below 10.5 V, the test is terminated. In this case, the battery is discharged with 15 Amps for 2 hours. Thus, 30 Ah hours are discharged from the battery (Equation 6-7-8).

$$I_n = \frac{C_n}{20} \quad (6)$$

$$I_n = \frac{60}{20} \quad (7)$$

$$I_n = 3A \quad (8)$$

As a second step, the accumulator is recharged with a constant voltage and a fixed-limited $5 \times I_n$ current for a maximum of 5 hours. The recharge capacity value is recorded throughout the charge and if it reaches $CR=1.08$, the charge is terminated.

Nominal capacity (C_n) = C20 (20 hours capacity, current-suppliable electric charge; Ah) (Equation 9).

$$CR = \frac{2Crch}{C_n} \quad (9)$$

$Crch$ = recharge capacity.

If the charging rate CR is lower than 1.08, the battery is

charged with constant current until the CR value in the table is reached, or it is continued until the maximum time reaches 1 hour. In this study, when the determined 60 Ah battery is calculated (Equation10-11),

$$1.08 = \frac{2Crch}{60} \quad (10)$$

$$Crch = 32.4Ah \quad (11)$$

is charged.

After completing step 1 and step 2, this loop represents a cycle. In cycle batteries, these steps are repeated until the voltage limit during discharge is reached or the number of cycles defined in Table 1 is reached. If one of these two conditions is met, the cycle test is completed.

Table 1. Cycle classes

| Requirement level | Number of cycles |
|-------------------|------------------|
| E1 | 80 |
| E2 | 150 |
| E3 | 230 |
| E4 | 360 |

2.6. Charge Acceptance Test

The accumulator must be discharged at a temperature of 25 °C ± 2 °C for 5 hours with a current I0 (Equation 12),

$$I_0 = \frac{Ce}{10} \quad (12)$$

Ce= It is the maximum Ah (capacity) value that the battery gives when discharging until it drops to 10.5 V.

Within a maximum period of 10 minutes after discharge, the accumulator should be placed in a cooling chamber and cooled until the temperature of its middle cells is 0 °C ± 1 °C. This period should be at least 15 hours.

At this temperature the accumulator is operated with a constant voltage of 14.40 V ± 0.05 V and I_{max} = 50 A for batteries with dimensions defined in EN 50342-2 and I_{max} = 100 A for batteries with dimensions defined in EN 50342-4 must be charged. According to these conditions, the battery we used in the thesis is classified as I_{max}=50 A.

After 10 minutes the charging current I_{ca} should be recorded (Equation 13) as a condition.

$$I_{ca} \geq 1I_0 \quad (13)$$

2.7. Response Surface Method (RSM)

Experimental data were evaluated using the Surface Response Method (RSM). This method was used in order to obtain maximum efficiency with a minimum of experimental work Uslu and Celik (2020). In this study, when the 2D picture (Figure 6) of the relationship between lead percentage and yield is examined, it is seen that the highest yield is obtained at 26% lead yield and

the yield is inversely proportional with the increase in lead percentage.

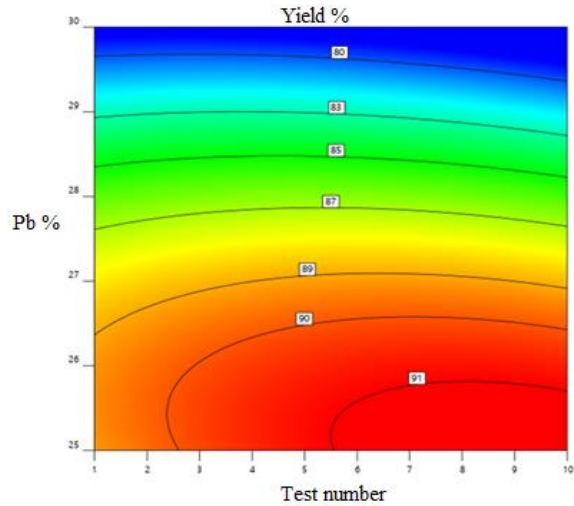


Figure 6. Lead percentage and yield graph.

When the 3D Picture (Figure 7-8) is examined, the correctness of the thought behavior is seen. It is seen that the maximum efficiency is in the region containing 26% lead. It is thought that this situation may be due to the effect of particle size and therefore the effect of changing surface area on yield.

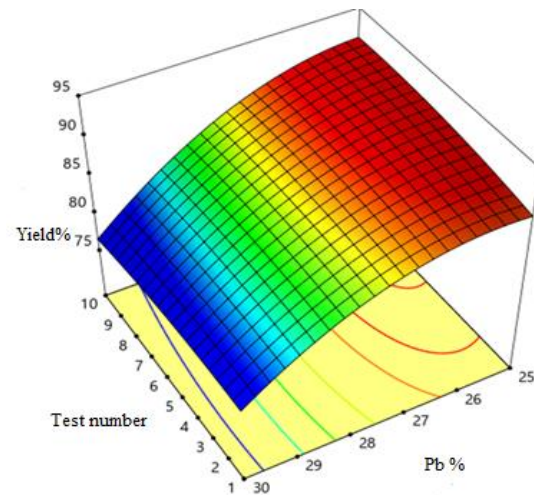


Figure 7. Evaluation of experimental data in 3D.

When the normal distribution graph of the residual points is examined, it is seen that there is not much deviation from the linear line. This means that the model is compatible. When the estimated values and the actual value table are examined, deviations from linearity are observed to be negligible. This situation can be interpreted as the result of systematic errors in experimental studies. In addition, the evaluations according to the optimization results are shown in Figure 9.

When the graphs between "Desired" and "Efficiency" are examined, some differences can be seen in the "Desired" graph. These differences are thought to be due to systematic errors (Vahedi et al., 2020).

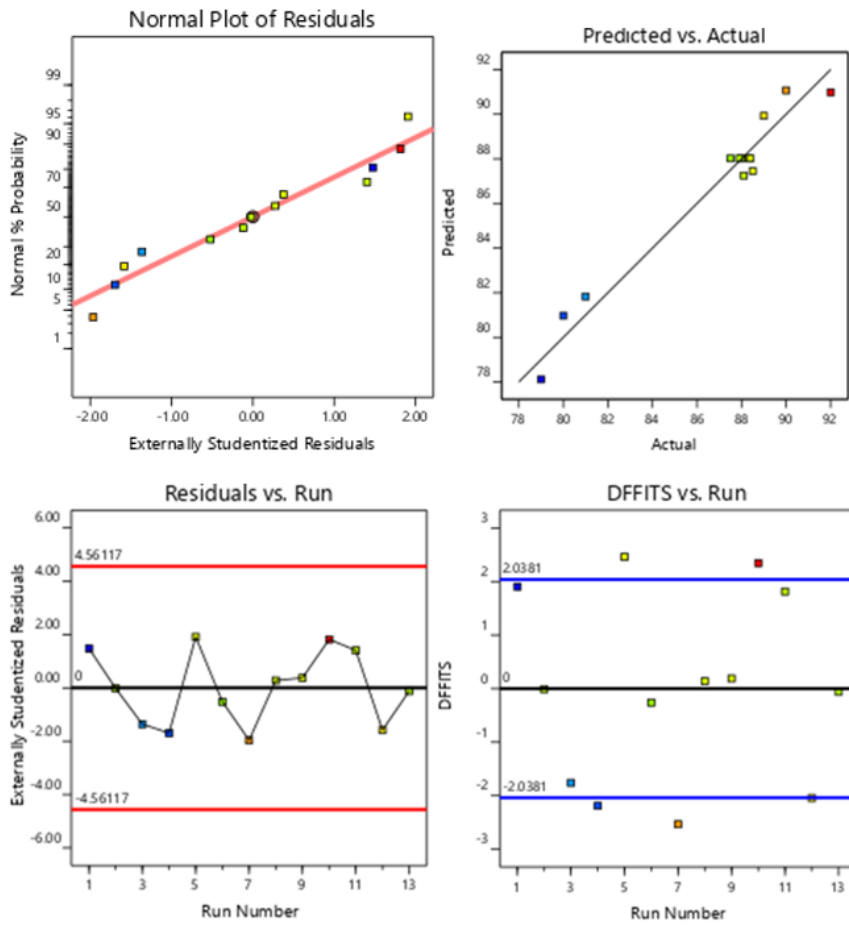


Figure 8. Compatibility of experimental data and model results.

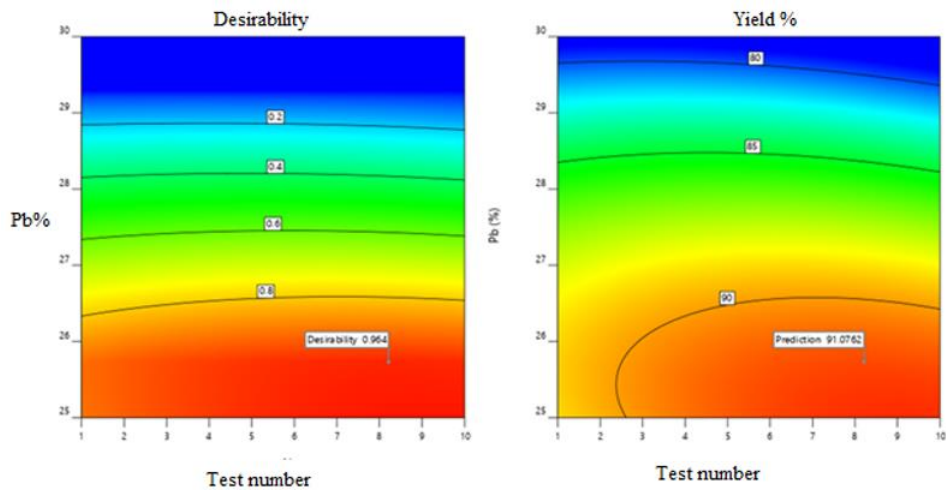


Figure 9. Evaluations according to the optimization results.

Here, a high R² value indicates that the results are successful (Table 2).

Table 2. Statistical analysis results

| | | | |
|-----------|-------|-------------------------|--------|
| Std. Dev. | 1.05 | R ² | 0.9601 |
| Mean | 86.75 | Adjusted R ² | 0.9317 |
| C.V. % | 1.22 | | |

$$\text{Yield (\%)} = -275.66575 + 2.83062 \cdot \text{No} + 28.45210 \cdot \text{Pb (\%)} - 0.088889 \cdot \text{No} * \text{Pb (\%)} - 0.033086 \cdot \text{No}^2 - 0.555200 \cdot \text{Pb (\%)}^2 \quad (14)$$

With this obtained equation, it is possible to achieve the desired efficiency when the work is repeated.

When statistical modeling is done, it is seen from the results given in the table above that the Quadratic model is more effective than other models and therefore it is recommended (Table 3).

The model equation found as given in Equation 14,

As can be seen in the analysis table for the Anova Quadratik model, when the model is examined with the 95% confidence interval and the P value of 0.05 as a reference, it is seen that the parameters that are effective

in the specified model are B and B². It is understood that other parameters are not very effective in the specified conditions (Table 4).

Table 3. Statistical evaluation

| Source | Sum of Squares | df | Mean Square | F-value | P value | |
|--------------------|----------------|----|-------------|---------|---------|-----------|
| Mean vs Total | 97823.64 | 1 | 97823.64 | | | |
| Linear vs Mean | 165.52 | 2 | 82.76 | 27.76 | <0.0001 | |
| 2FI vs Linear | 1.0000 | 1 | 1.0000 | 0.3124 | 0.5899 | |
| Quadratic vs 2FI | 21.02 | 2 | 10.51 | 9.45 | 0.0103 | Suggested |
| Cubic vs Quadratic | 0.0585 | 2 | 0.0293 | 0.0189 | 0.9813 | Aliased |
| Residual | 7.73 | 5 | 1.55 | | | |
| Total | 98018.97 | 13 | 7539.92 | | | |

Table 4. ANOVA for Quadratic model

| Source | Sum of Squares | df | Mean Square | F-value | P value | |
|----------------|----------------|----|-------------|---------|----------|-------------|
| Model | 187.55 | 5 | 37.51 | 33.72 | < 0.0001 | significant |
| A-No | 0.0400 | 1 | 0.0400 | 0.0360 | 0.8550 | |
| B-Pb (%) | 165.48 | 1 | 165.48 | 148.77 | < 0.0001 | |
| AB | 1.0000 | 1 | 1.0000 | 0.8990 | 0.3746 | |
| A ² | 0.7807 | 1 | 0.7807 | 0.7018 | 0.4298 | |
| B ² | 20.94 | 1 | 20.94 | 18.83 | 0.0034 | |
| Residual | 7.79 | 7 | 1.11 | | | |
| Lack of Fit | 7.28 | 3 | 2.43 | 19.10 | 0.0078 | significant |
| Pure Error | 0.5080 | 4 | 0.1270 | | | |
| Cor Total | 195.33 | 12 | | | | |

3. Results

3.1. Pb% Test in Product after Lead Oxide Production

The products produced in the oxide line were made according to the %Pb test instructions in the product after the lead oxide production according to the TS EN 13086 standard, and results of 25% and 30% were obtained from the results from 2 different production lots. According to this result, batteries were made from these oxides by following the batch.

3.2. Evaluation of Capacity Test Results

The capacity test was carried out to calculate the initial charging efficiency and the effective capacity of the charged batteries. Capacity test was performed on the batteries twice. When the first charge efficiency of the batteries was evaluated according to the results of the 1st capacity test, it was determined that as the amount of free lead of the produced lead oxides decreased, the first charge efficiency was between 88-92%, while the samples with high free lead were between 79-81% (Figure 10).

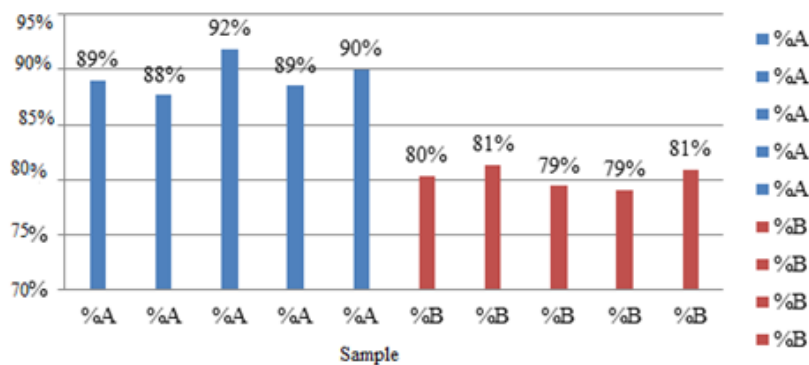


Figure 10. Initial charge efficiency graph (25%Pb-75%PbO mix (sample A), 30% Pb-70% PbO (B sample)).

It is believed that the changes in plate morphology during the curing process are the primary reason for this phenomenon, as they affect the initial charge efficiency and charge acceptance of the batteries. During the curing process, the crystals in the dough bond to the plate surface and to each other, resulting in larger crystal structures. Prior to curing, the plate's moisture level was measured at 9%, which decreased to 0.65% after curing. The water particles on the plate surface evaporated during curing, resulting in the formation of stronger structures, including 3BS, 4BS, and PbO structures.

The 3BS structures have a fine particle structure, creating a large surface area, which is an important factor affecting the battery's starting power and charge acceptance. On the other hand, the 4BS structures are coarser and contribute to the battery's cycle life. Due to the high free lead content of the plates undergoing curing, the 4BS ratio was observed to be higher (as shown in Figure 11). The SEM analysis visualized these structures by reducing the size by 10.000 μm .

In this case, it is thought that the plates in the form of 4BS on the right are structurally larger than the plates in the form of 3BS, which increases the internal resistance in the batteries during the charging process. Batteries with high internal resistance can be seen from the maximum temperature value during charging. Since the charge acceptance rate of 3BS structures is higher than 4BS structures, it has been observed that the current given in the 4BS structured batteries increases the reaction temperature without affecting the conversion in the reaction. While the charging temperature of 3BS batteries reaches a maximum of 60 °C (Figure 12). It has found 66 °C in batteries with 4BS. It is also seen from the test results in Figure 12 and Figure 13 that the charge acceptance effect of 3BS structures is more efficient.

In the BET analyzes performed, it was seen that the BET analysis of the A-ratio plate was 1.388 m^2/g , while the B-ratio BET analysis was 0.9260 m^2/g . In this case, it was observed that the surface area of the samples with A ratio was more than B.

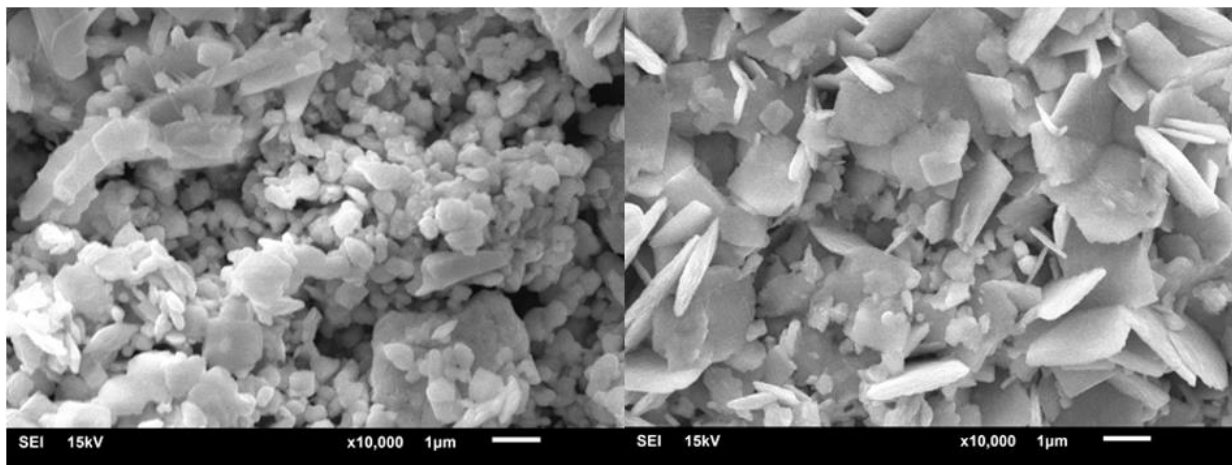


Figure 11. Plate curing manufactured from A, SEM image of end of curing plate made from B SEM image of end.

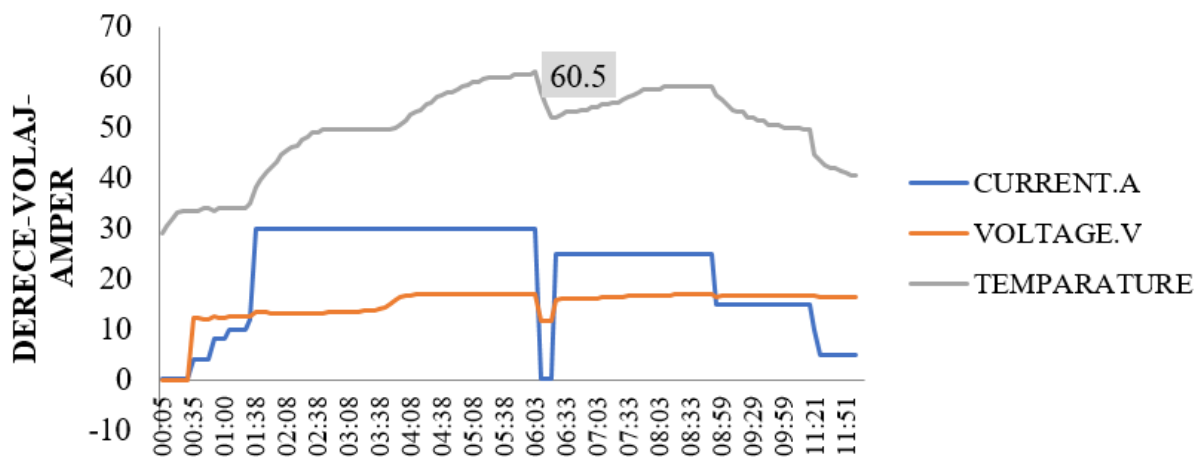


Figure 12. A Sample charge graph (25%Pb-75%PbO mix A sample mix).

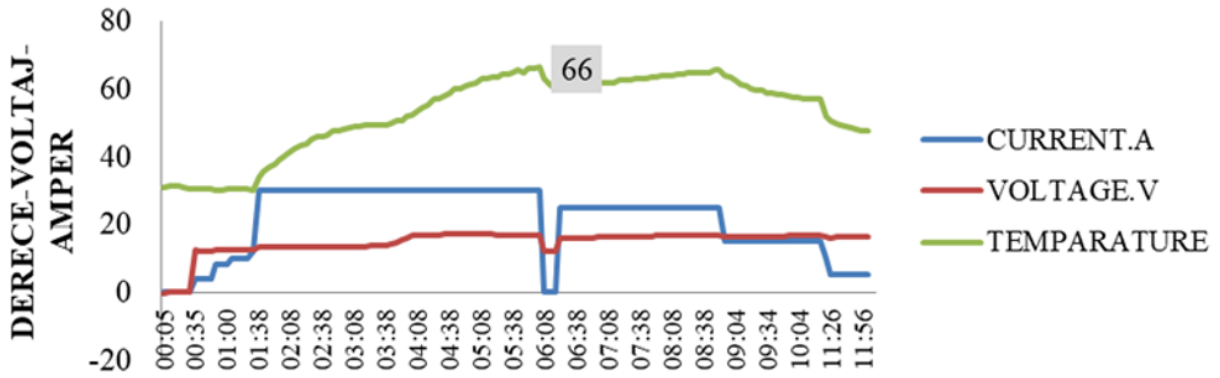


Figure 13. B Sample charge graph (30% Pb-70% PbO (B sample) mix).

3.3. Evaluation of Start Test Results

This test was carried out according to the test instruction specified in the TS EN 50342-1 standard. The purpose of this test is to determine the starting power of the batteries. When the tests were performed according to the standard, no positive or negative effect of both conditions on the starting power was observed in the results. It is seen that the effect is not much in the results obtained (Figure 14).

A test was conducted following the TS EN 50342-1 standard to determine the cycle life of the batteries by measuring the number of charge-discharge cycles. The impact of 3BS and 4BS structures on the battery performance was also investigated in this study while examining the previous capacity test. It was anticipated that 3BS structures with smaller particle size would have a shorter cycle life due to quicker spillage compared to 4BS structures with larger particles. However, if there is no spillage, the battery with better charge acceptance is expected to perform more efficiently in the cycle. The results of the test showed that batteries made from A-rated plates completed 180 cycles, while B-rated

batteries completed 165 cycles (Figure 15).

3.4. Evaluation of Charge Acceptance Test Results

This test was carried out according to the test instruction specified in the TS EN 50342-1 standard. The purpose of this test is to measure the charging capability of the batteries after deep discharge. Since the current value given to the fully discharged batteries is charged in the constant current constant voltage method, the current value will start to decrease when the voltage value reaches the limit. When the current values taken after 10 minutes were compared during this period, it was seen that sample A received 18.45 A current, while sample B received 11.04 A current. This indicated that the charge acceptance of sample A was higher (Figure 16). When the result is evaluated according to the TS EN 50342-1 standard;

$$I_0 = 60/10$$

$$I_0 = 6 \text{ Amper}$$

Conditions (Equation 15)

$$I_{ca} \geq 2I_0 \tag{15}$$

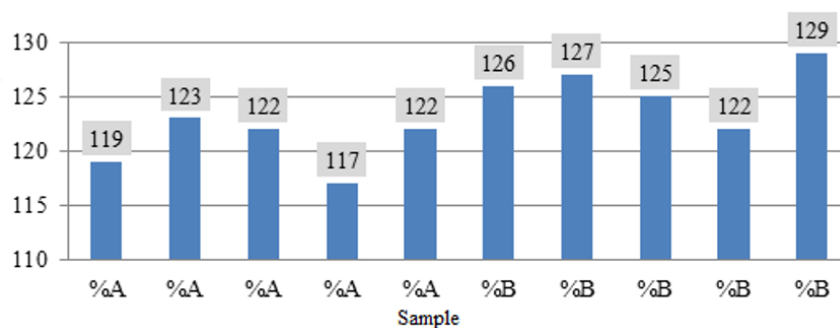


Figure 14. Starting performance test result t6 volt duration condition>90 seconds evaluation of cycle test results(25%Pb-75%PbO mix (A sample) , 30% Pb-70% PbO (B sample) mix).

4. Discussion

This study aimed to investigate the impact of lead oxide production on lead acid battery quality. Specifically, the effects of two different ratios of lead oxide production (25% Pb-75% PbO and 30% Pb-70% PbO) on battery performance were evaluated. As the oxidized lead ratio increased in the lead oxide production, it was observed that the plates contained more 3BS structures after the

curing process, with smaller crystal structures in samples with low oxidized lead content. In terms of charge acceptance, it was observed that the batteries with 3BS structures had higher charge acceptance. The first charge efficiency of samples with high lead oxide content was around 90% on average, while those with low lead oxide content remained at 80%. Additionally, samples with higher charge acceptance cycled more.

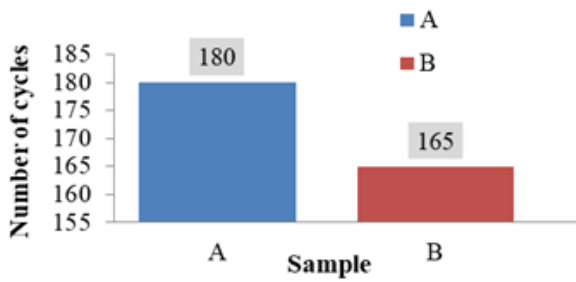


Figure 15. Cycle test result (25%Pb-75%PbO mix (A sample), 30% Pb-70% PbO (B sample) mix).

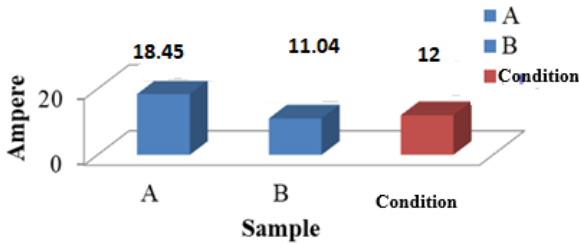


Figure 16. Charge acceptance test result (25%Pb-75%PbO mix (A sample), 30% Pb-70% PbO (B sample) mix).

Sample A was found to be 12% more effective in initial charging efficiency than sample B, 67% more efficient in charge acceptance tests, and 6.5% more efficient in cycle tests. Furthermore, it was observed that the initial charge efficiency, charge acceptance, and cycle life decreased as the %Pb ratio in the lead oxide product increased. The relationship between lead percentage and yield was analyzed using the response surface method, revealing that the highest yield was obtained at a 26% lead yield, with the yield being inversely proportional to the increase in lead percentage due to the effect of particle size and changing surface area.

Author Contributions

The percentage of the author(s) contributions is presented below. All authors reviewed and approved the final version of the manuscript.

| | E.P. | Z.G.Y. |
|-----|------|--------|
| C | 40 | 60 |
| D | 40 | 60 |
| S | 30 | 70 |
| DCP | 60 | 40 |
| DAI | 40 | 60 |
| L | 50 | 50 |
| W | 20 | 80 |
| CR | 20 | 80 |
| SR | 20 | 80 |
| PM | 40 | 60 |
| FA | 40 | 60 |

C=Concept, D= design, S= supervision, DCP= data collection and/or processing, DAI= data analysis and/or interpretation, L= literature search, W= writing, CR= critical review, SR= submission and revision, PM= project management, FA= funding acquisition.

Conflict of Interest

The authors declared that there is no conflict of interest.

Ethical Consideration

Ethics committee approval was not required for this study because of there was no study on animals or humans.

Acknowledgements

In this department, Emrah Pıçakçı, a graduate student and working at Ako Battery Factory, conducted experiments at the factory. Her advisor, Zehra Gülten Yalçın, carried out the studies of designing the experiments, reviewing the literature, applying the RSM model and writing the article by interpreting it. SEM and BET analyzes were performed at Çankırı Karatekin University. We thank the Ako Battery Factory Authorities in Çankırı for providing laboratory facilities in the study.

References

- Arun S, Kiran KUV, Mayavan S. 2020. Effects of carbon surface area and morphology on performance of stationary lead acid battery. *J Energy Stor*, 32: 101763.
- Bao J, Lin N, Dan Y, Gao W, Liu Z, Lin H. 2021. Anodic co-electrodeposition of hierarchical porous nano-SiO₂+ PbO₂ composite for enhanced performance of advanced lead-carbon batteries. *J Energy Stor*, 35: 102285.
- Bode H. 1977. *Lead-acid Batteries, Handbook of Batteries*, 3rd ed. John Wiley & Sons Inc., Hoboken, US.
- Bode H. 1979. Lead-acid batteries. *J Power Sour*, 4(3): 252-255.
- Chen T, Huang H, Ma H, Kong D. 2013. Effects of surface morphology of nanostructured PbO₂ thin films on their electrochemical properties. *Electrochimica Acta*, 88: 79-85.
- Chemistry Specialization Group. 2008. Lead and lead alloys-Lead oxides. TS EN 13086, April 4, 2008.
- Dayton TC, Edwards DB. 2000. Improving the performance of a high power, lead-acid battery with paste additives. *J Power Sour*, 85(1): 137-144.

- Draper NR, Pukelsheim F. 1996. An overview of design of experiments. *Stat Papers*, 37: 1-32.
- Elkelawy M, El Shenawy EA, Bastawissi HAE, Shams MM, Panchal H. 2022. A comprehensive review on the effects of diesel/biofuel blends with nanofluid additives on compression ignition engine by response surface methodology. *Energy Convers Manag*: X: 100177.
- Eydemir Y. 2019. Strengthened battery design in start-stop vehicles. MSc Thesis, Gazi University, Faculty of Technology, Energy Systems Engineering, Ankara, Türkiye, pp: 93.
- Garche J. 1990. On the historical development of the lead/acid battery, especially in Europe. *J Power Sour*, 31(1-4): 401-406.
- Gutiérrez AS, Eras JJC, Santos VS, Herrera HH, Hens L, Vandecasteele C. 2018. Electricity management in the production of lead-acid batteries: The industrial case of a production plant in Colombia. *J Clean Prod*, 198: 1443-1458.
- Jensen WA. 2017. Response surface methodology: process and product optimization using designed experiments. *J Quality Technol*, 49(2): 186.
- Jia X, Liu C, Neale ZG, Yang J, Cao G. 2020. Active materials for aqueous zinc ion batteries: synthesis, crystal structure, morphology, and electrochemistry. *Chemical Rev*, 120(15): 7795-7866.
- Karimi MA, Karami H, Mahdipour M. 2006. Sodium sulfate as an efficient additive of negative paste for lead-acid batteries. *J Power Sour*, 160(2): 1414-1419.
- Kocakulak T, Halis S, Ardebili SMS, Babagiray M, Haşimoğlu C, Rabeti M, Calam A. 2023. Predictive modelling and optimization of performance and emissions of an auto-ignited heavy naphtha/n-heptane fueled HCCI engine using RSM. *Fuel*, 333: 126519.
- Kwiecien M, Badeda J, Huck M, Komut K, Duman D, Sauer DU. 2018. Determination of SoH of lead-acid batteries by electrochemical impedance spectroscopy. *Appl Sci*, 8(6): 873.
- Lach J, Wróbel K, Wróbel J, Podsadni P, Czerwiński A. 2019. Applications of carbon in lead-acid batteries: a review. *J Solid State Electrochem*, 23: 693-705.
- Liu J, Yang D, Gao L, Zhu X, Li L, Yang J. 2011. Effect of iron doped lead oxide on the performance of lead acid batteries. *J Power Sour*, 196(20): 8802-8808.
- Lu Y, Zhao CZ, Yuan H, Hu JK, Huang JQ, Zhang Q. 2022. Dry electrode technology, the rising star in solid-state battery industrialization. *Matter*, 5(3): 876-898.
- Mayer MG, Rand DAJ. 1996. Lead oxide for lead/acid battery positive plates: scope for improvement?. *J Power Sour*, 59(1-2): 17-24.
- Mitchell P, Zhong L, Xi X, Zou B. 2009. Dry particle based adhesive and dry film and methods of making same. US7508651.
- Pavlov D. 2011. Lead-acid batteries: science and technology. Elsevier, New York, US, pp: 707.
- Pıçakçı E, Yalçın ZG, Dağ M, Aydoğmuş E. 2021. The Effects of Using High Rate Lead (II) Oxide(PBO) on Battery. *EasyChair Preprint* № 692. URL: https://easychair.org/publications/preprint_download/Lrkj [accessed date: February 10, 2023].
- Sagbas A. 2022. Analysis and optimization of process parameters in wire electrical discharge machining based on RSM: A case study. In *Response Surface Methodology- Research Advances and Applications*. IntechOpen, DOI: 10.5772/intechopen.102317.
- Shang L, Yan Y, Zhan Y, Ke X, Shao Y, Liu Y, Lin M. 2021. A regulatory network involving Rpo, Gac and RSM for nitrogen-fixing biofilm formation by *Pseudomonas stutzeri*. *NPJ Biofilms Microbiomes*, 7(1): 54.
- Tong P, Zhao R, Zhang R, Yi F, Shi G, Li A, Chen H. 2015. Characterization of lead (II)-containing activated carbon and its excellent performance of extending lead-acid battery cycle life for high-rate partial-state-of-charge operation. *J Power Sour*, 286: 91-102.
- Technical Board. 2016. Lead-acid starter batteries-Part 1: General requirements and methods of test. TS EN 50342-1.
- Uslu S, Celik MB. 2020. Performance and exhaust emission prediction of a SI engine fueled with I-amyl alcohol-gasoline blends: an ANN coupled RSM based optimization. *Fuel*, 265: 116922.
- Vahedi Torshizi M, Azadbakht M, Kashaninejad M. 2020. A study on the energy and exergy of Ohmic heating (OH) process of sour orange juice using an artificial neural network (ANN) and response surface methodology (RSM). *Food Sci Nutrit*, 8(8): 4432-4445.
- Wang J, Li M, Hu J, Ke Y, Yu W, Wang Z, Yang J. 2020. Effect of particle size on phase transitions of positive active materials made from novel lead oxide during soaking process and its influence on lead-acid battery capacity. *J Energy Stor*, 28: 101175.
- Wang S, Xia B, Yin G, Shi P. 1995. Effects of additives on the discharge behaviour of positive electrodes in lead/acid batteries. *J Power Sour*, 55(1): 47-52.
- Xie L, Zhou Y, Xiao S, Miao X, Murzataev A, Kong D, Wang L. 2022. Research on basalt fiber reinforced phosphogypsum-based composites based on single factor test and RSM test. *Construct Build Mater*, 316: 126084.
- Yang W, Gao Z, Ma J, Wang J, Wang B, Liu L. 2013. Effects of solvent on the morphology of nanostructured Co₃O₄ and its application for high-performance supercapacitors. *Electrochimica Acta*, 112: 378-385.
- Yin J, Lin Z, Liu D, Wang C, Lin H, Zhang W. 2019. Effect of polyvinyl alcohol/nano-carbon colloid on the electrochemical performance of negative plates of lead acid battery. *J Electroanalytical Chem*, 832: 152-157.
- Zhang FY, Zhou HY, Yuan JQ, Li QH, Diaoyu YW, Zhang LJ, Du L. 2022. Optimization of nitrosation reaction for synthesis of 4-aminoantipyrine by response surface methodology and its reaction mechanism. *Organic Process Res Devel*, 26(11): 3051-3066.
- Zhang K, Liu W, Ma B, Mezaal MA, Li G, Zhang R, Lei L. 2016. Lead sulfate used as the positive active material of lead acid batteries. *J Solid State Electrochem*, 20: 2267-2273.
- Zhang WL, Yin J, Lin ZQ, Shi J, Wang C, Liu DB, Lin HB. 2017. Lead-carbon electrode designed for renewable energy storage with superior performance in partial state of charge operation. *J Power Sour*, 342: 183-191.



CORN DISEASE DETECTION USING TRANSFER LEARNING

Cevher OZDEN^{1, 2*}

¹Akdeniz University, Faculty of Engineering, Department of Computer Science Engineering, 07058, Antalya, Türkiye


²Cukurova University, Faculty of Agriculture, Department of Agricultural Economics, 01380, Adana, Türkiye

Abstract: Detecting plant disease is a complicated yet important task to enable sustainable production in agriculture. Especially, early and on-field disease detection provides an opportunity to producers to take necessary precautions before it causes dramatic losses. Corn is one of the most important agricultural products for many countries around the world. It constitutes the main nutrient intake for large populations. This study examines and analyzes the applicability of the pretrained models in corn disease detection. A number of well-known pretrained models including Xception, ResNet50, VGG16, EfficientNetB0, MobileNet and InceptionV3 have been employed for this purpose. SMOTE is employed to solve the imbalanced data and resulting bias problem, which is a common problem in plant disease dataset. The study results indicate that SMOTE provides a good solution to the imbalanced data problem and MobileNet, VGG16 and Xception can be used as base models to develop AI applications to detect corn diseases.

Keywords: Disease detection, Classification, Transfer learning, Imbalanced data

*Corresponding author: Akdeniz University, Faculty of Engineering, Department of Computer Science Engineering, 07058, Antalya, Türkiye

E mail: efeozden@gmail.com (C. OZDEN)

Cevher OZDEN  <https://orcid.org/0000-0002-8445-4629>

Received: July 05, 2023

Accepted: August 31, 2023

Published: October 15, 2023

Cite as: Ozden C. 2023. Corn disease detection using transfer learning. BSI Eng Sci, 6(4): 387-393.

1. Introduction

Plant diseases constitute a major problem in agricultural production. Plants exposed to diseases may experience disruptions in their growth processes, decrease in product yield and loss of quality. This leads to economic losses in the agricultural sector. In particular, agriculture is an important economic activity for many countries, and agricultural products are a major source of income for both domestic consumption and exports. Plant diseases can negatively affect this potential in agricultural production.

Plant diseases can also affect product quality, which reduces the marketability of the product and lowers the commercial value. Also, some plant diseases can produce toxins in plant tissues and threaten human health when consumed. Such situations further increase the economic effects of plant diseases.

Economic losses affect not only producer farmers but also other stakeholders along the entire agricultural value chain. Plant diseases can also cause problems in the food processing and packaging industries. Processing poor quality and diseased products can affect the quality of end products and tarnish marketing image. In addition, the storage and transportation of diseased plant material can also lead to economic losses.

Plant diseases also affect trading activities. Trade in diseased plants can lead to the spread of plant diseases between countries. This poses a serious risk for both exporting and importing countries. Diseased plant material can cause new infections or epidemics in other

countries. This could accelerate the global spread of plant diseases and create barriers to agribusiness.

Corn production is a key component of the agricultural sector of many countries and plays a critical role in food production, economy and trade. Corn is a product of great importance for Türkiye in terms of agricultural production and economy. Türkiye is an important player in corn production and produces this product for both domestic consumption and export. According to statistics, Türkiye's corn production has increased continuously in recent years. Türkiye's corn production in 2020 was approximately 6.5 million tons (TUIK, 2022). This amount of production helped Türkiye to meet its own corn needs and reduced the need for imports. At the same time, Türkiye shows a significant increase in its corn export. Türkiye's corn export in 2020 was recorded as 1.2 million tons (TUIK, 2022).

However, diseases can reduce the yield in corn production and even cause complete destruction of the product. These diseases are caused by fungi, bacteria, viruses and other microorganisms called plant pathogens. In addition, environmental factors, pests, nutrient deficiencies and other stress conditions can also contribute to the emergence of plant diseases.

Artificial intelligence (AI) technologies play an important role in plant disease diagnosis. AI accelerates the detection of plant diseases and increases its accuracy thanks to its capabilities such as big data analysis, image processing and pattern recognition. These technologies help to minimize losses in agricultural production by enabling early detection of plant diseases. Diagnosis of



plant diseases is often visually based. However, it is a difficult task for people to have expert knowledge of thousands of plant species and disease symptoms. AI can automatically diagnose plant diseases using image processing and pattern recognition algorithms. For example, artificial neural networks can determine the type of disease by analyzing spot symptoms on plant

leaves. These methods make it possible to obtain fast and accurate results.

Plant disease detection has been a hot research topic among scientists. There have been a number of studies implemented using artificial intelligence methods. The recent studies are summarized in Table 1.

Table 1. Recent studies implemented using transfer learning on plant disease detection

| Researchers | Methods | Data | Performance |
|------------------------------|---|---|--|
| Paymode et al. 2021 | VGG16, ResNet50 | Plant Village | 98.40% Accuracy |
| Mukti and Biswas, 2019 | ResNet50, VGG16, VGG19, AlexNet | Salathegroup Data | 99.8% Accuracy |
| Khasawneh et al. 2022 | DenseNet-201, SqueezeNet, GoogLeNet, Inceptionv3, MobileNetv2, ResNet-101, ResNet-50, ResNet-18, Xception, ShuffleNet, DarkNet-53 | Tomato, Mendeley Data | 99.2% F1 Score |
| Bir et al., 2020 | EfficientNetB0, MobileNetv2, VGG19 | Tomato Plant Village | 98.6% Accuracy |
| Chen et al., 2020 | Dens-Incep (DenseNet + Inception) | Rice Plant locally collected | 92.22% Accuracy |
| Feng et al., 2021 | Deep CORAL, Deep Domain Confusion, CNN | Rice Plant China Rice Research Institute | 88.0% Accuracy |
| Kathiresan et al., 2021 | RiceDenseNet, MobileNet, ResNet50, ResNet101, Xception, Inceptionv3 | Rice Plant Combination of three open source datasets | 97.71% Accuracy |
| Shahoveisi et al., 2023 | ResNet50, Xception, EfficientNetB4, MobileNet | Rust Disease Detection on various plants | 93.52% Accuracy |
| Abbas et al., 2021 | Conditional Generative Adversarial Network + DenseNet121 | Tomato PlantVillage | 99.51% Accuracy |
| Hasan et al., 2019 | Inception | Tomato PlantVillage | 99.0% Accuracy |
| Vallabhajosyula et al., 2021 | Deep Ensemble Neural Network, ResNet50, ResNet101, Inceptionv3, DenseNet121, DenseNet201, MobileNetv3, NasNet | PlantVillage | 99.9% Accuracy (NasNet, DenseNet201, ResNet101) |
| Reddy and Rekka, 2021 | Deep Leaf Disease Prediction Framework (CNN+AlexNet+ GoogLeNet) | Apple PlantVillage | 97.62% |

The main problem of plant disease detection studies is that datasets contain imbalanced number of classes. In order to eliminate the bias problem that can arise from the dominant class, certain techniques such as under sampling, oversampling, data augmentation and synthetic data creation are employed during data preprocessing phase. Oversampling through duplicating examples in the minority class or under sampling through removing examples in the majority class can make the dataset balanced but both techniques do not provide any additional information, and under sampling even degrades the information further. The solution can be synthesizing new examples using the information in the minority class. The most common approach in literature is Synthetic Minority Oversampling Technique -SMOTE (Chawla et al., 2011). SMOTE is effective as it produces new synthetic examples from the minority class that are relatively close to representing the features of

the existing examples. In this study, SMOTE is preferred to eliminate imbalanced data structure and a number of popular pre-trained models are employed to test their applicability and robustness in detecting the diseases of corn products.

2. Materials and Methods

In this study, Plant Village dataset is used. Plant Village is a research unit of Penn State University that aims to alleviate poverty through offering cheap and affordable technologies to farmers. They offer a large collection of databases and resources on plant diseases (Hughes and Salathé, 2015). This platform aims to assist agronomists, farmers, researchers and other interested parties in the diagnosis, identification and management of plant diseases. The database contains thousands of plant disease images, plant damage images, symptoms of plant diseases, and descriptive information. The dataset

provides users with information to diagnose plant diseases, recognize disease symptoms, learn appropriate treatment methods and protect their agricultural production. Plant Village dataset consists of 54303 healthy and unhealthy leaf images separated into 38 categories by diseases and species. The dataset contains a total of 3.852 images of corn product which consists of 513 gray leaf spot, 1.192 common rust, 1.162 healthy and

985 northern leaf blight categories. There is imbalance among classes as three classes contains approximately close number of instances; however, the number of instance in gray leaf spot is about half of the other three classes. In order to eliminate the bias problem, Synthetic Minority Sampling Technique (SMOTE) technique has been employed. SMOTE brings balance to the dataset by augmenting the samples in minority classes (Figure 1).

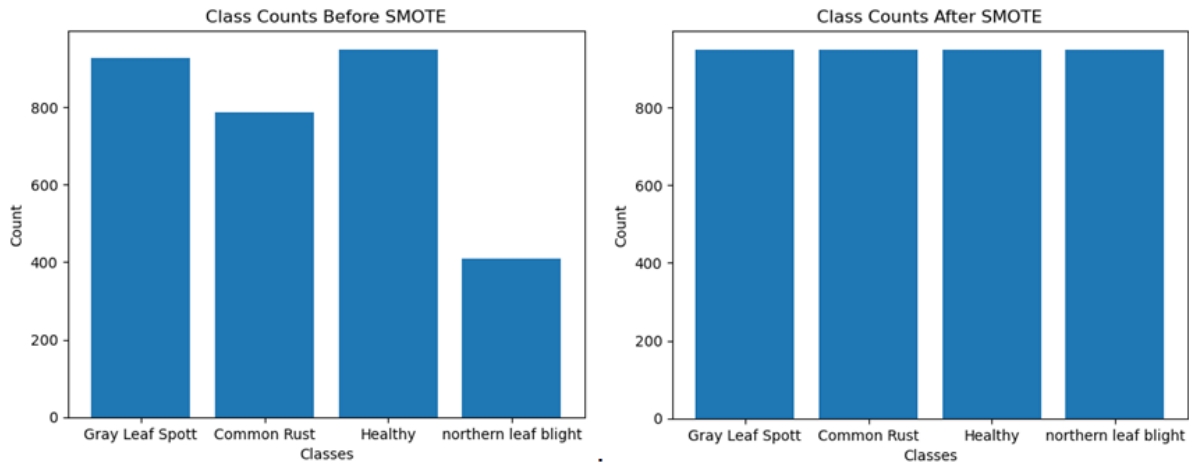


Figure 1. The distribution of classes before and after SMOTE.

SMOTE analyzes the immediate neighbors of the minority class samples and uses the relationships between these samples to generate new synthetic samples. SMOTE method generates synthetic samples through interpolating between the feature values of the base instance and its nearest neighbors given by the user. For each synthetic sample to be generated, (i) it chooses one of the k nearest neighbors randomly, (ii) computes the difference between the feature values of the base instance and the chosen neighbor, (iii) multiplies this difference by a random value between 0 and 1, and (iv) adds the scaled difference to the feature values of the base instance, generating a new synthetic instance. While SMOTE augments samples belonging to the minority class, it also adds random variations to allow for variation and variability between samples. Furthermore, edge-based image segmentation has been applied to separate leaves from their backgrounds (Figure 2).



Figure 2. Corn Leaf images before and after segmentation

Transfer learning has been preferred in the study, because it allows to employ information gained from one

dataset to another, especially the second dataset is smaller or different such as the case in this study. Leveraging the information gained from large dataset can provide a good head start and potentially better performance. Transfer learning means transferring information learned in one task to another task. It is a method used in the field of machine learning and enables a model to use the information learned by a pre-trained model in a new task. Transfer learning allows using the weights and learned features of this pre-trained model in a new task. The new task is a different dataset or a different problem but may generally contain the same type of data or similar features. That is, the pre-trained model may perform better on the new dataset with less training or less data. The use of a pre-trained model can be used as a starting point for the new task. This can reduce training time because the model does not have to relearn some layers or features.

- This study employs the most-commonly used pretrained models including Xception, EfficientNetV2B0, InceptionV3, MobileNet, VGG16 and ResNet50 (Figure 3). The top layers of the models have been truncated to make them appropriate for the input images. Also, the models have been extended using a Flatten Layer, a Dense Layer (256 neurons), a Dropout Layer (0.3) and an output Dense Layer for 4 classes. Some of the base features of these models are summarized in Table 2. In the table, Time per inference step is reported as the average of 30 batches and 10 repetitions on a computer with CPU: AMD EPYC Processor (with IBPB) (92 core), RAM: 1.7T, GPU: Tesla A100 and batch size: 32.

- Data is separated into 80% training, 10% validation and 10% test sets. All models have been set to train for 50 epochs. Early stopping criteria have been employed to stop training if the validation accuracy does not improve in three successive epochs. RMSprop is used as optimizer with a learning rate of

0.001 and categorical cross entropy is used as loss function. The layers of the pretrained models have been frozen, which means that the weights of these layers are nontrainable because the number of images in the dataset is not sufficient for meaningful update.

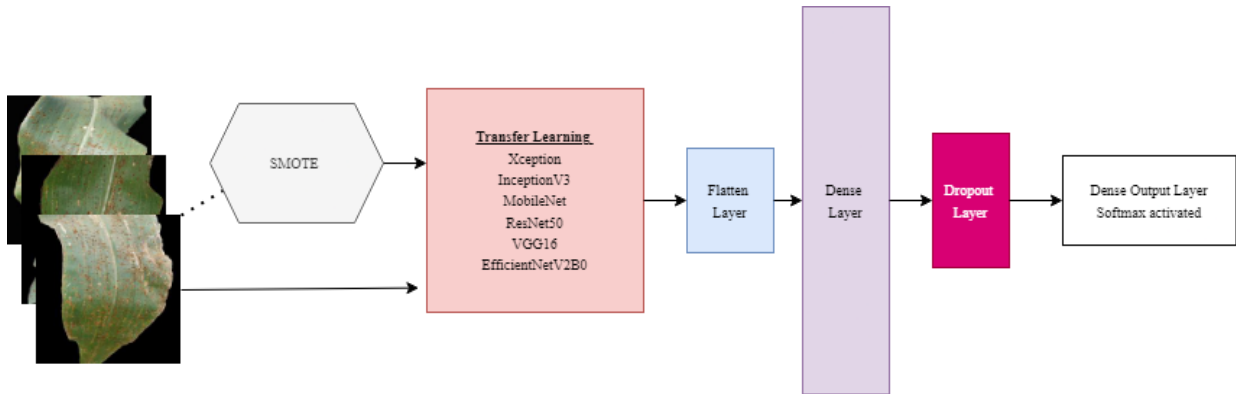


Figure 3. Flowchart of the applied algorithm

Table 2. Model specifications*

| Pretrained Networks | Size (MB) ¹ | Top-1 Accuracy ² | Top-5 Accuracy ³ | Parameters | Depth ⁴ | Time (ms) per inference step (CPU) | Time (ms) per inference step (GPU) |
|---------------------|------------------------|-----------------------------|-----------------------------|------------|--------------------|------------------------------------|------------------------------------|
| Xception | 88 | 79.00% | 94.50% | 22.9M | 81 | 109.4 | 8.1 |
| VGG16 | 528 | 71.30% | 90.10% | 138.4M | 16 | 69.5 | 4.2 |
| InceptionV3 | 92 | 77.90% | 93.70% | 23.9M | 189 | 42.2 | 6.9 |
| ResNet50 | 98 | 74.90% | 92.10% | 25.6M | 107 | 58.2 | 4.6 |
| EfficientNetV2B0 | 29 | 78.70% | 94.30% | 7.2M | 132 | 46 | 4.9 |

*Source: <https://keras.io/api/applications/>

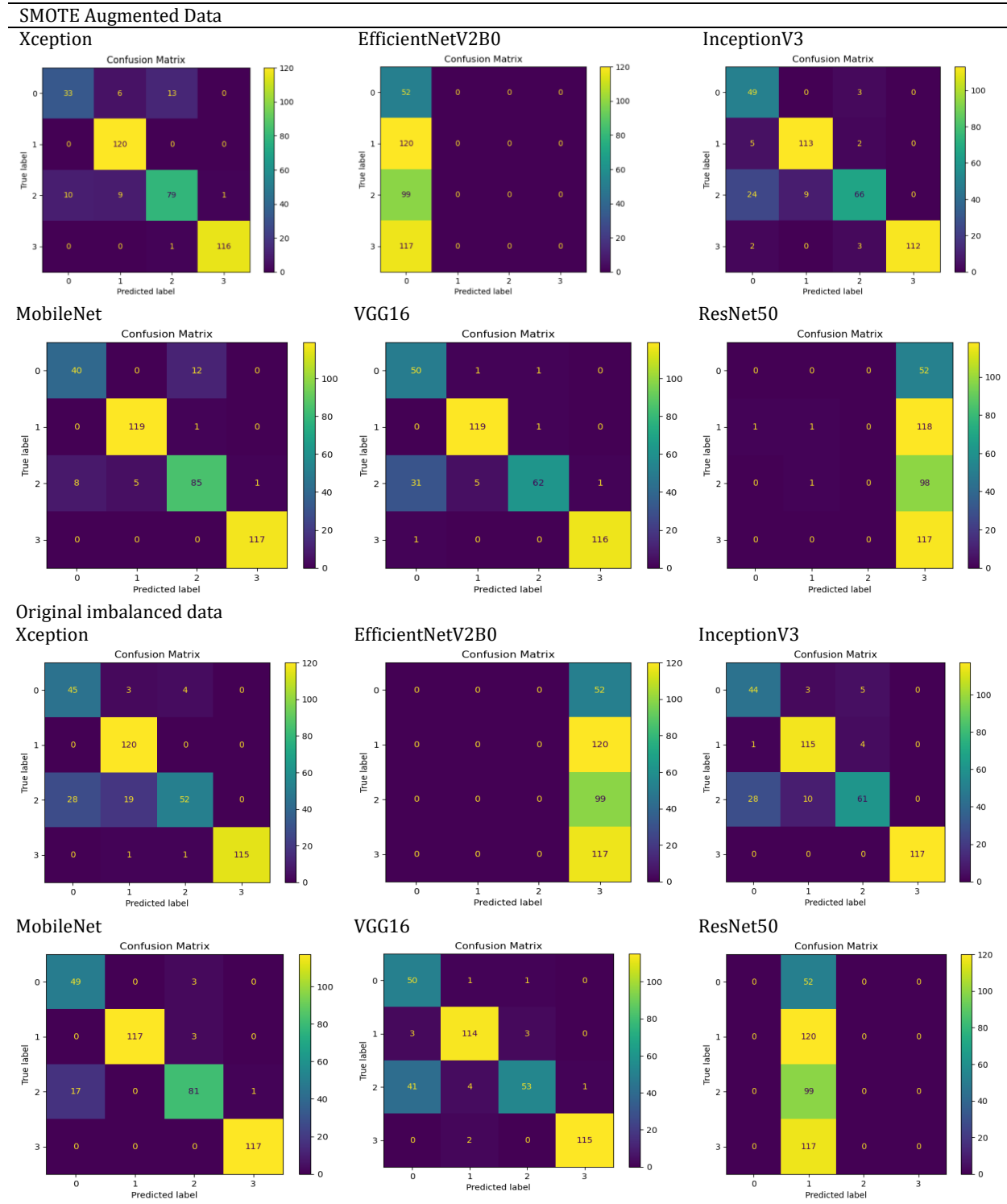
¹Download size of models, ²Top-1 accuracy considers the model's most confident prediction. This is the standard accuracy metric where only the single most probable prediction is considered, ³Top-5 accuracy measures the percentage of images for which the ground truth label is among the model's top five predicted labels, Top-1 and Top-5 accuracy refers to the model's performance on the ImageNet validation dataset, ⁴Number of layers in the model architecture.

3. Results

The prediction accuracies of the models are given as confusion matrices in Table 3. The results indicate that models have difficulty in separating health corns from gray leaf spot disease class. EfficientNetV2B0 and VGG16 ResNet50 yielded quite poor classification accuracies. On the other hand, the other models achieved reliable accuracies in classification task. The reason behind the poor classification accuracies of EfficientV2B0 and ResNet50 could be attributed to several possible reasons.

One is the domain mismatch which arises when there's a significant difference between the domain of the pre-trained data and the data for your target task. However, all the pre-trained models are reported to be trained on the same ImageNet dataset, which rules out this possibility. Another reason could be architecture suitability that happens when the pre-trained model is designed with specific architectures optimized for particular types of tasks, which is different from the target task.

Table 3. Confusion matrices of the models



Model performances on SMOTE and original imbalanced dataset are given in Table 4. With respect to performance results on Smote augmented data, MobileNet pretrained model achieved the highest accuracy with over 93% on test set. This is closely followed by Xception (90%), VGG16 (89%) and InceptionV3 (88%), while EfficientNet and ResNet50 proved to be quite poor classifier for the study task. InceptionV3 yielded the highest performance by F1 and Recall metrics, which is followed by VGG16, Xception and MobileNet. F1 and Recall metrics provides a better comparison when dealing with imbalanced classes

as Accuracy only takes into account the general accuracy, while Recall considers the incorrectly classified instances in the target class, and F1 considers incorrectly classified instances in the target and other classes. When the results on both SMOTE augmented and original imbalanced datasets are compared, model performances are increased by 5-10% on average with the use of SMOTE. The results clearly indicate that SMOTE prevents models to be biased towards the majority class, and has increased the performance on the minority class. This technique can be used to provide a practical and effective

solution to mitigate the challenges posed by class imbalance. Paymode and Malode (2022) employed Generative Adversarial Network and Neural Style Transfer along with several other data augmentation techniques like image cropping, flipping, rotation and color transformation on tomato leaf diseases. They used VGG16 as transfer learning base model and reported 98.89% validation accuracy. The downside of their study is that they separated data into training and validation subsets and tested the highest model on field images. However, the study lacks the performance metrics for on-field image testing. Considering the fact that training and validation images are captured in fixed conditions like fixed camera angle, distance and background, it would be quite difficult for such a model to perform well on real field conditions. Mukti and Biswas (2019) used the whole data in salathegroup dataset which contains over 80.000 images in 38 classes. They separated the images into training and validation subsets and used VGG16, VGG19 and AlexNet as transfer learning base models. They

employed data augmentation such as flipping, rotation, shifting. They reported that ResNet50 based model yielded highest accuracy on training images with 99.80%. The main drawback of their study is that they did not give any performance result on testing data. The high accuracy in training set could be resulted from the memorization of the data pattern. Khasawneh et al. (2022) employed transfer learning on 9 tomato leaf diseases. They did not use any data preprocessing technique. They used DarkNet-53, DenseNet-201, GoogLeNet, Inceptionv3, MobileNetv2, ResNet-18, ResNet-50, ResNet-101, ShuffleNet, SqueezeNet and Xception. They used 10-fold cross validation using training and validation subsets and reported that DenseNet-201 yielded highest F1 score with 98.5%. The main novelty of the current study is that synthetic data creation method is used with Smote method and the model performances are evaluated on test dataset, which are unseen to models during training phase.

Table 4. Performance metrics of the models

| | Model | Train Accuracy | Validation Accuracy | Test Accuracy | F1 on Test Set | Recall on Test Set |
|--------------------------|------------------|----------------|---------------------|---------------|----------------|--------------------|
| SMOTE | Xception | 0.9513 | 0.8923 | 0.8969 | 0.8047 | 0.8168 |
| | EfficientNetV2B0 | 0.2346 | 0.3923 | 0.1340 | 0.1181 | 0.2500 |
| | InceptionV3 | 0.9269 | 0.8615 | 0.8763 | 0.9116 | 0.9178 |
| | MobileNet | 0.9752 | 0.8692 | 0.9304 | 0.7803 | 0.8292 |
| | VGG16 | 0.9669 | 0.9000 | 0.8943 | 0.8524 | 0.8820 |
| | ResNet50 | 0.2490 | 0.007 | 0.3004 | 0.1147 | 0.2663 |
| Original Imbalanced Data | Xception | 0.8867 | 0.8000 | 0.85567 | 0.8226 | 0.8434 |
| | EfficientNetV2B0 | 0.2921 | 0.0000 | 0.30154 | 0.1158 | 0.2500 |
| | InceptionV3 | 0.8527 | 0.8077 | 0.8685 | 0.8383 | 0.8551 |
| | MobileNet | 0.9208 | 0.8462 | 0.938144 | 0.9211 | 0.9339 |
| | VGG16 | 0.8451 | 0.7692 | 0.85567 | 0.8244 | 0.8574 |
| | ResNet50 | 0.3189 | 0.6077 | 0.3092 | 0.1181 | 0.2500 |

5. Conclusion

The study aims to analyze the efficiency of the pretrained models in predicting and classifying corn diseases. Popular pretrained models have been used for transfer learning and their accuracies have been compared. The study results indicate that corn diseases can be can be successfully identified using several of the pretrained networks including Xception, VGG16 and InceptionV3 Smote data augmentation clearly improved the prediction results in all models. The model accuracies can be further improved through larger data collected and labeled in the same manner as the Plant Village dataset. In this way, model weights can be set to trainable and updated accordingly. No parameter fine-tuning is made and all parameters are kept the same for each models in order to provide a comparison basis. However, future studies can be implemented to see effects of different parameter fine-tunings on the performance of pretrained models. Further studies can also be carried out to test other pretrained models enabling their layers as

trainable. The main limitation of the study is that images in dataset are collected under certain fixed conditions that are remotely related to on-field conditions including many noise and varying backgrounds. Further studies are advice to be implemented with on-field experiments.

Author Contributions

The percentage of the author contributions is presented below. The author reviewed and approved the final version of the manuscript.

| | C.O. |
|-----|------|
| C | 100 |
| D | 100 |
| S | 100 |
| DCP | 100 |
| DAI | 100 |
| L | 100 |
| W | 100 |
| CR | 100 |
| SR | 100 |
| PM | 100 |
| FA | 100 |

C=Concept, D= design, S= supervision, DCP= data collection and/or processing, DAI= data analysis and/or interpretation, L= literature search, W= writing, CR= critical review, SR= submission and revision, PM= project management, FA= funding acquisition.

Conflict of Interest

The author declared that there is no conflict of interest.

Ethical Consideration

Ethics committee approval was not required for this study because of there was no study on animals or humans. The authors confirm that the ethical policies of the journal, as noted on the journal's author guidelines page, have been adhered to.

References

Abbas A, Jain S, Gour M, Vankudothu S. 2021. Tomato plant disease detection using transfer learning with C-GAN synthetic images. *Comput Electron Agri*, 187: 106279. 10.1016/j.compag.2021.106279.

Bir P, Kumar R, Singh G. 2020. Transfer learning based tomato leaf disease detection for mobile applications. *Proceedings of 2020 IEEE International Conference on Computing, Power and Communication Technologies (GUCON)*, Oct 2-4, 2020, Galgotias University, Greater Noida, UP, India, pp: 34-39.

Chawla N, Bowyer K, Hall L, Kegelmeyer W. 2002. SMOTE: Synthetic minority over-sampling technique. *J Artif Intell Res*,

16: 321-357. 10.1613/jair.953.

Chen J, Zhang D, Nanehkaran Y, Li D. 2020. Detection of rice plant diseases based on deep transfer learning. *J Sci Food Agri*, 2020: 100. 10.1002/jsfa.10365.

Hasan M, Tanawala B, Patel K. 2019. Deep learning precision farming: Tomato leaf disease detection by transfer learning. *SSRN Electronic J*, 2019: 1-5. 10.2139/ssrn.3349597.

Hughes DP, Salathé M. 2015. An open access repository of images on plant health to enable the development of mobile disease diagnostics through machine learning and crowdsourcing. URL: <https://arxiv.org/abs/1511.08060> (accessed date: March 23, 2022).

Feng L, Wu B, He Y, Zhang C. 2021. Hyperspectral imaging combined with deep transfer learning for rice disease detection. *Frontiers Plant Sci*, 12: 693521. 10.3389/fpls.2021.693521.

Kathiresan G, Anirudh M, Mathimariappan N, Ramamurthy K. 2021. Disease detection in rice leaves using transfer learning techniques. *J Physics*, 1911: 012004. 10.1088/1742-6596/1911/1/012004.

Khasawneh N, Faouri E, Fraiwan M. 2022. Automatic detection of tomato diseases using deep transfer learning. *Applied Sci*, 12: 8467. 10.3390/app12178467.

Mukti I, Biswas D. 2019. Transfer learning based plant diseases detection using ResNet50. *Proceedings of International Conference on Electrical Information and Communication Technology (EICT)*, Oct 2-4, 2020, Greater Noida, UP, India, pp: 1-6. 10.1109/EICT48899.2019.9068805.

Paymode AS, Malode VB. 2022. Transfer learning for multi-crop leaf disease image classification using convolutional neural network VGG. *Artificial Intell Agric*, 2022: 23-33. 10.1016/j.aiaa.2021.12.002.

Reddy T, Rekha K. 2021. Deep leaf disease prediction framework (dlpdf) with transfer learning for automatic leaf disease detection. 1408-1415. *Proceedings of 5th International Conference on Computing Methodologies and Communication (ICCMC 2021)*, 8 - 10 April 2021, Erode, India, pp: 1-6.

Shahoveisi F, Taheri GH, Shahabi S. 2023. Application of image processing and transfer learning for the detection of rust disease. *Sci Rep*, 13: 5133. <https://doi.org/10.1038/s41598-023-31942-9>.

TUIK. 2022. *Plant Production Statistics*. URL: <https://data.tuik.gov.tr/Bulten/Index?p=Bitkisel-Uretim-Istatistikleri-2022-45504>. (accessed data: August 2, 2023).

Vallabhajosyula S, Sistla V, Kolli V. K. K. 2021. Transfer learning-based deep ensemble neural network for plant leaf disease detection. *J Plant Diseases Protect*, 129: 1-14. 10.1007/s41348-021-00465-8.



AKUT AKCİĞER HASARI MODELİNDE HİSPİDULİNİN HEPATOPROTEKTİF ROLÜNÜN KARACİĞER BİYOMOLEKÜLER KOMPOZİSYONU DEĞİŞİMLERİ AÇISINDAN DEĞERLENDİRİLMESİ

Nihal ŞİMSEK ÖZEK^{1,2*}

¹Atatürk University, Faculty of Science, Department of Biology, 25240, Erzurum, Türkiye

²Atatürk University, East Anatolia High Technology Application and Research Center (DAYTAM), 25240, Erzurum, Türkiye

Özet: Akut solunum sıkıntısı sendromu (ARDS), ciddi hipoksemi, pulmoner ödem, pulmoner hücresel infiltrasyon ve yaygın alveoler hasar ile karakterize edilen ani solunum yetmezliğinin bir çeşit semptom kompleksidir. ARDS olan kritik hastalar, karaciğer fonksiyonunun bozulması açısından yüksek risk altındadır çünkü karaciğer, mediatörleri düzenleyen ve enflamatuar bozukluklar sırasında organ etkileşimlerini modüle eden önemli bir organdır. Bu nedenle ARDSli hastalarda karaciğeri koruyacak hepatoprotektif özellikte yeni ajanların belirlenmesine ihtiyaç vardır. Bu çalışmada, oleik asit kaynaklı akut akciğer hasarı sıçan modelinde Hispidulin'in potansiyel hepatoprotektif aktivitesi, Fourier Dönüşümlü Kızılötesi Spektroskopisi ve denetimsiz örüntü tanıma yöntemleri kullanılarak biyokimyasal kompozisyon değişiklikleri açısından belirlenmiştir. Çalışmada erkek Sprague Dawley cinsi sıçanlardan I. Kontrol, II. ARDS, III. ARDS + Hispidulin olmak üzere 3 grup oluşturulmuştur. Kontrol grubu hariç diğer iki gruba 50µL Oleik asit intravenöz olarak verilmiştir. Grup III'teki hayvanlara Oleik asit enjeksiyonlarından bir saat önce 80 mg/kg intraperitoneal Hispidulin uygulanmıştır. Gruplar arasındaki bağıntıları ve biyomoleküler değişimleri belirlemek için elde edilen spektrumlara temel bileşen analizi (TBA) ve hiyerarşik kümeleme analizi (HCA) uygulandı. PCA skor ve HCA dendrogram grafiklerine göre, ARDS grubu %100 doğruluk, özgüllük ve duyarlılık değeri ile diğer iki gruptan ayrı bir yerde konumlanmıştır. PCA analizinde elde edilen yüklem grafikleri özellikle ARDS kaynaklı karaciğer protein, lipit, kollajen ve nükleit asit içeriğinde değişimlerin olduğunu, hispidulin önuygulamasının bu değişimlerin oluşmasını engellediğini, akut akciğer hasarında hepatoprotektif potansiyeli olduğunu göstermektedir.

Anahtar kelimeler: ATR-FTIR spektroskopisi, Hispidulin, ARDS, Temel bileşen analizi, Hiyerarşik kümeleme analizi, Biyomoleküler kompozisyon


Evaluation of Hepatoprotective Role of Hispidulin in Terms of Liver Biomolecular Composition Changes in Acute Lung Injury Model

Abstract: Acute respiratory distress syndrome (ARDS) is a symptom complex of sudden respiratory failure characterized by severe hypoxemia, pulmonary edema, pulmonary cellular infiltration, and diffuse alveolar damage. Critically ill patients with ARDS are at high risk for impaired liver function because the liver is a vital organ that regulates mediators and modulates organ interactions during inflammatory disorders. Therefore, there is a need to identify new hepatoprotective agents to protect the liver in patients with ARDS. In the present study, the potential hepatoprotective activity of Hispidulin in the oleic acid-induced ARDS rat model was determined regarding biochemical composition changes using Fourier Transform Infrared Spectroscopy and unsupervised pattern recognition methods. In this study, three groups of male Sprague Dawley rats were formed as I. Control, II. ARDS, III. ARDS + Hispidulin. Except for the control group, the other two groups received 50µL Oleic acid intravenously. Group III animals were administered Hispidulin 80 mg/kg intraperitoneally one hour before Oleic acid injections. Principal component analysis (PCA) and hierarchical cluster analysis (HCA) were applied to IR spectra to determine the relationships and biomolecular changes between the groups. According to the PCA score and HCA dendrogram graphs, the ARDS group was well discriminated from the other two groups with 100% accuracy, sensitivity and specificity. The PCA loading plot showed the changes in liver protein, lipid, collagen, and nucleic acid contents, mainly due to ARDS; hispidulin preadministration prevented these changes, indicating the hepatoprotective potential of hispidulin in acute lung injury.

Keywords: ATR-FTIR spectroscopy, Hispidulin, ARDS, Principal component analysis, Hierarchical cluster analysis, Biomolecular composition

*Sorumlu yazar (Corresponding author): Atatürk University, Faculty of Science, Department of Biology, 25240, Erzurum, Türkiye

E mail: nsozek@yahoo.com (N. ŞİMSEK ÖZEK)

Nihal ŞİMSEK ÖZEK  <https://orcid.org/0000-0002-7326-5670>

Gönderi: 13 Temmuz 2023

Kabul: 04 Eylül 2023

Yayınlanma: 15 Ekim 2023

Received: July 13, 2023

Accepted: September 04, 2023

Published: October 15, 2023

Cite as: Şimsek Özek N. 2023. Evaluation of hepatoprotective role of hispidulin in terms of liver biomolecular composition changes in acute lung injury model. BSJ Eng Sci, 6(4): 394-400.



1. Giriş

Akut solunum sıkıntısı sendromu (ARDS), ciddi hipoksemi, pulmoner ödem, pulmoner hücrel infiltrasyon ve yaygın alveoler hasar ile karakterize edilen ani solunum yetmezliğinin bir çeşit semptom kompleksidir (Meyer ve ark., 2021). ARDS, toksik gazlar, çoklu travma, sepsis, grip virüsü enfeksiyonu, pankreatit ve gastrik muhtevanın aspirasyonu gibi çeşitli etmenler nedeniyle oluşabilmektedir (Anan ve ark., 2018). Bu etmenlerin yanı sıra, şiddetli Akut Solunum Sendromu-Coronavirus-2'nin (SARS-CoV-2) neden olduğu koronavirüs 2019 (COVID-19) formuna sahip hastalarda da ARDS tablosu hızla gelişmektedir (Kaya ve Kaya, 2020; Kamyshnyi ve ark., 2020). Günümüzde COVID-19'a yakalanan hastaların %96,7'sinde önde gelen ölüm nedeninin ARDS olduğu rapor edilmiştir (Aydın ve Çöl, 2020; Nardo ve ark., 2021). Küresel bakımdan ise ARDS, yoğun bakım ünitesi kabullerinin %10'unu ve mekanik ventilasyonların %23'ünü oluşturmaktadır ve yılda yaklaşık 3 milyon kişinin hayatını tehdit etmektedir (Bellani ve ark., 2016; Papazian ve ark., 2019).

ARDS, organlarda ve organ sistemlerinde önemli yapısal ve hücrel değişikliklere neden olabilir. Organlar içerisinde karaciğer hasarı, en yaygın görülen ARDS komplikasyonudur (Herrero ve ark., 2020). COVID-19 hastalarında da karaciğerin akciğerlerden sonra en çok hasar gören ikinci organ olduğu görülmektedir (Hu ve ark., 2020; Li ve Fan 2020). ARDS'li hastalarda pulmoner immünoisitler tarafından üretilen IL-1, IL-6 ve TNF- α gibi proinflamatuvar sinyal molekülleri, sistemik dolaşıma katılmak üzere akciğerleri terk ederek karaciğerde akut faz yanıtına sebep olmaktadır (Guillot ve Tacke 2019). ARDS, hipoksemi, sistemik inflamatuvar yanıt aktivasyonu ve kardiyovasküler değişimlere neden olarak karaciğer fonksiyonunu bozabilmekte (Yang ve ark., 2019) ve şiddetli ARDS vakaları, sarılık, asit, karaciğer ensefalopatisi ve hipoagülasyon ile karakterize edilen karaciğer yetmezliği ile sonuçlanabilmektedir (Cai ve ark., 2015). Karaciğer, mediatörleri düzenleyen ve enflamatuvar bozukluklar sırasında organ etkileşimlerini modüle eden önemli bir organdır. Dolayısıyla karaciğer fonksiyonu, akut solunum sıkıntısı sendromunun patogenezi ve çözümünde kritik bir tanı olarak tanınmakta ve bu hastaların prognozunu önemli ölçüde etkilemektedir (Redko ve ark., 2021).

Bitkiler ve bitkisel kaynaklı ürünler, uzun süredir hem geleneksel hem de modern klinik çalışmalarda yaygın olarak kullanılmaktadır. Hispidulin, bitkilerde bulunan güçlü antioksidan, anti-inflamatuvar, antikanser ve anti-trombotik dahil olmak üzere çok çeşitli biyolojik aktivitelere sahip doğal bir flavonoiddir (Liu ve ark., 2020). Şimdiye kadar yapılan yapılan in vivo ve in vitro çalışmalarda hispidulinin karaciğer üzerine olumlu etkisinin olduğu rapor edilmiştir (Wu ve ark., 2018; Wang ve ark., 2019; Lee ve ark., 2022). ARDS'nin patogenezi karaciğer-akciğer etkileşiminin ve özellikle hispidulinin hepatoprotektif etkisinin değerlendirilmesinde biyomoleküler içerik açısından

değişimlere yönelik herhangi bir çalışma bulunmamaktadır. ARDS kaynaklı karaciğer bozukluğunu engellemek için özellikle uzun vadeli bir COVID-19 pandemisi göz önüne alındığında hepatoprotektif aktivitenin değerlendirilmesine dayalı yeni araştırmaların yapılması gereklidir. Bu nedenle, söz konusu çalışmada sıçanlarda oleik asitle oluşturulan akut akciğer hasarı modelinde, hispidulinin koruyucu potansiyelinin doku lipit, protein ve nükleik asit kompozisyonundaki değişimler açısından belirlenmesi amaçlanmıştır. Söz konusu değişimleri belirlemek ve değişimlere dayalı gruplar arasındaki bağlantıları ortaya koymak için Fourier Dönüşüm Kızılötesi (FTIR) Spektroskopisi tekniği ile birlikte gözetimsiz örüntü tanımlama teknikleri kullanılmıştır. FTIR spektroskopisi kemometrik analizlerle birlikte hücre ve doku olmak üzere çalışılan tüm materyallerde içeriksel değişimleri kullanıcıdan bağımsız, kısa süreli, düşük maliyetli, doğru ve güvenilir bir şekilde ortaya koyan tekrarlanabilirliği yüksek bir metod olduğu için çeşitli disiplinlerde yaygın olarak kullanılan bir tekniktir (Türker-Kaya ve ark., 2020; Elibol ve ark., 2022; Yonar ve ark., 2022).

2. Materyal ve Yöntem

2.1. Deneysel Hayvanları ve ARDS Modelinin Oluşturulması

Bu çalışma için Atatürk Üniversitesi Tıbbi Deneysel Araştırma ve Uygulama Merkezi (ATADEM)'den erkek Sprague Dawley sıçanlar (300-350 g) temin edildi. Sıçanlar deneysel prosedüre başlamadan önce standart koşullarda muhafaza edildi (20-22 °C sıcaklık, %40-50 nem, 12 saat ışık/gün döngüsü).

Hayvanların olası acı çekmelerini en aza indirmek için her türlü çaba gösterildi ve çalışma, ABD Ulusal Sağlık Enstitüleri tarafından yayınlanan Labnortuar Hayvanlarının Bakımı ve Kullanımı Kılavuzuna göre yapıldı. Tüm hayvanlar, her grupta 6 hayvan olmak üzere rastgele seçilerek 3 gruba ayrıldı:

Grup I (6 hayvan) —Kontrol (Sağlıklı Grup)

Grup II (6 hayvan) —Oleik asit (ARDS)

Grup III (9 hayvan) —Oleik asit + Hispidulin (ARDS+HİS)

Grup II ve III sıçanlarına %1 lik BSA içinde hazırlanmış 50 mcl oleik asit kuyruk venlerinden uygulandı, Grup II sıçanlarına uygulamadan bir saat önce 80 mg/kg hispidulin intraperitoneal olarak verildi. 24 saat sonra akut akciğer hasarı en yüksek seviyeye ulaşınca sıçanlar yüksek doz ketamin anestezisiyle birlikte intrakardiyak yöntemle kan alınarak ötenazi edildi ve deney sonlandırıldı. Daha sonra karaciğer doku örneklerinden bir kısmı biyokimyasal testler ve FTIR analizi için steril plastik petrilere alınıp -80 °C'de saklandı.

2.2. Karaciğer Dokularından FTIR Spektrumunun Toplanması

Karaciğer dokularının spektrumları, 4000-400 cm^{-1} aralığında 4 cm^{-1} spektral çözünürlük ve 32 tarama ile ATR modlu (Bruker Vertex 70 FTIR spektrometre,

Ettlingen, Almanya) FTIR spektroskopisi kullanılarak toplandı. Atmosferik su buharı ve CO₂'nin katkısını önlemek için arka plan spektrumu toplandı ve doku spektrumlarından otomatik olarak çıkarıldı. Her örnekten 3er kez spektrum elde edildi ve her alınan spektrumların ortalaması alındı. Her bir grup için 6 adet spektrum toplanmış oldu. Spektral verilerin toplanması ve sinyal işleminde OPUS 7.5 yazılımı (Bruker Optics, GmbH) kullanıldı.

2.3. FTIR Spektrumlarının Kemometrik Analizi

Kemometrik analiz öncesi spektrumlara, gürültüyü elimine etmek amacıyla Savitzky Golay düzleştirme (düzleştirme noktası:9), sonrasında baseline düzleştirme (concave-rubber band baseline correction) yapıldı. İşlenmiş spektrumlara 3670-900 cm⁻¹ spektral bölgede çoklu değişkenli gözetimsiz (unsupervised) kemometrik analiz yöntemlerinden temel bileşen analizi (principle component analysis-PCA) ve hiyerarşik kümeleme analizi (hierarchical cluster analysis-HCA) uygulandı. Kemometrik analizler Unscrambler X 10.3 (CAMO Software AS., Oslo, Norveç) yazılımı kullanılarak yapıldı. PCA sonuçları skor ve yüklem grafiği olarak, HCA ise Ward algoritmasından elde edilen dendrogram grafiği olarak verildi. HCA dendrogram grafiğinden Tablo 1'de verilen gruplar göz önüne alınarak, formüller yardımıyla doğruluk, özgüllük ve duyarlılık hesaplandı. Yüklem grafiğinde elde edilen spektral bantların her bir temel bileşendeki yüzde varyasyon katkı değerleri belirtildi.

Tablo 1. Duyarlılık, özgüllük ve doğruluk değerlerinin hesaplanması

| Gruplar | HCA Dendrogram Sonucu | |
|--------------------------|-----------------------|---------|
| | Pozitif | Negatif |
| ARDS | A | B |
| Kontrol, ARDS+Hispidulin | C | D |

Duyarlılık= $(Ax100) / (A+B)$, Özgüllük= $(Dx100) / (C+D)$,
Doğruluk = $[(A+D) X100] / (A+D+B+C)$.

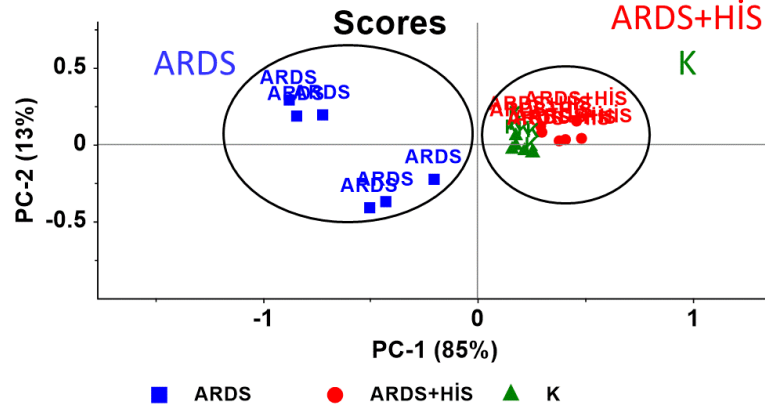
3. Bulgular ve Tartışma

Karaciğer, metabolik homeostazın düzenlenmesinde önemli rol oynayan bir organ olduğu için karaciğer fonksiyonunun bozulması, enerji arzının kesilmesi nedeniyle diğer organları da etkilemektedir (Rui, 2014). Ayrıca karaciğer, toksin ve ilaç metabolizmasında, sistemik inflamatuvar yanıt düzenlenmesinde ve immün korumada görevlidir. Hepatobilier sistem, sistemik dolaşımdaki proinflamatuvar sitokinleri, vazoaktif mediatörleri ve eikozanoidleri etkisiz hale getirdiği ve detoksifiye ettiği için akciğerleri ve diğer organları hasardan koruyan bir organdır (Guillot ve Tacke 2019). Dolayısıyla karaciğerin normal çalışması, akciğerlerin korunması veya akciğerlerin geçirdiği herhangi bir hasar sonrasında iyileşmesi için gereklidir (Herrero ve ark., 2020). Diğer taraftan karaciğer ve akciğerler arasındaki bağlantının dengesizliği, ARDS'nin ilerlemesinde ve çoklu organ yetmezliğinin ortaya çıkmasında önemli bir

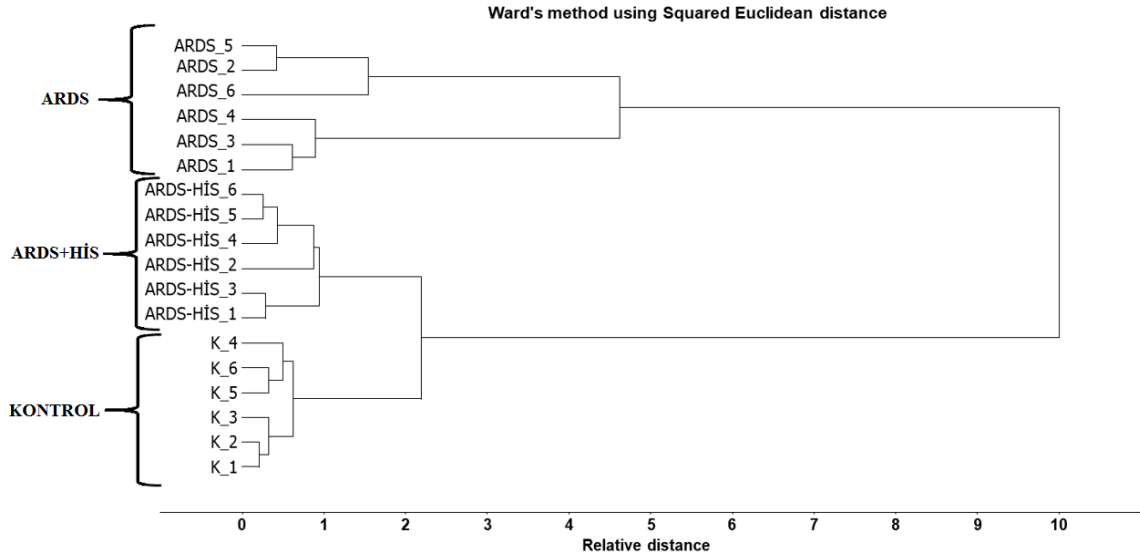
faktördür (Hilliard ve ark., 2015). Bu çalışmada ARDS kaynaklı karaciğer doku biyomoleküllerinde içeriksel değişimlerini belirlemek amacıyla FTIR spektroskopi metodu kullanılmıştır. Çünkü örneklere ait FTIR spektrumu örneğe karakteristik parmak izi niteliğinde biyomoleküllere ait fonksiyonel grup titreşimlerinden kaynaklanan spektral bantlar içermektedir (Severcan ve Haris, 2012). Bu bantlardan kalitatif ve kantitatif spektral analizler yapılarak biyomoleküler kompozisyon değişimlerini belirlemek mümkündür. Ancak IR spektrumunda toplanan spektral bant aralığı dalga sayısı ve absorbans değerleri açısından dikkate alındığında, tek bir örneğe ait spektrumda dahi binlerce veri bulunmaktadır. Spektral verinin bant alanı, bant genişliği ile bant dalgasayısı gibi kantitatif spektral analizler manuel olarak yapıldığından uzun zaman almaktadır. Son yıllarda spektroskopi temelli yapılan çalışmalarda spektral analizlerde hem analiz süresini kısaltmak, hem de doğru ve etkin bir analiz yapmak için çok değişkenli analiz yöntemi olan kemometrik analiz metodları yaygın olarak kullanılmaktadır (Craig ve ark., 2013; Sauzier ve ark., 2021). Bu metodlar çok değişkenli spektral varyasyonlara dayalı olarak gruplar arasındaki farklılıkların ortaya konulmasını ve örnek içindeki spesifik analit miktarının belirlenmesini sağlar. Gruplar arasındaki ilişkileri, kümeleşmeleri belirlemek için herhangi bir ön bilgi gerektirmeyen gözetimsiz kemometrik analiz yöntemlerinden Temel Bileşen Analizi (PCA) ile Hiyerarşik Kümeleme Analizi (HCA) yaygın olarak kullanılmaktadır (Severcan ve Haris 2012; Abbas ve ark., 2018; Sauzier ve ark., 2021). Son yıllarda, diyabetten kansere kadar birçok farklı hastalığın teşhisinde, bitki özütü veya farklı bileşiklerin koruyucu ve/veya tedavi edici özelliklerinin belirlenmesine yönelik yapılan çalışmalarda FTIR spektroskopisi ile birlikte bu analiz metodlarının etkin olarak kullanılabilmesi gösterilmiştir (Severcan ve Haris 2012; Gok ve ark., 2016; Gurbanov ve ark., 2016; Abbas ve ark., 2018; Faelelbom ve ark., 2022). Bu nedenlerden ötürü, K, ARDS ve HİS+ARDS gruplarında gruplar arasındaki bağlantıları belirlemek amacıyla karaciğer spektrumlarına PCA analizi uygulanmıştır. Bu bağlantılar PCA'dan elde edilen skor ve yüklem grafiklerinin değerlendirilmesi ile ortaya konulmaktadır (Roggo ve ark., 2007; Gurbanov ve ark., 2018). Şekil 1'de her üç gruba ait PCA skor grafiği verilmektedir. Skor grafiği verilerine göre ARDS group diğer iki gruptan ayrı bir yerde konumlanmaktadır. K ve HİS+ARDS gruplarında ise yer alan örnekler aynı bölgede yer almaktadır. Skor grafiklerinde ise gruplar arasında yer alan spektral varyasyonlar temel bileşenler (Principal Component, PC), % olarak ifade edilmektedir. En çok varyasyon PC1, diğer varyasyonların en yükseği ise PC2 ile ifade edilmektedir (Gurbanov ve ark., 2018; Dizaji ve ark., 2021). Her üç gruba ait skor grafiklerine bakıldığında PC1 ve PC2 için %86 ve %12 varyasyon değerleri elde edilmiş gruplar arasında toplam varyasyon oranı %98 olarak bulunmuştur. Bu değer, gruplar arasında özellikle ARDS

ve diğer iki grup arasında spektral biyokompozisyonda önemli oranda değişimlerin olduğunu ortaya koymaktadır. PCA skor grafiğinde elde edilen gruplaşma bulgularını desteklemek amacıyla gözetimsiz kemometrik analiz yöntemlerinden sınıflandırma metodu olan HCA uygulanmıştır. HCAda sınıflar dendrogramda yer alan clusterlar ile gösterilmektedir (Roggo ve ark., 2007; Gurbanov ve ark., 2018; Dizaji ve ark., 2021). Benzer örnekler aynı clusterda, farklı örnekler ise farklı clusterda yer almaktadır. Örnekler arasındaki farklılıklar uzaklık/heterojenlik birimi ile ifade edilmektedir. Aynı

clusterda yer alan örneklerin birbiri arasındaki uzaklık değeri yüksektir (Siqueira ve Lima, 2016). Şekil 2'de K, ARDS ve ARDS+HİS gruplarına ait HCA dendrogram grafiği verilmektedir. PCA bulguları ile benzer olarak ARDS, K ve ARDS+HİS gruplarına göre farklı bir clusterda yer almakta olup, uzaklık değeri olarak 10 elde edilmiştir. ARDS ayrımında %100 duyarlılık, özgüllük ve doğruluk değeri elde edilmiştir. K ve ARDS+HİS gruplarında ise bu değer 2 olarak elde edilmiştir, değer düşük olması her iki grup arasında karaciğer doku biyokimyasal kompozisyonun benzer olduğunu göstermektedir.



Şekil 1. Kontrol, ARDS, ve ARDS-HİS gruplarına ait 3670-900 cm⁻¹ spektral bölgede uygulanan PCA skor grafiği.



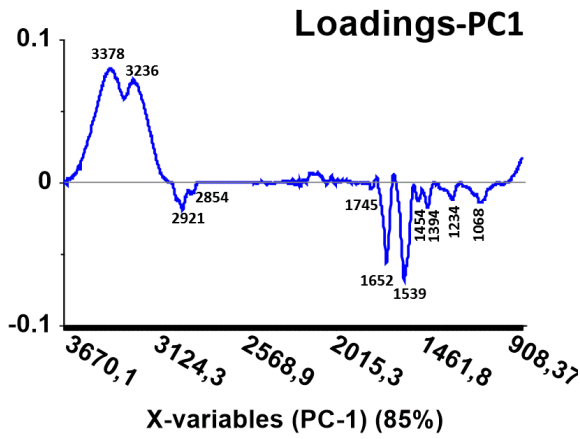
Şekil 2. Kontrol, ARDS, ve ARDS-HİS gruplarına ait 3670-900 cm⁻¹ spektral bölgede uygulanan HCA dendrogram grafiği.

ARDS ve hispidulin uygulanmasına bağlı, gruplar arası ayrıma neden olan karaciğer dokusu biyomoleküllerindeki kalitatif ve kantitatif değişimleri belirlemek için PCA yükleme grafikleri kullanılmaktadır. Yükleme grafikleri, örnek spektrumlarına benzer grafiklerdir. Bu nedenle yükleme grafiğinin kalitatif ve kantitatif analiz, spectral bantlarının daha iyi yorumlamasını sağlar (Pocasap ve ark., 2020; Dizaji ve ark., 2021). Grafikte x eksenı dalgasayısına karşılık gelen spektral bantlar, y eksenı ise bu bantlara karşılık elde edilen eigen değerleri ile gösterilmektedir. Yüksek pozitif eigen ve negatif eigen değeri, spektral varyasyon

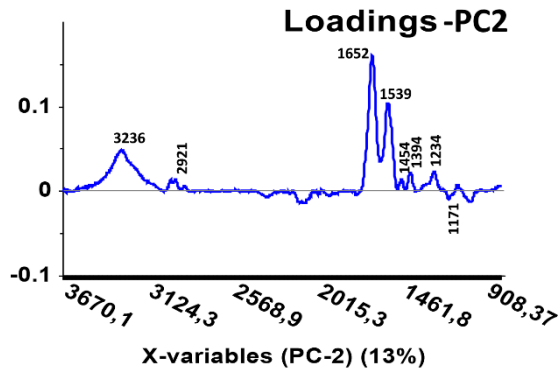
değerinin yüksek olduğunu ve gruplar arasındaki ayrıma katkı oranının önemli olduğunu belirtmektedir. PC1 ve PC2 için yükleme grafikleri Şekil 3 ve 4'de verilmektedir. Her iki PC de, 3700-2800 ile 1800-900 cm⁻¹ spektral bölgesinde eigen değeri yüksek birçok spektral bant elde edilmiştir. Varyasyonları ve bunları PClere olan katkısını belirlemek için, bantların konumu ile bant tanımları belirlenerek PC1 ve PC2 için bant varyasyonları hesaplanmıştır (Tablo 2).

Tablo 2. PCA yüklem grafiklerinde yer alan IR spektral bantların tanımı ve PC1 ve PC2deki açıklanan % varyasyonları

| Bant Konumu | PC1 | PC2 | Bant Tanımı | Referans |
|-------------|-------|-------|---|-------------------------------|
| 3378 | 98,93 | 99,95 | Amit A: peptit N-H gerilme, titreşimi,-OH gerilme | Dominguez-Vidal ve ark., 2016 |
| 3236 | 96,48 | 99,90 | Amit A: peptit N-H gerilme, titreşimi,-OH gerilme | Dominguez-Vidal ve ark., 2016 |
| 2921 | 91,28 | 95,45 | CH ₂ asimetrik gerilme: lipit | Zohdi ve ark., 2015 |
| 2854 | 91,19 | 92,45 | CH ₂ simetrik gerilme:lipit | Zohdi ve ark., 2015 |
| 1745 | 80,58 | 90,22 | C=O gerilme trigliserit kolesterol ester | Gautam ve ark., 2016 |
| 1652 | 50,19 | 99,54 | amit I—α-helix, protein | Çakmak ve ark., 2003 |
| 1539 | 73,40 | 99,91 | Amit II, protein | Çakmak ve ark., 2003 |
| 1454 | 87,01 | 98,07 | CH ₃ makaslama titreşimi:lipit | Severcan ve ark., 2000 |
| 1394 | 81,77 | 99,53 | CH ₃ simetrik bükülme titreşimi: proten ve lipit | Mihály ve ark., 2017 |
| 1234 | 61,44 | 94,86 | PO ₂ - antisimetrik gerilme:Fosfolipit, nükleik asit | Mehra ve ark., 2020 |
| 1171 | 93,60 | 94,64 | kollajen | Zohdi ve ark., 2015 |
| 1068 | 71,20 | 71,87 | C-O gerilme fosfodiester, riboz | Ashtarinezhad ve ark.,2014 |
| 921 | 79,27 | 81,52 | Nükleik asit, RNA riboz | Ami ve ark.,2013 |



Şekil 3. Kontrol, ARDS, ve ARDS-HİS gruplarına ait 3670-900 cm⁻¹ spektral bölgede uygulanan PCA analizi PC1'e ait yüklem grafiği.



Şekil 4. Kontrol, ARDS, ve ARDS-HİS gruplarına ait 3670-900 cm⁻¹ spektral bölgede uygulanan PCA analizi PC2'e ait yüklem grafiği.

PC1 yüklem grafiğinde en yüksek eigen değerine sahip bant 3378,3236,1652,1539 cm⁻¹, PC2 de ise en yüksek eigen değerleri 1652, 1539 cm⁻¹ bantlar için elde edilmiştir. Protein kaynaklı bu iki bantın % değerleri PC2 de %99,54 ve 99,91 olarak bulunmuştur. PC1 da

varyasyon yüzdelerinde yükseklik bakımından diğer bantlar incelendiğinde 2921 için % 91,28, 2854 için % 91,19 elde edilmiştir. Kollajen kaynaklı 1171 bantı için bu oran %93,60, nükleik asit kaynaklı 1234 bant için PC2de %94,86 olarak hesaplanmıştır. RNA kaynaklı 921 cm⁻¹ de yer alan bant için varyasyon yüzdesi %81,52 olarak bulunmuştur. Söz konusu bantlardaki yüksek varyasyon değerleri belirtilen makromoleküllerde gruplar arası değişimlerin yüksek olduğunu göstermektedir. Özellikle PCA ve HCA analizlerinde ARDS grubunu diğer çalışılan iki gruba göre ayrı yerde konumlanması, ARDS kaynaklı karaciğer doku lipit nükleik asit ve protein içeriğinde kantitatif değişimlerin oluşmasını engellediğini ortaya koymaktadır. ARDS grubunda oluşan içeriksel değişimler, hastalık kaynaklı artan oksidatif stresle ilgili olabilir. Çünkü artan oksidatif stres doku biomoleküler kompozisyonunda yıkımlara neden olmaktadır. Hispidulin protektif amaçlı uygulamasında bu tür değişimlerin engellenmesi molekülün antioksidant özelliği ile ilgili olabilir. Hispidulinin karaciğerde antioksidan özelliği Ferrandiz ve ark. (1994) tarafından yapılan çalışma ile gösterilmiştir. Bu çalışmada, 50-150 mg/kg doz aralığında hispidulin uygulamasının karaciğerde lipit peroksidasyonu azalttığı, 150 mg/kg dozun MDA oluşumunu engellediği belirtilmiştir. CCl₄ karaciğer toksisitesine karşı hispidulinin hepaprotektif özelliği Jin ve ark. (2011) ile yapılan çalışma ile gösterilmiş ve 300 mg/kg dozda hispidulin uygulamasının karaciğer enzimleri olan ALT'de 7 kat, AST'de ise 2 kat azalmaya neden olduğu ifade edilmiştir. ARDS kaynaklı lipit, protein ve nükleik asitlerdeki degradasyonun hispidulin uygulanmış sıçanlarda görülmesi ve bu grubun kontrol grubu ile aynı yerde konumlanması söz konusu bileşiğin hepatoprotektif rolünü ve bu bağlamda ARDS hastalarında kullanılabilme potansiyelini ortaya koymaktadır.

4. Sonuç

Karaciğer-akciğer ekseninin daha iyi anlaşılması, ARDS'lu veya riskini taşıyan hastalarda klinik müdahale için yeni teşhislerin ve terapötik stratejilerin hakkında bilgi sağlanması açısından önemlidir. Günümüzde ARDS tedavisi ve olası komplikasyonları, COVID-19 salgını nedeniyle daha önemli hale gelmektedir. Modern bilimsel veriler, en yaygın ARDS komplikasyonunun karaciğer hasarı olduğunu göstermektedir. ARDS'ye bağlı karaciğer yetmezliği olan hastaların tedavi stratejilerine hispidulinin eklenmesi yaşam kalitelerini artıracaktır.

Katkı Oranı Beyanı

Yazarın katkı yüzdesi aşağıda verilmiştir. Yazar makaleyi incelemiş ve onaylamıştır.

| | N.Ş.Ö. |
|-----|--------|
| K | 100 |
| T | 100 |
| Y | 100 |
| VTI | 100 |
| VAY | 100 |
| KT | 100 |
| YZ | 100 |
| KI | 100 |
| GR | 100 |
| PY | 100 |
| FA | 100 |

K= kavram, T= tasarım, Y= yönetim, VTI= veri toplama ve/veya işleme, VAY= veri analizi ve/veya yorumlama, KT= kaynak tarama, YZ= Yazım, KI= kritik inceleme, GR= gönderim ve revizyon, PY= proje yönetimi, FA= fon alımı.

Çatışma Beyanı

Yazarlar bu çalışmada hiçbir çıkar ilişkisi olmadığını beyan etmektedirler.

Etik Onay Beyanı

Bu araştırma Atatürk Üniversitesi Hayvan Deneyleri Yerel Etik Kurulu tarafından onaylanmıştır (onay tarihi: 22 Aralık 2022, onay numarası: 2022/14).

Destek ve Teşekkür Beyanı

Sağladığı imkânlardan dolayı Atatürk Üniversitesi DAYTAM (Doğu Anadolu Yüksek Teknoloji Uygulama ve Araştırma Merkezi)'a teşekkür ederim.

Kaynaklar

Abbas S, Simsek Ozek N, Emri S, Koksall D, Severcan M, Severcan F. 2018. Diagnosis of malignant pleural mesothelioma from pleural fluid by Fourier transform-infrared spectroscopy coupled with chemometrics. *J Biomed Opt*, 23(10): 105003.

Ami D, Mereghetti P, Doglia SM. 2013. Multivariate analysis for Fourier transform infrared spectra of complex biological systems and processes. *Multivariate Analysis Manag Eng Sci*, 2013: 189-220.

Anan K, Kawamura K, Suga M, Ichikado K. 2018. Clinical differences between pulmonary and extrapulmonary acute respiratory distress syndrome: a retrospective cohort study of prospectively collected data in Japan. *J Thorac Dis*, 10: 5796.

Ashtarinezhad A, Shirazi FH, Vatanpour H, Mohamzadehasl B, Panahyab A, Nakhjavani M. 2014. FTIR-microspectroscopy detection of metronidazole teratogenic effects on mice fetus. *Iran J Pharm Res*, 13: 101.

Aydın S, Çöl M. 2020. İtalya'daki COVID-19 salgınına genel bir bakış, Editors: Osman Memikoğlu, Volkan Genç, Covid-19, Ankara Üniversitesi Tıp Fakültesi, Ankara, Türkiye, pp: 75.

Bellani G, Laffey JG, Pham T. 2016. Epidemiology, patterns of care, and mortality for patients with acute respiratory distress syndrome in intensive care units in 50 countries. *JAMA*, 315: 788-800.

Cai Y, Zou Z, Liu L, Chen S, Chen Y, Lin Z, Chen Y. 2015. Bone marrow-derived mesenchymal stem cells inhibits hepatocyte apoptosis after acute liver injury. *Int J Clin Exp*, 8(1): 107.

Craig AP, Franca AS, Irudayaraj J. 2013. Pattern recognition applied to spectroscopy: Conventional methods and future directions: Pattern Recognition: Practices, Perspectives and Challenges. Vincent, Eddimburg, UK, pp: 1-46.

Çakmak G, Togan I, Uğuz C, Severcan F. 2003. FT-IR spectroscopic analysis of rainbow trout liver exposed to nonylphenol. *Appl Spectrosc*, 57(7): 835-841.

Dizaji AN, Ozek NS, Yilmaz A, Aysin F, Yilmaz M. 2021. Gold nanorod arrays enable highly sensitive bacterial detection via surface-enhanced infrared absorption (SEIRA) spectroscopy. *Colloids Surf B Biointerfaces*, 206: 111939.

Dominguez-Vidal A, Pantoja-de la Rosa J, Cuadros-Rodríguez L, Ayora-Cañada MJ. 2016. Authentication of canned fish packing oils by means of Fourier transform infrared spectroscopy. *Food Chem*, 190: 122-127.

Elibol B, Severcan M, JakubowskaDogru E, Dursun I, Severcan F. 2022. The structural effects of Vitamin A deficiency on biological macromolecules due to ethanol consumption and withdrawal: An FTIR study with chemometrics. *J Biophotonics*, 15(7): e202100377.

Fahelbom KM, Saleh A, Al-Tabakha MM, Ashames AA. 2022. Recent applications of quantitative analytical FTIR spectroscopy in pharmaceutical, biomedical, and clinical fields: A brief review. *Rev Anal Chem*, 41(1): 21-33.

Ferrandiz ML, Bustos G, Paya M, Gunasegaran R, Alcaraz MJ. 1994. Hispidulin protection against hepatotoxicity induced by bromobenzene in mice. *Life Sci*, 55(8): PL145-PL150.

Gautam R, Deobagkar-Lele M, Majumdar S, Chandrasekar B, Victor E, Ahmed SM, Nandi D. 2016. Molecular profiling of sepsis in mice using Fourier Transform Infrared Microspectroscopy. *J Biophotonics*, 9(1-2): 67-82.

Gok S, Aydın OZ, Sural YS, Zorlu F, Bayol U, Severcan F. 2016. Bladder cancer diagnosis from bladder wash by Fourier transform infrared spectroscopy as a novel test for tumor recurrence. *J Biophotonics*, 9(9): 967-975.

Guillot A, Tacke F. 2019. Liver macrophages: old dogmas and new insights. *HepatoL Commun*, 3(6): 730-743.

Gurbanov R, Bilgin M, Severcan F. 2016. Restoring effect of selenium on the molecular content, structure and fluidity of diabetic rat kidney brush border cell membrane. *Biochim Biophys Acta Biomembr*, 1858(4): 845-854.

Gurbanov R, Gozen AG, Severcan, F. 2018. Rapid classification of heavy metal-exposed freshwater bacteria by infrared spectroscopy coupled with chemometrics using supervised method. *Spectrochim Acta A Mol Biomol Spectrosc*, 189: 282-290.

Herrero R, Sánchez G, Asensio I, López E, Ferruelo A, Vaquero J. 2020. Liver-lung interactions in acute respiratory distress syndrome. *Intensive Care Med Exp*, 8(1): 1-13.

Hilliard KL, Allen E, Traber KE, Yamamoto K, Stauffer NM, Wasserman GA. 2015. The lung-liver axis: a requirement for

- maximal innate immunity and hepatoprotection during pneumonia. *Am J Respir Cell Mol Biol*, 53(3): 378-390.
- Hu LL, Wang WJ, Zhu QJ, Yang L. 2020. Novel coronavirus pneumonia-related liver injury: etiological analysis and treatment strategy. *Chinese J Hepatol*, 28(2): 97-99.
- Jin XF, Qian J, Lu YH. 2011. The role of hepatoprotective effect of a flavonoid-rich extract of *Salvia plebeia* R. Br. on carbon tetrachloride-induced acute hepatic injury in mice. *J Medic Plant Res*, 5(9): 1558-1563.
- Kamysynyi A, Krynytska I, Matskevych V, Marushchak M, Lushchak O. 2020. Arterial hypertension as a risk comorbidity associated with COVID-19 pathology. *Int J Hypertens*, 2020: 8019360.
- Kaya AG, Kaya A. 2020. Klinik yaklaşım: Solunum sistemi. Editors: Osman Memikoğlu Volkan Genç, Covid-19, Ankara Üniversitesi Tıp Fakültesi, Ankara, Türkiye, pp: 75.
- Lee D, Lee JH, Kim BH, Lee S, Kim DW, Kang KS. 2022. Phytochemical combination (p-Synephrine, p-octopamine hydrochloride, and hispidulin) for improving obesity in obese mice induced by high-fat diet. *Nutrients*, 14(10): 2164.
- Li J, Fan JG. 2020. Characteristics and mechanism of liver injury in 2019 coronavirus disease. *J Clin Transl Hepatol*, 8(1): 13.
- Liu K, Zhao F, Yan J, Xia Z, Jiang D, Ma P. 2020. Hispidulin: A promising flavonoid with diverse anti-cancer properties. *Life Sci*, 259: 118395.
- Mehra S, Chadha P. 2020. Alterations in structure of biomolecules using ATR-FTIR and histopathological variations in brain tissue of *Channa punctatus* exposed to 2Naphthalene sulfonate. *Toxicol Res*, 9(4): 530-536.
- Meyer NJ, Gattinoni L, Calfee CS. 2021. Acute respiratory distress syndrome. *Lancet*, 398: 622-637.
- Mihály J, Deák R, Szigyártó I.C, Bóta A, Beke-Somfai T, Varga Z. 2017. Characterization of extracellular vesicles by IR spectroscopy: fast and simple classification based on amide and CH stretching vibrations. *Biochim Biophys Acta Biomembr*, 1859(3): 459-466.
- Nardo AD, Schneeweiss-Gleixner M, Bakail M, Dixon ED, Lax SF, Trauner M. 2021. Pathophysiological mechanisms of liver injury in COVID-19. *Liver Int*, 41(1): 32.
- Papazian L, Aubron C, Brochard L. 2019. Formal guidelines: management of acute respiratory distress syndrome. *Ann Intens Care*, 9: 69.
- Pocasap P, Weerapreeyakul N, Junhom C, Phiboonchaiyanan PP, Srisayam M, Nonpunya A, Barusrux S. 2020. FTIR microspectroscopy for the assessment of mycoplasmas in HepG2 cell culture. *Appl Sci*, 10(11): 3766.
- Redko O, Dovgalyuk A, Dovbush A, Nebesna Z, Yakubyshtyna L, Krynytska I. 2021. Liver injury associated with acute respiratory distress syndrome and the prospects of mesenchymal stromal cells therapy for liver failure. *Therapy*, 8(12): 14-21.
- Roggo Y, Chalus P, Maurer L, Lema-Martinez C, Edmond A, Jent N. 2007. A review of near infrared spectroscopy and chemometrics in pharmaceutical technologies. *J Pharm Biomed Anal*, 44(3): 683-700.
- Rui L. 2014. Energy metabolism in the liver. *Compr Physiol*, 4(1): 177.
- Sauzier G, van Bronswijk W, Lewis SW. 2021. Chemometrics in forensic science: approaches and applications. *Analyst*, 146(8): 2415-2448.
- Severcan F, Haris PI. 2012. Introduction to vibrational spectroscopy in diagnosis and screening in "Vibrational Spectroscopy in Diagnosis and Screening" *Adv Biomedic Spectrosc*, 6: 1-10.
- Severcan F, Toyran N, Kaptan N, Turan B. 2000. Fourier transform infrared study of the effect of diabetes on rat liver and heart tissues in the C-H region. *Talanta*, 53(1): 55-59.
- Siqueira LF, Lima KM. 2016. MIR-biospectroscopy coupled with chemometrics in cancer studies. *Analyst*, 141(16): 4833-4847.
- Türker-Kaya S, İlbay G. 2020. Analysis of rat blood plasma upon acute epileptic seizures by infrared spectroscopy with chemometrics. *Vib Spectrosc*, 109: 103074.
- Wang Y, Alkhalidy H, Luo J, Liu D. 2019. Antidiabetic effects of hispidulin in streptozotocin-induced insulin deficient mice. *The FASEB J*, 33(S1): 834-838.
- Wu F, Li S, Zhang N, Huang W, Li X, Wang M, Han B. 2018. Hispidulin alleviates high-glucose-induced podocyte injury by regulating protective autophagy. *Biomed Pharmacother*, 104: 307-314.
- Yang P, Formanek P, Scaglione S, Afshar M. 2019. Risk factors and outcomes of acute respiratory distress syndrome in critically ill patients with cirrhosis. *Hepatol Res.*, 49(3): 335-343.
- Yonar D, Severcan M, Gurbanov R, Sandal A, Yilmaz U, Emri S, Severcan F. 2022. Rapid diagnosis of malignant pleural mesothelioma and its discrimination from lung cancer and benign exudative effusions using blood serum. *Biochim Biophys Acta Mol Basis Dis*, 1868(10): 166473.
- Zohdi V, Whelan DR, Wood BR, Pearson JT, Bambery KR, Black M. 2015. Importance of tissue preparation methods in FTIR micro-spectroscopical analysis of biological tissues: traps for new users. *PLoS One*, 10(2): e0116491.



ON DARBOUX FRAMES OF INDICATRICES OF SPACELIKE SALKOWSKI CURVE WITH SPACELIKE BINORMAL IN E_1^3

Birkan AKSAN¹, Sümeyye GÜR MAZLUM^{2*}

¹Gümüşhane University, Institute of Graduate Education, Department of Mathematical Engineering, 29100, Gümüşhane, Türkiye


²Gümüşhane University, Kelkit Aydın Doğan Vocational School, Department of Computer Technology, 29600, Gümüşhane, Türkiye


Abstract: The aim of this study is to examine Darboux frames and some other geometric properties (geodesic curvatures, geodesic torsions, normal curvatures, Darboux derivative formulas, Darboux vectors, angles, etc.) of the spherical indicatrices on Lorentzian unit sphere S_1^2 and hyperbolic unit sphere H_0^2 of the spacelike Salkowski curve with spacelike binormal in Lorentzian 3-space E_1^3 . In this context, new and interesting results have been obtained for this curve. Thus, relationships between the newly obtained curvatures and torsions and the curvature and torsion of the original curve are given. Moreover, the matrix relationship between the Darboux and Frenet frames of these indicatrices is shown. Finally, the Darboux vectors belong to the Darboux frames and the Darboux vectors belong to the Frenet frames of these curves are compared.

Keywords: Lorentzian space, Salkowski curve, Darboux frame, Spherical indicatrices, Curvatures

*Corresponding author: Gümüşhane University, Kelkit Aydın Doğan Vocational School, Department of Computer Technology, 29600, Gümüşhane, Türkiye

E mail: sumeyyegur@gumushane.edu.tr (S. GÜR MAZLUM)

Birkan AKSAN  <https://orcid.org/0000-0002-1533-6557>

Sümeyye GÜR MAZLUM  <https://orcid.org/0000-0003-2471-1627>

Received: August 04, 2023

Accepted: September 04, 2023

Published: October 15, 2023

Cite as: Aksan B, Gür Mazlum S. 2023. On darbox frames of indicatrices of spacelike salkowski curve with spacelike binormal in E_1^3 . BSJ Eng Sci, 6(4): 401-413.

1. Introduction

Darboux frame, one of the tools used to study the differential geometry of a curve on a surface, consists of the tangent of the curve, the normal of the surface, and a third vector consisting of vector product of these two vectors. Therefore, the Darboux frame is an element of curves passing through the tangent plane or surface's normal at any point on the surface. Using Darboux frame's vectors, the normal and geodesic curvatures and geodesic torsion of the curve on a surface are obtained. Studies on the Darboux frame of a curve are available in (Uğurlu and Kocayiğit, 1996; Uğurlu and Çalışkan, 2012; Şentürk and Yüce, 2015; Yakıcı et al., 2016; Özdemir, 2020; Li et al., 2023). There are relationships between these elements and the main curvatures of the curve. Another relationship is found between the Frenet and Darboux frames of the curve. In addition, just as the Darboux instantaneous rotation axis belong to the Frenet frame can be calculated, a rotation axis of the Darboux frame can also be calculated (Fenchel, 1951). While drawing a curve in E^3 , at every moment t , the Frenet vectors of the curve also form curves on unit sphere S^2 . These curves are called spherical indicatrices of the main curve. Geometric features such as curvatures and radii of curvature of the surface on it are examined with the spherical indicatrices. Moreover, Darboux frames of the curves and other geometric elements mentioned above can be calculated, since the spherical indicatrices of any curve are on the surface. Studies on the spherical indicatrices of the curve can be found in sources (Hacısalıhoğlu, 1983; Aksan and Gür Mazlum, 2023; Bilici and Çalışkan, 2019; Kula and

Yaylı, 2005; Gür and Şenyurt, 2010). The aim of this study is to examine the Darboux frames and some geometric properties (curvatures, torsions, Darboux vectors, angles etc.) of the spherical indicatrices on unit spheres S_1^2 and H_0^2 of the spacelike Salkowski curve with spacelike binormal, which is one of the forms in Lorentzian 3-space of the well-known Salkowski curve (Salkowski, 1909; Monerde 2009) in differential geometry. For basic information and various studies on Lorentzian space, which is one of the current fields in which physicists and geometers frequently work, the sources (O'Neill, 1983; Birman and Nomizu, 1984; Ratcliffe, 1994; Uğurlu and Kocayiğit, 1996; Uğurlu, 1997; Kahveci and Yaylı, 2002; Bükcü and Karacan, 2007; Uğurlu and Çalışkan, 2012; Lopez, 2014; Yüksel et al., 2014; Yakıcı et al., 2016; Babaarslan and Yaylı, 2017; Li et al., 2023) can be examined. In addition, other studies on the Salkowski curves are available in (Gür and Şenyurt, 2010; Ali, 2011; Gür Mazlum et al., 2022; Aksan and Gür Mazlum, 2023).

2. Preliminaries

The inner and vector product functions are defined as respectively:

$$\langle \cdot, \cdot \rangle : E_1^3 \times E_1^3 \rightarrow R, \langle \vec{Z}_1, \vec{Z}_2 \rangle = Z_{11}Z_{21} + Z_{12}Z_{22} - Z_{13}Z_{23}, \quad (1)$$

$$\wedge : E_1^3 \times E_1^3 \rightarrow E_1^3,$$

$$\vec{Z}_1 \wedge \vec{Z}_2 = (Z_{13}Z_{22} - Z_{12}Z_{23}, Z_{11}Z_{23} - Z_{13}Z_{21}, Z_{11}Z_{22} - Z_{12}Z_{21}), \quad (2)$$



for the vectors $\vec{Z}_1 = (Z_{11}, Z_{12}, Z_{13}) \in E_1^3$ and $\vec{Z}_2 = (Z_{21}, Z_{22}, Z_{23}) \in E_1^3$. Here, $\langle \cdot, \cdot \rangle$ is Lorentzian metric. E^3 with the metric is called Lorentzian 3-space and is denoted by E_1^3 . $\vec{Z}_1 \in E_1^3$ is spacelike (sl) vector, if $\langle \vec{Z}_1, \vec{Z}_1 \rangle > 0$ or $\vec{Z}_1 = 0$, $\vec{Z}_1 \in E_1^3$ is timelike (tl) vector, if $\langle \vec{Z}_1, \vec{Z}_1 \rangle < 0$, $\vec{Z}_1 \in E_1^3$ is lightlike or null vector, if $\langle \vec{Z}_1, \vec{Z}_1 \rangle = 0$ and $\vec{Z}_1 \neq 0$. Besides, $\vec{Z}_1 \in E_1^3$ is future pointing (fp) timelike vector, if $\langle \vec{Z}_1, \vec{E} \rangle < 0$ or \vec{Z}_1 is past pointing (pp) timelike vector, if $\langle \vec{Z}_1, \vec{E} \rangle > 0$, where $\vec{E} = (0, 0, 1)$. The vectors $\vec{Z}_1, \vec{Z}_2 \in E_1^3$ are Lorentz orthogonal vectors, if $\langle \vec{Z}_1, \vec{Z}_2 \rangle = 0$. Let $\vec{Z}_1, \vec{Z}_2 \in E_1^3$ be nonzero Lorentz orthogonal vectors in E_1^3 , if \vec{Z}_1 is timelike, then \vec{Z}_2 is spacelike, (Ratcliffe, 1994). The norm of $\vec{Z}_1 \in E_1^3$ is $\|\vec{Z}_1\| = \sqrt{|\langle \vec{Z}_1, \vec{Z}_1 \rangle|}$. If $\|\vec{Z}_1\| = 1$, $\vec{Z}_1 \in E_1^3$ is a unit vector. The sets

$$S_1^2 = \{ \vec{Z}_1 \in E_1^3 \mid \vec{Z}_1 \text{ is unit spacelike vector} \},$$

$$H_0^2 = \{ \vec{Z}_1 \in E_1^3 \mid \vec{Z}_1 \text{ is unit timelike vector} \},$$

$$\Lambda = \{ \vec{Z}_1 \in E_1^3 \mid \vec{Z}_1 \text{ is unit lightlike vector} \}$$

are Lorentzian and hyperbolic unit spheres, and light cone, respectively. In E_1^3 , timelike vectors are located inside the light cone, lightlike vectors are located on the light cone, and spacelike vectors are located outside the light cone, Figure 1.

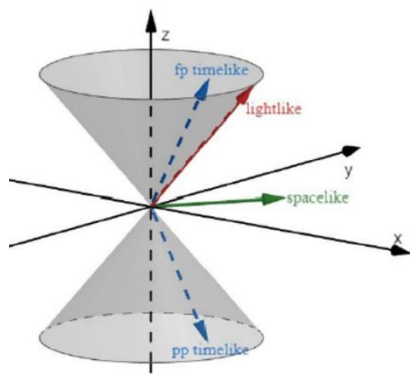


Figure 1. The vectors in E_1^3 .

In E_1^3 , the angle between two vectors is defined as follows: (O'Neill, 1983; Ratcliffe, 1994).

- If $\vec{Z}_1, \vec{Z}_2 \in E_1^3$ are future pointing (or past pointing) timelike vectors at the same time, then the hyperbolic angle between the vectors is

$$\langle \vec{Z}_1, \vec{Z}_2 \rangle = -\|\vec{Z}_1\| \|\vec{Z}_2\| \cosh \varphi.$$

- If $\vec{Z}_1 \in E_1^3$ is future pointing and $\vec{Z}_2 \in E_1^3$ is past pointing timelike vector, then the hyperbolic angle between the vectors is

$$\langle \vec{Z}_1, \vec{Z}_2 \rangle = \|\vec{Z}_1\| \|\vec{Z}_2\| \cosh \varphi.$$

- If $\vec{Z}_1, \vec{Z}_2 \in E_1^3$ are spacelike vectors lying in a spacelike plane, then the real angle between the vectors is

$$\langle \vec{Z}_1, \vec{Z}_2 \rangle = \|\vec{Z}_1\| \|\vec{Z}_2\| \cos \varphi.$$

- If $\vec{Z}_1, \vec{Z}_2 \in E_1^3$ are spacelike vectors lying in a timelike plane, then the hyperbolic angle between the vectors is

$$|\langle \vec{Z}_1, \vec{Z}_2 \rangle| = \|\vec{Z}_1\| \|\vec{Z}_2\| \cosh \varphi.$$

- If $\vec{Z}_1 \in E_1^3$ is a spacelike and $\vec{Z}_2 \in E_1^3$ is a timelike vector, then the hyperbolic angle between the vectors is

$$|\langle \vec{Z}_1, \vec{Z}_2 \rangle| = \|\vec{Z}_1\| \|\vec{Z}_2\| \sinh \varphi.$$

An curve $(\vec{\alpha})$ in E_1^3 is timelike, spacelike or lightlike curve, if all of the velocity vector of the curve are the timelike, spacelike or lightlike, respectively. When plotting a spacelike curve with the spacelike binormal $(\vec{\alpha})$ in E_1^3 , the endpoints of the spacelike tangent, timelike principal normal and spacelike binormal vectors \vec{T}, \vec{N} and \vec{B} of $(\vec{\alpha})$ draw

the spacelike indicatrices (\vec{T}) and (\vec{B}) on the Lorentz unit sphere S_1^2 and the timelike indicatrix (\vec{N}) on the hyperbolic unit sphere H_0^2 (Uğurlu and Çalışkan, 2012). A surface in E_1^3 is a spacelike (timelike), if the normal vector field of the surface at every points is timelike (spacelike). Let's assume that the regular spacelike curve $(\vec{\alpha}) = \vec{\alpha}(t)$ is on a timelike surface. The Darboux frame of this curve is $\{\vec{T}(t), \vec{g}(t), \vec{n}(t)\}$, where $\vec{n}(t)$ is the spacelike normal vector of the timelike surface and $\vec{g}(t) = \vec{n}(t) \wedge \vec{T}(t)$ is timelike (Uğurlu and Çalışkan, 2012).

3. On Darboux Frames of Indicatrices of Spacelike Salkowski Curve with Spacelike Binormal in E_1^3

Definition 2.1. For $m \in \mathbb{R}$ and $n = \frac{m}{\sqrt{m^2 - 1}}$, the parametric

equation of spacelike Salkowski curve with the spacelike binormal in E_1^3 is given as (Ali, 2011):

$$\vec{\gamma}_m(t) = \left(2 \sin t - \frac{1+n}{1-2n} \sin[(1-2n)t] - \frac{1-n}{1+2n} \sin[(1+2n)t], \right. \\ \left. 2 \cos t - \frac{1+n}{1-2n} \cos[(1-2n)t] - \frac{1-n}{1+2n} \cos[(1+2n)t], \right. \\ \left. \frac{1}{m} \cos(2nt) \right),$$

where, $m > 1$ or $m < -1$, Figure 2. Besides

$$\|\vec{\gamma}'_m(t)\| = v(t) = \frac{\sin(nt)}{\sqrt{m^2 - 1}}.$$

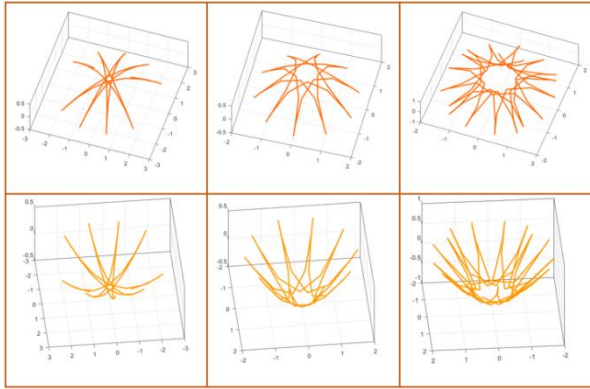


Figure 2. Salkowski curves for $m = -\frac{5}{2}, -\frac{5}{4}, -\frac{9}{8}, \frac{5}{2}, \frac{5}{4}, \frac{9}{8}$.

The Frenet vectors of $\vec{\gamma}_m(t)$ are (Ali, 2011)

$$\begin{cases} \vec{T}(t) = (\sin(nt)\cos t - n\cos(nt)\sin t, \\ \quad -\sin(nt)\sin t - n\cos(nt)\cos t, -\frac{n}{m}\cos(nt)) \quad (\text{sl}), \\ \vec{N}(t) = \frac{n}{m}(\sin t, \cos t, m) \quad (\text{tl}), \\ \vec{B}(t) = (-\cos(nt)\cos t - n\sin(nt)\sin t, \\ \quad \cos(nt)\sin t - n\sin(nt)\cos t, -\frac{n}{m}\sin(nt)) \quad (\text{sl}). \end{cases} \quad (3)$$

The timelike tangent indicatrix (\vec{T}) of $\vec{\gamma}_m(t)$ is a helix on S_1^2 , the spacelike principal normal indicatrix (\vec{N}) of $\vec{\gamma}_m(t)$ is a planar circle of radius $\frac{n}{m}$ on H_0^{2+} and the timelike binormal indicatrix (\vec{B}) of $\vec{\gamma}_m(t)$ is a helix on S_1^2 (Aksan and Gür Mazlum, 2023), Figure 3. Besides, for the curves

$$\begin{cases} v_T(t) = \|\vec{T}'(t)\| = \frac{n}{m}\sin(nt), \\ v_N(t) = \|\vec{N}'(t)\| = \frac{n}{m}, \\ v_B(t) = \|\vec{B}'(t)\| = \frac{n}{m}\cos(nt), \end{cases} \quad (4)$$

(Aksan and Gür Mazlum, 2023).

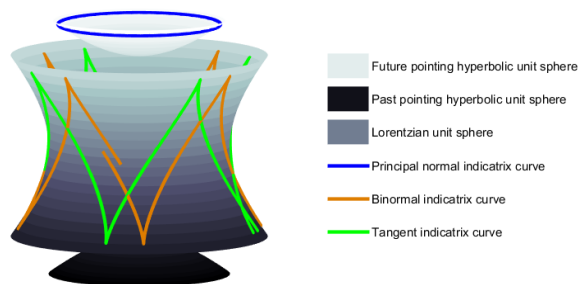


Figure 3. Spherical indicatrices on S_1^2 and H_0^2 of $\vec{\gamma}_m(t)$.

3.1. The Darboux Frame of the Tangent Indicatrix (\vec{T}) of $\vec{\gamma}_m(t)$

The Frenet frame $\{\vec{T}_T(t), \vec{N}_T(t), \vec{B}_T(t)\}$, curvature $\kappa_T(t)$ and torsion $\tau_T(t)$ of the timelike tangent indicatrix (\vec{T}) on S_1^2 of the curve $\vec{\gamma}_m(t)$ in E_1^3 are as follows, respectively (Aksan and Gür Mazlum, 2023):

$$\begin{cases} \vec{T}_T(t) = \left(\frac{n}{m}\sin t, \frac{n}{m}\cos t, n\right) \quad (\text{tl}), \\ \vec{N}_T(t) = (\cos t, -\sin t, 0) \quad (\text{sl}), \\ \vec{B}_T(t) = \left(n\sin t, n\cos t, \frac{n}{m}\right) \quad (\text{sl}), \\ \vec{F}_T(t) = (0, 0, 1) \quad (\text{tl}), \end{cases} \quad (5)$$

$$\kappa_T(t) = \frac{1}{\sin(nt)} \quad \text{and} \quad \tau_T(t) = \frac{m}{\sin(nt)}. \quad (6)$$

Theorem 3.1. The Darboux frame $\{\vec{T}_T(t), \vec{g}_T(t), \vec{n}_T(t)\}$ of the timelike tangent indicatrix (\vec{T}) on S_1^2 is as follows:

$$\begin{cases} \vec{T}_T(t) = \left(\frac{n}{m}\sin t, \frac{n}{m}\cos t, n\right) \quad (\text{tl}), \\ \vec{g}_T(t) = (-\cos(nt)\cos t - n\sin(nt)\sin t, \\ \quad \cos(nt)\sin t - n\sin(nt)\cos t, -\frac{n}{m}\sin(nt)) \quad (\text{sl}), \\ \vec{n}_T(t) = (\sin(nt)\cos t - n\cos(nt)\sin t, \\ \quad -\sin(nt)\sin t - n\cos(nt)\cos t, -\frac{n}{m}\cos(nt)) \quad (\text{sl}). \end{cases} \quad (7)$$

Proof: Since $\vec{T}_T(t)$ is timelike and $\vec{T}(t)$ is spacelike, $\vec{g}_T(t) = -\vec{T}(t) \wedge \vec{T}_T(t)$. From (3) and (5), we get the vector $\vec{g}_T(t)$ in (7). Besides, $\vec{T}(t)$ can be taken as the surface's normal for (\vec{T}) on S_1^2 , that is $\vec{n}_T(t) = \vec{T}(t)$ as in (3). Thus, the Darboux frame is obtained as in (7).

Theorem 3.2. The normal curvature $(\kappa_n)_T(t)$ of the tangent indicatrix (\vec{T}) on S_1^2 of $\vec{\gamma}_m(t)$ is as follows:

$$(\kappa_n)_T(t) = 1 \quad (8)$$

Proof: The normal curvature of (\vec{T}) is calculated by

$$(\kappa_n)_T(t) = \frac{\langle \vec{n}_T(t), \vec{T}''(t) \rangle}{v_T^2(t)}, \quad (9)$$

(Uğurlu and Çalışkan, 2012). From (3), we get

$$\begin{aligned} \overline{T}''(t) = & \left(\frac{n^2}{m^2} \sin(nt) \cos t + \frac{n^3}{m^2} \cos(nt) \sin t, \right. \\ & \left. -\frac{n^2}{m^2} \sin(nt) \sin t + \frac{n^3}{m^2} \cos(nt) \cos t, \frac{n^3}{m} \cos(nt) \right). \end{aligned} \quad (10)$$

From (7) and (10), we have

$$\langle \overline{n}_T(t), \overline{T}''(t) \rangle = \frac{n^2}{m^2} \sin^2(nt). \quad (11)$$

If we substitute (4) and (11) in (9), we obtain the normal curvature of (\overline{T}) as in (8).

Theorem 3.3. The geodesic curvature $(\kappa_g)_T(t)$ of the tangent indicatrix (\overline{T}) on S_1^2 of $\overline{\gamma}_m(t)$ is as follows:

$$(\kappa_g)_T(t) = -\frac{\cos(nt)}{\sin(nt)}. \quad (12)$$

Proof: The geodesic curvature $(\kappa_g)_T(t)$ of the tangent indicatrix (\overline{T}) is calculated by

$$(\kappa_g)_T(t) = \frac{\langle \overline{g}_T(t), \overline{T}''(t) \rangle}{v_T^2(t)}. \quad (13)$$

From (7) and (10), we have

$$\langle \overline{g}_T(t), \overline{T}''(t) \rangle = -\frac{n^2}{m^2} \cos(nt) \sin(nt). \quad (14)$$

If we substitute (4) and (14) in (13), we obtain the geodesic curvature of (\overline{T}) as in (12).

Theorem 3.4. The geodesic torsion $(\tau_g)_T(t)$ of the tangent indicatrix (\overline{T}) on S_1^2 of $\overline{\gamma}_m(t)$ is as follows:

$$(\tau_g)_T(t) = 0. \quad (15)$$

Proof: The geodesic torsion $(\tau_g)_T(t)$ of (\overline{T}) is calculated by

$$(\tau_g)_T(t) = -\frac{\langle \overline{g}_T(t), \overline{n}_T'(t) \rangle}{v_T^2(t)}. \quad (16)$$

From (7), we have

$$\overline{n}_T'(t) = \left(\frac{n^2}{m^2} \sin(nt) \sin t, \frac{n^2}{m^2} \sin(nt) \cos t, \frac{n^2}{m} \sin(nt) \right). \quad (17)$$

So, from (7) and (17), we get

$$\langle \overline{g}_T(t), \overline{n}_T'(t) \rangle = 0. \quad (18)$$

If we substitute (4) and (18) in (16), we obtain the geodesic torsion of (\overline{T}) as in (15).

Corollary 3.1. The timelike tangent indicatrix (\overline{T}) on S_1^2 of $\overline{\gamma}_m(t)$ is a curvature line.

Theorem 3.5. Let $\{\overline{T}_T(t), \overline{g}_T(t), \overline{n}_T(t)\}$ be Darboux frame of the timelike tangent indicatrix (\overline{T}) on S_1^2 of $\overline{\gamma}_m(t)$.

Darboux frame equations of (\overline{T}) are as follows:

$$\begin{bmatrix} \overline{T}_T'(t) \\ \overline{g}_T'(t) \\ \overline{n}_T'(t) \end{bmatrix} = \begin{bmatrix} 0 & -\frac{n}{m} \cos(nt) & \frac{n}{m} \sin(nt) \\ \frac{n}{m} \cos(nt) & 0 & 0 \\ \frac{n}{m} \sin(nt) & 0 & 0 \end{bmatrix} \begin{bmatrix} \overline{T}_T(t) \\ \overline{g}_T(t) \\ \overline{n}_T(t) \end{bmatrix}. \quad (19)$$

Proof: We can construct the following matrix equation between Darboux vectors and their derivatives:

$$\begin{bmatrix} \overline{T}_T'(t) \\ \overline{g}_T'(t) \\ \overline{n}_T'(t) \end{bmatrix} = \begin{bmatrix} a_1 & b_1 & c_1 \\ d_1 & e_1 & f_1 \\ k_1 & l_1 & m_1 \end{bmatrix} \begin{bmatrix} \overline{T}_T(t) \\ \overline{g}_T(t) \\ \overline{n}_T(t) \end{bmatrix}, \quad (20)$$

where $a_1, b_1, c_1, d_1, e_1, f_1, k_1, l_1, m_1$ are arbitrary functions of t . Now let's find these coefficients in order. From (20), we write the equation below:

$$\overline{T}_T'(t) = a_1 \overline{T}_T(t) + b_1 \overline{g}_T(t) + c_1 \overline{n}_T(t). \quad (21)$$

Let's apply the inner product of the vectors $\overline{T}_T'(t), \overline{g}_T(t)$ and $\overline{n}_T(t)$ to both sides of (21), respectively. So, we have

$$\begin{aligned} a_1 &= \langle \overline{T}_T'(t), \overline{T}_T(t) \rangle, \\ b_1 &= -\langle \overline{g}_T(t), \overline{T}_T'(t) \rangle, \\ c_1 &= \langle \overline{n}_T(t), \overline{T}_T'(t) \rangle. \end{aligned} \quad (22)$$

From (7), we get

$$\overline{T}_T'(t) = \left(\frac{n}{m} \cos t, -\frac{n}{m} \sin t, 0 \right). \quad (23)$$

From (7), (22) and (23), we have

$$a_1 = 0, \quad b_1 = -\frac{n}{m} \cos(nt), \quad c_1 = \frac{n}{m} \sin(nt). \quad (24)$$

From (20), we write the equation below:

$$\overline{g}_T'(t) = d_1 \overline{T}_T(t) + e_1 \overline{g}_T(t) + f_1 \overline{n}_T(t) \quad (25)$$

Let's apply the inner product of the vectors $\vec{T}_T(t)$, $\vec{g}_T(t)$ and $\vec{n}_T(t)$ to both sides of (25), respectively. So, we have

$$\begin{aligned} d_1 &= \langle \vec{T}_T(t), \vec{g}_T'(t) \rangle, \\ e_1 &= \langle \vec{g}_T(t), \vec{g}_T'(t) \rangle, \\ f_1 &= \langle \vec{n}_T(t), \vec{g}_T'(t) \rangle. \end{aligned} \tag{26}$$

From (7), we get

$$\vec{g}_T'(t) = -\frac{n^2}{m^2} \cos(nt) (\sin t, \cos t, 1). \tag{27}$$

From (7), (26) and (27), we have

$$d_1 = \frac{n}{m} \cos(nt), \quad e_1 = 0, \quad f_1 = 0. \tag{28}$$

From (20), we write the equation below:

$$\vec{n}_T'(t) = k_1 \vec{T}_T(t) + l_1 \vec{g}_T(t) + m_1 \vec{n}_T(t). \tag{29}$$

Let's apply the inner product of the vectors $\vec{T}_T(t)$, $\vec{g}_T(t)$ and $\vec{n}_T(t)$ to both sides of (29), respectively. So, we have

$$\begin{aligned} k_1 &= \langle \vec{T}_T(t), \vec{n}_T'(t) \rangle, \\ l_1 &= \langle \vec{g}_T(t), \vec{n}_T'(t) \rangle, \\ m_1 &= \langle \vec{n}_T(t), \vec{n}_T'(t) \rangle. \end{aligned} \tag{30}$$

From (7), (17) and (30), we have

$$k_1 = \frac{n}{m} \sin(nt), \quad l_1 = 0, \quad m_1 = 0. \tag{31}$$

If we substitute (24), (28) and (31) in (20), we get the expression (19).

Theorem 3.6. Let $\{\vec{T}_T(t), \vec{N}_T(t), \vec{B}_T(t)\}$ and $\{\vec{T}_T(t), \vec{g}_T(t), \vec{n}_T(t)\}$ be the Frenet and Darboux frames of the timelike tangent indicatrix (\vec{T}) on S_1^2 of $\vec{\gamma}_m(t)$, respectively. The real angle $\theta_T(t)$ between $\vec{n}_T(t)$ and $\vec{N}_T(t)$ is as follows:

$$\theta_T(t) = \frac{\pi}{2} + nt. \tag{32}$$

Proof: For the real angle $\theta_T(t)$ between the spacelike vectors $\vec{n}_T(t)$ and $\vec{N}_T(t)$, Figure 4, we write

$$\langle \vec{n}_T(t), \vec{N}_T(t) \rangle = \|\vec{n}_T(t)\| \|\vec{N}_T(t)\| \cos \theta_T(t). \tag{33}$$

Since $\vec{n}_T(t)$ and $\vec{N}_T(t)$ are unit vectors and using (5) and (7), from the inner product of these vectors in (33), we have

$$\langle \vec{n}_T(t), \vec{N}_T(t) \rangle = \sin(nt) = \cos \theta_T. \tag{34}$$

Similarly, using (5) and (7), from the inner product of $\vec{n}_T(t)$ and $\vec{B}_T(t)$, we get

$$\langle \vec{n}_T(t), \vec{B}_T(t) \rangle = \sin \theta_T(t) = -\cos(nt). \tag{35}$$

So, from (34) and (35), we obtain the expression (32).

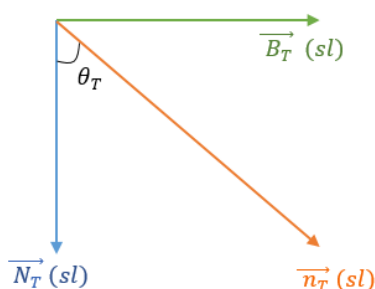


Figure 4. The real angle $\theta_T(t)$ between $\vec{n}_T(t)$ and $\vec{N}_T(t)$.

Theorem 3.7. The spacelike Darboux vector $\vec{W}_T(t)$ of Darboux frame of the timelike tangent indicatrix (\vec{T}) on S_1^2 of $\vec{\gamma}_m(t)$ is as follows:

$$\vec{W}_T(t) = \left(-\frac{n^2}{m} \sin t, -\frac{n^2}{m} \cos t, -\frac{n^2}{m^2} \right) \quad (sl). \tag{36}$$

Proof: For the Darboux vector $\vec{W}_T(t)$ belong to the Darboux frame, we know

$$\begin{aligned} \vec{T}_T'(t) &= \vec{W}_T(t) \wedge \vec{T}_T(t), \\ \vec{g}_T'(t) &= \vec{W}_T(t) \wedge \vec{g}_T(t), \\ \vec{n}_T'(t) &= \vec{W}_T(t) \wedge \vec{n}_T(t), \end{aligned} \tag{37}$$

(Uğurlu and Çalıřkan, 2012). From (37), using (7) and (17), we have (36).

Corollary 3.2. The spacelike Darboux vector $\vec{W}_T(t)$ of Darboux frame of timelike tangent indicatrix (\vec{T}) on S_1^2 of $\vec{\gamma}_m(t)$ is as follows:

$$\vec{W}_T(t) = \frac{n}{m} \sin(nt) \vec{g}_T(t) + \frac{n}{m} \cos(nt) \vec{n}_T(t). \tag{38}$$

Proof: We write the vector $\vec{W}_T(t)$ as follows:

$$\vec{W}_T(t) = \rho \vec{T}_T(t) + \sigma \vec{g}_T(t) + \zeta \vec{n}_T(t), \tag{39}$$

where ρ, σ, ζ are arbitrary functions of t . For (32) and (37) to be satisfied simultaneously, we have

$$\begin{aligned} \rho &= \nu_T(t) (\tau_g)_T(t), \\ \sigma &= \nu_T(t) (\kappa_n)_T(t), \\ \zeta &= -\nu_T(t) (\kappa_g)_T(t) \end{aligned}$$

in (39). If we substitute these values in (39), we obtain

$$\overline{W}_T(t) = \nu_T(t) \begin{bmatrix} (\tau_g)_T(t) \overline{T}_T(t) + (\kappa_n)_T(t) \overline{g}_T(t) \\ -(\kappa_g)_T(t) \overline{n}_T(t) \end{bmatrix}, \quad (40)$$

(Uğurlu and Çalışkan, 2012). If we substitute (4), (8), (12) and (15) in (40), we get (38). Moreover, if we substitute (8) in (39) also, it is clear that we get the expression (37).

Theorem 3.8. There are the following relations between the normal curvature $(K_n)_T(t)$, geodesic curvature $(K_g)_T(t)$, geodesic torsion $(\tau_g)_T(t)$ and torsion $\tau_T(t)$, curvature $K_T(t)$ of the timelike tangent indicatrix (\overline{T}) on S_1^2 of $\overline{\gamma}_m(t)$:

$$\begin{cases} (\kappa_n)_T(t) = \kappa_T(t) \sin(nt), \\ (\kappa_g)_T(t) = -\kappa_T(t) \cos(nt), \\ (\tau_g)_T(t) = \tau_T(t) - \frac{m}{\sin(nt)}. \end{cases} \quad (41)$$

Proof: For Darboux vector $\overline{F}_T(t)$ of Frenet frame of (\overline{T}) , we write

$$\overline{T}'_T(t) = \overline{F}_T(t) \wedge \overline{T}_T(t), \quad (42)$$

(Uğurlu and Çalışkan, 2012). From the equality of (37) and (42), we have

$$\overline{T}'_T(t) \wedge (\overline{F}_T(t) - \overline{W}_T(t)) = \vec{0}, \quad (43)$$

where

$$\overline{F}_T(t) = (0, 0, 1) = \nu_T(t) [\tau_T(t) \overline{T}_T(t) - \kappa_T(t) \overline{B}_T(t)] \quad (44)$$

(Aksan and Gür Mazlum, 2023). If we substitute (40) and (44) in (43), we get

$$\kappa_T(t) \overline{N}_T(t) - (\kappa_n)_T(t) \overline{n}_T(t) - (\kappa_g)_T(t) \overline{g}_T(t) = \vec{0}. \quad (45)$$

If we apply the inner product with $\overline{n}_T(t)$ and $\overline{g}_T(t)$ on both

sides of (45), respectively, we get

$$\begin{cases} (\kappa_n)_T(t) = \kappa_T(t) \langle \overline{N}_T(t), \overline{n}_T(t) \rangle \\ \quad - (\kappa_g)_T(t) \langle \overline{g}_T(t), \overline{n}_T(t) \rangle, \\ (\kappa_g)_T(t) = \kappa_T(t) \langle \overline{N}_T(t), \overline{g}_T(t) \rangle \\ \quad - (\kappa_n)_T(t) \langle \overline{g}_T(t), \overline{n}_T(t) \rangle. \end{cases} \quad (46)$$

From (5) and (7), we get

$$\langle \overline{N}_T(t), \overline{g}_T(t) \rangle = -\cos(nt). \quad (47)$$

If we substitute (34) and (47) in (46), we have

$$\begin{aligned} (\kappa_n)_T(t) &= \kappa_T(t) \sin(nt), \\ (\kappa_g)_T(t) &= -\kappa_T(t) \cos(nt). \end{aligned} \quad (48)$$

Besides, if we take the derivative of both sides of $\langle \overline{n}_T(t), \overline{N}_T(t) \rangle = \sinh \theta_T(t)$ in (34), we get

$$\langle \overline{N}_T(t), \overline{n}'_T(t) \rangle + \langle \overline{N}'_T(t), \overline{n}_T(t) \rangle = -\sin \theta_T(t) \frac{d\theta_T(t)}{dt}. \quad (49)$$

From the derivative formulas (Uğurlu and Çalışkan, 2012), we obtain

$$\begin{aligned} \nu_T(t) \left((\tau_g)_T(t) \langle \overline{N}_T(t), \overline{g}_T(t) \rangle - \tau_T(t) \langle \overline{B}_T(t), \overline{n}_T(t) \rangle \right) \\ = -\sin \theta_T(t) \frac{d\theta_T(t)}{dt}. \end{aligned} \quad (50)$$

If we substitute (32), (35) and (47) in (50), we have

$$(\tau_g)_T(t) = \tau_T(t) - \frac{1}{\nu_T(t)} \frac{d\theta_T}{dt}. \quad (51)$$

Also, from (4) and (32), we get

$$(\tau_g)_T(t) = \tau_T(t) - \frac{m}{\sin(nt)}. \quad (52)$$

From (48) and (52), we obtain (41).

Theorem 3.9. Let $\{\overline{T}_T(t), \overline{N}_T(t), \overline{B}_T(t)\}$ and $\{\overline{T}_T(t), \overline{g}_T(t), \overline{n}_T(t)\}$ be the Frenet and Darboux frames of the timelike tangent indicatrix (\overline{T}) on S_1^2 of $\overline{\gamma}_m(t)$, respectively. There is the following relationship between these frames:

$$\begin{bmatrix} \overline{T}_T(t) \\ \overline{N}_T(t) \\ \overline{B}_T(t) \end{bmatrix} = \begin{bmatrix} 1 & 0 & 0 \\ 0 & -\cos(nt) & \sin(nt) \\ 0 & -\sin(nt) & -\cos(nt) \end{bmatrix} \begin{bmatrix} \overline{T}_T(t) \\ \overline{g}_T(t) \\ \overline{n}_T(t) \end{bmatrix}. \quad (53)$$

Proof: We can construct the following matrix equation between the vectors of the Frenet and Darboux frames:

$$\begin{bmatrix} \overline{T}_T(t) \\ \overline{N}_T(t) \\ \overline{B}_T(t) \end{bmatrix} = \begin{bmatrix} a_2 & b_2 & c_2 \\ d_2 & e_2 & f_2 \\ k_2 & l_2 & m_2 \end{bmatrix} \begin{bmatrix} \overline{T}_T(t) \\ \overline{g}_T(t) \\ \overline{n}_T(t) \end{bmatrix}, \quad (54)$$

where $a_2, b_2, c_2, d_2, e_2, f_2, k_2, l_2, m_2$ are arbitrary functions of t . Now let's find these coefficients in order. From (54), we write the equation below:

$$\overline{T}_T(t) = a_2 \overline{T}_T(t) + b_2 \overline{g}_T(t) + c_2 \overline{n}_T(t). \quad (55)$$

Let's apply the inner product of the vectors $\overline{T}_T(t), \overline{g}_T(t)$ and $\overline{n}_T(t)$ to both sides of (55), respectively. So, it is clear that

$$a_2 = 1, \quad b_2 = 0, \quad c_2 = 0. \quad (56)$$

Similarly, from (54), we write

$$\overline{N}_T(t) = d_2 \overline{T}_T(t) + e_2 \overline{g}_T(t) + f_2 \overline{n}_T(t). \quad (57)$$

Let's apply the inner product of the vectors $\overline{T}_T(t), \overline{g}_T(t)$ and $\overline{n}_T(t)$ to both sides of (57), respectively. From (34) and (47), we get

$$d_2 = 0, \quad e_2 = -\cos(nt), \quad f_2 = \sin(nt). \quad (58)$$

Similarly, from (54), we write

$$\overline{B}_T(t) = k_2 \overline{T}_T(t) + l_2 \overline{g}_T(t) + m_2 \overline{n}_T(t). \quad (59)$$

Let's apply the inner product of the vectors $\overline{T}_T(t), \overline{g}_T(t)$ and $\overline{n}_T(t)$ to both sides of (59), respectively. From (35) and (59), we have

$$k_2 = 0, \quad l_2 = -\sin(nt), \quad m_2 = \cos(nt). \quad (60)$$

If we substitute (56), (58) and (60) in (54), we obtain the expression (53).

Theorem 3.10. Let $\{\overline{T}_T(t), \overline{g}_T(t), \overline{n}_T(t)\}$ be the Darboux frame of the timelike tangent indicatrix (\vec{T}) on S_1^2 of $\overline{\gamma}_m(t)$. There is the following relationship between the Darboux vectors $\overline{F}_T(t)$ and $\overline{W}_T(t)$ belong to the Frenet and Darboux frames, respectively:

$$\overline{W}_T(t) = \overline{F}_T(t) - n \overline{T}_T(t). \quad (61)$$

Proof: It is clear that (5), (36) and (44).

Theorem 3.11. The real angle $\varphi_T(t)$ between $\overline{W}_T(t)$ and $\overline{g}_T(t)$ of the timelike tangent indicatrix (\vec{T}) on S_1^2 of $\overline{\gamma}_m(t)$ is as follows:

$$\varphi_T(t) = \arcsin\left(\frac{n}{m}\right) + nt. \quad (62)$$

Proof: For the real angle $\varphi_T(t)$ between the unit spacelike vectors $\overline{W}_T(t)$ and $\overline{g}_T(t)$, Figure 5, we write

$$\langle \overline{g}_T(t), \overline{W}_T(t) \rangle = \cos \varphi_T(t). \quad (63)$$

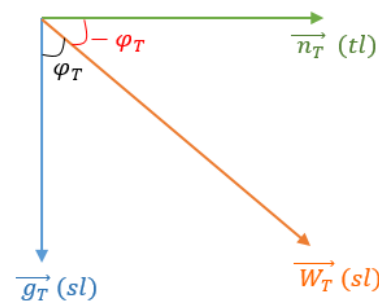


Figure 5. The real angle $\varphi_T(t)$ between $\overline{W}_T(t)$ and $\overline{g}_T(t)$.

Besides, since timelike $\overline{n}_T(t)$ and spacelike $\overline{g}_T(t)$ are perpendicular, the angle between them is zero in the Lorentzian sense, we write

$$\langle \overline{n}_T(t), \overline{W}_T(t) \rangle = \sinh(-\varphi_T(t)) = -\sinh \varphi_T(t). \quad (64)$$

On the other hand, from (7) and (36), we get

$$\langle \overline{g}_T(t), \overline{W}_T(t) \rangle = \frac{n}{m} \sin(nt), \quad (65)$$

$$\langle \overline{n}_T(t), \overline{W}_T(t) \rangle = \frac{n}{m} \cos(nt).$$

From (66), (67) and (68), we obtain

$$\cosh \varphi_T(t) = \frac{n}{m} \sin(nt), \quad (66)$$

$$\sinh \varphi_T(t) = -\frac{n}{m} \cos(nt).$$

From (66), we get

$$\begin{aligned} & \cosh \varphi_T(t) \sin(nt) - \sinh \varphi_T(t) \cos(nt) \\ &= \sin(\varphi_T(t) - nt) = \frac{n}{m}. \end{aligned} \quad (67)$$

3.2. The Darboux Frame of the Principal Normal indicatrix of $\overrightarrow{\gamma}_m(t)$

The Frenet frame $\{\overrightarrow{T}_N(t), \overrightarrow{N}_N(t), \overrightarrow{B}_N(t)\}$, Darboux vector belong to Frenet frame $F_N(t)$, curvature $K_N(t)$ and torsion $\tau_N(t)$ of spacelike principal normal indicatrix (\overrightarrow{N}) on H_0^{2+} of $\overrightarrow{\gamma}_m(t)$ are

$$\begin{cases} \overrightarrow{T}_N(t) = (\cos t, -\sin t, 0) & (\text{sl}), \\ \overrightarrow{N}_N(t) = (-\sin t, -\cos t, 0) & (\text{sl}), \\ \overrightarrow{B}_N(t) = (0, 0, -1) & (\text{tl}), \\ \overrightarrow{F}_N(t) = (0, 0, 1) & (\text{tl}), \end{cases} \quad (68)$$

$$\kappa_N(t) = \frac{m}{n} \quad \text{and} \quad \tau_N(t) = 0, \quad (69)$$

respectively, (Uğurlu and Çalışkan, 2012).

Theorem 4.1. The Darboux frame $\{\overrightarrow{T}_N(t), \overrightarrow{g}_N(t), \overrightarrow{n}_N(t)\}$ of spacelike principal normal indicatrix (\overrightarrow{N}) on H_0^{2+} of $\overrightarrow{\gamma}_m(t)$ is as follows:

$$\begin{cases} \overrightarrow{T}_N(t) = (\cos t, -\sin t, 0) & (\text{sl}), \\ \overrightarrow{g}_N(t) = \left(n \sin t, n \cos t, \frac{n}{m} \right) & (\text{sl}), \\ \overrightarrow{n}_N(t) = \left(\frac{n}{m} \sin t, \frac{n}{m} \cos t, n \right) & (\text{tl}). \end{cases} \quad (70)$$

Proof: Since $\overrightarrow{T}_N(t)$ is spacelike and $\overrightarrow{N}(t)$ is timelike, $\overrightarrow{g}_N(t) = -N(t) \wedge \overrightarrow{T}_N(t)$. From (3) and (68), we get the vector $\overrightarrow{g}_N(t)$ in (70). Besides, $\overrightarrow{N}(t)$ can be taken as the normal vector of the surface for (\overrightarrow{N}) on H_0^{2+} , that is $\overrightarrow{n}(t) = \overrightarrow{N}(t)$ as in (3). Thus, the Darboux frame is as in (70).

Theorem 4.2. The normal curvature $(K_n)_N(t)$ of principal normal indicatrix (\overrightarrow{N}) on H_0^{2+} of $\overrightarrow{\gamma}_m(t)$ is as follows:

$$(K_n)_N(t) = 1. \quad (71)$$

Proof: The normal curvature of (\overrightarrow{N}) is calculated by

$$(K_n)_N(t) = -\frac{\langle \overrightarrow{n}_N(t), \overrightarrow{N}''(t) \rangle}{v_N^2(t)}, \quad (72)$$

(Uğurlu and Çalışkan, 2012). From (3), we obtain

$$\overrightarrow{N}''(t) = \left(-\frac{n}{m} \sin t, -\frac{n}{m} \cos t, 0 \right). \quad (73)$$

From (70) and (73), we have

$$\langle \overrightarrow{n}_N(t), \overrightarrow{N}''(t) \rangle = -\frac{n^2}{m^2}. \quad (74)$$

If we substitute (4) and (74) in (72), we obtain the normal curvature of (\overrightarrow{N}) as in (71).

Theorem 4.3. The geodesic curvature $(K_g)_N(t)$ of principal normal indicatrix (\overrightarrow{N}) on H_0^{2+} of $\overrightarrow{\gamma}_m(t)$ is as follows:

$$(K_g)_N(t) = -m. \quad (75)$$

Proof: $(K_g)_N(t)$ for (\overrightarrow{N}) is calculated by

$$(K_g)_N(t) = \frac{\langle \overrightarrow{g}_N(t), \overrightarrow{N}''(t) \rangle}{v_N^2(t)}, \quad (76)$$

(Uğurlu and Çalışkan, 2012). From (70) and (73), we get

$$\langle \overrightarrow{g}_N(t), \overrightarrow{N}''(t) \rangle = -\frac{n^2}{m}. \quad (77)$$

If we substitute (4) and (77) in (76), we obtain the geodesic curvature of (\overrightarrow{N}) as in (75).

Theorem 4.4. The geodesic torsion $(\tau_g)_N(t)$ of principal normal indicatrix (\overrightarrow{N}) on H_0^{2+} of $\overrightarrow{\gamma}_m(t)$ is as follows:

$$(\tau_g)_N(t) = 0. \quad (78)$$

Proof: $(\tau_g)_N(t)$ for (\overrightarrow{N}) is calculated by

$$(\tau_g)_N(t) = -\frac{\langle \overrightarrow{g}_N(t), \overrightarrow{n}_N'(t) \rangle}{v_N^2(t)}, \quad (79)$$

(Uğurlu and Çalışkan, 2012). From (7), we have

$$\overrightarrow{n}_N'(t) = \left(\frac{n}{m} \cos t, -\frac{n}{m} \sin t, 0 \right). \quad (80)$$

So, from (7) and (80), we get

$$\langle \overrightarrow{g}_N(t), \overrightarrow{n}_N'(t) \rangle = 0. \quad (81)$$

If we substitute (4) and (81) in (79), we obtain the geodesic torsion of (\overrightarrow{N}) as in (78).

Corollary 4.1. The spacelike principal normal indicatrix (\overrightarrow{N}) on H_0^{2+} of $\overrightarrow{\gamma}_m(t)$ is a curvature line.

Theorem 4.5. Let $\{\overrightarrow{T}_N(t), \overrightarrow{g}_N(t), \overrightarrow{n}_N(t)\}$ be Darboux frame of spacelike principal normal indicatrix (\overrightarrow{N}) on H_0^{2+} of $\overrightarrow{\gamma}_m(t)$. Darboux frame equations of (\overrightarrow{N}) are as follows:

$$\begin{bmatrix} \overrightarrow{T'_N}(t) \\ \overrightarrow{g'_N}(t) \\ \overrightarrow{n'_N}(t) \end{bmatrix} = \begin{bmatrix} 0 & -n & \frac{n}{m} \\ n & 0 & 0 \\ \frac{n}{m} & 0 & 0 \end{bmatrix} \begin{bmatrix} \overrightarrow{T_N}(t) \\ \overrightarrow{g_N}(t) \\ \overrightarrow{n_N}(t) \end{bmatrix}.$$

Proof: The proof can be done similarly to the proof of Theorem 3.5.

Theorem 4.6. Let $\{\overrightarrow{T_N}(t), \overrightarrow{N_N}(t), \overrightarrow{B_N}(t)\}$ and $\{\overrightarrow{T_N}(t), \overrightarrow{g_N}(t), \overrightarrow{n_N}(t)\}$ be Frenet and Darboux frames of spacelike principal normal indicatrix (\vec{N}) on H_0^{2+} of $\overrightarrow{\gamma_m}(t)$, respectively. The hyperbolic angle $\theta_N(t)$ between $\overrightarrow{B_N}(t)$ and $\overrightarrow{n_N}(t)$ is as follows:

$$\theta_N(t) = \operatorname{arctan} h\left(\frac{1}{m}\right) = \frac{1}{2} \ln\left(\frac{m+1}{m-1}\right). \quad (82)$$

Proof: From the inner product of $\overrightarrow{B_N}(t)$ and $\overrightarrow{n_N}(t)$ in (68) and (70), for the angle $\theta_N(t)$ between unit timelike vectors $\overrightarrow{B_N}(t)$ (future pointing) and $\overrightarrow{n_N}(t)$ (past pointing), Figure 6, we have

$$\langle \overrightarrow{B_N}(t), \overrightarrow{n_N}(t) \rangle = \cosh \theta_N = n. \quad (83)$$

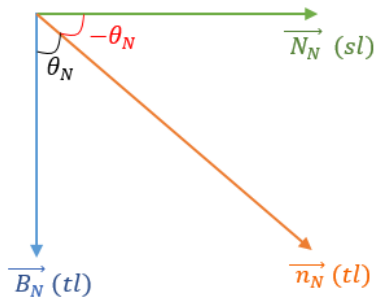


Figure 6. The real angle $\theta_N(t)$ between $\overrightarrow{B_N}(t)$ and $\overrightarrow{n_N}(t)$.

Similarly, from inner product of unit spacelike $\overrightarrow{N_N}(t)$ and unit timelike $\overrightarrow{n_N}(t)$ vectors, (here since timelike $\overrightarrow{B_N}(t)$ and spacelike $\overrightarrow{N_N}(t)$ are perpendicular, the angle between them is zero in the Lorentzian sense), we have

$$\langle \overrightarrow{N_N}(t), \overrightarrow{n_N}(t) \rangle = \sinh(-\theta_N) = -\sinh(\theta_N) = -\frac{n}{m}. \quad (84)$$

So, from (83) and (84), we obtain the expression (82).

Theorem 4.7. The timelike Darboux vector $\overrightarrow{W_N}(t)$ of Darboux frame of spacelike principal normal indicatrix (\vec{N}) on H_0^{2+} of $\overrightarrow{\gamma_m}(t)$ is as follows:

$$\overrightarrow{W_N}(t) = (0, 0, 1) \quad (tl). \quad (85)$$

Proof: For the Darboux vector $\overrightarrow{W_N}(t)$ belong to the Darboux frame, we know

$$\begin{aligned} \overrightarrow{T'_N}(t) &= \overrightarrow{W_N}(t) \wedge \overrightarrow{T_N}(t), \\ \overrightarrow{g'_N}(t) &= \overrightarrow{W_N}(t) \wedge \overrightarrow{g_N}(t), \\ \overrightarrow{n'_N}(t) &= \overrightarrow{W_N}(t) \wedge \overrightarrow{n_N}(t), \end{aligned} \quad (86)$$

(Uğurlu and Çalışkan, 2012). From (86), using (70) and (80), we get (85).

Corollary 4.2. The timelike Darboux vector $\overrightarrow{W_N}(t)$ of Darboux frame of spacelike principal normal indicatrix (\vec{N}) on H_0^{2+} of $\overrightarrow{\gamma_m}(t)$ is as follows:

$$\overrightarrow{W_N}(t) = -\frac{n}{m} \overrightarrow{g_N}(t) + n \overrightarrow{n_N}(t).$$

Proof: The proof can be done similarly to Corollary 3.2.

Theorem 4.8. There are the following relations between the normal curvature $(K_n)_N(t)$, geodesic curvatures $(K_g)_N(t)$, geodesic torsion $(\tau_g)_N(t)$ and curvature $K_N(t)$, torsion $\tau_N(t)$ of spacelike principal normal indicatrix (\vec{N}) on H_0^{2+} of $\overrightarrow{\gamma_m}(t)$:

$$\begin{cases} (\kappa_n)_N(t) = \frac{n}{m} \kappa_N(t), \\ (\kappa_g)_N(t) = -n \kappa_N(t), \\ (\tau_g)_N(t) = \tau_N(t). \end{cases}$$

Proof: The proof is similar to Theorem 3.8.

Theorem 4.9. Let $\{\overrightarrow{T_N}(t), \overrightarrow{N_N}(t), \overrightarrow{B_N}(t)\}$ and $\{\overrightarrow{T_N}(t), \overrightarrow{g_N}(t), \overrightarrow{n_N}(t)\}$ be the Frenet and Darboux frames of spacelike principal normal indicatrix (\vec{N}) on H_0^{2+} of $\overrightarrow{\gamma_m}(t)$, respectively. There is the following relation between the frames:

$$\begin{bmatrix} \overrightarrow{T_N}(t) \\ \overrightarrow{N_N}(t) \\ \overrightarrow{B_N}(t) \end{bmatrix} = \begin{bmatrix} 1 & 0 & 0 \\ 0 & -n & -\frac{n}{m} \\ 0 & -\frac{n}{m} & -n \end{bmatrix} \begin{bmatrix} \overrightarrow{T_N}(t) \\ \overrightarrow{g_N}(t) \\ \overrightarrow{n_N}(t) \end{bmatrix}.$$

Proof: The proof can be done similarly to Theorem 3.9.

Theorem 4.10. Let $\{\overrightarrow{T_N}(t), \overrightarrow{g_N}(t), \overrightarrow{n_N}(t)\}$ be Darboux frame of spacelike principal normal indicatrix (\vec{N}) on H_0^{2+} of $\overrightarrow{\gamma_m}(t)$. There is the following relation between Darboux vectors $\overrightarrow{F_N}(t)$ and $\overrightarrow{W_N}(t)$ belong to the Frenet and Darboux frames, respectively:

$$\overrightarrow{W_N}(t) = \overrightarrow{F_N}(t).$$

Proof: It is clear that (68) and (85).

Theorem 4.11. The hyperbolic angle $\varphi_N(t)$ between $\overline{W}_N(t)$ and $\overline{n}_N(t)$ of spacelike principal normal indicatrix (\overline{N}) on H_0^{2+} of $\overline{\gamma}_m(t)$ is as follows:

$$\varphi_N(t) = \operatorname{arctanh} \left(\frac{1}{m} \right). \quad (87)$$

Proof: For hyperbolic angle $\varphi_N(t)$ between unit timelike (past pointing) vectors $\overline{W}_N(t)$ and $\overline{n}_N(t)$, Figure 7, we know

$$\langle \overline{n}_N(t), \overline{W}_N(t) \rangle = -\cosh \varphi_N(t). \quad (88)$$

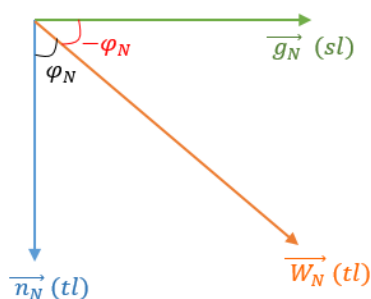


Figure 7. The real angle $\varphi_N(t)$ between $\overline{W}_N(t)$ and $\overline{n}_N(t)$.

Besides, since timelike $\overline{n}_N(t)$ and spacelike $\overline{g}_N(t)$ are perpendicular, the angle between them is zero in the Lorentzian sense, we have

$$\langle \overline{g}_N(t), \overline{W}_N(t) \rangle = \sinh(-\varphi_N(t)) = -\sinh \varphi_N(t). \quad (89)$$

On the other hand, from (70) and (85), we get

$$\langle \overline{n}_N(t), \overline{W}_N(t) \rangle = -n, \quad \langle \overline{g}_N(t), \overline{W}_N(t) \rangle = -\frac{n}{m}. \quad (90)$$

From (88), (89) and (90), we obtain

$$\cosh \varphi_N(t) = n \quad \text{and} \quad \sinh \varphi_N(t) = \frac{n}{m}. \quad (91)$$

From (91), we have (87).

3.3. The Darboux Frame of Binormal Indicatrix (\overline{B}) of $\overline{\gamma}_m(t)$

The Frenet frame $\{\overline{T}_B(t), \overline{N}_B(t), \overline{B}_B(t)\}$, Darboux vector belong to Frenet frame $\overline{F}_B(t)$, curvature $K_B(t)$ and torsion $\tau_B(t)$ of the timelike binormal indicatrix (\overline{B}) on S_1^2 of $\overline{\gamma}_m(t)$ are

$$\begin{cases} \overline{T}_B(t) = \left(-\frac{n}{m} \sin t, -\frac{n}{m} \cos t, -n \right) & (\text{tl}), \\ \overline{N}_B(t) = (-\cos t, \sin t, 0) & (\text{sl}), \\ \overline{B}_B(t) = \left(n \sin t, n \cos t, \frac{n}{m} \right) & (\text{sl}), \\ \overline{F}_B(t) = (0, 0, 1), \end{cases} \quad (92)$$

$$\kappa_B(t) = \frac{1}{\cos(nt)} \quad \text{and} \quad \tau_B(t) = -\frac{m}{\cos(nt)} \quad (93)$$

respectively, (Uğurlu and Çalışkan, 2012).

Theorem 5.1. The Darboux frame $\{\overline{T}_B(t), \overline{g}_B(t), \overline{n}_B(t)\}$, of the timelike binormal indicatrix (\overline{B}) on S_1^2 of $\overline{\gamma}_m(t)$ is as follows:

$$\begin{cases} \overline{T}_B(t) = \left(-\frac{n}{m} \sin t, -\frac{n}{m} \cos t, -n \right) & (\text{tl}), \\ \overline{g}_B(t) = \left(\sin(nt) \cos t - n \cos(nt) \sin t, \right. \\ \quad \left. \sin(nt) \sin t - n \cos(nt) \cos t, -\frac{n}{m} \cos(nt) \right) & (\text{sl}), \\ \overline{n}_B(t) = \left(-\cos(nt) \cos t - n \sin(nt) \sin t, \right. \\ \quad \left. \cos(nt) \sin t - n \sin(nt) \cos t, -\frac{n}{m} \sin(nt) \right) & (\text{sl}). \end{cases} \quad (94)$$

Proof: Since $\overline{T}_B(t)$ is timelike and $\overline{B}(t)$ is spacelike, $\overline{g}_B(t) = -\overline{B}(t) \wedge \overline{T}_B(t)$. From (3) and (92), we get the vector $\overline{g}_B(t)$ in (94). Besides $\overline{B}(t)$ of $\overline{\gamma}_m(t)$ can be taken as the normal vector of the surface for (\overline{B}) on S_1^2 , that is $\overline{n}_B(t) = \overline{B}(t)$ as in (3). Thus, Darboux frame is as in (94).

Theorem 5.2. The normal curvature $(K_n)_B(t)$ of binormal indicatrix (\overline{B}) on S_1^2 of $\overline{\gamma}_m(t)$ is as follows:

$$(\kappa_n)_B(t) = 1. \quad (95)$$

Proof: The normal curvature of (\overline{B}) is calculated by

$$(\kappa_n)_B(t) = \frac{\langle \overline{n}_B(t), \overline{B}''(t) \rangle}{v_B^2(t)}, \quad (96)$$

(Uğurlu and Çalışkan, 2012). From (3), we get

$$\overline{B}''(t) = \frac{n^2}{m^2} \left(-\cos(nt) \cos t + n \sin(nt) \sin t, \right. \\ \left. \cos(nt) \sin t + n \sin(nt) \cos t, nm \sin(nt) \right). \quad (97)$$

From (94) and (97), we have

$$\langle \overline{n}_B(t), \overline{B}''(t) \rangle = \frac{n^2}{m^2} \cos^2(nt). \quad (98)$$

If we substitute (4) and (98) in (96), we obtain the normal curvature of (\overline{B}) as in (95).

Theorem 5.3. The geodesic curvature $(K_g)_B(t)$ of binormal indicatrix (\overline{B}) on S_1^2 of $\overline{\gamma}_m(t)$ is as follows:

$$(\kappa_g)_B(t) = -\frac{\sin(nt)}{\cos(nt)}. \quad (99)$$

Proof: $(\kappa_g)_B(t)$ for (\vec{B}) is calculated by

$$(\kappa_g)_B(t) = \frac{\langle \overline{g_B}(t), \overline{B''}(t) \rangle}{v_B^2(t)}. \quad (100)$$

(Uğurlu and Çalışkan, 2012). From (94) and (97), we have

$$\langle \overline{g_B}(t), \overline{B''}(t) \rangle = -\frac{n^2}{m^2} \cos(nt) \sin(nt). \quad (101)$$

If we substitute (4) and (101) in (100), we obtain the geodesic curvature of (\vec{B}) as in (99).

Theorem 5.4. The geodesic torsion $(\tau_g)_B(t)$ of binormal indicatrix (\vec{B}) on S_1^2 of $\overline{\gamma_m}(t)$ is as follows:

$$(\tau_g)_B(t) = 0. \quad (102)$$

Proof: $(\tau_g)_B(t)$ for (\vec{B}) is calculated by

$$(\tau_g)_B(t) = -\frac{\langle \overline{g_B}(t), \overline{n_B}'(t) \rangle}{v_B^2(t)}, \quad (103)$$

(Uğurlu and Çalışkan, 2012). From (7), we have

$$\overline{n_B}'(t) = -\left(\frac{n^2}{m^2} \cos(nt) \sin t, \frac{n^2}{m^2} \cos(nt) \cos t, \frac{n^2}{m} \cos(nt) \right). \quad (104)$$

So, from (7) and (104), we get

$$\langle \overline{n_B}'(t), \overline{g_B}(t) \rangle = 0. \quad (105)$$

If we substitute (4) and (105) in (103), we obtain the geodesic torsion of (\vec{B}) as in (102).

Corollary 5.1. The timelike binormal indicatrix (\vec{B}) on S_1^2 of $\overline{\gamma_m}(t)$ is a curvature line.

Theorem 5.5. Let $\{\overline{T_B}(t), \overline{g_B}(t), \overline{n_B}(t)\}$ be Darboux frame of timelike binormal indicatrix (\vec{B}) on S_1^2 of $\overline{\gamma_m}(t)$. Darboux frame equations of (\vec{B}) are as follows:

$$\begin{bmatrix} \overline{T_B}'(t) \\ \overline{g_B}'(t) \\ \overline{n_B}'(t) \end{bmatrix} = \begin{bmatrix} 0 & -\frac{n}{m} \sin(nt) & \frac{n}{m} \cos(nt) \\ -\frac{n}{m} \sin(nt) & 0 & 0 \\ \frac{n}{m} \cos(nt) & 0 & 0 \end{bmatrix} \begin{bmatrix} \overline{T_B}(t) \\ \overline{g_B}(t) \\ \overline{n_B}(t) \end{bmatrix}$$

Proof: The proof can be done similarly to Theorem 3.5.

Theorem 5.6. Let $\{\overline{T_B}(t), \overline{N_B}(t), \overline{B_B}(t)\}$ and $\{\overline{T_B}(t), \overline{g_B}(t), \overline{n_B}(t)\}$ be the Frenet and Darboux frames of the timelike binormal indicatrix (\vec{B}) on S_1^2 of $\overline{\gamma_m}(t)$,

respectively. The angle $\theta_B(t)$ between $\overline{N_B}(t)$ and $\overline{n_B}(t)$ is as follows:

$$\theta_B(t) = -nt. \quad (106)$$

Proof: From the inner product of $\overline{N_B}(t)$ and $\overline{n_B}(t)$ in (92) and (94), for the real angle $\theta_B(t)$ between unit spacelike vectors $\overline{N_B}(t)$ and $\overline{n_B}(t)$, Figure 8, we get

$$\langle \overline{N_B}(t), \overline{n_B}(t) \rangle = \cos \theta_B(t) = \cos(nt). \quad (107)$$

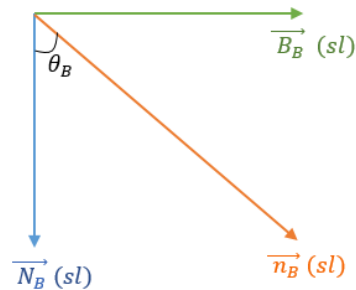


Figure 8. The real angle $\theta_B(t)$ between $\overline{N_B}(t)$ and $\overline{n_B}(t)$.

Similarly, we have

$$\langle \overline{B_B}(t), \overline{n_B}(t) \rangle = \sin \theta_B(t) = -\sin(nt). \quad (108)$$

So, from (107) and (108), we obtain the expression (106).

Theorem 5.7. The spacelike Darboux vector $\overline{W_B}(t)$ of Darboux frame of the timelike binormal indicatrix (\vec{B}) on S_1^2 of $\overline{\gamma_m}(t)$ is as follows:

$$\overline{W_B}(t) = \left(-\frac{n^2}{m} \sin t, -\frac{n^2}{m} \cos t, -\frac{n^2}{m} \right) \text{ (sl)}. \quad (109)$$

Proof: For the Darboux vector $\overline{W_B}(t)$ belong to the Darboux frame, we know

$$\begin{aligned} \overline{T_B}'(t) &= \overline{W_B}(t) \wedge \overline{T_B}(t), \\ \overline{g_B}'(t) &= \overline{W_B}(t) \wedge \overline{g_B}(t), \\ \overline{n_B}'(t) &= \overline{W_B}(t) \wedge \overline{n_B}(t), \end{aligned} \quad (110)$$

(Uğurlu and Çalışkan, 2012). From (110), using (94) and (104), we get the expression (109).

Corollary 5.2. The spacelike Darboux vector $\overline{W_B}(t)$ of Darboux frame of timelike binormal indicatrix (\vec{B}) on S_1^2 of $\overline{\gamma_m}(t)$ is as follows:

$$\overline{W_B}(t) = \frac{n}{m} \cos(nt) \overline{g_B}(t) + \frac{n}{m} \sin(nt) \overline{n_B}(t).$$

Proof: The proof can be done similarly to Corollary 3.2.

Theorem 5.8. There are the following relations between the normal curvature $(K_n)_B(t)$, geodesic curvatures $(K_g)_B(t)$, geodesic torsion $(\tau_g)_B(t)$ and curvature $K_B(t)$, torsion $\tau_B(t)$ of the timelike binormal indicatrix (\vec{B}) on S_1^2 of $\vec{\gamma}_m(t)$:

$$\begin{cases} (\kappa_n)_B(t) = \kappa_B(t) \cos(nt), \\ (\kappa_g)_B(t) = -\kappa_B(t) \sin(nt), \\ (\tau_g)_B(t) = \tau_B(t) + \frac{m}{\cos(nt)}. \end{cases}$$

Proof: The proof is similar to Theorem 3.8.

Theorem 5.9. Let $\{\vec{T}_B(t), \vec{N}_B(t), \vec{B}_B(t)\}$ and $\{\vec{T}_B(t), \vec{g}_B(t), \vec{n}_B(t)\}$ be Frenet and Darboux frames of timelike binormal indicatrix (\vec{B}) on S_1^2 of $\vec{\gamma}_m(t)$, respectively. There is the following relation between the frames:

$$\begin{bmatrix} \vec{T}_B(t) \\ \vec{N}_B(t) \\ \vec{B}_B(t) \end{bmatrix} = \begin{bmatrix} 1 & 0 & 0 \\ 0 & -\sin(nt) & \cos(nt) \\ 0 & -\cos(nt) & -\sin(nt) \end{bmatrix} \begin{bmatrix} \vec{T}_B(t) \\ \vec{g}_B(t) \\ \vec{n}_B(t) \end{bmatrix}.$$

Proof: The proof can be done similarly to Theorem 3.9.

Theorem 5.10. Let $\{\vec{T}_B(t), \vec{g}_B(t), \vec{n}_B(t)\}$ be the Darboux frame of the timelike binormal indicatrix (\vec{B}) on S_1^2 of $\vec{\gamma}_m(t)$. There is the following relationship between the Darboux vectors $\vec{F}_B(t)$ and $\vec{W}_B(t)$ belong to the Frenet and Darboux frames, respectively:

$$\vec{W}_B(t) = \vec{F}_B(t) + n\vec{T}_B(t).$$

Proof: It is clear that (92) and (109).

Theorem 5.11. The angle $\varphi_B(t)$ between $\vec{W}_B(t)$ and $\vec{g}_B(t)$ of timelike binormal indicatrix (\vec{B}) on S_1^2 of $\vec{\gamma}_m(t)$ is as follows:

$$\varphi_B(t) = \arccos\left(\frac{n}{m}\right) + nt. \tag{111}$$

Proof: For the real angle $\varphi_B(t)$ between unit spacelike vectors $\vec{W}_B(t)$ and $\vec{g}_B(t)$, Figure 9, we know

$$\langle \vec{W}_B(t), \vec{g}_B(t) \rangle = \cos \varphi_B(t). \tag{112}$$

Besides, we have

$$\langle \vec{W}_B(t), \vec{n}_B(t) \rangle = \sin \varphi_B(t). \tag{113}$$

On the other hand, from (70) and (85), we get

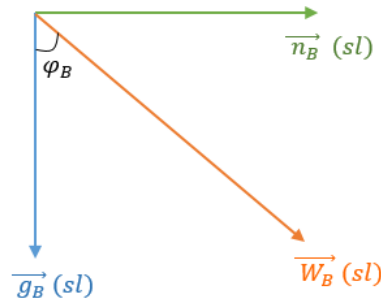


Figure 9. The real angle $\varphi_B(t)$ between $\vec{W}_B(t)$ and $\vec{g}_B(t)$.

$$\langle \vec{W}_B(t), \vec{g}_B(t) \rangle = \frac{n}{m} \cos(nt), \tag{114}$$

$$\langle \vec{W}_B(t), \vec{n}_B(t) \rangle = \frac{n}{m} \sin(nt).$$

From (112), (113) and (114), we obtain

$$\begin{aligned} \cos \varphi_B(t) \cos(nt) + \sin \varphi_B(t) \sin(nt) \\ = \cos(\varphi_B(t) - nt) = \frac{n}{m} \end{aligned} \tag{115}$$

From (115), we have (111).

4. Discussion and Conclusion

In this study, the some geometric elements (Darboux frames, curvatures, torsions, Darboux vectors, angles etc.) of timelike tangent indicatrix (\vec{T}) and timelike binormal indicatrix (\vec{B}) on the Lorentzian unit sphere S_1^2 , spacelike principal normal indicatrix (\vec{N}) on the hyperbolic unit sphere H_0^2 of the spacelike Salkowski curve with spacelike binormal in Lorentzian 3-space E_1^3 are obtained. And the relationships between these elements are studied. Similar studies can also be done on other types of Salkowski curves in Lorentzian 3-space or other well-done curves.

Author Contributions

The percentage of the author(s) contributions is presented below. All authors reviewed and approved the final version of the manuscript.

| | B.A. | S.G.M. |
|-----|------|--------|
| C | 10 | 90 |
| D | 50 | 50 |
| S | | 100 |
| DCP | 60 | 40 |
| DAI | | 100 |
| L | 70 | 30 |
| W | 40 | 60 |
| CR | | 100 |
| SR | | 100 |

C=Concept, D= design, S= supervision, DCP= data collection and/or processing, DAI= data analysis and/or interpretation, L= literature search, W= writing, CR= critical review, SR= submission and revision, PM= project management, FA= funding acquisition.

Conflict of Interest

The authors declared that there is no conflict of interest.

Ethical Consideration

Ethics committee approval was not required for this study because of there was no study on animals or humans.

References

- Aksan B, Gür Mazlum S. 2023. On the Spherical Indicatrix Curves of the Spacelike Salkowski Curve with Timelike Principal Normal in Lorentzian 3-Space. *Honam Math J*, 45(3): 513-541.
- Ali AT. 2011. Spacelike Salkowski and anti-Salkowski curves with timelike principal normal in Minkowski 3-space. *Math Aeterna*, 1(4): 201-210.
- Babaarslan M, Yaylı Y. 2017. On space-like constant slope surfaces and bertrand curves in Minkowski 3-space. *Analele Stiintifice ale Universitatii Al I Cuza din Iasi-Matematica*, 63(F2): 323-339.
- Bilici M, Çalışkan M. 2019. Some new results on the curvatures of the spherical indicatrix curves of the involutes of a spacelike curve with a spacelike binormal in Minkowski 3-space. *MathLAB J*, 2(1): 110-119.
- Birman GS, Nomizu K. 1984. Trigonometry in Lorentzian geometry. *Ann Math Mont*, 91: 534-549.
- Bükcü B, Karacan MK. 2007. On the involute and evolute curves of the spacelike curve with a spacelike binormal in Minkowski 3-space. *Int J Contemp Math Sci*, 2(5): 221-232.
- Fenchel W. 1951. On the differential geometry of closed space curves. *Bull Am Math Soc*, 57: 44-54.
- Gür Mazlum S, Şenyurt S, Bektaş M. 2022. Salkowski curves and their modified orthogonal frames in E3. *J New Theory*, 40: 12-26.
- Gür Mazlum S. 2023. Geometric properties of timelike surfaces in Lorentz-Minkowski 3-space. *Filomat*, 37(17): 5735-5749.
- Gür S, Şenyurt S. 2010. Frenet vectors and geodesic curvatures of spheric indicatrix curves of Salkowski curve in E3. *Hadronic J*, 33(5): 485-512.
- Hacısalıhoğlu HH. 1983. *Differential geometry*. İnönü University, Publication of Faculty of Sciences and Arts, Malatya, Türkiye.
- Kahveci D, Yaylı Y. 2002. Geometric kinematics of persistent rigid motions in three-dimensional Minkowski space. *Mechanism Machine Theory*, 167: 104535.
- Kula L, Yaylı Y. 2005. On slant helix and its spherical indicatrix. *Appl Math Comput*, 169(1): 600-607.
- Li Y, Gür Mazlum S, Şenyurt S. 2023. The Darboux trihedrons of timelike surfaces in the Lorentzian 3-space. *Internationa J Geomet Methods Modern Physics*, 20(2): 2350030-82.
- Lopez R. 2014. Differential geometry of curves and surfaces in Lorentz-Minkowski space. *Int E-J Geomet*, 7: 44-107.
- Monterde J. 2009. Salkowski curves revisited: A family of curves with constant curvature and non-constant torsion. *Comp Aided Geomet Design*, 26(3): 271-278.
- O'Neill B. 1983. *Semi-Riemannian geometry with applications to relativity*. Academic Press, London, UK, pp: 488.
- Özdemir M. 2020. *Diferansiyel geometri*. Altın Nokta Yayınevi, İzmir, Türkiye, pp: 132.
- Ratcliffe JG. 1994. *Foundations of hyperbolic manifolds*. Springer-Verlag, Tokyo, Japan, pp: 779.
- Salkowski E. 1909. Zur transformation von raumkurven. *Math Annalen*, 66(4): 517-557.
- Şentürk GY, Yüce S. 2015. Characteristic properties of the ruled surface with Darboux frame in E-3. *Kuwait J Sci*, 42(2), 14-33.
- Uğurlu HH, Çalışkan A. 2012. *Darboux ani dönme vektörleri ile spacelike ve timelike yüzeyler geometrisi*. Celal Bayar University Press, Manisa, Türkiye, pp: 12.
- Uğurlu HH, Kocayiğit H. 1996. The Frenet and Darboux instantaneous rotation vectors of curves on time-like surface. *Math Comp Appl*, 1(2): 133-141.
- Uğurlu HH. 1997. On the geometry of time-like surfaces. *Communications, Faculty of Sciences, University of Ankara, A1 Series*, No: 46, pp: 211-223.
- Yakıcı Topbaş ES, Gök İ, Ekmekci FN, Yaylı Y. 2016. Darboux frame of a curve lying on a lightlike surface. *Math Sci Appl E-Notes*, 4(2): 121-130.
- Yüksel N, Saltık B, Damar E. 2014. Parallel curves in Minkowski 3-space. *Gümüşhane Univ J Sci Tech*, 12(2): 480-486.



BIBLIOMETRIC ANALYSIS OF THE STUDIES DETERMINED BY THE MONTE CARLO SIMULATION TECHNIQUE OF THE POWER OF THE TEST

Malik ERGIN^{1*}, Rabia ALBAYRAK DELIALIOĞLU², Yasin ALTAY³, Özgür KOŞKAN¹

¹Isparta University of Applied Sciences, Faculty of Agriculture, Department of Animal Science, 32000, Isparta, Türkiye

²Ankara University, Faculty of Agriculture, Department of Animal Science, 06000, Ankara, Türkiye

³Eskişehir Osmangazi University, Faculty of Agriculture, Department of Animal Science, 26000, Eskişehir, Türkiye

Abstract: In order to give detailed information about the characteristics of scientific studies related to the power of the test, a bibliometric analysis of studies in which the power of the tests used in statistical data analysis was determined with the aid of Monte Carlo simulation techniques was carried out. The Web of Science (WoS) database's 1309 scientific studies in which the power of the test was determined by using Monte Carlo simulation techniques served as the study's material of data. The analysis includes the number of studies by year, average citation count by year, the number of articles published in scientific journals, countries of responsible authors, and the most relevant words in the studies. It was observed that Communications in Statistics-Simulation and Computation and Journal of Statistical Computation and Simulation are the journals with the highest number of published articles. The United States of America (USA) takes the lead when considering the countries of corresponding authors, while Türkiye is in 8th place. The most used keywords in the ten-year time period of scientific studies were respectively "power", "test", "skewness", "model" and "inference". As a result, it can be concluded that test power studies can be obtained safely using the Monte Carlo simulation technique.

Keywords: Type I error probability, Test power, Bibliometric analysis, Monte Carlo, Simulation

*Corresponding author: Isparta University of Applied Sciences, Faculty of Agriculture, Department of Animal Science, 32000, Isparta, Türkiye

E mail: malikergin@isparta.edu.tr (Malik ERGIN)

Malik ERGIN  <https://orcid.org/0000-0003-1810-6754>

Rabia ALBAYRAK DELIALIOĞLU  <https://orcid.org/0000-0002-1969-4319>

Yasin ALTAY  <https://orcid.org/0000-0003-4049-8301>

Özgür KOŞKAN  <https://orcid.org/0000-0002-5089-6250>

Received: August 01, 2023

Accepted: September 05, 2023

Published: October 15, 2023

Cite as: Ergin M, Albayrak Delialioğlu R, Altay Y, Koşkan Ö. 2023. Bibliometric analysis of the studies determined by the monte carlo simulation technique of the power of the test. BSJ Eng Sci, 6(4): 414-420.

1. Introduction

Thanks to the progress in computer technology, statistical simulation techniques have also rapidly developed. With the rapid advancement of programming power in computer technology, the behaviors of various statistical methods can be evaluated using the Monte Carlo simulation method by generating random numbers from specific statistical distributions (Kroese et al., 2014; Morris et al., 2019). Depending on the purpose of the simulation study, various combinations can be designed when comparing means between two or more groups (Burton et al., 2006). These combinations include variance ratios between groups, sample sizes, distributions of populations from which observations are taken, and standard deviation differences between or among group means. These simulation combinations help in investigating the results shown by variance analysis techniques (ANOVA) or alternative methods more clearly. The advantage provided by the simulation technique is the ability to determine the parameters of populations in advance. When evaluating many statistical methods through simulation experiments, the literature mostly considers Type I error and power values of the

test. In recent years, various statistical methods are still being examined using the Monte Carlo simulation technique (Patric, 2009; Koşkan ve Gürbüz, 2008; Ferreira et al., 2012; Lantz, 2013). In the field of medicine, through the Monte Carlo simulation technique, a newly developed mathematical technique can be evaluated by creating various simulation designs. In addition, when designing a study based on the assumptions required by a statistical method to be used in real-life data (such as variance analysis, t-test, etc.), comparing two or more methods, or calculating values such as sample size or test power can be used (Morris et al., 2019).

When evaluating the performance of any test, the criterion we focus on can be the test power. The test power or empirical power is the probability of being able to detect a difference when there is a difference between group means. If there is a 0.75 standard deviation difference between or among group means, the ratio at which the null hypothesis (H_0) is rejected at a significance level of 5.0% after 100000 simulation trials is expressed as the test power. There is a generally accepted measure in the literature regarding the level of



power that is considered sufficient for test performance. Murphy and Myors (2014) stated that if the power of the test is 80% or higher, it can be considered adequate. There are also mathematical approaches developed to assess the test power. Studies have suggested that it is not appropriate to compare the test power when the probabilities of Type I errors are not equal (Zhang and Boos, 1994; Lloyd, 2005). While a test maintains a Type I error rate of 5%, it can have lower power values compared to other tests (Çavuş, 2020). In Monte Carlo simulation studies, the test power is investigated by many researchers. Mahapoonyanont et al. (2010) compared the power of the test using original and transformed data in analysis of variance. Öztuna et al. (2006) compared the power of Lilliefors corrected Kolmogorov-Smirnov, D'Agostino Pearson, Jarque-Bera, and Shapiro-Wilk tests, where normality assumption can be checked. In conclusion, it was reported that the Shapiro-Wilk test yielded better results in terms of power for small sample sizes. In addition, Başpınar and Gürbüz (2000) evaluated the power of variance analysis using randomly generated numbers from symmetric, right-skewed, and left-skewed distributions. The researchers emphasized that the distribution shapes of populations do not have significance in achieving the desired power.

Evaluating the results and some bibliometric data of previous studies in the literature regarding the subject at hand enables research to progress faster and in a more interconnected manner. Therefore, a bibliometric study helps the researcher assess the literature related to the research subject of interest by employing quantitative approaches on the bibliometric data (Büyükkıdık, 2022). Donthu et al. (2021) emphasized the use of bibliometric analysis in cases where the scope of evaluation is broad and when manually reviewing data from studies becomes inconvenient. The most common databases where bibliometric data can be generated include Web of Science (WOS), Scopus, Google Scholar, Microsoft Academic, and Dimensions. Thanks to libraries developed in open-source programming languages such as Python or R, such as Bibliometrix, BiblioTools, Citan, Metaknowledge, Scientopy, and scientoText, bibliometric analyses can now be easily conducted (Moral-Munoz et al., 2020).

The lack of sufficient knowledge about the progress made despite years of studying the power of any test using Monte Carlo simulation techniques is an important factor in determining the status of research conducted. In this study, a bibliometric analysis was conducted on studies examining the power of tests using Monte Carlo simulation technique in the Web of Science (WOS) database.

2. Materials and Methods

Bibliometric analysis is a technique supported by computer technology to review the literature on a specific area and to network these studies (Han et al.

2020). The simulation studies conducted between 1980 and 2023 were used in the literature review stage by utilizing the Web of Science database. Due to the various interpretations of the simulation technique in different disciplines, a literature search was conducted focusing on “test power” and “Monte Carlo simulation” keywords. After the WOS search, Monte Carlo Simulation and Power test words were review, and 1309 scientific studies were reached by selecting the research areas related to statistics. To construct the list of reviewed documents, each paper included in a single dataset and repeated papers were eliminated. The collected data set included the number of studies by year, average citation count by year, number of articles published in scientific journals, countries of corresponding authors, and commonly used keywords in the studies.

All analyses conducted in the following steps:

- (1) Extracting data on statistical studies related to the test power and Monte Carlo simulation from the WOS database
- (2) Uniting and reorganizing the dataset
- (3) Determining a relationship among these studies reviewed in a certain year period and visualizing this relationship with different ways
- (4) Interpretation of the results obtained.

Bibliometric analysis was conducted with a total of 1309 papers via Bibliometric package developed in the R programming language (Aria and Cuccurullo, 2017).

3. Results and Discussion

Based on the literature available in WOS, a total of 1309 papers constitute the body of simulation studies published between 1980 and 2023. Within these 1309 publications, there are subcategories such as research articles, book chapters, full-text conference papers, and reviews. The findings obtained from bibliometric analysis in this study were evaluated in terms of the number of studies by year, average citation count by year, number of articles published in scientific journals, countries of responsible authors, and the commonly used keywords.

As seen in Figure 1, according to the studies in the WOS database, the first years in which the Monte Carlo simulation technique was used date back to 1980. It is noteworthy that any study was not conducted until the early 1990s, and the number of studies gradually increased in the subsequent years. In 2008, there was a significant increase with 42 studies, and the highest number of studies occurred in 2017 with 87 studies. Although the number of studies did not decrease rapidly in the following years, it remained limited to 29 studies within the year 2023. As a result, it is clearly observed that simulation studies still have a widespread presence and are of interest to researchers nowadays.

The average citation counts of simulation studies in the WOS database are presented by year in Figure 2. The highest average citation count per year is 4.76 in 2007. If we observe the number of studies by year shown in Figure 1, the rapid increase in 2007 can be considered as

the reason for the increase in citation count. However, the average citation counts significantly decreased in the subsequent years.

The knowledge of which journals published studies conducted using the Monte Carlo simulation technique can significantly impact researchers' future work plans. Figure 3 displays the number of articles published in various journals for simulation studies conducted within

the specified years in the WOS database. A total of 357 scientific journals in the WOS database have published simulation studies. Among them, the journal named as "Communications in Statistics-Simulation and Computation" takes the lead with 140 articles. Following closely is the "Journal of Statistical Computation and Simulation" with 111 articles.

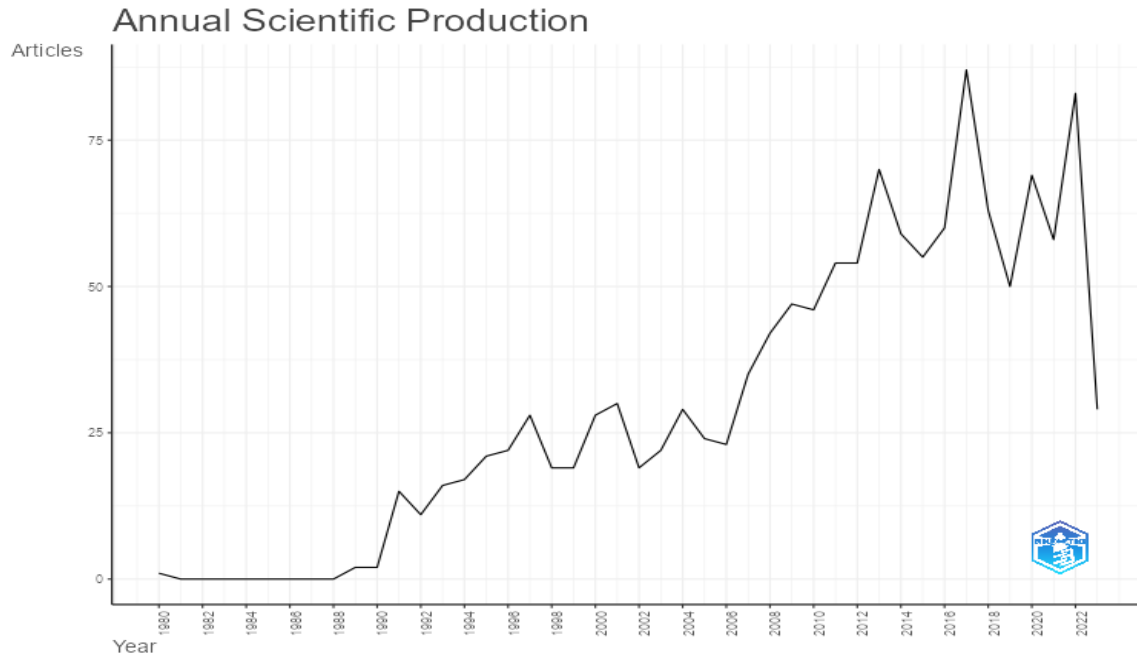


Figure 1. Annual Scientific Production (between 1980 – 2023).

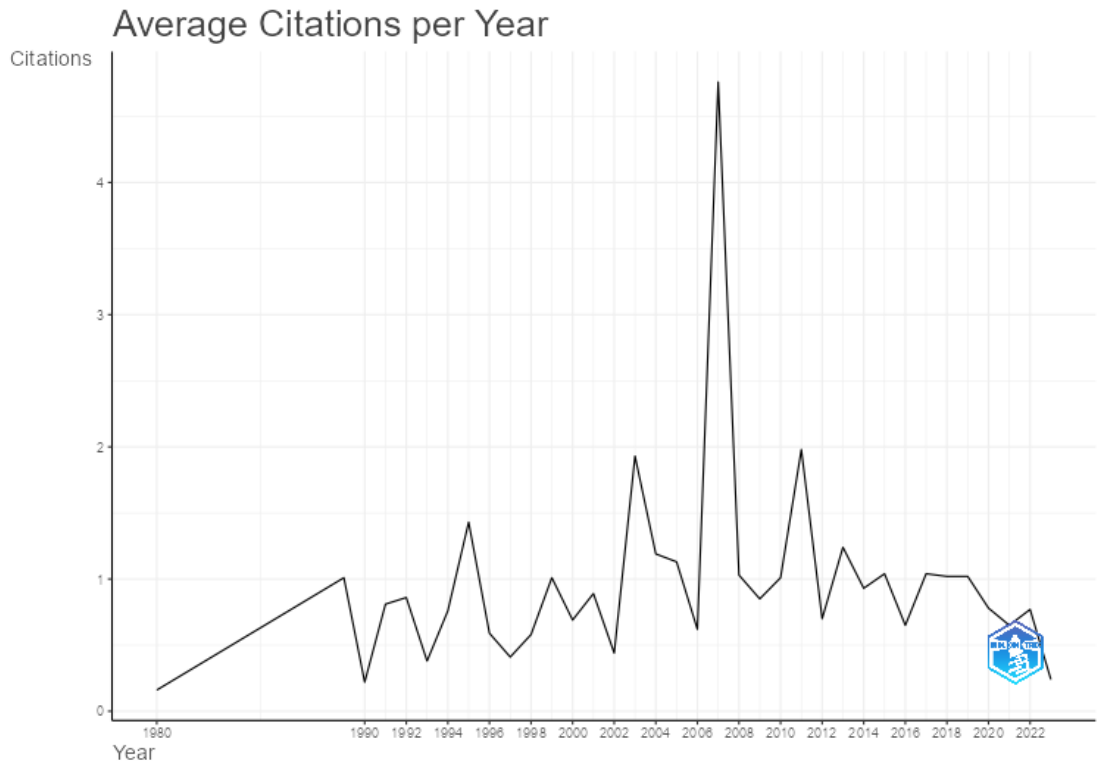


Figure 2. Average citations per year.

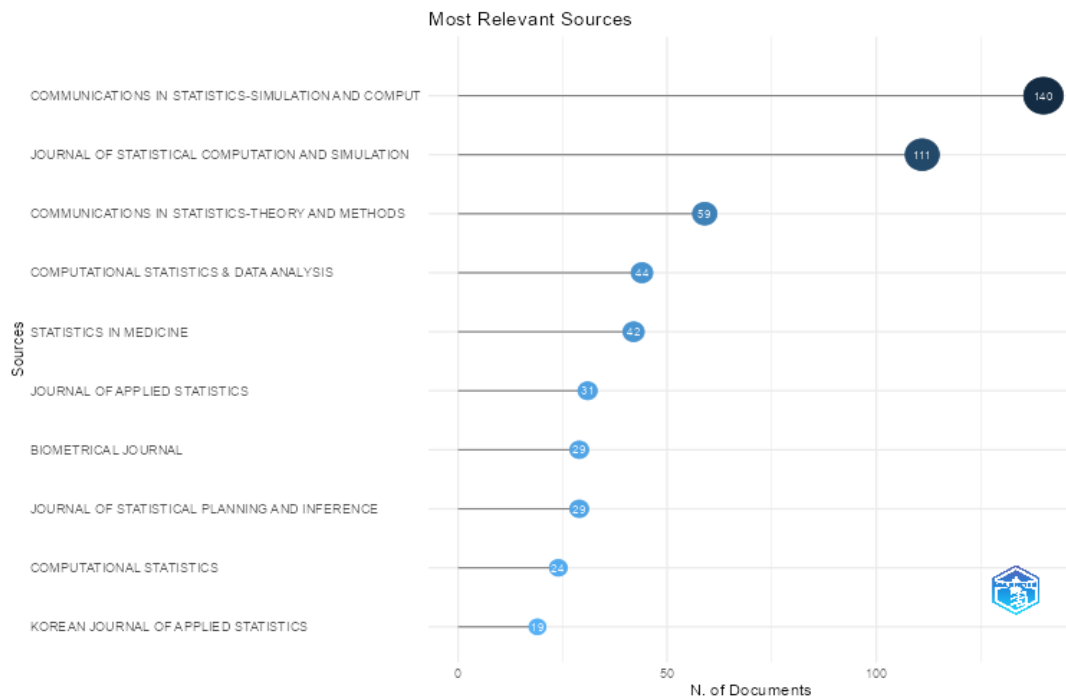


Figure 3. Most relevant journals.

The countries of the corresponding authors for the papers are shown in Figure 4. The parts highlighted with Single Country Publications (SCP) and Multiple Country Publications (MCP) in the graph respectively represent the number of publications made by researchers from the same country and the number of publications made by researchers from multiple countries. Considering the countries of the corresponding authors, the United States of America (USA) ranks first with 332 publications (SCP: 276, MCP: 56), followed by China with 170 publications (SCP: 129, MCP: 41). Türkiye ranks 8th among 66 countries with 50 publications (SCP: 48, MCP: 2). The most relevant words within the scope of 1309 studies included in the data are presented in Figure 5.

Accordingly, the words tests ($f = 116$), power ($f = 86$), statistics ($f = 82$), models ($f = 74$) are widely used.

In Figure 6, the frequency of the most used words by years is presented in Figure 6. While there are years between 1980-2023 on the X axis, the cumulative frequencies are on the Y axis. The cumulative frequencies of the words tests, powers, statistics, and model resulted as 116, 86, 82 and 74 in 2023, respectively.

In Figure 7, the most used words are visualized with a Sankey diagram according to specific year periods. Accordingly, the keywords generally vary within each year interval. It can be said that words became more prevalent between 2001-2010 and 2011-2020 periods.

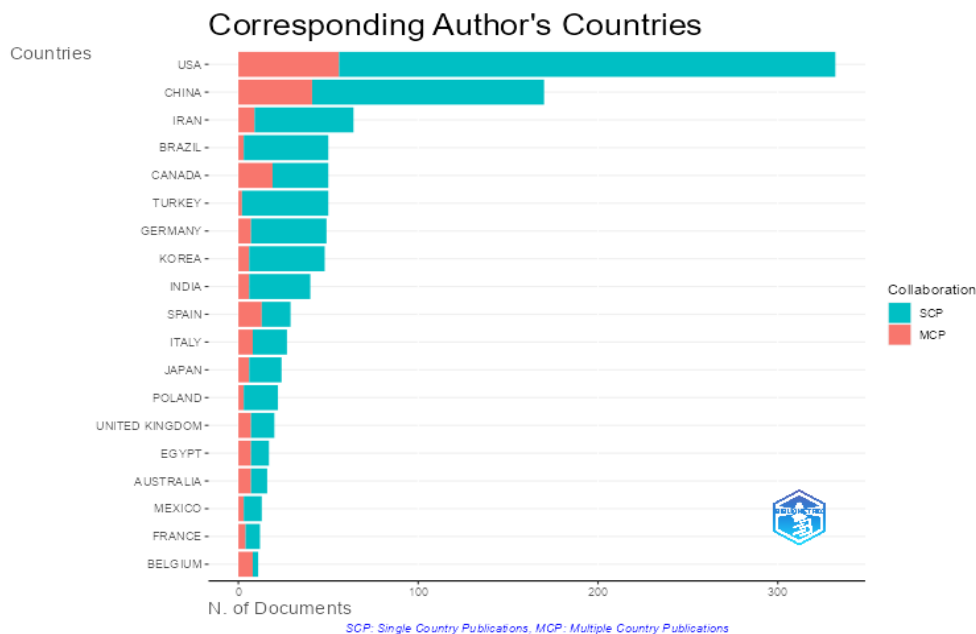


Figure 4. Corresponding authors's countries.

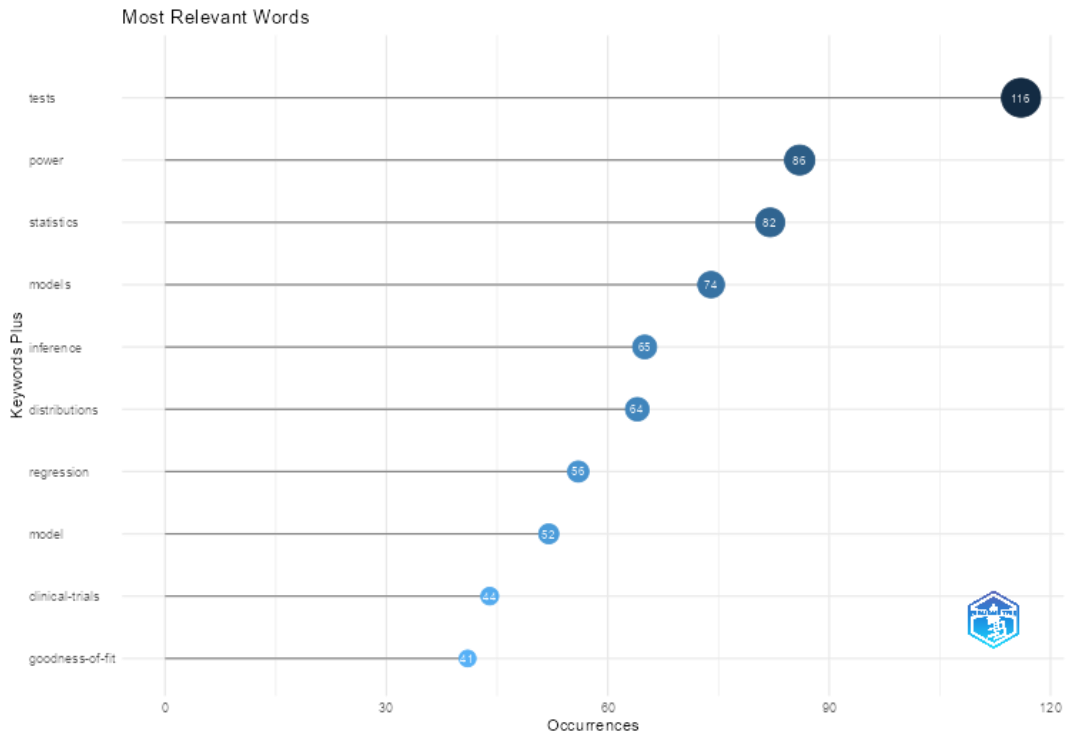


Figure 5. Most relevant words.

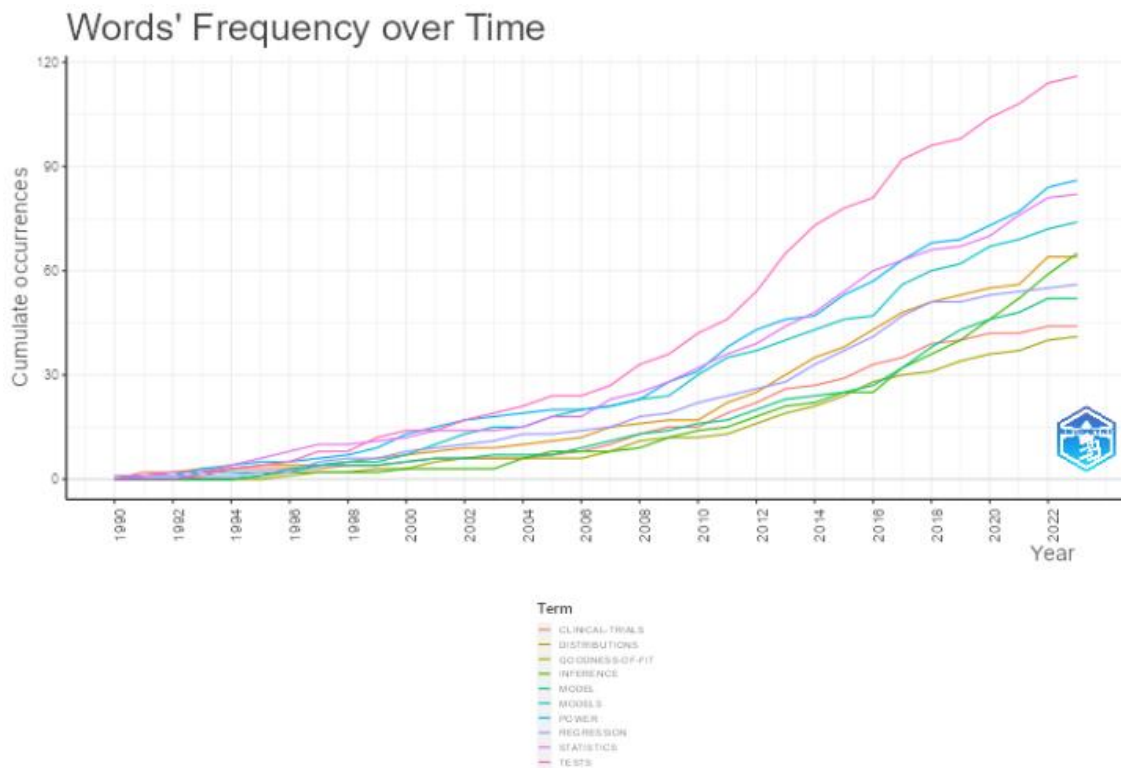


Figure 6. Word's frequency over time.

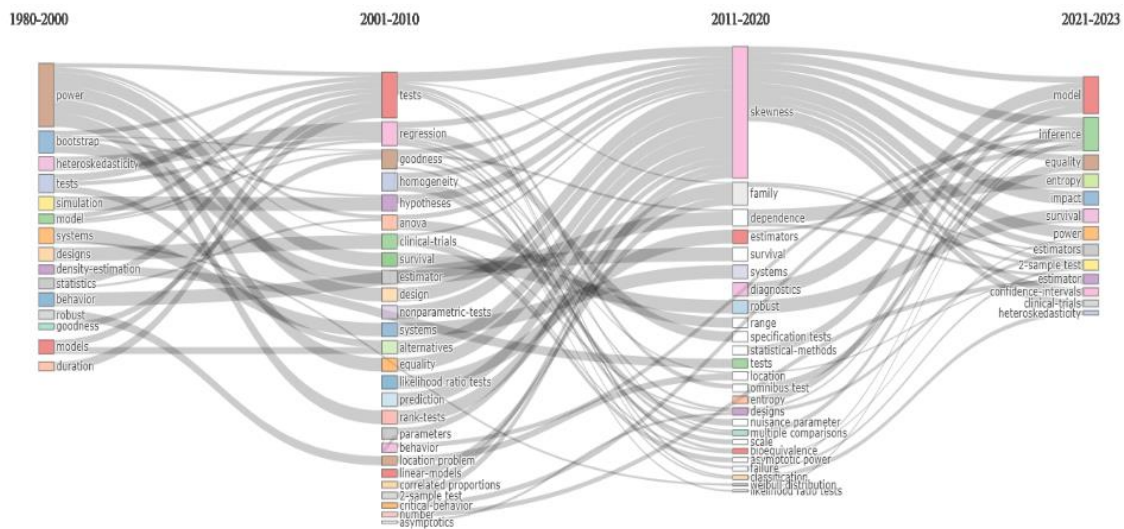


Figure 7. Sankey diagram of most relevant words within certain years.

5. Conclusion

The indication that the findings obtained through bibliometric analysis can be validated by determining the power of tests using the Monte Carlo simulation technique is recognized by the scientific community. Furthermore, when examining the distribution of publications in this field, it is evident that the significance of the subject has never diminished. The reason for this is that the reliability of newly developed tests may be established through studies on the power of the test. It is believed that this study can serve as a guide for researchers in identifying journals where they can publish their simulation studies. Although it is noteworthy that the number of simulation studies has slightly decreased compared to previous years in the present era, they still maintain their relevance even in 2023.

Author Contributions

The percentage of the author(s) contributions is presented below. All authors reviewed and approved the final version of the manuscript.

| | M.E. | R.A.D. | Y.A. | Ö.K. |
|-----|------|--------|------|------|
| C | 30 | 20 | 30 | 20 |
| D | 30 | 20 | 30 | 20 |
| S | | | | 100 |
| DCP | | | 100 | |
| DAI | 40 | 10 | 40 | 10 |
| L | 30 | 20 | 30 | 20 |
| W | 30 | 20 | 30 | 20 |
| CR | 25 | 25 | 25 | 25 |
| SR | 50 | | 50 | |
| PM | 25 | 25 | 25 | 25 |
| FA | 25 | 25 | 25 | 25 |

C=Concept, D= design, S= supervision, DCP= data collection and/or processing, DAI= data analysis and/or interpretation, L= literature search, W= writing, CR= critical review, SR= submission and revision, PM= project management, FA= funding acquisition.

Conflict of Interest

The authors declared that there is no conflict of interest.

Ethical Consideration

Ethics committee approval was not required for this study because of there was no study on animals or humans. The authors confirm that the ethical policies of the journal, as noted on the journal's author guidelines page, have been adhered to.

Acknowledgements

This study is the expanded full text of the abstract presentation titled "Bibliometric Analysis of The Studies Determined by the Monte Carlo Simulation Technique of The Power of The Test" that was presented at the 7th International Conference on Medical & Health Sciences. The previous abstract summarized the main findings of this study; however, this study presents the existing findings in more depth.

References

Aria M, Cuccurullo C. 2017. Bibliometrix: An R-tool for comprehensive science mapping analysis. *J Informetr*, 11(4): 959-975.

Baspinar E, Gurbuz F. 2000. The power of the test in the samples of various sample sizes were taken from the binary combinations of the normal, beta, gamma and Weibull distributions. *J Agric Sci*, 6(1): 116-127.

Burton A, Altman DG, Royston P, Holder RL. 2006. The design of simulation studies in medical statistics. *Stat Med*, 25(24): 4279-4292.

Büyükkidik S. 2022. A Bibliometric Analysis: A tutorial for the bibliometrix package in r using IRT literature. *J Meas Eval*, 13(3): 164-193.

Çavuş M. 2020. The Computational approach tests for testing the equality of population means under two-parameter exponential distribution. PhD thesis, Eskisehir Technical University, Institute of Graduate Programs, Eskisehir, Türkiye, pp: 105.

Donthu N, Kumar S, Mukherjee D, Pandey N, Lim WM. 2021. How to conduct a bibliometric analysis: An overview and

- guidelines. *J Bus Res*, 133: 285-296.
- Ferreira EB, Rocha MC, Mequelino DB. 2012. Monte Carlo evaluation of the ANOVA's F and Kruskal-Wallis tests under binomial distribution. *Sigmae*, 1(1): 126-139.
- Han J, Kang HJ, Kim M, Kwon GH. 2020. Mapping the intellectual structure of research on surgery with mixed reality: Bibliometric network analysis (2000–2019). *J Biomed Inform*, 109: 103516.
- Koşkan Ö, Gürbüz F. 2009. Comparison of F test and resampling approach for type I error rate and test power by simulation method. *J Agric Sci*, 15(1): 105-111.
- Kroese DP, Brereton T, Taimre T, Botev ZI. 2014. Why the Monte Carlo method is so important today. *Interdiscip Rev Comput Stat*, 6: 386-392.
- Lantz B. 2013. The impact of sample nonnormality on ANOVA and alternative methods. *Br J Math Stat Psychol*, 66(2): 224–244.
- Lloyd CJ. 2005. Estimating test power adjusted for size. *J Stat Comput Simul*, 75(11): 921-933.
- Mahapoonyanont N, Mahapoonyanont T, Pengkaew N, Kamhangkit R. 2010. Power of the test of one-way anova after transforming with large sample size data. *Procedia Soc*, 9: 993-937.
- Moral-Muñoz JA, Herrera-Viedma E, Santisteban-Espejo A, Cobo MJ. 2020. Software tools for conducting bibliometric analysis in science: An up-to-date review. *Prof de la Inf*, 29(1).
- Morris TP, White IR, Crowther MJ. 2019. Using simulation studies to evaluate statistical methods. *Stat Med*, 38: 2074–2102.
- Murphy KR, Myers B, Wolach A. 2014. Statistical power analysis: a simple and general model for traditional and modern hypothesis tests. Routledge, New York, USA, pp: 244.
- Öztuna D, Elhan AH, Tüccar E. 2006. Investigation of four different normality tests in terms of type I error rate and power under different distributions. *Turk J Med Sci*, 36(3): 171-176.
- Patric JD. 2009. Simulations to analyze type I error and power in the anova F test and nonparametric alternatives. Master Thesis, University of West Florida, Florida, USA, pp: 80.
- Zhang J, Boos DD. 1994. Adjusted power estimates in Monte Carlo experiments. *Commun Stat Simul*, 23(1): 165-173.



FORECASTING COVID-19 CASES IN TÜRKİYE WITH THE HELP OF LSTM

Nurgül GÖKGÖZ KÜÇÜKSAKALLI^{1*}

¹Çankaya University, Faculty of Arts and Sciences, Department of Mathematics, 06790, Ankara, Türkiye

Abstract: Even though, it is thought that the pandemic has come to an end, the humanity is still under the danger of upcoming pandemics. In that sense, every effort to understand or predict the nature of an infectious disease is very precious since those efforts will provide experience for upcoming infectious disease epidemic/pandemic. Mathematical models provide a common way to analyze the nature of the pandemic. Apart from those mathematical models that mostly determine which variables should be used in the model to predict the nature of the epidemic and at which rate the disease will spread, deep learning models can also provide a fast and practical tool. Moreover, they can shed a light on which variables should be taken into account in the construction of a mathematical model. And also, deep learning methods give rapid results in the robust forecasting trends of the number of new patients that a country will deal with. In this work, a deep learning model that forecasts time series data using a long short-term memory (LSTM) network is used. The time series data used in this project is COVID-19 data taken from the Health Ministry of Republic of Türkiye. The weekend isolation and vaccination are not considered in the deep learning model. It is seen that even though the graph is consistent and similar to the graph of real number of patients, and LSTM is an effective tool to forecast new cases, those parameters, isolation and vaccination, must be taken into account in the construction of mathematical models and also in deep learning models as well.

Keywords: Long-Short Term Memory (LSTM), COVID-19, Forecasting, Modeling

*Corresponding author: Çankaya University, Faculty of Arts and Sciences, Department of Mathematics, 06790, Ankara, Türkiye

E mail: ngokgoz@cankaya.edu.tr (N. GÖKGÖZ KÜÇÜKSAKALLI)

Nurgül GÖKGÖZ KÜÇÜKSAKALLI  <https://orcid.org/0000-0002-9640-4194>

Received: February 27, 2023

Accepted: September 10, 2023

Published: October 15, 2023

Cite as: Gökgöz Küçüksakalli N. 2023. Forecasting COVID-19 cases in Türkiye with the help of LSTM. BSE Eng Sci, 6(4): 421-425.

1. Introduction

The world is still fighting against the coronavirus disease 2019 (COVID-19) caused by the novel coronavirus, SARS-CoV-2, which is thought as a highly contagious virus that affects the human respiratory system as a first step. Many researchers from different fields started to work on this topic to find a treatment, to understand the nature of the disease or to forecast the trend in the case numbers or death numbers.

To provide a solid background to the biological data, mathematical models provide a powerful tool (Belen et al., 2011; Peadar et al., 2012; Brauer et al., 2019). In that sense, many mathematical models are investigated to estimate the trend in the case/death numbers or to decide how contagious is this disease. The mathematical approach used in the model aside (ordinary differential equations, partial differential equations, difference equations, etc.), how many variables are considered make a difference in the arrangement of the model. It is certain that some simplifications and therefore assumptions must be made in order to be able to analyze the model. From the mathematical modeling perspective, some of the works disregard the incubation period (Arino et al., 2020), some works include the social isolation period in their model (Vega, 2020), some consider both social isolation and vaccination (Demirci,

2023). With those models, basic reproduction number, i.e., the number of next generation cases produced by the present generation, stability of the model and numerical simulations are obtained (Demirci, 2023). However, which variables must be taken into account, which parameters should be included, basically which simplifications or assumptions we are allowed to make for a more realistic mathematical model must be determined. In that sense, apart from mathematical models, deep learning, machine learning, and artificial intelligence models are very popular in identification (Subramanian et al., 2022; Paul et al., 2023) and forecasting the trend of any real world problem (Livieris et al. 2020), and also COVID-19 cases (Xu et al. 2022). Apart from their effectiveness in the forecast of the trends, deep learning models can be used to overcome the difficulties we face listed above in the use of mathematical models. The model should be fast, reliable and practical as possible as to allow government to take action before the pandemic spreads quickly.

Basically, deep learning refers to an artificial neural network with feature learning. It uses multiple layers in the architecture of the network and that is the reason why it is called as deep learning. When we talk about the deep learning methods, it has to be mentioned that one of the extensive types of artificial networks is Recurrent Neural Networks (RNN) which is capable of using



arbitrary data from their internal states (Tealab 2018). However, they can capture data only from a few steps earlier. A long-short term memory (LSTM) networks which is a kind of RNN has been proved to be successful in many applications (Graves et al., 2008). Throughout the years many different applications of LSTM have been conducted to various fields (Wang et al. 2020; Xu et al., 2022) and proved to be successful and therefore, they are still extensively used.

In this project, an LSTM network is used where the LSTM network learns to predict the value of the next time step. The data is COVID-19 data from 27th April 2021 to 21st June 2021 taken from the Health Ministry of Republic of Türkiye (one may check <https://covid19.saglik.gov.tr/EN-69532/general-coronavirus-table.html>).

2.1. Related Work

When the use of machine learning is searched throughout the literature, it can be seen that they are both used in the identification of a pattern and in the forecasting of some cases. When COVID-19 cases are considered, deep learning or machine learning networks are used both in detection and prediction of it (Paul et al., 2023; Subramanian et al., 2022; Xu et al., 2022; Jin et al., 2021). To be more precise, machine learning models that predict antibody response using antibody sequences (Magar et al., 2021), using chest X-rays to determine if the patient is infected or not (Toğaçar et al., 2020), forecasting cases of COVID-19 (Xu et al., 2022; Wang et al., 2020).

Making a prediction using time series data play an important role in many areas, and especially multi-step time-series forecast is challenging and essential in many real world problems e.g. forecasting stock-price, river flow, disease cases, etc. The most effective multi-step model is Long Short Term Memory (LSTM) because of its structure that allows capturing the long-term dependencies. There are works on the literature that apply LSTM on different data patterns (Yunpeng et al., 2017). To name a few of them, there are works on financial data (Siami-Namini et al., 2018), petroleum production, gold price (Sagheer et al., 2019; Livieris et al., 2020). Forecasting COVID-19 cases using LSTM networks plays an important role in the literature as well. It has been shown that it is more effective than convolutional neural networks (CNN), and a combination of LSTM-CNN (Xu et al. 2022). Therefore, in this work, we use LSTM networks to forecast COVID-19 cases in Türkiye.

2. Materials and Methods

In this section, the data used in the experiment and the steps used to construct the model are explained in detailed. The model is constructed and implemented on MATLAB R2019b. For a better explanation, figures of the data, forecasted data, graphs of RMSE are given.

2.1. Dataset

The data includes a single time series where time steps are days and the values are the number of COVID-19 cases in Türkiye. The data is a cell array, where each element is a time step (Figure 1). Then the data is divided into two groups as the training and the test data. The training is done on the first 90% of the sequence and the test is done on the remaining 10%. At this point, a standardization of the data has been applied. It is crucial because, it allows data exchange in different models or computers. Moreover, it improves quality of the data and therefore leads to a better decision-making. Therefore, standardization on the training data is done in order to obtain a better fit and to get away from the divergence of the training. By this way, the training data have zero mean and unit variance. Later on, the test data is standardized using the same parameters as the training data. During the overall process, CPU is used since the data is rather small collection of data.

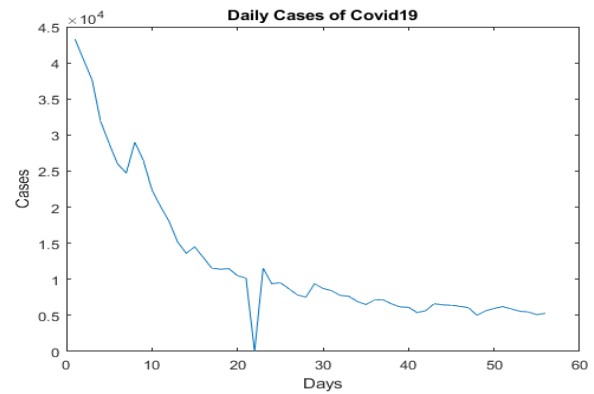


Figure 1. COVID-19 daily dataset of Türkiye (starts on 27th April 2021, ends on 21st June 2021).

2.2. Procedure

After data preparation step, an LSTM network is constructed. A flowchart of the general workflow of this structure can be seen from Figure 2.

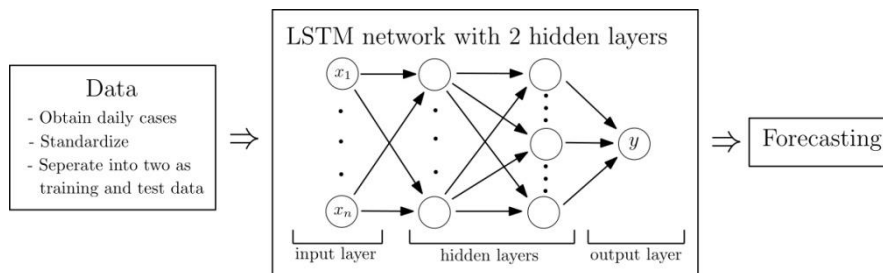


Figure 2. Flowchart that shows the workflow of the LSTM network to forecast cases of COVID-19 according to daily dataset of Türkiye.

At every time step of the input sequence, the network learns to forecast the next time step's value. In this work, the LSTM layer has 200 hidden units. The training is executed for 250 epochs with the solver 'adam'. The get away from the problem of gradient exploding, gradient threshold is chosen as 1. Moreover, the learning rate is initially is chosen as 0.005 and dropped to 0.001 after the halfway of the training. A standardization is applied on the test data using the same parameters as the training data. A detailed list of hyper parameter optimization and model architecture is given in Table 1.

Table 1. Parameters for the architecture for the LSTM network

| Model | LSTM |
|---------------|-------|
| Hidden Layer | 2 |
| Hidden Units | 200 |
| Learning Rate | 0.005 |
| Optimizer | Adam |
| Epoch | 250 |

Using the training progress plot, the root-mean-square error (RMSE) may be calculated from the standardized data. In this work, for the error calculation root-mean-square error (RMSE) is used. Even though, it is not scale invariant, using standardized data overcomes this disadvantage. Moreover, it is mostly used to check the model performance. In the literature, (RMSE) formula (equation 1) is given by

$$RMSE = \sqrt{\frac{\sum_{i=1}^n (\hat{y}_i - y_i)^2}{n}}, \quad (1)$$

where y_i values are observed values, \hat{y}_i are predicted values and n is the number of observations. In our model, the MATLAB output for the RMSE measure (equation 2) is

$$RMSE = 528.0957. \quad (2)$$

One may see the forecasted values (Figure 3). We may compare the forecasted values with the test data (Figure 4). Since we have the actual values of time steps between predictions as well, then we update the network state with the observed values (Figure 5).

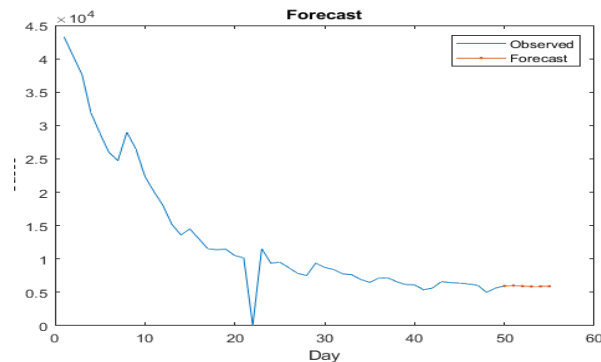


Figure 3. Forecasted data. The red curve indicates the

forecasted data in the graph.

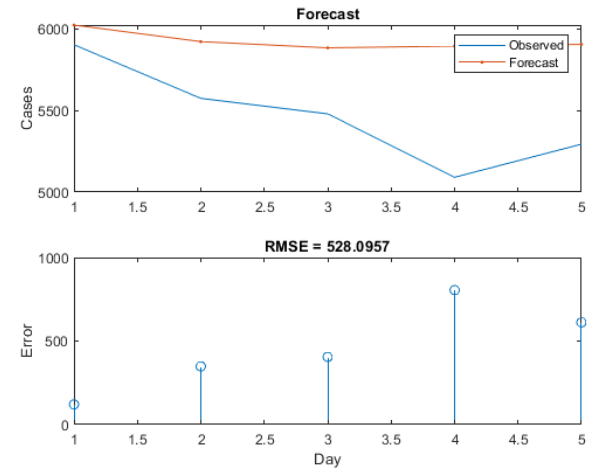


Figure 4. Forecasted values with the test data (with predicted values).

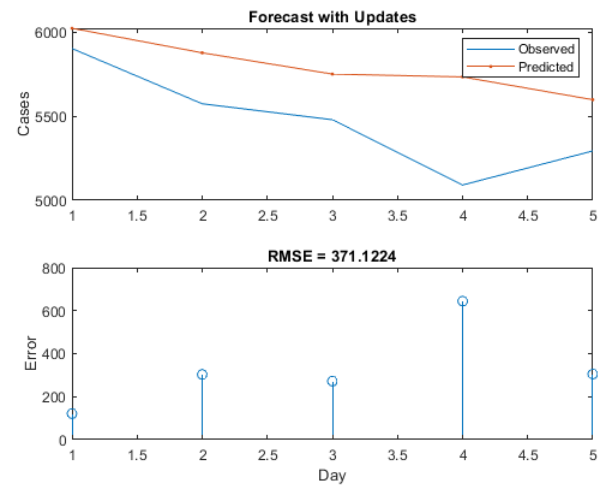


Figure 5. Forecasted values with the test data (with actual values).

In that case, the MATLAB output for the RMSE measure (equation 3) is

$$RMSE = 371.1224. \quad (3)$$

As expected, in that case, we have a more accurate prediction. Moreover, it can be concluded that, by investigating Figure 4 and Figure 5, observed values and the forecasted values show a similar trend. Therefore, even though the error value, since the general behavior of the system is captured, it can be stated that the model should include the disregarded variables such as isolation and vaccination.

3. Results and Discussion

In this work, forecasting of the number of cases for COVID-19 which is a time series data is considered. Obtaining a future prediction in the number of cases is very important from different aspects as explained earlier. In the literature, LSTM networks are proved to be efficient among different deep learning networks among

other deep learning models (Xu et al., 2022; Wang et al. 2020). In this work, we use LSTM networks to determine which parameters will be used in a mathematical model. We conclude that, even though the RMSE value is high, this study shows that predicting of the number of cases is available by using LSTM. That is because the tendency of the observed and the forecasted values are similar to each other in the graphs (Figure 4 and Figure 5). High RMSE value is depending on the vaccination of different age groups and occupation groups started before and during this period of time and the quarantine applied during weekends. Moreover, high RMSE value is known to be causing from the outliers in the dataset. In this case, we may conclude that a mathematical model should include those parameters, as well. This result is also compatible with the mathematical models considered in the literature (Demirci, 2023). Therefore, we conclude that even though LSTM is an effective tool to predict number of cases, other factors (like vaccination, quarantine) must be considered in the future models. In the literature, there are works that consider different deep learning networks and compare them according to different error measures (Xu et al., 2022). As a future work, a comparison of the LSTM model with different deep learning networks with different error measures may be considered. Moreover, using LSTM networks to determine which parameters to include in a mathematical model may be extended to different real world problems. To name a few of them, it may be used in tumor-immune system (Gokgoz et al., 2021), HIV/AIDS transmission (Padamallu et al., 2012), rumour model (Belen et al. 2011) or fishery model (Çifdalöz, 2022). By this way, by adding more variables in the mathematical models better reproduction number, more realistic stability results, etc. will be obtained.

Author Contributions

The percentage of the author contributions is presented below. The author reviewed and approved the final version of the manuscript.

| | N.G.K. |
|-----|--------|
| C | 100 |
| D | 100 |
| S | 100 |
| DCP | 100 |
| DAI | 100 |
| L | 100 |
| W | 100 |
| CR | 100 |
| SR | 100 |
| PM | 100 |
| FA | 100 |

C=Concept, D= design, S= supervision, DCP= data collection and/or processing, DAI= data analysis and/or interpretation, L= literature search, W= writing, CR= critical review, SR= submission and revision, PM= project management, FA= funding acquisition.

Conflict of Interest

The author declared that there is no conflict of interest.

Ethical Consideration

Ethics committee approval was not required for this study because of there was no study on animals or humans. The authors confirm that the ethical policies of the journal, as noted on the journal's author guidelines page, have been adhered to.

References

Arino J, Protet S. 2020. A simple model for COVID-19. *Infectious Disease Modelling*, 5: 309-315.

Belen S, Kropat, E, Weber, GW. 2011. On the classical Maki-Thompson rumour model in continuous time. *Cent Eur J Oper Res*, 19: 1-17.

Brauer F, Castillo-Chavez C, Feng Z. 2019. *Mathematical models in epidemiology*. Springer-Verlag, New York, USA, First Edition, pp: 254.

Çifdalöz, O. 2022. Sustainable Management of a Renewable Fishery Resource with Depensation Dynamics from a Control Systems Perspective. *Gazi University J Sci*, 35 (3): 936-955.

Demirci E. 2023. A Novel Mathematical Model of the Dynamics of COVID-19. *GU J Sci*, 36(3): 1302-1309.

Gokgoz N, Oktem H. 2021. Modeling of tumor-immune system interaction with stochastic hybrid systems with memory: a piecewise linear approach. *Advances in the Theory of Nonlinear Analysis and its Application*, 5(1): 25-38.

Graves A, Schmidhuber J. 2008. Offline handwriting recognition with multidimensional recurrent neural networks. *Advances in neural information processing systems*, 21, 545-552.

Jin W, Stokes JM, Eastman RT, Itkin Z, Zakharov AV, Collins JJ, Jaakkola TS, Barzilay R. 2021. Deep learning identifies synergistic drug combinations for treating COVID-19. In: *Proceedings of the National Academy of Sciences of the United States of America*, 118(39): e21105070118.

Livieris IE, Pintelas E, Pintelas, P A. 2020. CNN-LSTM model for gold price time-series forecasting. *Neural Comput Applic*, 32: 17351-17360.

Magar R, Yadav P, Farimani AB. 2021. Potential neutralizing antibodies discovered for novel corona virus using machine learning. *Sci Rep*, 11: 5261.

Paul SG, Saha A, Biswas A, Zulfiker S, Arefin MS, Rahman M, Reza AW. 2023. Combating Covid-19 using machine learning and deep learning: Applications, challenges, and future perspectives. *Array*, 2023: 100271.

Padamallu CS, Özdamar L, Kropat E, Weber GW. 2012. A system dynamics model for intentional transmission of HIV/AIDS using cross impact analysis. *CEJOR*, 20(2): 319-336.

Sagheer A, Kotb M. 2019. Time series forecasting of petroleum production using deep LSTM recurrent networks. *Neurocomput*, 323: 203-213.

Siami-Namini S, Tavakoli N, Siami Namin A. 2018. A Comparison of ARIMA and LSTM in Forecasting Time Series. In: *17th IEEE International Conference on Machine Learning and Applications (ICMLA)*: pp: 1394-1401. doi: 10.1109/ICMLA.2018.

Subramanian N, Elharrouss O, Al-Maadeed S, Chowdhury M. 2022. A review of deep learning-based detection methods for COVID-19. *Computers Biol Med*, 2022: 105233

Tealab A. 2018. Time series forecasting using artificial neural networks methodologies: A systematic review. *Future Computing Informatics J*, 3(2): 334-340.

- Toğaçar M, Ergen B, Cömert Z. 2020. COVID-19 detection using deep learning models to exploit social mimic optimization and structured chest X-ray images using fuzzy color and stacking approaches. *Comput Biol Med*, 121: 103805.
- Vega DI. 2020. Lockdown, one, two, none, or smart. Modeling containing COVID-19 infection. A conceptual model. *Sci Total Environ*, 730: 138917.
- Wang P, Zheng X, Ai G, Liu D, Zhu B. 2020. Time series prediction for the epidemic trends of COVID-19 using the improved LSTM deep learning method: case studies in Russia, Peru and Iran. *Chaos Solit Fractals*, 140.
- Xu L, Magar R, Farimani AB. 2022. Forecasting COVID-19 new cases using deep learning methods. *Computers Biol Med*, 2022: 105342.
- Yunpeng L, Di H, Junpeng B, Yong Q. 2017. Multi-step ahead time series forecasting for different data patterns based on lstm recurrent neural network. In: 14th Web Information Systems and Applications Conference (WISA): pp: 305-310. doi: 10.1109/WISA.2017.25.



ETLİK PİLİÇ YETİŞTİRİCİLİĞİNDE ÇEVRE KOŞULLARININ İZLENMESİNE YÖNELİK WEB TABANLI BİR UZAK İZLEME SİSTEMİNİN GELİŞTİRİLMESİ

Hayrettin KARADÖL^{1*}, Ali ÇAYLI¹, Adil AKYÜZ¹, Serdar ÜÇOK¹

¹Kahramanmaraş Sütçü İmam University, Department of Biosystem Engineering, 46100 Kahramanmaraş, Türkiye

Özet: Etlik piliç yetiştiriciliği artan talep doğrultusunda giderek yaygınlaşan üretim kollarından biri haline gelmiştir. Kümes ortamında ortaya çıkan Karbondioksit, Amonyak, Hidrojen Sülfür gibi zararlı gazlar, atmosfer, kanatlı sağlığı ve dolayısıyla insan sağlığı açısından önemli etkilere sahiptir. Bu durum, etlik piliç yetiştiriciliğinde süreçlerinin hassas kontrolünü ön plana çıkarmaktadır. Bu çalışmada, etlik piliç üretimi yapan 2 katlı bir çiftliğe ait kümes içi ortam koşulları (sıcaklık, bağıl nem, karbondioksit ve amonyak,) 2 yetiştirme dönemi süresince sensörlerle okunmuştur. Daha sonra geliştirilen bir web server uygulaması ile uzak izleme sistemi oluşturulmuştur. 1. üretim döneminde kümes ortamının başlangıç sıcaklığı ortalama 34 °C, bağıl nem değerleri ise % 50 seviyelerinde gerçekleşmiştir. İlerleyen haftalarda sıcaklık değerinin kademeli olarak düştüğü ve üretim döneminin son günlerinde minimum sıcaklık değerinin 20 °C, bağıl nem değerinin ise %70 seviyelerine ulaştığı belirlenmiştir. 2. üretim dönemi süresince 9. günden itibaren yapılan ölçümlerde, ortalama sıcaklık değerinin 25 °C, bağıl nem değerleri ise % 50 seviyelerinde gerçekleşmiştir. İlerleyen haftalarda sıcaklık değerinin kademeli olarak düştüğü ve üretim döneminin son günlerinde minimum sıcaklık değerinin 14 °C, bağıl nem değerinin ise %70 seviyelerine ulaştığı belirlenmiştir. CO₂ değeri ise 1. üretim döneminde her iki kat için genel olarak kabul edilebilir sınır değer olan 3000 ppm değerini sadece 1. katta 2-3 saat süre ile aştığı diğer zamanlarda kabul edilebilir sınırlar içerisinde olduğu görülmüştür. Ancak havaların soğumasıyla birlikte 2. üretim döneminde 10-15. günlerde civcivlerin zemin katta 12 saatten daha fazla süreyle 3000 ppm'in üzerinde CO₂'e maruz kaldığı, 1. katta ise birkaç saat süre ile 5000 ppm seviyelerine kadar çıktığı görülmüştür. Her iki üretim dönemi için NH₃ değerinin son hafta içerisinde artış gösterme eğiliminde olduğu ve bu artışın maksimum 8 ppm değerine ulaştığı belirlenmiştir.

Anahtar kelimeler: PLC, Web sunucu, Etlik piliç


Development of a Web Based Remote Monitoring System for Environmental Conditions in Broiler Chicken Farming


Abstract: Broiler chicken farming has become one of the increasingly widespread branches of production due to rising demand. Harmful gases such as carbon dioxide, ammonia, and hydrogen sulfide that emerge in the poultry house environment have significant effects on the atmosphere, avian health, and consequently human health. This situation emphasizes the need for precise control over the processes in broiler chicken farming. In this study, indoor environmental conditions (temperature, relative humidity, carbon dioxide, and ammonia) of a 2-story poultry farm engaged in broiler production were monitored using sensors during 2 growing periods. Subsequently, a remote monitoring system was established through a developed web server application. During the 1st production period, the initial temperature of the poultry house environment averaged around 34 °C, while relative humidity values were at around 50%. In the following weeks, the temperature gradually decreased, and in the last days of the production period, the minimum temperature was determined to be 20 °C, and the relative humidity reached around 70%. Throughout the 2nd production period, starting from the 9th day, the average temperature was 25 °C, and relative humidity values were around 50%. As the weeks progressed, the temperature gradually decreased, and in the last days of the production period, the minimum temperature was found to be 14 °C, and the relative humidity reached around 70%. The CO₂ value during the 1st production period generally remained within acceptable limits for both floors, exceeding the widely accepted threshold of 3000 ppm only on the 1st floor for 2-3 hours and remaining within acceptable limits at other times. However, during the 2nd production period, with the cooling weather, it was observed that on days 10-15, chicks on the ground floor were exposed to CO₂ levels exceeding 3000 ppm for more than 12 hours, and on the 1st floor, CO₂ levels reached up to 5000 ppm for a few hours. For both production periods, the NH₃ value showed a tendency to increase in the last week, and this increase reached a maximum value of 8 ppm.


Keywords: PLC, Web server, Broiler


*Sorumlu yazar (Corresponding author): Kahramanmaraş Sütçü İmam University, Department of Biosystem Engineering, 46100 Kahramanmaraş, Türkiye

E mail: hayrettinkaradol@gmail.com (H. KARADÖL)

Hayrettin KARADÖL  <https://orcid.org/0000-0002-5062-0887>

Ali ÇAYLI  <https://orcid.org/0000-0001-8332-2264>

Adil AKYÜZ  <https://orcid.org/0000-0002-2120-0680>

Serdar ÜÇOK  <https://orcid.org/0000-0002-7158-669X>

Gönderi: 07 Ağustos 2023

Kabul: 10 Eylül 2023

Yayınlanma: 15 Ekim 2023

Received: August 07, 2023

Accepted: September 10, 2023

Published: October 15, 2023

Cite as: Karadol H, Çaylı A, Akyüz A, Üçok S. 2023. Development of a web based remote monitoring system for environmental conditions in broiler chicken farming. *BSJ Eng Sci*, 6(4): 426-433.



1. Giriş

Hızla artan Dünya nüfusuyla birlikte gıda ihtiyacı giderek artmaktadır. Bu durum birçok gıda alanında olduğu gibi etlik piliç üretiminin de artmasına neden olmaktadır. Etlik piliç yetiştiriciliğinde kümes ortamında oluşan zararlı gazlar hayvanların sağlığı ve elde edilecek ürün kalitesi açısından oldukça önemlidir. Kümeslerde kabul edilebilir iç ortam hava kalitesi oluşturmak için iç ortamdaki kirli havanın temiz hava ile değiştirilmesi gerekmektedir. Etlik piliçlere sağlanan kümes içi koşullar karkas kalitesinde belirleyici rol oynamaktadır (Yıldız ve ark., 2001; Sözlü ve Koyuncu, 2015). Yetiştirme süresince kümeslerde ortaya çıkan, hayvan sağlığını ve üretimini etkileyen en önemli kirleticiler amonyak, karbondioksit, su buharı, diğer zararlı gazlar ve altlık içerisindeki mikroorganizmalardır. Bu zararlı gazların kümes içerisindeki seviyeleri mutlaka göz önüne alınmalıdır (Kılıç ve Şimşek, 2009; Atılğan ve ark., 2010; Gürdil ve Yıldız, 2010; Yıldız ve ark., 2010; Dağtekin, 2012; Boyacı, 2018). Bu durum, yeni üretim tekniklerinin uygulamaya girmesini gerekli kılmış ve profesyonel üretim adı altında, otomasyon ve bilgisayar teknolojileri gibi faktörlerin üretim süreçlerinde kullanımını arttırmıştır (Avşaroğlu, 2008).

Kümes iç ortam koşullarının optimum seviyede tutulabilmesi için ortama ait veriler hassas sensörler kullanılarak algılanmaktadır. Algılanan bu veriler ise bir kontrolör tarafından değerlendirilerek, kümes havalandırma sisteminin kontrolü gerçekleştirilmektedir. Mikro işlemci temelli uzak kontrol sistemleri son yıllarda oldukça ilgi gören konulardan biridir. Günümüzde, tarımsal yapılarda kullanılan kontrol cihazlarının hala büyük bir çoğunluğunun ithal edilmesi, kaynak israfı ve teknik destek problemleri gibi sorunlara neden olmaktadır. Sera ve hayvan barınakları gibi yapılarda mikroişlemci temelli sistemlerin kullanılması, zaman, iş gücü ve verim açısından önemli avantajlar sağlamaktadır. Otomasyon sistemlerinin merkezinde bulunan mikroişlemcilerin çevre birimleri ile yaptığı iletişim protokolleri son yıllarda giderek artmaktadır. Örneğin modern PLC'ler (Programmable Logic Controller - Programlanabilir Mantık Denetleyicisi) herhangi bir standart web tarayıcısı aracılığıyla görüntülenebilen ve gerçek zamanlı olarak bilgilere ve teşhislere açık uzak erişim sağlayan gömülü web sunucuları içermektedir. Böylece, kullanıcılar PLC'ye fiziksel olarak yakın olmak zorunda kalmadan, internet üzerinden erişim sağlayabilir ve kontrol işlemlerini gerçekleştirebilmektedirler. PLC web sunucusu genellikle bir ethernet bağlantısı üzerinden internet ağına bağlanmakta ve kullanıcılara çeşitli işlevler sunmaktadır bunlar; (1) PLC'nin çalışma durumunu, giriş/çıkış durumunu ve diğer değişkenlerin durumunu izleme, (2) PLC'nin parametrelerini, hedef değerleri ve çalışma modlarını ayarlama ve değiştirme (Da'na ve ark., 2008), (3) PLC'ye yeni kontrol programları yüklemek veya var olan programları düzenlemek için bir programlama arayüz sağlama, (4) uygulama performansını değerlendirmek, üretim

verimliliğini analiz etmek ve hataları tespit etmek amacıyla, PLC tarafından üretilen verileri kaydetme, raporlama ve analiz etme ve (5) PLC tarafından üretilen alarm ve hata mesajlarını izleme ve yönetme imkanı sağlamaktadır (Siemens, 2023).

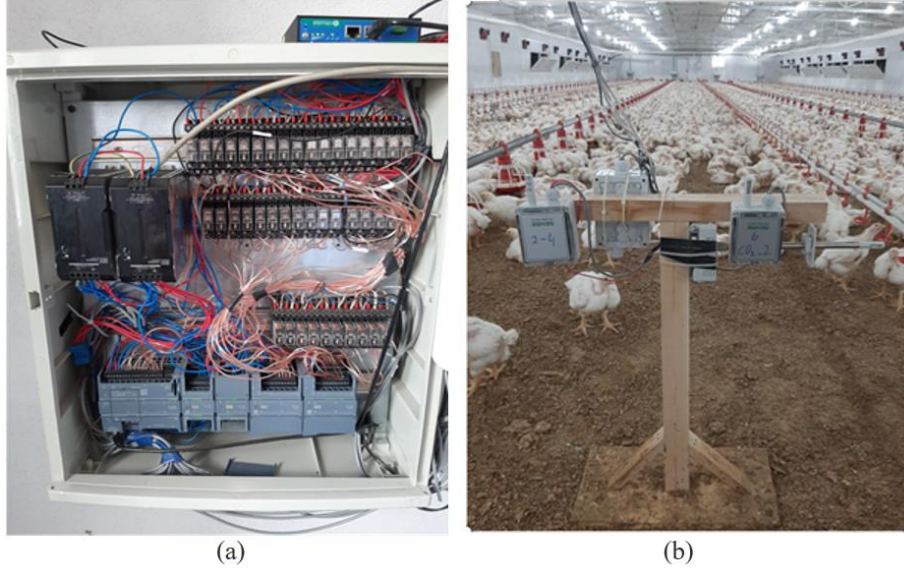
Etlik piliç yetiştiriciliğinde özellikle kış aylarında piliçlerin istediği sıcaklık değerlerinin yüksek olduğu düşünüldüğünde kümes içi çevre koşullarının optimum değerlerin altında ya da üzerinde olması, verim ve enerji kayıpları açısından oldukça önemlidir. Bu nedenle kümes çevre koşullarının, otomasyon sistemleriyle izlenmesi ve gerekli durumlarda hızlı bir şekilde müdahalelerin gerçekleştirilmesi bu kayıpları önemli ölçüde azaltabilecektir. Bu araştırmanın amacı, etlik piliç çiftliğine ait ortam koşullarını (sıcaklık, nem, amonyak ve karbondioksit) sensörlerle okumak, bu sensör verilerine ait değişkenleri PLC web sunucu uygulamasına aktarılacak ve ilgili verilerin uzak veri tabanı sunucusu (UVTS) üzerinde tarih ve saat etiketleriyle izlenmesini sağlamaktır. Ayrıca oluşturulan web sayfası üzerinden PLC değişkenlerine erişilerek, kümese ait aktuatörlerin çalışma durumları, internet üzerinden değiştirilebilmektedir.

2. Materyal ve Yöntem

Çalışma, Kahramanmaraş Türkoğlu bölgesinde bulunan ticari etlik piliç yetiştiriciliği yapan bir kümeste gerçekleştirilmiştir. Kümes 2 katlı olup her bir katta kontrol panoları bulunmaktadır. Her bir kontrol panosunda bulunan; 12 tünel fan kontağının, 4 minimum havalandırma fanı kontağının, 2 klepe kontağının (aç-kapa), 2 soğutma peteği kontağının (aç-kapa), 1 adet ısıtıcı kontağının ve 1 adet su pompası kontağının kontrol terminalleri PLC dijital girişlerine bağlanmıştır. Sensörler her iki katta kümesin merkezinde bulunan yerden 60 cm yüksekliğe sahip bir ahşap ayak üzerine monte edilmiştir. Sensörlerin elektriksel beslemesi ve data bilgilerini okumak amacıyla giriş kata bir kontrol panosu monte edilmiştir. Sensör-pano arası bağlantı için yaklaşık 60 m uzunluğunda kablolar kullanılmıştır. Kümese ait aktuatörleri tetikleyebilmek amacıyla, PLC çıkış terminalleri ile kümese ait yüksek gerilim panolarında bulunan kontaktörler arasında 36 adet DC/AC 220 V röleler kullanılmıştır (Şekil 1 a ve b). Çalışmada sistemin kontrolü için 1 adet S7-1200 PLC (6ES7214-1AG40-0XB0, 14 dijital giriş 10 dijital çıkış ve 2 adet 0-10 V analog giriş), 2 adet analog giriş modülü (SM 1234, 4 Analog giriş, 2 Analog çıkış) ve 2 adet dijital giriş-çıkış modülü (SM 1223 16 dijital giriş/ 16 Dijital çıkış) kullanılmıştır. Çalışmada sıcaklık-nem (SHO.355), karbondioksit (SCD.W51) ve amonyak (SNH.W51) sensörleri olmak üzere 3 farklı sensör kullanılmıştır. Sensörlerin çıkış sinyal tipi ve ölçüm aralıkları Tablo 1'de sunulmuştur. Çalışmada sensör verilerini izlemek ve kümese ait tüm aktuatörlerin uzak kontrolünü gerçekleştirmek için PLC dahili web sunucusu üzerinden alınan verilerin uzak veri tabanı sunucusuna aktarılması amacıyla, bir 4G modem (Robustel R2000-4L) kullanılmıştır.

Tablo 1. Araştırmada kullanılan sensör özellikleri

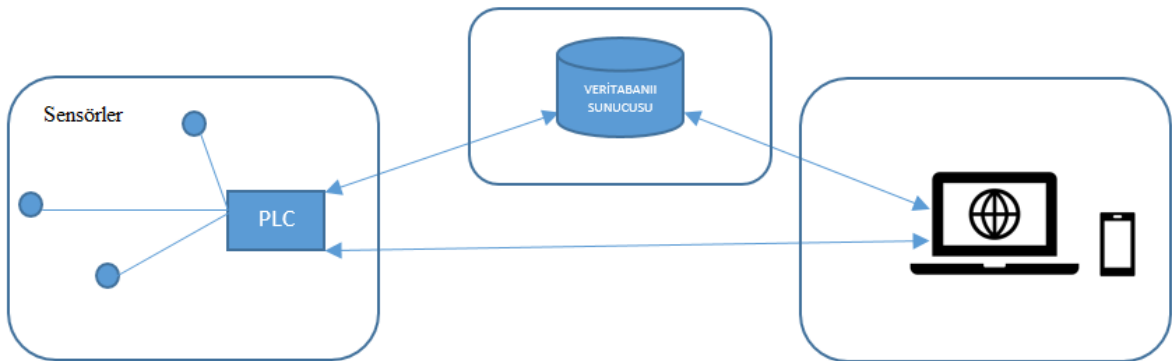
| Ölçülen değişken | Çıkış sinyali | Ölçüm aralığı |
|------------------|---------------|--------------------|
| Sıcaklık-nem | 4-20 mA | 0-100 °C - %0-%100 |
| CO ₂ | 4-20 mA | 400-10000 ppm |
| NH ₃ | 0-10 Volt | 0-100 ppm |



Şekil 1. Oluşturulan kontrol panosu (a) ve sensörler (b).

Sensör verilerinin doğrudan PLC web sunucusu (PWS) üzerinden görüntülenmesi için index.htm dosyası oluşturulmuştur. Bu dosya içerisinde, PLC dokümanlarında belirtilen yöntem ile değişkenlere atanmış olan sensör veri çıkışları, sunucu ara yüzünden anlık olarak görüntülenmiştir. Ana sayfa dosyası olan index.htm dosyasında JavaScript kitaplıklarının avantajlarını kullanmak için JQuery kitaplığı kullanılmıştır (JQuery, 2020). Benzer şekilde, web sayfasının stili ve biçimlendirmesi de CSS stil sayfaları dahil edilerek yapılmıştır (Bootstrap, 2020). Aynı zamanda analiz ve raporlama amaçlı PLC sensör verilerinin İnternet ağı üzerinden uzak veri tabanı sunucusuna kaydedilmesi için, modem üzerinden PLC yerel ip adresine yönlendirme yapılarak PWS'ye İnternet üzerinden erişim sağlanmıştır. UVTS olarak Centos 7 GNU/Linux işletim sistemi üzerinde çalışan MariaDB veritabanı sunucusu kullanılmıştır (MariaDB Foundation,

2020). Sistemin diyagramı Şekil 2'de verilmiştir. PWS'de index.htm dosyasından farklı olarak bir de json.htm dosyası oluşturulmuş ve bu dosya ile tüm PLC sensör verileri ile PLC tarafından kontrol edilen aktuatörlerin durumlarına ait veriler JSON formatında PWS'den uzak sunucuya her 5 dakikada bir aktarılmıştır. Uzak sunucu üzerinde bu işlem için kabuk ortamında çalışan bir betik geliştirilmiştir. PWS'den alınan veriler PHP programla dili ile geliştirilen bir kod ile ayrıştırılıp verinin tutarlılığı kontrol edilerek UVTS'ye aktarılmış ve sensör numarası, tarih-saat ve sensör ölçüm değerleri şeklinde oluşturulan tablolara kaydedilmiştir (Şekil 3). Araştırma süresince sadece sensör verileri kaydedilmiştir. Kümese ait bir PLC kontrol sistemi bulunması nedeniyle aktüatörlere herhangi bir müdahale bulunulmamıştır. Bu nedenle aktüatörlerin durumu sunucu üzerinden izlenmiş ancak kaydedilmemiştir.



Şekil 2. PLC'den uzak sunucu üzerinde çalışan UVTS'ye veri aktarımı.

| Kümeslerde Ortam Koşullarının Denetlenmesi İçin Bir Uzak Kontrol Sisteminin Geliştirilmesi Projesi Yeni Dev: 01.2023.11.13.0317+0309 (0317+0309) | |
|---|------------|
| Zemin | Kat 1 |
| SICAKLIK (°C) | 19.01 °C |
| BAGIL NEM (%) | 19.25 °C |
| KARBONDİOKSİT (CO2) (ppm) | 67.25 % |
| AMONYAK (NH3) (ppm) | 78.25 % |
| HAVAKİMLİK (m/s) | 450.69 ppm |
| BASINÇ FARKI (pa) | 452.78 ppm |
| DIĞ ORTAM | 0 ppm |
| Sıcaklık | 0 m/s |
| Bağıl Nem | 0 pa |
| | 0 °C |

| ÖLÇÜLER | | | | |
|--|--|---|---|--|
| Zemin Kat Petek Kapak İçerisi KAPALI | Zemin Kat Petek Aç İçerisi KAPALI | Zemin Kat Klape Kapak İçerisi KAPALI | Zemin Kat Klape Aç İçerisi KAPALI | Zemin Kat Isılma İçerisi KAPALI |
| Zemin Kat Su Pompası İçerisi KAPALI | Zemin Kat Min Fan 1 İçerisi KAPALI | Zemin Kat Min Fan 2 İçerisi KAPALI | Zemin Kat Min Fan 3-4 İçerisi KAPALI | Zemin Kat Min Fan 3-4 İçerisi KAPALI |
| Zemin Kat Tünel Fan 1 İçerisi KAPALI | Zemin Kat Tünel Fan 2 İçerisi KAPALI | Zemin Kat Tünel Fan 3 İçerisi KAPALI | Zemin Kat Tünel Fan 4 İçerisi KAPALI | Zemin Kat Tünel Fan 5 İçerisi KAPALI |
| Zemin Kat Tünel Fan 6 İçerisi KAPALI | Zemin Kat Tünel Fan 7 İçerisi KAPALI | Zemin Kat Tünel Fan 8 İçerisi KAPALI | Zemin Kat Tünel Fan 9 İçerisi KAPALI | Zemin Kat Tünel Fan 10 İçerisi KAPALI |
| Zemin Kat Tünel Fan 11 İçerisi KAPALI | Zemin Kat Tünel Fan 12 İçerisi KAPALI | Zemin Kat Diğ. İçerisi KAPALI | 1. Kat Klape Aç İçerisi KAPALI | 1. Kat Klape Kapak İçerisi KAPALI |

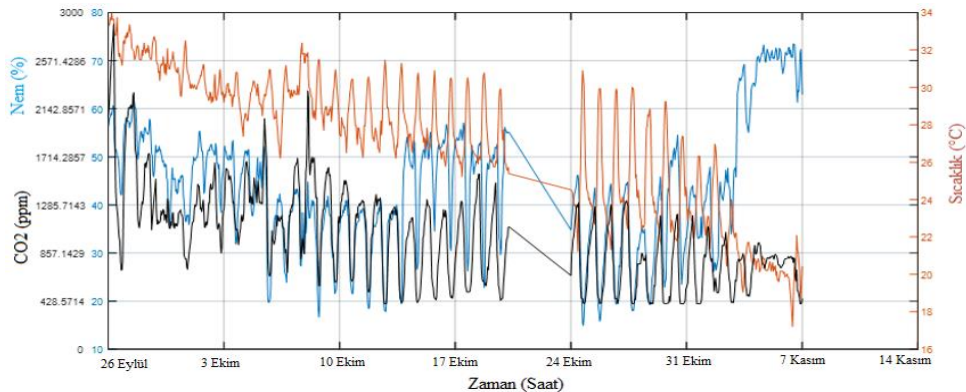
Şekil 3. Web sunucu ara yüzü.

Çalışmada, bir etlik piliç üretimi yapan 2 katlı bir çiftliğe ait ortam koşulları (sıcaklık, nem, karbondioksit, amonyak, ve hava akışı hızı) 2 yetiştirme dönemi süresince sensörlerle okunmuş ve geliştirilen bir web server uygulaması ile uzak izleme sistemi oluşturulmuştur. 1. üretim dönemi ölçümleri 25 Eylül- 6 Kasım tarihleri arası ve 2. üretim dönemi ölçümleri ise 9 Aralık-16 Ocak tarihleri arasında gerçekleştirilmiştir. Uzak sunucu üzerinden elde edilen veriler hem gerçek zamanlı olarak izlenmiş hem de 5 dk. aralıklarla veri tabanına tarih ve saat etiketleriyle birlikte kaydedilmiştir. Kaydedilen bu değerler daha anlaşılır ve sade bir görünüm elde etmek amacıyla grafikler saatlik olarak oluşturulmuştur. İlk olarak her iki üretim dönemi için kümes ortamında oluşan sıcaklık, nem ve karbondioksit değerleri, daha sonra son haftada oluşan nem, CO₂ ve amonyak değerleri birlikte sunulmuştur. 2. üretim dönemi ölçümleri civcivlerin kümes ortamına girişinden 9 gün sonra başlanmıştır. Ayrıca 1. üretim döneminde 19 Ekim 24 Ekim tarihleri arasında kümeslerde oluşan elektriksel bir sorun nedeniyle 5 gün

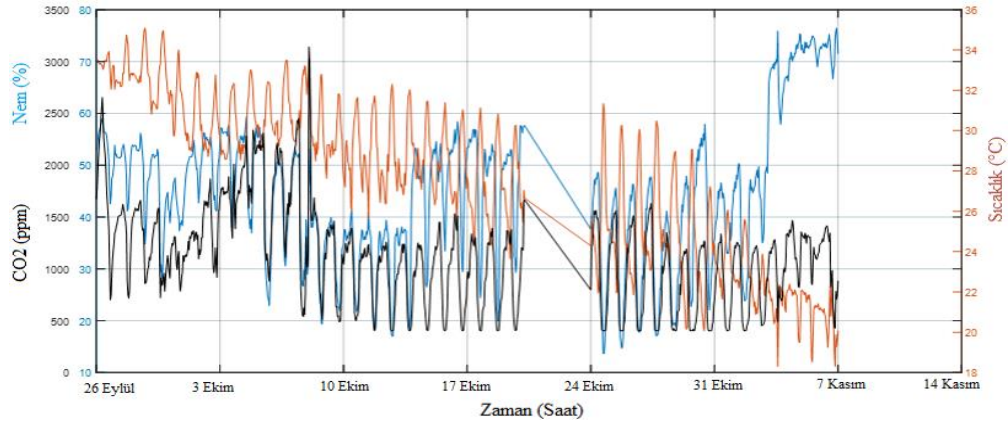
süre ile veri kaydedilememiştir.

3. Bulgular ve Tartışma

1. üretim döneminde her iki kat için kümes ortamının başlangıç sıcaklığı yaklaşık 34 °C olduğu, nem değerlerinin yaklaşık %50 seviyesinde olduğu görülmektedir. Sıcaklık değerinin her iki kat için 32-34°C seviyelerinde olduğu takip eden günlerde kademeli olarak düştüğü ve son günlerde yaklaşık 18 °C seviyesine kadar düştüğü görülmektedir. Nem değerinin ise başlangıç günlerinde her iki kat için ortalama %50 seviyesinde olduğu, 2. haftadan itibaren ise gündüz saatlerinde %20 seviyelerine kadar düştüğü ve son günlerde hızlı bir şekilde artarak %70 seviyelerine çıktığı görülmektedir. CO₂ açısından bakıldığında ise 1. üretim döneminde her iki kat için genel olarak kabul edilebilir sınır değer olan 3000 ppm değerini sadece 1. katta 2-3 saat süre ile aştığı (bu süreçte üretici uyarılmış ve manuel havalandırma devreye alınmıştır) diğer zamanlarda kabul edilebilir sınırlar içerisinde olduğu görülmektedir (Şekil 4 ve 5).



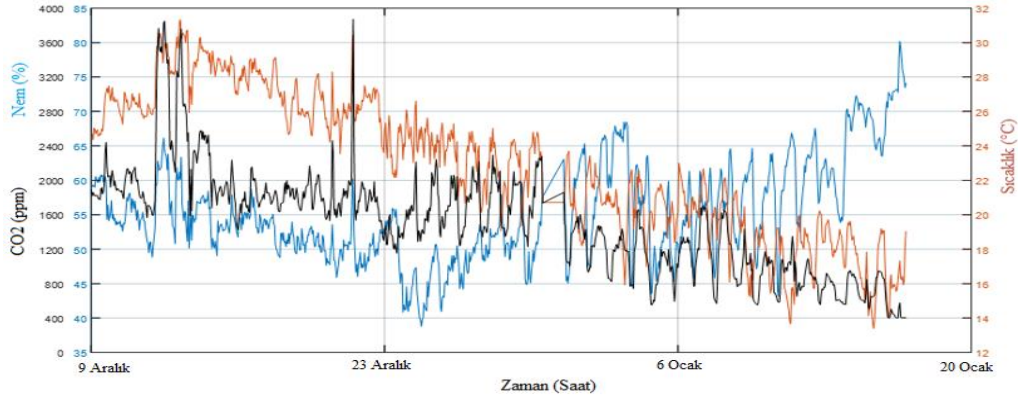
Şekil 4. 1. Üretim dönemi zemin kat CO₂, sıcaklık ve nem değerleri.



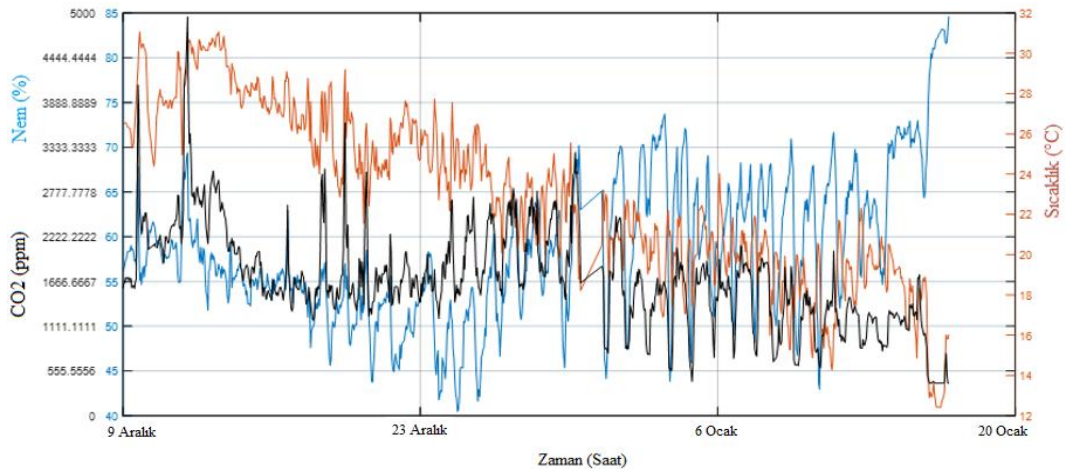
Şekil 5. 1. Üretim dönemi 1. kat CO₂, sıcaklık ve nem değerleri.

2. üretim dönemi süresince 9. günden itibaren yapılan ölçümlerde, sıcaklık değerinin her iki kat için 24-26°C seviyelerinde olduğu takip eden günlerde her iki kat için de 30 °C değerine çıktığı ve daha sonra kademeli olarak düşerek son günlerde yaklaşık 14 °C seviyesine kadar düştüğü görülmüştür. Nem değerinin ise başlangıç

günlerinde her iki kat için yaklaşık %55-65 seviyelerinde olduğu, 2. haftadan itibaren gündüz saatlerinde minimum %40 seviyelerine düştüğü ve son günlerde hızlı bir şekilde artarak %70 seviyelerine çıktığı görülmektedir (Şekil 6 ve 7).



Şekil 6. 2. Üretim dönemi zemin kat CO₂, sıcaklık ve nem değerleri.



Şekil 7. 2. Üretim dönemi 1. kat CO₂, sıcaklık ve nem değerleri.

Havaların soğumasıyla birlikte 2. üretim döneminde 10-15. günlerde civcivlerin zemin katta 12 saatten daha fazla süreyle 3000 ppm'in üzerinde CO₂ 'e maruz kaldığı, 1. katta ise birkaç saat süre ile 5000 ppm seviyelerine kadar çıktığı görülmüştür. İlk iki hafta süresince kümes iç bölgesinin bölünerek civcivler için daha küçük bir

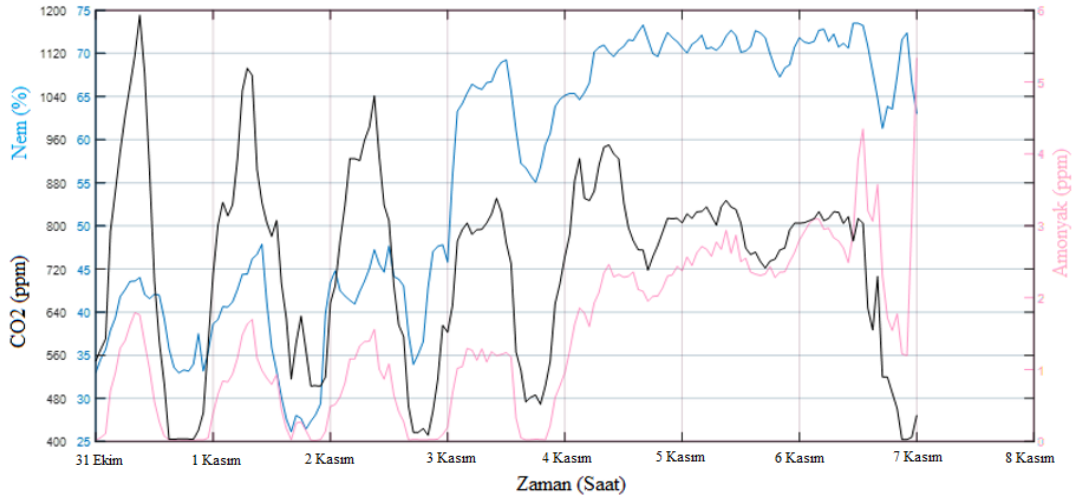
hacmin oluşturulması sonucunda CO₂ değerinde sınır değerinin üzerine çıkılmasına neden olduğu anlaşılmaktadır. Civciv döneminde yüksek CO₂ konsantrasyonunun 24 saatten fazla devam etmesi durumunda geç dönem (30. günden sonra) ölüm oranı artış göstermektedir (Olanrewaju ve ark., 2008). Her iki

üretim dönemi için ilk 3 haftalık sürede CO₂ miktarının çoğunlukla nem değeri ile orantılı olarak artış gösterdiği görülmektedir ancak bu sonuç nem oranının, CO₂ seviyesiyle kesin bir ilişkisi olduğunu göstermemektedir. Çünkü son hafta içerisinde nem değerinin %70-80 seviyelerine ulaştığı görülmüş, ancak CO₂ değerinin aynı hızda artmadığı görülmüştür. Bu durum, son hafta içerisinde çalışan havalandırma fanı sayısındaki artışa bağlı olarak ortamdaki CO₂ gazının bir miktar uzaklaştırıldığı ancak nemin yeterince uzaklaştırılmadığını göstermektedir.

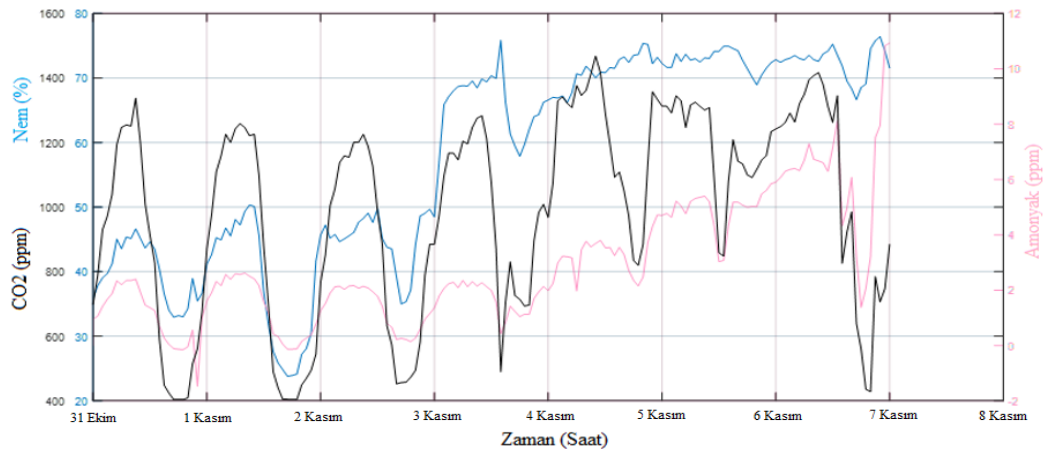
Etlük piliç kümeslerinde sıcaklığın ilk haftada 30 ila 33°C arasında olması gerektiğini ve daha sonra sıcaklığın 6. haftaya kadar 2 ila 3 °C arasında kademeli olarak düşürülmesi gerektiğini ve kesim sürecine kadar 18-21°C'lik sıcaklık değerinin muhafaza edilmesi gerektiğini bildirmiştir (Maton ve ark., 1985). Bu kümeslerde ideal nem değerinin ise % 60-80 aralığında tutulması gerektiği bildirilmektedir (Poltryhub, 2023). Bu araştırmada 2.

üretim döneminde her iki küme sıcaklık değerinin son hafta içerisinde ideal sıcaklık değerinin 3-4 °C altına düştüğü, nem değerinin ise 1. üretim döneminde özellikle gündüz saatlerinde %20 seviyelerine düştüğü belirlenmiştir. Küme içindeki düşük nem kümes içerisindeki havada dolaşan kuru toz oranının artmasına neden olmaktadır.

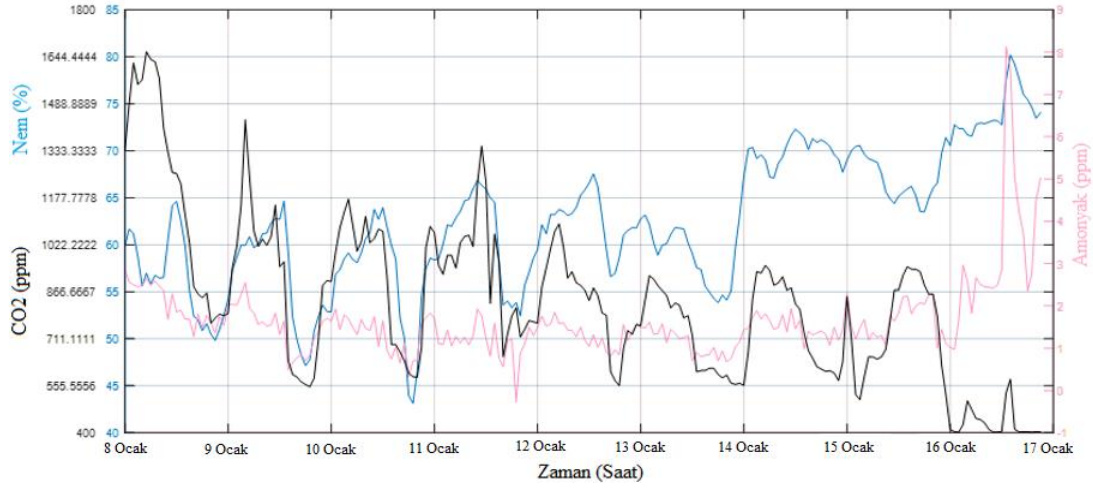
Her iki üretim dönemi için NH₃ değerinin son hafta içerisinde artış gösterme eğiliminde olduğu ve bu artışın maksimum 1. üretim döneminde 1. katta 8-10 ppm civarında olduğu görülmüştür. Her iki üretim dönemi için amonyak değerinin zarar eşik değeri olarak kabul edilen 20 ppm (Al-Mashhadani ve Beck, 1985) değerine ulaşmadığı görülmüştür. Özellikle gece saatlerinde nem değerinin artmasıyla birlikte CO₂ ve NH₃ değerlerinin de arttığı görülmektedir. Ancak yetiştirme periyodunun son günlerinde CO₂ ve NH₃ değerleri düşerken nem değerindeki artış devam etmektedir. Bu durum Şekil 8, 9, 10 ve 11'de daha ayrıntılı olarak görülmektedir.



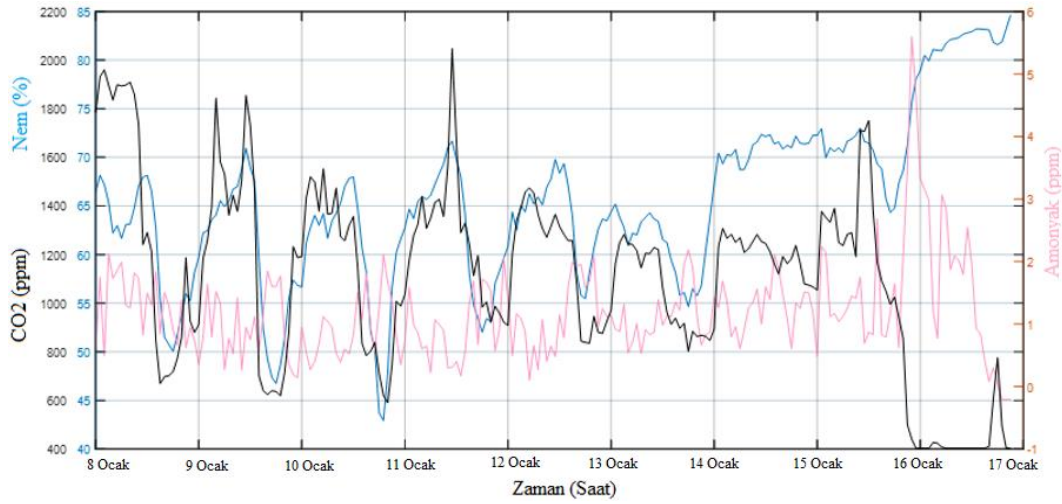
Şekil 8. 1. Üretim dönemi 34-42. günler zemin kat CO₂, amonyak ve nem değerleri.



Şekil 9. 1. Üretim dönemi 34-42. günler 1. kat CO₂, amonyak ve nem değerleri.



Şekil 10. 2. Üretim dönemi 34-42. günler zemin kat CO₂, amonyak ve nem değerleri.



Şekil 11. 2. Üretim dönemi 34-42. günler 1. kat CO₂, amonyak ve nem değerleri.

4. Sonuç

Üretim süreci boyunca kümes içi sıcaklık değerinin 1. üretim döneminde başlangıç günlerinde, kabul edilebilir sıcaklık değerinden 1-2 °C daha fazla olduğu, 2. üretim döneminde ise her iki katta sıcaklık değerinin kabul edilebilir seviyeden 3-4 °C daha az olduğu görülmüştür. Hava bağıl nem değerleri ise yetiştiricilik dönemi boyunca kabul edilebilir sınır değerleri arasında kalmıştır. Kümes içerisinde civcivleri ısıtmak amacıyla ilk iki hafta süresince kümes hacminin küçültülmesi sonucunda CO₂ seviyesinin eşik değerden daha yüksek seviyelere ulaşmasına neden olmuştur. Ayrıca ölçüm sürecinde her iki kat için yaklaşık ilk 3 hafta süresince CO₂ ve hava bağıl nem değerlerinin birbiriyle paralel olarak arttığı gözlenmiştir. Amonyak değerinin ise her iki üretim döneminde de zarar eşik değerine ulaşmadığı görülmüştür. Bu çalışmada, genel olarak bir kümese ait ortam verileri internet ağı üzerinden gerçek zamanlı olarak izlenmiş ve istenmeyen bir durumla karşılaşılması halinde işletme sahibi bilgilendirilerek gereken önlemler alınabilmesi sağlanmıştır. Bu araştırma, maliyet ve iş gücü açısından daha efektif olabilecek mikrodenetleyici tabanlı kablosuz haberleşme yöntemine altyapı oluşturmuştur.

Katkı Oranı Beyanı

Yazar(lar)ın katkı yüzdesi aşağıda verilmiştir. Tüm yazarlar makaleyi incelemiş ve onaylamıştır.

| | H.K. | A.Ç. | A.A. | S.Ü. |
|-----|------|------|------|------|
| K | 40 | 20 | 20 | 20 |
| T | 70 | 30 | | |
| Y | 40 | 20 | 20 | 20 |
| VTI | 50 | 50 | | |
| VAY | 100 | | | |
| KT | 70 | 30 | | |
| YZ | 70 | 30 | | |
| KI | 40 | 20 | 20 | 20 |
| GR | 100 | | | |
| PY | 40 | 20 | 20 | 20 |
| FA | 40 | 20 | 20 | 20 |

K= kavram, T= tasarım, Y= yönetim, VTI= veri toplama ve/veya işleme, VAY= veri analizi ve/veya yorumlama, KT= kaynak tarama, YZ= Yazım, KI= kritik inceleme, GR= gönderim ve revizyon, PY= proje yönetimi, FA= fon alımı.

Çatışma Beyanı

Yazarlar bu çalışmada hiçbir çıkar ilişkisi olmadığını beyan etmektedirler.

Etik Onay Beyanı

Bu arařtırmada hayvanlar ve insanlar üzerinde herhangi bir alıřma yapılmadıđı için etik kurul onayı alınmamıřtır.

Destek ve Teřekkür Beyanı

Bu arařtırma Kahramanmarař Sütü İmam Üniversitesini Bilimsel Arařtırmalar Proje (BAP) Koordinasyon Birimi tarafından desteklenmiřtir (Proje No: 2019/3-19 M). BAP Koordinasyon Birimi'ne desteklerinden dolayı teřekkür ederiz.

Kaynaklar

- Al-Mashhadani E, Beck M.M 1985. Effect of atmospheric ammonia on the surface ultrastructure of the lung and trachea of broiler chicks. *Poultry Sci*, 64(11): 2056-2061.
- Atılđan A, Cořkan A, Öz H, İřler E. 2010. Etlik pili kümesinde kiř döneminde amonyak gaz düzeyinin vakum sistemi ile azaltılması. *Kafkas Univ Vet Fak Derg*, 16(2): 257-262.
- Avřarođlu, H. 2008. ukurova kořullarında Broiler Kümeslerinde Kullanılan Bir Pedli Serinletme Sisteminin Performans Özellikleri ve Kümes İi Sıcaklık Dađılımı. Yüksek Lisans Tezi, ukurova Üniversitesi, Fen Bilimleri Enstitüsü, Adana, Türkiye, pp: 47.
- Bootstrap. 2020. Bootstrap Basic Table. https://www.w3schools.com/bootstrap/bootstrap_tables.asp (eriřim tarihi: 12 Ocak 2022).
- Boyacı S. 2018. Etlik pili kümeslerinde, ısıtma ve sođutma derece gün deđerlerinin derece gün yöntemiyle belirlenmesi: Kırřehir ili örneđi. *Nevřehir Bil Teknol Derg*, 7(1): 75-82.
- Dađtekin M. 2012. Etlik pili kümeslerinin serinletilmesinde güneř enerjisi kullanımının tekno-ekonomik analizi. *ukurova Üniv Zir Fak Derg*, 27(2): 11-20.
- Da'na, S, Sagahyoon A, Elrayes A, Al-Ali AR, Al-Aydi, R. 2008. Development of a monitoring and control platform for PLC-based applications. *Comp Stand Interfaces*, 30(3): 157-166.
- Gürdil GA, Yıldız Y. 2010. Kümeslerde havalandırma

- sistemlerinin tasarımına yönelik bir programın geliřtirilmesi üzerinde bir arařtırma. Doktora Tezi, ukurova Üniversitesi, Fen Bilimleri Enstitüsü, Adana, Türkiye, pp: 237.
- jQuery. 2023. jQuery html Method. URL: https://www.w3schools.com/jquery/html_html.asp (eriřim tarihi: 22 Mayıs 2022).
- Kılı İ, řimřek E. 2009. Hayvan barınaklarından kaynaklanan gaz emisyonları ve çevresel etkileri. *Uludađ Üniv MühMimarlık Fak Derg*, 14(2): 151-160.
- MariaDB Foundation. 2020. MariaDB Server. URL: https://mariadb.org/download/?t=mariadb&p=mariadb&r=11.2.0&os=windows&cpu=x86_64&kg=msi&m=truenetwork (eriřim tarihi: 10 Mayıs 2022).
- Maton A, Daelemans J, Lambrecht J. 1985. *Housing of Animals*. Elsevier Science Publishing Company Inc., Newyork, US, pp: 458.
- Olanrewaju HA, Dozier WA, Purswell JL, Branton SL, Miles DM, Lott BD, Thaxton JP. 2008. Growth performance and physiological variables for broiler chickens subjected to short-term elevated carbon dioxide concentrations. *Int J Poultry Sci*, 7(8):738-742.
- Poltryhub. 2023. Climate in Poultry Houses. URL: <https://www.poultryhub.org/all-about-poultry/husbandry-management/climate-in-poultry-houses> (eriřim tarihi: 2 Ađustos 2023).
- Siemens. 2023. S7/1200 PLC. URL: <https://www.siemens.com/global/en/products/automation/systems/industrial/plc/s7-1200.html> (eriřim tarihi: 18 Aralık 2021).
- Sözcü A, Koyuncu M. 2015. Etlik pili yetiřtiriciliđinde çevresel kořulların ve beslemenin karkas kalitesi üzerine etkileri. *Uludađ Üniv Zir Fak Derg*, 29(1): 115-122.
- Yıldız Y, Gürdil GAK, Dađtekin M. 2001. Adana çevresi etlik yetiřtirme kümeslerinde amonyak NH3 ve hidrojen sülfür H2S gazlarının oluřum düzeyleri. *Tarımsal Mekanizasyon 20. Ulusal Kongresi, řanlıurfa, Türkiye*, 13 - 15 Eylül 2001, pp: 317-323.
- Yıldız Y, Karaca C, Dađtekin M. 2010. Hayvan barınaklarında çevre denetim. *Hasad Yayıncılık*, Adana, Türkiye, pp: 256.



A NEW SOLUBLE COPPER PHTHALOCYANINE DERIVATIVE AS A SMART MATERIAL

Fuat ERDEN¹, Ebru YABAŞ^{2*}

¹Sivas University of Science and Technology, Department of Aeronautical Engineering, 58000 Sivas, Türkiye


²Sivas Cumhuriyet University, Advanced Technology Application and Research Center, 58140, Sivas, Türkiye


Abstract: Copper phthalocyanine (CuPc) and its derivatives are considered as candidate materials in many applications. Particularly, easy and sensitive film-forming ability, commercial availability, chemical stability, and ease in tailoring its molecular structure make CuPc a versatile material. On the other hand, main challenge that Pcs often exhibit is their poor solubility in organic solvents. In this sense, this work involves designing of new CuPc derivatives by introducing suitable substitutions to improve the solubility in organic solvents. Specifically, [2,9,16,23-tetra{(4,5-Diphenyl-1H-imidazole)-2-yl-thio}phthalocyaninato-copper(II)] (1) and [2,9,16,23-tetra{(4,5-Diphenyl-1-methyl-1H-imidazole)-2-yl-thio}phthalocyaninato-copper(II)] (2) were prepared. The results show that compound 1 is soluble in tetrahydrofuran (THF), dimethylformamide (DMF), and dimethyl sulfoxide (DMSO), and compound 2 is soluble in chloroform, acetone, methanol, THF, DMF, and DMSO. Optical and spectroscopic properties of the synthesized compounds were also investigated, and it was determined that the energy band gaps of compounds 1 and 2 are 1.70 eV and 1.56 eV, respectively. Strikingly, we demonstrate that compound 1 is exhibiting a rapid and reversible color change behavior upon altering pH in the entire pH spectrum. As it is known, materials that respond reversibly to chemical and/or physical stimuli in a controllable fashion are regarded as smart materials. Hence, we report that compound 1 is actually a smart material that can be used as a simple yet efficient pH sensor.

Keywords: Phthalocyanine, Copper, pH sensor, Aggregation, Band gap

*Corresponding author: Sivas Cumhuriyet University, Advanced Technology Application and Research Center, 58140, Sivas, Türkiye

E mail: eyabas@cumhuriyet.edu.tr (E. YABAŞ)

Fuat ERDEN  <https://orcid.org/0000-0002-8261-4844>

Ebru YABAŞ  <https://orcid.org/0000-0001-7163-3057>

Received: August 11, 2023

Accepted: September 10, 2023

Published: October 15, 2023

Cite as: Erden F, Yabaş E. 2023. A new soluble copper phthalocyanine derivative as a smart material. BSJ Eng Sci, 6(4): 434-441.

1. Introduction

Organic semiconductor materials are receiving a considerable interest for many potential applications. Unlike their inorganic counterparts, the organic semiconductors are lightweight, flexible, cheap, and exhibit improved light absorption over a wide wavelength range. Besides, they also have tunable molecular structures to obtain desired optical and electronic properties (Claessens et al., 2001; Alosabi et al., 2022). Metallophthalocyanines, from the well-known organic semiconductor class, are one of the most promising candidates due to their properties such as favorable band gap and chemical and thermal stability. Stable metallophthalocyanines with 18 delocalized π electrons have a wide range of synthetic variations (Claessens et al., 2001; Afify et al., 2015; Ai et al. 2018). Among the metallophthalocyanines, copper phthalocyanine is widely preferred in organic electronic applications, thanks to its chemical stability, high molecular symmetry, easy and sensitive film-forming ability, commercial availability, and excellent optical and electronic properties (Djurisic et al., 2002; Farag, 2007; Tong et al., 2007; Mali et al., 2012; Sánchez-Vergara et al., 2012; Afify et al., 2015; McAfee et al., 2016; Dakoğlu-Gülmez et al., 2017; Hamam, 2017; Ai et al. 2018).

In fact, copper phthalocyanines have the potential to be used in almost all types of organic electronic devices, including diodes, transistors, photovoltaics, light emitting diodes, photodetectors, rectifiers, temperature sensors, radiation dosimeters, and chemical sensors (Djurisic et al., 2002; Farag, 2007; Tong et al., 2007; Mali et al., 2012; Sánchez-Vergara et al., 2012; Afify et al., 2015; McAfee et al., 2016; Dakoğlu-Gülmez et al., 2017; Hamam, 2017; Ai et al. 2018). Because, copper phthalocyanine is a square planar molecule that forms a stack of different polymorphs with varying molecular arrangements and orientations. Hence, it could be predicted that the diversity in applications might further increase with the modification of the chemical environment of the molecule. For instance, while Raval et al. demonstrated that copper phthalocyanine based organic electronic devices could be used as sensors for ionizing radiation of γ -rays (Raval et al., 2013), Chaure et al. (2011) used 1,4,8,11,15,18,22,25-octakis(hexyl) copper phthalocyanine films in the fabrication of organic field-effect transistors (Chaure et al., 2011). In another work, Wang et al. (2017) showed that tetra-alkyl-substituted copper phthalocyanines could be used as dopant-free hole transport layers in planar perovskite solar cells (Wang et al., 2017). Overall, while copper phthalocyanine



is promising in terms of ease in altering its molecular arrangement to adapt it to countless of different applications, the phthalocyanines usually exhibit poor solubility in organic solvents, which hinders them to reach their true potential.

In this context, we aimed at improving the solubility of copper phthalocyanine in organic solvents by designing its new derivatives through selection of suitable substituents. Namely, we prepared [2,9,16,23-tetra{(4,5-Diphenyl-1H-imidazole)-2-yl-thio}phthalocyaninato-copper(II)] (1) and [2,9,16,23-tetra{(4,5-Diphenyl-1-methyl-1H-imidazole)-2-yl-thio}phthalocyaninato-copper(II)] (2), and demonstrated that the compound 1 was soluble in THF, DMF, and DMSO, and the compound 2 was soluble in chloroform (CHCl₃), acetone, methanol (MeOH), THF, DMF, and DMSO. Actually, in designing of any copper phthalocyanine derivatives, examination of the spectroscopic and optical properties is essential to reveal the true potential of the new molecule. Accordingly, we also investigated the optical and

spectroscopic properties of the Compounds 1 and 2. Further, we report that while Compound 1 demonstrated colorimetric pH sensor properties, Compound 2 did not exhibit such performance at all.

2. Materials and Methods

2.1 Synthesis

The synthesis reactions were carried out under argon gas and all the solvents used were dried by special methods and on molecular sieves (Armarego et al., 2003). The imidazole-substituted phthalonitrile derivative, which is used as a starting material in the synthesis of imidazole-substituted copper phthalocyanine, was synthesized as a result of the reaction of 4-nitrophthalonitrile and 4,5-diphenyl-2-imidazolethiol according to the literature (Yabaş et al., 2011). The synthesis of the new copper phthalocyanine derivatives are described below and schematized in Figure 1.

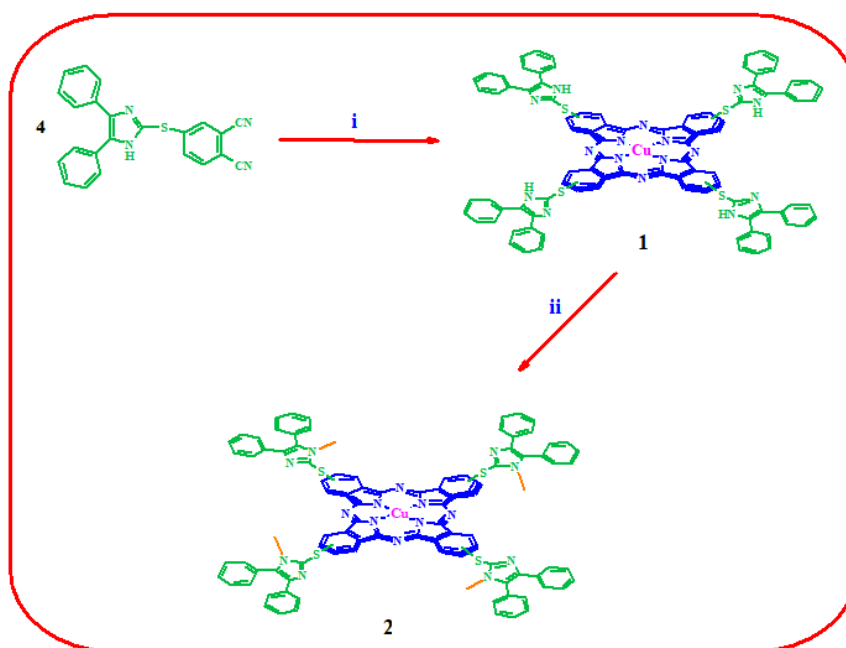


Figure 1. Synthesis of copper phthalocyanine compounds. (i: n-pentanol, CuCl₂, DBU, 15 hr, 180°C ii: DMF, CH₃I, K₂CO₃, 10 hr, RT).

[2,9,16,23-tetra{(4,5-Diphenyl-1H-imidazole)-2-yl-thio}phthalocyaninato-copper(II)]

Imidazole substituted phthalonitrile (200.0 mg, 0.52 mmol) was dissolved in 3 mL of pentanol, and copper(II) chloride (CuCl₂) (18.0 mg, 0.13 mmol) was added to this solution. This mixture was kept at 180°C for 15 hours in the presence of 1,8-diazabicyclo[5.4.0]undec-7-ene (DBU). After the reaction was complete, the mixture was cooled to room temperature, and was precipitated with ether, filtered and dried. The crude product was washed sequentially with MeOH and acetone until the filtrate lightened in color and dried in vacuum. The resulting green powder was soluble in THF, DMF and DMSO. Yield:

49% (100.0 mg). M.p.: >300°C. UV-Vis (DMSO) λ_{\max}/nm : 669, 600, 351. FT-IR (KBr pellet) ν (cm⁻¹): 3433; 3047; 2924; 2851; 1642; 1598; 1523; 1483; 1444; 1403; 1314; 1140; 699. MS (MALDI-TOF) m/z: 1577 [M]⁺. Anal. Calc. for C₉₂H₅₆N₁₆S₄Cu: C, 70.05; H, 3.58; N, 14.21%. Found: C, 70.95; H, 3.71; N, 14.43%.

[2,9,16,23-tetra{(4,5-Diphenyl-1-methyl-1H-imidazole)-2-yl-thio}phthalocyaninato-copper(II)]

CH₃I (78.0 mg, 0.55 mmol) and K₂CO₃ (90.0 mg, 0.65 mmol) were added to a solution of synthesized copper(II) phthalocyanine 1 (200.0 mg, 0.13 mmol) in 4 mL of DMF. This mixture was stirred at room temperature for 10 hours. After the reaction was complete, DMF was

evaporated under reduced pressure, and the resulting crude residue was dissolved in CHCl_3 and filtered. Next, the organic phase was concentrated, precipitated by the addition of n-hexane, filtered, and the solid was dried in a vacuum. The resulting dark green powder was soluble in CHCl_3 , acetone, methanol, THF, DMF, and DMSO. Yield: 75% (160.0 mg). M.p.: $>300^\circ\text{C}$. UV-Vis (DMSO) $\lambda_{\text{max}}/\text{nm}$: 683, 613, 353. IR (KBr pellet) ν (cm^{-1}): 3430; 3241; 3052; 3017; 2927; 2859; 2798; 1712; 1642; 1596; 1497; 1445; 1382; 1321; 697. MS (MALDI-TOF) m/z : 1639 $[\text{M}+\text{H}]^+$. Anal.Calc. for $\text{C}_9\text{H}_6\text{N}_{16}\text{S}_4\text{Cu}$: C, 70.41; H, 4.19; N, 13.69%. Found: C, 70.66; H, 4.31; N, 13.94%.

2.2. Characterization

FT-IR and UV-Vis spectra were recorded on a Bruker Tensor II FT-IR spectrophotometer and a Shimadzu UV-1800 UV-Vis spectrophotometer, respectively. The Cary 5000 UV-Vis-NIR spectrophotometer was used for optical characterization, and the optical band gaps were determined by using Tauc plot. The Electrothermal 9100 melting point detector was used to determine the melting points of the synthesized compounds. The pH of the compounds was measured with a glass electrode in an electronic pH meter using perchloric acid (HClO_4) and tetrabutylammonium hydroxide (TBAOH) in DMSO solution.

3. Results and Discussions

As summarized in Figure 1, tetrasubstituted copper(II) phthalocyanine 1 was synthesized in high yield as a

result of tetramerization reaction of phthalonitrile derivative in the presence of CuCl_2 . N-methylated copper(II) phthalocyanine 2 was synthesized by N-alkylation reaction of synthesized copper(II) phthalocyanine 1 with CH_3I in basic medium. Compounds were purified by using solubility differences, and then were characterized by FT-IR, UV-Vis, MALDI-TOF MS and elemental analysis.

The FT-IR spectra of compounds 1 and 2 were shown in Figure 2. It can be said that the peaks appearing in the range of 3241-2798 cm^{-1} in the FT-IR spectrum of compound 2 were C-H peaks belonging to the alkyl groups. This indicates that the N-H bonds were converted to N- CH_3 . At the same time, it was observed that the sharp $\text{C}\equiv\text{N}$ characteristic vibration band of the phthalonitrile derivative, which appeared at 2233 cm^{-1} according to our previous study (Yabaş et al., 2011), disappeared in the FT-IR spectrum of compound 1. This suggests that phthalocyanine compound was formed as a result of the tetramerization reaction. In addition, in the FT-IR spectra of compounds 1 and 2, aromatic $\text{C}=\text{C}$ stretching bands were observed in the range of 1598-1596 cm^{-1} and the stretching bands of $\text{C}=\text{N}$ were observed in the range of 1497-1483 cm^{-1} , while vibration bands of the substituted benzene ring were observed in the range of 699-697 cm^{-1} , all of which were in good accordance with previous reports (Yabaş et al., 2018; Yabaş, 2023).

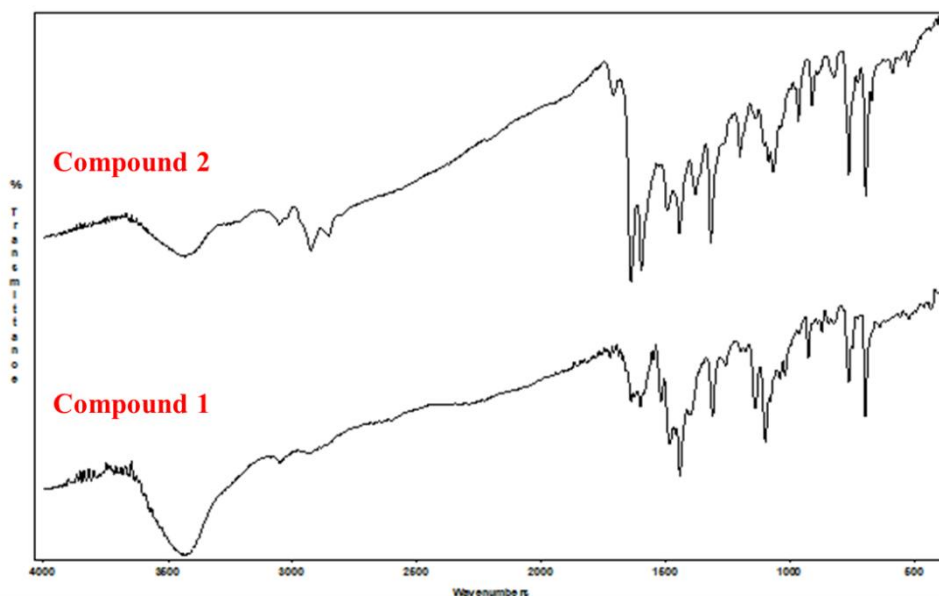


Figure 2. FT-IR Spectra of compounds 1 and 2.

UV-Vis spectroscopy is one of the most basic characterization methods showing the structural formation of phthalocyanines. Two intense bands associated with $\pi-\pi^*$ transitions dominate the UV-Vis spectra of the phthalocyanine ring, and these characteristic bands prove the formation of phthalocyanine. These two bands are defined as the Q-band, which occurs around 600-700 nm, and the B-band,

which occurs at about 300-400 nm. The characteristic Q-band is caused by the transition of the Pc ring from the Highest Occupied Molecular Orbital (HOMO) to the Lowest Unoccupied Molecular Orbital (LUMO) $\pi-\pi^*$. The characteristic B-band is due to deep $\pi-\pi^*$ transitions (Nyokong, 2007; Nyokong, 2010; Yabaş et al., 2011; Yabaş et al., 2023). The UV-Vis spectra of the synthesized

copper phthalocyanine compounds were shown in Figure 3. The absorption spectra of compounds 1 and 2 exhibited sharp Q-band and B-band in the desired range. Q-bands of compounds 1 and 2 appeared at 669 nm and 683 nm, respectively, while B-bands appeared at 351 nm and 353 nm, respectively. These characteristic peaks suggest that phthalocyanine compounds were

successfully formed as a result of the tetramerization reaction. Comparing the UV spectra of compounds 1 and 2, it can be observed that the Q-band position of compound 2 is red-shifted as compared to compound 1. This might be ascribed to the electron donor effect of the methyl groups attached to the structure (van Leeuwen et al., 2014).

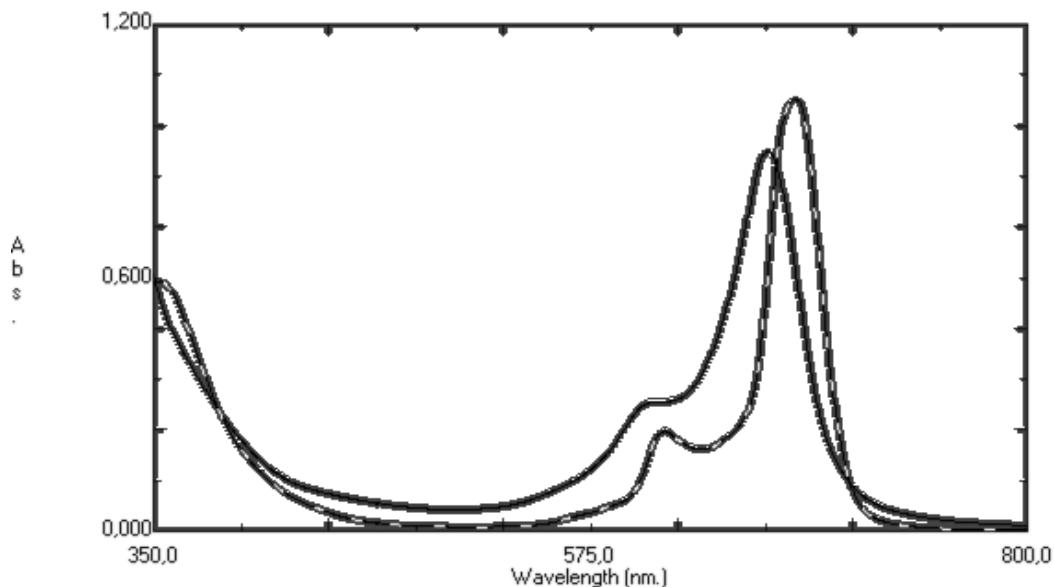


Figure 3. UV-Vis spectra of compounds 1 (-) and 2 (--) in DMSO.

The MALDI-TOF MS results of the synthesized compounds were shown in the experimental part, and were in agreement with the calculated molar masses. In addition, elemental analysis results of the compounds were also consistent with the calculated results. These results further confirm that the compounds were successfully synthesized.

NMR analysis of the synthesized phthalocyanine compounds could not be performed because it is difficult to realize consistent results due to the paramagnetic nature of the copper ion (He et al., 2008).

Phthalocyanines tend to exhibit aggregation behavior as a result of electronic interactions between the rings of two or more molecules. The aggregation behavior of phthalocyanines varies depending on the type of metal

ions, the nature of the substituents and the substitution location. Since aggregation in phthalocyanines reduces energy efficiency, it is desirable that the materials to be used in applications do not show aggregation tendency (Yabaş, 2023; Nyokong, 2007; Nyokong, 2010). Aggregation behavior of compounds 1 and 2 in different solvents (THF, DMF, DMSO) and different concentrations in DMF (10×10^{-6} , 8×10^{-6} , 6×10^{-6} , 4×10^{-6} , 2×10^{-6} M) was easily examined by UV-Vis spectrophotometer. As seen in the concentration-dependent aggregation behavior of compounds 1 and 2 in Figure 4, a proportional decrease in the peaks was observed with the decrease of the concentration, but no shift or new peak formation was detected. Similar results were also observed in different solvents.

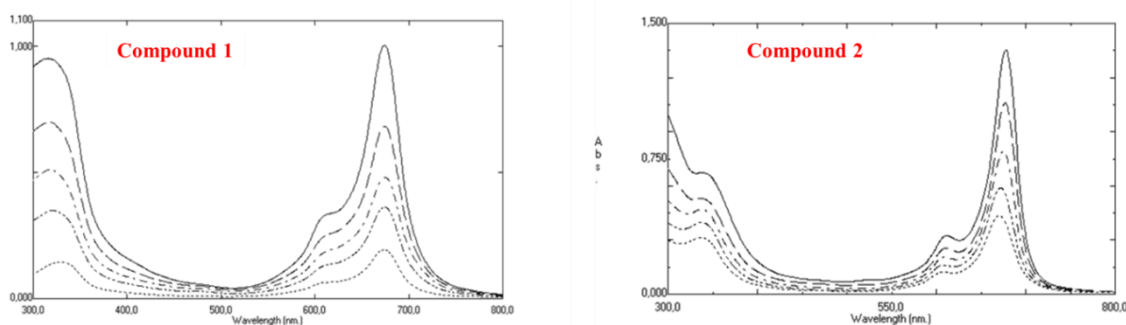


Figure 4. UV-Vis spectra of compounds 1 and 2 at different concentrations in DMF.

According to these results, it can be said that the synthesized copper phthalocyanine compounds did not show a significant aggregation behavior. On the other

hand, imidazole substituted copper phthalocyanine 1 showed interesting color changes under acidic and basic conditions. When the color changes of N-alkylated

imidazole substituted copper phthalocyanine 2 under acidic and basic conditions were examined, it was observed that the same color change was not observed. According to the literature (Yabaş, 2023), this was thought to be caused by the protonation/deprotonation of the imidazole groups, as schematized in Figure 5. Because no color change was observed after the conversion of the N-H group to N-CH₃ in the substituted imidazole groups on the phthalocyanine ring. In addition, it is thought that the methyl group attached to the imidazole groups changes the electron density of compound 2, thus preventing the color change of the compound in acidic medium.

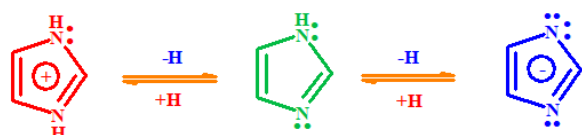


Figure 5. Schematic representation of the protonation/deprotonation of the imidazole group.

Solutions of compounds 1 and 2 at different pHs under acidic and basic conditions were prepared using HClO₄ and TBAOH in DMSO with a glass electrode in an electronic pH meter. The spectroscopic changes of the solutions prepared in the pH range of 13.8-3.1 were examined by UV-Vis spectrophotometer, but no significant change was observed in the UV-Vis spectra of both compounds. The color changes at different pHs for compounds 1 and 2 were shown in Figure 6.

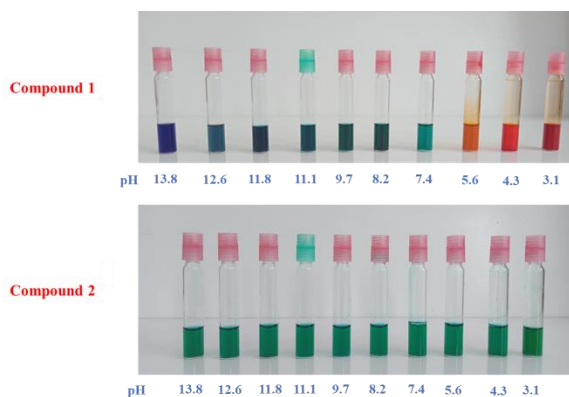


Figure 6. Color changes of compounds 1 and 2 at different pH ranges.

It can be said that compound 1 has colorimetric pH sensor properties in a very wide pH range, with color

transformations caused by protonation/deprotonation of imidazole groups (Figure 7), and accordingly electron density changes of the molecule.

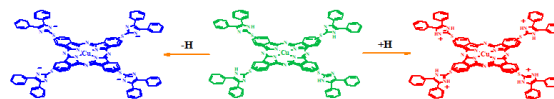


Figure 7. Schematic representation of the protonation/deprotonation of compound 1.

Also, the energy band gaps of compounds 1 and 2 were spectroscopically determined. Because, the optical properties of materials provide information about their electronic structures and optical transition types, and hence, are important in determining their potential for use in optoelectronic applications (Cherian et al., 2008; Yabaş, 2023). Thin films were prepared by dropping solutions of the compounds in THF onto glass substrates and then drying the solvent at room temperature. Then, the energy band gaps were determined by UV-Vis spectrophotometer through Tauc plot by using equation 1 (El Nhas et al., 2001; Hamam et al., 2017):

$$\alpha h\nu = \alpha_0(h\nu - E_g)^n \quad (1)$$

where α is absorption coefficient, $h\nu$ is the energy of the incident photons and E_g is the value of the optical band gap energy (eV) corresponding to the transitions denoted by the n value. The α_0 is a constant that depends on the transition probability. The best linear fit for semiconductors was found for $n = 0.5$, indicating that direct transitions were allowed in the material (Kim et al., 2012; Hamam et al., 2017; Mobtakeri et al., 2021). The corresponding absorbance and transmittance spectra of the thin films were given in Figure 8.

Calculations were made from the obtained data according to equation 1 and a Tauc plot was drawn for each compound as seen in Figure 9. As it is known, extrapolating the Tauc plot to the abscissa gives the value of the energy band gap. As a result of the calculations and measurements, the energy band gaps for compounds 1 and 2 were determined as 1.70 eV and 1.56 eV, respectively. These values might indicate that particularly the compounds 2 might have a potential to be used in solar cell applications, since an ideal band gap in photovoltaic applications are usually considered to be around 1.4 eV in terms of absorbing more photons from sunlight (Yu et al., 2017; Polat et al., 2020; Yabaş et al., 2023).

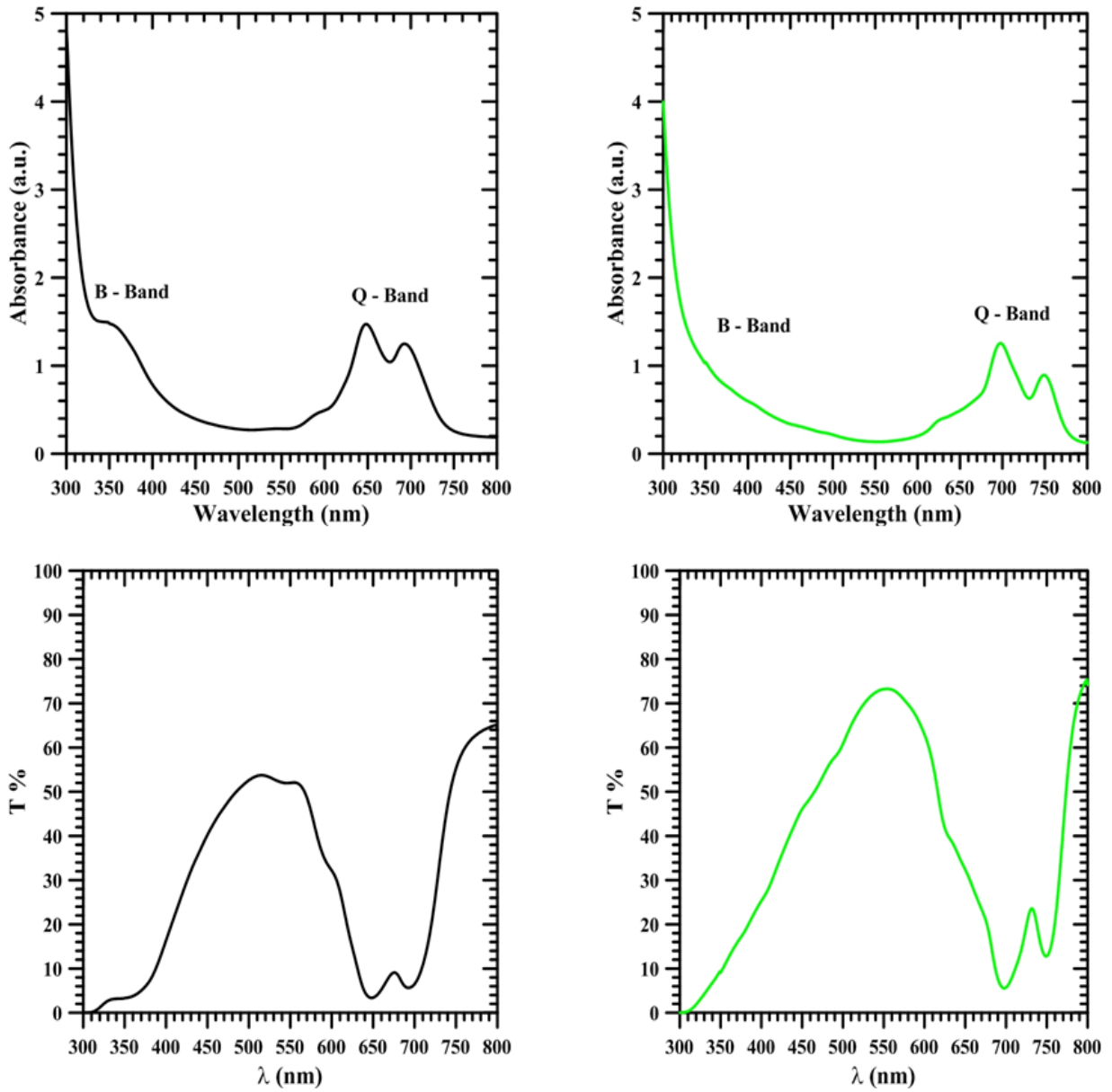


Figure 8. The transmittance and absorption spectrum of compounds 1 (black) and 2 (green) thin film.

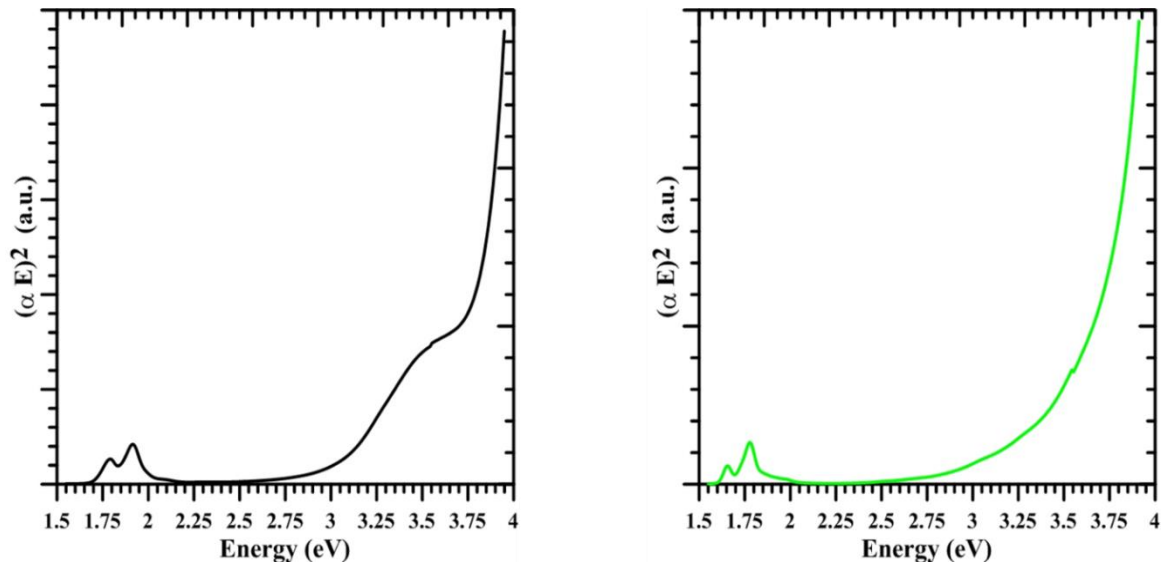


Figure 9. Determination of the band gap of compounds 1 (black) and 2 (green).

4. Conclusions

In this study, new imidazole tetrasubstituted copper phthalocyanine compounds were synthesized as copper phthalocyanine derivatives. These compounds, which were easily purified by washing with different solvents, were characterized by UV-Vis, FTIR, MALDI-TOF MS, and elemental analysis. Also, the band gaps of compounds 1 and 2 were found to be 1.70 eV and 1.56 eV, respectively. These results suggest that the newly synthesized phthalocyanines might have the potential to be used in optoelectronic applications. In addition, we report that the synthesized compounds did not exhibit a significant aggregation problem, and were actually soluble in organic solvents. This is important, as it is well-known that phthalocyanines usually show aggregation tendencies and aggregation is naturally undesirable in many applications. This situation further increases the potential of the newly synthesized compounds for practical applications. Finally, we showed that compound 1 is actually a smart material that can be used as a simple but effective pH sensor over a wide pH range.

Author Contributions

The percentage of the author(s) contributions is presented below. All authors reviewed and approved the final version of the manuscript.

| | F.E. | E.Y. |
|-----|------|------|
| C | 60 | 40 |
| D | 90 | 10 |
| S | 75 | 25 |
| DCP | 60 | 40 |
| DAI | 70 | 30 |
| L | 50 | 50 |
| W | 50 | 50 |
| CR | 50 | 50 |
| SR | 50 | 50 |
| PM | 50 | 50 |
| FA | 50 | 50 |

C=Concept, D= design, S= supervision, DCP= data collection and/or processing, DAI= data analysis and/or interpretation, L= literature search, W= writing, CR= critical review, SR= submission and revision, PM= project management, FA= funding acquisition.

Conflict of Interest

There is no conflict of interest. The funders had no role in the design of the study; in the collection, analyses, or interpretation of data; in the writing of the manuscript, or in the decision to publish the results.

Ethical Consideration

Ethics committee approval was not required for this study because of there was no study on animals or humans. The authors confirm that the ethical policies of the journal, as noted on the journal's author guidelines page, have been adhered to.

References

- Affify HA, Gadallah AS, El-Nahass MM, Atta Khedr M. 2015. Effect of thermal annealing on the structural and optical properties of spin coated copper phthalocyanine thin films. *J Mol Struct*, 1098: 161-166.
- Ai X, Lin J, Chang Y, Zhou L, Zhang X, Qin G. 2018. Phase modification of copper phthalocyanine semiconductor by converting powder to thin film. *Appl Surf Sci*, 428: 788-792.
- Alosabi AQ, Al-Muntaser AA, El-Nahass MM, Oraby AH. 2022. Structural, optical and DFT studies of disodium phthalocyanine thin films for optoelectronic devices applications. *Opt Laser Technol*, 155: 108372-108381.
- Armarego WLF, Chai CLL. 2003. Purification of Laboratory Chemicals. 5 third ed.; Butterworth/Heinemann, Tokyo.
- Chaure NB, Cammidge AN, Chambrier I, Cook MJ, Cain MG, Murphy CE, Pal C, Ray AK. 2011. High-mobility solution-processed copper phthalocyanine-based organic field-effect transistors. *Sci Technol Adv Mater*, 12(2): 025001.
- Cherian RC, Menon CS. 2008. Preparation and characterization of thermally evaporated titanium phthalocyanine dichloride thin films. *J Phys Chem*, 69: 2858-2863.
- Claessens CG, Blau WJ, Cook M, Hanack M, Nolte RJM, Torres T, Wöhrle D. 2001. Phthalocyanines and Phthalocyanine Analogues: The Quest for Applicable Optical Properties. *Monatsh Chem*, 132: 3-11.
- Dakoğlu-Gülmez A, Polyakov MS, Volchek VV, Tuncel-Kostakoğlu S, Esenpinar AA, Basova TV, Durmuş M, Gürek AG, Ahsen V, Banimuslem HA, Hassan AK. 2017. Tetrasubstituted copper phthalocyanines: Correlation between liquidcrystalline properties, films alignment and sensing properties. *Sens Actuators B Chem*, 241: 364-375.
- Djurisic AB, Kwong CY, Lau TW, Guo WL, Li EH, Liu ZT, Kwok HS, Lam LSM, Chan WK. 2002. Optical properties of copper phthalocyanine. *Opt Commun*, 205: 155-162.
- El Nhass MM, Sollman BS, Metwally BS, Farid AM, Farag AAM, El Shazly AA. 2001. Optical properties of evaporated iron phthalocyanine (FePc) thin films. *J Opt*, 30: 121-129.
- Farag AAM. 2007. Optical absorption studies of copper phthalocyanine thin films. *Opt Laser Technol*, 39: 728-732.
- Hamam KJ, Alomari MI. 2017. A study of the optical band gap of zinc phthalocyanine nanoparticles using UV-Vis spectroscopy and DFT function. *Appl Nanosci*, 7: 261-268.
- He N, Chen Y, Doyle J, Liu Y, Blau WJ. 2008. Optical and nonlinear optical properties of an octasubstituted liquid crystalline copper phthalocyanine. *Dyes Pigm*, 76: 569-573.
- Kim HJ, Kim JW, Lee HH, Lee B, Kim JJ. 2012. Initial growth mode, nanostructure, and molecular stacking of a ZnPc:C60 bulk heterojunction. *Adv Funct Mater*, 22: 4244-4248.
- Mali SS, Dalavi DS, Bhosale PN, Betty CA, Chauhan AK, Patil PS. 2012. Electro-optical properties of copper phthalocyanines (CuPc) vacuum deposited thin films. *RSC Adv*, 2: 2100-2104.
- McAfee T, Hoffman BC, You X, Atkin JM, Ade H, Dougherty DB. 2016. Morphological, Optical, and Electronic Consequences of Coexisting Crystal Orientations in β -Copper Phthalocyanine Thin Films. *J Phys Chem C*, 120: 18616-18621.
- Mobtakeri S, Akaltun Y, Özer A, Kılıç M, Tüzemen EŞ, Gür E. 2021. Gallium oxide films deposition by RF magnetron sputtering; a detailed analysis on the effects of deposition pressure and sputtering power and annealing. *Ceram Int*, 47: 1721-1727.
- Nyokong T. 2007. Effects of substituents on the photochemical and photophysical properties of main group metal phthalocyanines. *Coord Chem Rev*, 251: 1707-1722.
- Nyokong T. 2010. Electronic spectral and electrochemical

- behavior of near infrared absorbing metallophthalocyanines. *Struct Bond*, 135: 45-88.
- Polat O, Caglar M, Coskun FM, Sobola D, Konecny M, Coskun M, Caglar Y, Turut A. 2020. Examination of optical properties of YbFeO₃ films via doping transition element osmium. *Opt Mater*, 105: 109911.
- Raval HN, Sutar DS, Rao VR. 2013. Copper(II) phthalocyanine based organic electronic devices for ionizing radiation dosimetry applications. *Org Electron*, 14(5): 1281-1290.
- Sánchez-Vergara ME, Alonso-Huitron JC, Rodríguez-Gómez A, Reider-Burstin JN. 2012. Determination of the Optical GAP in Thin Films of Amorphous Dilithium Phthalocyanine Using the Tauc and Cody Models. *Molecules*, 17: 10000-10013.
- Tong WY, Djurišić AB, Ng AMC, Chan WK. 2007. Synthesis and properties of copper phthalocyanine nanowires. *Thin Solid Films*, 515: 5270-5274.
- van Leeuwen M, Beeby A, Fernandes I, Ashworth SH. 2014. The photochemistry and photophysics of a series of alpha octa(alkyl-substituted) silicon, zinc and palladium phthalocyanines. *Photochem Photobio Sci*, 13: 62-69.
- Wang Y, Liu X, Shan H, Chen Q, Liu T, Sun X, Ma D, Zhang Z, Xu J, Xu Z-J. 2017. Tetra-alkyl-substituted copper (II) phthalocyanines as dopant-free hole-transport layers for planar perovskite solar cells with enhanced open circuit voltage and stability. *Dyes Pigm*, 139: 619-626.
- Yabaş E, Erden F. 2023. Water-Soluble Quaternized Serotonin Substituted Zinc-Phthalocyanine for Photodynamic Therapy Applications. *Cumhuriyet Sci J*, 44(1): 99-105.
- Yabaş E, Sülü M, Dumludağ F, Salih B, Bekaroğlu Ö. 2018. Imidazole octasubstituted novel mono and double-decker phthalocyanines: Synthesis, characterization, electrical and gas sensing properties. *Polyhedron*, 153: 51-63.
- Yabaş E, Sülü M, Saydam S, Dumludağ F, Salih B, Bekaroğlu Ö. 2011. Synthesis, characterization and investigation of electrical and electrochemical properties of imidazole substituted phthalocyanines. *Inorganica Chim Acta*, 1(365): 340-348.
- Yabaş E, Şenadim-Tuzemen E, Kaya S, Maslov MM, Erden F. 2023. Incorporation of graphene oxide to metal-free phthalocyanine through hydrogen bonding for optoelectronic applications: An experimental and computational study. *J Phys Org Chem*, e4496.
- Yabaş E. 2023. The new soluble tetra-substituted oxo-titanium phthalocyanines: Synthesis, characterization, spectral and colorimetric pH sensing properties. *J Mol Struct*, 1284: 135435-135443.
- Yu ZL, Ma QR, Liu B, Zhao YQ, Wang LZ, Zhou H, Cai MQ. 2017. Oriented tuning the photovoltaic properties of γ -RbGeX₃ by strain-induced electron effective mass mutation. *J Phys D*, 50: 465101.



NEUROANATOMY OF ENTREPRENEURSHIP AND BIBLIOMETRIC ANALYSIS OF STUDIES WITH VOSVIEWER

Abdullah BALLI^{1*}

¹National Defense Department, 06530, Ankara, Türkiye

Abstract: Entrepreneurship has been at the focus of many scientists doing research in the field of social sciences. Studies have focused on entrepreneurial intention, entrepreneurial disposition and entrepreneurial behavior. Generally, empirical methods have been used in studies, but the neurophysiological, neuropsychological and psychoneuroendocrinological reasons behind the individual's entrepreneurship have been neglected. In short, genetic factors, hormones, behavioral genetic factors related to the individual's being an entrepreneur were not taken into account in the studies. However, with the use and development of neuroscience methods, tools and approaches in different fields, the opportunities offered by neuroscience in research on entrepreneurship in the field of Social Sciences have recently begun to be utilized. This has facilitated the neuroanatomical examination of entrepreneurial individuals. Entrepreneurship research focuses on the individual's family, environmental, social and educational interactions. In order for entrepreneurship to be understood in a multidimensional way, it is necessary to consider human behavior in terms of genetic transfers, hormones, behavioral genetics and the interactions of these factors with each other. For this reason, studies on the concepts of "entrepreneurship and neuroscience", "entrepreneurship and genetics", "entrepreneurship and biology" and "neuroentrepreneurship" gain importance. The aim of this study is to provide information about the neuroscience methods, tools and approaches used in entrepreneurship research, to make a detailed bibliometric analysis of the researches, to identify the trends and gaps related to the mentioned concepts and to bring them to the attention of researchers and to make suggestions about what should be done in future studies. Since a better understanding of entrepreneurial thought, intention and behavior will contribute to the development of entrepreneurship, mapping the studies in the literature in terms of the neuroanatomy of entrepreneurship and analyzing them within the scope of quantitative data makes the study unique. The study consists of five parts. In the first part of the study, studies carried out for a better understanding of entrepreneurship in terms of neurophysiology, hormones and genetics are given by making use of neuroscience methods, tools and approaches in the literature. In the second part, neuroscience tools, methods and approaches used in entrepreneurship research are explained. In the third part, the method of the research and in the fourth part, the bibliometric analysis findings are given. In the last part, the discussion and conclusion, the deficiencies identified in the field and recommendations for future studies are made. As the analysis unit, bibliometric data of different types of papers scanned in the Web of Science (WoS) database and published between 2006 and 2023 was taken as a basis. As a result of the research, 379 publications related to the words "entrepreneurship" and "neuroscience" were identified and the most studied 260 of them were neuroscience, neurology, 53 business economics and 47 mathematical computational biology. 346 publications on "entrepreneurship" and "genetics" have been identified and the most studied 146 of them are genetic inheritance, 44 are biochemistry, molecular biology and 35 are business economics. 183 publications on "entrepreneurship" and "biology" were found, 58 of which were studied the most, multidisciplinary sciences, 55 related to genetic inheritance and 44 of them related to business. Within the scope of the study, only 9 publications related to "neuroentrepreneurship", which are directly related to entrepreneurship and neuroscience, were identified in the Web of Science (WoS) database. In the last part, discussion and conclusion, what needs to be done in entrepreneurship research and suggestions are presented.

Keywords: Entrepreneurship and neuroscience, Entrepreneurship and genetics, Entrepreneurship and biology, Neuroentrepreneurship

*Corresponding author: National Defense Department, 06530, Ankara, Türkiye

E mail: abduallah.balli@ostimteknik.edu.tr (A. BALLI)

Abdullah BALLI  <https://orcid.org/0000-0003-2689-6610>

Received: August 20, 2023

Accepted: September 11, 2023

Published: October 15, 2023

Cite as: Ballı A. 2023. Neuroanatomy of entrepreneurship and bibliometric analysis of studies with VOSviewer. BSJ Eng Sci, 6(4): 442-457.

1. Introduction

Thoughts, movements, feelings and emotions arise in response to chemical and electrical signals triggered by the brain and then transmitted to organs or produced in response to peripheral events (for example, pain after a wound). Psychophysiology studies the physiological activation that occurs by manipulating psychological variables in experimental settings. It is aimed to reach the underlying causes of behavior by observing the

interactions between physiological changes and psychological processes. For example; it is possible to determine the relationship between certain behaviors (such as risk seeking, risk aversion, emotional responses to certain stimuli) and somatic indices (heart rate, blood pressure or brain activity). Psychophysiology studies phenomena such as emotions, stress, decision making, and cognitive processes. By combining psychophysiological approaches, scientists have



developed various approaches to how emotions can be measured. For example; Psychophysiology offers researchers a deep perspective in cases such as examining the relationship between entrepreneurship and success, evaluating the implicit (unconscious) reactions to certain situations such as failure, changes in the brain when the entrepreneurial decision is made, predicting certain behaviors such as entrepreneurial intention.

Human psychophysiology has been widely studied, and there are now numerous tools available to scientists to explore the relationships between cognitive, psychological, emotional events and the resulting bodily responses. Since psychophysiology studies the activity of both the central nervous system (brain) and the peripheral nervous system (organs and glands), it has developed common approaches to the functions of the brain (central system) and common approaches to the discovery of bodily responses as a result of behavior (peripheral system). Thanks to neuroscience methods, tools and approaches, significant gains have been achieved in entrepreneurship research. Neuroscience provides important insights into understanding the reasons behind entrepreneurial emotion, thought, intention, and behavior. For example; "Quantitative genetics" and "molecular genetics" methods used to reveal the relationship between genetics and entrepreneurship have been used in important studies in this field. To show separately the effects of genes and environmental factors in entrepreneurial behavior, twins and adoptees were included in quantitative genetic studies. Molecular genetics, on the other hand, is based on the use of certain variants together for the detection of the gene that causes the individual to become entrepreneurs.

Some studies in the literature have shown that the genetic makeup of the individual affects the tendency to be entrepreneurial. Nicolaou et al. (2011) found that there may be a gene associated with entrepreneurship in the dopamine receptor in their study, which they hypothesized to have an entrepreneurial gene in individuals. However, molecular genetic research has been used less frequently due to its limitations. In studies on individuals' willingness to start their own businesses (Nicolaou et al., 2008; Zhang et al., 2009), genetic factors accounted for 48% of the variance of being self-employed, 40% of the variance in starting a new business, and 43% of the variance in the process of establishing a company. (Lindquist et al., 2015; Zunino, 2016; Nofal et al., 2018). Other studies in the field have examined the influence of genes on other entrepreneurial outcomes, such as opportunity recognition and entrepreneurial intentions. For example; Evidence was obtained that genetics contributed 45% of the variance in recognizing opportunities (Shane and Nicolaou, 2015b) and 42% of the variance in entrepreneurial intentions (Nicolaou and Shane, 2010).

Some of the important findings in entrepreneurship

research have been obtained from hormone studies. Key findings include that testosterone affects people's tendency to be self-employed (White et al., 2007; Greene et al., 2014). The relationship between the effect of testosterone on risk taking, which is an indicator of entrepreneurial behavior, and individuals' willingness to start their own business has been examined (White et al., 2007; Bönte et al., 2016). Nicolaou et al., (2018) conducted twin experiments on men and women to show that testosterone highly affects an individual's tendency to be entrepreneurial. As a result of the study, it was concluded that high testosterone level increased the entrepreneurial tendency. Unger et al. (2015) examined the relationship between entrepreneurs operating in more than one different field and the need for success and testosterone hormone, and a significant relationship was found between them. In other studies, it has been determined that there is a certain relationship between the stress hormones "cortisol" and epinephrine and the tendency to be entrepreneurial (Wolfe and Patel, 2017). It appears that individuals with high epinephrine levels are more likely to make risky decisions when their cortisol levels are low.

Studies conducted with neuroscientific methods and tools have revealed the necessity of further research on the correlations of entrepreneurship with a holistic approach in neurophysiological, neuropsychological and psychoneuroendocrinological aspects. Although researches show that entrepreneurs and non-entrepreneurs respond differently to neurologically different neural networks, more studies are needed to reveal the changes that occur in the brain during entrepreneurial behavior (Laureiro-Martinez et al., 2015; Nofal et al., 2018; Shane et al., 2019). For this reason, the neuroanatomical approach to entrepreneurship has an important place in the success of entrepreneurship research. In this context, studies on the concepts of "entrepreneurship and neuroscience", "entrepreneurship and genetics", "entrepreneurship and biology" and "neuroentrepreneurship" gain importance. The aim of this study is to provide information about the neuroscience methods, tools and approaches used in entrepreneurship research, to make a detailed bibliometric analysis of the researches, to identify the trends and gaps related to the mentioned concepts and to bring them to the attention of researchers and to make suggestions about what should be done in future studies. Since a better understanding of entrepreneurial thought, intention and behavior will contribute to the development of entrepreneurship, mapping the studies in the literature in terms of the neuroanatomy of entrepreneurship and analyzing them within the scope of quantitative data makes the study unique. The study consists of five parts. In the first part of the study, studies carried out for a better understanding of entrepreneurship in terms of neurophysiology, hormones and genetics are given by making use of neuroscience methods, tools and approaches in the

literature. In the second part, neuroscience tools, methods and approaches used in entrepreneurship research are explained. The methods and findings are described in the third and fourth sections. In the last part, discussion and conclusion, what needs to be done in entrepreneurship research and suggestions are presented.

2. Literature Review

The field of neuroscience has expanded significantly in recent years. Although researchers have used neuroscientific techniques to examine various phenomena in the fields of entrepreneurship, business, economics, and marketing, until now, entrepreneurship researchers have not sufficiently benefited from neuroscience methods and tools (Krueger and Welpel, 2014). In the last decade, there has been a significant increase in the number of articles on the biology of entrepreneurship and more than 300 articles have been published in this field (Nofal et al., 2018).

Biologically-based approaches in entrepreneurship research are defined as the whole of research examining the role of genetics (Nicolaou et al., 2009), physiology (White et al., 2007), neuroscience (de Holan, 2014; Shane et al., 2020) and neurodevelopment (Lerner et al., 2018; Wiklund et al., 2017). Entrepreneurship takes place at the nexus of entrepreneurial individuals and valuable opportunities (Venkataraman, 1997). Considering the

biology of entrepreneurial individuals will help us to understand the difference between entrepreneurial and non-entrepreneurial individuals and to learn how likely it is that entrepreneurial individuals will achieve the material and moral gains they will gain from entrepreneurship. In addition, thanks to entrepreneurs' ability to seek and create opportunities (Alvarez and Barney, 2020), it is stated that biologically dopamine (Muda et al., 2018) can affect the individual neurophysiologically during the recognition of opportunities.

Research on the genetic sequence has examined the role of genes in the probability of entrepreneurial individuals to become entrepreneurs (Nicolaou et al., 2008; Zhang et al., 2009). Genes are the basic building blocks of DNA and the basis of the human body (Nicolaou et al., 2009). Increasingly, it is assumed that genes may also be associated with behavior through the action of the mind-brain complex. Twin and adoption studies are quasi-experiments used to examine the heritability of entrepreneurial traits. Heritability refers to the proportion of individual differences in entrepreneurship that can be attributed to the genetic profile of a particular population (Plomin et al., 2012). In entrepreneurship research, various studies have been carried out with different subjects and tools. Some of them are given in Table 1.

Table 1. Researches in the field of entrepreneurship with neuroscience methods and tools

| Researcher | Research Subject | Findings |
|----------------------------|--|---|
| White et al. (2007) | Does testosterone influence entrepreneurship? | Testosterone levels are associated with entrepreneurship and this is partially mediated by risk propensity |
| Nicolaou et al. (2008) | Is there a genetic predisposition to entrepreneurship? | Heritability estimates between 0.37 and 0.48 for entrepreneurship depending on the operationalization of the construct |
| Zhang et al. (2009) | Do extraversion and neuroticism partly mediate the genetic predisposition to entrepreneurship? | Neuroticism and extraversion mediate the genetic predisposition to entrepreneurship for women |
| Logan (2009) | Is dyslexia associated with entrepreneurship? | Dyslexics are more likely than corporate managers to engage in entrepreneurship |
| Shane et al. (2010) | Do genetic factors account for part of the covariance between the Big Five and entrepreneurship? | Common genetic factors influence the covariation between openness to experience and extraversion and entrepreneurship |
| van der Loos et al. (2013) | Molecular genetics of self-employment | 55% of the variance in self-employment due to additive genetic effects; 25% of variance in self-employment explained by additive effects of common SNPs; no genome-wide SNPs identified |
| Lindquist et al. (2015) | Decomposition of the intergenerational transmission of entrepreneurship into pre-birth and post- birth factors | Both biological and adoptive parents contribute to the likelihood that adopted children become entrepreneurs |
| Bönte et al. (2016) | Does prenatal testosterone exposure influence entrepreneurship? | Prenatal testosterone exposure is associated with entrepreneurship |

Table 1. Researches in the field of entrepreneurship with neuroscience methods and tools (continue)

| Researcher | Research Subject | Findings |
|----------------------------|--|--|
| Unger et al. (2015) | Do biological factors interact with psychological factors in influencing entrepreneurship? | Need for achievement moderated the effects of prenatal testosterone on entrepreneurial impact |
| Wiklund et al. (2016) | How does ADHD influence the decision to become an entrepreneur and entrepreneurial performance? | Inattention and hyperfocus significantly influence entrepreneurship |
| Wolfe and Patel (2017) | Does cortisol modulate the relationship between epinephrine and self-employment? | At lower levels of cortisol, higher epinephrine levels are associated with self-employment |
| Wiklund et al. (2017) | How does ADHD influence entrepreneurship? | Hyperactivity is positively but inattention negatively correlated with entrepreneurship |
| Wolfe and Patel (2017) | Is obsessive compulsive personality disorder associated with self-employment? | Individuals with obsessive compulsive personality disorder have a higher likelihood of engaging in self-employment |
| Nicolaou et al. (2018) | Does testosterone increase the likelihood of self-employment? | Serum testosterone levels are positively associated with self-employment for males; lower 2d:4d (higher prenatal testosterone) in left hand associated with self-employment; support for testosterone transfer hypothesis |
| Weinberger et al. (2018) | How does recovery from work stress influence entrepreneurs' generation of new ideas? | Sleep efficiency and work-related problem solving pondering positively associated with entrepreneurs' creativity |
| Lahti et al. (2019) | Why and how do founding entrepreneurs bond with their ventures? | Entrepreneurs showed similar signs of affective bonding to parents |
| Shane et al. (2020) | How does variation in entrepreneurs' displayed passion influence investor interest? | Passionate founders raise investor neural engagement and interest in the start-up |
| Moore et al. (2021) | ADHD-Related neurodiversity and the entrepreneurial mindset | How neurodiversity (neurobiological/brain-related differences) relates to entrepreneurial cognition is better understood. |
| Sharma et al. (2021) | Is it possible to investigate entrepreneurial intention with six neuroscience methods? | Entrepreneurial intention is influenced by five factors: recognition of entrepreneurial opportunities, evaluation and risk taking, entrepreneurial cognition, entrepreneurial behavior and entrepreneurial decision making.. |
| Bai et al (2022) | Sensitive assessment of creativity and entrepreneurship education to achieve professional differentiation. | The BP (Backpropagation) neural network model is highly generalizable to students' creative enterprise abilities, |
| Egana-delSol et al. (2023) | Neurophysiological markers of emotion regulation predict efficacy of entrepreneurship education | Programs designed to develop social-emotional skills are effective in improving entrepreneurial outcomes as they develop students' ability to regulate their emotions. |

Source: Created by the author using Nicolau et al. (2021).

Of course, the work done is not limited to these. Hatak and Zhou (2019) conceptualized entrepreneurial health as an important dimension of human capital (measured as subsequent annual income and subsequent subjective well-being) that drives entrepreneurial success. Shane et al., (2020) found that the neural interaction of the investor increases when entrepreneurs showcase their desired ventures in front of the investors, which in turn affects their interest in investing in the new venture.

Lahti et al. (2019) investigated the emotional bonds that entrepreneurs have with their start-ups and found that these are similar to the emotional bonds between parents and children. According to studies claiming that testosterone positively affects the tendency to be entrepreneurial in men and women (White et al., 2006; Greene et al., 2014; Unger et al., 2015; Bönte et al., 2016; Nicolaou et al., 2018), hormones have an effect on decision making. These

studies examined serum and prenatal testosterone levels as well as testosterone transfer in both same-sex and opposite-sex twins. As a result of the studies, it has been understood that testosterone has a significant effect on being an entrepreneur. Other research has shown an interaction between cortisol and epinephrine (Wolfe and Patel, 2017) and testosterone and the need for success (Unger et al., 2015) in entrepreneurs.

3. Neuroscience Methods, Tools and Approaches Used in Entrepreneurship Research

Modern technological advances have led to the production of small, portable devices and electrodes that are used largely in marketing efforts and can potentially be very proficient at exploring the entrepreneurial mind in a real environment. In particular, there have been significant advances in understanding entrepreneurial neurophysiology. EEG (Electroencephalogram) is one of the most frequently used tools in this sense. Studer et al., (2013) investigated the relationship between resting brain activity, psychological traits (such as sensitivity to punishment and reward), and risk-taking behavior through a modern EEG (and fMRI) approach. Their results showed that the prefrontal cortex (an important brain area for high-level cognitive processes, behavioral control and decision making) certain core activity of the brain and psychological traits can predict risk-taking behavior. In the study by Vieito et al., (2015), brain activity of 20 (volunteer) investors was monitored using EEG during different financial activities (such as selling, buying and holding) to investigate whether certain market outcomes affect brain activity and responses.

Another neuroscience tool used in entrepreneurship research is MEG (Magnetoencephalogram). This method is based on the principle that the electrical activity produced by populations of neurons is accompanied by the generation of magnetic fields. Ioannides et al. (2000) in their study to investigate how the brain responds to cognitive and emotional stimuli, found that the brain responds differently to cognitive and emotional stimuli. Tallon-Baudry et al. (2011) investigated how the human brain is activated when participants are presented with money and neutral stimuli. It has been observed that money activates the reward system in the brain like other physiological incentives and can be distinguished in a much shorter time than other stimuli.

Functional Magnetic Resonance Imaging (fMRI) is the tool used in entrepreneurship research and provides much more detailed information than other neuroimaging methods. (fMRI) Functional magnetic resonance imaging (fMRI), unlike EEG and MEG devices, allows the visualization of changes in blood flow in the brain (Morin, 2011).

When the entrepreneur makes an investment decision in a risky environment or takes action to seize an opportunity, there are some differences in heart rate and

blood pressure compared to other individuals. The neuroscience tool used to detect these changes is the EKG (Electrocardiogram). As Krueger and Welpel (2014) point out, "entrepreneurial action has important emotional bases". Considering how the heart relates to our emotional perception, investigating how heart rate (or blood pressure) changes under certain stimuli or situations provides important information for entrepreneurial decision making.

Since it is suggested that emotional stimuli involuntarily activate facial expressions, the EMG (Electromyogram) approach ignores the voluntary control of emotion and detects involuntary differences. It is the most commonly used face EMG in entrepreneurship research. Balconi and Pagani (2015) explored social hierarchies and emotions using facial EMG along with EEG and other behavioral measures. Experimental results have shown that negative emotions (for example, involuntary positive activity) and poorer cognitive performance follow a decline in social status. Künecke et al. (2014) tested the relationship between involuntary movement and emotion using facial EMG. During the research, the participants' perception of face and emotion in multitasking were examined and it was concluded that facial fold activity was related to individual emotion perception activity.

Sight is man's most developed sense. While the areas related to vision make up 30 percent of the cerebral cortex, each of the other sensory areas is less than 10 percent (Colosio et al., 2017). Therefore, it is important for entrepreneurship scholars to focus on eye-related processes as the first stage of sensory perception and cognitive processing. Two methodologies are used to detect visual activity. These are: Electrooculography (EOG) and eye tracking. Hüsser and Wirth (2014) used eye tracking to investigate the effect of limited attentional resources on investors' investment decision-making behaviors. In the research, it has been determined that there is a relationship between attention to past performance and investors' purchase intentions.

Another of the neuroscience methods used in entrepreneurship research is the tools that enable the measurement of electrodermal activity. Lo and Repin (2002) included ten professional traders in their study to investigate the role of emotions in financial decision making, taking into account skin conductivity and blood parameters. The role of emotions in decision making through the skin conductivity response is supported by other articles (Bechara et al., 1999; Bechara et al., 2005). This makes it easier to identify the changes physically created by the processes related to entrepreneurial decision making and risk taking.

The turning point of entrepreneurship research is the emergence of approaches that assume that one of the most important reasons for an individual to be an entrepreneur is genetically based. As a matter of fact, Nicolaou et al. (2011) in a study on twins suggested that there is a possible link between the presence of a gene

(DRD3) that encodes a type of dopamine receptor (special protein molecules selectively activated by dopamine) and entrepreneurship. It has been found that individuals with a certain genetic makeup (ie, people with a specific genetic makeup of the DRD3 gene) are more likely to engage in entrepreneurial behavior or other thrill-seeking activities. An interesting study by Barnea et al. (2010) found that there is a significant relationship between the family environment and the behavior of young investors. Other researchers have compared entrepreneurial tendencies in adopted children (Lindquist et al., 2015). Contrary to previous evidence, the authors showed that the influence of adoptive parents (entrepreneurs) is twice as significant as the genetic contribution (biological parents). Zhang et al. (2009) included both identical and fraternal twins in their study. As a result of the research, it has been concluded that the tendency of women to be entrepreneurs is genetically based, while men are caused by the external environment.

In the human body, decision making works through two complementary systems: the nervous system, which is

based on neurotransmitters (chemicals that enable communication between nerve cells or between a nerve cell and another type of cell, such as dopamine or serotonin) and the endocrine system, which is mediated by hormones. The most common neurotransmitters are dopamine, GABA, serotonin and norepinephrine. Hormones, on the other hand, are chemicals secreted directly into the blood from glands and organs such as the thyroid, pancreas, gonads and pineal gland (Colosio et al., 2017). Simeon et al., (2007) stated that there is a relationship between cortisol and psychological resilience, while Yildırım and Derksen (2012) state that there is a relationship between testosterone and leadership and aggression. Mehta and Prasad (2015) found an interaction between testosterone and cortisol in risk-taking behaviors. Neuroscience tools and methods used in entrepreneurship research are not limited to those described in the study. However, the mentioned tools and methods are the most used in entrepreneurship research. Neuroscience tools and methods used in entrepreneurship research are shown in Figure 1.

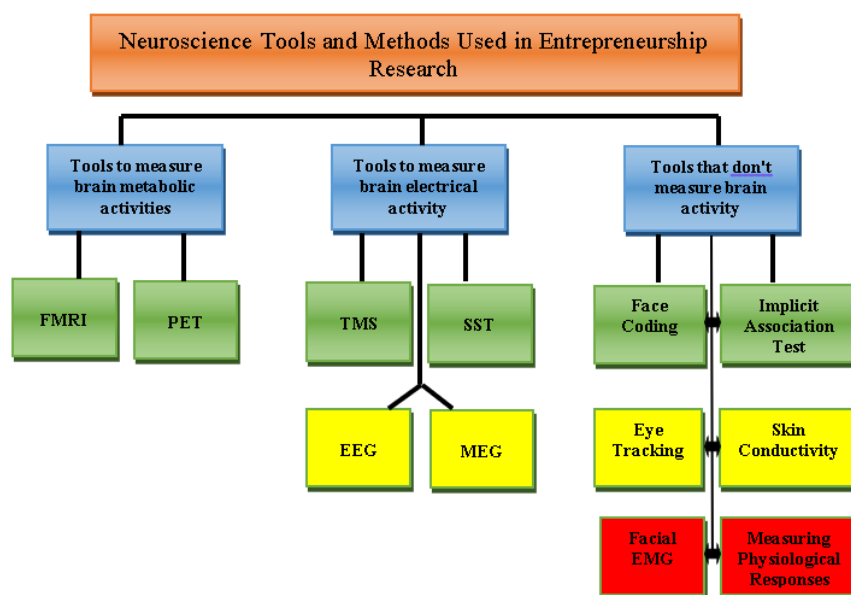


Figure 1. Neuroscience tools and methods used in entrepreneurship research (Bercea, 2013).

4. Method

Within the scope of the research, bibliometric analysis method was used to evaluate the relationship between the themes in the literature. The basic idea of bibliometrics is to measure the academic output of individuals and institutions (Ball, 2018). In the research, studies in the international literature on entrepreneurship and neuroscience were examined. Web of Science (WoS) was used in the creation of the data set to be examined within the scope of the research. Due to the fact that entrepreneurship studies take place quite a lot in the literature, a screening limitation was put in the relevant citation indexes between the years 2006-2023. Another limitation is that the studies in the literature were searched only on Web of Science (WoS), and other

international databases such as Scopus, PubMed and Elsevier ScienceDirect were excluded. In addition, choosing the language of the studies conducted in English is another limitation of the study. In this part of the study, bibliometric analyzes of the concepts of "entrepreneurship and neuroscience", "entrepreneurship and genetics", "entrepreneurship and biology" and "neuroentrepreneurship" are included.

4.1. Purpose of the Research

In the scope of the research; As a result of the bibliometric analyzes made on the concepts of entrepreneurship and neuroscience, entrepreneurship and genetics, entrepreneurship and biology and neuroentrepreneurship as a result of quantitative data and numerical measurement indicators, it is aimed to

present the studies on the concepts to the attention of researchers with a holistic perspective and to offer suggestions about what needs to be done in future studies.

4.2. Data and Analytics

Different bibliometric analysis tools are used in the literature. In this study, the VOSviewer program was preferred because of its strengths in terms of functionality. It is considered to be an important program that provides convenience to researchers in order to discover evolutions, relationships and new concepts in the literature. In addition, it enables in-depth analysis of data sets as it provides visualization, mapping and multidimensional analysis. It is based on the bibliometric data of different types of papers scanned in the Web of Science (WoS) database on 14.03.2023 and published between 2006 and 2023. As a result of the research, 379 publications on the words “entrepreneurship” and “neuroscience”, 346 publications on “entrepreneurship” and “genetics”, 183 publications on “entrepreneurship” and “biology”, and only 9 publications on “neuroentrepreneurship” were identified. The contents indexed in Web of Science (WoS) were examined as

criteria through the obtained data, author-citation-journal-country-institution and keyword analysis.

5. Results

The findings obtained from the bibliometric analyzes performed under this title are presented. Bibliometric analyzes of studies published between 2006 and 2023 are included. Within the scope of the research, 917 studies were evaluated. The results of this evaluation are included in the research through graphics and tables.

5.1. General Descriptive Statistics

The number of the most studied areas among the 379 studies on “entrepreneurship” and “neuroscience” is shown in Table 2, and the most studied areas are shown in Figure 2. Of these, 260 are related to neuroscience neurology, 53 are related to business economics, and 47 are related to mathematical computational biology. Among the 346 publications on “entrepreneurship” and “genetics”, 146 of the most studied publications are related to genetics heredity, 44 of them are about biochemistry molecular biology and 35 of them are about business economics, and the fields of study are shown in Figure 3.

Table 2. Number of studies by fields

| Research Areas | Record Count | % of 379 |
|------------------------------------|--------------|----------|
| Neurosciences neurology | 260 | 68.602 |
| Business Economics | 53 | 13.984 |
| Mathematical Computational Biology | 47 | 12.401 |
| Psychology | 32 | 8.443 |
| Pharmacology pharmacy | 24 | 6.332 |

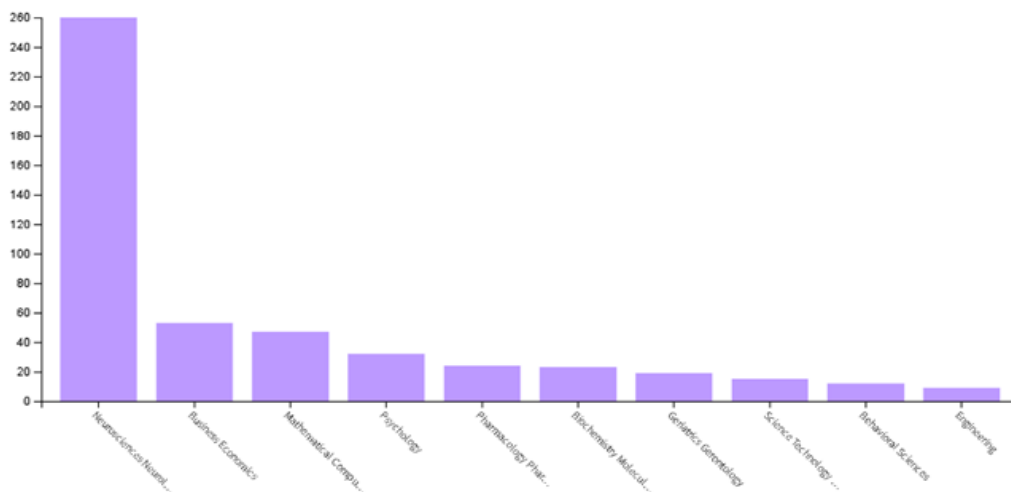


Figure 2. Areas with the most study.

Table 3. Number of studies by fields

| Research Areas | Record Count | % of 346 |
|--------------------------------|--------------|----------|
| Genetics heredity | 146 | 42.197 |
| Biochemistry molecular biology | 44 | 12.717 |
| Business economics | 35 | 10.116 |
| Agriculture | 21 | 6.069 |
| Plant sciences | 17 | 4.913 |

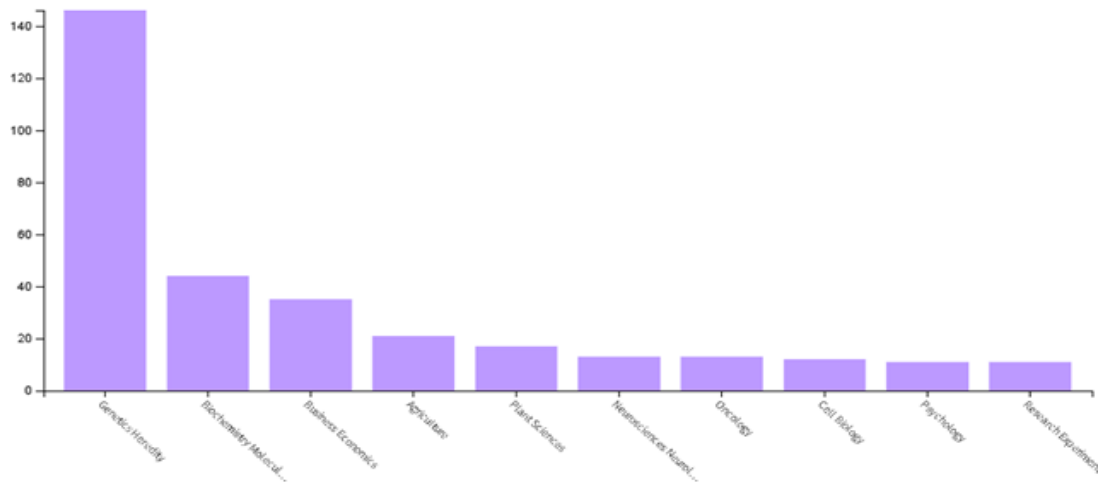


Figure 3. Areas with the most study.

183 publications related to "entrepreneurship" and "biology" were found, the most studied of which was 58 multidisciplinary sciences, 55 related to genetic inheritance and 44 of them related to business (Table 4). These areas are shown in Figure 4.

Within the scope of the study, only 9 publications related to "neuroentrepreneurship", which are directly related to entrepreneurship and neuroscience, were identified in the Web of Science (WoS) database.

5.2. Co-authorship of Author Analysis

According to the co-authorship analysis of the authors, a network map was created by determining at least 1 publication and at least 1 citation criteria in order to

identify the most connected and collaborating authors. It is understood from Figure 6 that the data are mapped in 3 groups, namely the red cluster with 21 authors, the green cluster with 11 authors, and the blue cluster with 7 authors. According to the analysis made among the names with the highest connection, 39 authors in the three clusters have 314 connections. Figure 7 shows that the authors who produced the most publications (12 publications Nicolau Nicos and 11 publications Shane Scott) were the most relevant authors in the analysis of at least 5 publications and at least 5 citations for each author.

Table 4. Number of studies by fields

| Research Areas | Record Count | % of 183 |
|------------------------------------|--------------|----------|
| Multidisciplinary Sciences | 58 | 31.694 |
| Genetics heredity | 55 | 30.055 |
| Business | 44 | 24.044 |
| Management | 24 | 13.115 |
| Biotechnology applied microbiology | 20 | 10.929 |

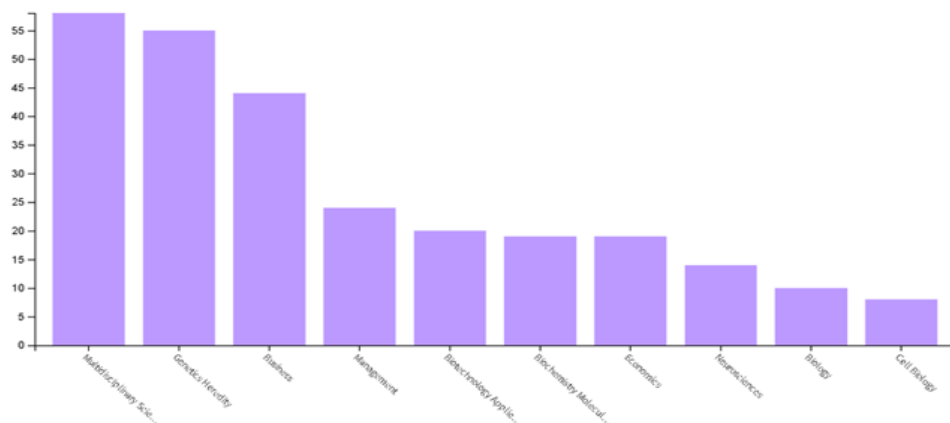


Figure 4. Areas with the most study.

Table 5. Number of studies by fields

| Research Areas | Record Count | % of 9 |
|--------------------------------|--------------|--------|
| Business economics | 8 | 88.889 |
| Development studies | 1 | 11.111 |
| Education educational research | 1 | 11.111 |
| Psychology | 1 | 11.111 |

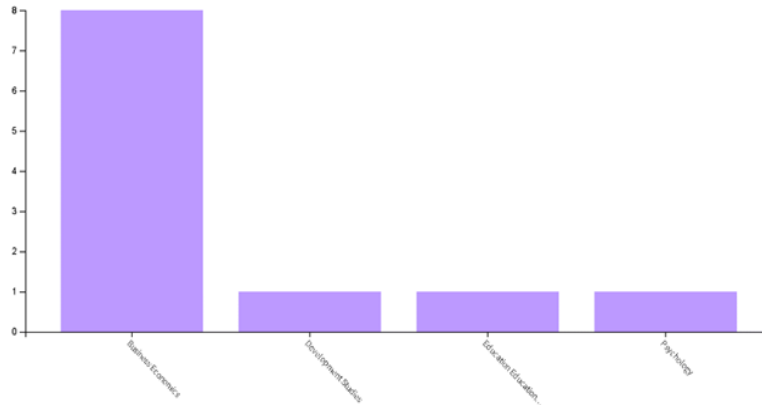


Figure 5. Areas with the most study.

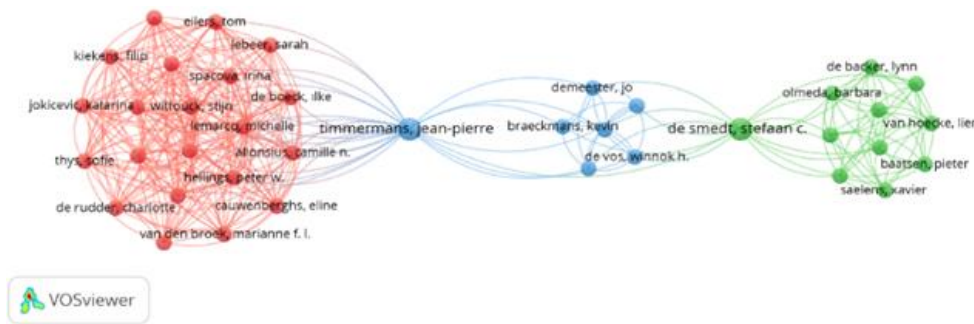


Figure 6. Co-author analysis.

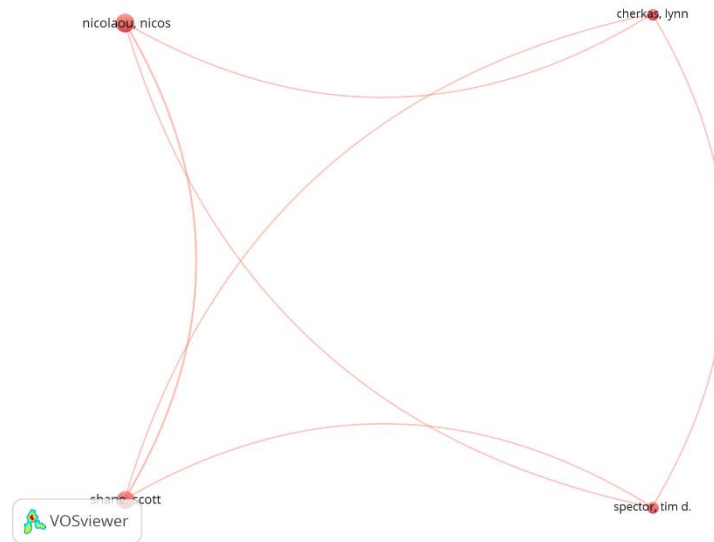


Figure 7. Collaboration between authors and co-author ties.

5.3. Citation of Author Analysis

In order to determine the citation networks, a network map of at least 1 publication and at least 1 citation criteria and author citation analysis was created. In the analysis made on 688 units, which are seen to be

interconnected, a total of 7 clusters and the total connection strength were determined as 833, and these connections are shown in Figure 8. The most cited authors were Shane Scott with 723 citations and Nicolau Nicos with 703 citations.

54. Citation of Countries Analysis

In order to create a network map of the citations of the publications according to their country of origin, analysis was carried out on 38 observation units that were related to each other within the scope of the criteria of publishing at least 1 work and receiving 1 citation by a country. 6 clusters, total connection strength was determined as 713. The most cited countries were the USA (3201 citations), China (1671 citations), and England (1487 citations). In terms of number of works, the ranking is USA (57 publications), China (48 publications) and England (24 publications).

5.5. Citation of Organizations Analysis

Figure 10 shows the result of the analysis made on 310 related observation units within the scope of the criterion of publishing at least 1 publication and receiving 1 citation by an institution in order to create a network map of citations between institutions. Case Western Reserve University (12 publications), Cyprus University (10 publications), Ghent University (7 publications) are the institutions with the most publications, while the ranking is the same in terms of the number of citations (Case Western Reserve University 746 citations, Cyprus University 680 citations, Ghent University 419 citation). A total of 11 clusters and the total connection strength were determined as 1162.

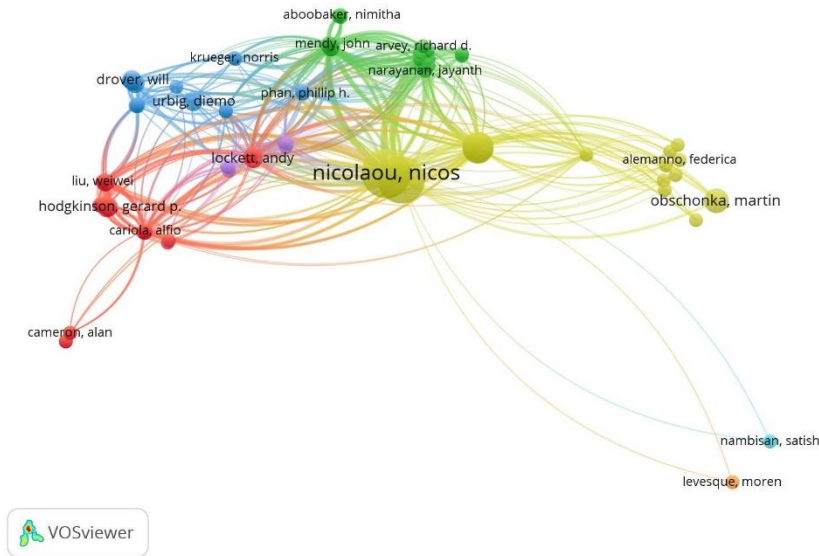


Figure 8. Citation links of authors.

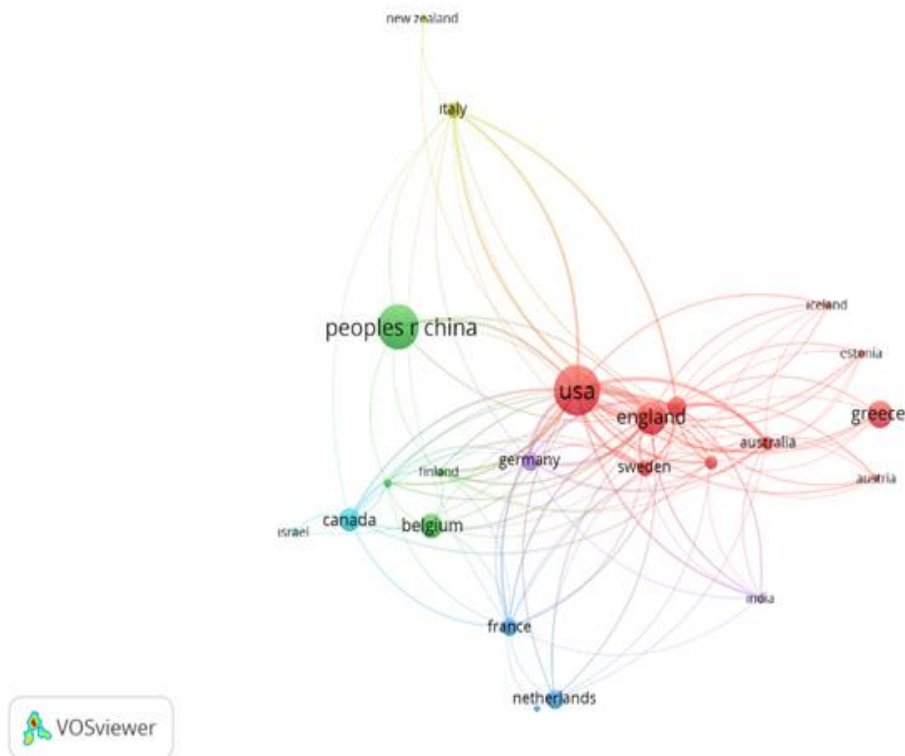


Figure 9. Country citation ties.

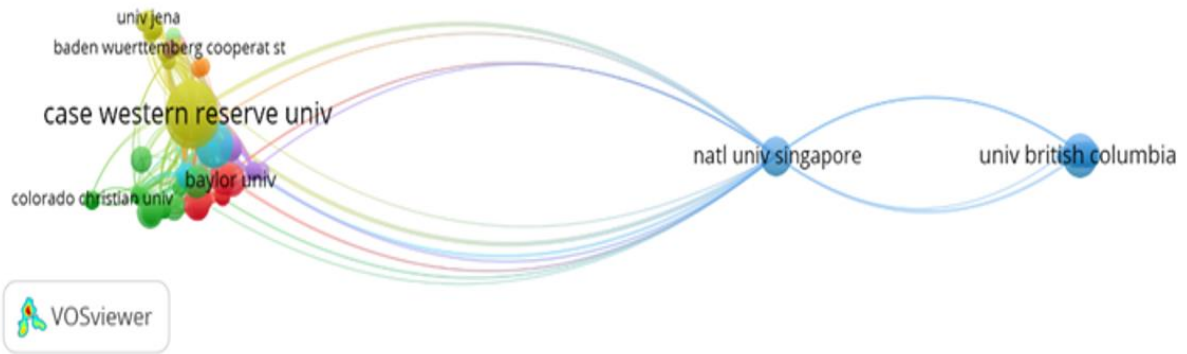


Figure 10. Citation ties of institutions.

5.6. Co-occurrence of Author Keywords Analysis

In the analysis of the most frequently used keywords in the studies carried out by the authors, it is understood from Figure 11 that there are 19 clusters according to the criterion of having at least 1 word in common, and that the most frequently used keywords are 181. Among these words, the word entrepreneurship was in the first place with 19 repetitions, neuroscience was in the second place with 10 repetitions, and the word biology was in the third place with 10 repetitions.

5.7. Co-citation Cited References Analysis

According to the analysis made according to the authors' reference to similar sources in their studies, it is understood that a reference cited is 77 studies and 3 clusters, the minimum number of citations of which is determined as at least 5. It has been determined that the total link strength is 4675, and the most commonly cited studies are Shane (2000) with 20 citations and Nicolau (2008) with 17 citations.

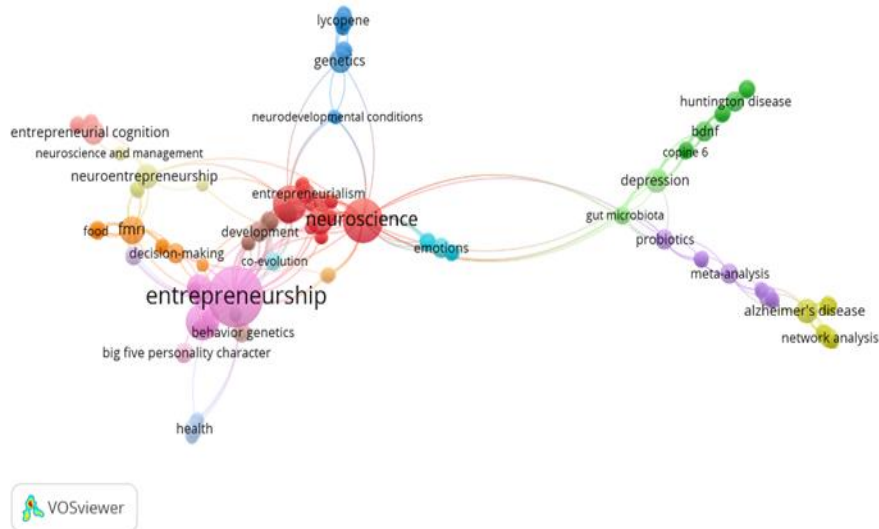


Figure 11. Most common keyword links.

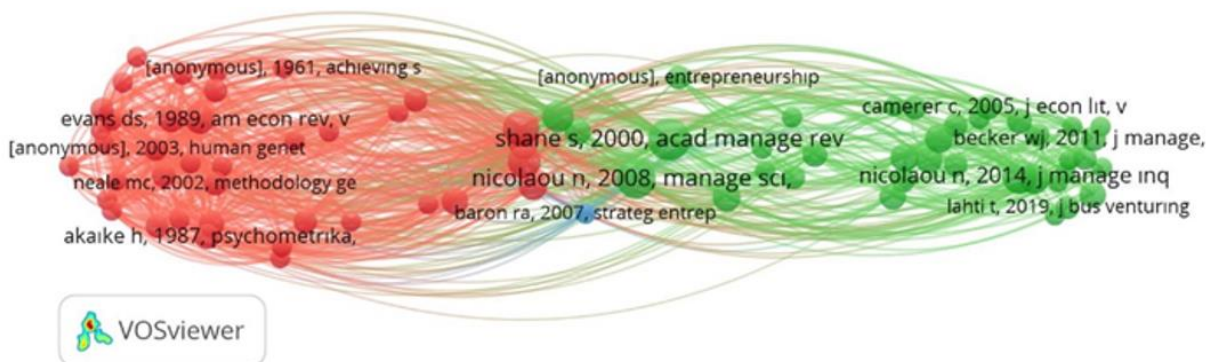


Figure 12. Co-cited authors.

6. Discussion and Conclusion

Entrepreneurship is one of the fields of interest today as a field of study. The importance of neuroscience methods, tools, techniques and approaches in entrepreneurship research is increasing day by day. It has become a necessity to reveal the trends needed in this field. Therefore, this study presents a comprehensive literature review on the neuroanatomy of entrepreneurship using bibliometric analysis techniques. It also provides some data and guides by visualizing the relationships between influential studies and researchers in the field. By including only the studies in WoS and choosing English in terms of language, 917 studies published between 2006 and 2023 were accessed as findings. In the research, published studies on entrepreneurship and neuroscience are analyzed bibliometrically from various aspects and provide valuable information for a better understanding and promotion of the subject.

The most researched areas within the scope of the study; business, business economics, genetic inheritance, biochemistry, molecular biology, multidisciplinary sciences and neuroscience. In the review of co-author analysis, Nicolau Nicos with 12 publications and Shane Scott with 11 publications were also found to be the authors with the highest link. In the citation analysis of the authors, the most cited authors were Shane Scott with 723 citations and Nicolau Nicos with 703 citations. Within the scope of the citation analysis of countries, the most cited countries were the USA (3201 citations), China (1671 citations) and England (1487 citations). In terms of number of works, the ranking is USA (57 publications), China (48 publications) and England (24 publications). In the evaluation of the citation analysis of institutions, Case Western Reserve University (12 publications), Cyprus University (10 publications), Ghent University (7 publications) are the institutions with the highest number of publications. In terms of the number of citations, Case Western Reserve University received 746 citations, Cyprus University 680 citations, and Ghent University 419 citations. As a result of the author's keyword analysis, the word entrepreneurship was in the first place with 19 repetitions, neuroscience was in the second place with 10 repetitions, and the word biology was in the third place with 10 repetitions. As a result of the bibliographic match analysis of the texts, the publications with the most bibliographic matches were Kruschke (2012) with 266 citations, Pouladi (2013) with 240 citations, and Boglione (2013) with 225 citations. Nicolau (2008a; 2008b; 2019) took the first three places as the work with the highest total connection strength. As a result of the co-cited references analysis, it was understood that the most commonly cited studies were Shane (2000) with 20 citations and Nicolau (2008) with 17 citations. As a result of the bibliometric analyzes, it has been understood that some fields of study that can be done with the help of neuroscience in the field of entrepreneurship are missing. In particular, studies in

which genetics, hormones, neurophysiological fields, the effect of environment-biology, behavioral genetics and these components will be handled together will guide future studies.

Parts of the ventral tegmental area, basal nuclei, prefrontal cortex, insular cortex, limbic areas (such as hippocampus and amygdala), nucleus accumbens, thalamus and hypothalamus (Songur, 2022) are the main reward system areas in the human brain. The ventral tegmental area is a dopamine-producing center that manages impulses such as reward, motivation, and cravings. When this area becomes aware of a potential reward, it starts producing a chemical called a neurotransmitter called dopamine. Oxytocin is a hormone that is released in the body at certain times. When oxytocin, known as the hormone of commitment (even when unsuccessful, does not give up being an entrepreneur) interacts with dopamine, the reward system in the brain is activated. One of the most important reward centers in the brain, the ventral tegmental area and the nucleus accumbens (Songur, 2022) are activated in the calculation of gains and losses and in making high-risk decisions. It is a deficiency that studies in the field of entrepreneurship do not examine the relationship between oxytocin, dopamine, ventral tegmental area and nucleus accumbens. Hormones and mediators such as dopamine, vasopressin (ADH) and oxytocin secreted from the hypothalamus, where the most important reward areas of the brain are located (Songur, 2022), have an important place in the stimulation of the reward system. In the studies carried out, the relationships and interactions of these areas or hormones with each other can greatly contribute to the explanation of entrepreneurial behavior. For this reason, the absence of such studies causes the desired results in entrepreneurship research to not be achieved and some questions remain unanswered. For a better understanding of entrepreneurship neurophysiologically, it is very important to examine the active centers and neural networks in the brain due to the reactions given during entrepreneurial decision making and behavior. Entrepreneurship research, which will be conducted using neuroscience tools and methods together, will contribute more to the field. The most important reason for this is that entrepreneurship is multifaceted, complex and consists of more than one element. For this reason, it is very difficult to elucidate such a complex process with the help of a single method, approach or tool.

Many studies have focused on certain characteristics of entrepreneurship or have made use of certain methods, tools and techniques. For this reason, complete and precise information about the processes related to entrepreneurial thought, behavior and decision making could not be reached. Although the development of neuroscience and its use with different disciplines allow promising results in entrepreneurship research, the desired level has not been reached yet. The fact that scientists who do research in the field of social sciences

do not have the culture and knowledge of working with different disciplines (neuroscience) has made the subject even more difficult. Entrepreneurship research, which requires a multidisciplinary approach, cannot benefit from neuroscience sufficiently. The fact that entrepreneurial behavior consists of many different components has made the subject even more difficult. In future studies, neurological, physiological, and genetic and psychoneuroendocrinological approaches should be used together. Otherwise, parts of the whole will always be missing and some questions will not be answered.

Studies advocating that biology and environmental factors should be considered together have advocated a holistic approach with the sentence "We are all biological creatures and our biology affects all aspects of our behavior, including our work" (Nofal et al., 2018). As a result of the interaction of environmental factors and genetic inheritance, individuals are more prone to become entrepreneurs (Nicolaou et al., 2008; Shane et al., 2010a; Shane and Nicolaou, 2013; Nicolaou, 2015b; Wolfe and Patel, 2017; Wolfe and Patel, 2018; Anglin et al., 2018; Shane et al. 2019). A study similar to the study by Studer et al. (2013) design will make a great contribution to the understanding of entrepreneurial behavior.

Lawrence et al. (2008) in their study investigating the phenomenon of "functional impulsivity" among entrepreneurs and managers, discovered that functional impulsivity allows people to seize opportunities in rapidly changing environments. Researchers recorded various parameters such as neurocognitive assessment (to test their decision-making skills) and demonstrated their relationship to the performance of behavioral tasks. The study, which tested whether entrepreneurs and managers differ in terms of impulsivity and risk taking, showed that entrepreneurs and managers performed equally on behavioral tasks that required "cold" cognition (rational analysis), but entrepreneurs outperformed managers in "hot" cognition. These results will help us understand why entrepreneurs are more successful at tasks that require both rational and emotional thinking.

In particular, the investigation of psychophysiological indices will contribute to a better understanding of the nature of entrepreneurial behavior. Future studies can build on this literature and compare cardiovascular parameters between male and female entrepreneurs or investors (Bellavitis et al., 2016; Bellavitis et al., 2017). The study could explore how the two groups react in different situations, such as risk taking, failure, success or uncertainty. Further research will help us understand whether different entrepreneurial attempts trigger different emotional states, leading an entrepreneur to choose a particular venture based on emotions rather than economic profit maximisation. Since the ultimate goal of the ever-evolving field of neuroentrepreneurship is to understand the psychological and biological factors that determine entrepreneurial outcomes (e.g. behavior, success), entrepreneurship and business scholars can

gain great insights by exploring psychophysiological indices. Understanding the emotions of entrepreneurs will shed light on many processes that are difficult to resolve. Lawrence et al. (2008) have shown that neuroscience can be a powerful tool to answer such research questions. In particular, the investigation of psychophysiological indices will contribute to a better understanding of the nature of entrepreneurial behavior.

The use of psychoneuroendocrinology will enable many questions to be answered in entrepreneurship research. Analysis of different hormones can offer interesting insights into entrepreneurial behavior. A different level of dopamine precursors or receptors may explain risk-seeking behavior and may be implicated as a determinant of entrepreneurial instincts. For example, Nicolaou et al. (2011) suggested a possible link between the presence of a gene (DRD3) encoding a type of dopamine receptor (special protein molecules selectively activated by dopamine) and entrepreneurship. This may be due to the higher dopamine levels these individuals need to "activate" the reward circuits in their brains. However, it should be emphasized that this study could not be replicated in larger samples (van der Loos et al., 2011). In this context, it would be beneficial to examine the responses of the brain's reward-related centers to entrepreneurial behavior. For example; In the event of a risky economic decision, the changes that occur in the "accumbens" nucleus in the brain and the measurement of the responses will provide important insights in the understanding of entrepreneurial behavior.

Using the skin conductivity method, in which electrodermal activity is measured, will be useful in detecting some changes in the body caused by entrepreneurial behavior and in obtaining information about emotional arousal, decision-making and behavior. It can also contribute to discovering unsuccessful entrepreneurial decision-making strategies. Similar studies can be conducted to explore the differences between a person who takes the entrepreneurial decision for the first time and those who have previously engaged in entrepreneurial activities. For example; New insights can be gained by comparing electrodermal activity, how partners form a successful cooperation (credibility) or how investors (e.g. venture capitalists) respond to certain investment offers, emotional responses to investment opportunities, and experience-related responses.

Understanding how events in the entrepreneurial ecosystem shape an entrepreneur's motivation or a particular decision-making process will allow significant gains. Building on the paper of Vieito et al. (2015), entrepreneurship researchers can explore important dynamics of the venture finance industry, including equity crowdfunding. The most important questions we will face in the research are: Are the investment decisions of venture capitalists affected by certain market conditions? How do venture capitalists react when the companies they invest in underperform or have

a conflict with management? What types of information affect investors' brain activity the most, and how does this affect their decision to invest (or not)?

There is little information about the correlation between biological structure and environment and individuals' preference for environments that positively affect entrepreneurship (Plomin et al., 2001; Nicolaou and Shane, 2009). Therefore, genetics can be crucial for advancing the field of entrepreneurship and offer an innovative and powerful set of tools for investigating the behavioral and cognitive patterns of entrepreneurs. Scientists can indirectly investigate the neural and physiological correlates of human behavior. A better understanding of how genetics and environment shape a person's choices (such as being an entrepreneur), behaviors, and skills (such as leadership or decision-making skills) will help to better understand entrepreneurial behavior. One of the most important elements of entrepreneurial behavior and decision making is hormones. For this reason, the relationship and effect of hormones and body chemicals on entrepreneurial thinking, intention and behavior, together with environmental or genetic factors, must be investigated. Emerging neuroscience methods, tools, techniques, and approaches allow researchers to explore the antecedents of behavior, including entrepreneurial behavior. These tools can shed light on important questions about the natural (genetic-based) or acquired (education-based) origins of entrepreneurial attitudes and the individual differences between successful and unsuccessful entrepreneurs. One of the most frequently asked questions, is there an "entrepreneurship gene"? If so, how and under what conditions does this gene affect an individual's tendency to be an entrepreneur? The answer to all these questions will only be revealed if research is carried out with a holistic approach.

Author Contributions

The percentage of the author(s) contributions is presented below. All authors reviewed and approved the final version of the manuscript.

| | A.B. |
|-----|------|
| C | 100 |
| D | 100 |
| S | 100 |
| DCP | 100 |
| DAI | 100 |
| L | 100 |
| W | 100 |
| CR | 100 |
| SR | 100 |
| PM | 100 |
| FA | 100 |

C=Concept, D= design, S= supervision, DCP= data collection and/or processing, DAI= data analysis and/or interpretation, L= literature search, W= writing, CR= critical review, SR= submission and revision, PM= project management, FA= funding acquisition.

Conflict of Interest

The authors declared that there is no conflict of interest.

Ethical Consideration

Ethics committee approval was not required for this study because of there was no study on animals or humans.

References

Alvarez S, Barney JB. 2020. Has the concept of opportunities been fruitful in the field of entrepreneurship? *Acad Manag Perspect*, 34(3): 300-310.

Anglin AH, Wolfe MT, Short JC, McKenny AF, Pidduck RJ. 2018. Narcissistic rhetoric and crowdfunding performance: A social role theory perspective. *J Business Vent*, 33(6): 780-812. DOI: 10.1016/j.jbusvent.2018.04.004.

Bai L, Sun F, Wang W. 2022. Innovative application of artificial intelligence in the field of innovation and entrepreneurship of college students in internet colleges and universities. *Comput Intel Neurosci*, 2022: 3538755.

Balconi M, Pagani S. 2015. Social hierarchies and emotions: cortical prefrontal activity, facial feedback (EMG), and cognitive performance in a dynamic interaction. *Soc Neurosci*, 10(2): 166-178.

Ball R. 2018. Bibliometric methods: Basic principles and indicators. Ball R. (Ed), *An introduction to bibliometrics*, Chandos Publishing, London, UK, pp: 15-56.

Barnea A, Cronqvist H, Siegel S. 2010. Nature or nurture: what determines investor behavior?. *J Finan Econ*, 98(3): 583-604.

Bechara A, Damasio H, Damasio AR, Lee GP. 1999. Different contributions of the human amygdala and ventromedial prefrontal cortex to decision-making. *J Neurosci*, 19(13): 5473-5481.

Bechara A, Damasio H, Tranel D, Damasio AR. 2005. The Iowa Gambling Task and the somatic marker hypothesis: some questions and answers. *Trends Cognit Sci*, 9(4): 159-162.

Bellavitis C, Filatotchev I, Kamuriwo DS, Vanacker T. 2017. "Entrepreneurial finance: New frontiers of research and practice. *Venture Capital*, 19(1-2): 1-16.

Bellavitis C, Filatotchev I, Souitaris V. 2016. The impact of investment networks on venture capital firm performance: A contingency framework. *British J Manag*, 28: 102-119.

Bercea MD. 2013. Anatomy of methodologies for measuring consumer behavior in neuromarketing research. URL: http://www.lcbroonline.com/index_files/proceedingsemc12/12emc023.pdf.E.T. (accessed date: January 09, 2023).

Boglione C, Gisbert E, Gavaia PE, Witten P, Moren M, Fontagné S, Koumoundouros G. 2013. Skeletal anomalies in reared European fish larvae and juveniles. Part 2: main typologies, occurrences and causative factors. *Rev Aquaculture*, 5: S121-S167.

Bönte W, Procher VD, Urbig D. 2016. Biology and selection into entrepreneurship: The relevance of prenatal testosterone exposure. *Entrepreneurship Theory Pract*, 40(5): 1121-1148. DOI: 10.1111/etap.12165.

Colosio M, Bellavitis C, Gorin AA. 2017. Human psychophysiological and genetic approaches in neuroentrepreneurship. In *Handbook of Research Methodologies and Design in Neuroentrepreneurship*. Edward Elgar Publishing Ltd., London, UK, pp: 54-93.

de Holan PM. 2014. It's all in your head: Why we need neuroentrepreneurship. *J Manag Inquiry*, 23(1): 93-97.

Egana-delSol P, Sun X, Sajda P. 2023. Neurophysiological markers of emotion regulation predict efficacy of

- entrepreneurship education. *Scient Rep*, 13(1): 7206.
- Greene FJ, Han L, Martin S, Zhang S, Wittert G. 2014. Testosterone is associated with self-employment among Australian men. *Econ Human Biol*, 13: 76-84.
- Hatak I, Zhou H. 2019. Health as human capital in entrepreneurship: Individual, extension, and substitution effects on entrepreneurial success. *Entrepreneurship Theory Pract*, 127(1): 104225871986755.
- Hüsser A, Wirth W. 2014. Do investors show an attentional bias toward past performance? An eye-tracking experiment on visual attention to mutual fund disclosures in simplified fund prospectuses. *J Financ Serv Mark*, 19: 169-185.
- Ioannides AA, Liu L, Theofilou D, Dammers J, Burne T, Ambler T, Rose S. 2000. Real time processing of affective and cognitive stimuli in the human brain extracted from MEG signals. *Brain Topography*, 13(1): 11-16.
- Krueger N, Welpe I. 2014. Neuroentrepreneurship: what can entrepreneurship learn from neuroscience?" in Michael H. Morris (ed), *Annals of Entrepreneurship: Education and Pedagogy*. United States Association for Small Business and Entrepreneurship, Washington, US.
- Kruschke JK, Aguinis H, Joo H. 2012. The time has come: Bayesian methods for data analysis in the organizational sciences. *Organizat Res Methods*, 15(4): 722-752.
- Künecke J, Hildebrandt A, Recio G, Sommer W, Wilhelm O. 2014. Facial EMG responses to emotional expressions are related to emotion perception ability. *PloS One*, 9(1): e84053.
- Lahti T, Halko ML, Karagozoglu N, Wincent J. 2019. Why and how do founding entrepreneurs bond with their ventures? Neural correlates of entrepreneurial and parental bonding. *J Business Vent*, 34(2): 368-388. DOI: 10.1016/j.jbusvent.2018.05.001
- Laureiro-Martínez D, Venkatraman V, Cappa S, Zollo M, Brusoni S. 2015. Cognitive neurosciences and strategic management: Challenges and opportunities in tying the knot. *Cognit Strat*, 32: 351-370.
- Lawrence A, Clark L, Labuzetta JN, Sahakian B, Vyakarnum S. 2008. The innovative brain. *Nature*, 456(7219): 168-169.
- Lerner DA, Hunt RA, Verheul I. 2018. Dueling banjos: Harmony and discord between ADHD and entrepreneurship. *Acad Manag Perspect*, 32(2): 266-286. DOI: 10.5465/amp.2016.0178.
- Lindquist MJ, Sol J, Van Praag M. 2015. Why do entrepreneurial parents have entrepreneurial children?. *J Labor Econ*, 33(2): 269-296.
- Lo AW, Repin Dmitry D. 2002. The psychophysiology of real-time financial risk processing. *J Cognit Neurosci*, 8508: 323-339.
- Logan J. 2009. Dyslexic entrepreneurs: The incidence; their coping strategies and their business skills. *Dyslexia*, 15(4): 328-346.
- Mehta PH, Prasad S. 2015. The dual-hormone hypothesis: a brief review and future research agenda. *Curr Opin Behav Sci*, 3: 163-168.
- Moore CB, McIntyre NH, Lanivich SE. 2021. ADHD-related neurodiversity and the entrepreneurial mindset. *Entrepreneurship Theory Pract*, 45(1): 64-91.
- Morin C. 2011. Neuromarketing. *New Sci Consumer Behav*, 48(2): 131-135.
- Muda R, Kicia M, Michalak-Wojnowska M, Ginszt M, Filip A, Gawda P, Majcher P. 2018. The dopamine receptor D4 gene (DRD4) and financial risk-taking: Stimulating and instrumental risk-taking propensity and motivation to engage in investment activity. *Front Behav Neurosci*, 12: 34. DOI: 10.3389/fnbeh.2018.00034.
- Nicolaou N, Patel PC, Wolfe MT. 2018. Testosterone and tendency to engage in self-employment. *Manag Sci*, 64(4): 1825-1841. DOI: 10.1287/mnsc.2016.2664.
- Nicolaou N, Phan PH, Stephan U. 2021. The biological perspective in entrepreneurship research. *Entrepreneurship Theory Pract*, 45(1): 3-17.
- Nicolaou N, Shane S, Adi G, Mangino M, Harris J. 2011. A polymorphism associated with entrepreneurship: evidence from dopamine receptor candidate genes. *Small Busin Econ*, 36(2): 151-155.
- Nicolaou N, Shane S, Cherkas L, Hunkin J, Spector TO. 2008. Is the tendency to engage in entrepreneurship genetic?. *Manag Sci*, 54(1): 167-179.
- Nicolaou N, Shane S, Cherkas L, Spector TD. 2009. Opportunity recognition and the tendency to be an entrepreneur: a bivariate genetics perspective. *Organiz Behav Human Decis Proces*, 110(2): 108-117.
- Nicolaou N, Shane S. 2010. Entrepreneurship and occupational choice: genetic and environmental influences. *J Econ Behav Organizat*, 76(1): 3-14.
- Nofal AM, Nicolaou N, Symeonidou N, Shane S. 2018. Biology and management: A review, critique, and research agenda. *J Manag*, 44(1): 7-31. DOI: 10.1177/0149206317720723.
- Plomin R, DeFries JC, Knopik VS, Neiderhiser JM. 2012. Behavioral genetics. Worth Publishers, New York, US, pp: 74.
- Plomin R, DeFries JC, McClearn GE, McGuffin P. 2001. Behavioral genetics (4th ed). Worth Publishers, Worth Publishers, New York, US, pp: 127.
- Pouladi MA, Morton AJ, Hayden MR. 2013. Choosing an animal model for the study of Huntington's disease. *Nature Rev Neurosci*, 14(10): 708-721.
- Shane S, Drover W, Clingsmith D, Cerf M. 2019. Founder passion, neural engagement and informal investor interest in startup pitches: An fMRI study. *J Busin Ventur*, 35(4): 105949.
- Shane S, Nicolaou N, Cherkas L, Spector TD. 2010. Genetics, the big five, and the tendency to be self-employed. *J Appl Psychol*, 95(6): 1154-1162. DOI: 10.1037/a0020294.
- Shane S, Nicolaou N, Cherkas L, Spector TD. 2010a. Do openness to experience and recognizing opportunities have the same genetic source? *Human Resour Manag*, 49(2): 291-303. DOI: 10.1002/hrm.20343.
- Shane S, Nicolaou N. 2015b. Creative personality, opportunity recognition and the tendency to start businesses: A study of their genetic predispositions. *J Busin Ventur*, 30(3): 407-419.
- Sharma GD, Paul J, Srivastava M, Yadav A, Mendy J, Sarker T, Bansal S. 2021. Neuroentrepreneurship: an integrative review and research agenda. *Entrepren Regional Devel*, 33(9-10): 863-893.
- Simeon D, Yehuda R, Cunill R, Knutelska M, Putnam FW, Smith LM. 2007. Factors associated with resilience in healthy adults. *Psychoneuroendocrinol*, 32(8-10): 1149-52.
- Songur A. 2022. Aşkın nöroanatomi. *LabMedia Mag*, 13(77): 26-27.
- Studer B, Pedroni A, Rieskamp J. 2013. Predicting risk-taking behavior from prefrontal resting-state activity and personality. *PloS One*, 8(10): e76861.
- Tallon-Baudry C, Meyniel F, Bourgeois-Gironde S. 2011. Fast and automatic activation of an abstract representation of money in the human ventral visual pathway. *PloS One*, 6(11): e28229.
- Unger JM, Rauch A, Weis SE, Frese M. 2015. Biology (prenatal testosterone), psychology (achievement need) and entrepreneurial impact. *J Busin Ventur Insights*, 4: 1-5.
- van der Loos MJHM, Koellinger PD, Groenen PJF, Rietveld CA,

- Rivadeneira F, van Rooij FJA, Thurik AR. 2011. Candidate gene studies and the quest for the entrepreneurial gene. *Small Busin Econ*, 37(3): 269-275.
- van der Loos MJHM, Rietveld CA, Eklund N, Koellinger PD, Rivadeneira F, Abecasis GR, Ankra-Badu GA, Baumeister SE, Benjamin DJ, Biffar R, Blankenberg S, Boomsma DI, Cesarini D, Cucca F, de Geus EJC, Dedoussis G, Deloukas P, Dimitriou M, Eiriksdottir G, Thurik AR. 2013. The molecular genetic architecture of self-employment. *PLoS ONE*, 8(4): e60542.
- Venkataraman S. 1997. The distinctive domain of entrepreneurship research. *JAI Press*, 3: 119-138.
- Vieito JP, da Rocha AF, Rocha FT. 2015. Brain activity of the investor's stock market financial decision. *J Behav Finan*, 16(3): 220-230.
- Weinberger E, Wach D, Stephan U, Wegge J. 2018. Having a creative day: Understanding entrepreneurs' daily idea generation through a recovery lens. *J Busin Ventur*, 33(1): 1-19. DOI: 10.1016/j.jbusvent.2017.09.001.
- White RE, Thornhill S, Hampson E. 2006. Entrepreneurs and evolutionary biology: The relationship between testosterone and new venture creation. *Organizat Behav Human Decis Proces*, 100(1): 21-34. DOI: 10.1016/j.obhdp.2005.11.001.
- White RE, Thornhill S, Hampson E. 2007. A biosocial model of entrepreneurship: The combined effects of nurture and nature. *J Organiz Behav*, 28(4): 451-466.
- Wiklund J, Patzelt H, Dimov D. 2016. Entrepreneurship and psychological disorders: How ADHD can be productively harnessed. *J Busin Ventur Insights*, 6: 14-20.
- Wiklund J, Yu W, Tucker R, Marino LD. 2017. ADHD, Impulsivity and Entrepreneurship. *J Busin Ventur*, 32(6): 627-656.
- Wolfe MT, Patel PC. 2017. Two are better than one: Cortisol as a contingency in the association between epinephrine and self-employment. *J Busin Ventur Insights*, 8: 78-86.
- Wolfe MT, Patel PC. 2018. Racing to get self-employed? Life history models and self-employment. *J Busin Ventur Insights*, 10: e00093.
- Yıldırım BO, Derksen JJ. 2012. A review on the relationship between testosterone and life-course persistent antisocial behavior. *Psychiatry Res*, 200(2-3): 984-1010.
- Zhang Z, Zyphur MJ, Narayanan J, Arvey RD, Chaturvedi S, Avolio BJ, Larsson G. 2009. The genetic basis of entrepreneurship: effects of gender and personality. *Organizat Behav Human Decis Proces*, 110(2): 93-107.
- Zunino D. 2016. Are genetics and environment substitutes or complements in affecting entrepreneurial choice? *Acad Manag Proceed*, 2016(1): 12173. DOI: 10.5465/ambpp.2016.12173abstract.



MECHANICAL PERFORMANCE OF SALVADORA PERSICAL (MISWAK) REINFORCED POLYLACTIC ACID MATRIX COMPOSITES FOR THREE DIMENSIONAL PRINTING

Fuat KARTAL^{1*}, Arslan KAPTAN²

¹Kastamonu University, Faculty of Engineering and Architecture, Department of Mechanical Engineering, 37150, Kastamonu, Türkiye


²Sivas Cumhuriyet University, Sivas Technical Sciences Vocational School, Department of Motor Vehicles and Transportation Technologies, 58140, Sivas, Türkiye


Abstract: This study examines the mechanical performance of polylactic acid (PLA) matrix composites reinforced with *Salvadora Persica* (Miswak). With the increasing use of environmentally friendly materials, researchers are focusing on the production of biodegradable materials. However, incompatibility between PLA and filler materials used in PLA composites causes mechanical problems during production. This study deals with the production and characterization of PLA composites containing lignocellulosic and inorganic fillers using maleic anhydride grafted polylactic acid (PLA/g/MA) as a matrix. The aim of the research is to examine the mechanical specifications of Miswak powder reinforced PLA composites and to evaluate their suitability for practical applications. PLA was used as the matrix material and PLA/g/MA was used as the compatibilizer. Composites containing Miswak powder at different weight concentrations (5%, 10%, 15% and 20%) were characterized using scanning electron microscopy along with tensile and bending tests. The obtained results showed that different Miswak concentrations affect the mechanical specifications of the composites. Composites at 5% concentration demonstrated excellent interlayer adhesion and high mechanical strength, demonstrating favorable mechanical specifications. The findings show that Miswak powder is a potential filling material to improve the mechanical specifications of PLA composites and provide antimicrobial benefits. The results of this study shed light on the mechanical performance of Miswak reinforced PLA matrix composites, which are promising for 3D printing applications. In addition, it is stated that the materials used, such as natural filling materials, contribute to the development of sustainable and environmentally friendly materials by reducing the environmental impact.

Keywords: *Salvadora Persica*, Miswak powder, Polylactic acid, PLA composites, Mechanical specifications, 3D printing

*Corresponding author: Kastamonu University, Faculty of Engineering and Architecture, Department of Mechanical Engineering, 37150, Kastamonu, Türkiye

E mail: fkartal@kastamonu.edu.tr (F. KARTAL)

Fuat KARTAL  <https://orcid.org/0000-0002-2567-9705>

Arslan KAPTAN  <https://orcid.org/0000-0002-2431-9329>

Received: July 15, 2023

Accepted: September 18, 2023

Published: October 15, 2023

Cite as: Kartal F, Kaptan A. 2023. Mechanical performance of salvadora persical (Miswak) reinforced polylactic acid matrix composites for three dimensional printing. BSJ Eng Sci, 6(4): 458-468.

1. Introduction

Poly(lactic acid) (PLA) has gained significant attention as a potential alternative to petroleum-based plastics due to its renewable nature and biodegradability (Rujitanaroj et al., 2015). However, PLA exhibits certain limitations in terms of its mechanical properties, such as low tensile strength and impact resistance (Garlotta, 2001). To overcome these limitations, researchers have focused on the development of PLA composites by incorporating compatible fillers that can enhance its mechanical performance (Averous, 2008). Among the various fillers investigated, natural fillers have garnered interest due to their abundance, renewability, and potential cost advantages (Zhang and Jiang, 2018). *Salvadora Persica* (*S. Persica*, Miswak) stands out as a promising natural filler for reinforcing PLA composites (Hassan and Hassan, 2019). Miswak is derived from the Miswak tree and possesses bioactive compounds with antimicrobial, antioxidant, and anti-inflammatory properties. These

properties make Miswak an attractive candidate for improving the mechanical specifications of PLA composites while also providing additional benefits (Almas, 2002). Miswak has been traditionally used as a natural oral hygiene tool in many cultures (Dar-Odeh et al., 2019). Several studies have highlighted the oral health benefits of Miswak, including its antimicrobial and plaque-reducing properties (Baeshen et al., 2017; Winarni et al., 2019). Miswak has also been compared to conventional toothbrushes, demonstrating comparable or even superior oral hygiene outcomes (Chauhan et al., 2020). Mechanical (tensile strength, percent elongation, bending strength, impact resistance and compressive strength) and abrasive wear properties of Miswak reinforced polymer composites were examined (Savas, 2018; Khalaf, 2013; Oleiwi et al., 2017). Its mechanical specifications, such as flexibility and toughness, make it suitable for chewing and maintaining oral hygiene (Bramantoro et al., 2018). The incorporation of Miswak into PLA composites holds great potential for various



applications, including 3D printing. However, limited research has been conducted to explore the mechanical performance of Miswak reinforced PLA composites specifically for 3D printing applications. Therefore, this study aims to investigate the mechanical specifications of Miswak powder reinforced PLA composites and evaluate their suitability for 3D printing.

Here is a summary of the key points:

Objective: The aim of the research is to investigate the mechanical performance of PLA composites reinforced with Miswak powder and evaluate their suitability for practical applications, particularly in 3D printing.

Background: The increasing demand for environmentally friendly materials has led researchers to explore biodegradable options such as PLA. However, PLA has limitations in terms of mechanical properties, which can be addressed by reinforcing it with compatible fillers.

Miswak as a Reinforcing Filler: Miswak, derived from the Miswak tree, is considered a promising natural filler for strengthening PLA composites. Miswak contains bioactive compounds with antimicrobial properties, making it an attractive candidate for enhancing the mechanical specifications of PLA composites.

Composite Production and Characterization: The study utilizes PLA/g/MA as a matrix and Miswak powder as the reinforcing filler. Composites with different weight concentrations of Miswak (5%, 10%, 15%, and 20%) are produced and characterized using scanning electron microscopy (SEM), as well as tensile and bending tests.

Mechanical Property Effects: The results indicate that the mechanical specifications of the composites are influenced by the concentration of Miswak. Composites with a 5% Miswak concentration exhibit excellent interlayer adhesion and high mechanical strength, demonstrating favorable mechanical properties. However, as the Miswak concentration increases, the mechanical specifications of the composites may be affected differently.

Significance: The findings of this study shed light on the mechanical performance of Miswak reinforced PLA matrix composites, highlighting their potential for 3D printing applications. Additionally, the use of natural fillers like Miswak contributes to the development of sustainable and environmentally friendly materials by reducing their environmental impact. Although Miswak is a candidate material for the production of natural fiber-reinforced polymer matrix composites due to its fiber-like structure, there are very few studies on this subject. There are a limited number of studies on the mechanical properties of Miswak-added polymer matrix composites. In this study, a PLA matrix is reinforced with Miswak powder at different weight concentrations. The mechanical specifications of the composites have been characterized using a variety of tests, including tensile and bending tests. The morphology and interface interactions between Miswak powder and PLA matrix were investigated using SEM. Additionally, thermal properties and compatibility of composites will be

analyzed. The findings of this research contribute to the understanding of the mechanical performance of *S. persica* (Miwak) reinforced PLA composites and their potential for 3D printing applications. Also, the use of Miswak as a natural filler in PLA composites has the potential to lead to the development of sustainable and environmentally friendly materials.

2. Materials and Methods

S. persica has a natural fiber structure and is among the most commonly used medicinal plants for oral hygiene (Sher et al., 2010). *S. persica* is chemically composed of butanediamide, N-benzyl 2-phenylacetamide, benzyl isothiocyanate, salvadorin, alkaloids, chlorides, high amounts of fluoride and silica, sulfur, vitamin C, essential oils, small amounts of tannins, saponins, flavonoids and sterols (Darout et al. al., 2000). Sulfur, alkaloids, butanediamide and N-benzyl-2-phenylacetamide in Miswak are agents that provide antimicrobial effect (Dutta and Shaikh, 2012). In the literature, it was stated that *S. persica* extracts showed antimicrobial activity against *Staphylococcus aureus*, *Streptococcus mutans*, *Lactobacillus acidophilus*, *E. coli* and *Pseudomonas aeruginosa*. Miswak is being used for different applications due to its low cost and ready availability as well as its antibacterial effect. On the other hand, it is known that Miswak improves mechanical properties due to its fiber-like structure. Miswak sticks were obtained from a Türkiye-based e-commerce platform and stored in hygienic vacuum packaging. These Miswak products were imported by the Kureyshi Essence Company. Miswak sticks have been specially processed and turned into Miswak powder with various physical and chemical properties. The process involved peeling, breaking, drying, grinding and drying the sticks. The obtained Miswak powder was stored in airtight plastic bags. Miswak powder is an ingredient obtained from the Miswak plant. This powder contains ingredients such as cellulose, hemicellulose, and lignin, which contain organic compounds. It also contains functional groups such as phenolic, carboxylic, alcoholic and amine groups. Miswak powder contains various phytochemicals such as sulfur, chloride, fluoride, vitamin C, tannins, silica, alkaloids and essential oils. Also, chemical components include beta-sitosterol, glycosides, pyrrolidine, pyrrole and piperidine. Other properties of Miswak powder such as pH value and conductivity were also determined. Miswak powder has been characterized for use as a filler in PLA composites. Miswak fibers mixed with PLA were mixed using a twin screw extruder and then extruded using a single screw extruder. The resulting Miswak PLA Composite filament was prepared for use in 3D printing. This filament offers a sustainable and environmentally friendly alternative to traditional filaments. The natural antibacterial properties of Miswak powder stand out as additional benefits of the composite material. Miswak/PLA composite filament was used to create tensile test specimens in accordance with ASTM 638

Type IV standards. This composite filament is evaluated as a promising material for various applications by combining the advantages of PLA as well as the natural properties obtained from the Miswak plant. Table 1 shows the mixing ratios of samples containing polylactic acid (PLA), PLA/g/MA (polylactic acid modified with maleic acid), and Miswak fiber (Miswak). The PLA/W0 sample contains only 100% PLA, while the PLA/W5 sample has 94% PLA, 1% PLA/g/MA and 5% Miswak content. Similarly, 88% PLA, 2% PLA/g/MA and 10%

Miswak in the PLA/W10 sample, 81% PLA, 4% PLA/g/MA and 15% Miswak in the PLA/W15 sample, and 74% in the PLA/W20 sample. It has PLA, 6% PLA/g/MA and 20% Miswak content. These mixing ratios show the compositions of the composite samples and the percentage of materials they contain. These ratios can affect the properties and performance of the composite material. The schematic illustration of composite filament preparation typically involves several steps (Figure 1).

Table 1. Sample combination rates

| Sample name | PLA (wt%) | PLA/g/MA (wt%) | Miswak (wt%) |
|-------------|-----------|----------------|--------------|
| PLA/W0 | 100 | 0 | 0 |
| PLA/W5 | 94 | 1 | 5 |
| PLA/W10 | 88 | 2 | 10 |
| PLA/W15 | 81 | 4 | 15 |
| PLA/W20 | 74 | 6 | 20 |



Figure 1. PLA/MF preparation and printing cycle.

Here is a general description of the process:

Selection of Matrix Material: A suitable matrix material is selected, such as PLA or another compatible polymer.

Selection of Reinforcement Material: Reinforcement material is selected, in this case this material can be Miswak powder or any desired filler.

Mixing: Matrix material and reinforcement material are mixed thoroughly. This can be achieved using a twin screw extruder or other mixing techniques to ensure uniform distribution of the filler in the matrix.

Extrusion: The mixed material is fed into a single screw extruder. The extruder melts the composite mix and pushes it through a die of the desired filament diameter, forming a continuous filament.

Cooling and Solidification: The extruded filament is cooled rapidly to solidify the material and maintain its shape. This can be done using cooling baths or air cooling.

Winding: The solidified filament is wound onto a spool or bobbin for storage and later use in 3D printing.

Better Distribution: Smaller particles provide a more homogeneous distribution in the polymer matrix. This homogeneous distribution can improve the overall properties of the material, eg. mechanical properties or thermal properties.

Increased Surface Area: Reducing the particle size increases the overall surface area. This can enable the Miswak to better interact and bond with the polymer, which can affect the overall properties and performance of the material. However, reducing the particle size too much can sometimes lead to undesirable results. For example, agglomeration of nanoscale particles can be a problem. This means that the particles clump together and form large clumps, which can negatively affect the material's properties. The Miswak powders used in this study were sieved at an average size of 10 microns.

3. Results and Discussion

Density values of composite samples containing PLA and Miswak fiber (MF) are given in Table 2. It is observed that there is an increase in the density of PLA-MF composites as the MF content increases. While the density of PLA sample is 1.240 g/cm³, the density of PLA-MF10 sample containing 10% MF is 1.255 g/cm³, the density of PLA-MF20 sample containing 20% MF is 1.283 g/cm³ and the density of PLA-MF30 sample containing 30% MF is 1.308 g/cm³ has been determined. These results show that Miswak fiber increases the density of composites. Density increase can affect the physical properties of the composite material and can be an important factor in applications.

Table 2. Specifications of PLA-MF composite density

| Specimens | Density (g/cm ³) | Density increment, % |
|-----------|------------------------------|----------------------|
| PLA | 1.240 | — |
| PLA-MF10 | 1.255 | 1.21% |
| PLA-MF20 | 1.283 | 2.23% |
| PLA-MF30 | 1.308 | 5.48% |

The composition of natural fibers significantly affects the performance of composite materials. Current research shows that MF has a lower cellulose concentration compared to other natural fibers. However, it is stated that it is difficult to obtain pure cellulose because it is closely related to lignin and hemicellulose. MF has the highest hemicellulose content compared to other natural fibers and is characterized by hemicellulosic binding microfibrils that provide structural reinforcement. Lignin, on the other hand, acts as an adhesive between cells in the cell wall, maintaining the flexibility, properties and structure of the fiber.

3.1. Tensile Properties of PLA-MF Composites

The tensile test, commonly referred to as the tension test, is a crucial mechanical evaluation that assesses a material's resistance to forces trying to pull it apart. Initiated with a specific goal, this test establishes the material's reaction to uniaxial forces and fetches data on

properties like the ultimate tensile strength, yield strength, Young's modulus, and more. Preparing for the test involves using specimens often shaped like a dog-bone to ensure the highest stress occurs in the gauge section (Figure 2).

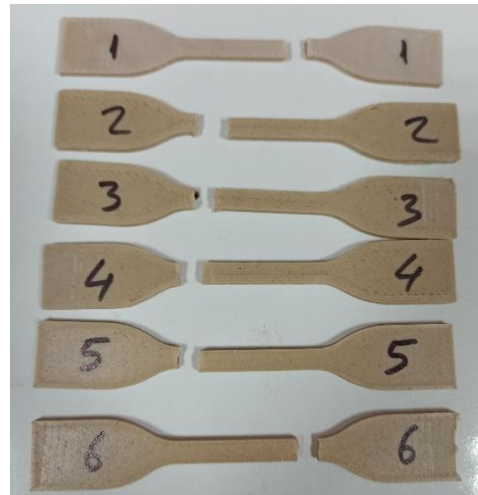


Figure 2. Tensile tested samples.

Anisotropic materials might necessitate specimens cut in varied orientations, such as longitudinal or transverse. The primary equipment used is the universal testing machine (UTM), which has a movable upper grip and a fixed lower one, ensuring the specimen is held firmly. As the test proceeds, the UTM exerts an increasing axial force on the specimen, with its elongation consistently monitored, often through an extensometer, until the sample fractures or reaches a set strain. The outcomes, typically showcased as a stress-strain curve, denote various material properties, including its elasticity, yield point, and UTS, along with its elongation that signifies ductility as a percentage increase from its initial size. The tensile properties of PLA samples with different MF contents are given in Table 3.

Table 3. The percentage of fiber content is detailed

| Specimen | σ (MPa) | E (MPa) | ϵ (%) |
|----------|----------------|---------|----------------|
| PLA/W0 | 58.48 | 2985 | 3.94 |
| PLA/W5 | 51.36 | 2940 | 3.12 |
| PLA/W10 | 44.24 | 2895 | 2.3 |
| PLA/W15 | 37.12 | 2850 | 1.48 |
| PLA/W20 | 30 | 2805 | 0.66 |

σ = tensile strength, E= young's modulus, ϵ = elongation at break

As the MF content of the samples increases, the tensile strength (σ) decreases. The PLA/W0 sample (0% MF) has the highest tensile strength, while the PLA/W20 sample (20% MF) has the lowest tensile strength. Similarly, the Young's modulus (E) value also decreases as the MF content increases. Elongation at break (ϵ) value decreases as the MF content increases. These results show that the addition of MF negatively affects the mechanical specifications of PLA composites (Figure 3).

That is, higher MF content reduces the toughness and flexibility of the samples. These findings suggest that MF

content should be considered to evaluate and optimize the effect of composite on performance.

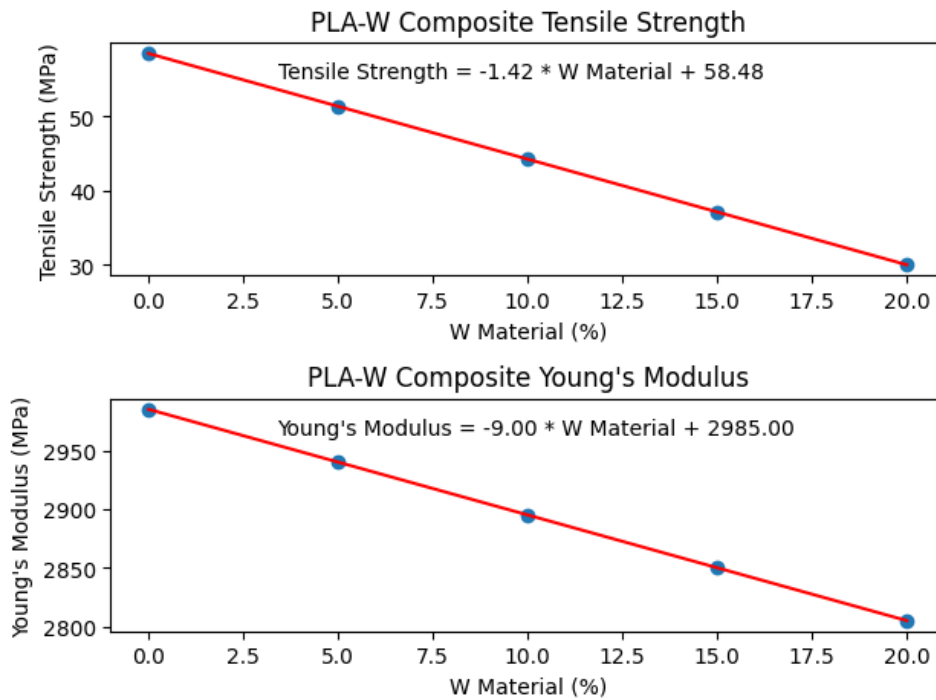


Figure 3. Tensile strength and the Young’s modulus of PLA-MF composites.

Miswak fiber contains extractants as well as components such as lignin, hemicellulose and cellulose. MF can be classified as a drought-resistant natural fiber obtained from *S. persica*, a tropical tree species. This fiber has a high hemicellulose content compared to other natural fibers and is characterized by hemicellulosic binder microfibrils that provide structural reinforcement. Lignin plays an important role in maintaining the flexibility, properties and structure of the fiber. MF, when combined with PLA polymer, affects the mechanical and thermal properties of the composite. The results presented in Table 3 show that PLA composites containing MF cause a decrease in tensile strength and E values. As the amount of MF increases, the strength properties of the composite material decrease. The reason for this can be shown as insufficient adhesion of the fibers with the matrix and the resulting voids. However, the addition of MF resulted in an increase in E values compared to polymers. In the design of fiber-reinforced composite materials, a solid connection at the fiber-matrix interface and minimizing gaps are important. In addition, it is seen that the

parameters used in the production process of the composite affect the fiber distribution and mechanical properties.

3.2. Flexural Specifications and Shore D Hardness of PLA-MF Composites

The bending properties of composite specimens are given in Table 4. With the increase of MF content in composite samples, flexural strength and flexural E values decrease. PLA/W0 sample has the highest flexural strength and E, while PLA/W20 sample has the lowest values. These results show that the bending performance of the composite decreases as the MF content increases. This may be due to poor adhesion and voids formed at the fiber-matrix interface. Insufficient wetting of the fibers can cause voids to form and reduce the mechanical specifications of the composite. Therefore, it is important to pay attention to factors such as fiber-matrix interaction and filler material distribution in order to improve the bending performance of composites containing MF (Figure 4).

Table 4. Flexural specifications of composite specimens

| Specimen | Flexural Strength (MPa) | Flexural Young's Modulus (GPa) |
|----------|-------------------------|--------------------------------|
| PLA/W0 | 89.15 | 3.35 |
| PLA/W5 | 78.81 | 3.25 |
| PLA/W10 | 68.47 | 3.15 |
| PLA/W15 | 58.13 | 3.05 |
| PLA/W20 | 47.79 | 2.95 |

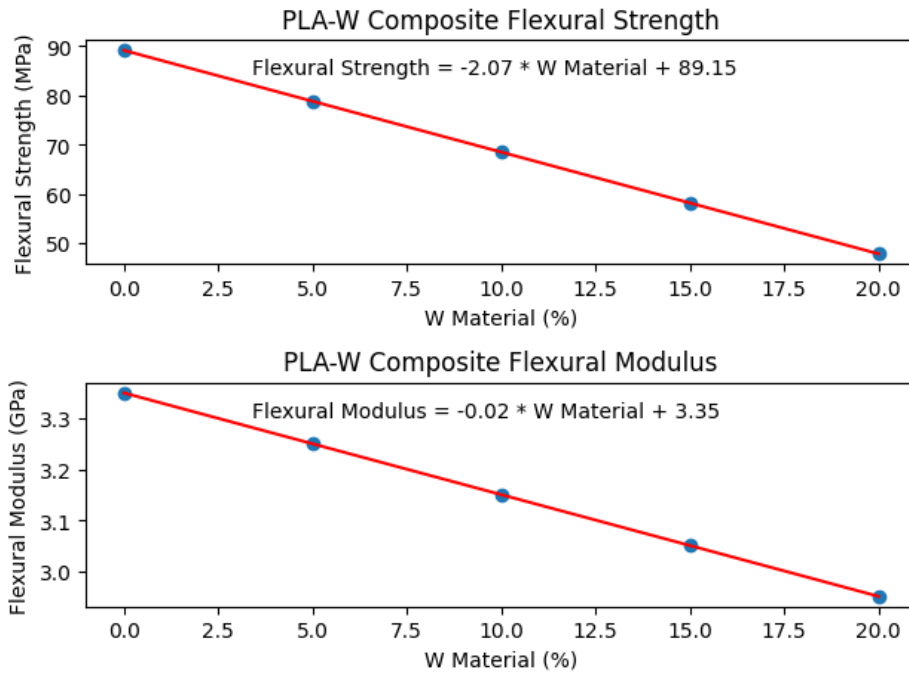


Figure 4. Flexural strength and the flexural modulus of PLA/-MF composites.

Bending properties of composite samples are given in Table 4. With the increase of MF content, flexural strength and flexural E values decrease. PLA/W0 sample has the highest flexural strength and E, while PLA/W20 sample has the lowest values. The results show that insufficient interfacial bonding in composites containing MF increases porosity and causes a decrease in properties. These results are also consistent with SEM findings in previous studies. In addition, changes in the flexural strength and modulus of different natural fiber reinforced PLA composites were observed in other studies in the literature (Diyana et al., 2022; Pérez, 2021). These studies show that attenuation at the fiber-matrix interface can reduce the stiffness of the composite. The Miswak-reinforced PLA composite exhibited a Shore D hardness value of 68.5 HD (Figure 5). This value signifies a comparison with pure PLA noticeable improvement over pure PLA.

The increase in hardness can be attributed to the inherent properties of Miswak fibers and their interaction with the PLA matrix. The adhesion between the Miswak fibers and the PLA matrix, as well as the dispersion of fibers within the matrix, play a pivotal role in determining the hardness. The observed Shore D hardness suggests that the Miswak fibers offer a promising avenue for improving the mechanical properties of PLA, especially for applications where enhanced hardness is beneficial.

3.3. Scanning Electron Microscope of PLA-MF Composites

Based on the data in Table 2, 3 and 4, the properties of MF reinforced PLA composites were evaluated. The SEM images shown in Figures 6.a and 6.b show the microstructure of samples with different proportions of MF. In the sample containing 10% MF (Figure 6.a), it was observed that there was no homogeneous bonding between the fibers and the matrix, and voids were formed. Factors such as production and processing conditions, fiber volume ratio, and fiber length can contribute to void formation in polymer composites. In addition, other variables such as matrix material and moisture content may also have an effect on void formation. The presence of MF disrupted the flow of molten resin, resulting in the formation of meso- and micro-voids. The irregularity of the air permeability of the MF caused the formation of more voids and weakened the matrix-fiber connection. These gaps can act as stress concentration points under loading conditions, leading to earlier failure of samples. These results are also consistent with the findings of previous studies (Chauhan et al. 2020; Bramantoro et al., 2018; Rafiqah et al., 2023).

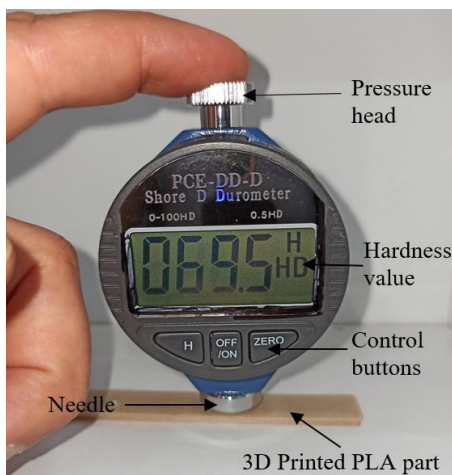


Figure 5. Shore D hardness measurement of Miswak reinforced PLA composite part.

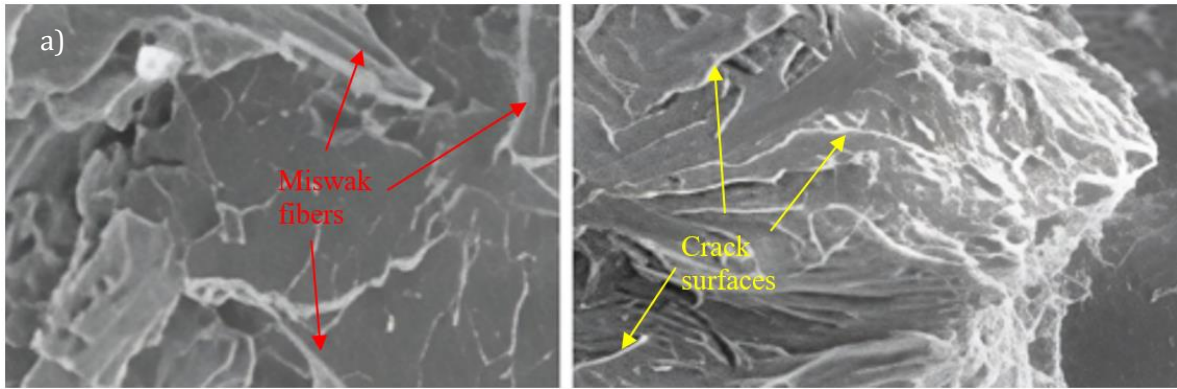


Figure 6. SEM micrograph of stretched surfaces of PLA-MF composites with different loading ratios. (a) shows the stretched surface of the PLA-MF10 10% wt sample at 100 times magnification, while (b) shows the PLA-MF20 stretched surface of the 20% wt sample.

On the other hand, the image in Figure 6.b shows the presence of voids indicating ineffective interfacial bonding between the hydrophilic matrix and the hydrophobic natural fiber. Also, incomplete fiber wetting can be observed due to poor matrix adhesion on the impurity-rich fiber surface. This results in complete separation of the matrix from the fibers under the applied tensile forces. Examination of Figure 6.b reveals that a fiber breakage and fiber drawing scenario can be seen. Microscopic examinations show composite fracture caused by fiber-fiber interactions within the matrix. This observation is in line with previous studies (Nur Diyana et al., 2022; Rafiqah et al., 2023; Savaş, 2019; Chaaben et al., 2022). Based on these analyses, polylactic acid/Miswak fiber (PLA-MF) composites are likely to exhibit low mechanical specifications due to factors such as inappropriate fiber use, weak fiber-matrix interactions, and matrix separation. Nur Diyana et al. (2022) studied the chemical, physical and mechanical specifications of MF to investigate the use of MF as a potential supplement for toothbrush materials (Nur Diyana et al., 2022). Researchers fabricated MF reinforced composites at different weight percentages (0%, 10%, 20%, and 30%) in a PLA matrix and performed various tests. Chemical analyzes revealed a high content of cellulose in MF. This can be considered as a feature that can facilitate the equal transfer of the stress load between the fiber and the matrix. However, it has been observed that the low cellulosic content in MF negatively affects the interfacial bond between fiber and matrix. When the physical properties were examined, it was observed that the density increased as the fiber content increased. This result indicates that MF may be suitable for applications such as toothbrush handles. SEM analysis revealed that voids in composites contribute to the reduction in mechanical properties. Mechanical test results showed that the proposed material performed comparable to commercially used materials. The thermal analysis results showed that the composite material has a similar melting point with pure PLA, which means that both materials have similar processing temperatures.

Dynamic mechanical analysis (DMA) results revealed that PLA-MF 30 composite has a higher storage modulus (2062 MPa) and a lower $\tan \delta$ value (0.6) compared to other PLA-MF composites. These results show the effects of pretreatments and/or adapters. In conclusion, the study of Diyana et al. revealed the potential of using MF as a supplement in toothbrush materials. The chemical and physical properties of MF affect the mechanical specifications of composites. The results show that the proposed composite exhibits similar performance to commercially used materials and may be a viable option for toothbrush materials. The study by Rafiqah et al. (2023) investigates the mechanical and thermal properties of alkali-treated MF and PLA composites. The study addresses the difficulty of the hydrophilic nature of Miswak fiber, which complicates its interaction with the hydrophobic PLA matrix (Rafiqah et al., 2023). The composites were treated with different concentrations of sodium hydroxide (NaOH): 1%, 2% and 3% by weight. The characterization of the composites was carried out using methods such as Fourier Transform Infrared Spectroscopy (FTIR), tensile testing, thermogravimetric analysis (TGA), DMA and SEM. The results show that the alkali treatment did not significantly improve the interfacial bonding, which is supported by the uneven tensile strength data. However, it was observed that the treated fiber surface showed an increase in the tensile strength of PLA composites reinforced with Miswak fiber. Tensile strength increased by 18.01%, 6.48% and 14.50% in composites treated with 1%, 2% and 3% wt NaOH concentrations, respectively. A slight increase in tensile modulus (0.7%) was observed in only 2% wt of processed fiber, whereas at 1% wt and 3% wt NaOH concentrations the modulus decreased by 4.15% and 19.7%. TGA for thermal stability analysis showed that alkali-treated fiber composites showed a slight improvement in thermal stability, especially at elevated temperatures. The DMA results reveal that surface-treated composites show higher storage modulus, especially for PLA reinforced with 2%wt alkali-treated MF. This suggests that alkaline treatment is effective. In

summary, the work of Rafiqah et al. highlights the influence on the mechanical and thermal properties of alkali-treated reinforced Miswak fiber and PLA composites. The findings reveal improvements in tensile strength and thermal stability with the treated fiber surface, but indicate that further improvements are needed in interfacial bonding. The study conducted by Savaş (2018) focuses on investigating the structural, mechanical, and tribological properties of Miswak powder reinforced polypropylene (PP) composites (Savaş, 2019). The composites were prepared using a PP matrix and a maleic anhydride-grafted PP (PP/g/MA) copolymer as a coupling agent. Different concentrations of Miswak powder (5, 10, 20, and 30 wt%) were incorporated into the composites. Various characterization techniques were employed to evaluate the properties of the composites. Tensile and flexural tests were performed to assess the mechanical behavior, DMA was conducted to examine the viscoelastic properties, X-ray diffraction was used to analyze the crystalline structure, SEM allowed for microstructural analysis, a goniometer measured the contact angles and surface energy, water uptake tests evaluated the moisture absorption capacity, and a ball-on-disc test assessed the tribological performance of the composites. The results indicate that the addition of Miswak powder at different concentrations positively influenced the properties of the composites. Particularly, composites with lower Miswak concentrations (5% and 10%) exhibited improved mechanical and tribological properties while maintaining good surface integrity. The 5% Miswak reinforcement showed promising performance even under wet conditions, making it suitable for potential applications in medical parts. In summary, the study highlights the potential of Miswak powder reinforced PP composites by demonstrating their enhanced structural, mechanical, and tribological properties. The findings suggest that composites with lower Miswak concentrations can fulfill the requirements for effective adhesion, high surface energy, and desirable mechanical and tribological performance. This research opens up possibilities for utilizing Miswak-reinforced composites in various applications, including medical parts. The study conducted by Rihem Chaaben et al. (2020) focuses on the development of a novel biocomposite for dental materials by incorporating Miswak powders into poly (methyl methacrylate) (PMMA) resin (Chaaben et al., 2022). The use of Miswak has been investigated to improve the bioactive properties of dental restoration materials. Material characterization was performed on both the individual components and the developed biocomposite, which contained 30 wt% of *S. persica*. X-ray diffraction, FTIR, differential scanning calorimetry, and high-performance liquid chromatography techniques were employed to analyze and characterize the materials. The results revealed the presence of organic chemical compounds from Miswak that are responsible for biological activities, as well as

mineral chemical compounds that are beneficial for dental applications and oral health. The absence of toxic residual monomers was also confirmed, ensuring the safety of the developed composite. Furthermore, the composite demonstrated antioxidant activities, as evidenced by its total polyphenol flavonoid content. The study also demonstrated the antibacterial activity of both Miswak and the composite material. In summary, this study introduces a novel biocomposite by incorporating Miswak powders into PMMA resin for dental applications. The characterization results confirm the presence of bioactive organic and mineral compounds, the absence of toxic residual monomers, and the antioxidant and antibacterial activities of the composite material.

The present study investigated the mechanical performance of Miswak reinforced PLA matrix composites for 3D printing applications. The incorporation of Miswak powder at different weight concentrations (5%, 10%, 15%, and 20%) was explored, and PLA/g/MA was used as a compatibilizer to improve the compatibility between the filler and matrix. The results obtained from the tensile and flexural testing demonstrated that the addition of Miswak powder positively influenced the mechanical specifications of the PLA composites. Specifically, the composite with 5% Miswak concentration exhibited excellent interlayer adhesion and high mechanical strength. This enhancement can be attributed to several factors. First, Miswak powder contains natural fibers rich in cellulose, which can effectively transfer stress from the matrix to the reinforcement, thereby improving the load-bearing capability of the composite. Additionally, the use of PLA/g/MA as a compatibilizer promoted better adhesion between the Miswak powder and PLA matrix, leading to improved mechanical performance. SEM analysis provided insights into the microstructure of the composites. The images revealed a homogeneous distribution of Miswak powder within the PLA matrix, indicating good dispersion and interfacial bonding. Furthermore, the presence of Miswak powder helped to reduce the formation of voids and microcracks, contributing to enhanced mechanical properties. The findings of this study suggest that Miswak powder has significant potential as a reinforcing material for PLA composites in 3D printing applications. The improved mechanical properties, including increased strength and interlayer adhesion, indicate the suitability of these composites for load-bearing applications. Moreover, the antimicrobial properties associated with Miswak powder provide additional benefits, making these composites suitable for applications requiring antimicrobial characteristics. The utilization of natural fillers like Miswak powder in PLA composites offers a sustainable and eco-friendly alternative to conventional plastic materials. By incorporating Miswak powder, the environmental impact can be reduced while maintaining or even enhancing the performance of the composites. In

conclusion, the present study successfully demonstrated the mechanical performance of Miswak reinforced PLA matrix composites for 3D printing applications. The findings indicate that Miswak powder can effectively improve the mechanical specifications of PLA composites, making them suitable for various practical applications.

Miswak powder was incorporated at varying concentrations. A significant finding was that the 5% Miswak concentration yielded excellent mechanical strength and adhesion. SEM images corroborated these findings, showing a homogeneous distribution of Miswak powder in the PLA matrix. This enhancement in properties is due to Miswak's rich cellulose content and the use of a compatibilizer. The composites could have potential applications in areas that require antimicrobial properties, presenting an eco-friendly alternative to conventional plastics. In essence, while Miswak fiber holds promise as a reinforcing material in various composites, challenges persist in terms of achieving consistent and strong interfacial bonding. The current study on 3D printing applications, however, reveals promising mechanical properties, especially at lower Miswak concentrations.

Figure 6's Scanning Electron Microscope (SEM) images shed light on the microstructural complexities of PLA-MF composites, serving as direct visual support for experimental conclusions. Figure 6.a, representing a sample with 10% MF, displays a conspicuous lack of uniform bonding, evident voids, and disrupted matrix continuity due to MF, suggesting potential production issues and the impact of fiber volume ratio. Figure 6.b accentuates the gaps hinting at poor interfacial bonding, possibly due to hydrophilic-hydrophobic disparities, incomplete fiber wetting implying impurity-driven adhesion issues, and discernible fiber breakage indicative of weaker interactions. Additionally, fiber-fiber interactions seem more prominent than fiber-matrix ones. These SEM revelations underscore concerns about PLA-MF composites' mechanical performance, emphasizing the significance of optimal fiber dispersion, adhesion, and bonding. Improved production and processing could lead to enhanced mechanical properties, broadening their application potential.

4. Conclusion

In this study, the mechanical performance of Miswak reinforced polylactic acid (PLA) matrix composites was investigated. The results shed light on the potential use of Miswak powder as a natural filler in PLA composites for 3D printing applications. The following conclusions can be drawn from the study:

- i.) Miswak powder, obtained from the Miswak tree, contains lignin, hemicellulose, cellulose, and other organic compounds. It has a high hemicellulose content compared to other natural fibers, which provides structural reinforcement to the composite.
- ii.) The addition of Miswak fiber to PLA composites

affects their mechanical properties. As the Miswak fiber content increases, there is a decrease in tensile strength, E, flexural strength, and flexural E values of the composites.

- iii.) The decrease in mechanical specifications can be attributed to insufficient adhesion between the fibers and the matrix, resulting in the formation of voids. The presence of voids acts as stress concentration points, leading to earlier failure of the composites.
- iv.) Despite the decrease in mechanical properties, Miswak powder offers additional antimicrobial benefits to the PLA composites, making them potentially useful for applications requiring antimicrobial properties.
- v.) The density of PLA/Miswak composites increases with increasing Miswak fiber content. This density increment can affect the physical properties of the composites.
- vi.) The morphology analysis using SEM revealed the presence of voids and ineffective interfacial bonding between the matrix and the Miswak fibers, further confirming the mechanical performance of the composites.

The results highlight the importance of optimizing the fiber-matrix interaction and filler material distribution in order to improve the mechanical specifications of Miswak reinforced PLA composites. The findings of this study contribute to the development of sustainable and environmentally friendly materials by utilizing natural fillers such as Miswak powder. Further research and experimental analysis are required to better understand the effects of Miswak fiber on composite performance and to optimize the manufacturing processes for enhanced mechanical specifications.

Limitation and Future Works

By addressing the following limitations and the suggested future works, researchers can further advance the knowledge and application of Miswak reinforced PLA composites, paving the way for sustainable and high-performance materials in various industries.

Limitations:

Limited research: The research in this specific area is limited, indicating a gap in the existing literature. Further studies are needed to explore other aspects such as the printability, dimensional stability, and surface quality of these composites in the context of 3D printing.

Optimal Miswak concentration: The present study investigates Miswak powder concentrations at different weight percentages. However, the optimal concentration for achieving the best mechanical specifications and other desirable characteristics of the composites is yet to be determined. Further research is required to identify the ideal Miswak concentration that balances mechanical performance, printability, and other relevant factors.

Future works:

Printability assessment: Evaluating the printability of

Miswak reinforced PLA composites is an important aspect for their application in 3D printing. Future research should focus on assessing the printability parameters, such as extrudability, adhesion between layers, and dimensional accuracy, to ensure successful and reliable printing of the composites.

Optimization of processing parameters: Investigating the effect of processing parameters, temperature, nozzle size, and printing speed, on the mechanical specifications and overall performance of Miswak reinforced PLA composites is crucial. Optimizing these parameters can help achieve enhanced mechanical specifications and better compatibility between the Miswak filler and PLA matrix.

Characterization of functional properties: In addition to mechanical properties, future studies should explore the functional properties of Miswak reinforced PLA composites, such as antimicrobial activity and biocompatibility. Understanding these properties will broaden the potential applications of these composites, particularly in the field of dental materials and other biomedical applications.

Long-term durability assessment: Assessing the long-term durability and stability of Miswak reinforced PLA composites is essential to ensure their reliability and suitability for real-world applications. Investigating the effects of environmental factors, aging, and repeated loading on the mechanical performance and structural integrity of these composites will provide valuable insights for their practical use.

Comparative studies: Conducting comparative studies with other reinforcement materials, such as synthetic fibers or nanoparticles, can provide a better understanding of the advantages and limitations of Miswak reinforced PLA composites. Comparative analyses will aid in determining the unique properties and potential niche applications of Miswak-based composites in the realm of 3D printing and beyond.

Author Contributions

The percentage of the author(s) contributions is presented below. All authors reviewed and approved the final version of the manuscript.

| | F.K. | A.K. |
|-----|------|------|
| C | 60 | 40 |
| D | 100 | |
| S | | 100 |
| DCP | 70 | 30 |
| DAI | | 100 |
| L | 50 | 50 |
| W | 70 | 30 |
| CR | 40 | 60 |
| SR | 100 | |
| PM | 80 | 20 |
| F | 100 | |

C=Concept, D= design, S= supervision, DCP= data collection and/or processing, DAI= data analysis and/or interpretation, L= literature search, W= writing, CR= critical review, SR= submission and revision, PM= project management, FA= funding acquisition.

Conflict of Interest

There is no conflict of interest. The funders had no role in the design of the study; in the collection, analyses, or interpretation of data; in the writing of the manuscript, or in the decision to publish the results.

Ethical Consideration

Ethics committee approval was not required for this study because of there was no study on animals or humans. The authors confirm that the ethical policies of the journal, as noted on the journal's author guidelines page, have been adhered to.

Acknowledgments

We would like to thank Kastamonu University Scientific Research Coordinatorship for supporting this study with project number KÜBAP-01/2022-38.

References

- Açıkbaş, G. 2022. Miswak, borik asit ve porselen atığı takviyeli polyester matrisli kompozitler. *El-Cezeri*, 9(1): 335-349.
- Almas K. 2002. The effect of *salvadora persica* extract (miswak) and chlorhexidine gluconate on human dentin: A SEM study. *J Contemporary Dental Practice*, 3(3): 27-35.
- Avérous L. 2008. Polylactic acid: Synthesis, properties, and applications. *Monomers, Polymers Composit Renew Resourc*, 2008: 433-450.
- Baeshen HA, Lingawi MM, Bajonaid AM, Al-Malik MI. 2017. Oral hygiene habits among Saudi Arabian infants and toddlers in Riyadh city. *J Clinical Pediatric Dentistry*, 41(4): 301-305.
- Bramantoro T, Bramantoro T, Primasari S, Tondas AE, Putri MA. 2018. *Salvadora Persica* extract chewing stick: Physical and mechanical properties. *Indian J Dental Res*, 29(2): 151-156.
- Chaaben R, Taktak R, Mnif B, Guermazi N, Elleuch K. 2022.

- Innovative biocomposite development based on the incorporation of *Salvadora Persica* in acrylic resin for dental material. *J Thermoplastic Composite Mater*, 35(11): 1815-1831.
- Chauhan AS, Chauhan VS, Choudhury PK. 2020. Comparative evaluation of Miswak chewing stick (*Salvadora Persica*) and conventional toothbrush on oral hygiene status: A clinical study. *J Family Med Primary Care*, 9(2): 924-929.
- Dar-Odeh N, Alnazzawi A, Shayyab M, Abu-Hammad S. 2019. Oral health awareness and practices among university students in Jordan. *J Inter Soc Prevent Commun Dentistry*, 9(6): 595-602.
- Darout IA, Christy AA, Skaug N, Egeberg PK. 2000. Identification and quantification of some potentially antimicrobial anionic components in Miswak extract. *Ind J Pharmacol*, 32: 11-14.
- Dutta S, Shaikh, A. 2012. The active chemical constituent and biological activity of *Salvadora Persica* (Miwak). *Int J Curr Pharmaceut Rev Res*, 3(1): 1-14.
- Garlotta D. 2001. A Literature review of Poly(lactic acid). *J Polymers Environ*, 9(2): 63-84.
- Hassan EA, Hassan ML. 2019. Lignocellulosic fibers reinforced polylactic acid composites: a review. *Polymer Composit*, 40(S1): E62-E82.
- Khalaf HAR. 2013. Effect of siwak on certain mechanical properties of acrylic resin. *J Oral Res*, 1(1): 39-49.
- Nur Diyana AF, Khalina A, Sapuan MS, Lee CH, Aisyah HA, Nurazzi MN, Ayu RS. 2022. Physical, mechanical, and thermal properties and characterization of natural fiber composites reinforced poly (lactic acid): Miswak (*Salvadora Persica* L.) fibers. *Inter J Polymer Sci*, 2022: 273.
- Olewi JK, Salih SI, Fadhil HS. 2017. Effect of siwak and bamboo fibers on tensile properties of self-cure acrylic resin used for denture applications. *J Mater Sci Engin*, 6(5): 1-6.
- Pérez, E. 2021. Mechanical performance of in vitro degraded polylactic acid/hydroxyapatite composites. *J Mater Sci*, 56: 19915-19935.
- Rafiqah SA, Diyana AN, Abdan K, Sapuan SM. 2023. Effect of alkaline treatment on mechanical and thermal properties of miswak (*Salvadora Persica*) fiber-reinforced polylactic acid. *Polymers*, 15(9): 2228.
- Rujitanaroj PO, Petchwattana N, Rujitanaroj P. 2015. Advances in packaging materials: perspectives on polylactic acid (PLA) and derived nanocomposites. *AIMS Mater Sci*, 2(4): 418-428.
- Savaş S. 2019. Structural properties and mechanical performance of *Salvadora Persica* L. (Miwak) reinforced polypropylene composites. *Polymer Composit*, 40(S1): E663-E677.
- Savaş S., 2018. Misvak'ın Abrazif Aşınma Özellikleri ve Diş Hekimliği Protez Kaide Malzemelerinde Takviye Fazı Olarak Kullanımı. *Afyon Kocatepe Üniv Fen Müh Bilim Derg*, 18(3): 1043-1057.
- Sher H, Al-Yemeni MN, Masrahi YS, Shah AH. 2010. Ethnomedicinal and ethnoecological evaluation of *Salvadora Persica* L.: A threatened medicinal plant in Arabian Peninsula. *J Med Plants Res*, 4(12): 1209-1215.
- Winarni DI, Rakhmawati RA, Wibowo A, Soeroso Y. 2019. Efficacy of Miswak extract mouthwash on dental plaque and gingival inflammation. *Pesquisa Brasileira em Odontoped Clínica Integr*, 19(1): 1-7.
- Zhang Y, Jiang L. 2018. Advances in the development of PLA composites: a review. *J Mater Sci*, 53(15): 8109-8131.



THE ANGULAR USE OF LIGHT IN ARCHITECTURE AND THE CONCEPT OF SPACE

Mehmet Sait CENGİZ^{1*}


¹Bitlis Eren University, 13000, Bitlis, Türkiye

Abstract: In this study, the analysis of the understanding of space under the influence of light was made. The content of the study touched on the effect of light and space on human perception, both architecturally and computationally. The identity that the light adds to the space, the interaction of the material with the light, and the illusory properties of the light are explained. While examining these abstract concepts, the illumination area of the light was calculated with a computational application. The fact that light is one of the most effective elements used in space has revealed the necessity of designing form, material, and lighting together. It is understood that the effect of basic elements that make up space, such as form and material color, can be increased with angular lighting. It has been understood that if a textured surface is illuminated with a directional light, the visual effect of the surface will increase. However, it has been understood that a material with a smooth structure and a material with a rough structure cannot be illuminated with the same lighting method, and this visual effect will create negativity. For original lighting designs, it is necessary to make accented or homogeneous lighting according to the need, and it is possible to provide this with designed-planned lighting.

Keywords: Architectural lighting, Artificial lighting, Daylight, Lighting engineering

*Corresponding author: Bitlis Eren University, 13000, Bitlis, Türkiye

E mail: mesace@gmail.com (M. S. CENGİZ)

Mehmet Sait CENGİZ  <https://orcid.org/0000-0003-3029-3388>

Received: August 19, 2023

Accepted: September 18, 2023

Published: October 01, 2023

Cite as: Cengiz MS. 2023. The angular use of light in architecture and the concept of space. BSJ Eng Sci, 6(4): 469-476.

1. Introduction

People look at the world from the perspective of their cultural repertoire. Thus, it distinguishes the inner space from the outer space, and the light from the dark, and chooses its boundaries. Human first considers visual stimuli in their relationship with their environment, and these visual stimuli contribute to the person's recognition of their location, boundaries, and all other features. As a result, the person perceives the space or the object with the help of these physical and visual elements. How the space or object is perceived by the users and then the reactions to the space or object are related to how the space is visually presented to the user. Space is a suitable space for people to continue their activities by separating them from the physical environment in which they live at a certain rate. The materials with different properties and the lighting design used by the function and aesthetics of the space on all surfaces of the space are among the most important factors that make the space different from other spaces (Göler, 2009; Turgay and Altuncu, 2011; Esen et al., 2020). Surfaces play an essential role in spaces where a large part of human life passes. The surfaces, which have the characteristics of the materials used in its construction, make the space comfortable and give that space an identity. It is the material of the surface that provides the shape of a surface and gives its texture and color. It is the visual characteristics of the materials

used on the surfaces, such as the form, texture, and color that give the space its identity. Light is also accepted as a building material like concrete or steel materials in space design. Despite the need for all materials that provide the physical definition of space, light is distinguished from other building materials with a feature it has, because light gains its physical existence only if it is seen by the human eye. The ability of the eye to see the light occurs as a result of the contact of the light with a surface (Göler, 2009; Innes, 2012; Cengiz and Cengiz, 2018; Çağal, 2020; Duman et al., 2023). Thus, it is understood that there is an inevitable relationship between surfaces and light. In the 1st picture the light was applied from the top and in the 2nd picture the light was applied from the bottom. In Figure 1, the same shape creates the perception that the pictures are different with the effect of light in different directions.

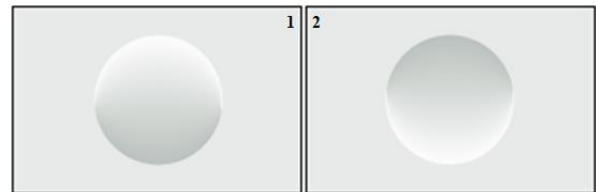


Figure 1. Light effect of the same shape in a different direction (Ganslandt and Hoffman, 1992).

Just as the form, texture, and color of surfaces can be seen by users, depending on the presence of light, light



finds value and is shaped in space only as a result of its relationship with surfaces. In space design, successful results can be obtained if the mutual relationship between the surfaces that make up the space and the light is correctly established. This situation highlights the need for lighting design in space design. In architectural lighting design, lighting design principles should be followed. Knowing the material properties of the surfaces in the space in terms of light (such as reflection or absorption) plays an active role in achieving the purpose of the design. A successful lighting design increases the functionality, reliability, and aesthetic value of the space.

2. Interaction of Visuality and Light

Spaces gain an identity as a result of the combination of human perception ability with light. Because most of the spaces designed with the right lighting are not the spaces seen with the designed light unless there is light. In the absence of light, the colors and forms of the materials in the space lose all their impressiveness. It is possible to design in a wide variety of spaces, from provocative effects to creating a religious environment with light. With the shadow effect created by the light, visual effects such as size changes and expression differences can be obtained in three-dimensional forms. The interaction between light and surfaces visually defines the material properties of the objects and surfaces that make up the space. Light appears as a result of contact with a surface

that will reflect or transmit it. Surfaces have some form, texture, and reflective properties depending on their visual structure. The surfaces can be in various textures such as patterned, matte, glossy, rough, and smooth. In addition, there are various shape features such as concave, convex, pointed, oval, bumpy, and flat. All these visual features are directly effective in the way surfaces reflect light (Unver, 1985; Turgay and Altuncu, 2011; Yumurtaci, 2013; Esen, 2020). A simple change in the wall covering of a space or the addition of a mirror or a polished painting can dramatically change the illuminated appearance of a space. If it is effective on the visibility of the materials with its features such as the visual properties of the surfaces have a great effect on the lighting of the space due to light. From this point of view, it is possible to say that light is a design element that has a passive structure as well as an active one. Although lighting is included in the building after the formation of form and material in space designs, it is an element designed together with other elements beforehand. The fact that light is one of the most effective elements used in the interior reveals the necessity of designing form, material, and lighting together. The effect of the designed lighting on the basic elements that make up the space, such as form and material color, shows how important lighting is. The use of lighting in different designs in the space is seen in Figure 2.

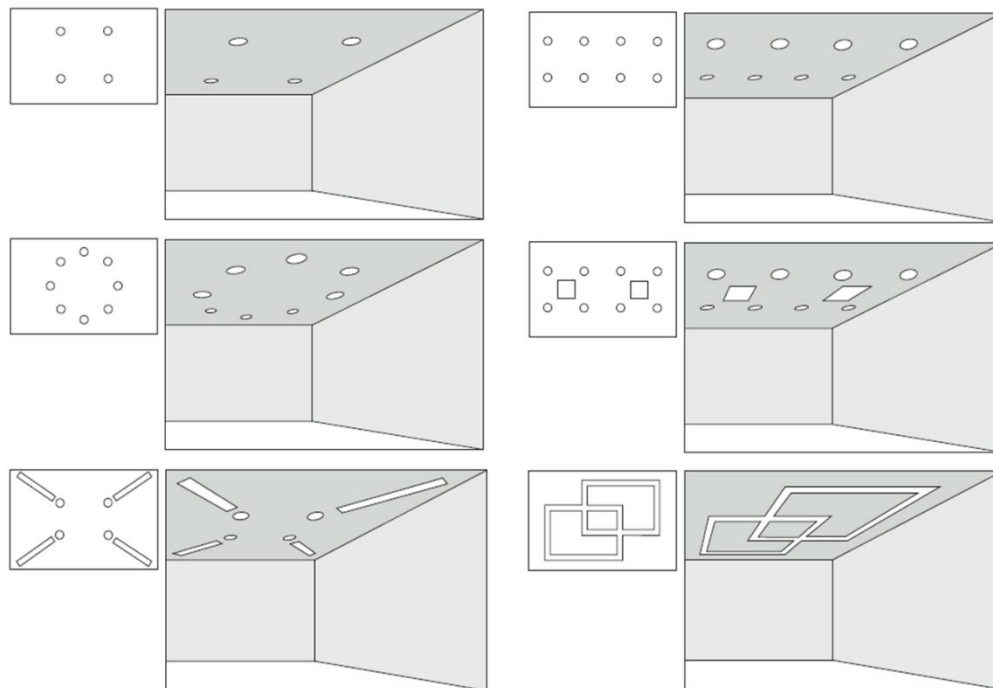


Figure 2. The use of lighting in different designs in the space (Ganslandt and Hoffman, 1992).

2.1. Formalism and Light Influence

Light is an indispensable element in the design of space in terms of facilitating our acquisition of knowledge of the forms around us. The use of light in three different ways directional, diffuse, and dominant direction determines the visibility of the form, its quality, and the

structure of the shadows. In Figure 3, the effects on the shape and shadow structure as a result of the application of light on a shape in different directions are seen. Directed light (left column) produces distinctive shadows and strong effects. The form is emphasized while the details on the surface are hidden by the shadow.

Dominant lighting (middle column) creates soft shadows. The shape is recognizable and there are no disturbing shadows. Diffused lighting (right column) almost does not create shadows but does not sufficiently introduce the form. In Figure 3, some forms and surface structures can be seen at different lighting angles.

Sometimes, it is desired that the shape of a wall or any object that makes up the space is unimportant, creates an uncomfortable image, or is imperfect so that it cannot be noticed by users (Göler, 2009; Çağal, 2020). In such a case, it shows that it would be beneficial to use diffused lighting as needed. Conversely, when the shape is expected to attract extra attention by creating sharp shadows, the emphasis on form can be increased by applying directional lighting. It is necessary to ensure the

harmony between the number and location of the light sources to be used, the direction and direction of the light is applied. Otherwise, light effects that are incompatible with the form will occur. For example, Figure 4 shows the wall surface with curvilinear shape and texture. For this wall lighting, angled lighting suitable for the purpose is used. In the first angle lighting, the light angle was applied as 62%. In the second-angle wall lighting, the light angle was applied to 75%, creating a targeted space perception. In this way, the shape of the wall draws extra attention by creating sharp shadows with angled lighting in Figure 4, and the emphasis on form is increased by applying directional lighting. Figure 4 shows examples of angled lighting suitable for the purpose.

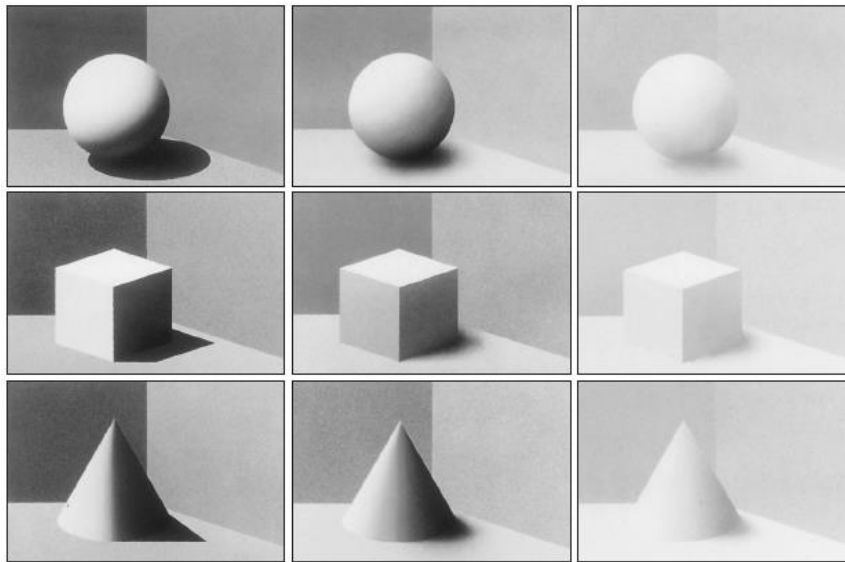


Figure 3. Some forms and surface structures at different lighting angles (Ganslandt and Hoffman, 1992).



Figure 4. Examples of purpose-built angled lighting.

Incorrect positioning of the fixture to the wall shape will cause the surface to be perceived incorrectly. Again, just like wall lighting, the correct and incorrectly positioned angular lighting in the painting lighting in a museum serves the purpose or causes a bad appearance to be perceived by deviating from its main purpose. Figure 5 shows the correct and incorrect positioning of the angular lighting (Ganslandt and Hoffman, 1992).

2.2. Surface Texture and Lighting Effect

The texture features of the surfaces are one of the most important elements that affect the perceived size of the space and determine its volumetric expression. It affects the spatial width estimation, such as the perception of surfaces as far or near the user in line with the user's perspective.

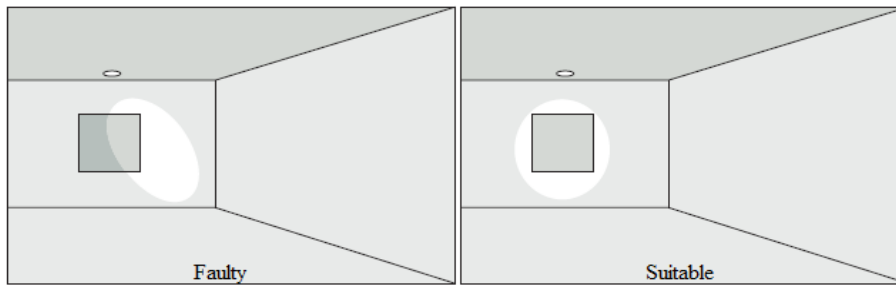


Figure 5. Correct and incorrect positioning of angular lighting.

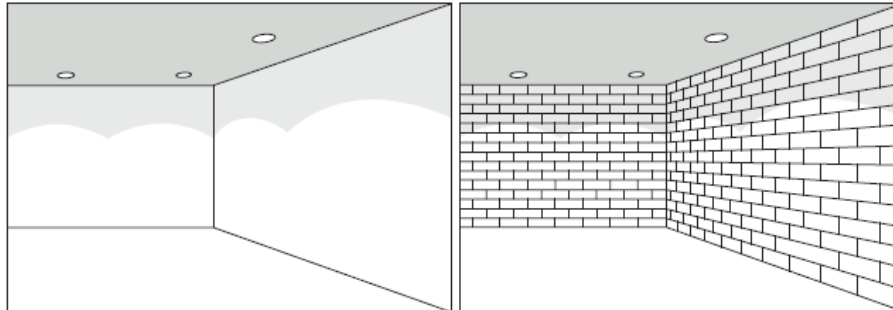


Figure 6. Light effect on the plastered and unplastered wall surface.

The most important reason why texture has such an effect on the perception of space is its interaction with light. It is possible to convey the effect desired to be created in the space with the texture used, to the user, with the help of artificial light, which makes the texture visible and increases its impressiveness with its features such as type, color, direction, and location. Light has properties such as making a soft texture look like a hard texture or creating shadow plays on the surface. Not applying the appropriate lighting solution only to the surface texture causes the visual effect of the space to decrease. If the relationship between texture and light is established incorrectly, unwanted images will occur and the perception of space will change. It is seen that two different types of luminaires are used as linear and spotlighting in Figure 4. With the linear luminaire, the light first touches the ceiling and then the textured surface. With spot luminaires, the light is transmitted on the surface in a directional manner and at an angle of 45 degrees. Two different effects are seen on the surface as a result of the change in the position, direction, and direction of the light. As a result, it should be decided what the desired effect is and accordingly, the type of luminaire, its location, etc. should be determined and selected.

Illuminating a textured surface with a directional light increases the visual effect of the surface. On a surface illuminated by a diffused light, the applied light reduces the visual effect of the texture and even obscures the three-dimensional feature. Diffused light prevents the texture effect from reaching the user, causing the space to be monotonous and unemotional. A surface texture illuminated by a point light source directionally may appear different from its real state because the textural details on it are enlarged, creating harsh and sharp

shadows. In this application, the small size of the light source and the hard shadows formed accordingly create exaggerated images on some parts of the surface. Again, in directional lighting, small differences in the texture as a result of shadows and penumbras are difficult to distinguish as the size of the light source increases, but on the other hand, this soft shaded illumination provides the perceptibility of the concave-convexity of the surface and the three-dimensional structure of the tissue. The angle of the directional light, on the other hand, affects the hardness of the tissue depending on the shadows it creates on the surface texture, causing its appearance to change. For example, if a directional light hits a textured surface at a right angle, shadow formation is very low, thus reducing the visual effect of the texture (Aytug, 1989; Kazanasmaz, 2003; Çagal, 2020). While the illumination distribution on an unplastered wall is the dominant feature, the same illumination distribution on a plastered-even wall is interpreted as the background. In Figure 6, a light effect can be seen on the plastered and unplastered wall surface (Ganslandt and Hoffman, 1992). Figure 7 shows the use of the light angle as a background or disturbing decor. A light distribution that is not compatible with the architectural structure of the space is perceived as disturbing patterns that have nothing to do with the space. The light angle determines whether the light is perceived as a background or as a disturbing shape.

2.3. Orientation of Light

The effective transmission of the light emanating from the light source to the desired location is the main issue of lighting. In addition, necessary precautions must be taken to prevent this light from creating glare. Materials with reflection, refraction, absorption, and diffusion properties are used to direct the light. Under normal

conditions, only a small amount of light falling on a surface is reflected. This reflectance rate depends on the type of surface, the angle of the light, and the spectral composition of the light. Depending on the surface type; It is classified as specular reflection (glossy surfaces such as aluminum and glass), diffuse reflection (matte and rough surfaces), and mixed reflection (glossy paper and

glazed ceramic surfaces) (Kazanasmaz, 2003; Sirel, 2007; Cengiz et al, 2015). In Figure 8, light reflection is seen according to the surface type. Figure 9 shows the refraction of light (absorption and reflection), that is, the passage of light between two surfaces of different intensities.

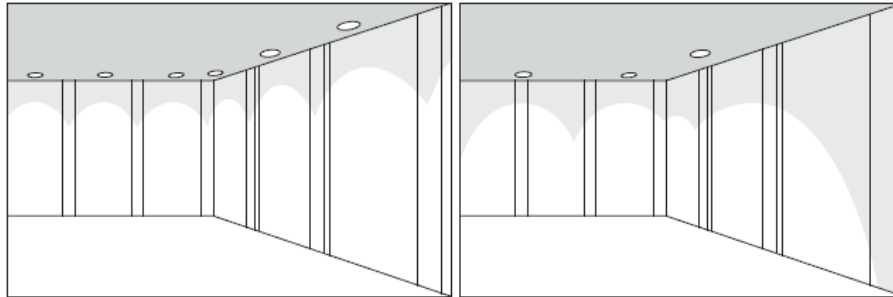


Figure 7. Use of light angle as background decor or disturbing décor.



Figure 8. Reflecting light by surface type.

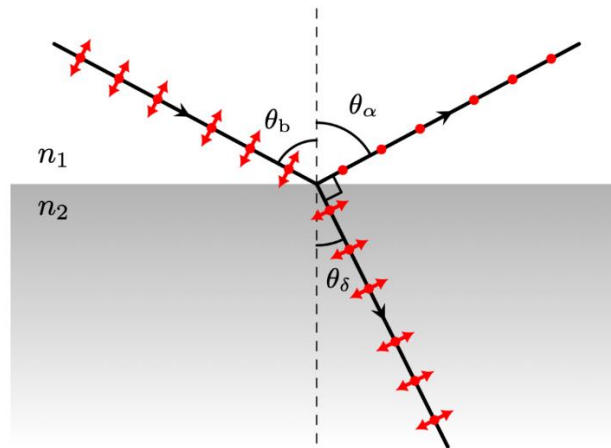


Figure 9. Refraction of light (absorption and reflection).

In lighting design, spaces, where highly reflective materials and colors are used, are illuminated more efficiently. These spaces are seen as wider and warmer than the spaces where low-reflective materials are used. For this reason, it is necessary to know the reflectivity of the material used before the lighting design is made in the space. Illumination of a surface with a bright texture on which fine works are worked on, with a directional light source will cause specular reflection on the surface, causing the image of the user and the light source to be reflected from the surface. As a result of this, it will cause the work to be invisible, make it difficult to perceive, glare, and therefore errors. Therefore, it is very important to pay attention to the way the surfaces reflect light in the space and to choose the light source on the surface characteristics and the function performed. If the surface of the material is not completely reflective or

permeable, some of the light is absorbed by the surface. The light disappears and turns into heat. The absorption of light makes an object dark relative to the wavelength of the incident radiation. Wood is opaque to visible light. Some materials are opaque to some frequencies of light but transparent to others. Glass is opaque to ultraviolet radiation below a certain wavelength, but transparent to visible light. The properties of the surfaces that make up the space increase or decrease the dispersion of the light coming from its source. Therefore, the relationship between surface materials and lighting elements is of great importance for a successful lighting design. The texture features of the surfaces can be emphasized or hidden by choosing and positioning the appropriate luminaires. With the use of a glossy surface, the form of glare can be controlled (Kazanasmaz, 2003; Şerefhanoglu, 2003; Sirel, 2007).

3. Space Design by Light Angle

Today, the increasing demand for original lighting design forces differentiated lighting designs to be produced. Differentiated lighting requires angular lighting designed to cope with specific lighting tasks. For example, to achieve angular lighting on a wall in a hall or exhibition space, or to highlight a single object, completely different angular lighting is needed. Today, the development of technical possibilities and lighting applications has led to a fruitful correlation. Advances in lamp technology and luminaire design continue to evolve to suit the specific applications required by lighting designers. New lighting developments have allowed spatial differentiation and more flexible lighting. From the place of open incandescent and fluorescent lamps to the illumination of large surfaces using wall ceilings or highlighting a defined area, the era of purposefully directing light to certain areas or objects has begun.

The expression that describes how a light source scatters light is called beam angle. The light angle is expressed in degrees, its symbol is ($^{\circ}$). Light sources can be classified as narrow-angle from 5 degrees to 45 degrees and wide-angle from 45 degrees to 120 degrees. In illumination, the light angle is calculated with the Full Width and Half Maximum management. Because at the point where the light is scattered, it is practically impossible to measure the light on both sides without limit. The angle specified as the light angle is the angle at which the light beam falls below 50 percent of its initial intensity. In another saying; the center of the light beam, that is, the point where the light intensity is highest (Şerefhanoglu, 2003; Kazanasmaz, 2003; Sirel, 2007; Turan et al., 2016). Then, it goes towards the beam up to half of this value in one direction. The angle of light is obtained by taking twice the angle found. In Figure 10, the view of the illumination area of the light angle is given.

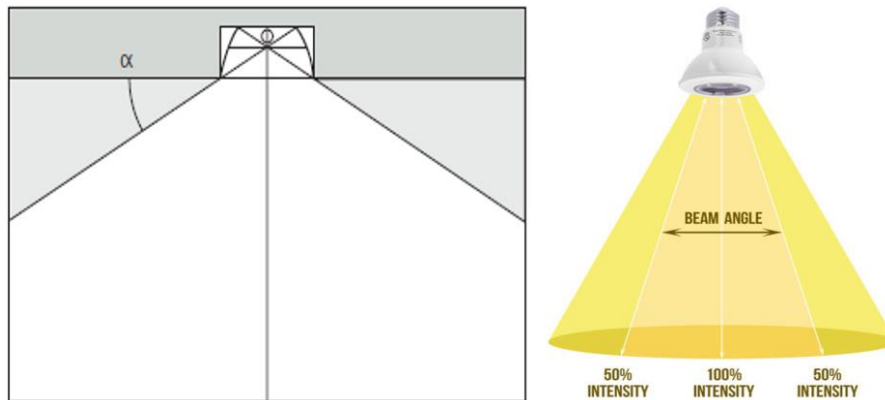


Figure 10. The view of the lighting area of the light angle.

The light angle is determined by the ceiling height indoors and by the height of the pole or mounting location outdoors. If the lighting element is to be placed at a high point, it should be narrow, and if it is to be positioned at a low point, it should be chosen with a wide angle. Lighting elements with a wide angle of light do not emit more light than light sources with a narrow angle. It just scatters the light more widely. When the light angle is narrowed, the luminous flux, that is, the lumen value, remains constant, but the luminous intensity that is, the candela value, increases. The light of wide-angle lighting elements cannot reach far points. For this reason, narrow-angle skylights are usually chosen when lighting from high points. For example, lighting elements in buildings with high ceiling heights generally emit light at a narrow angle. In interior lighting where the ceiling height is low, lighting elements with a wide light angle are used as much as possible. In this way, the formation of dark and very bright spots is prevented, and more homogeneous lighting is provided. As the ceiling height increases indoors, the illuminated surface becomes larger, that is, the light spreads over a wider area. However, in such a case, a decrease in the level of illumination is observed. LEDs, which are light sources, usually emit light at an angle of 120 degrees when no

optical material is used (Şerefhanoglu, 2003; Sirel, 2007; Kaynaklı et al., 2016; Efe and Varhan, 2020). However, in some LED types, such as Power LED, the optical material called primary optics may be located on the LED light source. In this way, the LED package itself can have a light angle of 30, 60, or 90 degrees. To use all these angled lighting sources, it is necessary to know the height of the space between the ceiling and the floor. In addition, the spot opening in the pan should be known. The ceiling spot opening directly affects the area of light falling on the surface. This variable should not be neglected in the calculation. According to this information, while the ceiling height is 5m and 10m, the light area illuminated on the floor surface is calculated in Table 1.

3. Results and Discussion

It is the light and material duo that responds to the many needs of the space, determines the character of the space, keeps the space alive, and surrounds the space. Light and material are two important and indispensable elements that have a great impact on the general appearance of the space, the feelings of the user, the perception of space, the experience of the space, and the interpretation of the space.

Table 1. Light angle and surface illumination areas by distance

| Distance between light - surface (m) | Light angle (°) | Minimum spotlight diameter (m) | Light field on the surface (m ²) |
|--------------------------------------|-----------------|--------------------------------|--|
| 5 | 15 | 1.32 | 1.37 |
| | 30 | 2.68 | 5.44 |
| | 45 | 4.14 | 13.45 |
| | 60 | 5.77 | 26.13 |
| | 75 | 7.67 | 46.18 |
| | 90 | 10.0 | 78.50 |
| 10 | 15 | 2.63 | 5.43 |
| | 30 | 5.36 | 22.55 |
| | 45 | 8.28 | 53.82 |
| | 60 | 11.55 | 104.72 |
| | 75 | 15.35 | 184.96 |
| | 90 | 20.0 | 314 |

Without the texture, color, and form in the material, every space would be the same. In other words, in the absence of light, spaces would be undefined and emotionless. In addition, if there was no light, the visual properties of the materials would not make any sense in the space. Therefore, the materials and the light that makes the materials visible strengthen the perception of space by emphasizing the texture, form, and color of the materials. Light and objects in space are not separate from each other, on the contrary, the light-space duo must take place in space as part of each other. In architectural design, it is important to choose the materials according to the function and concept of the space, as well as to illuminate each different building material by considering its characteristics. The appearance of each material in the face of light application varies. For this reason, material properties are effective in determining the color, direction, angle, and position of the light source to be located in the space. The fact that the light used changes the perception of space significantly as a result of its effect on the surface shape, color, direction, and quality of the shadows, reveals the necessity of constructing the relationship between material and light in the best way. In order not to cause unwanted images while creating this setup and to increase the efficiency to be obtained, lighting design by considering the visual comfort conditions ensures the most correct decision for the space and the most effective solution.

The use of various materials in the space and the combination of lighting design should nurture and strengthen the design of the space and make the design interesting. Material and light source properties should be compatible with each other to avoid random light effects. The principle that a material with a smooth structure and a material with a rough structure cannot be illuminated with the same lighting method should be followed. The color of the light should be chosen in harmony with the color of the surface for the material colors to look close to their color, suitable for the desired color and not to mislead the user. The color rendering of the selected artificial light should also be high.

5. Conclusion

The direction and angle of the light source create various shadow effects on the surface. Care should be taken to determine the effect desired to be created with a textured surface used in the space before the light application and to determine the direction and angle of the light source in this direction. Since light-colored surfaces reflect the light at a higher rate than dark-colored surfaces, in other words, they have more brightness, light-colored materials can be preferred more for energy saving in a place where a high level of illumination is desired. After the change in the form, texture, and color of the materials in the space designed with a certain lighting scheme, the level of illumination will also change. Because the light, which is a design element, will appear dimmer or brighter in terms of illuminance, depending on the color of the new materials. For this reason, the characteristics of the light source such as direction, color, and angle are also changing. Since different actions are carried out in the space, lighting the space with a single lighting scheme is a weakness in terms of light design. For this reason, lighting composition should be created with different lighting schemes such as general daylighting, (homogeneous) lighting, task lighting, accent lighting, or decorative lighting. Such need-oriented lighting will increase the functionality of the space and positively change the aesthetic appearance of the space.

Today, the increasing demand for original lighting design forces differentiated lighting designs to be produced. Differentiated lighting requires angular lighting designed to cope with specific lighting tasks. For example, completely different angular lighting is needed as it is used to achieve angular lighting on a wall in a hall or exhibition space or to highlight a single object. Today, the development of technical possibilities and lighting applications has led to a fruitful correlation. Advances in lamp technology and luminaire design continue to evolve to suit the specific applications required by lighting designers. New lighting developments have allowed spatial differentiation and more flexible lighting.

Author Contributions

The percentage of the author(s) contributions is presented below. All authors reviewed and approved the final version of the manuscript.

| | M.S.C. |
|-----|--------|
| C | 100 |
| D | 100 |
| S | 100 |
| DCP | 100 |
| DAI | 100 |
| L | 100 |
| W | 100 |
| CR | 100 |
| SR | 100 |
| PM | 100 |
| FA | 100 |

C=Concept, D= design, S= supervision, DCP= data collection and/or processing, DAI= data analysis and/or interpretation, L= literature search, W= writing, CR= critical review, SR= submission and revision, PM= project management, FA= funding acquisition.

Conflict of Interest

The author declared that there is no conflict of interest.

Ethical Consideration

Ethics committee approval was not required for this study because of there was no study on animals or humans.

References

- Aytuğ A. 1989. Görsel çevrenin oluşturulmasında doku ve aydınlatma ile ilişkisi. 2. Ulusal Ergonomi Kongresi, May 1989, Adana, Türkiye, pp: 422-431.
- Çağal Taşdelen D. 2020. Principles of lighting design and analysis of its importance in interior architectural design process through interior models with different functions. PhD Thesis, Mimar Sinan Güzel Sanatlar University, Istitute of Sciece, İstanbul, Türkiye, pp: 269.
- Cengiz MS, Cengiz C. 2018. Numerical analysis of tunnel lighting maintenance factor. *Int Isl U Malaysia IIUM Eng J*, 19: 154-163.
- Cengiz MS, Mamis MS, Akdag M, Cengiz C. 2015. A review of prices for photovoltaic systems. *Int J Tech Phy Prob Eng*, 7: 8-

13.

- Duman S, Özbay H, Çelik, Efe SB, İşen E. Duman B. 2023. Improvement of the fitness-distance balance-based supply-demand optimization algorithm for solving the combined heat and power economic dispatch problem. *Iranian J Sci Tech Transact Electr Eng*, 47(2): 513-548.
- Efe SB, Varhan D. 2020. Interior lighting of a historical building by using LED luminaires a case study of Fatih Paşa Mosque. *Light Eng*, 28: 77-83.
- Esen V, Sağlam Ş, Oral, B, Esen ÖC. 2020. Spectrum measurement of variable irradiance controlled LED-based solar simulator. *Int J Renew Energy Res*, 10(1): 109-116.
- Ganslandt R, Hofmann H. 1992. Handbook of lighting design. ERCO, Berlin, Germany, pp: 289.
- Göler S. 2009. Style, color, material, texture and light effects on the location of perception. MSc Thesis, Mimar Sinan Güzel Sanatlar University, Istitute of Sciece, İstanbul, Türkiye, pp: 236.
- Innes M. 2012. Lighting for interior Design. Laurence King Publishing Ltd., London, UK, pp: 192.
- Kaynaklı M, Palta O, Yurci Y, Cengiz Ç. 2016. Cooperation of conventional electric power grids and smart power grids. *J Elect Electron Eng*, 11: 23-27.
- Kazanasmaz T. 2003. Müzelerin aydınlatma tasarımı- ODTÜ Müzesi. EMO II. Ulusal Aydınlatma Sempozyumu, 8-10 Ekim, Diyarbakır, Türkiye.
- Şerefhanoglu Sözen M. 2003. Aydınlatma tasarımında mimarın ve elektrik mühendisinin rolü. EMO II. Ulusal Aydınlatma Sempozyumu, 8-10 Ekim, Diyarbakır, Türkiye.
- Sirel Ş. 2007. Aydınlatma tekniği seminer notları. URL: <http://www.sazisirel.com/yayinlar.html> (accessed date: July 14, 2023).
- Turan B, Eskikurt HI, Can MS. 2016. An application based on artificial neural network for determining viewpoint coordinates on a screen. *Elektronika Ir Elektrotechnika*, 22(2): 86-91.
- Turgay O. Altuncu D. 2011. İç mekanda kullanılan yapay aydınlatmanın kullanıcı açısından etkileri. *Çankaya Univ J Sci Eng*, 8: 167-181.
- Ünver R. 1985. Yapıların içinde ışık ve renk ilişkisi. PhD Thesis, Yıldız University, Istitute of Science, İstanbul, Türkiye, pp: 263.
- Yumurtacı R. 2013. Role of energy management in hybrid renewable energy systems case study based analysis considering varying seasonal conditions. *Turkish J Electr Eng Comp Sci*, 21(4): 1077-1091.



A PARALLEL ALGORITHM FOR DESIGNING PRIMER AND PROBE FOR ACCURATE DETECTION OF SEVERE ACUTE RESPIRATORY SYNDROME CORONAVIRUS

Hilal ARSLAN^{1*}, Rıza DURMAZ²

¹Ankara Yıldırım Beyazıt University, Faculty of Engineering and Natural Sciences, Department of Software Engineering, 06010, Ankara, Türkiye


²Ankara Yıldırım Beyazıt University, Faculty of Medicine, Department of Clinical Microbiology, 06010, Ankara, Türkiye


Abstract: The spread of the SARS-CoV-2 in many countries has led to multiple SARS-CoV-2 variants, and this makes accurate detection of SARS-CoV-2 difficult. The reverse transcription real-time polymerase chain reaction (RT-PCR) is a widely used gold-standard method to detect SARS-CoV-2, and accurate designing of primers and probes is crucial to prevent false negative results, especially with the rise of new dangerous variants. Therefore, it is significant to determine primers and probes targeting conserved regions in the genome sequence to diagnose many variants of SARS-CoV-2. In this paper, we propose a novel and efficient method for identifying PCR primers and probe sequences by evaluating sequences belonging to SARS-CoV-2 variant of concern and variants of interest. We propose 13 primer and probe sets by analyzing 54,524 sequences in Alpha variant, 25,465 sequences in Beta variant, 53,501 sequences in Gamma variant, 46,225 sequences in Delta variant, and 43,682 sequences in Omicron variant from GISAID. Furthermore, we analyzed 1,008 sequences in Lambda variant as well as 5,844 sequences in Mu variant to extract primer and probe sets from GISAID. The proposed primer and probe sets were validated in 406,757 new SARS-CoV-2 unique genomes collected from NCBI. In silico evaluation presented that the proposed set of primers and probes are found inside about 99% of SARS-CoV-2 genome sequences. Designed primers present a higher potential to detect the main SARS-CoV-2 recent variant of concerns and the variants of interests. The superiority of the proposed method is also highlighted by comparing the state-of-the-art PCR primer and probe sets based on the number of mismatches for various types of SARS-CoV-2 genomes.

Keywords: COVID-19, SARS-CoV-2, SARS-CoV-2 variants, Primer and Probe, Real Time PCR

*Corresponding author: Ankara Yıldırım Beyazıt University, Faculty of Engineering and Natural Sciences, Department of Software Engineering, 06010, Ankara, Türkiye

E mail: hilalararslaneng@gmail.com (H. ARSLAN)

Hilal ARSLAN  <https://orcid.org/0000-0002-6449-6952>

Rıza DURMAZ  <https://orcid.org/0000-0001-6561-778X>

Received: July 09, 2023

Accepted: September 26, 2023

Published: October 15, 2023

Cite as: Arslan H, Durmaz R. 2023. A parallel algorithm for designing primer and probe for accurate detection of severe acute respiratory syndrome coronavirus. *BSJ Eng Sci*, 6(4): 477-485.

1. Introduction

SARS-CoV-2 detected in 2019 caused a disease called COVID-19 by spreading rapidly around the world. The spread of the SARS-CoV-2 in many countries has led to multiple SARS-CoV-2 variants and accurate detection of SARS-CoV-2 variants is crucial to fight the COVID-19 pandemic. Recent dominant variants of SARS-CoV-2 are B.1.1.7 (Alpha), B.1.351 (Beta), P.1. (Gamma), B.1.617 (Delta), and B.1.1.529 (Omicron). Alpha variant (Volz et al., 2021) was first identified in the United Kingdom in the fall of 2020, and it spread ~ 50% more quickly than the original SARS-CoV-2 (Lauring and Malani, 2021). Although current treatments against the Alpha variant are effective, the Alpha variant may cause more severe COVID-19 disease (Yaniv et al., 2021). The Beta variant (Tegally et al., 2021) first detected in South Africa and the Gamma variant (Sabino et al., 2021) first detected in Brazil at the end of 2020 spread less quickly than the Alpha variant; however, current treatments against the Beta and Gamma variants are less effective. The Delta variant (Mlcochova et

al., 2021) first identified in India may cause more severe disease when compared to the other variants. Furthermore, the Delta variant spreads 100% more quickly than the original SARS-CoV-2 (Lauring and Malani, 2021). It is not adequate information on whether it causes more severe COVID-19 disease, or not. The Lambda variant (Baj et al., 2021) first identified in Peru in August 2020, and it was designated as the Lambda variant by the World Health Organization (WHO) in June 2021 (Wink et al., 2021). The Mu variant (Uriu et al., 2021) first identified in Colombia was designated as a variant of interest in August, 2021 by the WHO. It is not known whether the Lambda and Mu variants are more contagious or more pathogenic than other variants. Finally, the Omicron variant (Sahoo and Samal, 2021) first identified in South Africa in November 2021, and it may spread more easily than other variants including the Delta. Xue et al. (2022) investigated factors that affect the recovery of patients and they applied machine learning techniques to estimate the duration of recovery during Omicron pandemic.



Irudayasamy et al. (2022) investigated the effect of Omicron on unvaccinated community. Their results showed that vaccination decreases mortality risk in a significant degree. Arslan (2022b) predicted mortality of patients with COVID-19 in an acceptable accuracy.

The RT-PCR (Cobb et al., 2021; Bustin et al., 2009) is a widely known method to detect SARS-CoV-2 although optimization of the RT-PCR may include a complicated process. Rapid tests for detecting SARS-CoV-2 are based on RT-PCR, and these tests require a forward primer, reverse primer and probe sequences which together are utilized to amplify the signal from the virus within a sample. Although this approach provides specific detection of the virus and does not rely on tissue culture or cell models of animals, new mutations on the primer binding sites may be occurred because of the rapid evolution of the SARS-CoV-2 (Lownick et al., 2021; Osorio and Correia-Neves, 2021). Thus, it is critical to the well design of the primer sets, and these primer sets need to be updated and evaluated regularly (Nayar et al., 2021; Jain et al., 2021).

Various types of studies are published to detect SARS-CoV-2 (Jiang et al., 2020; Zoabi, Deri-Rozov, and Shomron, 2021; Muhammad et al., 2021; Shi et al., 2021; Mohamadou et al., 2020; Arslan and Arslan, 2021; Arslan, 2021a; Arslan and Aygun, 2021; Arslan, 2021b; Togrul and Arslan, 2022). Furthermore, there exist efficient methods for detecting SARS-CoV-2 variants (Ali et al., 2021; Ogiela and Ogiela, 2021; Jamil and Rahman, 2021; Arslan, 2022a; Arslan, 2023). Park et al. (Park et al., 2020) introduced a guideline including three steps to design and optimization of primer sets. After they selected the primer sets for target genes, they performed in silico validation of the primer. Finally, they optimized the PCR conditions for specific hybridization. Alignment-based methods may be used to detect conserved regions that are used for the design of universal primers and probes (Anantharajah et al., 2021). Davi et al. (2021) determined 26 conserved regions in the SARS-CoV-2 genome as a result of the alignments of 2,341 full genome sequences. They selected nine candidate systems including primers and probes. They also analyzed their systems using 211,833 SARS-CoV-2 genome sequences. However, these methods are expensive and require a lot of time. Rincon et al. (2021) used an artificial intelligence technique to identify primers to detect SARS-CoV-2. They identified 12 unique 21-bps sequences to appear only SARS-CoV-2 sequences using Convolutional Neural Network (CNN). They validated their results by using 52,645 SARS-CoV-2 sequences. Langer et al. (2020) investigated the accuracy of artificial intelligence for predicting RT-PCR results for detecting SARS-CoV-2 using the main knowledge provided by emergence departments.

In this study, we propose a parallel algorithm to identify the most conserved segments in the SARS-CoV-2 genomes. To determine these segments, we analyze a various number of SARS-CoV-2 genome sequences including the main SARS-CoV-2 variants of concern and interest. After

the conserved region is determined, online Primer3Plus (2022) is employed to detect primers and probes using the conserved region. The proposed primer and probe sets are evaluated using specific types of SARS-CoV-2 and also evaluated using 406,757 genome sequences belonging to various types of SARS-CoV-2. The rest of this study is organized as follows. The proposed method is presented in Section 2. Experimental results are evaluated and compared in Section 3. Finally, Section 4 includes the conclusion.

2. Materials and Methods

In this section, we present a rapid and accurate method to determine forward primers, reverse primers and probes used in RT-PCR. The main idea behind the proposed method is to determine the most conserved region of the sequenced SARS-CoV-2 genomes using a sliding window approach in a parallel manner. The algorithm takes complete genome sequences of SARS-CoV-2 and the length of the conserved region and returns forward primers, reverse primers, and probes that are determined for the conserved region. The basic steps of the proposed algorithm are described in Algorithm 1. The length of the conserved region is fixed to 100 base pairs (bps). The first sequence in the dataset is fixed to perform a 100-bp sliding window approach in Step 1. There is a for loop between Steps 4-16 and this loop is executed in parallel by OpenMP threads. In this loop, we iterate over all the possible beginnings of the 100 bp ranges. For each range, we check whether a genome sequence in the dataset includes the 100-bp substring in parallel to find the total number of matches. At the end of for loop, we determine the most repeated 100-bp substring that has the highest match score. After identifying the most repeated 100-bp sequences, we employ online Primer3Plus to pick primers and probes from the most repeated substring in Step 17.

2.1. Primer and Probes Design

We follow the steps defined in Algorithm 1 to determine the most conserved region of the genome sequences of SARS-CoV-2. In the following, we briefly explain the genome sequences of SARS-CoV-2 used in this study. Whole human genome sequences of SARS-CoV-2 are obtained from the Global Initiative on Sharing All Influenza Data (GISAID) (Shu and McCauley, 2017). We download high-quality and complete sequences to minimize sequencing errors. Recently, five variants of concern of SARS-CoV-2, which are B.1.1.7, B.1.351, P.1, B.1.617.2, and B.1.1.529, have been reported. Furthermore, we analyze two variants of interest of SARS-CoV-2, which are C.7 and B.1.621, recently. WHO Label, Scientific Names, date of designation, and the number of sequences used in this study are presented in Table 1. Next, we run online Primer3Plus to design primer pairs and probes adopting the criteria shown in Table 2.

Table 1. Properties of the SARS-CoV-2 sequences used in this study

| Variant Name | WHO Label | Scientific Name | Date of Designation | # of sequences |
|----------------------|-----------|-----------------|---------------------|----------------|
| Variant of Concerns | Alpha | B.1.1.7 | October, 2020 | 54,524 |
| | Beta | B.1.351 | December, 2020 | 25,465 |
| | Gamma | P.1 | January, 2021 | 53,501 |
| | Delta | B.1.617.2 | October, 202 | 46,225 |
| | Omicron | B.1.1.529 | November, 2021 | 43,682 |
| Variants of Interest | Lambda | C.7 | August, 2020 | 1,008 |
| | Mu | B.1.621 | January, 2021 | 5,844 |

Table 2. General conditions for designing primers and probes

| Condition | Minimum | Optimum | Maximum |
|---------------|---------|---------|---------|
| Primer Size | 18 | 20 | 23 |
| Primer Tm (C) | 57 | 59 | 62 |
| Primer GC % | 30 | 50 | 70 |
| Probe Size | 18 | 20 | 27 |
| Probe Tm (C) | 57 | 60 | 63 |
| Probe GC % | 20 | 50 | 80 |

Algorithm 1. Proposed Parallel Algorithm

Require: dataSeqs: SARS-CoV-2 genome sequences and size: length of the conserved region

Ensure: Determine forward and reverse primers as well as probe

```

1: seq ← dataSeqs[0]
2: n ← length(seq) - size
3: maxSeq ← 0
4: parfor k = 1:n do
5: count ← 0
6: overlapSeq ← seq[k:k+size]
7: parfor genSeq in dataSeqs do
8: if overlapSeq in genSeq then
9: count = count + 1
10: end if
11: end parfor
12: if count > maxSeq then
13: maxOverlapSeq = overlapSeq
14: maxSeq = count
15: end if
16: end parfor
17: Use Primer3Plus to design primers and probes using maxOverlapSeq
    
```

Table 3 presents the primer and probe sequences identified in this study. Furthermore, we present primer and probe sizes, melting temperatures (Tm), percentage of G and C (GC% = G + C). The "SELF" and "ANY" present the possibility which the primer will bond to itself composing dimers and hairpins. Alpha-1 and Alpha-2 primers and probes are obtained by running Algorithm 1 on a set of sequences containing B.1.1.7 variant. Similarly, Beta, Gamma, Delta, and Omicron primers and probes are obtained by running Algorithm 1 on a specific set of sequences including B.1.351, P.1, B.1.617.2, and B.1.1.529 variant of concerns. Furthermore, Lambda and Mu

primers and probes are obtained by running Algorithm 1 on a set of sequences containing C.7 and B.1.621 variants of interest and shown in Table 3. The suitability of the proposed primers was checked by using PCR Primer Stats program (2022) and we achieved acceptable results. Furthermore, the uniqueness of proposed primers and probes was verified using the tool UCSC In-Slico PCR (Stothard, 2020; Kent et al., 2002).

3. Results and Discussion

In this section, we evaluate primers and probes proposed in this study based on the number of sequences that the primers and probes found. The proposed primers are validated in five datasets containing SARS-CoV-2 variants of concern, which include the Alpha (54,524 sequences), Beta (25,465 sequences), Gamma (53,501 sequences), Delta (46,225 sequences), and Omicron (43,682 sequences). They are also validated in two datasets including SARS-CoV-2 variants of interest, the Lambda (1,008 sequences) and Mu (5,844 sequences). Finally, we validate the proposed primers using 406,757 whole genome sequences including a recent variant of concerns and interests of SARS-CoV-2, which is referred to as the Mixed dataset. We note that we downloaded all possible complete SARS-CoV-2 genome sequences (*.fasta format) from NCBI database (NCBISD, 2021) on March 4th, 2021. Table 4 summarizes the total number of sequences that proposed primers are found against a specific set of sequences. The percentage is also shown. Considering B.1.1.7 (Alpha) variant of sequences, the appearance of the proposed primer sets ranged from 54,165 sequences (99.34%) to 54,447 sequences (99.86%). The best score is achieved with Mu-1 primers, and only 77 out of 54,524 sequences do not appear. When considering B.1.351 (Beta) variant of sequences, the appearance of the proposed primer sets ranged from 25,069 sequences

(98.44%) to 25,443 sequences (99.91%). The Mu-1 primer achieves the best frequency of appearance and only 22 out of 25,465 sequences do not appear. When considering P.1 (Gamma) variant of sequences, the appearance of the proposed primer sets ranged from 52,467 sequences (98.07%) to 53,456 sequences (99.92%). The Mu-1 primer achieves the best frequency of appearance and only 45 out of 53,501 sequences do not appear. For B.1.617.2 (Delta) variant of sequences, the appearance of the proposed primer sets ranged from 44,904 sequences (97.14%) to 46,141 sequences (99.82%). The Mu-1 primer achieves the best frequency of

appearance and only 84 out of 46,225 sequences do not appear. For B.1.1.529 (Omicron) variant of sequences, the appearance of the proposed primer sets ranged from 43,069 sequences (98.6%) to 43,670 sequences (99.97%). The Mu-1 and Beta-4 primers achieve the best frequency of appearance and only 12 out of 43,682 sequences do not appear. When we analyze the frequency results on two SARS-CoV-2 variants of interest, for C.8 (Lambda) variant of sequences, the Beta-2, Beta-4, and Omicron-1 primers achieve 100% frequency of appearance. For B.1.1.529 (Mu) variant of sequences, the Mu-1 primer achieves 100% frequency of appearance.

Table 3. The properties of the primer and probe sequences identified in this study. F forward primer; R reverse primer; P probe

| Primer Name | Sequence | Size | Tm | GC(%) | ANY | SELF | Target |
|-------------|-----------------------------|------|------|-------|-----|------|--------|
| Alpha-1-F | GGCCGGCTGTTTTGTAGAT | 19 | 59.3 | 52 | 6 | 0 | ORF1ab |
| Alpha-1-P | TGATTGAACGGTTCGTGTCT | 20 | 59.1 | 45 | 7 | 1 | ORF1ab |
| Alpha-1-R | GGATGTTTAGTAAGTGGGTAAGCA | 24 | 58.7 | 41.7 | 5 | 3 | ORF1ab |
| Alpha-2-F | CAGTTTATGATCCTTTGCAACC | 22 | 58.6 | 40.9 | 6 | 2 | S |
| Alpha-2-P | TGAATTAGACTCATTCAAGGAGGA | 24 | 59.3 | 37.5 | 11 | 3 | S |
| Alpha-2-R | ATGTCACCTAAATCAACATCTGG | 23 | 58 | 39.1 | 4 | 2 | S |
| Beta-1-F | CATGCGAAATGCTGGTATTG | 20 | 60.1 | 45 | 4 | 2 | ORF1ab |
| Beta-1-P | GGTAACTGGTATGATTTTCGGTGA | 23 | 60.1 | 43.5 | 3 | 3 | ORF1ab |
| Beta-1-R | CTACCTGGCGTGGTTTGTATG | 21 | 60.4 | 52.4 | 4 | 0 | ORF1ab |
| Beta-2-F | ACAATTCTGTGATGCCATGC | 20 | 59.5 | 45 | 5 | 3 | ORF1ab |
| Beta-2-P | GAAATGCTGGTATTGTTGGTG | 21 | 58 | 42.9 | 4 | 0 | ORF1ab |
| Beta-2-R | TACCTGGCGTGGTTTGTATG | 20 | 59.5 | 50 | 4 | 0 | ORF1ab |
| Beta-3-F | GTAACAGCTTTAAGGGCCAAT | 21 | 57.5 | 42.9 | 6 | 2 | ORF1ab |
| Beta-3-P | CCTGTTGCACTACGACAGATG | 21 | 59.4 | 52.4 | 7 | 2 | ORF1ab |
| Beta-3-R | TTTGTGTAGTACCGGCAGCA | 20 | 60.3 | 50 | 5 | 2 | ORF1ab |
| Beta-4-F | GGCTGTTGCTAATGGTGATT | 20 | 57.7 | 45 | 3 | 2 | ORF1ab |
| Beta-4-P | TCTGAATTTGACCGTGATGC | 20 | 59.7 | 45 | 4 | 2 | ORF1ab |
| Beta-4-R | TTCCAACCTTACGTTGCATGG | 20 | 59.6 | 45 | 8 | 2 | ORF1ab |
| Gamma-1-F | GTGCAGTGCTGCATTACA | 19 | 59.4 | 52.6 | 7 | 3 | S |
| Gamma-1-P | CATTTGCTATGCAAATGGCTT | 21 | 60.1 | 38.1 | 12 | 3 | S |
| Gamma-1-R | GGTTGGCAATCAATTTTGG | 20 | 60.2 | 40 | 5 | 2 | S |
| Gamma-2-F | CTGGTTGGACCTTTGGTG | 18 | 57.4 | 55.6 | 3 | 1 | S |
| Gamma-2-P | CATTTGCTATGCAAATGGCTT | 21 | 60.1 | 38.1 | 12 | 3 | S |
| Gamma-2-R | TAGAGAACATTCTGTGTAACCTCCAAT | 26 | 57.6 | 34.6 | 6 | 3 | S |
| Delta-1-F | AGCTCCAATTTTGGTGCAAT | 20 | 59.6 | 40 | 8 | 2 | S |
| Delta-1-P | AAGTTGAGGCTGAAGTGCAAA | 21 | 60 | 42.9 | 5 | 0 | S |
| Delta-1-R | TGCCTGTGATCAACCTATCAA | 21 | 59.1 | 42.9 | 6 | 1 | S |
| Delta-2-F | AGCTCCAATTTTGGTGCAAT | 20 | 59.6 | 40 | 8 | 2 | S |
| Delta-2-P | TGAGGCTGAAGTGCAAATTG | 20 | 60 | 45 | 5 | 5 | S |
| Delta-2-R | GAAGTCTGCCTGTGATCAACC | 20 | 59.7 | 52.4 | 6 | 2 | S |
| Omicron-1-F | ACAATTCTGTGATGCCATGC | 20 | 59.5 | 45 | 5 | 3 | ORF1ab |
| Omicron-1-P | GAAATGCTGGTATTGTTGGTG | 21 | 58 | 42.9 | 4 | 0 | ORF1ab |
| Omicron-1-R | TGGCGTGGTTTGTATGAAAT | 20 | 58.9 | 40 | 3 | 2 | ORF1ab |
| Lambda-1-F | CCATCATATGCAGCTTTTGC | 20 | 59.3 | 45 | 6 | 3 | ORF1ab |
| Lambda-1-P | AGCAGGCTGTTGCTAATGGT | 20 | 59.9 | 50 | 5 | 0 | ORF1ab |
| Lambda-1-R | GCCACATTCAAAGACTTCTTCA | 22 | 59.4 | 40.9 | 6 | 2 | ORF1ab |
| Mu-1-F | AGGACCTCATGAATTTTGCTC | 21 | 58.3 | 42.9 | 6 | 0 | ORF1ab |
| Mu-1-P | TGTGTACCTTCCTTACCCAGATC | 23 | 59.4 | 47.8 | 4 | 4 | ORF1ab |
| Mu-1-R | GGCCCTAGGATTCTTGATG | 20 | 60.8 | 55 | 6 | 2 | ORF1ab |

Table 4. The percentage and total number of sequences that proposed primers are found in the corresponding dataset.

| Primer Name | B.1.1.7 (Alpha) | B.1.351 (Beta) | P.1 (Gamma) | B.1.617.2 (Delta) | C.8 (Lambda) | B.1.621 (Mu) | B.1.1.529 (Omicron) | Mixed Dataset |
|-------------|--------------------|--------------------|--------------------|--------------------|------------------|-------------------|---------------------|---------------------|
| Alpha-1 | 54,257 (99.51%) | 25,352 (99.56%) | 52,467 (98.07%) | 46,026 (99.57%) | 1,004 (99.6%) | 5,675 (97.11%) | 43,634 (99.89%) | 402,892 (99.05%) |
| Alpha-2 | 54,380 (99.74%) | 25,069 (98.44%) | 53,210 (99.46%) | 45,440 (98.3%) | 1,006 (99.8%) | 5,740 (98.22%) | 43,275 (99.07%) | 403,665 (99.24%) |
| Beta-1 | 54,293 (99.58%) | 25,369 (99.62%) | 53,437 (99.88%) | 45,572 (98.59%) | 1,006 (99.8%) | 5,838 (99.9%) | 43,585 (99.78%) | 404,793 (99.52%) |
| Beta-2 | 54,165 (99.34%) | 25,422 (99.83%) | 53,359 (99.73%) | 44,904 (97.14%) | 1,008 (100%) | 5,841 (99.95%) | 43,650 (99.93%) | 404,698 (99.49%) |
| Beta-3 | 54,222 (99.45%) | 25,403 (99.76%) | 53,320 (99.66%) | 46,036 (99.59%) | 979 (97.12%) | 5,831 (99.78%) | 43,644 (99.91%) | 404,808 (99.52%) |
| Beta-4 | 54,301 (99.59%) | 25,432 (99.87%) | 53,383 (99.78%) | 46,127 (99.79%) | 1,008 (100%) | 5,841 (99.95%) | 43,670 (99.97%) | 405,247 (99.63%) |
| Gamma-1 | 54,166 (99.34%) | 25,280 (99.27%) | 53,422 (99.85%) | 45,935 (99.37%) | 1,007 (99.9%) | 5,805 (99.33%) | 43,093 (98.65%) | 402,564 (98.97%) |
| Gamma-2 | 54,361 (99.7%) | 25,362 (99.6%) | 53,443 (99.89%) | 45,998 (99.51%) | 1,006 (99.8%) | 5,813 (99.47%) | 43,069 (98.6%) | 402,615 (98.98%) |
| Delta-1 | 54,292 (99.57%) | 25,379 (99.66%) | 53,434 (99.87%) | 46,098 (99.73%) | 1,007 (99.9%) | 5,821 (99.61%) | 43,630 (99.88%) | 403,766 (99.26%) |
| Delta-2 | 54,292 (99.57%) | 25,379 (99.66%) | 53,434 (99.87%) | 46,098 (99.73%) | 1,007 (99.9%) | 5,821 (99.61%) | 43,630 (99.88%) | 403,766 (99.26%) |
| Omicron-1 | 54,165 (99.34%) | 25,422 (99.83%) | 53,359 (99.73%) | 44,904 (97.14%) | 1,008 (100%) | 5,841 (99.95%) | 43,650 (99.93%) | 404,698 (99.49%) |
| Lambda-1 | 54,427 (99.82%) | 25,362 (99.6%) | 53,428 (99.86%) | 45,943 (99.39%) | 1,007 (99.9%) | 5,833 (99.81%) | 43,668 (99.97%) | 404,798 (99.52%) |
| Mu-1 | 54,447 (99.86%) | 25,443 (99.91%) | 53,456 (99.92%) | 46,141 (99.82%) | 1,007 (99.9%) | 5,844 (100%) | 43,670 (99.97%) | 405,415 (99.67%) |

Finally, we analyze the frequency of appearance on the Mixed dataset. The proposed primer sets ranged from 402,564 sequences (98.97%) to 405,415 sequences (99.67%). The Mu-1 primer achieves the best frequency of appearance and only 1342 out of 406,757 sequences do not appear. In silico analysis presents that the sets of primers and probes proposed in this study potentially anneal to a highly conserved region of the SARS-CoV-2. Designed primers are also analyzed using Oligo 7 software (Rychlik, 2007) based on duplex formation and hairpin formation. Moreover, Oligo 7 program analyzes primers by calculating an efficiency score that is a possibility that a given oligonucleotide is going to prime at a given site on the sequence currently analyzed. It is noted that when efficiency scores of the primers are between 450 and 500, excellent results are obtained for multiplex PCR, and the priming is more likely when this score is over 220 (threshold) (Rychlik, 2007). Figure 1 presents efficiency values of forward primers, reverse primers, and probes designed in this study. When the proposed primers are evaluated based on primer efficiency, as you can see in Figure 1, the efficiencies of the primers and probes are above the threshold and the designed primers either fall

in 450-500 primer efficiency range or close to this range. This points out that the proposed primers may be achieved excellent for multiplex PCR.

3.1. Comparison with Existing Primers

In this section, we present results related to the primers reported by Davi et al. (2021). The properties of the primers and probes shown by Davi et al. (2021) are given in Table 5. Furthermore, the percentages of appearance for each primer designed by Davi et al. (2021) against the different datasets including the main SARS-CoV-2 concerns and two types of SARS-CoV-2 variant of interests are presented in Table 6. The results revealed that the UFRN-5, UFRN-6, and UFRN-7 primers cannot accurately detect the sequences belonging to the Mu variant. Furthermore, the UFRN-8 and UFRN-9 primers have a lower percentage of appearance on the Mixed dataset and appear in only 60.12% of the sequences including recent variants of SARS-CoV-2.

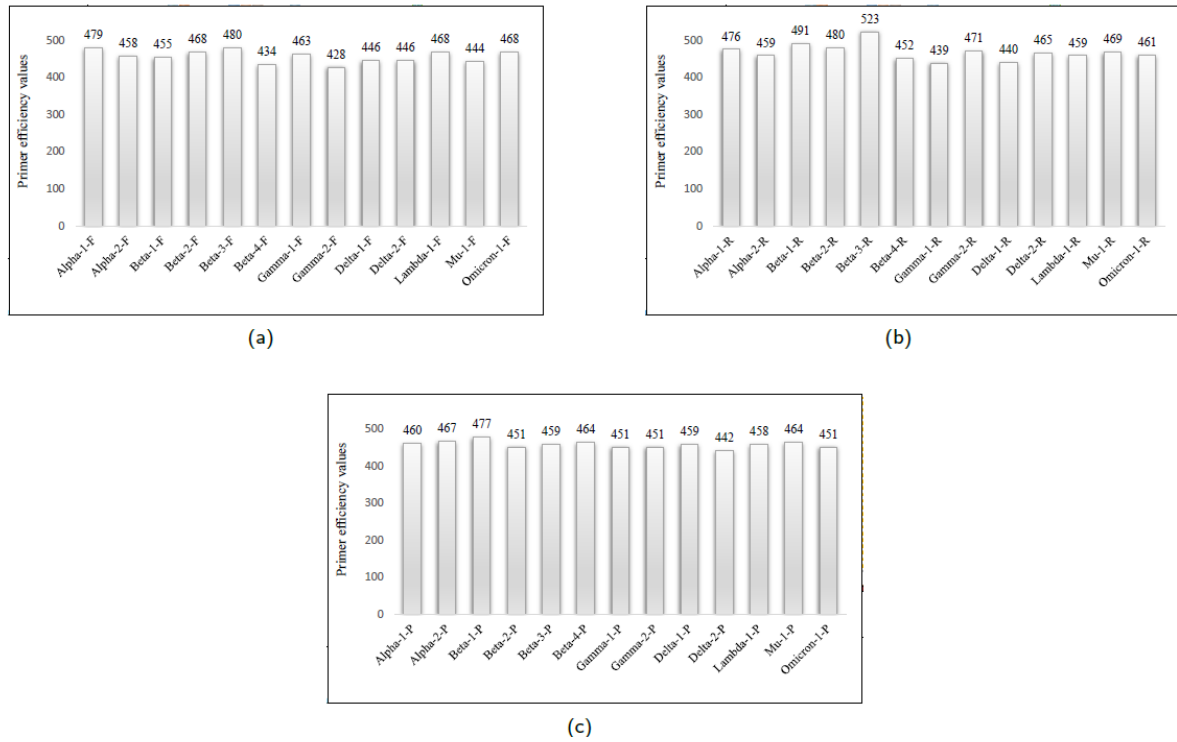


Figure 1. Efficiency scores of (a) forward primers (b) reverse primers (c) probes designed in this study.

Table 5. The information regarding the primers and probes shown by Davi et al. (2021)

| Primer Name | Sequence | Length | Tm | GC(%) | Target | Size |
|-------------|------------------------------|--------|-------|-------|--------|------|
| UFRN-1-F | GGGCATACACTCGCTATGTC | 20 | 58.22 | 55 | ORF1a | 101 |
| UFRN-1-R | GCATGAAGCTTTACCAGCAC | 20 | 57.73 | 50 | ORF1a | 101 |
| UFRN-1-P | TCTGTGGCCCTGATGGCTACCCT | 23 | 67.22 | 60.87 | ORF1a | 101 |
| UFRN-2-F | GGCTACTAACAAATGCCATGC | 20 | 57.22 | 50 | ORF1a | 137 |
| UFRN-2-R | TAACATTTGGGCCGACAACA | 20 | 58.02 | 45 | ORF1a | 137 |
| UFRN-2-P | GGGTGGTAGTTGTGTTTTAAGCGG | 24 | 62.33 | 50 | ORF1a | 137 |
| UFRN-3-F | TTCATGTTGTCGCCCAAAT | 20 | 58.37 | 45 | ORF1a | 98 |
| UFRN-3-R | TGGTGCAAGTAGAACTTCGT | 20 | 57.1 | 45 | ORF1a | 98 |
| UFRN-3-P | GAAGACATTCAACTTCTTAAGAGTGC | 26 | 58.71 | 38.46 | ORF1a | 98 |
| UFRN-4-F | TGGTGCTAGGAGAGTGTGG | 19 | 58.33 | 87.89 | ORF1a | 95 |
| UFRN-4-R | CCCACATGGAAATGGCTTGAT | 21 | 58.89 | 47.62 | ORF1a | 95 |
| UFRN-4-P | CTTATGAATGTCTTGACACTCGTTTATA | 28 | 58.01 | 32.14 | ORF1a | 95 |
| UFRN-5-F | AGGGCACACTAGAACCAGAA | 20 | 58.27 | 50 | ORF1b | 105 |
| UFRN-5-R | CAATTCAGCAGGACAACGC | 20 | 58.31 | 50 | ORF1b | 105 |
| UFRN-5-P | GGTCCAGACATGTTCTCGGAACT | 24 | 64.18 | 54.17 | ORF1b | 105 |
| UFRN-6-F | TCTTCACGACATTGGTAACCC | 21 | 57.95 | 47.62 | ORF1b | 90 |
| UFRN-6-R | TCACTACAAGGCTGTGCATC | 20 | 57.9 | 50 | ORF1b | 90 |
| UFRN-6-P | TACCTCAAGCTGATGTAGAATGGAAG | 26 | 60.41 | 42.31 | ORF1b | 90 |
| UFRN-7-F | CTTCACGACATTGGTAACCT | 21 | 57.95 | 47.62 | ORF1b | 90 |
| UFRN-7-R | GTCCTACAAGGCTGTGCAT | 20 | 58.19 | 50 | ORF1b | 90 |
| UFRN-7-P | GTGTACCTCAAGCTGATGTAGAATGG | 26 | 61.4 | 46.15 | ORF1b | 90 |
| UFRN-8-F | GGCACAGGTGTTCTTACTGA | 20 | 57.46 | 50 | S | 107 |
| UFRN-8-R | TCAAGTGTCTGTGGATCACG | 20 | 57.56 | 50 | S | 107 |
| UFRN-8-P | CCAACAATTTGGCAGAGACATTGC | 24 | 61.62 | 45.83 | S | 107 |
| UFRN-9-F | AGGCACAGGTGTTCTTACTG | 20 | 57.45 | 50 | S | 93 |
| UFRN-9-R | TCACGGACAGCATCAGTAGT | 20 | 58.45 | 50 | S | 93 |
| UFRN-9-P | TCCAACAATTTGGCAGAGACATTGC | 25 | 62.75 | 44 | S | 93 |

Table 6. The percentage of appearance for each primer designed by Davi et al. (2021) against the different datasets including the main SARS-CoV-2 concerns and two types of SARS-CoV-2 variant of interests

| Primer Name | B.1.1.7 (Alpha) | B.1.351 (Beta) | P.1 (Gamma) | B.1.617.2 (Delta) | C.8 (Lambda) | B.1.621 (Mu) | B.1.1.529 (Omicron) | Mixed Dataset |
|-------------|-----------------|----------------|-------------|-------------------|--------------|--------------|---------------------|---------------|
| UFRN-1 | 98% | 98.83% | 99.38% | 99.05% | 99.8% | 98.36% | 99.86% | 98.15% |
| UFRN-2 | 98.89% | 99.37% | 96.95% | 99.07% | 98.81% | 99.16% | 99.63% | 98.35% |
| UFRN-3 | 98.51% | 98.7% | 88.31% | 98.96% | 99.7% | 99.49% | 99.42% | 98.28% |
| UFRN-4 | 99.31% | 98.96% | 99.5% | 99.1% | 100% | 99.81% | 99.96% | 97.07% |
| UFRN-5 | 99.34% | 99.79% | 99.87% | 99.37% | 99.8% | 0.29% | 99.95% | 98.33% |
| UFRN-6 | 99.56% | 99.72% | 99.71% | 99.36% | 99.5% | 5.18% | 99.97% | 99.18% |
| UFRN-7 | 99.58% | 99.71% | 99.71% | 99.34% | 99.40% | 5.18% | 99.97% | 99.18% |
| UFRN-8 | 99.78% | 99.7% | 99.8% | 99.48% | 99.9% | 99.9% | 99.89% | 60.12% |
| UFRN-9 | 99.79% | 99.7% | 99.8% | 99.69% | 99.31% | 99.9% | 99.89% | 60.12% |

Next, we choose the best-performing primer sets developed by Davi et al. (2021) and WHO to compare against the best primer set obtained by the proposed method. They are chosen based on the highest frequency of appearance on the mixed dataset. Table 7 presents the properties of the primers and probes. Experimental results present that the proposed primer and probe have

a higher frequency of appearance on the main SARS-CoV-2 variants of concern and interest. On the other hand, the frequency of appearance of the primer proposed by WHO is lower in the sequences belonging Lambda variant. Furthermore, the primer proposed by Davi et al. (2021) cannot accurately detect the Mu variant.

Table 7. The properties of the best-performing primers and probes developed by Davi et al. (2021), WHO, and the proposed method

| Study | Primer Name | Sequence | Length | Tm | GC(%) |
|--------------------|--------------|----------------------------|--------|-------|-------|
| Davi et al. (2021) | UFRN-6-F | TCTTCACGACATTGGTAACCC | 21 | 57.95 | 47.62 |
| | UFRN-6-P | TACCTCAAGCTGATGTAGAATGGAAG | 26 | 60.41 | 42.31 |
| | UFRN-6-R | TCACTACAAGGCTGTGCATC | 20 | 57.9 | 50 |
| WHO | N_Sarbeco_F1 | CACATTGGCACCCGCAATC | 19 | 60.15 | 57.89 |
| | N_Sarbeco_P1 | ACTTCCTCAAGGAACAACATTGCCA | 25 | 63.15 | 44 |
| | N_Sarbeco_R1 | GAGGAACGAGAAGAGGCTTG | 20 | 58 | 55 |
| Proposed Study | Mu-1-F | AGGACCTCATGAATTTTGCTC | 21 | 58.3 | 42.9 |
| | Mu-1-P | TGTGTACCTTCCTTACCCAGATC | 23 | 59.4 | 47.8 |
| | Mu-1-R | GGCCCTAGGATTCTTGATG | 20 | 60.8 | 55 |

4. Conclusion

In this study, we propose an efficient parallel method to identify primers and probes for real-time PCR. Compared to the alignment-based method, the proposed method is effectively detected to the conserved region. We analyze the performance of the proposed primers and probes based on the number of matches of the PCR primers for genome sequences of SARS-CoV-2. Experimental results present that the proposed primers and probes have about 99% matches for the genome sequences including the recent variants of SARS-CoV-2. In future, other pandemics may occur as a result of the increasing population and growing interaction between people. We believe that the proposed method can be applied to develop more accurate primers and probes for identifying any type of virus and contribute treatment for the rapidly propagating virus as well as help limit the spread of the virus. In future studies, we will also provide laboratory results of the primers and probes. Furthermore, we will extend the proposed technique for other types of virus.

Author Contributions

The percentage of the author(s) contributions is presented below. All authors reviewed and approved the final version of the manuscript.

| | H.A. | R.D. |
|-----|------|------|
| C | 50 | 50 |
| D | 100 | |
| S | | 100 |
| DCP | 100 | |
| DAI | 20 | 80 |
| L | 50 | 50 |
| W | 80 | 20 |
| CR | 20 | 80 |
| SR | 80 | 20 |

C=Concept, D= design, S= supervision, DCP= data collection and/or processing, DAI= data analysis and/or interpretation, L= literature search, W= writing, CR= critical review, SR= submission and revision.

Conflict of Interest

The authors declared that there is no conflict of interest.

Ethical Consideration

Ethics committee approval was not required for this study because of there was no study on animals or humans. The authors confirm that the ethical policies of the journal, as noted on the journal's author guidelines page, have been adhered to.

References

Ali S, Tamkanat-E-Ali Khan MA, Khan I, Patterson M. 2021. Effective and scalable clustering of sars-cov-2 sequences. Proceedings of the 5th International Conference on Big Data Research, September 23-25, Qingdao, China, pp: 42-49.

Anantharajah A, Helaers R, Defour J.-P, Olive N, Kabera F, Croonen L, Kabamba-Mukadi B. 2021. How to choose the right real-time RT-PCR primer sets for the SARS-CoV-2 genome detection. *J Virol Methods*, 295: 114197.

Arslan H. 2021a. COVID-19 prediction based on genome similarity of human SARS-CoV-2 and bat SARS-CoV-like coronavirus. *Comput Indust Engin*, 161: 107666.

Arslan H. 2021b. Machine learning methods for Covid-19 prediction using human genomic data. *Proceed 74 (1)*: 20.

Arslan H, Arslan H. 2021. A new covid-19 detection method from human genome sequences using cpg island features and knn classifier. *Engin Sci Technol Inter J*, 24(4): 839-847.

Arslan H, Aygun B. 2021. Performance analysis of machine learning algorithms in detection of covid-19 from common symptoms. *Proceeding of 29th Signal Processing and Communications Applications Conference*, June 9-11, Istanbul, Türkiye, pp: 1-4.

Arslan H. 2022a. Classification of SARS-CoV-2 Variants in Turkey. *J Turkish Operat Manage*, 6(1): 1092-1101.

Arslan H. 2022b. Bagging and boosting for predicting mortality of patients with COVID-19. *Dicle Univ J Engin*, 13(2): 221-226.

Arslan H. 2023. A k-mer based metaheuristic approach for detecting COVID-19 variants. *Dicle Univ J Engin*, 14(1): 17-26.

Baj A, Novazzi F, Ferrante FD, Genoni A, Cassani G, Prestia M, Maggi F. 2021. Introduction of SARS-COV-2 c.37 (WHO VOI lambda) from Peru to Italy. *J Medical Virol*, 93(12): 6460-6461.

Bustin SA, Benes V, Garson JA, Hellems J, Huggett J, Kubista M, Wittwer CT. 2009. The MIQE guidelines: Minimum information for publication of quantitative realtime PCR experiments. *Clin Chem*, 55(4): 611-622.

Cobb BR, Vaks JE, Do T, Vilchez RA. 2011. Evolution in the sensitivity of quantitative HIV-1 viral load tests. *J Clin Virol*, 52 S77-S82.

Davi MJP, Jeronimo SMB, Lima JPMS, Lanza DCF. 2021. Design and in silico validation of polymerase chain reaction primers to detect severe acute respiratory syndrome coronavirus 2 (SARS-CoV-2). *Sci Rep*, 11(1): 12565.

Irudayasamy A, Ganesh D, Natesh M. 2022. Big data analytics on the impact ofOMICRON and its influence on unvaccinated community through advanced machine learning concepts. *Int J Syst Assur Eng Manag*, 2022: 1-10.

Jain A, Rophina M, Mahajan S, Krishnan BB, Sharma M, Mandal S, Scaria V. 2021. Analysis of the potential impact of genomic variants in global sars-cov-2 genomes on molecular diagnostic assays. *Inter J Infect Diseases*, 102: 460-462.

Jamil S, Rahman M. 2021. A dual-stage vocabulary of features (vof)-based technique for covid-19 variants' classification. *Applied Sci*, 11 (24): 11902.

Jiang X, Coffee M, Bari A, Wang J, Jiang X, Huang J, Huang Y. 2020. Towards an Artificial Intelligence Framework for Data-Driven Prediction of Coronavirus Clinical Severity. *Comput Mater Contin*, 62(3): 537-551.

Kent WJ, Sugnet CW, Furey TS, Roskin KM, Pringle TH, Zahler AM, Haussler D. 2002. The human genome browser at UCSC. *Genome Res*, 12(6): 996-1006.

Langer T, Favarato M, Giudici R, Bassi G, Garberi R, Villa F, Fumagalli R. 2020. Development of machine learning models to predict RT-PCR results for severe acute respiratory syndrome coronavirus 2 (SARS-CoV-2) in patients with influenza-like symptoms using only basic clinical data. *Scandinavian J Trauma Resuscit Emerg Med*, 28 (1): 113.

Lauring AS, Malani PN. 2021. Variants of SARS-CoV-2. *JAMA*, 326(9): 880-880.

Lopez-Rincon A, Tonda A, Mendoza-Maldonado L, Mulders DGJC, Molenkamp R, Perez-Romero CA, Kraneveld AD. 2021. Classification and specific primer design for accurate detection of SARS-CoV-2 using deep learning. *Sci Reports* 11(1): 947.

Lownik JC, Farrar JS, Way GW, McKay A, Roychoudhury P, Greninger AL, Martin RK. 2021. Fast sars-cov-2 variant detection using snapback primer high-resolution melting. *Diagnostics*, 11(10): 1788.

Mlcochova P, Kemp SA, Dhar MS. 2021. SARS-CoV-2 b.1.617.2 delta variant replication and immune evasion. *Nature*, 599(7883): 114-119.

Mohamadou Y, Halidou A, Kapen PT. 2020 November. A review of mathematical modeling artificial intelligence and datasets used in the study prediction and management of COVID- 19. *Applied Intell*, 50(11): 3913-3925.

Muhammad LJ, Algehyne EA, Usman SS, Ahmad A, Chakraborty C, Mohammed IA. 2021 February. Supervised machine learning models for prediction of Covid-19 infection using epidemiology dataset. *SN Computer Sci*, 2(1): 11.

NCBI/SD. 2021. National center for biotechnology information search database. URL: <https://www.ncbi.nlm.nih.gov/sars-cov-2/>. (accessed date: December 04, 2021).

Nayar G, Seabolt EE, Kunitomi M, Agarwal A, Beck KL, Mukherjee V, Kaufman JH. 2021. Analysis and forecasting of global real time RT-PCR primers and probes for SARS-CoV-2. *Sci Reports*, 11 (1): 8988.

Ogiela MR, Ogiela U. 2021. Linguistic methods in healthcare application and COVID-19 variants classification. *Neural Comput Applicat*, 35: 13935-13940

Os'orio NS, Correia-Neves M. 2021. Implication of SARS-CoV-2 evolution in the sensitivity of RT-qPCR diagnostic assays. *The Lancet Infect Diseases*, 21(2): 166-167.

Park M, Won J, Choi BY, Lee CJ. 2020. Optimization of primer sets and detection protocols for SARS-CoV-2 of coronavirus disease 2019 (COVID-19) using PCR and real-time PCR. *Experiment Molec Med*, 52(6): 963-977.

PCR Primer Stats. 2022. URL: <https://www.bioinformatics.org/sms2/pcrprimerstats.html>. (accessed date October 01, 2022).

Primer3plus. 2022. URL: <https://www.bioinformatics.nl/cgi-bin/primer3plus/primer3plus.cgi>. (accessed date October 01, 2022).

Rychlik W. 2007. OLIGO 7 primer analysis software. *Humana Press In PCR primer design*, New York, USA, pp: 35-59.

Sabino EC, Buss LF, Carvalho MPS. 2021. Resurgence of COVID-19 in manaus brazil despite high seroprevalence. *The Lancet*, 397(10273): 452-455.

Sahoo JP, Samal KC. 2021. World on alert: WHO designated south

- african new COVID strain (Omicron/B.1.1.529) as a variant of concern. *Biotica Res Today*, 3(11): 1086–1088.
- Shi F, Wang J, Shi J, Wu Z, Wang Q, Tang Z, Shen D. 2021. Review of artificial intelligence techniques in imaging data acquisition segmentation and diagnosis for covid-19. *IEEE Rev Biomed Eng*, 14 4-15.
- Shu Y, McCauley J. 2017. GISAID: Global initiative on sharing all influenza data - from vision to reality. *Eurosurveillance*, 22(13): 30494.
- Stothard P. 2000. The sequence manipulation suite: JavaScript programs for analyzing and formatting protein and DNA sequences. *BioTechniques*, 28(6): 1102–1104.
- Tegally H, Wilkinson E, Giovanetti M. 2021 March. Detection of a SARS-CoV-2 variant of concern in South Africa. *Nature*, 592(7854): 438–443.
- Togrul M, Arslan H. 2022. Detection of SARS-CoV-2 main variants of concerns using deep learning. *Proceeding of Innovations in Intelligent Systems and Applications Conference*, September 07-09, Antalya, Türkiye, pp: 32.
- UCSC In-silico PCR. 2022. URL: <https://genome.ucsc.edu/cgi-bin/hgPcr>. (accessed date October 01, 2022).
- Uriu K, Kimura I, Shirakawa K, Takaori-Kondo A, aki Nakada T, Kaneda A, Sato K. 2021. Neutralization of the SARS-CoV-2 mu variant by convalescent and vaccine serum. *New England J Med*, 385(25): 2397–2399.
- Volz E, Mishra S, Chand M, Barrett J. 2021. Assessing transmissibility of SARS-CoV-2 lineage b.1.1.7 in England. *Nature*, 593(7858): 266–269.
- Wink PL, Volpato FCZ, Monteiro FL, Willig JB, Zavascki AP, Barth AL, Martins AF. 2021. First identification of SARS-CoV-2 lambda (c.37) variant in southern Brazil. *Infect Control Hospital Epidemiol*, 2021: 1–2.
- Xu Y, Ye W, Song Q, Shen L, Liu Y, Guo Y, Liu G, Wu H, Wang X, Sun X, Bai L, Luo C, Liao T, Chen H, Song C, Huang C, Wu Y, Xu Z. 2022. Using machine learning models to predict the duration of the recovery of COVID-19 patients hospitalized in Fangcang shelter hospital during the Omicron BA. 2.2 pandemic. *In Frontiers Med*, 9: 1001801.
- Yaniv K, Ozer E, Shagan M, Lakkakula S, Plotkin N, Bhandarkar NS, Kushmaro A. 2021. Direct RT-QPCR assay for sars-cov-2 variants of concern (alpha b.1.1.7 and beta b.1.351) detection and quantification in wastewater. *Environ Res*, 201: 111653.
- Zoabi Y, Deri-Rozov S, Shomron N. 2021. Machine learning-based prediction of COVID-19 diagnosis based on symptoms. *NPJ Digital Medi*, 4(1): 3.



INVESTIGATION OF USE OF HYDROCHARS OBTAINED FROM LEGUME WASTES AS FUEL AND THEIR CONVERSION INTO ACTIVATED CARBON FOR AMOXICILLIN REMOVAL


İsmail Cem KANTARLI^{1*}

¹Ege University, Atatürk Medical Technology Vocational Training School, 35100, Izmir, Türkiye

Abstract: Legume wastes, pinto bean peel (PBP) and pea shell (PS), were hydrothermally carbonized in subcritical water at various temperatures (200-240 °C) with the aim of obtaining a solid fuel, hydrochar. Fuel characteristics and chemical properties of hydrochars were determined by standard fuel analysis methods. Hydrochar yield decreased sharply with the increase of temperature due to the enhanced degradation of legume wastes. The weight percent of initial carbon in the legume wastes retained in the obtained hydrochars was lower than those in the literature due to the low hydrochar yields. The effect of temperature on carbon content and hence higher heating value (HHV) of hydrochar became noticeable at 240°C. As a result of this effect, bituminous coal-like and lignite-like hydrochars with HHV of 31.2 and 28.1 MJ.kg⁻¹ were obtained from PBP and PS, respectively. Hydrochars obtained at 220 °C were chemically activated with ZnCl₂ to produce activated carbons (PBP-AHC and PS-AHC). The activated carbons were characterized by elemental analysis, FTIR spectroscopy, BET surface area analysis and Scanning Electron Microscopy (SEM). BET surface area, total pore volume, and mesopore volume of PS-HC were determined as 1205 m². g⁻¹, 0.686 m³. g⁻¹ and 0.144 m³. g⁻¹, respectively. PBP-AHC was found to have higher BET surface area (1350 m². g⁻¹), total pore volume (0.723 m³. g⁻¹), and mesopore volume (0.249 m³. g⁻¹) than PS-AHC. Activated carbons were tested as adsorbent for removal of amoxicillin (AMX) from aqueous solutions with the batch adsorption studies carried out at different initial concentrations, adsorbent dosage, and contact time. The compatibility of the adsorption data with the Langmuir and Freundlich isotherm models was checked to determine the adsorption capacity of activated carbons. The maximum Langmuir adsorption capacity (Q_{max}) was calculated as 188.7 and 70.9 mg. g⁻¹ for PBP-AHC and PS-AHC, respectively. Adsorption kinetic analysis revealed that AMX adsorption on PBP-AHC and PS-AHC best fits with the pseudo-second order kinetic model. AMX adsorption was found to be faster on PBP-AHC than PS-AHC due to its higher surface area and more mesoporous character. ZnCl₂ activation of PBP-derived hydrochar produced a potential adsorbent for amoxicillin removal.

Keywords: Hydrochar, Activated carbon, Adsorption, Amoxicillin, Pinto bean peel, Pea shell

*Corresponding author: Ege University, Atatürk Medical Technology Vocational Training School, 35100, Izmir, Türkiye
E mail: ismail.cem.kantarli@ege.edu.tr (I.C. KANTARLI)

İsmail Cem KANTARLI  <https://orcid.org/0000-0002-5911-3152>

Received: August 21, 2023

Accepted: September 26, 2023

Published: October 15, 2023

Cite as: Kantarlı İC. 2023. Investigation of use of hydrochars obtained from legume wastes as fuel and their conversion into activated carbon for amoxicillin removal. *BSJ Eng Sci*, 6(4): 486-501.

1. Introduction

Renewable energy is a fast growing energy sector and biomass is the only renewable energy source that can be used as a carbon-based fuel. However, the direct use of biomass as fuel is not economical due to its high pre-treatment cost, low energy density and low calorific value (Akogun and Waheed, 2019). In order for all kinds of biomass to be processed in the same combustion plant, they need to have a homogeneous structure and converting them into biochar would provide this condition. Two different thermochemical processes, dry and wet carbonization, are generally applied at low temperatures to transform biomass into stable, energy-intensive solid, biochar. With dry carbonization (DC), biomass is thermally decomposed in an inert gas atmosphere at low temperatures (200-300 °C) in short residence times (30-60 minutes). At the end of the process, biochar with a mass yield of 60-90% and an energy yield of 80-95% is obtained. Various studies exist

in the literature which investigated the effects of parameters such as process temperature, heating rate and residence time on the mass yield, physicochemical properties and fuel properties of biochar obtained from different types of biomass (Yan et al., 2009; Ciolkosz and Wallace, 2011; Larsson et al., 2013; Satpathy et al., 2014). Production of biochar with DC of biomass with high water content is limited by the cost of pre-drying of the biomass. On the other hand, using wet carbonization method, also known as hydrothermal carbonization (HTC), it is possible to convert biomass containing up to 80% water to hydrochar, which has a higher energy density than biomass, under subcritical water conditions (usually in the temperature range of 180-260 °C, ambient pressure < 22.1 MPa), under inert gas atmosphere and with short residence times without the need for drying. The resulting hydrochars have combustion characteristics and caloric values similar to lignite coal, and also better dewatering properties (Funke et al., 2013). Temperature



is the most effective process parameter in HTC. Residence time and the biomass: water ratio of the fed waste are the other parameters effective on the fuel characteristics of the produced hydrochar (Heilmann et al., 2010, 2011). Since water is a very good solvent under subcritical conditions, it can dissolve inorganic substances in biomass. Therefore, it is possible to obtain hydrochars with low ash content after HTC (Pala et al., 2014). Low ash content will reduce the tendency of hydrochars to cause problems such as fouling and slagging in combustion systems and will increase their preferability as a solid fuel. Dried legumes are used as a cheap protein and calorie source worldwide and especially in developing countries. Pinto bean (*Phaseolus vulgaris* L.) and pea (*Pisum sativum* Linn.) are the most widely grown legumes worldwide (Verma et al., 2011). They are also grown in abundance in Türkiye. The peel remaining after the separation of pinto bean (PBP) has a dietary fiber content of approximately 67% (Martínez-Castaño et al., 2020). It has been stated that the remaining part of the shell after the separation of pea grain (PS) has a dietary fiber content of approximately 50% and is a perishable waste (Mateos-Aparicio et al., 2010). PBP and PS to be used in the study are both lignocellulosic wastes and have high water content (~77%). These features make these wastes interesting as raw material for the production of solid fuel, hydrochar, by HTC. While there is no study on the HTC of PBP in the literature, only one study on the HTC of PS exist in the literature (Dong et al., 2019).

There are many studies in the literature on the production of activated carbon from different biomass/waste until today (Horikawa et al., 2010; Lim et al., 2010; Rashid et al., 2016; Limousy et al., 2017; Rodrigues et al., 2020; Yi et al., 2021). The common goal in these studies was generally to reduce the cost of activated carbon production. In the production of activated carbon from biomass, two methods are generally applied, namely chemical activation and physical activation. Physical activation method is applied in commercial activated carbon production (Yi et al., 2021). However, more studies on chemical activation exist in the literature due to its advantages such as lower process temperature, higher efficiency, more controllable pore formation and size compared to physical activation. In these studies, H_3PO_4 , $ZnCl_2$ and alkali hydroxides were generally used as chemical activators (Limousy et al., 2017; Rodrigues et al., 2020; Rashid et al., 2016).

The properties required in activated carbon depend on its application area. For example, high mesoporosity is required for its usage as adsorbent in dye adsorption (Swan and Zaini, 2019), while surface functional groups are required for metal adsorption (Yang et al., 2019). It has been observed in the previous studies that pre-treatment of the biomass before activation improves the surface properties of the obtained activated carbon. It has been determined that the activation of biochar obtained by dry carbonization with strong acids forms carboxylic groups on its surface and increases the surface area due to its

micropores (Hadjittofi et al., 2014; Qian et al., 2013; Iriarte-Velasco et al., 2016). For example, it was observed that the activation of biochar obtained from cactus fibers with HNO_3 increased the carboxyl groups on the surface, increasing the Cu^{2+} binding capacity (Hadjittofi et al., 2014). On the other hand, it has been reported that the activation of biochar obtained from glass wood with H_2O_2 increases the adsorption capacity of metal ions by increasing the cation exchange capacity due to the oxygenated groups on the surface (Huff and Lee, 2016). Similarly, activation of biochar with metal hydroxides has been observed to increase the adsorption capacity of metal ions by increasing the number of oxygenated groups, surface area and porosity in the obtained activated carbon (Petrović et al., 2016; Goswami et al., 2016; Hamid et al., 2014). In the studies of Angin et al., activated carbons with a surface area of $1277\text{ m}^2\text{ g}^{-1}$ and a surface area of $801\text{ m}^2\text{ g}^{-1}$ were obtained from biochars activated with KOH , H_3PO_4 and $ZnCl_2$, and these active carbons has been effective in removing reactive dyestuffs from water (Angin et al., 2013a, 2013b).

In addition to biochars, hydrochar can also be used as raw material in the production of activated carbon. The difference of hydrochars from biochars is that they have less aromatic structure and generally more alkyl groups. A study by Sun et al. showed that hydrochars have the capacity to adsorb more amount of polar and non-polar organics than biochars (Sun et al., 2011). In some of the studies, hydrochars were directly used in the removal of dyestuffs (Parshetti et al., 2014; Flora et al., 2013), copper and cadmium (Regmi et al., 2012), and Pb^{2+} and Cd^{2+} (Elaiwu et al., 2014) from water. Studies focusing on the activation of hydrochars also exists in literature. Roman et al. found that the production of activated carbon with controlled surface chemistry and porosity from hydrochar can be achieved by physical activation with carbon dioxide (Roman et al., 2013). Pari et al also produced porous carbon spheres from hydrochars by chemical activation with KOH (Pari et al., 2014). Similarly, Laginhas et al. reported that a combination of HTC and $CaCO_3$ or K_2CO_3 activation can successfully produce activated carbon from chitosan (Laginhas et al., 2016). Sevilla and Fuertes reported that activated carbons with very high surface area can be produced by HTC of polysaccharide and wood powder followed by chemical activation with KOH (Sevilla and Fuertes, 2011).

Considering other studies on the production of activated carbon by chemical activation of hydrochars, it was found that $NaOH$ activation of coconut shell hydrochar produced activated carbon suitable for cationic dye adsorption (Islam et al., 2017); $FeCl_3$ activation of *Salix psammophila* hydrochar produced activated carbon with high mesoporosity and a surface area of $349\text{ m}^2\text{ g}^{-1}$ (Zhu et al., 2014); H_3PO_4 activation of orange peel hydrochar produced activated carbon with mesopore volume of $0.102\text{ cm}^3\text{ g}^{-1}$ (Fernandez et al., 2015); $NaOH$ activation of waste tea hydrochar produced activated carbon with mesopore volume of $0.21\text{ cm}^3\text{ g}^{-1}$ and surface area of

368.92 m².g⁻¹ (Islam et al., 2015). Unlike the above studies, when wet carbonization of coconut shell in the presence of ZnCl₂ was performed, it was found that the mesopore volume increased by 67% (Jain et al., 2014). Eom et al., in his study, impregnated hydrochar obtained from brewed black tea waste at 200 °C for 12 hours with KOH in varying ratios of hydrochar: activating agent (between 1:2 and 1:4) and activated them at pyrolysis temperatures of 600 °C and 700 °C (Eom et al., 2021). As a result of activation, they have obtained active carbons with BET surface area varying in the 174 to 1398 m².g⁻¹ range and micropore volume varying in the 0.05 to 0.69 cm³.g⁻¹ range. PBP and PS, which are the wastes to be used in this study with high water content (>77%), can be similarly evaluated as feedstock in the production of activated carbon with a two-step process.

Pharmaceutical compounds, especially antibiotics, are widely used in medical treatment of both humans and animals throughout the world and have emerged as a new class of pollutants. They bio-accumulate in the waters and pose a risk to the aquatic ecosystem, since they are released to water sources without being completely metabolized in the human/animal body and degrade very little after they are released (Yu et al., 2016; Garoma et al., 2010). Therefore, it is necessary to remove pharmaceutical substances from wastewater. Methods used for the removal of pharmaceuticals from wastewater include techniques such as ozonation, membrane filtration, photodegradation and biological treatment. The adsorption technique, which is more advantageous in terms of efficiency and cost compared to these techniques, is also frequently used for the removal of pharmaceutical substances from wastewater (Hayati et al., 2018). It is also stated in the literature that especially activated carbon adsorption is an effective approach in the removal of pharmaceuticals from wastewater (Redding et al., 2009). Amoxicillin (AMX) is a common penicillin-type antibiotic which is used in a wide spectrum against various bacteria in both human and veterinary medicine. It was reported to be present in surface water, domestic, industrial and hospital wastewater in concentration ranges of ng L⁻¹ to mg L⁻¹ (Elmolla and Chaudhuri, 2010; Zuccato et al., 2010; Serna-Galvis et al., 2017). As mentioned for pharmaceuticals removal above, adsorption process was

reported to be more efficient than the other methods also for AMX removal. A number of studies exist in literature using different adsorbents including commercial granular activated carbon (De Franco et al., 2017), lignocellulosic waste based activated carbon (Pezoti et al., 2016; Laksaci et al., 2023; Limousy et al., 2017), carbon nanotubes (Balarak et al., 2016; Unutkan et al., 2018; Fazelirad et al., 2015), magnetic activated carbon (Saucier et al., 2017), magnetic graphene oxide (Moradi, 2015; Kerkez-Kuyumcu et al., 2016), metal-organic framework (Abazari and Mahjoub, 2018) and activated hydrochar (Ajala et al., 2023; Li et al., 2017). However, using activated hydrochar obtained from PBP and PS as adsorbent for AMX removal has not been studied before.

In this study, utilization of PBP and PS as energy feedstock and adsorbent was aimed by the application of a two-step process which followed the hydrothermal carbonization and chemical activation sequence. The aim of first step was to homogenize these wastes by converting them into hydrochars and to examine the feasibility of their direct use as fuel or use as precursor for activated carbon production. Variation of the fuel characteristics of derived hydrochars was investigated with respect to temperature. In the second step, feasibility of producing activated carbon from hydrochar by ZnCl₂ activation was investigated with the motivation of using it as adsorbent in treatment of wastewater streams. The chemical and morphological properties of activated hydrochars were compared according to the legume waste type. Additionally, AMX adsorption studies were carried out to check the potential of activated hydrochars as adsorbent and to examine the relation between their properties and AMX adsorption capacities.

2. Materials and Methods

2.1. Materials

All the chemicals and reagents used in this research were of analytical grade. The legume wastes, PBP and PS, were supplied by a local restaurant in Bornova, Izmir. PBP and PS had solid content of 19.6% and 22.9%, respectively. The legume wastes were dried at 60 °C overnight. Some properties of dried legume wastes were given in Table 1.

Table 1. Some properties of legume wastes

| Legume waste | Proximate analysis, (dry basis, wt. %) | | | | Ultimate analysis, (dry basis, wt. %) | | | | | HHV (MJ/kg) |
|--------------|--|-----|--------------|------------|---------------------------------------|------|------|------|-------|-------------|
| | Volatile matter | Ash | Fixed carbon | Fuel ratio | C | H | N | S | O | |
| PBP | 78.4 | 3.8 | 17.8 | 0.23 | 44.04 | 6.06 | 1.07 | 0.00 | 43.79 | 22.30 |
| PS | 77.5 | 5.0 | 17.5 | 0.23 | 43.39 | 5.75 | 4.19 | 0.02 | 42.85 | 21.41 |

HHV= higher heating value

As can be seen from Table 1, legume wastes have high volatile matter content and low fixed carbon content. High volatile matter contents of legume wastes is a disadvantage for their utilization as feedstock in existing

gasification plants since it leads to tar formation (Maitlo et al., 2022). High volatile matter might cause a rapid and incomplete burning and hence emissions of high amount of pollutants such as CO, polycyclic aromatic

hydrocarbons, unburned products, etc. (Vassilev et al., 2015).

2.2. Hydrothermal Carbonization Experiments

A 0.5 L stainless steel autoclave with a magnetic stirrer was used for HTC experiments (Balmuk et al., 2023). Both heating and cooling system exists in the oven. A PID controller regulates and fixes the process temperature. It was observed in a previous study that HTC of biomass at temperature below 200 °C led to ineffective carbonization of biomass and produced hydrochar which had TG curve similar to that of biomass (Kantarli et al., 2016). Therefore, HTC experiments were performed at reaction temperature of 200, 220 and 240 °C at autogeneous pressure as duplicates. The heating rate was 5 °C. min⁻¹. The water: solid ratio was selected as 7: 1 in order to provide homogenous stirring of the mixture in autoclave reactor. 25 g of dried legume waste was mixed with 175 mL of distilled water. After loading the dried legume waste + water mixture to the reactor, the reactor was sealed. Next, the sealed reactor was purged with N₂ to remove the air inside, heated to the pre-determined temperature and held at this temperature for 60 min. At the end of 60 min., the reactor was cooled and the gaseous products were released to the atmosphere. The solid product, hydrochar, was separated from aqueous phase by filtration of the slurry mixture inside the reactor. The hydrochar was washed with 100 mL water and dried at 105 °C for 24 h. The dried hydrochar was weighed and the mass yield was calculated accordingly. Hydrochars were abbreviated in the order of "feedstock type-HC-temperature". For example, PBP-HC-200 corresponds to the hydrochar obtained from pinto bean peel at 200 °C for 60 min.

2.3. Chemical Activation of Hydrochars

Hydrochars derived from legume wastes, PBP-HC-220 and PS-HC-220, were chemically activated by ZnCl₂. ZnCl₂ activation experiments were done once without replications. ZnCl₂:precursor ratio was chosen as 1:1 in order to consume less chemical. As the first step of activation, ZnCl₂ solution was prepared by dissolving 10 g of ZnCl₂ in approximately 20 mL of water. 10 g of hydrochar was impregnated with the ZnCl₂ solution. The mixture was dried in an oven at 100 °C overnight. The dried mixture was loaded in a pyrolysis reactor and activated at 500 °C under N₂ flow (100 mL/min) for 1 h. At the end of 1 h, the reactor was cooled. Then, the reactor residue was collected in a boiling flask, mixed with 150 mL of 10% HCl solution and refluxed for 1 h. Next, the mixture was filtered under vacuum. The acid treated solid residue separated from the mixture was washed with hot distilled water until no chloride ions was observed in filtrate. Finally, the activated hydrochar samples (PBP-AHC and PS-AHC) were dried at 100 °C for 24 h and sieved to the particle size <100 µm for AMX batch adsorption studies.

2.4. Analysis

The ash content and the volatile matter content of legume wastes and their hydrochars were determined according to the standard methods NREL/TP-510-42622 and ASTM D3175-89a, respectively. C, H, N, S content of legume

wastes and their hydrochars were determined by a ELEMENTAR Vario Micro Cube Organic elemental analyzer. The higher heating value (HHV) of legume wastes and their hydrochars were calculated according to the Equation 1 given in the literature (Channiwala and Parikh, 2002), which is as follows (equation 1):

$$HHV, \left(\frac{MJ}{kg}\right) = 0.3491 * C + 1.1783 * H + 0.1005 * S - 0.1034 * O - 0.0151 * N - 0.0211 * Ash \quad (1)$$

C, H, O, N, S, and Ash correspond to the mass percentages of carbon, hydrogen, oxygen, nitrogen, sulphur, and ash in the sample, respectively.

The FTIR spectra of legume wastes, hydrochars and activated carbons were taken with ATR-FTIR spectrometer (Spectrum 100, PerkinElmer, Waltham, MA, USA). Brunauer, Emmett and Teller (BET) surface area and pore volume of activated carbons were analyzed by performing N₂ adsorption at 77 K (Micrometrics Gemini V). Degassing of activated carbon was carried out at 300 °C for a duration of 3 h before the measurement. The surface morphologies of legume wastes, hydrochars, and activated carbons were examined by Scanning Electron Microscope (SEM). A FEI QUANTA 250 FEG was used to take SEM images of samples at different magnitudes.

2.5. Adsorption Tests

The potential of activated hydrochars for AMX removal was checked with the batch adsorption studies carried out at different initial concentrations (75–250 mg.L⁻¹), times (5 min–1440 min) and activated carbon dosage (0.5–3 g.L⁻¹).

In each experiment, 25 mL of AMX solution was poured into a 50 mL flask containing activated carbon and no pH adjustment was done. The suspensions were placed on an orbital shaker and shaken at 200 rpm at room temperature for pre-determined period of time. At the end of time period, the suspension was filtered through a filter paper for separation of activated carbon from solution of residual AMX, filtrate. The filtrates was analyzed for residual AMX concentration using a UV-vis spectrometer (UV-160A, Shimadzu) at a wavelength of 196 nm.

The adsorbed amount of AMX per unit mass of activated carbon at any time *t* (*Q_t*) and the percentage of removal efficiency were calculated by equations 2 and 3 as follows (Liu et al., 2016):

$$Q_t = \frac{C_i - C_f}{m} \times V \quad (2)$$

$$Removal\ efficiency, \% = 100 \times \frac{C_i - C_f}{C_i} \quad (3)$$

where *C_i* (mg.L⁻¹) is initial concentration, *C_f* (mg.L⁻¹) is the concentration at the end of batch experiment, *V*(L) is the volume of AMX solution and *m* (g) is the mass of activated carbon.

Kinetic data was obtained by batch experiments varying the time from 5 to 1440 min and analysed using pseudo-first order kinetic model, pseudo-second order kinetic

models and intra-particle diffusion model. The mathematical equations of pseudo-first order kinetic model, pseudo-second order kinetic model and intra-particle diffusion kinetic model are given in equations 4, 5, 6, respectively, as follows (Chayid and Ahmed, 2015):

$$\ln(Q_e - Q_t) = \ln Q_e - k_1 t \quad (4)$$

$$\frac{t}{Q_t} = \frac{1}{k_2 Q_e^2} - \frac{t}{Q_e} \quad (5)$$

$$Q_t = k_i t^{0.5} + C_i \quad (6)$$

Q_t and Q_e (mg.g⁻¹) are amount of AMX adsorbed at any time t (min) and at equilibrium time, respectively. k_1 , k_2 and k_i are rate constants of first order, pseudo second order, and intra-particle diffusion kinetic model, respectively. C_i (mg.g⁻¹) is the boundary layer thickness.

Adsorption equilibrium experiments were carried out with AMX solutions at different initial concentrations (75-250 mg.L⁻¹) for an equilibrium time of 24 h in order to determine the AMX adsorption capacity of activated carbons in equilibrium state. At the end of experiments, AMX equilibrium concentration, C_e and quantity of AMX adsorbed by 1 g activated carbon, Q_e were determined. The relation between C_e and Q_e was established using Equations 7 and 8 specific to Freundlich and Langmuir adsorption isotherm models, respectively, given as follows (Moussavi et al., 2013):

$$\frac{C_e}{Q_e} = \frac{1}{K_L Q_{max}} + \frac{1}{Q_{max}} C_e \quad (7)$$

$$\log Q_e = \log K_F + \frac{1}{n} \log C_e \quad (8)$$

where Q_{max} is the maximum monolayer adsorption capacity, K_L is the equilibrium constant, K_F is the Freundlich constant, an empirical parameter related with the adsorption capacity, and $1/n$ is the heterogeneity factor taking values usually in the range of 0-1. The $1/n$ values closer to 0 indicates a more heterogeneous adsorbent surface (Edet and Ifebugue, 2020). In addition, separation factor (R_L), which is specific to Langmuir model, was calculated by equation 9 given below (Moussavi et al., 2013):

$$R_L = \frac{1}{1 + C_i K_L} \quad (9)$$

The value of R_L helps to identify adsorption process as irreversible ($R_L = 0$), favorable ($0 < R_L < 1$), linear ($R_L = 1$), or unfavorable ($R_L > 1$) (Araújo et al., 2021).

3. Results and Discussion

3.1. Mass Yields and Carbon Recovery of Hydrochars

The mass yield and carbon recovery of hydrochars produced from legume wastes at different process temperature is given in Figure 1.

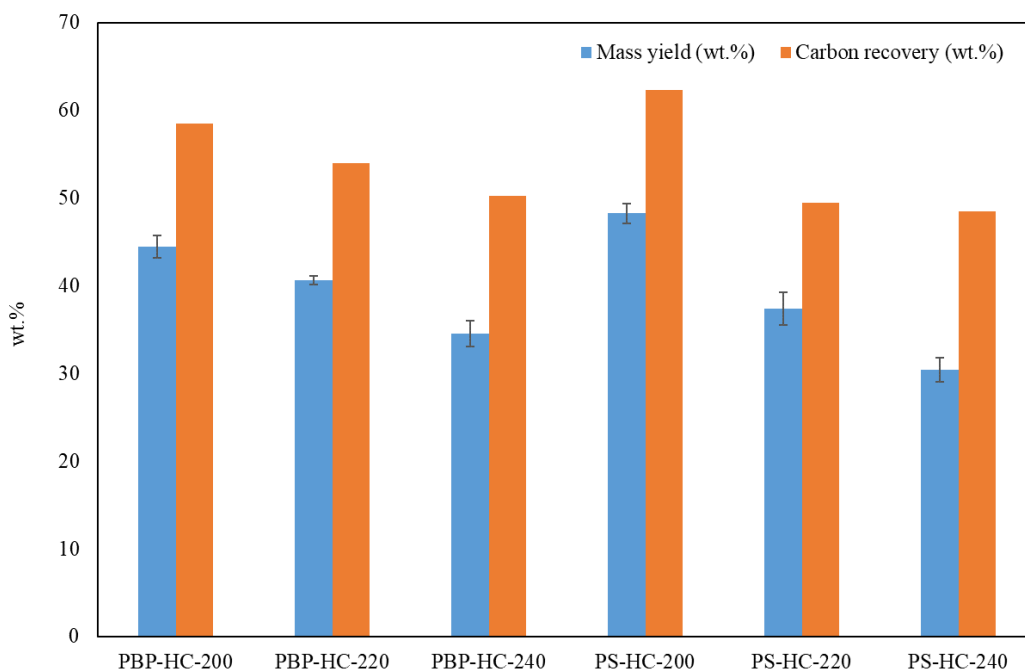


Figure 1. Mass yield and carbon recovery of hydrochars produced from dried legume wastes at different temperatures (dry basis) (wt.%).

As can be seen from Figure 1, a sharp decrease is observed in hydrochar yield with the increase of process temperature. It must be noted that PBP and PS have high holocellulose content which were reported as 79% (De Sa

et al., 2022) and 61% (Verma et al., 2011) in the literature, respectively. Therefore, the sharp decrease of hydrochar yield with increasing process temperature was attributed to the enhanced degradation of legume wastes occurring

mainly as the hydrolysis of hemicellulose and cellulose in legume wastes (Kambo and Dutta, 2015; Makela et al., 2015). The carbon recovery of hydrochars was also shown in Figure 1. The weight percentage of carbon in legume waste recovered in hydrochar varied in the range of 48-57 wt% and 44-63 wt% in case of PBP and PS, respectively. These values were found to be lower than the carbon recovery results given in the literature (Kantarli, 2023;

Balmuk et al., 2023; Pala et al., 2014; Hoffmann et al., 2019) mainly due to the lower hydrochar yields obtained as a result of degradation of the higher holocellulose content of legume wastes in this study.

3.2. Fuel Properties of Hydrochars

Proximate, elemental, and energy analysis results of hydrochars derived from legume wastes at different process temperatures are given in Table 2.

Table 2. Proximate, elemental and energy analysis of hydrochars (dry basis)

| | Proximate analysis, %wt., dry basis | | | | Elemental analysis, %wt., dry basis | | | | | Energy analysis | | |
|------------|-------------------------------------|------|------|------|-------------------------------------|------|------|------|-------|-----------------|------|-------|
| | Ash | VM | FC | FR | C | H | N | S | O | HHV [MJ/kg] | EDR | EY |
| PBP-HC-200 | 1.0 | 72.9 | 26.1 | 0.36 | 56.86 | 5.98 | 1.12 | 0.00 | 31.55 | 26.76 | 1.20 | 53.29 |
| PBP-HC-220 | 1.1 | 67.9 | 30.9 | 0.45 | 58.26 | 5.68 | 1.10 | 0.00 | 29.56 | 26.89 | 1.20 | 48.97 |
| PBP-HC-240 | 1.2 | 59.8 | 39.0 | 0.65 | 70.12 | 5.86 | 1.49 | 0.00 | 18.05 | 31.21 | 1.40 | 42.46 |
| PS-HC-200 | 4.5 | 67.9 | 27.6 | 0.41 | 57.13 | 5.38 | 3.97 | 0.00 | 32.50 | 25.77 | 1.21 | 58.19 |
| PS-HC-220 | 5.4 | 65.5 | 29.1 | 0.44 | 57.66 | 5.61 | 3.42 | 0.00 | 32.17 | 26.27 | 1.23 | 49.42 |
| PS-HC-240 | 4.5 | 65.5 | 30.0 | 0.46 | 63.07 | 5.57 | 4.14 | 0.01 | 26.01 | 28.06 | 1.31 | 39.97 |

VM= volatile matter; FC= fixed carbon; FR (Fuel ratio)= FC / VM; HHV= higher heating value; EDR (energy densification ratio)= HHVhydrochar / HHVbiomass; EY (energy yield) = mass yield × EDR; O% = 100 - (C+H+N+S+Ash).

The ash contents of PBP-derived hydrochars were lower than that of PBP owing to the solubility of inorganics under subcritical water conditions (Tables 1-2). Calculations depending on the hydrochar yield and ash contents revealed that 12-9 % of initial ash in PBP were retained in the resultant hydrochar depending on the process temperature. On the contrary to PBP-derived hydrochars, PS-derived hydrochars had ash contents only slightly lower/higher than that of PS due to the less solubility of inorganics under subcritical water conditions. Therefore, percentage of initial ash retained in PS-derived hydrochars were calculated to be in the range of 43-27% which were much higher than that retained in PBP-derived hydrochars. As can be seen from Table 2, HTC decreased the VM content of legume wastes, while it increased the FC content of legume wastes. This indicated the improvement of the carbon stability by HTC treatment. In case of PS, VM content of obtained hydrochar decreased only slightly (from 67.9% to 65.5%) and its FC content increased slightly (from 27.6% to 30.0%) with increasing temperature from 200 °C to 240 °C. Hence, HTC of PS led to the limited increase of FR of raw waste only from 0.23 to 0.44 which was still lower than 0.6 reported for lignite coal (Odeh, 2015). Compared to PS, VM content of PBP-derived hydrochar decreased pronouncedly from 72.9% to 59.8%, while its FC content increased pronouncedly from 26.1% to 39.0% with increasing temperature from 200°C to 240°C. HTC of PBP led to a higher increase of FR of raw biomass from 0.23 to 0.65 which is even higher than 0.6 reported for lignite coal (Odeh, 2015). Hydrochars had higher carbon content and lower oxygen content than legume wastes as a result of HTC. The effect of HTC temperature on carbon content of hydrochar was

noticeable at 240 °C. C content of PBP-derived hydrochar and PS-derived hydrochar increased to 70.1% and 63.1% with the increase of HTC temperature to 240 °C, respectively. C content of PS-HC-240 was found to be higher than those of hydrochars obtained from pea pods at 230 °C for a duration of 30-480 min (Dong et al., 2019). The variation of HHV and ED of hydrochars showed similarity with the variation of carbon content. HHV of PBP-HC-240 was found to be higher than that of PS-HC-240 due to its higher C content. Comparison of the results with those in literature revealed that HHV of PBP-HC-240 was comparable to HHVs of hydrochars obtained by HTC of two-phase olive mill waste at 240-260 °C for 1-4 h (Balmuk et al., 2023), walnut and hazelnut shells at 250 °C for 24 h. (Pavkov et al., 2022) and from food waste at 230-260 °C for 30 min. (McGaughy and Reza, 2018) and higher than HHVs of hydrochars obtained by HTC of hornbeam wood at 275 °C for 1 h (Ercan et al., 2023), pineapple peelings at 250-270 °C for 5h (Bote et al., 2023), loquat seeds at 150-250 °C for 2-6 h (Kalderis et al., 2023), sunflower stalks at 180-280 °C for 45 min. (Nawaz and Kumar, 2023), cannabis waste at 170-230 °C for 1 h (Kanchanatip et al., 2022) and agricultural wastes at 180-260 °C for 1 h. (Wu et al., 2023). EY of PBP-derived hydrochars and PS-derived hydrochars decreased from 53.3% to 42.5% and from 58.2 % to 40.0 % with increasing temperature. The decreasing trend of EY with the increase of temperature, which was consistent with the literature (Kanchanatip et al., 2022; Kalderis et al., 2023), was mainly attributed to the dominance of reduction in mass yield over the increase of ED. EY values of hydrochars obtained in this study was similar to those observed by Kalderis et al. (2023) owing to the low mass

yield, while they were lower than those observed by Kanchanatip et al. (2022) owing to much higher mass yield obtained in their study. The atomic H/C ratio versus O/C ratio of hydrochars were plotted on the van Krevelen

diagram, given in Figure 2, in order to follow the carbonization degree and identify the main reaction pathways during HTC.

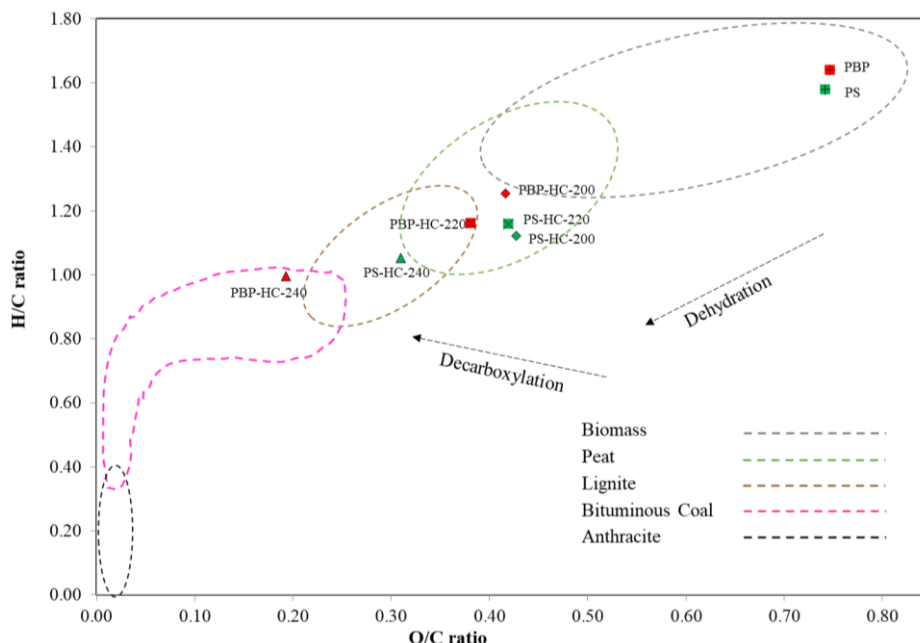


Figure 2. Van Krevelen diagram of hydrochars produced from legume wastes at different temperatures.

Examination of Figure 2 shows that dehydration reactions mainly occur at 200 °C, while decarboxylation reactions start to accompany dehydration reactions at 220 °C during HTC of PS. On the other hand, decarboxylation reactions accompany dehydration reactions at each temperature during HTC of PBP. Therefore, PBP-derived hydrochars had better carbonization degree than PS-derived hydrochars. As can be seen from Figure 2, PBP-HC-240 fall within the H/C and O/C ratio range of bituminous coal, while PS-HC-240 could only fall within the H/C and O/C ratio range of lignite. PS-HC-200 and PS-HC-220 fall in the region of peat which is consistent with the results obtained from HTC of pea pods at less severe conditions by Dong et al. (2019).

3.3 Activated Carbon Characteristics

PBP-HC-220 and PS-HC-220 were selected as activated carbon precursor in the ZnCl₂ activation experiments at 500 °C in order to obtain activated carbon with developed porosity at acceptable yield. Activated carbons obtained from PBP-derived and PS-derived hydrochars were abbreviated as PBP-AHC and PS-AHC, respectively.

3.3.1. Elemental composition and yields of activated carbons

Elemental analysis and mass yields of PBP-AHC and PS-AHC are presented in Table 3. Mass yield of activated carbon was calculated as the ratio of weight of activated carbon to weight of dried legume waste.

Table 3. Elemental analysis and mass yields of PBP-AHC and PS-AHC

| | Elemental analysis, wt% | | | | Yield, wt% |
|---------|-------------------------|------|------|-------|------------|
| | C | H | N | O | |
| PBP-AHC | 88.43 | 2.59 | 1.86 | 7.12 | 21.2 |
| PS-AHC | 82.02 | 2.91 | 4.63 | 10.44 | 22.6 |

The mass yields of PBP-AHC and PS-AHC were found as 21.2 and 22.6 %, respectively (Table 3). These mass yields were lower than those obtained by chemical activation of lignocellulosic waste-derived hydrochars given in the literature (Kantarli, 2023; Chen et al., 2017). Activation of hydrochars resulted in further increase of C contents accompanied by the decrease of H and O contents of resultant activated carbons which implied the enhancement of aromaticity in hydrochars.

3.3.2. BET surface area and pore volumes of activated carbons

BET surface area, mesopore volumes, and pore volumes of PBP-AHC and PS-AHC are given in Table 4. ZnCl₂ activation seems to be effective on the porosity development of legume waste-derived hydrochars (Table 4). As a result, both of the activated carbons had high surface area and total pore volume, which were comparable to or higher than those of activated carbons obtained by ZnCl₂ activation of wood sawdust hydrochar (Nirmaladevi and

Palanisamy, 2021), brewed tea waste hydrochar (Kantarli, 2023); KOH activation of garlic peel hydrochars (Huang et al., 2019) and raw coffee husk hydrochar (Tran et al, 2021) and K₂CO₃ activation of rice straw hydrochar (Liu et

al., 2014). PBP-AHC was found to have a higher BET surface area and more developed porosity than PS-AHC. This result was consistent with the higher C content observed for PBP-AHC (Table 3).

Table 4. BET surface area, mesopore volume, and pore volumes of PBP-AHC and PS-AHC

| | BET Surface area (m ² .g ⁻¹) | Mesopore area (m ² .g ⁻¹) | Total pore volume (cm ³ .g ⁻¹) | Mesopore volume (cm ³ .g ⁻¹) |
|---------|--|---|--|--|
| PBP-AHC | 1350 | 399 | 0.723 | 0.249 |
| PS-AHC | 1205 | 152 | 0.686 | 0.144 |

3.4. FTIR Analysis of Legume Wastes, Hydrochars and Activated Carbons

FTIR analysis of legume wastes, their hydrochars obtained at 200°C and activated carbons was performed in order to

detect the changes of chemical structure during HTC of legume wastes and chemical activation of hydrochars, respectively. FTIR spectra of legume wastes, their hydrochars, and activated carbon are given in Figure 3.

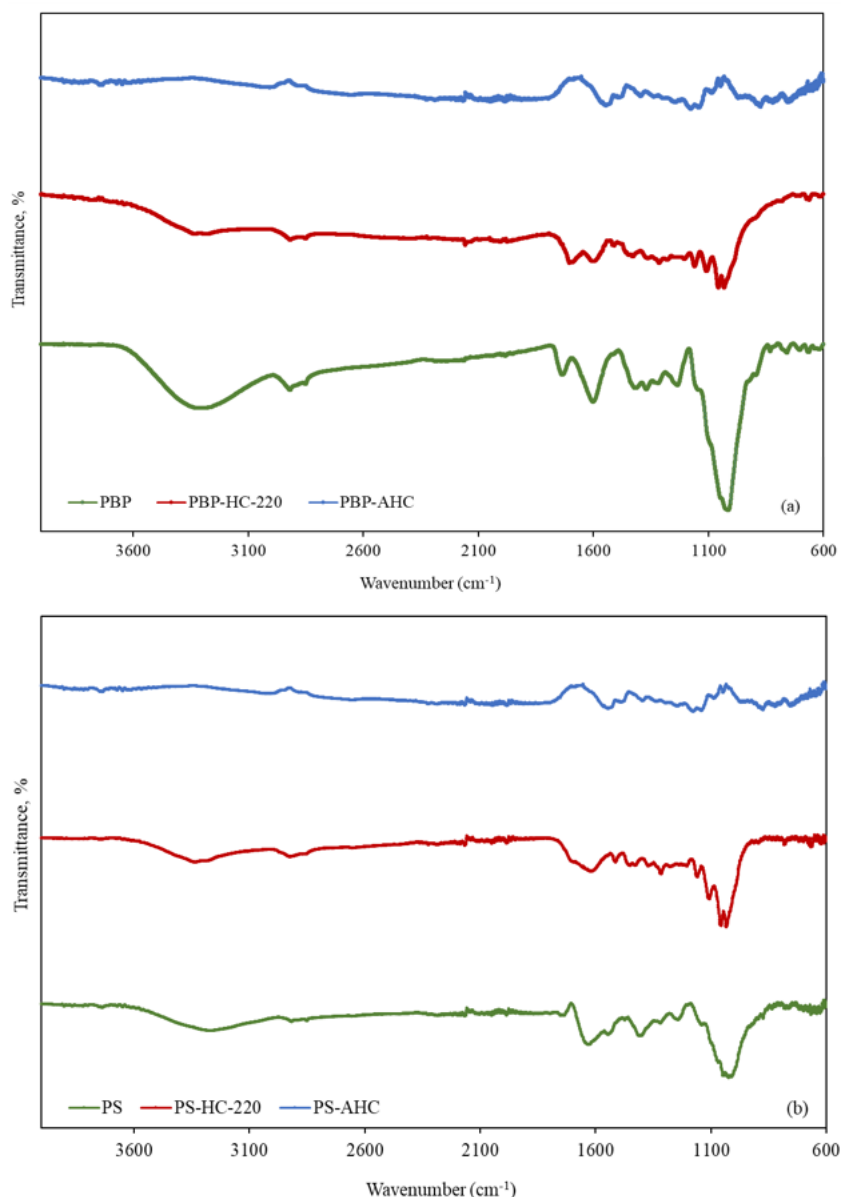


Figure 3. FTIR spectra of (a)PBP, PBP-HC-200, and PBP-AHC; (b)PS, PS-HC-200, and PS-AHC.

A wide peak was noticed in the spectra of PBP, PS, and all hydrochars at 3160-3600 cm⁻¹. This peak was attributed to the O-H stretching of the hydroxyl or carboxyl group. It must be noted that this peak was weaker in the spectra of

hydrochars as a result of dehydration during HTC and almost disappeared after ZnCl₂ activation. The peak at 2925-2850 cm⁻¹ was more strongly observed in the spectra of PBP and its hydrochar and attributed to the

aliphatic C-H stretching vibration of methylene groups of lignin (Missaoui et al., 2017). The existence of this peak in the spectra of both hydrochars implied that lignin was not completely decomposed during HTC. After activation, this peak was observed to be very weak which implied that further degradation of lignin occurred during activation. The intensity of the peak around 1030 cm^{-1} corresponding to the C-O stretching of hemicellulose and cellulose (Missaoui et al., 2017) weakened as a result of their partial degradation during HTC. This peak almost disappeared after ZnCl_2 activation showing that degradation of holocellulose in legume wastes was almost completed. The peak at 1740 cm^{-1} existing in the spectra of legume wastes corresponds to the C=O stretching of ester group of hemicellulose. This peak disappeared due to the degradation of hemicellulose after HTC (Dong et al., 2019)

and a new peak appeared at 1690 cm^{-1} implying the formation of carbonyl/carboxyl groups conjugated to a benzene ring or C=C bond. The peak which was observed at 1635 cm^{-1} in the spectrum of legume wastes and shifted to 1610 cm^{-1} in the spectra of hydrochars was assigned to C=C aromatic stretching (Wang et al., 2018; Dong et al., 2019). The C=O peaks disappeared and C=C peaks shifted to lower wavenumbers after ZnCl_2 activation of both type of hydrochars implying the enhancement of decarboxylation and improvement of aromaticity.

3.5. SEM Analysis of Legume Wastes, Hydrochars and Activated Carbons

The SEM images of legume wastes, their hydrochars, and activated carbons taken at $\times 2500$ magnitude are given in Figure 4.

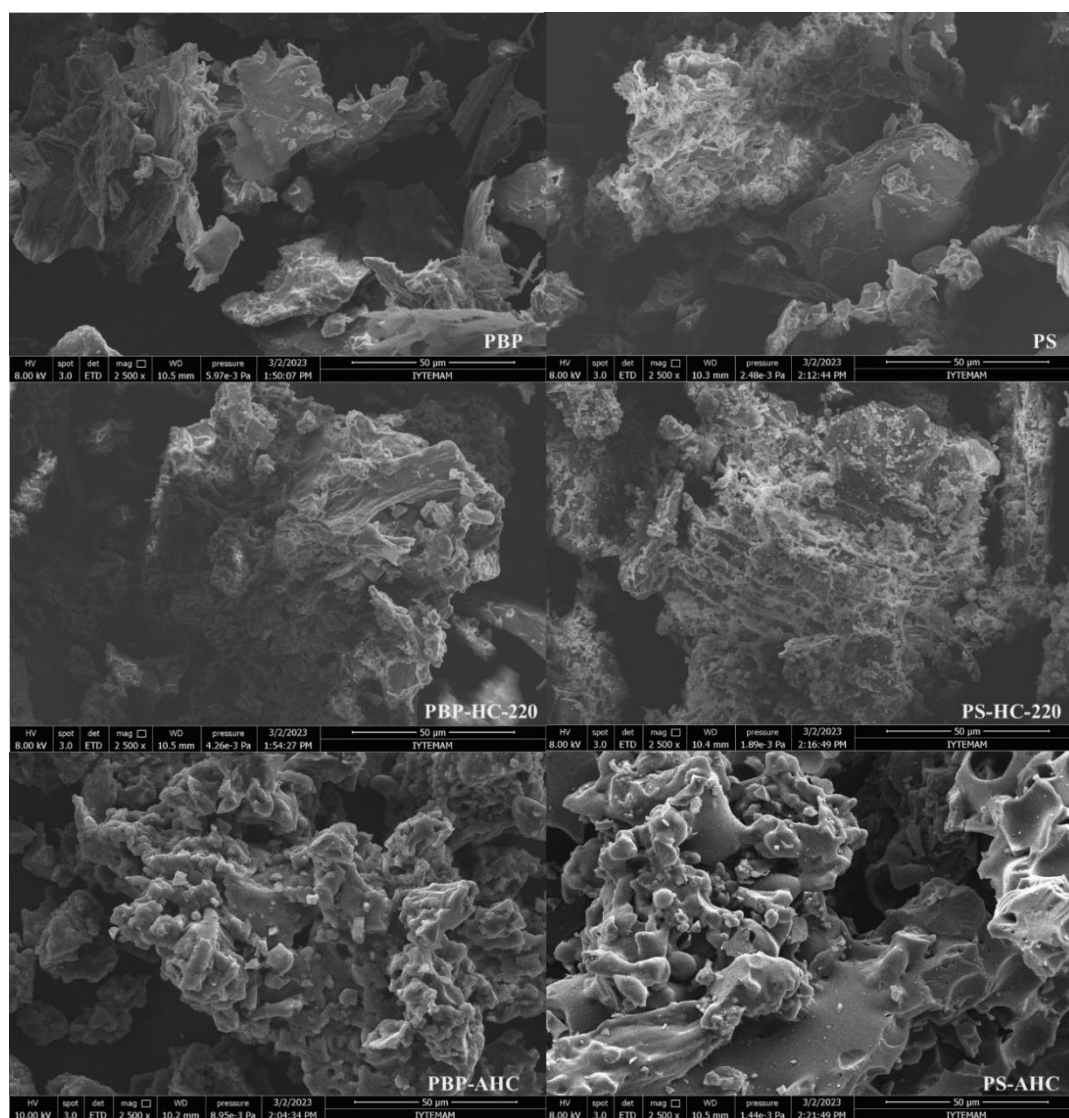


Figure 4. SEM images of legume wastes, their hydrochars, and activated carbons ($\times 2500$ magnitude).

The changes in morphologies of legume wastes after HTC and ZnCl_2 activation can be followed from SEM images given in Figure 4. The surface of legume wastes was smooth. On the other hand, the surface of hydrochars was observed to be relatively rough and deformed compared

to that of legume wastes which was attributed to the degradation of hemicellulose and cellulose into smaller fragments during HTC (Hamid and Subramaniam, 2022). According to Chen et al. (2017), these smaller fragments might combine to form spherical particles on the surface

of hydrochars during HTC. Similarly, a number of spherical particles was detected on the surface of hydrochars in this study. Also, a small number of rudimentary pores was observed on the surface of hydrochars which might have occurred through removal of internal volatile fraction in legume wastes. Further treatment of hydrochars by ZnCl₂ activation resulted in more porous morphology as can be seen from SEM images of activated carbons given in Figure 4. Spherical particles seem to retain on the surface even after activation of hydrochars.

3.6. AMX Adsorption Study

3.6.1. Effect of time on AMX removal efficiency and adsorption kinetics

Batch adsorption experiments were carried out for PBP-

AHC and PS-AHC at adsorption times varying between 1 and 24 h with an amount of 0.075 g (3 g.L⁻¹) in a 25 mL of 200 ppm AMX solution in order to determine the equilibrium time. Variation of removal efficiency with time was presented in Table 5. PBP-AHC showed higher removal efficiency in shorter adsorption time probably due to its higher surface area which probably enabled a faster mass transfer (Table 5). Therefore, AMX removal efficiency of PBP-AHC changed very slightly with the increase of adsorption time. None of the activated carbons was able to achieve a removal efficiency of 100% even for an adsorption time of 24 h which was attributed to the high initial concentration of AMX. 24 h was chosen as the equilibrium time in order to guarantee the establishment of adsorption equilibrium for both activated carbons.

Table 5. Removal efficiency of activated carbon at different adsorption times, %

| | | Adsorption time, hour | | | | |
|------------------------|---------|-----------------------|------|------|------|------|
| | | 1 | 2 | 4 | 6 | 24 |
| Removal efficiency (%) | PBP-AHC | 86.9 | 87.4 | 87.9 | 88.2 | 89.7 |
| | PS-AHC | 77.2 | 81.8 | 83.1 | 84.1 | 87.3 |

Adsorption kinetic study was carried out at an initial AMX concentration of 200 ppm varying the time between 10 and 1440 minutes. Q_t versus time was plotted using the data obtained and was shown in Figure 5. As can be seen

from the figure, AMX adsorption rate was fast at the initial stage of adsorption and got slower with the increase of time.

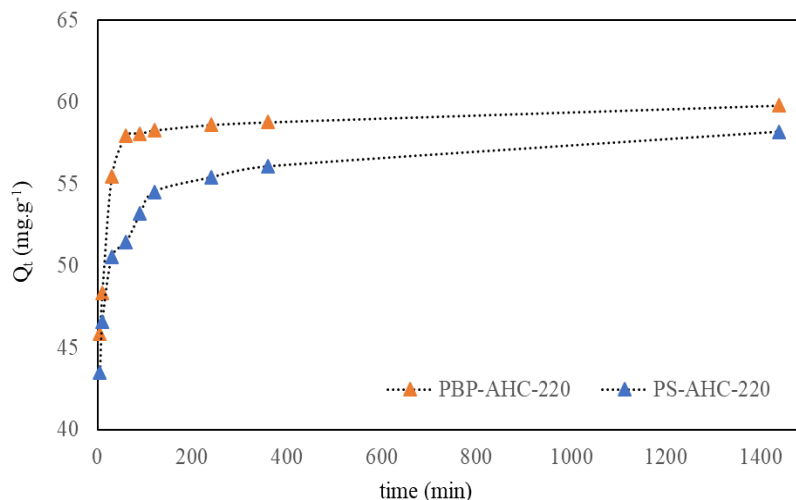


Figure 5. Plot of adsorbed amount of AMX per unit mass of activated carbon (Q_t) versus time.

Kinetic parameters of AMX adsorption on PBP-AHC and PS-AHC obtained from the analysis of kinetic data using pseudo-first order kinetic model, pseudo-second order kinetic model and intra-particle diffusion kinetic model were presented in Table 6.

The comparison of R² values in Table 6 revealed that AMX adsorption on PBP-AHC and PS-AHC best fits with the pseudo-second order kinetic model and hence AMX adsorption rate is controlled mainly by chemisorption. Q_{e,2} values calculated from pseudo-second order model were found to be more proximate to Q_{e,experimental} values than Q_e values calculated from other models. Comparison of k₂ values showed that AMX adsorption rate of PBP-AHC was

faster than that of PS-AHC. The compatibility of pseudo-second order kinetic model for AMX adsorption on activated carbon was also reported by other researchers in the literature (Chayid and Ahmed, 2015; Budyanto et al., 2008; Moussavi et al., 2013).

3.6.2. Effect of activated carbon dosage on AMX removal efficiency

Effect of activated carbon dosage on AMX removal efficiency of both activated carbon was investigated and depicted in Figure 6. As can be seen from Figure 6, removal efficiency of AMX increased proportionally (from 30.0% and 28.8% to 82.8% and 83.0% for PBP-AHC and PS-AHC, respectively) with increasing activated carbon dosage

from 0.5 to 2 g.L⁻¹. Further increase of activated carbon dosage caused only a slight increase in removal efficiency of AMX without achieving 100% removal.

3.6.3. Adsorption isotherms

Adsorption isotherm study was performed at an activated carbon dosage of 3 g. L⁻¹ at varying initial AMX concentrations (75 - 250 ppm) for an equilibrium time of

24 h. Activated carbon dosage was selected as 3 g. L⁻¹, since maximum AMX removal efficiency was achieved at this dosage (Figure 6). Isotherm constants and R² values of Langmuir and Freundlich models obtained by application of Equations 7 and 8 to the C_e and Q_e values determined at different initial concentrations are given in Table 7.

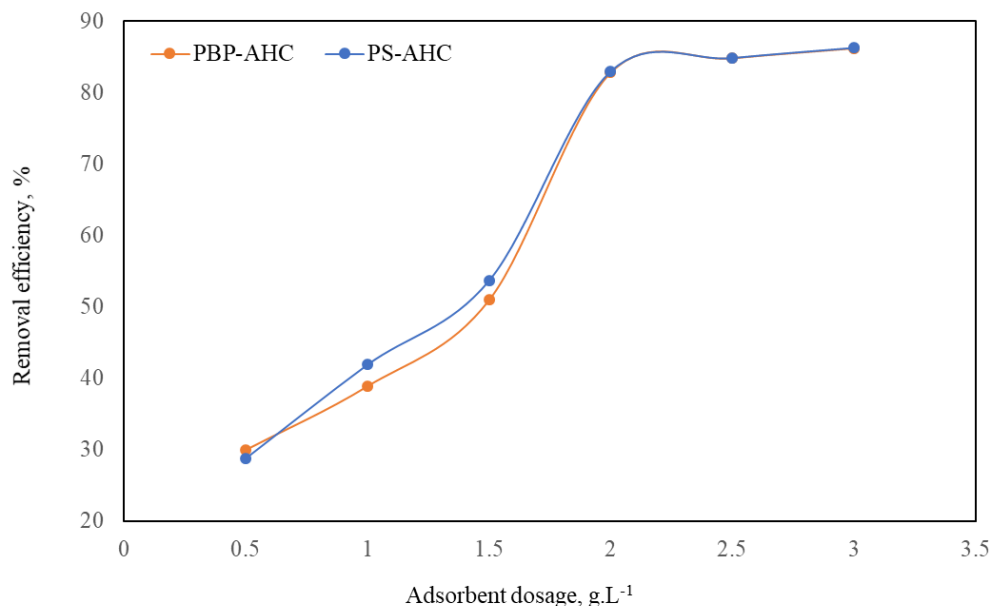


Figure 6. Effect of activated carbon dosage on removal efficiency of AMX.

Table 6. Kinetic parameters of AMX adsorption on PBP-AHC and PS-AHC.

| | PBP-AHC | PS-AHC |
|--------------------------------|---------|--------|
| $Q_{e,exp}$ | 59.79 | 58.18 |
| Pseudo-first order model | | |
| k_1 | 0.0103 | 0.0049 |
| $Q_{e1} (mg.g^{-1})$ | 7.79 | 10.25 |
| R^2 | 0.664 | 0.883 |
| Pseudo-second order model | | |
| k_2 | 0.0084 | 0.0048 |
| $Q_{e2} (mg.g^{-1})$ | 59.17 | 56.49 |
| R^2 | 0.999 | 0.999 |
| Intra-particle diffusion model | | |
| $C_{i1} (mg.g^{-1})$ | 39.32 | 41.46 |
| $C_{i2} (mg.g^{-1})$ | 57.24 | 51.05 |
| k_{i1} | 2.81 | 1.41 |
| k_{i2} | 0.09 | 0.27 |
| R^2_1 | 0.962 | 0.892 |
| R^2_2 | 0.987 | 0.895 |

$Q_{e,exp} (mg.g^{-1})$ = amount of AMX adsorbed at equilibrium obtained in experiments, k_p = pseudo-first order, model rate constant, $Q_{e1} (mg.g^{-1})$ = amount of AMX adsorbed at equilibrium time calculated by pseudo-first, order model, k_2 = pseudo-second order model rate constant, $Q_{e2} (mg.g^{-1})$ = amount of AMX adsorbed, at equilibrium time calculated by pseudo-second order model, k_{i1} = intra-particle diffusion model first, stage rate constant, k_{i2} = intra-particle diffusion model second stage rate constant, $C_{i1} (mg.g^{-1})$ = the first, stage boundary layer thickness, $C_{i2} (mg.g^{-1})$ = the second stage boundary layer thickness.

Table 7. Langmuir and Freundlich isotherm constants and R^2 values for AMX adsorption on PBP-AHC and PS-AHC

| | PBP-AHC | PS-AHC |
|----------------------|---------|--------|
| Langmuir | | |
| $Q_{max}(mg.g^{-1})$ | 188.7 | 70.9 |
| $K_L(L.mg^{-1})$ | 0.02 | 0.23 |
| R_L | 0.155 | 0.017 |
| R^2 | 0.96 | 0.98 |
| Freundlich | | |
| $1/n(mg.g^{-1})$ | 0.73 | 0.29 |
| $K_F(L.mg^{-1})$ | 6.26 | 22.85 |
| R^2 | 0.99 | 0.95 |

Q_{max} = maximum monolayer adsorption capacity, K_L = equilibrium constant, R_L : separation factor, K_F = Freundlich constant, $1/n$ = heterogeneity factor.

R^2 values of Langmuir and Freundlich isotherms presented in Table 7 indicated that experimental isotherm data of PBP-AHC and PS-AHC were highly correlated with both of the models. In case of AMX adsorption on PS-AHC, Freundlich isotherm showed more satisfactory fit with the experimental data. This indicated that adsorption took place on the surface of PS-AHC which was energetically heterogeneous. On the other hand, Langmuir isotherm was found to be more compatible with the experimental data of PBP-AHC indicating that AMX molecules covered the surface of PBP-AHC, which was homogeneous, as monolayer.

Examination of Langmuir isotherm constants revealed that AMX adsorption onto PBP-AHC was favorable ($0 < R_L < 1$), while that on PS-AHC was nearly irreversible ($R_L \approx 0$) (Araújo et al., 2021). Similarly, $1/n$ values calculated from Freundlich isotherm model also indicated a favorable AMX adsorption on both activated carbons (Kalam et al., 2021).

Q_{max} values are known to be very useful for determination and comparison of adsorption capacities of adsorbents. As can be seen from Table 7, PBP-AHC has much higher AMX adsorption capacity than PS-AHC due to its more developed porosity with more mesoporous character and higher surface area. Rodrigues et al. stated that predominantly mesoporous activated carbons having oxygenated groups in abundance and high specific area shows an efficient and fast AMX adsorption (Rodrigues et al., 2020). Hence, it can be stated that PBP derived hydrochar is a more promising precursor in production of activated carbon with a good AMX adsorption capacity. Q_{max} of AMX on other activated carbons was calculated as 345 mg. g⁻¹ for KOH activated giant reed (Chayid and Ahmed, 2015); 233 mg.g⁻¹ for coconut shell based commercial activated carbon (Budyanto et al., 2008); 439 mg.g⁻¹ for NH₄Cl activated pomegranate wood (Moussavi et al., 2013); 175 and 268 mg.g⁻¹ for two types of magnetic activated carbon (Saucier et al., 2017); 122 and 132 mg.g⁻¹ for Mn-impregnated *Phragmites australis* based activated carbons (Liu et al., 2016) and 130 and 176 mg.g⁻¹ for two types of ZnCl₂ activated solid olive-mill waste (Rodrigues et al., 2020) in literature. Depending on the literature results, KOH or NH₄Cl activation of PBP-HC-220

and PS-HC-220 can be investigated in further studies to obtain a higher AMX adsorption capacity.

4. Conclusion

In this study, use of hydrochars obtained from legume wastes as fuel and their conversion into activated carbon for amoxicillin removal was investigated. Two types of legume wastes, pinto bean peels and pea shells, were used for hydrochar production. Hydrothermal carbonization of legume wastes was carried out at different temperatures in order to examine its effect on fuel properties of derived hydrochars. Hydrothermal carbonization at 240 °C had significant effect on the enhancement of hydrochar fuel properties such as higher heating value and fuel ratio. This effect was more noticeable in case of pinto bean shells. Van Krevelen Diagram depicted the formation of bituminous coal-like and lignite-like hydrochars from pinto bean peels and pea shells at 240 °C, respectively. Initial ash in pinto bean peels retained in the resultant hydrochar was lower than that in pea shell retained in the resultant hydrochar. This was attributed to the difference in ash composition of legume wastes. ZnCl₂ activation of hydrochars obtained at 220 °C produced activated carbons with enhanced surface area and pore volume that varied according to the legume waste type. Pinto bean peel yielded an activated carbon with higher BET surface area, total pore volume, mesopore volume and hence maximum amoxicillin adsorption capacity and rate. Overall, it can be concluded that hydrothermal carbonization can be considered as a promising treatment method of legume wastes for enhancing their fuel properties and as a promising pretreatment method of legume wastes for activated carbon production by chemical activation.

Author Contributions

Percentages of the author contributions is present below. The author reviewed and approved final version of the manuscript.

| | i.C.K. |
|-----|--------|
| C | 100 |
| D | 100 |
| S | 100 |
| DCP | 100 |
| DAI | 100 |
| L | 100 |
| W | 100 |
| CR | 100 |
| SR | 100 |

C= concept, D= design, S= supervision, DCP= data collection and/or processing, DAI= data analysis and/or interpretation, L= literature search, W= writing, CR= critical review, SR= submission and revision.

Conflict of Interest

The author declared that there is no conflict of interest.

Ethical Consideration

Ethics committee approval was not required for this study because of there was no study on animals or humans.

Acknowledgments

The author thanks Prof. Dr. Jale Yanik for granting permission to use Industrial Organic Laboratory facilities at Chemistry Department, Ege University, Türkiye. The author would like to acknowledge TAUM (Erciyes University) and IYTE-MAM (Izmir Institute of Technology) for BET analysis, ODUMARAL (Ordu University) for elemental analysis, and IYTE-MAM (Izmir Institute of Technology) for SEM images.

References

Abazari R, Mahjoub AR. 2018. Ultrasound-assisted synthesis of Zinc(II)-based metal organic framework nanoparticles in the presence of modulator for adsorption enhancement of 2,4-dichlorophenol and amoxicillin. *Ultrason Sonochem*, 42: 577-584. DOI: 10.1016/j.ultsonch.2017.12.027.

Ajala OO, Akinawo SO, Bamisaye A, Adedipe DT, Adesina MO, Okon-Akan OA, Adebisuyi TA, Ojedokun AT, Adegoke KA, Bello OS. 2023. Adsorptive removal of antibiotic pollutants from wastewater using biomass/biochar-based adsorbents. *RSC Adv*, 13: 4678-4712 DOI:10.1039/d2ra06436g.

Akogun OA, Waheed MA. 2019. Property upgrades of some raw Nigerian biomass through torrefaction pre-treatment- a review. *J Phys*, 1378: 032026. DOI:10.1088/1742-6596/1378/3/032026.

Angın D, Köse TE, Selengil U. 2013a. Production and characterization of activated carbon prepared from safflower seed cake biochar and its ability to absorb reactive dyestuff. *Appl Surf Sci*, 280: 705-710. DOI: 10.1016/j.apsusc.2013.05.046.

Angın D, Altıntig E, Köse TE. 2013b. Influence of process

parameters on the surface and chemical properties of activated carbon obtained from biochar by chemical activation. *Bioresour Technol*, 148: 542-549. DOI: 10.1016/j.biortech.2013.08.164.

Araújo LK, Albuquerque AA, Ramos WC, Santos AT, Carvalho SH, Soletti JI, Bispo MD. 2021. Elaeis guineensis-activated carbon for methylene blue removal: adsorption capacity and optimization using CCD-RSM, *Environ Dev Sustain* 1-19. DOI: 10.1016/j.crgsc.2022.100325.

Balarak D, Mahdavi Y, Maleki A, Daraei H, Sadeghi S. 2016. Studies on the removal of amoxicillin by single walled carbon nanotubes. *Br J Pharmaceut Res*, 10(4): 1-9. DOI: 10.9734/BJPR/2016/24150.

Balmuk G, Cay H, Duman G, Kantarli IC, Yanik J. 2023. Hydrothermal carbonization of olive oil industry waste into solid fuel: Fuel characteristics and combustion performance. *Energy*, 278:127803. DOI: 10.1016/j.energy.2023.127803.

Bote JG, Castasus NFP, Layug KM, Vicente RZ, Yambao PJT, Rubi RVC, Roque EC, Olay JG. 2023. Production of hydrochar using pineapple (*Ananas comosus*) peelings via hydrothermal carbonization, *Mater Today-Proc*. Article in press. DOI:10.1016/j.matpr.2023.05.464.

Budyanto S, Soedjono S, Irawaty W, Indraswati N. 2008. Studies of adsorption equilibria and kinetics of amoxicillin from simulated wastewater using activated carbon and natural bentonite. *J Environ Prot Sci*, 2: 72-80.

Channiwala SA, Parikh PP. 2002. A unified correlation for estimating HHV of solid, liquid and gaseous fuels. *Fuel*, 81(8): 1051-1063. DOI: 10.1016/S0016-2361(01)00131-4.

Chayid M, Ahmed MJ. 2015. Amoxicillin adsorption on microwave prepared activated carbon from *Arundo donax* Linn: Isotherms, kinetics, and thermodynamics studies. *J Environ Chem Eng*, 3: 1592-1601. DOI: 10.1016/j.jece.2015.05.021.

Chen J, Zhang L, Yang G, Wang Q, Li R, Lucia LA. 2017. Preparation and characterization of activated carbon from hydrochar by phosphoric acid activation and its adsorption performance in prehydrolysis liquor. *BioRes*, 12(3): 5928-5941. DOI: 10.15376/biores.12.3.5928-5941.

Ciolkosz D, Wallace R. 2011. A review of torrefaction for bioenergy feedstock production. *Biofuel Bioprod Bior*, 5(3): 317-329. DOI: 10.1002/bbb.275.

De Franco MAE, de Carvalho CB, Bonetto MM, de Pelegrini Soares R, Feris LA. 2017. Removal of amoxicillin from water by adsorption onto activated carbon in batch process and fixed bed column: Kinetics, isotherms, experimental design and breakthrough curves modelling. *J Clean Prod*, 161: 947-956. DOI: 10.1016/j.jclepro.2017.05.197.

De Sa IC, De Oliveira P, Nossol E, Borges PHS, Lepri FG, Semaan FS, Pacheco WF. 2022. Modified dry bean pod waste (*Phaseolus vulgaris*) as a biosorbent for fluorescein removal from aqueous media: batch and fixed bed studies. *J Hazard Mater*, 424: 127723. DOI: 10.1016/j.jhazmat.2021.127723.

Dong X, Guo S, Wang H, Wang Z, Gao X. 2019. Physicochemical characteristics and FTIR-derived structural parameters of hydrochar produced by hydrothermal carbonisation of pea pod (*Pisum sativum* Linn.) waste. *Biomass Conv Bioref*, 9: 531-540. DOI: 10.1007/s13399-018-0363-1.

Edet UA, Ifealebuegu AO. 2020. Kinetics, isotherms, and thermodynamic modeling of the adsorption of phosphates from model wastewater using recycled brick waste. *Processes*, 8(6): 665. DOI: 10.3390/pr8060665.

Elaigwu, SE, Rocher V, Kyriakou G, Greenway GM. 2014. Removal of Pb²⁺ and Cd²⁺ from aqueous solution using chars from pyrolysis and microwave-assisted hydrothermal

- carbonization of *Prosopis Africana* Shell. *J Ind Eng Chem*, 20: 3467-73. DOI: doi.org/10.1016/j.micromeso.2012.08.006.
- Elmolla ES, Chaudhuri M. 2010. Degradation of amoxicillin, ampicillin and cloxacillin antibiotics in aqueous solution by the UV/ZnO photocatalytic process. *J Hazard Mater*, 173: 445-449. DOI: 10.1016/j.jhazmat.2009.08.104.
- Eom H, Kim J, Nam I, Bae S. 2021. Recycling black tea waste biomass as activated porous carbon for long life cycle supercapacitor electrodes. *Materials*, 14(21): Article 6592. DOI: 10.3390/ma14216592.
- Ercan B, Alper K, Ucar S, Karagoz S. 2023. Comparative studies of hydrochars and biochars produced from lignocellulosic biomass via hydrothermal carbonization, torrefaction and pyrolysis. *Journal of the Energy Institute*, 109:101298. DOI: 10.1016/j.joei.2023.101298.
- Fazelirad H, Ranjbar M, Taher MA, Sargazi G. 2015. Preparation of magnetic multi-walled carbon nanotubes for an efficient adsorption and spectrophotometric determination of amoxicillin. *J Ind Eng Chem*, 21: 889-892. DOI: 10.1016/j.jiec.2014.04.028.
- Fernandez ME, Ledesma B, Roman S, Bonelli PR, Cukierman AL. 2015. Development and characterization of activated hydrochars from orange peels as potential adsorbents for emerging organic contaminants. *Bioresour Technol*, 183: 221-228. DOI: 10.1016/j.biortech.2015.02.035.
- Flora JFR, Lu X, Li L, Flora JRV, Berge ND. 2013. The effects of alkalinity and acidity of process water and hydrochar washing on the adsorption of atrazine on hydrothermally produced hydrochar. *Chemosphere*, 93: 1989-96. DOI: 10.1016/j.chemosphere.2013.07.018.
- Funke A, Reebes F, Kruse A. 2013. Experimental comparison of hydrothermal and vapothermal carbonization. *Fuel Process Technol*, 115: 261-269. DOI: 10.1016/j.fuproc.2013.04.020.
- Garoma T, Umamaheshwar SH, Mumper A. 2010. Removal of sulfadiazine, sulfamethizole, sulfamethoxazole, and sulfathiazole from aqueous solution by ozonation. *Chemosphere*, 79: 814-20. DOI: 10.1016/j.chemosphere.2010.02.060.
- Goswami R, Shim J, Deka S, Kumari D, Katak R, Kumar M. 2016. Characterization of cadmium removal from aqueous solution by biochar produced from *Ipomoea fistulosa* at different pyrolytic temperatures. *Ecol Eng*, 97: 444-451. DOI: 10.1016/j.ecoleng.2016.10.007.
- Hadjittofi L, Prodromou M, Pashalidis I. 2014. Activated biochar derived from cactus fibres – Preparation, characterization and application on Cu(II) removal from aqueous solutions. *Bioresour Technol*, 159: 460-464. DOI: 10.1016/j.biortech.2014.03.073.
- Hamid SBA, Chowdhury ZZ, Zain SM. 2014. Base catalytic approach: A promising technique for the activation of biochar for equilibrium sorption studies of copper, Cu (II) ions in single solute system. *Materials*, 7 (4): 2815-2832. DOI: 10.3390/ma7042815.
- Hamid NA, Subramaniam T. 2022. Physicochemical properties of hydrochars produced from *Khaya senegalensis* leaves using hydrothermal carbonisation. *Journal of Engineering Science and Technology*, 17(3): 1781-91.
- Hayati B, Maleki A, Najafi F, Gharibi F, McKay G, Gupta VK, Puttaiah SH, Marzban N. 2018. Heavy metal adsorption using PAMAM/CNT nanocomposite from aqueous solution in batch and continuous fixed bed systems. *Chem Eng J*, 346: 258-270. DOI: 10.1016/j.cej.2018.03.172.
- Heilmann SM, Davis HT, Jader LR, Lefebvre PA, Sadowsky MJ, Schendel FJ, Von Keitz MG, Valentas KJ. 2010. Hydrothermal carbonization of microalgae. *Biomass Bioenergy*, 34: 875-882. DOI: 10.1016/j.biombioe.2010.01.032.
- Heilmann SM, Jader LR, Sadowsky MJ, Schendel FJ, Von Keitz MG, Valentas KJ. 2011. Hydrothermal carbonization of distiller's grains. *Biomass Bioenergy*, 35: 2526-2533. DOI: 10.1016/j.biombioe.2011.02.022
- Hoffmann V, Jung D, Zimmermann J, Rodriguez Correa C, Elleuch A. 2019. Conductive carbon materials from the hydrothermal carbonization of vineyard residues for the application in electrochemical double-layer capacitors (EDLCs) and direct carbon fuel cells (DCFCs). *Materials*, 12(10): 1-33. DOI: 10.3390/ma12101703.
- Horikawa T, Kitakaze Y, Sekida T, Hayashi J, Katoh M. 2010. Characteristics and humidity control capacity of activated carbon from bamboo. *Bioresour Technol*, 101: 3964-3969. DOI: 10.1016/j.biortech.2010.01.032
- Huang GG, Liu YF, Wu XX, Cai JJ. 2019. Activated carbons prepared by the KOH activation of a hydrochar from garlic peel and their CO₂ adsorption performance. *New Carbon Mater*, 34(3): 247-257. DOI: 10.1016/S1872-5805(19)60014-4
- Huff MD, Lee JW. 2016. Biochar-surface oxygenation with hydrogen peroxide. *J Environ Manage*, 165: 17-21. DOI: 10.1016/j.jenvman.2015.08.046.
- Iriarte-Velasco U, Sierra I, Zudaire L, Ayastuy JL. 2016. Preparation of a porous biochar from the acid activation of pork bones. *Food Bioprod Process*, 98: 341-353. DOI: 10.1016/j.fbp.2016.03.003.
- Islam MA, Benhouria A, Asif M, Hameed BH. 2015. Methylene blue adsorption on factory-rejected tea activated carbon prepared by conjunction of hydrothermal carbonization and sodium hydroxide activation processes. *J Taiwan Inst Chem Eng*, 52: 57-64. DOI: doi.org/10.1016/j.jtice.2015.02.010.
- Islam MA, Ahmed MJ, Khanday WA, Asif M, Hameed BH. 2017. Mesoporous activated coconut shell-derived hydrochar prepared via hydrothermal carbonization-NaOH activation for methylene blue adsorption. *J Environ Manage*, 203: 237-244. DOI: 10.1016/j.jenvman.2017.07.029.
- Jain A, Jayaraman S, Balasubramanian R, Srinivasan MP. 2014. Hydrothermal pre-treatment for mesoporous carbon synthesis: enhancement of chemical activation. *J Mater Chem A*, 2: 520-528. DOI: 10.1039/C3TA12648J.
- Kalam S, Abu-Khamsin SA, Kamal MS, Patil S. 2021. Surfactant adsorption isotherms: a review. *ACS Omega*, 6 (48): 32342-348. DOI: 10.1021/acsomega.1c04661.
- Kalderis D, Görmez Ö, Sağlı B, Çalhan SD, Gözmen B. 2023. Valorization of loquat seeds by hydrothermal carbonization for the production of hydrochars and aqueous phases as added-value products. *J Environ Manage*, 344: 118612. DOI: 10.1016/j.jenvman.2023.118612.
- Kambo HS, Dutta A. 2015. Comparative evaluation of torrefaction and hydrothermal carbonization of lignocellulosic biomass for the production of solid biofuel. *Energy Convers Manage*, 105: 746-755. DOI: /10.1016/j.enconman.2015.08.031.
- Kanchanatip E, Prasertsung N, Thasnas N, Grisdanurak N, Wantala K. 2022. Valorization of cannabis waste via hydrothermal carbonization: solid fuel production and characterization. *Environ Sci Pollut Res*. DOI:10.1007/s11356-022-24123-0
- Kantarli IC, Kabadayi A, Ucar S, Yanik, J. 2016. Conversion of poultry wastes into energy feedstocks. *Waste Manage*, 56: 530-539. DOI: 10.1016/j.wasman.2016.07.019.
- Kantarli IC. 2023. Conversion of brewed tea waste into hydrochar and activated carbon. *Int J Glob Warming*, 29(1-2):1-15. DOI: 10.1504/IJGW.2023.128832.
- Kerkez-Kuyumcu O, Bayazit SS, Salam MA. 2016. Antibiotic

- amoxicillin removal from aqueous solution using magnetically modified graphene nanoplatelets. *J Ind Eng Chem*, 36:198-205. DOI: 10.1016/j.jiec.2016.01.040.
- Laginhas C, Valente Nabais JM, Titirici MM. 2016. Activated carbons with high nitrogen content by a combination of hydrothermal carbonization with activation. *Microporous and Mesoporous Mater*, 226: 125-132. DOI: doi.org/10.1016/j.micromeso.2015.12.047.
- Laksaci H, Belhamdi B, Khelif O, Khelif A, Trari M. 2023. Elimination of amoxicillin by adsorption on coffee waste based activated carbon. *J Mol Struct*, 1274: 134500.
- Larsson SH, Rudolfsson M, Nordwaeger M, Olofsson I, Samuelsson R. 2013. Effect of moisture content, torrefaction temperature and die temperature in pilot scale pelletizing of torrefied Norway spruce. *App Energy*, 102: 827-832. DOI: 10.1016/j.apenergy.2012.08.046.
- Limousy L, Ghouma I, Ouederni A, Jeguirim M. 2017. Amoxicillin removal from aqueous solution using activated carbon prepared by chemical activation of olive stone. *Environ Sci Pollut Res*, 24 (11): 9993-10004. DOI: 10.1007/s11356-016-7404-8.
- Li H, Hu J, Cao Y, Li X, Wang X. 2017. Development and assessment of a functional activated fore-modified biohydrochar for amoxicillin removal. *Bioresour Technol*, 246:168-175. DOI: 10.1016/j.biortech.2017.06.112.
- Lim WC, Srinivasakannan C, Balasubramanian N. 2010. Activation of palm shells by phosphoric acid impregnation for high yielding activated carbon. *J Anal Appl Pyrolysis*, 88: 181-186. DOI: 10.1016/j.jaap.2010.04.004
- Liu Y, Zhu X, Qian F, Zhang S, Chen J. 2014. Magnetic activated carbon prepared from rice straw-derived hydrochar for triclosan removal. *RSC Adv*, 4(109): 63620-63626. DOI: 10.1039/c4ra11815d.
- Liu H, Hu Z, Liu H, Xie H, Lu S, Wang Q, Zhang J. 2016. Adsorption of Amoxicillin by Mn-impregnated activated carbons: performance and mechanisms. *RSC Adv*, 6(14): 11454-11460. DOI: 10.1039/C5RA23256B.
- Maitlo G, Ali I, Mangi KH, Ali S, Maitlo HA, Unar IN, Pirzada AM. 2022. Thermochemical conversion of biomass for syngas production: current status and future trends. *Sustainability*, 14(5):2596. DOI: 10.3390/su14052596.
- Makela M, Benavente V, Fullana A. 2015. Hydrothermal carbonization of lignocellulosic biomass: effect of process conditions on hydrochar properties. *Appl Energy*, 155:576-84. DOI: 10.1016/j.apenergy.2015.06.022.
- Martínez-Castaño M, Mejía Díaz DP, Contreras-Calderón J, Gallardo Cabrera C. 2020. Physicochemical properties of bean pod (*Phaseolus vulgaris*) flour and its potential as a raw material for the food industry. *Revista Facultad Nacional de Agronomía Medellín*, 73(2): 9179-9187. DOI: 10.15446/rfnam.v73n2.81564.
- Mateos-Aparicio I, Redondo-Cuenca A, Villanueva-Suárez MJ, Zapata-Revilla MA, Tenorio-Sanz, MD. 2010. Pea pod, broad bean pod and okara, potential sources of functional compounds. *LWT- Food Sci Technol*, 43:1467-1470. DOI: 10.1016/j.lwt.2010.05.008.
- McGaughy K, Toufiq Reza M. 2018. Hydrothermal carbonization of food waste: simplified process simulation model based on experimental results. *Biomass Conv Bioref*, 8: 283-292. DOI: 10.1007/s13399-017-0276-4.
- Missaoui A, Bostyn S, Belandria V, Cagnon B, Sarh B, Gokalp I. 2017. Hydrothermal carbonization of dried olive pomace: energy potential and process performances. *J Anal Appl Pyrolysis*, 128: 281-90. DOI: 10.1016/j.jaap.2017.09.022.
- Moradi SE. 2015. Highly efficient removal of amoxicillin from water by magnetic graphene oxide adsorbent. *Chem Bull 'Politehnica' University Timisoara, Rom Ser Chem Environ Eng*, 60: 41-48.
- Moussavi G, Alahabadi A, Yaghmaei K, Eskandari M. 2013. Preparation, characterization and adsorption potential of the NH₄Cl-induced activated carbon for the removal of amoxicillin antibiotic from water. *Chem Eng J*, 217: 119-128. DOI:10.1016/j.cej.2012.11.069.
- Nawaz A, Kumar P. 2023. Impact of temperature severity on hydrothermal carbonization: fuel properties, kinetic and thermodynamic parameters. *Fuel*, 336:127166. DOI: 10.1016/j.fuel.2022.127166.
- Nirmaladevi S, Palanisamy PN. 2021. Adsorptive behavior of biochar and zinc chloride activated hydrochar prepared from *Acacia leucophloea* wood sawdust: kinetic equilibrium and thermodynamic studies. *Desalination Water Treat*, 209: 170-181. DOI: 10.5004/dwt.2021.26515
- Odeh AO. 2015. Comprehensive conventional analysis of southern hemisphere coal chars of different ranks for fixed bed gasification. *Global Journals of Research in Engineering*, 15(4): 5-16.
- Pala M, Kantarli IC, Buyukisik HB, Yanik J. 2014. Hydrothermal carbonization and torrefaction of grape pomace: A comparative evaluation. *Bioresour Technol*, 161: 255-262. DOI: 10.1016/j.biortech.2014.03.052.
- Pari G, Darmawan S, Bambang Prihandoko B. 2014. Porous carbon spheres from hydrothermal carbonization and koh activation on cassava and tapioca flour raw material. *Procedia Environmental Sciences*, 20: 342-51. DOI: 10.1016/j.proenv.2014.03.043.
- Parshetti GK, Chowdhury S, Balasubramanian R. 2014. Hydrothermal conversion of urban food waste to chars for removal of textile dyes from contaminated waters. *Bioresour Technol*, 161: 310-319. DOI: 10.1016/j.biortech.2014.03.087.
- Pavkov I, Radojčin M, Stamenković Z, Bikić S, Tomić M, Bukurov M, Despotović B. 2022. Hydrothermal carbonization of agricultural biomass: Characterization of hydrochar for energy production. *Solid Fuel Chem*, 56: 225-235. DOI: 10.3103/S0361521922030077.
- Petrović JT, Stojanović MD, Milojković JV, Petrović MS, Šoštarić TD, Laušević MD, Mihajlović ML. 2016. Alkali modified hydrochar of grape pomace as a perspective adsorbent of Pb²⁺ from aqueous solution. *J Environ Manage*, 182: 292-300. DOI: 10.1016/j.jenvman.2016.07.081.
- Pezoti O, Cazetta AL, Bedin KC, Souza LS, Martins AC, Silva TL, Júnior OOS, Visentainer JV, Almeida VC. 2016. NaOH-activated carbon of high surface area produced from guava seeds as a high-efficiency adsorbent for amoxicillin removal: Kinetic, isotherm and thermodynamic studies. *Chem Eng J*; 288: 778-788.
- Qian K, Kumar A, Patil K, Bellmer D, Wang D, Yuan W, Huhnke RL. 2013. Effects of biomass feedstocks and gasification conditions on the physicochemical properties of char. *Energies*, 6 (8): 3972-3986. DOI: 10.3390/en6083972
- Rashid RA, Jawad AH, Ishak MAM, Kasim NN. 2016. KOH-activated carbon developed from biomass waste: adsorption equilibrium, kinetic and thermodynamic studies for methylene blue uptake. *Desalin Water Treat*, 57:27226-27236. DOI: 10.1080/19443994.2016.1167630.
- Redding AM, Cannon FS, Snyder SA, Vanderford BJ. 2009. A QSAR-like analysis of the adsorption of endocrine disrupting compounds, pharmaceuticals, and personal care products on modified activated carbons. *Water Res*, 43(15): 3849-3861. DOI: 10.1016/j.watres.2009.05.026.
- Regmi P, Moscoso JLG, Kumar S, Cao X, Mao J, Schafran G. 2012.

- Removal of copper and cadmium from aqueous solution using switchgrass biochar produced via hydrothermal carbonization process. *J Environ Manage*, 109: 61-69. DOI: 10.1016/j.jenvman.2012.04.047.
- Rodrigues DLC, Machado FM, Osorio AG, Azevedo CFD, Lima EC, Silva RSD, Lima DR, FM Gonçalves. 2020. Adsorption of amoxicillin onto high surface area-activated carbons based on olive biomass: kinetic and equilibrium studies. *Environ Sci Pollut Res*, 27: 41394-41404. DOI: 10.1007/s11356-020-09583-6.
- Roman S, Nabais JMV, Ledesma B, Gonzalez, JF, Laginhas C, Titrici MM. 2013. Production of low-cost adsorbents with tunable surface chemistry by conjunction of hydrothermal carbonization and activation processes. *Microporous and Mesoporous Mater*, 165: 127-133. DOI: 10.1016/j.micromeso.2012.08.006.
- Satpathy SK, Tabil LG, Meda V, Naik SN, Prasad R. 2014. Torrefaction of wheat and barley straw after microwave heating. *Fuel*, 124: 269-278. DOI: 10.1016/j.fuel.2014.01.102.
- Saucier C, Karthickeyan P, Ranjithkumar V, Lima EC, Dos Reis GS, De Brum IAS. 2017. Efficient removal of amoxicillin and paracetamol from aqueous solutions using magnetic activated carbon. *Environ Sci Pollut Res*, 2017, 24(6): 5918-5932. DOI:10.1007/s11356-016-8304-7.
- Serna-Galvis EA, Ferraro F, Silva-Agredo J, Torres-Palma RA. 2017. Degradation of highly consumed fluoroquinolones, penicillins and cephalosporins in distilled water and simulated hospital wastewater by UV254 and UV254/persulfate processes. *Water Res*, 122: 128-138. DOI: 10.1016/j.watres.2017.05.065.
- Sevilla M, Fuertes AB. 2011. Sustainable porous carbons with a superior performance for CO₂ capture. *Energy Environ Sci*, 4: 1765-71. DOI: 10.1039/C0EE00784F.
- Sun K, Ro K, Guo M, Novak J, Mashayekhi H, Xing B. 2011. Sorption of bisphenol-A, alpha-ethinyl estradiol and phenanthrene on thermally and hydrothermally produced biochars. *Bioresour Technol*, 102: 5757-63. DOI: 10.1016/j.biortech.2011.03.038.
- Swan NB, Zaini MAA. 2019. Adsorption of malachite green and congo red dyes from water: recent progress and future outlook. *Ecol Chem Eng S*, 26(1):119-132. DOI: 10.1515/eces-2019-0009.
- Tran TH, Le HH, Pham TH, Nguyen DT, La DD, Chang SW, Lee SM, Chung WJ, Nguyen DD. 2021. Comparative study on methylene blue adsorption behavior of coffee husk-derived activated carbon materials prepared using hydrothermal and soaking methods. *J Environ Chem Eng*, 9: 105362. DOI:10.1016/j.jece.2021.105362.
- Unutkan T, Bakirdere S, Keyf S. 2018. Development of an analytical method for the determination of amoxicillin in commercial drugs and wastewater samples, and assessing its stability in simulated gastric digestion. *J Chromatogr Sci*, 56(1): 36-40. DOI: 10.1093/chromsci/bmx078.
- Vassilev SV, Vassileva CG, Vassilev VS. 2015. Advantages and disadvantages of composition and properties of biomass in comparison with coal: An overview. *Fuel*, 158: 330-350, DOI:10.1016/j.fuel.2015.05.050.
- Verma N, Bansal MC, Kumar V. 2011. Pea peel waste: a lignocellulosic waste and its utility in cellulase production by *Trichoderma reesei* under solid state cultivation. *BioResource*, 6: 1505-1519.
- Wang T, Zhai Y, Zhu Y, Li C, Zeng G. 2018. A review of the hydrothermal carbonization of biomass waste for hydrochar formation: process conditions, fundamentals, and physicochemical properties. *Renew Sustain Energy Rev*, 90: 223-47. DOI: doi.org/10.1016/j.rser.2018.03.071.
- Wu S, Wang Q, Cui D, Sun H, H Yin, Xu F, Wang Z. 2023. Evaluation of fuel properties and combustion behaviour of hydrochar derived from hydrothermal carbonisation of agricultural wastes, *Journal of the Energy Institute*, 108: 101209. DOI:10.1016/j.joei.2023.101209.
- Yan W, Acharjee TC, Coronella CJ, Victor R, Vásquez VR. 2009. Thermal pretreatment of lignocellulosic biomass. *Environ Prog Sustain Energy*, 28: 435-440. DOI: 10.1002/ep.10385.
- Yang X, Wan Y, Zheng Y, F He, Z Yu, Huang J, Wang H, YS Ok, Jiang Y, Gao B. 2019. Surface functional groups of carbon-based adsorbents and their roles in the removal of heavy metals from aqueous solutions: A critical review. *Chem Eng J*, 366: 608-621. DOI: 10.1016/j.cej.2019.02.119.
- Yi H, Nakabayashi K, Yoon SH, Miyawaki J. 2021. Pressurized physical activation: A simple production method for activated carbon with a highly developed pore structure. *Carbon*, 183: 735-742. DOI: 10.1016/j.carbon.2021.07.061.
- Yu F, Li Y, Han S, Ma J. 2016. Adsorptive removal of antibiotics from aqueous solution using carbon materials. *Chemosphere*, 153: 365-385. DOI: 10.1016/j.chemosphere.2016.03.083.
- Zhu X, Liu Y, Qian F, Zhou C, Zhang S, Chen J. 2014. Preparation of magnetic porous carbon from waste hydrochar by simultaneous activation and magnetization for tetracycline removal. *Bioresour Technol*, 154: 209-214. DOI: 10.1016/j.biortech.2013.12.019.
- Zuccato E, Castiglioni S, Bagnati R, Melis M, Fanelli R. 2010. Source, occurrence and fate of antibiotics in the Italian aquatic environment. *J Hazard Mater*, 179(1-3): 1042-1048. DOI: 10.1016/j.jhazmat.2010.03.110.



BIODIVERSITY OF ACTINOBACTERIA ISOLATED FROM MARMARA AND AVŞA ISLANDS IN TÜRKİYE

Ahmet Ridvan TOPKARA^{1,2*}, Kamil ISIK¹

¹Ondokuz Mayıs University, Faculty of Science, Department of Biology, 55139, Samsun, Türkiye


²Çankırı Karatekin University, Central Research Laboratory Application and Research Center, 18100, Çankırı, Türkiye


Abstract: The main purpose of this study is to investigate the microbial diversity of *Actinobacteria*, living in soils in the “Marmara” and “Avşa” Islands and to identify species at genus level based on 16S rRNA gene sequences. These islands are located in the southwest of the Sea of Marmara and in the literature review, no *Actinobacteria* biodiversity studies related to Marmara and Avşa Islands were found. Such unexplored ecological habitats are potentially rich source for discovery sources of novel species and bioactive molecule. *Actinobacteria* play an important role in many natural phenomena such as nitrogen fixation, roles of these prokaryotic microorganisms. In this article, we focused on the presence and the diversity of *Actinobacteria* on the Islands by examining multiple sampling sites and using different selective isolation media. A total of 400 culturable *Actinobacteria* were isolated using ten different isolation media by dilution-plating method. Among the 400 isolates, 112 isolates were selected according to their morphology in different culture media. The isolates were characterized on the basis of 16S ribosomal RNA gene sequencing and phylogenetic analysis. The results showed a high level of actinobacterial diversity with 16 different genera. These genera obtained as a result of phylogenetic analyzes are *Streptomyces*, *Nonomuraea*, *Nocardia*, *Actinomadura*, *Micromonospora*, *Kribbella*, *Mycolicibacterium*, *Microbispora*, *Saccharopolyspora*, *Jiangella*, *Rhodococcus*, *Actinopolymorpha*, *Geodermatophilus*, *Dactylosporangium*, *Pseudonocardia* and *Nocardioides*. Many isolates are identified as new species by our current research. Findings from this study showed that the soil of Marmara and Avşa Islands can be a good source of isolation for *Actinobacteria*.

Keywords: *Actinobacteria*, Isolation, 16S rRNA gene, Island soil, Biodiversity

*Corresponding author: Çankırı Karatekin University, Central Research Laboratory Application and Research Center, 18100, Çankırı, Türkiye

E mail: ahmetridvantopkara@karatekin.edu.tr (A. R. TOPKARA)

Ahmet Ridvan TOPKARA  <https://orcid.org/0000-0001-5813-1095>

Kamil ISIK  <https://orcid.org/0000-0003-1764-8113>

Received: September 04, 2023

Accepted: September 28, 2023

Published: October 15, 2023

Cite as: Topkara AR, Isik K. 2023. Biodiversity of actinobacteria isolated from Marmara and Avşa islands in Türkiye. BSJ Eng Sci, 6(4): 502-521.

1. Introduction

Actinobacteria, one of the largest bacterial phyla within the Bacteria domain; It is a group of microorganisms consisting of members widely distributed in various terrestrial and aquatic ecosystems. *Actinobacteria* (Küster, 1968), consisting of aerobic and gram-positive bacteria, help the nutrient cycle by degrading different organic compounds due to their wide distribution in nature and their saprophytic properties (Goodfellow and Williams, 1983; Hasegawa et al., 2006).

Actinobacteria, which are widely distributed in the soil microbiota, have been isolated from aquatic environments such as hot springs (Barabote et al., 2009; Mokrane et al., 2016; Amin et al., 2017), swamps (Suzuki et al., 1994; Tanasupawat et al., 2016), sea sponges (Kämpfer et al., 2015; Huang et al., 2016; Thawai et al., 2017), and sediments (Deng et al., 2015; Phongsopitanun et al., 2015; Veyisoglu et al., 2016) and from different habitats such as marble surface (Montero-Calasanz et al., 2014), underground caves (Groth et al., 1999; Také et al., 2018), plant rhizosphere (Zhang et al., 2011; Wang et al., 2014; Corretto et al., 2016; Sujarit et al., 2016), rocks (Trujillo et al., 2017), desert (Röttig et al., 2017; Idris et al., 2017; Saygin et al., 2019) and Island soils (Saricaoğlu

et al., 2014).

The best-known feature of *Actinobacteria* is that they have the potential to produce a wide range of bioactive molecules, especially antibiotics (Lazzarini et al., 2000; Prescott et al., 2002). Investigation of these powerful potentials has allowed the discovery of more than 120 antibiotics, different enzymes, enzyme inhibitors and many useful products from actinobacterial sources (Wink et al., 2017). In addition, microorganisms such as *Actinobacteria*, which increase soil fertility and contribute to plant development, are called "biofertilizers" and are used in the preparation of microbial vaccine materials in agriculture. Most of the rare actinomycetes are used as "phytostimulators" or plant growth promoters in the soil because they produce substances (e.g., vitamins and plant hormones) that increase plant health and contribute to high yields (El-Tarabily and Sivasithamparam, 2006; Koçak, 2019). At the same time, *Actinobacteria* members are also used as biocontrol agents because they support plant growth by inactivating many plant pathogens that cause disease in plant roots with the bioactive agents they produce endophytically (El-Tarabily and Sivasithamparam, 2006; Kurtboke, 2000; Kurtboke et al., 2007).



In this study, we examined *Actinobacteria* in two regions: Marmara and Avşa Islands, which are part of the "Marmara" region. To our knowledge, the biodiversity of *Actinobacteria* of inhabiting these regions (Marmara-Avşa) has not been studied yet. The aims of the present study were to detect the diversity of *Actinobacteria* of islands (Marmara-Avşa), the presence of the secondary metabolite genes in the isolates and reveal whether soils investigated in islands represents a valuable source for new species. As a result of 16S ribosomal RNA gene analysis, A large number of isolates from two different islands were accepted as potentially new species.

2. Materials and Methods

2.1. Collection of Soil Sample and Geographical Locations

Soil samples were collected from different parts of the two islands in November 2020 as shown in Figure 1. The soil samples were randomly taken from ten different areas within Avşa and Marmara islands. Samples taken from 10 cm depth of the soil surface were placed in sterile tubes (10 g). The lands of the island of Marmara were later combined, sifted, and thoroughly mixed. Labeled samples were transferred to sterile plastic bags, transported to the laboratory, and stored at 4 °C for analysis.

2.2. Selective Isolation of *Actinobacteria* from Island Soils

First of all, soil samples were left to dry for 14 days at room temperature in a sterile petri dish. The dried soil samples are pulverized with a mortar so that they do not mix with each other. Each of the prepared solutions was shaken for 30 minutes. Soil samples weighing 1 g were added to 9 ml of Ringer's solution and tubes with a dilution ratio of 10^{-1} were obtained. Dilutions of 10^{-2} and 10^{-3} were prepared by serial dilution. For each dilution, 2 plates were prepared. The two hundred microliters

solutions taken from each diluted suspensions with the help of an automatic pipette were inoculated on different media surfaces and incubated at 28 °C for 21 days. The isolation process was carried out using the dilution plate method. A total of 10 diverse media were used for the selective isolation of *Actinobacteria* members. The media commonly used for the isolation of *Actinomycetes* are shown in Table 1. Various antibiotics (Table 1) have been added to all media to eliminate unwanted gram negative and fungal growth. Inoculated plates were incubated at 28 °C for 3 weeks.



Figure 1. Map of the islands showing sample areas

Table 1. List of selective media used and antibiotics

| Number | Name of medium | Antibiotics | Reference |
|--------|-----------------------------------|--|------------------------------|
| 1 | Czapek-Dox Agar* | Rifampicin (5 µg/ml) | Waksman, 1967 |
| 2 | Marine Agar* | Rifampicin (5 µg/ml) | ZoBell, 1941 |
| 3 | R2A Agar* | Nalidixic acid (10 µg/ml) | Reasoner and Geldreich, 1985 |
| 4 | Raffinose-Histidine Agar* | Rifampicin (5 µg/ml), Nalidixic acid (10 µg/ml) | Vickers et al.1984 |
| 5 | Humic Acid-Vitamin Agar* | Nalidixic acid (10 µg/ml) | Taechowison et al. 1993 |
| 6 | M1 Agar* | Neomycin sulphate (4 µg/ml) | Mincer et al. 2002 |
| 7 | Gause Synthetic Agar* | Neomycin (4 µg/ml), | Tan et al. 2006 |
| 8 | SM3 Agar* | Nalidixic acid (10 µg/ml), Neomycin (10 µg/ml) | Tan et al. 2006 |
| 9 | Sodium Succinate Asparagine Agar* | Neomycin sulphate (4 µg/ml) | Piao et al. 2017 |
| 10 | Starch-Casein Agar* | Rifampicin (5 µg/ml), Nalidixic acid (10 µg/ml) | Küster and Williams, 1964 |

*Cycloheximide (50 µg/ml) and nystatin (50 µg/ml) were added to each isolation medium.

2.3. Selection, Purification and Storage of Isolates

Colonies that were likely to be *Actinobacteria* in terms of features such as morphology and spore formation were selected from the incubated colonies. In order to obtain pure cultures of these colonies, passage was carried out by streaking on the surface of International *Streptomyces* Project Medium No.2 (ISP2; Shirling and Gottlieb, 1966) agar using sterile loop. Pure isolates were obtained from transferred plates after 14 days of incubation at 28 °C. The pure cultures obtained were transferred into glycerol stock solution (20%, v/v) and finally stored at -80 °C until the time of use.

2.4. Genomic DNA Extraction from Pure Cultures

PureLink® Genomic DNA Isolation Kit (Invitrogen, USA) was used to perform genomic DNA isolations of isolates for molecular identification and phylogenetic analysis (Zothanpuia et al., 2017). The presence of products obtained following DNA isolation will be checked in 1% agarose gel electrophoresis. With the Nanodrop, DNA purities and concentrations were checked using a spectrophotometer (Thermo Scientific Multiskan GO microplate reader) with an optical density ratio of

260/280.

2.5. Identification and 16S rDNA Amplification of Actinobacterial Isolates

The 16S rRNA gene region polymerase chain reaction (PCR) amplifications were performed on a Thermal Cycler (MyGenie-96 Gradient Thermal Cycler, Korea) using the universal primers 27F and 1525R (Table 2). A reaction mix of 50 µl was prepared for 16S rRNA PCR of each test isolate. The components of this mixture are GoTaq® Hot Start Colorless Master mix (Promega), primer 27F, primer 1525R, genomic DNA and deionized water. In the mixture, these components were added as 25 µl, 1 µl, 1 µl, 1 µl and 22 µl, respectively. PCR amplification (MyGenie-96 Gradient Thermal Cycler, Korea) contains the following parameters: Pre-denaturation at 95 °C for 2 min, denaturation at 95 °C for 1 min, consisting of 30 cycles, 1.5 min bonding at 55 °C and elongation at 72 °C for 3 min, end at 72 °C for 10 min and 4 It consists of storage stages at 4°C. Amplification products were then checked by gel electrophoresis using 4 µL of PCR product in 1.5% agarose gel (Merck) and performed using the Gel imaging system (Bio-RAD).

Table 2. Oligonucleotide primers used for 16S rRNA PCR amplification and sequencing

| Primer code | Sequences (5'-3') | Base length | References |
|-------------|----------------------|-------------|-----------------------------|
| 27F | AGAGTTTGATCMTGGCTCAG | 20 | Weisburg, 1991 |
| 518F | CCAGCAGCCGCGTAAT | 17 | Buchholz-Cleven et al, 1997 |
| 800R | TACCAGGGTATCTAATCC | 18 | Chun and Goodfellow, 1995 |
| MG5F | AAACTCAAAGGAATTGACGG | 20 | Chun and Goodfellow, 1995 |
| 1525R | AAGGAGGTGWTCCARCC | 17 | Lane, 1991 |

*M; adenine or cytosine, R; adenine or guanine, W; adenine or thymine.

2.6. 16S rRNA Gene Analysis

Chromatogram files in ABI format obtained as a result of sequencing PCR products were checked using the Chromas version 1.7.6 (C. McCarthy, School of Health Sciences, Griffith University, Queensland, Australia) program and 16S rRNA gene nucleotide sequences were obtained in FASTA format for each organism by overlapping the reads of the primers. Sequences were analyzed and corrected manually. All sequences were compared to other sequences in the EzBioCloud database (Yoon et al., 2017) as well as to GenBank of the NCBI website by the BLAST program (Altschul et al., 1990). MEGA X program was used for phylogenetic analysis (Tamura et al., 2013). Multiple alignments were performed with the option Clustal_W (Tamura et al., 2013). Phylogenetic dendrograms were created based on neighbor-joining (Saitou and Nei, 1987), maximum-

likelihood (Felsenstein, 1981) and maximum-parsimony (Fitch, 1971) algorithms. The Jukes-Cantor (Jukes and Cantor, 1969) matrix was used as the phylogenetic distance matrix. Bootstrap analyzes of the obtained phylogenetic trees were performed with 1000 repetitions (Felsenstein, 1985). The 16S rRNA gene sequences of *Actinobacteria* isolates in this study were stored in the NCBI GenBank database.

3. Results

3.1. Physicochemical Properties of Soil Samples

Soil samples were taken by GPS from different localities (considering variables such as vegetation, soil type, topography, and parent material) of two different islands (Avşa; 36 km² and Marmara; 117 km², Balıkesir-South Marmara Islands) in the Marmara region included in the study (Table 3).

Table 3. Locality and Geographical coordinates of soil samples

| Soil No | Locality | Geographical coordinates |
|---------|----------|----------------------------------|
| 1 | Avşa | 40°31'52.73"K 27°30'39.60"D |
| 2 | Avşa | 40°31'39.91"K 27°31'33.27"D |
| 3 | Avşa | 40°31'12.17"K 27°32'3.82"D |
| 4 | Avşa | 40°30'49.52"K 27°32'13.12"D |
| 5 | Avşa | 40°29'26.17"K 27°32'5.83"D |
| 6 | Avşa | 40°29'11.66"K 27°30'57.66"D |
| 7 | Avşa | 40°29'38.01"K 27°30'23.03"D |
| 8 | Avşa | 40°30'18.95"K 27°30'21.38"D |
| 9 | Avşa | 40°29'29.69"K 27°29'11.73"D |
| 10 | Avşa | 40°28'22.47"K 27°29'31.80"D |
| 11 | Marmara | 40°35'31.37"K 27°33'7.013"D |
| 12 | Marmara | 40°35'44.498"K 27°32'57.156"D |
| 13 | Marmara | 40°34'42.964"K 27°34'18.318"D |
| 14 | Marmara | 40°35'42.677"K 27°35'7.879"D |
| 15 | Marmara | 40°35'13.358"K 27°36'29.398"D |
| 16 | Marmara | 40°36'32.803"K 27°41'1.835"D |
| 17 | Marmara | 40°38'21.293"K 27°41'58.909"D |
| 18 | Marmara | 40°38'59.093"K 27°41'52.127"D |

Physicochemical properties of soil samples such as electrical conductivity, amount of organic matter, moisture content, and lime content (CaCO₃) were determined (Table 4-5).

Physicochemical analyzes of Marmara and Avşa soils are shown in Table 4-5. The pH values of Avşa soil samples generally vary between 4.67 and 6.90, while the pH values of Marmara soil samples generally vary between 4.98 and 7.93. Organic matter amount of Avşa soil samples varies between 0.36 and 2.74, while organic matter amount of Marmara soil samples varies between 0.44 and 1.95. These soils are also loamy-clay-sandy and have low moisture and organic matter ratios.

3.2. Morphological Analysis of Culturable *Actinobacteria*

As a result of soil isolation, a total of 400 isolates obtained from Marmara and Avşa Islands were divided into 40 color groups according to colony morphology and pigmentation characteristics (Kelly, 1964). After color grouping, 112 isolates were selected for 16S rRNA gene

region analysis, taking into account features such as 10 different selective media, substrate mycelium, air mycelium and soil physicochemical properties, and phylogenetic analyzes were performed.

Among the actinomycete isolates, 18 strains were isolated on starch casein agar, 5 strains from Marine agar, 5 strains from R2A agar, 2 strains from SM3 agar, 2 strains from M1 agar, 15 strains from Humic acid vitamin agar, 23 strains from Gause agar, 20 strains from Czapek dox agar, 8 strains from Raffinose-Histidine agar, 14 strains from Sodium-Succinate agar and incubated at 28 °C for about 21 days (Table 6).

These results plainly showed that Gause agar was the most suitable medium for the isolation of *Actinobacteria* from islands and provided about 20% of the total isolates followed by Czapek dox agar (17%). In total, 112 culturable actinobacterial isolates were isolated from the ten different stations of the Islands: 32 isolates from the Marmara soil, 80 isolates from Avşa soil.

Table 4. Physicochemical properties of soil samples taken from Avşa Island

| Sample code | EC | pH | %OC | %OM | %CaCO ₃ | %Clay | %Silt | %Sand | Texture |
|-------------|-------|------|------|------|--------------------|-------|-------|-------|------------|
| Avşa 1 | 445,7 | 6,90 | 0,44 | 0,76 | 1,52 | 41,30 | 18,98 | 39,72 | clay |
| Avşa 2 | 143,8 | 6,75 | 0,19 | 0,32 | 2,15 | 5,03 | 3,72 | 91,25 | sand |
| Avşa 3 | 826,5 | 4,67 | 1,07 | 1,84 | 2,15 | 11,05 | 9,81 | 79,14 | sand loamy |
| Avşa 4 | 782,3 | 6,63 | 0,87 | 1,50 | 1,43 | 19,17 | 13,94 | 66,89 | sand loamy |
| Avşa 5 | 216,7 | 5,52 | 1,59 | 2,74 | 2,15 | 15,27 | 15,92 | 68,80 | sand loamy |
| Avşa 6 | 98,1 | 6,18 | 0,23 | 0,40 | 2,15 | 7,04 | 9,86 | 83,09 | sand loamy |
| Avşa 7 | 303,2 | 5,89 | 0,44 | 0,76 | 1,46 | 11,20 | 11,77 | 77,02 | sand clay |
| Avşa 8 | 368,9 | 6,18 | 0,55 | 0,95 | 1,46 | 17,34 | 16,02 | 66,64 | sand loamy |
| Avşa 9 | 254,0 | 5,89 | 0,21 | 0,36 | 1,52 | 41,24 | 16,64 | 42,12 | clay |
| Avşa 10 | 227,9 | 6,30 | 0,94 | 1,62 | 1,44 | 6,98 | 9,70 | 83,33 | sand loamy |

EC = Electrical Conductivity, OM= Organic Matter, CaCO₃= Lime Quantities.

Table 5. Physicochemical properties of soil samples taken from Marmara Island

| Sample code | EC | pH | %OC | %OM | %CaCO ₃ | %Clay | %Silt | %Sand | Texture |
|-------------|-------|------|------|------|--------------------|-------|-------|-------|------------|
| M1 | 203,6 | 6,45 | 0,52 | 0,90 | 1,44 | 14,93 | 7,85 | 77,22 | sand loamy |
| M2 | 363,3 | 7,48 | 0,72 | 1,25 | 3,67 | 19,33 | 32,30 | 48,36 | loamy clay |
| M3 | 145,3 | 6,56 | 0,86 | 1,47 | 2,19 | 31,90 | 32,77 | 35,33 | loamy clay |
| M4 | 220,7 | 4,98 | 0,30 | 0,51 | 1,45 | 15,46 | 41,42 | 43,12 | loamy clay |
| M5 | 225,9 | 6,11 | 0,57 | 0,98 | 0,78 | 29,24 | 28,06 | 42,70 | loamy sand |
| M6 | 144,4 | 7,05 | 1,13 | 1,95 | 1,43 | 12,93 | 19,92 | 67,16 | loamy sand |
| M7 | 237,0 | 7,93 | 0,85 | 1,47 | 116,90 | 35,88 | 9,92 | 54,20 | sand clay |
| M8 | 93,8 | 7,50 | 0,25 | 0,44 | 1,43 | 8,95 | 15,80 | 75,25 | sand loamy |

*EC = Electrical Conductivity, OM= Organic Matter, CaCO₃= Lime Quantities.

Table 6. Comparison of the isolation success of each culture media in function of the number of isolates/genera obtained.

| Number | Name of medium | Isolates | Genera |
|--------|--------------------------|----------|--------|
| 1 | Czapek-Dox Agar | 20 | 6 |
| 2 | Marine Agar | 5 | 6 |
| 3 | R2A Agar | 5 | 3 |
| 4 | Raffinose-Histidine Agar | 8 | 6 |
| 5 | Humic Acid-Vitamin Agar | 15 | 6 |
| 6 | M1 Agar | 2 | 2 |
| 7 | Gause Synthetic Agar | 23 | 12 |
| 8 | SM3 Agar | 2 | 2 |
| 9 | Sodium Succinate | 14 | 5 |
| 10 | Starch-Casein Agar | 18 | 6 |

3.3. Biodiversity of Culturable *Actinobacteria*

As a result of 16S rRNA gene region nucleotide sequence analysis, 112 isolates were determined to be members of the *Actinobacteria* phylum. When 112 *Actinobacteria* members were examined; It was determined that the

genera *Streptomyces* (36 isolates), *Nonomuraea* (17 isolates), *Nocardia* (11 isolates) and *Actinomadura* (11 isolates) were the dominant genera found in the island environments and the other strains belonged to the genera *Micromonospora* (6 isolates), *Kribbella* (6

isolates), *Mycolicibacterium* (2 isolates), *Microbispora* (7 isolates), *Saccharopolyspora* (3 isolates), *Jiangella* (1 isolates), *Rhodococcus* (2 isolates), *Actinopolymorpha* (3 isolates), *Geodermatophilus* (1 isolates),

Dactylosporangium (3 isolates), *Nocardioides* (1 isolates) and *Pseudonocardia* (2 isolates). Finally, results obtained in this study showed a very significant level of diversity with 16 different genera of *Actinobacteria* (Figure 2).

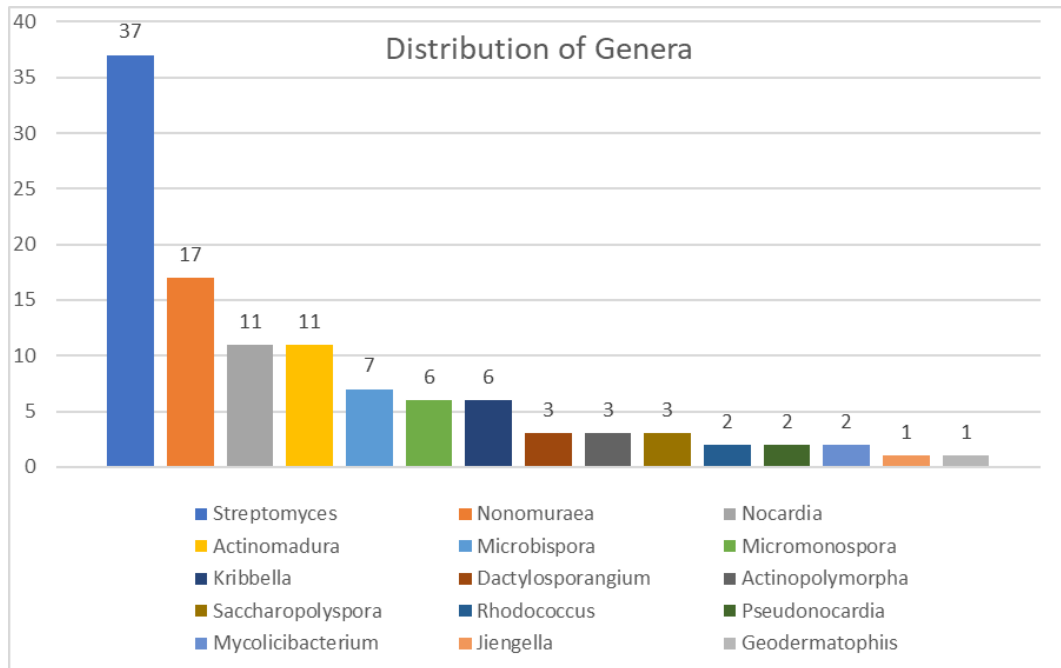


Figure 2. Distribution of *Actinobacteria* isolates by genus.

3.4. Phylogenetic Analysis of the Isolates

Phylogenetic trees based on 16S rRNA sequences were constructed to investigate the evolutionary relationships between the *Actinobacteria* isolates in this study and their closest taxonomic relatives. The molecular identification of isolates by amplification of 16S rRNA gene was done by using universal primers 518F, 800R and MG5F (Table 2). All the isolates of *Actinomadura* were found to be closely related to the genus *Actinomadura* and shared 16S rRNA gene similarity ranging from 98.19-100.00% (Figure 3). Isolates of the genera *Microbispora*, *Kribbella*, *Jiangella*, *Nocardioides*, *Actinopolymorpha*, *Geodermatophilus*, *Micromonospora*, *Dactylosporangium*, *Nocardia*, *Rhodococcus*, *Mycolicibacterium*, *Saccharopolyspora* and *Pseudonocardia* were clustered together with their closest relatives (Figure 3, 4, 5, 6, 7). The phylogenetic

tree, according to the neighbor-joining algorithm indicated that 17 strains were members of the genus *Nonomuraea* (Figure 8). Seventeen *Nonomuraea* isolates showed close 16S rRNA gene sequence similarity with the type strain of *Nonomuraea*, which are 97.78% and 99.79% (Table 7). Based on 16S rRNA gene sequence analysis, 37 isolates were identified as *Streptomyces* spp. The phylogenetic tree, according to the neighbor-joining algorithm, indicated that nineteen strains were members of the genus *Streptomyces* (Figure 9-10; Table 7). According to the 16S ribosomal RNA gene sequence analysis, 37 *Streptomyces* isolates showed close 16S rRNA gene sequence similarity to the *Streptomyces* type strains, which are 99.86% and 98.00%, respectively. The percentage of 16S ribosomal RNA gene sequence similarity of the isolates with their closest relatives is shown in Table 7.

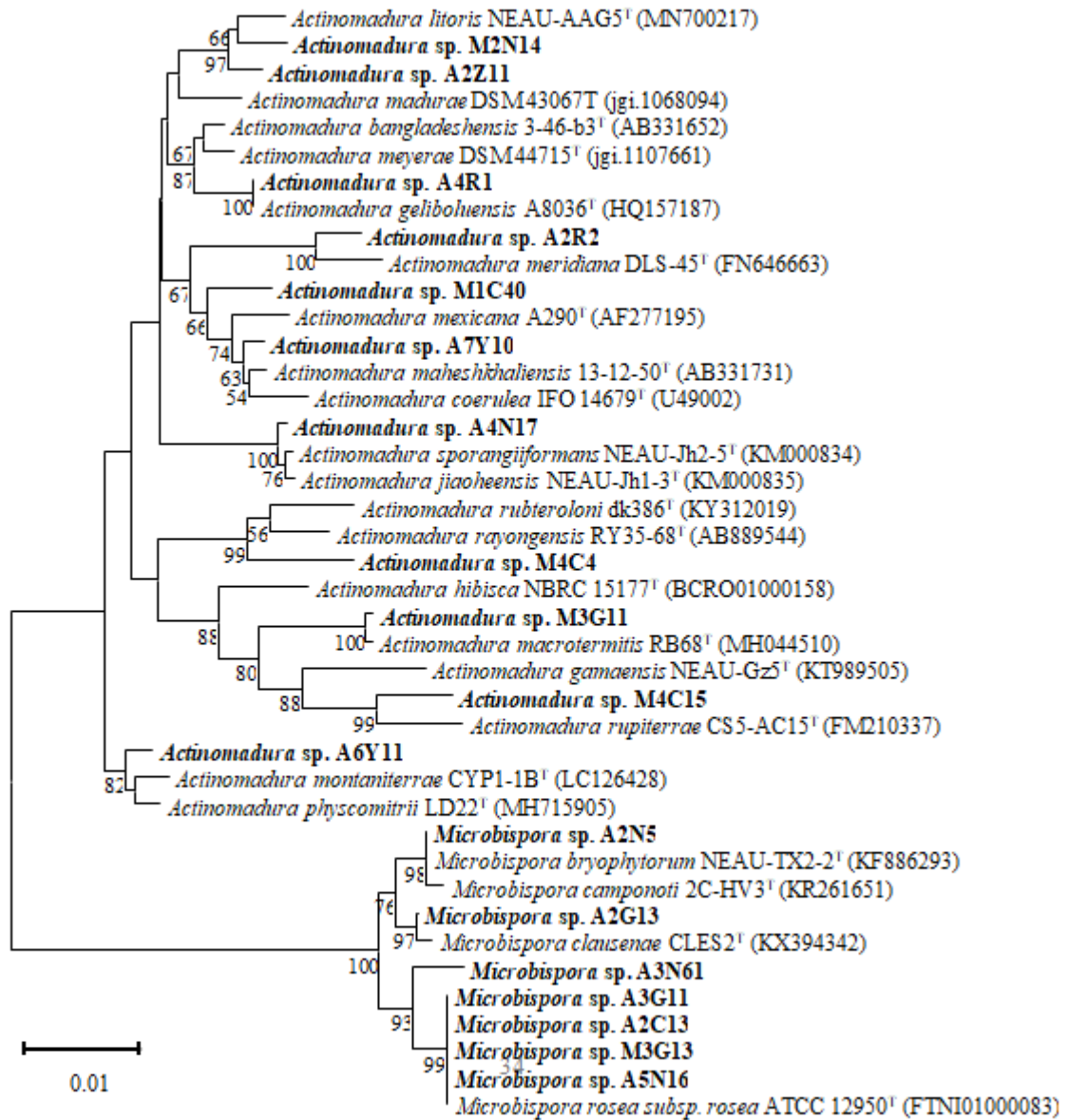


Figure 3. Phylogenetic tree showing the relationship of the actinobacterial isolates in group *Actinomadura*, group *Microbispora*, and related type strains. Phylogenetic tree was based on the Neighbor-joining method using MEGA X software. Bootstrap values above 50% (for 1000 replications) are shown. The scale bar indicates 0.01 substitutions per nucleotide position.

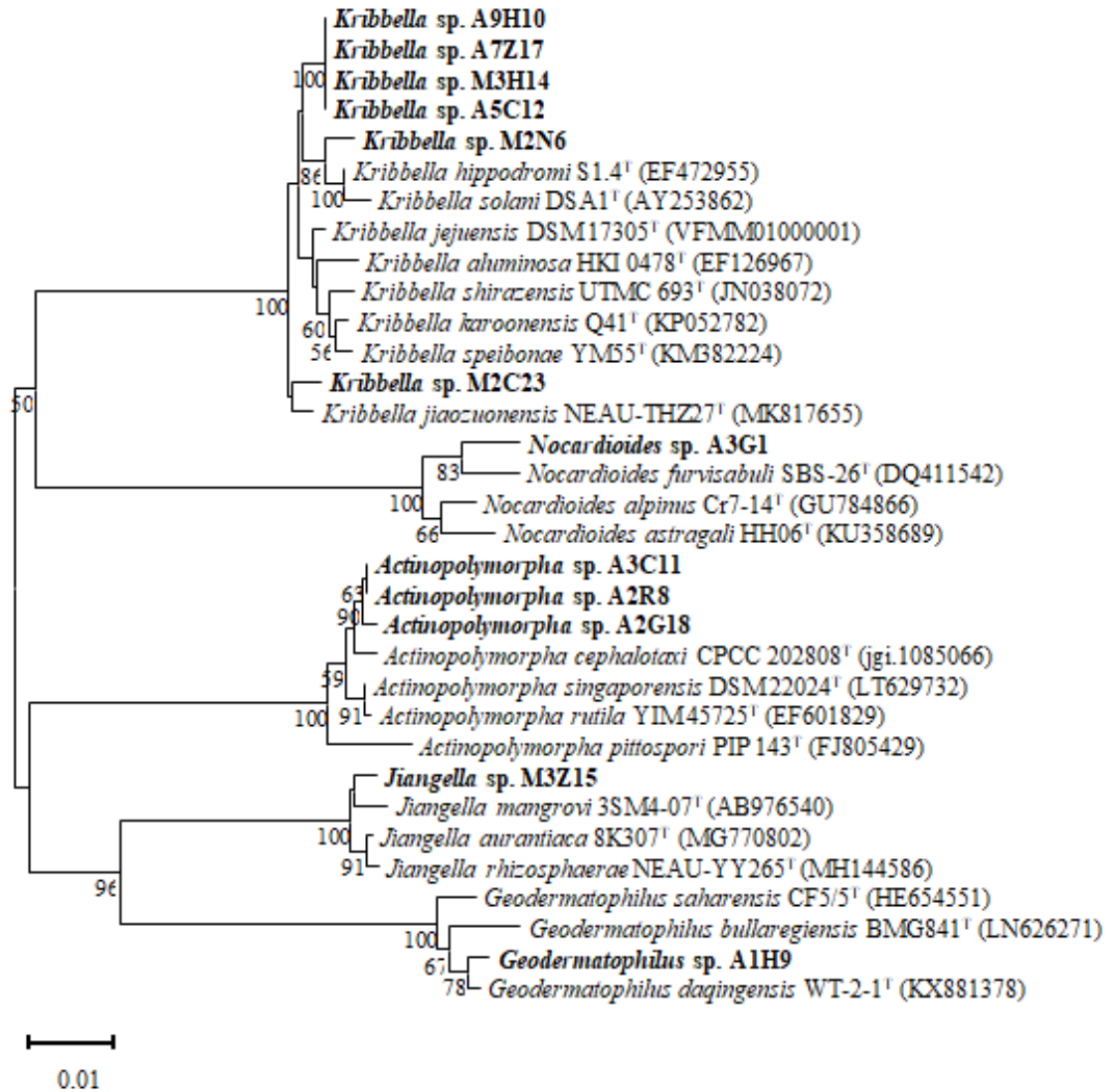


Figure 4. Phylogenetic tree showing the relationship of the actinobacterial isolates in group *Kribbella*, group *Nocardioides*, group *Actinopolymorpha*, group *Jiangella*, group *Geodermatophilus*, and related type strains. Phylogenetic tree was based on the Neighbor-joining method using MEGA X software. Bootstrap values above 50% (for 1000 replications) are shown. The scale bar indicates 0.01 substitutions per nucleotide position.

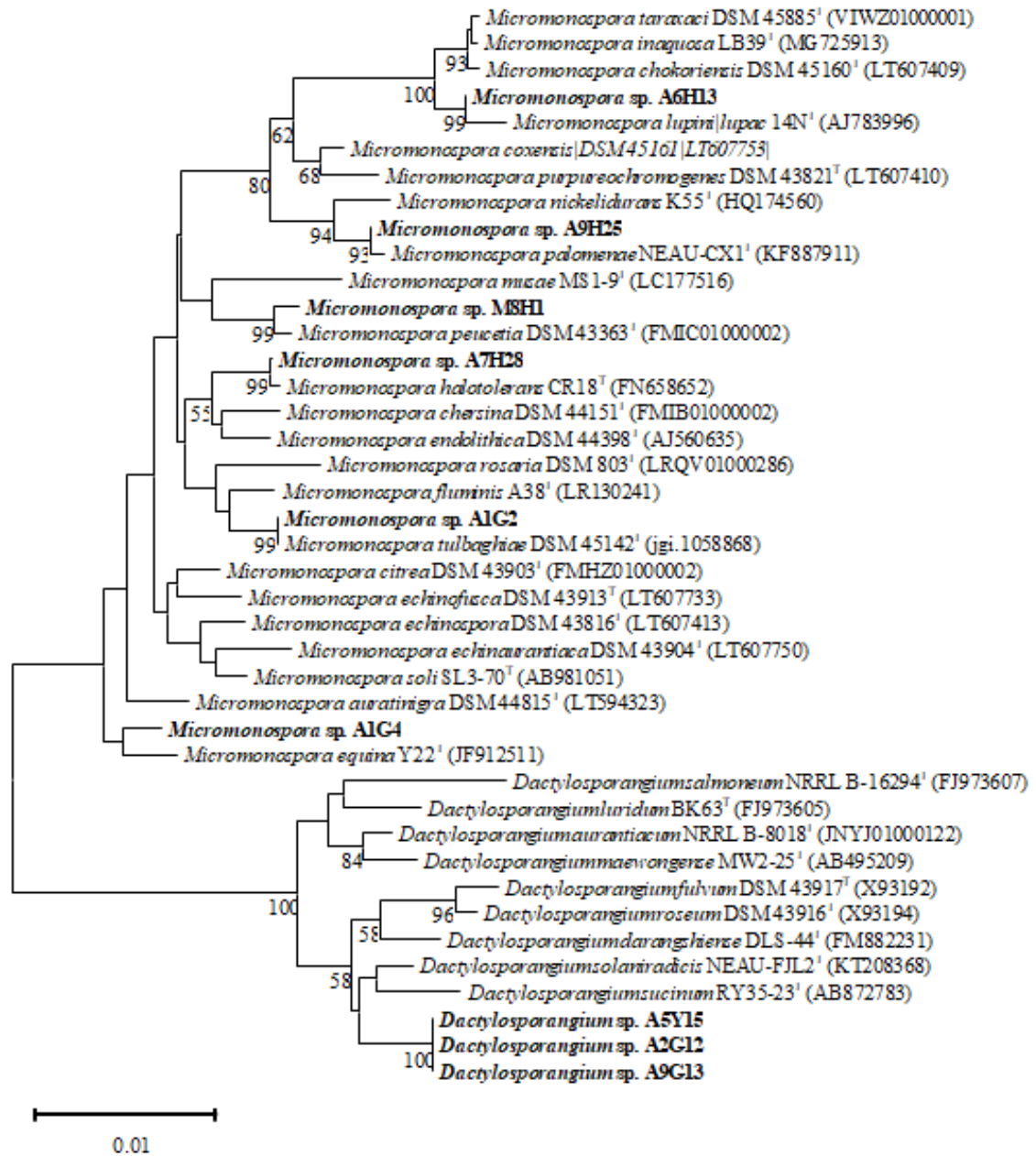


Figure 5. Phylogenetic tree showing the relationship of the actinobacterial isolates in group *Micromonospora*, group *Dactylosporangium*, and related type strains. Phylogenetic tree was based on the Neighbor-joining method using MEGA X software. Bootstrap values above 50% (for 1000 replications) are shown. The scale bar indicates 0.01 substitutions per nucleotide position.

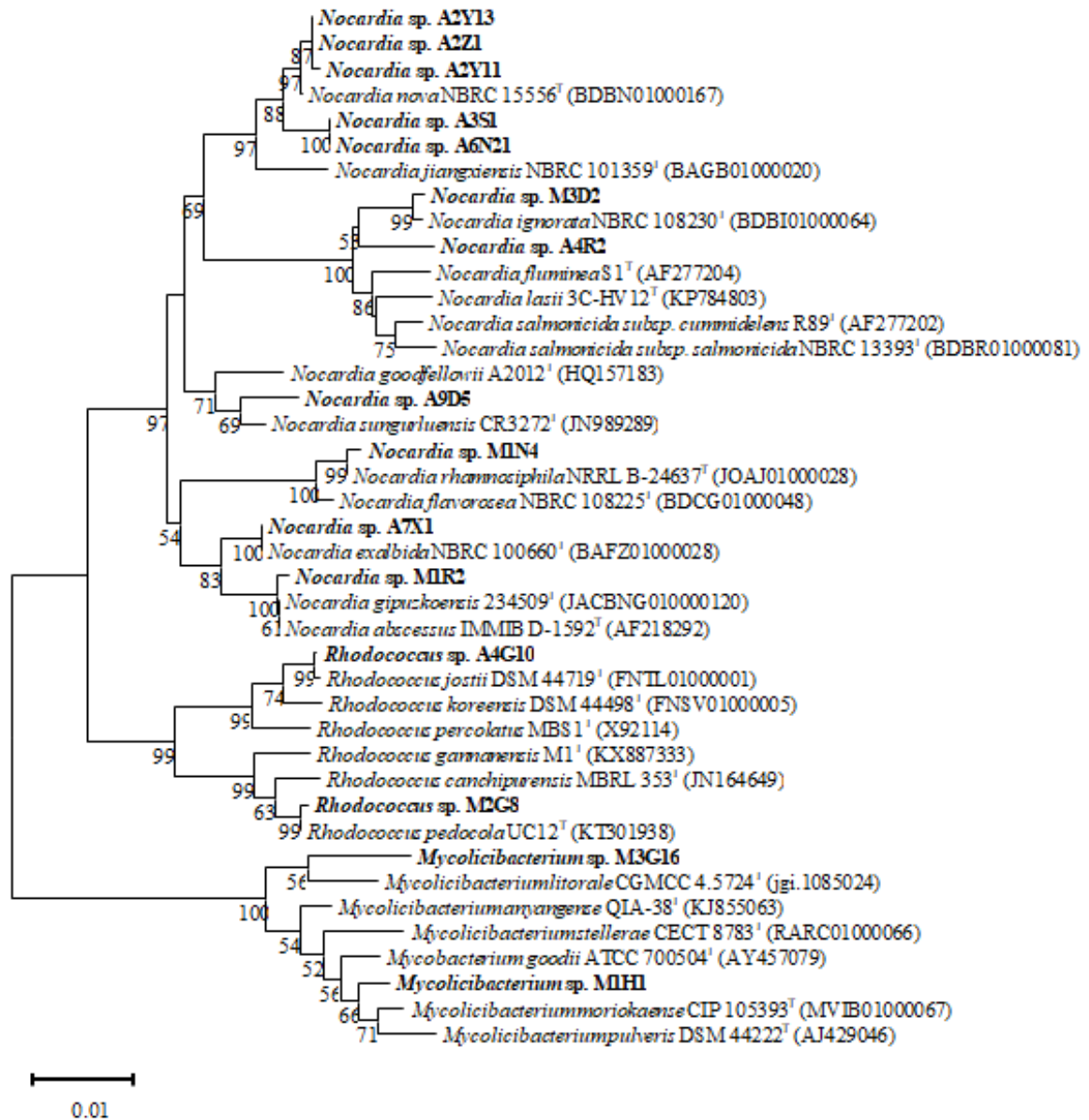


Figure 6. Phylogenetic tree showing the relationship of the actinobacterial isolates in group *Nocardia*, group *Rhodococcus*, group *Mycolicibacterium*, and related type strains. Phylogenetic tree was based on the Neighbor-joining method using MEGA X software. Bootstrap values above 50% (for 1000 replications) are shown. The scale bar indicates 0.01 substitutions per nucleotide position.

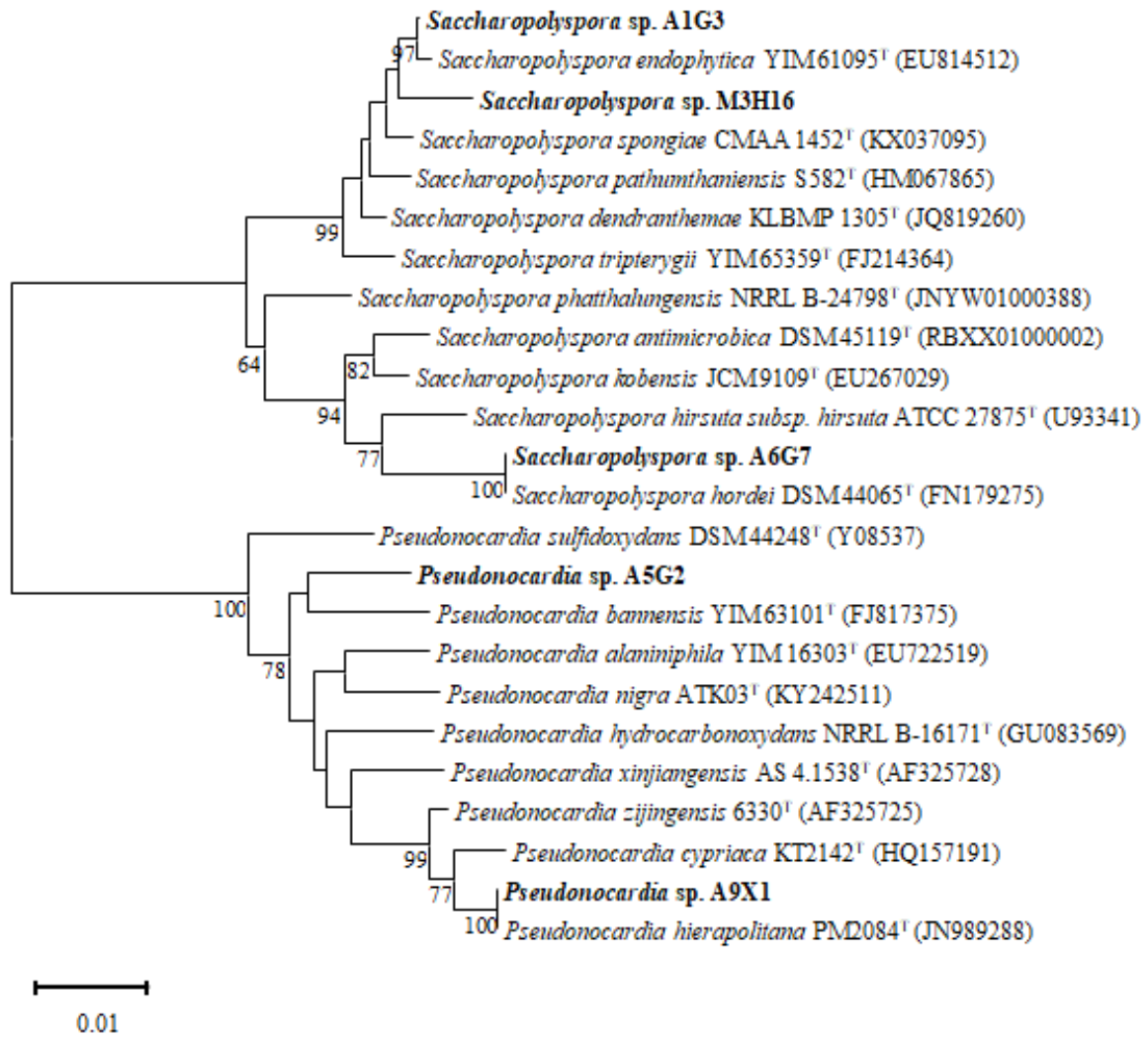


Figure 7. Phylogenetic tree showing the relationship of the actinobacterial isolates in group *Saccharopolyspora*, group *Pseudonocardia*, and related type strains. Phylogenetic tree was based on the Neighbor-joining method using MEGA X software. Bootstrap values above 50% (for 1000 replications) are shown. The scale bar indicates 0.01 substitutions per nucleotide position.

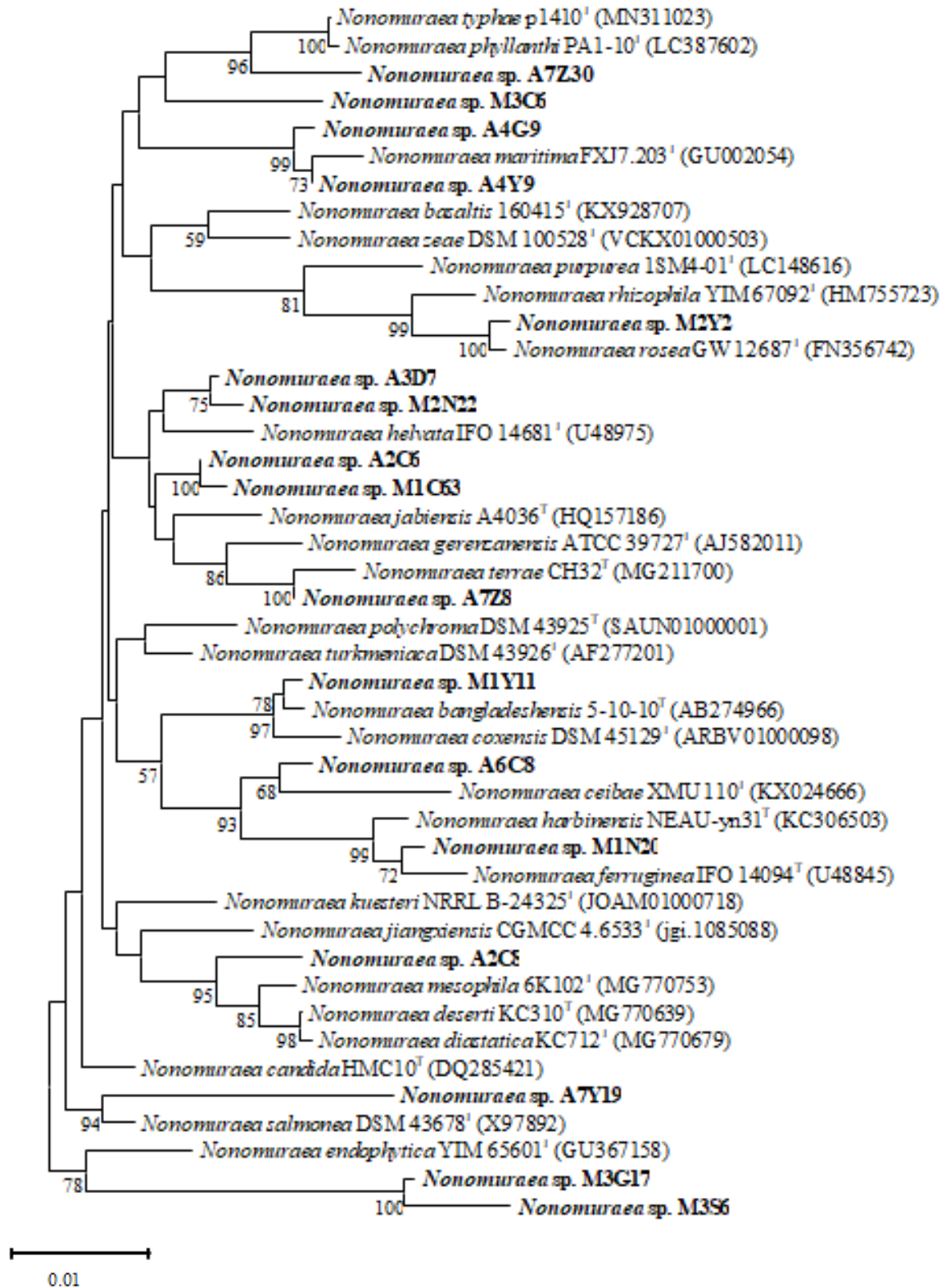


Figure 8. Phylogenetic tree showing the relationship of the actinobacterial isolates in group *Nonomuraea*, and related type strains. Phylogenetic tree was based on the Neighbor-joining method using MEGA X software. Bootstrap values above 50% (for 1000 replications) are shown. The scale bar indicates 0.01 substitutions per nucleotide position.

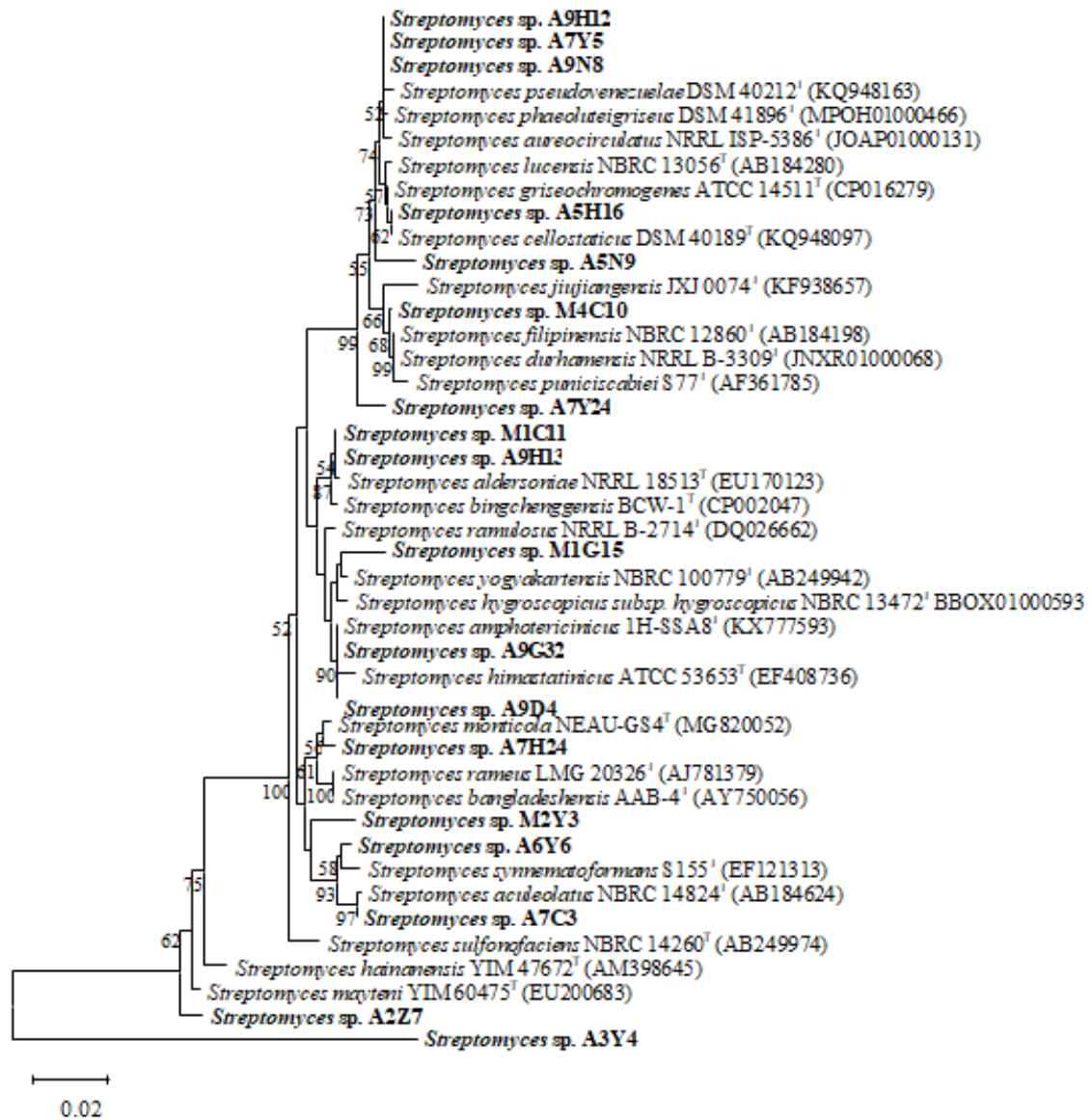


Figure 9. Phylogenetic relationships based on 16S rRNA sequences amongst 43 *Streptomyces* strains in relation to closely related validly described species. Phylogenetic tree was based on the Neighbor-joining method using MEGA X software. Bootstrap values above 50% (for 1000 replications) are shown. The scale bar indicates 0.02 substitutions per nucleotide position.

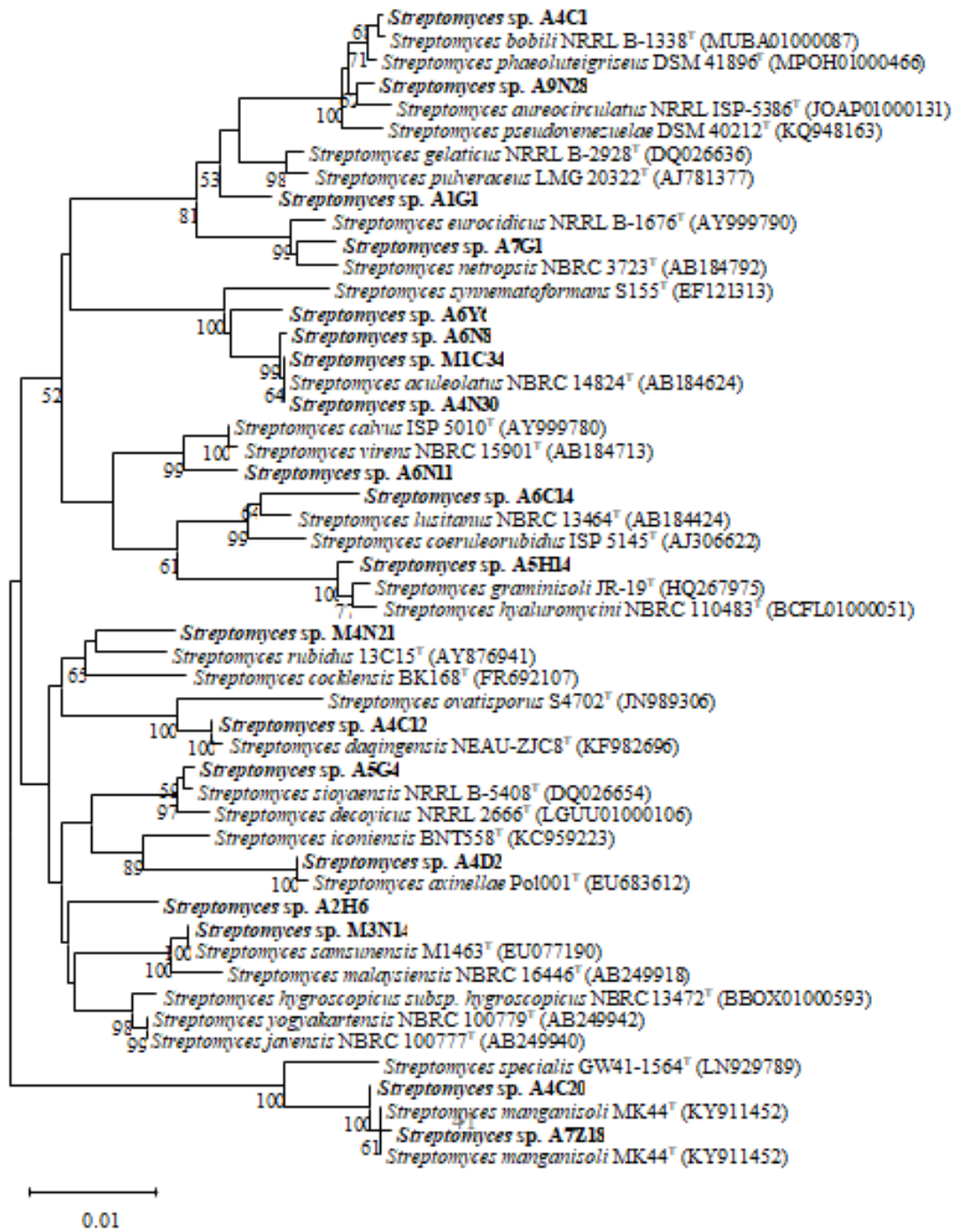


Figure 10. Phylogenetic relationships based on 16S rRNA sequences amongst 51 *Streptomyces* strains in relation to closely related validly described species. Phylogenetic tree was based on the Neighbor-joining method using MEGA X software. Bootstrap values above 50% (for 1000 replications) are shown. The scale bar indicates 0.01 substitutions per nucleotide position.

Table 7. Summary of information on 16S rRNA sequence determination of isolated strains

| Number | Strain | Locality | Highest match | Similarity (%) Nucleotide difference |
|--------|--------|----------|--|---|
| 1. | A2R2 | Avşa | <i>Actinomadura meridiana</i> DLS-45 ^T | 98.60 - 20/1426 |
| 2. | A2Z11 | Avşa | <i>Actinomadura litoris</i> NEAU-AAG5 ^T | 99.17 - 12/1438 |
| 3. | A4N17 | Avşa | <i>Actinomadura sporangiiformans</i> NEAU-Jh2-5 ^T | 99.79 - 3/1440 |
| 4. | A4R1 | Avşa | <i>Actinomadura geliboluensis</i> A8036 ^T | 100.00 - 0/1441 |
| 5. | A6Y11 | Avşa | <i>Actinomadura montaniterrae</i> CYP1-1B ^T | 99.31 - 10/1440 |
| 6. | A7Y10 | Avşa | <i>Actinomadura maheshkhaliensis</i> 13-12-50 ^T | 99.58 - 6/1417 |
| 7. | M1C40 | Avşa | <i>Actinomadura maheshkhaliensis</i> 13-12-50 ^T | 99.08 - 13/1420 |
| 8. | M2N14 | Marmara | <i>Actinomadura litoris</i> NEAU-AAG5 ^T | 99.03 - 14/1438 |
| 9. | M3G11 | Marmara | <i>Actinomadura macrotermis</i> RB68 ^T | 99.86 - 2/1442 |
| 10. | M4C4 | Marmara | <i>Actinomadura rubteroloni</i> dk386 ^T | 98.19 - 26/1438 |
| 11. | M4C15 | Marmara | <i>Actinomadura rupiterrae</i> CS5-AC15 ^T | 98.25 - 25/1427 |
| 12. | A2G18 | Avşa | <i>Actinopolymorpha cephalotaxi</i> CPCC 202808 ^T | 99.44 - 8/1439 |
| 13. | M3Z15 | Marmara | <i>Jiangella aurantiaca</i> 8K307 ^T | 99.51 - 7/1441 |
| 14. | A1H9 | Avşa | <i>Geodermatophilus daqingensis</i> WT-2-1 ^T | 99.58 - 6/1443 |
| 15. | A2G12 | Avşa | <i>Dactylosporangium solaniradicis</i> NEAU-FJL2 ^T | 99.16 - 12/1437 |
| 16. | A5Y15 | Avşa | <i>Dactylosporangium solaniradicis</i> NEAU-FJL2 ^T | 99.16 - 12/1437 |
| 17. | A9G13 | Avşa | <i>Dactylosporangium solaniradicis</i> NEAU-FJL2 ^T | 99.16 - 12/1437 |
| 18. | A5G2 | Avşa | <i>Pseudonocardia xinjiangensis</i> AS 4.1538 ^T | 97.74 - 30/1325 |
| 19. | A9X1 | Avşa | <i>Pseudonocardia hierapolitana</i> PM2084 ^T | 99.79 - 3/1443 |
| 20. | A1G3 | Avşa | <i>Saccharopolyspora endophytica</i> YIM 61095 ^T | 99.86 - 2/1445 |
| 21. | A6G7 | Avşa | <i>Saccharopolyspora hordei</i> DSM 44065 ^T | 99.86 - 2/1448 |
| 22. | M3H16 | Marmara | <i>Saccharopolyspora spongiae</i> CMAA 1452 ^T | 98.75 - 18/1443 |
| 23. | A4G10 | Avşa | <i>Rhodococcus jostii</i> DSM 44719 ^T | 99.93 - 1/1440 |
| 24. | M2G8 | Marmara | <i>Rhodococcus pedocola</i> UC12 ^T | 99.93 - 1/1441 |
| 25. | M1H1 | Marmara | <i>Mycolicibacterium moriokaense</i> CIP 105393 ^T | 99.10 - 13/1444 |
| 26. | M3G16 | Marmara | <i>Mycolicibacterium litorale</i> CGMCC 4.5724 ^T | 98.40 - 23/1442 |
| 27. | A5C12 | Avşa | <i>Kribbella jejuensis</i> DSM 17305 ^T | 99.52 - 7/1447 |
| 28. | A7Z17 | Avşa | <i>Kribbella jejuensis</i> DSM 17305 ^T | 99.52 - 7/1447 |
| 29. | A9H10 | Avşa | <i>Kribbella jejuensis</i> DSM 17305 ^T | 99.52 - 7/1447 |
| 30. | M2C23 | Marmara | <i>Kribbella karoonensis</i> Q41 ^T | 99.45 - 8/1447 |
| 31. | M2N6 | Marmara | <i>Kribbella hippodromi</i> S1.4 ^T | 99.35 - 9/1389 |
| 32. | M3H14 | Marmara | <i>Kribbella jejuensis</i> DSM 17305 ^T | 99.52 - 7/1445 |
| 33. | A2C13 | Avşa | <i>Microbispora rosea</i> subsp. <i>rosea</i> ATCC 12950 ^T | 100.00 - 0/1443 |
| 34. | A2G13 | Avşa | <i>Microbispora clausenae</i> CLES2 ^T | 99.79 - 3/1443 |
| 35. | A2N5 | Avşa | <i>Microbispora bryophytorum</i> NEAU-TX2-2 ^T | 100.00 - 0/1443 |
| 36. | A3G11 | Avşa | <i>Microbispora rosea</i> subsp. <i>rosea</i> ATCC 12950 ^T | 100.00 - 0/1443 |
| 37. | A3N61 | Avşa | <i>Microbispora rosea</i> subsp. <i>rosea</i> ATCC 12950 ^T | 99.17 - 12/1443 |
| 38. | A5N16 | Avşa | <i>Microbispora rosea</i> subsp. <i>rosea</i> ATCC 12950 ^T | 100.00 - 0/1443 |
| 39. | M3G13 | Marmara | <i>Microbispora rosea</i> subsp. <i>rosea</i> ATCC 12950 ^T | 100.00 - 0/1443 |
| 40. | A1G4 | Avşa | <i>Micromonospora echinaurantiaca</i> DSM 43904 ^T | 99.24 - 11/1439 |
| 41. | A1G2 | Avşa | <i>Micromonospora tulbaghia</i> DSM 45142 ^T | 100.00 - 0/1437 |
| 42. | A6H13 | Avşa | <i>Micromonospora taraxaci</i> DSM 45885 ^T | 99.65 - 5/1437 |
| 43. | A7H28 | Avşa | <i>Micromonospora halotolerans</i> CR18 ^T | 99.93 - 1/1429 |
| 44. | A9H25 | Avşa | <i>Micromonospora palomenae</i> NEAU-CX1 ^T | 99.93 - 1/1438 |
| 45. | M4H1 | Avşa | <i>Streptomyces aculeolatus</i> NBRC 14824 ^T | 99.72 - 4/1442 |
| 46. | A2Y11 | Avşa | <i>Nocardia nova</i> NBRC 15556 ^T | 99.79 - 3/1439 |
| 47. | A2Y13 | Avşa | <i>Nocardia nova</i> NBRC 15556 ^T | 99.86 - 2/1438 |
| 48. | A2Z1 | Avşa | <i>Nocardia nova</i> NBRC 15556 ^T | 99.86 - 2/1439 |
| 49. | A3S1 | Avşa | <i>Nocardia nova</i> NBRC 15556 ^T | 99.37 - 9/1439 |
| 50. | A4R2 | Avşa | <i>Nocardia salmonicida</i> subsp. <i>cummidelens</i> R89 ^T | 98.60 - 20/1425 |
| 51. | A6N21 | Avşa | <i>Nocardia nova</i> NBRC 15556 ^T | 99.30 - 10/1438 |
| 52. | A7X1 | Avşa | <i>Nocardia exalbida</i> NBRC 100660 ^T | 100.00 - 0/1441 |
| 53. | A9D5 | Avşa | <i>Nocardia sungurluensis</i> CR3272 ^T | 99.24 - 11/1441 |
| 54. | M1N4 | Marmara | <i>Nocardia rhamnosiphila</i> NRRL B-24637 ^T | 99.86 - 2/1439 |
| 55. | M1R2 | Marmara | <i>Nocardia gipuzkoensis</i> 234509 ^T | 99.86 - 2/1441 |
| 56. | M3D2 | Marmara | <i>Nocardia ignorata</i> NBRC 108230 ^T | 99.72 - 4/1441 |
| 57. | A2C6 | Avşa | <i>Nonomuraea jabiensis</i> A4036 ^T | 99.31 - 10/1442 |

Table 7. Summary of information on 16S rRNA sequence determination of isolated strains (continuing)

| Number | Strain | Locality | Highest match | Similarity (%) Nucleotide difference |
|--------|--------|----------|---|---|
| 58. | A2C8 | Avşa | <i>Nonomuraea deserti</i> KC310 ^T | 98.96 - 15/1443 |
| 59. | A3D7 | Avşa | <i>Nonomuraea helvata</i> IFO 14681 ^T | 98.65 - 19/1409 |
| 60. | A4G9 | Avşa | <i>Nonomuraea maritima</i> FXJ7.203 ^T | 99.51 - 7/1441 |
| 61. | A4Y9 | Avşa | <i>Nonomuraea maritima</i> FXJ7.203 ^T | 99.72 - 4/1441 |
| 62. | A6C8 | Avşa | <i>Nonomuraea ceibae</i> XMU 110 ^T | 98.89 - 16/1437 |
| 63. | A7Y19 | Avşa | <i>Nonomuraea salmonea</i> DSM 43678 ^T | 97.49 - 36/1436 |
| 64. | A7Z8 | Avşa | <i>Nonomuraea terrae</i> CH32 ^T | 99.65 - 5/1441 |
| 65. | A7Z30 | Avşa | <i>Nonomuraea nitratreducens</i> WYY166 ^T | 98.89 - 16/1444 |
| 66. | M1N20 | Marmara | <i>Nonomuraea harbinensis</i> NEAU-yn31 ^T | 99.65 - 5/1447 |
| 67. | M1Y11 | Marmara | <i>Nonomuraea bangladeshensis</i> 5-10-10 ^T | 99.79 - 3/1441 |
| 68. | M1C63 | Marmara | <i>Nonomuraea jabiensis</i> A4036 ^T | 99.17 - 12/1442 |
| 69. | M2Y2 | Marmara | <i>Nonomuraea rosea</i> GW 12687 ^T | 99.78 - 3/1375 |
| 70. | M2N22 | Marmara | <i>Nonomuraea jabiensis</i> A4036 ^T | 98.82 - 17/1441 |
| 71. | M3C6 | Marmara | <i>Nonomuraea basaltis</i> 160415 ^T | 98.68 - 19/1443 |
| 72. | M3S6 | Marmara | <i>Nonomuraea endophytica</i> YIM 65601 ^T | 97.28 - 39/1434 |
| 73. | M3G17 | Marmara | <i>Nonomuraea endophytica</i> YIM 65601 ^T | 97.78 - 32/1444 |
| 74. | A3G1 | Avşa | <i>Nocardioides furvisabuli</i> SBS-26(T) | 98.57 - 20/1398 |
| 75. | A1G1 | Avşa | <i>Streptomyces gelaticus</i> NRRL B-2928 ^T | 99.03 - 14/1448 |
| 76. | A2H6 | Avşa | <i>Streptomyces hygrosopicus</i> subsp. NBRC 13472 ^T | 98.47 - 22/1442 |
| 77. | A2Z7 | Avşa | <i>Streptomyces mayteni</i> YIM 60475 ^T | 99.27 - 10/1378 |
| 78. | A3Y4 | Avşa | <i>Streptomyces mayteni</i> YIM 60475 ^T | 89.67 - 142/1374 |
| 79. | A4C1 | Avşa | <i>Streptomyces bobili</i> NRRL B-1338 ^T | 99.86 - 2/1448 |
| 80. | A4C12 | Avşa | <i>Streptomyces daqingensis</i> NEAU-ZJC8 ^T | 99.79 - 3/1450 |
| 81. | A4C20 | Avşa | <i>Streptomyces manganisoli</i> MK44 ^T | 99.64 - 5/1405 |
| 82. | A4D2 | Avşa | <i>Streptomyces axinellae</i> Pol001 ^T | 99.86 - 2/1422 |
| 83. | A4N30 | Avşa | <i>Streptomyces aculeolatus</i> NBRC 14824 ^T | 99.51 - 7/1440 |
| 84. | A5G4 | Avşa | <i>Streptomyces sioyaensis</i> NRRL B-5408 ^T | 99.79 - 3/1451 |
| 85. | A5H14 | Avşa | <i>Streptomyces graminisoli</i> JR-19 ^T | 99.72 - 4/1446 |
| 86. | A5H16 | Avşa | <i>Streptomyces cellostaticus</i> DSM 40189 ^T | 99.59 - 6/1448 |
| 87. | A5N9 | Avşa | <i>Streptomyces lucensis</i> NBRC 13056 ^T | 98.74 - 18/1426 |
| 88. | A6C14 | Avşa | <i>Streptomyces lusitanus</i> NBRC 13464 ^T | 98.67 - 19/1427 |
| 89. | A6N8 | Avşa | <i>Streptomyces aculeolatus</i> NBRC 14824 ^T | 99.58 - 6/1440 |
| 90. | A6N11 | Avşa | <i>Streptomyces calvus</i> ISP 5010 ^T | 99.10 - 13/1447 |
| 91. | A6Y6 | Avşa | <i>Streptomyces aculeolatus</i> NBRC 14824 ^T | 98.75 - 18/1440 |
| 92. | A7C3 | Avşa | <i>Streptomyces aculeolatus</i> NBRC 14824 ^T | 99.72 - 4/1442 |
| 93. | A7G1 | Avşa | <i>Streptomyces netropsis</i> NBRC 3723 ^T | 99.24 - 11/1445 |
| 94. | A7Y5 | Avşa | <i>Streptomyces aureocirculatus</i> NRRL ISP-5386 ^T | 99.52 - 7/1450 |
| 95. | A7H24 | Avşa | <i>Streptomyces rameus</i> LMG 20326 ^T | 99.10 - 13/1446 |
| 96. | A7Y24 | Avşa | <i>Streptomyces durhamensis</i> NRRL B-3309 ^T | 98.62 - 20/1448 |
| 97. | A7Z18 | Avşa | <i>Streptomyces manganisoli</i> MK44 ^T | 99.57 - 6/1405 |
| 98. | A9D4 | Avşa | <i>Streptomyces amphotericinicus</i> 1H-SSA8 ^T | 99.24 - 11/1449 |
| 99. | A9G32 | Avşa | <i>Streptomyces amphotericinicus</i> 1H-SSA8 ^T | 99.52 - 7/1449 |
| 100. | A9H12 | Avşa | <i>Streptomyces pseudovenezuelae</i> DSM 40212 ^T | 99.38 - 9/1450 |
| 101. | A9H13 | Avşa | <i>Streptomyces aldersoniae</i> NRRL 18513 ^T | 99.79 - 3/1420 |
| 102. | A9N8 | Avşa | <i>Streptomyces aureocirculatus</i> NRRL ISP-5386 ^T | 99.78 - 2/911 |
| 103. | A9N28 | Avşa | <i>Streptomyces aureocirculatus</i> NRRL ISP-5386 ^T | 99.52 - 7/1450 |
| 104. | M1C11 | Marmara | <i>Streptomyces aldersoniae</i> NRRL 18513 ^T | 99.51 - 7/1420 |
| 105. | M1C34 | Marmara | <i>Streptomyces aculeolatus</i> NBRC 14824 ^T | 99.86 - 2/1440 |
| 106. | M2Y3 | Marmara | <i>Streptomyces sulfonofaciens</i> NBRC 14260 ^T | 98.00 - 29/1448 |
| 107. | M3N14 | Marmara | <i>Streptomyces samsunensis</i> M1463 ^T | 99.86 - 2/1425 |
| 108. | M4C10 | Marmara | <i>Streptomyces filipinensis</i> NBRC 12860 ^T | 99.24 - 11/1445 |
| 109. | M4N21 | Marmara | <i>Streptomyces rubidus</i> 13C15 ^T | 98.58 - 20/1413 |
| 110. | M8H1 | Marmara | <i>Micromonospora peucetia</i> DSM 43363 ^T | 99.58 - 6/1437 |
| 111. | A2R8 | Avşa | <i>Actinopolymorpha singaporensis</i> DSM 22024 ^T | 99.51 - 7/1439 |
| 112. | M1G15 | Marmara | <i>Streptomyces hygrosopicus</i> subsp. NBRC 13472 ^T | 98.61 - 20/1442 |

4. Discussion

Actinobacteria have been isolated from many different habitats so far. Among these habitats, Island environments attract more attention in terms of their new species hosting potential. At the same time, culture media was an inflection point for the success in the number of isolates and genera. Pek Lim Chu et al identified 36 actinobacterial isolates based on 16S rRNA gene sequence analysis in a study from 15 soil samples collected at South Shetland Island. They used five different media during isolation. They concluded that 36 actinobacterial isolates were separated into a common genus (*Streptomyces*) and nine rare genera (*Micromonospora*, *Micrococcus*, *Kocuria*, *Dermacoccus*, *Brachybacterium*, *Brevibacterium*, *Rhodococcus*, *Microbacterium* and *Rothia*) (Lim et al., 2017).

According to a study conducted in 2021, 6 soil samples were taken from Sichang Island, Chonburi Province, Thailand and the culture-dependent method was employed to obtain *Actinobacteria* (Phongsopitanuna et al., 2021). A total of 55 culturable *actinobacteria* were isolated and 3 different genera (*Streptomyces*, *Nocardia* and *Saccharothrix*) were obtained by comparative analysis of partial 16S rRNA gene sequences. The dominant genus was *Streptomyces*, followed by *Nocardia*. Only humic acid vitamin (HV) agar was used during isolation.

In another study carried out in 2020, a total of 32 isolates were isolated from soil samples of different forest locations of Bisle Ghat and Virjapet situated in Western Ghats of Karnataka, India. The isolates were identified as species of *Streptomyces*, *Nocardiopsis*, and *Nocardioides* by cultural, morphological, and molecular studies. isolates were obtained on starch casein agar and Actinomycetes isolation agar (Siddharth et al., 2020).

In our study, 112 isolates were obtained as a result of isolation from the Islands using 10 different media. In the effort of isolating *Actinobacteria* from Islands, Gause Agar was the most efficient isolation medium and capable of recovering the highest diversity of *Streptomyces* and rare *Actinobacteria*. In this study, 20% of the *Actinobacteria* isolates were recovered from Gause Agar. Interestingly, all *Rhodococcus* and *Nocardioides* isolates were only recovered on Gause Agar, while *Streptomyces* isolates were recovered on 80 percent of the media used. This finding could relate to the natural ecological role of *Actinobacteria* in recycling and decomposition of organic materials in soils, and their prevalence distribution in humus-rich soils (Goodfellow and Williams 1983; Ventura et al., 2007).

Rare *Actinobacteria* are an important resource for the discovery of new antibiotics (Tiwari et al., 2012). Rare *Actinobacteria* are defined as certain types of *Actinobacteria* that are difficult to isolate. In our study, about 10 genera belonging to rare *Actinobacteria* members were obtained (*Micromonospora*, *Actinomadura*, *Nonomuraea*, *Nocardia*, *Pseudanocardia*,

Rhodococcus, *Kribbella*, *Dactylosporangium*, *Saccharopolyspora*, *Microbispora*). Considering these studies, it is seen that the genus and biodiversity of *Actinobacteria* strains obtained with the use of different media in isolation studies and the increase in the number of isolated samples increased.

In 2014, Kim et al suggested that a value of 98.65% 16S rRNA gene sequence similarity could be used as the threshold for differentiating two bacterial species. Based on this data, A7Z30, A2C8, M3C6, A6C8, A3D7 and M3G17 strains may be new species belonging to the genus *Nonomuraea*. These isolates had 98.96%, 98.68%, 98.89%, 98.65% and 97.78% 16S rRNA gene sequence similarity with the closest *Nonomuraea* type species, respectively. A2R2 and M4C4 strains showed close 16S rRNA gene sequence similarity, 98.60% and 98.19%, with the type strain of *Actinomadura*, A5G2 strain showed 97.74% 16S rRNA gene sequence similarity with *Pseudanocardia* type strain, M3G16 strain showed close 16S rRNA gene sequence similarity, 98.47% with the type strain of *Mycolicibacterium*, M2Y3 strain showed close 16S rRNA gene sequence similarity, 98.00% with the type strain of *Streptomyces*. 16S rRNA gene sequence similarity ratios of other species are given in the Table 7. In this study, the 16S rRNA gene similarity of the above-mentioned isolates was lower than 98.65%, indicating that these isolates are candidates for a new species of actinobacterial taxa.

5. Conclusion

This research is the first to examine the diversity of *Actinobacteria* in the soils of "Marmara" and "Avşa" in Türkiye with the dilution plating method. In this study, a large number of *Actinobacteria* were effectively isolated and identified from two different islands. Our primary data based on the 16S rRNA gene revealed that the actinobacterial community is very diverse. In addition to the genera of *Actinobacteria* found in the two studied regions, some unknown members that do not belong to the class *Actinobacteria* were also identified.

According to the results of 16S rRNA gene region % similarity and nucleotide difference, *Actinomadura* sp. M4C4, *Actinomadura* sp. A2R2, *Mycolicibacterium* sp. M3G16, *Nonomuraea* sp. A7Z30, *Nonomuraea* sp. A2C8, *Nonomuraea* sp. M3C6, *Nonomuraea* sp. A6C8, *Nonomuraea* sp. A3D7, *Nonomuraea* sp. M3G17, *Saccharopolyspora* sp. M3H16, *Pseudanocardia* sp. A5G2, *Nocardia* sp. A4R2, *Streptomyces* sp. M2Y3, *Streptomyces* sp. A5N9, *Streptomyces* sp. A7Y24, *Streptomyces* sp. M4N21, *Streptomyces* sp. A6Y6, *Streptomyces* sp. A6C14 and *Streptomyces* sp. A2H6 isolates are thought to be most likely new species. In addition, all our new isolates may be important candidates for biotechnological applications.

After this work, a large number of new species were revealed, thus determining the diversity and distribution of *Actinobacteria* in island environments. Thereby,

Islands were shown to be a valuable resource for *Actinobacteria* strains with a high rate of putative new and rare species.

Two aspects appear of primary importance in regard to the high degree of novelty and diversity of *Actinobacteria* found. First, the application of various culture media significantly increased the number of species and genera obtained. Second, the geographical isolation is considered to be of importance regarding the actinobacterial novelty found.

Author Contributions

The percentage of the author(s) contributions is presented below. All authors reviewed and approved the final version of the manuscript.

| | A.R.T. | K.I. |
|-----|--------|------|
| C | 50 | 50 |
| D | 50 | 50 |
| S | 50 | 50 |
| DCP | 50 | 50 |
| DAI | 50 | 50 |
| L | 50 | 50 |
| W | 50 | 50 |
| CR | 50 | 50 |
| SR | 50 | 50 |
| PM | 50 | 50 |
| FA | 50 | 50 |

C=Concept, D= design, S= supervision, DCP= data collection and/or processing, DAI= data analysis and/or interpretation, L= literature search, W= writing, CR= critical review, SR= submission and revision, PM= project management, FA= funding acquisition.

Conflict of Interest

The authors declared that there is no conflict of interest.

Ethical Consideration

Ethics committee approval was not required for this study because of there was no study on animals or humans. The authors confirm that the ethical policies of the journal, as noted on the journal's author guidelines page, have been adhered to.

Acknowledgements

This study was supported by Ondokuz Mayıs University Scientific Research Projects Coordination Unit (BAPKOB) under the project number PYO.FEN.1904.21.006.

References

Altschul SF, Gish W, Miller W. 1990. Basic local alignment search tool. *J Mol Biol*, 215: 403-410.

Amin A, Ahmed I, Khalid N, Osman G, Khan IU, Xiao M, Li WJ. 2017. *Streptomyces caldifontis* sp. nov., isolated from a hot water spring of Tatta Pani, Kotli, Pakistan. *Antonie van Leeuwenhoek*, 110(1): 77-86.

Barabote RD, Xie G, Leu DH, Normand P, Necsulea A, Daubin V, Me'digue C, Adney WS, Xu XC, Lapidus A, Parales RE, Detter C, Pujic P, Bruce D, Lavire C, Challacombe JF, Brettin TS, Berry AM. 2009. Complete genome of the cellulolytic thermophile

Acidothermus cellulolyticus 11B provides insights into its ecophysiological and evolutionary adaptations. *Genome Res*, 19: 1033-1043.

Buchholz-Cleven BEE, Rattunde B, Straub KL. 1997. Screening for genetic diversity of isolates of anaerobic Fe (II)-oxidizing bacteria using DGGE and whole-cell hybridization. *Syst Appl Microbiol*, 20(2): 301-309.

Chaouch FC, Bouras N, Mokrane S, Zitouni A, Schumann P, Spröer C, Sabaou N, Klenk HP. 2016. *Streptosporangium becharensense* sp. nov., an actinobacterium isolated from desert soil. *International Journal of Systematic and Evolutionary Microbiology*, 64(7): 2484-2490.

Chun J, Goodfellow MA. 1995. Phylogenetic analysis of the genus *Nocardia* with 16S rRNA gene sequences. *Int J Syst Bacteriol*, 45(2): 240-245.

Corretto E, Antonielli L, Sessitsch A, Compant S, Gorfer M, Kuffner M, Brader G. 2016. *Agromyces aureus* sp. nov., isolated from the rhizosphere of *Salix caprea* L. grown in a heavy-metal-contaminated soil. *Int J Syst Evol Microbiol*, 66(9): 3749-3754.

Deng S, Chang X, Zhang Y, Ren L, Jiang F, Qu Z, Peng F. 2015. *Nocardioides antarcticus* sp. nov., isolated from marine sediment. *Int J Syst Evol Microbiol*, 65(8): 2615-2621.

El-Tarabily KA, Hardy GESJ, Sivasithamparam K, Kurtböke ID. 1996. Microbiological differences between limed and unlimed soils and their relationship with cavity spot disease of carrots (*Daucus carota* L.) caused by *Pythium coloratum* in Western Australia. *Plant and Soil*, 183(2): 279-290.

El-Tarabily KA, Sivasithamparam K. 2006. Non-streptomycete actinomycetes as biocontrol agents of soil-borne fungal plant pathogens and as plant growth promoters. *Soil Biology and Biochemistry*, 38(7): 1505-1520.

Felsenstein J. 1981. Evolutionary trees from DNA sequences: a maximum likelihood approach. *Journal of Molecular Evolution*, 17(6): 368-376.

Felsenstein J. 1985. Confidence limits on phylogeny: an approach using the bootstrap. *Evolution*, 39: 783-791.

Fitch WM. 1971. Toward defining the course of evolution: minimum change for a specific tree topology. *Systematic Biol*, 20(4): 406-416.

Goodfellow M, Williams ST. 1983. Ecology of actinomycetes. *Annu Rev Microbiol*, 37: 189-216.

Groth I, Vettermann R, Schuetze B, Schumann P, Sáiz-Jiménez C. 1999. Actinomycetes in karstic caves of northern Spain (Altamira and Tito Bustillo). *Journal of Microbiological Methods*, 36(1-2): 115-122.

Hasegawa S, Meguro A, Shimizu M, Nishimura T, Kunoh H. 2006. Endophytic *Actinomycetes* and their interactions with host plants. *Actinomycetologica*, 20(2): 72-81.

Huang X, Zhou S, Huang D, Chen J, Zhu W. 2016. *Streptomyces spongiicola* sp. nov., an Actinomycete derived from marine sponge. *Int J Syst Evol Microbiol*, 66(2): 738-743.

Jukes TH, Cantor CR. 1969. Evolution of protein molecules. In: Munro HN, editor. *Mammalian Protein Metabolism*, Academic Press, New York, USA, pp: 21-132.

Kämpfer P, Glaeser SP, Busse HJ, Abdelmohsen UR, Ahmed S, Hentschel U. 2015. *Actinokineospora spheciospongiae* sp. nov., isolated from the marine sponge *Sphaciospongia vagabunda*. *Int J Syst Evol Microbiol*, 65(3): 879-884.

Kelly KL. 1964. Color-name charts illustrated with centroid colors. Inter-Society Color Council-National Bureau of Standards, Supplement to NBS Circ. 533, Standard sample No. 2106, Chicago.

Kim M, Oh HS, Park SC, Chun J. 2014. Towards a taxonomic coherence between average nucleotide identity and 16S

- rRNA gene sequence similarity for species demarcation of prokaryotes. *Int J Syst Evol Microbiol* 64: 346-351.
- Koçak FÖ. 2019. "Identification of *Streptomyces* strains isolated from *Humulus lupulus* rhizosphere and determination of plant growth promotion potential of selected strains," *Turkish Journal of Biology*, 43(6):5.
- Kurane R, Suzuki T, Fukuoka S. 1984. Purification and some properties of a phthalate ester hydrolyzing enzyme from *Nocardia erythropolis*. *Applied Microbiology and Biotechnology*, 20(6): 378-383.
- Kurtboke I. 2000. Australian actinomycetes: An unexhausted source for biotechnological applications. *Actinomycetologica*, 14(2): 43-53.
- Kurtböke DI, Neller RJ, Bellgard SE. 2007. Mesophilic actinomycetes in the natural and reconstructed Antonie van Leeuwenhoek, 77(3-4): 399-405.
- Küster E. 1968. Taxonomy of soil Actinomycetes and Related organisms. In: *Ecology of soil bacteria*, Liverpool University Press, Liverpool, pp: 322-336.
- Küster E, Williams ST. 1964. Selection of media for isolation of *streptomycetes*. *Nature*, 202: 928-929.
- Lazzarini A, Cavaletti L, Toppo G, Marinelli F. 2000. Rare genera of actinomycetes as potential producers of new antibiotics. *Antonie van Leeuwenhoek*, 78(3-4): 399-405.
- Lane DJ. 1991. 16S/23S rRNA sequencing. In *Stackebrandt, E, Goodfellow M. Nucleic acid techniques in bacterial systematics*, Wiley, New York, pp: 115-175.
- Lim CP, Hoon KC, Cheah YK. 2017. *Actinobacteria* from Greenwich Island and Dee Island: Isolation, diversity and distribution. *Life Sciences, Medicine and Biomedicine*, 1-1.
- Mincer TJ, Jensen PR, Kauffman CA, Fenical W. 2002. Widespread and persistent populations of a major new marine actinomycete taxon in ocean sediments. *Appl Environ Microbiol*, 68: 5005-5011.
- Montero-Calasanz MDC, Hofner B, Göker M, Rohde M, Spröer C, Hezbri K, Klenk H. P. 2014. *Geodermatophilus poikilotrophi* sp. nov., amultitolerant actinomycete isolated from dolomitic marble. *BioMed Research International*, 1-11.
- Phongsopitanun W, Kudo T, Mori M, Shiomi K, Pittayakhajonwut P, Suwanborirux K, Tanasupawat S. 2015. *Micromonospora fluostatini* sp. nov., isolated from marine sediment. *Int J Syst Evol Microbiol*, 65(12): 4417-4423.
- Phongsopitanuna W, Sripreehasakb P, Sangvichien E, Tanasupawat S. 2021. Diversity, antimicrobial activity, and susceptibility of culturable soil *actinobacteria* isolated from Sichang Island. *ScienceAsia*, 47: 673-681.
- Piao CY, Zheng WW, Li Y, Liu CX, Jin LY, Song W, Yan K, Wang XJ, Xiang WS. 2017. Two new species of the genus *Streptomyces*: *Streptomyces camponoti* sp. nov. and *Streptomyces cuticulae* sp. nov., isolated from the cuticle of *Camponotus japonicus* Mayr. *Arch Microbiol*, 199: 963-970.
- Prescott LM, Harley JP, Klein DA. 2002. *Microbial taxonomy*. In: *Microbiology*, The McGraw-Hill Companies, Inc. Boston, USA. 5th ed., pp: 421-449.
- Reasoner DJ, Geldreich EE. 1985. A new medium for the enumeration and subculture of bacteria from potable water. *Appl Environ Microbiol*, 49(1):1-7.
- Röttig A, Atasayar E, Meier-Kolthoff JP, Spröer C, Schumann P, Schauer J, Steinbüchel A. 2017. *Streptomyces jeddahensis* sp. nov., an oleaginous bacterium isolated from desert soil. *Int J Syst Evol Microbiol*, 67(6): 1676-1682.
- Saitou N, Nei M. 1987. The neighbor-joining method: A new method for reconstructing phylogenetic trees. *Molecular Biology and Evolution*, 4:406-425.
- Saygin H, Ay H, Guven K, Cetin D, Sahin N. 2019. *Desertiactinospora gelatinilytica* gen. nov., sp. nov., a new member of the family *Streptosporangiaceae* isolated from the Karakum Desert. *Antonie van Leeuwenhoek*, 112(3):409-423.
- Sarıcaoğlu S, Işık K, Veyisoglu A, Saygin H, Çetin D, Güven K, Sproeer C, Klenk H, Şahin N. 2014. *Streptomyces burgazadensis* sp. nov., isolated from soil. *Int J Syst Evol Microbiol*, 64: 4043-4048.
- Shirling EB, Gottlieb D. 1966. Methods for characterisation of *Streptomyces* species. *International Journal of Systematic Bacteriology*, 16(3): 313-340.
- Siddharth S, Vittal RR, Wink J, Steinert M. 2020. Diversity and Bioactive Potential of *Actinobacteria* from Unexplored Regions of Western Ghats, India. *Microorganisms*, 8(2): 225.
- Sujarit K, Kudo T, Ohkuma M, Pathom-Aree W, Lumyong S. 2016. *Streptomyces palmae* sp. nov., isolated from oil palm (*Elaeis guineensis*) rhizosphere soil. *Int J Syst Evol Microbiol*, 66(10): 3983-3988.
- Taechowison Tanaka YT, Omura S. 1993. Agroactive compounds of microbial origin. *Annu Rev Microbiol*, 47: 57-87.
- Také A, Inahashi Y, Ōmura S, Takahashi Y, Matsumoto A. 2018. *Streptomyces boninensis* sp. nov., isolated from soil from a limestone cave in the Ogasawara Islands. *Int J Syst Evol Microbiol*, 68(5): 1795-1799.
- Tamura K, Stecher G, Peterson D, Filipinski A, Kumar S. 2013. MEGA: molecular evolutionary genetics analysis version 6.0. *Molecular Biology and Evolution*, 30(12): 2725-2729.
- Tan GYA, Ward AC, Goodfellow M. 2006. Exploration of *Amycolatopsis* diversity in soil using genus-specific primers and novel selective media. *Syst Appl Microbiol*, 29: 557-569.
- Tanasupawat S, Phongsopitanun W, Suwanborirux K, Ohkuma M, Kudo T. 2016. *Streptomyces actinomycinicus* sp. nov., isolated from soil of a peat swamp forest. *Int J Syst Evol Microbiol*, 66(1): 290-295.
- Thawai C, Rungjindamai N, Klanbu TK, Tanasupawa TS. 2017. *Nocardia xestospongiae* sp. nov., isolated from a marine sponge in the Andaman Sea. *International Journal of Systematic and Evolutionary Microbiology*, 67(5):1451-1456.
- Tiwari K, Gupta RK. 2012. Rare actinomycetes: a potential storehouse for novel antibiotics. *Crit Rev Biotechnol*, 32(2): 108-132.
- Trujillo ME, Idris H, Riesco R, Nouioui I, Igual JM, Bull AT, Goodfellow M. 2017. *Pseudonocardia nigra* sp. nov., isolated from Atacama Desert rock. *International journal of systematic and evolutionary microbiology*, 67(8): 2980-2985.
- Vickers JC, Williams ST, Ross GW. 1984. A taxonomic approach to selective isolation of *streptomycetes* from soil. In: *Ortiz-Ortiz L, Bojalil LF, Yakoleff V (eds) Bio- logical, biochemical and biomedical aspects of actinomycetes*. Academic Press, London, 553-561.
- Ventura M, Canchaya C, Tauch A, Chandra G, Fitzgerald GF, Chater KF, van Sinderen D. 2007. *Genomics of Actinobacteria: Tracing the evolutionary history of an ancient phylum*. *Microbiol Mol Biol Rev*, 71:495-548.
- Veyisoglu A, Carro L, Cetin D, Guven K, Spröer C, Pötter G, Goodfellow M. 2016. *Micromonospora profundus* sp. nov., isolated from deep marine sediment. *Int J Syst Evol Microbiol*, 66(11): 4735-4743.
- Wang HF, Zhang YG, Chen JY, Hozzein WN, Li L, Wadaan MA, Li WJ. 2014. *Nesterenkonia rhizosphaerae* sp. nov., an alkaliphilic actinobacterium isolated from rhizosphere soil in a saline-alkaline desert. *Int J Syst Evol Microbiol*, 64(12): 4021-4026.
- Waksman, SA. 1967. *The Actinomycetes. A summary of current knowledge*. The Actinomycetes. A summary of current

- knowledge, 286.
- Weisburg WG, Barns SM, Pelletier DA, et al. 1991. 16S ribosomal DNA amplification for phylogenetic study. *J Bacteriol*, 173(2): 697–703.
- Williams ST, Goodfellow M, Alderson G, Wellington EMH, Sneath PHA, Sackin MJ. 1983. Numerical classification of *Streptomyces* and related genera. *Microbiology*, 129:6, 1743-1813.
- Wink J, Schumann P, Atasayar E, Klenk HP, Zaburannyi N, Westermann M, Kämpfer P. 2017. '*Streptomyces caelicus*', an antibiotic-producing species of the genus *Streptomyces*, and *Streptomyces canchipurensis* Li et al. 2015 are later heterotypic synonyms of *Streptomyces muensis* Ningthoujam et al. 2014. *International Journal of Systematic and Evolutionary Microbiology*, 67(3): 548-556.
- Yoon SH, Ha SM, Kwon S. 2017. Introducing EzBioCloud: a taxonomically united database of 16S rRNA gene sequences and whole-genome assemblies. *Int J Syst Evol Microbiol*, 67(5): 1613–1617.
- Zhang YQ, Chen J, Liu HY, Zhang YQ, Li, WJ, Yu LY. 2011. *Geodermatophilus ruber* sp. nov., isolated from rhizosphere soil of a medicinal plant. *International Journal of Systematic and Evolutionary Microbiology*, 61(1): 190-193.
- Zothanpuia Passari AK, Chandra P, Leo VV. 2017. Production of potent antimicrobial compounds from *Streptomyces cyaneofuscatus* associated with freshwater sediment. *Front Microbiol*, 8:68.
- ZoBell CE. 1941. Studies on marine bacteria. I. The cultural requirements of heterotrophic aerobes. *Journal of Marine Resources*, 4: 41-75.



DETERMINATION OF HMF VALUE AND DIASTASE ACTIVITIES IN STRAINED HONEYS SOLD IN MARKETS

Seda Dicle KORKMAZ^{1*}


¹Giresun University, Espiye Vocational School, Food Processing Department, 28600, Giresun, Türkiye

Abstract: This study aimed to determine HMF values and diastase activities of the strained honeys collected from various markets in Türkiye and to evaluate their suitability to Turkish Food Codex, Directive on Honey. The samples were obtained with original package and their shelf lives were remarked by companies. A total of 90 honey samples, 45 were flower honey and 45 were honeydew honey, were analysed for HMF using High Performance Liquid Chromatography and for diastase activity using UV spectrophotometer. According to the results, it was observed that the 35.5% of flower honey samples and the 20% of honeydew honey samples were not fulfilled the HMF value and/or diastase activity standards of the Turkish Food Codex. The highest HMF value of the samples was 119.8 mg/kg, while the lowest diastase activity of samples was 0.9. Furthermore, 15 of 45 flower honey and 8 of 45 honeydew honey samples were in critical limits for the mentioned standards. In conclusion, in strained honey offered for consumption, either heat treatment that is applied during the production or increasing HMF value and decreasing diastase activity depending on storage temperature limit the product's shelf life. HMF in honey is known to be a potential risk for food safety and public health. Appropriate production and storage conditions for honey should be ensured until it reaches the consumer, and all quality criteria, especially HMF and diastase, should be targeted to comply with the Turkish Food Codex Directive on Honey, until the end of the shelf life. Thus, it will be possible to ensure food safety by protecting both public health and producer rights. In addition, raising consumers' awareness on the subject will enable the development of internal control at both manufacturers and markets.

Keywords: Honey, HMF, Shelf life, Diastase activity, Storage temperature, HPLC

*Corresponding author: Giresun University, Espiye Vocational School, Food Processing Department, 28600, Giresun, Türkiye

E mail: diclekahraman@gmail.com (S. D. KORKMAZ)

Seda Dicle KORKMAZ  <https://orcid.org/0000-0002-4272-300X>

Received: August 24, 2023

Accepted: September 28, 2023

Published: October 15, 2023

Cite as: Korkmaz SD. 2023. Determination of HMF value and diastase activities in strained honeys sold in markets. BSJ Eng Sci, 6(4): 522-526.

1. Introduction

Türkiye has a very rich structure in term of geography, climate, and flora in honey production and bee breeding. Türkiye takes first place in world rankings with its increasing number of bee hives (4.734.938) and its 118.297 tons of honey production. It is very important to increase quality standards in honey in order to increase this potential in exportation. (TUIK, 2022).

The amount of hydroxymethyl furfural (HMF) and diastase activity are two important parameters in evaluating the quality and freshness of honey (An Ajlouni and Sujirapinyokul, 2009; Castro-Vazquez et al., 2008). The source of diastase, which is the most important enzymes that gives honey the quality of easy digestibility, is the salivary gland secretion of bees. The heat treatment applied to honey and time dependent disintegration of this enzyme are important indicators in identifying the freshness of honey. However, enzyme activity varies within hide limit even in fresh honey (Sancho et al., 1992; Belitz and Grosch, 1999). According to the standards of Turkish Food Codex (TGK), Directive on Honey diastase activity is determined as at least 8 for flower honey and honeydew honey and at least 3 for citrus honey. Diastase activity which is used in the measurement of enzyme is defined as ml of starch solution (% 1) which is hidrolized

by enzyme in 1 g honey in one hour at 38-40 °C (TGK, 2012).

Hydroxymethyl furfural is an important quality criteria which occurs as a result of the dehydration of hexoses in honey in acidic ambient and which changes according to chemical properties of honey (sugar, pH, total acidity), honey processing or storage temperature (Sahinler, 2007; Fallico et al. 2008). HMF is a cytotoxic, genotoxic, and organotoxic compound. Also, it is a byproduct formed during hexose decomposition in an acidic environment or during to Maillard reaction (Islam et al., 2014; Pasiyas et al., 2017; Shapla et al., 2018). According to TGK, Directive on Honey, HMF value is determined as maximum 40 mg/kg in flower honey and honeydew honey (TGK, 2012).

It is known that as a result of heat treatment applied to honey during the production stage in order not to undergo fermentation and to prevent it from crystallization (Zappala et al., 2005; Morales et al., 2009; Korkmaz and Küplülü, 2017). Honey is preserved from crystallization and it increases marketing quality of honey. However HMF is found in very small amounts in fresh honey (in harvest period) and it increases with high and long term heat treatment. This increases the HMF in the beginning on the shelf, depending on inappropriate storage temperature increasing effect of HMF shelf life is shorten (Ramirez et



al., 2000; Sanz et al., 2003; Tosi et al., 2022). The quality criteria reported in the TGK Honey communiqué (no. 2005/49) were revised in 2012 without making any changes, and it is stated that honey should be kept under 25°C by protecting it from direct sunlight at all stages until it is delivered to the consumer (TGK, 2005; TGK 2012). Also it causes the reduction of nutritional value by the disintegration of diastase enzyme which has an important role in honey digestion and quality lost by creating changes in taste, flavor and color (Cocco et al., 1996; Kalabova et al., 2003).

In this study, strained honey the shelf life of which is determined by firms in their original package and marketed in the markets was used. The suitability were evaluated according to Turkish Food Codex Honey Commission by identifying the diastase activities and HMF values, storage time determined concerning the dates of analysis.

2. Materials and Methods

2.1. Honey Samples

In this study a total of 90 honey samples, 45 were flower honey and 45 were honeydew honey bought from various markets in several cities of Türkiye (Ankara, Antalya, Muğla, Hatay, İzmir, Konya, Adana) in their original package and shelf lives remarked by companies and which had different expiration date were used as material. Also, all honey samples used in the study were collected in 2020.

2.2. HMF Analysis

HMF determination of samples were analyzed by using HPLC-UV sensor according to Harmonised Methods of the International Honey Commission (Bogdanov, 2009). For the instrument calibration, the standard of 99% pure 5-hydroxymethyl- furan-2-carbaldehyde (HMF) (Merck 820 678) standard was used. The working standards for 1, 2, 5 and 10 mg/L were prepared daily. After their preliminary preparations, the samples were taken into 2 ml vials and introduced to HPLC device with UV detector capable of measuring at a wavelength of 285 nm. The analyses were made by using C18-reversed phase (Hypersil ODS 5µm, 125x4 mm), under the instrument conditions with 90% distilled water- 10% methanol at mobile phase, with a flow rate of 1.0 ml/minute and injection amount of 20 µl.

2.3. Diastase Analysis

Diastase numbers of honey samples were determined by using UV -Spectrophotometer (Rayleigh, VIS- 723G, England), according to the Harmonised Methods of The International Honey Commission (Bogdanov, 2009). Calibration of the starch solution to be used during the analysis was provided in the UV-Spectrophotometer with an absorbency value of 600 nm; and the solution of sodium chloride-acetate buffer required for analysis was prepared. Honey solution was prepared by taking 10 g from the samples, and adding acetate buffer solution. 10

ml honey solution and 5 ml starch solution taken into tubes were kept waiting in water for 15 minutes, at 40 °C. At the end of the period, they were mixed again and taken to the water bath. 5 ml diluted iodine solution was added to the 0,5 ml honey- starch solution taken into the tubes containing 11 ml distilled water, after being kept with 5-minute intervals; and the absorbance value at the 5th, 10th, 15th and 20th minutes were read through 600 nm UV-Spectrophotometer for determining its diastase activity.

3. Results

In the study, totally 90 honey samples consisting of 45 flower honey and 45 honeydew samples were analyzed. 4, 2 and 10 of the 45 flower honey samples analyzed were not found to be in accordance with the T.F.C. Directive on Honey, in terms of their HMF values, diastase activities, and both HMF values and diastase activities, respectively. Accordingly, the HMF values of the 14 honey samples analyzed, which were higher than the limit values, were found to be 119.8, 114.6, 102.4, 100.3, 98.5, 87.6, 87.4, 73.3, 53.6, 49.2, 48.2, 46.7, 42.5 and 40.2 mg/kg, respectively; and the diastase activities of the 12 honey samples, which were determined to be lower than the limit value, were 0.9, 1.5, 5.4, 5.6, 5.9, 6.0, 6.2, 6.4, 7.2, 7.5, 7.6, 7.7, respectively. 45 honeydew honey samples were examined, and HMF value of 6 of totally 9 samples were not suitable for T.G.K. Honey Communiqué, while diastase activity of 3 samples were not found in accordance with T.G.K. Honey Communiqué. Accordingly, the amount of HMF exceeding the limit value in 9 of the pine honey samples was 82.5, 54.6, 52.4, 50.2, 46.4, 45.5, 44.7, 42.5, 40.6 mg/kg, respectively, while the diastase activity of 3 samples was found to be 7.5, below the limit value (Table 1 and Table 2).

This study found that among 90 honey samples, 16 flower honey and 9 honeydew honey were not suitable for the limit value specified in the Turkish Food Codex Directive on Honey. Furthermore, as a result of the analysis, it was determined that 10 flower honey and 8 honeydew honey samples were in proximity to the HMF limit value, while 5 flower honey samples were found close to the limit value with diastase activity. Given the samples' expiration dates, there is concern that this situation might pose a potential public health risk.

In addition, closed to the limit value HMF amounts were found to be between 35-40 mg/kg (35.3, 35.6, 36.0, 37.2, 38.0, 38.6, 38.9, 39.1, 39.4, 39.8 mg/kg) in 10 flower honey and 8 honeydew honey samples, while closed to the limit value of diastase activities in 5 flower honey samples were determined as (8.8, 8.5, 8.5, 8.3, 8) respectively. The samples were evaluated considering the packaging dates and the analysis date. According to the findings, the minimum and maximum HMF values and diastase activities of honey samples are shown in Table 3.

Table 1. HMF value and diastase activities of flower honey samples

| Sample no | *Analysis time (month) | **Shelf life (month) | HMF(mg/kg) | Diastase activity |
|-----------|------------------------|----------------------|------------|-------------------|
| 1 | 6th | 24 | 119.8 | 0.9 |
| 2 | 16th | 24 | 114.6 | 5.9 |
| 3 | 22nd | 24 | 102.4 | 1.5 |
| 4 | 28th | 36 | 100.3 | 6.0 |
| 5 | 19th | 24 | 98.5 | 5.6, |
| 6 | 24th | 36 | 87.6 | 7.2 |
| 7 | 20th | 24 | 87.4 | 10 |
| 8 | 20th | 24 | 73.3 | 7.6 |
| 9 | 12th | 18 | 53.6 | 5.4 |
| 10 | 7th | 18 | 49.2 | 7.5 |
| 11 | 10th | 18 | 48.2 | 6.2 |
| 12 | 18th | 24 | 46.7 | 11.5 |
| 13 | 12th | 24 | 42.5 | 10.6 |
| 14 | 8th | 18 | 40.2 | 14.2 |
| 15 | 11th | 18 | 30.8 | 7.7 |
| 16 | 8th | 18 | 32.2 | 6.4 |

*Analysis time= time from packaging date to analysis date, **Shelf Life= the period between the packaging date and the expiration date on the labels of honey samples.

Table 2. HMF value and diastase activities of honeydew honey samples

| Sample no | *Analysis time (month) | **Shelf life | HMF(mg/kg) | Diastase activity |
|-----------|------------------------|--------------|------------|-------------------|
| 1 | 6th | 24 | 82.5 | 7.5 |
| 2 | 6th | 18 | 54.6 | 9.2 |
| 3 | 9th | 18 | 52.4 | 7.5 |
| 4 | 17th | 24 | 50.2 | 12.8 |
| 5 | 8th | 18 | 46.4 | 7.5 |
| 6 | 18th | 24 | 45.5 | 11.4 |
| 7 | 4th | 24 | 44.7 | 13.2 |
| 8 | 6th | 18 | 42.5 | 15.6 |
| 9 | 14th | 18 | 40.6 | 10.5 |

*Analysis time= time from packaging date to analysis date, **Shelf Life= the period between the packaging date and the expiration date on the labels of honey samples.

Table 3. Maximum and minimum values of HMF and diastase activities of honey samples

| Parametres | Type | Number of samples | Min. value | Max. value |
|-------------------|----------|-------------------|------------|-------------|
| HMF (mg/kg) | Flower | 45 | 19.8 mg/kg | 119.8 mg/kg |
| | Honeydew | 45 | 11.5 mg/kg | 82.5 mg/kg |
| Diastase activity | Flower | 45 | 0.9 | 15.8 |
| | Honeydew | 45 | 7.5 | 19.6 |

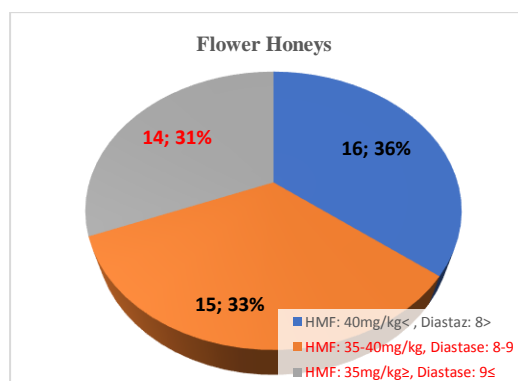


Figure 1. HMF values and diastase activity rates of flower honeys (%).

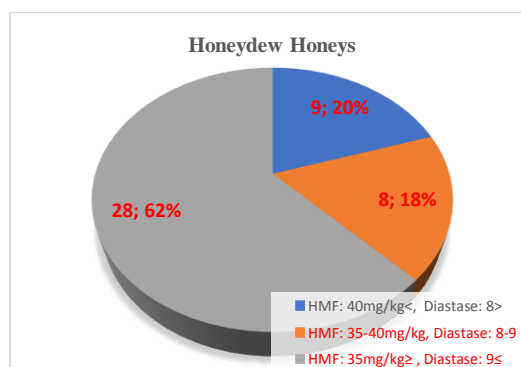


Figure 2. HMF values and diastase activity rates of honeydew honeys (%).

4. Discussion and Conclusion

In this study HMF values of 45 flower honey samples of 90 honey samples collected from various markets in their original package were determined as 19.8-119.8 mg/kg and diastase of them were determined as 0.9- 15.8. According to the data, in terms of HMF value 4 of them, in terms of diastase activity 2 of them, in terms of both HMF value and diastase activity 10 of them are not suitable for TGK Directive on Honey. Moreover, HMF values of 45 honeydew honey were found as 10.6-82.5 mg/kg and their diastase activities were found as 7.5-19.6. With reference to this in terms of HMF value 6 of the samples, in terms of both HMF value and diastase activity 3 of the samples were not suitable for TGK Directive on Honey. When retention periods and markets with their expiry dates and analysis date were taken into consideration, it's thought that the reason of improper HMF values and diastase activities were because of the adverse storage conditions. Also initial HMF values and diastase activities were important facts. When storage periods, expiration dates, and analysis dates are taken into consideration, the combination of high HMF values and low diastase activities indicates that the honeys might be subjected to unfavorable storage conditions within the markets. As it is specified in the transportation and storage section of the revised TGK (NO:2012/58) communiqué, ensuring the healthiness of the shelf life and the food safety of honeys that meet the quality standards set by the honey regulations when they reach the retail stage is crucial. This involves maintaining suitable storage conditions consistently from the point of sale to the end consumer. Thus, it will become feasible to safeguard both the rights of producers and the health of consumers, thereby guaranteeing food safety.

Study by Guler (2005) suggests HMF values of 30 honey samples collected from Eastern Black Sea region producers were determined as 3.83-11.0 mg/kg and they were found quite lower than other HMF values in the study. Furthermore in their study, Sahinler and Gul (2004) found average HMF values of untreated flower and sunflower honey quite lower than other values in the study. They were 5.73, 2.17 mg/kg and their diastase activities were higher than other with the 17.9, 18. Turgay (2009) reported that 50 honey samples (different floral feature), HMF values were found to be 31.46-40.70 mg/kg and diastase activities as 8-25.4. Bölükbaşı (2007) determined the HMF values as 0-38.6 mg/kg in 47 honey samples collected from different parts of Türkiye. It is thought that the reasons why HMF values were found higher and diastase activities lower were high and long-term temperature treatment and improper storage conditions. In another study conducted by Al-Diab et al. (2015), various types of honey obtained from markets exhibited an increase in HMF levels following a 6-month storage period at 25°C. The most significant rise, amounting to 14.7%, was observed in a polyfloral honey sample that initially contained 39.7±3.3 mg/kg of HMF. The samples in our study were analyzed directly without

being kept in a controlled storage temperature. Nevertheless, the substantial elevation in HMF values indicates that the samples have likely been exposed to increased temperatures both during the production and storage processes. In another study carried out within Saudi Arabia, the highest HMF value among 14 honey samples collected from local markets was found to be 28.97 mg/kg. It was concluded that the honeys were not heat-treated and were fresh since the HMF values were at relatively low level (Alghamdi et al., 2020). Although the HMF limit value in countries with tropical ambient temperatures is 80 mg/kg according to Codex Alimentarius (2019), the HMF values of the honey samples in our study, which exceeded the limit value (40 mg/kg) in Türkiye, indicate that the samples were exposed to inappropriate storage conditions in markets after being distributed from factories under controlled conditions. Similarly, a study conducted in the Aydın province involved a total of 40 honey samples, including 20 honey samples taken directly from the beehives and 20 honey samples taken from the market. In the study, it was reported that the average HMF values of the market samples were 56.70±3.83 mg/kg, and the HMF values of all market samples exceeded the limit value. Diastase activities were found to be lower than the values of the samples in our study, with an average of 7.4±0.24 (Aypak et al., 2019).

In this study 16 flower honeys and 9 honeydew honeys of 90 honey samples were improper according to the limit values of T.G.K. Directive on Honey. Also in terms of HMF value on 10 flower honey and 8 honeydew honey and in terms of diastase activities 5 flower honey were found close to limit value. Therefore, it is thought that when expiry dates are taken into consideration they are potential risks for human health.

In conclusion, HMF forming in honey is known to be a potential risk in terms of food safety and public health. Suitability of the all quality criteria- HMF and diastase criteria in particular- to the Turkish Food Codex Directive on Honey should be ensured throughout the shelf life determined by companies for strained honeys offered for consumption. As revised with this aim, as stated in TGK (NO: 2012/58), it is crucial to store honey under appropriate conditions (especially <25 °C. from markets to consumers to maintain quality criteria. This will ensure food safety while protecting both public health and producer rights. Moreover, raising consumer awareness on this issue will facilitate the development of internal controls at both the production and markets. Suitability of the all quality criteria- HMF and diastase criteria in particular- to the Turkish Food Codex Directive on Honey should be ensured throughout the shelf life determined by companies for strained honeys offered for consumption.

Author Contributions

The percentage of the author contributions is presented below. The author reviewed and approved the final version of the manuscript.

| | S.D.K. |
|-----|--------|
| C | 100 |
| D | 100 |
| S | 100 |
| DCP | 100 |
| DAI | 100 |
| L | 100 |
| W | 100 |
| CR | 100 |
| SR | 100 |
| PM | 100 |
| FA | 100 |

C=Concept, D= design, S= supervision, DCP= data collection and/or processing, DAI= data analysis and/or interpretation, L= literature search, W= writing, CR= critical review, SR= submission and revision, PM= project management, FA= funding acquisition.

Conflict of Interest

The author declared that there is no conflict of interest.

Ethical Consideration

Ethics committee approval was not required for this study because of there was no study on animals or humans.

References

Al-Diab D, Jarkos B. 2015. Effect of storage and thermal treatment on the quality of some local brands of honey from Latakia markets. *J Ento Zoo Stud*, 3: 328-334.

Alghamdi BA, Alshumrani ES, Bin Saeed MS, Ghufra MR, Alharthi NA, Baeshen MN, Helmi NM, Alam MZ, Suhail M. 2020. Analysis of sugar composition and pesticides using HPLC and GC-MS techniques in honey samples collected from Saudi Arabian markets. *Saudi J Biol Sci*, 27(12): 3720-3726.

An Ajlouni S, Sujirapinyokul P. 2009. Hydroxymethylfurfuraldehyde and amylase contents in Australian honey. *Food Chem*, 119: 1000-1005.

Aypak SÜ, İnci A, Bakırcı S, Fidan ED, Soysal M. 2019. Comparison of the antioksidant activity and HMF levels in honey taken from hives and markets. *Gıda*, 44(1): 86-92.

Belitz HD, Grosch W. 1999. *Food chemistry*, 2th. Edition. Springer, Berlin, Germany, pp: 145-157.

Bogdanov S. 2009. Harmonised Methods of the international honey commission. IHC responsible for the methods. *Bee Product Sci*, 2009: 9-54.

Bölükbaşı DN. 2007. Ambalajlı balların melitopalnolojik, kimyasal ve organoleptik analizleri. MSc Thesis, Hacettepe University, Institute of Science, Ankara, Türkiye, pp: 27-28.

Castro-Vazquez L, Diaz-Maroto MC, Gonzalez-Vinas MA, De La Fuente E, Perez- Coello MS. 2008. influence of storage conditions on chemical composition and sensory properties of citrus honey. *J Agricult Food Chem*, 56: 1999-2006.

Cocco LF, Valentini C, Novelli V, Ceccon L. 1996; High-performance liquid chromatography determination of 2-

furaldehyde and 5-hydroxymethyl-2-furaldehyde in honey. *J Cromatogr A*, 749: 95-102.

Fallico B, Arena E, Zappala M. 2008. Degradation of 5-Hydroxymethylfurfural in honey. *J Food Sci*, 73: 625-631.

Güler Z. 2005. Doğu Karadeniz Bölgesi'nde üretilen balların kimyasal ve duyuusal nitelikleri. *Gıda*, 30: 379-384.

Islam N, Khalil L, Islam A, Gan SH. 2014. Toxic compounds in honey. *J Appl Toxicol*, 34: 733-742.

Kalabova K, Vorlova L, Borkovcova I, Smutna M, Vecerek V. 2003. Hydroxymethylfurfural in Czech honeys. *Czech J Anim Sci*, 48: 551-557.

Korkmaz SD, Küplülü Ö. 2017. Effects of storage temperature on HMF and diastase activity of strained honeys. *Ankara Üniv Vet Fak Derg*, 64: 281-287.

Morales V, Sanz ML, Martin-Alvarez PJ, Corzo N. 2009. Combined use of HMF and furosine to assess fresh honey quality. *J Sci Food Agric*, 89: 1332-1338.

Pasias IN, Kiriakou IK, Proestos C. 2017. HMF and diastase activity in honeys: A fully validated approach and a chemometric analysis for identification of honey freshness and adulteration. *Food Chem*, 229: 425-431.

Ramirez MA, Gonzales SA, Sauri E. 2000. Effect of the temporary thermic treatment of honey on variation of the quality of the same during storage. *Apiacta*, 35: 162-170.

Sahinler N, Gül A. 2004. Chemical composition and physical properties of honey produced in Turkey from sunflower, cotton, orange and pine. *First European Conference of Apidology*, September 19-23, 2004, Udine Italy, pp: 136-137.

Sahinler N. 2007. Effects of heating and storage on hydroxy methylfurfural and diastase activity of different Turkish honeys. *J Apicult Res*, 46: 34-39.

Sancho TM, Muniata S, Huidobro FJ, Lozano SJ. 1992. Aging of Honey. *J Agricult Food Chem*, 40: 134-138.

Sanz ML, Castillo MD, Corzo N, Olano A. 2003. 2-Furoylmethyl amino acids and Hydroxymethylfurfural as indicators of honey quality. *J Agric Food Chem*, 51: 4278-4283.

Shapla UM, Soleyman M, Alam N, Khalil MI, Gan SH. 2018. 5-Hydroxymethylfurfural (HMF) levels in honey and other food products: effects on bees and human health. *Chem Cent J*, 12: 2-18.

Tosi E, Ciappini M, Re E, Lucero, H. 2022. Honey thermal treatment effects on hydroxymethylfurfural content. *Food Chem*, 77(1): 71-74.

TUIK. 2022. İstatistik Veri Portalı; Arıcılık. URL: <https://data.tuik.gov.tr/Kategori/GetKategori?p=tarim-111&dil=18> (accessed date: June 8, 2022).

Turgay O. 2009. Characteristic properties of Kahramanmaraş honey samples. *KSU Doğa Bil Derg*, 12: 21-24.

Türk Gıda Kodeksi Bal Tebliği, No: 2005/49, 17/12/2005 Türkiye. URL: <https://www.resmigazete.gov.tr/eskiler/2020/04/2020042-2-13.htm> (accessed date: Agust 13, 2020).

Türk Gıda Kodeksi Bal Tebliği, No: 2012/58, 27/07/2012 Türkiye. URL:<http://mevzuat.basbakanlik.gov.tr/Metin.Aspx?MevzuatKod=9.5.16425&MevzuatIliski=0&sourceXmlSearch=BAL> (accessed date: Agust 12, 2020).

Zappala M, Fallico B, Arena E, Verzera A. 2005. Methods for the determination of HMF in honey: a comparison. *Food Control*, 16(3): 273-277.



INVESTIGATION OF DEFECTS OCCURRING IN THE CASTING SHOP PROCESS OF CERAMIC SANITARYWARE ON THE FINAL PRODUCT

Nihal Derin COSKUN^{1*}, Eray CASIN², Cumhur Eren ISIK³

¹Ordu University, Faculty of Fine Arts, Department of Ceramics and Glass, 52200, Ordu, Türkiye

²Genesis Technological Products Industry and Trade. Inc., 19010, Çorum, Türkiye


³Kütahya Dumlupınar University, Faculty of Fine Arts, Department of Handicraft Design and Production, 43020, Kütahya, Türkiye


Abstract: When the export values of ceramic sanitaryware in Türkiye are analyzed, it is seen that the data for the year 2022 of ~660 million dollars continues to increase. In the sector, which reaches an annual average increase of 100 million dollars, the amount of production as well as the design demands change and shape the market. The most important difficulty factors in design are due to the fact that the products in the sector have large sizes, complex shapes and the most human-made production stages. When these factors are compared with other ceramic sectors, it is revealed that although industrialization has increased in the production of ceramic sanitaryware, the lack of production amount and the excess of faults are among the biggest problems. Glaze faults are the leading faults observed in the final product, and since this problem is not recyclable, it harms the ceramic sanitaryware industry in terms of cost. In this study, the glaze faults reflected in the final glazed products originating from the casting shop stage, which attracts attention in this field due to its large size and whiteness and there is not much data for the vitreous ware industry in the literature, have been studied. In the study, which was carried out with the aim of detecting and eliminating some faults in industrial production and creating data for the literature, faults arising from mechanical evenings used in classical and pressure casting benches and material residues used in retouching processes were determined. These faults were produced on the basis of the laboratory and the characterization of the glazed faulty products was made. It is concluded that production losses can be reduced by eliminating these problems, consequently increasing quality and productivity.


Keywords: Sanitaryware, Casting department, Glazing, Ceramic manufacturing defects

*Corresponding author: Ordu University, Faculty of Fine Arts, Department of Ceramics and Glass, 52200, Ordu, Türkiye

E mail: nihalderincoskun@odu.edu.tr (N. D. COSKUN)

Nihal Derin COSKUN  <https://orcid.org/0000-0002-3024-9443>

Eray CASIN  <https://orcid.org/0000-0003-3698-2248>

Cumhur Eren ISIK  <https://orcid.org/0000-0002-1129-2497>

Received: August 21, 2023

Accepted: September 28, 2023

Published: October 15, 2023

Cite as: Coskun ND, Casin E, Isik CE. 2023. Investigation of defects occurring in the casting shop process of ceramic sanitaryware on the final product. *BSJ Eng Sci*, 6(4): 527-534.

1. Introduction

Ceramics is an area that consists mainly of shaping and firing kaolin, quartz, feldspar and clay raw materials and provides functional use in the industrial sense. Sanitaryware (also known as vitrified ceramics) serves the industry as an important industrial production branch of ceramics, which has an important place in the ceramic industry in terms of providing hygiene and ease of life to people. Washbasins, toilet bowls, urinals, shower trays, etc. are the articles manufactured in this sector. The products are sintered at ~1200-1250°C and are in the scale of products that are difficult to manufacture, as they are large-sized, durable and low-water absorption products with a glassy glaze layer covering them. Although these products can be colored, they are preferably produced in white color as it is suitable for customer demand (Canduran ve Ural, 2019; Mete, 2020; Taykurt Daday, 2012).

As seen in Figure 1, different textures and impurities provide artistic effects in artistic ceramic production.

However, in vitrified products, which are an industrial production branch, these images visually distort the effect as seen in Figure 2. Since they are relatively large in size, these products go to waste which has a negative impact on production in terms of raw materials, labor, energy and time. These faults can also be seen in a porcelain plate or ceramic tile product, but the biggest loss is more visible in the sanitaryware industry due to its larger size (Fortuna and Fortuna, 2017; Fraser, 2005). Many studies have been done and are being carried out on ceramic defects in areas such as tableware and the tile sector, which require more patterns and designs. Efforts to eliminate these faults and possible causes of defects are determined, and some of the main faults in the literature are seen in Figure 3.





Figure 1. Some glaze defects used as artistic effects in artistic ceramic products (Berberoğlu, 2015; Genç ve ark., 2018; Genç, 2010; Taşkın, 2009).



Figure 2. Manufacturing defects on some vitrified products.



Figure 3. Some ceramic glaze defects (Hopper, 2023).

Casting shop related defects in vitreous ware are generally in the literature; voids, points, lines, cracking, explosions due to plaster residues, deformations caused by uneven drying and air bubbles during filling. However, there are also faults that appear in the final product. These faults can be caused by various components and, in a sense, by human faults (Fortuna and Fortuna, 2017; Kurama ve Sarı, 2013).

In this study, the effects of defects occurring from the casting shop may occur in the final product stage besides the pre-sintering stage, and especially the effects of defects originating material based issues and their effects on the microstructure were investigated.

2. Materials and Method

Five of the materials utilized in the slip casting that cause the most faults were selected and these materials were applied on the specimen plates. Although the visuals of the faults on the plates in the experimental studies seem to be major, these defects are considered as minor in production. In fact, due to the plastic or polymeric

materials used, it may move away from the body at ~250 °C during the sintering phase and cause defects such as air, crater or pinhole defects. Semi-finished products and raw materials used in factory conditions and production were supplied from Ece Bathroom production facility. Microstructure studies (SEM) of the study were performed by scanning electron microscope and chemical composition analysis (EDX). SEM/EDX images were measured with Zeiss Supra 50VP Brand device.

2.1. Casting Shop based Faults

2.1.1. Defects due to green scotch

Green scotch is a material that is generally used for retouching the surfaces of semi-finished products containing 18% moisture from casting. It is especially used for rounding corners. It can also be used in semi-finished products after drying. Many apparatuses are used during the retouching in the casting shop, but since the green scotch comes into contact with the product with plenty of water, they can be buried in the product from time to time and cannot be noticed in the process (Figure 4).



Figure 4. Green scotch (Right) and defects due to green scotch (Left).

2.1.2. Die casting machine materials

Pressure casting benches are different from conventional casting benches, they are more mechanical and have many moving and rotating parts. Machine elements such as belts or bearings are used in the rotational movements of these machine parts or the movements of the moving parts. Lubrication processes are also carried out to prevent the wear of these elements. The presence of water in the working environment causes these oils to clump and stick to the products in cases where cleaning processes are not carried out in a controlled manner. In addition, the abrasions that may occur due to the friction of some parts against each other and the resulting metal slags also cause the formation of metallic stains (Figure 5).



Figure 5. Die casting machine slag materials (Right) and defects caused by them (Left).

Many sanitaryware products such as sinks and toilet bowls are produced on the pressure casting benches as seen in Figure 6. However, while the molds are being opened, especially in products such as large-sized toilet bowls or similar shower trays, metallic parts that are

poured from the upper part of the counter due to friction cannot be detected because they are taken into the system by robots without human touch. These types of defects also appear as stain faults at the exit of the kiln.



Figure 6. Vitrified die casting machine from Ece Banyo.

2.1.3. Strip tape abrasive based defects

Strip tape abrasive is a hard, metallic abrasive type used in ceramic sanitaryware at the stage of semi-finished product control. This abrasive, which is generally preferred in the retouching processes carried out under the control of the products after drying, is used to ensure the rapid flow of semi-finished products. The reason for this is that it has a high ability to retouch, since it is a hard abrasive. After using this abrasive in the semi-finished product control process, the surface should be wiped with a damp cloth again and the touch-up marks on the surface should be closed. Since it is a metal-based material, it causes staining in case of any wear or breakage (Figure 7).



Figure 7. Strip tape abrasive (Left) and defects (Right) due to this abrasion.

2.1.4. Faults from abrasive materials

Box shaped abrasives are a different type of abrasive used in casting shop and used to perform surface treatments of products. It is a material that can be touched up without damaging the surfaces, since the eroding part is soft, box-shaped and has a sponge in the middle. In some cases, stains can be seen if this abrasive

(silicon carbide) wears off and the wearing parts adhere to the surfaces. In addition, abrasive particles that dissolve in the retouching waters in the casting shop and adhere to the surface with slip particles also cause staining (Figure 8).



Figure 8. Box Abrasive (Left) and Related Defects (Right).

2.1.5. White abrasive based defects

This type of abrasives is generally used in the semi-finished product control phase. White color is the chief reason for this abrasive to be utilized in the retouching process of the semi-finished product, because the upper area of the product is alumina-based. This type of abrasive is more preferred because black spots are observed in silicon alumina based abrasives. However, it is observed that this material also causes defects (Figure 9).



Figure 9. White Abrasive (Left) and its related defects (Right).

3. Results and Discussion

3.1. SEM /EDX Analysis

3.1.1. SEM/EDX analysis of green scotch based defects

The green scotch-based defects seen in Figure 9 cause inclusions in the structure since the material is polymer-based. In the samples studied in a major scale, the material appears as a mound because it does not completely melt in the glaze. However, it is not completely combined in the glassy phase, and it shows itself as a separate formation from the structure, as seen the figures (Figure 10).

Since the green scotch is a polymeric material, it does not leave any residue after firing. The earlier melting temperature of the material, which is embedded in the glaze (i.e., if parts remain within the body), causes defect on the glaze surface.

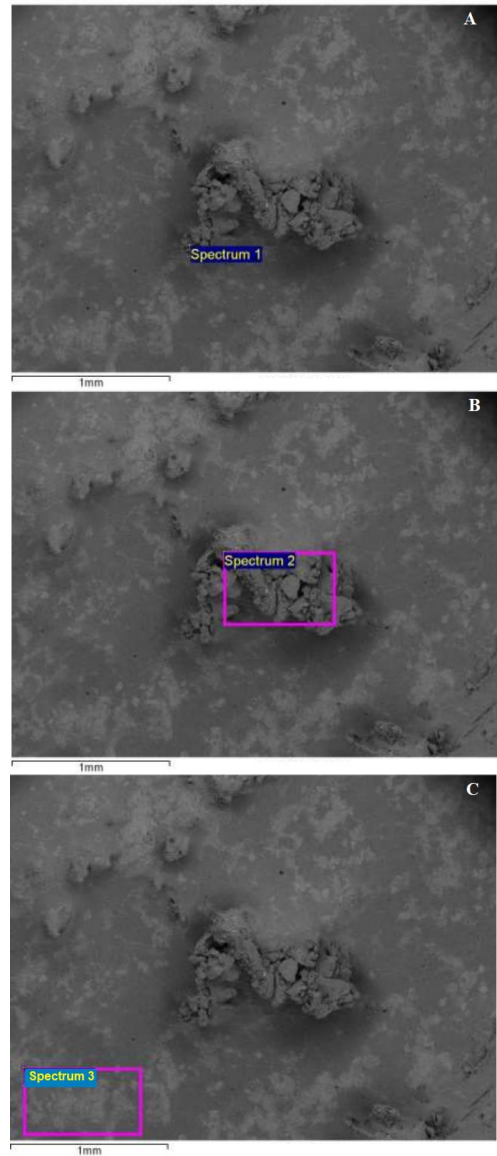


Figure 10. Some SEM Analysis of Green Scotch Based Defects A, B, C (Table 1 displays EDX analysis of the defects).

Since the green scotch is a polymeric material, it does not leave any residue after firing. The earlier melting temperature of the material, which is embedded in the glaze (i.e., if parts remain within the body), causes defect on the glaze surface.

Table 1. EDX analysis of green scotch based defects in Figure 10.

| Ex. No | MgO | Al ₂ O ₃ | CaO | ZnO | SiO ₂ | Na ₂ O | K ₂ O | ZrO ₂ | Total |
|--------|------|--------------------------------|------|------|------------------|-------------------|------------------|------------------|-------|
| A | 0 | 30.89 | 6.67 | 0 | 55.43 | 7.01 | 0 | 0 | 100 |
| B | 0 | 24.94 | 6.87 | 0 | 64.46 | 2.77 | 0.96 | 0 | 100 |
| C | 1.16 | 9.62 | 8.14 | 1.72 | 57.9 | 3.21 | 0.75 | 17.5 | 100 |

As seen in Table 1, in the analysis of the points where the Al₂O₃ ratio higher, ZrO₂ ratio is not observed in the structure, indicating the green scotch is causing defects in the regions. The defect of the natural opaque glaze structure is evidenced by the zircon ratio.

3.1.2. SEM/EDX analysis of defects due to die casting machine materials

Since there are iron particles in the machine oil, and the viscosity of the oil increases and becomes semi-solid due to friction, iron defects are encountered on the product surface. Also, assuming that the oil lowers the surface tension, it is likely to cause glaze collection in cases where the body absorbs the oil (Figure 11).

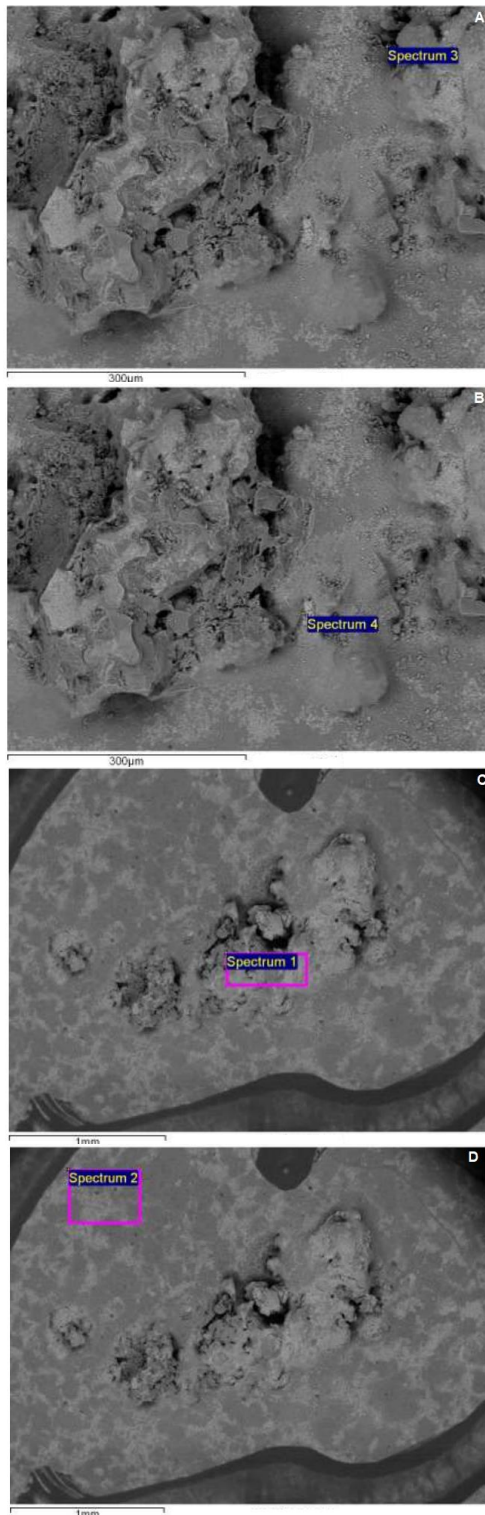


Figure 11. Some SEM Analysis of Defects Due to Die Casting Machine Materials (A, B, C, D) (Table 2 displays EDX analysis of the defects).

The high Fe₂O₃ ratio in the point analyzes in Table 2 shows that the parts poured over the machine are iron-containing. However, although there is a structure that creates a depression in the iron structure, it is seen that the other impurities that come with the iron do not melt completely, allowing the structure to remain rigid.

Table 2. EDX analysis of defects in figure 11 due to die casting machine materials

| Ex. No | MgO | Al ₂ O ₃ | CaO | Fe ₂ O ₃ | ZnO | SiO ₂ | Na ₂ O | K ₂ O | ZrO ₂ | MnO | Total |
|--------|------|--------------------------------|------|--------------------------------|------|------------------|-------------------|------------------|------------------|------|-------|
| A | 0 | 35.22 | 0 | 3.3 | 0 | 58.1 | 2.76 | 0 | 0 | 0.61 | 99.99 |
| B | 0 | 0 | 0 | 100 | 0 | 0 | 0 | 0 | 0 | 0 | 100 |
| C | 4.55 | 17.66 | 4.1 | 24.47 | 4.18 | 43.27 | 0 | 0.85 | 0 | 0.92 | 100 |
| D | 1.14 | 9.27 | 6.21 | 0 | 1.39 | 58.96 | 2.84 | 0 | 20.2 | 0 | 100 |

3.1.3. SEM/EDX analysis of tape abrasive based defects

The tape abrasive is made of hard metallic materials. When seen under the glaze, it creates iron stains on the glaze surface. It has been observed that since it is placed as a whole piece in the figure, it does not spoil the glaze surface and behaves like a glaze in EDX analyses (Figure 12).

Due to the application of the defect as a major part in the experimental studies, the abrasive remained under the glaze surface without melting and it was observed that there were glaze surfaces in the SEM/EDX analyzes. It has been determined that the EDX analysis, which provides a homogeneous image of the structure, also supports this idea (Table 3).

Table 3. EDX analysis of tape abrasive-based defects in figure 12

| Ex. No | MgO | Al ₂ O ₃ | CaO | ZnO | SiO ₂ | Na ₂ O | K ₂ O | ZrO ₂ | Total |
|--------|------|--------------------------------|------|------|------------------|-------------------|------------------|------------------|--------|
| A | 1.28 | 11.47 | 7.5 | 0.72 | 70.77 | 4.66 | 0.51 | 3.09 | 100 |
| B | 0 | 4.24 | 5.66 | 0 | 43.97 | 2.2 | 0 | 43.93 | 100 |
| C | 1.05 | 7.9 | 8 | 0 | 56.22 | 3.77 | 0 | 23.07 | 100.01 |

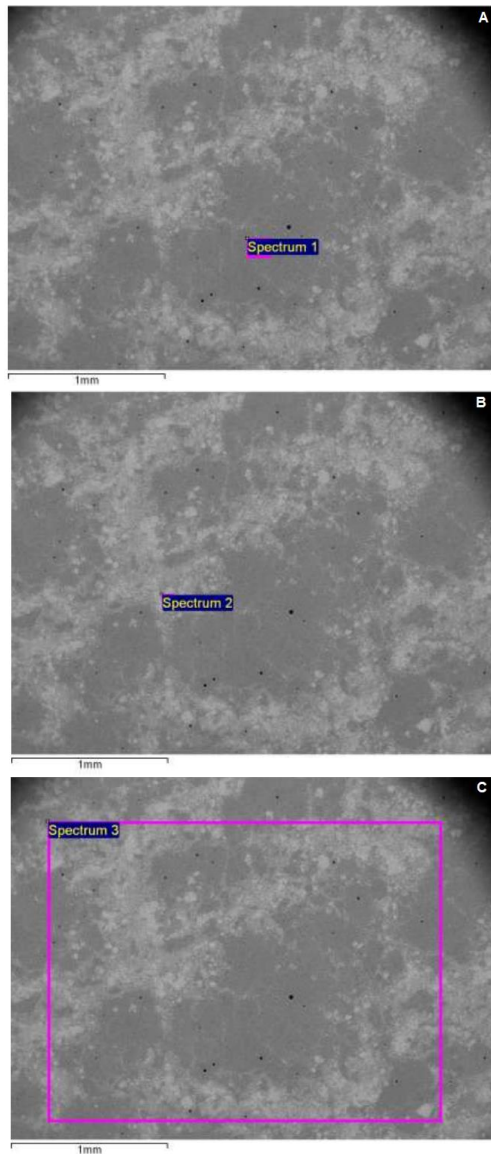


Figure 12. Some SEM/EDX Analysis of Tape Abrasive Based Defects (A, B, C) (Table 3 displays EDX analysis of the defects).

3.1.4. SEM/EDX analysis of box abrasive based defects

Box abrasives are applied on semi-wet products in the casting process. Especially the inner chambers of the toilet bowls and the fluffy parts on the outer surfaces are cleaned with these abrasives. For this reason, it is desired that this product should be hard. However, in the SEM images, it is seen that the SiC particles cause crystallization in the structure and are clustered locally (Figure 13).

As seen in Table 4, CO₂ formation was found that was not observed in other EDX analyzes. Another oxide seen here is SiO₂, proving that the material is SiC. In the results obtained from the faulty areas, it was determined that the glaze deteriorated on the surface and the ZrO₂ ratio was not found because the SiC material remained unmelted (Hasanuzzaman et al., 2022).

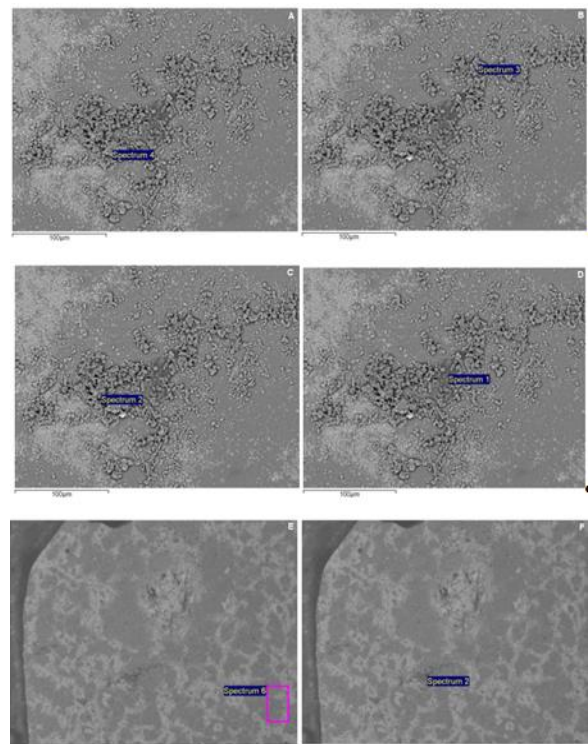


Figure 13. Some SEM/EDX Analysis of Box Abrasive Based Defects (A, B, C, D, E, F) (Table 4 displays EDX analysis of the defects).

Table 4. EDX analysis of box abrasive based defects in figure 13

| Ex. No | MgO | Al ₂ O ₃ | CaO | ZnO | SiO ₂ | Na ₂ O | K ₂ O | ZrO ₂ | CO ₂ | Total |
|--------|------|--------------------------------|------|------|------------------|-------------------|------------------|------------------|-----------------|-------|
| A | 0 | 20.16 | 0 | 0 | 79.84 | 0 | 0 | 0 | 0 | 100 |
| B | 0 | 1.4 | 0 | 0 | 98.6 | 0 | 0 | 0 | 0 | 100 |
| C | 0 | 33.11 | 0 | 0 | 66.89 | 0 | 0 | 0 | 0 | 100 |
| D | 1.05 | 3.37 | 2 | 0 | 16.97 | 0 | 0 | 0 | 76.61 | 100 |
| E | 0 | 2.65 | 1.11 | 0 | 14.22 | 0 | 0 | 0 | 82.02 | 100 |
| F | 1.09 | 9.7 | 6.68 | 1.71 | 66.03 | 2.97 | 0.38 | 11.43 | 0 | 99.99 |

3.1.5. SEM/EDX analysis of white abrasive based defects

Since white abrasives are based on alumina silicate, it causes deterioration on the surface. The black spots seen on it are caused by the falling of the sponge pieces caused by friction and burning on the surface. The appearance of abrasive pieces on the glaze surface ensures that there are regions in the glaze structure as in the 2nd figure in Figure 14. As examined in the SEM images, it is seen that the alumina silicate layers deposited on the surface tend to mullite structures and begin to turn into a rod-like form. This causes refractory structures within the glaze, thereby distorting the appearance of the glaze (Figure 14).

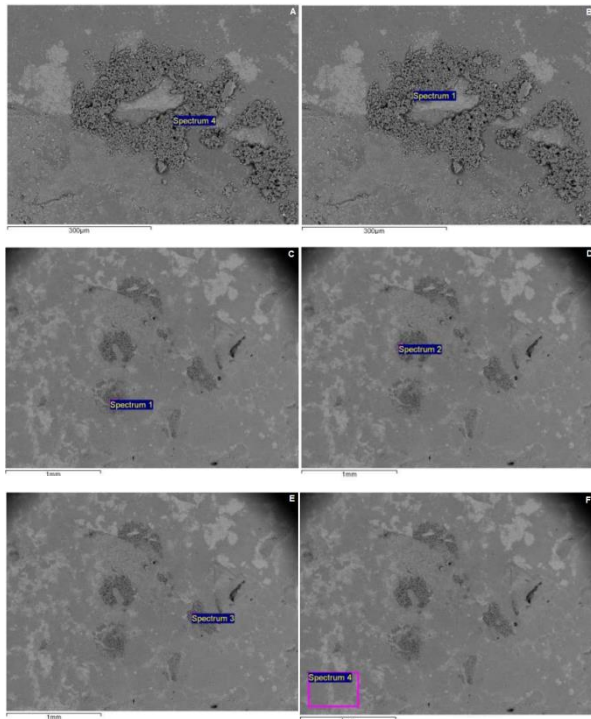


Figure 14. Some SEM/EDX Analysis of White Abrasive Based Defects (A, B, C, D, E, F) (Table 5 displays EDX analysis of the defects).

It also shows itself in EDX analyzes with the decrease in zircon ratios in which the glaze structure is deteriorated. The increased alumina ratio coincides with the EDX values taken from the samples (Table 5).

Table 5. EDX analysis of white abrasive-based defects in figure 14

| Ex. No | MgO | Al ₂ O ₃ | CaO | SiO ₂ | Na ₂ O | K ₂ O | ZrO ₂ | Total |
|--------|------|--------------------------------|------|------------------|-------------------|------------------|------------------|-------|
| A | 0 | 25.77 | 0 | 74.23 | 0 | 0 | 0 | 100 |
| B | 0 | 16.14 | 0 | 83.86 | 0 | 0 | 0 | 100 |
| C | 0 | 32.55 | 0 | 67.45 | 0 | 0 | 0 | 100 |
| D | 0 | 23.25 | 0 | 76.75 | 0 | 0 | 0 | 100 |
| E | 0 | 32.47 | 0 | 67.53 | 0 | 0 | 0 | 100 |
| F | 1.46 | 9.78 | 5.56 | 63 | 5.95 | 0.29 | 13.94 | 99.98 |

4. Conclusion

The casting is one of the first stages of production, and the defects that occur here are sought in the next process rather than the final product. However, in the study, it is revealed that these defects can also affect the final product and the use of the materials utilized properly and by changing will affect the quality of the final product. In this respect, it can be said that some types of defects, which are generally seen as workmanship defects, may also be caused by material deformations and it is important to detect this by the production foremen. It has been observed that material-related defects may be polymer-based, as well as from hard materials with refractory properties such as metallic or SiC. When these defects are characterized, they can differentiate from the

normal opaque vitrified glaze structure and create crystallized or deformational images. Sometimes the change in the ratio of alumina, sometimes silica, and in some cases, zircon, guides us to determine the damages caused by these materials to the structure.

Even if the ratio of the materials used is relatively low, it has been observed that it affects the crystallization in the glaze structure and causes staining and deterioration on the final product. SEM/EDX analyzes play an active role in determining the extent of damage to the product at the final stage.

Thus, it is concluded that production losses can be minimized by eliminating these problems, consequently increasing quality and productivity.

Author Contributions

The percentage of the author(s) contributions is presented below. All authors reviewed and approved the final version of the manuscript.

| | N.D.C. | E.C. | C.E.I. |
|-----|--------|------|--------|
| C | 50 | 25 | 25 |
| D | 50 | 25 | 25 |
| S | 50 | 25 | 25 |
| DCP | 50 | 25 | 25 |
| DAI | 50 | 25 | 25 |
| L | 50 | 25 | 25 |
| W | 50 | 25 | 25 |
| CR | 50 | 25 | 25 |
| SR | 50 | 25 | 25 |
| PM | 50 | 25 | 25 |
| FA | 50 | 25 | 25 |

C=Concept, D= design, S= supervision, DCP= data collection and/or processing, DAI= data analysis and/or interpretation, L= literature search, W= writing, CR= critical review, SR= submission and revision, PM= project management, FA= funding acquisition.

Conflict of Interest

The authors declared that there is no conflict of interest.

Ethical Consideration

Ethics committee approval was not required for this study because of there was no study on animals or humans. The authors confirm that the ethical policies of the journal, as noted on the journal's author guidelines page, have been adhered to.

Acknowledgements

We would like to thank the Ceramic Research Center (SAM), for assisting the characterizations and also Ece Banyo Inc. for providing factories facilities.

References

- Berberoğlu FE. 2015. Seramik form ve yüzeylerde organik doku araştırmaları. Yüksek Lisans Tezi, Hacettepe Üniversitesi, Güzel Sanatlar Enstitüsü, Seramik Anasanat Dalı, İstanbul, Türkiye, ss: 61.
- Canduran K, Ural M. 2019. Seramik sağlık gereçleri üretiminde

- deformasyon oluşumunu önlemek için kullanılan aparatlar. Akademik Sanat, 4(8): 66–79.
- Daday MT. 2012. Seramik sağlık gereçlerinde damar hatalarının giderilmesi. Doktora Tezi, Anadolu Üniversitesi, Fen Bilimleri Enstitüsü, Seramik Mühendisliği Anabilim Dalı, Eskişehir, ss: 28-31.
- Fortuna A, Fortuna DM. 2017. An industrial approach to ceramics: sanitaryware. Plinius, 2017: 43.
- Fraser H. 2005. Ceramic faults and their remedies. A & C Black Publishers Ltd, New York, USA, pp: 138.
- Genç S, Öztürk RE, Göksel MM. 2018. Obrava pişirim tekniğinin bisküvi renkli ve sırlı bünyeler üzerinde etkileri. Anadolu Üniv Sanat Tasarım Derg, 2018:156–169.
- Genç S. 2010. Kapadokya güray müze - Kapadokya yeraltı seramik müzesi. URL: <https://www.guraymuze.com/icerik/156/soner-genc/> (accessed date: August 20, 2023).
- Hasanuzzaman M, Islam F, Rashid ARMH. 2022. Investigation of methods to prevent pin-holing defect in tableware ceramic industry. Inter J Ceramic Engin Sci, 4(6): 416–425. <https://doi.org/10.1002/CES2.10164>
- Hopper R. 2023. 5 Glaze defects and expert solutions for fixing them. URL: <https://ceramicartsnetwork.org/daily/article/How-to-Correct-Five-Common-Ceramic-Glaze-Defects> (accessed date: August 20, 2023).
- Kurama S, Sarı H. 2013. Seramik sağlık gereçleri bünyelerinde camı faz kompozisyonunun pişirim sıcaklıklarına etkisi. Gazi Üniv Müh Mim Fak Der, 28(3) 445–454.
- Mete Z. 2020. Seramik kimyası. Tıbyan Yayıncılık, İzmir, Türkiye, ss: 365.
- Taşkın Z. 2009. Krakle ve toplanmalı sırlar üzerine bir araştırma. Yüksek Lisans Tezi, Dokuz Eylül Üniversitesi, Güzel Sanatlar Enstitüsü, Seramik Anasanat Dalı, İzmir, Türkiye, ss: 108.



DAYLIGHT ANALYSIS IN TERMS OF BUILDING DIRECTION AND ONE-WAY ROOF

Mehmet Sait CENGİZ^{1*}


¹Bitlis Eren University, Vocational School of Technical Sciences, 13000, Bitlis, Türkiye

Abstract: The location of the buildings in the residential area is very important in protecting or benefiting from sunlight. The dynamic structure of the sun, which constantly changes according to time and seasons, directly affects the building's architecture and urban formation. Ignoring the sun's use of the structures during the construction of the buildings can cause significant disturbances to the residents. Daylight strategies, which are also influenced by climate, depend on the availability of natural light, determined by the latitude of the building site and the instantaneous conditions around the building. High latitudes have different summer and winter conditions, with lower daylight levels in winter. At these latitudes, designers often aim to maximize daylight penetration in buildings. In the tropics, where daylight levels are high throughout the year, the design emphasis is often on preventing over heating by limiting the amount of sunlight entering the building. Daylight availability depends not only on latitude, but also on the orientation of a building, and each facade and material of the building requires a different design importance. Therefore, daylight and architectural design strategies are two inseparable phenomena. In this respect, examining traditional architecture and successful natural lighting designs in the past is very useful for understanding climate-balanced building design. For this purpose, determining the roof slope according to the sun angle in architectural structures by calculating according to the location provides efficiency in many issues from energy efficiency to human health.

Keywords: Daylight, Building Direction, Lighting, Efficiency

*Corresponding author: Bitlis Eren University, Vocational School of Technical Sciences, 13000, Bitlis, Türkiye

E mail: mesace@gmail.com (M. S. CENGİZ)

Mehmet Sait CENGİZ  <https://orcid.org/0000-0003-3029-3388>

Received: September 02, 2023

Accepted: September 28, 2023

Published: October 15, 2023

Cite as: Cengiz MS. 2023. Daylight analysis in terms of building direction and one-way roof. BSJ Eng Sci, 6(4): 535-539.

1. Introduction

Daylight lighting design in architectural lighting is a design that aims to bring the light entering the building together, taking into account the regional climate, latitude, mass, and location of the architectural structure, other structures in the region, and all surfaces that can reflect. In natural lighting calculations, natural light does not only consist of rays from the sun. Daylight is the sum of sunlight and light from reflection. In this sense, the sum of the direct sunlight of the sun and the effect of the light reflected from the sky on the earth constitutes daylight. In natural lighting design, environmental, geographical, and atmospheric conditions should be examined first. Thus, by calculating the shadows that may fall on the building at different times of the day and year, it can be decided from where the building will receive the optimum daylight (Aykal et al. 2011: Baker and Steemers, 2014 Kaynaklı et al., 2016: Kim and Kim, 2010: Kurtay, 2002). After deciding on the location, form, and height of the building, the daylight entering the interiors is optimized. In this sense, the function of the building, its openings, and interior reflectors will determine the amount and direction of daylight that will enter the building. There are many reasons why a building is illuminated by daylight, both subjective and objective. While natural lighting creates a pleasant and

inviting effect in spaces, when designed correctly, it can improve the visual environment by providing a dynamic and enjoyable environment, increasing user satisfaction, improving circadian rhythm, and reducing the load of artificial lighting, thus saving energy. Parameters related to the location, environment, and volume of the building are effective in benefiting from daylight in buildings (Brown and Dekay, 2001: Oakley et al., 2000) The parameters related to the location of the building can be listed as the natural and artificial obstacles around it, the heights of these obstacles, and their light reflection properties. Parameters related to the building's environment are related to the orientation, form, and dimensions of the building, while parameters related to the volume are related to the form and size of the space, the position of the ceiling, the wall, and the dimensions of the building. ground. materials and furniture used in the space and their surface properties. With the right lighting strategies, users in the space can perform their visual activities without difficulty, make optimum use of daylight, create better health conditions, and increase performance for efficiency (Demircan and Gültekin, 2017: Yüceer, 2010: Canan, 2008).



2. Materials and Methods

2.1. Direction of Architectural Design by Daylight

Orientation refers to how a building is positioned relative to its changing paths during different seasons, as well as to prevailing wind patterns. The most important factors to consider to obtain a good orientation include the climate of the building location, the choice of the south façade for the building (if in the northern hemisphere), the sun angles, and the climate zone (Özmen, 2010; Cengiz and Cengiz, 2018; Phillips, 2004; Cengiz et al., 2015). The effects of climate change should also be considered for optimum building design. Some climates require passive heating, while some climates require passive cooling as the case may be. To create an energy-efficient building, energy-saving projects must be implemented during the construction process with the help of simulations at the design stage. Energy-efficient solutions should be used to reduce the environmental and economic effects of excessive energy use and to provide maximum energy savings in the building. For example, the orientation of the building is the most important parameter. Because in terms of energy costs, building orientation provides great savings in energy consumption. Apart from this, energy-efficient systems such as natural ventilation, Low-e glass, hot water production from solar energy, heat recovery, 30% better heat transmission coefficient on the walls, and high-efficiency lighting fixtures offer useful solutions. Figure 1 shows the perspective view, features, and solar path of a building modeled in the northern hemisphere.

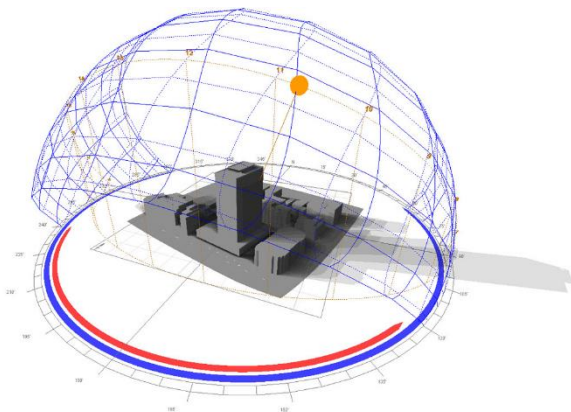


Figure 1. Perspective view, features, and solar path of a building modeled in the Northern Hemisphere (URL-1).

Suitable for passive heating is using the sun to heat a space in winter and keeping unwanted sun out in summer. Orientation for passive heating is best suited for places with a cold climate in winter. Passive heating of the one-way roof and south-facing window is shown in Figure 2.

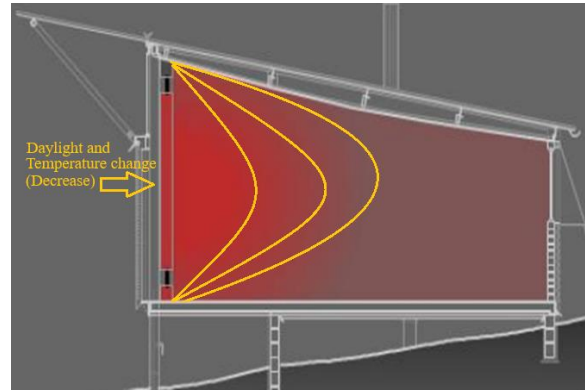


Figure 2. Passive heating of the one-way roof and south-facing window.

In a climate zone suitable for passive heating, living areas, and windows are placed on south-facing walls to let the low-angle (higher) winter sun in. Daylight efficiency is achieved by using horizontal shading devices to exclude the high-angle (lower) summer sun. Due to the movement of the earth, the sun moves from a low angle in summer to a high angle in winter. In terms of location, the best orientation for living spaces in Türkiye is south; however, directions up to 15° west of south and 25° east of south still allow good passive solar access.

2.2. Determination of Direction and Angle

2.2.1. Facade Direction and Sun Angles

The main sun access in Türkiye comes from the south side. In the passive house concept, when people talk about orientation, they mean how the house and especially the living spaces are oriented relative to the south. Solar south can differ significantly from magnetic south based on location. In addition, it will be necessary to determine the angle of the sun in different seasons for the region, because the position of the sun varies according to the regions. Knowing the angle of the sun at different times of the day and in different seasons causes the design of windows and shading elements to best capture or block the sunlight depending on the needs.

South-facing walls and windows receive more solar radiation in winter than in summer, as the sun is lower in the sky. East- and west-facing walls and windows get more sun in the early morning and late afternoon when the sun is lower in the sky in summer. The building design and south-facing walls will determine how much sun access the house will receive. Figure 3 shows the altitude positions of the sun in winter and summer.

The amount of solar access required varies by season and climate. Accordingly, if analysis is made for some climate scenarios; for a place with a hot humid (summer)-warm (winter), hot humid (summer)-temperate (winter), and hot dry (summer)-warm (winter) climate, the shading should be done on all fronts. Shading is a must to minimize direct sunlight. In a place where summer is hot and dry and winter is cold, the aim is to provide a balance of winter sun and summer shade for a place with a mild climate in all seasons. The south aspect of their habitat is

preferred because the sun's position in the sky allows for full sun access in winter. In these climates, the south facades can be easily shaded with simple horizontal arrangements such as eaves in summer. In places like Bitlis, which have a cold climate in winter and a temperate climate in summer, the aim is to maximize the

use of the sun. The south aspect of the living spaces requires making the most of solar access to heat the home, along with appropriate glazing and thermal mass. Solar access to south façades should be increased in regions with cooling breezes or high-altitude climates.

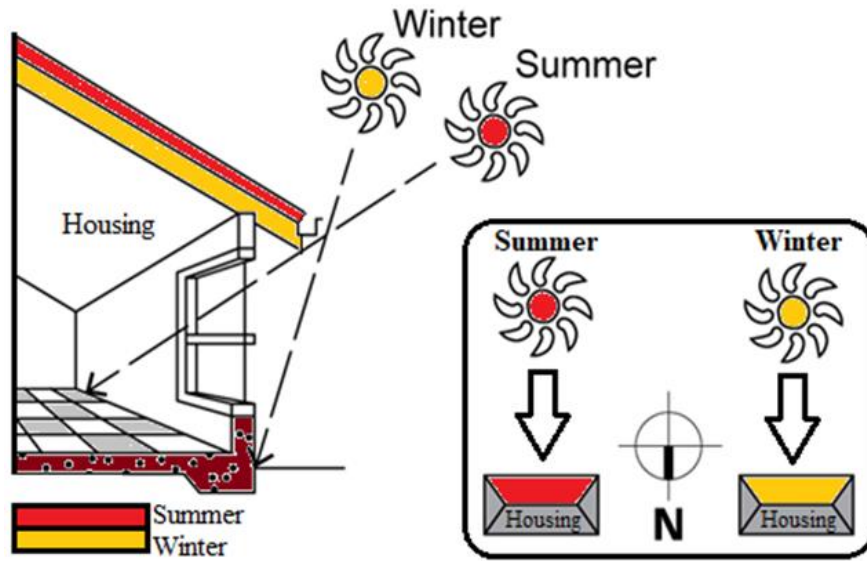


Figure3. Elevation positions of the sun in winter and summer.

2.2.2. Position Effect

When constructing a building, it is necessary to know the direction of the building. The orientation of the building will receive the sun at its highest efficiency when oriented fully towards the sun. Although it seems like a simple idea to make a building by directing the direction of the building to the sun; The sun is in different positions at different times of the year. It constantly changes during the day. Therefore, an optimal direction must be chosen (Costanzo et al. 2017: Efe and Varhan, 2020: Guzowski, 2000). For a country in the northern hemisphere, a south-facing setup provides optimal efficiency. The direction of the building is determined by the location of the place where it will be installed. In countries located in the northern hemisphere such as Türkiye, the direction of the Building is directed to the south. In countries located in the southern hemisphere, it is oriented to the north. For example, applications where the direction of the building is oriented east or west are wrong. In every city in Türkiye, the direction of the Building should face south.

The latitude value of the Building Location can be converted to the required tilt angle with the help of various formulas (Alshami et al. 2015: Bekkering et al., 2021: Beşiroğlu and Özmen, 2022). When the direction of the building is chosen optimally, it is ensured that it can benefit from the sun at the maximum level throughout the day. If the roof of the building will be used as a living space or if the light will enter the interior from the roof of the building, the slope angle of the building roof is calculated with the help of the latitude value. This angle is calculated by multiplying by 0.87 if the latitude value is

less than 25. If the latitude value is between 25 and 50, multiply by 0.87 and add 3.1 degrees to the result. Since Türkiye is located between 36-42 degrees latitude, this calculation method should be used for all installations in our country. To be used in all cities in Türkiye, Equation 1 can be used for the slope angle calculation of the roof of the building.

$$\text{Optimum Roof Slope} = (\text{Latitude} \times 0.87 + 3.1) \quad (1)$$

The angle of inclination to be found with the help of calculation expresses the angle between the roof of the building and the ground. In other words, a zero-degree slope means full horizontal positioning, 90-degree building roof full vertical positioning. If a calculation is made for the location of Bitlis, which is the subject of this study; The latitude value is 38.39379 and the longitude value is 42.12318. Accordingly, the calculation is done as in Equation 2.

$$\text{Optimum Roof Slope} = 38.3 \times 0.87 + 3.1 = 36.42 \quad (2)$$

As a result of this calculation, for a building in Bitlis province, its fixed direction should be directed to the south and the slope of the roof of this building should be directed at an angle of 36.42 degrees. In this way, energy savings are achieved both in the south and in the optimum roof slope. The optimum angle of 36.42 degrees should be used since the roof on the building that transfers the daylight to the interior is fixed. Since Türkiye is located in the Northern hemisphere, one-way roofs for daylight are directed toward the South. Figure 4 shows a one-way roof.



Figure 4. One-way roof.

3. Results and Discussion

Differences in east and west orientation can have advantages. For example, in cold climates, orienting a space slightly west or south increases afternoon sun gains that are most desirable for evening comfort. But the southeast can warm the home's living areas more in the morning and increase daytime comfort. If it is accepted that the world will warm up more due to climate change, in warmer climates, directing the space to catch local breezes will increase comfort. The breezes may vary from region to region, depending on the local topography and climate zone. Poor orientation and lack of proper shading can prevent the winter sun from getting into the space. Or, as a result of the low-angle east/west sun hitting the glass surfaces at steeper angles, it can increase the sunshine duration and cause overheating in the summer. South-facing slopes may be better suited to moderate density if design strategies are used to overcome the effects of shading. For example, side walls can be designed to provide thermal buffers and smaller floor areas can be solar heated with carefully designed and shaded east or west-facing windows using the right type of glass. For passive heating, the ideal orientation for living spaces is 15° west and 20° east of true or solar south. Standard eaves overhangs will allow the winter sun to warm the building and let the occupants out of the summer sun without any effort or additional cost. Poor orientation can block out the winter sun and allow low-angle east or west sun to hit glass surfaces, causing overheating in the summer. Orientation for passive cooling keeps out unwanted sun and hot winds while providing access to cooling breezes. Some passive cooling is required in most hot climates. In hot, humid climates where the winters are not cool, orientation should often maximize access to cooling breezes while keeping out direct sunlight and radiant heat from nearby structures at all times of the year.

4. Conclusions

Orientation in architecture is the position of a space or house relative to the path of the sun and the prevailing wind in your area. Since the direction of the sun in Türkiye is in the south, the orientation is generally related to the living areas of the house facing south. This is because south-facing rooms get the longest amount of sun in winter and are easily shaded by roof eaves in summer. Optimum orientation significantly increases ambient comfort. It also contributes to energy efficiency and reduces the need for heating and cooling. The best orientation for a building is one suitable for the climate zone.

The routing requirement for a building's passive heating, passive cooling, or both should be selected according to the climate zone. The passive heating orientation maximizes the south exposure of walls and windows to prevent overheating during the summer months. However, it aims to keep the east and west fronts to a minimum. The orientation towards passive cooling aims to eliminate sun access and maximize access to cooling breezes with proper shading (particularly east and west). Orientation for heating in the winter and cooling in the summer should aim to maximize the southward exposure of walls and windows but block sun access in summer with suitable eaves and other shading. With careful design, good orientation can be achieved even in almost any structure. Good orientation is best achieved when purchasing or building a structure, but some improvements can also be made through renovation.

The warming of the earth's climate must be taken into account when deciding on the best orientation for a structure. Considering that extreme temperatures will be seen more and hot summers will be experienced more frequently, planning in this direction is essential. Passive heating is still highly desirable in most climate zones, but passive cooling is becoming more and more important.

Extra consideration should be given to exposing windows and walls (especially west-facing) to shading, wind directions, and other forms of natural cooling.

Author Contributions

The percentage of the author contributions is presented below. The author reviewed and approved the final version of the manuscript.

| | M.S.C. |
|-----|--------|
| C | 100 |
| D | 100 |
| S | 100 |
| DCP | 100 |
| DAI | 100 |
| L | 100 |
| W | 100 |
| CR | 100 |
| SR | 100 |
| PM | 100 |
| FA | 100 |

C=Concept, D= design, S= supervision, DCP= data collection and/or processing, DAI= data analysis and/or interpretation, L= literature search, W= writing, CR= critical review, SR= submission and revision, PM= project management, FA= funding acquisition.

Conflict of Interest

The author declared that there is no conflict of interest.

Ethical Consideration

Ethics committee approval was not required for this study because of there was no study on animals or humans.

References

- Alshami M, Atwa M, Fathy A, Saleh A. 2015. Parametric Patterns Inspired by Nature for Responsive Building Façade. *Inter J Innovative Res Sci Engin Technol*, 4(2): 8009-8018.
- Aykal FD, Gümüş B, Ünver FR, Özgür M. 2011. An approach in evaluation of re-functioned historical buildings in view of natural lighting a case study in Diyarbakır Turkey. *Light Engin*. 19(2): 64-76.
- Baker N, Steemers K. 2014. *Daylight design of buildings: a handbook for architects and engineers*. Abingdon: Routledge, 2014: 116-170.
- Bekkering J, Schröder T, Zhong W. 2021. Biophilic design in

- architecture and its contributions to health, well-being, and sustainability: A critical review. *Frontiers of Architectural Res*, 11(1): 114-141.
- Beşiroğlu Ş, Özmen E. 2022. Sürdürülebilir mimarlık kapsamında ekolojik bina ve enerji etkin binanın basit toplamlı ağırlıklandırma yöntemi ile karşılaştırılması. *Tasarım Kuram J*, 18(35): 194-205.
- Brown G.Z, Dekay M. 2001. *Sun, Wind & Light, Architectural Design Strategies* John Wiley & Sons Inc., New York, USA, 222-223.
- Canan F. 2008. Enerji etkin tasarımda parametrelerin denetlenmesi için bir model denemesi. *Doktora Tezi, Selçuk Üniversitesi, Fen Bilimleri Enstitüsü, Konya Türkiye*, ss: 259.
- Cengiz MS, Cengiz C. 2018. Numerical analysis of tunnel lighting maintenance factor. *Int Isl U Malaysia IIUM Engin J*, 19: 154-163.
- Cengiz MS, Mamis MS, Akdag M, Cengiz, C. 2015. A review of prices for photovoltaic systems. *Int J Tech Phy Prob Eng*, 7: 8-13.
- Costanzo V, Evola G, Marletta L. 2017. A review of daylighting strategies in schools: state of the art and expected future trends, *Buildings*, 7: 41.
- Demircan R, Gültekin A.B. 2017. Binalarda pasif ve aktif güneş sistemlerinin incelenmesi. *TÜBAV Bilim Der*, 10(1): 36-51.
- Efe SB, Varhan D. 2020. Interior lighting of a historical building by using LED luminaires a case study of Fatih Paşa Mosque. *Light Engin*, 28: 77-83.
- Guzowski M, 2000. *Daylighting for sustainable design*. McGraw-Hill, New York, USA, pp: 87.
- Kaynaklı M, Palta O, Yurci Y, Cengiz Ç. 2016. Cooperation of conventional electric power grids and smart power grids. *J Electrical Electron Engin*, 11: 23-27.
- Kim G, Kim J.T. 2010. Healthy-daylighting design for the living environment in apartments in Korea. *Building Environ*, 45(2): 287-294.
- Kurtay C. 2002. İç hacimlerde uygun gün ışığı için dış çevrenin tasarımı, *Gazi Üniv Müh Mimar Fak Derg*, 17(3): 75-87.
- Oakley G, Riffat S, Shao L. 2000. Daylight performance of light pipes. *Solar Energy*, 69(2): 89-98.
- Özmen P. 2010. 20. Yüzyıl başlarından 1980'lere kadar uzanan süreçte modern mimarlıkta doğal ışık kullanımının irdelenmesi. *Yüksek Lisans Tezi, Fen Bilimleri Enstitüsü, Dokuz Eylül Üniversitesi, İzmir, Türkiye*, ss: 163.
- Phillips D. 2004. *Daylighting natural light in architecture*. Architectural Press, Oxford, UK, pp: 37.
- URL1. 2023. <https://www.voltimum.com.tr/haberler/mimari-aydinlatmada-dogal-isik> (accessed date: 1 June 2023)
- Yüceer NS. 2010. Gölge elemanı tasarımına bir yaklaşım ve Adana örneği. *METU JFA*, 27: 19.



INVESTIGATION OF THE GENOTOXIC EFFECTS OF THE ANALGESIC DRUGS PIROXICAM AND TENOXICAM IN HUMAN LYMPHOCYTES

Humeyra GUL¹, Ece AVULOGLU YILMAZ^{2*}

¹Amasya University, Institute of Natural and Applied Sciences, Department of Biology, 05000, Amasya, Türkiye


²Amasya University, Vocational School of Technical Sciences, Department of Health Information Systems, 05000, Amasya, Türkiye


Abstract: Analgesics are one of the most widely used drug groups in the world. Since the genotoxic and carcinogenic effects of some analgesic drugs have been detected, studies investigating these effects have increased. In this study, the genotoxic effects of the analgesic drugs Tenoxicam and Piroxicam were investigated *in vitro* in human peripheral lymphocytes by chromosomal aberrations (CAs) and micronucleus (MN) assays. In addition, mitotic index (MI) and nuclear division index (NDI) values were also determined. As a result, no difference in chromosomal abnormalities was observed in both 24 and 48 hours of Piroxicam treatment. Micronucleus frequency was increased at the three highest concentrations (0.94, 1.88 and 3.75 µg/mL) compared to the control. Piroxicam significantly decreased MI compared to both control and solvent control at concentrations of 1.88 and 3.75 µg/mL at all exposure times. Tenoxicam showed a statistically significant increase at the highest concentration (10 µg/mL) compared to the control in the 24 h CA treatment. On the other hand, no effect was observed in 48-hour CA treatment. It was concluded that tenoxicam did not cause a toxic effect at any concentration except the highest concentration (10 µg/mL) in the MN assay results. Mitotic index (MI) significantly decreased at concentrations of 1.25, 2.5, 5 and 10 µg/mL. Nuclear division index (NDI) results did not change for both agents. In conclusion, both agents were found to be genotoxic only at high concentrations and the effect was weak. This study is pioneering as there have been no previous *in vitro* studies in human peripheral lymphocytes for both Piroxicam and Tenoxicam. These results need to be supported by different cell groups and *in vivo* assays.

Keywords: Piroxicam, Tenoxicam, Chromosomal aberrations, Micronucleus, Genotoxicity, Human lymphocytes

*Corresponding author: Amasya University, Vocational School of Technical Sciences, Department of Health Information Systems, 05000, Amasya, Türkiye

E mail: ece.yilmaz@amasya.edu.tr (E. AVULOGLU YILMAZ)

Humeyra GUL  <https://orcid.org/0000-0001-5258-8051>

Ece Avuloglu YILMAZ  <https://orcid.org/0000-0002-5164-3431>

Received: August 10, 2023

Accepted: September 29, 2023

Published: October 15, 2023

Cite as: Gul H, Avuloglu Yilmaz E. 2023. Investigation of the genotoxic effects of the analgesic drugs piroxicam and tenoxicam in human lymphocytes. BSJ Eng Sci, 6(4): 540-549.

1. Introduction

Pain is one of the most common conditions for which medication is preferred. Analgesic use is one of the leading pain treatment methods. They also known as painkillers, are the common name of the drug types preferred to provide pain relief. Analgesics are one of the most widely used drug groups in the world. They are used in the treatment of certain pains such as cancer pain, bone pain, neck pain and low back pain (Kılıç and Tuylu 2020). Analgesic drugs can be divided into six groups: opioids, pyrilazones, cannabinoids, anilides, NSAIDs (Non-Steroidal Anti-Inflammatory Drugs) and atypical drugs. Non-steroidal anti-inflammatory drugs (NSAIDs) are often prescribed to relieve pain, but they also have anti-inflammatory and antipyretic effects. Oxcams are in the NSAID group due to their chemical structure. They are analgesics used in the treatment of rheumatoid arthritis, osteoarthritis, acute gout and acute muscle pain. Their half-life is 20-60 hours. Since they are weakly acidic and easily absorbed in the stomach. They are usually transported by binding to albumin, a plasma

protein (Yilmaz et al., 2017).

Piroxicam is an analgesic among the oxcams, a class of NSAIDs that are often preferred in the treatment of rheumatoid and ostoid arthritis because they have a relatively strong analgesic effect. Besides being analgesic, it also has antipyretic and anti-inflammatory effect. Piroxicam is a cheap and easily accessible drug. Although it has more side effects such as headache, dizziness and depression compared to other NSAIDs, its benefits outweigh these negative effects (Mirza et al., 2010; Shohin et al., 2014; Islami et al., 2020). Tenoxicam is also an oxcam and is a thionethionine derivative drug active substance in the NSAID group with analgesic, anti-inflammatory and platelet aggregation suppressing effect. Tenoxicam has been shown to act as a cofactor in reducing the activity of peroxidase in neutrophils, one of the blood cell groups, and this activity has been shown to be an anti-inflammatory property (Balkaya et al., 2021). Genetic toxicity or genotoxicity is a general term covering damage to the nucleus, chromosome and DNA structure such as DNA insertions, DNA breaks, gene mutations,



chromosome abnormalities, clastogenicity and aneuploidy. Genotoxic substances that interact with enzymes that enable the copying of the genome DNA or cause mutation and damage to DNA or cause some changes are defined as genotoxins. Agents or mutagens that cause mutations in the DNA molecule show their effects on DNA either directly or indirectly by binding to proteins synthesised according to genomic information (Bagatir et al., 2022; Siivola et al., 2022).

Defects in key molecules and pathways involved in DNA damage lead to tissue damage, ageing, cancer, infertility and some genetic and multifactorial diseases. The relationship between genotoxicity and carcinogenicity was examined in many studies and it was shown that many compounds that are carcinogenic to humans are genotoxic. The demonstration of a strong correlation between the mutagenic effects of chemical substances and their carcinogenic potential has led to the use of genotoxicity tests as screening tests by industrial organisations to investigate the carcinogenic risks of chemical substances (Alonso-Jauregui et al., 2023; Sherif et al., 2023). For this purpose, Chromosomal abnormality and Micronucleus tests are frequently preferred tests for genotoxicity evaluations. Chromosomal abnormalities are usually caused by a failure to separate chromosomes correctly during division and/or a failure to repair errors in the chromosomes. Epidemiological studies show that an increase in the frequency of errors occurring in chromosomes can lead cells to cancer (Hagmar et al., 2004; Mamur et al., 2018). Micronuclei are small nuclei formed during mitosis in cells, which are not attached to the nucleus, originating from a whole chromosome or an acentric chromosome fragment. It is preferred for the detection of carcinogens in cultured human lymphocytes. Further studies allow this test to be used in the determination of agents causing aneuploidy (Ustuner, 2011; Yuzbasioglu and Avuloglu Yilmaz, 2022).

In this study, the possible genotoxic potentials of Piroxicam and Tenoxicam were examined by two genotoxicity tests, chromosomal abnormality and micronucleus tests, which have proven to be reliable and sensitive. Both test systems (*in vitro* chromosomal aberration assay test number: 473, *in vitro* micronucleus assay test number: 487) were accepted by the OECD for their validity and safety in testing chemicals and performed for many years (OECD, 2016a; OECD, 2016b). The aim of this study was to investigate the genotoxic effects of the commonly used analgesic drugs active ingredients Piroxicam and Tenoxicam. There is no study investigating the genotoxic effects of these two active ingredients in human peripheral lymphocytes. For this purpose, chromosomal aberration and micronucleus assays were performed in *in vitro* human peripheral lymphocytes.

2. Materials and Methods

Cultured human peripheral lymphocyte cells were used to evaluate the genotoxic effects of Piroxicam and

Tenoxicam. For this purpose, peripheral blood was collected from two female donors who had no health problems, did not smoke or drink alcohol, were between 18-25 years of age and had not been exposed to any genotoxic agent for at least three months. Drug active ingredients were purchased from Sigma-Aldrich.

2.1. Determination of concentrations

In this study, in determining the concentrations used in both Chromosomal Aberrations (CA) and Micronucleus (MN) tests, the LD50 concentrations of the substance determined in the studies conducted with experimental animals in the literature were taken as reference. Based on these concentrations, preliminary experiments were conducted to determine the concentrations to be used in the study. Piroxicam concentrations of 0.23, 0.47, 0.94, 1.88, 3.75, 7.5, 15, 30, 60, 120 µg/mL were tested and 0.23, 0.47, 0.94, 1.88, 3.75 µg/mL concentrations were selected. Tenoxicam concentrations of 0.31, 0.63, 1.25, 2.5, 5, 10, 20, 40 µg/mL were tested and concentrations of 0.63, 1.25, 2.5, 5, 10 µg/mL were selected.

2.2. Chromosomal aberration assay

The chromosomal aberration (CA) assay was performed according to various revisions (Yuzbasioglu et al., 2006) of the method of Evans et al. (1984). Heparinised blood obtained from donors was added to tubes containing of medium. The cells were treated with the above-mentioned concentrations of Piroxicam and Tenoxicam after 24 and 48 hours after the start of culture. On the other hand, distilled water was used as negative control and Mitomycin-C (MMC) at a concentration of 0.20 µg/mL was used as positive control. DMSO (4.81 µg/mL) and methanol (3.70 µg/mL) were used as solvent control for Piroxicam and Tenoxicam respectively. At 70 h after the start of culture, 0.06 µg/mL colchicine solution was added to each tube. The purpose of this procedure is to pre-treat the cells. At the end of the 72nd hour, culture tubes were centrifuged at 1200rpm for 10 minutes, KCl (0.075M) was added to the tubes and incubated at 37°C for 30 minutes. Then, centrifugation was performed again. Cells were fixed with 3:1 methanol: acetic acid mixture at +4°C for 45 minutes. Afterwards, this cold fixation process was repeated for 2 times. Cells remaining at the bottom of each tube were homogenised by pipetting. These suspensions were spread by dropping onto clean, cooled slides. The dried slides were stained with 5% Giemsa and fixed with entellan.

For the determination of chromosome aberrations, a total of 400 metaphases (200 metaphases from each donor) with well observable chromosomes were analysed for each concentration. The percentage of abnormal cells among the analysed metaphases and the chromosome abnormality per cell were determined. Quantification of mitotic index (MI), 2000 cells from the slides prepared for all concentrations (4000 cells in total) were analysed. Mitotic index was calculated as the ratio of the number of dividing cells to the total number of cells in percentage.

2.3. Micronucleus assay

Micronucleus (MN) test was performed according to various revisions of the method of Fenech et al. (2000). For this purpose, firstly, heparinised blood was collected from each donor to prevent clotting and 0.2 mL was added to each tube containing medium. These tubes were incubated at 37°C for 72 hours. At the 48th hour of culture, the cells in culture were treated with the previously mentioned concentrations of Piroxicam and Tenoxicam. In addition, negative, positive and solvent control groups were maintained at the concentrations described in the chromosomal aberration assay. At 44 h, Cytochalasin-B (5.2 µg/ml) was added to the culture to inhibit cytokinesis. After 72 hours, each tube was centrifuged at 1000 rpm and the supernatants were removed. KCl solution was added to the remaining part and centrifugation was repeated. Fixative (3:1 methanol:acetic acid) was added to the culture tubes and they were kept at +4 for 15 min. This process was repeated twice and formaldehyde was added to the fixative solution in the last treatment. Then centrifugation was performed for the last time. The supernatant in each tube was removed, the cells were homogenised and spread on the cold slides which were previously cleaned. Slides were allowed to dry at room temperature and stained with Giemsa (5 % pH:6.8).

For the determination of micronuclei, 2000 binucleates were counted from each slide (total 4000) for each concentration. The formula $[1x(1MN)+2x(2MN)+3x(3MN+4MN)]/N$ was used for MN/Cell. Here, N refers to the total number of cells analysed.

Nuclear division index (NDI) was determined by counting 1000 cells from each donor at each concentration and 2000 cells in total. NDI was calculated according to the formula $[1x(1N)+ 2x(2N)+3x(3N+4N)]/n$. n refers to the total number of cells and (1N) mononuclear, binuclear (2N), trinuclear (3N) or tetranuclear (4N) cells.

3. Results

3.1. The results of Piroxicam treatment

Piroxicam treatment of CA results is given in Table 1 and it was observed that it did not significantly increase the percentage of abnormal cells at any concentration compared to the control at both 24 and 48 hours. Similarly, the number of abnormalities per cell was not statistically increased at any concentration compared to both control and solvent control (Table 1). The structural abnormalities detected on cultured human lymphocytes for 24 and 48 hours' treatments were chromatid break (29.82%), chromosome break (25.44%), sister chromatid union (9.65%), dicentric chromosome (15.79%), fragment (4.39%) and chromatid exchange (14.91%). No numerical abnormality was observed as a result of piroxicam treatment.

Piroxicam significantly decreased the mitotic index at the two highest concentrations (1.88 and 3.75 µg/mL) compared to the control and solvent control at both

treatment times (Table 2). This decrease was not concentration dependent ($r = -0.14$ for 24 h, $r = -0.24$ for 48 h).

Piroxicam increased the MN frequency at the three highest concentrations (0.94, 1.88 and 3.75 µg/mL) compared to the negative control with concentration-depend ($r=0.96$). No statistical difference was detected in MN frequency compared to the solvent control. Additionally, Piroxicam did not cause any change in NDI (Table 3).

3.2. The results of Tenoxicam treatment

The CA test results of Tenoxicam are given in Table 4. Tenoxicam treatment significantly increased the percentage of abnormal cells at 24 hours compared to the negative control only at the highest concentration (10 µg/mL). Similarly, the number of abnormalities per cell was significantly increased only at the highest concentration (10 µg/mL) compared to both negative and solvent controls. These increases were concentration dependent (percentage of abnormal cells and abnormalities per cell for 24 hours $r=0.80$). On the other hand, 48 hours of Tenoxicam treatment did not significantly affect the frequency of chromosomal abnormalities and percentage of abnormal cells per cell at any concentration. Tenoxicam was induced six different structural abnormalities in human lymphocytes at 24- and 48-hours treatments (chromatid break (34%), chromosome break (26%), sister chromatid union (24%), dicentric chromosome (8%), fragment (6%) and chromatid exchange (2%).

Tenoxicam decreased the mitotic index at all concentrations except the lowest concentration (0.63 µg/mL), however, this decrease was not concentration dependent ($r=-0.31$) in 24-h treatment compared to the negative control. In addition, mitotic index decreased significantly at the three highest concentrations compared to the solvent control. In 48 h treatment, similarly, mitotic index decreased significantly compared to the negative control at all concentrations except the lowest concentration (0.63 µg/mL). However, there was a significant decrease only at the highest concentration compared to the solvent control. The correlation between the decrease in MI values and concentrations was weak ($r=-0.42$) (Table 5).

Tenoxicam statistically increased the micronucleus frequency at the three highest concentrations (2.5, 5 and 10 µg/mL) compared to the negative control, but only at the highest concentration compared to the solvent control. In addition, these increases were concentration dependently ($r=0.95$). It was determined that Tenoxicam treatment did not affect NDI values (Table 6).

Table 1. Chromosomal abnormalities in human peripheral lymphocytes induced by piroxicam

| Test substance | Treatment | | Abnormalities | | | | | | Abnormal cell ± SE (%) | CA/cell ± SE |
|--------------------------------|------------------|--------------------------|---------------|-------|------|-------|-------|------|---------------------------|-----------------|
| | Period (hour) | Concentration (µg/mL) | ctb | csb | scu | dic | ex | f | | |
| | | | | | | | | | | |
| Control | 24 | 0.00 | 5 | - | - | - | 2 | - | 1.5±0.60 | 0.0175±0.0489 |
| MMC | 24 | 0.20 | 6 | 2 | 1 | 6 | 65 | 1 | 17.5±1.89 | 0.2025±0.2213 |
| DMSO | 24 | 4.81 (µl/mL) | 1 | 1 | 1 | 2 | 3 | - | 1.75±0.64 | 0.0200±0.0700 |
| Piroxicam | 24 | 0.23 | 1 | 2 | - | 2 | 1 | 1 | 1.25±0.54 | 0.0175±0.0489 |
| | | 0.47 | 1 | 2 | - | 3 | 3 | - | 2.25±0.73 | 0.0220±0.0700 |
| | | 0.94 | 2 | 3 | 1 | 3 | 1 | 1 | 2.25±0.73 | 0.0275±0.0700 |
| | | 1.88 | 3 | 4 | 1 | 3 | 1 | 1 | 2.75±0.81 | 0.0325±0.0860 |
| | | 3.75 | 4 | 4 | 3 | 2 | - | - | 2.25±0.73 | 0.0325±0.0860 |
| Control | 48 | 0.00 | 3 | 1 | 1 | - | 2 | 1 | 2.00±0.70 | 0.0200±0.0700 |
| MMC | 48 | 0.20 | 3 | 2 | 1 | 8 | 69 | 2 | 18.25±1.92 | 0.2125±0.2236 |
| DMSO | 48 | 4,81 (µl/mL) | 2 | 4 | 1 | - | 5 | 1 | 2.75±0.81 | 0.0322±0.0860 |
| Piroxicam | 48 | 0.23 | 2 | 2 | - | 1 | 1 | - | 1.50±0.60 | 0.0150±0.0489 |
| | | 0.47 | 3 | 4 | 1 | 1 | 2 | 1 | 1.75±0.64 | 0.0300±0.0860 |
| | | 0.94 | 3 | 3 | 1 | - | 2 | - | 2.25±0.73 | 0.0222±0.0700 |
| | | 1.88 | 3 | 3 | 2 | 2 | 1 | - | 2.50±0.77 | 0.0275±0.0700 |
| | | 3.75 | 4 | 2 | 2 | 1 | 5 | 1 | 3.00±0.84 | 0.0375±0.0860 |
| Frequency of abnormalities (%) | | | 29.82 | 25.44 | 9.65 | 15.79 | 14.91 | 4.39 | | |

ctb= chromatid break, csb= chromosome break, scu= sister chromatid union, dic= dicentric chromosome, ex= chromatid exchange, f= fragment.

Table 2. Mitotic index values observed in lymphocytes with piroxicam treatment

| Test substance | Treatment | | MI |
|----------------|---------------|-----------------------|------------------------------|
| | Period (hour) | Concentration (µg/mL) | |
| Control | 24 | 0.00 | 6.78 ± 0.40 |
| DMSO | 24 | 4.81 (µl/mL) | 6.53 ± 0.39 |
| MMC | 24 | 0.20 | 3.25 ± 0.28 |
| Piroxicam | 24 | 0.23 | 6.88 ± 0.40 |
| | | 0.47 | 6.48 ± 0.39 |
| | | 0.94 | 5.75 ± 0.37 |
| | | 1.88 | 5.25 ± 0.35**a ₁ |
| | | 3.75 | 2.53 ± 0.25***a ₃ |
| Control | 48 | 0.00 | 6.68 ± 0.39 |
| DMSO | 48 | 4.81 (µl/mL) | 6.28 ± 0.38 |
| MMC | 48 | 0.20 | 3.00 ± 0.27 |
| Piroxicam | 48 | 0.23 | 6.55 ± 0.39 |
| | | 0.47 | 6.23 ± 0.38 |
| | | 0.94 | 5.68 ± 0.37 |
| | | 1.88 | 5.20 ± 0.35** a ₁ |
| | | 3.75 | 3.18 ± 0.28***a ₃ |

* Significantly different from the negative control P<0.05 (z test), ** Significantly different from the negative control P<0.01 (z test), *** Significantly different from the negative control P<0.001 (z test), a₁ Significantly different from the solvent control P<0.05 (z test), a₂ Significantly different from the solvent control P<0.01 (z test), a₃ Significantly different from the solvent control P<0.001 (z test).

Table 3. Effect of piroxicam on micronucleus frequencies and nuclear division index in human lymphocytes

| Test substance | Treatment | | Binucleated cells (BN) scored | Distribution of BN cells according to the number of MN | | | MN ± SE (%) | Nuclear division index (NDI) ± SE |
|----------------|---------------|-----------------------|-------------------------------|--|-----|-----|--------------|-----------------------------------|
| | Period (hour) | Concentration (µg/mL) | | (1) | (2) | (3) | | |
| Control | 48 | 0.00 | 4000 | 19 | - | - | 0.48±0.11 | 0.73±0.19 |
| MMC | 48 | 0.20 | 4000 | 138 | - | - | 3.45±0.30 | 0.67±0.18 |
| DMSO | 48 | 4.81 (µl/mL) | 4000 | 30 | - | - | 0.75±0.14 | 0.69±0.18 |
| Piroxicam | 48 | 0.23 | 4000 | 18 | - | - | 0.43±0.10 | 0.75±0.19 |
| | | 0.47 | 4000 | 25 | - | - | 0.63±0.12 | 0.76±0.19 |
| | | 0.94 | 4000 | 39 | - | - | 0.98±0.16** | 0.74±0.19 |
| | | 1.88 | 4000 | 43 | - | - | 1.08±0.16** | 0.74±0.19 |
| | | 3.75 | 4000 | 45 | - | - | 1.13±0.17*** | 0.77±0.19 |

** Significantly different from the negative control P<0.01 (z test), *** Significantly different from the negative control P<0.001 (z test).

Table 4. Chromosomal abnormalities in human peripheral lymphocytes induced by tenoxicam

| Test substance | Treatment | | Abnormal cell ± SE (%) | | | | | | CA/cell ± SE | |
|----------------|---------------|-----------------------|------------------------|-------|-------|------|------|------|--------------|----------------------------|
| | Period (hour) | Concentration (µg/mL) | Abnormalities | | | | | | | |
| | | | ctb | csb | scu | dic | ex | f | | |
| Control | 24 | 0.00 | 3 | - | - | - | - | - | 0.50 ±0,353 | 0.0075±0.0043 |
| MMC | 24 | 0.20 | 31 | 18 | 10 | 11 | - | 3 | 17.25±1.890 | 0.1825±0.0193 |
| Methanol | 24 | 3.70 (µl/mL) | 3 | - | - | 3 | - | - | 1,00 ±0.498 | 0.0150±0.0061 |
| Tenoxicam | 24 | 0.63 | - | 1 | - | - | - | - | 0.25 ±0.250 | 0.0025±0.0025 |
| | | 1.25 | - | 2 | - | - | - | - | 0.50 ±0.353 | 0.0050±0.0035 |
| | | 2.50 | - | - | 1 | 1 | - | - | 0.25 ±0.250 | 0.0050±0.0035 |
| | | 5.00 | 1 | 2 | 1 | - | - | - | 0.75 ±0.431 | 0.0100±0.0048 |
| | | 10.00 | 6 | 2 | 1 | 1 | - | 3 | 2.50 ±0.781* | 0.0325±0.0089 ^c |
| Control | 48 | 0.00 | 3 | 1 | 1 | - | - | - | 1,00±0.498 | 0.0125±0.0055 |
| MMC | 48 | 0.20 | 37 | 10 | 21 | 5 | - | - | 16.25±1.84 | 0.1825 ±0.0193 |
| Methanol | 48 | 3.70 (µl/mL) | - | - | - | 2 | 5 | - | 1.25±0.550 | 0.0175±0.0065 |
| Tenoxicam | 48 | 0.63 | - | - | 1 | - | - | - | 0.25±0.062 | 0.0025±0.0024 |
| | | 1.25 | 1 | 1 | 2 | - | - | - | 0.75±0.431 | 0.0100±0.0350 |
| | | 2.50 | 1 | 1 | 1 | 1 | - | - | 0.75±0.431 | 0.0100±0.0350 |
| | | 5.00 | 2 | 2 | 2 | - | - | - | 1.50±0.607 | 0.0150±0.0060 |
| | | 10.00 | 3 | 2 | 3 | 1 | 1 | - | 1.75±0.429 | 0.0250±0.0078 |
| FA (%) | | | 34.00 | 26.00 | 24.00 | 8.00 | 2.00 | 6.00 | | |

FA= frequency of abnormalities, ctb= chromatid break, csb= chromosome break, scu= sister chromatid union, dic= dicentric chromosome, ex= chromatid exchange, f= fragment.

* Significantly different from the negative control P<0.05 (z test), ^cSignificantly different from the solvent control P<0.001 (z test)

Table 5. Mitotic index values observed in lymphocytes with tenoxicam treatment

| Test substance | Treatment | | MI MI±SE % |
|----------------|---------------|-----------------------|------------------------------|
| | Period (hour) | Concentration (µg/ml) | |
| Control | 24 | 0.00 | 7.00 ± 0.40 |
| DMSO | 24 | 3.70 (µl/mL) | 6.68 ± 0.39 |
| MMC | 24 | 0.20 | 3.40 ± 0.29 |
| Tenoxicam | 24 | 0.63 | 6.50 ± 0.39 |
| | | 1.25 | 5.80 ± 0.37* |
| | | 2.50 | 5.58 ± 0.36**a ₁ |
| | | 5.00 | 5.23 ± 0.35**a ₂ |
| | | 10.00 | 3.63 ± 0.30***a ₃ |
| Control | 48 | 0.00 | 7.25 ± 0.41 |
| DMSO | 48 | 3.70 (µl/mL) | 6.38 ± 0.39 |
| MMC | 48 | 0.20 | 3.90±0.31 |
| Tenoxicam | 48 | 0.63 | 6.25 ± 0.38 |
| | | 1.25 | 5.88 ± 0.37* |
| | | 2.50 | 5.60 ± 0.36** |
| | | 5.00 | 5.48 ± 0.36** |
| | | 10.00 | 4.20 ± 0.32***a ₃ |

* Significantly different from the negative control P<0.05 (z test), ** Significantly different from the negative control P<0.01 (z test), *** Significantly different from the negative control P<0.001 (z test), a₁Significantly different from the solvent control P<0.05 (z test), a₂ Significantly different from the solvent control P<0.01 (z test), a₃ Significantly different from the solvent control P<0.001 (z test).

Table 6. Effect of tenoxicam on micronucleus frequencies and nuclear division index in human lymphocytes

| Test substance | Treatment | | Binucleated cells (BN) scored | Distribution of BN cells according to the number of MN | | | MN ± SE (%) | Nuclear division index (NDI) ± SE |
|----------------|---------------|-----------------------|-------------------------------|--|-----|-----|----------------------------|-----------------------------------|
| | Period (hour) | Concentration (µg/mL) | | (1) | (2) | (3) | | |
| Control | 48 | 0.00 | 4000 | 21 | - | - | 0.53 ± 0.11 | 0.71 ± 0.18 |
| MMC | 48 | 0.20 | 4000 | 130 | - | - | 3.25 ± 0.28 | 0.65 ± 0.18 |
| Methanol | 48 | 3,70 (µl/mL) | 4000 | 27 | - | - | 0.68 ± 0.13 | 0.70 ± 0.18 |
| Tenoxicam | 48 | 0.63 | 4000 | 19 | - | - | 0.48 ± 0.11 | 0.67 ± 0.18 |
| | | 1.25 | 4000 | 22 | - | - | 0.55 ± 0.12 | 0.69 ± 0.18 |
| | | 2.50 | 4000 | 40 | - | - | 1.00 ± 0.16* | 0.66 ± 0.18 |
| | | 5.00 | 4000 | 36 | - | - | 0.90 ± 0.15* | 0.66 ± 0.18 |
| | | 10.00 | 4000 | 47 | - | - | 1.18 ±0.17**a ₁ | 0.73 ± 0.19 |

* Significantly different from the negative control P<0.05 (z test), ** Significantly different from the negative control P<0.01 (z test), a₁Significantly different from the solvent control P<0.05 (z test).

4. Discussion

In this study, CA and MN tests were performed in human lymphocytes to determine the *in vitro* genotoxic effects of Piroxicam and Tenoxicam, the active ingredients of NSAIDs analgesic drugs. NSAIDs show their effects through COX (cyclooxygenase) enzymes. As a result of the translation from arachidonic acid to prostoglandin, they act by non-selectively inhibiting COX enzymes. NSAIDs inhibit prostoglandin synthesis after tissue damage. These drugs are needed to prevent both pain and inflammation in damaged tissues. NSAID group analgesics have significant side effects. The most frequently observed side effect of this group of drugs is on the gastrointestinal system due to inhibition of COX enzymes. NSAIDs provide reversible or irreversible

inhibition of COX by competing with arachidonic acid for the active site of the enzyme. (Himly et al., 2003; Becker and Phero, 2005; Ali et al., 2023)

CA and MN test results showed that piroxicam did not induce the formation of chromosomal abnormalities but induced micronucleus formation at the three highest concentrations (0.94, 1.88, 3.75 µg/mL). The other analgesic Tenoxicam, whose genotoxic potential was examined in the study, is induced chromosomal abnormality formation only at the highest concentration (10 µg/mL) and induced micronucleus formation at concentrations of 2.5, 5 and 10 µg/mL. In addition, Piroxicam was found to decrease mitotic index at the two highest concentrations and Tenoxicam caused a significant decrease in mitotic index values. However,

nuclear division index (NDI) did not change for treatment of both analgesics.

The concept of genotoxicity refers to damage to the structure or quantity of chromosomes or DNA caused by any physical, biological or chemical agent. The chromosomal aberration (CA) assay detects the structure and number of any changes that occur in the chromosome or in the sister chromatids that make up the chromosome. Micronuclei are caused by defects in kinetochore and spindle threads during the karyokinesis stage of cell division, deficiencies in genes that control cell division, and finally damage to chromosomes (Bonassi et al., 2011). Cytogenetic modifications, which are changes in chromosome structure and number, have been described as the types of genetic changes that contribute to the development and progression of cancer (Norppa et al. 2006, Ewing et al., 2023). Furthermore, Micronuclei (MNi) and other nuclear abnormalities such as nucleoplasmic bridges (NPBs) and (NBUDs) are known to be biomarkers of genotoxicity and indicators of chromosomal instability that often occur in cancer (El-Zein et al., 2011, Raj and Rajitha, 2023).

Exposure to biological, physical and chemical agents causes differences in either the structure or the number of chromosomes. Structural abnormalities are chromatid breaks, chromosome breaks, fragments, dysentric chromosomes, sister chromatid unions. Polyploidy is an example of numerical abnormalities. If the effect of the chemical occurs in the first phase of interphase (G1), chromosome-type abnormalities; if it occurs in the second phase (G2), chromatid-type abnormalities; if it occurs in the synthesis phase (S), both types of abnormalities may be observed. Chromosomal abnormalities are usually caused by the misjoining or non-joining of chromosome ends originating from DNA single and double strand breaks. As expected, as the number of DNA strand breaks increases, the number of misjoins or failures to join may increase. The formation of two breaks on two different chromosomes can result in a dysentric chromosome with two centromeres, or an acentric fragment with reciprocal translocation where both chromosomes have one centromere. On the other hand, fragments are also known to be formed as a result of breaks in chromosomes or chromatids as well as terminal deletions (Natarajan and Boei, 2003; Timoroglu et al., 2014; Ila and Husunet, 2022).

Damages occurring in the genome are effective in the occurrence of micronuclei. Clastogenic, mutagenic or carcinogenic factors are important in the formation of these damages. In micronuclei caused by any reason, the damage that has occurred anywhere along the genome cannot be repaired or even if it is repaired, it may not be fully repaired. In addition, mutations in kinetochores, which are special proteins, or in centromeres that join chromatids or in spindle threads originating from the centrosome organelle can also cause micronucleus formation. However, errors can also occur in the genes responsible for the repair of these errors in DNA. In such

a case, an increase in the frequency of micronucleus formation is an expected result since repair of errors is not possible (Fenech, 1993; Choy, 2001; Ellwanger et al., 2023). Although piroxicam did not induce chromosomal abnormalities, it may have increased the frequency of MNs due to the failure to repair defects in mitotic apparatus, spindle threads or centrosome responsible for spindle thread formation and centrioles originating from centrosome. In addition, defects in repair mechanisms may not have been repaired and the cell may have lost its viability spontaneously (Fenech, 2000; Ellwanger et al., 2023).

Mitotic Index (MI) is used to evaluate the cytotoxicity of different chemical agents. It is a preferred parameter to obtain information about the mitosis process. Most chemical agents that cause cytotoxicity cause a decrease in mitotic index values. The reason for this decrease in mitotic index is the inhibition of the G2 phase, which initiates mitosis of cells, and the suppression of enzymes involved in DNA replication and forming spindle threads. The decrease in mitotic index is also caused by the loss of the cell's ability to divide and the presence of factors that cause cell death (Van't Hof, 1968; Jain and Sorbhoy, 1988; Takebayashia et al., 2023). In this study, the decrease in MI values of both drug active ingredients, except at low concentrations, indicates that cell cycle progression is prevented and/or capacity is reduced (Riss and Moravec, 2004).

In order to examine the genotoxic effects of drug active ingredients, the guidelines established by the Organisation for Economic Cooperation and Development (OECD) for the testing of chemicals are considered. Genotoxicity tests that should be performed if the active substance is intended to be placed on the market are gene mutation test in bacteria, cytogenetic examination of *in vitro* chromosomal damage in mammalian cells or gene mutation test in *in vitro* mammalian cells and lastly *in vivo* chromosomal damage test using rodent haematopoietic cells (OECD, 2008). However, the lack of genotoxicity studies on Piroxicam and Tenoxicam drug active ingredients is noteworthy. This is the first study to investigate the genotoxicity of both drug active ingredients in human lymphocytes *in vitro*.

Since some analgesic drug active ingredients were found to have genotoxic and carcinogenic effects, the number of studies examining the effects of these substances were increased. In order to investigate the genotoxicity of Piroxicam, *in vitro* MN assay (50, 1000 and 1500 µg/mL) was performed in mouse, rat, monkey, dog and human liver cells. The results showed that Piroxicam did not increase the MN frequency and therefore did not show any genotoxic effect (Kishino, et al., 2019). The genotoxic effect of piroxicam was investigated in 20-25 g healthy *Mus musculus* treated at a dose of 0.3 mg/kg for 24 hours by CA assay. At the same time, cytotoxicity was also evaluated using mitotic index. As a result, no significant increase in chromosomal abnormalities and no change in

mitotic index frequency were observed (Dkhil et al., 2011).

RAW 264.7 macrophages were treated with Piroxicam and liposome-coated Piroxicam concentrations of 0.1, 0.2 and 0.4 mg/ml for 24 hours and cytotoxicity was evaluated using MTT assay. It was observed that Piroxicam treatments did not significantly decrease cell viability, while liposome-coated Piroxicam significantly decreased cell viability at the highest concentration (Chiong et al., 2013). In patients exposed to tenoxicam, piroxicam and lornoxicam at a dose of 20 mg/day for 2 weeks, the *in vivo* frequency of sister chromatid exchanges (SCEs) was increased, except in piroxicam-treated patients. It was indicated that treatment with oxicams may indicate a genotoxic risk due to elevated SCE levels (Kulich and Klein 1986; Brambilla and Martelli, 2009). Ames test was performed with *Bacillus subtilis*, *S. typhimurium* strains TA98, TA100, TA1535, TA1537, TA1538 and *E. coli* WP2 uvrA strain with 1000 g/plate concentration of tenoxicam and it was reported that it did not induce mutation (Brambilla and Martelli, 2009).

Genotoxicity studies with Piroxicam and Tenoxicam are very limited. However, studies investigating the genotoxic potential of different analgesic drug active ingredients were encountered. The genotoxicity of ibuprofen (oral doses of 10, 20, 40 and 60 mg/kg) was investigated in mice by *in vivo* CA assay. It was observed that mitotic index values decreased at doses of 40 and 60 mg/kg and chromosomal abnormality frequencies increased dose-dependently in bone marrow cells of mice (Rina et al., 2012). In another study, the genotoxicity of dexketoprofen trometamol in human lymphocytes was investigated by MN and comet assays. For this, cells were exposed to concentrations in the range of 100-1000 mg/ml for 24 and 48 hours. As a result, it was observed that MN frequency and comet tail length and intensity increased especially at high concentrations (Kilic and Tuylu, 2020).

The effects of repeated doses of meloxicam, an NSAID from the oxicam group, on genotoxicity, oxidative stress and histopathological changes in mice were evaluated. For this purpose, 0.1, 0.5 and 1 mg/kg meloxicam were given to animals for 28 days. The highest concentration was not change MN frequency but induced DNA damage in comet test. Meloxicam did not affect catalase activity but increased plasma ferric reduction capacity (FRAP) (1 mg/kg). It was evaluated that meloxicam could potentially cause cardiac pathological changes and genotoxic effects (da Silva et al., 2022) These effects can be explained by the induction of ROS formation by anti-inflammatory drugs and analgesics. Although studies indicate that NSAIDs reduce ROS formation by inhibition of COX enzyme, it is also a fact that ROS production caused by them endangers DNA integrity. Studies in the literature show that especially prolonged exposure to NSAIDs may have genotoxic effects (Bhattacharya et al.2000; Fernandes et al.2003; Pandey and Rizvi 2010; da

Silva et al., 2022). The genotoxic effects of Piroxicam and Tenoxicam observed in this study may be due to aromatic amines. Despite their known and proven mutagenicity and carcinogenicity, aromatic amines are frequently found in drug molecules, including oxicams, due to their usefulness in synthesis (Harding et al., 2015). Additionally, oxicams are characterized by the presence of the 4-hydroxybenzothiazine heterocycle. Piroxicam, known to have gastrointestinal toxicity *in vivo*, did not show significant PGHS-1 selectivity *in vitro*. The cytochrome P450 (CYP) oxidase system is responsible for most NSAID metabolism and CYP2C9 is the most important oxidase primarily responsible for the metabolism of a wide range of NSAIDs, including piroxicam and tenoxicam (Bindu et al., 2020).

In this study, the genotoxic effects of Piroxicam and Tenoxicam, the active ingredients of analgesic drugs, were investigated by performed chromosomal aberrations and micronucleus assays. It was determined that the risk of genotoxic effects increased as the concentration increased in different test systems of both active substances and similar results were valid for cytotoxicity. However, when the data obtained are evaluated collectively, it is possible to state that Piroxicam and Tenoxicam exhibit a weak genotoxic effect. It is thought that *in vivo* studies, especially for high concentrations, will contribute to the understanding of their genotoxic potential and mechanisms of action.

Author Contributions

The percentage of the author(s) contributions is presented below. All authors reviewed and approved the final version of the manuscript.

| | H.G. | E.A.Y. |
|-----|------|--------|
| C | 50 | 50 |
| D | 50 | 50 |
| S | 20 | 80 |
| DCP | 80 | 20 |
| DAI | 60 | 40 |
| L | 70 | 30 |
| W | 20 | 80 |
| CR | 20 | 80 |
| SR | 10 | 90 |
| PM | 50 | 50 |
| FA | 30 | 70 |

C=Concept, D= design, S= supervision, DCP= data collection and/or processing, DAI= data analysis and/or interpretation, L= literature search, W= writing, CR= critical review, SR= submission and revision, PM= project management, FA= funding acquisition.

Conflict of Interest

The authors declared that there is no conflict of interest.

Ethical Consideration

This study was conducted with the permission of Amasya University Clinical Ethics Committee (approval date: 3 June 2021 and protocol code: 86). The authors confirm that the ethical policies of the journal, as noted on the journal's author guidelines page, have been adhered to.

Acknowledgements

This study is based on Humeyra Gul's master thesis. Ece Avuloglu Yilmaz is the supervisor of the thesis.

References

- Ali KA, Maity A, Roy SD, Pramanik SD, Das PP, Shaharyar MA. 2023. Insight into the mechanism of steroidal and non-steroidal anti-inflammatory drugs. In: Kazmi I, Karmakar S, Shaharyar A, Afzal M, Al-Abbasi FA, editors. How synthetic drugs work. Academic Press, Cambridge, Massachusetts, USA, pp: 61-94.
- Alonso-Jauregui M, López de Cerain A, Azqueta A, Rodríguez-Garraus A, Gil AG, González-Peñas E, Vettorazzi A. 2023. In vivo genotoxicity and toxicity assessment of sterigmatocystin individually and in mixture with aflatoxin B1. *Toxins*, 15(8): 491.
- Bagatir G, Kaya M, Suer I, Cefle K, Palanduz A, Palanduz S, Becerir EB, Kocyigit M, Ozturk S. 2022. The effect of anzer honey on X-ray induced genotoxicity in human lymphocytes: an in vitro study. *Microsc Res Tech*, 85(6): 2241-2250.
- Balkaya AN, Kaya FN, Filiz TA, Karaca U. 2021. Postoperatif ağrı kontrolünde preemtif ve postoperatif tek doz tenoksikam uygulamasının etkinliğinin karşılaştırılması. *BUÜTF Dergisi*, 47(1): 97-104.
- Becker DE, Phero JC. 2005. Drug therapy in dental practice: nonopioid and opioid analgesics. *Anesth Prog*, 52:140- 149.
- Bhattacharya SK. 2000. Antioxidant activity of bacopa monniera in rat frontal cortex, striatum and hippocampus. *Phytother Res*, 14 (3): 174-179.
- Bindu S, Mazumder M, Bandyopadhyay U. 2020. Non-steroidal anti-inflammatory drugs (NSAIDs) and organ damage: a current perspective. *Biochem Pharmacol*, 180: 114147.
- Bonassi S, El-Zein R, Bolognesi C, Fenec M. 2011. Micronuclei frequency in peripheral blood lymphocytes and cancer risk: evidence from human studies. *Mutagenesis*, 26(1): 93-100.
- Brammilla G, Martelli A. 2009. Genotoxicity and carcinogenicity studies of analgesics, anti-inflammatory drugs and antipyretics. *Pharmacol Res*, 60: 1-17.
- Chiong HS, Yong YK, Ahmad Z, Sulaiman MR, Zakaria ZA, Yuen KH, Hakim MN. 2013. Cytoprotective and enhanced anti-inflammatory activities of liposomal piroxicam formulation in lipopolysaccharide-stimulated RAW 264.7 macrophages. *Int J Nanomedicine*, 8: 1245-1255.
- Choy WN. 2001. Genetic toxicology and cancer risk assessment. First edition, CRC Press, New York, USA, pp: 29-47.
- da Silva JCG, Dallegrave E, Rodrigues GZP, Bigolin C, Neumann TMSDO, Schuster AC, et al. 2022. Repeated dose of meloxicam induces genotoxicity and histopathological changes in cardiac tissue of mice. *Drug Chemical Toxicol*, 45(2): 822-833.
- Dkhil MA, Tohamy A, Gabry MS. 2011. Chromosomal aberrations induced in bone marrow cells of mice due to the administration of the non-steroidal anti-inflammatory drug, Piroxicam. *Afr J Pharm Pharmacol*, 5(1): 98-103.
- Ellwanger JH, Kulmann-Leal B, Ziliotto M, Chies JAB. 2023. HIV Infection, chromosome instability, and micronucleus formation. *Viruses*, 15(1): 155.
- El-Zein R, Vral A, Etzel CJ. 2011. Cytokinesis-blocked micronucleus assay and cancer risk assessment. *Mutagenesis*, 26(1): 101-106.
- Evans HJ, (1984) Human peripheral blood lymphocytes for the analysis of chromosome aberrations in mutagen tests. In: Kilbey B J, Legator M, Nichols W, Ramel C editors, Handbook of mutagenicity test procedures, Elsevier Sciences, Amsterdam, pp: 405-424.
- Ewing LE, Pathak R, Landes RD, Skinner CM, Binz R, Young SG, et al. 2023. Cytogenetic and epigenetic aberrations in peripheral lymphocytes of northwest Arkansas Marshallese. *Int J Radiat Biol*, 99(4): 644-655.
- Fenec M. 2000. The *in vitro* micronucleus technique. *Mutat Res*, 455: 81-95.
- Fenec M. 1993. The cytokinesis-block micronucleus technique and its application to genotoxicity studies in human populations. *Environ Health Perspect*, 101(3): 101-107.
- Fernandes E, Toste SA, Lima JL, Reis S. 2003. The metabolism of sulindac enhances its scavenging activity against reactive oxygen and nitrogen species. *Free Radic Biol Med*, 35(9):1008-1017.
- Hagmar L, Strömberg U, Bonassi S, Hansteen IL, Knudsen LE, Lindholm C, Norppa H. 2004. Impact of types of lymphocyte chromosomal aberrations on human cancer risk results from nordic and italian cohorts. *Cancer Res*, 64(6): 2258-2263.
- Harding AP, Popelier PL, Harvey J, Giddings A, Foster G, Kranz M. 2015. Evaluation of aromatic amines with different purities and different solvent vehicles in the Ames test. *Regul Toxicol Pharmacol*, 71(2): 244-250.
- Himly M, Jahn-Schmid B, Pittertschatscher K, Bohle B, Grubmayr K, Ferreira F. 2003. IgE- mediated immediate-type hypersensitivity to the pyrazolone drug propyphenazone. *Journal Allergy Clin Immunol*, 111: 882-888.
- Ila, H. B., and Husunet, M.T. 2022. Kromozom anormallikleri testi. In: Unal F, Yuzbasioglu D, editors. *Genetik Toksikoloji*, Ankara, Palme; 2022:153-179.
- Islami A, Sopyan I, Gozali D, Hairunnisa H. 2020. Review Modifikasi Kelarutan Piroksikam. *Jurnal Ilmiah Farmako Bahari*, 11(1): 89-102.
- Jain AK, Sorbhoy RK.1988. Cytogenetical studies on the effects of some chlorinated pesticides. *Cytologia*, 53: 427-436.
- Kilic M, Tuylu BA. 2020. An in vitro investigation of genotoxic effects of dexketoprofen trometamol on healthy human lymphocytes. *Drug Chem Toxicol*, 43(2): 174-181.
- Kishino Y, Hasegawa T, Yamoto T, Mori K. 2019. Species differences in micronucleus induction of the clastogenic compounds associated with drug metabolic profile. *J Toxicol Sci*, 44(10): 701-709.
- Kullich W, Klein G. 1986. Investigations of the influence of nonsteroidal antirheumatic drugs on the rates of sister-chromatid exchange. *Mutat Res Lett*, 174(2): 131-134.
- Mamur S, Ataseven N, Ünal F, Yüzbaşıoğlu D. 2018. Gıdalarda koruyucu katkı maddesi olarak kullanılan sodyum benzoat ve potasyum sorbat karışımının genotoksik eşiğin mikronükleus testi ile belirlenmesi. *Balikesir Üniversitesi Fen Bilimleri Enstitüsü Dergisi*, 20 (2): 235-245.
- Mirza S, Miroshnyk I, Habib MJ, Brausch JF, Hussain MD. 2010. Enhanced dissolution and oral bioavailability of piroxicam formulations: modulating effect of phospholipids. *Pharmaceutics*, 2(4): 339-350.
- Natarajan A T, Boei JJWA. 2003. Formation of chromosome aberrations: insights from FISH. *Mutat Res*, 544(2): 299-304.
- Norppa H, Bonassi S, Hansteen IL, Hagmar L, Strömberg U, Rössner P, et al. 2006. Chromosomal aberrations and SCEs as biomarkers of cancer risk. *Mutat Res*, 600(1-2): 37-45.

- Organization for Economic Co-operation and Development (OECD) 2016a. Test No. 473: In Vitro Mammalian Chromosomal Aberration Test, OECD Guidelines for the Testing of Chemicals, Section 4, OECD Publishing, Paris, <https://doi.org/10.1787/9789264264649-en>
- Organization for Economic Co-operation and Development (OECD) 2016b. Test No. 487: In Vitro Mammalian Cell Micronucleus Test, OECD Guidelines for the Testing of Chemicals, Section 4, OECD Publishing, Paris, <https://doi.org/10.1787/9789264264861-en>
- Organization for Economic Co-operation and Development (OECD), 2008. OECD Guidelines for the Testing of Chemicals, Health Effects, 4: 471-486
- Pandey KB, Rizvi SI, 2010. Markers of oxidative stress in erythrocytes and plasma during aging in humans. *Oxid Med Cell Longev*, 3(1): 2-12.
- Raj SG, Rajitha V. 2023. Assessment of genotoxic instability markers in peripheral blood lymphocytes of breast cancer patients: a case control study. *J Biomol Struct Dyn*, 2023: 1-5.
- Rina T, Shyam SP, Pankaj T. 2012. Genotoxicity of ibuprofen in mouse bone marrow cells in vivo. *Drug and Chem Toxicol*, 27: 940-951.
- Riss TL, Moravec RA. 2004. Use of multiple assay endpoints to investigate the effects of incubation time, dose of toxin and plating density in cell-based cytotoxicity assays. *Assay Drug Dev Technol*, 2(1): 51- 62.
- Sherif M, Makame KR, Östlundh L, Paulo MS, Nemmar A, Ali BR, et al. 2023. Genotoxicity of occupational pesticide exposures among agricultural workers in arab countries: a systematic review and meta-analysis. *Toxics*, 11(8): 663.
- Shohin IE, Kulinich JI, Ramenskaya GV, Abrahamsson B, Kopp S, Langguth P, et al. 2014. Biowaiver monographs for immediate release solid oral dosage forms: piroxicam. *J Pharm Sci*, 103(2): 367-377.
- Siivola KK, Burgum MJ, Suárez-Merino B, Clift MJ, Doak SH, Catalán J. 2022. A systematic quality evaluation and review of nanomaterial genotoxicity studies: a regulatory perspective. *Part Fibre Toxicol*, 19(1): 1-24.
- Takebayashi K, Echizenya K, Kameya Y, et al. 2023. Mitotic index maximization with no effect on radiation-induced dicentric chromosome frequency. *Int J Radiat Biol*, 99(5):750-759.
- Timoroglu İ, Yuzbasioglu D, Unal F, Yilmaz S, Aksoy H, Celik M. 2014. Assessment of the genotoxic effects of organophosphorus insecticides phorate and trichlorfon in human lymphocytes. *Environ toxicol*, 29(5): 577-587.
- Ustuner D. 2011. Kromozom kırıkları ve mikronükleus-apoptoz bağlantısı. *TÜBAV Bilim Dergisi*, 4(1): 64-69.
- Van't Hof J. 1968. The action of iaa and kinetin on the mitotic cycle of proliferative and stationary phase excised root meristems. *Exp Cell Res*, 51(1): 167-176.
- Yilmaz I, Tutar N, Yenigun S, Ozer Simsek Z, Gulmez I. 2017. Tenoxicam-induced fixed drug eruption confirmed by skin patch test. *Asthma Allergy Immunol*, 15(3): 162-164.
- Yuzbasioglu D, Celik M, Yilmaz S, Unal F, Aksoy H. 2006. Clastogenicity of the fungicide afugan in cultured human lymphocytes. *Mutat Res*, 604: 53-59.
- Yuzbasioglu D, Avuloglu-Yilmaz E. Mikronükleus testi. In: Unal F, Yuzbasioglu D, editors. *Genetik Toksikoloji*, Ankara, Palme; 2022: 219-249.



SCATTERING FROM PARABOLIC CYLINDRICAL REFLECTOR ANTENNA USING PHYSICAL OPTICS

Fadıl KUYUCUOĞLU^{1*}


¹Manisa Celal Bayar University, Faculty of Engineering, Department of Electrical-Electronics Engineering, 45140, Manisa, Türkiye

Abstract: In this study, numerical analysis of scattering from a dielectric-coated metallic reflector is presented. The reflector has a parabolic cross-sectional cylindrical geometry. Radiation patterns and aperture efficiency parameters are analyzed using physical optics. A complex source point located at the focal point of the parabolic reflector is used as the source of radiation. The dielectric-coated metallic reflector is considered as an antenna, and an impedance boundary is utilized. The effects of coating on radiation patterns are analyzed in terms of dielectric thickness and dielectric permittivity. Numerical results are presented for various parameters, including dielectric permittivity, dielectric layer thickness, complex source point width, and focal distance.

Keywords: Scattering, Physical optics, Impenetrable sheet, Cylindrical parabolic reflector

*Corresponding author: Manisa Celal Bayar University, Faculty of Engineering, Department of Electrical-Electronics Engineering, 45140, Manisa, Türkiye

E mail: fadil.kuyucuoglu@cbu.edu.tr (F. KUYUCUOĞLU)

Fadıl KUYUCUOĞLU  <https://orcid.org/0000-0002-0134-0491>

Received: August 07, 2023

Accepted: September 29, 2023

Published: October 15, 2023

Cite as: Kuyucuoglu F. 2023. Scattering from parabolic cylindrical reflector antenna using physical optics. BSJ Eng Sci, 6(4): 550-556.

1. Introduction

In antenna design, reflector antennas have been widely used in applications such as satellite communications, radio astronomy, remote sensing, and radar (Rahmat-Samii and Haupt, 2015; Lu and Qu, 2023). Among reflector antennas, the parabolic reflector is the most preferred type due to its improved overall radiation characteristics (Balanis, 2016). Parabolic reflectors exhibit lower sidelobes and higher beam efficiencies compared to other reflectors (Wu et al., 2016).

However, in parabolic reflector antennas with fixed geometry, the performance depends on the feeder located along the focus axis of the reflector. Adjusting the focal length is crucial for achieving higher gain. Unfortunately, locating the feeder causes aperture-blocking effects, negatively affecting the radiation patterns and gain of the antenna (Qudrat and Shafai, 2012). To increase the gain of the antenna, a common and simple approach is to add a perfect electric conductor (PEC) on the reflector surface (Ge et al., 2018; Chang et al., 2021; Wu et al., 2021). Additionally, a high focal-to-diameter (f/D) ratio enables a high aperture efficiency for the reflector antenna (Galuscak et al., 2018; Granet et al., 2005; Wang et al., 2020).

It is worth mentioning that the characteristics of reflector surfaces also significantly impact the radiation properties of antennas. Impedance surfaces find considerable applications in the modeling of reflector antennas in optics and electromagnetics studies (Bhattacharyya, 1995). Many studies have presented the scattering from impedance surfaces (Kuyucuoglu et al., 2014; Maliuzhinets, 1959; Tiberio et al., 1985; Volakis, 1986;

Umul, 2006; Umul, 2007; Bie et al., 2023).

In this study, scattering from a dielectric-coated perfectly electric conductor (PEC) cylindrical parabolic reflector antenna is analyzed. The complex source point is used as the feed and is located at the focus of the reflector. Impedance boundary conditions are utilized, and the physical optics (PO) method is used to obtain the radiation pattern, as explained in (Umul, 2008). The impedance of the surface is evaluated using the expressions given in (Bleszynski et al., 1993) as impenetrable thin layer systems.

By using the PO method, the surface integrals are evaluated asymptotically. The performance of the reflector is analyzed for several dielectric thickness and focal length parameters. Throughout the paper, a time factor $\exp(-j\omega t)$ is used and omitted.

2. Materials and Methods

The cylindrical parabolic reflector antenna shown in Figure 1 is fed by a complex source point (CSP), with the feed located precisely at the focus (f) of the parabolic reflector. The aperture of the reflector is represented by the symbol D . The antenna is constructed using infinitely thin PEC (Perfect Electric Conductor) material, and this PEC material is coated with a dielectric material. The antenna lies on the x - y plane and extends infinitely in the z -axis direction. The cross-sectional shape of the reflector is parabolic, and the feed is precisely placed at the focus of this parabolic geometry.



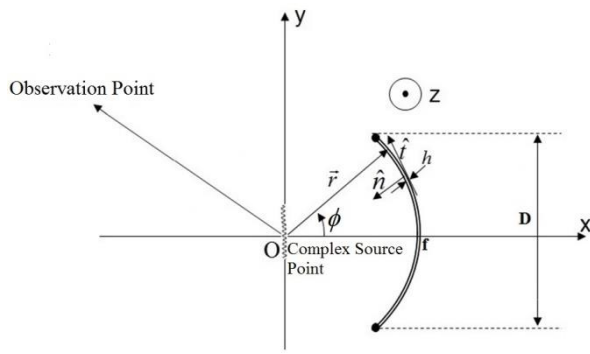


Figure 1. Problem geometry

In the case of E-polarization, electric and magnetic field components are taken as E_z , H_x and H_y respectively. If we choose E_z as the basic component and denote it, complex source point can be expressed as (equation 1):

$$U^{in}(\vec{r}) = H_0^{(1)}(k_0|\vec{r} - (\vec{r}_0 + i\vec{b})|) \quad (1)$$

where $H_0^{(1)}$ is the Hankel function of the first kind, \vec{r} is the position vector, \vec{r}_0 is the real source position vector of the CSP, b is the aperture width of the CSP and k_0 is the wavenumber in free space.

In order to model the surface of the reflector, impenetrable boundary condition is utilized. We can write the impedance of the sheet face in (equation 2) as described in (Bleszynski et al., 1993) for nonmagnetic materials.

$$Z = -i \frac{Z_0}{\sqrt{\epsilon_r}} \tan(\sqrt{\epsilon_r} k_0 d) \quad (2)$$

In equation (2), the variable d is defined as the thickness of the dielectric coating, and ϵ_r is the relative dielectric constant of the material.

After defining the feed and antenna impedance, the next step is to write the sum of the scattered field and the incident field using the physical optics as in Equation (3). The integral for the electrical line source and impedance surface in this equation is described in detail in (Umul, 2008). However, for the current study, this theory is being modified to account for a complex source point feed and several coatings on the PEC reflector.

The physical optics method takes into consideration the effects of the complex source point feed and the multiple dielectric coatings on the reflector's surface. These modifications allow for a more accurate representation of the radiation pattern and characteristics of the reflector antenna. The scattering and radiation behavior are now computed considering the presence of the complex source point and the interactions with the impedance surface of the dielectric-coated reflector.

By incorporating these modifications into the theoretical framework, the study aims to obtain a comprehensive understanding of the antenna's performance when fed by a complex source point and coated with various dielectric materials. The detailed analysis presented in (Umul, 2008) for the electrical line source and impedance

surface is extended and adapted to suit the current scenario with a complex source point and multiple coatings on the PEC reflector.

$$E_{tot} = \frac{e^{jk_0 r}}{\sqrt{kr}} \left(e^{jb \cos(\phi)} + \frac{ke^{j\pi/4}}{\sqrt{2\pi}} \int_{-b}^b \frac{\sin(\alpha) - (Z_0/Z)}{\sin(\alpha) + (Z_0/Z)} \sin(\alpha) \left[\frac{e^{jkr'(\phi)} e^{-jk_0 b \cos(\phi)} e^{-jkr'(\phi) \cos(\phi - \phi')}}{\sqrt{k}} \right] \frac{\sqrt{f}}{\cos^2(\phi'/2)} d\phi' \right) \quad (3)$$

In equation (3), total field expression is given where

$\alpha = \left(\frac{\pi}{2}\right) - \left(\frac{\phi'}{2}\right)$, $r'(\phi') = f/\cos^2(\frac{\phi'}{2})$, f is the focal length of reflector, Z_0 is the free space impedance, ϕ_0 is the angle of the aperture of the reflector. CSP is located at the focus where we can write $\vec{r}_0 = 0$.

After obtaining total fields, forward directivity (D_0) is calculated taking the integral of total field given in Equation (3). Besides, aperture efficiency can be calculated as in Equation (4) easily.

$$\epsilon_{eff} = \frac{D_0}{2\pi D} \quad (4)$$

In the following section, antenna performance is presented with several coating thicknesses, CSP width, focal distances.

3. Results and Discussion

In the analysis, an impenetrable, impedance surface, parabolic reflector antenna is studied under E-polarized CSP (Complex Source Point) illumination. All metric parameters are given in terms of free space wavelength (λ_0).

Initially, the total radiated field is calculated for a PEC reflector with dielectric coatings with various thicknesses. The variation of the total field is presented in dB scale in Figure 2. For this calculation, the width of the CSP (kb) is chosen as 3 and the aperture width of the antenna (D) is selected as 10. The focus of the parabolic reflector is set at 5.

Several coatings are considered for the reflector antenna. Specifically, tantalum oxide with $\epsilon_r=20$ and silicon with $\epsilon_r=11.7$ are investigated. This study examines the impact of different dielectric thicknesses (d) on the levels of backside radiation.

As shown in Figure 2, for the tantalum oxide coating ($\epsilon_r=20$) with $\lambda_0/200$ thickness case, minimum backside radiation occurs. However, as the magnitude of the impedance of the dielectric coating increases, higher levels of backside radiation are observed between 120° and 180° . Front side radiation levels are nearly the same for all the cases under investigation. In order to prove the correctness of the backside radiation of PO, method of analytical regularization (MAR) results are used for comparison purposes. It can be seen that, front side radiations are nearly same for PO and MAR as expected but small deviations are observed at the backside region.

The results of the analysis highlight the importance of the dielectric coating and its thickness in shaping the radiation pattern of the reflector antenna. Different

dielectric materials with distinct permittivity values yield varying levels of backside radiation, while the front side radiation remains relatively consistent. These findings

contribute to a deeper understanding of the antenna's performance and may guide the selection of suitable dielectric coatings for desired radiation characteristics.

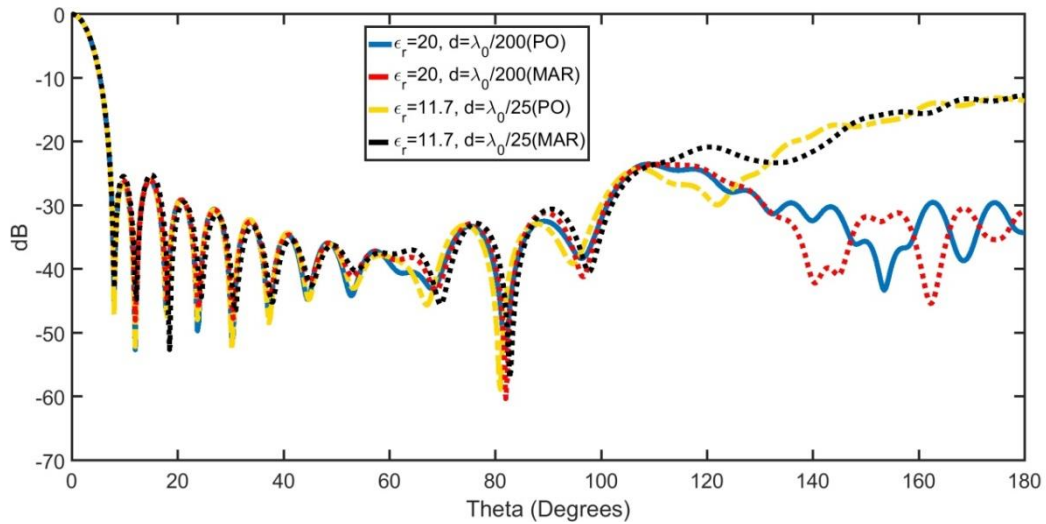


Figure 2. Total radiated fields (normalized) of the reflector in dB versus observation angle in degrees (f=5, D=10, kb=3)

If we wish to observe the effect of the dielectric coating for various parameters, we can refer to Figure 3. In this figure, the total radiated fields are plotted for several cases with different dielectric and coating thickness values.

The problem parameters are chosen as follows: the focal length (f) is 5 or 7, the aperture width (D) is 10, the width of the complex source point (kb) is 5 or 7, and the dielectric thickness (d) is $\lambda_0/50$ or $\lambda_0/25$.

As depicted in Figure 3, the back radiation levels of the coated cases (PEC coated with silicon and PEC coated with tantalum oxide) are different from each other. This difference is because the impedances of the surface with these coatings, kb values and focal lengths are different. As expected, choosing thin and higher permittivity coating reduces radiation at the backside of the reflector

antenna. MAR results are also plotted to prove the correctness of PO results. Small deviations occurred at the backside as expected. Front side sidelobes are nearly same for PO and MAR.

These results provide valuable insights into the impact of dielectric coatings on the antenna's radiation pattern, particularly with regard to tune backside radiation. The difference of the impedance values for the two coatings may indicate that, under the specified parameters, the choice of either silicon or tantalum oxide as the dielectric material will yield different back radiation reduction effects. Further analysis and parameter exploration may help in understanding the nuances and optimizing the performance of the reflector antenna for specific applications.

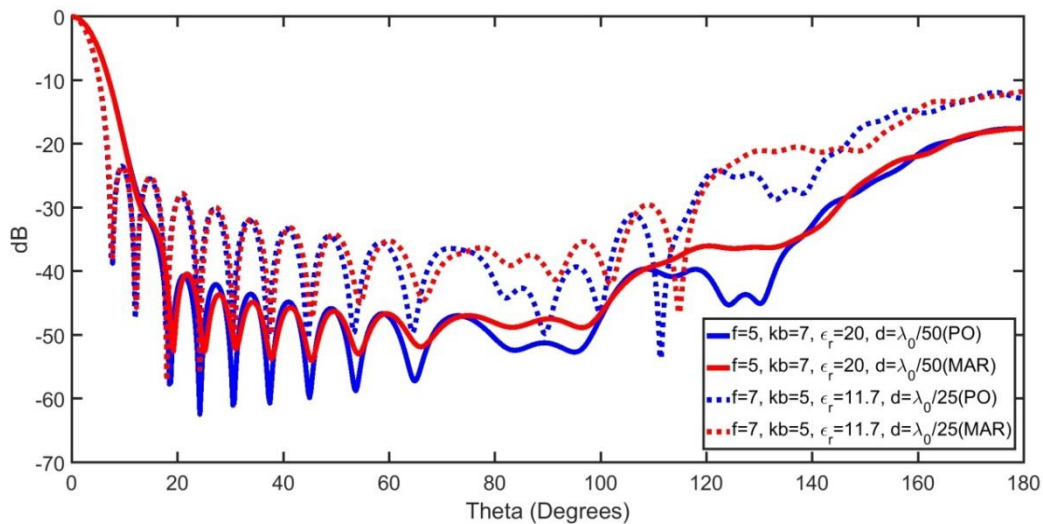


Figure 3. Total radiated fields (normalized) of the reflector in dB versus observation angle in degrees

After obtaining the directivity of the antenna using the radiation pattern distribution, the aperture efficiency is

calculated as described in equation (4). In this context, the antenna is coated with tantalum oxide, with a relative

permittivity of $\epsilon_r=20$. The antenna aperture width is $D=10$, and the thickness of the coating is chosen as $1/100$ of the wavelength ($d=\lambda_0/100$).

The analysis explores how changing the focus of the reflector affects the aperture efficiency, and the results are presented in Figure 4. Three different values of focal length (f) are considered: $f=3$, $f=5$, and $f=7$.

When $f=3$, the aperture efficiency slowly increases and reaches its maximum value around $kb=1$, then it starts to decline as kb increases. On the other hand, when $f=5$, the antenna exhibits low aperture efficiencies at low kb values, but the maximum aperture efficiency is higher

than that of $f=3$, occurring around $kb=2$. The highest aperture efficiency is obtained when $f=7$, and it gradually increases up to $kb=5$.

These results indicate that the focal length of the reflector significantly impacts the aperture efficiency of the antenna. Different focal lengths lead to distinct patterns of aperture efficiency variation with respect to kb . The focal length of $f=7$ yields the highest overall aperture efficiency, while different focal lengths may exhibit varying trends in aperture efficiency behavior as a function of kb .

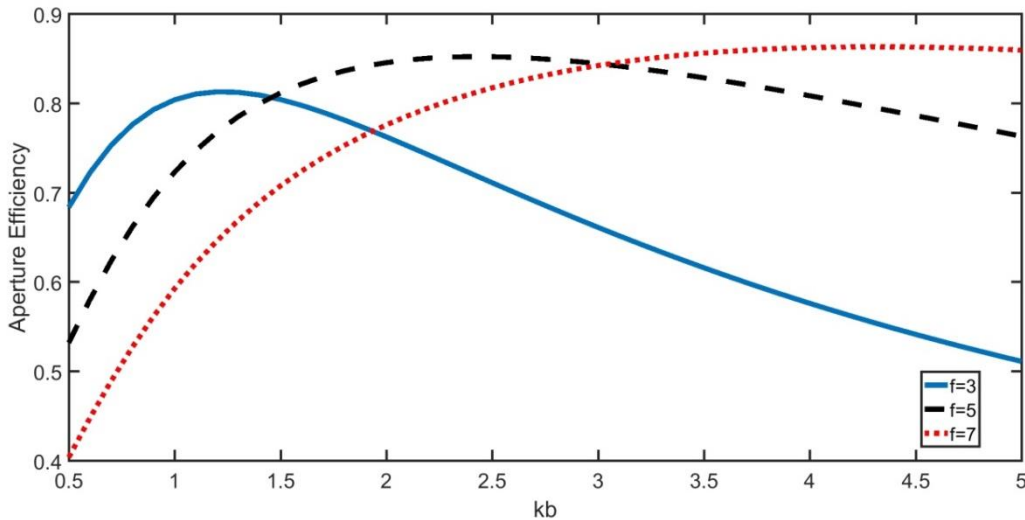


Figure 4. Aperture efficiency versus CSP width (kb) ($D=10$, $\epsilon_r=20$, $h=\lambda_0/100$)

We present the variation of aperture efficiency versus focal distance for several CSP widths (kb) in Figure 5. Problem parameters are $D=10$, $d=\lambda_0/100$ and $\epsilon_r=20$. Based on the results, we can observe that for all kb cases, the aperture efficiencies are low when the focal distance is $f=1$. As the focal distance increases, the aperture efficiency gradually improves, reaching its maximum value at certain focal distances, and then it starts to decrease.

This trend indicates that the focal distance plays a critical role in determining the antenna's aperture efficiency. For focal distances less than the optimum value, the antenna performance suffers, resulting in lower aperture efficiencies. However, as the focal distance increases beyond the optimum, the antenna's performance also degrades, leading to decreased aperture efficiency.

It is essential to identify the optimal focal distance for a specific CSP width (kb) to achieve the highest aperture efficiency for the reflector antenna. Understanding these trends enables antenna designers to make informed

decisions in selecting the appropriate focal distance, ensuring optimal performance for their intended applications.

To examine the influence of relative permittivity on directivity and aperture efficiency, Figures 6(a) and 6(b) are instructive. In Figure 6(a) and (b), variations in directivity and aperture efficiency are presented for different thicknesses concerning the relative dielectric constant of the coating material.

It's evident from these figures that higher thickness values result in lower directivity and aperture efficiencies. Conversely, reducing the coating thickness leads to higher directivities and enhanced aperture efficiencies. Furthermore, it can be noted that as the relative dielectric constant of the material increases, there is a significant decrease in directivity and aperture efficiency, particularly when the thickness is high. However, the effect of dielectric constant on directivity is relatively small when the thickness is low.

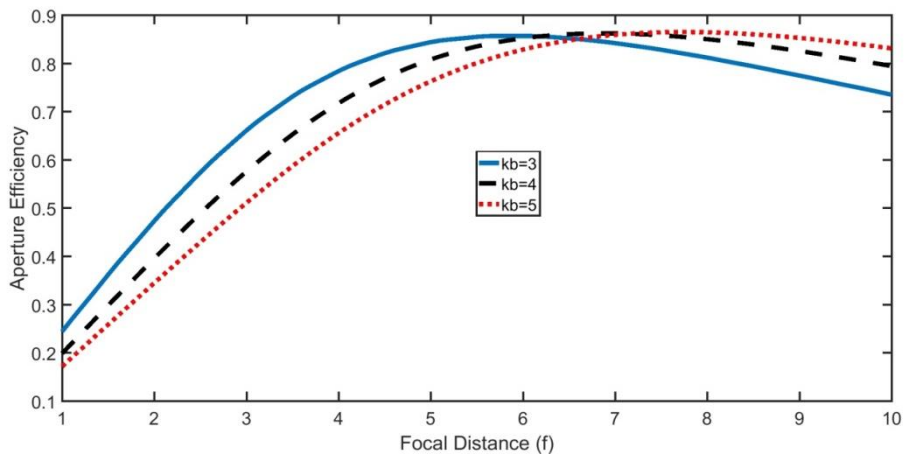


Figure 5. Aperture efficiency versus focal distance (f) ($D=10$, $\epsilon_r=20$, $h=\lambda_0/100$)

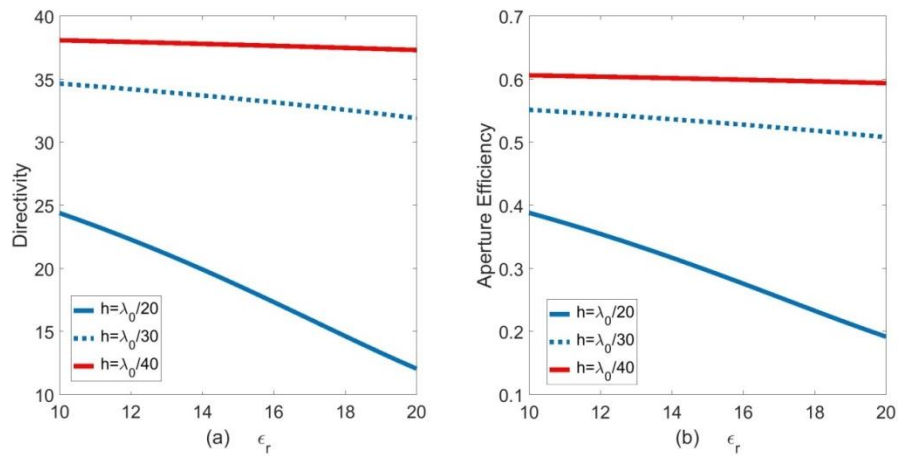


Figure 6. Directivity and aperture efficiency versus relative dielectric constant ($D=10$, $f=3$, $kb=3$)

In the final analysis, the impact of coating thickness is assessed for various dielectric constants, focal distances, and CSP width values, as illustrated in Figures 7(a) and (b). It is evident from these figures that the dielectric constant's effect on the coating becomes more dominant when the thickness is high. Reducing the thickness results in nearly identical directivity and aperture efficiency values for two different dielectric coatings. The highest directivities and aperture efficiencies are achieved when the focal distance (f) is set to 5 and the

CSP width (kb) is 3, using a specific thickness. Decreasing the focal distance (f) while keeping kb constant leads to the expected results of reduced directivity and aperture efficiencies.

In summary, these observations highlight the interplay between coating thickness, dielectric constant, focal distance, and CSP width in determining the performance of the system, with certain configurations yielding higher directivity and aperture efficiency values.

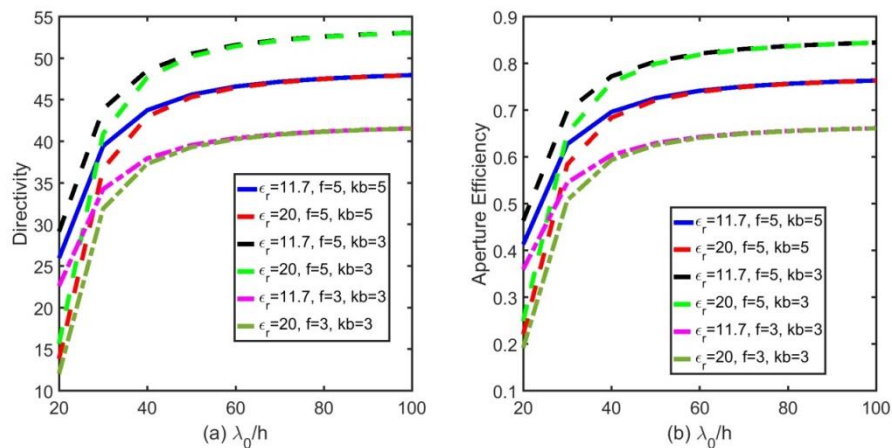


Figure 7. Directivity and aperture efficiency versus thickness of coating

4. Conclusion

The numerical investigation of a parabolic, cylindrical, dielectric-coated PEC reflector antenna's radiation performance yielded promising results. The study utilized the physical optics method to calculate radiated fields, total fields, and antenna efficiency parameters. The results demonstrated high aperture efficiency and tunable backside radiation levels achievable by changing the coating material on the reflector.

One notable advantage of the study was the use of the PO method, which allowed for obtaining fast and accurate results in a significantly reduced computing time. This efficiency in computation is crucial in antenna design and analysis, as it enables researchers and engineers to explore various scenarios and optimize antenna performance effectively.

The findings from this investigation can be leveraged in future studies to analyze the effects of different coatings on antenna performance. The ability to control backside radiation levels by varying the dielectric coating opens up possibilities for tailoring the antenna characteristics to suit specific applications.

In conclusion, the research presented in this study provides valuable insights into the radiation behavior of dielectric-coated PEC reflector antennas. The use of the physical optics method contributes to faster and accurate simulations, making it a powerful tool for future antenna design and analysis studies involving coatings and other parameters.

Author Contributions

The percentage of the author contributions is presented below. The author reviewed and approved the final version of the manuscript.

| | F.K. |
|-----|------|
| C | 100 |
| D | 100 |
| S | 100 |
| DCP | 100 |
| DAI | 100 |
| L | 100 |
| W | 100 |
| CR | 100 |
| SR | 100 |
| PM | 100 |
| FA | 100 |

C=Concept, D= design, S= supervision, DCP= data collection and/or processing, DAI= data analysis and/or interpretation, L= literature search, W= writing, CR= critical review, SR= submission and revision, PM= project management, FA= funding acquisition.

Conflict of Interest

The author declared that there is no conflict of interest.

Ethical Consideration

Ethics committee approval was not required for this study because of there was no study on animals or humans. The authors confirm that the ethical policies of the journal, as noted on the journal's author guidelines page, have been adhered to.

References

Balanis CA. 2016. Antenna theory: analysis and design. John Wiley Sons, New Jersey, USA, 4th ed., pp: 875–920.

Bhattacharyya AK. 1995. High-frequency electromagnetic techniques: recent advances and applications. Wiley-Interscience, New York USA, pp: 487.

Bie M, Peng M, Jiang ZH, Werner DH. 2023. Modal expansion analysis inverse-design and experimental verification of a broadband high-aperture efficiency circular short backfire antenna loaded with anisotropic impedance surfaces. *IEEE Transactions Anten Propag*, 71(6): 4783-4798.

Bleszynski EH, Bleszynski MK, Jaroszewicz T. 1993. Surface-integral equations for electromagnetic scattering from impenetrable and penetrable sheets. *IEEE Antennas Propag Mag*, 35(6): 14-25.

Chang L, Chen L-L, Zhang J-Q, Chen Z-Z. 2021. A compact wideband dipole antenna with wide beamwidth. *IEEE Antennas Wirel Propag Lett*, 20(9):1701-1705.

Galuscak R, Mazanek M, Hazdra P, Kabourek V. 2018. A dual-band reflector feed in coaxial configuration for satellite communication. *IEEE Antennas Propag Mag*, 60: 89–94.

Ge L, Gao S, Zhang D, Li M. 2018. Magnetolectric dipole antenna with low profile. *IEEE Antennas Wirel Propag Lett*, 17(10): 1760-1763.

Granet C, Zhang HZ, Forsyth AR, Graves GR, Doherty P, Greene KJ, James GL, Sykes P, Bird TS, Sinclair MW, Moorey G, Manchester RN. 2005. The designing manufacturing and testing of a dual-band feed system for the Parkes radio telescopes. *IEEE Antennas Propag Mag*, 47: 13–19.

Kuyucuoglu F, Oğuzer T, Avgin I, Altintas A. 2014. Analysis of an arbitrary-profile cylindrical impedance reflector surface illuminated by an E-polarized complex line source beam. *J Electromag Waves Applicati*, 28(3): 360-377.

Lu S, Qu SW. 2023. Low-profile dual-band reflector antenna for high-frequency applications. *Sensors*, 23(13): 5781.

Maliuzhinets G. D. 1959. Excitation reflection and emission of surface waves from a wedge with given face impedance. *Sov Phys Dokl*, 3: 752–755.

Qudrat-E-Maula M, Shafai L. 2012. Low-cost microstrip-fed printed dipole for prime focus reflector feed. *IEEE Trans Antennas Propag*, 60(11): 5428-5433.

Rahmat-Samii Y, Haupt R. 2015. Reflector antenna developments: A perspective on the past present and future. *IEEE Antennas Propag Mag*, 57 (2): 85–95.

Tiberio R, Pelosi G, Manara G. 1985. A uniform GTD formulation for the diffraction by a wedge with impedance faces. *IEEE Trans Antennas Propag*, 33: 867–873.

Umul YZ. 2006. Modified theory of the physical-optics approach to the impedance wedge problem. *Opt Lett*, 31: 401–403.

Umul YZ. 2007. Edge-dislocation waves in the diffraction process by an impedance half-plane. *J Opt Soc Am A*, 24: 507–511.

Umul YZ. 2008. Scattering of a line source by a cylindrical parabolic impedance surface. *JOSA A* 25(7): 1652-1659.

Volakis JL. 1986. A uniform geometrical theory of diffraction for an imperfectly conducting half-plane *IEEE Trans. Antennas Propag*, 34: 172–180.



- Wang C, Wu J, Ma B-Y, Guo Y-X. 2020. A 3D-printed K/Ka-band dual circularly polarized feed for offset-fed reflector antennas. In: Proceedings of the IEEE Asia-Pacific Microwave Conference, December 8–11, Hong Kong, China, pp. 558–560.
- Wu L, Peng S, Xu J, Xiao Z. 2016. A W-band radiometer with the offset parabolic antenna for radiometric measurements. Int J Antennas Propag, 2016: 1–9.
- Wu R, Xue Q, Chu QX, Chen FC. 2021. Ultrawideband dual-polarized antenna for LTE600/LTE700/GSM850/GSM900 application. IEEE Antennas Wirel Propag Lett, 20(7): 1135–1139.



COMPREHENSIVE ANALYSIS AND EVALUATION OF DC-DC CONVERTERS: ADVANCEMENTS, APPLICATIONS, AND CHALLENGES

Fuad ALHAJ OMAR^{1*}


¹Zonguldak Bulent Ecevit University, Department of Electric and Energy, 67100, Zonguldak, Türkiye

Abstract: Power electronics stand as the cornerstone of our electrified world, and versatile DC-DC converters are a key component of this technology. In this comprehensive analysis, we investigate deeply the realm of DC-DC converters, examining their pivotal role in modern power systems. From the evolution of converter topologies to their wide-ranging applications, we explore the advancements that propel this field forward. Whether maintaining continuous power in portable devices or facilitating renewable energy integration, DC-DC converters are the fundamental components. Yet, they face formidable challenges, from complex control strategies to voltage stress management. This study reveals the complex configuration of DC-DC converters, detailing a narrative of adaptability, resilience, and innovation in response to the increasing energy demands of our time.

Keywords: DC-DC converters, Power electronics, DC-DC converter topologies, DC-DC converter advantages, DC-DC converter applications and converter challenges

*Corresponding author: Zonguldak Bulent Ecevit University, Department of Electric and Energy, 67100, Zonguldak, Türkiye

E mail: fuad.a@beun.edu.tr (F. ALHAJ OMAR)

Fuad ALHAJ OMAR  <https://orcid.org/0000-0001-5969-2513>

Received: September 09, 2023

Accepted: September 29, 2023

Published: October 15, 2023

Cite as: Alhaj Omar F. 2023. Comprehensive analysis and evaluation of DC-DC converters: advancements, applications, and challenges. BSJ Eng Sci, 6(4): 557-571.

1. Introduction

In the ever-expanding landscape of modern electronics, the efficient conversion and management of electrical energy have evolved from being merely a necessity to becoming a driving force. At the heart of this electrifying transformation lies DC-DC converters, unassuming yet indispensable devices that modify and regulate power in our digital age. These converters serve as power bridges, seamlessly shifting voltages, managing power flows, and ensuring a reliable supply to the many electronic devices in our world (Raghavendra et al., 2019). They have firmly established themselves as the preferred choice for medium and high-power applications in power electronic conversion and have reached maturity as a proven technology (Hossain and Rahim 2018). DC-DC converters are now integrated into both standard and customized products, serving a wide range of applications. These applications include photovoltaic (PV) power systems, offshore wind turbines (Forouzesh et al., 2017), electric/hybrid/fuel cell vehicles (İnci et al., 2021), medium-voltage DC (MVDC) and high-voltage DC (HVDC) power systems (Alhurayyis, Elkhateb and Morrow 2020, Li et al., 2018), telecommunication power supplies, shipboard power systems, and offshore oil and gas applications, including subsea compressors (Revathi and Prabhakar 2016), among others. Although they are well-established technology, they still present several challenges, yet offer a variety of possibilities, which

continue to fuel ongoing research efforts worldwide. These efforts aim to enhance conversion efficiency, power density, reliability, control techniques, simplicity, and cost while exploring new application domains (Saeedifard et al., 2010).

The realm of DC-DC converters has been characterized by a continuous wave of innovation and development. Advancements in topology, control strategies, and efficiency optimization have propelled these devices into the forefront of modern electronics. Among the notable innovations, the versatile workhorse Buck-Boost converter subtly steps up or down voltages, precisely accommodating input power changes (Khaligh and Onar 2017). It has evolved into a fundamental component in portable electronics, adapting to fluctuating battery voltages and facilitating device operation even as the battery discharges. Meanwhile, the Cuk converter, with its unique ability to maintain a continuous output voltage amidst turbulent input fluctuations, has emerged as a linchpin in the renewable energy era, harnessing energy from solar panels with unparalleled efficiency (Erickson and Maksimovic 2007). Its versatility in both step-up and step-down voltage conversion makes it invaluable in scenarios where a stable power supply is essential, such as in photovoltaic systems and LED lighting applications. The Full-Bridge Converter, which serves bi-directional power flow, demonstrates its effectiveness in high-power applications, proving its ability for robust power



conversion (Lipo 2017). Its capability to efficiently handle large currents and voltages positions it as a key component in industries such as electric vehicles, renewable energy systems, and high-power industrial equipment. The advancements in these converter topologies reflect the dynamic nature of the field, as engineers are constantly developing tools to manage power effectively. These developments are not limited to the theoretical realm; rather, it is reflected across diverse industries and applications. In the field of portable electronics, the Buck-Boost converter is emerging as an effective voltage continuity tool, ensuring uninterrupted operation as batteries are running low. Its adaptability to varying input voltages and maintaining a constant output voltage is crucial in extending the operational life of battery-powered devices. In the field of renewable energy conversion, Cuk inverters are proving highly effective, extracting energy from solar panels and leading the global transition towards sustainable energy (Erickson and Maksimovic 2007). Their ability to efficiently regulate voltage and manage power harvested from solar panels makes them pivotal in photovoltaic systems and solar inverters. Cuk converters also play a vital role in LED lighting applications, maintaining consistent brightness despite variations in input voltage and load. On the other hand, Flyback converters diligently power low-wattage electronics, such as power adapters and battery chargers, while Push-Pull converters manage the amplification of audio signals in class D audio amplifiers and drive the precision of electric motors in industrial automation and robotics (Ivanovic and Knezic 2022, Krishnan 2017). The Half-Bridge converter, with its simplicity, finds a niche in motor drives and uninterruptible power supplies (Skvarenina 2018). Moreover, the rise of LLC resonant converters, with their zero voltage switching (ZVS) and zero current switching (ZCS) capabilities, is reshaping high-frequency and high-power systems, underpinning the infrastructure of data centers and revolutionizing renewable energy applications (Wei, Luo and Mantooh 2020). The adaptability of these converters to a wide range of applications underscores their significance in the modern technological world.

However, these advancements are not devoid of challenges. The quest for precise voltage regulation while simultaneously mitigating voltage stress across the switches continues to be a complex engineering issue that demands workable solutions (Lipo 2017). In converters like the Forward Converter, where transformer design is pivotal, achieving optimization in efficiency requires an understanding of core materials, winding ratios, and parasitic elements (Krishnan 2017). The challenges of optimizing voltage transformation while maintaining efficiency are particularly prominent in the context of Full-Bridge converters, where intricate control strategies are essential for harnessing their bidirectional power flow capabilities (Bakas et al., 2016). Additionally, the balance between simplicity and

functionality, which is a feature of the Half-Bridge converter, presents its own set of challenges, particularly when extending its use to moderate power applications (Skvarenina 2018). Challenges such as control strategies, electromagnetic interference, and heat dissipation loom large in the realm of Push-Pull converters (Ivanovic and Knezic 2022). Achieving efficient zero voltage switching and zero current switching in LLC resonant converters, while promising for high-frequency and high-power systems, demands intricate control mechanisms and transformative approaches to transformer design (Mohan, Undeland and Robbins 2003). These challenges, although formidable, serve as catalysts for innovation in the domain of DC-DC converters, pushing engineers to craft increasingly efficient, reliable, and versatile solutions to meet the ever-evolving demands of modern electronics.

As we initiate this comprehensive analysis of the DC-DC converters, we will reveal the delicate interplay between innovation and practicality. Through this extensive analysis, we will carefully examine the intricacies of these converters, exploring their fundamental principles, practical applications, and the challenges that persistently drive innovation in this field. We will gain a deep understanding of how these converters have shaped our electrified world in order to influence continued development and innovation.

2. Materials and Methods

The field of DC-DC converters encompasses a wide range of topologies (as shown in Figure 1), and each is designed to meet specific requirements in power conversion, voltage regulation, and power management. These diverse topologies serve different application domains, ranging from renewable energy systems to electric vehicles and communications. This section provides an in-depth analysis of prominent DC-DC converter topologies with their distinct characteristics and applications.

2.1. Buck Converter (Step-Down Converter)

The Buck converter, also referred to as the Step-Down converter, is a fundamental DC-DC converter topology widely utilized for reducing the input voltage to a lower, regulated output voltage (Pressman 2009). Its simplicity, efficiency, and reliable operation make it a cornerstone in power electronics, finding applications in a variety of fields such as power supplies, voltage regulators, and battery-powered devices (Luo and Ye 2016, Rashid 2010).

2.1.1. Operating principle

The Buck converter operates based on the principle of energy storage and transfer through an inductor and a switching element (usually a transistor), accompanied by a diode for rectification (Basso 2008). The process involves alternating between two states: the ON state (switch closed) and the OFF state (switch open).

During the ON state, the switch connects the input voltage source to the inductor. This allows current to

flow through the inductor, building up energy in its magnetic field. The output voltage is determined by the duty cycle of the switching signal, which controls the amount of time the switch remains closed.

When the switch transitions to the OFF state, the inductor's stored energy continues to flow, but now through a diode connected to the output. This diode prevents the inductor's current from reversing and directs it towards the output capacitor, maintaining a continuous output current (Kazimierczuk 2015).

2.1.2. Advantages

The Buck converter offers several advantages, contributing to its widespread use:

- 1) **Efficiency:** Buck converters are known for their high efficiency, especially when the input-output voltage difference is moderate. Since there is no isolation transformer and minimal energy storage components, power losses are relatively low.
- 2) **Simplicity:** The Buck converter has a straightforward topology with fewer components, making it cost-effective and reliable.
- 3) **Fast Transient Response:** The inherent energy storage in the inductor allows for a rapid response to load changes, providing good transient performance.
- 4) **Compact Size:** The reduced number of components and absence of an isolation transformer contribute to a compact design, making it suitable for space-constrained applications.

2.1.3. Applications

The Buck converter demonstrates its versatility across a spectrum of scenarios necessitating voltage reduction while upholding elevated efficiency standards. Its applications encompass:

- 1) **Voltage Regulation:** Serving as a steadfast source of a stable output voltage, the Buck converter caters to the needs of microcontrollers, digital circuits, and sensors.
- 2) **Battery Charging:** Exhibiting proficiency in battery charging operations, the Buck converter efficiently recharges batteries within devices like mobile phones, laptops, and portable electronics.
- 3) **Voltage Regulator Modules (VRMs):** In the realm of computer motherboards, the Buck converter plays a crucial role by regulating the voltage supply to processors, underscoring its significance in enhancing operational stability.
- 4) **Power Supplies:** The Buck converter assumes a pivotal role in delivering regulated voltage levels to a wide range of electronic devices, thereby facilitating smooth functionality.

2.1.4. Challenges and Considerations

Despite the manifold benefits conferred by the Buck converter, several considerations warrant attention:

- 1) **Limited Voltage Conversion:** One of the intrinsic limitations of the Buck converter pertains to its ability to solely reduce voltage; it lacks the capacity to elevate the output voltage beyond the input level.
- 2) **Inductor Selection:** The right selection of the

inductor emerges as a pivotal factor in achieving desired performance benchmarks and operational efficiency.

- 3) **Switching Losses:** The efficiency of the Buck converter can be impacted by switching losses in the switching element (transistor).

- 4) **Output Ripple:** The energy transfer process can result in output voltage ripple, which may require filtering for noise-sensitive applications.

2.2. Boost Converter (Step-Up Converter)

The Boost converter, commonly denoted as the Step-Up converter, occupies a pivotal position among DC-DC converter topologies, stepping up the input voltage to a regulated and higher output voltage. With applications including battery charging, power supplies, and renewable energy systems, this converter topology plays an important role wherever demand for high voltage levels prevails (Nouri, Nouri and Vosoughi 2019, Wu, Ruan and Ye 2014).

2.2.1. Operating principle

The operation of the Boost converter is rooted in the concept of inductor energy storage and transfer, facilitated by a switching element (typically a transistor) and a diode (Rashid 2017). Analogous to other DC-DC converters, the Boost converter cycles between two operational modes: the ON state (switch closed) and the OFF state (switch open). In the ON state, the switch links the input voltage source to the inductor, enabling the flow of current through the inductor and leading to energy accumulation within its magnetic field. The magnitude of the output voltage is dictated by the duty cycle of the switching signal, which governs the duration the switch remains closed. During the OFF state transition, the stored energy within the inductor is discharged. The diode prevents the inductor's current from reversing, channeling it towards the output capacitor and load. Consequently, this mechanism elevates the output voltage beyond the input voltage level (Tseng and Huang 2013).

2.2.2. Advantages

The Boost converter is characterized by a set of advantages that increase its significance:

- 1) **Voltage Boosting:** The Boost converter steps up the input voltage to a higher, regulated output voltage, making it ideal for applications requiring voltage multiplication.
- 2) **Simple Structure:** The Boost topology features an arrangement with minimal components, which is attributed to its cost-effectiveness and high reliability.
- 3) **Diverse Applicability:** Boost converters exhibit their utility across diverse sectors, encompassing industries such as renewable energy systems, battery-powered devices, and electric vehicles.
- 4) **Stable Output Regulation:** The Boost converter supplies a regulated output voltage despite fluctuations in input voltage.

2.2.3. Applications:

The Boost converter is essential in applications that

require increased output voltages while maintaining operational efficiency. Applications include a range of domains:

- 1) **Battery Charging:** Boost converters facilitate the elevation of voltage from low-voltage batteries to levels conducive to effective charging.
- 2) **Photovoltaic Systems:** In solar energy systems, Boost converters increase the output voltage of solar panels, aligning it harmoniously with grid or battery storage requisites.
- 3) **LED Drivers:** Boost converters prove their effectiveness by driving LEDs and providing high voltages that match their operational requirements.
- 4) **Uninterruptible Power Supplies (UPS):** Boost converters raise the voltage from low battery levels to a suitable threshold for meeting standby power requirements.
- 5) **Electric Vehicles (EVs):** Boost converters demonstrate their versatility by stepping up the voltage of battery packs to levels that exactly match the operating requirements of an electric motor.

2.2.4. Challenges and considerations

While Boost converters offer various advantages, there are considerations to be aware of:

- 1) **Voltage Stress:** The operation of Boost converters entails higher voltage levels than the input, which can impose stress on components, mandating meticulous selection of voltage ratings to ensure system robustness.
- 2) **Inductor Design:** Attaining the desired performance and efficiency hinges upon meticulous selection and design of inductors, making it an essential aspect of the system's optimization.
- 3) **Switching Losses:** The efficiency of Boost converters may encounter a setback due to switching losses that transpire in the switching element, predominantly the transistor, necessitating mitigation strategies for enhanced performance.
- 4) **Output Ripple:** The energy transfer process might engender output voltage ripple, underscoring the necessity for suitable filtering techniques, particularly in applications sensitive to noise.

2.3. Buck-Boost Converter

The Buck-Boost converter is a versatile DC-DC converter topology that enables both step-down and step-up voltage conversion. This capability makes it a viable solution for applications where the input voltage can vary widely, and the output voltage needs to be adjusted to match specific requirements (Gorji et al., 2019).

2.3.1. Operating principle

The Buck-Boost converter combines the principles of both the Buck (Step-Down) and Boost (Step-Up) converters to achieve its dual functionality. It employs an inductor, a switching element (typically a transistor), a diode, and an output capacitor (Chen, Maksimović and Erickson 2001, Gorji et al., 2019).

During the ON state, when the switch is closed, the inductor charges and stores energy. Similar to the Buck

converter, current flows through the inductor and diode, and energy is stored in the inductor's magnetic field.

When the switch transitions to the OFF state, the inductor's stored energy is released. However, the diode prevents the inductor's current from reversing and directs it toward the output capacitor and load, resulting in an output voltage that can be either higher or lower than the input voltage, depending on the duty cycle of the switching signal.

2.3.2. Advantages

The advantages of the Buck-Boost converter can greatly enhance its utility in various applications:

Bidirectional Voltage Conversion:

- 1) **The Buck-Boost converter provides bidirectional voltage conversion, allowing for step-up and step-down voltage regulation in a single topology.**
- 2) **Input Voltage Variability:** It's particularly useful in applications with input voltage variations, as it can handle both lower and higher input voltages, ensuring stable output voltage regardless of fluctuations in the power source.
- 3) **Simple Control:** The control scheme employed by the Buck-Boost converter is relatively uncomplicated. It relies on Pulse Width Modulation (PWM) control to adjust the duty cycle, allowing for precise and efficient voltage regulation. This simplicity contributes to ease of implementation and control.

- 4) **Compact Design:** The Buck-Boost's single-inductor design is an advantage for applications with limited space. This compact structure enables it to fit into space-constrained environments, making it an attractive choice for miniaturized electronic devices and systems.

Collectively, these advantages position the Buck-Boost converter as a valuable tool in power electronics, capable of meeting voltage regulation challenges across a range of practical applications.

2.3.3. Applications

The Buck-Boost converter serves a wide range of applications, demonstrating its adaptability in various scenarios:

- 1) **Battery-Powered Devices:** In portable electronics and battery-powered devices, the Buck-Boost converter plays a pivotal role. It helps to uphold a consistent output voltage even as the battery discharges, ensuring uninterrupted and stable device operation.
- 2) **Uninterruptible Power Supplies (UPS):** During power fluctuations or outages, maintaining a stable and reliable power supply is critical. The Buck-Boost converter excels in this role, efficiently regulating voltage to provide a continuous power source to connected devices.
- 3) **Energy Harvesting:** Renewable energy systems, such as those utilizing solar panels or wind turbines, often face variable energy generation. Buck-Boost converters are instrumental in efficiently storing energy from these sources, allowing for effective

utilization and storage of harvested power.

4) **Battery Charging:** Battery charging systems can include batteries with voltages above or below the charging voltage requirements. Here, the Buck-Boost converter comes into play, ensuring that the batteries are charged correctly and safely, regardless of their initial voltage levels.

5) **LED Drivers:** Maintaining consistent brightness in LED lighting systems is crucial for many applications, including automotive, signage, and general illumination. Buck-Boost converters are employed to regulate voltage, ensuring that LEDs emit a steady and uniform light output despite variations in the input voltage.

These applications underscore the versatility and significance of the Buck-Boost converter in the power electronics field, where voltage regulation is a fundamental requirement.

2.3.4. Challenges and considerations

While the Buck-Boost converter offers valuable advantages, it is necessary to acknowledge and address challenges:

1) **Voltage Stress:** In certain operating conditions, the voltage across the switching element can exceed the input voltage. This requires careful component selection, particularly when selecting components with appropriate voltage ratings to ensure system durability and reliability.

2) **Efficiency Trade-Offs:** Achieving high efficiency in both step-up and step-down modes can be challenging due to varying duty cycles.

3) **Inductor Design:** Designing the inductor to handle both modes efficiently requires careful consideration.

Addressing these challenges requires a deep understanding of the Buck-Boost converter's operation, careful component selection, and advanced control strategies. Despite these challenges, the Buck-Boost converter remains a valuable tool in power electronics, providing bidirectional voltage conversion in a wide range of applications.

2.4. Cuk Converter

The Cuk converter, named after its inventor Slobodan Cuk, is a versatile DC-DC converter topology that combines the advantages of both step-up and step-down voltage conversion. It is known for its ability to provide a continuous output voltage, even when the input voltage fluctuates. This makes it particularly useful in applications where a stable output voltage is crucial (Al-Obaidi, Abbas and Khazaal 2022, Mumtaz et al., 2021).

2.4.1. Operating principle

The Cuk converter consists of an inductor, two capacitors, and two switches. Unlike other conventional converters, it employs a coupled inductor, which enables its unique voltage conversion capabilities (Al-Obaidi, Abbas and Khazaal 2022).

During the ON state of the first switch, energy is stored in the inductor and transferred to the output through the

diode and the second switch. The voltage across the coupled inductor can be either higher or lower than the input voltage, depending on the duty cycle of the switching signal.

In the OFF state of the first switch, the energy stored in the inductor is delivered to the output capacitor and the load through the second switch and the diode. By regulating the duty cycle of the switches, the output voltage can be adjusted.

2.4.2. Advantages

1) **Continuous Output Voltage:** The Cuk converter maintains a consistent output voltage, irrespective of fluctuations in the input voltage or variations in the load. This reliability is crucial for applications demanding stable power delivery.

2) **Inherent Voltage Conversion:** Its design inherently allows for voltage conversion, which can be either step-up or step-down. This inherent versatility makes it suitable for a wide range of applications, where flexible voltage regulation is required.

3) **Isolation Option:** The Cuk converter can be easily adapted to include an isolation transformer, enhancing its suitability for applications that necessitate galvanic isolation. This feature extends its usability to fields requiring electrical separation for safety or functional reasons.

4) **Reduced Voltage Stress:** Compared to some other converter topologies, the Cuk converter imposes lower voltage stress across the switching components. This characteristic not only enhances overall system reliability but also contributes to improved efficiency.

These advantages collectively position the Cuk converter as a valuable choice in various power electronics applications, ensuring stable output voltage, adaptability, and enhanced reliability.

2.4.3. Applications

The Cuk converter finds applications in a range of scenarios due to its continuous voltage conversion ability and other advantages:

1) **Portable Devices:** The Cuk converter is extensively utilized in battery-operated devices to ensure a stable output voltage throughout the battery discharge cycle. This capability is crucial for maintaining consistent device performance and maximizing battery life.

2) **Photovoltaic Systems:** In the realm of solar energy systems, the Cuk converter plays a pivotal role. It is employed to regulate voltage and efficiently manage the power generated from solar panels. This aids in optimizing energy utilization and grid integration.

3) **LED Lighting:** The Cuk converter finds application in LED lighting systems, where it serves to uphold a steady brightness level. It effectively compensates for variations in input voltage and load, ensuring uniform and reliable illumination.

4) **Voltage Regulators:** Cuk converters are employed as voltage regulators in scenarios demanding

effective management of input voltage variations. Their ability to provide continuous output voltage makes them valuable for stabilizing power supply across a variety of applications.

These diverse applications underscore the adaptability and significance of the Cuk converter in modern power electronics, addressing the needs of everything from portable devices to renewable energy solutions.

2.4.4. Challenges and considerations

Despite its benefits, the Cuk converter comes with certain challenges:

- 1) **Complex Control:** The Cuk converter presents challenges in terms of control strategy due to the presence of multiple reactive components and coupled inductors. Achieving precise regulation and efficiency can require intricate control algorithms and circuitry.
- 2) **Voltage Ripple:** Depending on the specific design and operating conditions, the Cuk converter's output voltage may exhibit ripple. Managing this ripple effectively calls for the implementation of proper filtering techniques and advanced control methods.
- 3) **Isolation Challenges:** When the Cuk converter is used in conjunction with an isolation transformer, additional considerations come into play. Issues related to leakage inductance and maintaining a robust isolation barrier must be carefully addressed to ensure safe and reliable operation.

These considerations highlight the need for a thorough understanding of the Cuk converter's intricacies and the importance of tailored solutions to overcome its challenges.

2.5. Flyback Converter

The Flyback Converter, also known as the Flyback Transformer, is a widely used isolated DC-DC converter topology known for its simplicity, cost-effectiveness, and versatility. It provides galvanic isolation between the input and output, making it suitable for applications requiring voltage transformation and electrical isolation (Davari et al., 2012, Erickson, Madigan and Singer 1990).

2.5.1. Operating principle

The Flyback Converter operates based on the principles of energy storage and transfer. It typically consists of a transformer, an input capacitor, an output diode, and a control circuit that regulates the switching of the semiconductor switches (Davari et al., 2012, Erickson, Madigan and Singer 1990).

Switch-On State: When the semiconductor switch (usually a MOSFET) is turned on, current flows through the primary winding of the transformer, storing energy in the magnetic field created around the winding.

Energy Transfer: When the switch turns off, the energy stored in the magnetic field induces a voltage in the secondary winding of the transformer. This voltage is rectified by the output diode and transferred to the output capacitor, resulting in voltage transformation.

Output Regulation: By controlling the duty cycle (ratio of switch-on time to total cycle time), the output voltage can be regulated. Feedback control loops are often employed

to adjust the duty cycle based on the desired output voltage.

2.5.2. Advantages

- 1) **Galvanic Isolation:** The Flyback Converter offers galvanic isolation between the input and output, providing electrical separation and safety between different circuits.
- 2) **Simplicity:** Its simple structure with fewer components reduces cost and complexity, making it suitable for various applications.
- 3) **Multiple Outputs:** The Flyback Converter can provide multiple outputs by adding secondary windings to the transformer.
- 4) **Energy Storage:** Its energy storage capability allows for buffering energy and accommodating transient loads.

These advantages collectively underscore the Flyback Converter's significance in power electronics, offering a combination of isolation, simplicity, versatility, and energy management capabilities to meet the demands of diverse and complex applications.

2.5.3. Applications

The Flyback Converter finds applications in diverse fields due to its isolation and simplicity:

- 1) **Low-Power Electronics:** The Flyback Converter is a good choice for low-power electronic devices, including power adapters, battery chargers, and auxiliary power supplies. Its ability to efficiently provide isolated power makes it well-suited for these applications.
- 2) **LED Drivers:** In LED lighting systems, Flyback converters play a crucial role by delivering constant current or voltage to LEDs. This ensures consistent brightness and stable performance, making it an ideal choice for automotive, signage, and general illumination applications.
- 3) **Isolated Power Supplies:** It's suitable for applications requiring isolated power sources, such as industrial control systems and medical devices.
- 4) **Automotive:** Within the automotive industry, Flyback converters power various components, including sensors, lighting systems, and infotainment units. Their ability to efficiently manage power distribution in the challenging automotive environment underscores their importance in modern vehicles.

These applications highlight the adaptability of the Flyback Converter, making it a valuable solution in domains where isolation, simplicity, and precise power regulation are paramount.

2.5.4. Challenges and Considerations

While the Flyback Converter offers significant advantages, it also presents certain challenges that require careful consideration:

- 1) **Voltage Regulation:** Achieving precise voltage regulation can be challenging, especially under varying load conditions. Designing control strategies that can effectively handle load fluctuations is essential to ensure stable output voltage.

2) **Transformer Design:** The design of the transformer in a Flyback Converter is a critical aspect that influences overall performance. The transformer design must consider factors like core material, winding ratios, and leakage inductance to optimize efficiency and performance.

3) **Voltage Stress:** The voltage stress experienced by the semiconductor switch can be substantial in Flyback Converters, particularly during switching transitions. Proper selection of switches and the implementation of voltage clamping techniques are vital to mitigate voltage stress and enhance the converter's reliability.

Addressing these challenges requires a profound comprehension of the converter's operation, implementation of advanced control strategies, and meticulous transformer design. By managing these considerations effectively, the full potential of the Flyback converter can be utilized while ensuring reliable and efficient power conversion.

2.6. Forward Converter

The Forward Converter stands as a prominent and widely employed DC-DC converter topology, esteemed for its efficiency, simplicity, and adaptability in applications necessitating voltage transformation and isolation. Operating on the fundamental principle of energy transfer facilitated by a transformer, this converter topology finds a foothold across a wide range of industries, catering to a wide range of low to medium-power applications (Zhang, Jovanovic and Lee 1998).

2.6.1. Operating principle

The Forward Converter consists of a transformer, semiconductor switches (usually MOSFETs), an input capacitor, an output diode, and a control circuit. The operation of the Forward Converter can be divided into several key stages (Tan 2002, Zhang, Jovanovic and Lee 1998):

Switch-On State: During this stage, one of the MOSFET switches is turned on, allowing current to flow through the primary winding of the transformer. Energy is stored in the transformer's magnetic field.

Energy Transfer: When the primary switch turns off, the stored energy in the magnetic field is transferred to the secondary winding of the transformer. This induces a voltage in secondary winding, which is rectified by the output diode and transferred to the output capacitor.

Voltage Regulation: The output voltage can be regulated by controlling the duty cycle of the switches. Feedback control loops are often used to adjust the duty cycle and maintain the desired output voltage.

Isolation: The transformer provides galvanic isolation between the input and output, enhancing safety and allowing voltage transformation.

2.6.2. Advantages

1) **Efficiency:** The Forward Converter takes center stage with its remarkable efficiency, captivating the users with reduced switching losses and an optimized transformer design that ensures a high performance in

energy conversion.

2) **Isolation:** Galvanic isolation between input and output enhances safety and allows voltage transformation.

3) **Compact Design:** Its simple structure and fewer components contribute to a compact and cost-effective design.

4) **Versatility:** The Forward Converter can be configured for various output voltages and power levels, making it suitable for a wide range of applications.

2.6.3. Applications

The Forward Converter finds applications in different industries due to its efficiency and voltage transformation capabilities:

1) **Power Supplies:** It takes the leading role in power supplies, catering to the energy needs of computers, televisions, and industrial equipment, delivering a stellar performance in providing stable and efficient power.

2) **Telecommunications:** Forward converters provide isolated voltage conversion in telecom power supplies and equipment.

3) **Automotive:** They are used in automotive applications for powering infotainment systems, sensors, and control units.

4) **Renewable Energy:** Forward converters can be part of renewable energy systems, such as wind turbine converters.

2.6.4. Challenges and considerations

Amidst its many advantages, the Forward Converter isn't without its set of challenges:

1) **Transformer Design:** Crafting an efficient transformer demands meticulous attention to winding ratios, core material selection, and the management of parasitic elements. This intricate process is critical to optimizing both efficiency and performance.

2) **Magnetic Core Saturation:** The risk of transformer core saturation lurks, potentially causing distortion and efficiency dips. Combatting this issue necessitates astute design choices and adept control techniques.

3) **Voltage Stress:** Excessive voltage stress on the switches can lead to undesirable consequences like breakdown and ringing. To navigate this challenge, the employment of voltage clamping mechanisms and snubber circuits may become a necessity.

2.7. Full-Bridge Converter

The Full-Bridge Converter is a versatile and widely used topology in the field of DC-DC power conversion. It offers voltage transformation, isolation, and bidirectional power flow, making it suitable for various applications across industries. The Full-Bridge Converter operates by utilizing a bridge configuration of semiconductor switches and is known for its ability to efficiently handle high-power levels (Bakas et al., 2016, Chen et al., 1995).

2.7.1. Operating principle

The Full-Bridge Converter consists of four semiconductor switches arranged in a bridge configuration. These switches can be either diodes or transistors, such as MOSFETs or IGBTs. The converter can operate in two modes: buck (step-down) mode and boost (step-up) mode (Wang, Lee and Lai 2000).

Buck Mode: In this mode, the upper switches are alternately turned on and off while the lower switches remain off. When the upper-left switch is on, current flows through the load and the upper-right diode, effectively stepping down the voltage. The energy stored in the inductor is transferred to the output.

Boost Mode: In this mode, the lower switches are alternately turned on and off while the upper switches remain off. When the lower-left switch is on, current flows through the inductor, storing energy. When the lower-right switch is turned on, the stored energy is transferred to the load and the output voltage is boosted. By carefully controlling the switching sequence and timing of the switches, the Full-Bridge Converter can achieve bidirectional power flow, allowing energy to be transferred in both buck and boost modes.

2.7.2. Advantages

- 1) **Bidirectional Operation:** The Full-Bridge Converter's capacity to function in both buck and boost modes renders it highly versatile, making it an excellent choice for applications necessitating voltage step-up and step-down capabilities.
- 2) **Isolation:** When paired with a high-frequency transformer, the Full-Bridge Converter can deliver galvanic isolation between the input and output, significantly enhancing safety and permitting voltage transformation.
- 3) **High Power Handling:** This converter topology exhibits exceptional suitability for high-power applications. It can efficiently manage substantial currents and voltages, which is pivotal in applications demanding robust power handling.
- 4) **Voltage Regulation:** Precise control over the output voltage is achieved by fine-tuning the duty cycle of the switches, ensuring reliable and accurate voltage regulation for various applications.

2.7.3. Applications

The Full-Bridge Converter has a wide range of applications in various industries:

- 1) **Power Supplies:** The Full-Bridge Converter plays a pivotal role in high-power supplies across diverse sectors, including industrial equipment, data centers, and telecommunications. Its robust power handling capabilities make it a dependable choice for ensuring stable and efficient power delivery.
- 2) **Renewable Energy:** Full-Bridge Converters are instrumental in the realm of renewable energy systems, finding application in solar inverters and wind turbine converters. They serve as vital components for interfacing with the grid, managing power flow, and optimizing the utilization of energy harvested from

renewable sources.

- 3) **Electric Vehicles:** Within the domain of electric vehicles (EVs), Full-Bridge Converters are integrated into power electronics systems. They facilitate critical functions such as battery charging and power distribution, contributing to the efficient and reliable operation of EVs.
- 4) **Motor Drives:** Full-Bridge Converters are extensively employed in motor drive applications, where precise control of electric motors is imperative. Their utilization in industrial automation and robotics enables accurate and efficient motor control, enhancing productivity and performance in various industries.

2.7.4. Challenges and Considerations:

- 1) **Switching Losses:** Operating at high power levels can result in substantial switching losses within the Full-Bridge Converter. These losses can have a detrimental impact on overall efficiency. To mitigate this challenge, it's crucial to carefully select appropriate switching devices and implement advanced control techniques.
- 2) **Heat Dissipation:** Efficient heat dissipation mechanisms are vital when dealing with high-power applications. The substantial power levels involved can lead to significant heat generation, potentially affecting the reliability and longevity of the converter. Adequate cooling systems and thermal management strategies must be in place to ensure safe and reliable operation.
- 3) **Complex Control:** The bidirectional operation and multi-mode control capabilities of the Full-Bridge Converter necessitate sophisticated control strategies and circuitry. Achieving precise control over voltage regulation and power flow in high-power systems can be complex and requires in-depth knowledge of power electronics and control theory. Careful design and robust control algorithms are essential to meet the demands of such applications.

2.8. Half-Bridge Converter

The Half-Bridge Converter stands as a foundational topology extensively utilized across diverse power electronic applications, offering a balance between simplicity and functionality. It is particularly used for moderate power levels and is often implemented in motor drives, power supplies, and other applications where voltage transformation and control are essential (Steigerwald 1988).

2.8.1. Operating principle

The Half-Bridge Converter consists of two semiconductor switches (usually transistors or MOSFETs) and a center-tapped DC input voltage source. These switches are arranged in a configuration that allows voltage inversion across the load.

When one of the switches is turned on, current flows from the center tap of the input voltage source through the load and the switch. This results in a positive output voltage across the load. Conversely, when the other switch is turned on, the current direction is reversed, leading to a negative output voltage (Chen, Xu and Lee

2001, Steigerwald 1988).

2.8.1. Advantages

The Half-Bridge Converter offers several notable advantages:

- 1) **Simplicity:** The Half-Bridge Converter has a straightforward structure with only two switches, making it relatively easy to control and implement.
- 2) **Voltage Transformation:** The topology enables voltage inversion, allowing both positive and negative output voltages to be generated from the input voltage source.
- 3) **Space Efficiency:** With only two switches, the Half-Bridge Converter occupies less physical space compared to other topologies with multiple switches.

2.8.2. Applications

The Half-Bridge Converter finds application in various areas due to its simplicity and effectiveness:

- 1) **Motor Drives:** In the realm of motor control, the Half-Bridge Converter plays a pivotal role. It is widely used to control the speed and direction of electric motors, making it an integral component in applications ranging from industrial automation to robotics.
- 2) **Uninterruptible Power Supplies (UPS):** Half-Bridge Converters find essential use in UPS systems. Here, they excel in converting DC power sourced from batteries into AC power, ensuring a continuous and reliable power supply to critical loads during mains power interruptions.
- 3) **Induction Heating:** The Half-Bridge Converter's precise and controlled voltage inversion capabilities make it well-suited for induction heating systems. These systems are employed in various industries for the efficient and controlled heating of metals and other materials, playing a crucial role in processes like metal hardening and cooking appliances.
- 4) **Power Supplies:** In power electronics, the Half-Bridge Converter is a trusted workhorse for power supplies where voltage inversion and control are prerequisites. Its effectiveness in generating both positive and negative output voltages from a DC source makes it a versatile choice in diverse applications requiring flexible voltage regulation.

These applications underscore the adaptability and effectiveness of the Half-Bridge Converter in addressing the voltage transformation and control needs of various industries and technologies.

2.8.3. Challenges and considerations

- 1) **Limited Voltage Transformation Ratio:** One of the inherent limitations of the Half-Bridge Converter is its ability to generate only positive and negative output voltages concerning the center-tapped DC source. This restricted voltage transformation capability can be a constraint in applications requiring a wider range of output voltage options.
- 2) **Limited Output Power:** The Half-Bridge Converter is well-suited for moderate power applications. However, for scenarios demanding higher

power levels, it might be necessary to parallel multiple Half-Bridge Converters to meet the power requirements effectively. This consideration adds complexity to the system, necessitating synchronization and control mechanisms for parallel operation.

Addressing these challenges entails a comprehensive understanding of the Half-Bridge Converter's operational boundaries and careful system design to ensure it aligns with the specific demands of the intended application. Despite these limitations, its simplicity and efficiency continue to make it a valuable choice in numerous power electronic scenarios.

2.9. Push-Pull Converter

The Push-Pull Converter is a prominent topology in the field of power electronics, highly regarded for its proficiency in voltage transformation, high efficiency, and provision of electrical isolation. Its versatility finds extensive utilization in diverse applications such as power supplies, motor drives, and various scenarios where precise voltage conversion holds paramount importance (Ivanovic and Knezic 2022, Kim and Kwon 2009).

2.9.1. Operating principle

The Push-Pull Converter consists of two sets of switches (typically transistors or MOSFETs) arranged in a symmetric configuration. These switches are operated alternately to create a transformer action. The primary winding of the transformer is connected to a DC input source, while the secondary winding is connected to the load (Ivanovic and Knezic 2022).

The operation of the Push-Pull Converter involves two phases:

Positive Half-Cycle: During this phase, one set of switches is turned on while the other set is turned off. This allows current to flow through the primary winding, storing energy in the transformer's core. The secondary winding delivers energy to the load, resulting in an output voltage across the load.

Negative Half-Cycle: In this phase, the state of the switches is reversed, turning off the previously active set and turning on the other set. This reverses the current flow through the primary winding, causing energy to be transferred to the secondary winding and the load. This phase generates an output voltage with reversed polarity (Kim et al., 2013).

2.9.2. Advantages

- 1) **Efficiency:** Push-pull converters excel in efficiency, thanks to the symmetrical operation of their switches, which minimizes power losses during operation.
- 2) **Voltage Transformation:** This converter's transformer-based design facilitates voltage transformation, enabling the generation of output voltages that can be either higher or lower than the input voltage, catering to a wide range of applications.
- 3) **Isolation:** The presence of a transformer in Push-Pull Converters ensures galvanic isolation

between the input and output, enhancing safety by preventing direct electrical connection between the two, and improving noise immunity in sensitive applications.

2.9.3. Applications

Push-pull converters are utilized in a diverse array of applications where voltage transformation and isolation are paramount:

- 1) **Power Supplies:** They find widespread use in both AC-DC and DC-DC power supplies, effectively and efficiently generating regulated output voltages.
- 2) **Audio Amplifiers:** Push-pull converters are a key component in class D audio amplifiers, enabling the conversion of low-voltage audio signals into high-power amplified signals, vital for high-quality audio
- 3) **Motor Drives:** They play a pivotal role in motor drives, providing precise control over voltage and frequency for AC motors, a fundamental requirement in industrial automation and electric vehicle propulsion.
- 4) **High-Frequency Transformers:** Push-pull converters are indispensable in the design of high-frequency transformers, serving a multitude of applications, including telecommunications and efficient power distribution systems.

2.9.4. Challenges and considerations

- 1) **Complexity:** The Push-Pull Converter demands intricate control and precise synchronization of the switching operation to guarantee proper functionality and minimize switching losses.
- 2) **Transformer Design:** Achieving optimal voltage transformation and efficiency hinges on the effective design of the transformer, emphasizing factors such as core material, winding ratios, and parasitic elements.

2.10. Resonant Converters: LLC, ZVS, and ZCS

Resonant converters are a class of power electronic converters that utilize resonant components such as inductors, capacitors, and switches to achieve efficient energy conversion. These converters leverage the properties of resonance to achieve soft switching, reduced switching losses, and improved efficiency (Yang et al., 2002). Among the resonant converters, the LLC resonant converter, along with Zero Voltage Switching (ZVS) and Zero Current Switching (ZCS) techniques, have gained significant attention for their advantages in high-frequency and high-power applications (Kundu, Yenduri and Sensarma 2016, Park, Kim and Choi 2014).

2.10.1. LLC Resonant converter

The LLC resonant converter is a popular topology known for its ability to provide high efficiency over a wide load range. The name "LLC" stands for the three resonant components used in the topology: the resonant inductor (L), the resonant capacitor (C), and the leakage inductance of the transformer (L). The LLC resonant converter operates by creating resonant tank circuits that enable zero voltage switching for the switches, reducing switching losses (Yang et al., 2002, Zeng et al., 2020).

2.10.1. Advantages:

- 1) **High Efficiency:** The LLC resonant converter offers high efficiency due to its ability to achieve zero voltage switching and minimize switching losses.
- 2) **Wide Load Range:** LLC converters maintain high efficiency across a wide range of load conditions, making them suitable for variable load applications.
- 3) **Reduced Electromagnetic Interference (EMI):** The soft-switching characteristics of the LLC converter lead to lower EMI emissions, making it suitable for applications with stringent EMI requirements.

2.10.2. Zero Voltage Switching (ZVS)

Zero Voltage Switching (ZVS) is a technique applied to switching converters where the switching devices (usually transistors) are turned on or off when the voltage across them is zero (Kundu, Yenduri and Sensarma 2016). This technique eliminates the switching losses associated with hard switching and enhances converter efficiency.

2.10.2.1. Advantages

- 1) **Reduced Switching Losses:** ZVS eliminates the energy dissipated during hard switching, resulting in lower overall losses and increased efficiency.
- 2) **Improved Reliability:** Since ZVS reduces stress on the switching devices, it can contribute to improved reliability and longer device lifetimes.

2.10.3. Zero Current Switching (ZCS)

Zero Current Switching (ZCS) is a technique similar to ZVS, but it focuses on turning on or off the switching devices when the current through them is zero (Park, Kim and Choi 2014). ZCS minimizes the current-related losses associated with hard switching.

2.10.3.1. Advantages

- 1) **Lower Current Stress:** ZCS reduces the stress on the switching devices, leading to lower conduction losses and potentially extending the operational life of the components.
- 2) **Higher Efficiency:** By eliminating current-related losses, ZCS contributes to higher converter efficiency.

2.10.4. Applications

Resonant converters, often integrated with Zero Voltage Switching (ZVS) and Zero Current Switching (ZCS) techniques, find extensive applications in high-frequency and high-power systems:

- 1) **High-Frequency Power Supplies:** Resonant converters, when combined with ZVS and ZCS, are employed in high-frequency power supplies catering to critical sectors like telecommunications and data centers. The efficient and controlled power conversion they offer is essential for the reliable operation of these applications.
- 2) **Renewable Energy Systems:** Resonant converters, often utilizing ZVS and ZCS techniques, play a pivotal role in renewable energy systems such as solar inverters and wind energy converters. They are instrumental in efficiently converting and managing the power generated from renewable sources, contributing

to the sustainability of these systems.

- 3) Inductive Heating: Resonant converters, especially when implementing ZVS and ZCS, find significant use in inductive heating applications. Their ability to deliver efficient and controlled heating is invaluable in various industrial processes that rely on precise temperature control and rapid heating capabilities.

2.10.5. Challenges and Considerations:

- 1) Control Complexity: Designing control systems for resonant converters requires careful consideration of resonant frequencies, load variations, and switching characteristics.
- 2) Component Selection: Proper selection of resonant components, such as inductors and capacitors, is essential for achieving desired resonant frequencies and minimizing losses.

Indeed, the diversity of DC-DC converter topologies helps meet power conversion challenges. Whether the goal is precise voltage regulation, accommodating bidirectional power flow, optimizing efficiency, or ensuring galvanic isolation, these converter topologies offer customized solutions. This adaptability underscores the significance of power electronics in a wide array of applications, from portable devices to renewable energy systems, and highlights the role of innovation in continuously improving and expanding the capabilities of these converters to meet evolving technological demands. Table 1 provides an overview of the advantages, applications, and challenges associated with each DC-DC converter topology.

3. Results and Discussion

In the field of electrical engineering and power electronics, DC-DC converters stand as versatile and indispensable components, serving as the cornerstone for many applications. This comprehensive discussion includes an examination of DC-DC converters, exploring their diverse topologies, operating principles, advantages, and challenges. From the commonly used Buck converter, which is adept at efficiently stepping down voltage, to the Buck-Boost converter, which provides the flexibility of step-up and step-down voltage conversion, these structures meet a wide range of voltage regulation needs. The Cuk converter, with its continuous output voltage and voltage conversion abilities, finds its niche in applications demanding stability despite fluctuating input conditions. Meanwhile, the Flyback converter's isolation and simplicity make it a mainstay in low-power electronics. The Forward converter, renowned for its efficiency, and the Full-Bridge converter, lauded for its high-power handling capabilities, find places in various industries. The Half-Bridge converter, a model of simplicity and efficiency, is widely used in motor drives and power supplies. For its ability to convert voltage with precise isolation, the push-pull converter is used in power supply applications, amplifiers and motor drives. In the high-frequency domain, LLC resonant converters reduce switching losses

and EMI, enhancing efficiency and mitigating interference. These converters do not just stand as standalone components; they form the bedrock of many applications, from battery-powered devices to renewable energy systems. However, DC-DC converters still suffer from their complexities, as voltage stress, efficiency trade-offs, and complex control strategies often challenge engineers. Still, researchers continue to work and strive for innovation in the ever-evolving world of power electronics. In conclusion, DC-DC converters are the cornerstone, the power mediators, and the precision instruments, seamlessly adapting voltage to the needs of our electrified world.

4. Conclusion

In this comprehensive analysis of DC-DC converters, the advancements, applications, and challenges shaping this critical technology are explored and examined. These converters, with their diverse structures and operating principles, have redefined how electrical energy is managed and processed. From the humble Buck converter, offering efficient voltage reduction, to the complex Full-Bridge converter, capable of handling substantial power levels, each topology serves a specific purpose. Advancements in DC-DC converter topologies have pushed the field forward, providing engineers with a versatile toolkit to meet the demands of ever-evolving power applications. The Buck-Boost converter is a prime example, bridging the gap between step-up and step-down voltage conversion smoothly and precisely. Meanwhile, the Cuk converter's ability to maintain continuous output voltage amidst input fluctuations showcases the innovation required to address the needs of modern electronics.

Advantages such as high efficiency, bidirectional operation, galvanic isolation, and reduced voltage stress make these converters invaluable across a wide spectrum of applications. The power our portable devices, light up our LED systems, regulate voltage in photovoltaic installations, and drive motors in industrial automation. They are the unsung heroes, ensuring our electronics run smoothly and reliably and keeping the technological ecosystem running.

However, the operation of these converters is not without challenges. Complex control strategies, stress management and efficiency optimization present formidable obstacles that researchers must continually seek innovative solutions to overcome. Achieving greater efficiency and reliability requires meticulous design and innovative solutions.

In a world where energy efficiency, reliability, and precise voltage control are critical, DC-DC converters have emerged as the cornerstone of modern power electronics. As developments continue and applications expand, DC-DC converters remain at the forefront. They are the innovation meeting necessity, of technology shaping our world, and of challenges met with ingenuity.

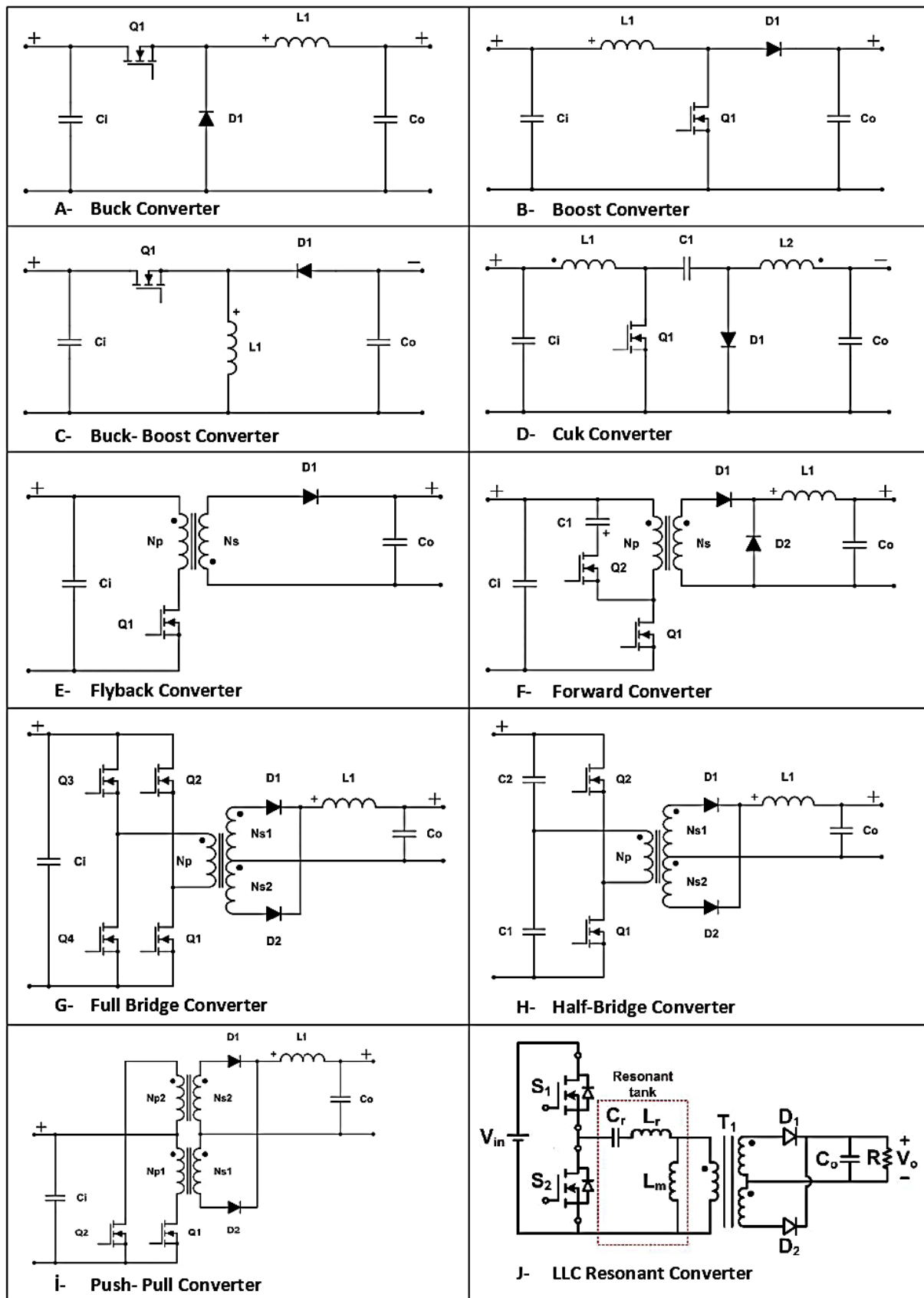


Figure 1. DC-DC converter topologies.

Table 1: characteristics associated with each DC-DC converter topology.

| Converter Topology | Advantages | Applications | Challenges and Considerations |
|------------------------|---|---|---|
| Buck Converter | <ul style="list-style-type: none"> - Efficient step-down voltage conversion - Simplicity and high efficiency - Low voltage stress on switches | <ul style="list-style-type: none"> - Battery-powered devices - LED drivers - Voltage regulators | <ul style="list-style-type: none"> - Limited to step-down voltage conversion - Output voltage fixed below input voltage |
| Boost Converter | <ul style="list-style-type: none"> - Efficient step-up voltage conversion - Simplicity and high efficiency - Low voltage stress on switches | <ul style="list-style-type: none"> - Power supplies - Battery chargers - LED drivers | <ul style="list-style-type: none"> - Limited to step-up voltage conversion - Output voltage fixed above input voltage |
| Buck-Boost Converter | <ul style="list-style-type: none"> - Can perform both step-up and step-down voltage conversion - Continuous output voltage | <ul style="list-style-type: none"> - Portable electronics - Battery-powered devices - LED drivers | <ul style="list-style-type: none"> - Complex control due to dual operation - Voltage ripple in some operating conditions |
| Cuk Converter | <ul style="list-style-type: none"> - Continuous output voltage - Inherent voltage conversion - Isolation option with a transformer - Reduced voltage stress on switches | <ul style="list-style-type: none"> - Portable devices - Photovoltaic systems - LED lighting - Voltage regulators | <ul style="list-style-type: none"> - Complex control due to coupled inductors - Voltage ripple in some operating conditions - Isolation challenges when using a transformer |
| Flyback Converter | <ul style="list-style-type: none"> - Galvanic isolation - Simplicity and cost-effective - Multiple outputs with secondary windings - Energy storage capability | <ul style="list-style-type: none"> - Low-power electronics - LED drivers - Isolated power supplies - Automotive | <ul style="list-style-type: none"> - Voltage regulation challenges under varying loads - Transformer design complexities - Voltage stress on switches |
| Forward Converter | <ul style="list-style-type: none"> - High efficiency - Galvanic isolation - Compact design - Versatility in output voltages | <ul style="list-style-type: none"> - Power supplies - Telecommunications - Automotive - Renewable energy systems | <ul style="list-style-type: none"> - Transformer design complexities - Transformer core saturation - Voltage stress on switches |
| Full-Bridge Converter | <ul style="list-style-type: none"> - Bidirectional operation - Galvanic isolation - High power handling - Voltage regulation | <ul style="list-style-type: none"> - Power supplies for industrial equipment, data centers, telecommunications, etc. - Renewable energy systems - Motor drives - Uninterruptible power supplies | <ul style="list-style-type: none"> - High-power operation may lead to switching losses - Efficient cooling systems are essential for heat dissipation - Complex control strategies |
| Half-Bridge Converter | <ul style="list-style-type: none"> - Simplicity - Voltage transformation - Space efficiency | <ul style="list-style-type: none"> - Induction heating - Power supplies with voltage inversion and control required | <ul style="list-style-type: none"> - Limited voltage transformation ratio - Limited output power for high-power applications |
| Push-Pull Converter | <ul style="list-style-type: none"> - High efficiency - Voltage transformation - Galvanic isolation | <ul style="list-style-type: none"> - Power supplies - Audio amplifiers - Motor drives - High-frequency transformers | <ul style="list-style-type: none"> - Control and synchronization complexities - Transformer design complexities |
| LLC Resonant Converter | <ul style="list-style-type: none"> - High efficiency - Wide load range - Reduced EMI emissions | <ul style="list-style-type: none"> - High-frequency power supplies - Renewable energy systems - Inductive heating | <ul style="list-style-type: none"> - Complex control and synchronization - Transformer design complexities - High-power operation may require efficient cooling systems |

Author Contributions

The percentage of the author contributions is presented below. The author reviewed and approved the final version of the manuscript.

| | F.A.O. |
|-----|--------|
| C | 100 |
| D | 100 |
| S | 100 |
| DCP | 100 |
| DAI | 100 |
| L | 100 |
| W | 100 |
| CR | 100 |
| SR | 100 |
| PM | 100 |
| FA | 100 |

C=Concept, D= design, S= supervision, DCP= data collection and/or processing, DAI= data analysis and/or interpretation, L= literature search, W= writing, CR= critical review, SR= submission and revision, PM= project management, FA= funding acquisition.

Conflict of Interest

The author declared that there is no conflict of interest.

Ethical Consideration

Ethics committee approval was not required for this study because of there was no study on animals or humans.

References

Alhurayyis I, Elkhateb A, Morrow J. 2020. Isolated and nonisolated dc-to-dc converters for medium-voltage dc networks: a review. *IEEE J Emerg Sel*, 9(6): 7486-500.

Al-Obaidi NA, Abbas RA, Khazaa HF. 2022. A review of non-isolated bidirectional dc-dc converters for hybrid energy storage system. In: 5th International Conference On Engineering Technology And Its Applications (IICETA), 31 May - 1 June, Al-Najaf, Iraq, pp: 248-253.

Bakas P, Harnefors L, Norrga S, Nami A, Ilves K, Dijkhuizen F, Nee HP. 2016. A review of hybrid topologies combining line-commutated and cascaded full-bridge converters. *IEEE J Emerg Sel*, 32(10): 7435-48.

Basso C. 2008. Switch-mode power supplies: spice simulations and practical designs. McGraw-Hill, New York, USA, 2th ed., pp: 321.

Chen J, Maksimović D, Erickson R. 2001. Buck-boost pwm converters having two independently controlled switches. In: IEEE 32nd Annual Power Electronics Specialists Conference (IEEE Cat. No. 01CH37230), 17-21 June, Vancouver, BC, Canada, pp: 736-741.

Chen, W, Lee FC, Jovanovic MM, Sabate JA. 1995. A comparative study of a class of full bridge zero-voltage-switched pwm converters. In: Proceedings of 1995 IEEE Applied Power Electronics Conference and Exposition-APEC'95, 5-9 March, Dallas, TX, USA, pp: 893-899.

Chen W, Xu P, Lee FC. 2001. The optimization of asymmetric half bridge converter. In: Sixteenth Annual IEEE Applied Power Electronics Conference and Exposition (Cat. No. 01CH37181), 4-8 March, Anaheim, CA, USA, pp: 703-707.

Davari P, Zare F, Ghosh A, Akiyama H. 2012. High-voltage

modular power supply using parallel and series configurations of flyback converter for pulsed power applications. *IEEE Trans Plasma Sci IEEE Nucl Plasma Sci Soc*, 40(10): 2578-87.

Erickson R, Madigan M, Singer S. 1990. Design of a simple high-power-factor rectifier based on the flyback converter. In: Fifth Annual Proceedings on Applied Power Electronics Conference and Exposition, 11-16 March, Los Angeles, CA, USA, pp: 792-801.

Erickson R, Dragan M. 2007. Fundamentals of power electronics. Springer science & business media, London, UK, 2th ed., pp: 253.

Forouzesh M, Siwakoti YP, Gorji SA, Blaabjerg F, Lehman B. 2017. Step-up dc-dc converters: a comprehensive review of voltage-boosting techniques, topologies, and applications. *IEEE Trans. Power Electron*, 32(12): 9143-78.

Gorji SA, Mostaan A, My HT, Ektesabi M. 2019. Non-isolated buck-boost dc-dc converter with quadratic voltage gain ratio. *IET Power Electron*, 12(6): 1425-33.

Hossain MZ, Rahim NA. 2018. Recent progress and development on power dc-dc converter topology, control, design and applications: a review. *Renew. Sust Energ Rev*, 81:205-30.

İnci M, Büyük M, Demir MH, İlbey G. 2021. A review and research on fuel cell electric vehicles: topologies, power electronic converters, energy management methods, technical challenges, marketing and future aspects. *Renew Sust Energ Rev*, 137: 110648.

Ivanovic Z, Knezic M. 2022. Modeling push-pull converter for efficiency improvement. *J Electron*, 11(17): 2713.

Kazimierczuk MK. 2015. Pulse-width modulated dc-dc power converters: John Wiley & Sons, London, UK, pp: 143.

Khaligh A, Onar OC. 2017. Energy harvesting: solar, wind, and ocean energy conversion systems, CRC press, London, UK, pp: 218.

Kim EH, Kwon BH. 2009. High step-up resonant push-pull converter with high efficiency. *IET Power Electron*, 2(1): 79-89.

Kim YH, Soo CS, Lee JH, Yong CJ, Chung YW. 2013. Soft-switching current-fed push-pull converter for 250-w ac module applications. *IEEE Trans Power Electron*, 29(2): 863-872.

Krishnan R. 2017. Switched reluctance motor drives: modeling, simulation, analysis, design, and applications: CRC press, London, UK, pp: 142.

Kundu U, Yenduri K, Sensarma P. 2016. Accurate zvs analysis for magnetic design and efficiency improvement of full-bridge llc resonant converter. *IEEE Trans Power Electron*, 32(3): 1703-1706.

Li Z, Ruopei Z, Yazhou L, Yan H, Jinming H, Xiaoling Z, Xiao-Ping Z. 2018. Recent developments in HVDC transmission systems to support renewable energy integration. *Glob Energy Interconnect*, 1(5): 595-607.

Lipo TA. 2017. Introduction to ac machine design. John Wiley & Sons, London, UK, pp: 154.

Luo FL, Ye H. 2016. Advanced Dc/Dc converters. CRC press, London, UK, pp: 125.

Mohan N, Undeland TM, Robbins WP. 2003. Power electronics: converters, applications, and design: John Wiley & Sons, London, UK, pp: 121.

Mumtaz F, Yahaya NZ, Meraj ST, Singh B, Kannan R, Ibrahim O. 2021. Review on non-isolated dc-dc converters and their control techniques for renewable energy applications. *Ain Shams Eng J*, 12(4): 3747-3763.

Nouri T, Nouri N, Vosoughi N. 2019. A novel high step-up high

- efficiency interleaved dc–dc converter with coupled inductor and built-in transformer for renewable energy systems. *IEEE Trans Power Electron*, 67(8): 6505-6516.
- Park J, Kim M, Choi S. 2014. Zero-current switching series loaded resonant converter insensitive to resonant component tolerance for battery charger. *IET Power Electron*, 7(10): 2517-2524.
- Pressman A. 2009. *Switching power supply design*. McGraw-Hill Education, London, UK, pp: 102.
- Raghavendra KVG, Zeb K, Muthusamy A, Krishna TNV, Kumar SVSVP, Kim DH, Kim MS, Cho HG, Kim HJ. 2019. A comprehensive review of dc–dc converter topologies and modulation strategies with recent advances in solar photovoltaic systems. *J Electron*, 9(1): 31.
- Rashid MH. 2010. *Power electronics circuits devices and application*. Pearson, London, UK, pp: 101.
- Rashid MH. 2017. *Power electronics handbook*. Butterworth-heinemann, London, UK, pp: 124.
- Revathi BS, Prabhakar M. 2016. Non isolated high gain dc-dc converter topologies for pv applications—a comprehensive review. *Renew Sust Energ Rev*, 66: 920-933.
- Saeedifard M, Graovac M, Dias RF, Iravani R. 2010. Dc power systems: challenges and opportunities. In: *IEEE PES general meeting: IEEE*, 25-29 July, Minneapolis, MN, USA, pp: 1-7
- Skvarenina T. L. 2018. *The power electronics handbook*. CRC press, London, UK, pp: 97.
- Steigerwald RL. 1988. A comparison of half-bridge resonant converter topologies. *IEEE Trans. Power Electron*, 3(2): 174-182.
- Tan FD. 2002. The forward converter: from the classic to the contemporary. In: *APEC. Seventeenth Annual IEEE Applied Power Electronics Conference and Exposition (Cat. No. 02CH37335)*, 10-14 March, Dallas, TX, USA, pp: 857-863.
- Tseng KC, Huang CC. 2013. High step-up high-efficiency interleaved converter with voltage multiplier module for renewable energy system. *IEEE Trans Ind Electron*, 61(3): 1311-1319.
- Wang K, Lee FC, Lai J. 2000. Operation principles of bi-directional full-bridge dc/dc converter with unified soft-switching scheme and soft-starting capability. In: *Fifteenth Annual IEEE Applied Power Electronics Conference and Exposition (Cat. No. 00CH37058)*, 6-10 Feb, New Orleans, LA, USA, pp: 111-118
- Wei Y, Luo Q, Mantooth A. 2020. Overview of modulation strategies for llc resonant converter. *IEEE Trans. Power Electron*, 35(10): 10423-10443.
- Wu G, Ruan X, Ye Z. 2014. Nonisolated high step-up dc-dc converters adopting switched-capacitor cell. *IEEE Trans. Ind Electron*, 62(1): 383-393.
- Yang B, Lee FC, Zhang AJ, Huang G. 2002. Llc resonant converter for front end dc/dc conversion. In: *Seventeenth Annual IEEE Applied Power Electronics Conference and Exposition (Cat. No. 02CH37335)*, 10-14 March, Dallas, TX, pp: 1108-1112.
- Zeng J, Zhang G, Yu SS, Zhang B, Zhang Y. 2020. LLC resonant converter topologies and industrial applications—a review. *Chin J Electr Eng*, 6(3): 73-84.
- Zhang MT, Jovanovic MM, Lee FCY. 1998. Analysis and evaluation of interleaving techniques in forward converters. *IEEE Trans Power Electron*, 13(4): 690-698.



ELEVATING THYME SPECIES IDENTIFICATION: EXPLOITING KEY CHLOROPLAST GENES (*matK*, *rbcl*, AND *psbA-trnH*) THROUGH DNA BARCODING AND PHYLOGENETIC ANALYSIS

Mehmet Alp FURAN^{1*}


¹Van Yüzüncü Yıl University, Agriculture Faculty, Department of Agricultural Biotechnology, 65090, Van, Türkiye

Abstract: Understanding genetic relationships and diversity among species is crucial for unraveling evolutionary processes, ecological interactions, and conservation strategies. DNA sequence analysis serves as a powerful tool in this endeavor. This study focuses on the *Thymus* genus, a collection of notable species, to investigate its genetic framework. Leveraging DNA sequences from key regions (*matK*, *rbcl*, and *psbA-trnH*), we aim to elucidate genetic connections within the *Thymus* genus and uncover mechanisms driving its diversity. The *Thymus* genus, with its diverse species and ecological characteristics, provides a captivating platform for genetic exploration. Through DNA sequence analysis, we aim to unveil genetic interconnections, biodiversity patterns, and the factors shaping the genus's evolution. Our findings are aligned with previous studies, and this consistency highlights the presence of polymorphism within potential sequences. Employing coding loci and spacer regions, our study contributes to Lamiaceae family barcoding research. Despite variations across gene regions, the concatenation of sequences enhances result reliability. We analyzed the suitability of *matK*, *rbcl*, and *psbA* sequences for *Thymus* identification, observing *rbcl* and *psbA* outperforming *matK*. Our novel approach, rooted in chloroplast DNA, presents a promising method for species discernment. By analyzing multiple chloroplast gene regions, this technique offers a fresh perspective on genetic affinity assessment using DNA barcodes. In conclusion, this study not only contributes to *Thymus* germplasm resource preservation but also exemplifies a novel approach to discerning *Thymus* species through DNA analysis. This methodology carries the potential for broader application, enriching our understanding of genetic relationships and diversity in the plant kingdom.

Keywords: *Thymus*, DNA barcoding, Chloroplast genes, Phylogenetic analysis

*Corresponding author: Van Yüzüncü Yıl University, Agriculture Faculty, Department of Agricultural Biotechnology, 65090, Van, Türkiye

E mail: alp@furan@yyu.edu.tr (M. A. FURAN)

Mehmet Alp FURAN  <https://orcid.org/0000-0002-0171-0405>

Received: August 31, 2023

Accepted: September 29, 2023

Published: October 15, 2023

Cite as: Furan MA. 2023. Elevating thyme species identification: exploiting key chloroplast genes (*matK*, *rbcl*, and *psbA-trnH*) through DNA barcoding and phylogenetic analysis. *BSJ Eng Sci*, 6(4): 572-582.

1. Introduction

The genus *Thymus* has over 350 species of fragrant perennial herbaceous plants and subshrubs, reaching a height of up to 40 cm. Within the family Labiate, which contains approximately 220 genera, the genus *Thymus* is one of the eight most important genera in terms of species, although this number fluctuates depending on the taxonomic perspective. The genus *Thymus* yields a variety of commercial items, including as essential oils, oleoresins, fresh and dried herbs, and landscape plants. The genus *Thymus* encompasses approximately 350 species, although only five of them have gained significant economic significance, albeit for different reasons. These species include *Thymus capitatus* (L.), which has recently been reclassified as *Thymbra capitata* (L.) Cav. (Hoffmanns and Link) (https://en.wikipedia.org/wiki/Thymbra_capitata) and is commonly known as Spanish oregano or conehead thyme. Another economically important species is *T. mastichina* L., also known as Spanish marjoram or mastic thyme. Additionally, *T. serpyllum* L., commonly referred to as wild thyme or mother-of-thyme, *T. vulgaris* L.,

known as common thyme, and *T. zygoides* L., referred to as Spanish thyme, have also achieved economic significance (El Ouariachi et al., 2011; Cutillas et al., 2018; Radi et al., 2021; Rahimi et al., 2022; Tomanić et al., 2022). While the essential oils derived from these species are commonly traded goods, thyme oil is mostly extracted from *T. zygoides*, but both *T. zygoides* and *T. vulgaris* serve as the primary sources for the dried and fresh herb (Lawrence et al., 2002). These plants belong to the family Lamiaceae and are naturally found in temperate climates across Europe, North Africa, and Asia (Uritu et al., 2018). The genus *Thymus* occupies a prominent place within the esteemed Lamiaceae family, also known as the Mint family. This botanical ancestry includes a variety of plants that have made significant contributions to numerous human endeavors due to their aromatic foliage and diverse applications (Mosavat et al., 2019). Among these, the genus *Thymus* stands out as a charismatic protagonist with a legacy spanning culinary, medicinal, and ornamental uses. *Thymus* species have intricately woven their aromatic threads into the fabric of international cuisine, which is at the core of its



significance (Honorato et al., 2023). Thyme leaves have enriched culinary experiences across cultures and continents by bestowing dishes with a range of flavors, from robust to delicate (Nair, 2023). Thyme leaves leave an indelible impression on the palette, whether they are utilized as a vital component in hearty stews, a fragrant seasoning for roasted meats, or a nuanced accent in salads. The adaptability of *Thymus* species extends beyond the kitchen, demonstrating their seamless incorporation into human existence. These plants have also left their impact on the field of herbal medicine, as their potential has received global recognition. Essential oils containing antibacterial, antiviral, and antioxidant compounds, such as thymol and carvacrol, are extracted from the leaves and petals of *Thymus* (Ansarifar and Farid, 2022; Kim et al., 2022; Morshdy et al., 2022). These qualities make treatments infused with Thyme useful for treating respiratory, digestive, and immune disorders (Mohammadi et al., 2018; Nabissi et al., 2018; Salehi et al., 2018; Taher et al., 2021). Through diffusers, massage oils, and fragrant products, the aromatic oils contribute to a calming atmosphere in aromatherapy and holistic wellness. In addition to their culinary and medicinal uses, *Thymus* species serve as cultural symbols. Thyme's aromatic qualities have made their way into rituals, festivities, and celebrations due to its widespread veneration as a symbol of courage, strength, and memory. Whether they are dusted on food or infused into oils, they impart both color and flavor. When used as groundcovers in landscapes, these plants also contribute to sustainable gardening by preventing soil erosion and enticing beneficial insects. Notably, Thyme's influence extends beyond conventional domains to include beekeeping. *Thymus* species generate nectar, which beekeepers use to produce aromatic thyme honey, which is prized for its flavor and potential health benefits (Alissandrakis et al., 2007; Rodríguez et al., 2021). This multifaceted (culinary, medicinal, cultural, and ecological) approach highlights the intrinsic value of *Thymus* species. In spite of their significance, however, accurate species identification and germplasm preservation present formidable obstacles. Given the intricacy of the *Thymus* genus, it can be difficult to identify specific species. Innovative DNA-based techniques, such as DNA barcoding, can provide accurate species identification, even among cryptic or closely related forms, to address this issue (Furan, 2023). To preserve the genetic diversity of *Thymus* species for future generations, germplasm preservation is of the utmost importance. Detailed genetic analyses disclose species-specific genetic markers, thereby facilitating reintroduction or cultivation efforts and aiding in the prevention of extinction (Joshi et al., 2004; Singh, 2020). In addition, DNA testing is essential for authenticating botanical items, ensuring the quality and authenticity of herbal, cosmetic, and aromatic products (Trindade, 2010; Polaiah et al., 2023). This verification procedure fosters confidence and reduces misrepresentation among

regulatory bodies, industries, and consumers. In the field of plant genetics, *Thymus* species are examined for enhanced characteristics such as flavor, aroma, and disease resistance. Researchers can utilize genetic markers to accelerate breeding programs, potentially resulting in novel cultivars that contribute to biodiversity and human welfare. A comprehensive comprehension of the ecological roles and characteristics of *Thymus* species facilitates sustainable harvesting, cultivation, and management practices, thereby securing the future of these resources. The existence of a universal barcode for animals has been shown; however, its use as a universal barcode for plants is limited due to its lower nucleotide replacement rate (Johnson et al., 2023). In order to produce DNA barcodes for plant species, researchers have investigated the use of plastid DNA sequences as a viable alternative. The utilization of DNA barcodes for the identification of plant specimens has been proposed as an effective, reliable, and uncomplicated pharmacognostic approach to address challenges associated with morphological identification ambiguity (Nongbet and Chrungoo, 2023). This study examines the genetic diversity of the *Thymus* genus using three essential chloroplast genes: *matK*, *rbcl*, and *psbA-trnH*. Each gene provides a distinct perspective, with *matK*'s adaptability to species-specific signals, *rbcl*'s stability providing a foundation for phylogenetic studies, and *psbA-trnH*'s dynamic variations facilitating differentiation. The integration of these genes produces a symphony of genetic information that resonates with species differentiation and sheds light on the intricate genetic tapestry of the *Thymus* genus. The overarching goal of this study is to improve species identification techniques and germplasm conservation procedures within the genus *Thymus*. Over the past few decades, a considerable number of researchers have made noteworthy advancements in the exploration and utilization of barcodes in plants. Additionally, scientists have carried out numerous phylogenetic analyses on medicinal and aromatic plants from diverse families or subfamilies. These studies have been conducted by various researchers, including Michel et al. (2016), Wang et al. (2017), Yu et al. (2021), Chinnkar and Jadhav (2023) Abdulrahman et al. (2023), and Jiang et al. (2023). We investigate the complex genetic markers of *Thymus* species and subspecies by employing DNA barcoding and phylogenetic analysis. Our findings reverberate throughout scientific research and practical applications, illuminating the central function of genetic exploration within the genus *Thymus*. This study advances our understanding of genetic diversity and provides tangible benefits by improving the accuracy of species identification using DNA-based methods. These findings not only empower regulators to uphold quality standards, but also enhance consumer confidence and the credibility of the industry. The genetic markers identified in our selected genes serve as the basis for personalized germplasm conservation strategies,

providing resource managers and conservationists with tools to protect the genetic diversity of *Thymus* species and subspecies. This effort contributes to the preservation of natural ecosystems and the establishment of plant populations able to adapt to fluctuating environmental conditions. Beyond individual sequences, our study reverberates as a genetic symphony that reflects the nuanced beauty and intricate complexity of the *Thymus* genus. DNA research of *Thymus* genus plant species' genetic diversity and linkages provides vital information. The study can add to the literature: Identification and Authentication; *Thymus* genus plants are identical in appearance, making identification and verification difficult. This study may help identify and verify plants by providing *Thymus* species DNA markers. The findings may help comprehend *Thymus*'s genetic diversity and establish conservation methods. *Thymus* plants are utilized in food, medicine, and cosmetics. This work may help the business and consumers employ DNA-based herbal product quality control methods. This discovery may help explain plant evolution and genetic variety. The study may help plant barcoding researchers find genomic areas that can identify *Thymus* species. This work will contribute to practical applications, scientific research, and conservation efforts for genetic diversity and verification of the *Thymus* genus plant. This can help plant scientists, botanists, conservationists, and industry representatives.

2. Materials and Methods

2.1. Nucleotide Sequences

In this investigation, data pertaining to gene loci as well as an intergenic spacer region were consolidated by utilizing information provided from the 2023 database. The researchers employed the NCBI nucleotide database to gather *Thymus* species belonging to the Lamiaceae family. The selection of plastid barcode locus genes (*matK*, *rbcl*) and one intergenic spacer (*psbA-trnH*) was based on their high suitability for this purpose. Furthermore, the MEGA11 software program was utilized to acquire concatenated sequences of *matK* + *psbA* and *rbcl* + *psbA*. Following a process of manual screening, nucleotide sequences of short length were removed, leaving behind a subset of sequences that underwent manual editing and trimming to guarantee proper alignment.

2.2. Sequence Alignment and Data Analysis

The main aim of this study was to investigate the species belonging to the *Thymus* genus within the Lamiaceae family. These species are frequently misidentified as a result of their same physical characteristics. The plastid DNA reference sequences *matK*, *rbcl*, and *psbA-trnH* were obtained from the National Center for Biotechnology Information (NCBI) website (<https://www.ncbi.nlm.nih.gov/>) in order to facilitate species identification. The sequencing data for the *matK*, *rbcl*, and *psbA-trnH* loci of each species were carefully examined and organized based on their gene regions in

order to ease comparisons. Additional examination was conducted on the sequencing data, with the utilization of MEGA11 software to ascertain the length of the aligned sequence, the various counts of nucleotides, the overall count of parsimony informative sites, and the mean GC content (Tamura et al., 2021). The study employed a pairwise genetic distance technique and phylogenetic tree-based analysis to assess the discriminatory power of the three selected barcode loci in differentiating across species. The process of Bayesian inference (BI) was carried out utilizing the MEGA11 model option. The T92 (Tamura 3 parameter) substitution model, which demonstrated the most optimal fit, was chosen for subsequent investigation. The Tamura 3-parameter distance model (T92) in MEGA 11 was employed in the pairwise genetic distance approach to compute both interspecific and intraspecific nucleotide divergence. The software program DNA Sequence Polymorphism version 5 (DNA SP v5) was employed to compute the number of polymorphic sites, genetic diversity indices, and neutrality tests, namely Fu's F_s 49 and Tajima's D_{50} (Sardar et al., 2023; Debrah et al., 2023). Distinct evolutionary pressures can cause various parts of DNA or amino acid sequences to alter, leading to the frequent utilization of the entire deletion option. In this work, the full deletion option was employed to exclude sites with gaps and missing data from the analysis of pairwise distances. Following the alignment and modification of all sequencing sites, a neighbor-joining (NJ) analysis was conducted using MEGA 11 software. The p-distance model was employed as the tree-based phylogenetic technique for this research. The evaluation of relationships involved the utilization of 1,000 bootstrap replicates. For each unique sequence site, a neighbor-joining tree was formed using the sequences from the three loci. Subsequently, the relationships were assessed.

3. Results

3.1. DNA Sequence Analysis

This study involved the analysis of DNA sequences from several notable species of the *Thymus* genus. The *matK* sequences of eight species, the *rbcl* sequences of eight species, and the *psbA-trnH* sequences of the same species were obtained from the NCBI nucleotide database (<https://www.ncbi.nlm.nih.gov/>). The combined sequences of the regions under investigation were collectively assessed. Following the process of trimming and editing, the determined lengths of *matK*, *rbcl*, and *psbA-trnH* were found to be 6.261 bp, 4.549 bp, and 3.032 bp, respectively. Additionally, the combined lengths of the concatenated sequences *matK+psbA* and *rbcl+psbA* were calculated to be 9.293 bp and 7.581 bp, respectively. Table 1 presents the overall mean frequencies of nucleotide bases, the nucleotide sequences, and the distribution of the four bases in potential nucleotide sequences identified across various codon coding sites. Table 2 presents the average number of identical pairs (ii) observed in possible nucleotide

sequences. Table 2 provides a comprehensive account of the transitional (si) and transversional (sv) pairings of nucleotide sequences. A potential correlation could exist between the occurrence of transitional and transversional bases within genetic sequences and the observed variations among different species. Table 3 presents an examination of potential polymorphic locations within the nucleotide sequence. The *rbcl*

sequence has the lowest number of mutation sites (1.7%) among all the individual and combined sequences. Conversely, the *matK* sequence demonstrates the highest rate of conservative sites (99.1%). The *psbA* sequence has a higher proportion of mutation sites (50.4%) and a lower proportion of conservative sites (38.3%) in comparison to the *psbA* concatenated sequences it aligns with.

Table 1. The nucleotide base frequencies analysis of candidate nucleotide sequences in *Thymus* species.

| Sequences | Base content | | | | | | | | | | |
|-------------|--------------|------|------|------|------|------|------|------|------|------|------|
| | A | T | C | G | GC | AT-1 | GC-1 | AT-2 | GC-2 | AT-3 | GC-3 |
| <i>matK</i> | 29.1 | 36.0 | 18.3 | 16.6 | 34.9 | 66.9 | 32.9 | 67.8 | 32.2 | 60.7 | 39.3 |
| <i>rbcl</i> | 27.3 | 28.8 | 20.9 | 22.9 | 43.8 | 43.6 | 56.4 | 55.6 | 44.4 | 69.2 | 30.8 |

Table 2. The analysis of nucleotide pair frequencies of candidate nucleotide sequences of *Thymus* species. ii Identical Pairs, si Transitionsal Pairs, sv Transversional Pairs, R si/sv.

| Sequence | ii | | | | si | | | | sv | | | | R | | | |
|------------------|-----|-----|-----|-----|-----|-----|-----|-----|-----|-----|-----|-----|-----|-----|-----|------|
| | Avg | 1st | 2nd | 3rd | Avg | 1st | 2nd | 3rd | Avg | 1st | 2nd | 3rd | Avg | 1st | 2nd | 3rd |
| <i>matK</i> | 718 | 240 | 238 | 240 | 5 | 1 | 2 | 1 | 2 | 1 | 1 | 0 | 1.9 | 1.3 | 2.0 | 2.9 |
| <i>rbcl</i> | 532 | 178 | 178 | 176 | 2 | 0 | 0 | 2 | 1 | 0 | 0 | 0 | 2.5 | 0.0 | 1.4 | 12.5 |
| <i>matK+psbA</i> | 955 | 317 | 318 | 320 | 40 | 12 | 14 | 15 | 44 | 16 | 16 | 12 | 0.9 | 0.8 | 0.9 | 1.2 |
| <i>rbcl+psbA</i> | 776 | 260 | 261 | 256 | 44 | 12 | 14 | 17 | 47 | 17 | 16 | 14 | 0.9 | 0.7 | 0.9 | 1.2 |

Table 3. The analysis of variation of candidate barcode sequences in *Thymus* species.

| Sequence | Conserved site | Variable site | Parsimony-informative site | Sigon site |
|--------------------|----------------|---------------|----------------------------|------------|
| <i>matK</i> | 846 (94.6%) | 28 (3.1%) | 3 | 25 |
| <i>rbcl</i> | 615 (89.9%) | 12 (1.7%) | 2 | 10 |
| <i>psbA</i> | 193 (38.3%) | 254 (50.4%) | 117 | 125 |
| <i>matK + psbA</i> | 1059 (74.3%) | 278 (19.5%) | 92 | 177 |
| <i>rbcl + psbA</i> | 753 (65.3%) | 295 (25.5%) | 111 | 165 |

3.2. Genetic Diversity

The presence of genetic variation based on species differences is inferred due to the utilization of data derived from many species within the same genus for study. The genetic diversity indices presented in Table 4 are derived via calculations involving pairwise nucleotide differences and nucleotide diversity. The validity of these indices was verified through the application of Tajima's neutrality test. According to the cumulative Eta value, the *matK+psbA* sequences exhibit the highest level of genetic variety, characterized by a collective count of 178 mutations. When comparing the *rbcl* sequences, it is observed that there are only six distinct mutation changes in total. Both neutrality tests yielded results indicating that there were substantial differences across all sequences. However, only a limited number of sequences exhibited significant differences based on the probability value (P-value) obtained from Fu's Fs test and Tajima's D test (Table 4). This finding highlights the importance of genetic variety. Comparable to the Tajima test statistic, namely the D value, which is utilized to assess neutrality in genetic sequences, the genetic variation observed in *rbcl* sequences exhibits a modest

increase, measuring at -0.63262. Nevertheless, the *matK* region exhibits a limited number of polymorphisms within the designated regions, which might be attributed to its high conservative site percentage of 94.6% (Table 3). In the case of combined sequences, the *rbcl* sequences exhibited a higher degree of genetic variation (-0.63262) compared to the *matK* sequence, which had values reaching up to -1.65200. Furthermore, the observed difference in genetic variation between the two sequences was found to be statistically insignificant, as indicated by the P value. The *rbcl* sequences demonstrate the highest Fu's Fs value for sequence variation (0.01238), as indicated in Table 4. In comparison to the other three region sequences, the *rbcl* sequence is the only one that exhibits a distinct value (0.01238).

3.3. Phylogenetic Analysis

In this study, we conducted an analysis to determine the evolutionary relationships across species by utilizing the *matK*, *rbcl*, *psbA-trnH*, and concatenated sequences. The MEGA 11 software was employed, employing the neighbor-joining method and the T92 (Tamura 3 parameter) model. In light of the topological

arrangement of the evolutionary tree, the genes *matK*, *rbcl*, and *psbA* present potential for investigation, although their utility in species identification within discrete subfamilies may be limited. Hence, the concatenated sequences of gene loci, namely *matK+psbA*, and *rbcl+psbA*, were assessed in order to determine their overall efficacy for identification purposes. The phylogenetic outcomes obtained from

both unique gene sections and an intergenic spacer exhibited a clearly visible divergence. Phylogenetic classifications based on concatenated data have also observed similar occurrences, wherein the findings from both two essential gene regions and concatenated data, as well as intergenic spacer data, are presented in Figures 1, 2, 3, 4, and 5.

Table 4. Genetic diversity calculation of *Thymus* species based on candidate barcode sequences by the DnaSP v5 software. *Eta* Total number of mutations, *n* number of sequences, *k* Average number of nucleotide difference, *S* Number of segregating sites, θ nucleotide substitution rate, π nucleotide diversity, *Hd* haplotype diversity, *Fu's Fs* is variance of haplotypes diversity, *D* is the Tajima test statistic.

| Sequences | n | Nucleotide diversity | | | | | π | Neutrality tests | | | |
|--------------------|---|----------------------|--------|-----|-------|----------|---------|------------------|---------|----------|---------|
| | | S | k | Eta | Hd | θ | | Fu's Fs | P-value | D | P-value |
| <i>matK</i> | 8 | 21 | 5.536 | 21 | 1.000 | 0.014061 | 0.00961 | 0.00391 | > 0.10 | -1.65200 | >0.05 |
| <i>rbcl</i> | 8 | 8 | 2.000 | 6 | 0.893 | 0.004485 | 0.00388 | 0.01238 | >0.10 | -0.63262 | >0.10 |
| <i>matK + psbA</i> | 8 | 146 | 57.071 | 178 | 1.000 | 0.073223 | 0.07422 | 0.00391 | > 0.10 | -0.92259 | >0.10 |
| <i>rbcl + psbA</i> | 8 | 128 | 53.571 | 165 | 1.000 | 0.070624 | 0.0764 | 0.00391 | > 0.10 | -0.86471 | >0.10 |

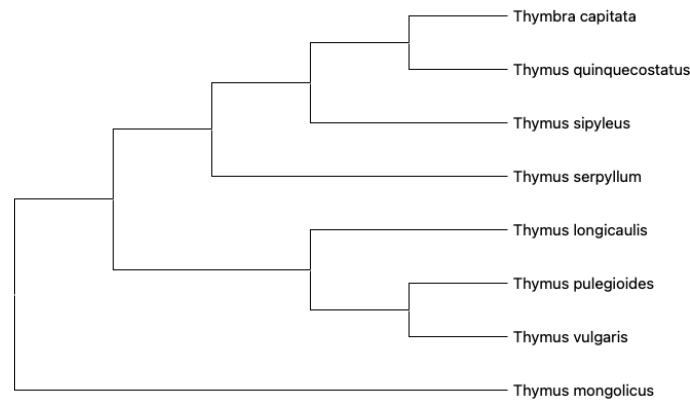


Figure 1. *Thymus* species NJ tree is derived from a study of the cpDNA *matK* sequence using the Tamura 3 model. The branches represent the 1000 bootstrap replications test.

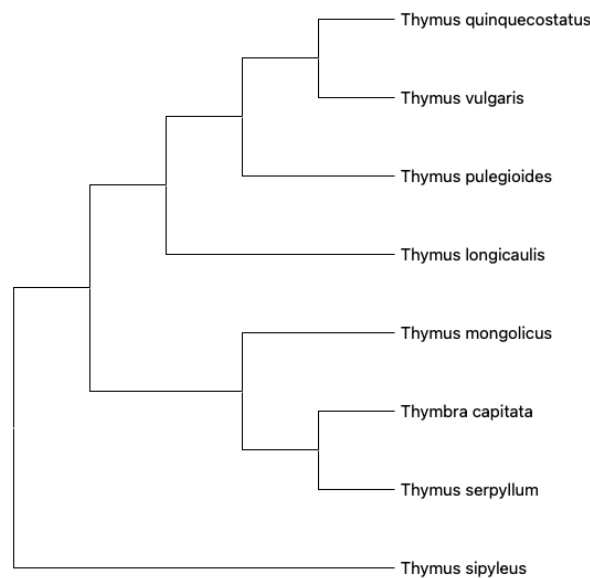


Figure 2. *Thymus* species NJ tree is derived from a study of the cpDNA *rbcl* sequence using the Tamura 3 model. The branches represent the 1000 bootstrap replications test.

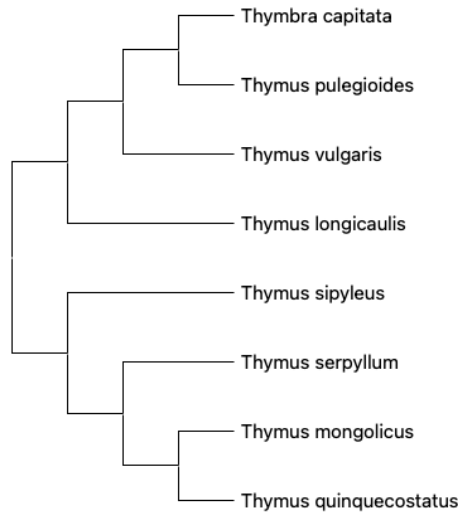


Figure 3. Thymus species NJ tree is derived from a study of the cpDNA psbA sequence using the Tamura 3 model. The branches represent the 1000 bootstrap replications test.

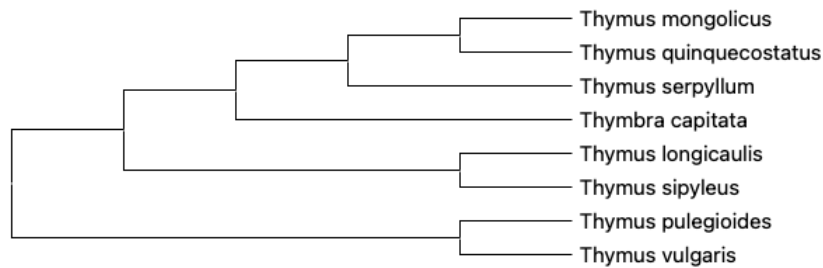


Figure 4. Thymus species NJ tree is derived from a study of the concatenated cpDNA matK+psbA sequence using the Tamura 3 model. The branches represent the 1000 bootstrap replications test.

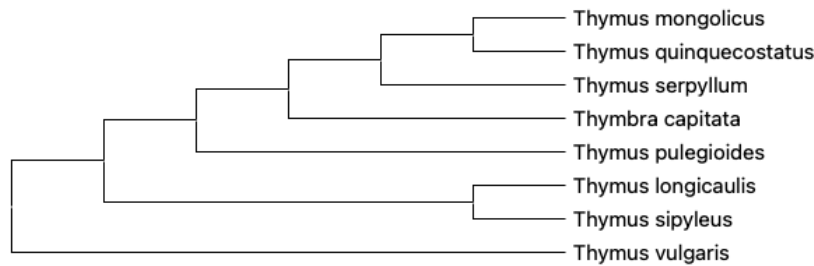


Figure 5. Thymus species NJ tree is derived from a study of the concatenated cpDNA rbcL+psbA sequence using the Tamura 3 model. The branches represent the 1000 bootstrap replications test.

3.4. Analysis of Barcoding Gap

According to Li et al. (2021), it is necessary for the interspecific genetic variance to exceed the intraspecific genetic variation in order to establish a suitable DNA barcoding sequence for the purpose of species identification. In order to accurately assess the individual chloroplast genes and combined sequences in thymus species and validate the suitability of potential sequences, an examination of the barcoding gap was conducted using frequency distribution. Among the three barcoding loci utilized, it is shown that the *matK* locus exhibits the longest aligned sequence length, measuring 6.261 base pairs (bp). Subsequently, the *rbcL* locus demonstrates a length of 4.549 bp, while the *psbA-trnH* locus possesses a length of 3.032 bp. The gene *psbA* exhibits the greatest number of parsimony-informative sites, with a count of 117, depending on the specific

dataset. Following *psbA*, *matK* demonstrates 3 parsimony-informative sites, while *rbcL* exhibits 2. Within the genus *Thymus*, the *psbA-trnH* region exhibits the greatest proportion of variant sites (50.4%), with *matK* (3.1%) and *rbcL* (1.7%) following suit. The computation of Tamura's 3-parameter model-based genetic distances between intra and interspecific species was performed using MEGA 11. Within the *Thymus* species, the *matK+psbA* gene combination exhibits the highest level of intraspecific divergence, with a distance of 0.10%. Conversely, the *rbcL* gene does not exhibit any variation at the intraspecific level, as indicated in Table 5. The interspecific distance among thymus species is found to be highest in the combined sequence *rbcL+psbA* (0.13%) region. However, it is worth noting that the *rbcL* region does not exhibit any significant variations in interspecific distance levels.

Table 5. Summary of the pairwise intraspecific and interspecific distances in the barcode loci of *Thymus* species

| Barcode locus | Intraspecific distances (%) | | Overall Mean | Interspecific distances (%) | |
|------------------|-----------------------------|---------|--------------|-----------------------------|---------|
| | Minimum | Maximum | | Minimum | Maximum |
| <i>matK</i> | 0 | 0.01 | 0.01 | 0 | 0.01 |
| <i>rbcl</i> | 0 | 0 | 0.004 | 0 | 0 |
| <i>matK+psbA</i> | 0.01 | 0.10 | 0.08 | 0.02 | 0.08 |
| <i>rbcl+psbA</i> | 0 | 0.09 | 0.08 | 0.1 | 0.13 |

4. Discussion

The examination of genetic links and diversity among species has significant importance in comprehending evolutionary processes, ecological interactions, and conservation endeavors. The examination of DNA sequences is a valuable technique for elucidating these complexities (Coissac et al., 2016; Amiteye, 2021). The Lamiaceae family has a total of roughly 7173 species that are geographically dispersed over the Mediterranean basin and Central Asia. The aforementioned botanical group plays a significant role as a primary supplier of fragrant oils and secondary metabolites. In order to ensure the safe utilization of medicinal plants belonging to the Lamiaceae family, it is necessary to possess a reliable methodology for verifying the authenticity of species (Thakur et al., 2021). This study aims to investigate the *Thymus* genus, which has a collection of noteworthy species, in order to examine the genetic framework that influences their existence. Our objective is to utilize the stored information within the DNA sequences to elucidate the genetic links within the *Thymus* genus and reveal the fundamental mechanisms that contribute to their variety. The examination of DNA sequences has significantly transformed our capacity to examine the genetic foundations of living organisms. By analyzing the sequence of nucleotides in DNA, valuable information may be obtained on the molecular patterns that determine the traits and attributes of living creatures (Li et al., 2021). This methodology enables the investigation of the common lineage and evolutionary trajectories of organisms, while also providing insights into the underlying processes accountable for their unique characteristics and adaptations (Techen et al., 2014; Michel et al., 2016; Raskoti and Ale, 2021; Chen et al., 2023; Hua, et al., 2023). The *Thymus* genus, which comprises a variety of species exhibiting a wide array of ecological and physical characteristics, is an intriguing platform for genetic investigation. Thyme, a widely recognized fragrant herb, possesses not only culinary value but also provides unique insights into the development of plants (Aneva et al., 2022; Halat et al., 2022; Kim et al., 2022). Through the analysis of DNA sequences from many species within this genus, our objective is to elucidate the underlying connections that unite these plants and differentiate them from other related organisms. This study represents a notable contribution to the field of barcoding research in the Lamiaceae family, since it encompasses a substantial sample size and employs various coding loci (*matK*, *rbcl*,

and *psbA*) in combination. The primary focus of this investigation is directed towards species belonging to the *Thymus* genus. The results obtained from conducting sequence analysis on the average GC content indicate that the GC content of *Thymus* candidate sequences is notably lower than AT content and significantly lower than the GC content observed in approximately 50% of common angiosperms. The obtained results are consistent with the findings reported in Li et al. (2021)'s investigation on orchids and the outcomes of Furan's research conducted in 2023 on *Origanum* species. All of the regions that were looked at, including the gene regions, the spacer regions, and the data from all of them together, show a greater variety of haploid types and a relatively low variety of nucleotides. This suggests that potential sequences have polymorphism. DNA barcoding is a widely employed technique for species identification, which involves the sequencing of a specific and standardized section of DNA. Nevertheless, an agreement has not yet been reached about the appropriate locations to be utilized for the purpose of barcoding terrestrial plant species. According to Hollingworth et al. (2009), the Consortium for the Barcode of Life (CBOL) advocates for the use of *matK* and *rbcl* as universally accepted barcodes for the plant kingdom. This study utilizes DNA sequences obtained from certain areas of the genome, including *matK*, *rbcl*, and *psbA-trnH*, as a means to examine the *Thymus* genus. These areas, renowned for their informative characteristics, enable us to get insights into the genetic variants that have accrued over a span of time. Through the process of sequence analysis, our objective is to elucidate the genetic interconnections between various species, unveil intricate patterns of biodiversity, and acquire a more profound comprehension of the factors that have influenced the evolutionary trajectory of the *Thymus* genus. The results obtained from the analysis of the *matK* gene region were found to be distinct from those obtained from the analysis of the *rbcl* gene region, as shown by phylogenetic analyses. Nevertheless, the findings derived from the *psbA* intergenic region corroborated the outcomes of both gene sections and exhibited a higher degree of concordance with *rbcl*. The utilization of concatenated data in phylogenetic analysis has contributed to the enhancement of result dependability. Upon examination of the phylogenetic perspective derived from the aforementioned data, it was noticed that the outcomes acquired from the *matK+psbA* analysis closely aligned with those obtained from the *rbcl* gene

region analysis. The proposition that the discriminatory capacity of the *matK* region is comparatively limited in thymus species aligns with the findings of Furan (2023)'s investigation on origanum species. The MEGA software does not include gap sites in the MP analysis. However, there are three distinct approaches to handling these gap sites. One approach entails the entire exclusion of some websites from the study of data. The "complete deletion" option is frequently used in light of the diverse evolutionary pressures exerted on distinct segments of DNA or amino acid sequences. Nevertheless, in cases when the impact of a gap on the number of nucleotides (or amino acids) is minimal and the gaps are distributed in a very haphazard manner, it is plausible to consider including these locations as instances of missing data. As a result, the presence of gaps and missing data is not considered when calculating the length of a tree. Partial deletion, as a third alternative, involves the removal of gaps that constitute a proportion of the data below a predetermined threshold (unambiguous). The focus of the study is to differentiate species within a certain genus. The data collected from different areas vary in terms of the number of individuals used for species discrimination within the genus. Consequently, each gene region plays a role in the development of separate branches. Coding areas are predominantly utilized in phylogenetic barcoding investigations due to their possession of the requisite genetic information for protein synthesis and their presumed stability and functional significance. The identification of nucleotide sequences inside these specific locations can serve as a valuable tool in elucidating genetic variances among species and facilitating the determination of phylogenetic connections. Noncoding regions, also known as non-coding DNA segments, are sections of DNA that do not possess the ability to code for proteins. The nucleotide sequences inside these areas have the potential to undergo fast alterations, hence providing significant phylogenetic resolution in certain cases. However, noncoding areas possess significant limitations. For example, rapid evolution across many groups of organisms might provide difficulties in achieving consistent outcomes in phylogenetic analysis. Furthermore, the process of resolving and aligning sequences in these locations may be a complex challenge. Therefore, coding areas are commonly selected as the best option for conducting phylogenetic barcoding studies. However, depending on the particular group of organisms and the aims of the research, it may also be necessary to include noncoding areas. The *rbcl* gene is responsible for encoding the large subunit of Rubisco, a pivotal enzyme involved in the process of photosynthesis in plants. The *rbcl* gene is present in the DNA of chloroplasts and serves as a valuable tool for investigating evolutionary connections across plant species. The *rbcl* gene is a gene region that has a high degree of conservation across plant species and is extensively employed in phylogenetic investigations. This

study utilized variable site data between sequences to evaluate the suitability of *rbcl*, *psbA*, and *matK* sequences for identifying the Thymus genus, species, and subspecies. The findings indicate that the *rbcl* and *psbA* sequences outperformed the *matK* sequences in this regard. Furthermore, combining the sequences may offer an effective means of distinguishing Thymus species and subspecies, provided that the objectives of the study and the specific species under investigation are taken into consideration. The *matK* sequence area is commonly employed in combination with other variables to classify plant species (Wang et al., 2017). Additionally, *matK* alone has been identified as a potential barcode for several plant species (Hollingsworth, 2011; Abdulrahman et al., 2023). Based on the findings of this study, it is recommended to employ a combination of several areas and their concatenated data. The investigation revealed that the *rbcl* sequence had the lowest number of mutation sites. Nevertheless, despite the relatively low variability and resolution, it is necessary to acknowledge the significance of the conservative nature of the *rbcl* data for Thymus species and the consequent reliability of the obtained results in the context of this investigation. The *psbA* sequence exhibited the highest proportion of mutation sites and the lowest proportion of conserved sites in comparison to the other sequences. The utilization of species-specific DNA barcodes of Thymus was effectively employed to discriminate between different species based on single nucleotide polymorphism (SNP) sites. The concatenation of sequences exhibited a higher level of distinction at the species level compared to chloroplast genes. This disparity can perhaps be attributed to the fact that concatenated sequences offer a greater number of mutation sites and single nucleotide polymorphism (SNP) sites. Variations in the specificities of gene combinations were observed among Thymus plants. When comparing the effectiveness of *matK*, *rbcl*, and *psbA* as genetic markers, it has been shown that the concatenation of two sequences (*matK* + *psbA*, *rbcl* + *psbA*) provides distinct and specific distinguishing characteristics for Thymus species. In summary, our research introduces a unique approach to accurately and effectively discerning Thymus species by using chloroplast DNA. This approach serves as a complementary way to the current procedures employed in the identification of thymus plants. This work aims to investigate DNA-level variations by employing several chloroplast gene areas and analyzing their concatenated data. This methodology has the potential to serve as a novel method for assessing the genetic affinities across Thymus species through the utilization of DNA barcodes. Consequently, it establishes a foundation for the preservation, assessment, inventive use, and safeguarding of Thymus germplasm resources.

4. Conclusion

In the realm of biological exploration, understanding genetic relationships and diversity among species holds paramount importance, offering insights into evolutionary mechanisms, ecological dynamics, and conservation strategies. DNA sequence analysis stands as a powerful tool to unravel these intricate phenomena (Coissac et al., 2016; Amiteye, 2021). Within the vast Lamiaceae family, with its distribution spanning the Mediterranean basin and Central Asia, a mosaic of approximately 7173 species thrives. These botanical entities not only play a pivotal role in providing fragrant oils and secondary metabolites but also hold implications for medicinal applications within a framework of authenticity verification (Thakur et al., 2021). Our study delves into the *Thymus* genus, a collection of noteworthy species, aiming to unravel the genetic underpinnings shaping their existence. Leveraging the genetic information encoded in DNA sequences, we've embarked on a journey to illuminate the genetic connections within the *Thymus* genus and unearth the fundamental mechanisms underpinning its diversity. DNA sequence analysis has revolutionized our ability to dissect genetic foundations, shedding light on molecular blueprints that define the intricate traits of living beings (Li et al., 2021). This technique allows us to decipher common lineages, evolutionary trajectories, and distinctive adaptations that characterize each species (Techen et al., 2014; Michel et al., 2016; Raskoti and Ale, 2021; Chen et al., 2023; Hua et al., 2023). The *Thymus* genus, encompassing a spectrum of species with diverse ecological and physical attributes, emerges as an intriguing canvas for genetic exploration. Thyme, a fragrant herb with both culinary and scientific significance, provides unique insights into plant development (Aneva et al., 2022; Hamoudi et al., 2022; Kim et al., 2022). By unraveling DNA sequences across various species within this genus, our quest is to unravel the threads that connect these plants while distinguishing them from their botanical peers. Our study is a big step forward in barcoding research for the Lamiaceae family. It has a large sample size and a mix of coding loci (*matK*, *rbcl*, and *psbA*). This exploration concentrates its lens on the *Thymus* genus, as the results of average GC content analysis highlight a distinctive pattern. The GC content of *Thymus* candidate sequences stands in contrast to AT content and deviates markedly from the GC content observed in approximately 50% of common angiosperms. Our findings resonate with Guo et al.'s orchid investigation and Furan's study on *Origanum* species conducted in 2023, aligning across gene and spacer regions. These findings collectively underscore the presence of polymorphism within potential sequences. DNA barcoding, a widely adopted technique for species identification, involves sequencing specific standardized DNA sections. Nonetheless, consensus on optimal barcode regions for terrestrial plant species remains elusive. According to Hollingworth et al. (2009), the Consortium for the Barcode of Life (CBOL) advocates

for *matK* and *rbcl* as universally accepted barcodes. Our study employs sequences from *matK*, *rbcl*, and *psbA-trnH* regions to probe the *Thymus* genus. These regions, recognized for their informativeness, facilitate a journey into the genetic diversity accumulated over time. Through this sequence analysis, our endeavor is to unveil genetic interconnections among species, decipher intricate biodiversity patterns, and gain a profound understanding of the forces steering the evolutionary trajectory of the *Thymus* genus. Phylogenetic analyses demonstrate distinctions between *rbcl* and *matK* gene regions, while *psbA*'s intergenic region reinforces both gene outcomes and aligns more closely with *rbcl*. In our pursuit of understanding genetic affinities, the concatenation of sequences emerges as a means to enhance the reliability of results. The *matK+psbA* analysis's congruence with *rbcl* outcomes parallels Furan (2023)'s findings, suggesting limited discriminatory capacity in *Thymus* species. Although the MEGA software doesn't incorporate gap sites in the MP analysis, strategies for handling gaps complete deletion, partial deletion, and inclusion as missing data augment data interpretation. Coding regions get a lot of attention in phylogenetic barcoding because of how stable and important they are for function. This helps find genetic differences between species and show their phylogenetic connections. While noncoding regions offer rapid alteration potential and resolution, their variability across organism groups poses challenges in maintaining analytical consistency. The *rbcl* gene, pivotal in photosynthesis, provides evolutionary insights across plant species. Our investigation employs variable site data to evaluate *rbcl*, *psbA*, and *matK* for thymus identification. Results indicate the potential of *rbcl* and *psbA* in species differentiation. As we conclude, our research introduces a novel approach to distinguishing *Thymus* species through chloroplast DNA, enriching the palette of plant identification methods. This method, based on a composite of chloroplast gene areas, has the potential to revolutionize genetic affinity assessment across *Thymus* species using DNA barcodes. In sum, this study forms a solid foundation for the preservation, assessment, and innovative utilization of *Thymus* germplasm resources, ensuring both the safeguarding of botanical diversity and informed conservation efforts.

Author Contributions

The percentage of the author contributions is presented below. The author reviewed and approved the final version of the manuscript.

| | M.A.F. |
|-----|--------|
| C | 100 |
| D | 100 |
| S | 100 |
| DCP | 100 |
| DAI | 100 |
| L | 100 |
| W | 100 |
| CR | 100 |
| SR | 100 |
| PM | 100 |
| FA | 100 |

C=Concept, D= design, S= supervision, DCP= data collection and/or processing, DAI= data analysis and/or interpretation, L= literature search, W= writing, CR= critical review, SR= submission and revision, PM= project management, FA= funding acquisition.

Conflict of Interest

The author declared that there is no conflict of interest.

Ethical Consideration

Ethics committee approval was not required for this study because of there was no study on animals or humans.

References

Abdulrahman SS, Daştan SD, Shahbaz SE, Selamoglu Z. 2023. Phylogenetic analysis of Prunus genus using nuclear and chloroplast gene markers as a bioorganic structure profiling. *J Mol Struct*, 1284: 135300. Doi: 10.1016/j.molstruc.2023.135300.

Alissandrakis E, Tarantilis PA, Harizanis PC, Polissiou M. 2007. Comparison of the volatile composition in thyme honeys from several origins in Greece. *J Agri Food Chem*, 55(20): 8152-8157. DOI: 10.1021/jf071442y.

Amiteye S. 2021. Basic concepts and methodologies of DNA marker systems in plant molecular breeding. *Heliyon*, 7(10): 202. DOI: 10.1016/j.heliyon.2021.e08093.

Aneva I, Zhelev P, Bonchev G, Boycheva I, Simeonova S, Kancheva D. 2022. DNA Barcoding Study of Representative Thymus Species in Bulgaria. *Plants*, 11(3): 270. DOI: 10.3390/plants11030270.

Ansarifar E, Moradinezhad F. 2022. Encapsulation of thyme essential oil using electrospun zein fiber for strawberry preservation, *Chem Biol Techn Agri*, 9: 2. DOI: 10.1186/s40538-021-00267-y.

Chen S, Yin X, Han J, Sun W, Yao H, Song J, Li X. 2023. DNA barcoding in herbal medicine: retrospective and prospective. *J Pharm Anal*, 13(5): 431-441. DOI: 10.1016/j.jpha.2023.03.008.

Chinnkar M, Jadhav P. 2023. Evaluating DNA barcoding using five loci (matK, ITS, trnH- psbA, rpoB, and rbcL) for species identification and phylogenetic analysis of Capsicum frutescens. *J Appl Biol Biotech*, 11(3): 97103. DOI: 10.7324/JABB.2023.57526.

Coissac E, Hollingsworth PM, Lavergne S. 2016. From barcodes

to genomes: extending the concept of DNA barcoding. *Mol Ecol*, 25: 423-1428. DOI: 10.1111/mec.13549.

Cutillas AB, Carrasco A, Gutierrez RM, Tomas V, Tudela J. 2018. Thymus mastichina L. essential oils from Murcia (Spain): Composition and antioxidant, antienzymatic and antimicrobial bioactivities. *PLoS ONE*, 13(1): e0190790. DOI: 10.1371/journal.pone.0190790.

Debrah I, Ochwedo KO, Otambo WO, Machani MG, Mago- mere EO, Onyango SA, Zhong D, Amoah LE, Githeko AK, Afrane YA, Yan G. 2023. Genetic diversity and population structure of anopheles funestus in Western Kenya based on mitochondrial DNA marker COII. *InSects*, 14: 273. DOI: 10.3390/insects14030273.

El Ouariachi EM, Paolini J, Bouyanzer A, Tomi P, Hammouti B, Salghi R, Majidi L, Costa J. 2011. Chemical composition and antioxidant activity of essential oils and solvent extracts of Thymus capitatus (L.) Hoffmanns and link from Morocco. *J Medic Plants Res*, 5: 5773-5778.

Furan MA. 2023. Species identification and germplasm conservation of origanum based on chloroplast genes. *Genet Resour Crop Evol*, DOI: 10.1007/s10722-023-01679-5.

Hammoudi Halat D, Krayem M, Khaled S, Younes S. 2022. A Focused Insight into Thyme: Biological, Chemical, and Therapeutic Properties of an Indigenous Mediterranean Herb Nutrients, 14(10): 2104. DOI: 10.3390/nu14102104.

Hollingsworth PM, Forrest LL, Little DP. 2009 A DNA barcode for land plants. *PNAS*, 106: 12794-12797. DOI: 10.1073/pnas.0905845106.

Honorato AC, Nohara GA, Assis RMA, Maciel JFA, Carvalho AA, Pinto JEBP, Bertolucci SKV. 2023. Colored shade nets and different harvest times alter the growth, antioxidant status, and quantitative attributes of glandular trichomes and essential oil of Thymus vulgaris L. *J Appl Res Medic Arom Plants*, 35: 100474. DOI: 10.1016/j.jarmap.2023.100474.

Hua Z, Jiang C, Song S, Tian D, Chen Z, Jin Y, Zhao Y, Zhou J, Zhang Z, Huang L, Yuan Y. 2023. Accurate identification of taxon-specific molecular markers in plants based on DNA signature sequence. *Mol Ecol Resour*, 23: 106-117. DOI: 10.1111/1755-0998.13697.

Jiang Y, Zhu C, Wang S, Wang F, Sun Z. 2023. Identification of three cultivated varieties of Scutellaria baicalensis using the complete chloroplast genome as a super-barcode. *Sci Rep*, 13: 5602. DOI: 10.1038/s41598-023-32493-9.

Johnson MS, Venkataram S, Kryazhimskiy S. 2023. Best practices in designing, sequencing, and identifying random DNA barcodes. *J Mol Evol*, 91: 283-280. DOI: 10.1007/s00239-022-10083-z.

Joshi K, Chavan P, Warude D, Patwardhan B. 2004. Molecular markers in herbal drug technology. *Current Sci*, 159-165.

Kim M, Sowndhararajan K, Kim S. 2022. The chemical composition and biological activities of essential oil from Korean native thyme Bak-Ri-Hyang (Thymus quinquecostatus Celak.). *Molecules*, 27(13): 4251. DOI: 10.3390/molecules27134251.

Kryvtsova M, Hrytsyna M, Salamon I, Skybitska M, Novykevuch O. 2022. Chemotypes of Species of the Genus Thymus L. in Carpathians region of Ukraine their essential oil qualitative and quantitative characteristics and antimicrobial activity. *Horticulturae*, 8(12): 1218. DOI: 10.3390/horticulturae8121218.

Lawrence BM, Tucker AO. 2002 The genus Thymus as a source of commercial products. Taylor & Francis Group, Hamburg Germany, pp: 11.

Li H, Xiao W, Tong T, Li Y, Zhang M, Lin X, Zou X, Wu Q, Guo X. 2021. The specific DNA barcodes based on chloroplast genes

- for species identification of Orchidaceae plants. *Sci Rep*, 11: 1424. DOI: 10.1038/s41598-021-81087-w.
- Michel CI, Meyer RS, Taveras Y, Molina J. 2016. The nuclear internal transcribed spacer (ITS2) as a practical plant DNA barcode for herbal medicines. *J Appl Res Med Aromat Plants*, 3: 94-100. DOI: 10.1016/j.jarmap.2016.02.002.
- Mohammadi A, Mahjoub S, Ghafarzadegan K, Nouri HR. 2018. Immunomodulatory effects of Thymol through modulation of redox status and trace element content in experimental model of asthma. *Biomed Pharmacother*, 105: 856-861, DOI: 10.1016/j.biopha.2018.05.154.
- Morshdy AEMA, El-tahlawy AS, Qari SH, Qumsani AT, Bay DH, Sami R, Althubaiti EH, Mansour AMA, Aljahani AH, Hafez AE-SE, Mohmoud AFA, Bayomi RME, Hussein MA. 2022. Antibiofilms' activity of garlic and thyme essential oils against *Salmonella typhimurium*. *Molecules*, 27(7): 2182. DOI: 10.3390/molecules27072182.
- Mosavat N, Golkar P, Youseffard M, Javed R. 2019. Modulation of callus growth and secondary metabolites in different *Thymus* species and *Zataria multiflora* micropropagated under ZnO nanoparticles stress, *Biotechnol Appl Biochem*, 66: 316-322. DOI: 10.1002/bab.1727.
- Nabissi M, Marinelli O, Morelli MB, Nicotra G, Iannarelli R, Amantini C, Santoni G, Maggi F. 2018. Thyme extract increases mucociliary-beating frequency in primary cell lines from chronic obstructive pulmonary disease patients, *Biomedic Pharmacother*, 105: 1248-1253. DOI: 10.1016/j.biopha.2018.06.004.
- Nair KP. 2023. Thyme. In: a compendium of unique and rare spices. Springer Cham, pp: 85-92. DOI: 10.1007/978-3-031-20249-0_8.
- Nongbet A, Chrungoo NK. 2023. Distribution mapping and diversity assessment of *Ilex venulosa* from meghalaya using internal transcribed spacer regions, *matK* and *rbcl*. In: Uppaluri RVS, Rangan L (eds) Conservation of biodiversity in the North Eastern States of India. Springer, Singapore, pp: 83-87. DOI: 10.1007/978-981-99-0945-2_5.
- Polaiah AC, Damor PR, Reddy RN, Manivel P, Shivakumara KT, Suthar MK, Thondaiman V, Manjesh GN, Bindu KH, Kumar J. 2023. Development of genomic SSR markers in *Gymnema sylvestre* (Retz.) R.Br. ex Sm. using next generation DNA sequencing and their application in genetic diversity analysis. *J Appl Res Med Aromat Plants*, 34: 100455. DOI: 10.1016/j.jarmap.2022.100455.
- Radi FZ, Bouhrim M, Mechchate H, Al-Zahrani M, Qurtam AA, Aleissa AM, Drioiche A, Handaq N, Zair T. 2021. Phytochemical analysis, antimicrobial and antioxidant properties of *Thymus zygis* L. and *Thymus wilddenowii* Boiss. essential oils. *Plants*, 11(1): 15. DOI: 10.3390/plants11010015.
- Rahimi A, Mohammadi MM, Moghaddam SS, Heydarzadeh S, Gitari H. 2022. Effects of stress modifier biostimulants on vegetative growth, nutrients, and antioxidants contents of garden thyme (*Thymus vulgaris* L.) under water deficit conditions. *J Plant Growth Regul*, 41: 2059-2072. DOI: 10.1007/s00344-022-10604-6.
- Raskoti BB, Ale R. 2021. DNA barcoding of medicinal orchids in Asia. *Sci Rep*, 11: 23651. DOI: 10.1038/s41598-021-03025-0.
- Rodríguez I, Tananaki C, Galán-Soldevilla H, Pérez-Cacho PR, Herrano S. 2021. Sensory profile of greek islands thyme honey. *Appl Sci*, 11(20): 9548. DOI: 10.3390/app11209548.
- Salehi B, Mishra AP, Shukla I, Rad MS, Contreras MM, Carretero AS, Fathi H, Nasrabadi NN, Kobarfard F, Rad JS. 2018. Thymol, thyme, and other plant sources: Health and potential uses. *Phytother Res*, 32: 1688-1706. DOI: 10.1002/ptr.6109.
- Sardar SK, Ghosal A, Haldar T, Maruf M, Das K, Saito-Nakano Y, Kobayashi S, Dutta S, Nozaki T, Ganguly S. 2023. Prevalence and molecular characterization of Enta-moeba moshkovskii in diarrheal patients from Eastern India. *PLoS Negl Trop Dis*, 17(5): e0011287. DOI: 10.1371/journal.pntd.0011287.
- Singh RB, Mahenderakar MD, Jugran AK, Singh RK, Srivastava RK. 2020. Assessing genetic diversity and population structure of sugarcane cultivars, progenitor species and genera using microsatellite (SSR) markers. *Gene*, 753: DOI: 10.1016/j.gene.2020.144800.
- Taher MS, Salloom YF, Hussein Al-Asadi RAU, Al-Mousswi ZJ, Alamrani HA. 2021. The medicinal importance of Thyme plant (*Thymus vulgaris*). *Biomedicine*, 41(3): 531-534.
- Tamura K, Stecher G, Kumar S. 2021. MEGA 11: molecular evolutionary genetics analysis version 11. *Mol Biol Evol*, 38(7): 3022-3027. DOI: 10.1093/molbev/msab120.
- Techen N, Parveen I, Pan Z, Khan IA. 2014. DNA barcoding of medicinal plant material for identification. *Current Opin Biotechnol*, 25: 103-110. DOI: 10.1016/j.copbio.2013.09.010.
- Thakur VV, Tripathi N, Tiwari S. 2021. DNA barcoding of some medicinally important plant species of lamiaceae family in India. *Mol Biol Rep*, 48: 3097-3106. DOI: 10.1007/s11033-021-06356-3.
- Tomanić D, Božin B, Kladar N, Stanojević J, Čabarkapa I, Stilinović N, Apić J, Božić DD, Kovačević Z. 2022. Environmental bovine mastitis pathogens: Prevalence, antimicrobial susceptibility, and sensitivity to *Thymus vulgaris* L., *Thymus serpyllum* L., and *Origanum vulgare* L. essential oils. *Antibiotics*, 11(8): 1077. DOI: 10.3390/antibiotics11081077.
- Trindade H. 2010. Molecular biology of aromatic plants and spices. A review. *Flavour Fragr J*, 25(5): 272-281. DOI: 10.1002/ffj.1974.
- Uritu CM, Mihai CT, Stanciu GD, Dodi G, Stratulat TA, Luca A, Constantin MML, Stefanescu R, Bild V, Melnic S, Tamba BI. 2018. Review article medicinal plants of the family Lamiaceae in pain therapy. *Pain Res Manag*, 2018: 1-45 DOI: 10.1155/2018/7801543.
- Wang Y, Dietrich CH, Zhang Y. 2017. Phylogeny and historical biogeography of leafhopper subfamily Evacanthinae (Hemiptera: Cicadellidae) based on morphological and molecular data. *Sci Rep*, 7: 45387. DOI: 10.1038/srep45387.
- Yu J, Wu X, Liu C, Newmaster S, Ragupathy S, Kress WJ. 2021. Progress in the use of DNA barcodes in the identification and classification of medicinal plants. *Ecotoxicol Environ Saf*, 208: 111691. DOI: 10.1016/j.ecoenv.2020.111691.



3 BOYUTLU GÖRÜNTÜLEME KULLANILARAK BİR AĞAÇ GÖVDE ÇAP ÖLÇÜM UYGULAMASININ GELİŞTİRİLMESİ

Hayrettin KARADÖL^{1*}, Mehmet GÖK², Mehmet TEKEREK³

¹Kahramanmaraş Sütçü İmam University, Department of Biosystem Engineering, 46100, Kahramanmaraş, Türkiye

²Kahramanmaraş İstiklal University, Department of Digital Game Desing, 46100, Kahramanmaraş, Türkiye

³Ankara University, Department of Computer Education and Instructional Technology, 06590, Ankara Türkiye

Özet: Orman işletmelerinde sürekli ve rasyonel bir çalışma gerçekleştirebilmek için ağaçların odun hacim ve artım miktarının periyodik olarak belirlenmesi önemlidir. Ağaçlardan elde edilecek materyallerin farklı kullanım amaçları için ağaçların odun hacimlerini belirlemede ağaç gövde çapının hassas bir şekilde ölçülmesi gerekmektedir. Ağaç gövde çapları çoğunlukla manuel olarak kumpaslarla ölçülmektedir. Bu işlem sürecinde bir orman işçisi kumpasla ağacın gövde çapını ölçmekte ve başka bir işçi ise bu ölçüm bilgisini dikili ağaç ölçüm tutanağına kaydetmekte ve daha sonra analiz için bu veriler bilgisayar ortamına aktarılmaktadır. Tüm bu süreçler zaman, iş gücü ve ölçüm hataları gibi sorunları da beraberinde getirmektedir. Bu çalışmada, ağaç gövde çaplarını ölçebilmek amacıyla derinlik bilgisi içeren bir kamera, tek kart bilgisayar ve diğer çevre birimlerden oluşan düşük maliyetli taşınabilir bir ölçüm sisteminin tasarımı ortaya konmuş ve ön testleri gerçekleştirmek amacıyla deneysel bir sistem oluşturulmuştur. Hedef plan doğrultusunda oluşturulan görüntüleme sistemi ile bazı ön testler gerçekleştirilmiştir. Derinlik bilgisi içeren görüntülerde, hedeflenen bir ağaç gövdesinin dış aydınlatma ortamından etkilenmeksizin ön plana çıkarabiliyor olması, ağaç gövde çapının hassas bir şekilde belirlenmesini sağlamaktadır. Kamera sensörü-ağaç gövdesi arası mesafe belirli bir sınır değer içerisinde (20-100cm) olması koşuluyla 15 farklı ölçüm gerçekleştirilmiş ve manuel kumpas ölçümüne göre ağaç gövde çapları maksimum 1.975 cm hata değeri ile belirlenmiştir.

Anahtar kelimeler: Orman amenajmanı, Görüntü bölütleme, Üç boyutlu görü


Development of a Tree Trunk Diameter Measurement System Using 3D Imaging


Abstract: In order to carry out a continuous and rational work in forest enterprises, it is important to determine the wood volume and increment amount of the trees periodically. It is necessary to measure the tree trunk diameter precisely in determining the wood volume of the trees for the different uses of the materials to be obtained from the trees. Tree trunk diameters are mostly measured manually with calipers. In this process, a forest worker measures the trunk diameter of the tree with a caliper, and another worker records this measurement information in the standing tree measurement report and then this information is transferred to the computer for further analysis. All these processes bring problems such as time, labor and measurement errors. In this study, it is planned to develop a low-cost portable measurement system consisting of a depth camera, single board computer and other peripherals with depth information in order to measure tree trunk diameters, and an experimental system was created to carry out preliminary tests. Some preliminary tests were carried out with the imaging system created in line with the target plan. In images containing depth information, the fact that a targeted tree trunk can be highlighted without being affected by the external lighting environment enables the tree trunk diameter to be determined precisely. 15 different measurements were performed, provided that the distance between the camera sensor and the tree trunk was within a certain limit value (20-100 cm), and tree trunk diameters were determined with a maximum error value of 1.975 cm according to manual caliper measurement.


Keywords: Forest management planning, Image segmentation, Three dimensional measurement

*Sorumlu yazar (Corresponding author): Kahramanmaraş Sütçü İmam University, Department of Biosystem Engineering, 46100, Kahramanmaraş, Türkiye

E mail: hayrettinkaradol@gmail.com (H. KARADÖL)

Hayrettin KARADÖL  <https://orcid.org/0000-0002-5062-0887>

Mehmet GÖK  <https://orcid.org/0000-0003-1656-5770>

Mehmet TEKEREK  <https://orcid.org/0000-0001-6112-3651>

Gönderi: 30 Ağustos 2023

Kabul: 29 Eylül 2023

Yayınlanma: 15 Ekim 2023

Received: August 30, 2023

Accepted: September 29, 2023

Published: October 15, 2023

Cite as: Karadöl H, Gök M, Tekerek M. 2023. Development of a tree trunk diameter measurement system using 3D imaging. BSJ Eng Sci, 6(4): 583-588.

1. Giriş

Orman envanteri ağaç türleri, göğüs yüksekliğindeki çap ve ağaç yüksekliği kullanılarak oluşturulan yüksek doğrulukta tahmin edilebilir (Liang ve ark., 2016; Celes ve ark., 2019). Bir ormanlık alanda kesilen ya da herhangi bir nedenle devrilen ağaçların pratik bir şekilde kabuklu gövde hacimlerinin tahmini gerekebilir (Durgun ve ark., 2022). Ormanlık çalışmalarının planlama, karar verme ve yönetim aşamalarında nitelikli ve hassas veriye büyük

bir ihtiyaç bulunmaktadır (Eker ve Özer, 2015; Buğday, 2016). Bir bölgedeki ağaçlara ait hacim artım kontrolünün yapılabilmesi için, ağaçların çapları günümüzde çoğunlukla mekanik çap ölçerler (kumpas) ile ölçülmektedir. Bu ölçme yöntemi, her ne kadar kullanılan araç ve ölçme güvenilirliği açısından kabul edilmiş bir yöntem olsa da önemli ölçüde zaman ve iş gücü gerektirmektedir. Ayrıca, arazide meydana gelebilen insan kaynaklı hatalar (yanlış ölçüm, kayıt



hatası vb.) veri güvenilirliğini riske atabilmektedir. (Vatandaşlar ve ark., 2022).

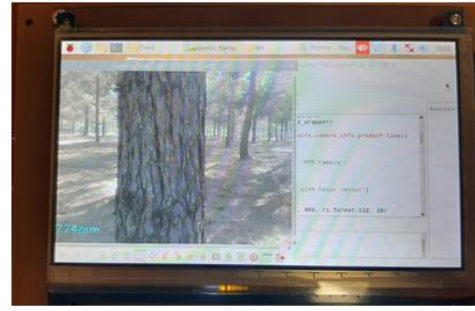
Son yıllarda uzaktan algılama teknolojileri ve Nesnelerin İnterneti (IoT) tabanlı sistemlerin orman envanteri belirleme yöntemlerinde kullanıldığı görülmektedir (Barrett ve ark., 2016; Suci ve ark., 2017; Gougherty ve ark., 2018; Alcarria ve ark., 2018). Bu alanda LIDAR (Laser Imaging Detection and Ranging) teknolojilerine dayanan 3D görüntüleme sistemi yaygın olarak kullanılan sistemlerden biridir. Ağaç gövde çapı ve yükseklik tahmini (Omasa ve ark., 2007; Chen ve ark., 2017), yaprak yoğunluğu (Hosoi ve ark., 2006) ve dikili ağaç hacmi (Hosoi ve ark., 2013) gibi uygulamalar bu çalışmalardan bazılarıdır. Uzaktan algılama teknolojileri, çalışma prensipleri açısından orman alanları söz konusu olduğunda uygulanabilir araçlar olarak görülebilir. Hatta LIDAR sisteminin otonom araçlar ve dronlarla birlikte kullanılarak (Elaksher ve ark., 2017) geniş ormanlık alanlara ilişkin envanter bilgileri elde edilebilmektedir. Ancak bu tür algılayıcıların renk bilgisi içermemesi ve hassas ölçüm süreçlerinde iş gücü ihtiyacını azaltmaması, LIDAR vb. sistem bileşenlerinin günümüzde hala fayda/maliyet açısından avantajlı teknoloji olarak görülmemesine neden olmaktadır. Ayrıca bu sistemler çoğunlukla ithalat yoluyla elde edildikleri için sistemin geliştirilmesi mümkün olamamaktadır.

LIDAR yöntemi, göğüs çapı 8 cm'e yakın olan ağaçların yoğun olarak yer aldığı ab, b ve bc gelişme çağlarındaki yapraklı karışık meşcerelerin bakım yapılmayan sahalarında verimli çalışmamasının yanında büyük miktarda verinin işlenmesi ve depolanması için güçlü donanım ihtiyacı duymaktadır (Vatandaşlar ve ark., 2022). LIDAR ile orman içerisinde çalışma yaparken birim alandaki gövde sayısı fazla olduğundan LIDAR ile gövdeler arasındaki mesafe azaldığından dolayı ağaçların birbirlerini gölgeleme etkisi artmaktadır. Bu nedenle meşcerelerde göğüs çapı gibi kolay ölçülebilen bir özelliğin bile elde edilmesi mümkün olamamaktadır (Özdemir, 2013). LIDAR cihazı ile arazide toplanan verilerin ofiste depolanması ve işlenmesi gerekmektedir. Bu çalışmada, 3D görüntüleme için bünyesinde kızılötesi ışık kaynağı barındıran ve ışık kaynağının nesneye çarpıp dönüşü ile elde edilen görüntüleri kullanarak piksel-derinlik değerini hesaplayabilen derinlik kamerası kullanılmıştır. Kapalı oda ortamında ve dış aydınlatma (gölge ve güneşli) ortamlarında farklı teknolojilere (PMD CamBoard, PMD CamCube ve SwissRanger SR4000) sahip üç ToF kamera ile gerçekleştirilen testlerde, güneş ışığı altında en başarılı sonucun PMD (Photonic Mixer Devices) sensör teknolojisine sahip kameranın olduğu belirlenmiştir (Kazmi ve ark., 2014). Derinlik kameraları günümüzde cep telefonlarında, artırılmış gerçeklik (AR) uygulamaları ve 3D tarama işlemleri için kullanılmakta ve giderek yaygınlaşmaktadır. Bu durum, bu tür algoritmaların, Android ve iOS gibi işletim sistemlerine de taşınabileceğini ve yaygınlık kazanabileceğini göstermektedir. Bu araştırmanın amacı, 3 boyutlu görüntüleme tekniği ile gerçek zamanlı olarak ağaca ait

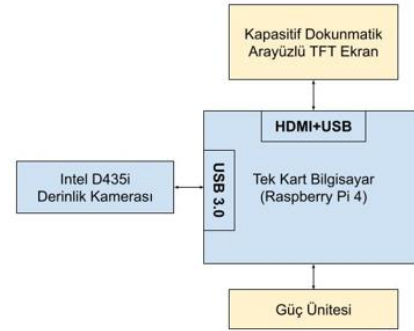
görüntü bölgesinin fotoğraftan ayrıştırılarak gövde ölçümünün yapılmasına ilişkin bilgi işlemsel bir yöntemin geliştirilmesidir.

2. Materyal ve Yöntem

Ağaç gövde çapı belirleme amacı ile tasarımı yapılan sistemin genel yapısı; Raspberry Pi 4 tek kart bilgisayarı, derinlik kamerası (Intel D435i; derinlik görüntü çözünürlüğü 1280X720, 30 FPS), TFT ekran ve bataryadan oluşmaktadır. Tek kart bilgisayar (Raspberry Pi 4), kamera, kapasitif dokunmatik ekran ve güç kaynağı elemanlarının bağlantıları gerçekleştirilerek, 3D yazıcıda oluşturulan bir çerçeve içerisinde yerleştirilmiştir (Şekil 1a). Şekil 1b'de ise oluşturulan görüntüleme sisteminin blok diyagramı görülmektedir.



(a)



(b)

Şekil 1. Görüntüleme sistemi.

Derinlik kameraları, görüntüleme açısına giren nesnelerle kamera arasındaki mesafeyi hesaplayarak piksel-derinlik bilgisi üretebilen kameralardır. Intel D435i eş zamanlı olarak hem derinlik görüntüsü üretebilen hem de renkli görüntü yakalayabilen düşük maliyetli bir derinlik kamerası olup günümüzde robotik ve üretim izleme gibi alanlarda kullanılmaktadır (Tadic ve ark., 2019; Zhang ve ark., 2020). Söz konusu kamera, genel anlamda Intel Görüntü İşlemcisi (Vision Processor) D4 ve derinlik ünitesinden oluşmaktadır. Derinlik modülünde, bir adet RGB kamera, iki adet kızılötesi kamera ve bir adet kızılötesi projektör yer almaktadır. Kızılötesi projektör bir nokta deseni üretirken, kamera açısına giren nesnelere yansıyan desen görüntüsü kızılötesi kameralar tarafından yakalanarak D4 işlemcisi tarafından işlenir. D4 işlemcisi stereo görüntüleme (stereo vision) tekniği ile piksel derinliklerini hesaplayarak RGB kameradan gelen görüntüyü de

kullanarak derinlik görüntüsünü (depth image) üretir. D435i derinlik kamerasında yer alan derinlik algılama bileşenleri Şekil 2’de verilmiştir.



Şekil 2. Intel 435i derinlik kamerası.

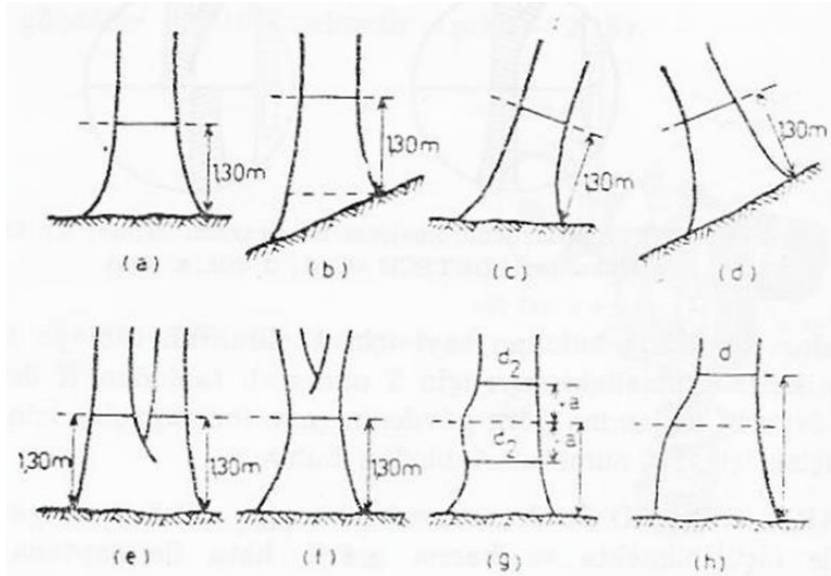
D435i derinlik kamerası, derinlik görüntüsünü dahili olarak üretebilmekte olup USB 3.1 Gen 1 bağlantı arayüzü ile de yüksek hızda görüntü aktarımı sunabilmektedir. Bununla birlikte, stereo kameralardan farklı olarak dahili kalibrasyon ile görüntü düzeltme desteğini de tümleşik olarak sunmaktadır. Intel tarafından sağlanan açık kaynak kodlu yazılım geliştirme kütüphanesi *librealsense* ile D435i derinlik kamerası, C/C++, Python ve Matlab ortamlarında da kolaylıkla kullanılabilir (Tadic ve ark., 2019).

Raspberry Pi 4, sahip olduğu USB 3.0 bağlantı arayüzü D435i derinlik kamerasını direkt olarak çalıştırabilmektedir. Sunulan çalışmada, çap ölçüsünün belirlenebilmesi için gerekli hesaplamalarını gerçekleştiren görüntü işleme yazılımı *librealsense*, OpenCV 4.3 ve wxPython kütüphaneleri kullanılarak Python 3 programlama dili ile gerçekleştirilmiştir. Bu

yazılım, Raspberry Pi 4 tek kart bilgisayarı için kullanılan Debian Linux tabanlı Raspberry Pi OS işletim sistemi üzerinde çalışmaktadır. Böylelikle, ağ bağlantısı ve depolama gibi yüksek seviyeli yazılım gereksinimleri kolaylıkla sağlanabilmektedir. wxPython kütüphanesi kullanılarak tasarlanan kullanıcı arayüzü de TFT LCD ve kapasitif dokunmatik arayüz sayesinde kolaylıkla kullanılabilir.

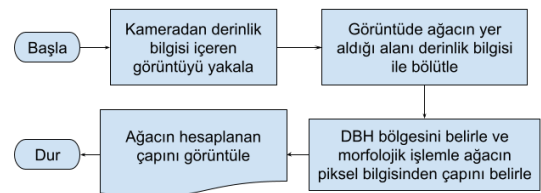
Ağaç çap ölçümleri Kahramanmaraş Sütçü İmam Üniversitesi kampüsü içerisinde bulunan ağaçlık alanda gerçekleştirilmiştir. Çalışmada ağaçla gövde çapları yerden 1,30 m yüksekten ölçülmüştür. Ağacın kamera sensörüne olan mesafesini doğru bir şekilde belirlemek amacıyla görüntünün merkezine dairesel bir belirteç çizilmiştir. Şekil 1 (a)’da sol alt köşede kamera sensörünün ağaç gövdesine (kırmızı imleç) olan mesafesini göstermektedir. Oluşturulan ölçüm cihazının blok diyagramı Şekil 1 (b)’de görülmektedir.

Ağacın bulunduğu arazinin düz ya da eğimli oluşuna, gövdenin değişik durumlarına göre uygulanacak çap ölçme yöntemleri farklılıklar göstermektedir (Şekil 3). Eğimli arazilerde ağacın üst kısmından ölçülmesi (b ve d), eğik gövdelerde yüksekliğin gövde eksenine paralel alınması (c ve d), dipten çatallı ağacın iki ayrı gövde sayılması ve yukarıdaki çatalın dikkate alınmaması (e ve f), ölçüm yerinin şişkin olması halinde “a” kadar aşağıdan ve yukarıdan ölçülerek ortalama alınması (g), dip kısmı anormal kütüklü olan gövdelerde daha yukarıdan ölçüm yapılması (h) gerekmektedir (Kalıpsız, 1999).



Şekil 3. Araziye ve ağacın durumuna göre göğüs çapının ölçüm yerleri.

Araştırmada, genel olarak dört farklı aşamada ağacın çap bilgisine ulaşılması hedeflenmiştir; Bunlar (1) derinlik görüntüsünün elde edilmesi, (2) derinlik bilgisinden yararlanılarak arka plan segmentasyonunun gerçekleştirilmesi, (3) görüntü üzerinde hedeflenen bölgenin (DBH, diameter at breast height) belirlenmesi, (4) morfolojik işlemler ve ağaç gövde çapının belirlenmesidir (Şekil 4).



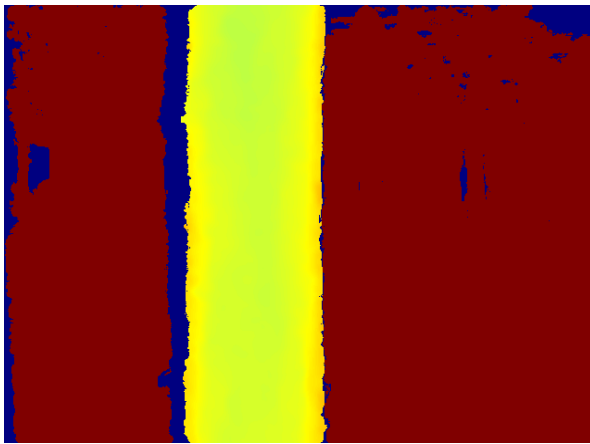
Şekil 4. Akış şeması.

3. Bulgular ve Tartışma

Çalışmada ağaç gövdeleri 50-100 cm mesafeden 14 farklı ağaca ait değişen mesafelerden toplam 15 görüntü elde edilmiştir. Bölgedeki ağaçların gövde çapı damgalama çalışmaları için uygun olmasalar da ağaç çapının büyüklüğü ölçüm sonuçlarını etkilemeyecektir. Şekil 5'te örnek bir ağaçtan elde edilen RGB görüntü sunulmuştur. Şekil 6'da örnek ağaca ait renkli derinlik görüntüsü, Şekil 7'de ise otomatik eşikleme (Otsu, 1979) kullanılarak elde edilen ikili görüntü sunulmuştur. Elde edilen ikili görüntü 3 piksel genişliğinde ve 50 piksel yüksekliğinde (3X50) bir yapısal elemanla aşındırma işlemine tabi tutulmuştur. Daha sonra görüntü üzerinde ağaç gövdesini temsil eden bölgenin merkez noktası baz alınarak oluşturulan dikdörtgensel bir ilgi alanı kesilmiştir. Kesilen bu bölge içerisindeki yatay yönlü en kısa ve en uzun genişlik değerlerinin ortalaması alınmış ve ilgili ağaç gövdesine ait çap değeri (32,25 cm) belirlenmiştir.



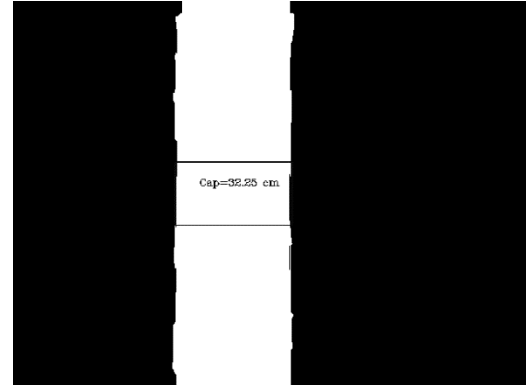
Şekil 5. Örnek bir ağaçtan elde edilen görüntü.



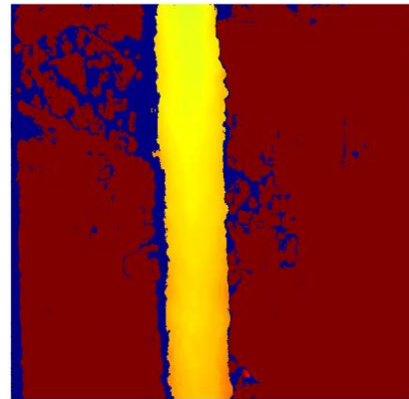
Şekil 6. Örnek ağaca ait renkli derinlik görüntüsü.

Orman arazilerinde standart 2D kameralarla ağaç gövde çap ve uzunluk ölçümleri gerçekleştirilebilmektedir (Pérez ve ark., 2014; Karadöl ve Aybek, 2019). Orman kaynak bilgisi oluşturmada 2D görüntüleme görüntü işleme çalışmalarının başlıca zorlukları; arka planda benzer birçok nesnenin bulunması, bölgedeki ağaçların gövde renk özelliklerinin büyük oranda benzer olması olarak ifade edilebilir. Bu zorluklar ve iki boyutlu

görüntülerde kesişen nesnelerin segmentasyonu için çözülmesi gereken problemlerden biridir. 3D görüntüleme temel amaç arka planı elimine etmek olduğu için görüntü çekimleri esnasında ağaç gövdesi arka planında nesnelerin ya da farklı ağaç gövdelerinin bulunduğu görüntüler incelenmiştir. Sistemin arka plan segmentasyonunu başarılı bir şekilde elimine ettiği görülmektedir (Şekil 8). Diğer taraftan görüntü çekimi esnasında kullanıcı ekrandan ağaç gövdesine ait ikili görüntüyü görebildiği için kamera açısında ve derinlik mesafesinde küçük değişiklikler yaparak doğru ölçümler elde edebilmektedir.



Şekil 7. Örnek ağaca ait gövde çapını içeren ikili görüntü.



Şekil 8. Derinlik bilgisi kullanılarak arka plan segmentasyonunun gerçekleştirilmesi.

Ağaç gövdelerinin elde edilmesi sürecinde ilk olarak ilgili ağacın gövde çapı bir kumpas aracılığı ile ölçülmüştür. Tablo 1'de kumpas ölçüm sonuçları, görüntüler

üzerinden elde edilen gövde piksel sayısı ve kamera sensörü ile ağaç gövdesi arası mesafe görülmektedir. Ölçümler sonucunda maksimum hata değeri 1. ölçüm sonucunda (1,975 cm), minimum hata değeri ise 5. ölçüm sonucunda gerçekleşmiştir (0,091 cm). Eşitlik 1'de

çalışmada kullanılan kamera çözünürlüğüne (1280X720) ve kamera sensörü ile ağaç gövdesi arası mesafe değerlerine bağlı çoklu korelasyon yöntemi (SBSS 20, 2011) kullanılarak oluşturulan kumpas ölçüm değeri ile görüntüleme sistemi arasındaki ilişki görülmektedir.

Tablo 1. Manuel ölçüm ve görüntüleme yöntemi kullanılarak hesaplanan ağaç gövde çap değerleri görülmektedir

| No | Kumpas ölçümü (cm) | Piksel sayısı (adet) | Mesafe (mm) | Görüntüleme Ölçümü (cm) | Fark (cm) |
|----|--------------------|----------------------|-------------|-------------------------|-----------|
| 1 | 29 | 119 | 909 | 30,975 | -1,975 |
| 2 | 26 | 138 | 701 | 27,728 | -1,728 |
| 3 | 25 | 138 | 620 | 24,488 | 0,512 |
| 4 | 22 | 92 | 842 | 21,086 | 0,914 |
| 5 | 26 | 121 | 769 | 25,909 | 0,091 |
| 6 | 32 | 148 | 716 | 30,998 | 1,002 |
| 7 | 33 | 146 | 771 | 32,664 | 0,336 |
| 8 | 32 | 144 | 774 | 32,25 | -0,25 |
| 9 | 31 | 153 | 647 | 29,573 | 1,427 |
| 10 | 29 | 150 | 640 | 28,492 | 0,508 |
| 11 | 38 | 170 | 774 | 39,192 | -1,192 |
| 12 | 24 | 121 | 703 | 23,269 | 0,731 |
| 13 | 17 | 101 | 710 | 18,209 | -1,209 |
| 14 | 32 | 168 | 602 | 31,778 | 0,222 |
| 15 | 32 | 146 | 719 | 30,584 | 1,416 |

$$Kö = 0,267 * Ps + 0,040 * Öm - 37,158 \quad (1)$$

$$R^2 = 0,927$$

burada; Kö, Kumpas ölçümünü; Ps, Piksel sayısını ve Öm, Ölçüm mesafesini (kamera sensörü - ağaç gövdesi arası mesafe) belirtmektedir.

4. Sonuç

Bu çalışmada, ormancılık uygulamalarında geleneksel ölçüm sistemleri yerine geçebilecek görüntüleme sistemine dayanan ve maliyet açısından efektif bir ölçüm cihazı oluşturulması amaçlanmıştır. Araştırmada, 3 boyutlu görüntüleme tekniği ile gerçek zamanlı olarak ağaca ait görüntü bölgesinin fotoğraftan ayrıştırılarak gövde ölçümünün yapılmasına ilişkin bilgi işlemsel bir yöntem önerilmiştir. Oluşturulan ölçüm sisteminin klasik kumpas ölçüm sürecine göre zaman ve iş gücü açısından önemli avantajlar sağlayabileceği görülmüştür. 3D görüntüleme yöntemi kullanılarak ağaç gövdesine ait görüntülerde, orman ortamında benzer renk özelliklerine sahip karmaşık arka planının segmentasyonunun başarılı bir şekilde gerçekleştirilebildiği görülmüştür. Kamera sensörü-ağaç gövdesi arası mesafe belirli bir sınır değer içerisinde (20-100cm) olması koşuluyla 15 farklı ölçüm gerçekleştirilmiş ve manuel kumpas ölçümüne göre ağaç gövde çapları maksimum 1,975 cm hata değeri ile belirlenmiştir. Farklı orman arazilerinde, günün farklı saatlerinde daha fazla ölçümlerin yapılmasıyla sistemin yazılımsal ve donanımsal olarak hassasiyetinin artırılabilceği düşünülmektedir.

Katkı Oranı Beyanı

Yazar(lar)ın katkı yüzdesi aşağıda verilmiştir. Tüm yazarlar makaleyi incelemiş ve onaylamıştır.

| | H.K. | M.G. | M.T. |
|-----|------|------|------|
| K | 40 | 30 | 30 |
| T | 50 | 30 | 20 |
| Y | 40 | 30 | 30 |
| VTI | 100 | | |
| VAY | 80 | 10 | 10 |
| KT | 50 | 30 | 20 |
| YZ | 70 | 30 | |
| KI | 40 | 20 | 40 |
| GR | 100 | | |
| PY | 40 | 30 | 30 |
| FA | 40 | 30 | 30 |

K= kavram, T= tasarım, Y= yönetim, VTI= veri toplama ve/veya işleme, VAY= veri analizi ve/veya yorumlama, KT= kaynak tarama, YZ= Yazım, KI= kritik inceleme, GR= gönderim ve revizyon, PY= proje yönetimi, FA= fon alımı.

Çatışma Beyanı

Yazarlar bu çalışmada hiçbir çıkar ilişkisi olmadığını beyan etmektedirler.

Etik Onay Beyanı

Bu araştırmada hayvanlar ve insanlar üzerinde herhangi bir çalışma yapılmadığı için etik kurul onayı alınmamıştır.

Kaynaklar

Alcarria R, Bordel B, Manso M. A, Iturrioz T, Pérez M. 2018. Analyzing UAV-based remote sensing and WSN support for data fusion. In Proceedings of the International Conference on

- Information Technology & Systems, February 8-10, Cusco, Peru, pp: 756-766.
- Barrett F, McRoberts RE, Tomppo E, Cienciala E, Waser LT. 2016. A questionnaire-based review of the operational use of remotely sensed data by national forest inventories. *Remote Sens Environ*, 174: 279-289.
- Buğday E. 2016. Ormanlıkta üretimin planlaması ve hassas ormancılık anlayışı. *Anadolu Orman Araşt Derg*, 2(12): 54-57.
- Celes CHS, Araujo RFD, Emmert F, Lima AJN, Campos MAA. 2019. Digital approach for measuring tree diameters in the Amazon forest. *Floresta e Ambiente*, 26: 1-10
- Chen C, Wang Y, Li Y, Yue T, Wang X. 2017. Robust and parameter-free algorithm for constructing pit-free canopy height models. *ISPRS Int J Geo-Info*, 6(7): 219-232.
- Durgun H, Çoban H.O, Mehmet E. 2022. İnsansız hava aracıyla elde edilen hava fotoğraflarından kızılçam ağaçlarının çap ve boylarının ölçümü ve gövde hacminin tahmini. *Turkish J Forest*, 23(4): 255-267.
- Eker M. Özer D. 2015. Üretim işlerinde hassas ormancılık yaklaşımı: Kavramsal çerçeve. *Türkiye Ormanlık Derg*, 16(2): 183-194.
- Elaksher AF, Bhandari S, Carreon-Limonés CA, Lauf R. 2017. Potential of UAV lidar systems for geospatial mapping. *Lidar Remote Sens Environ Monit*, 2017(10406): 121-133.
- Gougherty AV, Keller SR, Kruger A, Stylinski CD, Elmore AJ, Fitzpatrick MC. 2018. Estimating tree phenology from high frequency tree movement data. *Agri Forest Meteorol*, 263: 217-224.
- Hosoi F, Omasa K. 2006. Voxel-based 3-D modeling of individual trees for estimating leaf area density using high-resolution portable scanning lidar. *IEEE Transact Geosci Remote Sens*, 44(12): 3610-3618.
- Hosoi F, Nakai Y, Omasa K. 2013. 3-D voxel-based solid modeling of a broad-leaved tree for accurate volume estimation using portable scanning lidar. *ISPRS J Photogrammet Remote Sens*, 82: 41-48.
- Kalıpsız A. 1999. Dendrometri. İstanbul Üniversitesi Orman Fakültesi Yayınları, İ.Ü. Yayın No: 3194, O.F. Yayın No: 354, İstanbul, Türkiye.
- Karadöl H, Aybek A. 2019. Determination of live tree trunk diameter with close-range imaging. 1st International Congress on Biosystems Engineering, September 24-27, 2019, Hatay, Türkiye, pp: 142-147.
- Kazmi W, Foix S, Alenyà G, Andersen HJ. 2014. Indoor and outdoor depth imaging of leaves with time-of-flight and stereo vision sensors: Analysis and comparison. *ISPRS J Photogrammet Remote Sens*, 88: 128-146.
- Liang X, Kankare V, Hyypä J, Wang Y, Kukko A, Haggrén H, Vastaranta M. 2016. Terrestrial laser scanning in forest inventories. *ISPRS J Photogrammet Remote Sens*, 115: 63-77.
- Omasa K, Hosoi F, Konishi A. 2007. 3D lidar imaging for detecting and understanding plant responses and canopy structure. *J Exper Botany*, 58(4): 881-898.
- Otsu N. 1979. A threshold selection method from gray-level histogram. *IEEE Transact Syst Man Cybernetics*, 9: 62-66.
- Özdemir İ. 2013. Yersel lazer tarama ile tek ağaç özelliklerinin belirlenmesi. *Turkish J Forestry*, 14(1): 40-47.
- Pérez DS, Bromberg F, Antivilo FG. 2014. Computer vision approach for low cost, high precision measurement of grapevine trunk diameter in outdoor conditions. *ArXiv Preprint arXiv*, 140:4845.
- SPSS. 2011. IBM SPSS statistics for Windows, version 20.0. Methods for soil characterization. In *Diagnosis and improvement of saline and alkali soils*. Agricultural Handbook 60. USDA Washington, US, pp: 83-147.
- Suciu G, Ciucuc R, Pasat A, Scheianu A. 2017. Remote sensing for forest environment preservation. proceedings of the 2017 world conference on information systems and Technologies. Madeira, Portugal, 13: 211-220.
- Tadic V, Odry A, Kecskes I, Burkus E, Kiraly Z, Odry P. 2019. Application of Intel realsense cameras for depth image generation in robotics. *WSEAS Transac Comput*, 18: 2224-2872.
- Vatandaşlar C, Zeybek M, Borucu S. 2022. Mobil LiDAR ile orman envanterlerinde farklı örnekleme tasarımlarının veri hassasiyeti ve iş verimliliğine etkisi: Rize Şenyuva örneği. *Bartın Orman Fak Derg*, 24(2): 258-271.
- Vatandaşlar C, Zeybek M, Çankaya EÇ, Demiraslan T, Şahin C, Gündüz Y. 2022. El tipi mobil LiDAR teknolojisinin orman envanterlerinde kullanımı: Artvin-Şavşat Örneği. *Orman Araşt Derg*, 9(1): 81-96.
- Zhang L, Xia H, Qiao Y. 2020. Texture synthesis repair of RealSense D435i depth images with object-oriented RGB Image Segmentation. *Sensors*, 20(23): 6725.



OPTI-WAFFLE: A TECHNOLOGICAL FURNITURE DESIGN AND MANUFACTURING MODEL

Erdem YILDIRIM^{1*}


¹Dokuz Eylül University, Faculty of Architecture, Department of Architecture, 35390, İzmir, Türkiye

Abstract: Parametric design allows the use of computers and systems that can make decisions beyond human capacity, such as machine learning, through optimization in design and manufacturing. From this point of view, it is aimed to shape and manufacture the design by minimizing the subjective decisions of the designers by using various algorithmic methods and structural optimization to provide ergonomics in a furniture design. As the subject of the study, a meeting table for 8 people was discussed. In the process, 'artificial intelligence supported inspiration board', 'parametric design', 'human-computer interaction and sensors', 'topology optimization', 'observation in augmented reality' and 'computer-aided manufacturing' techniques were used sequentially. After the assembly was completed, the product obtained was finally evaluated in terms of structure-function relationship.

Keywords: Parametric design, Topology optimization, Waffle structure, Computer-Aided ergonomics

*Corresponding author: Dokuz Eylül University, Faculty of Architecture, Department of Architecture, 35390, İzmir, Türkiye

E mail: erdem.yildirim@deu.edu.tr (E. YILDIRIM)

Erdem YILDIRIM  <https://orcid.org/0000-0002-8829-5274>

Received: August 16, 2023

Accepted: September 30, 2023

Published: October 15, 2023

Cite as: Yıldırım E. 2023. Opti-waffle: a technological furniture design and manufacturing model. BSJ Eng Sci, 6(4): 589-599.

1. Introduction

Architectural design and manufacturing research are diversifying and moving in new directions. Changes in technology, such as new materials, design methods, and construction techniques, are accelerating the need to advance and integrate design knowledge across disciplines. In design disciplines, the transition from computer-aided design methods to parametric design models enables designers to create more efficient and optimized designs, make decisions that are beyond the capabilities of humans through the use of machine learning and control manufacturing decisions through the digitization of production techniques.

The primary objective of the study is to develop a model that minimizes the subjective decisions of designers by utilizing various algorithmic methods in furniture design to shape the final product. The focus of the study is the design of an eight-person conference table. As the table size, a volume of 240*120 cm with a height of 72 cm has been selected according to anthropometric average scale. In production, the use of MDF plates measuring 120*80 by 1.8 cm has been selected. These decisions are the designer's most influential subjective parameters in forming the model. Structural Topology Optimization (STO) is a computational design methodology that employs mathematical algorithms to optimize the distribution of material within a predefined space, subject to constraints and performance objectives, in order to create structurally efficient forms, typically realized via techniques such as Finite Element Analysis and various optimization algorithms. STO technique has the greatest

influence on the design's outcome, out of the numerous algorithmic techniques employed in the study. This article does not invent any of the techniques utilized in the procedure. The unique aspect of this study is the development of an algorithmic model independent of the subjective decisions of the designer through the use of algorithmic methods in furniture design, with the combination of the techniques used in the planned order.

1.1. Literature Review

Due to the structure of parametric design, it is now possible to digitize the design action and optimize design decisions autonomously, allowing computers to make decisions automatically during the design process. Parametric design is central to the techniques applied in this study. Analytical algorithm-based design is the cornerstone of parametric design. Greg Lynn, one of the pioneers of parametric design, developed a computational approach to architectural design that employs digital tools and algorithms to create complex and difficult-to-design-and-implement outcomes (Lynn, 1998, 1999). Although "form follows function" was first proposed by early modernists, this phenomenon is literally realized in parametric design (Schumacher, 2009, 2011). The parameters that give parametric design its name define the function(s), and designers can transform various contextual data into form-giving elements. Parameters and algorithms form the basis of this study, which also shapes the design.

Although furniture design does not have a long history of artificial intelligence-supported optimization methods, ZHA CODE's ACADIA chair is one of the establishing



approaches in this field (Schumacher, 2017). Since production of models designed with topology optimization is better suited for 3D printing, an additive technique, the majority of current research is conducted accordingly (Kazakis et al., 2017; Ma et al., 2021; Cui et al., 2022).

Machine Learning is the fundamental computing field that enables visual synthesis, a technique used in the preliminary design phase. Processing data with reward and punishment logic via Artificial Neural Networks (ANN) (Jain and Mao, 1996), reading, understanding, and imitating human language via Natural Language Processing (NLP) (Nadkarni et al., 2011), and identifying and labeling objects via Computer Vision (Vinyals et al., 2015) all contribute to complex learning capability. Visual synthesis dates back to the ELIZA program at the MIT Artificial Intelligence Laboratory in the 1950s (Agassi and Wiezenbaum, 1976), but until recently, the ability to generate realistic images was limited. The development of Deep Convolutional Generative Adversarial Networks (DCGANs) (Goodfellow et al., 2014) represents the most significant milestone in the method's evolution. Text-to-3D model synthesis is an additional promising research area linked to image synthesis (Jain et al., 2022; Liu et al., 2022; Zhuang et al., 2023).

In the parametric design phases of the research, Rhinoceros – Grasshopper was utilized as software. According to Rutten, Grasshopper is the most effective program for parametric design and parametric architecture (Rutten and McNeel, 2007). Grasshopper's visual coding (visual scripting) or node-based programming structure, which is more perceptible to designers, allows for the optimization of generative designs (Davis and Peters, 2013). In addition, numerous researchers have created over 650 Grasshopper plugins (Food4Rhino, 2023). Thus, modeling, analysis, simulation, optimization, real-time responsiveness, and numerous other domains can be interacted with using the same interface.

The main solid design process of the study starts with Human-Computer Interaction (HCI). HCI is the technique used at the beginning of the parametric design process. It is the study of how people interact with technological devices and software (Eloy et al., 2016). This field aims to make technology useful to people and enable them to interact effectively with technological devices. Sensors are the fundamental tools for human-computer interaction. Kinect, which was used in the study, is a sensor that can be programmed using an open-source software development kit; as a result, it is utilized in research in a variety of fields (Lun and Zhao, 2015).

The main form-giving process to the study, Structural Topology Optimization (STO) is a form optimization method that employs machine learning models to optimize the arrangement of materials within a user-defined area for a particular set of loads, conditions, and constraints (Halle et al., 2021; Rade et al., 2021). STO optimizes the performance and efficiency of the design by

eliminating unnecessary materials from areas that do not need to carry significant loads in order to reduce weight. Although STO is currently computer-assisted, its origins date back to 1904 (Michell, 1904). Over time, the method has evolved, algorithms for numerical environments have been developed (Zhou and Rozvany, 1991), and it continues to be developed in accordance with contemporary technologies (Cui et al., 2022; Wynne et al., 2022). Aerospace (Niemann et al., 2013), automotive (Bikas et al., 2015), and medicine (Sun et al., 2019) are the primary applications for STO. In these fields where lightweight construction is essential, STO provides significant advantages. Although there are numerous alternatives to STO software (Tyflopoulos and Steinert, 2022), there are a few that stand out for the use in architecture.

The next process of the study is waffle structures. In this study, waffle structure, more specifically defined as interlocked planar slicing, is a modern manufacturing technique. The production method, named after the pattern on the food item "waffle," is formed by slicing the two planar dimensions of a defined volume at precise intervals. The most well-known architectural example of waffle structures is the Parasol building in Seville (Schmid, 2010). Waffle structure is employed not only at the building scale, but also at smaller scales, such as in pavilion and furniture design (Indrawan, 2016; Dumitraşcu et al., 2018).

Augmented Reality (AR) is the real-time display of digital data superimposed on images of the real world. AR technology is utilized in numerous industries, including design, education, and entertainment. The fundamental distinction between Virtual Reality (VR) and Augmented Reality (AR) concepts is that in VR, the subject visually detaches from their physical location using a tool to experience a computer-generated virtual environment. AR, on the other hand, 'enhances' the user's perception of the real space around them by superimposing virtual objects. In contrast to virtual reality, in which the user is completely immersed in a computer-generated virtual environment, augmented reality superimposes virtual objects on the image of the real world that the user sees (Milgram and Kishino, 1994). Therefore, unlike VR, AR augments rather than alters reality.

The final technology used in the study is Computer-Aided Manufacturing (CAM). Today, CAM technologies are widely employed in the industrial sector. These systems allow the manufacturing process to be carried out quickly and efficiently while simultaneously enhancing the quality of the product. Various industries use computer-aided manufacturing technologies, including the automotive, aerospace, medical device, and defense industries (Bickel et al., 2018). There is a procedural parallel between design thinking, physical models, and information in these fields. In conjunction with the digitalization of manufacturing and fabrication techniques, designers are developing new ways of thinking (Arpak et al., 2009). With this strategy, computer-aided use of machines such as CNC, laser

cutting, and 3D printers are anticipated to shape the architecture of the future via mass customization-based production methods.

Forms derived from STO are typically manufactured using additive manufacturing techniques, such as 3D printing, as they are not particularly difficult to produce conventionally. This disadvantage of STO is eliminated through the adaptation of STO-obtained forms to waffle structure manufacturing, which will be explained in the following section. In architectural concept studies, STO and waffle structure are frequently combined (Bañón and Raspall, 2021). However, in these studies, the structure is formed using optimization techniques based on surface tension, and there is no volumetric three-dimensional optimization. Combining structural topology optimization and waffle structures in furniture design, this research fills a void in the field of study.

In light of the evolving paradigms in furniture design and manufacturing, this study introduces a theoretical framework that centers on the integration of STO and waffle structures. This framework's attempt to automate

the design process while achieving mass customization and material efficiency is innovative. It integrates design knowledge from diverse technological domains, such as machine learning algorithms and augmented reality, to create an innovative and effective workflow. The framework aims to overcome traditional design constraints by leveraging computational tools that complement human intuition and creativity. This synergistic approach not only increases the effectiveness of the design process, but also pushes the limits of customization and sustainability in furniture design.

2. Materials and Methods

In the design process, sequential techniques such as 'artificial intelligence-aided mood board', 'human-computer interaction', 'parametric design', 'topology optimization', 'observation in augmented reality', and 'computer-aided manufacturing' have been utilized (Figure 1).

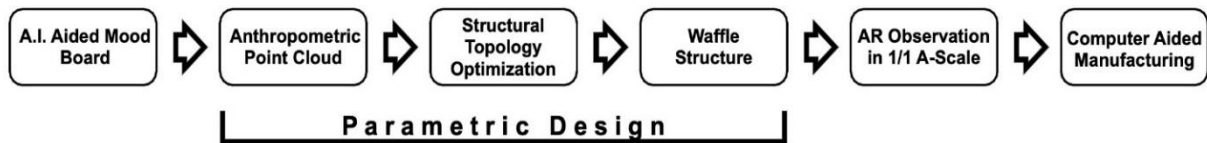


Figure 1. Design Process Procedure.

Initially, a brainstorming board was created using AI algorithms that perform visual synthesis. Then, instead of subjective design decisions, it was planned to develop the product of design decisions obtained through coding using parametric design methods. The parametric design scenario which is executed through the Rhinoceros Grasshopper plugin, begins with the collection of anthropometric data of the volume defined by the user's feet and legs using sensors to generate a point cloud. Then, this data was defined as a void in the topology-optimized structure of the parametric design environment. The mass formed as a result of topology optimization has been converted into an interlocked planar sliced structure using parametric design methods, and the resulting design has been experienced in augmented reality at a scale of 1/1. Using computer-aided manufacturing software, cut drawings were obtained, and the obtained drawings were checked and adapted to be manufactured on a CNC machine, and the assembled table was then evaluated.

3. Results and Discussion

3.1. Image Synthesis

At the outset of the research, algorithms that perform visual synthesis (text-to-image generation) were used to create a mood board and explore potentials. The terms 'meeting table,' 'parametric design,' 'topology optimization,' and 'waffle structure' were used as text in the application of these algorithms. The terms were entered as keywords, not to describe a specific design. Thus, it was desired that artificial intelligence's adaptability and creative synthesis yield an objective benefit.

The purpose of this technique is not to visualize a table in the mind of the designer using artificial intelligence, but rather to be inspired by the various visual syntheses of artificial intelligence. Not only was a single platform utilized, but also popular platforms such as Midjourney, Dall-E, Leonardo, DiffusionBee, Microsoft Designer, MotionLeap, Bluewillow, and FreewayML are used. Examining the results, it became evident that artificial intelligence typically evaluates waffle shape figuratively (Figure 2).

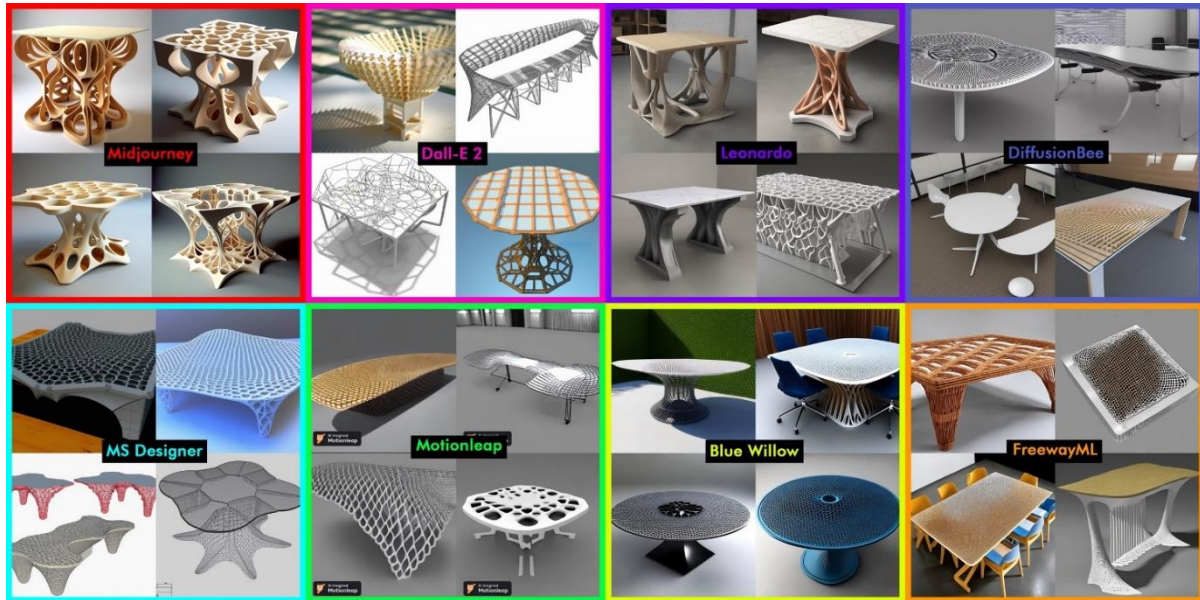


Figure 2. Visualizations created by various artificial intelligence systems utilizing the terms "table, waffle structure, parametric design, and topology optimization".

Aesthetically, Midjourney's visuals are far superior to Leonardo's, which are more realistically implemented. Blue Willow observed (top right) a single image containing the most appropriate visual for the imagined design. Nevertheless, it should be emphasized that this stage involves eye gymnastics. Even if it has no direct effect on the design, algorithms created with artificial intelligence enable the visualization of multiple variations by creating a mood board during the pre-design phase.

3.2. Parametric Design Environment

In a parametric design environment, the processes of transferring anthropometric data to design, topology optimization, and shaping waffle structures have been conceived. In conventional designs, performance-oriented decisions are made according to the following procedure: a design is created, the model is simulated, evaluation and improvement are made, the improved method is re-simulated, and this cycle continues until certain criteria are met. However, in designs created with algorithmic methods, simulation and parameter changes can be automated using various machine learning methods, allowing for the system's maximum efficiency to be realized. In the developed Structural Topology Optimized-Waffle model, parameters such as final dimensions, empty volume, loads, and support points are defined. By

controlling the above-mentioned parameters within a single software, the designer's subjective decision-making is minimized, and all these decisions and parameter changes can be observed in real time. The study utilizes the Millepede add-on of the RhinoCeros 6.0 software to implement the technique of structural topology optimization. In the following three sections, the hardware and software utilized in the parametric design environment are discussed more deeply, as well as the parameters.

3.3. Anthropometric Point Cloud

In the project, using the Kinect sensor, the foot and leg positions of three different heighted users were recorded at various times while working at a table, as well as their anthropometric data. The obtained point clouds from the recorded positions were combined to create a three-dimensional map of the action (Figure 3). The boundary of the cloud has been delineated by a curve comprised of over ten million points, which was then sectioned.

The purpose of rotating the section line derived from the point cloud to the table's perimeter is to improve ergonomics. Subtracting the volume of use created by the section line from the total volume of 240*120*72 cm, the volume limit of the table design is determined (Figure 4).

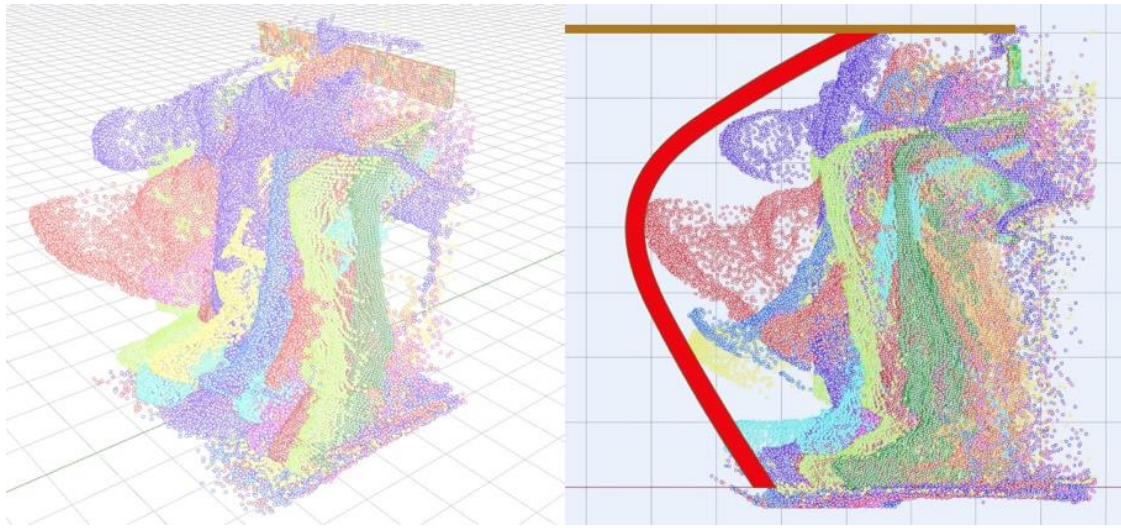


Figure 3. Point Cloud. (left) Sensor-obtained points; (right) section line derived from the point cloud.

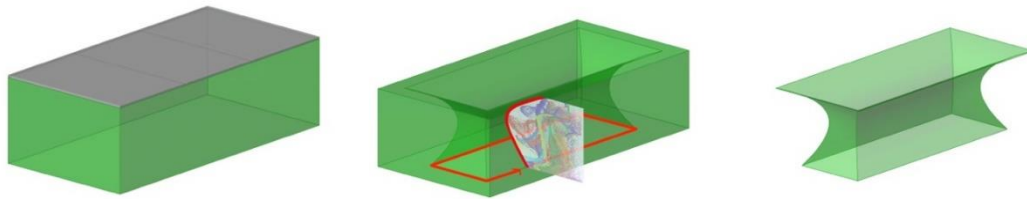


Figure 4. Volume definitions, (left) Total volume of 240*120*72 cm; (center) Volume defined by rotating the usage section curve around the table's perimeter; (right) Final design boundary.

3.4. Structural Topology Optimization

STO was used to design the table's fundamental shape. Taking into account the space and functions where the table will be used, as well as the fact that it will be subject to significant physical deformation and be frequently rearranged, the table's top has been designed in three sections. In production, MDF plates measuring 120 x 80 x 1.8 cm are planned. The three 120 x 80 cm tables will be attached to the substructure using L-profiles at the red points shown in Figure 5. In the topology optimization algorithm, it has been programmed that the load will be applied from these connection points, as load transfer will occur from these points. There are also vectors in the horizontal axis, as loads are not only in the -Z axis but also take into account that there will be lateral leanings from the load points toward the table's center of gravity. Figure 5 depicts the design volume, load, and support data entered into the STO algorithm.

In STO, "volume fraction" refers to the ratio of material volume to total design domain volume, which serves as a constraint for balancing structural performance and material efficiency. Masses obtained with different volume fractions and resolution parameters can be compared in Figure 6. When STO is conceived for objects created with the additive method, 3D printing, and the volume ratio is typically between 0.10 and 0.20. However, since the volume emptying in the waffle structure method that will be used after this stage will be much larger, the excessive volume fragmentation caused by these volume fractions compromises the structural integrity. Examining STO derivations, it has been subjectively predicted that the iteration with a volume fraction of 0.35 and a resolution of 70 will be appropriate for waffle structure construction. Examining the formation process of the iteration, it has been predicted that a resolution value of 70 will result in a more rigid structure (Figure 7).

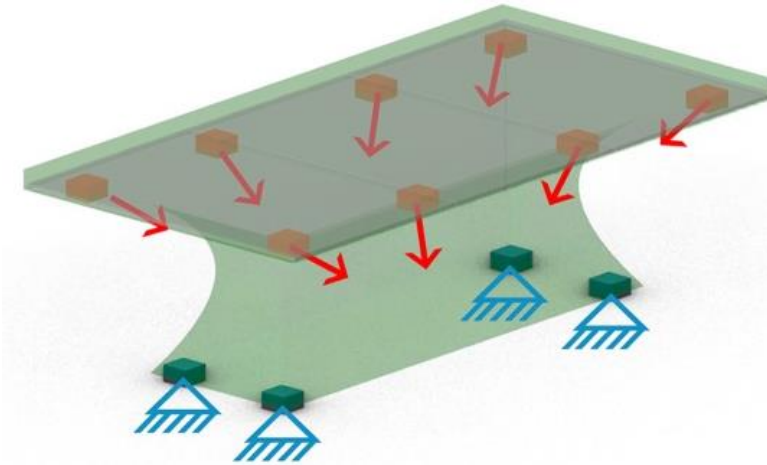


Figure 5. Volume specified in the tOpos plugin (green), loads (red), and supports (blue).

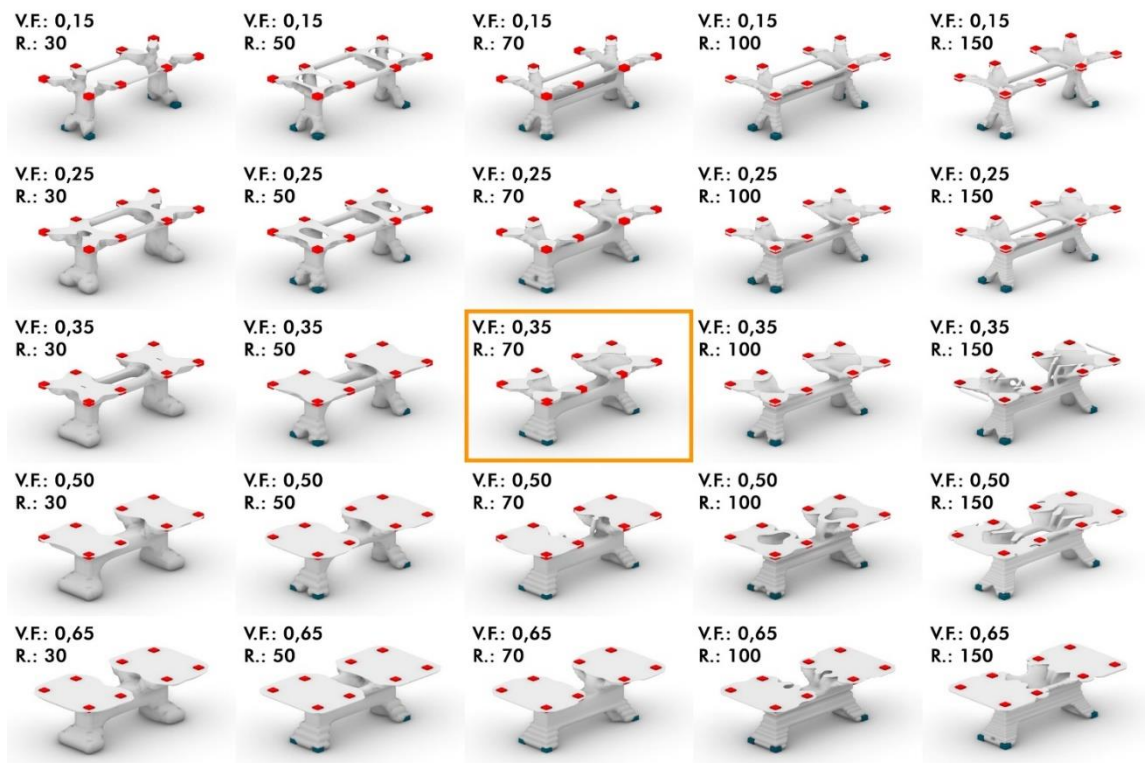


Figure 6. Different optimization parameter results and selected iteration (orange), V.F.: Volume Fraction, R.: Resolution.

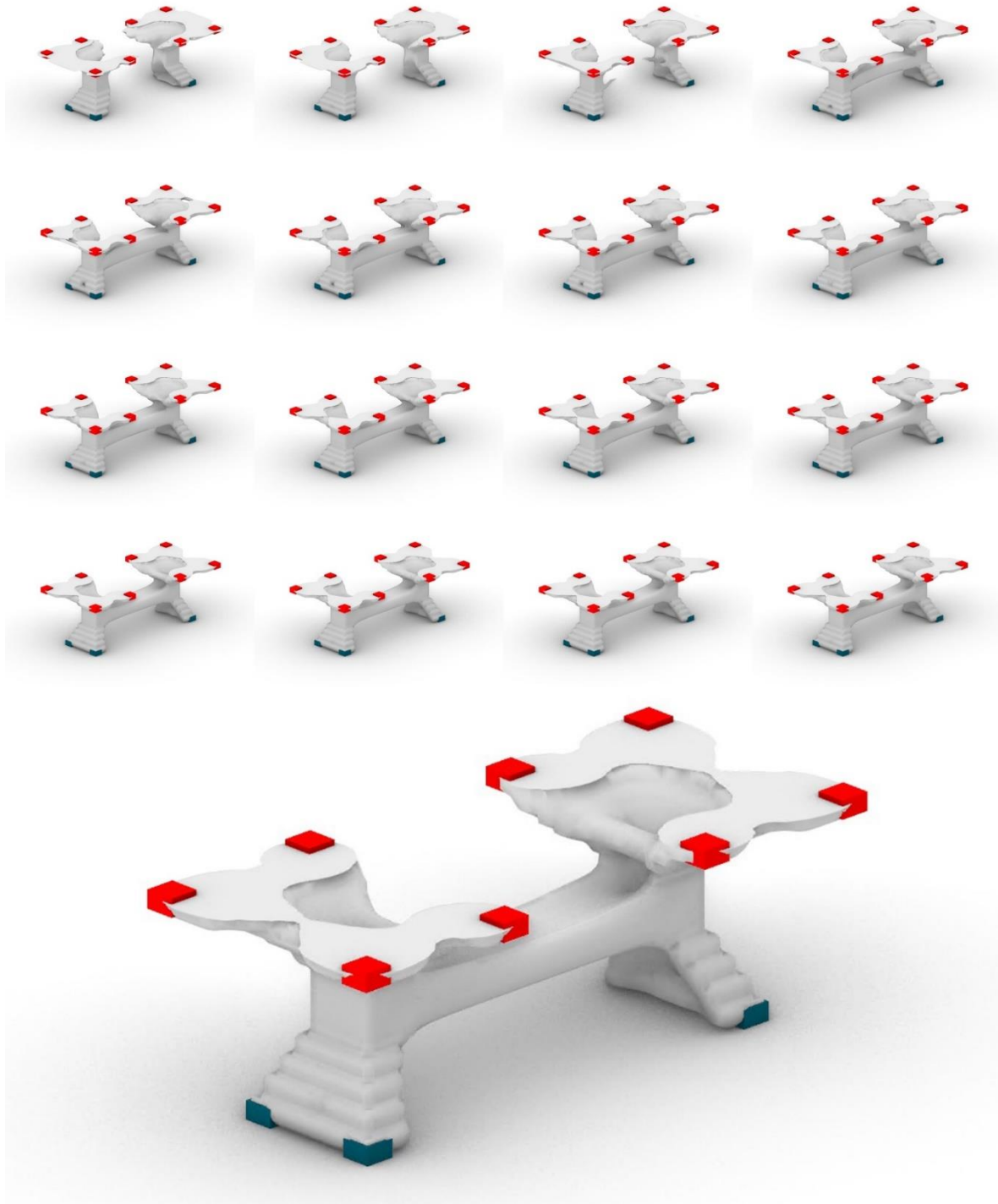


Figure 7. Iterations, (up) The formation procedure of the chosen iteration, (down) Final stage of iteration.

3.5. Waffle Structure

Lightweight structure is one of the primary advantages of waffle-structured furniture design. Using a grid-like structure reduces the amount of material required to construct the furniture, resulting in a lighter end product (Figure 8). When approximately 25 cm grid axes are used with the selected material of 1.8 cm thickness used for the study, there is a 92.8% reduction in volume. At this point, the total final volume reduction of the proposed model with a volume fraction of 0.35 entered as a parameter in topology optimization is roughly 97.5 percent.

There is no algorithmic method for determining the waffle structure's axis intervals. Despite the fact that the algorithm determines the cutting drawings, numerous axis numbers and width variations were tested when conceiving the axis layout. Consequently, it was anticipated that a 9 x 4 axis layout would provide sufficient stability when constructing the structure. When creating the waffle structure, the algorithm distributes all axis intervals equally with default preferences. Another advantage of the waffle structure during assembly is part classification and ease of assembly. The algorithm defines

the separation of part numbers according to the axes determined in the cutting drawing and the numbering of which part will go where. In addition, thanks to this

method's interlocking structure, the structure can be assembled without the use of any tools.



Figure 8. Waffle structure. (top) Volume reduction resulting from optimization; (middle) Installation sequences; (bottom) Final slices.

3.6. Observation via AR in 1/1 Scale

Observation at 1/1 scale using augmented reality technology, the designer virtually observes digital models in real environments (Figure 9). This allows for the demonstration of how the models will appear from various angles and how they will fit into the space. In this project, the developed design was viewed in an augmented reality environment using Arkio software, and the furniture was experienced in its intended location. Hence, the anthropometric data collected exhibited a high

level of consistency, with a scale of 1/1 being employed. Furthermore, it was ascertained that there was no intersection between the leg-foot and the structure when looking through AR image. A further advantage of AR for indoor furniture design is the established relationship between scale and space. The three-dimensional relationship that the furniture establishes with the spaces around it, other furniture, and objects can be observed using this method because the design is displayed at its actual scale in the area where it will be placed.



Figure 9. Augmented reality image of the table in the area where it will be placed. (This figure is blurry because it is a photograph of the image in the lens; in augmented reality, the image can only be viewed on the head-mounted display. In addition, the location's distinguishing characteristics are pixelated).

3.7. Computer-Aided Manufacturing and Assembly

In the project, laser cutting 18mm thick MDF was not favored due to its high-energy structure containing a fire hazard, and CNC was deemed suitable for obtaining the slices. CNC cutting has been incorporated into these modules based on the production with 120*80 cm panels taken at the outset of the design. In this instance, it is intended to produce the two main table slices in three

pieces each, and then assemble them during the assembly phase (Figure 10). The cutting drawings generated by the algorithm have been manually examined, and joints with acute angles that would pose a challenge for the CNC technique have been rounded. In addition, the waffle structure's required spacing has been increased from 18 mm to 18.5 mm. Thus, excessive friction force was avoided during assembly, thereby locking the system.



Figure 10. Image of the finished product

4. Conclusion

The integration of STO with waffle structure techniques in furniture design has opened new avenues in architectural design and digital culture. The innovative use of anthropometric data, parametric design, and augmented reality has not only enhanced the efficiency of the design process but also allowed for a more personalized approach. The ability to visualize designs in real space through augmented reality provides a tangible connection between the virtual and physical worlds, fostering a more immersive design experience.

While the study has achieved significant success in optimizing design, certain challenges were identified, such as the imbalance in weight distribution due to the lightweight structure, which might lead to instability. These challenges must be addressed in future research to ensure the practical applicability of the methods used.

The Opti-Waffle model developed in this study paves the way for mass customization in furniture design. It demonstrates how parametric design and computer-aided manufacturing can be employed to create unique pieces tailored to specific architectural spaces. This approach not only minimizes waste but also contributes to the creation of lightweight and efficient structures.

Furthermore, the study's methodology, which combines various fields such as machine learning, human-computer interaction, and augmented reality, reflects the growing trend of interdisciplinary collaboration in design.

This study has provided a comprehensive exploration of the potential for integrating STO with waffle structure techniques in architectural design, particularly with regard to the design of furniture. The research has demonstrated how cutting-edge technologies can revolutionize the design process while maintaining cost efficiency. This was accomplished through an approach that was both systematic and interdisciplinary.

The innovative use of anthropometric data to create personalized designs represents a significant advancement in the field. By tailoring designs to individual needs, the study has shown how technology can enhance both the functionality and aesthetics of architectural pieces. The application of waffle structure techniques for sustainability is another standout contribution, reducing material usage by 92.8% and contributing to global sustainability goals.

The utilization of augmented reality for real-space visualization has bridged the gap between virtual designs and physical reality, allowing designers to interact with their creations in a more tangible way. This integration of technology and design has broad implications for the future of architectural education and practice.

However, the study also highlights the need for further investigation into the challenges identified, particularly concerning stability and weight distribution. These challenges present opportunities for future research and development, paving the way for more robust and practical solutions.

Opti-Waffle model developed here offers a pathway

towards mass customization and sustainable design practices. It stands as a testament to the transformative power of technology in design, underscoring the endless possibilities that lie at the intersection of creativity, innovation, and interdisciplinary collaboration.

In conclusion, the findings of this research contribute significantly to the broader discourse on architecture design, parametric design, and digital culture. They provide valuable insights and directions for future exploration in these domains, highlighting the importance of continuous innovation and collaboration. The study serves as a source of inspiration for future researchers and practitioners, motivating them to expand the limits of architectural design and to explore novel approaches in the fusion of technology and creativity.

Author Contributions

The percentage of the author contributions is presented below. The author reviewed and approved the final version of the manuscript.

| | E.Y. |
|-----|------|
| C | 100 |
| D | 100 |
| S | 100 |
| DCP | 100 |
| DAI | 100 |
| L | 100 |
| W | 100 |
| CR | 100 |
| SR | 100 |
| PM | 100 |
| FA | 100 |

C=Concept, D= design, S= supervision, DCP= data collection and/or processing, DAI= data analysis and/or interpretation, L= literature search, W= writing, CR= critical review, SR= submission and revision, PM= project management, FA= funding acquisition.

Conflict of Interest

There is no conflict of interest. The funders had no role in the design of the study; in the collection, analyses, or interpretation of data; in the writing of the manuscript, or in the decision to publish the results.

Ethical Consideration

Ethics committee approval was not required for this study because of there was no study on animals or humans. The authors confirm that the ethical policies of the journal, as noted on the journal's author guidelines page, have been adhered to.

References

- Agassi J, Wiezenbaum J. 1976. Computer power and human reason: from judgment to calculation. *Technol Culture*, 17(4): 813-816.
- Arpak A, Sass L, Knight T. 2009. A meta-cognitive inquiry into digital fabrication exploring the activity of designing and

- making of a wall screen. Proceedings of the 27th Conference on Education and Research in Computer Aided Architectural Design in Europe, September 16-19, Istanbul, Türkiye, pp: 475-48.
- Bañón C, Raspall F. 2021. 3D Printing architecture workflows applications and trends. Springer, London, UK, pp: 127.
- Bickel B, Cignoni P, Malomo L, Pietroni N. 2018. State of the art on stylized fabrication. *Comput Graphics Forum*, 37(6): 325-342.
- Bikas H, Stavridis J, Stavropoulos P, Chryssolouris G. 2015. Design and topology optimization for additively manufactured structural parts: a formula student case study. Proceedings of the 6th BETA CAE International Conference, Jun 10-12, Thessaloniki, Greece, 1-6.
- Cui Q, Zhang H, Pawar S. S, Yu C, Feng X, Qiu S. 2022. Topology optimization for 3D- printable large-scale metallic hollow structures with self-supporting. Proceedings of the 27th Conference on Computer Aided Architectural Design Research in Asia (CAADRIA), 19-21 April, Nanjing, China, pp: 101-110.
- Davis D, Peters B. 2013. Design ecosystems: Customising the architectural design environment with software plug-ins. *Architectural Design*, 83(2): 124-131.
- Dumitraşcu AI, Hapurne TM, Bliuc I, Corduban CG, Nica RM. 2018. Waffle structure optimization in terms of energy efficiency and spatial geometry for a single family house. *Mater Sci Eng*, 444: 082013.
- Eloy S, Dias MS, Lopes PF, Vilar E. 2016. Digital technologies in architecture and engineering: exploring an engaged interaction within curricula. In Fonseca D, Redondo E, editors. *Handbook of Research on Applied E-Learning in Engineering and Architecture Education*. IGI Global PA, Hershey, USA, 368-402.
- Food4Rhino. 2023. URL: [https://www.food4rhino.com/en/browse?lang=en&df\[0\]=im_field_unified_type%3A773&df\[1\]=im_field_platform_app%3A720](https://www.food4rhino.com/en/browse?lang=en&df[0]=im_field_unified_type%3A773&df[1]=im_field_platform_app%3A720) (accessed date: February 17, 2023).
- Goodfellow IJ, Pouget-Abadie J, Mirza M, Xu B, Warde-Farley D, Ozair S, Bengio Y. 2014. Generative adversarial nets. *Advances Neural Inform Proc Syst*, 3(1): 2672-2680.
- Halle A, Campanile LF, Hasse A. 2021. An artificial intelligence-assisted design method for topology optimization without pre-optimized training data. *Applied Sci*, 11(19): 1-17.
- Indrawan SE. 2016. Design for environment and form findings through digital fabrication. *J Architect Built Environ*, 44(2): 171-178.
- Jain AK, Mao J. 1996. Artificial neural networks: A Tutorial. *Comput*, 29(3): 31-44.
- Jain A, Mildenhall B, Barron JT, Abbeel P, Poole B. 2022. Zero-shot text-guided object generation with dream fields. *Comput Sci*, 2022: 857-866.
- Kazakis G, Kanellopoulos I, Sotiropoulos S, Lagaros ND. 2017. Topology optimization aided structural design: Interpretation computational aspects and 3D printing. *Heliyon* 3(10): 1-33.
- Liu Z, Wang Y, Qi X, Fu C.-W. 2022. Towards implicit text-guided 3d shape generation. Proceedings of the IEEE/CVF Conference on Computer Vision and Pattern Recognition (CVPR), June 14-19, Seattle, WA, USA, 17896-17906.
- Lun R, Zhao W. 2015. A survey of applications and human motion recognition with microsoft kinect. *Inter J Pattern Recog Artificial Intel*, 5: 1555008.
- Lynn G. 1998. *Folds bodies, blobs : collected essays*. Bruxelles: La Lettre Volée, New Jersey, USA, 240.
- Lynn G. 1999. *Animate form*. Princeton Architectural Press, New Jersey, USA, 128.
- Ma J, Li Z, Zhao ZL, Xie YM. 2021. Creating novel furniture through topology optimization and advanced manufacturing. *Rapid Prototyping J*, 27(9): 1749-1758.
- Micell AGM. 1904. The limits of economy of material in frames structures. *Philosophical Magazine*, 6(8): 589-597.
- Milgram P, Kishino F. 1994. A Taxonomy of mixed reality visual displays. *IEICE Transactions Inform Syst*, E77-D(12): 1-15.
- Nadkarni PM, Ohno-Machado L, Chapman WW. 2011. Natural language processing: An introduction. *J American Medl Inform Assoc*, 18: 544-551.
- Niemann S, Kolesnikov B, Lohse-Busch H, Hühne C, Querin O, Toropov VV, Liu D. 2013. The use of topology optimisation in the conceptual design of next generation lattice composite aircraft fuselage structures. *Aeronautical J*, 117(3978): 1139-1154.
- Rade J, Balu A, Herron E, Pathak J, Ranade R, Sarkar S, Krishnamurthy A. 2021. Algorithmically-consistent deep learning frameworks for structural topology optimization. *Engin Applicat Artificial Intell* 106(11): 104483.
- Rutten D, McNeel R. 2007. *Grasshopper3D*. Seattle: Robert McNeel, Associates, Seattle, WA, USA, 251.
- Schmid V. 2010. Metropoli parasol: A new plaza and a unique timber mega structure right in the heart of Seville. *Large Struct Infrastructures Environment Constr Urban Areas*, 2010: 196-197.
- Schumacher P. 2009. Parametricism: A new global style for architecture and urban design. *Architectural Design*, 79(4): 14-23.
- Schumacher P. 2011. *The Autopoiesis of architecture volume I: a new framework for architecture*. John Wiley, Sons Ltd, London, UK, 480.
- Schumacher P. 2017. Tectonism in architecture design and fashion: Innovations in digital fabrication as stylistic drivers. *Architectural Design*, 87(6): 106-113.
- Sun Y, Liu Y, Xu L, Lueth TC. 2019. Design of a disposable compliant medical forceps using topology optimization techniques. Proceedings of IEEE International Conference on Robotics and Biomimetics ROBIO, December 6-8, Dali, China, 1-6.
- Tyflopoulos E, Steinert M. 2022. A comparative study of the application of different commercial software for topology optimization. *Applied Sci*, 12(2): 1- 23.
- Vinyals O, Toshev A, Bengio S, Erhan D. 2015. Show and tell: a neural image caption generator. Proceedings of IEEE Conference on Computer Vision and Pattern Recognition (CVPR), June 7-12, Boston, MA, USA, 3156-3164.
- Wynne Z, Buchanan C, Kyvelou P, Gardner L, Kromanis R, Stratford T, Reynolds TPS. 2022. Dynamic testing and analysis of the world's first metal 3d printed bridge. *Case Stud Construct Mater*, 17(e01541): 1-15.
- Zhou M, Rozvany GIN. 1991. The COC algorithm Part II: Topological geometrical and generalized shape optimization. *Comput Methods Appl Mechan Engin*, 89: 309-336.
- Zhuang X, Ju Y, Yang A, Luisa Caldas. 2023. Synthesis and generation for 3D architecture volume with generative modeling. *Inter J Architect Comput*, 1(1): 1-18.



CHROMOSOME BANDING PROPERTIES OF *Neogobius fluviatilis* (PALLAS, 1814) (PERCIFORMES, GOBIIDAE)

Sevgi UNAL-KARAKUS^{1*}, Muradiye KARASU-AYATA², Muhammet GAFFAROĞLU³

¹Bartın University, Faculty of Science, Department of Molecular Biology and Genetics, 74100, Bartın, Türkiye

²Kırşehir Ahi Evran University, Faculty of Health, Department of Nutrition and Dietetics, 40100, Kırşehir, Türkiye

³Kırşehir Ahi Evran University, Faculty of Science and Arts, Department of Molecular Biology and Genetics, 40100, Kırşehir, Türkiye

Abstract: The monkey goby, *Neogobius fluviatilis* (Pallas, 1814) that distributed in Türkiye was studied cytogenetically for the first time. In this context, diploid chromosome number, chromosome morphology and also chromosomal banding properties (C-banding and Ag-NOR staining) of *N. fluviatilis* were revealed out. Chromosome slides were prepared from head kidney cells according to the air-drying technique. Chromosome slides were observed under the microscope and metaphases were photographed. The chromosomes were measured by digital caliper and karyotype was arranged manually. The diploid chromosome number was found as 46. Karyotype was composed with all uniarmed chromosomes. Fundamental arm number was calculated as 46 too. No heteromorphic sex chromosomes were determined in the karyotype. C-bands were detected on the pericentromeres of almost all chromosomes. Otherwise, two Ag-NORs were found in the silver-stained metaphases. This study revealed out chromosomal properties of *N. fluviatilis* from Türkiye with conventional cytogenetic techniques. This report may improve the cytogenetic data of the genus *Neogobius*.

Keywords: Karyotype, C-banding, Nucleolus Organizer Region, Monkey Goby

*Corresponding author: Bartın University, Faculty of Science, Department of Molecular Biology and Genetics, 74100, Bartın, Türkiye

E mail: sunal@bartin.edu.tr (S. Unal-Karakus)

Sevgi UNAL-KARAKUS



<https://orcid.org/0000-0002-6409-7783>

Muradiye KARASU-AYATA



<https://orcid.org/0000-0001-8890-8547>

Muhammet GAFFAROĞLU



<https://orcid.org/0000-0001-7436-5828>

Received: September 05, 2023

Accepted: September 30, 2023

Published: October 15, 2023

Cite as: Unal-Karakus S, Karasu-Ayata M, Gaffaroglu M. 2023. Chromosome banding properties of *Neogobius fluviatilis* (Pallas, 1814) (Perciformes, Gobiidae). BSJ Eng Sci, 6(4): 600-603.

1. Introduction

Transboundary waters play an important role in the spreading of fishes to different countries. Many fish species entered into the inland waters of Türkiye from European or other countries. One of the threatened factors in the inland waters of Türkiye is the presence of non-native or invasive fish species. These species should be accelerating the loss of native species (Özuluğ et al., 2023). The family Gobiidae Cuvier, 1816 is one of the largest family that comprises about 200 genera and 2000 species (Karakuş et al., 2018). Gobiids are mostly marine fish but also found in shallow coastal waters (Esmaily and Kalbassi, 2008). The subfamily Gobiinae Cuvier, 1816 belonging to the family Gobiidae contains 18 species that are distributed in the inland waters of Türkiye (Çiçek et al., 2020). From these species, only two *Neogobius* species were listed, *N. fluviatilis* and *N. melanostomus* (Çiçek et al., 2020). An invasive fish is the monkey goby, *N. fluviatilis* distributes in the benthic areas that inhabits nearshore marine to brackish and freshwaters. This species tends high biological plasticity depending on the environment (Karakuş et al., 2018).

Chromosomal studies are important in cytotaxonomy of the gobiids (Ene, 2003). However, fish species have large numbers of relatively small chromosomes that makes cytogenetic studies difficult (Ergene-Gözükara and Çavaş, 2002). Chromosomal reports about non-native fish

species from the order Perciformes that are distributed in Türkiye have been reported in limited studies like *Gobius paganellus* (Ergene-Gözükara and Çavaş, 2002) and *Sander lucioperca* (Unal-Karakus et al., 2023). There is no data about the karyological properties of *N. fluviatilis* from Türkiye. In this study it is aimed to reveal out chromosomal properties of *N. fluviatilis* with conventional cytogenetic techniques.

2. Material and Methods

Four individuals (three females and one male) of *N. fluviatilis* were collected from Sakarya Creek, Tozman Village, Bilecik prov., Türkiye (40° 02' N; 30° 28' E). The individuals were transported alive to the laboratory and kept in a well-aerated aquarium until analysis. For karyological studies, air drying technique of Bertollo et al. (2015) was followed. The process was approved by the Local Animal Ethics Committee of Türkiye (Protocol Number: 68429034/09). Each individual was injected intra-peritoneally with a colchicine solution (0.1%; 1 ml/100 g body weight). The individuals were kept in a well-aerated aquarium and after two hours head kidney tissue was extracted and placed in a hypotonic solution of 0.56% KCl. After this step, the cellular suspension was centrifuged at 1200 rpm for 10 minutes. The hypotonic solution was discarded, and the pellet was suspended and washed 3 times in methanol: glacial acetic acid (3: 1). After



centrifugation at 1200 rpm for 10 minutes, the drops of cellular suspension were put on a clean slide. The slides were allowed to air dry. Some of them were stained with 10% Giemsa for 20 minutes. At least 10 slide was prepared from each specimen. Otherwise, C-banding was followed by using the method given by Sumner (1972) with slight modifications. For silver staining of the chromosomes, the method given by Howell and Black (1980) was followed. The all prepared slides were observed under a Leica DM3000 microscope. Mitotic metaphase plaques (with Giemsa stained, C-banded and silver stained) were photographed by using AKAS software. Karyotype was prepared by arranging chromosomes in pairs by size. Chromosomes were

measured by digital caliper and arranged according to the criteria given by Levan et al. (1964).

3. Results

Karyotype of *N. fluviatilis* with $2n = 46$ (Fig. 1A) consisted subtelo-acrocentric chromosomes that gradually decreased in size (Fig. 1A). Fundamental arm number (FN) was 46. No sex chromosomes were observed. C-bands were localized on the pericentromeres of almost all chromosomes (Fig. 1B). Two Ag-NORs were determined on the terminal regions of No. 8 chromosome only pair (Fig. 1C).

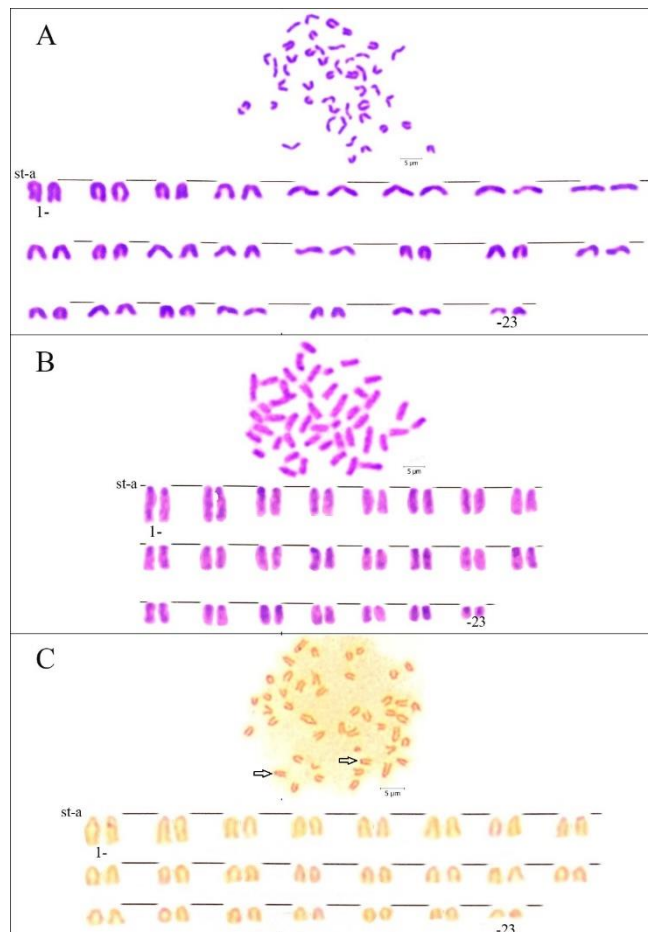


Figure 1. Metaphases and karyotypes of *Neogobius fluviatilis* A. Giemsa-stained metaphase and the arranged karyotype of Giemsa-stained metaphase; B. C-banded metaphase and the arranged karyotype of C-banded metaphase; C. Silver-stained metaphase (arrows indicate the Ag-NORs) and the arranged karyotype of silver-stained metaphase. Scale bar = 5 µm. st-a: subtelo-acrocentric.

4. Discussion and Conclusion

The gobiids are well studied karyologically, with dominant $2n = 44, 46$ and 48 . Other chromosome numbers appear to be exceptional (Ene, 2003). Karyotype with 46 unpaired chromosomes is considered to be basis for many gobiids including the genus *Neogobius* (Bigaliev et al., 2017). The ancestral $2n$ of Teleost fishes is 48 (Thode and Alvares, 1983). Otherwise, the ancestral gobiid karyotype consists of 46 mono-armed chromosomes (Ene, 2003). Thode and Alvares (1983) hypothesized that

decreasing in the $2n$, deletion should be occurred in the karyotype evolutions of gobiids. Also, it should be occurred after tandem fusion or Robertsonian translocation followed by pericentric inversions (Ocalewicz and Sapota, 2011). This reduction in the $2n$ should be taken place in the phylogeny of the group (Thode and Alvares, 1983).

In the order Perciformes, species are remarkably conservative in their karyotypes (Thode and Alvares 1983). According to the results of this study *N. fluviatilis*

with $2n = 46$ is represented in the diploid set mainly by uniarmed chromosomes like *Neogobius caspius*, *N. pallasii*, *N. melanostomus* (Bigaliev et al., 2017). *N. fluviatilis* from the Russian watersheds (Arai, 2011) shows similarity to this study in having 46 acrocentric chromosomes. With uniarmed 46 chromosomes, *N. fluviatilis* shows an ancestral karyotype pattern as three different species of the genus *Neogobius* (Arai, 2011), *N. kessleri* (Esmaily and Kalbassi, 2008), *N. caspius*, *N. pallasii* and *N. melanostomus* (Bigaliev et al., 2017). Otherwise, *N. fluviatilis* is different from *N. eurycephalus* (Ene, 2003) that has variable $2n = 30 - 32$.

Heteromorphic sex chromosomes were not reported on the other members of *Neogobius* (Ene, 2003; Ocalewicz and Sapota, 2011) or *Gobius* species (Ergene-Gözükara and Çavaş, 2002) like *N. fluviatilis*.

The location and number of NORs have descriptive characters in fish cytotaxonomy (Ene, 2003). Single chromosomal distribution of Ag-NORs also were described in *N. melanostomus* (Ocalewicz and Sapota, 2011) as this study. *N. fluviatilis* is similar to *N. eurycephalus* (Ene, 2003) in terms of Ag-NOR number. However, there are differences about the location of Ag-NORs that were reported in metacentric chromosomes in *N. eurycephalus* (Ene, 2003). Ag-NOR number and location of *Gobius niger* (Mandrioli et al., 2001) and *G. paganellus* (Caputo, 1998) are similar to *N. fluviatilis*. Ag-NOR size polymorphism that was reported in *N. eurycephalus* (Ene, 2003) is not observed in the silver-stained metaphases of *N. fluviatilis*.

Constitutive heterochromatin regions are observed by the application of a C-banding procedure (Sumner, 1972). These regions are an important tool in terms of chromosomal identification of the species. The differences in C-band localization could be used as a cytogenetic marker and reveal the chromosomal evolution between the species (Arslan and Arslan, 2007). C-band pattern of *N. fluviatilis* shows similarity to *N. eurycephalus* (Ene, 2003). Caputo (1998) reported that C-bands were localized at almost all the centromeric and telomeric chromosomal regions in *G. paganellus* and *G. niger*. In this context, *N. fluviatilis* is similar to above mentioned two species in terms of C-band pattern.

The cytogenetic data especially about chromosomal bandings for *Neogobius* species is limited to discuss their relationships in details. Also, $2n$ and chromosome morphology in the karyotype of *N. fluviatilis* from Russian (Arai, 2011) have been reported however no chromosomal banding features are available.

In conclusion, *N. fluviatilis* from Türkiye is not studied in terms of chromosome banding patterns. We conducted cytogenetic analysis with chromosomal bandings for the first time in Türkiye's population. Chromosomal studies of gobiids, contributed to their knowledge.

Author Contributions

Percentages of the author(s) contributions is present below. All authors reviewed and approved final version of the manuscript.

| | S.U.K. | M.K.A. | M.G. |
|-----|--------|--------|------|
| C | 40 | 30 | 30 |
| D | | 100 | |
| S | | | 100 |
| DCP | 50 | | 50 |
| DAI | 100 | | |
| L | 30 | 40 | 30 |
| W | 30 | 40 | 30 |
| CR | 40 | 30 | 30 |
| SR | 40 | 30 | 30 |
| PM | 30 | 30 | 40 |
| FA | 40 | 30 | 30 |

C= concept, D= design, S= supervision, DCP= data collection and/or processing, DAI= data analysis and/or interpretation, L= literature search, W= writing, CR= critical review, SR= submission and revision, PM= project management, FA= funding acquisition.

Conflict of Interest

The authors declared that there is no conflict of interest.

Ethical Consideration

The experimental procedures were approved by the Local Animal Care and Ethics Committee of Kirsehir Ahi Evran University (approval date: March 30, 2023 and protocol code: 68429034/09).

References

- Arai R. 2011. Fish karyotypes: A check list. Springer, Tokyo, Japan, pp: 340.
- Arslan A, Arslan E. 2007. Importance of C-banding (Constitutive Heterochromatin) in karyosystematic. Selçuk Univ J Sci Fac, 2(29): 121-126.
- Bertollo LAC, Cioffi MB, Moreira-Filho O. 2015. Direct chromosome preparation from freshwater teleost fishes. In: Ozouf-Costaz C, Pisano E, Foresti F, Toledo LFA, editors. Fish cytogenetic techniques, ray-fin fishes and chondrichthyans. CRC Press, New York, US, pp: 21-26.
- Bigaliev AB, Kobegenova SS, Adyrbekova KB, Gutsulyak SA. 2017. Diversity, morphology and karyotypes of species from genus *Neogobius* (Perciformes; Gobiidae) at coastal zone of the Caspian Sea (Aktau city). Int J Biol Chem, 10(1): 4-8.
- Caputo V. 1998. Nucleolar organizer (NOR) location and cytotaxonomic implications in six species of gobiid fishes (Perciformes, Gobiidae). Ital J Zool, 65(1): 93-99.
- Çiçek E, Sungur S, Fricke R. 2020. Freshwater lampreys and fishes of Turkey; a revised and updated annotated checklist 2020. Zootaxa, 4809(2): 241-270.
- Ene AC. 2003. Chromosomal polymorphism in the goby *Neogobius eurycephalus* (Perciformes: Gobiidae). Mar Biol, 142: 583-588.
- Ergene-Gözükara S, Çavaş T. 2002. Cytogenetic analysis of a Mediterranean gobiid fish *Gobius paganellus* L., 1758 from

- Turkey. *Folia Biol*, 50(1-2): 5-7.
- Esmaily AH, Kalbassi MR. 2008. Karyological study on bighead goby (*Neogobius kessleri*) from southern part of the Caspian Sea. *Iran J Fish Sci*, 7(2): 15-26.
- Howell WM, Black DA. 1980. Controlled silver-staining of nucleolus organizer regions with a protective colloidal developer: a 1-step method. *Experientia*, 36: 1014-1015.
- Karakuş U, Top N, Tepek y EG, Britton JR, Tarkan AS. 2018. Life history characteristics of the potentially invasive Ponto-Caspian goby *Neogobius fluviatilis* in natural lakes from its native range (Black Sea region of Turkey). *Mar Freshw Res*, 69: 1544-1556.
- Levan A, Fredga K, Sandberg AA. 1964. Nomenclature for centromeric position on chromosomes. *Hereditas*, 52: 201-220.
- Mandrioli M, Manicardi GC, Machella N, Caputo V. 2001. Molecular and cytogenetic analysis of the goby *Gobius niger* (Teleostei, Gobiidae). *Genetica*, 110: 73-78.
- Ocalewicz K, Sapota M. 2011. Cytogenetic characteristics of the round goby *Neogobius melanostomus* (Pallas, 1814) (Teleostei: Gobiidae: Benthophilinae). *Mar Biol Res*, 7(2): 195-201.
-  zuluđ M, Gaygusuz  , Gaygusuz  G, Kaya N, Sa  G. 2023. Fishes encountered in the Turkish Thrace River systems (NW Turkey). *Inland Water Biol*, 16(2): 341-356.
- Sumner AT. 1972. A simple technique for demonstrating centromeric heterochromatin. *Exp Cell Res*, 75: 304-306.
- Thode G, Alvares MC. 1983. The chromosome complements of two species of *Gobius* (Teleostei, Perciformes). *Experientia*, 39: 1312-1314.
- Unal-Karakus S, Gaffarođlu M, Karasu-Ayata M. 2023. Chromosomal analysis of *Sander lucioperca* (L., 1758) (Perciformes: Percidae) from Turkey. *Menba J Fisher Fac*, 9(1): 1-6.



ESTIMATION OF AIR LIGHT WITH DEEP LEARNING FOR A NEAR REAL-TIME IMAGE DEHAZING SYSTEM

Yücel ÇİMTAY^{1*}


¹TED University, Faculty of Engineering, Department of Computer Engineering, 06420, Ankara, Türkiye

Abstract: Haze which can be created by natural or synthetic factors, degrades the visual quality and human sight distance. Visible objects become invisible or scarcely visible. The physics of the degrading function due to haze has been modelled by Atmospheric Light Scattering (ALS) Model. Therefore, from a single hazy image, by using proper methods, it is possible to recover the original scene. In dehazing methods, which solve the ALS function, there are basically two steps: First one is the estimation of the air light present at the time of the image capturing and the second one is the estimation of transmission of the corresponding scene. One of the most effective method which is used for air light estimation is QuadTree decomposition. For this method, tests show that the most amount of the dehazing time is consumed to estimate the air light. For the case of High Definition (HD) imagery, the estimation of air light consumes huge time. Therefore, it cannot be possible to achieve a real-time or near real-time dehazing on traditional hardware. In this study, a novel convolutional neural network model is developed to estimate the air light directly from the hazy image quickly. The estimated air light then is used with Atmospheric Light Scattering model to handle the recovered image. Results show that the time cost is reduced by 56.0% and 65% for image resolutions of (640x480) and (1920x1080) compared to the QuadTree Decomposition method used in ALS based dehazing methods, without losing the visual quality of the dehazed image.

Keywords: Depth map, Image quality, Distortion, Image blur, Real-time systems

*Corresponding author: TED University, Faculty of Engineering, Department of Computer Engineering, 06420, Ankara, Türkiye

E mail: yuce.cimtay@tedu.edu.tr (Y. ÇİMTAY)

Yücel ÇİMTAY  <https://orcid.org/0000-0002-2254-9307>

Received: August 25, 2023

Accepted: September 30, 2023

Published: October 15, 2023

Cite as: Çimtay Y. 2023. Estimation of air light with deep learning for a near real-time image dehazing system. BSJ Eng Sci, 6(4): 604-612.

1. Introduction

Dehazing is crucial for a better human visual quality in the conditions of bad weather and for improving the success of the computer and machine vision applications needed in the field of transportation and military. For the last decade, many researchers have contributed to the subject of image enhancement and restoration (Wang and Yuan, 2017). As being one of the areas of image restoration, dehazing, depends on the estimation of the air light presents at the time of image capturing and the depth of the scene from the observing device. The success of dehazing is mostly determined by the success of these estimations. Another important problem related to dehazing is the homogeneity of the haze cover on the scene, since, it can be at local and/or global levels. Therefore the air light and transmission estimation may not be achieved properly for each pixel of the hazy image. The distance of the object from the scene is another important factor for the estimation of transmission term. As the distance from the sensor increases, the transmission of the light through the haze cover decreases and the estimation error becomes higher. In addition, as the amount of haze increases, the reconstruction error becomes larger and the success of dehazing goes down. Figure 1 shows the hazy images with low and high amount of haze, taken from CHIC

dataset (El Khoury et al., 2018) and the reconstructed images with Dark Channel Prior method (Park et al., 2014). It can be observed that when the amount of haze is higher the reconstruction performance is poor.

Fundamentally, there are 2 approaches in the context of image dehazing which are traditional methods and learning based methods. In traditional methods, contrast enhancement and image restoration are applied in the very first studies (Tan and Oakley, 2001; Kim et al., 2011; Hao et al., 2011; Al-Sammaraie, 2015). Secondly, ALS model of haze is studied to be solved. DCP and the DCP-based methods are frequently applied for this purpose (Kaiming et al., 2011; Park et al., 2014). Due to the limitations on the accurate estimation of transmission and/or air light, researchers have developed deep models to be trained with hazy and clear image pairs. Therefore, many learning based methods based on Convolutional Neural Network (CNN) (Cai et al., 2016; Li et al., 2018; Li et al., 2018; Rashid et al., 2019; Haouassi and Di, 2020), Generative Adversarial Networks (GAN) (Khatun et al., 2020; Ren et al., 2022), Vision Transformers (Guo et al., 2022; Li et al., 2023; Yuda et al., 2023) structures have been developed. By this way, several hazy image datasets were created and provided as open access (Ancuti et al., 2016; El Khoury et al., 2018; Ancuti et al., 2019; Ancuti et al., 2019; Li et al., 2019).



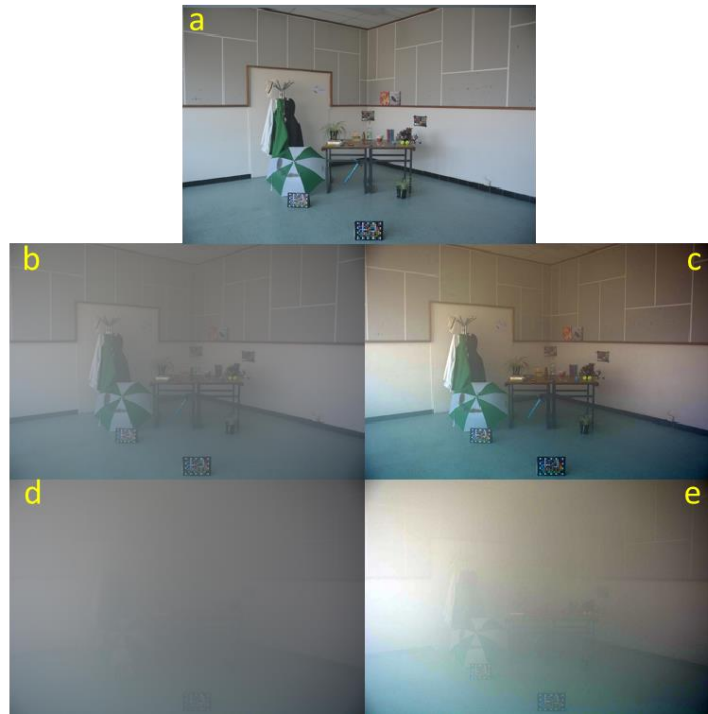


Figure 1. (a) Clear image, (b) low-level hazy image, (c) dehazed image from (b), (d) high-level hazy image, (e) dehazed image from (d).

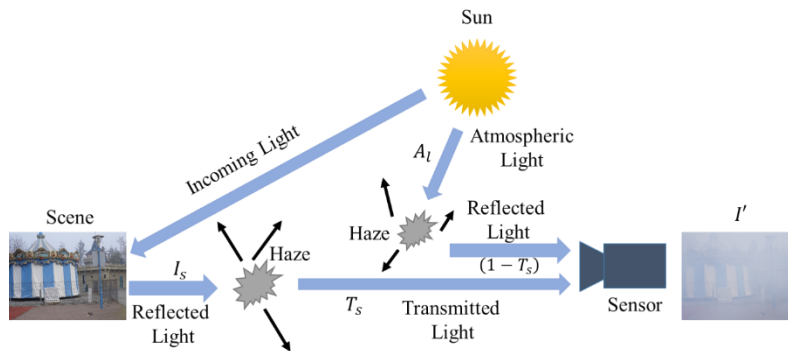


Figure 2. Atmospheric light scattering model.

However the most important bottleneck of the learning based methods are the capability of the generalization. A deep model which was trained on a specific dataset generally cannot achieve the same performance when tested on a different hazy image dataset. To solve this problem several studies based on domain adaptation have been employed for last 3-4 years (Shao et al., 2020; Meng et al., 2022).

In this study, we address the problem of real-time and/or near real-time dehazing which is needed in many real-time applications. When the complexity of the method or model increases, the response time to single image frame increases which makes real-time processing harder or impossible. Since the generalization capacity is more effective than many learning based models, (Park et al., 2014) is taken as the reference in this study. As shown in Figure 2, ALS model, needs the transmission map of the scene and air light (incoming light) present at the time of image capturing to be estimated from a hazy image.

According to the prior implementations, it was observed that the most percentage of the total dehazing process is spent in the air light estimation part (Cimtay, 2020; Cimtay, 2021). Therefore, as the image size increases, the estimation time also increases dramatically. In order to reduce this cost, in this study, the estimation of air light is embedded in a deep model which was trained with hazy images and the corresponding air light values handled by employing the Quadtree Decomposition method, applied in (Park et al., 2014). Therefore, the contribution of this study is, reducing the estimation time of air light by using a deep model and by this way achieving a near real-time dehazing performance on traditional hardware.

2. Motivation

ALS model formulates the physics of the deterioration due to haze, very well. Figure 2 shows the graphical structure of the formation of hazy image on the sensor. ALS equations are given in (Equation 1) where I' is the

hazy image, I_s is the clear image of the scene (ground truth), and A_l is the air light (incoming light in Figure 2).

$$I' = I_s * T_s + A_l * (1 - T_s) + E_r \quad (1)$$

The sensor integrates the air light reflected from haze particles and the light reflected from scene and transmitted through haze. In Equation 1, T_s is scene transmission map and E_r is the reconstruction error of ALS model. Although there will be still some amount of error due to the multiple reflections and/or transmission terms from/through haze particles and the absorbed energy by haze, for a perfect recover of the original scene from the hazy image, estimation of transmission and air light is crucial.

2.1. Preliminary Study

The time spent on the estimation of the transmission and air light is based on the size of the image to be dehazed. To measure the processing time, 3 images with various resolutions were dehazed by using (Park et al., 2014). The time spent for transmission estimation and air light estimation is measured and given in Table 1. It can be observed from the table, as the resolution of the image increases from 480p to 4K, the time spent for both transmission and air light increases. In addition the ratio of the spent time for air light estimation changes from 83% to 70.67%. This experiment shows that the most amount of the time spent for dehazing is used for the estimation of air light. In addition, time spent increases as the resolution of the image increases.

The interest point of this study is reducing the time spent for estimation of air light. By this way a real-time or near real-time dehazing can be achieved. Therefore, this study develops a deep CNN model which extracts the spatial features from the hazy images and employs a regression between these features and the estimated air light by (Park et al., 2014).

2.1. QuadTree Decomposition

The study in (Park et al., 2014) proposes an optimal approach to improve the previous air light estimation methods (Tan et al., 2001). It is presumed that air light which is present over much of the hazy image, has its intensity as greatest in a local region of the image scene. Then air light is estimated by using QuadTree subdivision on a transformed image. The grayscale version of the color hazy image is divided into non-overlapping sub-blocks with the size of $N \times N$.

The minimum value over each block is assigned to each

pixels inside each block, defined as B_k^{block} reduce the negative effects of a local object's bright values (Equation 2).

$$L_k^{block} = \min B(x), x \in B_k^{block} \quad (2)$$

N as the block size is chosen as 30×30 to keep the accuracy and reliability optimal. The transformed image has lower brightness values, in average, compare to the original gray image. As a result, the suggested QuadTree decomposition strategy can pick the candidate region to estimate the air light more accurately. By this way, after several iteration, the sky region in a sample image can be selected as the final candidate region even if the image includes some white floors. Air light is estimated more accurately by considering the final region. By calculating the Euclidean distance, given in Equation 3, for each pixel in that region, the color values of the pixel which minimizes the distance is chosen as the air light.

$$\|P_{(R,G,B)} - (1,1,1)\| \quad (3)$$

3. Related Work

Beyond the traditional dehazing methods, deep learning is the main technique used recently. For single-image dehazing, GANs and CNNs have lately been employed in the creation of deep learning-based techniques. The transmission maps and/or atmospheric light are directly learned from data using CNN-based algorithms (Cai et al., 2016; Boyi et al., 2017). It has also been demonstrated that utilizing multi-scale features collected by pyramid networks can enhance the effectiveness of CNN-based dehazing (Singh et al., 2020). GAN-based techniques (Zhang et al., 2018; Tran et al., 2022) have been developed to address the light attenuation effect caused by haze from the original scene.

However, the dehazing performance suffers if deep learning-based dehazing algorithms are unable to predict physical model parameters precisely. Furthermore, the success of the deep models are more accurate when tested on the same samples from the same dataset whereas the success reduces on different datasets. And due to the extensive training time and hardware requirements, deep learning-based dehazing methods are typically computationally inefficient. The literature has a lot of effective image dehazing approaches. The intricacy of the algorithms, hardware limitations, and high cost should all be taken into account when real-time implementation is the main focus.

Table 1. Time spent for various image resolutions

| Image resolution | Time Spent (ms) | | Ratio (%) |
|------------------|-----------------|--------------|-----------|
| | Air light | Transmission | |
| 640x480 | 130 | 20 | 86.6 |
| 1280x720 | 373 | 67 | 84.7 |
| 1920x1080 (HD) | 720 | 250 | 74.2 |
| 3840x2160 (4K) | 2530 | 1050 | 70.67 |

By combining the Central Process Unit (CPU) and Graphics Processing Unit (GPU), the study in (Yuanyuan and Yue, 2015) provides a parallel processing dehazing method for mobile devices and reports 1.12s per frame processing time for HD imagery on a Phone with Windows operating system. The researchers use a mean filter instead of the guided filter to speed up image processing in (Lu and Dong, 2019). A 25 frames per second processing rate is achieved over a DSP device (C6748 pure DSP device data sheet, 2023).

In the research in (Vazquez et al., 2020), a hazy color image is converted to an Hue, Saturation, Value (HSV) color space, and the value component is subjected to a global histogram flattening, the saturation component is changed to be consistent with the previous lowered value, and the value component is subjected to contrast enhancement. For HD images, it achieves 90ms of dehazing time on GPU. The study in (Yang et al., 2017) carries out two level image processing in an intelligent manner. If the final image satisfies the system requirements after applying histogram enhancement, no further action is necessary. If not, DCP is employed to clear the haze. It performs real-time processing and saves a lot of time by adopting a clever method.

The work in (Cheng et al., 2020) decomposes the picture into brightness and contrast components while parallelizing the fundamental Retinex model. Gamma correction and non-parametric mapping are used to restore the image, and the parallel GPU system achieves a processing time of 1.12ms for a high quality 1024x2048 image. Genetic programming is used in the work in (Hernandez et al., 2019) to create a transmission function estimator. The transmission map is then computed using this function. To obtain the haze-free pictures, a transmission map and a hazy image are utilized. The system processes both synthetic and real-world images at high rates. In (Kopf et al., 2008) to combine a virtual series of candidates for haze-free images into the desired single haze-free image, a unique pixel-level optimum dehazing criteria is suggested. By using every conceivable value of the discretely sampled depth of the scene, the calculation for this series of pictures is performed from the input hazy image. The benefit of this approach is that it can compute any individual pixel location without affecting the others. Therefore, employing a fully parallel GPU system makes it simple to implement this strategy.

In (Nguyen et al., 2022) a multiscale guided filtering-based real-time dehazing method is proposed. Since the estimation of the transmission map and atmospheric light in ALS model takes the longest time in the dehazing process, atmospheric light and transmission map are estimated by computing them in the low-resolution images which are created as image pyramids of the original hazy image. Then by using guided filtering for each pyramidal level, the transmission map is upsampled to the original resolution. (Shu-Juan et al., 2021), proposes a method for real-time video dehazing which

suppresses the visual artifacts by using incremental learning of transmission and spatial-temporal coherent regularization. A boundary limited dark channel model is provided to initialize the transmission map. Then, assuming a specific point on the scene produces highly correlated transmission values between the consecutive frames, a temporally coherent term is imposed for both maintaining the temporal consistency of the frame transmission values and continuously deriving an gradual transmission map to adapt the scene depth changes between the frames. In order to represent the scene depth, the study in (Zhu et al., 2015) builds a linear model and uses the color attenuation beforehand. This method prevents color distortion in the sky region, but the related dehazing results still contain some amount of visual distortions.

The study in (Chen et al., 2016) explores a gradient residual reduction approach for specifically eliminating any visual artifacts while concurrently recovering the haze-free image. Although this technique has successfully balanced haze removal with the reduction of visual artifacts, it frequently fails to maintain the image's fine details. The study in (Kim et al., 2013) attempts to make transmission values temporally consistent in the video sequence in an effort to decrease the visual contrast in a single frame and lessen flickering artifacts. Despite the fact that this method may generate outstanding dehazing results, it frequently results in oversaturated and blocking artifacts.

In this paper, the estimation of air light is automated on a deep model to get rid of the large amount of time spent for it. ALS model is then applied with the estimated air light and transmission map. By this way the processing time is reduced and near real-time dehazing is achieved. The rest of this paper is in section for proposed method is introduced in detail and in section 5 detail implementation results in terms of the obtained visual results and processing rates are presented. Finally, in the conclusion section a short summary of the proposed method and future studies are included.

4. Proposed Method

As stated in preliminary study part, the most amount time of dehazing with DCP (Park et al., 2014) is spent during the air light estimation. Therefore, in this study a deep CNN based estimation of air light is proposed. Firstly, RESIDE Indoor dataset (Boyi et al., 2017) is chosen to train the network. For each hazy image in RESIDE, QuadTree decomposition method in (Park et al., 2014) is employed and the corresponding air light values are handled. There are 13,990 hazy-clear image pairs in this dataset which is needed and sufficient to train a CNN model properly. The designed CNN model is shown in Figure 3 where the input is the hazy images and the output is the estimated air light by (Park et al., 2014). The shape of each of the convolutional, pooling and dense layers are shown on the figure. Also, the ratio of drop out layers are given. Drop out layers are very effective on

preventing the overfitting problem which is mostly faced in the training of deep models. Figure 3 is plotted by using *Visualkeras* library (VisualKeras Library, 2023). Batch size and learning rate are set to 32 and .0001, respectively. Number of epochs is set as 100. Input data is split in to training and validation sets with a ratio of 0.85 and 0.15. The training loss based on mean square error (MSE) for training and validation data is shown in Figure 4. It can be observed from the figure, training is very accurate. There is no overfitting and the amount of

MSE is in the order of 10^{-4} . Training is done on a computer with windows operating system, 8GB RAM, 11th Gen Intel(R) Core(TM) i7-1165G7 2.80 GHz processor and GeForce RTX 3060 model graphic card. Following acquiring the trained model, the real-time design of the proposed method is shown in Figure 5. In this study we employ the proposed real-time dehazing model on a computer with windows operating system. As the air light and transmission is estimated ALS model is used to reconstruct the dehazed image.

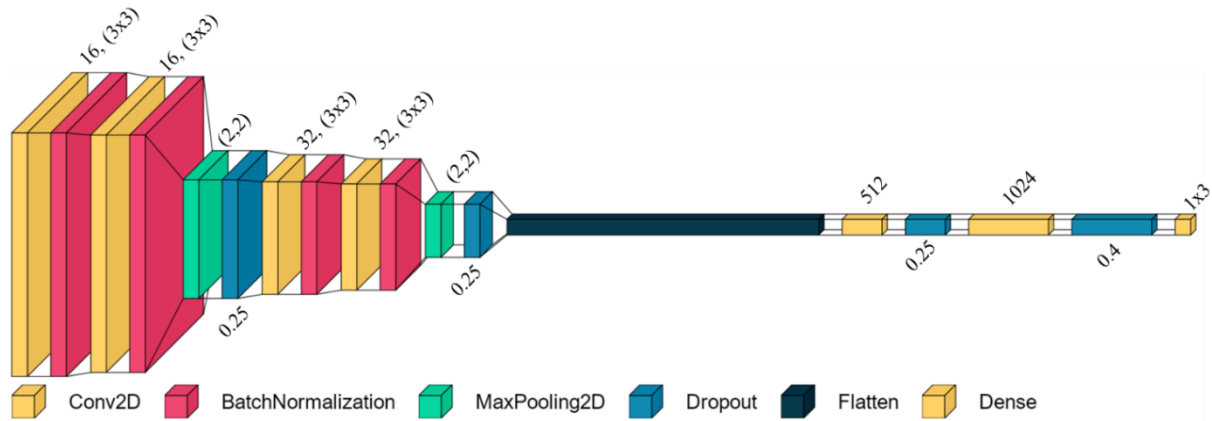


Figure 3. Proposed CNN model constructed with convolutional, normalization, pooling, dropout (ratio: 0.25) and dense layers.

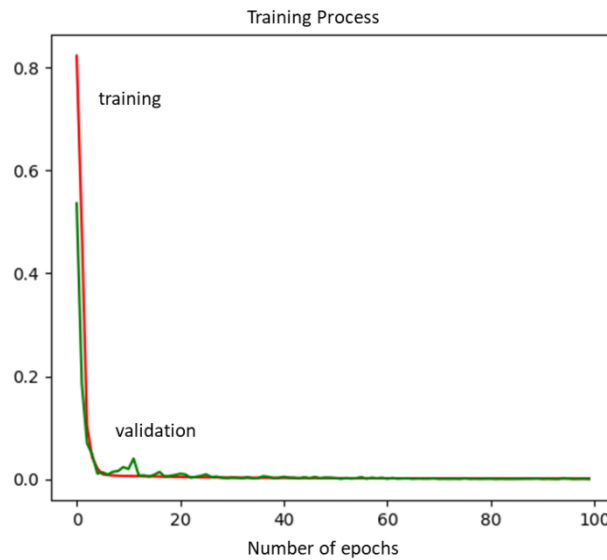


Figure 4. Training and validation loss.

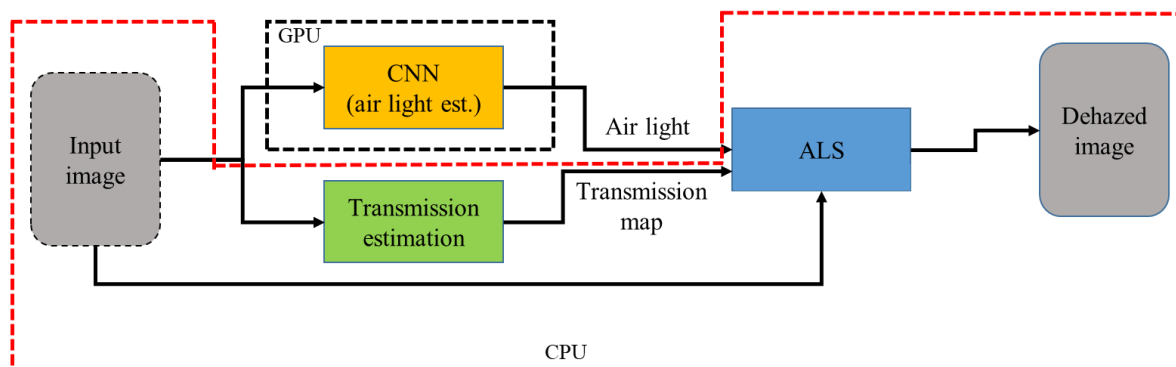


Figure 5. Proposed hybrid dehazing system.B

5. Results

In the application of (Park et al., 2014) the most time-consuming part of the dehazing process is the air light estimation. Instead of using the technique (Park et al., 2014) for air light estimation in this study a CNN is proposed. To measure the success of the proposed method, the system is run on a Windows PC. The time spent for air light estimation is given for three different resolutions: (640x480), (1280x720) and (1920x1080). By using the proposed deep model, air light estimation time is reduced for significant amount for each resolution as shown in Table 2. The time gain ratios for air light estimation are 65.1%, 84.3%, and 88.3% which is very promising.

Table 3 shows the overall dehazing time. This time is the summation of the time spent for air light, transmission and the solution of ALS model. Therefore it is higher than the values given in Table 2.

From Table 3, the frame processing time changes from 0.151 to 0.066, 0.442 to 0.126 and 0.972 to 0.336 s. for 480p, 720p and HD (High Definition) images, respectively. Therefore, approximately, 15.08, 7.89 and 2.97 frame rate is achieved. Frame rate reduces as the resolution increases. Since the air light is estimated by using a CNN running on GPU, due to the insufficient GPU memory, a 4K image could not be tested. The real-time performance of this study is compared with the results of the state of the art studies in Table 4.

Table 2. Air light estimation time on Windows PC

| Resolution | Processing Time (ms.) with (Park et al., 2014) | Processing Time (ms.) (proposed method) | Time gain (%) |
|----------------|--|---|---------------|
| 640x480 | 130 | 45.3 | 65.1 |
| 1280x720 | 373 | 58.3 | 84.3 |
| 1920x1080 (HD) | 720 | 84.2 | 88.3 |

Table 3. Dehazing speed on Windows PC

| Resolution | Method (Park et al., 2014) | | Proposed Method | |
|----------------|----------------------------|------------------|----------------------|------------------|
| | Tot. Proc. Time (ms) | Frame per Second | Tot. Proc. Time (ms) | Frame per second |
| 640x480 (480p) | 151 | 6.62 | 66.3 | 15.08 |
| 1280x720 | 442 | 2.26 | 126.7 | 7.89 |
| 1920x1080 (HD) | 972 | 1.02 | 336.2 | 2.97 |

Table 4. Benchmark results for per frame processing time (ms)

| Studies | (1920x1080) | (1280x720) | (640x480) |
|------------------------------------|-------------|------------|-----------|
| (Vazquez et al., 2020) with GPU | NA | 88.3 | NA |
| (Cheng et al., 2020) with Par. GPU | 1 | NA | NA |
| (Lu and Dong, 2019) | 40.1 | NA | NA |
| (Zhu et al., 2015) | 7093.5 | 3609 | 1471.2 |
| (Kim et al., 2013) | 904.0 | 410.1 | 125.1 |
| (Shu-Juan et al., 2021) | 709.3 | 304.6 | 91.02 |
| Proposed Method | 336.2 | 126.7 | 66.3 |

It can be understood from the benchmark table, for HD imagery, except the ones with DSP device and parallel GPU system, proposed method is the best. Similarly, for 480p imagery, proposed method is the best and for 1280x720 image, proposed method is the second best. The most important contribution and innovation of the proposed method is to provide near real-time image dehazing with traditional computers with a single GPU, as it has 15.08 and 2.97 fps for 480p and HD image. To provide the dehazing quality of the proposed method, dehazing results on different hazy samples from various datasets are also presented. In Figure 6, from top to down, the test results belong to Reside, CHIC, Dense-Haze, I-haze, O-haze datasets are shown. From left to right, clear image (ground truth), hazy image, dehazed

image with (Park et al., 2014) and dehazed image with proposed method are given. It can be observed that, for the proposed method, the visual quality of the dehazed image is kept well while increasing the frame rate.

Another important point is that the trained model performs a good generalization capacity. Although it was only trained on RESIDE hazy images, it can also perform well on estimation of the air light of other hazy images from different datasets. This is due to the fact that, the designed CNN structure is proper, dataset is rich and qualified, and there is only one parameter to be estimated which is the air light. Therefore, the proposed method is a kind of hybrid dehazing method based on traditional and deep learning based approaches which gets use of both approaches well.



Figure 6. Image dehazing results. Top to down: Samples from Reside, CHIC, Dense-Haze, I-haze, O-haze. Left to right: clear, hazy, Dehazed with DCP, Dehazed with Proposed Method.

6. Discussion and Conclusion

In this study, a deep learning based approach is proposed for the estimation of air light in ALS model on the hazy images. Since, the most amount of the processing time for dehazing is spent during air light estimation in (Park et al., 2014), this approach is crucial to reduce the estimation time, so overall dehazing time. The generalization performance of an end to end dehazing method based on deep learning is generally low when the model is tested on a different dataset which is different from the dataset used for training. For this reason, in this study an end-to-end dehazing model is not chosen instead the air light which can be estimated more properly independent of the dataset is estimated by using a pre-trained deep CNN model on GPU. By using a hybrid approach, then, air light and transmission map are used with ALS model for dehazing on CPU. Results show that proposed approach are superior or on par with the other state-of-the-art real-time dehazing applications. It reduces the time spent for air light estimation from 976

ms. to 336.2 ms. and increases the frame rate from 1.02 to 2.97 for HD imagery, which is very promising for real-time and/or near real-time dehazing applications on a traditional PC with a single GPU. Furthermore, while frame rate is increased, dehazed image quality is still kept which is the tradeoff in real-time and/or near real-time image dehazing applications. In the future this approach will be improved and the system will be applied on an FPGA hardware. This will be a challenging task due to the fact that it is hard to deploy a CNN model on FPGA hardware.

Author Contributions

The percentage of the author contributions is presented below. The author reviewed and approved the final version of the manuscript.

| | Y.Ç. |
|-----|------|
| C | 100 |
| D | 100 |
| S | 100 |
| DCP | 100 |
| DAI | 100 |
| L | 100 |
| W | 100 |
| CR | 100 |
| SR | 100 |
| PM | 100 |
| FA | 100 |

C=Concept, D= design, S= supervision, DCP= data collection and/or processing, DAI= data analysis and/or interpretation, L= literature search, W= writing, CR= critical review, SR= submission and revision, PM= project management, FA= funding acquisition.

Conflict of Interest

The author declared that there is no conflict of interest.

Ethical Consideration

Ethics committee approval was not required for this study because of there was no study on animals or humans.

Acknowledgements

This study is supported by The Scientific and Technological Research Council of Türkiye (TUBITAK) within the Project number: 122E333.

References

Al-Sammarai, MF. 2015. Contrast enhancement of roads images with foggy scenes based on histogram equalization. Proceedings of 10th International Conference on Computer Science & Education (ICCSE), June 22-24, Cambridge, UK, pp: 95-101.

Ancuti C, Ancuti CO, Vleschouwer CD. 2016. D-HAZY: A dataset to evaluate quantitatively dehazing algorithms journal. Proceedings of IEEE International Conference on Image Processing ICIP, September 25-28, Arizona, US, pp: 2226-2230.

Ancuti CO, Ancuti C, Sbert M, Timofte R. 2019. Dense haze: A benchmark for image dehazing with dense-haze and haze-free images. IEEE International Conference on Image Processing (ICIP), September 22-25, Taipei, Taiwan, pp: 1014-1018.

Ancuti CO, Ancuti C, Timofte R, Gool LV, Zhang L, Yang MH. 2019. NTIRE 2019 Image Dehazing Challenge Report. Proceedings of IEEE CVPR Workshop, June 16-17, Long Beach, CA, US, pp: 2241-2253.

Boyi L, Wenqi R, Dengpan F, Dacheng T, Feng D, Wenjun Z, Zhangyang W. 2017. Benchmarking Single-Image Dehazing and Beyond. IEEE Transact Image Proces, 28(1): 492-505.

C6748 pure DSP device data sheet. URL: https://www.ti.com/lit/ml/sprt6_33/sprt6_33.pdf?ts=15976

90676_332&ref_url=https%253A%252F%252Fww.google.com%252F (access date: June, 9, 2023).

Cai B, Xu X, Jia K, Qing C, Tao D. 2016. DehazeNet: An end-to-end system for single image haze removal. IEEE Transact Image Proces, 25(11): 5187-5198.

Chen C, Do MN, Wang J. 2016. Robust image and video dehazing with visual artifact suppression via gradient residual minimization. In: Proceedings of European Conference on Computer Vision, October 8-16, Amsterdam, Netherlands, pp: 576-591.

Cheng K, Yu Y, Zhou H, Zhou D. 2020. GPU fast restoration of nonuniform illumination images. J Real-Time Image Proces, 18(1): 75-83.

Cimtay Y. 2020. Towards real-time image dehazing on android operating system. Commun, Series A2-A3: Physical Sci Eng, 62(2): 177-188.

Cimtay Y. 2021. Smart and real-time image dehazing on mobile devices. J Real-Time Image Proces. 18: 2063-2072.

El Khoury J, Jean-Baptiste T, Alamin M. 2018. A database with reference for image dehazing evaluation. J Imag Sci Techn, 62(1): 010503-1-010503-13.

Guo C, Yan Q, Anwar S, Cong R, Ren W, Li C. 2022. Image dehazing transformer with transmission-aware 3D position embedding. IEEE/CVF Conference on Computer Vision and Pattern Recognition (CVPR), June 19-24, New Orleans, LA, US, pp: 5802-5810.

Hao W, He M, Ge H, Wang C, Qing-Wei G. 2011. Retinex-like method for image enhancement in poor visibility conditions. Procedia Eng, 15(1): 2798-2803.

Haouassi S, Di W. 2020. Image dehazing based on (CMTnet) cascaded multi-scale convolutional neural networks and efficient light estimation algorithm. Appl Sci, 10(3): 1-21.

Hernandez-Beltran J, Diaz-Ramirez V, Juarez-Salazar, R. 2019. Realtime image dehazing using genetic programming. J Opt Photonics Inf Proces, 11136: 222-230.

Kaiming H, Jian S, Xiaoou, T. 2011. Single image haze removal using dark channel prior. IEEE Transact Pattern Analy Machine Intell, 33(12): 2341-2353.

Khatun A, Haque M, Basri R, Uddin M. 2020. Single image dehazing: an analysis on generative adversarial network. J Comput Commun, 8(4): 127-137.

Kim JH, Jang WD, Sim JY, Kim CS. 2013. Optimized contrast enhancement for real-time image and video dehazing. J Visual Commun Image Represent, 24(3): 410-425.

Kim JH, Sim JY, Kim CS. 2011. Single image dehazing based on contrast enhancement. Proceedings of IEEE International Conference Acoustics, Speech and Signal Processing(ICASSP), May 22-27, Prague, Czech Republic, pp: 1273-1276.

Kopf J, Neubert B, Chen B, Cohen M, Cohen-Or D, Deussen O, Uyttendaele M, Lischinski D. 2008. Deep photo: modelbased photograph enhancement and viewing. ACM Trans Graph, 27(5): 1-10.

Li B, Peng X, Wang Z, Xu J, Feng D. 2017. Aod-net: All-in-one dehazing network. Proceedings of the IEEE international conference on computer vision, October 22-29, Venice, Italy, pp: 4770-4778.

Li C, Guo J, Porikli F, Fu H, Pang Y. 2018. A cascaded convolutional neural network for single image dehazing. IEEE Access, 6(1): 24877-24887.

Li H, Zhang Y, Liu J, Ma Y. 2023. GTMNet: a vision transformer with guided transmission map for single remote sensing image dehazing. Scient Rep, 13(1): 9222.

Li J, Li G, Fan H. 2018. Image dehazing using residual-based deep CNN. IEEE Access, 6(1): 26831-26842.

Lu J, Dong C. 2019. DSP-based image real-time dehazing

- optimization for improved dark-channel prior algorithm. *J Real-Time Image Proces*, 17(1): 1675-1684.
- Meng X, Feng Y, Su Z, Zhou F. 2022. Unsupervised domain adaptation image dehazing with contrastive nearest-farthest subspace distance. *Proceedings of IEEE International Conference on Multimedia and Expo (ICME)*, July 18-22, Taipei, Taiwan, pp: 1-6.
- Park D, Park, H, Han, DK, Ko, H. 2014. Single image dehazing with image entropy and information fidelity. *IEEE International Conference on Image Processing (ICIP)*, October 27-30, Paris, France, pp: 4037-4041
- Rashid H, Zafar N, Javed Iqbal M, Dawood H. 2019. Single Image Dehazing using CNN. *Procedia Comput Sci*, 147(1): 124-130.
- Ren W, Zhou L, Chen J. 2022. Unsupervised single image dehazing with generative adversarial network. *Multimed Syst*, 2022: 1-11.
- Shao Y, Li L, Ren W, Gao C, Sang N. 2020. Domain Adaptation for Image Dehazing. *Proceedings of IEEE/CVF Conference on Computer Vision and Pattern Recognition (CVPR)*, June 16-18, Seattle, WA, US, pp: 2805-2814.
- Shu-Juan P, Zhang H, Liu X, Wentao F, Zhong B, Ji-Xiang D. 2021. Real-time video dehazing via incremental transmission learning and spatial-temporally coherent regularization. *Neurocomputing*, 458: 602-614.
- Singh A, Bhave A, Prasad DK. 2020. Single image dehazing for a variety of haze scenarios using back projected pyramid network. *Proceedings of ECCV 2020 Workshops*, August 23-28, Glasgow, UK, pp: 166-181.
- Tan K, Oakley JP. 2001. Physics-based approach to color image enhancement in poor visibility conditions. *J Optical Soc America*, 18(10): 2460-2467.
- Tran LA, Moon S, Park DC. 2022. A novel encoder-decoder network with guided transmission map for single image dehazing. *Procedia Comput Sci*, 204(1): 682-689.
- Nguyen VT, Vien AG, Lee C. 2022. Real-time image and video dehazing based on multiscale guided filtering. *Multimed Tools Appl*, 8(1): 36567-36584.
- Vazquez-Corral J, Galdran A, Cyriac P, Bertalmio M. 2020. A fast image dehazing method that does not introduce color artifacts. *J Real-Time Image Proces*, 17(1): 607-622
- VisualKeras Library. 2023. URL: <https://pypi.org/project/visualkeras/> (access date: June, 8, 2023).
- Wang W, Yuan X. 2017. Recent advances in image dehazing. *IEEE/CAA J Automatica Sinica*, 4(3): 410-436.
- Yang J, Jiang B, Lv Z, Jiang N. 2017. A real-time image dehazing method considering dark channel and statistics features. *J Real-Time Image Proces*, 13(1): 479-490.
- Yuanyuan S, Yue M. 2015. Single image dehazing on mobile device based on GPU rendering technology. *J Roboti Network Artificial Life*, 2(2): 85-88.
- Yuda S, Zhuqing H, Hui Q, Xin D. 2023. Vision transformers for single image dehazing. *IEEE Transact Image Proces*, 32(1): 1927-1941.
- Zhang H, Patel VM. 2018. Densely connected pyramid dehazing network. *Proceedings of the IEEE conference on computer vision and pattern recognition*, June 18-23, Salt Lake City, UT, US, pp: 3194-3203.
- Zhu Q, Mai J, Shao L. 2015. A fast single image haze removal algorithm using color attenuation prior. *IEEE Transact Image Proces*, 24(11): 3522-3533.



ÇOK NOKTALI DERİN ÇEKME PROSESİNDE FARKLI PİM RADIUSLARININ ETKİSİNİN İNCELENMESİ

Kaan Emre ENGİN^{1*}

¹Adıyaman Üniversitesi, Mühendislik Fakültesi, Makine Mühendisliği Bölümü, 02040, Adıyaman, Türkiye

Özet: Derin çekme prosesi, metal levha şekillendirme endüstrisinde en çok tercih edilen proseslerden bir tanesidir. Özellikle seri üretim söz konusu olduğunda kap formundaki iş parçalarının düşük maliyetlerle üretilmesi mümkündür. Ancak, aynı durum seri üretim dışında farklı boyutlara sahip ürünlerin imal edilmesi esnasında geçerli olmayıp, kalıp yapım maliyetlerinden kaynaklı olarak prosesin ekonomikliğini büyük ölçüde kaybetmesiyle sonuçlanmaktadır. Bu dezavantajı gidermek amacıyla daha yeni yaklaşımların ve metodların geliştirilmesi gerekmektedir. Çok noktali derin çekme prosesi standart kalıp elemanları yerine yüksekliği ayarlanabilir pimler kullanılması vasıtasıyla farklı boyutlarda veya yüksekliklerde derin çekme işleminin yapılmasına müsaade eden bir yöntemdir. Ancak prosesin bir özelliği olan pim kullanımının etkilerinin araştırılması da önemlidir. Bu çalışmada 87 mm uzunluğunda, 12 mm çapa sahip pimlerden oluşan çok noktali derin çekme kalıbında farklı pim uç radyuslarının (1 mm, 3 mm, 6 mm) proses üzerine olan etkileri araştırılmıştır. Bu amaçla ilk önce 6 mm radyusa sahip pimlerden oluşan bir kalıp seti imal edilmiş ve 0,75 mm kalınlığa sahip AISI Al 3003 HX6 alüminyum alaşım üzerinde deneyler gerçekleştirilmiştir. Daha sonra aynı koşullar altında sonlu elemanlar yöntemi kullanılarak yapılan simülasyonlar sonucunda elde edilen değerler ve deneylerden elde edilen değerler karşılaştırılmıştır. Bulgular arasındaki tutarlılık sağlandıktan sonra çalışmanın 1 mm ve 3 mm radyusa sahip pimlerin etkisinin incelenmesini içeren aşamaları sonlu elemanlar yöntemi ile simüle edilerek, analizler gerçekleştirilmiştir. Sonuç olarak pim uç radyuslarının değerlerinin azaldıkça, iş parçası ile temas eden yüzeyin artmasına bağlı olarak gerekli yük değerinin arttığı ve iş parçasının daha düşük bir çekme derinliğinde yırtıldığı saptanmıştır. En iyi sonuçların 6 mm radyusa sahip pim kullanılması durumunda elde edildiği görülmüştür.

Anahtar kelimeler: Çok noktali şekillendirme, Derin çekme, Çok noktali derin çekme, Pim çapı, AISI Al 3003


Investigation of the Effect of Different Pin Radius in the Multi-Point Deep Drawing Process

Abstract: The deep drawing process is one of the most preferred processes in the sheet metal forming industry. Especially when it comes to mass production, it is possible to produce workpieces in the form of containers at low costs. However, the same situation is not valid during the production of products with different dimensions except for mass production, resulting in the process losing its economy to a large extent due to die manufacturing costs. In order to overcome this disadvantage, newer approaches and methods need to be developed. The multi-point deep drawing process is a method that allows deep drawing in different sizes or heights by using height-adjustable pins instead of standard die elements. However, it is also important to investigate the effects of the use of pins, which is a feature of the process. In this study, the effects of different pin end radii (1 mm, 3 mm, 6 mm) on the process were investigated in a multi-point deep drawing die consisting of pins with a length of 87 mm and a diameter of 12 mm. For this purpose, a die set consisting of pins with a radius of 6 mm was first manufactured and experiments were carried out on AISI Al 3003 HX6 aluminum alloy with a thickness of 0.75 mm. Then, the values obtained as a result of the simulations using the finite element method under the same conditions and the values obtained from the experiments were compared. After the consistency between the findings, the stages of the study including the examination of the effect of the pins with 1 mm and 3 mm radius were simulated by the finite element method and analyzes were carried out. As a result, it has been determined that as the values of the pin end radii decrease, the required load value increases due to the increase in the contact surface with the workpiece, and the workpiece ruptures at a lower drawing depth. It has been observed that the best results are obtained when using pins with a radius of 6 mm.

Keywords: Multi-point forming, Deep drawing, Multi-point deep drawing, Pin diameter, AISI Al 3003

*Sorumlu yazar (Corresponding author): Adıyaman Üniversitesi, Mühendislik Fakültesi, Makine Mühendisliği Bölümü, 02040, Adıyaman, Türkiye

E mail: kengin@adiyaman.edu.tr (K.E. ENGİN)

Kaan Emre Engin  <https://orcid.org/0000-0002-6439-7700>

Gönderi: 6 Eylül 2023

Kabul: 1 Ekim 2023

Yayınlanma: 15 Ekim 2023

Received: September 23, 2023

Accepted: October 1, 2023

Published: October 15, 2023

Cite as: Engin KE. 2023. Investigation of the Effect of Different Pin Radius in the Multi-Point Deep Drawing Process. BSE Eng Sci, 6(4): 613-623.

1. Giriş

Derin çekme prosesi, levha halindeki iş parçasının bir kalıp seti vasıtasıyla üç boyutlu derin bir kap formuna getirildiği yöntem olarak tanımlanabilir. Belirli bir geometriye sahip zımba, levhayı alt kalıp boşluğuna bastırarak, levhanın kalıp iç duvarına sıvanmasını ve bu

şekilde son halini almasını sağlar. Çeşitli parçaların yüksek kalitede ve hızlı olarak üretilebilmesi aynı zamanda da düşük maliyetlere sahip olması nedeniyle bu yöntem yaygın bir kullanıma sahiptir (Beglarzadeh ve Davoodi, 2016). Ancak, geleneksel metal levha şekillendirme yöntemlerin karşı karşıya oldukları en büyük sorunlardan bir tanesi kalıp sisteminin farklı



boyut ya da şekildeki parçaların üretimine göre ayarlanamaması ve ekonomikliğin ancak yüksek adetlerde üretim veya seri üretim söz konusu olduğunda sağlanabilmesidir (Zareh-Desari ve ark. 2017). Çünkü, farklı şekil ya da boyuttaki kalıp setlerinin üretilmesi ekstra maliyet gerektirmektedir ve küçük miktarda yapılacak üretimler açısından ekonomikliğin sağlanabilmesi zorlaşmaktadır. Bu dezavantajlı durum derin çekme prosesi içinde geçerlidir. Yeni yöntemlerin derin çekme prosesine uygulanması vasıtasıyla bu sorunun giderilmesi önem arz etmektedir.

Çok noktali şekillendirme prosesi belirtilen dezavantajlı durumları giderebilecek bir yöntem olarak kendini göstermektedir. Çok noktali şekillendirme, 3 boyutlu yüzeyler oluşturmak için esnek bir üretim yöntemidir. Ana fikri, tüm kalıbın düzenli ve doğru bir şekilde ayarlanabilen birçok pim'e bölünmesi şeklindedir. Çok noktali kalıp üzerinde bulunan pimlerin birbirinden bağımsız ve yüksekliklerinin ayarlanabiliyor oluşu, istenilen formların ve 3 boyutlu yüzeylerin oluşturabilmesine imkân tanır. Çok noktali şekillendirme yöntemi eğer derin çekme prosesine uygulanabilirse, geleneksel derin çekme prosesinin karşılaştığı sorunları ortadan kaldıracak potansiyele sahiptir.

Çok noktali şekillendirme prosesinin doğası gereği, bir bütün halindeyken parçalı bir forma dönüşen kalıp elemanlarından kaynaklanan ve incelenmesi gereken farklı parametrelerde ortaya çıkmaktadır. Aynı zamanda prosesin standart metal levha şekillendirme yöntemleri ile elde edilmesi ciddi zorluklar içeren şekillerin üretimini mümkün kılması da araştırmacıların bu özellikler üzerinde incelemeler yapmasına sebebiyet vermiştir.

Li ve ark., (1999), kalıp üzerinde bulunan pimlerin yüksekliklerinin ayarlanma şekline göre çok noktali şekillendirme prosesini dört çeşit olarak tanımlamışlardır. Çok noktali kalıp, çok noktali yarım kalıp, çok noktali pres ve çok noktali yarım pres adını verdikleri çeşitleri inceleyen araştırmacılar, metal levhanın şekillendirilmesi esnasında pimlerin dizilimini değiştirerek izlenen farklı yolların getirdiği şekil değiştirme miktarlarını ve özelliklerini incelemişlerdir. Li ve ark. (2002), sonlu elemanlar yöntemi kullanarak gerçekleştirdikleri bir diğer çalışmada, çok noktali şekillendirme prosesinde meydana gelen yüzey bozukluklarını incelemişlerdir. Esnek bir iş parçası tutucu (sıyırıcı) kullanarak parça yüzeyinde meydana gelen kırışmaları engellemeyi başaran araştırmacılar, prosesin kendine özgü en belirgin hatalarından olan ve birbirinden bağımsız pimlerin uyguladığı baskı sonucu iş parçası yüzeyinde şekillendirme esnasında meydana gelen çukurların farklı pim dizilimleri uygulanarak azaltılabileceğini belirtmişlerdir.

Cai ve Li (2005), sonlu elemanlar yöntemi kullanarak, çok noktali şekillendirme prosesi vasıtasıyla şekillendirilen metal levha için elastik-plastik malzeme modelini incelemişler ve güncellenmiş Lagrangian formülasyonunu temel alan bir yaklaşım

geliştirmişlerdir. Ayrıca levha üzerinde oluşan gerilmelerin entegrasyonu için de bir algoritma oluşturmuşlardır.

Liu ve ark. (2008), çok noktali şekillendirme prosesinin kalıp setinde yer alan pimleri bilgisayar kontrollü olacak şekilde tasarlamışlardır. Kullandıkları ekipmanların özelliklerinin ve pin boylarının hangi koşullara bağlı kalınarak ayarlanacağını, tasarım ilkelerinin ve ayar modlarının detaylarını paylaşan araştırmacılar daha sonrasında bu yöntemleri kullanarak geleneksel metal levha şekillendirme yöntemleri ile gerçekleştirilemeyecek düzeydeki formları oluşturmayı başarmışlardır.

Qian ve ark (2007), çok noktali şekillendirme yöntemine ait iki farklı şekillendirme tipini incelemişlerdir. Düz metal levhaya çanak formu vermek için kullanılan bu iki tipin ilkini çok adımlı şekillendirme olarak tanımlamışlardır. Metod, oluşturulması planlanan çanak formuna ait derinlik değerinin iş parçasına birkaç adımda verilmesi prensibine dayanmaktadır. İkinci tip olan kesit şekillendirme metodunda ise metal levhanın belirli kısımları parça parça çok noktali şekillendirme işlemine tabi tutulmaktadır. Araştırmacılar bu iki metodu kullanarak hem deneysel hem de nümerik çalışmaları yapmışlar ve iki metodun metal levhanın şekillendirilmesi esnasında olan etkilerini incelemişlerdir.

Zhu ve ark. (2019), kare pimlerin çok noktali şekillendirme prosesi üzerindeki etkilerini ve dış büyü olarak şekillendirilen farklı kalınlıklara sahip metal levhanın geri esneme davranışlarını araştırmışlardır. Metal levhanın şekillendirme mekanizmasını ve geri esneme özelliklerini analiz etmek için teorik denklemler türetmiş, elde ettikleri teorik ve analitik sonuçları deneysel sonuçlarla doğrulamış ve metal levhanın göstereceği davranışları tanımlamışlardır.

Tandoğan ve ark. (2020), değişik sayıdaki dizilime sahip ve farklı çapa sahip pimlerin sabit bir alt kalıp formu üzerinde şekillendirilen Al 1100 H14 alüminyum levha iş parçasına olan etkilerini incelemişlerdir. İlk dizilim 10 mm çapında 13 pim, ikinci dizilim ise 5 mm çapında olan 25 pimden oluşmakta ve her bir dizilimde pimler arasında 1 mm mesafe bulunmaktadır. Sonlu eleman analizinin kullanıldığı çalışmada farklı dizilimlerin levha üzerinde belirlenen noktalardaki yük dağılımlarına ve hasar oluşumlarına olan etkileri ortaya konulmuştur.

Tandoğan ve ark. (2023), yapmış oldukları bir başka çalışmada çok noktali şekillendirme prosesinde kullanılan pim çaplarının etkilerini gözlemlemişlerdir. 0,5 mm kalınlığındaki Al 1100 alüminyum alaşımından olan iş parçasına üç farklı form verilmiştir. Bu formların oluşturulması esnasında 10 mm, 12 mm, 14 mm çapa sahip pimlerin levhada meydana getirdiği stres dağılımı, yük dağılımı ve kalınlık dağılımlarının hem deneysel hem de sonlu elemanlar yöntemi ile analizini gerçekleştirerek sonuçları karşılaştırmışlardır.

Daha önce yapılan örnek çalışmalardan anlaşılacağı üzere çok noktali şekillendirme klasik şekillendirme yöntemleri

ile elde edilemeyecek şekillerin metal levha üzerinde verilebilmesine imkân sağlamaktadır. Bu sebeple derin çekme prosesine ait kalıp elemanlarının çok noktali şekillendirme elemanlarında olduğu gibi pimlerle değiştirilmesi sonucunda prosesin geliştirilmesine katkı sağlanabilecektir. Tıpkı çok noktali şekillendirme prosesinde olduğu gibi çok noktali derin çekme olarak isimlendirilen bu proses üzerine yapılan çalışmalarda bulunmaktadır.

Beglarzadeh ve Davoodi'nin (2016), deneysel ve sayısal teknikler kullanarak çok noktali derin çekme prosesine ilişkin yaptıkları çalışmada, sıyrıcının uyguladığı farklı kuvvet değerlerinin iş parçası yüzey kalitesine nasıl etki ettiğini araştırmışlardır. Çalışma da 300 adet pim kullanarak 1 mm kalınlığa sahip Al2024 alüminyum alaşımını kare formunda derin çekme işlemine tabi tutmuşlardır. Çukur oluşumlarının engellenmesi amacıyla 10 mm kalınlığında poliüretan ped kullanılmıştır. Sıyrıcı için 1200 N, 1600 N ve 2000 N olacak şekilde yük değerleri uygulanmıştır. Ayrıca, aynı koşullar ABAQUS/EXPLICIT yazılımı kullanılarak da simüle edilmiştir. Araştırmacılar, değişen sıyrıcı yüklerinin iş parçasında kırışıklık ve kopma oluşumu üzerindeki etkisini göstererek, 2000 N'lik yükün en iyi sonuçları verdiğini belirtmişlerdir.

Zareh-Desari ve ark. (2017), çok noktali derin çekme prosesini kullanarak derin çekme işlemini gerçekleştirmek amacıyla 1 mm kalınlığında ve 220x220 mm boyutlarında Al 2024-O alüminyum alaşımı iş parçası kullanmışlardır. Kalıp seti, 12 mm çapında dairesel pimlerden oluşmakta ve tamamen ayarlanabilir yapıdadır. Çukur oluşumlarının incelenmesi amacıyla her biri farklı sertlik değerlerine sahip kauçuk ve poliüretan gibi çeşitli tipte pedler kullanılmıştır. Her biri farklı boyutlarda iki ayrı kare iş parçası üretilmiş ve proses Abaqus/CAE 6.9.1 yazılımı kullanılarak da aynı koşullar altında proses simüle edilmiştir. Yırtılmaların iş parçası üzerindeki konumu ve kopma derinliği gibi özellikler gözlemlenmiştir. Daha yüksek sertliğe sahip ped kullanımının iş parçasının çekme derinliğini arttırdığını ve yüzeyde daha az çukur meydana getirdiğini belirtmişlerdir.

Yaşar ve ark. (2007), kalınlığı 0,8 mm olan DC04 çelik levhadan düzensiz şekilli dikdörtgen bir parçanın imalatını çok noktali derin çekme prosesini kullanarak gerçekleştirmişlerdir. Araştırmacılar, iş parçası üzerinde

herhangi bir kopma durumu olmadan etkili bir şekilde uygulanabilecek limit koşullarını belirlemek amacıyla derin çekme hızının, takım geometrisinin ve derin çekmenin diğer ilgili özelliklerin etkisini ortaya koymuşlardır.

Araştırmacılar tarafından yapılan çalışmalar incelendiğinde çok noktali derin çekme prosesi üzerine yapılan yayın sayısının azlığı dikkat çekmektedir. Bu sebeple prosese ait birçok parametrenin araştırılmamış olduğu ve literatürde bir boşluk yarattığı anlaşılmaktadır. Bu çalışmanın amacı, çok noktali derin çekme işleminde farklı pim uç radyus değerlerinin (1 mm, 3 mm ve 6 mm) etkisinin sonlu elemanlar analizi yöntemiyle incelenmesidir. Çalışma için 130x130 mm boyutlara sahip, 0,75 mm kalınlığında Al 3003 HX6 alüminyum alaşımı iş parçası temin edilmiştir. Ayrıca, sonlu eleman analizlerinden elde edilen sonuçların deneysel olarak da doğruluğunun sağlanması amacıyla bir adet çok noktali derin çekme seti tasarlanarak, imalatı gerçekleştirilmiştir. Gerçekleştirilen deneyler sonucunda elde edilen bulgular sonlu elemanlar analizinden elde edilen bulgularla karşılaştırılmıştır. Bulgular arasında tutarlılık sağlandıktan sonra geri kalan radyus değerleri için sonlu elemanlar yöntemiyle simülasyonlar yapılmış ve analizler gerçekleştirilmiştir. Radyuslarda olan değişimlerin yük dağılımına, hasar değerlerine ve stres dağılımına ne düzeyde etki ettiği incelenmiştir.

2. Materyal ve Yöntem

2.1. Deneysel Çalışma

Deneysel ve sonlu eleman analizleri için levha halinde, 0,75 mm kalınlığında AISI Al 3003 HX6 alüminyum alaşımı kullanılmıştır. Temin edilen levha 130x130 mm boyutlarda kare parçalar olarak kesilmiştir. AISI Al 3003 HX6 diğer alüminyum çeşitlerine göre daha sünek olup dövme, ekstrüzyon ve derin çekme gibi şekillendirme proseslerine gayet uygundur. Aşındırıcı atmosferik koşullara ve korozyona olan dayanıklılığı, bunun yanında kaynak edilebilirliği sebebiyle özellikle havacılık ve denizcilik sektöründe yaygın bir kullanıma sahiptir (Park ve ark., 2004). AISI Al 3003 HX6'nın kimyasal kompozisyonu Tablo 1.'de verilmiştir.

Temin edilen iş parçası ASTM E8 standardına bağlı kalınarak U-Test marka çekme testi cihazında, 0,5 s⁻¹ şekil değiştirme hızında çekme testine tabi tutulmuştur.

Tablo 1. AISI Al 3003 HX6' nın kimyasal kompozisyonu

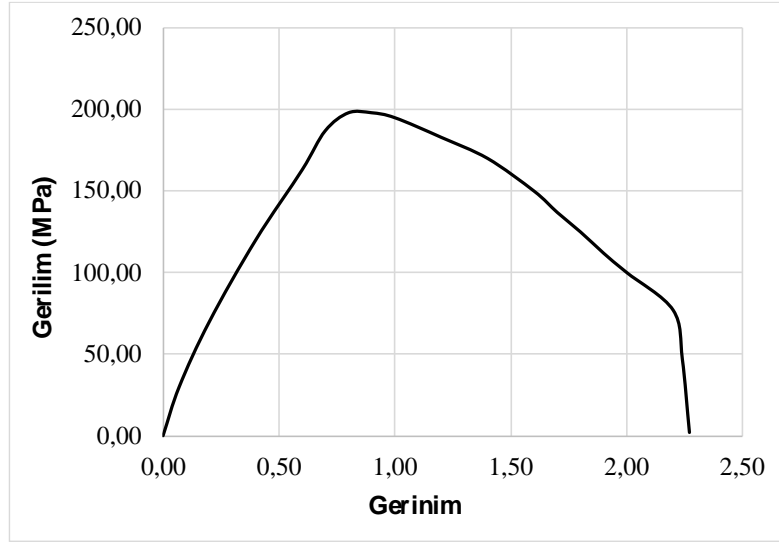
| Si | Cu | Mn | Zn | Fe | Al | Diğer |
|-----|-----|------|-----|------|-------|-------|
| 0,6 | 0,1 | 1,25 | 0,1 | 0,05 | Kalan | 0,15 |

Çekme testi 6 kez gerçekleştirilmiş ve elde edilen değerlerin ortalaması alınarak mühendislik gerilme-şekil değiştirme eğrisi oluşturulmuştur. Deneylerde kullanılan numunelerden bir tanesi örnek olarak Şekil 1' de

görülmektedir. Elde edilen gerilme-gerinim eğrisi ise Şekil 2' de verilmiştir.



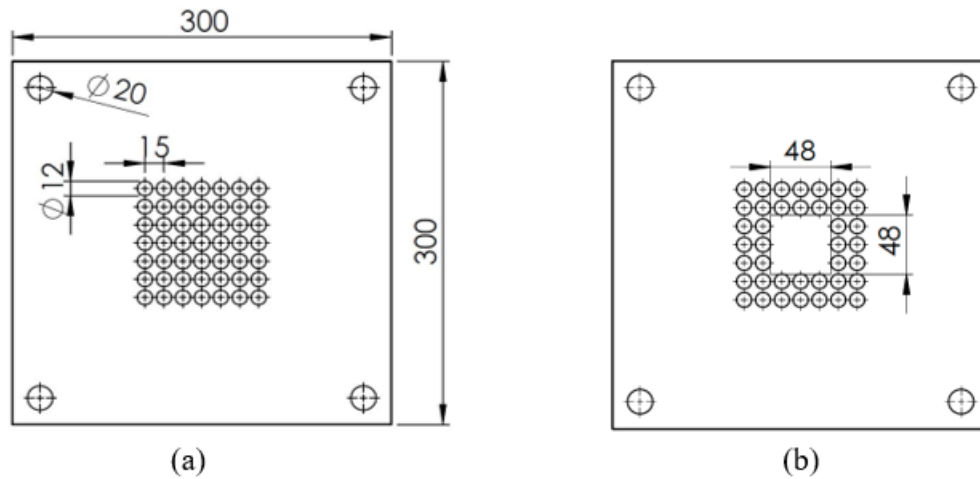
Şekil 1. Çekme testi numunesi.



Şekil 2. Al 3003 HX6 alüminyum iş parçası mühendislik gerilim-gerinim eğrisi.

Deneilerin gerçekleştirilmesi amacıyla bir adet çok noktalı derin çekme kalıp seti imal edilmiştir. Alt ve üst kalıbın tamamı 87 mm uzunluğunda, 12 mm çapında, 6 mm radyusa sahip pimlerden oluşacak ve 7x7'lik kare bir matris oluşturacak şekilde tasarlanan kalıbın tüm parçaları AISI 4140 çelik malzemeden üretilmiştir. Bu tip kalıp imalatı uygulamalarında kullanılan AISI 4140, tercih edilen ve dayanımı yüksek bir çelik türüdür (Borchers, 2021). Kalıpla aynı malzemeden imal edilen pimlerin dayanımının ve sertliğinin artırılması amacıyla tüm pimler ısıl işlem görmüştür. Alt ve üst kalıba 7x7'lik

bir matris oluşturacak şekilde dizilen pimlerin merkezleri birbirlerinden 15 mm uzaklıktadır. Pimlerin kalıba yerleştirilebilmesi için alt ve üst kalıplarda pimlerin geleceği yere M8 vida dişi açılmıştır. Aynı şekilde vidaların içerisine 45 mm uzunluğunda M8 kılavuz çekilmiştir. Alt kalıp içerisinde 48x48 mm'lik bir kalıp boşluğu oluşturulacak şekilde pimler eksiltilmiş, derin çekme işleminin gerçekleştirilebilmesi için üst kalıpta bulunan ve alt kalıp boşluğunun karşısına gelen pimler 30 mm uzatılmıştır. Oluşturulan (a) üst ve (b) alt kalıba ait teknik çizimler Şekil 3'te görülmektedir.

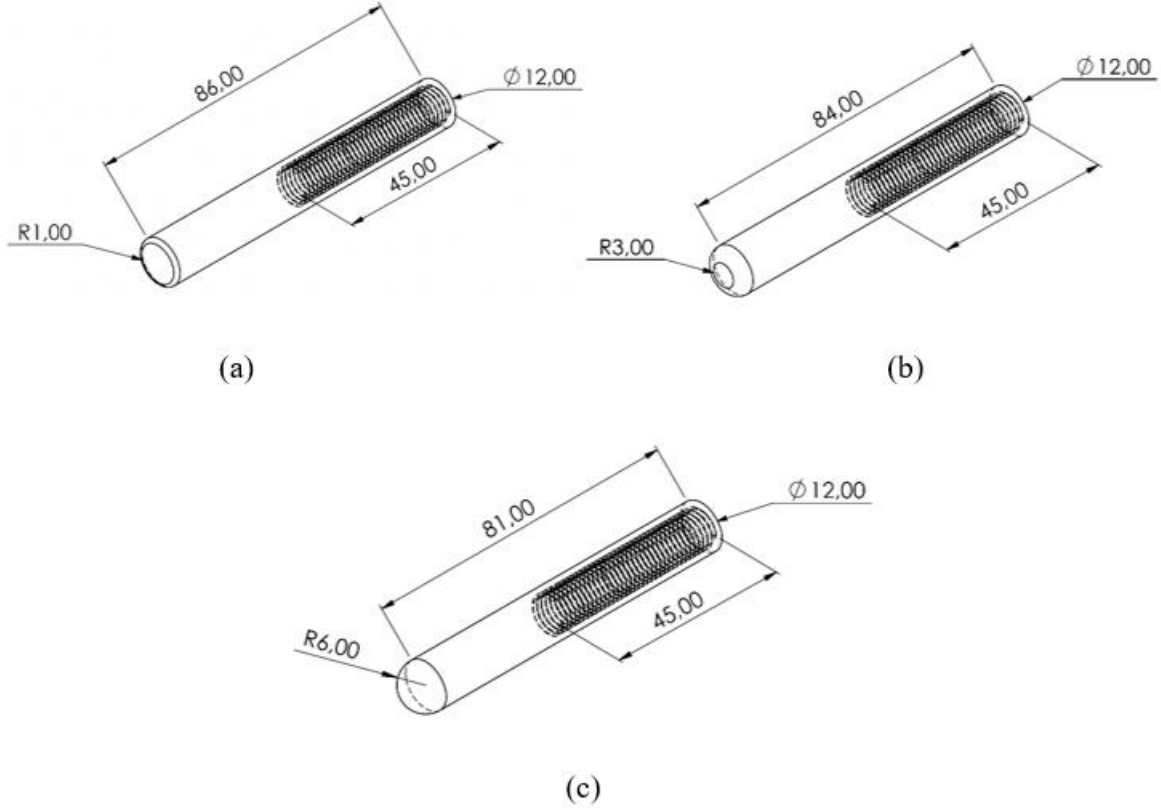


Şekil 3. İmal edilen çok noktalı derin çekme kalıp setine ait teknik çizimler (a) üst kalıp, (b) alt kalıp.

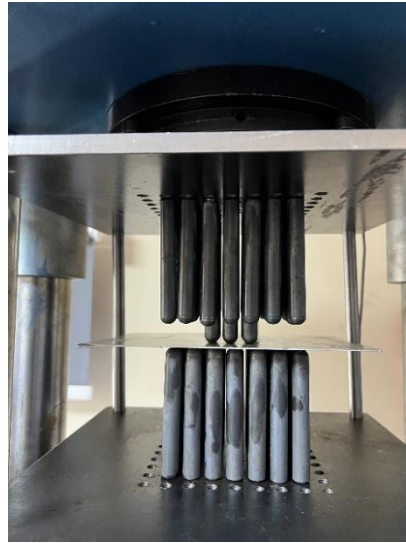
Çalışma da pimlerin radyuslarının etkisi inceleneceğinden dolayı aynı ölçülere sahip ancak uç radyusları 1 mm, 3 mm ve 6 mm olacak şekilde üç farklı pim tipi tasarlanmış ve daha önce de belirtildiği gibi bu tiplerden 6 mm uç radyusuna sahip olan pimin deneysel çalışma için imalatı gerçekleştirilmiştir. Çalışmada kullanılan pimlerin teknik çizimleri Şekil 4'te verilmiştir. Deneysel çalışma, Tarsus Organize Sanayi Bölgesi'nde

bulunan Berdan Civata tarafından sağlanan üniversal test makinesi kullanılarak gerçekleştirilmiştir. Makine 30 kN yük kapasitesine sahip olup deneyler 1 mm/dak hızında gerçekleştirilmiştir.

Pimler ile levha arasındaki yağlama, SEA 40 yağı kullanılarak sağlanmıştır. İmal edilen kalıp seti ve iş parçasına ait deney görüntüsü Şekil 5'te verilmiştir.



Şekil 4. Farklı uç radyuslarına sahip pimlerin teknik çizimleri (a) 1 mm, (b) 3 mm, (c) 6 mm.



Şekil 5. İmal edilen kalıp seti ve iş parçasına ait deney görüntüsü.

2.2. Sonlu Elemanlar Yöntemi

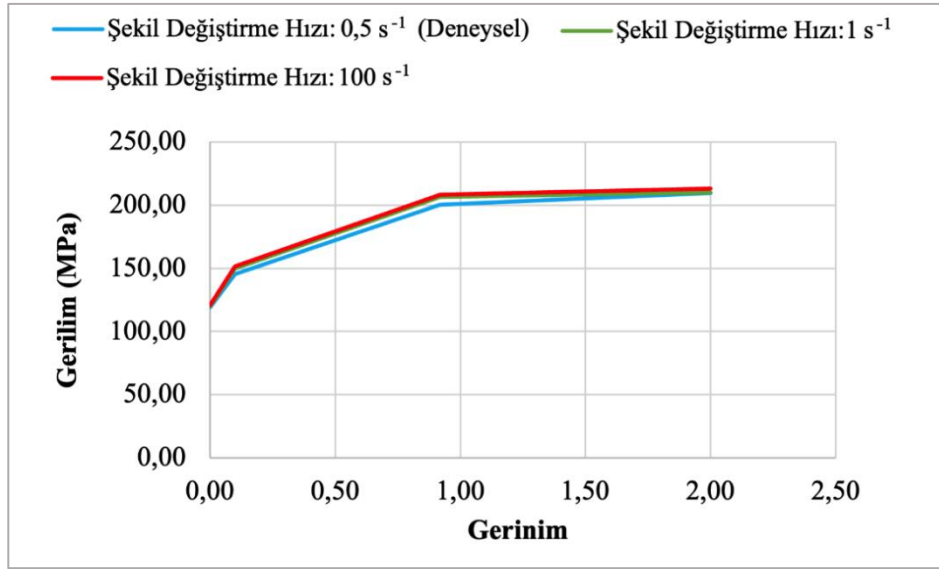
Sonlu elemanlar analizleri, Scientific Forming Technologies Corporation'a ait Deform-3D yazılımı kullanılarak gerçekleştirilmiştir. Prosesin 3 boyutlu olarak simüle edilmesi uzun bir zaman almaktadır. Çalışmanın ana hedefi iş parçası üzerinde oluşan etkileri incelemek olduğundan hesaplama hızının artırılması ve böylece simülasyon zamanlarının azaltılması amacıyla üst plaka, alt plaka ve pimler deforme olmayan katı gövdeler olarak tanımlanırken, iş parçası da elasto-plastik bir malzeme olarak tanımlanmıştır. Çekme testinden elde edilen değerler sonucunda, Al 3003 HX6 alüminyum malzemenin akış gerilimi eğrileri Holloman denklemi kullanarak bulunmuştur. Hollomon denklemi

Eşitlik 1'de verilmiştir;

$$\bar{\sigma} = K\epsilon^{-n} \quad (1)$$

Burada $\bar{\sigma}$; etkin gerilim, ϵ ; etkin gerinim, K; malzeme sabiti ve n; gerinim sertleşmesi katsayısını ifade etmektedir.

Elde edilen sonuçlar doğrultusunda çizilen akış gerilim eğrileri ve Deform-3D yazılımının veri tabanında Al 3003 alüminyum malzeme için bulunan akış gerilim eğrileri Şekil 6'da verilmiştir.



Şekil 6. Deneysel olarak elde edilen ve yazılım veri tabanında bulunan akış gerilimi eğrilerinin karşılaştırılması.

Görüldüğü üzere deneysel olarak elde edilen sonuçlar ve programın kendi veri tabanında bulunan değerler birbiri ile örtüşmektedir. Derin çekme işlemi sırasında önemli bir parametre olan yırtık (kırılma) oluşumunun simüle edilebilmesi için DEFORM-3D yazılımı içerisinde kırılma kriterinin tanımlanması gerekmektedir. Çok noktalı derin çekme işlemi için normalleştirilmiş Cockroft & Latham kırılma kriteridir seçilmiştir. Bu kriter, gerinim değerlerinin hassas şekilde ölçümüne imkân tanımaktadır. Kritere göre kırılma başlangıcı, etkili gerinim değerinin kritik değere (C) ulaştığı noktada meydana gelir. Kriter, Eşitlik 2'de verilmiştir;

$$\int_0^{\epsilon^{-f}} \left(\frac{\sigma^*}{\bar{\sigma}} \right) d\bar{\epsilon} = C, \quad (2)$$

σ^* ; maksimum asal çekme gerilmesini, ϵ^{-f} ; kırılma gerinimini ve C ise kritik kırılma değerini göstermektedir. $\bar{\sigma}$; efektif gerilim ve $\bar{\epsilon}$; efektif ve olarak ifade edilmiştir. Kritik değeri ifade eden C, çekme testi ile bulunmaktadır ve çalışma koşullarından bağımsızdır. Bu değer 0,35 olarak bulunmuştur.

İş parçası ile pimler arasındaki sürtünme katsayısının sabit kalacağı ve 0,1 olarak belirlenmiş bir değerle Coulomb modelini takip edeceği varsayılmıştır.

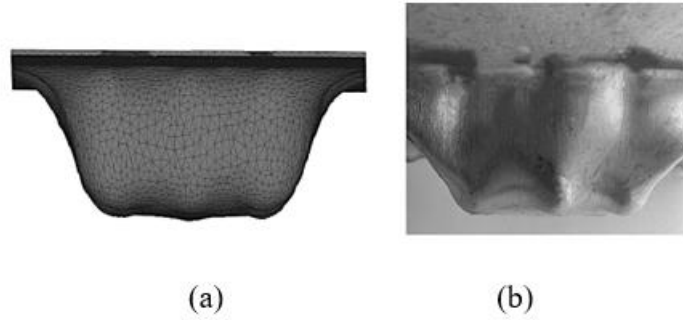
Deform-3D yazılımı, simülasyonları gerçekleştirirken iş parçası üzerinde oluşturduğu ağ elemanları vasıtasıyla şekil değiştirme ve gerilim değerlerini hesaplamakta, eğer ağ elemanlarından herhangi biri C ile belirtilen kırılma değerine ulaşırsa, ilgili ağ elemanını silmektedir. Yazılımın çok noktalı derin çekme işlemi en gerçekçi olarak simüle edebilmesi için ağ elemanı sayısının olabildiğince fazla olması gerekmektedir. Eğer ağ elemanı sayısı az olursa gerek görsel geri bildirim gerekse hesaplama hataları meydana gelmektedir. Deneysel sonuçlara olabildiğince uyumlu nümerik analiz sonuçları elde edebilmek için ağ elemanı sayısının olabildiğince fazla ve şekil değiştirme bölgelerinde yoğunlaşmış olması şarttır. Ancak, gereğinden fazla eleman kullanmakta simülasyon sürelerini ciddi derecede uzatmaktadır. Bu sebeple nümerik analizlere geçilmeden önce çalışmada kullanılan deney setine karşılık gelen ve 6 mm radyusa sahip pimlerle gerçekleştirilen çok noktalı derin çekme prosesi birçok kez farklı ağ elemanı sayıları ile simüle

edilmiş, tetrahedral (dört yüzlü) tip 340.000 adet ağ elemanı sayısına ulaşıldığında ve bu eleman sayısının daha üst değerlerine çıktığında sonuçların değişmediği belirlenmiştir. Ağ elemanı boyutu 0,03 mm olarak tanımlanmış ve kalıbın her 0,1 mm ilerlemesinde ağ elemanların yenilenmesi için yazılımın otomatik ağ yenileme özelliği kullanılmıştır. Gerek deneylerde gerekse simülasyonlarda sıyrıcı kullanılmamış ve malzemenin ne kadarlık bir kırılmaya uğrayacağı da incelenmiştir.

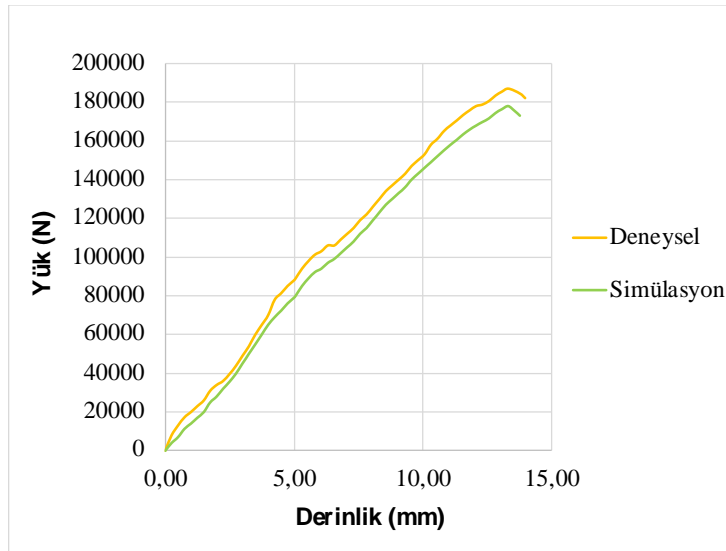
3. Bulgular ve Tartışma

Sonlu eleman analizlerinin sağlıklı olarak gerçekleştirilebilmesi için yapılan simülasyonlardan elde edilen sonuçların doğrulanması şarttır. Eğer deneysel

sonuçlar ile simülasyon sonuçları arasındaki fark büyükse, daha sonrasında gerçekleştirilecek analizler hatalı ve gerçekten uzak olacaktır. Hazırlanan çok noktalı derin çekme kalıp seti ile deneyler gerçekleştirilmiş ve aynı koşullar altında yürütülen simülasyon sonuçları ile karşılaştırılmıştır. Simülasyon sonucunda (a) iş parçası üzerinde elde edilen derin çekme formuna ait görüntü ve (b) deney sonrasında elde edilen görüntü Şekil 7’de verilmiştir. Şekil 7’den anlaşılacağı üzere, görsel olarak simülasyon ve deneysel sonuçları birbirleriyle uyumludur. Diğer bir karşılaştırma ise prosesin gerçekleştirilmesi esnasında uygulanan yükün değişimi üzerine yapılmış ve Şekil 8’de gösterilmiştir.



Şekil 7. Çok noktalı derin çekme görüntüleri (a) simülasyon, (b) deneysel.

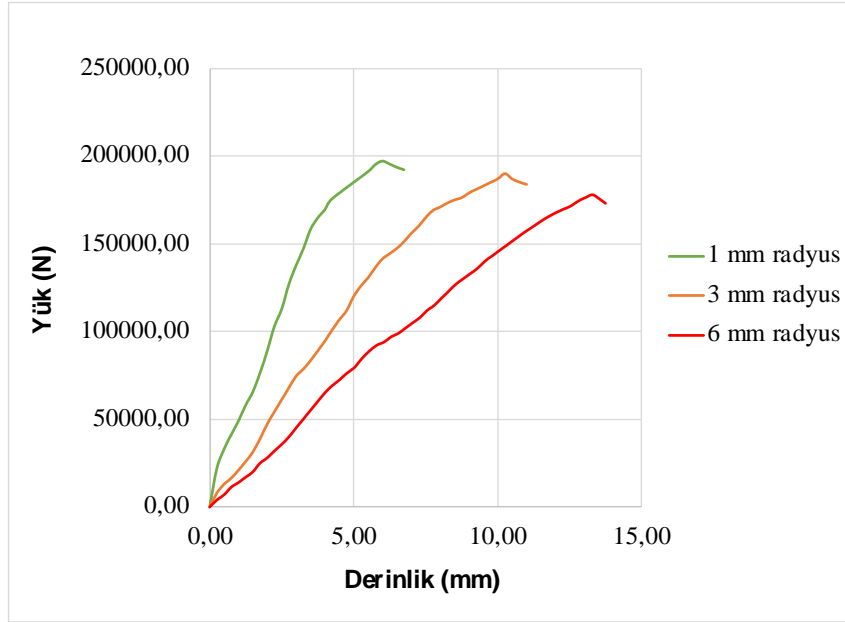


Şekil 8. Deney ve simülasyon sonrasında elde edilen yük değerlerinin karşılaştırılması.

Şekil 7 ve Şekil 8’den görülebileceği üzere deney ve simülasyon sonuçlarının birbiri ile uyumlu oldukları anlaşılmaktadır. Yük değişimleri karşılaştırıldığında yaklaşık %7,35’lik bir fark olduğu görülmektedir. Deney ve simülasyon sonuçlarının tutarlılığı sağlandıktan sonra geri kalan radyus değerlerine ait çok noktalı derin çekme işlemleri yine sonlu elemanlar yöntemi kullanılarak simülasyonlar vasıtasıyla gerçekleştirilmiştir.

3.1. Yük ve Hasar Sonuçları

Metal levha şekillendirme proseslerinde en önemli parametrelerden bir tanesi derin çekmenin gerçekleştirilmesi için gereken şekillendirme yüküdür. Yük değeri, kullanılması gereken pres kapasitesini direkt belirleyen bir parametredir. Simülasyon çalışmaları sonucunda 1 mm, 3 mm ve 6mm uç radyuslarına sahip olan pimlerle yapılan simülasyonlardan elde edilen yük değişimleri Şekil 9’da verilmiştir.



Şekil 9. Farklı radyuslara ait yük değerlerinin karşılaştırılması.

Şekil 9'dan anlaşılacağı üzere radyusların azalması, derin çekme için gereken yükü artırmıştır. Ortalama yük değerleri incelendiğinde 1 mm ve 3 mm radyusa sahip pimlerin oluşturduğu yük arasında % 3,70 oranında bir fark varken, 3 mm ve 6 mm radyusa sahip pim arasında % 16,83'lük bir fark olduğu görülmüştür.

Bu durum, pimlerin uç noktalarındaki temas alanında olan farklılıklar nedeniyle ortaya çıkmaktadır. Bir levha şekillendirme operasyonundaki yük büyüklüğü, zımbanın temas alanından doğrudan etkilenmektedir (Engin ve Eyercioglu, 2017). Çok noktalı derin çekme prosesinde zımbanın parçalı yapısının bir sonucu olarak, her bir pim, uygulanan yükü bağımsız olarak iş parçasına iletmektedir. Pimlerin uçlarına verilen radyus ne kadar büyükse levha üzerine temas eden pim yüzey alanı azalmaktadır. Bu durumda gerekli şekillendirme yükünü azaltmaktadır.

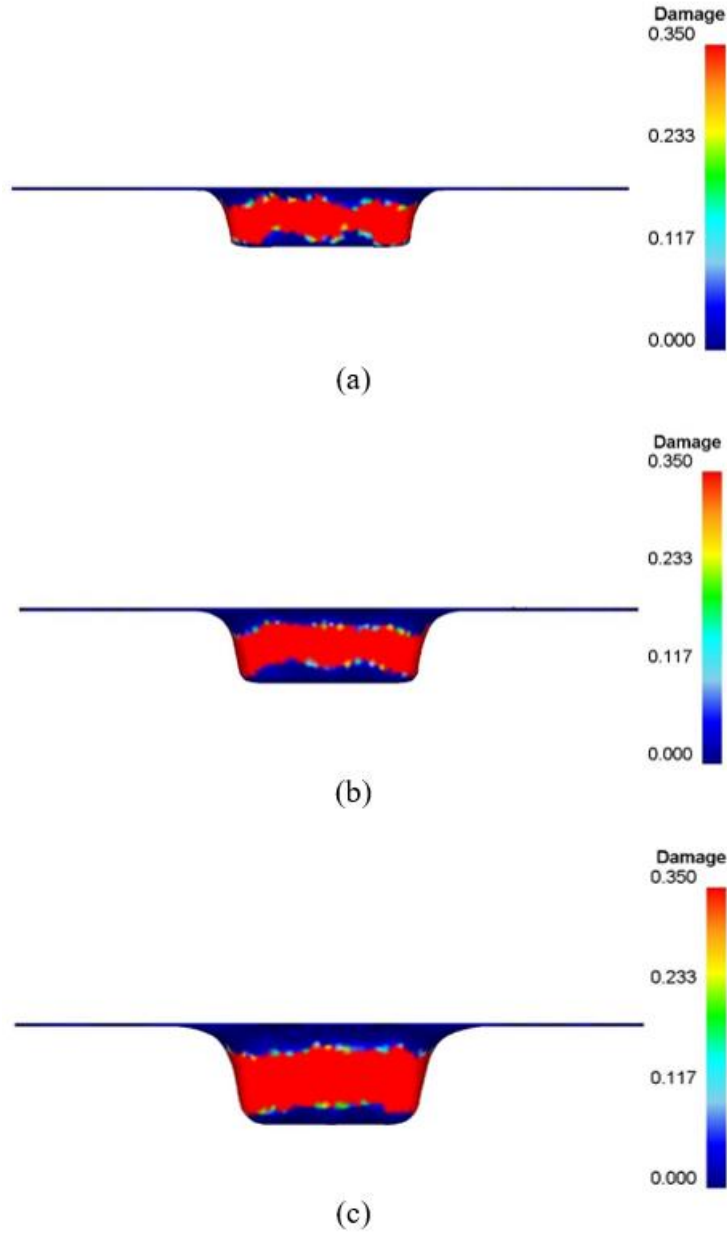
Şekil 9'da dikkat çeken diğer hususlardan bir tanesi de yük grafiklerinin yükseldikten sonra bir anda kesilmesidir. Bu kesilme noktaları malzeme üzerinde yırtık oluştuğu derinliği göstermektedir. Pimlerin uç radyusu arttıkça, malzemenin maksimum çekilebilme ve ilk yırtığın oluştuğu derinlik artmaktadır. 1 mm ve 3 mm uç radyusu olan pimler arasında %42,8'lik bir derinlik farkı olduğu hesaplanmıştır. Aynı şekilde 3 mm ve 6 mm

uç radyusu olan pimler arasında ise %30,56 derinlik farkı olduğu görülmüştür. Bu sonuçlardan hareketle radyusun azalmasının malzemenin çekme derinliğini azalttığı ve gereken şekillendirme yük değerini arttırdığı sonucuna varılmıştır.

Aynı şekilde Al 3003 HX6 alüminyum alaşım iş parçası üzerinde oluşan hasar miktarları da bu bulguları destekler durumdadır. İş parçası malzemesi için bulunan kritik değer C: 0,35 olarak tespit edildiği daha önce belirtilmiştir. Çok noktalı derin çekme işlemi esnasında yırtık oluşumunun hemen öncesinde kritik değere ulaşan bölgeleri belirten görseller (a) 1 mm radyusa sahip pim, (b) 3 mm radyusa sahip pim ve (c) 6 mm radyusa sahip pim için Şekil 10' da verilmiştir.

Şekil 10'da bulunan görsellerden anlaşılacağı üzere iş parçası üzerinde hasarın en çok oluştuğu bölgeler derin çekme prosesine özgü olarak malzemenin alt kalıp ve üst kalıp arasında kalan yan duvarlarıdır. Şekiller sırasıyla incelendiğinde radyusun artmasıyla beraber çekme derinliğinin de arttığı bir kez daha görülmüştür.

Radyusun azalması, pimlerin iş parçası ile temas eden yüzey alanını artırırken, aradaki sürtünme alanını da arttırmakta ve malzemenin şekil değişimi esnasında pim formu üzerindeki kayma hareketi daha az olmaktadır (Li ve ark., 2002).

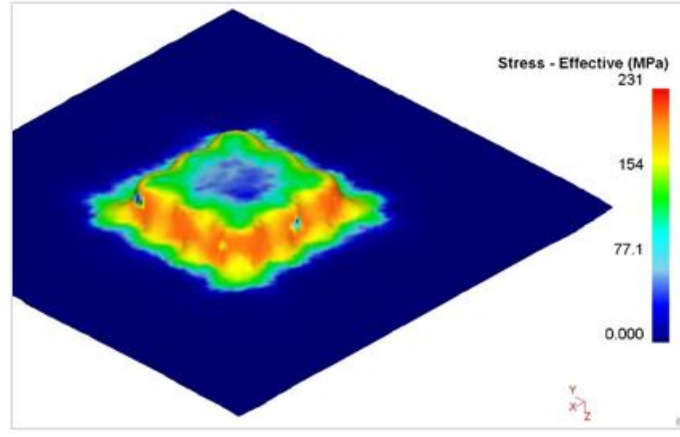


Şekil 10. Farklı radyusların oluşturduğu hasar durumları (a) 1 mm radyusa sahip pim, (b) 3 mm radyusa sahip pim ve (c) 6 mm radyusa sahip pim.

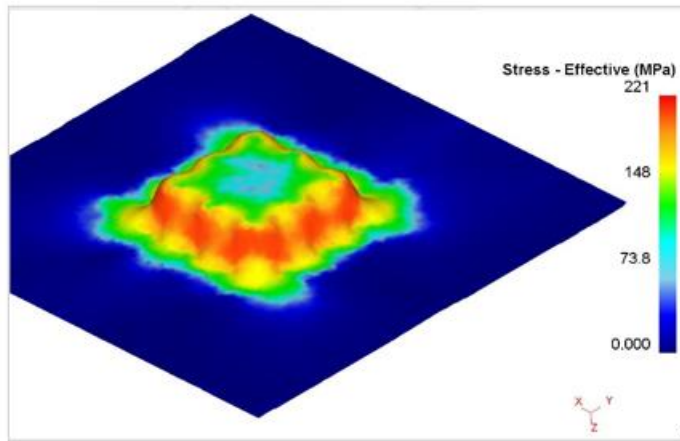
Ayrıca küçük radyus değerinden dolayı uçlardaki yuvarlaklığın azalması, malzemenin alt kalıp ve pim arasında daha fazla sıkışmasına sebebiyet vererek malzemenin yırtılmayla sonuçlanacak hasar değerine daha hızlı ulaşmasına neden olmuş, bu sebeple çekme derinliği azalmıştır.

3.2. Gerilim Dağılımı

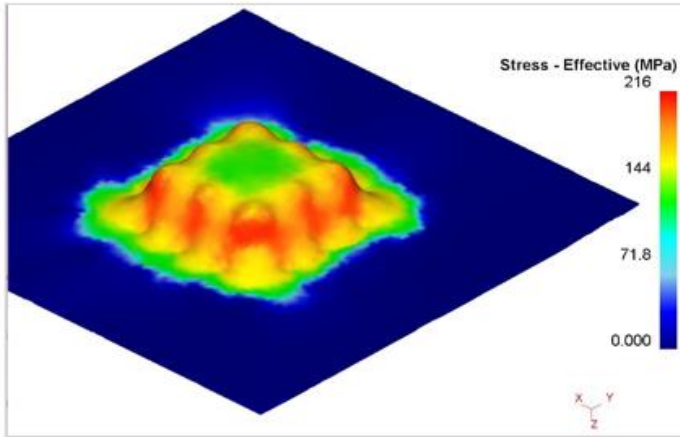
Malzeme üzerinde oluşan gerilim dağılımı, şekillendirilebilirlik üzerinde doğrudan etkili olan bir parametredir. Şekil 11' de Al 3030 HX6 alüminyum malzeme üzerinde oluşan gerilim dağılımları (a) 1 mm radyusa sahip pim, (b) 3 mm radyusa sahip pim ve (c) 6 mm radyusa sahip pim için verilmiştir.



(a)



(b)



(c)

Şekil 11. Farklı radyusların oluşturduğu gerilim dağılımları (a) 1 mm radyusa sahip pim, (b) 3 mm radyusa sahip pim ve (c) 6 mm radyusa sahip pim.

Şekil 11 incelendiğinde 1 mm radyusa sahip pim kullanımı sonucu elde edilen maksimum efektif gerilme değerinin 231 MPa, 3 mm radyusa sahip pim kullanımı sonucunda edilen maksimum efektif gerilme değerinin 221 MPa, 6 mm radyusa sahip pim kullanımı sonucunda elde maksimum efektif gerilme değerinin ise 216 Mpa

olduğu bulunmuştur. İş parçasının üzerinde oluşan maksimum gerilme değerlerinin pim radyusu ile ters orantılı olduğu anlaşılmaktadır. Daha önceki bulgularla uyumlu olarak, 1 mm radyusa sahip pim kullanımı sonucunda diğer radyus değerlerine göre daha düşük çekme derinliğinde, daha da yüksek efektif gerilme

değerine sahip olmaktadır. 1 mm radyus ile 3 mm radyusa sahip pimler arasında % 4,52, 3 mm ve 6 mm radyusa sahip pimler arasında ise % 2,31'lik bir efektif gerilme farkı olduğu hesaplanmıştır. Bu durumunda temel sebebi, daha düşük radyus olan sonucunda yüzey alanının artması ve lokal gerilmelerinde buna bağlı olarak artmasıdır (Tandoğan ve ark., 2023).

4. Sonuç

Bu çalışmada 0,75 mm kalınlığında AISI Al 3033 HX6 alüminyum alaşımı levha, çok noktalı derin çekme prosesi ile derin çekilmiş, çok noktalı kalıp setini oluşturan pimlerin uç raydus değerlerinin değişimi sonucunda (1 mm, 3 mm, 6 mm) proses çıktılarındaki değişimler incelenmiştir. Elde edilen sonuçlar şu şekilde özetlenebilir;

- Çok noktalı derin çekme prosesine özgü olarak kullanılan ve iş parçası ile temas eden pimlerin uç radyuslarının proses çıktıları üzerine etkisi olduğu görülmüştür.
- Radyus değerleri azaldıkça iş parçası ile temas eden yüzey alanı artmaktadır. Yüzey alanının artması, derin çekme prosesi için gerekli olan yük değerini ciddi derecede arttırmaktadır. Bu durum pres kapasitesinin de arttırılması ve daha fazla enerji harcanması manasına gelmektedir.
- Düşük radyus değerine sahip pimlerin kullanımı sonucunda maksimum efektif gerilmelerin ve hasar oranlarının daha düşük çekme derinliğinde, daha yüksek değerlere ulaştığı görülmüştür. Düşük radyus kullanımı malzemenin daha kısa bir çekme derinliğinde yırtılmasına sebebiyet vermektedir.
- Çekme derinliği ve gereken yük ihtiyacı olarak en iyi sonuçlara 6 mm uç radyusunun kullanımı sonucunda ulaşılmıştır.

Katkı Oranı Beyanı

Yazarın katkı yüzdesi aşağıda verilmiştir. Yazar makaleyi incelemiş ve onaylamıştır.

| | K.E.E |
|-----|-------|
| K | 100 |
| T | 100 |
| Y | 100 |
| VTI | 100 |
| VAY | 100 |
| KT | 100 |
| YZ | 100 |
| KI | 100 |
| GR | 100 |
| PY | 100 |
| FA | 100 |

K= kavram, T= tasarım, Y= yönetim, VTI= veri toplama ve/veya işleme, VAY= veri analizi ve/veya yorumlama, KT= kaynak tarama, YZ= Yazım, KI= kritik inceleme, GR= gönderim ve revizyon, PY= proje yönetimi, FA= fon alımı.

Çatışma Beyanı

Yazar, bu çalışmada hiçbir çıkar ilişkisi olmadığını beyan etmektedir.

Etik Onay Beyanı

Bu araştırmada hayvanlar ve insanlar üzerinde herhangi bir çalışma yapılmadığı için etik kurul onayı alınmamıştır.

Kaynaklar

- Beglarzadeh B, Davoodi B. 2016. Numerical simulation and experimental examination of forming defects in multi-point deep drawing process. *Mechanics*, 22(3):182-189.
- Borchers F, Clausen B, Ehle L.C, Eich M, Epp J, Frerichs F, Hettig M, Klink A, Kohls E, Lu Y, Meyer H, Rommes B, Schneider S, Strunk R, Zielinski T. 2021. The influence of former process steps on changes in hardness, lattice and micro structure of AISI 4140 due to manufacturing processes. *Metals*, 11(7): 1102.
- Cai ZY, Li MZ. 2005. Finite element simulation of multi-point sheet forming process based on implicit scheme. *J. Mater. Process. Technol*, 161(3):449-455.
- Engin K.E, Eyercioglu O. 2017. The effect of the thickness-to-die diameter ratio on the sheet metal blanking process. *Stroj. Vestn. J. Mech. Eng.*, 63(9): 501-509.
- Li M, Liu Y, Su S, Li G. 1999. Multi-point forming: A flexible manufacturing method for a 3-d surface sheet. *J. Mater. Process. Technol*, 87(1-3): 277-280.
- Li MZ, Cai ZY, Sui Z, Yan Q. 2002. Multi-point forming technology for sheet metal. *J. Mater. Process. Technol*, 129(1-3):333-338.
- Liu C, Li M, Fu W. 2008. Principles and apparatus of multi-point forming for sheet metal. *Int. J. Adv. Manuf. Technol*, 35: 1227-1233.
- Park C.S, Ku T.W, Kang B.S, Hwang S.M. 2004. Process design and blank modification in the multistage rectangular deep drawing of an extreme aspect ratio. *J. Mater. Process. Technol*, 153: 778-784.
- Qian ZR, Li MZ, Tan FX. 2007. The analyse on the process of multi-point forming for dish head. *J. Mater. Process. Technol*, 187:471-475.
- Tandoğan M, Eyercioglu Ö, Dülger M. 2020. Principles and finite element simulation of multi-point forming technology for sheet metal. *TIJMET*, 3(2): 120-130.
- Tandogan M, Eyercioglu O, Engin KE. 2023. Experimental and numerical investigation on effects of pin diameter on multi-point forming. *Processes*, 11(2):387.
- Yaşar M, Korkmaz Z, Gavas M. 2007. Forming sheet metals by means of multi-point deep drawing method. *Mater. Des.* 28(10): 2647-2653.
- Zareh-Desari B, Davoodi B, Vedaei-Sabegh A. 2017. Investigation of deep drawing concept of multi-point forming process in terms of prevalent defects. *Int. J. Mater. Form.*, 10: 193-203.
- Zhu L, Liang Q, Yu TX, Yuan P, Hu Y. 2019. Experimental and theoretical study of constant curvature multi-square punch forming process of strips under follower load. *Int. J. Mech. Sci.* 156: 462-473.



LAHANAGİLLER FAMILYASINA AİT BAZI SEBZE TÜRLERİNİN VEJETATİF BÜYÜME ÖZELLİKLERİNİN İNCELENMESİ

Dilek KANDEMİR^{1*}, Kübra PALA², Güldane Tuğba ŞAHİN², Ahmet BALKAYA³

¹Ondokuz Mayıs Üniversitesi, Samsun Meslek Yüksekokulu, Bitkisel ve Hayvansal Üretim Bölümü, 55139, Samsun, Türkiye

²Ondokuz Mayıs Üniversitesi, Lisansüstü Eğitim Enstitüsü, Bahçe Bitkileri ABD, 55139, Samsun, Türkiye

³Ondokuz Mayıs Üniversitesi, Ziraat Fakültesi, Bahçe Bitkileri Bölümü, Samsun, 55139, Türkiye

Özet: Lahanağil sebze türleri kışlık sebzeler içerisinde önemli bir yere sahiptir. Olumsuz çevre koşulları bu sebze türlerinde büyüme ve gelişmeyi olumsuz düzeyde etkileyebilmekte ve verim unsurlarında önemli azalışlara neden olmaktadır. Bu çalışmada, bazı lahanağil türlerine ait çeşitlerde fide dikiminden itibaren belirli aralıklarla yapılan kantitatif analizlerle vejetatif büyüme özellikleri yönünden karşılaştırılması ve ortaya çıkan farklılıkların fizyolojik parametrelerle incelenmesi amaçlanmıştır. Çalışmada, brokoli, karnabahar, Brüksel lahana, yaprak lahana, beyaz baş lahana ve kırmızı baş lahana türleri kullanılmıştır. Fide dikim tarihini takiben 45. güne kadar 15 gün aralıklı yapılan kantitatif analizlerde yaprak sayısı (adet/bitki), gövde çapı (mm), bitki boyu (cm), toprak üstü aksam yaş ve kuru ağırlığı (g), kök yaş ve kuru ağırlığı (g), bitki yaş ağırlık kuru ağırlığı (g) değerleri belirlenmiştir. Ayrıca, oransal toprak üstü aksam ağırlığı ve oransal kök ağırlığı değerleri de incelenmiştir. Araştırma sonucunda fide dikiminden itibaren 45. günde yapılan kantitatif analiz sonucunda lahanağil türlerinin vejetatif büyüme özellikleri yönünden önemli düzeyde farklılıklar gösterdiği tespit edilmiştir. Lahana grubu sebze türlerinde yaprak sayısı 11-14 adet/bitki arasında değişim göstermiş ve baş lahanaların yaprak sayısının diğer türlere oranla daha fazla olduğu belirlenmiştir. Bitki boyu değerleri 36 - 47 cm aralıklarında dağılım göstermiş ve en yüksek brokoli türünde ölçülmüştür. Toprak üstü aksamı kuru ağırlık değeri 7.31-10.31 g arasında değişim göstermiştir. Araştırmada kök kuru ağırlık değerleri 0.80-1.73 g değerleri arasında dağılım göstermiş ve en yüksek kök kuru ağırlık değerleri sırasıyla yaprak lahana ve Brüksel lahanasında tespit edilmiştir. Oransal kök ağırlığının 0.09-0.14 arasında değiştiği saptanmıştır. Araştırma sonuçlarının, simülasyon çalışmaları ile gelecekte diğer farklı kışlık çeşitlerde kullanımı ve üretim planlanmasında faydalı olacağı öngörülmektedir.

Anahtar kelimeler: Brassicaceae familyası, Tür, Vejetatif büyüme, Kantitatif analiz, Model

Investigation of Vegetative Growth Characteristics of Some Vegetable Species in Brassicaceae Family

Abstract: Brassicaceae vegetable types have an important place among winter vegetables. Adverse environmental conditions can adversely affect the growth and development of these vegetable species and cause serious reductions in yield elements. In this study, it was aimed to compare of some Brassicaceae species in terms of vegetative growth characteristics with quantitative analyses made at regular intervals from seedling planting and to examine the differences in physiological parameters. Six varieties were used in the study, including broccoli, cauliflower, Brussels cabbage, leaf cabbage, white head cabbage, and red head cabbage. Quantitative analyses performed at 15-day intervals until the 45th day following the planting date were determined by the number of leaves (pieces/plant), stem diameter (mm), plant length (cm), fresh and dry weight of the above-ground parts (g), root fresh and dry weight (g), plant fresh weight and dry weight (g) values were determined. In addition, the ratio of above-ground parts weight and the ratio of root weight values were also examined. As a result of the quantitative analysis performed on the 45th day from planting, it was determined that there were significant differences in terms of vegetative growth characteristics. The number of leaves varied between 11-14 and the number of leaves of the head cabbages was higher than the other species. Plant height ranged from 36 to 47 cm, and the highest stem height was obtained in broccoli. The dry weight of the above-ground parts varied between 7.31 - 10.31 g. The root dry weight values ranged between 0.80-1.73 g and the highest root dry weight was determined in leaf cabbage and Brussels cabbage. It was determined that the root weight ratio ranged between 0.09-0.14. It is predicted that the results of the research will be useful in simulation studies and production planning of other different winter varieties.

Keywords: Brassicaceae family, Species, Vegetative growth, Quantitative analysis, Model

*Sorumlu yazar (Corresponding author): Ondokuz Mayıs Üniversitesi, Samsun Meslek Yüksekokulu, Bitkisel ve Hayvansal Üretim Bölümü, 55139, Samsun, Türkiye

E mail: mdilek@omu.edu.tr (D. KANDEMİR)

Dilek KANDEMİR <https://orcid.org/0000-0002-3097-3394>

Kübra PALA <https://orcid.org/0000-0001-5005-4304>

Güldane Tuğba ŞAHİN <https://orcid.org/0000-0002-3409-4282>

Ahmet BALKAYA <https://orcid.org/0000-0001-9114-615X>

Gönderi: 08 Eylül 2023

Kabul: 03 Ekim 2023

Yayınlanma: 15 Ekim 2023

Received: September 08, 2023

Accepted: October 03, 2023

Published: October 15, 2023

Cite as: Kandemir D, Pala K, Şahin GT, Balkaya A. 2023. Investigation of vegetative growth characteristics of some vegetable species in Brassicaceae family. BSJ Eng Sci, 6(4): xx-xx.

1. Giriş

Brassicales takımına ait familyalar arasında yer alan Brassicaceae, Hardalgiller familyası olarak da adlandırılmaktadır (Balkaya ve Karaağaç 2021). Familya

360 cins ve yaklaşık 3709 türden oluşmaktadır. Literatürde Brassica cinsi içerisinde toplam 159 tür olduğu bildirilmiştir (Appel ve Al-Shehbaz 2003; Al-Shehbaz ve Warwick, 2006). Brassica grubu sebzeler,



Brassica oleracea ve *Brassica campestris* türlerine ait alt varyetelerde bulunmaktadır (Monteiro ve Lunn, 1998; Li ve ark., 2020; Balkaya ve Karaağaç, 2021). Önemli *Brassica* grubu sebzeler; baş lahanası (var. *capitata*), yaprak lahanası (var. *acephala*), karnabahar (var. *botrytis*), brokoli (var. *italica*), Brüksel lahanası (var. *gemmifera*), alabaş (var. *gongyloides*), Çin yaprak lahanası (var. *alboglabra*) ve kalın gövdeli yaprak lahanası (var. *medullosa*) olarak sıralanabilir (Song ve ark., 1990; Balkaya ve Karaağaç, 2021).

Lahanagil grubu sebze türleri bitkisel üretimde iklim seçiciliği yüksek olan türler arasında yer almaktadır (Zhiyuan ve ark., 2000; Balkaya, 2001; Balkaya, 2016; Balkaya ve Karaağaç, 2021; Balkaya ve ark., 2023). Yetiştiricilikte genel olarak serin iklim koşulları tercih edilmektedir. Son yıllarda yaşanan iklim değişiklikleri ve buna bağlı olarak ortaya çıkan kuraklık, tuzluluk, su basması gibi abiyotik stres faktörleri lahanagil sebze türlerinde büyüme, gelişme ve buna bağlı olarak verim ve ürün kalite unsurlarını olumsuz yönde etkilemektedir. Lahanagil grubu sebze türlerinin yetiştiriciliğinde bitki büyümesi ve gelişimi üzerine etkili olan diğer önemli bir faktör, bitkilerin kök mimarileri ve ortaya çıkan stres faktörleri altında köklenme yetenekleri ile köklerin topraktan aldığı su ve besin maddesi miktarlarıdır (Atasoy ve ark., 2023).

Lahanalar genel olarak soğuklara dayanıklıdır. Dayanıklılık, bitkilerin büyüme ve gelişme dönemleri ile düşük sıcaklık stresine bağlı olarak değişkenlik göstermektedir (Balkaya ve Karaağaç, 2021). Günümüzde lahanagil grubu sebze türlerinde su stresi nedeniyle bitki büyüme ve gelişmesinde ortaya çıkan olumsuzluklar ve verim değerlerindeki azalışlar ile ürün kalite kayıpları son yıllarda üzerinde önemle durulan güncel konulardan biridir (Ekinci ve ark., 2023). Lahanagillerde kuraklık stresi bitkilerde çeşitli fizyolojik bozukluklara neden olabilmektedir. Lahanagil sebzelerinde düzenli sulama bitki büyümesi, gelişimi ve ürün verimi yönünden büyük önem taşır. Lahanası bitkilerinin su stresine gösterdiği tepkiler bitki organlarına göre değişkenlik gösterdiği gibi bitkinin gelişim dönemlerine göre farklılıklar göstermektedir. Lahanada, gençlik aşamasında (3-4 gerçek yaprak) oluşan kuraklık, bitki büyüme ve gelişmesi ile bitkilerin homojen olgunlaşmalarını olumsuz yönde etkilemektedir (Welbaum, 2015). Shannon ve Grieve (1998), lahanada baş oluşum döneminin kuraklık stresine daha hassas olduğunu bildirmiştir. Lahanalarda yapılan bir çalışmada, bitki gelişiminin orta aşamasında meydana gelen kuraklık stresinin bitkilerde nem içeriğini azaltarak verimi düşürdüğü ve baş ağırlığının azalmasına neden olduğu saptanmıştır (Ackah ve Kotei, 2021). Kuraklık stresinin lahanası bitkilerinde sürgün gelişimini kökten daha fazla engellediği ve sürgün/kök oranında önemli bir düşüşe neden olduğu belirlenmiştir (Maggio ve ark., 2005). Baş lahanada oluşan yaprak sayısı bakımından bitki gelişiminin ilk aşaması, orta aşamalara göre kuraklığa daha duyarlı olmaktadır. Artan kuraklık stresi ile lahanası

bitkilerinde klorofil içeriğinde belirgin düzeylerde azalışlar meydana geldiği saptanmıştır (Ackah ve Kotei, 2021).

Bitki gelişimi sırasındaki su stresi, brokoli bitkisinde baş ve sapının büyüme ve kalitesini azaltır (Decoteau, 2000). Literatürde erken ve geç vejetatif dönemlerdeki su kısıtının, brokoli bitkisinde verim unsurları ve ürün kalitesinde önemli bir azalışa sebep olmadığı, fakat çiçeklenme dönemindeki su eksikliğinin verimde düşüşü artırdığı bildirilmiştir (Erken ve Oztokat, 2010). Diğer bir çalışmada, brokoli yetiştiriciliğinde bitki büyümesi sırasında düşük toprak su içeriğinin (0,40 MPa toprak su gerilimi) bitki ağırlığı ve yaprak boyutunu azalttığı tespit edilmiştir (Zaicovski ve ark., 2008).

Karnabahar yetiştiriciliğinde verim ve kalite özellikleri üzerine, birçok bitki türünde olduğu gibi genetik faktörler, çevresel faktörler ve yetiştiricilik koşulları önemli düzeylerde etkili olmaktadır (Ulukapı ve Şener, 2018). Su eksikliği karnabaharda bitki büyümesini baskılamakta, yaprak klorofil içeriğini, oransal su içeriği, sürgün ve kök P ve K iyon konsantrasyonları ile toplam çözünbilir protein konsantrasyonlarını da önemli ölçüde azaltmaktadır (Wu ve ark., 2012).

Kışlık sebze türleri içerisinde lahanagil grubu sebze türleri (baş lahanası, yaprak lahanası, karnabahar, brokoli, Brüksel lahanası vb.) en önemli ürün segment grubunu oluşturmaktadır. Bu sebze türlerinde çevresel stres faktörleri sonucunda büyüme ve gelişme olumsuz düzeyde etkilenmektedir. Günümüzde ancak bu stres faktörlerine tolerans gösteren çeşitlerin üretimde kullanılması ile yıl boyu üretim yapılması mümkün olabilmektedir. Ülkemizde yaygın olarak yetiştiriciliği yapılan lahanası grubu sebze türlerinde çeşitler esas alınarak mevsimlere göre vejetatif büyüme ve gelişme parametreleri yönünden performans düzeylerinin kantitatif analiz çalışmalarıyla ortaya koyulmasına yönelik bilimsel araştırma sayısı oldukça sınırlıdır. Bu araştırma ile sera koşullarında sonbahar döneminde bazı lahanagil sebze türlerine ait çeşitlerde 15 günlük aralıklarla yapılan kantitatif analizler sonucunda vejetatif büyüme özelliklerinin ayrıntılı olarak incelenmesi ve ortaya çıkan farklılıkların fizyolojik parametrelerle irdelenmesi amaçlanmıştır.

2. Materyal ve Yöntem

Bu araştırma, Ondokuz Mayıs Üniversitesi Ziraat Fakültesi sebze çoğaltma sera ünitesi ve deneme alanında bulunan ısıtmalı polikarbon plastik serada 2022 yılı Kasım-2023 yılı Ocak ayı arasında yürütülmüştür. Araştırmada, ülkemizde yaygın olarak yetiştiriciliği yapılan brokoli (B) karnabahar (K), yaprak lahanası (YL), Brüksel lahanası (BL), beyaz baş lahanası (BBL) ve kırmızı baş lahanası (KBL) türleri yer almıştır. Denemede bu türlere ait Atlantis (brokoli), Igloo (karnabahar), Karadere (yaprak lahanası), Brüksel (Brüksel lahanası), BT-Bafra (beyaz baş lahanası) ve Zencibaş (kırmızı baş lahanası) çeşitleri kullanılmıştır. Denemede çeşitler arasında bir örnekliğin sağlanması amacıyla tohum

ekimleri her çeşitte eş zamanda 1 Kasım 2022 tarihinde gerçekleştirilmiştir. Fideler 4-5 gerçek yapraklı döneme ulaştığında; içerisinde torf + perlit (3:1) karışımının bulunduğu 3 litrelik (19 x 17.5 cm) plastik saksılara, 12 Aralık 2022 tarihinde tesadüf parselleri deneme desenine uygun olarak üç tekerrürlü ve her tekerrürde 12 bitki olacak şekilde aynı tarihte dikimleri yapılmıştır. Fideler, ısıtılmı polikarbon serada 45 gün süresince yetiştirilmiş ve bitkilerinin ihtiyaç duyduğu besin elementleri yetiştiricilik dönemi boyunca 15 gün aralıklarla kademeli olarak iki kez uygulanmıştır.

Lahanagil grubu sebze türlerine ait çeşitlerde vejetatif büyüme özelliklerinin incelenmesi amacıyla fide dikiminden itibaren on beş gün aralıklarla 45. gün sonuna kadar toplam 3 kez (15. 30. ve 45. gün) kantitatif büyüme analizleri gerçekleştirilmiştir. Ölçümlerin yapıldığı günlerde bitkiler kökleri ile birlikte saksıdan çıkarılmıştır. Bitkilerin kök ve vejetatif kısımları birbirinden ayrılarak, kök kısımları dikkatli bir şekilde yıkanmış ve zarar görmeyecek şekilde kâğıt havlu ile kurutulmuştur. Vejetatif büyüme analizlerinde aşağıda belirtilen özellikler incelenmiştir (Uzun, 1996).

- Yaprak sayısı (adet/bitki): Bitkideki tüm yapraklar sayılarak belirlenmiştir.
- Gövde çapı (mm): Kök oluşumunun başladığı noktanın 1 cm üzerinden 0.01 mm'ye duyarlı dijital kumpas ile ölçülmüştür.
- Bitki boyu (cm): Gövdenin kök ile birleştiği başlangıç noktasından büyüme noktasına kadar olan mesafesinin cetvel ile ölçülmesiyle belirlenmiştir.
- Toprak üstü aksamı ve kök yaş ağırlığı (g): Kök ve bitkinin üst aksamı olan kısım birbirinden ayrılarak, 0.01 g'a duyarlı terazide tartılmışlardır.
- Toplam bitki yaş ağırlığı (g): Gövde yaş ağırlığı ile kök yaş ağırlığının toplanmasıyla hesaplanmıştır.
- Toprak üstü aksamı ve kök kuru ağırlığı (g): Bitkinin kök ve üst aksam kısımları ayrı ayrı olacak şekilde kese kâğıtlarına yerleştirilerek etüvde 60 °C'de 72 saat süreyle kurutulmuşlardır. Kurutma işleminden sonra hassas terazide (0.001 g) tartularak kuru ağırlıklar belirlenmiştir.

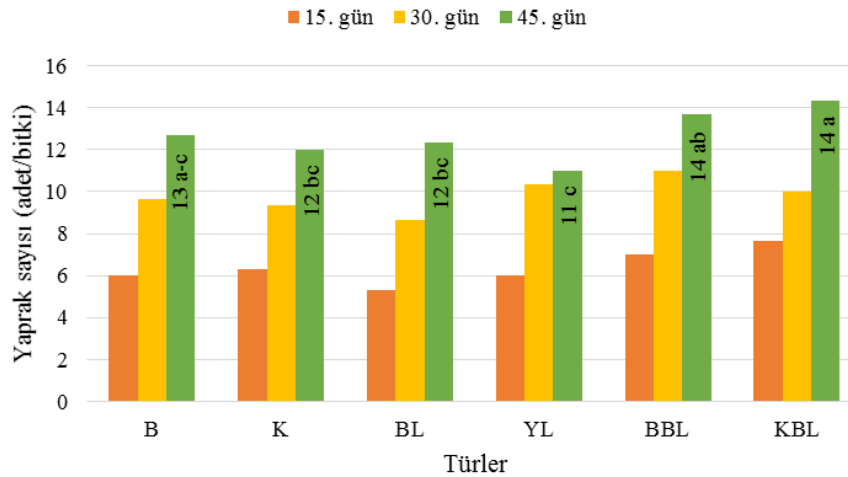
- Toplam bitki kuru ağırlığı (g): Gövde kuru ağırlığı ile kök kuru ağırlığının toplanmasıyla hesaplanmıştır.
- Oransal toprak üstü aksam kuru ağırlığı: Toplam toprak üstü kuru ağırlığının, toplam bitki kuru ağırlığına oranlanmasıyla hesap edilmiştir.
- Oransal kök ağırlığı (OKA): Toplam kök kuru ağırlığının, toplam bitki kuru ağırlığına oranlanmasıyla bulunmuştur.

Araştırma sonucunda elde edilen tüm verilerin değerlendirilmesinde, Microsoft Excel paket programı ve istatistiki analizlerde JMP 5.0.1 paket programı kullanılmıştır. Elde edilen veriler, istatistiki olarak varyans analizi (ANOVA) ile değerlendirmeye tabi tutulmuş ve önemli bulunan parametrelerde DUNCAN çoklu karşılaştırma ile çeşitler arasında gruplandırmalar yapılmıştır.

3. Bulgular ve Tartışma

Çalışmada, kışlık sebze türleri içerisinde önemli bir paya sahip olan lahanagil grubu 6 farklı sebze türünün vejetatif büyüme özellikleri belirlenmiştir. Yetiştiriciliğin 45. gününde elde edilen verilere göre yapılan varyans analizi sonucunda, incelenen bazı özelliklerde çeşitler arasında istatistiksel olarak önemli düzeyde farklılıklar olduğu tespit edilmiştir.

Araştırma sonucunda, lahanagil grubunda yer alan sebze türleri yaprak sayısı yönünden değerlendirildiğinde, 45. gün sonunda çeşitler arasında önemli düzeyde farklılık meydana geldiği saptanmıştır. Türler bazında yaprak sayısı 11-14 adet arasında değişim göstermiştir (Şekil 1). Kırmızı baş lahana ve beyaz baş lahana türleri en fazla, yaprak lahanaya türü ise diğer türlere göre daha az sayıda yaprak oluşturmuştur. Dikimden itibaren 15. gün sonunda belirlenen yaprak sayısı değerlerine göre 45. gündeki yaprak sayısı değerlerinin; brokolide 2,11 kat, karnabaharda 1.89 kat, Brüksel lahanasında 2,31 kat, yaprak lahanada 1.83 kat, beyaz baş lahanada 1,95 ve kırmızı baş lahanada ise 1.87 kat arttığı tespit edilmiştir. 45. gün sonunda en yüksek yaprak artış oranı (%131,25), beyaz baş lahana türünde kaydedilmiştir.

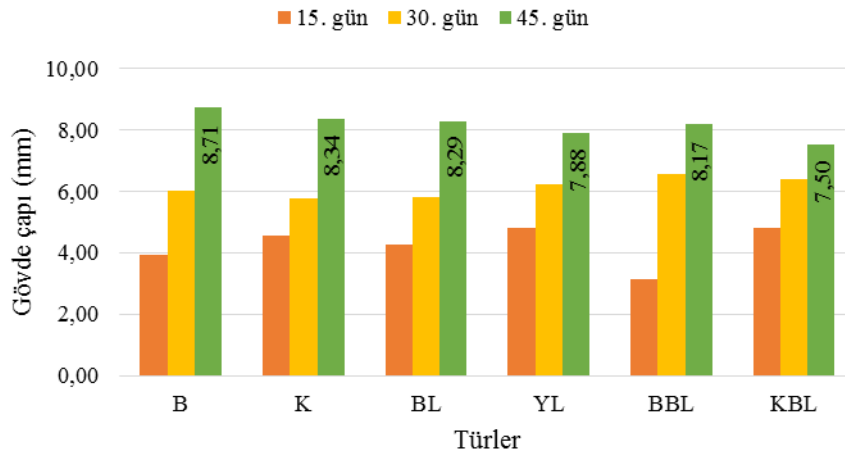


Şekil 1. Lahanagiller familyasına ait farklı türlerde dikimden itibaren 15 gün aralıklarla ortalama yaprak sayısı (adet/bitki) değerlerinin değişimi.

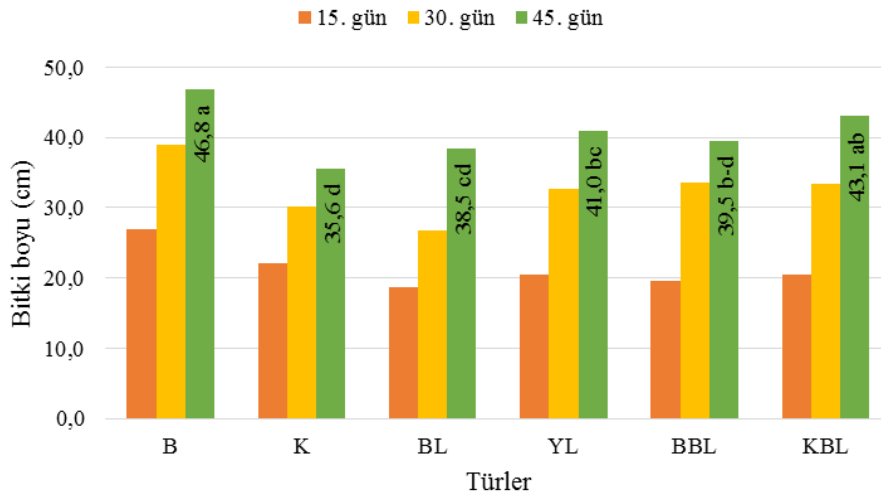
Bu çalışmada 45. günde yapılan ölçümler sonucunda; lahanagiller familyasında yer alan sebze türleri, istatistiki olarak önemli bulunmayan gövde çapı (mm) değerleri göstermişlerdir (Şekil 2). İstatistiksel olarak aynı grup içerisinde yer almalarına rağmen, sebze türlerinin gövde çapı değerleri 7.50-8.71 mm arasında değişiklik göstermiştir. Araştırmada 45. günde yapılan analizde en yüksek gövde çapı değeri brokoli türünde elde edilirken en düşük değer kırmızı baş lahana türünde kaydedilmiştir. Denemede 15. gün ile 45. gün arasındaki yetiştiricilik periyodunda gövde çapı artış oranı en yüksek BBL’de %159.47 olarak belirlenmiş olup, bunu %120.51 ile brokoli, %95.13 ile Brüksel lahanası, %82.82 ile karnabahar, %64.35 ile yaprak lahana ve %56.18 ile kırmızı baş lahana türleri takip etmiştir.

Bitki boyu (cm) değerleri bakımından lahanagil familyasında yer alan sebze türlerinin sahip oldukları genetik özellikler ve sera ortam koşullarının etkilerine bağlı olarak istatistiksel olarak ($P < 0.05$) önemli düzeyde

farklılık gösterdikleri saptanmıştır (Şekil 3). Araştırmada 15. günde yapılan ölçümde bitki boyu değerleri 18.7 cm (BL) - 27.0 cm (B) arasında, 30. gün analizinde 26.8 cm (BL) - 39.0 cm (B) arasında değişim göstermiştir. Lahanagil grubu incelenen çeşitlerde bitki boyunun 45. günde 35.6 - 46.8 cm arasında değişim gösterdiği kaydedilmiştir. Ayrıca, 15 ile 30 gün arasındaki bitki büyüme döneminde, türlere göre bitki boyu artış oranları sırasıyla %44.44 (B), %36.09 (K), %43.75 (BL), %59.87 (YL), %72.65 (BBL) ve %62.34 (KBL) olarak belirlenmiştir. Yine 30 ile 45 gün arasındaki 15 günlük süreçte ise bitki boyu artış oranı en düşük karnabahar türünde (% 60.6 oranında) hesaplanmıştır. Bununla birlikte araştırma sonucunda incelenen diğer 5 türde bitki boyu artış oranlarının %70’in üzerinde olduğu saptanmıştır.



Şekil 2. Lahanagiller familyasına ait farklı türlerde dikimden itibaren 15 gün aralıklarla ölçülen gövde çapı (mm) değerlerinin değişimleri.



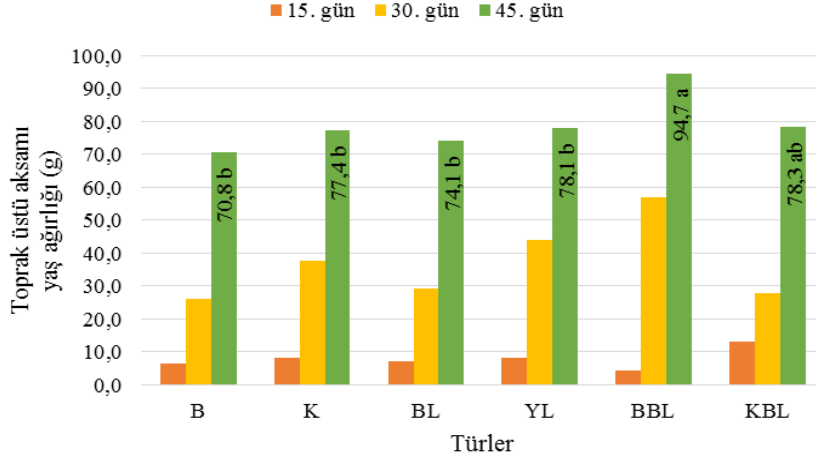
Şekil 3. Lahanagiller familyasına ait farklı türlerde dikimden itibaren 15 gün aralıklarla ölçülen bitki boyu (cm) değerlerinin değişimleri.

Araştırmada yer alan lahana grubu sebze türlerinde 15 gün aralıklarla yapılan kantitatif analizler sonucunda belirlenen toprak üstü kısmı yaş ağırlık (g) değerleri

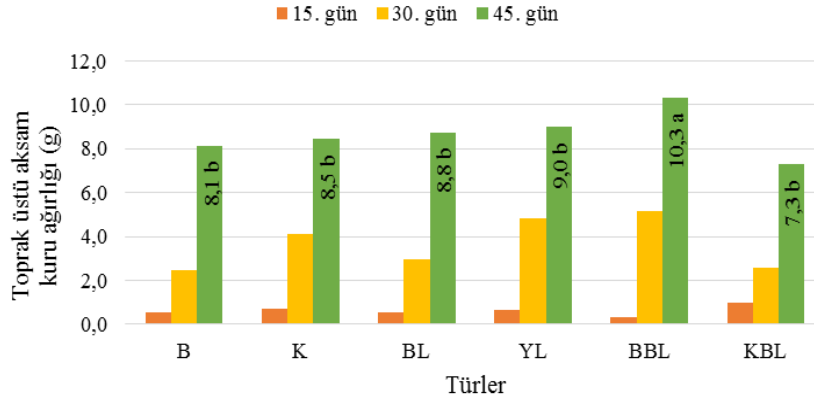
Şekil 4’te ve kuru ağırlık değerleri ise Şekil 5’te verilmiştir. Her iki özellik bakımından incelenen türler arasında istatistiksel olarak önemli düzeyde farklılıklar

olduğu bulunmuştur. Toprak üstü aksamı yaş ağırlık değerleri; 15. günde 4.23 (BBL) - 13.04 (KBL) g, 30. günde 26.12 (B) - 56.91 (BBL) g ve 45. günde ise 70,8 (B) - 94,7 (BBL) g arasında değişim göstermiştir. Araştırma sonucunda; 45. gün sonunda belirlenen yaş ağırlığı değerlerinin, 15. günde belirlenen yaş ağırlık değerlerine göre sırasıyla 6.01 kat (KBL), 9.39 kat (K), 9.44 kat (YL), 10.28 kat (BL), 10.77 kat (B) ve 22.38 kat (BBL) artış gösterdikleri tespit edilmiştir. Dikimden itibaren 45. gün sonunda belirlenen toprak

üstü aksamı kuru ağırlık değerleri, 7,3 - 10,3 g arasında değişim göstermiştir (Şekil 5). Yapılan varyans analizi sonucunda toprak üstü aksamı kuru ağırlık değerleri bakımından beyaz baş lahanada tür en yüksek değeri olarak istatistiki açıdan aynı grupta yer alan diğer türlerden farklı grupta yer almıştır. Ayrıca, beyaz baş lahanada 15. gün kaydedilen toprak üstü aksamı kuru ağırlık değerinin 45. gün sonucunda ölçülen değere göre yaklaşık 30.75 kat artış göstererek en yüksek değeri aldığı tespit edilmiştir.



Şekil 4. Lahanagiller familyasına ait farklı türlerde dikimden itibaren 15 gün aralıklarla belirlenen toprak üstü aksamı yaş ağırlık (g) değerleri.



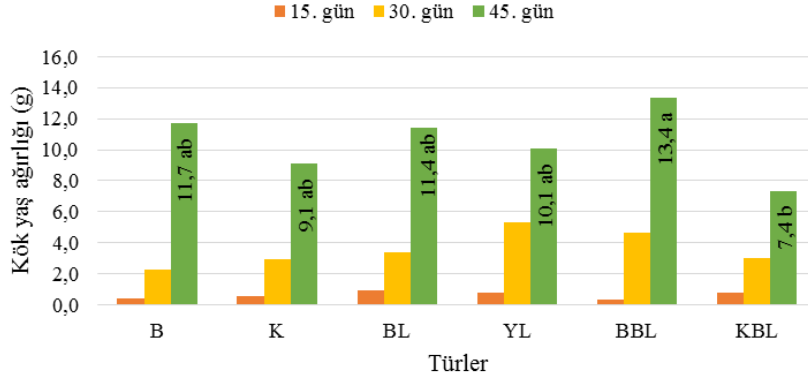
Şekil 5. Lahanagiller familyasına ait farklı türlerde dikimden itibaren 15 gün aralıklarla belirlenen toprak üstü aksamı kuru ağırlık (g) değerleri.

Lahanagiller familyasının farklı sebze türlerinde yapılan kantitatif analizleri sonucunda kök yaş ve kuru ağırlık değerleri yönünden elde edilen veriler Şekil 6 ve Şekil 7'de sunulmuştur. Fide dikiminden itibaren 45. günde yapılan analizlerde hem kök yaş ve hem de kuru ağırlık değerleri arasında istatistiksel olarak önemli düzeyde farkların olduğu tespit edilmiştir. En yüksek kök yaş ağırlık değeri beyaz baş lahanada türünde (13,4 g) belirlenmiş olmasına rağmen, en yüksek kök kuru ağırlık değerleri Brüksel lahanası (1,6 g) ile yaprak lahanada (1,7 g) kaydedilmiştir. Kök yaş ağırlığı bakımından brokoli, karnabahar, Brüksel lahanası ve yaprak lahanada türlerine ait çeşitler aynı istatistiki grupta yer almıştır. En düşük kök yaş ve kuru ağırlığı değerleri ise kırmızı baş lahanada sırasıyla 7,4 g ile 0,8 g olarak belirlenmiştir.

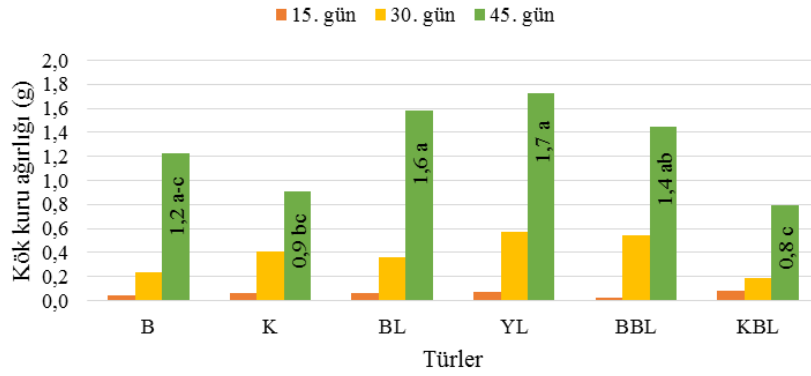
Araştırma sonucunda incelenen lahanagil türlerine ait çeşitlerde kök yaş ve kuru ağırlık değerlerinin özellikle 30. gün ve 45. gün arasındaki periyotta hızlı bir artış gösterdiği tespit edilmiştir. Kantitatif analizler sonucunda toplam bitki yaş ağırlık değerleri sırasıyla 15. günde sırasıyla türlere göre 4.58 g (BBL), 7.01 g (B), 8.11 g (BL), 8.79 g (K), 9.08 g (YL) ve 13.81 g (KBL); 30. günde 28.40 g (B), 31.03 g (KBL), 32.80 g (BL), 40.77 g (K), 49.15 g (YL) ve 61.55 g (BBL) olarak saptanmıştır (Şekil 8). Araştırmada 45. gün analiz sonuçlarına göre türlere göre bitki yaş ağırlığının 82.5 - 108.1 g; bitki kuru ağırlığının ise 8.1 - 11.8 g aralıklarında değerler aldığı ve bu özellikler bakımından türler arasında istatistiksel olarak önemli düzeyde farklılık olduğu tespit edilmiştir (Şekil 8, Şekil 9). En yüksek bitki yaş ve kuru ağırlığı

değerleri beyaz baş lahana türünde tespit edilmiştir. Brokoli (9.4 g), karnabahar (9.4 g) ve Brüksel lahanası (10.3 g) türleri bitki kuru ağırlık değerleri yönünden aynı

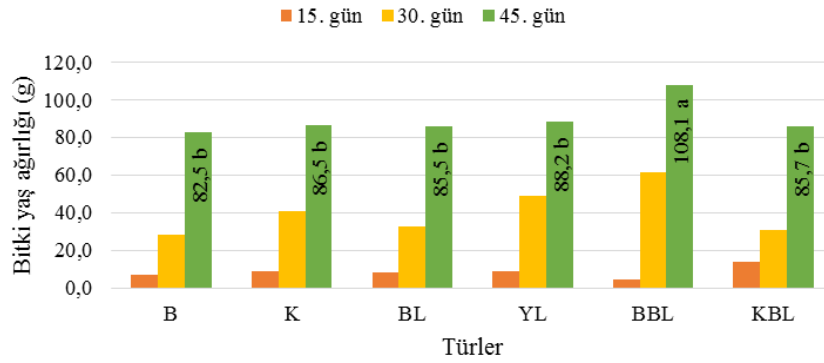
istatistiki grupta yer almıştır (Şekil 9). Araştırma sonucunda en düşük bitki kuru ağırlığı değeri, KBL türünde tespit edilmiştir.



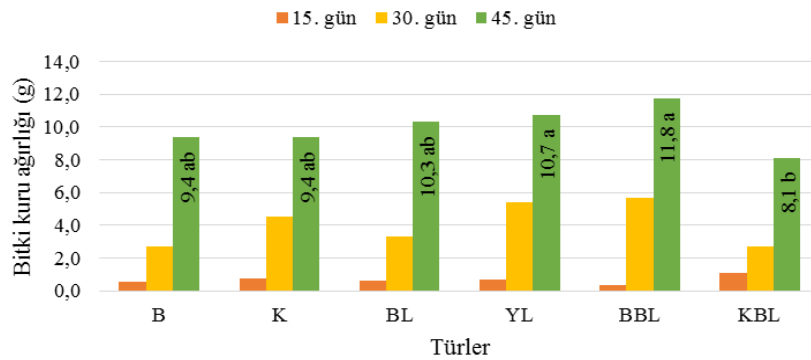
Şekil 6. Lahanagiller familyasına ait farklı türlerde dikimden itibaren 15 gün aralıklarla belirlenen kök yaş ağırlık (g) değerleri.



Şekil 7. Lahanagiller familyasına ait farklı türlerde dikimden itibaren 15 gün aralıklarla belirlenen kök kuru ağırlık (g) değerleri.



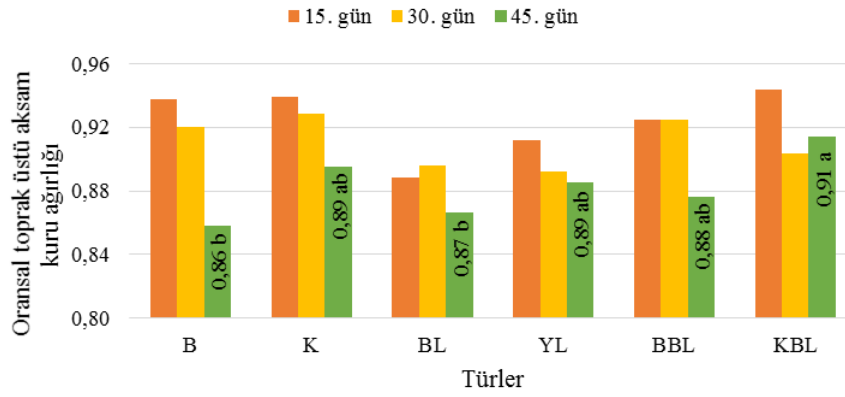
Şekil 8. Lahanagiller familyasına ait farklı türlerde dikimden itibaren 15 gün aralıklarla belirlenen toplam bitki yaş ağırlık (g) değerleri.



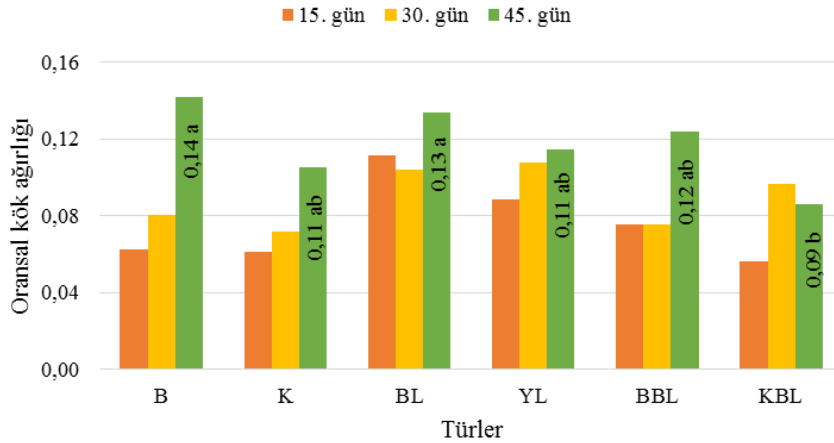
Şekil 9. Lahanagiller familyasına ait farklı türlerde dikimden itibaren 15 gün aralıklarla belirlenen toplam bitki kuru ağırlık (g) değerleri.

Araştırma sonucunda dikimden itibaren 45. gün için hesaplanan oransal toprak üstü aksam ağırlığı katsayıları incelendiğinde, lahanagil grubu sebze türlerine ait çeşitler arasında önemli düzeyde ($P<0.05$) farklılıklar olduğu tespit edilmiştir (Şekil 10). Bu değerler, 0.86 - 0.91 arasında değişim göstermiştir. Toprak üstü aksam kuru ağırlığının, toplam bitki kuru ağırlığı içerisindeki en yüksek oranı, 0.91 ile KBL türünde kaydedilmiştir. KBL, YL, K, BBL ve YL aynı istatistik grupta yer almışlardır. B ve BL ise aynı grupta ve daha düşük oransal toprak üstü aksam kuru ağırlık oranına sahip olmuşlardır. Bitkilerde var olan kök mimarisi yapısı, su ve besin alımı gibi farklı fizyolojik görevlere önemli miktarlarda tesir ederek, özellikle stres etmenleri altında bitki büyümesi,

gelişmesi, verimliliği ve ürün kalitesi açısından önemli düzeyde etkili olmaktadır (Atasoy ve ark. 2023). Toplam bitki kuru ağırlığı içerisinde kök kuru ağırlık miktarının belirlenmesi amacıyla yapılan hesaplama sonucu fide dikiminden itibaren 45. günde kök ağırlığı yönünden incelenen türler arasında istatistiksel olarak önemli düzeyde farklılık olduğu bulunmuştur (Şekil 11). Brokoli (0.14) ve Brüksel lahanası (0.13) türlerine ait çeşitlerde en yüksek oransal kök ağırlığı katsayı değerleri belirlenmiştir. En düşük oransal kök ağırlığı katsayısı ise KBL türünde kaydedilmiştir.



Şekil 10. Lahanagiller familyasına ait farklı türlerde dikimden itibaren 15 gün aralıklarla belirlenen oransal toprak üstü aksam kuru ağırlık oranı.



Şekil 11. Lahanagiller familyasına ait farklı türlerin dikimden itibaren 15 gün aralıklarla belirlenen toplam oransal kök ağırlık (OKA) değerleri

Sebzelerden yüksek verim ve kalite, birim alandaki bitki sayısına, sebze türüne ve çeşidine, olgunlaşma süresine, çevre ve özellikle de iklimsel koşullara göre değişen bir özelliktir. Büyüme ve gelişme açısından iklim şartları oldukça önemlidir. Vejetatif büyümesini tam olarak tamamlamış sebzelerde muhtemel verim artışlarının olması beklenmektedir (Uzun, 2000; Kandemir ve Uzun, 2019; Özkaplan ve Balkaya, 2020; Şahin ve ark., 2022). *Brassicaceae* familyası sebze türlerinde verim artışı ve kalite bakımından bitkilerin büyüme ve gelişme şartları, yani çevresel koşullara uyum yeteneği ile abiyotik stres

faktörlerine dayanıklılık oldukça önemlidir. Bu sebze türleri özellikle çevresel faktörlerden kaynaklı abiyotik stres faktörlerinden olumsuz yönde etkilenmekte ve vejetatif ile generatif büyüme hızları oldukça yavaşlamaktadır (Atasoy ve ark., 2023; Ekinci ve ark., 2023). Bu çalışmada optimum yetiştirme koşulları altında bazı lahanagil sebze türlerine ait çeşitlerde vejetatif büyüme özellikleri ayrıntılı olarak ortaya konulmuştur. Bununla birlikte lahanagillerde iyi bir büyüme ve gelişme sağlanması açısından genetik yapı (çeşit), iklim koşulları, sulama yöntemi; toprak tipi ve

diğer kültürel uygulamalara göre sistem dahilinde bir planlama yapılarak bitki yönetimleri gerçekleştirilmelidir. Yine diğer kışlık sebze türleri için büyüme ve gelişimine ve sonuçta verimine yönelik yapılan bu tür çalışmalarla pazara yıl içerisinde ne zaman ve ne kadar ürünle girilebileceği belirlenebilir ve bu sayede yetiştiricilerin üretim planlaması yapmaları sağlanabilir (Şahin ve ark., 2022).

4. Sonuç

Bu çalışma ile Samsun ekolojik şartlarında ısıtmasız serada bazı lahanagiller familyasında yer alan öne çıkan sebze türlerinde vejetatif büyüme özellikleri ortaya konulmuştur. Sebze türleri her ne kadar aynı familya içerisinde bulunsun bile türlerin büyüme ve gelişmelerinin ve sonuçta verim değerlerinin; yetiştirildikleri ekolojik faktörlere, kullanılan yetiştirme tekniğine ve çeşitlere göre farklılık gösterdiği bilinmektedir. Ülkemizde yetiştiriciliği yapılan bazı kışlık sebze türlerinde (brokoli, karnabahar, Brüksel lahanası, yaprak lahanası, beyaz ve kırmızı baş lahanası) çevre şartları, çeşit seçimi ile uygun ekim ve dikim zamanı ayarlanarak bitki büyüme ve gelişmesi kontrol altında tutulabilir ve böylece yılın her döneminde verim almak mümkün olabilir. Yazlık sebze türleri için büyüme, gelişme ve verim için modelleri vardır ve bu modeller sayesinde en iyi büyüme ve gelişme şartları ortaya konmuştur. Bu türlerde bitki büyüme model çalışmaları ile bitki büyümesi ile verim arasındaki ilişkiler detaylı olarak incelenmiştir. Kışlık sebze türlerinde ve özellikle lahanagiller familyasında yer alan sebze türlerinde böyle bir çalışmaya rastlanılmamıştır. Samsun ekolojik koşullarında ısıtmasız serada sonbahar dönemi yetiştiriciliğinde farklı lahanagiller sebze türlerinin vejetatif büyüme durumlarının saptanması ile elde edilen sonuçlar, bilimsel açıdan ileride diğer kışlık sebze türlerinde yapılacak büyüme ve verim model çalışmalarına yol gösterebilecektir. Elde edilecek bu modeller sayesinde bu sebze türleri için uygun şartlar ve çeşitler belirlenerek, yıl boyu üretim yapmak mümkün olabilir. Bu da ekonomik açıdan ülkemizde kışlık sebze üretim planlamasına olumlu yönde katkılar sağlayabilir.

Katkı Oranı Beyanı

Yazar(lar)ın katkı yüzdesi aşağıda verilmiştir. Tüm yazarlar makaleyi incelemiş ve onaylamıştır.

| | D.K. | K.P. | T.G.Ş | A.B. |
|-----|------|------|-------|------|
| K | 30 | 10 | 10 | 50 |
| T | 50 | | | 50 |
| Y | 50 | | | 50 |
| VTI | 30 | 40 | 40 | |
| VAY | 60 | 20 | 20 | |
| KT | 50 | | | 50 |
| YZ | 50 | | | 50 |
| KI | | | | |
| GR | 70 | | | 30 |

K= kavram, T= tasarım, Y= yönetim, VTI= veri toplama ve/veya işleme, VAY= veri analizi ve/veya yorumlama, KT= kaynak tarama, YZ= Yazım, KI= kritik inceleme, GR= gönderim ve revizyon.

Çatışma Beyanı

Yazarlar bu çalışmada hiçbir çıkar ilişkisi olmadığını beyan etmektedirler.

Etik Onay Beyanı

Hayvanlar ve insanlar üzerinde herhangi bir çalışma yapılmadığından dolayı bu araştırma için etik kurul onayı alınmamıştır.

Kaynaklar

- Ackah E, Kotei R. 2021. Effect of drought length on the performance of cabbage (*Brassica oleracea* var *capitata*) in the forest-savannah transition zone, Ghana. *Plant Physiology Rep*, 26: 74-83.
- Al-Shehbaz IA, Warwick SI. 2006. A synopsis of *Smelowskia* (*Brassicaceae*). *Harvard Papers in Botany*, 11: 91-100.
- Appel O, Al-Shehbaz IA. 2003. Cruciferae. In: Kubitzki, K., Bayer, C. (eds) *Flowering Plants-Dicotyledons. The Families and Genera of Vascular Plants*, vol 5. Springer, Berlin, pp: 75-174.
- Atasoy S, Şahin GT, Balkaya A. 2023. Lahanagil Sebze Türlerinin Kök Sistemi Mimarileri Yönünden Karşılaştırılması. *Inter J Life Sci Biotech*, 6: 193-207.
- Balkaya A. 2001. Çin lahanası yetiştiriciliğinde tohumu kalkmayı etkileyen faktörler. *OMÜ Zir Fak Der*, 16: 78-83.
- Balkaya A. 2016. Lahanası, Karnabahar, Brokoli, Yetiştiriciliği. Anadolu Üniversitesi Yayını No:2358. Açık Öğretim Fakültesi Yayını No:1355.
- Balkaya A, Karaağaç O. 2021. Lahanagiller (*Brassicaceae*) ıslahı, Bölüm:1 lahanası ıslahı, Gece Kitaplığı, s. 149-198.
- Balkaya A, Karaağaç O, Atasoy S. 2023. Geçmişten geleceğe Türkiye'de lahanagil sebzelerinin üretimi, sorunları ve çözüm önerileri. *Farklı Yönleriyle Lahanagiller Üzerine Bilimsel Çalışmalar*, İksad Publishing House, s. 3-36.
- Decoteau DR. 2000. *Vegetable crops* (No. 635 D3589v Ej. 1 025327). Prentice Hall.
- Erken O, Oztokat, C. 2010. Effects of water stress on yield and some quality parameters of Broccoli. In 2nd International Symposium on Sustainable Development. *Science Book*, pp: 231-237.
- Ekinci M, Örs S, Yıldırım E. 2023. Lahanagil sebze türlerinde sulama ve su stresi. Bölüm 6. *Farklı yönleriyle lahanagiller üzerine bilimsel çalışmalar*, pp: 181-214.
- Kandemir D, Uzun S. 2019. Modelling of the quantitative effects of different light and temperature values on growth

- parameters of pepper grown in greenhouse. *Anadolu Tar Bil Der*, 34: 1-11.
- Li Y, Liu GF, Ma LM, Liu TK, Zhang CW, Xiao D, Zheng HK, Chen F, Hou XL. 2020. A chromosome-level reference genome of non-heading Chinese cabbage [*Brassica campestris* (syn. *Brassica rapa*) ssp. *chinensis*]. *Hort Res*, 7.
- Maggio A, De Pascale S, Ruggiero C, Barbieri G. 2005. Physiological response of field-grown cabbage to salinity and drought stress. *Eur J Agron*, 23: 57-67.
- Monteiro A, Lunn T. 1998. Trends and perspectives of vegetable Brassica breeding World- Wide. World Conference on Horticultural Research. 17-20 June, Rome, Italy.
- Özkaplan M, Balkaya A. 2020. Topraksız tarımda domates yetiştiriciliğinde bitki gelişme parametreleri ile sıcaklık ve ışık arasındaki ilişkilerin modellenmesi. *Mediterr Agric Sci*, 33: 181-187.
- Shannon MC, Grieve CM. 1998. Tolerance of vegetable crops to salinity. *Sci Hort*, 78: 5-38
- Song K, Osborn TC., Williams P.H. 1990. Brassica taxonomy based on nuclear restriction fragment length polymorphisms (RFLPs): 3. Genome relationships in Brassica and related genera and the origin of *B. oleracea* and *B. rapa* (syn. *campestris*). *Theoretical and Applied Genetics*. 79: 497-506.
- Şahin G.T, Kandemir D, Balkaya A, Karaağaç O, Sarıbaş Ş. 2022. Sonbahar dönemi yetiştiriciliğinde kıvrıkcık (*Lactuca sativa* L. var. *crispa*) ve Yedikule (*Lactuca sativa* L. var. *longifolia*) tipi marul çeşitlerinin vejetatif büyüme düzeylerinin incelenmesi. *Bahçe*, 51: 1-10.
- Ulukapı K, Şener S. 2018. Farklı organik gübrelerin tarla ve örtüaltı koşullarında yetiştirilen karnabaharın bitki gelişimi ve verim parametreleri üzerine etkisi. *Selcuk J of Agr Food Sci*, 32: 510-515.
- Uzun S. 1996. The quantitative effects of Temperature and light environment on the growth, development and yield of tomato (*Lycopersicon esculentum* Mill.) and aubergine (*Solanum melongena* L.). Ph.D. Thesis, Reading University, England.
- Uzun S. 2000. Sıcaklık ve ışığın bitki büyüme, gelişme ve verimine etkisi (III Verim). *OMÜ Zir Fak Der*, 15: 105-108.
- Welbaum GE. 2015. Vegetable production and practices. CABI, Wallingford, UK.
- Wu H, Wu X, Li Z, Duan L, Zhang M. 2012. Physiological evaluation of drought stress tolerance and recovery in cauliflower (*Brassica oleracea* L.) seedlings treated with methyl jasmonate and coronatine. *J of Plant Growth Regulation*, 31: 113-123.
- Zaicovski CB, Zimmerman T, Nora L, Nora FR, Silva JA, Rombaldi CV. 2008. Water stress increases cytokinin biosynthesis and delays postharvest yellowing of broccoli florets. *Postharvest Bio and Tech*, 49: 436-439.
- Zhiyuan F, Wang X, Dongyu Q, Guangshu L. 2000. Hybrid seed production in cabbage. *J of New Seeds* 1: 109-129.



COMPARING OF CFD CONTOURS USING IMAGE ANALYSING METHOD: A STUDY ON VELOCITY DISTRIBUTIONS

Ahmet ERDOĞAN^{1,2*}, Mahmut DAŞKIN^{1,3}

¹Inönü University, Faculty of Engineering, Department of Mechanical Engineering, 44280, Malatya, Türkiye

²University of Nottingham, Faculty of Engineering, Advanced Materials Research Group, NG72RD, Nottingham, UK


³Cranfield University, Energy and Sustainability Theme, MK43 0AL, Cranfield, UK


Abstract: Contour plotting, a widely utilized graphical technique for visualizing CFD (Computational Fluid Dynamics) outcomes, is highly valuable. It provides an effective and practical approach to analysing distributions of magnitudes belonging to fluid domains such as; velocity, temperature, pressure, volume fraction, etc. Nevertheless, when analysing multiple contours, especially showing similar distribution, identifying the ideal contour can be difficult and open to speculation. In this research, the issue was addressed by employing the Image Analysis Method for the classification of velocity distribution contours. This led to determining which picture has the best distribution among a few of the contour's pictures. Firstly, velocity distribution contours downstream of the diffuser located in Air Handling Unit (AHU) unit were obtained by using CFD. The contour pictures were then transferred to MATLAB environment. With pixel analysis in MATLAB, the pictures were able to be classified based on which parameters had an effect on the velocity distribution. Variable parameters are the length of the fan channel (x) and the ratio of cross-sectional areas of the AHU (A/A_0). The results showed that $x=250$ mm and $A/A_0=0.5$ improved velocity distributions by 6% and 20%, respectively.

Keywords: Computational fluid dynamics, Image analysis method, Velocity distribution, Air handling unit

*Corresponding author: University of Nottingham, Faculty of Engineering, Advanced Materials Research Group, NG72RD, Nottingham, UK

E mail: ahmet.erdogan@inonu.edu.tr (A. ERDOĞAN)

Ahmet ERDOĞAN  <https://orcid.org/0000-0001-8349-0006>

Mahmut DAŞKIN  <https://orcid.org/0000-0001-7777-1821>

Received: June 06, 2023

Accepted: October 04, 2023

Published: October 15, 2023

Cite as: Erdoğan A, Daşkin M. 2023. Comparing of CFD contours using image analysing method: a study on velocity distributions. BSJ Eng Sci, 6(4): 633-638.

1. Introduction

Fluid flow problems are numerically solved using the principles of conservation of mass, momentum, and energy, also known as computational fluid dynamics (CFD) (Hu, 2012). The characteristics of fluid domains can be determined with CFD by revealing magnitudes belonging to the fluid domain such as; the velocity, pressure, shear stress, temperature, turbulence, and volume fraction (Anderson and Wendt, 1995; Versteeg and Malalasekera, 2007). CFD results can be visualized via contour plots, which provide valuable and useful graphical tools (Tu et al., 2023). It always challenging to find the optimal contour plot when comparing multiple contour plots with similar distributions. Interpreting CFD contour plots that show similar distributions to each other without subjecting them to a numerical analysis and deciding which one gives better results may vary from person to person and may lead to erroneous interpretations and decisions. To classify the CFD results, which are presented as contour plots showing the velocity distribution of airflows, this study includes a series of CFD simulations based on airflow in air handling units (AHUs).

Air handling units serve as part of ventilation, heating, and air conditioning systems (HVAC) to regulate and circulate air (Parsons, 1996; Xu et al., 1996). In many

applications of AHU, perforated diffusers are used to diffuse as homogeneously as possible the air supplied by the fan (Kamer et al., 2018). Otherwise, the air cannot entirely be in contact with the other units such as serpentine or humidifiers and AHUs may inefficiently work (Bayramgil et al., 1998). The pressure loss caused by perforated diffusers and velocity distributions downstream of them are two performance characteristics. The performance characteristics of V profile diffusers (Kamer et al., 2018), truncated pyramid diffusers (Bulut et al., 2011; Erdoğan, 2017), truncated cone diffusers (Sönmez, 2017), anemostat type diffusers (Vakkasoglu et al., 2021), and plate diffusers (Kerim Sönmez and Özmen, 2022) have been numerically studied. As with perforated diffusers, perforated plates are frequently used to manage flow in flow systems (Gan and Riffat, 1997; Özahi, 2015). Some researchers have reported the pressure losses and velocity distributions of perforated diffusers (Gaulke and Dreyer, 2015; Guo et al., 2013; Wang et al., 2020). In these studies, however, velocity distribution contours were interpreted without any image process which could assess the pictures. This might lead to a mistake in interpretation when contours showing small differences are considered.

Image analysing and image processes have been currently widely used in the assessment of CFD results of



different applications such as solar dryers (Benhamza et al., 2021), bubbles characteristics in the fluidised beds (Li et al., 2019), wind effect around buildings (He et al., 2021), and so on.

In this study, flow analyses were conducted using the Computational Fluid Dynamics (CFD) method considering two different geometric parameters, which have not been considered before, for a truncated pyramid perforated diffuser. The parameters considered were the length of fan channel (x) and the ratio of cross-sectional areas of the AHU (A/A_0). Velocity contours at the downstream region of the diffusers were obtained as a result of the CFD analysis with the grayscale contours colormap option. In this study, an initiative was taken to obtain parameter values resulting in optimal velocity distribution by transferring velocity contours to MATLAB software and analysing them using image matrices, rather than visually interpreting velocity contours.

2. Materials and Methods

In order to perform three-dimensional CFD analysis, solid models were firstly prepared and then transferred to the Ansys Fluent commercial software. Figure 1 depicts the solid model prepared for CFD analysis. In Figure 2, an AHU with diffuser is schematically shown

with its dimensions and details.

In the prepared model, air enters uniformly through inlet section that has A of cross-sectional area. This inlet section was identified “velocity inlet” boundary condition. Upon reaching the sudden expansion region, a portion of the air collides with the truncated pyramid perforated diffuser through its holes, while the remaining portion bypasses the diffuser and exits the flow domain through an 800×800 mm outlet section which was defined as “pressure outlet” boundary condition. All other boundaries were acknowledged as “wall” boundary conditioning with no slip condition. The height between the ceiling and the base of the square truncated pyramid perforated diffuser is 180 mm, with a thickness of 2 mm. Each face of the diffuser contains 45 holes. In Figure 2, x represents the length of the air supply channel, which is the first parameter. 100 mm, 150 mm, 200 mm, and 250 mm are the values in this study for x . Another parameter examined for its effect on diffuser velocity distributions is the ratio of cross-sectional areas of the AHU, symbolized by A/A_0 . For four different values (0.2, 0.3, 0.4, and 0.5) of A/A_0 , this parameter was considered to obtain velocity distribution contours at the downstream of the diffuser.

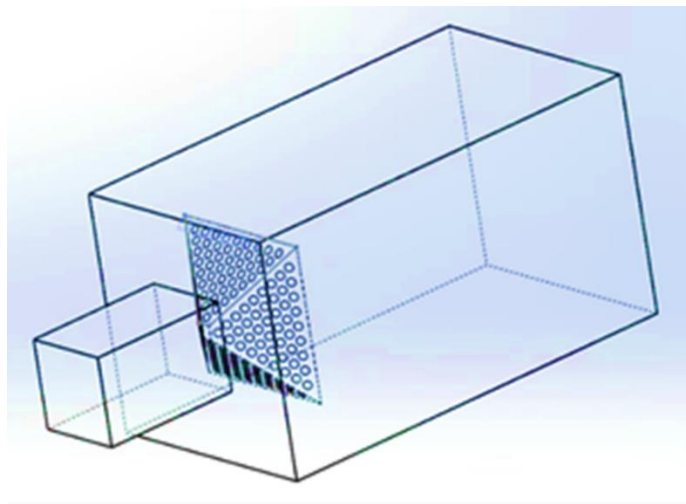


Figure 1. Solid model prepared for CFD.

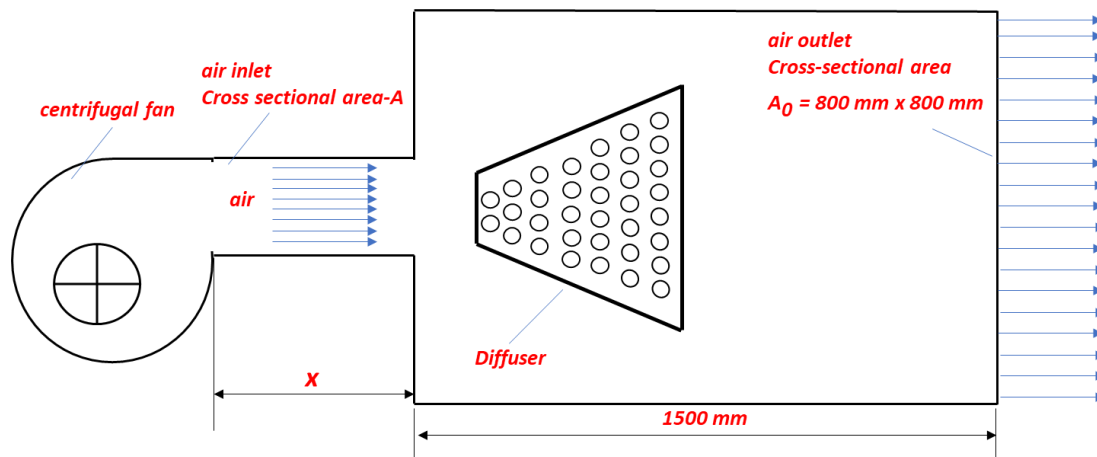


Figure 2. The dimensions and details of an AHU with diffusers.

In the models generated to perform CFD analyses, the mesh number is maintained at approximately $2.5 \cdot 10^6$. There was no significant difference in the results when the mesh number is increased or decreased by 50%. A tetrahedral mesh type was defined for the entire flow domain. A dense mesh structure was created on the diffuser surfaces and hole sections, with a mesh size of 3 mm on the diffuser surface and a maximum size of 15 mm throughout the entire flow volume. The maximum skewness value all the meshes was preserved at 0.84. The mesh was refined in all of flow domain. 18° is determined for the span angle of the mesh curvature. Fine and high options are selected as the relevance centre and mesh smoothing characteristics. The turbulence intensity at the inlet was set to 5%, and the hydraulic diameter was set to 0.3 m. The entire flow domain was analysed under steady flow conditions. A pressure-based solver with the SIMPLE algorithm was used for the resolution of all models. This model was discretized spatially using the First Order Upwind Scheme as a method of spatial discretization. A convergence criterion of 10^{-3} was applied to all variables. Parallel processing was carried out on 8 processors for each analysis. The principles of conservation of mass, momentum, and additional motion equations were applied to the flow domain using the Finite Volume Method. The RANS (Reynolds Averaging Navier-Stokes) governing equations of mass and momentum are solved in CFD analyses. The governing Equations 1 and 2:

$$\frac{\partial u_i}{\partial x_i} = 0 \tag{1}$$

$$\frac{\partial u_i u_j}{\partial x_j} = -\frac{\partial p}{\partial x_i} + \frac{\partial}{\partial x_j} \left[\mu \left(\frac{\partial u_i}{\partial x_j} + \frac{\partial u_j}{\partial x_i} \right) \right] - \frac{\partial}{\partial x_j} (\rho \overline{u'_i u'_j}) \tag{2}$$

where u and p are the velocity and pressure, respectively.

$\overline{u'_i u'_j}$ states Reynolds stress. Since giving a good agreement between numerical simulations and experimental measurements in the flow analysis within AHUs (Kamer et al., 2018; Vakkasoglu et al., 2021), the CFD analyses were solved using the Standard k-ε turbulence model. The equations of Standard k-ε turbulence model are given Equation 3 and equation 4 (Chen and Kim, 1987).

$$\frac{\partial(\rho k)}{\partial t} + \frac{\partial(\rho k u_i)}{\partial x_i} = \frac{\partial}{\partial x_j} \left[\left(\mu + \frac{\mu_t}{\sigma_k} \right) \frac{\partial k}{\partial x_j} \right] + G_k - \rho \varepsilon \tag{3}$$

$$\frac{\partial(\rho \varepsilon)}{\partial t} + \frac{\partial(\rho \varepsilon u_i)}{\partial x_i} = \frac{\partial}{\partial x_j} \left[\left(\mu + \frac{\mu_t}{\sigma_\varepsilon} \right) \frac{\partial \varepsilon}{\partial x_j} \right] + C_{1\varepsilon} \frac{\varepsilon}{k} G_k - C_{2\varepsilon} \rho \frac{\varepsilon^2}{k} \tag{4}$$

In equation 3 and equation 4, turbulence kinetic energy and turbulence dissipation rate are symbolised k and ε , respectively. μ_t states turbulent viscosity and calculated equation 5 illustrated below.

$$\mu_t = \rho C_\mu \frac{k^2}{\varepsilon} \tag{5}$$

The constants in these equations take the following values, respectively: $\sigma_k=1$, $\sigma_\varepsilon=1.3$, $C_{1\varepsilon}=1.44$, $C_{2\varepsilon}=1.92$, and $C_\mu=0.09$ (Fluent, 2009).

Velocity contours at the reference section downstream of the diffuser were obtained using the Ansys Fluent program. These velocity contours were transferred to the MATLAB environment as grayscale contours starting from black and ending with white. Investigation of these images was conducted in two stages using MATLAB program. Firstly, the pixel value corresponding to average velocity, which is desirable to have a velocity close to this level at every point on the cross-sectional area for a homogeneous velocity distribution, the value at the reference section downstream of the diffuser was determined. This process is illustrated in Figure 3.

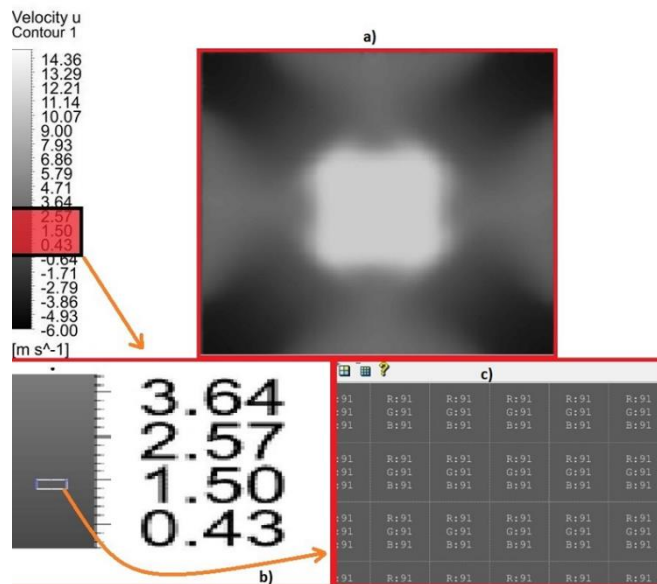


Figure 3. a) The velocity distribution contours obtained from CFD analysis. b) The region of interest where the average velocity is located. c) The image pixel values corresponding to the average velocity.

Secondly, the absolute difference between the pixel value corresponding to the average velocity and the matrix values of the respective velocity distribution images is obtained using the equation 6. This process yields an error value. This error computation was conducted across all pixels within the image, resulting in a comprehensive assessment of how closely the actual velocity distribution matched the desired average velocity. To facilitate a more meaningful comparison among different velocity distribution images, the obtained error values were normalized within the range of [0-1]. Normalization allowed for a consistent and fair evaluation of the images, regardless of their original scale or magnitude. Finally, the images were sorted based on their error values, providing a systematic way to identify and rank the performance of various diffuser configurations (Equation 6).

$$E = \sum_{x=1}^n \sum_{y=1}^n |\hat{I} - I_{xy}| \quad (6)$$

Here, E is the error, \hat{I} represents the pixel value corresponding to the average velocity, and I_{xy} states each pixel value associated with the image.

3. Results and Discussion

In this study, the velocity distribution characteristics of truncated pyramid perforated diffusers were examined. Velocity contours were obtained for a reference section located 400 mm horizontally from the sudden expansion section downstream of the diffuser using the ANSYS Fluent software package in the CFD analysis. Velocity distribution contours at the reference section for four different values of the length of the air supply channel ($x_1=100\text{ mm}$, $x_2=150\text{ mm}$, $x_3=200\text{ mm}$, and $x_4=250\text{ mm}$) are presented in Figure 4. Additionally, velocity contours obtained for the reference section in the downstream of the diffuser are provided in Figure 5 for four different values of the ratio of cross-sectional areas of the AHU ($A/A_0=0.2$, $A/A_0=0.3$, $A/A_0=0.4$, and $A/A_0=0.5$). It is obvious from Figures 4 and 5 that all pictures showing velocity distributions are not homogeneous. Moreover, Figure 4 illustrates the main objective of this study because the images showing velocity distribution are considerably close to each other.

In the studies where the performances of diffusers of different geometries used in AHUs were investigated by CFD, the images demonstrating contour plots were tried to be interpreted without any numerical analysis (A Erdođan, 2016; Kamer et al., 2018; Vakkasoglu et al., 2021). In contrast, in this study, images displaying contour plots were analysed and classified using image analysis. By applying equation 6, the pixel values of the velocity contours for different lengths of the air supply channel values were analysed, and the normalized error values obtained from the analysis are presented in Table 1. As can be seen in Table 1, the length of air supply channel providing more homogeneous airflow

distribution in the reference section is $x_2=250\text{ mm}$ since it has the minimum value among these normalized error values calculated for different lengths of air supply channel. At this point, as the air supply channel length increases, the airflow reaches the fully-developed turbulence flow profile (Gessner & Jones, 1965; Hussain & Reynolds, 1975) and may therefore result in improved diffuser performance.

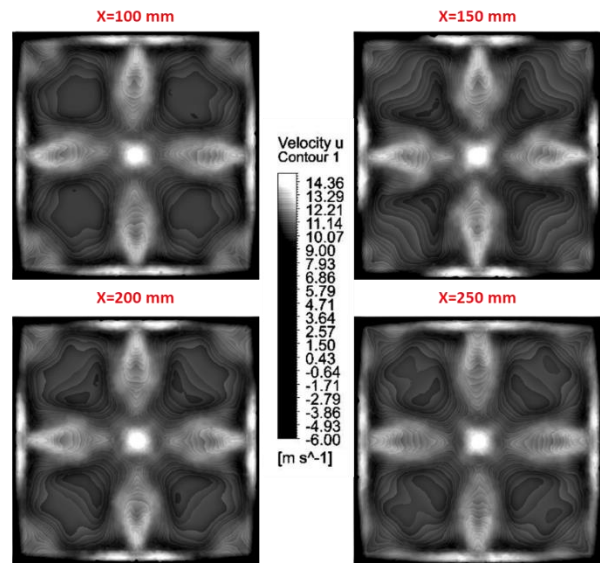


Figure 4. Velocity distribution contours obtained by CFD for the length of the air supply channel.

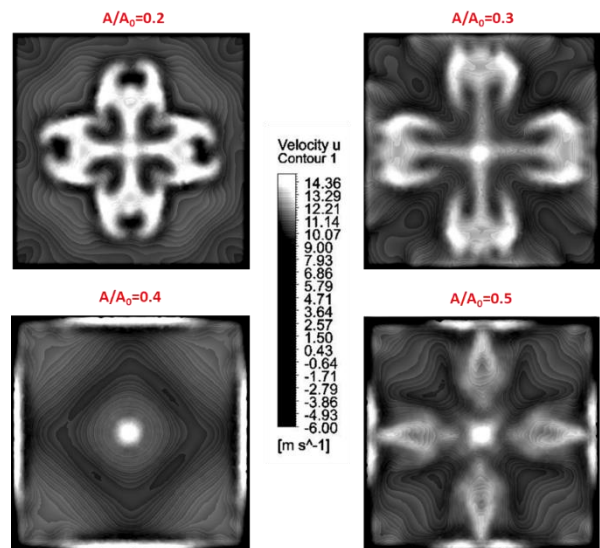


Figure 5. Velocity distribution contours obtained by CFD for the ratio of cross-sectional areas of the AHU.

Table 1. Normalised pixel errors values of the contours obtained for different lengths of the air supply channel

| Parameter and values | Error |
|----------------------|--------|
| $x_1=100\text{ mm}$ | 1.0000 |
| $x_2=150\text{ mm}$ | 0.9880 |
| $x_3=200\text{ mm}$ | 0.9715 |
| $x_4=250\text{ mm}$ | 0.9418 |

Table 2 gives normalized pixel error values of the contours obtained for different ratios of cross-sectional areas of the AHU. According to Table 2, the parameter value of $A/A_0 = 0.5$ is closest to the average velocity value corresponding to the reference cross-section highlighted in red in Figure 3 in terms of pixel value on the image. This shows that the diffuser with a ratio of cross-sectional areas of the AHU of $A/A_0 = 0.5$ possesses a lower error value and demonstrates superior distribution performance compared to other ratios of cross-sectional areas of the AHU.

Table 2. Normalised pixel error values of the contours obtained for different ratio of cross-sectional areas of the AHU

| Parameter and values | Error |
|----------------------|--------|
| $A/A_0 = 0.2$ | 1.0000 |
| $A/A_0 = 0.3$ | 0.9919 |
| $A/A_0 = 0.4$ | 0.9321 |
| $A/A_0 = 0.5$ | 0.8012 |

4. Conclusion

This study has focused on analysing velocity distribution contours using image analysis techniques to provide a numerical interpretation of computational fluid dynamics (CFD) contours, which are commonly presented in various CFD studies. To carry out this novelty, a few CFD simulations were conducted in AHU which has a diffuser. Velocity distribution contours at the reference cross-section downstream of the diffuser were obtained for two different parameters in the grayscale contour. Error values are calculated for each velocity contour to quantify the deviation from the contour representing the optimal velocity distribution. Within the scope of this study,

- It has been established that CFD outputs such as contour plots, which are often challenging to interpret or subject to debate, can be effectively interpreted using numerical image analysis techniques.
- Based on the image analysis, it appears that the minimum pixel error is reached if the length of air supply channel (x) is kept at 250 mm, and the velocity distribution could be improved by approximately 20%.
- In these ranges of parameters values, the pixel error obtained by the image analysis method can be minimised within these parameter scales if the ratio of AHU cross-sectional area (A/A_0) is 0.5. The velocity distribution is able to be developed by around 6% if the ratio of AHU cross-sectional area is 0.5.

In future studies, it is planned that this optimisation method could be applied to other CFD contours presenting such as temperature distribution, pressure distribution, and volume fraction of the fluid domain.

Author Contributions

The percentage of the author(s) contributions is presented below. All authors reviewed and approved the final version of the manuscript.

| | A.E. | M.D. |
|-----|------|------|
| C | 50 | 50 |
| D | 50 | 50 |
| S | 60 | 40 |
| DCP | 80 | 20 |
| DAI | 20 | 80 |
| L | 60 | 40 |
| W | 50 | 50 |
| CR | 50 | 50 |
| SR | 50 | 50 |
| PM | 50 | 50 |

C=Concept, D= design, S= supervision, DCP= data collection and/or processing, DAI= data analysis and/or interpretation, L= literature search, W= writing, CR= critical review, SR= submission and revision, PM= project management.

Conflict of Interest

The authors declared that there is no conflict of interest.

Ethical Consideration

Ethics committee approval was not required for this study because of there was no study on animals or humans.

References

- Anderson JD, Wendt J. 1995. Computational fluid dynamics. Springer, Berlin, Germany, pp: 3-14.
- Bayramgil V, Bayrak S, Yükselen M, Erim M. 1998. Experimental investigation of a diffuser for cooling and air conditioning system. 21st Congress of International Council of the Aeronautical Sciences, September 13-18, Melbourne, Australia, pp. 13-20.
- Benhamza A, Boubekri A, Atia A, Hadibi T, Arıcı M. 2021. Drying uniformity analysis of an indirect solar dryer based on computational fluid dynamics and image processing. Sustain Energy Techn Asses, 47: 101466.
- Bulut S, Unveren M, Arisoy A, Boke Y. 2011. Reducing internal losses in air handling units with CFD analysis method. TMMOB X. National Plumbing Engineering Congress and Exhibition, İzmir, Türkiye, pp: 291-326.
- Chen YS, Kim SW. 1987. Computation of turbulent flows using an extended k-epsilon turbulence closure model. URL: <https://ntrs.nasa.gov/citations/19880002587> (accessed date: January 15, 2023).
- Erdoğan A, Taçgün E, Canbazoğlu S, Aksoy İ G, Kaya A, Sönmez K, Kamer M S, Şahin H E. 2016. A numerical investigation on pressure loss in a chamber with truncated pyramid perforated diffuser designed for air handling units. 8th International Ege Energy Symposium and Exhibition, May 11-13, Afyon, Türkiye, pp. 823-828.
- Erdoğan A. 2017. Investigation of airflow in empty chambers with perforated diffuser designed for air handling units in terms of flow and acoustic. PhD Thesis, İnönü University, Institute of Science, Malatya, Türkiye, pp: 115.
- Fluent A. 2009. 12.0 User's guide. Ansys inc, 6, 552.
- Gan G, Riffat SB. 1997. Pressure loss characteristics of orifice and perforated plates. Experim Thermal Fluid Sci, 14(2): 160-

- 165.
- Gaulke D, Dreyer ME. 2015. CFD simulation of capillary transport of liquid between parallel perforated plates using Flow3D. *Micrograv Sci Tech*, 27: 261-271.
- Gessner F, Jones J. 1965. On some aspects of fully-developed turbulent flow in rectangular channels. *J Fluid Mechan*, 23(4): 689-713.
- Guo B, Hou Q, Yu A, Li L, Guo J. 2013. Numerical modelling of the gas flow through perforated plates. *Chem Eng Res Design*, 91(3): 403-408.
- He Y, Liu XH, Zhang HL, Zheng W, Zhao FY, Schnabel MA, Mei Y. 2021. Hybrid framework for rapid evaluation of wind environment around buildings through parametric design, CFD simulation, image processing and machine learning. *Sustain Cities Soc*, 73: 103092.
- Hu HH. 2012. *Computational fluid dynamics*. Elsevier, New York, US, pp: 421-472.
- Hussain A, Reynolds W. 1975. Measurements in fully developed turbulent channel flow. *J Fluids Eng*, 1975: 568-578.
- Kamer M, Erdoğan A, Tacgun E, Sonmez K, Kaya A, Aksoy I, Canbazoglu S. 2018. A performance analysis on pressure loss and airflow diffusion in a chamber with perforated V-profile diffuser designed for air handling units (AHUs). *J Appl Fluid Mechan*, 11(4): 1089-1100.
- Li J, Agarwal RK, Zhou L, Yang B. 2019. Investigation of a bubbling fluidized bed methanation reactor by using CFD-DEM and approximate image processing method. *Chem Eng Sci*, 207: 1107-1120.
- Özahi E. 2015. An analysis on the pressure loss through perforated plates at moderate Reynolds numbers in turbulent flow regime. *Flow Measur Instrumentat*, 43: 6-13.
- Parsons RA. 1996. 1996 Ashrae Handbook Heating, Ventilating, and Air-Conditioning Systems and Equipment: Inch-Pound Edition. ASHARE, Atlanta, US, pp: 667.
- Sönmez K, Özmen Y. 2022. Numerical investigation of the effects of plate diffusers in central air handling units on flow field and pressure drop. *Eng Machin*, 63(707): 333-358.
- Sönmez K. 2017. A numerical investigation of the effect of diffusion flow and pressure reduction of perforated cutting cone profile diffuser designed for empty cells in air handling units. MSc Thesis, Kahramanmaraş Sütçü İmam University, Institute of Science, Kahramanmaraş, Türkiye, pp: 68.
- Tu J, Yeoh GH, Liu C, Tao Y. 2023. *Computational fluid dynamics: a practical approach*. Elsevier, Heinemann, Germany, pp: 477.
- Vakkasoglu AV, Kamer MS, Kaya A. 2021. The effect of different diffusers designed for empty cells in central air handling units on flow and pressure drop. *Sci Tech Built Environ*, 27(1): 28-43.
- Versteeg HK, Malalasekera W. 2007. *An introduction to computational fluid dynamics: the finite volume method*. Pearson Education.
- Wang P, Pan W, Dai G. 2020. A CFD-based design scheme for the perforated distributor with the control of radial flow. *AIChE J*, 66(5): e16901.
- Xu Z, Gotham D, Collins M, Coney J, Sheppard C, Merdjani S. 1996. CFD prediction of turbulent recirculating flow in an industrial packaged air-conditioning unit. *HVAC&R Res*, 2(3): 195-213.



MAXIMUM LIKELIHOOD ESTIMATION FOR THE LOG-LOGISTIC DISTRIBUTION USING WHALE OPTIMIZATION ALGORITHM WITH APPLICATIONS

Adi Omaia FAOURI¹, Pelin KASAP^{1*}


¹Ondokuz Mayıs University, Faculty of Science, Department of Statistics, 55139, Samsun, Türkiye


Abstract: The log-logistic distribution has been widely used in several fields, including engineering, survival analysis, and economics. The method of maximum likelihood estimation is used in this study for estimating the shape and scale parameters for the log-logistic distribution, whereas in the case of the log-logistic distribution, likelihood equations lack explicit solutions. Therefore, problems with solving likelihood equations can be solved by using two highly efficient algorithms, which are the whale optimization algorithm and the Nelder-Mead algorithm, as well as by showing the applicability of this distribution by comparing it with other well-known classical distributions. To demonstrate the performance of each algorithm implemented, an extensive Monte Carlo simulation study has been conducted. The performance of maximum likelihood estimators for each algorithm has been evaluated in terms of mean square error and deficiency criteria. It has been seen that the whale optimization algorithm provides the best estimates for the log-logistic distribution parameters according to the simulation data.

Keywords: Maximum likelihood, Log-logistic distribution, Whale optimization, Monte-Carlo simulation

*Corresponding author: Ondokuz Mayıs University, Faculty of Science, Department of Statistics, 55139, Samsun, Türkiye

E mail: pelin.kasap@omu.edu.tr (P. KASAP)

Adi Omaia FAOURI  <https://orcid.org/0000-0003-4499-1240>

Pelin KASAP  <https://orcid.org/0000-0002-1106-710X>

Received: September 06, 2023

Accepted: October 04, 2023

Published: October 15, 2023

Cite as: Faouri AO, Kasap P. 2023. Maximum likelihood estimation for the log-logistic distribution using whale optimization algorithm with applications. *BSJ Eng Sci*, 6(4): 639-647.

1. Introduction

In many different fields of research, including medicine, economics and survival analysis, the log-logistic distribution is widely used. The log-logistic distribution can be obtained by applying a logarithmic transform to the logistic distribution. Similar to how the log-normal and normal distributions have a relation to one another, the log-logistic distribution has a relation to the logistic distribution. The log-logistic distribution looks similar to the log-normal distribution in terms of shape but with heavier tails. Burr distribution was introduced by Burr (1942) and log-logistic distribution is considered a special case of the Burr distribution family in Tadikamalla (1980) study. The log-logistic distribution's properties and characteristics were studied for the first time in 1963 (Shah & Dave, 1963). Systems of frequency curves are produced by applying three simple transformations to the logistic distribution (Tadikamalla and Johnson, 1982). Both the studies of Ali and Khan (1987) as well as Balakrishnan and Malik (1987) examined the use of moments of ordered statistics for estimating the unknown parameters of the log-logistic distribution. The initial application was to model the distribution of income and wealth (Fisk, 1961), and this distribution was used for modeling stream flow rates too (Shoukri et al., 1988). Kantam and Srinivasa (2002) in their study regarded maximum likelihood estimators

(MLEs) of the scale parameter when its shape parameter already exists and derived the modified maximum likelihood estimation (MLE) of this distribution. A Bayesian approach is applied to estimate the parameters of the log-logistic distribution and compared with the MLEs of the Abbas and Tang (2016) study. Regarding the estimation of the parameters of any distribution, there are several statistical methods that can be used. The maximum likelihood (ML) estimation method is the most popular method due to its great efficiency and well-known asymptotic characteristics for parameter estimators when compared to all other statistical approaches (Yuan and Schuster, 2013). One of the most commonly used techniques for calculating the MLEs of the parameters is the Newton-Raphson algorithm which is a gradient-based search algorithm. The fundamental issue with this technique is the requirement for the second derivatives for all iterations (Kus and Kaya, 2006). In order to avoid such restrictions another kind of classical iterative technique can be employed, such as the Nelder-Mead (NM) algorithm, that doesn't require the gradient information of the fitness function. However, all classical algorithms start from a randomly selected initial point and continue moving to the solution iteratively until the optimum solution is obtained, but the solution may remain at the local optimum with a lack of guarantee that the final result is globally reached (Pratihari, 2012).



The application of non-classical algorithms, such as meta-heuristic algorithms, is more desirable for solving advanced problems, especially when conventional algorithms fail, to avoid such difficulties. In addition, meta-heuristic algorithms, which are more flexible, simple, and derivation-free, ensure global convergence (Sreenivas and Kumar 2015). Recently, several distributions' parameters have been estimated using meta-heuristic algorithms, including an efficient new one known as the whale optimization algorithm (WOA) that was used by Mohammed (2021), Mohammed and Elmasry (2023), Al-Mhairat and Al-Quraan (2022), and many others in the literature. This study's main objective is to demonstrate the log-logistic distribution's usability in various fields and to estimate its scale and shape parameters. The main concern raised by this study is that explicit solutions to the likelihood equations do not exist for the log-logistic distribution. This issue is resolved by using iterative numerical techniques based on the NM algorithm as a conventional technique and the WOA as a meta-heuristic algorithm representing a non-conventional technique. The main contribution of this work is a comprehensive Monte-Carlo simulation study to compare and analyze the two optimization techniques and to provide the estimator's values for the log-logistic distribution parameters based on the WOA and NM algorithms. The remaining sections of this work will be arranged as follows: The log-logistic distribution and its basic properties are addressed in Section 2. The ML estimation method for both NM and WOA is discussed in Section (3). In Section (4), an extensive Monte-Carlo simulation study is performed to compare the performance of the parameter estimators. In Section (5), two real-world dataset applications are implemented. The study presents several conclusions in Section (6).

2. Log-logistic Distribution

If we have two random variables, X and Y , whose relationship is represented by Equation 1:

$$Y = \beta \ln\left(\frac{X}{\alpha}\right), \quad \beta > 0, \quad \alpha > 0, \quad (1)$$

where β is the shape parameter and α is the scale parameter, and Y is distributed logistically with the following (Equation 2) probability density function (pdf),

$$g(y) = \frac{e^y}{(1 + e^y)^2}, \quad y \in R. \quad (2)$$

Then X follows a two parameter log-logistic distribution, $X \sim \text{log-logistic}(\alpha, \beta)$, with the following (Equation 3) probability density function (pdf),

$$f(x; \alpha, \beta) = \frac{\left(\frac{\beta}{\alpha}\right) \left(\frac{x}{\alpha}\right)^{\beta-1}}{\left[1 + \left(\frac{x}{\alpha}\right)^\beta\right]^2}, \quad (3)$$

$x > 0, \beta > 0, \alpha > 0.$

X 's cumulative distribution function (Equation 4) (cdf) is:

$$F(x; \alpha, \beta) = \frac{1}{1 + \left(\frac{x}{\alpha}\right)^{-\beta}} \quad (4)$$

The plots of the log-logistic distribution for different values of β with fixed value of $\alpha = 2$ are shown in Figure 1. The log-logistic distribution's k^{th} moment exists only when k is less than β , and its general equation is given in Equation 5:

$$E(X^k) = \alpha^k B\left(1 - \frac{k}{\beta}, 1 + \frac{k}{\beta}\right) = \frac{\alpha^k \left(\frac{k\pi}{\beta}\right)}{\sin\left(\frac{k\pi}{\beta}\right)} \quad (5)$$

where B is the beta function. By using equation 5, The mean and variance of the random variable X can be calculated as follows (Equation 6-7):

$$E(X) = \frac{\alpha\pi}{\beta \sin\left(\frac{\pi}{\beta}\right)}, \quad \beta > 1 \quad (6)$$

$$Var(X) = \alpha^2 \left(\frac{2\left(\frac{\pi}{\beta}\right)}{\sin\left(\frac{2\pi}{\beta}\right)} - \frac{\left(\frac{\pi}{\beta}\right)^2}{\sin^2\left(\frac{\pi}{\beta}\right)} \right), \quad \beta > 2 \quad (7)$$

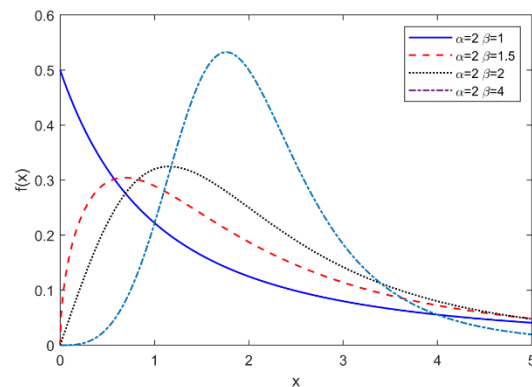


Figure 1. Log-logistic pdf for different parameter values for different values of β with fixed value of $\alpha = 2$

3. Maximum Likelihood Estimation

This method relies on identifying the values that maximize the likelihood function to its maximum; often, the logarithm of the likelihood function is used in order to simplify the calculations. The log-likelihood ($\log L$) function is provided in Equation 8 to estimate the unknown parameters for the log-logistic distribution in this study.

$$\log L(\alpha, \beta) = n \log(\beta) - n\beta \log(\alpha) + (\beta - 1) \sum_{i=1}^n \log(x_i) - 2 \sum_{i=1}^n \log\left[1 + \left(\frac{x_i}{\alpha}\right)^\beta\right] \quad (8)$$

The partial derivatives corresponding to the considered parameters are obtained and set to zero to estimate the likelihood parameters of the $\log L$ function for the log-logistic distribution. The likelihood equations are given as in Equation 9 and 10:

$$\frac{\partial \log L(\alpha, \beta)}{\partial \alpha} = \frac{n\beta}{\alpha} + \frac{2\beta}{\alpha} \sum_{i=1}^n \left(\frac{x_i}{\alpha}\right)^\beta + \left[1 + \left(\frac{x_i}{\alpha}\right)^\beta\right]^{-1} = 0 \quad (9)$$

and

$$\frac{\partial \ln L(\alpha, \beta)}{\partial \beta} = \frac{n}{\beta} - n \log(\alpha) + \sum_{i=1}^n \log(x_i) - 2 \sum_{i=1}^n \left(\frac{x_i}{\alpha}\right)^\beta \log\left(\frac{x_i}{\alpha}\right) + \left(\frac{x_i}{\alpha}\right)^\beta = 0 \quad (10)$$

Since the likelihood equations include nonlinear functions, as shown by equations (9) and (10), it is unlikely to find explicit solutions to them. Therefore, to solve these equations and obtain ML estimates for α and β , iterative numerical techniques are required. WOA and NM are two highly efficient algorithms that are used in this study as numerical techniques for estimating the likelihood estimators for the log-logistic distribution, and they are briefly introduced in the next few subsections.

3.1. Whale Optimization Algorithm (WOA)

The WOA is a new intelligent meta-heuristic algorithm that was developed by Mirjalili and Lewis (2016), in their study. It is modeled after the imitation of the humpback whale's bubble-net hunting technique, which involves creating a circle of bubbles around the prey and narrowing it or approaching the target in a spiral pattern while performing a random search, as discussed in Rana et al. (2020) as well as Hu et al. (2016) studies. Encircling the prey, the bubble-net attack mechanism, and the search for prey are the main three phases of this algorithm, and each phase is mathematically modeled (Yan et al., 2018). The population of humpback whales starts their search through a multi-dimensional search space, and their initial positions at the first iteration are represent the initial solutions in WOA. For mathematical modeling, there are many significant parameters should be known first, such as the following:

- Parameter (a), which is an essential parameter, declines linearly for each iteration from 2 to 0. The Equation 11 to obtain this parameter is:

$$a = 2 * \left(1 - \frac{t}{T_{max}}\right) \quad (11)$$

where t , is the current iteration and T_{max} is the total number of iterations.

- A and C coefficient vectors, whose equations 12 and 13 are:

$$A = 2a * r_1 - a \quad (12)$$

$$C = 2 * r_2 \quad (13)$$

where r_1 and r_2 are random vectors ranging in the closed interval [0,1].

- Parameter (b), which is a constant that determines how the logarithmic spiral is shaped, Parameter (l) is

a number chosen at random from the range [-1, 1], and parameter, p is a chance probability that can be any value between 0 and 1, to give an equal chance of encircling or spiraling movements of whales.

The fitness value for the main study's model, represented by the $\log L$ function (8), is used to evaluate each whale position, and the best position is then determined and stored. When $P < 0.5$ and $|A| < 1$, the currently in progress whale's position is updated using the following Equations 14 and 15:

$$D = |C \cdot X_p(t) - X(t)| \quad (14)$$

$$X(t+1) = X_p(t) - A * D \quad (15)$$

where the current vector's position at iteration t is represented by $X(t)$, and when iterating to the t^{th} time, the best solution's position vector is $X_p(t)$.

However, in case $|A| > 1$, one of the whales is picked at random, and the position is updated by applying the Equations 16 and 17 follow as:

$$D = |C \cdot X_{rand}(t) - X(t)| \quad (16)$$

$$X(t+1) = X_{rand}(t) - A * D \quad (17)$$

where X_{rand} is the position vector of any whale picked at random from the current whale population. On the other hand, the following Equations 18 and 19 update the position of the current whale when $P > 0.5$:

$$D' = |X_p(t) - X(t)| \quad (18)$$

$$X(t+1) = D' e^{bl} \cos(2\pi l) + X_p(t) \quad (19)$$

where D' indicates the distance between both the i^{th} whale and the available current best whale position (prey). Every iteration of WOA involves checking the updated whale's position to make sure it remains within the boundaries of the search space. The final solution positions indicate the values of WOA estimators, and this process continues until it reaches the final iteration needed to achieve convergence. Figure 2 shows the WOA's flowchart.

3.2. Nelder-Mead (NM)

The NM algorithm is a widely used deterministic search technique for locating optimal approximations of a fitness function in a space of multiple dimensions. It had been founded by the study of John Nelder and Roger Mead (1965). The NM algorithm depends on creating a geometric simplex figure with $n + 1$ vertex for n -dimensional problems. In this study, the function that needs to be minimized is $f(\theta) = -\log L(\theta)$, where $\theta = (\alpha, \beta) \in R \times R^+$. At each vertex, the fitness value $f(\theta)$ is calculated and put in ascending order as $\theta_1, \theta_2, \theta_3$, and then a mechanism for generating a new simplex by replacing the vertex that has the highest fitness value is done by applying four main operators. These operators are:

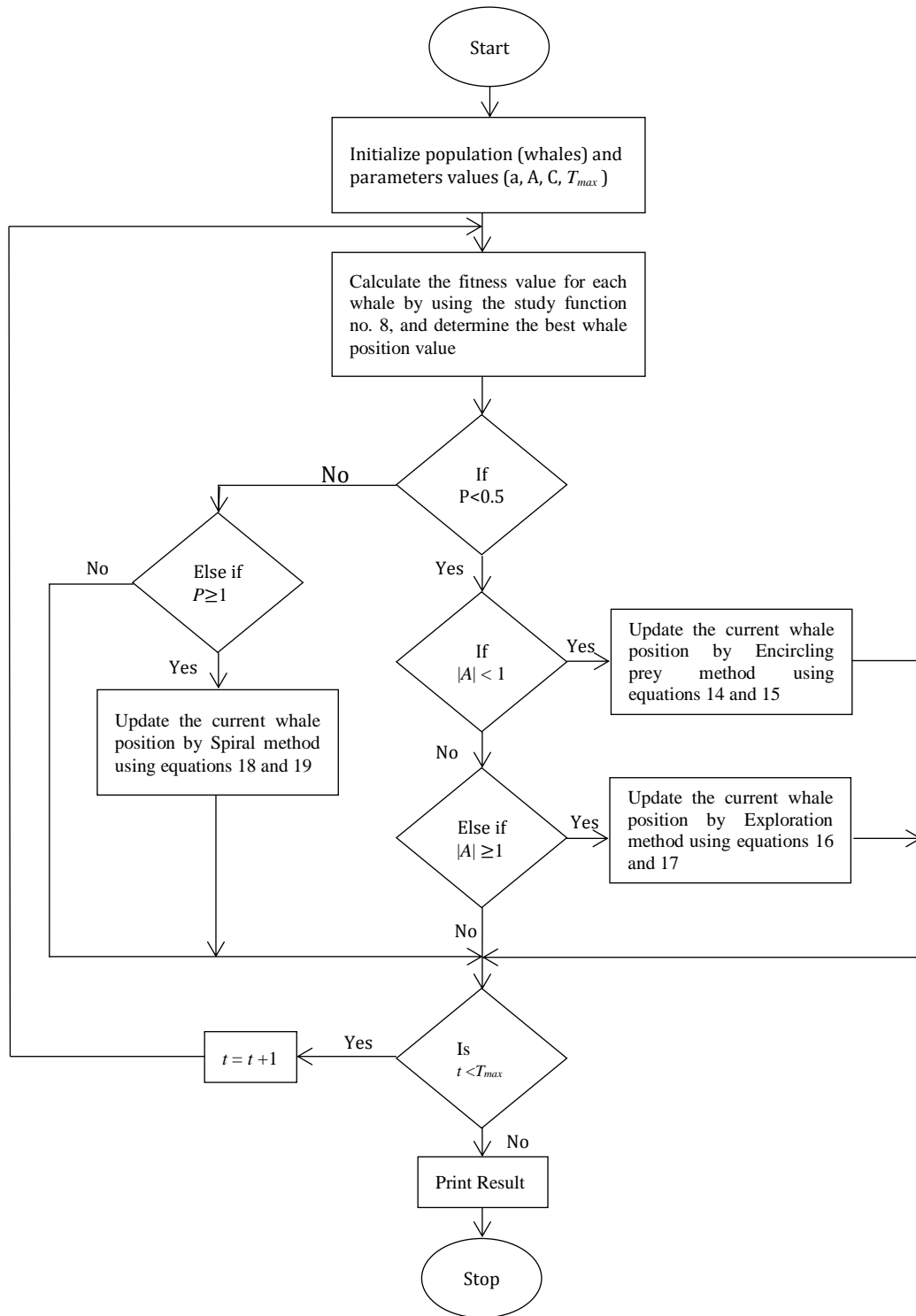


Figure 2. WOA flowchart.

- Reflection, for generating reflection points θ_r , which is defined as $\theta_r = \theta_0 + \alpha (\theta_0 - \theta_3)$, where θ_0 is the centroid, and α is the reflection coefficient. When $f(\theta_1) \leq f(\theta_r) \leq f(\theta_2)$ then θ_3 is replaced with θ_r .
- Expansion, for generating the expansion point θ_e and its related equation $\theta_e = \theta_0 + \gamma (\theta_r - \theta_0)$, where γ is the expansion coefficient. The use of expansion points happens when $f(\theta_r) < f(\theta_1)$ then θ_3 is replaced with θ_e if not, θ_0 is replaced with θ_r .
- Contraction, for generating the contraction point θ_c , which is defined as $\theta_c = \theta_0 + \rho (\theta_3 - \theta_0)$, where ρ is the contraction coefficient. The use of expansion

points happens when $f(\theta_2) \leq f(\theta_r)$, and if $f(\theta_c) < f(\theta_3)$ then a new simplex is generated with θ_3 is replaced with θ_c but if $f(\theta_c) > f(\theta_3)$ then the initial points will be shrunk by applying this equation $\theta_i = \theta_i + \beta (\theta_i - \theta_1)$ to all $i \in \{2,3\}$

This process is continuing until the convergence requirements are satisfied. According to many studies in the literature α , γ , ρ , and β are taken 1, 2, $\frac{1}{2}$ and $\frac{1}{2}$, respectively. The studies by Everitt (1984), Shamir (1987), Gao & Han (2012), and Kucukdeniz & Esnaf (2018) in the literature provide more information.

4. Monte-Carlo Simulations Study

In order to evaluate the efficiency of the ML estimator values for the model parameters using the WOA algorithm with the corresponding ML estimators using the NM algorithm, the numerical results from the Monte Carlo simulation study for various sample sizes are presented in this section of the paper. Matlab R2021a software is used to perform the computations for the simulation study. Every Monte Carlo simulation run is repeated 2,000 times. The scale parameter α remains constant at 1.0, but the shape parameter β is taken to be 1, 1.5, and 2, for a variety of sample sizes n that are assumed to be 10, 20, 30, 50, 100, 250, and 500. The range [0, 20] is chosen as the search space (SS) for the parameters, and as a result, $7 \times 4 \times 2000 = 56000$ unique samples are produced. The simulations' final results for the shape and scale parameters are indicated by the symbols $\hat{\alpha}$ and $\hat{\beta}$, respectively. The simulated mean, bias, variance, mean square error (MSE), and deficiency (Def) values provided by the equations 20-24 below are used in order to compare and evaluate the performance of the estimators (Equation 20-24).

$$Mean(\hat{\theta}) = \frac{\sum_{i=1}^n \hat{\theta}_i}{n} \tag{20}$$

$$Bias(\hat{\theta}) = E(\hat{\theta}) - \theta \tag{21}$$

$$Var(\hat{\theta}) = \frac{1}{n-1} \sum_{i=1}^n (\hat{\theta}_i - Mean \hat{\theta})^2 \tag{22}$$

$$MSE(\hat{\theta}) = Var(\hat{\theta}) + (Bias(\hat{\theta}))^2 \tag{23}$$

$$Def(\hat{\alpha}, \hat{\beta}) = MSE(\hat{\alpha}) + MSE(\hat{\beta}) \tag{24}$$

where, $\theta = (\alpha, \beta) \in R \times R^+$. The resulting simulated values of mean, bias, MSE, and Def for $\hat{\alpha}$ and $\hat{\beta}$ are given in Tables 1-3. In contrast to the NM algorithm, the simulated values demonstrate that the WOA produces the best performance. The values of the shape estimator $\hat{\beta}$ when $\alpha = 1$ and $\beta = 1$, have the least bias values for the NM technique, in accordance with the simulated results, with the exception of when the sample size is large ($n = 500$), in which case the WOA produces the least biased results as shown in Tables 1. However, tables 2 and 3 show that in all other remaining cases, the WOA produces the least biased results for $\hat{\alpha}$ and $\hat{\beta}$. In terms of MSE values, Tables 1-3 demonstrate that when $\alpha = 1$ and $\beta = 1$, simulated MSE values for $\hat{\beta}$ that belong to the NM algorithm are better than the WOA for all n values; otherwise, MSE values for the WOA outperform the NM algorithm in all other cases for $\hat{\alpha}$ and $\hat{\beta}$ estimators. The WOA shows excellence performance according to the Def criteria with the smallest values in contrast to the NM algorithm for all cases. All of this allows us to say that the WOA is an efficient algorithm for estimating the shape $\hat{\beta}$ and scale $\hat{\alpha}$ parameters for log-logistic distributions, and as a result of the NM algorithm's deficiency criterion values, it is inefficient for this distribution.

Table 1. Simulated mean, bias, variance, MSE, and Def values for the ML estimators $\hat{\alpha}$ and $\hat{\beta}$.

| n | Method | $\hat{\beta}$ | | | $\hat{\alpha}$ | | | Def |
|-------------------------|--------|---------------|--------|--------|----------------|--------|--------|--------|
| | | Mean | Bias | MSE | Mean | Bias | MSE | |
| $\alpha = 1, \beta = 1$ | | | | | | | | |
| 10 | WOA | 1.2775 | 0.1537 | 0.2307 | 0.9861 | 0.2690 | 0.2692 | 0.4999 |
| | NM | 1.2285 | 0.1301 | 0.1823 | 0.5500 | 0.9439 | 1.1464 | 1.3288 |
| 20 | WOA | 1.1874 | 0.0517 | 0.0868 | 0.9256 | 0.1133 | 0.1188 | 0.2056 |
| | NM | 1.1473 | 0.0386 | 0.0603 | 0.3715 | 0.7593 | 1.1542 | 1.2145 |
| 30 | WOA | 1.1575 | 0.0303 | 0.0551 | 0.8987 | 0.0728 | 0.0830 | 0.1382 |
| | NM | 1.1241 | 0.0214 | 0.0368 | 0.2971 | 0.7316 | 1.2257 | 1.2625 |
| 50 | WOA | 1.1474 | 0.0166 | 0.0384 | 0.8977 | 0.0401 | 0.0506 | 0.0889 |
| | NM | 1.1187 | 0.0134 | 0.0275 | 0.2272 | 0.7250 | 1.3222 | 1.3497 |
| 100 | WOA | 1.1315 | 0.0079 | 0.0252 | 0.8861 | 0.0197 | 0.0326 | 0.0578 |
| | NM | 1.1081 | 0.0068 | 0.0185 | 0.1800 | 0.6466 | 1.3190 | 1.3375 |
| 250 | WOA | 1.1474 | 0.0166 | 0.0384 | 0.8977 | 0.0401 | 0.0506 | 0.0889 |
| | NM | 1.1187 | 0.0134 | 0.0275 | 0.2272 | 0.7250 | 1.3222 | 1.3497 |
| 500 | WOA | 1.1141 | 0.0015 | 0.0145 | 0.8805 | 0.0041 | 0.0184 | 0.0329 |
| | NM | 1.0908 | 0.0029 | 0.0111 | 0.0207 | 0.6256 | 1.5846 | 1.5957 |

Table 2. Simulated mean, bias, variance, MSE, and Def values for the ML estimators $\hat{\alpha}$ and $\hat{\beta}$.

| n | Method | $\hat{\beta}$ | | | $\hat{\alpha}$ | | | Def |
|---------------------------|--------|---------------|--------|--------|----------------|--------|--------|--------|
| | | Mean | Bias | MSE | Mean | Bias | MSE | |
| $\alpha = 1, \beta = 1.5$ | | | | | | | | |
| 10 | WOA | 1.8014 | 0.3007 | 0.3915 | 1.0390 | 0.1628 | 0.1643 | 0.5558 |
| | NM | 1.6377 | 0.3465 | 0.3654 | 0.5746 | 0.7754 | 0.9564 | 1.3218 |
| 20 | WOA | 1.6600 | 0.1016 | 0.1272 | 1.0042 | 0.0666 | 0.0666 | 0.1938 |
| | NM | 1.4703 | 0.1383 | 0.1392 | 0.3761 | 0.7409 | 1.1302 | 1.2694 |
| 30 | WOA | 1.6122 | 0.0592 | 0.0718 | 0.9968 | 0.0427 | 0.0427 | 0.1145 |
| | NM | 1.4140 | 0.0927 | 0.1001 | 0.2665 | 0.7246 | 1.2627 | 1.3627 |
| 50 | WOA | 1.5932 | 0.0342 | 0.0429 | 0.9899 | 0.0264 | 0.0265 | 0.0694 |
| | NM | 1.3913 | 0.0691 | 0.0809 | 0.2288 | 0.6914 | 1.2861 | 1.3670 |
| 100 | WOA | 1.5695 | 0.0160 | 0.0209 | 0.9824 | 0.0122 | 0.0125 | 0.0333 |
| | NM | 1.3706 | 0.0494 | 0.0661 | 0.2015 | 0.6473 | 1.2850 | 1.3511 |
| 250 | WOA | 1.5629 | 0.0060 | 0.0100 | 0.9805 | 0.0051 | 0.0054 | 0.0154 |
| | NM | 1.3688 | 0.0424 | 0.0597 | 0.1837 | 0.6156 | 1.2820 | 1.3416 |
| 500 | WOA | 1.5564 | 0.0031 | 0.0063 | 0.9813 | 0.0024 | 0.0028 | 0.0091 |
| | NM | 1.3386 | 0.0378 | 0.0638 | 0.0752 | 0.5913 | 1.4466 | 1.5104 |

Table 3. Simulated Mean, Bias, Variance, MSE, and Def values for the ML estimators $\hat{\alpha}$ and $\hat{\beta}$.

| n | Method | $\hat{\beta}$ | | | $\hat{\alpha}$ | | | Def |
|-------------------------|--------|---------------|--------|--------|----------------|--------|--------|--------|
| | | Mean | Bias | MSE | Mean | Bias | MSE | |
| $\alpha = 1, \beta = 2$ | | | | | | | | |
| 10 | WOA | 2.3451 | 0.5763 | 0.6954 | 1.0284 | 0.0831 | 0.0840 | 0.7793 |
| | NM | 2.0404 | 0.7601 | 0.7617 | 0.5743 | 0.6409 | 0.8221 | 1.5838 |
| 20 | WOA | 2.1536 | 0.1758 | 0.1993 | 1.0196 | 0.0396 | 0.0400 | 0.2394 |
| | NM | 1.8372 | 0.3546 | 0.3811 | 0.4727 | 0.6469 | 0.9250 | 1.3061 |
| 30 | WOA | 2.1083 | 0.1100 | 0.1217 | 1.0072 | 0.0265 | 0.0265 | 0.1483 |
| | NM | 1.7689 | 0.2832 | 0.3366 | 0.4049 | 0.6334 | 0.9876 | 1.3242 |
| 50 | WOA | 2.0673 | 0.0612 | 0.0657 | 0.9984 | 0.0150 | 0.0150 | 0.0807 |
| | NM | 1.6866 | 0.2318 | 0.3300 | 0.3023 | 0.6292 | 1.1160 | 1.4460 |
| 100 | WOA | 2.0483 | 0.0300 | 0.0323 | 0.9986 | 0.0076 | 0.0076 | 0.0398 |
| | NM | 1.6543 | 0.1981 | 0.3176 | 0.2666 | 0.6149 | 1.1528 | 1.4703 |
| 250 | WOA | 2.0356 | 0.0107 | 0.0120 | 0.9976 | 0.0030 | 0.0030 | 0.0150 |
| | NM | 1.6459 | 0.1718 | 0.2972 | 0.2711 | 0.5909 | 1.1223 | 1.4195 |
| 500 | WOA | 2.0245 | 0.0054 | 0.0060 | 0.9985 | 0.0014 | 0.0014 | 0.0074 |
| | NM | 1.6363 | 0.1636 | 0.2958 | 0.2589 | 0.5837 | 1.1329 | 1.4288 |

5. Applications

For the sake of illustration of the practical applicability of this model, two real datasets with various sample sizes are modeled using the log-logistic distribution in this section. Well-known criteria concerning log-likelihood values, the Akaike Information Criterion (AIC), and the corrected AIC (AICc) are used for comparing the modeling performance of the log-logistic distribution with the performance of several other different distributions, which include Gamma, Weibull, Lognormal, Nakagami, Inverse Gaussian, logistic, Normal, Rayleigh, and Extreme Value distributions. Anderson et al. (1998) provided in their study more information on these criteria and how they are utilized in practice. Mathematically, these criteria are represented in Equation 25 and 26:

$$AIC = 2P - 2 \log L \tag{25}$$

$$AIC_c = AIC + \frac{2P(P + 1)}{n - P - 1} \tag{26}$$

where the likelihood function, the number of observations, and the total number of model parameters are represented by $\log L$, n , and p , respectively. When the probability model has the aforementioned criteria with lower values than other probability distributions, it is said to be the best-fit model.

5.1. Dataset

5.1.1. Remission time of bladders cancer patients

To demonstrate the implementation of the log-logistic distribution, the remission time of bladder cancer patients' dataset is used. Its 128 observations were originally analyzed by Lee and Wang in their study (2003) and used by other studies such as the study of Lemonte and Cordeiro (2011), the studies of Aldeni et al. (2017) as well as Ijaz et al. (2020) and Zea et al. (2012). The values of this dataset are as follows: 0.080, 0.200,

0.400, 0.500, 0.510, 0.810, 0.900, 1.050, 1.190,1.260,1.350, 1.400, 1.460, 1.760, 2.020, 2.020,2.070, 2.090, 2.230, 2.260, 2.460, 2.540, 2.620, 2.640, 2.690, 2.690, 2.750, 2.830, 2.870, 3.020,3.250, 3.310,3.360, 3.360, 3.480, 3.520, 3.570, 3.640, 3.700, 3.820,3.880, 4.180, 4.230, 4.260, 4.330, 4.340, 4.400, 4.500, 4.510, 4.870, 4.980, 5.060, 5.090, 5.170, 5.320, 5.320, 5.340, 5.410, 5.410, 5.490,5.620, 5.710, 5.850, 6.250, 6.540, 6.760, 6.930, 6.940, 6.970, 7.090, 7.260, 7.280, 7.320, 7.390, 7.590, 7.620, 7.630, 7.660, 7.870, 7.930,8.260, 8.370, 8.530, 8.650, 8.660, 9.020, 9.220, 9.470, 9.740, 10.06, 10.34, 10.66, 10.75, 11.25, 11.64, 11.79, 11.98, 12.02, 12.03, 12.07, 12.63, 13.11, 13.29, 13.80, 14.24, 14.76, 14.77, 14.83, 15.96, 16.62, 17.12, 17.14, 17.36, 18.10, 19.13, 20.28, 21.73, 22.69, 23.63, 25.74, 25.82, 26.31, 32.15, 34.26, 36.66, 43.01, 46.12, 79.05. Table 4 provides descriptive statistics, including sample size (n), minimum (min), mean, mode, median, maximum (max), variance (S²), skewness (γ₁), and kurtosis (γ₂).

Table 5 compares the modeling performance of the log-logistic distribution to that of other well-known distributions using the *log L*, *AIC*, and *AICc* criteria. The findings in Table 5 demonstrate that, in terms of the criteria taken into consideration, the log-logistic distribution's performance provides a better fit than other distributions.

5.2.2. A relief times (in minutes) of 20 patients receiving an analgesic

A relief time dataset of 20 patients receiving an analgesic was provided by Gross and Clark in their study (1975) and used in other statistical literature such as the studies of Shanker et al. (2016), Shukla (2019), and Marthin and Rao (2020). The dataset values are given as: 1.1, 1.4, 1.3, 1.7, 1.9, 1.8, 1.6, 2.2, 1.7, 2.7, 4.1, 1.8, 1.5, 1.2, 1.4, 3, 1.7, 2.3, 1.6, 2. The descriptive statistics for this dataset are displayed in Table 6 and Table 7 shows the results obtained after fitting this data to the log-logistic distribution model and comparing them to other distributions according to the chosen criteria.

Table 4. The descriptive statistics for the remission time of bladders cancer patient's data.

| n | Min | Mean | Mode | Median | Max | S ² | γ ₁ | γ ₂ |
|-----|------|--------|------|--------|-------|----------------|----------------|----------------|
| 128 | 0.08 | 9.3656 | 2.02 | 6.3950 | 79.05 | 1.1042 | 3.2866 | 18.4831 |

Table 5. Parameter estimates, *log L*, *AIC* and *AICc*, values for bladders cancer patient's data.

| | $\hat{\mu}$ | $\hat{\alpha}$ | $\hat{\beta}$ | <i>log L</i> | <i>AIC</i> | <i>AICc</i> |
|--------------|-------------|----------------|---------------|--------------|------------|-------------|
| Log-logistic | - | 6.0887 | 1.7254 | 411.4575 | 826.9150 | 827.011 |
| Gamma | - | 7.9877 | 1.1725 | 413.3680 | 830.7360 | 830.832 |
| Weibull | - | 9.5607 | 1.0478 | 414.0870 | 832.1740 | 832.27 |
| Lognormal | 1.7535 | 1.0773 | - | 415.0960 | 834.1920 | 834.288 |
| Nakagami | - | 197.2770 | 0.37420 | 426.6020 | 857.2040 | 857.3 |
| I-G | - | 9.3656 | 3.3820 | 440.3050 | 884.6100 | 884.706 |
| logistic | 7.5857 | 4.4825 | - | 456.6650 | 917.3300 | 917.426 |
| Normal | 9.3656 | 10.5083 | - | 486.2020 | 976.4040 | 976.5 |
| Rayleigh | - | 9.9317 | - | 491.2660 | 986.5320 | 986.628 |
| E-V | 15.8369 | 19.1518 | - | 549.1570 | 1102.3140 | 1102.41 |

I-G= inverse gaussian t, E-V = extreme value.

Table 6. The descriptive statistics for the relief times of 20 patients receiving an analgesic data.

| n | Min | Mean | Mode | Median | Max | S ² | γ ₁ | γ ₂ |
|----|-----|------|------|--------|-----|----------------|----------------|----------------|
| 20 | 1.1 | 1.9 | 1.7 | 1.7 | 4.1 | 0.4958 | 1.7197 | 5.9241 |

Table 7. Parameter estimates, *log L*, *AIC* and *AICc*, values for bladders cancer patient's data.

| | $\hat{\mu}$ | $\hat{\alpha}$ | $\hat{\beta}$ | <i>-ln L</i> | <i>AIC</i> | <i>AICc</i> |
|--------------|-------------|----------------|---------------|--------------|------------|-------------|
| Log-logistic | - | 1.7525 | 5.8895 | 16.4766 | 36.9532 | 37.65908 |
| I-G | - | 1.9000 | 18.6978 | 16.7723 | 37.5446 | 38.25048 |
| Lognormal | 0.5893 | 0.3185 | - | 16.7806 | 37.5612 | 38.26708 |
| Gamma | - | 0.1965 | 9.6695 | 17.8186 | 39.6372 | 40.34308 |
| Nakagami | - | 4.0810 | 2.3478 | 19.1701 | 42.3402 | 43.04608 |
| logistic | 1.7905 | 0.3390 | - | 19.2433 | 42.4866 | 43.19248 |
| Weibull | - | 2.1300 | 2.7870 | 20.5864 | 45.1728 | 45.87868 |
| Normal | 1.9000 | 0.7041 | - | 20.8627 | 45.7254 | 46.43128 |
| Rayleigh | - | 1.4285 | - | 22.4788 | 48.9576 | 49.66348 |
| E-V | 2.2913 | 0.9163 | - | 26.7927 | 57.5854 | 58.29128 |

I-G= inverse gaussian t, E-V = extreme value.

The findings demonstrate that, in terms of modeling performance, the log-logistic distribution is better than all other distributions.

6. Conclusion

In this study, estimation of the shape and scale parameters of the log-logistic distribution is considered. The ML estimates of the log-logistic distribution parameters via two iterative algorithms which are NM and WOA are obtained and then their performances compared to each other with respect to bias, MSE and Def criteria by conducting a Monte Carlo simulation study. Simulation results show that the WOA is more efficient than NM iterative algorithm in terms of these criteria in all cases. Two real datasets are employed to fit the log-logistic distribution, and the results demonstrate high performance for the log-logistic distribution in comparison with many well-known statistical distributions.

Author Contributions

The percentage of the author(s) contributions is presented below. All authors reviewed and approved the final version of the manuscript.

| | A.O.F. | P.K. |
|-----|--------|------|
| C | 50 | 50 |
| D | 50 | 50 |
| S | 50 | 50 |
| DCP | 50 | 50 |
| DAI | 50 | 50 |
| L | 50 | 50 |
| W | 50 | 50 |
| CR | 50 | 50 |
| SR | 50 | 50 |
| PM | 50 | 50 |
| FA | 50 | 50 |

C=Concept, D= design, S= supervision, DCP= data collection and/or processing, DAI= data analysis and/or interpretation, L= literature search, W= writing, CR= critical review, SR= submission and revision, PM= project management, FA= funding acquisition.

Conflict of Interest

The authors declared that there is no conflict of interest.

Ethical Consideration

Ethics committee approval was not required for this study because of there was no study on animals or humans.

References

Abbas K, Tang Y. 2016. Objective Bayesian analysis for log-logistic distribution. *Commun Stat-Simul Comput*, 45(8): 2782-2791. DOI: 10.1080/03610918.2014.925925.

Aldeni M, Lee C, Famoye F. 2017. Families of distributions arising from the quantile of generalized lambda distribution. *J Stat Distribut Appl*, 4: 1-18. DOI: 10.1186/s40488-017-0081-4.

Ali M, Khan A. 1987. On order statistics from the log-logistic distribution. *J Stat Plan Infer*, 17: 103-108. DOI: 10.1016/0378-3758(87)90104-2.

Al-Mhairat B, Al-Quraan A. 2022. Assessment of wind energy resources in Jordan using different optimization techniques. *Processes*, 10(1): 105. DOI: 10.3390/pr10010105.

Anderson D, Burnham K, White G. 1998. Comparison of Akaike information criterion and consistent Akaike information criterion for model selection and statistical inference from capture-recapture studies. *J Appl Stat*, 25(2): 263-282. DOI: 10.1080/02664769823250.

Balakrishnan N, Malik H. 1987. Moments of order statistics from truncated log-logistic distribution. *J Stat Plann Infer*, 17: 251-267. DOI: 10.1016/0378-3758(87)90117-0.

Burr I. 1942. Cumulative frequency functions. *Annals Math Stat*, 13(2): 215-232. DOI: 10.1214/aoms/1177731607.

Everitt B. 1984. Maximum likelihood estimation of the parameters in a mixture of two univariate normal distributions; a comparison of different algorithms. *J Royal Stat Soc Series D: The Statistician*, 33(2): 205-215. DOI: 10.2307/2987851.

Fisk P. 1961. The graduation of income distributions. *Econometrica*, 1961: 171-185. DOI: 10.2307/1909287.

Gao F, Han L. 2012. Implementing the Nelder-Mead simplex algorithm with adaptive parameters. *Comput Optimiz Appl*, 51(1): 259-277. DOI: 10.1007/s10589-010-9329-3.

Gross A, Clark V. 1975. *Survival distributions: Reliability applications in the biometrical sciences*. John Wiley, New York, US.

Hu H, Bai Y, Xu T. 2016. A whale optimization algorithm with inertia weight. *WSEAS Trans Comput*, 15: 319-326.

Ijaz M, Asim S, Alamgir, Farooq M, Khan S, Manzoor S. 2020. A Gull Alpha Power Weibull distribution with applications to real and simulated data. *Plos One*, 15(6): e0233080. DOI: 10.1371/journal.pone.0233080.

Kantam R, Srinivasa R. 2002. Log-logistic distribution: modified maximum likelihood estimation. *Gujarat Stat Rev*, 29(1): 25-36.

Kucukdeniz T, Esnaf S. 2018. Hybrid revised weighted fuzzy c-means clustering with Nelder-Mead simplex algorithm for generalized multisource Weber problem. *J Enterp Info Manag*, 31(6): 908-924. DOI: 10.1108/JEIM-01-2018-0002.

Kus C, Kaya M. 2006. Estimation of parameters of the loglogistic distribution based on progressive censoring using the EM algorithm. *Hacetatepe J Math Stat*, 35(2): 203-211.

Lee E, Wang J. 2003. *Statistical methods for survival data analysis*, John Wiley & Sons, New York, US, pp: 476.

Lemonte A, Cordeiro G. 2011. An extended Lomax distribution. *Statistics*, 47(4): 800-816. DOI: 10.1080/02331888.2011.568119.

Marthin P, Rao G. 2020. Generalized Weibull-Lindley (GWL) distribution in modeling lifetime data. *J Math*, 2020: 2049501. DOI: 10.1155/2020/2049501.

Mirjalili S, Lewis A. 2016. The whale optimization algorithm. *Adv Eng Software*, 95: 51-67. DOI: 10.1016/j.advengsoft.2016.01.008.

Mohammed W, Elmasry W. 2023. A comparative assessment of five different distributions based on five different optimization methods for modeling wind speed distribution. *Gazi Univ J Sci*, 2023: 1-1. DOI: 10.35378/gujs.1026834.

Mohammed W. 2021. Five different distributions and metaheuristics to model wind speed distribution. *J Thermal Eng*, 7(14): 1898-1920. DOI: 10.14744/jten.2021.xxxx.

Nelder J, Mead R. 1965. A simplex method for function minimization. *Comput J*, 7(4): 308-313. DOI:

- 10.1093/comjnl/7.4.308.
- Pratihari D. 2012. Traditional vs non-traditional optimization tools. In: Basu K (ed) Computational Optimization and Applications, Narosa Publishing House Pvt. Ltd, New Delhi, India, pp: 25-33.
- Rana N, Latiff M, Abdulhamid S, Chiroma H. 2020. Whale optimization algorithm: a systematic review of contemporary applications, modifications and developments. *Neural Comput Appl*, 32(20): 16245-16277. DOI: 10.1007/s00521-020-04849-z.
- Shah B, Dave P. 1963. A note on log-logistic distribution. *J MS Univ Baroda*, 12: 15-20.
- Shamir R. 1987. The efficiency of the simplex method: a survey. *Manag Sci*, 33(3): 301-334. DOI: 10.1287/mnsc.33.3.301.
- Shanker R, Shukla K, Shanker R, Leonida T. 2016. On modeling of lifetime data using two-parameter Gamma and Weibull distributions. *Biomet Biostat Int J*, 4(5): 201-206. DOI: 10.15406/bbij.2016.04.00107.
- Shoukri M, Mian I, Tracy D. 1988. Sampling properties of estimators of the log-logistic distribution with application to Canadian precipitation data. *Canadian J Stat*, 16(3): 223-236. DOI: 10.2307/3314729.
- Shukla K. 2019. A comparative study of one parameter lifetime distributions. *Biomet Biostat Int J*, 8(4): 111-123. DOI: 10.15406/bbij.2019.08.00280.
- Sreenivas P, Kumar S. 2015. A review on non-traditional optimization algorithm for simultaneous scheduling problems. *J Mech Civil Eng*, 12(2): 50-53. DOI: 10.9790/1684-12225053.
- Tadikamalla P, Johnson N. 1982. Systems of frequency curves generated by transformations of logistic variables. *Biometrika*, 69(2): 461-465. DOI: 10.1093/biomet/69.2.461.
- Tadikamalla P. 1980. A look at the Burr and related distributions. *Int Stat Rev*, 337-344. DOI: 10.2307/1402945.
- Yan Z, Wang S, Liu B, Li X. 2018. Application of whale optimization algorithm in optimal allocation of water resources. *E3S Web of Conferences*, 53: 04019. EDP Sciences. DOI: 10.1051/e3sconf/20185304019.
- Yuan K, Schuster C. 2013. Overview of statistical estimation methods. *The Oxford handbook of quantitative methods*. Oxford, UK. DOI: 10.1093/oxfordhb/9780199934874.013.0018.
- Zea L, Silva R, Bourguignon M, Santos A, Cordeiro G. 2012. The beta exponentiated Pareto distribution with application to bladder cancer susceptibility. *Int J Stat Probab*, 1(2): 8. DOI: 10.5539/ijsp.v1n2p8.



FARKLI ÖZELLİKLERİ VE ÖZEL YÖNLERİ İLE BİR BİTKİ HORMONLARI GRUBU: STRİGOLAKTONLAR

Özge DURMAZ^{1*}, Alper DURMAZ¹, Erdi Can AYTAR², Yasemin ÖZDENER KÖMPE¹

¹Ondokuz Mayıs University, Faculty of Science, Department of Biology, 55200 Samsun, Türkiye

²Uşak University, Faculty of Agriculture, Department of Horticulture, 64000, Uşak, Türkiye

Özet: Çok hücreli bir bitkinin yapısal değişimi ve fonksiyonu, organizmayı oluşturan hücreler arasındaki ilişkiye bağlıdır. Yüksek bitkilerde morfogenez, büyüme, metabolizmanın koordinasyonu ve düzenlenmesi, bitkinin bir kısmından diğer kısmına taşınan sinyal molekülleri ile sağlanmaktadır. Bitkiler, çeşitli sinyal molekülleri tarafından büyük ölçüde düzenlenen fizyolojik ve gelişimsel değişiklikler yoluyla çevresel tepkilere yanıt verir. Bu moleküller bitki büyüme düzenleyicileridir. Bitki büyüme düzenleyicileri, organizmalarda doğal olarak sentezlenen, büyüme ile buna bağlı diğer fizyolojik faaliyetleri kontrol eden ve sentezlendiği yerden diğer kısımlara taşıyıp, etkinliğini orada ve çok düşük konsantrasyonlarda gösteren organik maddelerdir. Yapılan çalışmalarla bitkilerde belirli işlevleri gerçekleştiren ve birbirleri ile etkileşim halinde olan birçok bitki büyüme düzenleyicileri belirlenmiştir. Strigolaktonlar da bitki yapısının kontrolünde önemli sinyaller olarak ortaya çıkan bitki büyüme düzenleyicilerinin yeni bir sınıfıdır. Strigolaktonlar, Orobanchaceae familyası türlerinde, tohum çimlenmesini uyarabilme yeteneğine sahipken, diğer birçok familyada da nodülasyonu arttırdığı düşünülmektedir. Nitekim, strigolaktonların moleküler yapısı, strigolaktonların görevleri, strigolaktonların bitki tarafından üretilmesi ve strigolaktonların diğer hormonlarla etkileşimleri konuları bu hormon grubunun daha iyi anlaşılmasını sağlayacaktır.

Anahtar kelimeler: Bitki büyüme düzenleyicileri, Tohum çimlenmesi, Fungus-bitki ilişkisi, Hormon yapısı

A Class of Plant hormones with Different Properties and Special Aspects: Strigolactones

Abstract: The structural change and function of a multicellular plant depend on the relationship between the cells of the organism. At the present, it is known that in high plants, the coordination and regulation of morphogenesis, growth and metabolism are provided by signals transmitted from one part of the plant to another. These signalling molecules are called hormones. Hormones are natural substances that are produced within an organism and play a significant role in regulating growth and other related physiological activities. They are transported to various parts of the organism from where they are synthesized, exerting their effects even at very low concentrations. Through various studies, researchers have identified specific hormones in plants that carry out specific functions and interact with each other. Strigolactone is also a new class of plant hormones that emerges as important signals in the control of plant structure. Strigolactones have the ability to stimulate seed germination in the Orobanchaceae family species, while it is thought to increase nodulation in many other families. Indeed, delving into topics such as the molecular structure of strigolactones, their functions, their biosynthesis within plants, and their interactions with other hormones will greatly contribute to a better comprehension of this group of hormones.

Keywords: Plant growth regulators, Seed germination, Fungus-plant relationship, Hormone structure

*Sorumlu yazar (Corresponding author): Ondokuz Mayıs Üniversitesi, Fen Fakültesi, Biyoloji Bölümü, 55200 Samsun, Türkiye

E mail: ozgebilici0811@gmail.com (Ö. DURMAZ)

Özge DURMAZ



<https://orcid.org/0000-0003-1180-0022>

Alper DURMAZ



<https://orcid.org/0000-0001-6927-3283>

Erdi Can AYTAR



<https://orcid.org/0000-0001-6045-0183>

Yasemin ÖZDENER KÖMPE



<https://orcid.org/0000-0003-1649-4298>

Gönderi: 05 Mayıs 2023

Kabul: 14 Ağustos 2023

Yayınlanma: 01 Ekim 2023

Received: May 05, 2023

Accepted: August 14, 2023

Published: October 01, 2023

Cite as: Durmaz Ö, Durmaz A, Aytar EC, Özden K. 2023. A class of plant hormones with different properties and special aspects: strigolactones. BSJ Eng Sci, 6(4): 648-657.

1. Giriş

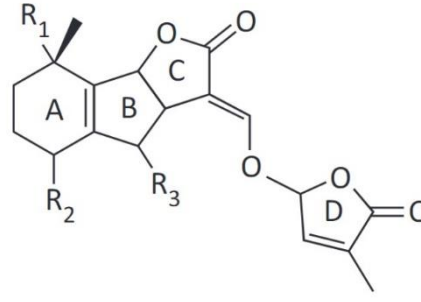
Başlangıçta parazitik bitkiler için tohum çimlenme uyarıcıları olarak kabul edilen strigolaktonlar, şimdi sürgün dallanması ve kök sistemi yapısı dahil olmak üzere bitki gelişiminin birçok yönünü etkileyen önemli endojen fitohormonlar olarak kabul edilmektedir (Wang ve ark., 2022). Orobanchaceae familyası türlerinin çoğu diğer bitkiler üzerinde parazit olarak yaşamaktadır (Smith, 2014). Strigolaktonlar, parazit bir bitki olan *Striga* spp. dahil Orobanchaceae familyasındaki kök paraziti bitkilerin tohumlarının çimlenmesini uyarabilme yeteneklerine sahiptir (Xie ve ark., 2010).

Strigolaktonların ilk defa tespit edilmesi; *Striga lutea* nın çimlenme stimülantı olarak pamuk köklerinden 1966 yılında saflaştırılmış ve kimyasal yapısı 1972 yılında tanımlanmıştır (Cook ve ark., 1966). Afrikada, bu yabancı otlar (*Striga* sp.) hiçbir uyarıcı olmadan rastgele ortaya çıktıkları ve ürünlere zarar verdikleri için çiftçiler tarafından "Cadı Otu" şeklinde adlandırılmıştır. Ayrıca, strigolaktonlar rizosferde arbusküler mikorizal funguslarla (AMF) bitki simbiyozu için sinyal molekülleri olarak görev alırlar (Besserer ve ark., 2006).



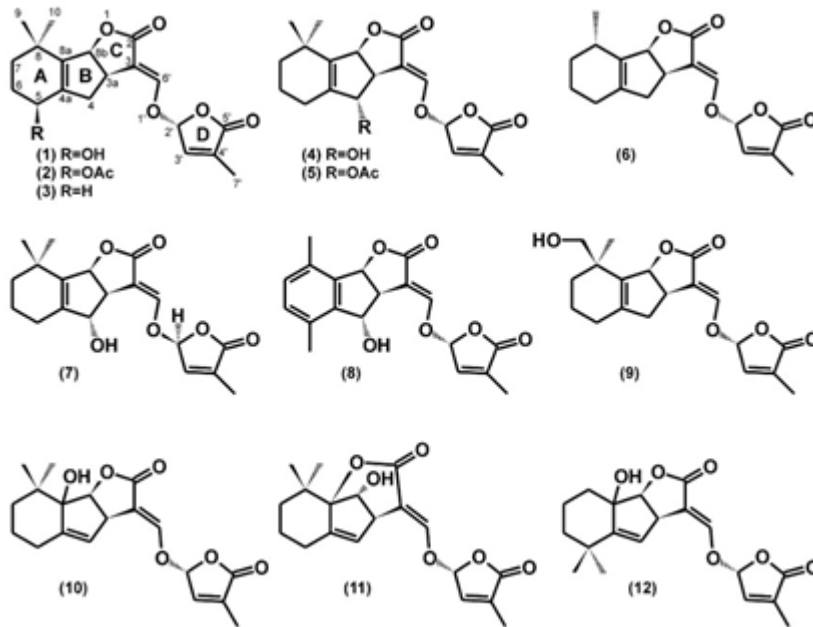
2. Strigolaktonların Moleküler Yapısı

Strigolaktonlar tipik lakton halkası içerir. Doğal strigolaktonlar, bir butenolid D-halkasına enol-eter köprüsü ile bağlanan trisiklik ABC lakton halka sisteminden oluşan çekirdeğe sahip karmaşık yapılardan oluşurlar (Zwanenburg ve Blanco-Ania, 2018). Strigolakton ailesinin üyeleri, çekirdek yapının kimyasal modifikasyonlarında ve stereokimyasal konformasyonlarında farklılık arz eder. Stereokimya, strigolaktona atfedilen biyolojik özelliklerinde çok önemli bir rol oynar (Scaffidi ve ark., 2013). Bu nedenle, Strigol ve Orobanchol, sırasıyla A ve B halkalarının oksitlendiği ve C halkasına göre B halkasının stereokimyasının farklı olduğu iki yaygın örnektir (Smith, 2014). B/C bağlantısının farklı yönelimine bağlı olarak doğal olarak oluşan strigolaktonlar Strigol ve Orobanchol olarak iki gruba ayrılabilir (Waters ve ark., 2017). Bunlar her zaman bir enol eter birimi vasıtasıyla bir butenolid halkasına (D-halkası) bağlanan üç halkalı yapı, ABC iskeleti içerir (Zwanenburg ve Pospíšil, 2013) (Şekil 1).



Şekil 1. Strigolaktonların genel yapısı (Ruyter-Spira ve ark., 2013)

5- deoksistrigol'den türevlenen birçok strigolakton vardır (Xie ve ark., 2010; Zwanenburg ve Pospíšil, 2013) (Şekil 2). Yapısal ve biyokimyasal olarak, şimdiye kadar yüksek bitkilerde belirlenen karotenoidler arasında muhtemel substrat adayı, 9 (Z) -β-karoten dir. Biyosentetik yollarda AB halkaları oksidasyon ve epoksidasyon, demetilasyon, dekarboksilasyon, protonasyon, hidroksilasyon, epoksidasyon, asetoksilasyon ile doğal Strigolaktonların mevcut olan yapısal çeşitliliğine yol açar (Al-Babili ve Bouwmeester, 2015). Sonuçta oluşan ara maddeler 5-deoksistrigol oluşmasını ve ardışık reaksiyonlarla strigolaktonların çeşitlerinin meydana gelmesini sağlar (Rani ve ark., 2008).



Şekil 2. Strigolaktonların yapısı: strigol (1), strigil asetat (2), 5-deoksistrigol (3), orobanchol (4), orobanchil asetat (5), sorgolakton (6), 20-epi-orobanchol (7), solanakol (8) ve sorgomol (9). Daha sonra orobanchil asetat olarak gösterilen alectrol için üç yapı (10,11,12) önerilmiştir (Rani ve ark., 2008).

Strigolaktonlar, kimyasal yapıları ve stereokimyası bakımından bitkiler arasında çeşitlilik gösterir. Yapısal çeşitlilikleri, trisiklik lakton halka kısmındaki yüksek düzeyde yapısal plastisitenin bir sonucu olarak, çok sayıda kiral karbonun ortaya çıkması, stereokimyasal

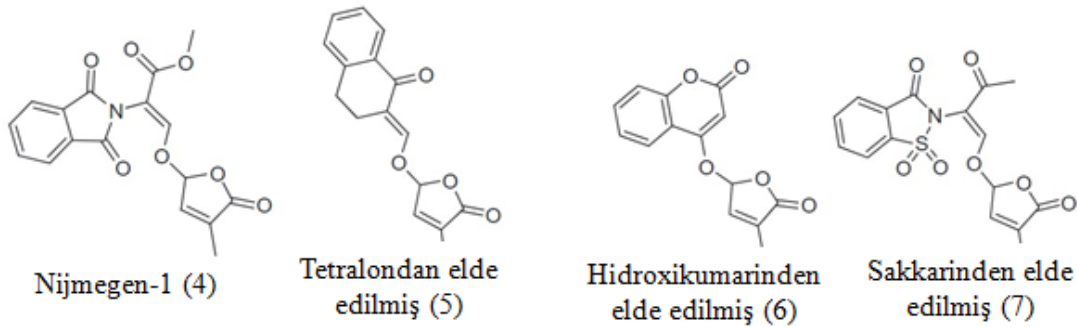
çeşitliliğinden sorumludur (Seto ve ark., 2014). Strigolaktonlar, trisiklik lakton halkasının varlığına/yokluğuna ve kimyasal yapısına göre gruplandırılır. Tam ABC halkasına sahip olanlar kanonik olarak adlandırılırken carlactone ve türevlerinde

görüldüğü gibi tam ABC halkasına sahip olmayanlar kanonik olmayan strigolaktonlar olarak adlandırılır (Waters ve ark., 2017). Bu çeşitliliklerin, strigolakton biyoaktiviteleri ve fonksiyonel özgüllük üzerinde önemli bir etkiye sahip olduğu gösterilmiştir (Boyer ve ark., 2012; Waters ve ark., 2017).

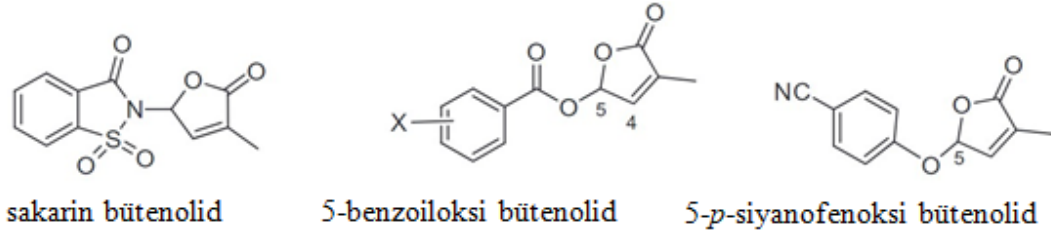
Strigolaktonların hem tarım hem de biyotıp alanlarında var olan potansiyeli düşünüldüğünde ve doğal Strigolaktonların mikromolar konsantrasyonda üretilmesi göz önüne alındığında, var olan potansiyellerinden yararlanmak için sentetik Strigolakton ürünlerinin elde edilmesi gerektiği kaçınılmaz bir gerçektir. Bu sentetik Strigolaktonların temel biyoaktivitesi, esas olarak D-halkasının varlığına bağlıdır (Boyer ve ark., 2012).

Pratik uygulama için bu doğal Strigolaktonlar çok karmaşık bir yapıya sahiptir ve bu nedenle, Strigolakton analogları daha basit bir yapı ile temel biyoaktiviteyi

muhafaza ederek geliştirilmiştir (Zwanenburg ve Pospíšil, 2013). Strigolakton analoglarının örnekleri, Nijmegen-1 (Nefkens ve ark., 1997) ve tetralondan türetilen analoglar (Mwakaboko ve Zwanenburg, 2011), hidroksi kumarin (Mwakaboko ve Zwanenburg, 2011) ve sakarindir (Nefkens ve ark., 1997). Strigolaktonun en çok bilinen analogu GR24'tür (Şekil 3) (Zwanenburg ve ark., 2013). Yeni keşfedilen Strigolakton taklitçileri ise sadece C-5'de uygun bir ayrılma grubu olan D-halkasına sahiptirler (Şekil 4). Strigolakton taklitçileri ve analogları arasında da büyük farklılıklar vardır. Analog Nijmegen-1 (4) (Şekil 3, 1 numaralı kimyasal) 'te butenolid halkasına fazladan bir metil grubu eklendiğinde çimlenme aktivitesi neredeyse etkilenmezken, taklit örneklerinde ekstra bir metil, aktivite kaybına neden olur. Davranıştaki bu farklılık, analogların ve taklitçilerin, farklı reseptör alanlarına sahip olduklarını kuvvetle göstermektedir (Zwanenburg ve ark., 2013).



Şekil 3. Analog GR24 ve yeni tasarlanmış Strigolakton analogları (Zwanenburg ve ark., 2013).



Şekil 4. Strigolakton taklitçileri (Zwanenburg ve ark., 2013).

3. Strigolaktonların Görevleri

Strigolaktonlar; sinyal molekülleri olarak ele alındığında oldukça ilginçtir; çünkü endojen bir hormon olarak bitki içinde ve kök hücre sinyali olarak da toprağın içinde hareket eder (Umehara ve ark., 2008). Birçok bitki türünde nitrat ve fosfor, strigolakton üretiminin düzenlemesini etkiler. Nitekim strigolaktonlar çevresel uyarılara karşı verilen yanıtların düzenleyicileri arasında da yer alır. Özellikle, besin maddesi kullanılabilirliği üzerine olan etkisi, strigolaktonlara karşı duyulan ilginin artmasına neden olmuştur (Yoneyama ve ark., 2012). Arbusküler mikoriza ve parazit yabancı otların etkileşimlerinin daha iyi belirlenmesi için yapılan çalışmalardan, tesadüfen strigolaktonlar ile ilgili sonuçlar elde edilmiştir. Strigolaktonların nodülasyonda, sürgün dallanmasında, ikincil büyümede ve kök büyümesinde önemli rollerinin olduğu ortaya çıkarılmıştır (Foo ve ark., 2013).

3.1 Kök ve Sürgün Dallanması

Bütün organizmalarda üniform bir büyüme ve yaşamın sürdürülebilmesi için ince ayarlanmış homeostazi vardır. Bitkiler de, canlılar arasında bu durum için bir istisna değildir. Bitki, sınırlı hareket kabiliyeti içinde faaliyet göstermek zorundadır ve pluripotent meristemler yoluyla yüksek bir esneklik seviyesine adapte olmuştur. Bir bitki içindeki tüm meristemlerin aktivitesi, çevresel koşullara yanıt olarak büyümeyi optimize etmek için sıkı bir şekilde koordine edilmektedir. Taşınabilen sinyaller (bitki büyüme düzenleyicileri -hormonlar), kontrollü ve sistematik gelişme ve büyüme için bitkilerde çok miktarda bulunur (Brewer ve ark., 2013).

2008'de yapılan çalışmalarda, köklerden sürgüne nakledilen önceden tanımlanmamış bir kimyasal sinyalin, ikincil sürgünlerin büyümesini bastırdığı fark edilmiş ve bu kimyasal sinyalin strigolakton olduğu düşünülmüştür (Shindo ve ark., 2018). Gözlemler sonucunda strigolakton

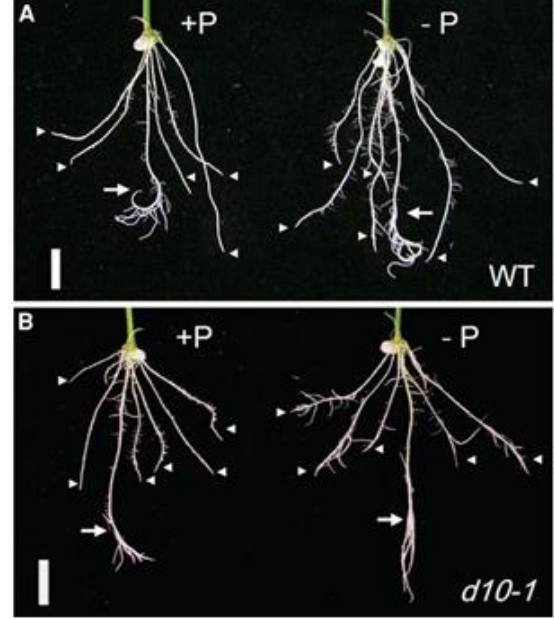
üretmeyen bitki mutantlarının birçok ikincil filiz ürettiği görülmüştür. Bunlara strigolakton sentetiği olan GR24 uygulayarak büyümeleri baskı altına alınmıştır. Daha sonra, strigolaktonların kökün sekonder kalınlaşmasına neden olduğu ve yan köklerin ve kök tüylerinin oluşumunu teşvik ettiği bulunmuştur. Elde edilen sonuçlar strigolaktonlar için kanıt olarak kabul edilir. (Brewer ve ark., 2013) (Şekil 5).



Şekil 5. d10-1 ve d14-1 mutantlarının fenotipi. A) 6 haftalık yabani tip bitkinin genel yapısı ve d10-1 ve d14-1 mutant bitkileri. B) Anaç d10-1, d14-1 mutantları ve WT bitkilerine ait anaçlarının kök görüntüleri. Ölçek çubuğu 10 cm (Arite ve ark., 2012).

Fosfor ve nitrat gibi toprak besin elementleri; kök ve sürgünlerin uzaması ve dallanmasında rol oynarlar. Bu nedenle bitkilerin gelişimleri üzerinde oldukça etkilidirler (S. M. Smith ve Waters, 2012). Strigolakton üretiminin topraktaki besin maddesi sınırlamasına yanıt olarak arttığı fark edildiğinde önemi daha da netlik kazanmaktadır. Strigolaktonların bu tür etkileri, kök sisteminin sürgün sistemine göre daha fazla büyümesine neden olur. (S. M. Smith, 2014). Besin eksikliği, köklerde daha fazla dallanmayı sağlarken sürgünlerde

dallanmanın azalmasını tetikler. Böylece köklerin potansiyellerini artırarak daha fazla besin elde etmesini sağlamış, sürgünlerin ise besin ihtiyacını azaltmış olur (S. M. Smith ve Waters, 2012). Tersine, mineral besin maddeleri bol olduğu zaman strigolakton üretimi düşer ve sürgünlere daha düşük miktarda taşınır. Buna bağlı olarak yeni ikincil filizler oluşur. Sonuçta bitki; güneş enerjisini ve atmosferdeki karbon dioksiti yakalamak için kapasitesini artıracak şekilde büyür (Şekil 6) (S. M. Smith, 2014). Ayrıca, son çalışmalar fotosentetik glikozun, pirinç bitkilerinde Strigolakton yolunu ve sürgün dallanmasını etkilediğini, sirkadiyen ritimlerin entegratörünü kontrol ettiğini ortaya koymuştur (Yoneyama ve Brewer, 2021)



Şekil 6. Fosfat eksikliği bitkilerin sürgün çoğalmasını engellerken, strigolakton varlığında ise sekonder köklerin sayısını ve uzamasını artırır (P içeren ortamda (600 μ M P, solda) ve P yokluğunda (sağda) büyütülen on dört günlük WT= yabani tip ve d10-1 mutant fideleri. (Arite ve ark., 2012).

3.2 Bitki ve Arbüsküler Mikorizal Fungusların Simbiyotik Yaşam Oluşturması

AMF zorunlu simbiyotlardır ve yaşam döngülerini tamamlamak için bitkileri konukçu olarak kullanırlar (Requena ve ark., 2007). AMF, en az 460 milyon yıl önce olduğu varsayılan Glomeromycota kökenli toprak canlılarıdır. Glomeromycota fungusları sürekli olarak yaşam içerisinde Angiosperm, Gymnosperm, Pteridofit ve bazı Bryofitlerin kökleri ile ortaklık içerisinde (J. E. Smith, 2009).

Strigolaktonların ilk önce endojen hormonlardan ziyade rizosfer sinyalleri olarak evrimleştiği öne sürülmüştür (Walker ve ark., 2019). Son veriler, *Marchantia paleacea*'da yeni tanımlanmış bir strigolakton olan biryosimbiol'ün büyüme ve gen ekspresyonu için gerekli olmadığını ancak AMF simbiyozu için gerekli olduğunu göstermektedir (Kodama ve ark., 2022). Simbiyoz esnasında, AMF konukçu bitkisinden karbonhidratları

alır ve karşılığında bitkiler funguslardan su ve mineral maddeleri (özellikle fosfor ve azot) elde eder (López-Ráez ve ark., 2011). Simbiyoz hem bitkinin besleme durumunu iyileştirir hem de stresli koşullara karşı daha dayanıklı olmasını sağlar (Parniske, 2008). Kimyasal iş birliği, iki canlı arasında herhangi bir temas gerçekleşmeden önce rhizosferde başlar. Strigolaktonlar hem bitki tepkilerini kontrol etmek için dahili sinyaller olarak hem de karşılıklılığı indüklemek için dışsal sinyaller olarak işlev görür. İki farklı canlı arasında bağlantı kurmanın en önemli nedeni inorganik besindir. Bitkiler besin mevcudiyetine, özellikle fosfata yanıt verir. Fosfat strigolakton üretimi ve eksüdasyonunu düzenler. Fosfat açlığı strigolakton üretimini önemli ölçüde artırırken, fosfat yeterliliği mikotropik bitkilerde bunu bastırır (Yoneyama, 2019). AMF simbiyozu, konukçu bitkiler tarafından inorganik besinlerin özellikle fosfatın alınmasında çok önemli roller oynadığından, bitkiler AMF simbiyozunu teşvik etmek için strigolakton salgısını artırır. Strigolaktonlar, bitki kökleri tarafından toprağa salındıktan sonra konak tespit sinyalleri olarak hareket ederek, AMF metabolizmalarını ve hif dallanmasını uyarırlar (Parniske, 2008).

Toprak içerisinde aseksüel sporlar hif üretir ve bitki köklerini kolonize eder. Bir appressorium vasıtasıyla kök yüzeyine hiflerin eklenmesinden sonra fungus kortekse nüfuz eder ve morfolojik olarak özel yapılar oluşturur. Strigolaktonların özellikle besin eksikliği durumunda AMF ile bitki arasındaki simbiyozu arttırdığı görülmüştür. Özellikle azot açlığı ise sorgum, mısır ve marul gibi bazı bitki türlerinde strigolakton üretimini ve eksüdasyonu artırır. Bu da bu bitkilerin nitrojen temini için AMF'ye bağlı olduğunu düşündürür (Yoneyama, 2019). Pirinçte sülfat eksikliği de strigolakton üretimini teşvik eder (Shindo ve ark., 2018). Fosfat eksikliği tüm strigolakton biyosentez genlerinin ekspresyonunu artırır (Yoneyama ve ark., 2020). Ancak sülfat eksikliğinde sadece D27 kuvvetli bir şekilde eksprese edilir, bu da D27'nin AMF simbiyozu yoluyla etkili kükürt kazanımında önemli bir rol oynayabileceğini düşündürür (Shindo ve ark., 2018).

Bitkilerin, değişen miktarlarda farklı strigolakton karışımları ürettiği bilinmektedir. Bunlar bitkinin gelişim aşaması ve ortam faktörlerinden etkilenmektedir (Al-Babili ve Bouwmeester, 2015). Bitki-mikoendofit simbiyotik birlikteliklerin, konukçunun gelişim aşaması ve ortam faktörlerinden önemli ölçüde etkilendiği göz önüne alındığında (Walters ve ark., 2008), gelişim aşamaları esnasında konak geçişi gerçekleşirken ve/veya abiyotik stres gibi değişen çevresel koşullar nedeniyle doku ve organların strigolakton çeşidindeki değişiklikler, mikoendofitik yaşam tarzlarını modüle etmek için bilgi kaynağı olarak kullanılabilirler (Jia ve ark., 2016).

Doku/organ tercihi veya özgülüğü, mikoendofitlerin sergilediği belirgin bir özelliktir (Qi ve ark., 2012). Örneğin, Qi ve ark., (2012) konukçu bitki materyallerinin yaşının mikoendofit çeşitliliğinin önemli bir belirleyicisi olmasına rağmen, doku tipinin

mikoendofit topluluğunu belirgin şekilde etkilediğini bulmuştur. Bu özelliğin bir önemi, mikoendofitlerin sınıflandırılmasında önemli bir faktör olabilir (Bamisile ve ark., 2018). Organ ve doku özgülüğü için önemli bir açıklama, bitki dokularının karakteristiği olan çeşitli fizyolojik koşullara mikoendofitik adaptasyondur. Benzer şekilde, belirli dokular, endofitleri etkileyen benzersiz bir dizi seçici baskı sağlar. Bu nedenle farklı mantar topluluğu, her doku tipine özgü karakteristik mikoendofit topluluklarının oluşumuna yol açan farklı dokularda baskındır. Strigolaktonlar, dokular ve organlar arasında çeşitli fizyolojik koşulların oluşmasına katkıda bulunabilir. Örneğin, strigolaktonlar, oksin taşınmasını ve ilişkili fizyolojik süreçleri kontrol eder. Bu durum bitki-mikoendofit etkileşimlerini de içerebilir. Çünkü oksinin, mikoendofit etkileşimini ve konak kolonizasyonunu kolaylaştırmak için kullanıldığı görülmüştür (Waqas ve ark., 2012).

Ayrıca, bitkiler içinde, strigolaktonların kökten sürgüne taşınmasının strigolaktonun yapısına ve stereokimyasına özgü olduğu gösterilmiştir (Waters ve ark., 2017). Bu aynı bitkinin farklı dokuları içinde yapısal veya stereokimyasal olarak farklı strigolaktonların birikmesine izin verir. Yukarıdakiler dikkate alındığında ve şu anda sadece AMF lerde doğrulanmış olmasına rağmen, fungus tepkilerinin farklı strigolakton moleküllerine göre değişiklik gösterdiği gerçeği ile strigolaktonların, mikoendofit dokusunu, organ tercihini ve özgülüğünü doğrudan etkileyerek bitki-mikoendofit etkileşimlerinin kurulmasında önemli bir rol oynaması mümkündür (Besserer ve ark., 2006; Tang ve Chu, 2020).

Strigolaktonların, simbiyoz oluştuktan sonra konukçu bitki içindeki seviyelerinin düzenlenmesinin öncelikleri vardır. López-Ráez ve ark., (2011) yılında strigolakton miktarının azalmasını domates ile yapmış oldukları bir çalışmada ortaya koymuşlardır. AMF simbiyozu ile strigolaktonların azaltılması ilk kez analitik olarak sıvı kromatografi-tandem kütle spektrometresi (LC-MS / MS) ile gösterilmiştir. Bu çalışmada *Glomus mosseae* (BEG12) ve *Glomus intraradices* (BEG 121) kullanılarak domates köklerinden elde edilen kök eksudatlarının *Phelipanche ramosa* tohumlarını çimlendirme yüzdesi kontrol edilmiştir. Sonuçta çimlenme miktarının yaklaşık %50 daha düşük olduğu görülmüştür (López-Ráez ve ark., 2011).

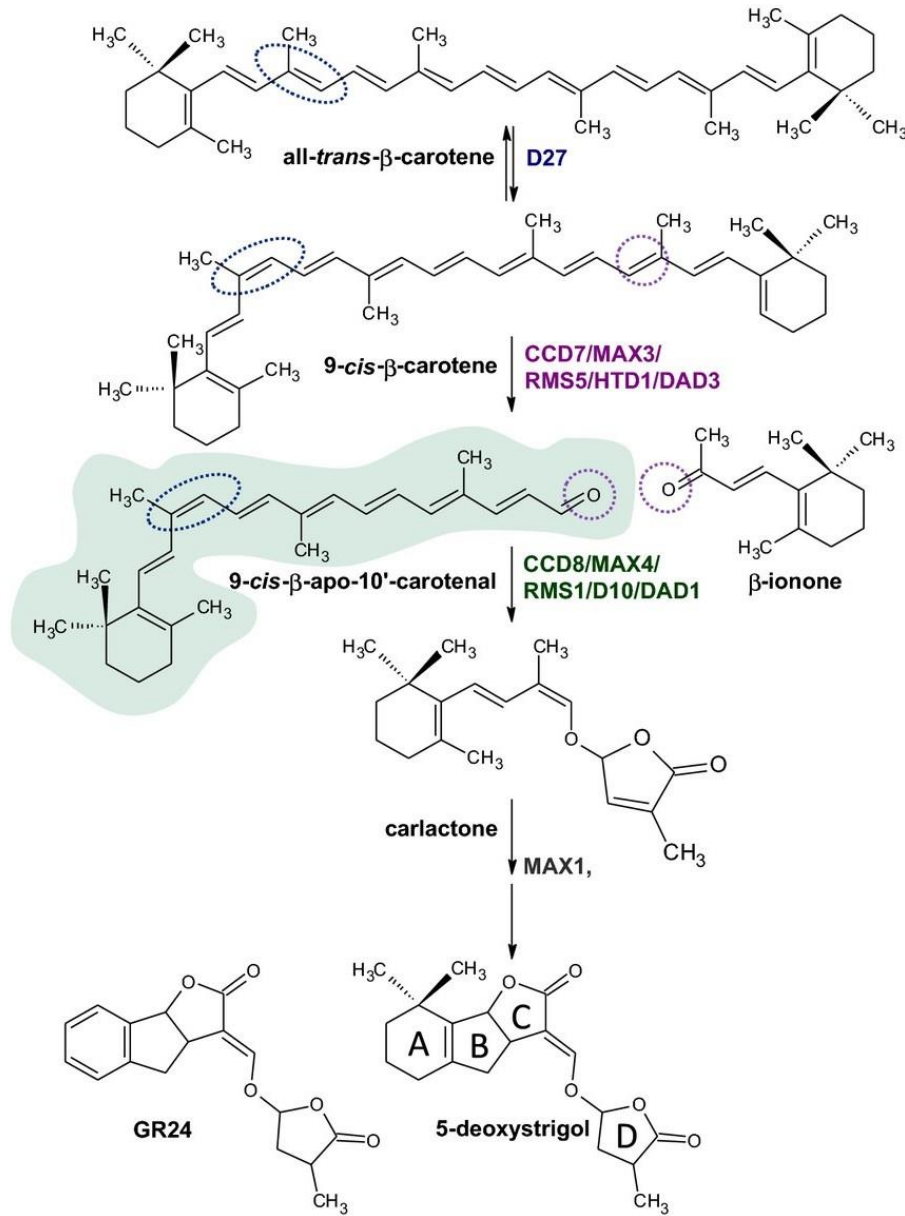
3.3 Nodülasyon Oluşumu

Rizosfer sinyali olan flavonoidler nodülasyon oluşumunu düşürür. Flavonoidlerin tersine sentetik strigolaktonların direk *Pisum sativum* ve *Medicago sativa* ya spesifik rizobiyal hücre kültürü şeklinde uygulanması büyümeyi arttırmazken nod faktörü üretimini ve kalsiyum artışını uyarmıştır (Soto ve ark., 2010). Mutantlarla yapılan son çalışmalar, strigolakton eksikliği bulunan bitkilerde nodül oluşumunun daha düşük olduğunu göstermiştir. Bu nedenle endojen strigolaktonların nodülasyonu arttırması gerektiği düşünülmüştür (Foo ve Davies, 2011).

3.4. Strigolaktonların Bitki Tarafından Üretilmesi

Strigolaktonlar karotenoidlerden oluşur ve bunlar terpenler veya izoprenler denilen yapı taşlarından yapılıdır. Bu nedenle karotenoidler ve dolayısıyla strigolaktonlar terpenoidler veya izoprenoitler olarak tanımlanabilir (Alder ve ark., 2012). Karotenoidler, muzda, havuç köklerinde ve domatesde gördüğümüz sarı, turuncu ve kırmızı renklerinin oluşmasını sağlar. Aynı zamanda ışık enerjisini absorbe etmek, fotosentezde kilit rol oynamak ve bitkiyi oksidatif hasara karşı korumak da dahil olmak üzere önemli işlevleri vardır (S. M. Smith, 2014). Bilinen tüm strigolaktonların türetildiği bitkilerde β -karoten biyosentezinin siyanobakteri kaynaklı olduğu bildirilmektedir (Sandmann, 2002). Strigolaktonların biyosentezinden sorumlu genler olan D27, CCD7, CCD8 hücre çekirdek DNA'sında kodlanmaktadır. Ancak, protein ürünleri plastidlerde görev yapar. Plastidlerle

ilişkili fonksiyonlar, hücre çekirdeğindeki genlerden genellikle siyanobakterilerin/plastidlerin atalarından türediği için (Gould ve ark., 2008; Timmis ve ark., 2004) D27/D27 benzeri, CCD7 ve CCD8 için bu gen ailelerinin erken siyanobakteriyel/plastidyal kökene sahip oldukları filogenetik analizlerle gösterilmiştir. Bitkilerdeki gen aileleri muhtemelen hücre içi gen transferi (IGT) yoluyla oluşmuş olabilir. Son çalışmalar, strigolaktonların çekirdek genler ve biyosentez yolunun ilk olarak angiospermlerde tanımlandığı gösterilirken, neredeyse tüm bitkilerde hatta bazı yeşil alglerde de bu biyosentez yolu ve çekirdek genlerin bulunduğu belirlenmiştir (Bonhomme ve Guillory, 2022; Kodama ve ark., 2022; Walker ve ark., 2019). Strigolaktonların biyosentetik yolunda, karlakton adı verilen β -karoteni bir laktona dönüştüren üç kloroplast enzimi içerdiği gösterilmiştir (Şekil 7)



Şekil 7. All-trans- β -karotenin öncü olarak kullanılarak strigolakton çeşitlerinin oluşmasını sağlayan 5-deoksistrigol'un sentez yolu. D27, CCD7 ve CCD8 tarafından katalize edilen moleküler yeniden düzenlemeler sırasıyla mavi, mor ve yeşil renkte vurgulanır. 5-Deoksistrigol'nin dört halkası A-D olarak adlandırılır (Waldie ve ark., 2014).

Yakın zamana kadar, seskiterpen laktonları olarak karakterize olmalarına rağmen, strigolaktonların biyosentetik kökeni bilinmemekteydi (Bouwmeester ve ark., 2003). Mısır (*Zea mays*) karotenoid mutantları ve mısır, kara fasulye (*Vigna unguiculata*) ve sorgum (*Sorghum bicolor*) bitkilerinde izoprenoid yollarının inhibitörleri kullanılarak, *Striga hermonthica* ve *Orobanche crenata*'nın kök salgısıyla tetiklenen çimlenmesi üzerinde etkilerini değerlendirdikleri çalışmalarında, bu üç konuk bitki türü ile iki parazit bitki türünde strigolakton çimlenme uyarıcılarının strigolaktonların seskiterpen formları olmadığını, bunların apokarotenoid olduğunu göstermiştir (López-Ráez ve ark., 2011). Bu keşfi takiben, karotenoid öncülünden bilinen tüm strigolaktonların oluşturulması için bir biyogenetik şema önerilmiştir (Matusova ve ark., 2005).

3.5. Strigolaktonların Diğer Hormonlarla Etkileşimleri

Oksinin miktarı, sürgün ucunun aktivitesiyle orantılıdır. Sürgünün altındaki dokulara büyüme durumu hakkında bilgi verir ve yanal büyüme hakkında karar vermesine izin verir (Li ve Bangerth, 1999). Oksinin, aksiller tomurcuk büyümesini engellemek ve kök büyümesini teşvik etmek için sürgünün tepe kısmından basipetal olarak taşınır. Birbirine antagonist çalışan strigolakton ve sitokininler, oksininin tomurcuk oluşumunu baskılayabilmesi veya etkisinin kırılması için ikincil haberci etkisi gösterirler. Strigolaktonlar tomurcuk büyümesini (Gomez-Roldan ve ark., 2008) ve sitokininler tomurcuk büyümesini teşvik eder ve her ikisi de tersine oksinin tarafından regüle edilir (Dun ve ark., 2013). Aksiller sürgün büyümesi, nitrata yanıt olarak köklerde üretilen ve karbonhidrat miktarına göre değişiklik gösteren sitokininler tarafından desteklenmektedir. Oksinin ve Strigolaktonlar, gövdelerde ve köklerde sekonder kalınlaşmayı teşvik etmek için birbirleri ile uyumlu bir etkileşime girer (Agusti ve ark., 2011). Böylece hem kök hem de filizden yayılan ve kaynak besin durumunu, apikal meristem aktivitesini bildiren sinyaller, hâkim olan koşullara göre bitki yapısını ve kaynak dağılımını ayarlamak amacıyla birlikte hareket eder.

Wang ve ark., (2013) yılında yapmış oldukları çalışmaların son gözlemleri, strigolakton ve brasinosteroid sinyalleme arasındaki potansiyel etkileşimleri göstermektedir (Y. Wang ve ark., 2013). Bu çalışmada, BES1'in MAX2 ile etkileşime girdiğini ve strigolakton-yanıt veren gen ifadesini düzenlemek için MAX2'nin substratı olarak işlev gördüğünü belirlenmiştir. Ayrıca, strigolakton ve brasinosteroid sinyal yollarının, aynı transkripsiyon faktörü olan BES1'i farklı şekillerde düzenlediği belirlenmiştir. Nitekim brasinosteroidler doğrudan kök dallanmasını etkilemese de BES1'in strigolaktona bağımlı tahrip edilmesi, potansiyel olarak brasinosteroid sinyalini zayıflatılabilir ve kök dallanması üzerinde bir kontrol mekanizması olarak işlev görebilir (Nakamura ve ark., 2013).

3.6. Biyomedikal Uygulamalar

Çeşitli bitki türevli biyoaktif bileşiklerin kanser hücresi büyümesini ve hayatta kalmasını engellediği gösterilmiştir (Fridlender ve ark., 2015). Strigolaktonların antiproliferatif aktivitesine ilişkin 2012'deki ilk raporda, strigolaktonların hücre replikasyonlarını bloke ederek bitkilerde sürgün dallanmasını engellediği gözlenmiştir. Bu ilk verilere dayanarak altı sentetik Strigolakton analogu göğüs kanseri hücre hattında test edilmiş ve meme kanseri hücrelerinin proliferasyonunu inhibe edebildiği ve Kanser hücrelerinin apoptozisini indükleyebildiği ve aynı zamanda 'kanseri olmayan' hatlar üzerinde çok daha az etkili olduğu rapor edilmiştir (Pollock ve ark., 2012). Daha sonra yapılan çalışmada, aynı strigolakton analoglarının prostat, kolon, akciğer, melanom, osteosarkom ve lösemi hücre hatları dahil olmak üzere katı ve katı olmayan kanser hücrelerini temsil eden bir dizi kanserden türetilmiş hücre hatlarının büyümesini ve hayatta kalmasını engellediği gösterilmiştir (Pollock ve ark., 2014).

Kanserle ilgili çalışmaların yanı sıra, daha yakın zamanda doğal Strigolaktonların ve analoglarının diğer biyomedikal alanlarda potansiyel aktiviteye sahip olduğu gösterilmiştir (Modi ve ark., 2018).

Alzheimer hastalığındaki nöropatolojik değişiklikler, beyindeki erken inflamatuvar mikro çevre ile doğrudan bağlantılıdır. Yakın tarihli bir çalışmada, strigolakton analog GR24 ya bir rasemik karışım olarak ya da saf enantiyomerler olarak SIM-A9 mikroglial hücre hattında fenotipik tarama aracında kullanılmış ve nöroinflamatuvarın baskılanmasında dikkate değer bir güç gösterildiği tespit edilmiştir (Kurt ve ark., 2020).

4. Sonuçlar ve Tartışma

Gittikçe artış gösteren dünya nüfusu için tarım ürünlerinin yeterli gelmediği bilinen bir gerçektir. Bu durum mevcut tarım ürünlerindeki kayıpların engellenmesini zorunlu kılmaktadır. Tarım ürünlerinde kullanılan azotlu gübrelerin zaman içinde tükenmesi ve mevcut bitkisel ürünleri koruma ve geliştirme yöntemlerinin yetersiz kalacağı göz önüne alındığında alternatif yolların geliştirilmesi zorunlu hale gelmiştir. Strigolaktonlar ileri için bitkisel üretim koruma ve tıbbi alanlar gibi daha birçok alanda alternatif yol olma olasılığı taşımaktadır. Bu nedenle nispeten yeni ortaya çıkmış olan bu hormonlar üzerine daha ileri araştırmalar yapılarak, yapıları ve muhtemel kullanım alanları detaylıca incelenmelidir.

Katkı Oranı Beyanı

Yazar(lar)ın katkı yüzdesi aşağıda verilmiştir. Tüm yazarlar makaleyi incelemiş ve onaylamıştır.

| | Ö.D. | A.D. | E.C.A | Y.Ö.K. |
|-----|------|------|-------|--------|
| K | 40 | 10 | 20 | 30 |
| T | 60 | 10 | 10 | 20 |
| Y | 70 | 10 | 10 | 10 |
| VTI | 70 | 10 | 10 | 10 |
| VAY | 70 | 10 | 10 | 10 |
| KT | 40 | 20 | 20 | 20 |
| YZ | 40 | 20 | 20 | 20 |
| KI | 40 | 20 | 20 | 20 |
| GR | 40 | 20 | 20 | 20 |

K= kavram, T= tasarım, Y= yönetim, VTI= veri toplama ve/veya işleme, VAY= veri analizi ve/veya yorumlama, KT= kaynak tarama, YZ= Yazım, KI= kritik inceleme, GR= gönderim ve revizyon.

Çalışma Beyanı

Yazarlar bu çalışmada hiçbir çıkar ilişkisi olmadığını beyan etmektedirler.

Kaynaklar

Agusti J, Herold S, Schwarz M, Sanchez P, Ljung K, Dun EA, Brewer PB, Beveridge CA, Sieberer T, Sehr E. M, Greb T. 2011. Strigolactone signaling is required for auxin-dependent stimulation of secondary growth in plants. *National Acad Sci United States of America*, 108(50): 20242-20247.

Al-Babili S, Bouwmeester HJ. 2015. Strigolactones a novel carotenoid-derived plant hormone. *Annu Rev Plant Biol*, 66: 161-186.

Alder A, Jamil M, Marzorati M, Bruno M, Vermathen M, Bigler P, Ghisla S, Bouwmeester H, Beyer P, Al-Babili S. 2012. The path from β -carotene to carlactone a strigolactone-like plant hormone. *Science* 335(6074): 1348-1351. <https://doi.org/10.1126/SCIENCE.1218094>.

Arite T, Kameoka H, Kyojuka J. 2012. Strigolactone positively controls crown root elongation in rice. *J Plant Growth Regul*, 31(2): 165-172. <https://doi.org/10.1007/S00344-011-9228-6/FIGURES/5>.

Bamisile BS, Dash CK, Akutse KS, Keppanan R, Wang L. 2018. Fungal endophytes: Beyond herbivore management. *Front Microbiology* 9(MAR): 544. <https://doi.org/10.3389/FMICB.2018.00544/BIBTEX>.

Bessener A, Puech-Pagès V, Kiefer P, Gomez-Roldan V, Jauneau A, Roy S, Portais JC, Roux C, Bécard G, Séjalon-Delmas N. 2006. Strigolactones stimulate arbuscular mycorrhizal fungi by activating mitochondria. *PLOS Biol*, 4(7): e226. <https://doi.org/10.1371/J.PBIO.0040226>.

Bonhomme S, Guillory A. 2022. Synthesis and signalling of strigolactone and KAI2-ligand signals in bryophytes. *J Experimental Botany*, 73(13): 4487-4495. <https://doi.org/10.1093/XB/ERAC186>.

Bouwmeester HJ, Matusova R, Zhongkui S, Beale MH. 2003. Secondary metabolite signalling in host-parasitic plant interactions. *Current Opinion Plant Biol*, 6(4): 358-364. [https://doi.org/10.1016/S1369-5266\(03\)00065-7](https://doi.org/10.1016/S1369-5266(03)00065-7).

Boyer FD, Germain A, de Saint Pillot JP, Pouvreau JB, Chen VX, Ramos S, Stévenin A, Simier P, Delavault P, Beau JM, Rameau C. 2012. Structure-Activity relationship studies of strigolactone-

related molecules for branching inhibition in garden pea: molecule design for shoot branching. *Plant Physiol*, 159(4): 1524-1544. <https://doi.org/10.1104/PP.112.195826>.

Brewer PB, Koltai H, Beveridge CA. 2013. Diverse roles of strigolactones in plant development. *Molec Plant*, 6(1): 18-28. <https://doi.org/10.1093/MP/SSS130>.

Cook CE, Whichard LP, Turner B, Wall M. E, Egle G. H. 1966. Germination of Witchweed (*Striga lutea* Lour.): Isolation and properties of a potent stimulant. *Sci*, 154(3753): 1189-1190. <https://doi.org/10.1126/SCIENCE.154.3753.1189>.

Dun EA, De Saint Germain A, Rameau C, Beveridge CA. 2013. Dynamics of strigolactone function and shoot branching responses in *pisum sativum*. *Molec Plant*, 6(1): 128-140. <https://doi.org/10.1093/MP/SSS131>.

Foo E, Davies NW. 2011. Strigolactones promote nodulation in pea. *Planta* 234(5): 1073-1081. <https://doi.org/10.1007/S00425-011-1516-7/FIGURES/4>.

Foo E, Yoneyama K, Huggill C, Quittenden LJ, Reid JB. 2013. Strigolactones. <https://doi.org/10.4161/psb.23168> 8(3). <https://doi.org/10.4161/PSB.23168>.

Fridlender M, Kapulnik Y, Koltai H. 2015. Plant derived substances with anti-cancer activity: From folklore to practice. *Frontiers in Plant Sci*, 6(OCTOBER): 799. <https://doi.org/10.3389/FPLS.2015.00799/BIBTEX>.

Gomez-Roldan V, Fermas S, Brewer PB, Puech-Pagès V, Dun EA, Pillot JP, Letisse F, Matusova R, Danoun S, Portais JC, Bouwmeester H, Bécard G, Beveridge CA, Rameau C, Rochange SF. 2008. Strigolactone inhibition of shoot branching. *Nature*, 455(7210): 189-194. <https://doi.org/10.1038/nature07271>.

Gould SB, Waller RF, McFadden GI. 2008. Plastid evolution. *Annu Rev Plant Biol*, 59: 491-517.

Jia M, Chen L, Xin HL, Zheng CJ, Rahman K, Han T, Qin LP. 2016. A friendly relationship between endophytic fungi and medicinal plants: A systematic review. *Frontiers in Microbiology* 7(JUN): 906. <https://doi.org/10.3389/FMICB.2016.00906/BIBTEX>.

Kodama K, Rich M. K, Yoda A, Shimazaki S, Xie X, Akiyama K, Mizuno Y, Komatsu A, Luo Y, Suzuki H, Kameoka H, Libourel C, Keller J, Sakakibara K, Nishiyama T, Nakagawa T, Mashiguchi K, Uchida K, Yoneyama K, ... Kyojuka J. 2022. An ancestral function of strigolactones as symbiotic rhizosphere signals. *Nature Commun*, 13(1): 1-15. <https://doi.org/10.1038/s41467-022-31708-3>.

Kurt B, Ozleyen A, Antika G, Yilmaz YB, Tumer TB. 2020. Multitarget profiling of a strigolactone analogue for early events of alzheimer's disease: in vitro therapeutic activities against neuroinflammation. *ACS Chemical Neurosci*, 11(4): 501-507. https://doi.org/10.1021/ACSCHEMNEURO.9B00694/SUPPL_FILE/CN9B00694_SI_001.PDF.

Li CJ, Bangerth F. 1999. Autoinhibition of indoleacetic acid transport in the shoots of two-branched pea (*Pisum sativum*): plants and its relationship to correlative dominance. *Physiologia Plantarum*, 106(4): 415-420. <https://doi.org/10.1034/J.1399-3054.1999.106409.X>.

López-Ráez JA, Charnikhova T, Fernández I, Bouwmeester H, Pozo MJ. 2011. Arbuscular mycorrhizal symbiosis decreases strigolactone production in tomato. *J Plant Physiol*, 168(3): 294-297. <https://doi.org/10.1016/J.JPLPH.2010.08.011>.

Matusova R, Rani K, Verstappen FWA, Franssen MCR, Beale MH, Bouwmeester HJ. 2005. The Strigolactone Germination Stimulants of the Plant-Parasitic *Striga* and *Orobanche* spp. Are Derived from the Carotenoid Pathway. *Plant Physiol*, 139(2): 920-934. <https://doi.org/10.1104/PP.105.061382>.

Modi S, Yaluri N, Kokkola T. 2018. Strigolactone GR24 and pinosylvin attenuate adipogenesis and inflammation of white

- adipocytes. *Biochemical and Biophysical Research Communications* 499(2): 164-169. <https://doi.org/10.1016/J.BBRC.2018.03.095>.
- Mwakaboko AS, Zwanenburg B. 2011. Single step synthesis of strigolactone analogues from cyclic keto enols germination stimulants for seeds of parasitic weeds. *Bioorganic Med Chem*, 19(16): 5006-5011. <https://doi.org/10.1016/J.BMC.2011.06.057>.
- Nakamura H, Xue YL, Miyakawa T, Hou F, Qin HM, Fukui K, Shi X, Ito E, Ito S, Park S. H, Miyauchi Y, Asano A, Totsuka N, Ueda T, Tanokura M, Asami T. 2013. Molecular mechanism of strigolactone perception by DWARF14. *Nature Commun*, 4(1): 1-10. <https://doi.org/10.1038/ncomms3613>.
- Nefkens GHL, Thuring JWJF, Beenackers MFM, Zwanenburg B. 1997. Synthesis of a Phthaloylglycine-Derived Strigolactone Analogue and Its Germination Stimulatory Activity toward Seeds of the Parasitic Weeds *Striga hermonthica* and *Orobancha crenata*. *J Agri Food Chem*, 45(6): 2273-2277. <https://doi.org/10.1021/JF9604504>.
- Parniske M. 2008. Arbuscular mycorrhiza: the mother of plant root endosymbioses. *Nature Reviews Microbiol*, 6(10): 763-775. <https://doi.org/10.1038/nrmicro1987>.
- Pollock CB, Koltai H, Kapulnik Y, Prandi C, Yarden RI. 2012. Strigolactones: A novel class of phytohormones that inhibit the growth and survival of breast cancer cells and breast cancer stem-like enriched mammosphere cells. *Breast Cancer Res Treatment*, 134(3): 1041-1055. <https://doi.org/10.1007/S10549-012-1992-X/FIGURES/11>.
- Pollock CB, McDonough S, Wang VS, Lee H, Ringer L, Li X, Prandi C, Lee RJ, Feldman AS, Koltai H, Kapulnik Y, Rodriguez OC, Schlegel R, Albanese C, Yarden RI. 2014. Strigolactone analogues induce apoptosis through activation of p38 and the stress response pathway in cancer cell lines and in conditionally reprogramed primary prostate cancer cells. *Oncotarget*, 5(6): 1683. <https://doi.org/10.18632/ONCOTARGET.1849>.
- Qi F, Jing T, Zhan Y. 2012. Characterization of endophytic fungi from acer ginnala maxim. in an artificial plantation: media effect and tissue-dependent variation. *PLOS ONE*, 7(10): e46785. <https://doi.org/10.1371/J.PONE.0046785>.
- Rani K, Zwanenburg B, Sugimoto Y, Yoneyama K, Bouwmeester HJ. 2008. Biosynthetic considerations could assist the structure elucidation of host plant produced rhizosphere signalling compounds (strigolactones): for arbuscular mycorrhizal fungi and parasitic plants. *Plant Physiol Biochem*, 46(7): 617-626. <https://doi.org/10.1016/J.PLAPHY.2008.04.012>.
- Requena N, Serrano E, Ocón A, Breuninger M. 2007. Plant signals and fungal perception during arbuscular mycorrhiza establishment. *Phytochem*, 68(1): 33-40. <https://doi.org/10.1016/J.PHYTOCHEM.2006.09.036>.
- Ruyter-Spira C, Al-Babili S, van der Krol S, Bouwmeester H. 2013. The biology of strigolactones. *Trends Plant Sci*, 18(2): 72-83. <https://doi.org/10.1016/J.TPLANTS.2012.10.003>.
- Sandmann G. 2002. Molecular evolution of carotenoid biosynthesis from bacteria to plants. *Physiologia Plantarum*, 116(4): 431-440. <https://doi.org/10.1034/J.1399-3054.2002.1160401.X>.
- Scaffidi A, Waters MT, Ghisalberti EL, Dixon KW, Flematti GR, Smith SM. 2013. Carlactone-independent seedling morphogenesis in *Arabidopsis*. *The Plant J*, 76(1): 1-9. <https://doi.org/10.1111/TPJ.12265>.
- Seto Y, Sado A, Asami K, Hanada A, Umehara M, Akiyama K, Yamaguchi S. 2014. Carlactone is an endogenous biosynthetic precursor for strigolactones. *National Academy Sci United States of America*, 111(4): 1640-1645. https://doi.org/10.1073/PNAS.1314805111/SUPPL_FILE/PNAS.201314805SI.PDF.
- Shindo M, Shimomura K, Yamaguchi S, Umehara M. 2018. Upregulation of DWARF27 is associated with increased strigolactone levels under sulfur deficiency in rice. *Plant Direct*, 2(4): e00050. <https://doi.org/10.1002/PLD3.50>.
- Smith JE. 2009. Mycorrhizal symbiosis. *Soil Sci Soc America J*, 73(2): 694-694. <https://doi.org/10.2136/SSSAJ2008.0015BR>
- Smith SM. 2014. Q&A: What are strigolactones and why are they important to plants and soil microbes? *BMC Biol*, 12(1): 1-7. <https://doi.org/10.1186/1741-7007-12-19/FIGURES/6>.
- Smith SM, Waters M. T. 2012. Strigolactones: Destruction-dependent perception? *Current Biol*, 22(21): R924-R927. <https://doi.org/10.1016/J.CUB.2012.09.016>.
- Soto MJ, Fernández-Aparicio M, Castellanos-Morales V, García-Garrido JM, Ocampo JA, Delgado MJ, Vierheilig H. 2010. First indications for the involvement of strigolactones on nodule formation in alfalfa *Medicago sativa*. *Soil Biol Biochem*, 42(2): 383-385. <https://doi.org/10.1016/J.SOILBIO.2009.11.007>.
- Tang J, Chu C. 2020. Strigolactone signaling: repressor proteins are transcription factors. *Trends Plant Sci*, 25(10): 960-963. <https://doi.org/10.1016/J.TPLANTS.2020.07.002>.
- Timmis JN, Ayliff MA, Huang CY, Martin W. 2004. Endosymbiotic gene transfer: organelle genomes forge eukaryotic chromosomes. *Nature Rev Genet*, 5(2): 123-135. <https://doi.org/10.1038/nrg1271>
- Umehara M, Hanada A, Yoshida S, Akiyama K, Arite T, Takeda-Kamiya N, Magome H, Kamiya Y, Shirasu K, Yoneyama K, Kyoizuka J, Yamaguchi S. 2008. Inhibition of shoot branching by new terpenoid plant hormones. *Nature*, 455(7210): 195-200. <https://doi.org/10.1038/nature07272>.
- Waldie T, McCulloch H, Leyser O. 2014. Strigolactones and the control of plant development: lessons from shoot branching. *The Plant J*, 79(4): 607-622. <https://doi.org/10.1111/TPJ.12488>.
- Walker CH, Siu-Ting K, Taylor A, O'Connell MJ, Bennett T. 2019. Strigolactone synthesis is ancestral in land plants but canonical strigolactone signalling is a flowering plant innovation. *BMC Biol*, 17(1): 70. <https://doi.org/10.1186/S12915-019-0689-6/FIGURES/9>.
- Walters DR, Havis ND, Oxley SJP. 2008. Ramularia collo-cygni: the biology of an emerging pathogen of barley. *FEMS Microbiol Letters*, 279(1): 1-7. <https://doi.org/10.1111/J.1574-6968.2007.00986.X>.
- Wang Q, Smith SM, Huang J. 2022. Origins of strigolactone and karrikin signaling in plants. *Trends Plant Sci*, 27(5): 450-459. <https://doi.org/10.1016/j.tplants.2021.11.009>.
- Wang Y, Sun S, Zhu W, Jia K, Yang H, Wang X. 2013. Strigolactone/MAX2-Induced degradation of brassinosteroid transcriptional effector bes1 regulates shoot branching. *Develop Cell*, 27(6): 681-688. <https://doi.org/10.1016/J.DEVCEL.2013.11.010>.
- Waqas M, Khan AL, Kamran M, Hamayun M, Kang SM, Kim YH, Lee IJ. 2012. Endophytic fungi produce gibberellins and indoleacetic acid and promotes host-plant growth during stress. *Molecules*, 17(9): 10754-10773. <https://doi.org/10.3390/MOLECULES170910754>.
- Waters MT, Gutjahr C, Bennett T, Nelson DC. 2017. Strigolactone signaling and evolution. *Annu Rev Plant Biol*, 68: 291-322.
- Xie X, Yoneyama K, Yoneyama K. 2010. The strigolactone story. *Annu Rev Phytopathol*, 48: 93-117.
- Yoneyama K. 2019. How Do Strigolactones ameliorate nutrient deficiencies in plants? *Cold Spring Harbor Perspect Biol*, 11(8): a034686.

- Yoneyama K, Brewer PB. 2021. Strigolactones how are they synthesized to regulate plant growth and development? *Current Opinion Plant Biol*, 63: 102072. <https://doi.org/10.1016/j.PBI.2021.102072>.
- Yoneyama K, Xie X, Kim H, Il Kisugi T, Nomura T, Sekimoto H, Yokota T, Yoneyama K. 2012. How do nitrogen and phosphorus deficiencies affect strigolactone production and exudation? *Planta*, 235(6): 1197-1207. <https://doi.org/10.1007/S00425-011-1568-8/FIGURES/4>.
- Yoneyama K, Xie X, Nomura T, Yoneyama K. 2020. Do phosphate and cytokinin interact to regulate strigolactone biosynthesis or act independently? *Frontiers Plant Sci*, 11: 438. <https://doi.org/10.3389/FPLS.2020.00438/BIBTEX>.
- Zwanenburg B, Blanco-Ania D. 2018. Strigolactones: new plant hormones in the spotlight. *J Experimental Botany*, 69(9): 2205-2218. <https://doi.org/10.1093/JXB/ERX487>.
- Zwanenburg B, Nayak S. K, Charnikhova TV, Bouwmeester HJ. 2013. New strigolactone mimics: Structure-activity relationship and mode of action as germinating stimulants for parasitic weeds. *Bioorganic Med Chem Letters*, 23(18): 5182-5186. <https://doi.org/10.1016/J.BMCL.2013.07.004>.
- Zwanenburg B, Pospíšil T. 2013. Structure and activity of strigolactones: New plant hormones with a rich future. *Molec Plant* 6(1): 38-62. <https://doi.org/10.1093/MP/SSS141>.



BULUT SERVİSLERİ VE BULUT GÜVENLİĞİ İÇİN ONTOLOJİ TABANLI HİZMET DÜZEYİ SÖZLEŞMELERİ

Sena YAKUT^{1*}, Özgü CAN²

¹Ege University, Institute of Science and Technology, 35100, İzmir, Türkiye

²Ege University, Faculty of Engineering, Computer Engineering, 35100, İzmir, Türkiye

Özet: Bulut bilişim, günümüzdeki en önemli teknolojik gelişim ve dönüşümlerinden biri olarak kabul edilmektedir. Bu teknolojinin gelişmesi ile veri tabanı servislerinin, sunucu ve depolama hizmetlerinin yönetimi ve kullanımı kolaylaşmış ve daha düşük maliyetler ile gerçekleştirilebilir bir hale gelmiştir. Son kullanıcılardan büyük ölçekli işletmelere kadar geniş bir kullanıcı kitlesine sahip olan bulut bilişimin popülerleşmesi bulut güvenliği kaygılarını da beraberinde getirmektedir. Farklı bulut servislerinin farklı hizmet katmanlarını karşılaması, atak yüzeylerinin geleneksel yöntemlerden çok daha fazla olması gibi sebepler, bulut güvenliğinin yönetimini zorlaştırmaktadır. Bulut servislerinin yönetimini ve bulut güvenliğini sağlamak amacı ile, bulut hizmetleri kullanıcılarının ve bulut sağlayıcılarının hizmetlerin güvenlik, kullanılabilirlik, yanıt verme düzeyleri gibi kritik özellikleri garanti eden Hizmet Düzeyi Sözleşmeleri (*Service Level Agreements, SLAs*) bulunur. Bu sözleşmelere uyumluluk ve sözleşme ihlallerin kontrolü üzerine bulut servisleri ve bulut güvenliği için geliştirilen ontoloji yapısı, bulut servisleri ve bulut güvenliği kavramlarının arasındaki ilişkileri tanımlamaktadır. Bu ontolojik tanımlama, SLA'ların daha iyi anlaşılmasını, yönetilmesini ve sürekli kontrol için otomasyonunu sağlamaktadır. Bu çalışmada, bulut servisleri ve bulut güvenliği kapsamında geliştirilen SLA ontolojileri üzerine kapsamlı bir araştırma ve inceleme sunulmaktadır. Gerçekleştirilen çalışma sonucunda, alandaki mevcut durum ve yaklaşımlar incelenerek kullanılan teknolojiler ve gelecek çalışmalara yönelik fırsatlar değerlendirilmektedir.

Anahtar kelimeler: Bulut bilişim, Bulut güvenliği, Ontoloji, Hizmet düzeyi sözleşmesi, Anlamsal ağ


Ontology-Based Service Level Agreements for Cloud Services and Cloud Security


Abstract: Cloud computing is defined as one of the most important technological developments and transformations nowadays. As cloud technology improves, handling and using services like databases, servers, and storage becomes simpler and cheaper. The popularization of cloud computing, which has a wide range of users from end users to large-scale enterprises, also brings cloud security concerns. Different cloud services have the ability to operate across multiple service layers, attack surfaces and scenarios are much more varied than traditional methods. Because of all these, keeping track of cloud security can be hard and complicated. In order to manage cloud services and provide cloud security, cloud users and cloud providers have Service Level Agreements (SLAs) that guarantee critical features of services such as security, availability, and responsiveness levels. Cloud services and cloud security ontology help to be compliant with these documents and control SLA violations by defining the relationships between cloud services and cloud security concepts. This ontological definition enables SLAs to be better understood, managed, and automated for continuous control. In this study, comprehensive research and review on SLA ontologies for cloud services and cloud are presented. As a result of the study, the current situation and approaches in the area are examined. Also, opportunities for future SLA ontology studies are evaluated.

Keywords: Cloud computing, Cloud security, Ontology, Service Level Agreement, Semantic network

*Sorumlu yazar (Corresponding author): Ege University, Institute of Science and Technology, 35100, İzmir, Türkiye

E mail: senayktt@gmail.com (S. YAKUT)

Sena YAKUT  <https://orcid.org/0000-0002-4666-7770>

Özgü CAN  <https://orcid.org/0000-0002-8064-2905>

Gönderi: 06 Haziran 2023

Kabul: 26 Ağustos 2023

Yayınlanma: 15 Ekim 2023

Received: June 06, 2023

Accepted: August 26, 2023

Published: October 15, 2023

Cite as: Yakut S, Can Ö. 2023. Ontology-based service level agreements for cloud services and cloud security. BSJ Eng Sci, 6(4): 658-667.

1. Giriş

Bulut bilişim teknolojisi, 21. yüzyılın en önemli teknolojik gelişimi ve dönüşümlerinden biridir. Temel olarak bulut bilişim, kullanıcılarının internet erişiminin olduğu herhangi bir yerden ve herhangi bir zamanda kaynaklarını kullanabileceği ve diğer kullanıcılarla paylaşabileceği hizmet olarak tanımlanmaktadır. Bulut bilişim teknolojisi ile, kullanıcılar tarafından her yerden erişilebilen, herkesle paylaşılabilen veriler ve uygulamalar oluşturulmakta ve kolayca kullanılmaktadır. Bulut bilişimin popülerleşmesinin temel sebebi,

geleneksel yöntemlere göre birçok kolaylık ve avantaj sağlamasıdır. Bu kolaylıklar, maliyet, hız, küresel ölçeklendirilebilirlik, verimlilik, performans, güvenilirlik (reliability) ve güvenlik olarak listelenmektedir (Avram, 2014).

Bulut bilişimin popülerleşmesi ile, bulut güvenliği de önem kazanmıştır. Bulut güvenliği, bulut tabanlı servislere gerçekleştirilecek olan potansiyel siber saldırılara karşı sistemleri güçlendirmek için alınmış önlemler, oluşturulmuş kurallar bütünü olarak tanımlanmaktadır (Singh ve ark., 2017). Bulut güvenliği



ile ilgili sorumluluklar, bulut sağlayıcısının sorumlulukları ve bulut hizmeti kullanıcılarının sorumlulukları olarak ikiye ayrılmıştır. Bu ayrıma paylaşılan sorumluluk modeli (*shared responsibility model*) adı verilmektedir. Bu modele göre, her iki taraf da sorumluluklarını bilip bulut tabanlı siber saldırılara karşı önlemler ve koruma çözümleri geliştirmekle yükümlüdür.

Hizmet düzeyi sözleşmesi (Service Level Agreement, SLA), bulut hizmetleri sağlayıcısı ve hizmet kullanıcısı arasında hizmetlerin güvenilirlik, kullanılabilirlik ve yanıt verme düzeylerini garanti eden, bir hizmet kesintisi olduğunda kimin yöneteceğini belirten ve belirtilen hizmetlerin düzeyleri karşılanmazsa konuyla ilgili yaptırım süreçlerini açıklayan sözleşmelerdir (Baset, 2012). Güvenlik tabanlı hizmet düzeyi sözleşmesi (*Security Based Service Level Agreement*) ise, bir bulut hizmeti sağlayıcısı ve bulut hizmetleri kullanıcısı arasında bulut hizmetlerinin güvenliği ile ilgili parametrelerin, metriklerin ve standartların tanımlandığı sözleşmelerdir. Bu tanımlamalara ek olarak, güvenlik standartlarına uyulmadığı durumda uygulanacak süreçlerin tanımlamalarını da kapsar. Bazı şirketler ve bulut sağlayıcıları tarafından güvenlik tabanlı SLA, SLA'ların bir parçası olarak belirlenmektedir. Bulut servisleri, bulut güvenliği SLA'nın birlikte düşünülüp, bir arada değerlendirilmesi oldukça önemlidir. Bulut hizmeti kullanıcılarının, sağlayıcılar tarafından paylaşılmış SLA dokümanlarını referans alarak net beklentileri oluşmaktadır. Örneğin, bir bulut hizmeti kullanıcısı, bir güvenlik servisinin her ayın %99,99'luk zaman diliminde sorunsuz şekilde çalışacağından emin olmak isteyecektir. Bulut sağlayıcısı ve bulut hizmeti kullanıcısının arasındaki SLA'lara ek olarak, bulut hizmeti kullanılarak oluşturulmuş bütün uygulamalar ve bu uygulama kullanıcıları arasında da SLA olması kaçınılmazdır.

SLA sözleşmeleri, performans başarısı, servis erişim hızı, hizmet çıktıları, hizmet takibi ve raporlama gibi detaylara sahiptir. Güvenlik tabanlı SLA dokümanlarında ise, bulut hizmetleri kullanılarak oluşturulmuş olan uygulamaların güvenliği, zafiyet yönetimi, güvenlik testleri, statik ve dinamik kod analizi, mimari güvenliği, siber olaylara müdahale ve analiz gibi başlıklara değinilmekte, bu sayede uygulama kullanıcıları da bu SLA'lardan uygulama güvenliği ile ilgili bilgi sahibi olabilmektedir.

SLA'ların bulut servisleri ve bulut güvenliği ile değerlendirilebilmesi için, otomasyon kurulması esastır. Bu gerekliliği karşılayabilmek için geliştirilebilecek ontolojik bir yapı, belirli bir alanda kavramlar ve ilişkileri sistemli bir şekilde tanımlar (Ontology, 2023). SLA'ların geliştirilmesinde ontoloji tabanlı bir yaklaşım, SLA'ların daha iyi anlaşılmasını, yönetilmesini ve SLA'larda tanımlanmış olan her bir denetimin gerçek zamanlı ya da yarı gerçek zamanlı olarak bulut sistemlerine entegrasyonunu sağlamaktadır.

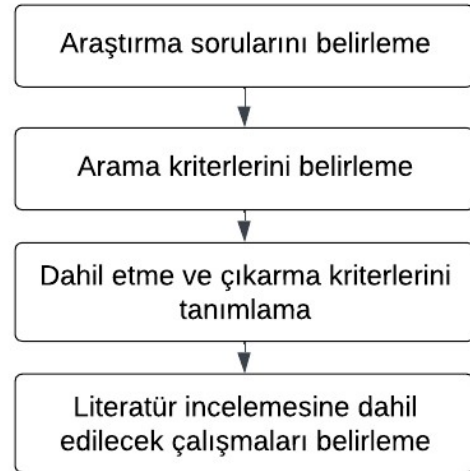
Bulut servisleri ve bulut güvenliği üzerine yapılan SLA ontolojileri ile ilgili çalışmaların araştırılması ve incelenmesi, bu konuda yapılacak olan gelecekteki

çalışmaların kapsamını belirleyecek ve geliştirilecek ontolojilerin hedeflerini net biçimde tanımlayacaktır. Araştırma ve inceleme çalışması, alanın daha iyi anlaşılmasını ve daha etkili güvenlik çözümleri geliştirilmesini sağlar.

Bu çalışmada, bulut servisleri ve bulut güvenliği için SLA ontolojileri oluşturulması üzerine kapsamlı bir araştırma ve inceleme yapılmıştır. Çalışmanın 2. bölümünde yapılan incelemenin yöntemi, araştırma soruları, arama stratejisi ve dahil etme/çıkarma kriterlerinin seçilmesi sağlanmıştır. 3. bölümde literatür incelemesi ile ilgili bulgulara yer verilmiştir. Çalışmanın son bölümü olan 4. bölümünde ise sonuçlar ve çıkarımlar eklenmiş, araştırma sorularına cevapların bulunabilirliği belirlenmiş, konu ile ilgili literatürdeki eksiklikler ve gelecekte yapılabilecek çalışmalar özetlenmiştir.

2. Yöntem

Çalışmada, bulut servisleri ve bulut güvenliği için SLA ontolojileri oluşturulması üzerine kapsamlı bir araştırma ve inceleme sunulmuştur. İnceleme kapsamında, Şekil 1'de gösterilmiş olan sistematik literatür taraması prosedürleri takip edilmiş (Kitchenham, 2004), yazılım mühendisliği alanında yapılması planlanan literatür incelemesi çalışmalarındaki kapsama uyulmuştur (Brereton ve ark., 2007). Bu prosedürler ve kapsam kullanılarak, literatürün tarafsız ve sistematik bir şekilde incelenmesi sağlanmıştır.



Şekil 1. Takip edilen yöntem özeti.

2.1. Araştırma Sorularını Belirleme

Literatürdeki çalışmaları kapsamlı şekilde tanımlama amacı ile, konu ile ilgili aşağıdaki 5 araştırma sorusu belirlenmiştir:

- AS1:Bulut servisleri ve bulut güvenliği SLA'ları için mevcut ontolojiler nelerdir ve hangi kavramları, ilişkileri kapsamaktadır?
- AS2:Bulut servisleri için SLA ontolojileri nasıl oluşturulur?
- AS3:Bulut servisleri için SLA ontolojileri, SLA uyumsuzluklarını belirlemede nasıl bir rol oynar?
- AS4:Bulut güvenliği için SLA ontolojileri, güvenlik

tabanlı SLA uyumsuzluklarını belirlemede nasıl bir rol oynar?

- AS5: Mevcut bulut servisleri ve bulut güvenliği SLA ontolojilerinin sınırlamaları nelerdir ve bu sınırlamaları aşmak için getirilmiş çözümler nelerdir?

Bu araştırma soruları kapsamında gerçekleştirilen sistematik literatür incelemesi, 2 ana başlık altında incelenmiş, elde edilen çalışmalarla ilgili tüm detaylar bu 2 başlık altında toplanmıştır:

- Bulut servisleri için SLA ontolojileri oluşturulması üzerine çalışmalar (AS1, AS2, AS3, AS5)
- Bulut güvenliği için SLA ontolojileri oluşturulması üzerine çalışmalar (AS1, AS4, AS5)

2.2. Arama Kriterlerini Belirleme

Bu çalışmada incelemede kullanılan kaynaklar, Google Scholar, Scopus, IEEE Xplore, ACM, Springer ve ResearchGate gibi elektronik bilgi ortamlarından elde edilmiştir. Seçilmiş olan elektronik bilgi ortamları, konuya dair tüm güncel ve tarafsız literatür çalışmalarını ve detaylarını içerdiğinden tercih edilmiştir. Literatür tarama ve inceleme çalışmalarının tamamı iki aylık süre içerisinde gerçekleştirilmiştir.

Araştırma sorularının belirlenmesinden sonra, bu araştırma sorularına cevap bulunacak şekilde, elektronik bilgi ortamları üzerinde yapılacak olan aramalarda temel

olarak "Cloud", "Cloud Computing", "Cloud Security", "SLA" ve "Security", "Ontology" kelimeleri seçilmiştir. Bu kelimeler ek olarak, araştırma kapsamında faydalı sonuçlar elde edilebilecek olan "Cloud Services Computing", "Service Level Agreement", "Security Based Service Level Agreement", "Cloud Services", "Cyber Security", "Cloud Computing Security" terimleri de aramalara eklenmiştir. Bu aramaları yapabilmek için gerekli olan IEEE Xplore'a ait sorgu örnekleri Tablo 1'de gösterilmiştir. Sorgu örneklerindeki mantıksal yapıya uygun olacak şekilde diğer elektronik bilgi ortamlarında da benzer sorgular kullanılmıştır.

IEEE Xplore, ACM, ResearchGate üzerinde ilgili sorgular kullanılarak yapılan araştırmalardan elde edilmiş çalışmaların toplam sayıları Tablo 2'de belirtilmiştir. Google Scholar ve ResearchGate'ten gelen sayıların çok fazla ilgisiz çalışma içermesi ve Google Scholar'ın diğer kaynakların çalışmalarını da sayı olarak üzerinde barındırması gibi durumlar düşünüldüğünde karışıklık yaratmaması için belirtilmiş olan tabloda çalışma sayılarına yer verilmemiştir. Tabloda bu sayıların eklenmemesine karşılık, sistematik literatür çalışması kapsamında elektronik bilgi kaynağı olarak kullanılmıştır. Elde edilen çalışmalar, kitap bölümü, makale, konferans bildirisi gibi türlerin tamamını içermektedir.

Tablo 1. Literatür aramalarında kullanılan örnek sorgular

| İlgili Çalışmalar | Sorgu Örnekleri |
|--|---|
| Bulut Servisleri ve SLA Ontoloji Odaklı Arama | ("All Metadata":Cloud Computing) AND ("All Metadata":Service Level Agreement) OR ("All Metadata":SLA) AND ("All Metadata":Ontology) |
| Bulut Güvenliği ve SLA Ontolojisi Odaklı Arama | ("All Metadata":Cloud Computing) AND ("All Metadata":Service Level Agreement) OR ("All Metadata":SLA) AND ("All Metadata":Ontology) AND ("All Metadata":Security) AND ("All Metadata":Cloud Security) |

Tablo 2. Elde edilen çalışmaların toplam sayısı

| Bilgi Ortamı | Bulut Servisleri ve SLA Ontoloji Odaklı Arama | Bulut Güvenliği ve SLA Ontolojisi Odaklı Arama | Yayın Yılları Aralığı |
|--------------|---|--|-----------------------|
| IEEE Xplore | 37 | 9 | 2010-2023 |
| ACM | 165 | 137 | 1980-2023 |
| Scopus | 69 | 13 | 2003-2023 |
| Springer | 318 | 236 | 2000-2023 |
| Toplam | 589 | 395 | - |

2.3. Dahil Etme ve Çıkarma Kriterlerinin Belirlenmesi

Yapılmış olan çalışmaların sayısı oldukça çok gibi gözükse de çoğu araştırma soruları ile değerlendirilip filtrelendiğinde kapsam dışı kalmaktadır. Springer ve ACM üzerindeki çalışmaların çoğunun hem eski tarihli hem de konu ile ilişkisiz olduğu görülmüştür. Bu çıkarma kriterine ek olarak, aşağıdaki kriterlere göre yapılacak literatür incelemesinde kullanılacak olan çalışmalar belirlenmiştir:

- Seçilmiş olan çalışmaların yazım dili İngilizce

olmalıdır.

- Seçilmiş olan çalışmalar 2013 yılı ve sonrasını kapsamalıdır. Zaman aralığı olarak son 10 yıl içerisinde yapılan çalışmalar belirlenmiştir. Bu kapsam, bulut bilişim teknolojisinin gelişmekte ve yenilenmekte olan bir teknoloji olması sebebi düşünülmüş olarak oluşturulmuştur.
- Kapsam açık şekilde tanımlanmış olmalı, kapsam dışı ya da daha geniş kapsamlı çalışmalar literatür incelemesine dahil edilmemelidir. Daha önceden belirlenmiş olan bulut servisleri için SLA ontolojileri

oluşturulması üzerine çalışmalar ve bulut güvenliği için SLA ontolojileri oluşturulması üzerine çalışmalar başlıklarını karşılar nitelikte olmalıdır.

2.4. Çalışmaların Seçilmesi

Belirtilmiş olan dahil etme ve çıkarma kriterleri kullanılarak seçilen çalışmalar, kullandıkları yöntemler ve uygulamalar, elde ettikleri sonuçlar ve gelecekte yapılması düşünülen çalışmalar gibi bakış açıları ile değerlendirilmiş ve bu literatür incelemesinde sunulmuştur. Çalışmaların seçilmesinde, dahil etme ve

çıkarma kriterlerinin yanı sıra, içerik olarak yalnızca bulut servisleri ve bulut güvenliği odaklı SLA ontolojisi çalışmaları değerlendirilmiştir. SLA ontolojilerinin oluşturulmadığı ve literatüre herhangi bir yenilik getirmemiş olan çalışmalar, sistematik literatür inceleme kapsamından çıkartılmıştır. Belirlenen çalışmalar bulut servisleri ya da bulut güvenliği odaklı olmak üzere 2 ayrı kategoriye ayrılmıştır. Toplamda kriterlere uygun 10 çalışma belirlenmiştir. Bu çalışmaların listesi Tablo 3'te görülmektedir.

Tablo 3. Seçilen çalışmaların adı, kategorisi ve yayın yılı

| Çalışmanın Adı | Kategori | Yayın Yılı |
|--|------------------------------------|------------|
| * An SLA Ontology to Support Service Discovery in Future Cloud Markets (Modica ve ark., 2013) | Bulut Servisleri, SLA ve Ontoloji | 2013 |
| * Automating Cloud Service Level Agreements using Semantic Technologies (Joshi ve Pearce , 2015) | Bulut Servisleri, SLA ve Ontoloji | 2015 |
| * Ontology of Secure Service Level Agreement (Lee ve ark., 2015a) | Bulut Güvenliği, SLA ve Ontoloji | 2015 |
| * Optimus: A Framework of Vulnerabilities, Attacks, Defenses and SLA Ontologies (Lee ve ark., 2015b) | Bulut Güvenliği, SLA ve Ontoloji | 2015 |
| * Automatic Extraction of Metrics from SLAs for Cloud Service Management (Mittal ve ark., 2016) | Bulut Servisleri, SLA ve Ontoloji | 2016 |
| * CSLAOnto: A Comprehensive Ontological SLA Model in Cloud Computing (Labidi ve ark.,2016) | Bulut Servisleri, SLA ve Ontoloji | 2016 |
| * Cloud SLA Modeling and Monitoring (Labidi ve ark., 2017a) | Bulut Servisleri, SLA ve Ontoloji | 2017 |
| * Ontology-Based SLA Negotiation and re-Negotiation for Cloud Computing (Labidi ve ark., 2017b) | Bulut Servisleri, SLA ve Ontoloji | 2017 |
| * Cloud SLA Terms Analysis Based On Ontology (Labidi ve ark., 2018) | Bulut Servisleri, SLA ve Ontoloji | 2018 |
| * A Semantically Rich Framework to Automate | Bulut Servisleri , SLA ve Ontoloji | 2022 |

3. Bulgular

Bu kısımda, bulut servisleri ve bulut güvenliği için SLA ontolojisi oluşturulması üzerine çalışmalar ve elde edilen bulgular belirtilmiştir.

3.1. Bulut Servisleri için SLA Ontolojileri Oluşturulması Üzerine Çalışmalar

2013 yılında yapılmış olan bulut hizmeti sağlayıcılarının arz ve talep eşleştirmesini desteklemek için anlamsal ontoloji çerçevesi geliştirildiği bu çalışmada (Modica ve ark., 2013), bulut servisleri için SLA ontolojisi geliştirme alanlarına 3 farklı perspektiften bakılmıştır: Bulut sağlayıcısına özgü ontolojiler, bulut kullanıcılarına özgü ontolojiler ve her iki tarafın da kullandığı paylaşılan ontolojiler. Geliştirilen ontoloji "Practical Guide to Cloud Service Level Agreements" (Meegan ve ark., 2012) belgesi örnek alınarak oluşturulmuştur. Bu belge, bulut sağlayıcıları ile bulut kullanıcıları arasındaki deneyimleri birleştirmeyi amaçlar. Çalışma kapsamında, çerçevenin bir prototipi uygulanmış ve test edilmiştir. Uygulama ve test süreçlerinde Pellet teknolojisi (Pellet, 2023) kullanılmıştır. Amazon (AWS SLA, 2023), Rackspace (Rackspace SLA, 2023), GoGrid (GoGrid, 2023) SLA'ları kapsama dahil edilmiştir. Çalışmada 2 ayrı senaryo oluşturulmuş ve bunların analizleri gerçekleştirilmiştir. İlk senaryoda, bulut hizmetleri kullanıcıları bir hizmet

olarak altyapı (*Infrastructure as a Service, IaaS*) servisini (Manvi ve Shyam, 2014) herhangi bir ücret ödmeden kullanmak istedikleri talebini iletir. Bu talep için oluşturulmuş olan ontoloji ve anlamsal çıkarım kuralına göre benzerlik oranı %100 olan servis ismi elde edilmiştir. Bunun yanı sıra, benzerlik oranı daha az olan servislerin çıkarımları da yapılmıştır. İkinci senaryoda ise, bulut hizmetleri kullanıcıları bir veri tabanı ve 3 özelliği SLA kapsamında tanımlanmış bir bulut servisi istenmiştir. Ontolojik çıkarım için, servis olarak yazılım (*Software as a Service, SaaS*) (WeiTek ve ark., 2014), uygulama için database, SLA parametreleri için ise ServiceAvailability, Confidentiality ve DataIntegrity belirlenmiştir. Geliştirilmiş olan ontoloji ve eklenen anlamsal ağ (*semantic web*) kurallarının sonucunda, veri tabanı servisi teklifi olarak oluşturulmuş servis çıktılarının benzerlik oranı en yüksek olanların AmazonRDSReservation ve MSAzureSQLFlat olduğu görülmüştür. Bu iki senaryodan yapılan çıkarımların sonuçları değerlendirildiğinde, geliştirilmiş ontolojinin ve anlamsal ağ kurallarının başarılı olduğu görülmektedir. Çalışmanın gelecek hedefleri olarak, bulut sağlayıcıları ve bulut hizmetleri kullanıcılarına ontolojik yapıya uygun talep ve teklifler oluşturmak için yarı otomatik uygulamalar sağlanacağı belirtilmiştir. Bu

uygulamalar sayesinde talep ve teklifler oluşturulması kolaylaşacaktır.

2015 yılında yapılmış olan diğer bir çalışmanın temel amacı (Joshi ve Pearce, 2015) bulut hizmetleri sağlayıcıları ve kullanıcıları arasında SLA kapsamında olan kontrolleri otomatize hale getirmektir. Bulut bilişim gündün güne popüler hale geldikçe SLA kapsamındaki metrikleri ve kontrolleri manuel şekilde kontrol etmek zorlaşmış, aynı zamanda vakit kaybı haline gelmiştir. Bu sorunu çözmek için geliştirilmiş olan SLA tabanlı ontolojide, bulut sağlayıcılarının SLA ontolojilerini daha zengin bir şekilde tanımlayabildiklerinden anlamsal ağ teknolojisini (*Web Ontology Language, OWL*) kullanmışlardır. Terimler arasındaki ilişkileri ontolojiye eklerken yaşanan temel zorluk, belirli ölçülerin farklı bulut sağlayıcılarında farklı kelimelerle belirtilmiş olmasıdır. Örneğin "availability" kelimesi, başka bir bulut sağlayıcısında "uptime" olarak belirtilmiştir. Bütün bu kapsamlar ve ilişkiler geliştirilmiş olan ontolojiye eklenmiştir. Bunun yanı sıra, bulut sağlayıcılarının SLA kapsamları güncellenip yenilenebilir. Bu güncellemelerin göz önünde bulundurulması için SLA'da yapılan değişikliklerin yeni bir kaynak tanımlama çerçevesi (Resource Description Framework, RDF) grafiği olarak saklanması gerektiğini savunmuşlardır. Bu sayede, herhangi bir bulut hizmeti için bütün SLA kayıtlarına sahip olunabilecek ve SLA takibini ve kullanım planlamasını kolaylaştıracaktır. Çalışmada, yalnızca 4 bulut sağlayıcısının belirli servisler için olan SLA'ları kullanılmıştır. Bunlar, Google for Google Apps (Google SLA., 2023), Microsoft for MS Azure (Azure SLA., 2023), Amazon EC2 (Amazon Compute SLA., 2023) ve Hewlett-Packard (HP SLA., 2023) olarak listelenmiştir. Çalışma ile ilgili gelecekte yapılacak aşamalar olarak, SLA'lara ek olarak gizlilik politikası belgeleri gibi bulut sağlayıcıları tarafından uygulanan gizlilik önlemleri ve denetimlerinin otomasyonu ve ontoloji çıkarımı ile ilgili çalışma yapılması hedeflenmektedir.

2016 yılında yapılmış olan çalışmada ise (Mittal ve ark., 2016), bulut tabanlı servisleri SLA'lar ile yönetmenin en kritik aşamalarından birinin SLA'ları sistemlerin anlayabileceği şekle dönüştürmek olduğundan bahsedilmiştir. SLA'ları sistemlerin anlayabileceği şekle dönüştürerek otomasyon ve düzenli izleme gibi konseptler bulut hizmetleri üzerinde uygulanabilmektedir. Bu motivasyondan yola çıkılarak çalışma kapsamında yazılım metinlerinden oluşan SLA'lar üzerinde metin madenciliği (*text mining*) ve ontoloji geliştirilmesi yapılmıştır. Bu geliştirmenin çıkarım yapan modülünde (*extractor*), SLA tanımlamaları, ilgili metriklerin, performans ölçütlerinin çıkarımı için desen tabanlı kurallar (*pattern based rules*) kullanılmıştır. Bu kurallar Stanford Pos Tagger (Stanford Pos Tagger, 2023) ve CMU Link Parser (Sleator ve Temperley, 1995). Çalışmanın değerlendirme (*assessor*) modülünde ise, bulut odaklı SLA ontolojisi oluşturulmuştur. SLA ontolojisinde, temel sınıflar bütün bulut uygulamalarında ortak olan özelliklerden oluşmaktadır. Örnek olarak

hizmet sağlama, hizmet kullanılabilirliği, veri silinmesi gibi başlıklar düşünülebilir. Çalışmada ontoloji kapsamında RDF, SPARQL gibi anlamsal ağ teknolojileri kullanılmıştır. Çalışma kapsamında, gelecekte yapılacak eklentiler olarak, farklı bulut sağlayıcılarının SLA'ları kullanılarak karşılaştırma ve farklılıkları belirleme yapılması planlanmaktadır. Ayrıca SLA dışında diğer legal belgeler, zorunluluklar ve sözleşmelerden çıkarım yapılması ve ontolojik yapıya dönüştürülmesi amaçlanmaktadır.

2016 yılında geliştirilmiş olan CSLAOnto adlı çerçeve, (Labidi ve ark., 2016), Methontology (Fernández ve ark., 1997) rehber alınarak oluşturulmuştur. Methontology, ontoloji geliştirme süreçlerini yönetmek ve düzenlemek için tasarlanmış bir metodoloji çerçevesi olarak tanımlanır. Bu çerçeveye göre oluşturulacak olan CSLAOnto 4 ana başlıktan oluşmaktadır. İlk başlık olan tanımlama (*spesification*), ontolojinin anlamsal yapısından faydalanılarak SLA'nın temeldeki yapısını iyileştirme hem sistemler hem de bulut sağlayıcıları için anlaşılabilir ve okunabilir bir model elde etmeyi içerir. Ek olarak, ontolojinin çıkarım yeteneklerinden ve çıkarım kurallarının gücünden faydalanılarak SLA ihlallerini otomatik olarak tespit etmeyi amaçlamışlardır. İkinci başlık olan kavramsallaştırma (*conceptualization*) aşamasında, ontoloji kapsamındaki kavramlar tanımlanmıştır. SLA kapsamları incelendiğinde kavramlar 3 ayrı gruba bölünmüştür. Bu gruplar, bağlam, taraflar ve şartlar olarak listelenmiştir. Resmileştirme (*formalization*) bölümünde, anlamsal ağ teknolojileri ve Protégé (Gennaria J. ve ark., 2003) uygulaması kullanılarak ontoloji oluşturulma tamamlanmıştır. Son başlık olan doğrulama (*validation*) aşamasında ise, ontolojinin otomatik olarak ihlalleri belirlemesi için izleme (*monitoring*) kuralları tanımlanması amaçlanmıştır. Ardından, SLA belgesi örneklerinde bu kurallar uygulanmıştır. Çalışma içerisinde daha önceden geliştirilmiş diğer ontolojilerle belirli parametreler üzerinden karşılaştırılmış bir tablo bulunmaktadır. Bu tabloya göre, CSLAOnto, genel olarak yapılmış diğer çalışmalardan daha geniş bir kapsam içerir. Buna ek olarak hizmet ve dağıtım bulutu modellerinin tamamını kapsayacak şekilde geliştirilmiştir. Gelecekte yapılacak olan detaylar kapsamında, geliştirdikleri ontolojinin esnekliğinden faydalanarak bulut üzerindeki servislerin SLA kapsamına uymaması durumunda otomatik düzeltme entegrasyonu yapılması planlanmaktadır.

2017 yılında yapılmış olan bir diğer çalışmada (Labidi ve ark., 2017a) ilk olarak SLA tabanlı izlemenin zorluklarından ve yapılan çalışmanın motivasyonlarından bahsedilmiştir. Her bir bulut sağlayıcısı farklı SLA belgelerine ve farklı izleme politikalarına sahiptir. Bu farklılıklar, belirli kontrollerin ve tanımların farklı şekilde temsil edilmesine yol açmaktadır. Aynı amaçla yazılmış olan bu SLA kontrollerini ve izleme yöntemlerini otomatize etmek, bu farklı temsil etme biçimlerinden dolayı zorlaşmaktadır. Farklı bulut sağlayıcılarının farklı şekilde tanımlanmış ve

yazılmış olan SLA'larına ek olarak, aynı bulut sağlayıcılarının farklı servisleri için tanımlanmış SLA'larda farklılıklar olabilmektedir. Bulut servislerinin yapıları farklıdır, bu sebeple servislerin farklı parametreleri ve farklı hesaplama biçimleri olacaktır. Bu şekildeki farklılıklar, SLA tabanlı izleme ve ihlallerle ilgili aksiyon almanın otomatikleştirilmesini zorlaştırır. Yapılmış olan çalışmada bu sorunları çözmek için ontoloji yapısının kullanılmasının gerekli olduğu vurgulanmaktadır. Ontoloji gerekliliği, 2 sebebe dayanır. Bunlardan ilki, ontoloji kullanıldığında SLA'ların daha okunabilir ve anlaşılabilir olmasıdır. Bir diğer sebep, kurulabilecek ontolojik bir yapıda bilgi çıkarımları (*knowledge extraction*) sayesinde, SLA ihlalleri ve bildirme gibi operasyonlar otomatize şekilde oluşturulmaktadır. Bu sebeplerden yola çıkılarak, bulut SLA'ları kullanarak ontoloji geliştirme ve ihlal durumlarını otomatik bildirme ve aksiyon alma çerçevesi tasarlanmıştır. Yaklaşım, 2 aşamalıdır. İlk aşamada, CSLAMOnto (Labidi ve ark., 2017a) çerçevesi, SLA dokümanlarını ontolojik bir yapıya dönüştürür. Bu dönüşümde OWL teknolojisi kullanılmıştır. Yaklaşımın ikinci aşamasında, oluşturulmuş olan SLA ontolojisi, SLA ihlallerini otomatize şekilde bildirmek için kullanılır. Bunun yapılabilmesi için Anlamsal Ağ Kural Dili (*Semantic Web Rule Language, SWRL*) kullanılmıştır. Yazılacak olan kurallara göre, ihlaller tespit edilip, gerekli aksiyonlar alınır. Yapılmış olan çalışmanın devamında, uygulanabilirliğini kanıtlamak amacı ile uygulanabilirlik kanıtlama (*Proof of Concept, PoC*) gerçekleştirilmiştir. Bu PoC'da, CSLA2M adıyla geliştirilmiş olan çerçeve kullanılmıştır. Bu çerçeve, farklı bulut sağlayıcılarının SLA'larını destekler. Bulut sağlayıcısı kullanıcı tarafında aktifleştirilmesi gereken bu çerçeve, SLA ihlallerini bildirmeye yöneliktir. Çerçevenin kullanılmasında, ilk olarak SLA'nın seçimi sağlanır. Sonrasında, SLA modelinin ontolojisi çerçeve üzerinden oluşturulur. Son olarak SLA'ya bağlı olarak izleme ve ihlal aşaması başlatılır. Burada, erişilebilirlik, hata oranı gibi belirli metriklerin izlenmesi sağlanır. Metriklerle ilgili verilerin toplanması ve çerçeveye gönderilmesi için PoC aşamasında CloudSim çerçevesi kullanılmıştır. CloudSim, bulut bilişim ortamlarını modellemek ve simüle etmek için tasarlanmış bir çerçevedir (CloudSim, 2023). Eklenen SWRL kuralları ile, geliştirilen çerçeve çeşitli hizmetlerin neden olduğu birden çok SLA ihlalinin verimli bir şekilde tespit edilmesini sağlamıştır. Son olarak, konu ile ilgili bir vaka analizi (*case study*) çalışması yapılmıştır. Bu analiz, geliştirilmiş olan SLA ontoloji modelleri ile karşılaştırma amaçlı gerçekleştirilmiştir. Yapılan çalışmada, Amazon EC2, S3 ve Microsoft Azure SLA'ları kullanılmış, rSLA (Mohamed ve ark., 2017) , CSLA (Kouki ve ark., 2012) ,SLAM (Moustafa ve ark., 2015), CSLAMOnto (Labidi T. ve ark., 2017a) ve Ontology-Base Service Monitoring (Dastjerdi ve ark., 2012) çalışmaları karşılaştırılmıştır. Yapılmış olan analizde ilk kriterde, SLA ontoloji modellerini oluşturmak ve kuralları yazmak için geçen süre

karşılaştırılmış ve CSLAMOnto'nun SLA ontolojiyi en kısa sürede oluşturduğu görülmüştür. Ardından, ontoloji kuralları kapsamında, CSLAMOnto'da 20 kural yazılmışken, diğerlerinde ortalama olarak 34 kurala ihtiyaç duyulduğu tespit edilmiştir. Daha fazla kurala ihtiyaç duyulması, diğer ontolojik sistemlerin daha karmaşık bir yapıda olduğunu kanıtlar. Vaka analizinde karşılaştırılan ikinci kriter ise, ihlal tespitindeki başarı oranlarını (*accuracy rate*) karşılaştırmaktır. Bu karşılaştırma sonucunda geliştirilen çerçevenin duyarlılık (*recall*) değerinin %80, kesinlik (*precision*) değerinin %88 olduğu görülmüştür. Duyarlılık ve kesinlik değerleri, diğer çalışmalardan daha fazladır.

Diğer bir çalışmada (Labidi ve ark., 2017b), bulut sağlayıcıları ve bulut kullanıcılarının SLA üzerinde anlaşmasını sağlamak için ontoloji tabanlı müzakere (*negotiation*) ve yeniden müzakere (*re-Negotiation*) yöntemi sunulmuştur. Yönteme dair çalışmalar gerçekleştirilirken, OWL ve SWRL teknolojileri kullanılmıştır. İlk olarak, modelleme aşamasında, bulut sağlayıcıları ve kullanıcıları iki ayrı ontoloji oluşturur. Eşleme (*mapping*) aşamasında, oluşturulmuş olan iki ontoloji arasında eşleştirme yapılır. İki tarafın arasındaki eşlenme sağlandığında, ontoloji oluşturulur. Ontoloji oluşturulma modeli ayrıca Cloud SLA Ontology (Labidi ve ark.,2016) çalışmasında da açıklanmıştır. Ontoloji oluşturulduktan sonra, bulut hizmetlerinde değişiklik algılandığında model otomatik olarak tetiklenmiştir. İlk olarak, SLA detaylarını etkileyebilecek parametreleri içeren bulut hizmeti ontolojisi tanımlanmıştır. Ardından, bulut hizmeti bağlamsal değişiklikleri hakkında akıl yürütme ve gerekirse SLA detaylarını sisteme için çıkarım kuralları oluşturulmuştur.

Geliştirilmiş olan SLA ontolojisi (Labidi ve ark., 2018) ile SLA'nın daha anlaşılabilir olmasını amaçlayan Labidi ve arkadaşları, müşteri isteklerine ve farklılıklarına göre akıl yürütme (*reasoning*) teknikleri kullanarak özelleştirmeyi de hedeflemişlerdir. Bunlara ek olarak, SLA terimlerinden yeni bilgi çıkarımları ile SLA ontoloji analiz süreçlerini iyileştirme, çalışmanın motivasyonları arasındadır. Geliştirilmiş olan ontoloji "Cloud SLA Analyzing Ontology" olarak isimlendirilmiştir. Kısaltması "CSLA2Onto" şeklindedir. Yapılmış olan SLA analizlerinde, SWRL kuralları oluşturularak çıkarımlar yapılması sağlanmıştır. Bu kurallar, zaman içerisinde yaşanabilecek SLA ya da bulut servisleri tabanlı değişikliklere uyum sağlayabilmek ve haberdar olabilmek için oluşturulmuştur. Analiz kısmında toplamda 3 farklı analiz türü belirtilmiştir. İlk model olan dinamik fiyatlandırma modelinde, verilecek olan fiyatlandırma modeli parametresine göre servislere ait fiyatlandırmanın hesaplanması ile ilgili kural eklenmiştir. Fiyatlandırma modelleri "PayAsYouGo", "PayForResource", "Subscription" olarak belirlenmiştir. Her bir model için özel olarak hesaplama kuralları tanımlanmıştır. Geliştirilen ikinci modelde bulut servisleri ile toplam ihlal ve ceza sayıları ile ilgili kural eklenmiştir. Son model olan otomatik SLA sonlandırma

ile ilgili modelde ise SLA'ya uymayan durumlar belirlendiğinde, SLA iptali, SLA sonlanması, kural ihlallerine göre güncelleme isteme gibi durumları otomatize şekilde belirleme amacıyla kural seti oluşturulmuştur. CSLA2Onto'ya ek olarak, "Cloud SLA Analyzing" diğer bir adıyla CSL2A prototipi geliştirilmiştir. Bu geliştirme, SLA analizini otomatikleştirmeyi bir adım öteye taşımaya hedeflemektedir. SLA ayrıştırma, ontolojinin yapısını zenginleştirme ve analiz modülleri bulunmaktadır. Çalışma kapsamında, gelecekte yapılacak olan çalışma olarak, SLA ihlalini otomatik olarak tahmin edip bu tahmine bağlı olarak yönetim süreci oluşturmak hedeflenmektedir.

Anlamsal ağ teknolojileri kullanılarak 2022 yılında yayınlanmış SLA ontoloji çerçevesinde (Ganapathy D. ve Josh K., 2022) , SLA üzerindeki terimler ve aralarındaki ilişkisel yapı oluşturulurken NIST standartlarıyla (NIST, 2023) eşleşecek şekilde geliştirilmiştir. NIST standartlarından, sınıflar ve bahsedilmiş olan terimler arasındaki ilişkisel yapılar temel alınmıştır. Geliştirilmiş olan çerçevede metodoloji şu şekildedir: İlk olarak farklı bulut sağlayıcılarının sahip olduğu farklı SLA'lar kullanılarak metin madenciliği yöntemiyle farklı bileşenlerin çıkarılması sağlanır. Bu bileşenler ontolojik yapı için sınıf, alt sınıf ve ilişkiler olarak tanımlanır. Bu çerçeve kullanılarak farklı sorgular ile farklı kullanıcı ihtiyaçlarına karşılık gelen en uygun bulut servis sağlayıcısı belirlenir. Bu çalışmada eğitim aşaması için kullanılan veri setleri, VMWare Cloud Air (VMWare Cloud Air., 2023) , Amazon Web Services (AWS SLA, 2023), Azure (Azure SLA, 2023), GCP (Google SLA., 2023), IBM Softlayer (IBM SLA, 2023) SLA dokümanları olarak listelenmiştir. Test için ise RackSpace (Rackspace SLA, 2023), SAP (SAP SLA, 2023) , Alibaba (Alibaba SLA, 2023) ve Oracle SLA'ları (Oracle SLA, 2023) kullanılmıştır. Veri setlerinden metin çıkarımı aşamalarında CMU Link Parser ve düzenli ifade (*regular expression*) entegrasyonları yapılmıştır. Çalışma kapsamında oluşturulmuş olan SLA ontoloji çerçevesinin sonuçlarının doğrulanması için katılımcı değerlendirmesi (*actor evaluation*) çalışmasında, ontoloji çıkarımlarının doğruluğunu kontrol etmek için anket çalışması yapılmıştır. Bu anket çalışmasına göre bulut SLA tabanlı 10 tane durum belirlenmiş ve geliştirilen ontolojinin çıkardığı sonuçlar ve çoğunluğun cevapları karşılaştırılmıştır. Bu anket çalışmasının temel amacı, insanların SLA dokümanlarından anlamlandırma ve SLA ontolojisinin yaptığı anlamsal çıkarımları karşılaştırmaktır. Karşılaştırma sonunda %90'lık başarı oranı olduğu görülmüştür. Yalnızca 1 durumda uyumsuzluk olduğu saptanmıştır. Bunun sebebi, durumun karmaşıklığıdır ve ontoloji çerçevesi kapsamında beklenen bir davranıştır. Çalışma kapsamında daha karmaşık bir kural eklenerek bu sorunun üstesinden gelinebileceğini belirtmişlerdir. Gelecekte yapılacak çalışmalar olarak, SLA dokümanlarına ek olarak bulut tabanlı uyumluluk, bulut

servisleri kapsamı ve sorumluluk sigortası gibi raporların ontoloji kapsamına eklenmesi planlanmaktadır. Buna ek olarak, daha karmaşık durumlara karşılık ontolojilerin anlamsal çıkarımlarının doğruluğunu artırma hedeflenmektedir. Yapılmak istenen bu çalışmalarda, veri setlerinin artırılması da amaçlanmaktadır.

Bulut güvenliği için SLA ontolojileri oluşturulması üzerine çalışmalar

Bulut sistemleri üzerinde güvenlik ve gizlilik (*privacy*) prensiplerini uygulamanın zor olduğu ve bulut tabanlı uygulamaların üzerindeki zafiyet sayısı arttıkça yönetimin de zor hale geldiğini vurgulayan bu çalışmada (Lee ve ark., 2015a), güvenlik tabanlı SLA ontolojisi geliştirilmiş ve SSLA olarak kısaltılmıştır. SSLA ontolojisi ile, güvenlik SLA'ları daha kolay anlaşılabilen, bulut hizmeti kullanıcıları ontolojileri karşılaştırarak kullanacağı bulut sağlayıcısına karar verebilmekte ve SLA tabanlı güvenlik izleme hizmetleri daha kolay hale gelmektedir. Bu avantajlar, ontoloji yapısının makine tarafından okunabilir (*machine readable*) ve kolayca entegre edilebilir olmasından kaynaklanmaktadır. Avantajlara ek olarak, geliştirilen çerçeve SSLA'nın uyumluluklar (*compliance*) için belirli düzenlemeleri karşılayıp karşılamadığını belirlemek için bir yöntem sağlar. Çalışmanın tartışma bölümü iki temel başlık altında incelenmiştir:

- **Taraflara faydaları:** Bulut altyapı sağlayıcısı tarafından bakıldığında, garanti edilen güvenlik düzeylerini sunmak ve sunulduğundan emin olmak için geliştirilen çerçeveyi kullanarak geliştirme yapabilir. Bulut servis sağlayıcısı tarafından bakıldığında ise, sağlanan hizmetlerle ilgili uyumluluk sorunlarını anlamak için geliştirilen çerçeveyi kullanabilir.
- **Veri ihlali (*Data Breach*):** Bir veri ihlali meydana geldiğinde, geliştirilmiş olan çerçeveye göre atak yüzeyi ve atağın getirebileceği olası zarar tespiti yapılabilir.

Gelecekte yapılacak çalışmalar olarak, geliştirilen çerçeveye dayalı WS-Anlaşması (*WS-Agreement*) tabanlı WSAG4J5'te SLA'yı SSLA'ya genişletmeyi planlamışlardır. WS-Agreement, SLA oluşturmak ve yönetmek için kullanılır (WSAG4J, 2023). Yapılacak bu geliştirme ile güvenlik tabanlı SLA yönetimi ve izlemesi gibi aksiyonlar otomatikleştirilecektir.

2015 yılında yapılmış diğer bir çalışma, (Lee ve ark., 2015b), "Ontology of Secure Service Level Agreement" çalışması geliştirilerek oluşturulmuştur. Geliştirilmiş olan Optimus çerçevesi, iki bölümden oluşmaktadır: Güvenlik tabanlı SLA ontolojisi ve güvenlik değerlendirmesi (*security assessment*). Güvenlik tabanlı SLA ontolojisi, bulut bilişimin güvenlik alanlarını kapsayan genelleştirilmiş SLA'lar kullanılarak modellenmiştir. Güvenlik değerlendirmesi, güvenlik tabanlı SLA ontolojisinin genişletilerek güvenlik açıkları, saldırılar ve savunma yöntemleri detaylarının eklenmesiyle ontoloji bilgi tabanları (*ontology knowledge bases - OKB*) oluşturulmak amacı ile geliştirilmiştir. Geliştirilen

güvenlik tabanlı SLA ontolojisinde toplam 13 sınıf (*class*) oluşturulmuştur. Bu sınıflardan bazılarının isimleri ve açıklamaları aşağıda belirtilmiştir:

- Networking (Ağ): Ağ yapıları ile ilgili tanımlanan sınıftır. TrafficIsolation, IndividualBandwidth, IPAddressQuantity alt sınıflarına sahiptir.
- Vulnerability (Zafiyet): Bilinen güvenlik açıklarını tespit etme ve çözümleri tanımlar.
- CryptoSpec (Kriptografik Spesifikasyonlar): Bulut sistemleri üzerindeki kriptografik geliştirmelerle ilgili olan sınıftır.
- AccessControl (Erişim Denetimi): Bu sınıf, erişim kimlik doğrulamasını, yetkilendirmeyi, mobil erişim şemaları ve kurallarını tanımlar.
- Compliance (Uyumluluk): Bulut hizmetlerinin, yasaların gerektirdiği şekilde güvenlik ve gizlilik standartları ve uygulamalarıyla uyumlu olduğu onaylanmalıdır. Bu sınıfın ontoloji içinde yer alması gerekliliktir.

Geliştirilen güvenlik değerlendirmesi ise, National Vulnerability Database (NVD), Common Vulnerability Scoring System (CVSS) metrikleri gibi detayların geliştirilmiş SLA ontolojisine eklenmesi ile oluşturulmuştur. Bu sayede güvenlik bilgi tabanları anlamsal olarak modellenmiştir. Güvenlik detaylarının anlamsal yapısı, her bir modeli nasıl temsil etmek istediğimize ve modellerin birbirleriyle nasıl etkileşime girdiğine ilişkin tanımlı verileri eklememize izin verir. Gelecekte yapılacak çalışmalar olarak, ontoloji ve güvenlik değerlendirmesi tabanlı farklı seviyelerde güvenlik yapılandırılmalarına sahip bulut hizmetleri sunmak amacıyla uygulama geliştirileceğini öngörmüştür.

4. Sonuç

Bu çalışmada bulut servisleri ve bulut güvenliği için SLA ontolojileri oluşturulması üzerine sistematik literatür incelemesi yapılmıştır. İlk olarak, yöntem, araştırma soruları, arama stratejisi ve dahil etme ve çıkarma kriterleri belirlenmiş, bu filtrelemelerin sonucunda toplamda 10 farklı çalışma inceleme kapsamına dahil edilmiştir. Çalışmalar seçilirken kapsamı ve araştırılan terimleri tam olarak karşılamasına özellikle dikkat edilmiştir. İnceleme kapsamında çıkarılan sonuçlar aşağıda özetlenmiştir:

- Bulut servisleri için SLA ontolojisi geliştirilme üzerine çalışmaların sayısının, bulut güvenliği için SLA ontolojisi geliştirilme çalışmalarının sayısından fazla olduğu görülmüştür. Gelecek çalışmalar olarak, bulut güvenliği ontolojilerine odaklanması bu çalışma kapsamında önerilmektedir.
- Seçilen çalışmaların geneline bakıldığında, belirli kişilerin bu konularda çalışma yaptığı dikkat çekmektedir. Bulut servisleri ve bulut güvenliği üzerine geliştirilecek SLA ontolojilerinin faydaları düşünüldüğünde, bulut servisleri ya da bulut güvenliği tabanlı teknolojilerle ilgili çalışma yapılacaksa, SLA ontolojisi kapsamına odaklanılabilir.

- Seçilen çalışmaların tamamında, belirli bulut sağlayıcılarının SLA'ları üzerinden yola çıkılmış, bunlara odaklı ontolojiler oluşturulmuştur. Günümüzde, bulut servislerinin kullanılabilirliği, maliyet analizi, dayanıklılığı gibi SLA parametreleri, bulut servislerinin sağladığı servisler tarafından kontrol edilebilmektedir. SLA ontolojisi tarafında eksik olan, bulut servislerini kullanarak uygulama geliştiren şirketlerin kendi SLA'larından ontoloji geliştirme ve güvenlik süreçlerine dahil etme ve otomatikleştirme süreçleridir. Daha önceden yapılmış çalışmalarda belirli bulut sağlayıcılarından yapılan çıkarımlarla oluşturulan ontolojilerin, özelleştirilmiş ve yapı olarak birbirinden farklı olabilecek diğer SLA yapılarını karşılayamayacağı öngörülmektedir. Bu sebeple, gelecek çalışma olarak, herhangi bir SLA dokümanı için otomatikleştirilmiş ontolojik çıkarım çalışmaları ve bunların bulut üzerinde çalışan uygulamaların süreçlerine dahil edilmesi düşünülebilir.

Yapılmış olan literatür çalışmasında, bulut servisleri ve bulut güvenliğine odaklı SLA ontolojileri ile ilgili güncel çalışmalar incelenmiş ve bir bütün olarak sunulmuştur. Daha önceden yapılmış olan çalışmalar incelendiğinde, bu konu ile ilgili bir literatür çalışması bulunmadığı görülmüştür. Bu çalışma ile birlikte, bulut servisleri ve bulut güvenliği tabanlı SLA ontolojilerinin literatürdeki yeri ve gelecekte yapılabilecek olan çalışmalar ile ilgili genel bir çerçeve oluşmuştur. Çalışmanın kapsamı SLA ontolojileri ile sınırlıdır, SLA'ların metin belgeleri olarak düzenlendiği düşünüldüğünde, metinler üzerinde uygulanabilecek doğal dil işleme uygulamalarının SLA'lar ile kullanımı ilgili literatür çalışmaları gelecekte yapılacak olan çalışmalardan biri olarak düşünülebilir.

Katkı Oranı Beyanı

Yazar(lar)ın katkı yüzdesi aşağıda verilmiştir. Tüm yazarlar makaleyi incelemiş ve onaylamıştır.

| | S.Y | Ö.C |
|-----|-----|-----|
| K | 70 | 30 |
| T | 70 | 30 |
| Y | 70 | 30 |
| VTI | 70 | 30 |
| VAY | 70 | 30 |
| KT | 70 | 30 |
| YZ | 80 | 20 |
| KI | 40 | 60 |
| GR | 40 | 60 |

K= kavram, T= tasarım, Y= yönetim, VTI= veri toplama ve/veya işleme, VAY= veri analizi ve/veya yorumlama, KT= kaynak tarama, YZ= Yazım, KI= kritik inceleme, GR= gönderim ve revizyon.

Çalışma Beyanı

Yazarlar bu çalışmada hiçbir çıkar ilişkisi olmadığını beyan etmektedirler.

Kaynaklar

- Alibaba SLA. 2023. Alibaba service level agreements. URL: <https://www.alibabacloud.com/help/en/legal/latest/product-sla>. (accessed date: 23 March, 2023).
- Amazon Web Services (AWS) SLA. 2023. AWS service level agreements (SLAs). URL: <https://aws.amazon.com/legal/service-level-agreements>. (accessed date: 23 March, 2023).
- Amazon Compute SLA. 2023. Amazon compute service level agreement. URL: <https://aws.amazon.com/compute/sla/>. (accessed date: 23 March, 2023).
- Avram MG. 2014. Advantages and challenges of adopting cloud computing from an enterprise perspective. *Procedia Technol*, 12: 529-534
- Azure SLA. 2023. Azure Service Level Agreements. URL: <https://www.azure.cn/en-us/support/legal/sla/>. (accessed date: 23 March, 2023).
- Baset S. 2012. Cloud SLAs: present and future. *ACM SIGOPS Operating Systems Rev*, 46: 57-66.
- Brereton P, Kitchenham A, Budgen D, Turner M, Khalil M. 2007. Lessons from applying the systematic literature review process within the software engineering domain. *Journal of Systems and Software*. Volume 80, 571-583.
- CloudSim. 2023. A framework for modeling and simulation of cloud computing infrastructures and services. URL: <https://github.com/Cloudslab/cloudsim>. (accessed date: 23 March, 2023).
- Dastjerdi A, Tabatabaei S, Buyya R. 2012. A dependency-aware ontology-based approach for deploying service level agreement monitoring services in cloud. *Softw Pract Exper*, 42(4): 501-518.
- Fernández M, Gómez-Pérez A, Juristo N. 1997. Methontology: From ontological art towards ontological engineering. *AAAI Technical Report*, 1997: 33-40
- Ganapathy D, Josh K. 2022. A semantically rich framework to automate cloud service level agreements. *IEEE Transactions on Services Computing*, 2022: 1-12.
- Gennaria J, Musen M, Fergerson R, Grosso W, Crubezy M, Eriksson H, Noy N, Tu S, 2003, The evolution of Protégé: an environment for knowledge-based systems development, *Inter J Human-Computer Stud*, 58(1): 89-123.
- Google SLA. 2023. Google cloud platform service level agreements. URL: <https://cloud.google.com/terms/sla> (accessed date: 23 March, 2023).
- GoGrid. 2023. What is GoGrid? URL: <https://en.wikipedia.org/wiki/GoGrid> (accessed date: 23 March, 2023).
- HP SLA. 2023. HP support service agreement terms & conditions. https://h20345.www2.hp.com/Resources/csndocs/elfpack/A_U_EN/Related%20Documents/Terms_and_conditions.pdf (accessed date: 23 March, 2023).
- IBM SLA. 2023. IBM service level agreements. URL: <https://cloud.ibm.com/docs/overview?topic=overview-slas> (accessed date: 23 March, 2023).
- Joshi K, Pearce C. 2015. Automating cloud service level agreements using semantic technologies. *Proceedings of IEEE International Conference on Cloud Engineering (IC2E)*, March 9-13 2015, Tempe, AZ, USA, pp: 1-6.
- Kitchenham B. 2004. Procedures for performing systematic reviews. Keele University, Technical Report, TR/SE-0401, Newcastle, UK, ISSN:1353-7776, pp: 33.
- Kouki Y, Ledoux T. 2012. CSLA: A language for improving cloud SLA management. *international conference on cloud computing and services science*. URL: <https://www.scitepress.org/papers/2012/39564/39564.pdf> (accessed date: 23 March, 2023).
- Labidi T, Mtibaa A, Brabra H. 2016. CSLAOnto: A comprehensive ontological sla model in cloud computing. *J Data Semant*, 5: 179-193.
- Labidi T, Mtibaa A, Gaaloul W, Tata S, Gargouri F. 2017a. Cloud SLA modeling and monitoring. *Proceedings of IEEE 14th International Conference on Services Computing*, June 25-30, 2017, Honolulu, Hawaii, USA, pp: 338-345. DOI: 10.1109/SCC.2017.50
- Labidi T, Mtibaa A, Gaaloul W, Gargouri F. 2017b. Ontology-Based SLA negotiation and re-negotiation for cloud computing. *Proceedings of IEEE 26th International Conference on Enabling Technologies: Infrastructure for Collaborative Enterprises*, 21-23 June, 2017, Tempe, AZ, USA, pp: 36-41. DOI: 10.1109/WETICE.2017.24
- Labidi T, Mtibaa A, Gargouri F. 2018. Cloud SLA terms analysis based on ontology. *Procedia Comput Sci*, 126: 292-301.
- Lee C, Kavi K, Raymond P, Gomathisankaran M. 2015a. Ontology of secure service level agreement. *Proceedings of 16th International Symposium on High Assurance Systems Engineering*, January 8-10, 2015, Daytona, USA, pp: 166-172. DOI: 10.1109/HASE.2015.33
- Lee C, Kamongi P, Kav K. 2015b. Optimus: A framework of vulnerabilities, attacks, defenses and SLA ontologies. *Inter J Next-Generation Comput*, 6(1): 42-56.
- Manvi S, Shyam G, 2014, Resource Management for Infrastructure as a Service (IaaS) in cloud computing: A survey. *J Network Comput Applicat*, 41: 424-440.
- Meegan J, Singh. G, Woodward, S, Salvatore V, Rak M, Harris D, Murray G, Martino B Di, Roux Le, McDonald J, Kean R, Edwards M, Russell D, Malekkos G, 2012, Practical guide to cloud service level agreements. URL: <https://parsec2.unicampania.it/venticinque/index.php/research/jr-project?view=publication&task=show&id=149> (accessed date: 03 June, 2023).
- Mittal S, Joshi K, Pearce C, Joshi A. 2016. Automatic extraction of metrics from slas for cloud service management. *Proceedings of IEEE International Conference on Cloud Engineering (IC2E)*, April 4-8, 2016, Berlin, Germany, pp: 1-4. DOI: 10.1109/IC2E.2016.14
- Modica G, Petralia G, Tomarchio O. 2013. An SLA ontology to support service discovery in future cloud markets. *Proceedings of 27th International Conference on Advanced Information Networking and Applications Workshops*, March 25-28, 2013, Barcelona, Spain, pp: 1-5. DOI: 10.1109/WAINA.2013.68
- Mohamed M, Anya O, Tata S, Mandagere N, Baracaldo N, Ludwig H. 2017. rSLA: An Approach for Managing Service Level Agreements in Cloud Environments. *Inter J Cooperat Inform Systems*, 26(2): 1742003. DOI: 10.1142/S0218843017420035
- Moustafa S, Elgazzar K, Martin P, Elsayed M. 2015. SLAM: SLA monitoring framework for federated cloud services. *Proceedings of IEEE/ACM 8th International Conference on Utility and Cloud Computing*, December 7-10, 2015, Limassol, Cyprus pp: 1-6. DOI: 10.1109/UCC.2015.90
- NIST. NIST ontological visualization interface for standards: user's guide. URL: <https://nvlpubs.nist.gov/nistpubs/ir/2013/NIST.IR.7945.pdf> / (accessed date: June 03, 2023).
- Ontology. 2023. What is Ontology? URL: <https://en.wikipedia.org/wiki/Ontology> (accessed date: 23 March, 2023).
- Oracle SLA. 2023. Oracle cloud infrastructure service level agreement (SLA). URL:

- <https://www.oracle.com/uk/cloud/sla/> (accessed date: 23 March, 2023).
- SAP SLA. 2023. SAP service level agreement. URL: https://help.sap.com/docs/HANA_SERVICE/319dbc7c518f4f31b7333060d0cc546c/9deb7aea417a4e1886d7845e198fc9b5.html (accessed date: 23 March, 2023).
- Singh A, Chatterjee K, 2017. Cloud security issues and challenges: A survey, *J Network Comput Applicat*, 79: 88-115.
- Sleator D, Temperley D. 1995. Parsing English with a link grammar. URL: <https://arxiv.org/pdf/cmp-lg/9508004.pdf> (accessed date: 23 March, 2023).
- Stanford PoS Tagger. 2023. The Stanford POS Tagger. URL: http://www.linguisticsweb.org/doku.php?id=linguisticsweb:tutorials:automaticannotation:stanford_pos_tagger (accessed date: 23 March, 2023).
- Pellet. 2023. What is pellet? URL: <https://www.w3.org/2001/sw/wiki/Pellet> (accessed date: 23 March, 2023).
- Rackspace SLA. 2023. Rackspace service level agreements. URL: <https://docs.rackspace.com/docs/vm-management/private-cloud/service-level-agreements> (accessed date: 23 March, 2023).
- VMWare Cloud Air. 2023. VMware vCloud air service description. URL: <https://www.vmware.com/files/au/pdf/vcloud-air/vcloud-air-Datasheet.pdf> (accessed date: 23 March, 2023).
- WeiTek T, XiaoYing BAI, Yu H. 2014. Software-as-a-service (SaaS): perspectives and challenges. *Sci China Inform Sci*, 57: 1-15.
- WSAG4J. 2023. Welcome to WSAG4J. URL: <https://wsag4j.sourceforge.net/site/index.html>. (accessed date: 23 March, 2023).